Innovation in Civil Engineering, Architecture and Sustainable Infrastructure

Edited by
Shunbo Zhao and Yi Min Xie

TRANS TECH PUBLICATIONS

Innovation in Civil Engineering, Architecture and Sustainable Infrastructure

Edited by
Shunbo Zhao
Yi Min Xie

Innovation in Civil Engineering, Architecture and Sustainable Infrastructure

Selected, peer reviewed papers from the
International Conference on
Civil Engineering, Architecture and Sustainable Infrastructure
(ICCEASI2012),
September 22-24, 2012, Zhengzhou, China

Edited by

Shunbo Zhao and Yi Min Xie

TTP

Copyright © 2012 Trans Tech Publications Ltd, Switzerland

All rights reserved. No part of the contents of this publication may be reproduced or transmitted in any form or by any means without the written permission of the publisher.

Trans Tech Publications Ltd
Kreuzstrasse 10
CH-8635 Durnten-Zurich
Switzerland
http://www.ttp.net

Volume 238 of
Applied Mechanics and Materials
ISSN print 1660-9336
ISSN cd 1660-9336
ISSN web 1662-7482

Full text available online at *http://www.scientific.net*

***Distributed** worldwide by*

Trans Tech Publications Ltd
Kreuzstrasse 10
CH-8635 Durnten-Zurich
Switzerland

Fax: +41 (44) 922 10 33
e-mail: sales@ttp.net

and in the Americas by

Trans Tech Publications Inc.
PO Box 699, May Street
Enfield, NH 03748
USA

Phone: +1 (603) 632-7377
Fax: +1 (603) 632-5611
e-mail: sales-usa@ttp.net

Preface

The International Conference on Civil Engineering, Architecture and Sustainable Infrastructure (ICCEASI2012) was held on September 22-24, 2012 in Zhengzhou, China. As the rising requirement of environmental and natural resources protection to achieve sustainable development, it brings more opportunities to the activities of civil engineering, architecture, hydraulic engineering and sustainable infrastructure. The aim of ICCEASI2012 is to provide a showcase for recent developments and advancements in these areas, and offer a forum for researchers and engineers in the word to discuss and debate future directions.

This book is a collection of the selected, peer-reviewed papers. All these accepted papers were subjected to strict peer-reviewed at least by 2 expert referees. This book aims to collect the latest development and applications of advanced and sustainable materials, the innovation in civil and hydraulic engineering, the innovation in architecture and building construction, and the innovation in bridge and underground engineering.

This issue was the product of the hard work and dedication of the authors. We would like to express our sincere appreciations to all the authors. We are indebted to all the referees for their constructive comments, time and effort. Thanks are also given to Trans Tech Publications for producing this volume.

Prof. Shunbo Zhao

North China University of Water Resources and Electric Power, China

Prof. Yi Min Xie

RMIT University, Australia

2012 International Conference on Civil Engineering, Architecture and Sustainable Infrastructure (ICCEASI2012)

Organized by

North China University of Water Resources and Electric Power, China
RMIT University, Australia

Co-organized by

Zhengzhou University, China
Wuhan University, China
Dalian University of Technology, China
Changsha University of Science and Technology, China
Fiber Concrete Committee, China Civil Engineering Society
Concrete Specialist Committee, China Association for Engineering Construction Standardization
Henan Civil Engineering and Architecture Society, China
Henan Highway and Transportation Society, China

Conference Organization

Co-chairman

Prof. Dakao Yan, North China University of Water Resources and Electric Power, China
Prof. Jianxin Xu, North China University of Water Resources and Electric Power, China
Prof. Yi Min Xie, RMIT University, Australia
Prof. Shunbo Zhao, North China University of Water Resources and Electric Power, China

International Scientific and Technical Committee

Prof. Chun Qing Li, RMIT University, Australia
Prof. Danying Gao, Zhengzhou University, China
Prof. Dakao Yan, North China University of Water Resources and Electric Power, China
Dr. David W. Law, RMIT University, Australia
Prof. Fengjun Zhou, Chinese Academy of Engineering, China
Prof. Guangqian Wang, Chinese Academy of Science, Tsinghua University, China
Dr. Guo Min Zhang, RMIT University, Australia
Prof. Handong Liu, North China University of Water Resources and Electric Power, China
Prof. Hao Wang, Chinese Academy of Engineering, China
Prof. Huai Chen, Zhengzhou University, China
Dr. Indubhushsan Patnaikuni, RMIT University, Australia
Prof. Jianhua Rong, Changsha University of Science and Technology, China

Prof. Jianxin Xu, North China University of Water Resources and Electric Power, China
Prof. Jitao Yao, Xi'an University of Architecture and Technology, China
Prof. Jinxin Gong, Dalian University of Technology, China
Prof. Qingbin Li, Tsinghua University, China
Prof. Qinghuai Liang, Beijing Jiaotong University, China
Dr. Rebecca Gravina, RMIT University, Australia
Prof. Renda Zhao, Southwest Jiaotong University, China
Prof. Shunbo Zhao, North China University of Water Resources and Electric Power, China
Prof. Songtao Ba, Henan Research Institute of Building Science, China
A/Prof. Sujeeva Setunge, RMIT University, Australia
A/Prof. Thomas Molyneaux, RMIT University, Australia
Prof. Wei Sun, Chinese Academy of Engineering, Southeast University, China
Prof. Weichen Xue, Tongji University, China
Prof. Weiliang Jin, Zhejiang University, China
Prof. Xiangtian Nie, North China University of Water Resources and Electric Power, China
A/Prof. Xueqing Zhang, Hong Kong University of Technology, China
Prof. Yi Min Xie, RMIT University, Australia
Prof. Yiyan Lu, Wuhan University, China
Prof. Yining Ding, Dalian University of Technology, China
Prof. Yongjian Liu, Chang'an University, China
Prof. Zhenmin Zhou, North China University of Water Resources and Electric Power, China
Prof. Zhimin Wu, Dalian University of Technology, China
Prof. Zhiquan Huang, North China University of Water Resources and Electric Power, China
Prof. Zongcai Deng, Beijing University of Technology, China

Organizing Committee

Co-chairs

Prof. Shunbo Zhao, North China University of Water Resources and Electric Power, China
Prof. Yi Min Xie, RMIT University, Australia

Secretary

Prof. Fenglan Li, North China University of Water Resources and Electric Power, China
A/Prof. Fule Han, North China University of Water Resources and Electric Power, China
A/Prof. Changyong Li, North China University of Water Resources and Electric Power, China
A/Prof. Yuping Tong, North China University of Water Resources and Electric Power, China
A/Prof. Fulai Qu, North China University of Water Resources and Electric Power, China
Ms. Xiaoyan Zhang, North China University of Water Resources and Electric Power, China
Ms. Xinxin Ding, North China University of Water Resources and Electric Power, China
Mr. Lixin Liu, North China University of Water Resources and Electric Power, China
Mr. Coffey ML Zhao, RMIT University, Australia

Member

Prof. Mingquan Sun, North China University of Water Resources and Electric Power, China
Prof. Yingbin Kang, North China University of Water Resources and Electric Power, China
Prof. Xiaoke Li, North China University of Water Resources and Electric Power, China
A/Prof. Jianwei Zhang, North China University of Water Resources and Electric Power, China
Dr. Jihao Chen, North China University of Water Resources and Electric Power, China
Dr. Junfeng Guan, North China University of Water Resources and Electric Power, China
Dr. Zhen Chen, North China University of Water Resources and Electric Power, China
Dr. Zhihao Wang, North China University of Water Resources and Electric Power, China
Dr. Xiaodong Huang, RMIT University, Australia
Dr. Shiwei Zhou, RMIT University, Australia
Dr. Zhihao Zuo, RMIT University, Australia

Table of Contents

Preface and Committees

Chapter 1: Advanced and Sustainable Materials

Luffa Sponge as a Sustainable Engineering Material
J.H. Shen, Y.M. Xie, X.D. Huang, S.W. Zhou and D. Ruan 3

Mechanical Properties Research on Concrete Block Doped Nano-TiO_2 under the Conditions of Common Conservation
Z.Y. Deng 9

Axial Compression Behaviors of Concrete Confined by Basalt Fiber Sheets
Z.C. Deng, J. Raphael-Daud and H.B. Xu 13

A Study on Structure and Properties of Basalt Fiber
F.J. Shi 17

Study of Road Property of Basalt Fiber Asphalt Concrete
Y.Z. Chen and Z.X. Li 22

A Review of Stee-Polypropylene Hybrid Fiber Reinforced Concrete
X.K. Li, L. Sun, Y.Y. Zhou and S.B. Zhao 26

Experimental Study on Flexural Toughness of SFRC
C.Y. Li, L.S. Song, L. Sun, C.J. Cao and T. Xing 33

Constitutive Model Based on Damage Mechanics of Fiber Reinforced Concrete (FRC): A Review
D.X. Zhang and Q.Y. Wang 37

Experimental Study on Full Stress-Strain Curve of SFRC in Axial Tension
H.Y. Huo, C.J. Cao, L. Sun, L.S. Song and T. Xing 41

Study on Damage Evolution Mechanism of Concrete under Uniaxial Tension
W.F. Bai, Y. Cui, Q. Wang, J.F. Guan and J.W. Zhang 46

Experimental Research on Sulfate Attack Resistance of Steel Fiber Reinforced Fly Ash Concrete
L. Cui, X.D. Ge and Q.Y. Ma 51

Toughness of ECC Evaluated by Nominal Fracture Energy
S.L. Gao, W. Shao, J.L. Qiao and L. Wang 57

A Review on the Connection of FRP Bars
G.Q. Yuan and N. Zhu 61

A Novel Internal Model Control Method for Non-Square System
L. Quan, H.L. Zhang and Y. Yang 66

Ocean Engineering Concrete Using High-Volume GGBS
K.L. Li 71

Mechanical Behaviors and Chloride Permeability of Rice Husk Ash Concrete
H.L. Wang, Q.W. Peng and X.Y. Sun 75

Square-Shaped $Nd_2Sn_2O_7$ Nanocrystals Prepared by Salt-Assistant Combustion Method
Y.P. Tong, X. Chen, S.B. Zhao and L.D. Lu 79

Safe and Sustainable for the Structural Silicone Sealant in Ultra High-Rise Building Curtains
H.L. Zhang and L. Quan 83

Research on Comprehensive Utilization of the Tail Ore
Y.J. Chen and G. Li 87

Experimental Study on Mechanical Behavior of Concrete Loading along Path (Constant Stress, Constant Strain, Increasing Strain)
Z. Wang, J. Li and R.J. Shang 91

Robust Statistics Analysis of Proficiency Test Result of Cement Chemical Composition
Y. Jia, X.T. Cheng and D. Wei 96

Influence of Sludge Content on Compressive Strength of Sintering Sludge-Shale Bricks
B.B. Huang, X.H. Zhang and J.Z. Zhu 101

Preparation of PZT Material with Different Zi/Ti Ratio by Sol-Gel Method
X. Chen 105

Toughness Properties of Concrete Modified with Water-Borne Polyurethane
B. Ding, X. Zhang, D.L. Zhou and C.W. Miao 109

Soil Stabilizer Prepared with Saline Soil and Industrial Solid Wastes
X.F. Zhang, J. Wang and W. Ni 118

An Improved Method to Calculate the Direction and Weight in Microplane Constitutive Model
M.X. Jia, S.S. Li and W. Xie 121

Experimental Study on Long-Term Exposure of Concrete in Magnesium Sulfate Solution
F.L. Li, X.X. Ding and L.H. Jin 129

Experimental Research on the Influence of Grain Size of Coarse Aggregate on Pebble Concrete Compressive Strength
W. Xie, Y.N. Jin and S.S. Li 133

Basic Mechanics Properties Test of Fly Ash Concrete
W. Xie, H.J. Zhang and S.S. Li 138

Bond-Slip Relation of Plain Steel Bar in Concrete with Machine-Made Sand
S.B. Zhao, X.X. Ding and C.Y. Li 142

Influence of Aggregate Gradation of Coarse Aggregates on Concrete Strength
W. Xie, D.K. Yuan and S.S. Li 147

Influence of Surface Treatment of Testing Specimens on Spacing Factor
M. Kostelecká and J. Kolísko 150

Investigation of Corrosion of Cement-Based Materials by Using of Rotating Disc Method
D. Dobiáš 153

Effect of Silica Fume on Workability and Water Impermeability of Concrete
F.H. Wang and S. Li 157

Effect of Silica Fume on Mechanical Properties and Carbonation Resistance of Concrete
Q.L. Wang and J.C. Bao 161

Effect of Silica Fume on Dry Shrinkage and Freezing-Thawing Durability of Concrete
F. Li and Z.P. Cui 165

A Kind of Simple Method for Mesh Generation of Concrete at Meso Level
J. Wang, L.B. Qing and J.F. Guan 169

Orthogonal Test on Large Content of Solid Waste in Building Binder
H.Q. Liu 173

Numerical Simulation of Bond Properties of Steel Bars in Concrete with Machine-Made Sand
S.B. Zhao, X.X. Ding and S.M. Liu 176

Brief Analysis on Crack of Unbonded Partially Prestressed RPC Beam
Q. Fu, B.F. Lv, X. Cao, L.Z. Jin and N. Deng 181

Experimental Research for Flexibility Properties of RC Beams Strengthened with Steel Wire-Polymer Mortar
C.Y. Zhao, S.M. Huang, Q.L. Yao and Y.J. Chen 185

Calculation Method of Crack Width of Steel Fiber Reinforced High-Strength Concrete Beams under Fatigue Load
D.Y. Gao and M. Zhang 190

Testing Researches on Mixing Proportion of Consolidator-Mixed Pile Composite Foundation
G.Z. Zhang, D.L. Xun, F.Q. Ji and Z. Yang 196

Analysis on Load Stress of Asphalt Pavements with Different Crack States
Y. Wang and Z.F. Liu 201

Chapter 2: Innovation in Civil and Hydraulic Engineering

Research Progress of Diffusion Absorption Refrigeration Technology
X.H. Ren and Y.Y. Tan 209

A Practical Technique for Generating Hexahedral Meshes
X.L. Bai, B. Ma and J.Y. Li 214

Three-Dimensional Two Material Transportation Method Based on the Volume Fractions Interface Algorithm
J.L. Wu, Z.Y. Wu, Y.P. Tong and P.R. Du 218

Numerical Simulation of Rural Brick Buildings Strengthened with CFRP under Flood Actions
Y.J. Liu, X.T. Ma and Y.M. Sun 223

Research of Viscous-Spring Artificial Boundary in Dynamic Analysis
H.Y. Zhang, L.W. Han, Z.T. Tao, L. Yao, S.P. Li and X.D. He 227

Study on Design Method for Scale and Layout of Road Passenger Station
Z.C. Li, Q.X. Sun and S.B. Zhao 231

Variation Rules of Warping Effect with Respect to Parameters of Cylindrical Helical Spring
Y. Hao and J.F. Guan 236

Calculation of Shear Capacity of Continuous Compound Spiral Hoop Reinforced Concrete Column
J.F. Guan and J. Wang 240

Research on Regional Dividing Technology for Liquefaction-Induced Lateral Spreads Based on MAPGIS
C.C. Li, W.M. Wang, R. Sun and Y.R. Li 244

The Dynamic Response Analysis on Train Liquid Storage Tanks under Harmonic Excitation
Q.H. Zhang 248

Stability Analysis of Concrete Gravity Dam
Z.H. Wen and J. Zhou 252

Stress Calculation of Gravity Dam Based on Elastic Mechanics
H.B. Cui, H.T. Zhu and J.C. Yue 256

Dynamic Analysis of Face Rockfill Dam Based on Finite Element Theory
Y. Zhao, S.Z. Cheng and J.W. Zhang 260

3D Finite Element Analysis of Concrete Face Rockfill Dam
J.W. Zhang, S.Z. Cheng, S.F. Yuan and Y. Zhao 264

Temperature Character Analysis of RCC Based on Stepwise Regression Model
Y.Q. Zhao 268

Temperature Control of RCC Dam in Yongding Project
X.D. Xu and J.C. Yue 272

Study on Fundamental Frequency of Runway Based on Winkler Model
X.M. Zhang, L. Liang and Z. Wei 278

S-Transform Analysis on Pulsating Water Pressure Acting on the Stop Log Gate
H. Huang, X.Y. Xu and J.W. Zhang 282

A Multiobjective Decision Framework for River Basin Management
X.Q. Zhang, H. Gao and X. Yu 288

Finite Element Analysis of Complicated Sedimentation Basin
X.Y. Zhang, X.C. Liu, S.Q. Yang and L.L. Dong 292

Study on Settling Efficiency of Sedimentation Basin of Coca Codo Sinclair Hydropower Station in Ecuador
X.Y. Guo, S.W. Chen and D.P. Sun 298

Application of MIKE21 MODEL on Flood Routing in the Lower Yellow River from Gaocun to Sunkou
X.L. Zhang and S.L. Guo 304

Analysis of Influence Factors of Irrigation Method in Detecting Compactness of Canal Bank
Y.B. Kang, K. Huang and A. Rjap 308

Numerical Simulation of Excavation of Abutment Slope at Left Bank in Dagangshan Hydropower Station
K. Yang, Z.C. Ma and H. Han 313

Application of High Pressure Jet Grouting Technology in Seepage Prevention of ChuLou Reservoir
S.B. Zhang and J. Wen 317

Reservoir Operating Policies Analysis by Using Genetic Algorithm
S.B. Zhang and J. Wen 321

Thermal Stress Analysis of Large Scale U-Shaped Aqueduct
J.H. Zhang 325

Analysis on Axial Stresses of Crossbars on Aqueduct
X.L. Bai, J.Y. Li and B. Ma 329

Design Analysis of Shuangji River Drainage Aqueduct Body with Large Flow
G.W. Feng and Y. Gao 333

Study on Lateral Dynamic Response of Pile Foundation in Liquefiable Soil by Using FBG Method
Y.R. Li, Y. Liang, X. Wei, Y.L. Wang and Z.Z. Cao 337

Research on Temperature Control and Cracking Prevention on Pier by Installing Expansion Reinforcing Bands during Construction
H.M. Li, S.S. Li and W. Xie 341

Application of BOTDA in Mass Concrete Temperature Monitoring
J.H. Xiong, L.J. Wang, W.Y. He and H.F. Xing 346

Australian Seaport Infrastructure Resilience to Climate Change
D. Kong, S. Setunge, T.C.K. Molyneaux, G.M. Zhang and D.W. Law 350

Study on the Inwall Crack Extension and Fatigue Life Evaluation for Deep-Sea Steel Catenary Riser under Wave and Current Action
B.J. Si and Q. Jin 358

System Identification Applications in Pavement Permittivity Back-Calculation
M.L. Meng, Y.C. Cai and B. Zhang 366

Calculation of Saturation Line of Groundwater under Reservoir Water Table Uniform Falling
Y.Y. Zhang 371

Research on the Relationship between Effective Porosity and Ratio of Cement to Stone of Non-Sand Concrete Well Pipe
C.J. Yan 378

Study on Influencing Factors of the Elderly Population Crossing Speed
C. Yin and X.N. Song 382

Determination Optimum Pipe Diameter Method of Tree Path Heating Pipe Network
M.J. Wang, W.M. Di and Y.K. Wang 385

Rural Drinking Water Security Evaluation and Simulation Based on MATLAB Digital and Vector Processing Technology
H.W. Pan, B.D. Xi, H.J. Lei, Z.M. Wei, X.S. He and Y.H. Jiang 390

Analysis of the City Waterfront Landscape Design in Central Plains Economic Zone
J.X. Liu and Z.Q. An 395

Orthogonal Enumeration Method for Optimum Seismic Strength of Water Supply Network
S.H. He 400

Effect of Electrochemical Pretreatment and Flocculation on the Degradation of Pharmaceutical Wastewater
X. Mi 405

Experimental Study of Ultrafiltration of Eutrophicated Source Water in Combination with Sand Filter and Biological Contact Oxidation
F.Z. Li, D. Cheng and X.W. Lv 409

Research on the Effect of Gas Leaking and Gas-Supplementing Measurements of Air Cushion Surge Chamber
G.J. Luo, Y.S. Hu and K. Huang 414

Study on Construction Technology of Geogrid Treatment for Slope of Swelling Rock
Y. Gao, T.H. Zhao and J. Bao 419

Study on Three-Dimensional Reconstruction of Macro/Meso-Structure Evolution of Expansive Soils with CT-Triaxial Apparatus
X. Li, S.J. Wang and Z.H. Chen 422

The Influence of Concentration of Pore Water Solution on the Swelling Characteristics of Expansive Soils
J.C. Jia, H. Li and Q.T. Bi 427

Study on the Impact of Long-Term Immersion on the Shear Strength of Compacted Lime Stabilized Expansive Soils
Y. Dong, W.Z. He and B.T. Wang 431

Analysis on Collapsibility and Microstructure of Unsaturated Loess Using Fractal Geometry
F.L. Ma, M. Wang, J. Yang and X.H. Bai 435

Study on Reasonable Feature of Compaction Loess with Air Porosities
J. Yang, L.H. Wang, F.L. Ma and X.H. Bai 441

Theoretical Solution to the Change of Site Predominant Period Caused by Soil Softening
B.R. Huang, Y.Z. Wang, W.M. Wang and X.M. Yuan 447

The Finite-Element Analysis of Characteristics of Soil Slopeseepage Field Change in Continuous Rain Condition
Z.M. He, W. Wu, L. Zeng and Z.X. Cai 451

Influence of Compaction Density of Soil Mass to the Seepage Build Capacity of Rain and Drainage Design Parameter
F.R. Zhao, Z.L. Cai and T.W. Zhang 455

The Study on Rainfall Threshold Induced Landslides in Yucheng District by Binary Logistic Model
Y.Y. Zhang 460

Application of New Soil Consolidator in Road-Construction Engineering
H. Zhang, D.L. Xun, Z. Yang and F.Q. Ji 466

Study on Updating Design Pattern of Using Solar Energy Hot Water System in High-Rise Residence
J.J. Zhang, M.B. Yu and Q. Liu 470

Application of Thermal Priority Strategy in Energy-Saving Optimization Design of Low-Cost Rural Residence
M.J. Lu and Z.F. Zheng 473

Simulation Study on Solar Collector - Air Source Heat Pump Combined System for Space Heating in Cold Region
Z.Q. Wang, Y. Chen and H.X. Wang 478

Analysis on Waterproof and Drainage Systems of Pit House in the West of Henan Province
G.X. Wang and H.G. Li 482

The Development of Low-Carbon Economy for Realizing Urban Sustainable Development: Taking the Example of Baotou
A.L. Zhang and H.Y. Zhang 486

Research on Fire Prevention and Evacuation Design of Large Sports Facilities
S.W. Zhang, L. Song and Z.M. Li 490

Research of Highway Alignment Design Safety Evaluation Using Curvature Change Rate
S.N. Hu 493

Cold Recycling Technology Application of Old Asphalt Pavement in Rural Road Alteration Engineering
Z.D. Guo, J. Liu and C.B. Li 497

Analysis of Dynamic Impedance Functions in Urban Traffic Flow Guidance System
Z.C. Li 503

Compensation Design of Highway Landscape
S.N. Hu, Q.D. Fan, Z.H. Hu and X.H. Xiao 507

Chapter 3: Innovation in Architecture and Building Construction

Critical Risks Influencing the Application of EERTs in Australian Green Office Buildings
G.M. Zhang, I. Mosly, S. Setunge and X.H. Jin 513

Thinking on Architectural Design of Rural Supermarket
L.J. Hao 525

Economic Thinking of Landscape Design in Residential District
N. Wang and W. Sun 529

Some Points about the Local Living Environment Research
H.G. Li, Y.Q. Liu and Y. Ding 532

Planning and Design of Urban Barrier Free Building Environment with Aging of Population
L. Song, S.W. Zhang and Z.M. Li 536

On the Elements of Contemporary Architectural Styling
C.H. Xu, Y. Song, S.C. Xu, Q. Feng and H. Wu 539

A Study on Architectural Style of Buildings along the Northern Foot of Qinling Mountains Taking Xi'an Garden as Example
Z.T. Xiao 543

Preservation and Renewal of Huaiyu Street Historical Blocks in Xunxian County
C.Z. Gao and Y.T. Song 547

A Tentative Research on Site Selection of Shanxi Buddhism Temple Architecture
Y.X. Li, X.D. Zhu and C.E. Wang 551

Application of Display List Group Technology in Forming of Complex Building Model
L.H. Li 555

Study of Natural Disasters Contract Conditions Based on the FIDIC Criteria
Z.L. Guo and H. Zhang 558

Discussion on Construction Contract Management
B.X. Cui 562

Partner Selection for Partnering Mode Based on Vertical Projection Method
X.T. Nie and J.H. Lan 565

Design and Analysis of a Light-Weight Steel Gabled Frames Structure
W.F. Du, Z.F. Sun, H. Zhang and F.D. Yu 572

Research on Secondary Stress for Steel-Pipe Truss under the Influence of Geometric Parameters
H. Wang 576

Comparative Study on the Design Schemes of Residential Steel Structure
Y.C. Xu and Z.P. Tang 581

Wind-Induced Response Analysis of Steel Tower Structure
C.F. Wan, J. Wang, H. Zhu, L. Huang, H. Wang and Z.D. Xu 585

Research on Ultimate Bearing Capacity of Single-Layer Cylinder Latticed Shells Considering the Influence of *P-δ* Effect
W.F. Du, Z.Y. Zhou and P. Zhu 589

Monitoring and Test on Load Bearing Transform of Large Span Steel Truss of Archaized Tower
X.K. Li, P.F. Han, Z.H. Wang and J. Liu 593

Design and Analysis of a Suspended Lattice Shell
W.F. Du, F.D. Yu, Z.Y. Zhou and L.M. Zhu 599

Development and Application of the Virtual Simulation Teaching System of Steel Structure Construction
Z.P. Tang and Y.C. Xu 603

Research Status and Development Application of Ceramsite Concrete Short Pier Shear Wall
B. Hu, R.Y. Zheng and B.F. Zhou 608

Application of Improved Response Surface Method Based on Kriging Model to Structural Reliability Analysis
B.Y. Jia, Q.S. Yan and X.L. Yu 611

A New Bending Stiffness Measurement Technique Based on Distributed FBG Sensing Technology
Y.L. Wang, X.M. Yuan, X.G. Cai and Y.Z. Wang 617

Fire and Post-Fire Performance of Space Grid Structures
G.Y. Wang, X.Q. Wang and G.W. Liu 621

Study of Building Design and Reinforcement Technology under the Mining Damage
Q.S. Li and T.C. Wang 625

Study on the Ductility of T-Shaped Short-Limb Shear Walls (I)
D. Guo, H. Feng, Z.P. Li and J.Y. Liu 631

Study on the Property of Ductility of T-Shaped Short-Shear Walls (II)
Z.P. Li, D. Guo, H. Feng and J.Y. Liu 635

Seismic Research and Development of Steel Plate Concrete Composite Shear Wall
Y.B. Yang 640

Testing and Control for Strands Embedded in Annular Concrete Foundation Beam of Steel Archaize Tower
X.K. Li, J. Liu, Z.H. Wang and P.F. Han 643

Free Vibration Analysis of Frame-Core Tube Structures Attached with Damped Outriggers
Z.H. Wang 648

Three-Spring Model for Spatial Walls
L.J. Si, G.L. Chen and H.L. Wang 652

Discussion on Masonry Structure Model Mechanical Property Test
G.L. Chen and L.J. Si 659

Manufacturing Technology of High-Strength Continuous Compound Spiral Hoop
J.F. Guan and Q. Zhang 663

Optimal Calculation Method of Eccentric Bearing Capacity of Concrete-Filled Steel Tube Short Columns
J.W. Zhang, X.J. Kuang, W.F. Bai and J. Wang 666

Experimental Studies on High Strength Concrete Beams Reinforced with Steel and GFRP Rebars
Y.H. Liu and Y. Yuan 669

Chapter 4: Innovation in Bridge and Underground Engineering

Key Design and Construction Techniques for Collisionproof Steel Cofferdam for Large Span Cable-Stayed Bridge
W.Z. Li, Z.J. Feng, Z.C. Hu, D.L. Xun, J. Zeng and Q. Peng 677

Study on Thermal and Structural Behavior of a Cable-Stayed Bridge under Potential Tanker Truck Fires
Y.J. Liu, B. Ning and Y. Wang 684

Rhombus Cradle System Checking Computation of Jinqinggang Bridge
S.M. Liu, Z.L. Yang and H. Zhao 689

Bridge Structure Performance Evaluation Based on Dynamic Load Test
Y. Zeng 694

Construction Technology of Transverse Bonded Structural Steel for Strengthening PPC Hollow Slab Bridge
J.H. Chen, L.H. Bai, S.B. Zhao, X.H. Yu and C. Chen 697

Checking Computation for Bracket Structure of Jinqinggang Bridge
S.M. Liu, H. Zhao and Z.L. Yang 701

Anti-Overturning Stability Numerical Analysis of Single Column Bridge
X.M. Zhang and B. Dong 705

Study on Construction Process of Suspension Bridge Based on a Co-Rotational Framework
B.J. Wang, J.Y. Song and J.M. Lu 709

Design of Mitigation Damper with Support Flexibility for Stay Cable under Bridge Deck Excitation
S. Luo, Q.S. Yan and H.J. Liu 714

Dynamic Analysis of Bridge-Approach Embankment Transition Segment
Z.X. Li and Y.Z. Chen 719

Simulation of Composite Strengthening Technique in Prestressed Concrete Continuous Box Beam Bridges
H.B. Jiao and S.H. He 723

Full-Scale Model Test for Anchorage Zone of Pylon of Cable-Stayed Bridge
X.L. Yu, B.Y. Jia, W.F. Wang and Q.S. Yan 728

Creep Effects on Simply Supported Prestressed Concrete Box Girder of High-Speed Railway with Ballastless Tracks
W. Fang, B. Han and S.K. Yang 733

Static Analysis of Reinforced Concrete Arch-Deck Bridge with Archaized Connective Corridors
X.K. Li, L.X. Liu, S.M. Liu and S.B. Zhao 738

Effect of Pile-Soil Action on Seismic Resistance of Prestressed Continuous Box-Girder Bridge with Changed Sections
F.L. Li, S.M. Zhang and S.M. Liu 743

The Research of Steel Bracket Jacking Experiment in Long Span Continuous Beam Bridge
C. Zhou, Q.S. Yan, H.B. Zheng and G. Wei 748

Research on Non-Quantification Risk Factors Control and Management of Bridges during Construction
Q.F. Li, H. Fu and W.K. Gan 753

Comparison Study on Crossbeam Web Cutout of Different Shapes for Orthotropic Steel Bridge Deck
L.Q. Gao, Q.H. Pu, B. Han and Z.B. Liu 758

Plastic Hinge Analysis of Seismic Performance of High Bridge Pier
R.H. Gao, R.L. Chen, S.G. Cao, Z. Tang, X.Q. Xiao and H.B. Hu 765

Theoretical Calculation and Parametric Analysis of Tunnel Settlements due to Neighboring Over-Length Pile Groups
K. Wang 769

Excavation Technology of Shield Tunneling in Mixed Ground
S.L. Xu 773

Safety Analysis on the Structure of an Existing Metro Station Impacted by the Construction of an Adjacent Building
L.H. Ma, Q.H. Liang, Y.F. Liu and M.R. He 777

Numerical Analysis of Effect of Blasting Vibration on Adjacent Roadway in 858 Mines
G.Y. Wang and J.C. Liu 783

Analysis of Plastic-Zone Radius Influenced by Mechanical Parameters in Tunnel Excavation and Support
Z.M. Su and R. Liu 787

Introduction of NO-NO_2-O_3 Recycle into Model for Air Pollutant Dispersion from Tunnel Portals
S.J. Miao and D.F. Fu 791

Underground Space Form Design of Large Centrifugal Shaker System and Analysis of Machine Foundation Vibration
Y.Z. Wang, Y.L. Wang, Z.S. Chen and X.M. Yuan 795

Research of Manually Excavated Pile Support for Large Foundation Pit
Z.Y. Deng 799

Analysis of Settlement Reasons and Mechanism in Immersed Tunnel
G. Wei, H.J. Qiu and X.J. Wei 803

Monitoring Analysis on Tunnel Portal Shallow Burying Segment of Center Diaphragm Construction Method
F. Zhou, Y.L. Xie and J.X. Lai 808

Stability Analysis of Underground Caverns by Jointed Finite Element Method
J.C. Wu, Y.M. Zhang and H.X. Li 814

Controlling Criterion for Differential Settlement of Widened Expressway
H.F. Xing and H.M. Li 818

Theory Study by CGM for Moving Force Identification
Z. Chen and J.L. Han 823

Numerical Simulation by CGM for Moving Force Identification
Z. Chen and J.L. Han 826

Chapter 5: Earthquake and Seismic Engineering

Mitigation of Seismic Risks to Soft-Storey Structures Using Toggle-Brace-Damper Systems
R.W.K. Chan and Z.F. Zhao 833

The Seismic Behavior of High-Strength Concrete Frame Joints
T.Y. Wang, J.W. Zhang and D.Y. Gao 838

Study on Relationship of Seismic and Pseudo Response Spectrums
G.L. Chen, W.F. Liu and G. Li 844

Feasibility of Vs Liquefication Evaluation Methods by Bachu Xinjiang Earthquake Data
Q.Y. Zhao, R. Sun, Y.R. Li and W.M. Wang 848

Study on *In Situ* Test Based on Survey of Bachu Earthquake
Z.Y. Li, W.M. Wang, Y.R. Li and L.W. Chen 852

Comparative Analysis on Liquefaction Macro-Characteristics of the Three Major Regions in Wenchuan Earthquake
W.M. Wang, Z.S. Chen, X.M. Yuan and Z.Z. Cao 856

Research on Zoning Technology of the Liquefaction Seismic Settlement Based on MAPGIS
X. Lu, R. Sun, Y.R. Li and L.W. Chen 860

Correlation of Site Characteristic Period with Predominant Period of Ground Acceleration by a Simplified Model
L.W. Chen, W.M. Wang and R. Sun 864

Study on Anti-Seismic Reliability of Urban Water Supply System
X.J. Li and F.M. Shen 868

A Study on the Analysis Method of Soil Layer Seismic Response in Seasonal Frozen Site
Z.S. Chen, S.J. Meng, Y.R. Li and L.W. Chen 872

Comparative Analysis of Seismic Responses of Different Layer Height Structures with Broken Stone Isolation Layers
X.Z. Zhang, L.J. Miao and K.D. Tang 876

Introduction to ASCE7 Seismic Design and the Comparison with Chinese Code GB 50011-2010
C. Song and H.J. Zheng 881

Analysis of Typical Example and Genesis of Landslide Triggered by Wenchuan Earthquake in China
J.Y. Dong, Z.L. Li, Z.Q. Huang, J.H. Yang and G.X. Yang 886

CHAPTER 1:

Advanced and Sustainable Materials

© (2012) Trans Tech Publications, Switzerland
doi:10.4028/www.scientific.net/AMM.238.3

Luffa Sponge as a Sustainable Engineering Material

Jianhu Shen[1, a], Yi Min Xie[1,b], Xiaodong Huang[1,c], Shiwei Zhou[1,d] and Dong Ruan[2,e]

[1]Centre for Innovative Structures and Materials, School of Civil, Environmental and Chemical Engineering, RMIT University, GPO Box 2476, Melbourne 3001, Australia

[2]Faculty of Engineering and Industrial Sciences, Swinburne University of Technology, John Street, Hawthorn, Victoria 3122, Australia

[a]jianhu.shen@rmit.edu.au, [b]mike.xie@rmit.edu.au (corresponding author), [c]huang.xiaodong@rmit.edu.au, [d]shiwei.zhou@rmit, [e]druan@groupwise.swin.edu.au

Keywords: Luffa sponge; mechanical properties; energy absorption; sustainability.

Abstract The paper presents the first scientific study of the stiffness, strength and energy absorption characteristics of the luffa sponge with a view to using it as an alternative sustainable engineering material for various practical applications. A series of compression tests on luffa sponge columns have been carried out. The stress-strain curves show a near constant plateau stress over a long strain range, which is ideal for energy absorption applications. It is found that the luffa sponge material exhibits remarkable stiffness, strength and energy absorption capacity that are comparable to those of some commonly-used metallic cellular materials. These properties are due to its light-weight base material, and its structural hierarchy at several length scales. Empirical formulae have been developed for stiffness, strength, densification strain and specific energy absorption at the macroscopic level by considering the luffa fiber as the base material. A comparative study shows that the luffa sponge material outperforms a variety of traditional engineering materials.

Introduction

Biological materials and structures have distinguished them from man-made counterparts because of their unique characteristics [1, 2]. The most attractive one is their long-term sustainability to the natural environment. The performance of the traditional man-made materials, notably various metals, metallic alloys, ceramics, plastics, as well as their composites, significantly surpass the biological materials [3, 4]. However, most of the man-made materials are not environmentally friendly and little has been concerned with their sustainability [4]. By contrast, those biological materials are based on relatively weak base materials such as minerals and proteins which are easily degradable, bio-compatible, pollution-free, recyclable and energy-efficient [4]. Furthermore, over millions of years to accommodate the natural environment to which they were exposed, a large number of biological systems evolve periodic cells with self-similar hierarchical microstructures.

Luffa sponge is one of such commercially viable and environmentally acceptable biological material derived from fruit of *Luffa Cylindrica* (LC) plant and having recycling capability and triggered biodegradability [5, 6]. It is relatively stable in their intended lifetime but would biodegrade after disposal in composting conditions. At the same time, the fruits of LC have a netting-like fibrous vascular system. When they are dried, the fibrous network structure serves like an open cell foam material. Due to the high strength-to-weight ratio of cellular materials, it may be used as a good packaging material and an excellent energy dissipation material. The importance of biological materials such as the luffa sponge is growing as we search for sustainable solutions using new materials.

Only a limited amount of research has been conducted on the luffa sponge as a source of bio-fibres and bio-composites in the last ten years. Those researches indicated that it is a potential alternative material for water absorption [7, 8] and waste water treatment [9, 10]. The luffa fibres were also used as reinforcement fibre for other materials and cell immobilization for biotechnology. At the same time, LC plants, the origin of luffa sponge material, have not yet had their potentialities fully

explored. With regard to industrial and technological development, the cost of fuel is on the increase. Oil is extracted from seeds of various plants for industrial use [7]. The seed of LC can also be used as oil sources. Actually, the oil extracted from LC is finding increasing use in the production of biodiesel which is now gaining wide acceptance because of low CO_2 emission and other considerations.

However, there is a lack of scientific data on the mechanical properties of luffa sponge material because up to now its main practical use has been as a body scrub in the bathroom. Due to the lack of experimental proofs, their complex hierarchy microstructures and other common limitations of biological materials, potential applications have not been applied in practice for luffa sponge material as well as luffa fibres.

To this end, the mechanical properties of luffa sponge columns were tested and compared with other cellular materials to check the performance of this light weight material. Uniaxial quasi-static compressive tests were conducted at a strain rate of 10^{-3} s^{-1} by using an Instron machine. Cylindrical specimens with different relative density were tested at a room temperature of 25ºC and a humidity of approximately 40%. An energy efficiency method was adopted to obtain the values of the densification strain and plateau stress, and thus the energy absorption capacity per unit volume. The experimental results are also discussed together with test results published by other researchers for other similar materials.

Experiments

Specimens. The luffa sponge used in our experiments was obtained from pharmacies in Australia which was sold as a bath sponge. The chemical composition of luffa sponge material depends on several factors, such as plant origin, weather condition, soil nature, pre-treatment, etc. A typical set of chemical compositions of luffa sponge can be referenced from a previous research [11].

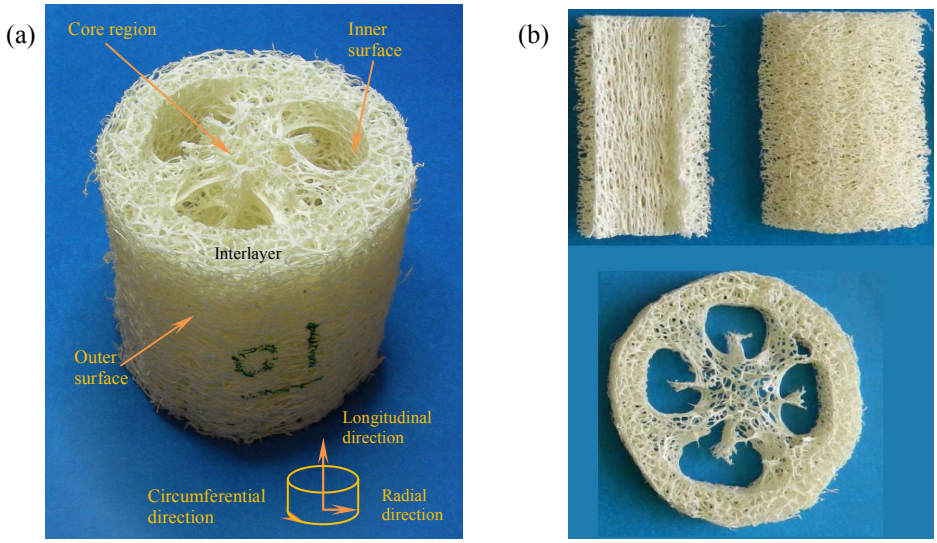


Fig. 1 Features of luffa sponge specimen for compressive tests: (a) different regions; (b) orientation of luffa fibres (top left: inner surface; top right: outer surface; bottom: cross section).

According to the standard of compressive tests and recent research [12] on other cellular material, the specimen size effect is negligible for foams when the dimension of specimen is sufficiently larger than the cell size, i.e. 7 times of the cell size for metallic foams. Thus the specimen for luffa sponge should be large enough to eliminate the specimen size effect. The available maximum size along radial direction for luffa sponge is the whole section of the luffa sponge column. It will be used as the cross section of the specimen which ranges from 55 mm to 86 mm in diameter. The height of the specimen was selected as approximately 50 mm in our test. A bandsaw cutting machine was used to cut the specimen from an initial dried luffa bath sponge. After the initial cutting, the specimens were sanded further to make the two cutting surface smooth and parallel. Besides the specimen, a separate slice was cut from the bath sponge to measure the section area of the specimen. For most of the bath sponge columns, the section area at two ends was different, thus two thin layers of luffa sponge slices

(about 5mm thick) were cut at each end to be used as samples to measure the cross section area of luffa sponge specimen. Because the cross section for most of the specimens was not perfectly circular, a photograph for each slice was taken and Photoshop was used to get the cross section area. Then the section area of the specimen was taken as the average value of these two slices. The volume of the luffa sponge specimen was the product of this cross section area and the height of the specimen. Fig. 1 (a) shows a typical cylindrical specimen for compression test.

Geometry Features and Standard Variation of Density. After the specimens were cut, three different core topologies were observed in our luffa sponge specimens. The major difference is the number of voids in the core region. Two, three and four voids were observed in the specimens. Fig. 1 (b) shows a topology with four voids. A large variation in specimen diameters and cross sectional area was also observed.

The luffa sponge column is composed of luffa fibres. Those fibres interconnect with each other and form networks with micro-trusses. The length of those micro-trusses represents the cell length of the luffa sponge material. A rough measurement indicates the average length of those micro-trusses was in the scale of millimeter (1 to 2 mm). The orientation of these luffa fibres in the luffa sponge columns exhibits a regular pattern. According to different orientation of the luffa fibre, the luffa sponge cylinder can be divided into four regions, namely, the inner surface, the outer surface, interlayer and core as shown in Fig. 1(a). On the inner surface, the thickest luffa fibre grows along longitudinal direction. While on the outer surface, the thickest luffa fibre grows along circumferential direction. In the core region, the strongest luffa fibre is along radial direction. In the interlayer between inner surface and outer surface, the fibre grows in all three directions.

Similar to other cellular materials, the mechanical properties of the luffa sponge material is closely related to its density rather than other geometric features mentioned above. Thus the specimens were grouped only according to their densities in order to obtain a reliable empirical formula to represent their mechanical performance. The specimen size and core topology will be disregarded in the current paper.

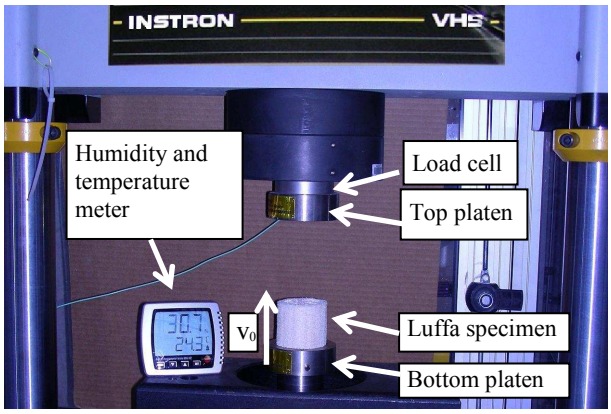


Fig. 2 Experimental set-up for mechanical tests of luffa sponge material.

Experimental Procedure. Uniaxial compressive tests were conducted at very low strain rates, namely, 10^{-3} s^{-1}, to obtain the mechanical properties under quasi-static loading. An Instron machine was used to conduct these tests as shown in Fig. 2. The displacement and load curves were recorded and the average compressive force, densification strain and energy absorption can be worked out using an energy efficiency method.

Like other natural sponges such as the sponge *Euplectella* aspergillum [13], the mechanical properties of luffa sponge are also influenced by the moisture. Thus the humidity during the test was monitored. The specimens were placed in the test room for at least 2 hours before the compressive test to eliminate the difference in temperature and humidity. The temperature in the test room was from 20ºC to 28ºC, but during each test its variation was less 1ºC. The humidity was between 30% and 44%, but during each test its variation was less 1.0%. Photographs were taken during the quasi-static compressive test at every 30 seconds which corresponded to a 1.5 mm displacement interval for the test rate used.

Experimental Results

Deformation Features. Force and displacement histories were obtained by the Instron machine (VHS 8800). Typical force displacement curves are shown in Fig. 3 (a). It shows clearly a fairly constant compressive force over a long stroke, which represents an ideal energy absorption feature. Nominal stress (defined as force over original cross sectional area) and nominal strain (defined as displacement over original height of the luffa sponge specimen) were calculated. The deformation patterns confirm that the overall compression strain of the specimen is axial along longitudinal direction rather than folding of the wall of the specimen. Similar to metallic foams, the compressive deformation process for luffa sponge material under quasi-static loading was not uniform. Localised crushing bands were observed which was similar to the static compression behaviour of metallic foams. Luffa fibres exhibited micro-truss-level distortions and rotations which was similar to the open-cell metallic foams.

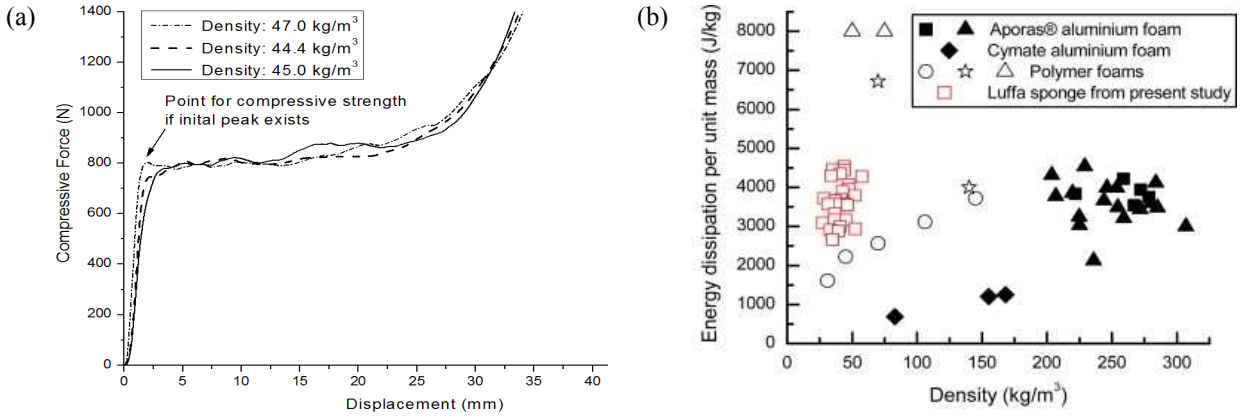


Fig. 3 Mechanical properties of luffa sponge columns crushed axially: (a) typical force-displacement curves; (b) comparison with other cellular materials.

Compressive Strength. Similar to other cellular materials [14], the compressive strength of the luffa sponge material was taken to be the initial peak stress if it existed. If there was no such peak stress, the stress at the intersection of two slopes was taken to be the compressive strength, namely, the slope for the initial loading and that for the stress plateau. It has been found by previous research that, like several other properties of cellular materials, compressive strength obeys a power law with the relative density,

$$\frac{\sigma_0}{\sigma_{yf}} = A\left(\frac{\rho_0}{\rho_f}\right)^B \tag{1}$$

Where σ_{yf} is the yield stress of the base luffa fibre, ρ_f is the density of luffa fibre, σ_0 and ρ_0 are the compressive strength and density of luffa sponge, A and B are two constants for luffa sponge material.

By fitting to Eq. (1) using the quasi-static data in our experiment together with the relevant data (ρ_f =353 kg/m^3, σ_{yf} =11.1 MPa) from literature for the similar luffa fibre [15], the parameters A and B are 0.37 and 1.28, respectively. The standard variation is pretty large, which will limit the practical application of luffa sponge material.

Elastic Modulus. Similar to metallic foams [12], the slope of the initial loading portion of the curve is lower than that of the unloading curve. It indicates that there is localized plastic deformation in the specimen at stresses well below the compressive strength of the luffa sponge material reducing the slope of the loading curve. However, the reloading curves after unloading roughly follow the initial loading curves. As a result, measurement of Young's modulus was made from the slope of the

initial loading curve in the current study. Thus, the slope between 25% and 75% of the compressive strength is taken as the elastic modulus of luffa sponge material. Following the same argument for the compressive strength, for Young's modulus, the empirical formula is:

$$\frac{E}{E_f} = 0.057\left(\frac{\rho_0}{\rho_f}\right)^{1.16} \tag{2}$$

Where E and E_f are the Young's moduli of luffa sponge and luffa fibre.

Comparison with Other Materials

As a cellular material, the luffa sponge is extremely light. Nevertheless, our research results show that, when the luffa column is compressed longitudinally, the amount of energy it can absorb per unit mass is comparable to that of the aluminium foam and several other commonly-used polymer foams [16], as shown in Fig. 3(b). It should be noted that Alporas® aluminium foam has superior specific energy absorption than other metallic foams when their density is lower than 300 kg/m^{-3}. As an important example, the comparison with a recently invented metallic microlattice of a similar density [17] shows that the average plateau stress of the luffa sponge (about 350 kPa) is significantly higher than that of the Ni-P microlattice (about 120 kPa). It should be noted that the strength decreases with density for any kind of cellular materials. These comparisons indicate that the luffa sponge material has better compressive strength than most of other available cellular material of similar density such as Cymat aluminium foam, expended polystyrene foams and Ni-P microlattices.

The experimental data presented in this paper about luffa sponge material may significantly expand the density range of previously studied natural materials [14] with respect to the strength, as shown in Fig. 4. This special feature provides an opportunity to widen the applications of natural cellular materials in general and the luffa sponge in particular, especially when the light-weight is a key design requirement.

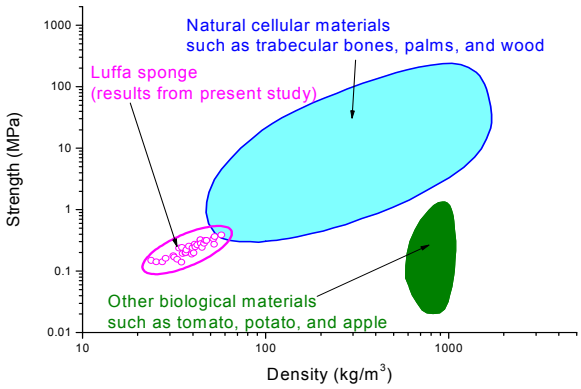


Fig. 4 Comparison between luffa sponge and other natural materials [14].

Conclusions

In this study, compressive tests were conducted to examine the stiffness, strength and energy absorption characteristics of the luffa sponge material under quasi-static compressive load. The stress-strain curves show a near constant plateau stress over a long strain range, which is ideal for energy absorption application. The stiffness, compressive strength, densification strain, plateau stress and energy absorption capacity of the luffa sponge material have been obtained for the first time. A set of empirical formulae have been proposed to predict the mechanical properties of luffa sponge material at the macroscopic scale. It is found that the luffa sponge material exhibits remarkable stiffness, strength and energy absorption capability that are comparable to those of some commonly-used metallic cellular materials. The results from the present study have clearly demonstrated that the luffa sponge has great potential to be used as an environmentally-friendly engineering material in various practical applications.

References

[1] J. Shen, Y. M. Xie, X. Huang, S. Zhou, D. Ruan, Mechanical properties of luffa sponge, J. Mech. Behav. Biomed. Mater., (2012) (in press and available online)
[2] M. A. Meyers, P.-Y. Chen, M.I. Lopez, Y. Seki, A.Y.M. Lin, Biological materials: a materials science approach, J. Mech. Behav. Biomed. Mater., 4 (2011) 626-657.
[3] L. J. Bonderer, A. R. Studart, L.J. Gauckler, Bioinspired design and assembly of platelet reinforced polymer films, Science, 319 (2008) 1069-1073.
[4] Z. Zhang, Y. Zhang, H. Gao, On optimal hierarchy of load-bearing biological materials, Proc. R. Soc. B, 278 (2011) 519-525.
[5] I. O. Oboh, E. O. Aluyor, Luffa cylindrica - an emerging cash crop, African J. Agr. Res., 4 (2009) 684-688.
[6] M. J. John, S. Thomas, Biofibres and biocomposites, Carbohydr. Polym., 71 (2008) 343-364.
[7] K. E. Bal, Y. Bal, Gross morphology and absorption capacity of cell-fibers from the fibrous vascular system of loofah (luffa cylindrica), Text. Res. J., 74 (2004) 241-247.
[8] H. Demir, U. Atikler, D. Balköse, F. TihmInlIoglu, The effect of fiber surface treatments on the tensile and water sorption properties of polypropylene-luffa fiber composites, Compos. Part A, 37 (2006) 447-456.
[9] I. O. Oboh, E. O. Aluyor, T. O. K. Audu, Application of luffa cylindrica in natural form as biosorbent to removal of divalent metals from aqueous solutions - kinetic and equilibrium study, in: F.S.G. Einschlag (Ed.) Waste Water - Treatment and Reutilization, InTech, 2011, pp. 195-212.
[10] Y. Laidani, S. Hanini, G. Henini, Use of fiber luffa cylindrica for waters traitement charged in copper, Study of the possibility of its regeneration by desorption chemical, Energy Procedia, 6 (2001) 381-388.
[11] G. Siqueira, J. Bras, A. Dufresne, Luffa cylindrica as a lignocellulosic source of fiber, microfibrillated cellulose, and cellulose nanocrystals, BioResources, 5 (2010) 727-740.
[12] M. F. Ashby, A. G. Evans, N. A. Fleck, L. J. Gibson, J. W. Hutchinson, H. N. G. Wadley, Metal foams: a design guide, Butterworth-Heinemann, Warrendale, 2000.
[13] M. Johnsona, S. L. Walterb, B. D. Flinnc, G. Mayerc, Influence of moisture on the mechanical behavior of a natural composite, Acta Biomater., 6 (2010) 2181-2188.
[14] L. J. Gibson, M. F. Ashby, B. A. Harley, Cellular Materials in Nature and Medicine, Cambridge University Press, Cambridge, 2010.
[15] M. A. Paglicawan, M. S. Cabillon, R. P. Cerbito, E. O. Santos, Loofah fiber as reinforcement material for composite, Philipp. J. Sci., 134 (2005) 113-120.
[16] M. Avalle, G. Belingardi, R. Montanini, Characterization of polymeric structural foams under compressive impact loading by means of energy-absorption diagram. Int. J. Impact Eng. 25 (2001) 455-472.
[17] T. A. Schaedler, A. J. Jacobsen, A. Torrents, A. E. Sorensen, J. Lian, J. R. Greer, L. Valdevit, W. B. Carter, Ultralight metallic microlattices, Science, 334 (2011) 962-965.

© (2012) Trans Tech Publications, Switzerland
doi:10.4028/www.scientific.net/AMM.238.9

Mechanical Properties Research on Concrete Block Doped Nano-TiO_2 under the Conditions of Common Conservation

Zhiyong Deng

Zhejiang Business Technology Institute, Ningbo 315012, China

ddzzyy2005@sohu.com

Keywords: concrete block; nano-TiO_2; mechanical properties.

Abstract. As a new high performance construction material, concrete doped nano-TiO_2 greatly expanded its application in engineering with the advantages of high strength and high durability. By compressive test of concrete block doped nano-TiO_2 under the conditions of common conservation, this paper respectively studies the regulation of compressive properties of the concrete block affected by the factors such as concrete strength and nano-TiO_2 dioxide.

Introduction

Modern engineering practice indicates that concrete is confronted with higher performance requirement in the complicated special structure, and how to make the high strength concrete becomes an important topic in the engineer field. Since the nano-material was used in civil areas in USA, the new materials industry has made a great development. With the development of nanotechnology and nano-materials, mixing excellent performance nanometer TiO_2 into the concrete is becoming a new trial.

Design of Experiment for Concrete Mixed TiO_2

Materials. Cement strength is the main source of cement concrete strength, its technical indexes is very important for the performance of the concrete. The P.S. 32.5 ordinary Portland cement used in this experiment that was made in Hebei JuDing cement co, Ltd. The technique indexes are listed as Table 1. The properties of NM- titanium dioxide are listed in Table 2.

Table 1 Properties of cement

Fineness (%)	Main component	Initial setting time (h)	Final setting time (h)	Compressive strength (MPa)	Color	Grade	Safety
1.2	slag silicate	3	4.25	17.9	grey	ordinary	qualified

Table 2 Properties of NM- titanium dioxide

Item		Index value
Main component		NM-TIO2
Purity (%)		＞99
Partical size (nm)		＜30
Crystalline phases		Rutile（R）
Appearance		white powder
Surface property		Hydrophilic
PH value		6-8
apparent density (g/cm³)		0.2±0.05
drying loss rate (%)		<1±0.5
Heavy metals content (ppm)	Pb	≤10
	As	≤5
	Hg	≤1

The crushed stone was used with apparent density of 2.653g/cm³ and bulk density of 1.392g/cm³.

The sand was the medium sand with 2.62 fineness modulus, apparent density of 2.67g/cm³ and bulk density of 1.52g/cm³.

The admixture was FDN-FZ efficient water reducer.

The water is the ordinary tap water of Ningbo.

Mixing Design. Selected standard test blocks size is 150mmx150mmx150mm, its mix proportion is in the Table 3.

Table 3 Proportion of concrete for mechanical property test

Item	water-cement ratio	sand ratio(%)	cement (g)	water (g)	sand (g)	crushed stone (g)	water reducer (g)	NM-TIO2 (g)
1	0.5	0.36	1148	517	2357	4190	13	0
2			1148	517	2357	4190	13	41
3			1148	517	2357	4190	13	62
4			1148	517	2357	4190	13	83
5	0.4	0.36	1293	517	2325	4134	13	0
6			1293	517	2325	4134	13	41
7			1293	517	2325	4134	13	62
8			1293	517	2325	4134	13	83
9	0.3	0.36	1723	517	2170	3858	13	0
10			1723	517	2170	3858	13	41
11			1723	517	2170	3858	13	62
12			1723	517	2170	3858	13	83

Production and Maintenance for Specimens

According to the test requirements and data of Tab 1, we determine thirty six specimens by three parameters that are concrete strength grade, curing period, and content of Nano SiO_2. Compression test use the cube specimens with side length of 150mm.

Specimen Preparation Methods.

(1) Mix: Weigh the raw materials According to the mix proportion; Put the cement, water reducer and NM-TiO_2 into the mixer, mix them evenly for two minutes; then add sand and crushed stone and mix them evenly. Finally, pour water into the mixer and mix them for three minutes. Pour out the mixture and test the slumps.

(2) Shaping: About the cube sample with side length of 150mm, divide into two equal layer and put into the module .Insert and smash along the wall of module by slice as loading the mixture. Shake it until the pulp come out of the concrete surface. Scrape off the redundant mixture and make the screed by slice.

(3) Split mold: Put the molds for 24 hours at 20±5 centigrade, split mold and sign numbers.

(4) Maintenance: Put the specimens in the environment with 20±3 centigrade and above 90% relative humidity and respectively maintain for 7 days, 14 days and 28 days.

Test equipment.

(1) Blender: concrete-mixer with volume of 250L.

(2) Shaking table: ZT-1X1 TYPE concrete trial shaking table.

(3) A number of Trial Mold.

Mechanical Property of Concrete Mixed NM-TiO_2

Concrete with NM-TiO_2 is a new type of composite building materials, its mechanical properties has different characters because of the complex material. It is worth to explore whether the conclusion and experiential formula are still suitable for concrete mixed NM-TiO_2 which are applicable to general concrete. Therefore, this article will study the concrete mixed NM-TiO_2 mechanical property experimental research, and make theoretical analyses for this research.

The Test Data of the Compressive Strength about Cube Specimens. In this experiment, we make 3 pieces of samples for each 3 group according to every combination ratio. Each sample has 3 ages, the total quantity is 36 pieces. We chose 12 pieces and calculate the cube specimens compressive strength after measuring the size of it, particular case is in the Table 4.

Table 4 The cube sample compressive strength value (MPa)

Sample item	7d	14d	28d	28d strength ratio
1	33	36	41	1
2	31	41	43	1.05
3	40	42	46	1.07
4	42	41	44	0.96
5	40	42	44	1
6	39	40	45	1.02
7	39	43	46	1.02
8	39	39	45	0.98
9	37	40	42	1
10	38	41	43	1.02
11	38	41	46	1.07
12	38	42	43	0.93

Data Analysis. The influence for compressive strength ratio is from the content of NM-TiO_2. Fig. 1 shows the relation between the compressive strength ratio and the content of NM-TiO_2 after making the samples in the fog room for 28 days. Where 1 represents nano-TiO_2 content of zero, 2 represents nano-TiO_2 content of 0.5%, 3 represents nano-TiO_2 content of 0.75%, 4 represents nano-TiO_2 content of 1%.

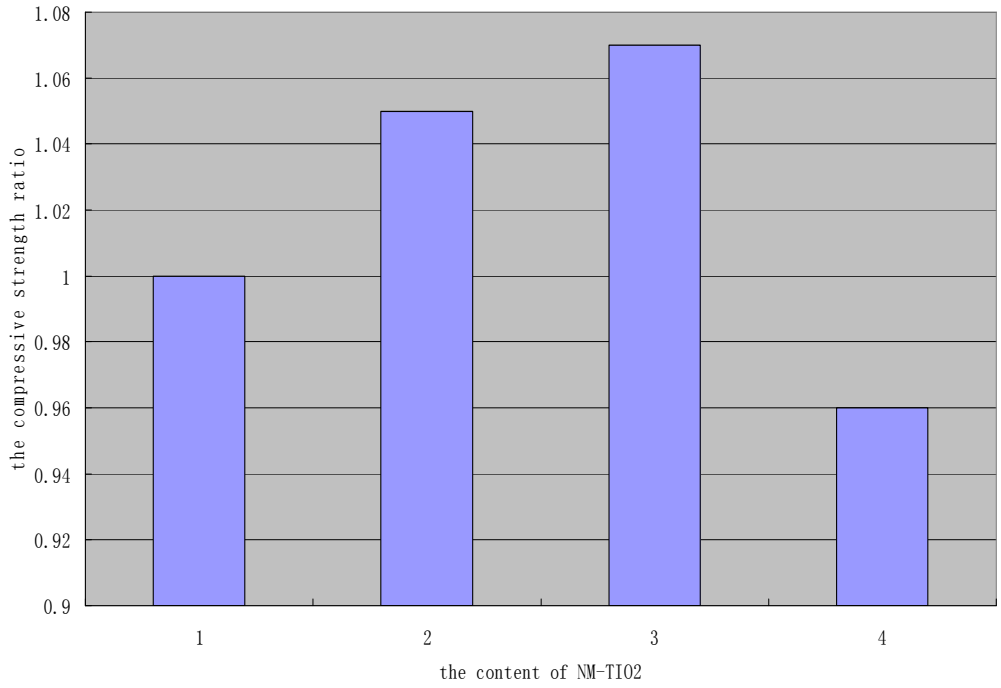


Fig. 1 Relation between the compressive strength ratio and the content of NM-TiO_2

Conclusions

With the content of NM-TiO_2 enhancing in the plain concrete, we can see that the concrete cube's total compressive strength raised firstly and then fell in this graph. The cube's total compressive strength ratio changed between 1 and 1.1. The compressive strength is the biggest when the content of NM-TiO_2 is 0.75%. In addition, NM-TiO_2 can improve the compressive strength of plain concrete at first.

References

[1] S. Zhang, Testing research on doped Nano-silica steel fiber reinforced concrete, Materials Thesis of Zhengzhou University, 2 (2010) 20-50.

[2] Z. Sun, Study on performance of P.I-portland cement by Nano-powders. D, Materials Thesis of Guangxi University, 3 (2010) 44-54.

[3] Information on http://www.zhulong.com

[4] Information on http://www.tydf.cn

© (2012) Trans Tech Publications, Switzerland
doi:10.4028/www.scientific.net/AMM.238.13

Axial Compression Behaviors of Concrete Confined by Basalt Fiber Sheets

Zongcai Deng [a], Jumbe Raphael-Daud [b] and Haibin Xu [c]

The Key Laboratory of Urban Security and Disaster Engineering, Ministry of Education, Beijing University of Technology, Beijing 100124, China

[a]dengzc@bjut.edu.cn, [b]daud@bjut.edu.cn, [c]xhb1979878@hpu.edu.cn

Keywords: Basalt fiber reinforcement polymers (BFRP); axial compression; stain; strength model.

Abstract. According to the axial compressive experiment of concrete cylindrical and quadrate specimens confined by Basalt fibers, the stress-strain curves, bearing capacity and peak strain were obtained. 12 quadrate and 12 cylindrical column specimens were prepared and wrapped with 2 to 4 layers of BFRP fibers. The results show that: (1) comparing with unconfined specimens, the compressive strength and peak strain of the specimens confined with Basalt fibers are improved significantly, not only cylindrical but also quadrate; (2) the compressive strength increases with the number of BFRP layers; with equal number of confinement layers, the compressive strength and peak strain of cylindrical specimens is higher than that of quadrate; (3) the wrapped fiber of quadrate specimens are more likely to rupture at the corners of specimen. Meanwhile, the compressive strength models of specimen confined by Basalt fibers were proposed, the theoretical values are in good agreement with the test data.

Introduction

The structures with lower seismic capacity have to be strengthened to improve their earthquake resistance. Fiber Reinforced Polymers (FRPs) are some of new materials being used in the reinforcement of concrete members [1]. FRPs are an ideal choice since they exhibit excellent characteristics such as lightweight, good corrosion resistance, high impact strength, easy work on etc [2].

Basalt fiber reinforced polymer (BFRP) is a new type FRP, and is very cheap in China, with good fire resistance, higher strength and elastic modulus [3]. It is the newest ideal strengthening material. In this paper, BFRP sheet has been used to confine cylindrical and quadrate concrete specimens and axial compressive experiment performed to research the confining effectiveness factors, including number of BFRP layers and specimen shape. From the experiment, the axial compressive stress-strain curve, strength, peak strain and fracture model were obtained.

Testing Program

Specimen Design. A total of 12 quadrate specimens of dimension 100mm×100mm×300mm, and 12 cylindrical specimens in 150mm diameter and 300mm height were prepared. Concrete proportions: cement 433kg/m^3, coarse aggregates 1260kg/m^3, fine aggregate 591kg/m^3, water165 kg/m^3, ordinary Portland cement P.O32.5, maximum aggregates with 20mm diameter. Steel molds were de-assembled 24 hours after being cast in molds, then placed in standard curing room for 28 days. 7 days after completion of curing, axial compression tests were performed.

Reinforcement Method. 12 Cylindrical specimens, three of which are control specimens, 9 reinforced specimens with reinforcement layers are 2, 3 and 4 respectively, each group with three specimens. Lap length of fibers is 100mm. 12 quadrate specimens, 9 reinforced specimens were similar to cylindrical ones; reinforced specimens chamfer radius 20mm.

Experimental Method. The experiment was conducted in the Beijing University of Technology laboratory using 2000kN MTS testing machine, data recorded using automatic IMP data collection system. Two circumferential strain gauges and two extensometers were fixed on each cylindrical and quadrate specimen, the gauge length is 300mm.

Experiment Results and Analysis

Failure Mode. Failure mode of various BFRP confined concrete cylindrical specimens is basically the same. As the loading approaches limit load, there is no significant lateral deformation of fibers, except for the creeping sound of cracking fiber. Once loading attains limit load, the BFRP suddenly break especially at the mid-height of the specimens, on subjection to external pressure, longitudinal fibers become disorganized therefore not evenly receiving stress, fibers failure exhibits brittle characteristic.

Complete Stress -Strain Curves. The stress-strain curves of confined cylindrical and quadrate specimens are similar, which can be divided into linear, strengthening and descending stages. At initial stage of loading, the stress and strain display a linear relationship, the confining effectiveness of the BFRP is not significant at this stage, and curves for confined and unconfined concrete column specimens take similar form. As the load increases, crack propagation increases in concrete, the lateral deformation increases. Due to BFRP effective confinement of the specimens, strain hardening stage follows, lateral deformation increases rapidly, the specimen stiffness significantly reduces. When loading reaches limit load, BFRP ruptures suddenly, causing an acute decrease in load-bearing capacity and the failure of specimens.

Experiment Data Analysis. Axial peak stress and peak strain of BFRP-confined concrete cylindrical and quadrate columns are listed in Table 1 and Table 2 respectively, where C and L show cylindrical specimens and quadrate specimens, the flowing numeral is the reinforcement layers.

Table 1 Bearing capacity and peak strain of concrete circular columns confined by BFRP

Number	Peak stress			Peak strain		
	Strength (MPa)	Average (MPa)	Increase (%)	Strain (10^{-6})	Average (10^{-6})	Increase (%)
C-0(1)	22.20			2980		
C-0(2)	29.09	27.88	—	3647	2912	—
C-0(3)	32.36			2110		
C-2(1)	51.76			14205		
C-2(2)	45.64	49.84	78.8	13200	12672	335.2
C-2(3)	52.13			10612		
C-3(1)	57.72			13446		
C-3(2)	54.72	56.52	102.7	12771	14674	403.9
C-3(3)	57.12			17806		
C-4(1)	66.91			18324		
C-4(2)	61.71	65.22	133.9	17301	18771	544.6
C-4(3)	67.04			20688		

Table 2 Bearing capacity and peak strain of concrete quadrate columns confined by BFRP

Number	Peak stress			Peak strain		
	Strength (MPa)	Average (MPa)	Increase (%)	Strain (10^{-6})	Average (10^{-6})	Increase (%)
L-0(1)	22.41			2024		
L-0(2)	19.41	19.67	—	3307	2745	—
L-0(3)	17.19			2903		
L-2(1)	44.65			13717		
L-2(2)	44.29	44.27	125.1	13683	14244	418.9
L-2(3)	43.88			15333		
L-3(1)	57.47			18875		
L-3(2)	56.06	56.84	189.0	16425	18189	562.6
L-3(3)	57.00			19268		
L-4(1)	60.35			16568		
L-4(2)	58.24	63.08	220.7	23834	21466	682.0
L-4(3)	70.65			23996		

Table 1 and 2 show that: (1) for cylindrical specimens, when the reinforcement layers are 2, 3 and 4, the peak-stress is higher than that of standard specimens by 78.8%, 102.7% and 133.9% respectively; whereas for quadrate specimens, when the reinforcement layers are 2, 3 and 4, the peak-stress is higher than that of standard specimens by 125.1%, 189.0% and 220.7% respectively. (2) for cylindrical specimens, when the reinforcement layers are 2, 3 and 4, the peak strain is higher than that of standard specimens by 335.2%, 403.9% and 544.6% respectively; for quadrate specimens, when reinforcement layers are 2, 3 and 4, the peak strain is higher than that of standard specimens by 418.9%, 562.6% and 682.0% respectively.

The data above indicates that the peak stress and peak strain of cylindrical and quadrate specimens significantly increased with the increase of reinforcement layers; applying BFRP confinement, the bearing capacity and ductility of specimens significantly improved.

Strength Model of BFRP Confined Specimens

Strength Model of Confined Cylindrical Specimens. Currently, FRP confined concrete strength models apply the form:

$$\frac{f'_{cc}}{f'_{c0}} = 1 + a\left(\frac{f_l}{f'_{c0}}\right)^b \tag{1}$$

Where f'_{c0}, f'_{cc} are unconfined and confined compressive strength of concrete respectively; f_l is the maximum lateral confinement stress produced on concrete when the tensile strength of FRP is attained, $f_l = 2t_f f_f / D$, t_f is the FRP thickness, f_f is the tensile strength of FRP, D is the diameter of the cylindrical column, a and b are the fitted regression function parameters.

Based on the data from this test, using nonlinear regression analysis methods, the strength of BFRP-confined concrete cylindrical columns is calculated as follows:

$$\frac{f'_{cc}}{f'_{c0}} = 1 + 3.6\left(\frac{f_l}{f'_{c0}}\right)^{1.18} \tag{2}$$

The average ratio of the experimental values of the model to calculated values is 0.997, the standard deviation is 0.052, which shows that the experimental data match the calculated values.

Strength Model of Confined Quadrate Specimens. For FRP-confined concrete quadrate columns, the lateral confinement is uneven, effective confinement is strongest near the diagonal angle, but relatively weaker between edges of the columns. In order to determine the effect of sectional shape on the confinement stress, cross-section shape factor K_s is considered, see equation (3) which is taken as the effective area to BFRP confinement region ratio:

$$k_s = \frac{b^2 - 4R^2 + \pi R^2 - 2W^2/3}{b^2 - 4R^2 + \pi R^2} \tag{3}$$

Due to stress concentration of the FRP fibers at the edges, failure is first observed at the corners. Tests have proved that, increase in the ratio between corner radius R, and side length b of square column, the confinement effectiveness is enhanced. In order to solve the problem of stress concentration around the corners, the lower corner stress concentration factor k_f is introduced, and calculated as shown in equation (4), where $k_i = 0.2121$.

$$k_f = \left\| 1 - \frac{\sqrt{2}}{2} k_i \right| \frac{2R}{b} + \frac{\sqrt{2}}{2} k_i \Bigg| \tag{4}$$

The compressive strength BFRP-confined concrete quadrate model takes the following form:

$$\frac{f'_{cc}}{f'_{c0}} = 1 + k_1 \frac{k_s k_f f_{el}}{f'_{c0}} \tag{5}$$

Where k_1 is the strength restraint factor, f_{el} is the BFRP lateral confinement stress, $f_{el} = 2t_f f_f / D$, where D is the equivalent circular cross-sectional column diameter taken as the diagonal length of the cross-section.

Based on the test data, using nonlinear regression analysis methods, strength restraint factor of BFRP-confined concrete quadrate columns is 9.10 and the strength is calculated as follows:

$$\frac{f'_{cc}}{f'_{c0}} = 1 + 9.10 \frac{k_s k_f f_{el}}{f'_{c0}} \quad (R^2=0.9692) \tag{6}$$

According to the above formula, the calculated results agree well with the test values.

Conclusions

The compression stress-strain complete curves of BFRP-confined concrete cylindrical and quadrate specimens were obtained. The stress-strain curve can be divided into three stages as ascending, strengthening and descending stages.

Compressive strength of BFRP-confined specimens increase with confinement layers, and the relationship is almost linear.

Compared with unconfined concrete specimens, the peak strain of 2-7 layers of BFRP-confined cylindrical and quadrate was increased by 3.4-8.4 and 4.2-9.6 times respectively.

With equal confinement layers, the compressive strength of cylindrical specimens is higher than that of quadrate specimens, as the stress concentration at the corners of quadrate specimens makes the fibers easy to rupture at the edges. Confinement effectiveness of quadrate specimens is lower than that of the cylindrical specimens.

References

[1] Z. Deng, D. Kan, X. Du, Experiment on behavior of concrete short columns confined by polyethylene fiber sheet under axial compression, Industrial Construction, 10 (2007) 69-72.

[2] J. G. Lam Teng, Strength models of fiber-reinforced plastic-confined concrete, Journal of Structural Engineering, 5 (2002) 612-623.

[3] Sergei, Properties of Basalt fibers and the prospect of its application in China, Fiber Glass, 4 (2005) 44-48.

[4] V. M. Karbhari, Y. Gao, Composite jacketed concrete confined under uni-axial compression-verification of simple design equations, Journal of Materials in Civil Engineering, ASCE, 4 (1997) 185-193.

[5] H. A. Toutanji, Stress-strain characteristics of concrete columns externally confined with advanced fiber composite fibers, ACI Materials Journal, 3 (1999) 397-404.

[6] A. Mirmiran, M. Shahawy, Behavior of concrete columns confined by fiber composites, Journal of Structural Engineering, 5 (1982) 583-590.

[7] Z. Deng, Y. Xu, Experiment and study on mechanical property of concrete square columns confined by IHFRP under axial compression, Highway, 7 (2011) 193-197.

© (2012) Trans Tech Publications, Switzerland
doi:10.4028/www.scientific.net/AMM.238.17

A Study on Structure and Properties of Basalt Fiber

Fengjun Shi

North China University of Water Resources and Electric Power, Zhengzhou 450011, China

shifengjun@126.com

Keywords: basalt fiber; composition; property.

Abstract. The structure and properties of a kind of domestic continuous basalt fiber is analyzed in the paper. Chemical composition, crystal structure, thermal properties, flammability, mechanical properties and morphology of the fiber are investigated. Element analysis experiment shows that the basalt fiber is a kind of aluminosilicate fiber which mainly composed of the oxides of such elements as Fe, Si, Ca, Al, K, Mo, Ti, Ba and so on. X-ray diffraction indicates that the bulk structure of the fiber is non-crystal with short range order. SEM observation finds that basalt fiber is circular in cross-section and smooth in longitudinal direction. Solubility experiment reveals the superior resistance of the fiber to acids, alkaline and organic solvents. DGA demonstrates there are three weight loss stages in the process of elevating temperature. There are, respectively, evaporation of moisture in the fiber at about 100^{o}C, decomposition of the residual carbonate minerals between 480^{o}C and 630^{o}C, and decomposition of newly generated carbonates between 850^{o}C~995^{o}C. In heatflow curve, there are also three endothermic peaks in which the first and the second correspond to the last two stages of weight loss and the third corresponds to melting process of the fiber and it onsets from 1122.14 ^{o}C, comes to its peak value at 1194.96 ^{o}C and ends at 1380 ^{o}C. The tensile strength of the basalt fiber is better than S-glass fiber, worse than carbon fiber. Flammability of the fiber is also analyzed.

Introduction

Basalt fiber is made from a single material, crushed basalt, which is composed of the minerals plagioclase, pyroxene, and olivine. Essentially no other materials are added. The basalt is simply washed and then sent to be melted down[1]. The manufacture of basalt fiber requires the melting of the quarried basalt rock at about 1,400°C (2,550°F). The molten rock is then extruded through small nozzles to produce continuous filaments of basalt fiber. The fibers typically have a filament diameter of between 9 and 13 μm which is far enough above the respiratory limit of 5 μm to make basalt fiber a suitable replacement for asbestos. They possess high thermal resistance, excellent corrosion and chemical durability. They also have a high elastic modulus, resulting in excellent specific tenacity—three times that of steel. They can be used as a fireproof textile in the aerospace and automotive industries and can also be used as a composite to produce products such as high pressure vessels (e.g. tanks and gas cylinders), load bearing profiles, windmill blades, and sports equipments. They can be used in concrete reinforcement (e.g. for bridges and buildings).

Although it is similar to glass fiber in manufacturing techniques, the processing of basalt fiber is more complicated and difficult because of its high melting point. There are only a few countries that are able to manufacture continuous basalt fiber at present[2]. So, as a kind of recently produced fiber, basalt fiber has not been thoroughly investigated in structure and properties. The chemical composition, structure, physical and mechanical properties of basalt fiber are measured in order to explain clearly fundamentals of the fiber and to provide the basis for further applications.

Experimental

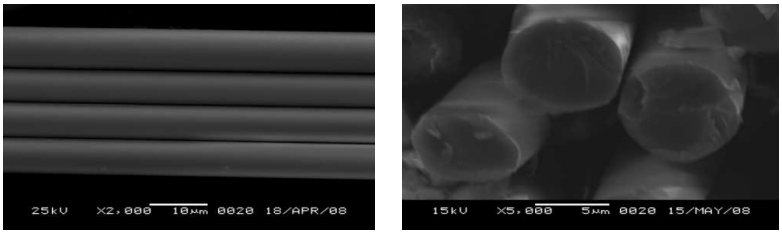
Specimen is twist-free basalt filaments with a linear density of XX tex. The diameter of the fiber is 10 mm.

Morphology of the basalt fiber is observed by JSM-6610 Scanning Electron Microscopy. The surface of the fiber is coated with a thin conducting layer. Here carbon is used for coating. The scanning voltage is 15 kv. The elements comprising the basalt fiber is quantitatively analyzed by

Shimadzu Energy dispersive X-ray Fluorescence Spectrometer EDX-720. The atmosphere is air and the collimator is 10 mm. Structure of the fiber is characterized by X-ray diffractometer. Scanning range is 0°～80°. Scanning speed is 4°/min. Thermal properties of the fiber are analyzed using Mettler Toledo TGA/DSC1, Differential Scanning Calorimeter and Thermogravimetric Analyzer. Sample is heated from room temperature to 1300 ^{o}C in 130 minutes. Tensile properties of the fiber are measured on USTERTENSOJET-4.

Results and Discussion

Scanning Electron Microscopy Observation. There has been some study by optical microscopy. The difficulty is not so much the limited resolution of the optical microscopy, but is the lack of depth of focus. So it can not show up clearly the complex shape of a broken fiber end. SEM has great depth of focus and can give a clear three-dimensional image. It can be found by SEM observation that Basalt fiber is circular in cross-section and smooth in longitudinal direction, as shown in Fig.1.



(a) longitudinal direction (b) cross section

Fig. 1 Scanning electron microscopy observation of basalt fiber

Composition. Energy-dispersive X-ray spectroscopy (EDS) is an analytical technique used for the elemental analysis or chemical characterization of a sample. Using the X-ray fluorescence spectrometer, elemental composition, especially metals, of sample can be rapidly determined. The elements comprising a basalt fiber is measured and listed in Table 1. It can be found that the main elements comprising the basalt fiber are Fe, Si, Ca, Al, K, Mo and so on. The sum of the elements Fe, Si, Ca and Al make up 87% of the total metal elements.

Table1 Quantitative result of basalt fiber

Analyte	Result (%)	Analyte	Result (%)	Analyte	Result (%)
Fe	36.020	Mo	2.066	S	0.429
Si	26.304	Ti	1.778	Cr	0.094
Ca	17.239	Ba	1.303	Zr	0.090
Al	7.432	Mn	0.610	Cu	0.080
K	6.028	Sr	0.479	Zn	0.049

The composition of the basalt fiber varies with its place of origin. The density of the continuous fiber is about 2.6-3.05g/cm^3. Main compositions of the fiber are listed in Table 2. Basalt fiber is composed of such oxides as SiO_2, Al_2O_3, CaO, FeO, MgO et al. The fiber is belonging to aluminosillicate fiber. So, main composition of the fiber is SiO_2 which contributes chemical stability and excellent mechanical properties. High mass ratio of Al_2O_3 gives the fiber durability, chemical and thermal stability, as well as tensile properties. Ferric oxide has effects on melting parameters and conductivity. It gives the fiber brown color [3]. The basic properties of Basalt fiber depends on its chemical composition and processing of production [4]. Silicon oxide, as main composition of the fiber, has favorable effect to elasticity and chemical stability of basalt fiber [5]. Iron oxide can change melting parameters and affect thermal conductivity of basalt fiber [6]. Alumina can improve the viscosity and chemical resistance of the basalt melt.

Table 2 Mass ratio of the oxide in Basalt fiber (%)

SiO_2	Al_2O_3	CaO	FeO	MgO	Na_2O	Fe_2O_3	K_2O	TiO_2	P_2O
51.4	14.83	10.26	8.47	5.92	2.42	1.73	1.20	0.84	0.32

X-ray Diffraction. X-ray diffraction pattern of a crystal is virtually a kind of sophisticated transformation of its microstructure. There is a correspondence between the structure and diffraction pattern for every crystal. Although a material may be composed of a variety of substances mixed together, the characteristic diffraction pattern for every substance does not change. The X-ray diffraction spectroscopy of basalt fiber is shown in Fig. 2. It can be seen there is no obvious diffraction peak but only a characteristic weak peak of typical glass state substances between 20°~30°. This indicates that basalt fiber is amorphous and there is no crystal in the fiber. Taking the composition of the fiber into account, bulk structure of the basalt fiber is a chainlike skeleton structure which mainly composed of 4 corner-sharing tetrahedral [SiO_4]. Al_2O_3 joins in the network structure in the form of [AlO_4]. And other oxides are either filled in the internal structure or absorbed around the network. So, there is short range order but without long range order in bulk structure of the basalt fiber [7].

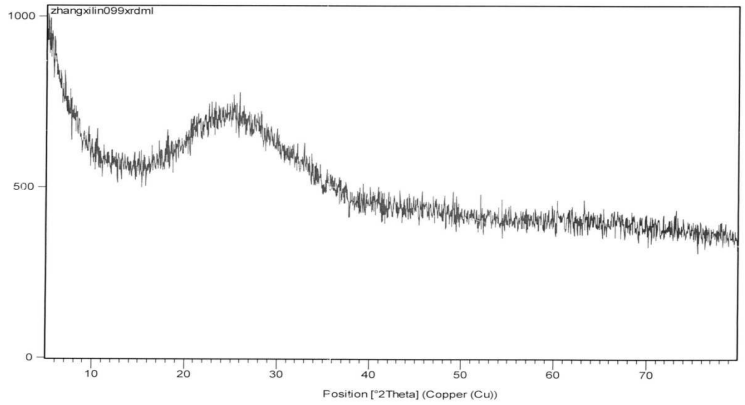


Fig. 2 The X-ray diffraction spectroscopy of basalt fiber

Chemical Properties. Unlike metal, basalt fiber is not affected by corrosive mediums. It has excellent resistance to alkalis as there are a variety of oxides(TiO_2, MgO, Fe_2O_3, Al_2O_3) in the fiber. Unlike fiber glass is almost not affected by acids. Basalt fiber possesses high corrosion resistance and good chemical durability to such solutions as salts, acids and, especially, alkalis [8, 9].

The solubility of materials in a solution changes with type and concentration of the solvent as well as temperature. Fibers can be identified by observing their solubility in different solvents. The solubility of basalt fiber in different solvents is listed in Table 3. It can be noted that the fiber does not dissolve in such inorganic solvents as 98% sulfuric acid, 65% hydrochloric acid, 68% nitric acid, 80% formic acid and 40% sodium hydroxide below 100°C. It is not soluble in organic solvents such as 75% formic acid—zinc chloride, glacial acetic acid, phenol, acetonitrile, nitrobenzene et al at temperature of 100°C. However, basalt fiber can be dissolved in Hydrofluoric acid at 25°C.

Table 3 Solubility of basalt fiber in different solvents

Solvent	Temperature (^oC)	Solubility
10% ~ 98% sulfuric acid	100	insoluble
10% ~ 65% hydrochloric acid	100	insoluble
10% ~68% nitric acid	100	insoluble
30% ~ 80% formic acid	100	insoluble
10% ~ 40% sodium hydroxide	100	insoluble
75% formic acid—Zinc chloride	100	insoluble
Glacial acetic acid	100	insoluble
Phenol	100	insoluble
Acetonitrile	100	insoluble
Nitrobenzene	100	insoluble
Hydrofluoric acid	25	soluble
Dimethyl sulfoxide	100	insoluble
Dichloromethane	100	insoluble
5% Ethyl acetate	100	insoluble
Carbon tetrachloride	100	insoluble
Xylene	100	insoluble
Pyridine	100	insoluble
65% Potassium thiocyanate	100	insoluble

Thermal Analysis. TGA/DSC1 Synchronous Thermal Analyzer can measure heat flow and weight variation of sample with the change of temperature or time. DGA/Heatflow curve of the basalt fiber is shown in Fig. 3. It can be observed there are three stages of weight loss in DGA curve. Firstly, the weight of the fiber decreases starting from 30 °C and ending at 150 °C in the DTG curve. Obviously, this is attributed to evaporation of the moisture absorbed in the fiber. The rate of weight loss for the desorption process is -2.48% which equals to water content of the fiber in magnitude. The second is a sharp reduction of 22.18% in weight of the fiber between 480 °C and 630 °C. This may be attributed to the decomposition of the residual carbonate minerals in the fiber. The third weight loss occurs at 850 °C ~995 °C, owing to the decomposition of newly generated carbonates [10]. The rate of weight loss is 1.06%. That is to say, the total weight loss of the fiber is only about 26% in the process of being heated from room temperature to high temperature of 1300 °C. It can clearly be seen that thermal stability of the fiber is very good.

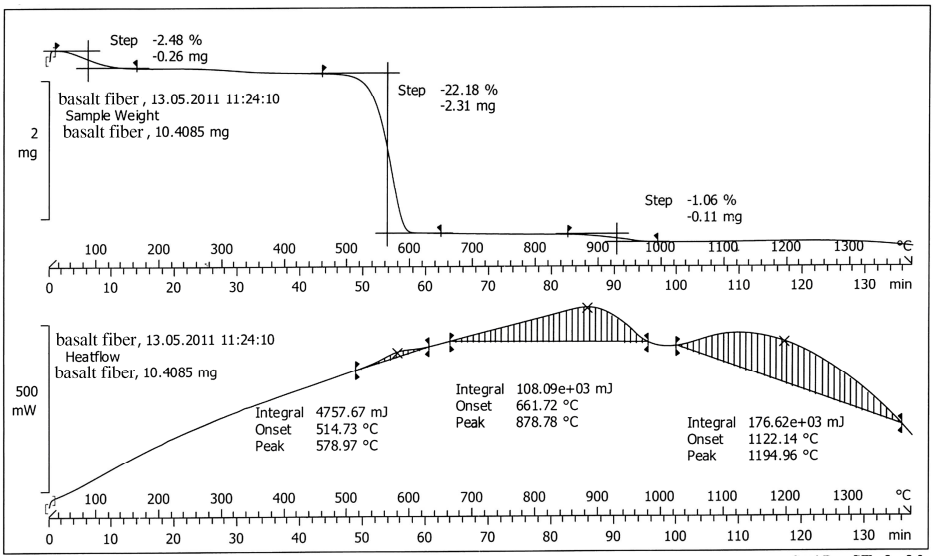


Fig. 3 DGA/Heatflow curve of the basalt fiber

There are also three endothermic peaks in corresponding heatflow curve of the fiber. The first takes place between 514.73 °C and 620 °C, with a peak value of 578.97 °C and integral heat of 4757.67 mJ. This is corresponding to the second weight loss stage in DGA curve. The second endothermic peak in heatflow curve onsets at 661.72 °C, reaches its summit at 878.78 °C and has a integral heat of 108.09×10^3 mJ. It is corresponding to the third weight loss stage in the DGA curve of the fiber. With the rising of temperature, there is third endothermic peak which begins from 1122.14 °C, comes to its peak value at 1194.96 °C, ends at 1380 °C and has an integral heat of 176.62×10^3 mJ. In this stage, there is almost no weight loss in the process of elevating temperature. So it indicates that the structure of the fiber is gradually destroyed and it melts continuously. The fiber melts completely at 1380 °C.

Flammability. Flammability of fibers in combustion process can be determined through observing the phenomenon occurred, order produced and ash left when it approaches the flame, is put in the flame and after it is removed from the flame.

Basalt fiber does not melt and shrink when it approaches flame. It will curl slightly and redden like an iron wire when it is contacted with the flame. And white smoke is given off when the fiber is gotten in touch with the fire. There is a little pungent flavor when burning. The fiber will stop burning when it leaves the flame. There is coke-like, crushable remains.

Table 4 Comparison of tensile properties of fibers

Property	Basalt Fiber	S-glass fiber	Carbon fiber
Tensile strength (GPa)	4.84	4.26	5.10
Elastic modulus (GPa)	89	85	241
Elongation at break (%)	3.15	5.3	1.5~2.0
Density (g/cm³)	2.65	2.49	1.80

Tensile Properties. Tensile properties of the fiber are tested and compared with S-glass fiber and carbon fiber, as listed in Table 4. It can be seen that the tensile strength and modulus of basalt fiber are larger than that of S-glass fiber, but smaller than that of carbon fiber. Its elongation at break is larger than that of S-glass fiber but smaller than that of carbon fiber. So, basalt fiber offers performance similar to S-2 glass fibers [11] at a price between S-2 glass and E-glass, and may offer manufacturers a less-expensive alternative to carbon fiber [1].

Conclusions

The basalt fiber is a kind of aluminosillicate fiber which mainly composed of the oxides of such elements as Fe, Si, Ca, Al, K, Mo, Ti, Ba and so on.

X-ray diffraction indicates that the bulk structure of the fibers is non-crystal with short range order but no long range order.

The fiber has a superior resistance to most acids, alkaline and organic solvents. It is only soluble in hydrofluoric acid in the extent of the experiment.

Thermal analysis shows that there three stages including a moisture evaporation and two decomposition process. The total weight loss in the temperature elevating process from room temperature to 1300 ^{o}C is about 26%. And the melting process onsets at 1122.14 ^{o}C, ends at about 1380 ^{o}C. The thermal stability of the basalt fiber is excellent.

References

[1] http://www.compositesworld.com/articles/basalt-fibers-alternative-to-glass.

[2] T. Czigany, K. Poloskei and J. Karger-Kocsis, Fracture and failure behavior of basalt fiber matreinforced vinylester/epoxy hybrid resins as a function of resin composition and fiber surface treatment, Journal of Materials Science, 2005.

[3] M. Swink, Cotinuous filament basalt--a unique fiber capable of leadership in high temperature applications, Techtextil North America Symposium, Atlanta, GA, USA, 2002.

[3] V. V. Gurev, E. I. Neproshin, G.E. Mostovoi, The effect of basalt fiber production technology on mechanical properties of fiber, Glass and Ceramics, 58 (2001) 62-65.

[4] L. Xu, A new high-performance fiber---applications of basalt fiber, New Textile, 9-10 (2005) 15-17.

[5] M. A. Sokolinskaya, L. K. Zabava, T. M. Tsybulya, et al, Strength properties of basalt fibers, Glass and Ceramics, 49 (1992) 435-437.

[6] B. Sang, S. Yang, Research progress of basalt fiber reinforced polymer composites, Chemical Industry and Engineering Progress, 8 (2011) 135-140.

[7] B. E. Ramachandran, V. Velpari, N. Balasubramanian, Chemical durability studies on basalt fibers, Journal of Materials Science, 16 (1998) 3393-3397.

[8] M. Wang, Z. Zhang, Y. Li, et al, Chemical durability and mechanical properties of alkali-proof basalt fiber and its reinforced epoxy composites, Journal of Reinforced Plastics and Composites, 27 (2008) 393-407.

[9] J. Lei, X. A. Dang, H. Zhang, J. Li, Analysis on basalt ore and crystallization temperature of basalt melt, Journal of Shaanxi University of Science & Technology, 25 (2007) 63-66.

[10] J. Militky, V. Kovacic, V. Bajzik, Mechanical properties of basalt filaments, Fibers & Textile in Eastern Europe, 15 (2007) 49-53.

© (2012) Trans Tech Publications, Switzerland
doi:10.4028/www.scientific.net/AMM.238.22

Study of Road Property of Basalt Fiber Asphalt Concrete

Yuanzhao Chen [a] and Zhenxia Li [b]

School of Civil Engineering and Communication, North China University of Water Resources and Electric Power, Zhengzhou 450011, China

[a] cyz740513@ncwu.edu.cn, [b] zhenxiali2009@ncwu.edu.cn

Keywords: road engineering; road property; study; asphalt concrete; stability; crack resistance.

Abstract. In order to discuss the effectiveness of basalt fiber in reinforcing pavement performance of asphalt mixtures, the pavement performances of basalt fiber asphalt mixtures were investigated by tests of high temperature stability, water stability and low temperature crack resistance, and compared with the pavement performance of asphalt mixtures with polyester fiber and xylogen fiber, and that of reference mixture. The results show that pavement performance of fiber asphalt mixture are improved and optimized comparing with reference asphalt mixture, the performance of asphalt mixture with basalt fiber are excelled than those with polyester fiber and xylogen fiber while the dosage of fibers is keeping at the optimum.

Introduction

Asphalt pavement has been widely used in express highway for its merits of smooth, comfortable travel, low-noise and so on. However, early damage of asphalt pavement becomes more and more serious with the continued increasing of axle load and traffic; therefore, asphalt concrete should be modified in some way to promote its pavement performance. Among those modifiers of asphalt concrete, fibers have obtained more and more attention for their excellent improvement effects and its merits of simple construction and economic cost. The mechanism of action and improvement effects of various types of fiber modifier such as methyl cellulose and polyester have been investigated in depth, moreover, some research finding have been gained. As a kind of new additive and stabilizer of asphalt concrete which appearing after methyl cellulose and polyester, basalt fiber obtained widely attention for its excellent technical characteristics. The basalt fiber not only makes up for the drawback of low strength, elastic ratio and weak high temperature resistance of organic fibers, but also overcomes the drawback of environmental pollution of mineral fibers such as asbestos fiber. In 1990s, the first basalt fibers modifier pavement was built in of the American state of Georgia and showed excellent pavement performance. Up to now the research about the pavement performance of basalt fiber asphalt binder is limited in china. To study the pavement performances of basalt fiber-reinforcing asphalt concrete by tests of high temperature stability test, water stability test and low temperature crack resistance test are carried out, moreover compared with pavement performance of polyester fiber, xylogen fiber, and control mixture.

Materials and Mineral Mixtures Grading

Mineral Mixtures Selection and Grading. Limestone and limestone mineral admixture produced by Yongli quarry in Liaoyang. Selected mix gradation of test is shown in Table.1.

Table 1 Mineral mixtures grading

Gradation type AC-16	Mass percent which passed the following sieves (mm)										
	19	16	12.5	9.5	4.75	2.36	1.18	0.6	0.3	0.15	0.075
Upper limit of standard	100	100	90	80	62	48	36	26	18	14	8
Lower limit of standard	100	95	75	58	42	32	22	16	11	7	4
Selected gradation	100	98	85	66	50	42	31	22	15.2	8.5	6.5

The Major Indexes of Fibers. The major technical indexes of experimentation fibers are showed in Table.2.

Table 2 Major technical indexes of experimentation fibers

Test items	Basalt fiber	Polyester fiber	Xylogen fiber
Color	Silver gray	white	
Diameter of fiber (μm)	15	15	45
Length (mm)	12	12	1.2
Specific gravity (g/cm^3)	2.56-3.05	1.38	0.91
Melting point (^{o}C)	1050	>256	170
Moisture content (%)	<0.1	2.0	12-15
Tensile strength (MPa)	3000-4840	500	<300
Young's modulus of elasticity (GPa)	>40	16-19	3.5
Elongation at break (%)	3.2	15-30	15-25

High Temperature Rutting Test. In accordance with literature, measured the 60 ^{o}C dynamic stability of comparison group of AC-16 asphalt concrete, the basalt fiber, polyester fiber and xylogen fiber asphalt concrete (fiber content was 0.15%, 0.30% and 0.45% separately) under the condition of each optimum bitumen-aggregate ratio. The test results were shown in Fig. 1.

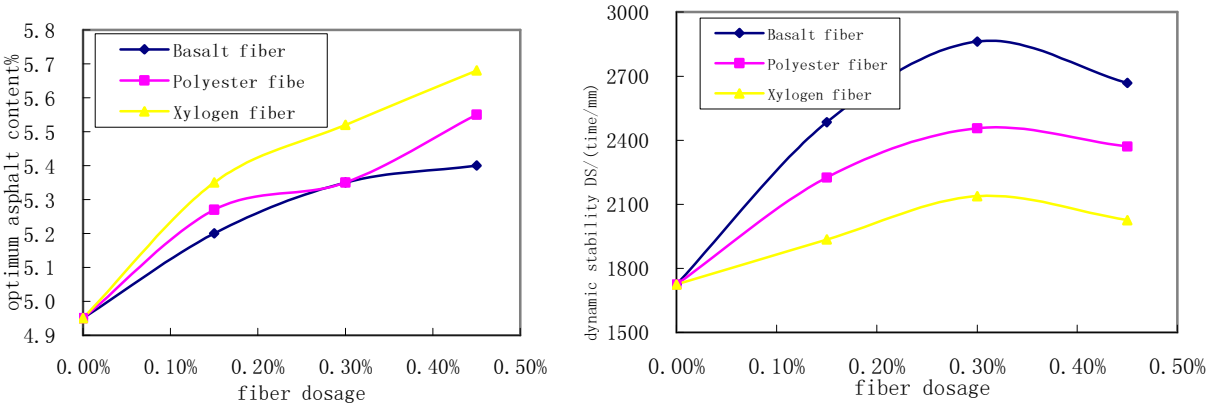


Fig. 1 Relationships between fiber content and asphalt content, dynamic stability

Compared with control asphalt concrete, the dynamic stability of fiber asphalt concrete by has improved significantly. When the fiber dosage was 0.30%, the dynamic stability of basalt fiber, polyester fiber and xylogen fiber asphalt concrete increased 66%, 42% and 24%, respectively. Thus, the addition of fiber can significantly improve the high temperature performance of asphalt concrete. Analysis of its causes, on the one hand the bridge joint effects formed by a large number of crisscross distribution fibers interloped and complemented with asphalt mortar cohesion, which would prevent the slippage of aggregate, to withstand the temperature generated as tensile stress make up the cohesion of the asphalt, thus resulting in improving of high temperature stability of asphalt concrete; the other hand, fiber diameter generally less than 20μm, the surface area per gram of fiber up to a few square meters, and its huge surface area and asphalt infiltration form the interface layer which buffers the stress among various phases of asphalt concrete as a kind of composite material, modified asphalt by fibers and the formation of chemical bonds in the interface layer increased the viscosity of asphalt, reducing the temperature susceptibility of asphalt, thereby high temperature stability of asphalt concrete is increased. It is can be seen from the Fig. 1, at certain dosage the fiber reinforced effect for high temperature properties of asphalt concrete achieves the best, which is called the optimum dosage, the optimum dosages of basalt fiber, polyester fiber are about 0.30%, for xylogen fiber is about 0.25%. When the fiber dosage exceed optimum content, the dynamic stability of fiber mixture began to decreasing or instability wave, the reason is excessive fibers lead to the decreasing of its dispensability, and those undiversified fiber bundle and becomes "flaw point" of asphalt concrete, the effect of modification, viscosity, and reinforced of fiber cannot be exploited fully, or even reduces the high temperature stability of asphalt concrete.

Water Resistance Test

Test calculation results were shown in Table 3. It can be seen that the residual stability of three asphalt concrete all meet the requirements of standard and increased in some degree, compared with polyester fiber and xylogen fibers, basalt fibers the effect of basalt for improving the Marshall stability and immersed stability of asphalt concrete was more significant. Under the optimum fiber dosage, immersion Marshall stability of basalt fiber, polyester fiber and xylogen fiber asphalt concrete was increased by 61.2%, 39.6% and 22.2%, residual stability was increased by 10.3%, 7.5% and 5.7%, respectably. Analysis of the main reasons are because the addition of fiber increased the dosage of asphalt in mixture, which increased the effective film thickness of mineral materials, thus effectively reducing the possibility of water effective between asphalt interface and mineral aggregate, and further increased residual stability of asphalt mix; besides, addition of fiber can fill in some void of asphalt mix, and decreasing the void ratio inside asphalt mix, and the addition of fiber also increased viscosity of asphalt. From the freeze-thaw test results it can be seen comparing to control mix the freezing splitting tensile strength and not freezing splitting tensile strength of fiber asphalt concrete are improved to some extent, not freeze-thaw splitting strength of basalt fiber, polyester fiber and xylogen fiber asphalt concrete increased by 36.4%, 15.4% and 6.2%, freeze-thaw splitting strength increased by 55.2%, 28.7% and 14.5%. The reason is mainly due to more porosity of control mixture comparing to fiber mix, during the freezing and thawing process; the water generated frost stress on void wall, and promoted the spilling between asphalt and aggregate.

Table 3 Test result of water stability of fiber reinforced asphalt concrete

Mix type	The immersed Marshall test			The freeze-thaw splitting test		
	Stability (kN)	Immersed stability (kN)	Residual stability (%)	Splitting tensile strength without freezing (MPa)	Freezing splitting tensile strength (MPa)	Not freeze-thaw splitting intensity ratio (%)
Control	8.52	7.27	85.4	0.825	0.670	81.2
Basalt fiber	12.45	11.72	94.2	1.125	1.040	92.5
Polyester fiber	11.06	10.15	91.8	0.952	0.862	90.5
Xylogen fiber	9.83	8.87	90.2	0.905	0.767	84.8

Low Temperature Crack Resistance Test

The low temperature cracking is one of the main damage of asphalt pavement, which seriously affects the pavement serve life. According to literature, The bending test of small beam at low temperature -10^{o}C was employed to evaluate the effect on low temperature resistance crack of basalt fibers. The MTS material tester imported from USA was employed to carry out the test, and the method of load is centralization loading, the test data were collected by computer automatically. The test results were showed in Table 4.

Table 4 Test result of low temperature crack-resistance of fiber reinforced asphalt concrete

Mix type	Limiting flexural-tensile strength (MPa)	Failure strain ε_{μ} (10^{-3})	Curveing stiffness modulus (MPa)
Control	9.134	7.45	8980
Basalt fiber	10.747	10.78	11925.1
Polyester fiber	10.523	10.15	10132.5
Xylogen fiber	10.236	9.85	9835.2

Test results show that limiting flexural-tensile strength, failure strain and curveing stiffness modulus of fiber mixture were all improved significantly comparing with control mixture. The reasons are that addition of fiber makes the best asphalt dosage increased which result in the improving of stress relaxation performance and bending strength of the asphalt concrete on the one hand, on the other hand, the reinforcement effects of fiber itself on asphalt concrete ensure the improve of flexural-tensile strength of asphalt concrete, thus, the low temperature crack resistance of asphalt concrete can be improved by fibers. Compared with the polyester fiber and xylogen fiber, the reinforcement effects of basalt fiber on low temperature crack resistance performance is more obvious. The flexure strength, failure strain and bending strength modulus has improve 17.7%, 44.7% and 32.8% respectively.

Conclusions

Through test of various fibers dosage, optimum basalt fiber dosage (weight) was gained as 0.3% which corresponding with the optimum asphalt ratio of 5.35%. The test results shown rutting stability of asphalt mix can be improved significantly for addition of fiber. Compared with polyester fiber and xylogen fiber, the improved effects of basalt fiber for high temperature stability of asphalt mix is more effectively. Rutting stabilities of basalt fiber asphalt concrete increase by 66% and 47%.

Under optimum fiber dosage, water stability of asphalt mix can be improved effectively by addition of fibers, and immersed residual stability and freeze-thaw splitting strength were all improved markedly. Compared with polyester fiber and xylogen fiber, under the same experimental conditions, the basalt fiber can more effectively improve the water stability performance of asphalt concrete. Its immersion Marshall stability, residual stability, freeze-thaw splitting strength and no freeze-thaw splitting strength ration increase by 61.2%, 10.3%, 55.2% and 13.9% respectively.

The results show that the improvement effects for low temperature crack resistance of asphalt concrete are remarkable by addition of fiber, and compared with polyester fiber and xylogen fiber, the improvement effects of basalt fiber is better. Its flexural-tensile strength, failure strain and b Curveing stiffness modulus increase by 17.7%, 44.7% and 32.8%.

Test results demonstrate that the basalt fibers improve pavement performance of asphalt concrete, significantly, and among these three types of fiber, basalt fiber shows the most integrated positive effect on pavement performances, thus, is worth promotion and application.

References

[1] Asi Ibrahim, Shalabi Faisal, Naji Jamil, Use of basalt in asphalt concrete mixes, Construction and Building Materials, 23 (2009) 498–506.

[2] S. Wu et al, Effects of fiber additive on the high temperature property of asphalt binder, J Wuhan Univ. Technol., 21 (2006) 28–31.

[3] Q. Ye, S. Wu, N. Li, Investigation of the dynamic and fatigue properties of fiber-modified asphalt mixtures, International Journal of Fatigue, 31 (2009) 1598–1602.

[4] J. P. Serfass, Application and behavior of fiber modified asphalt, AAPT, 64 (1995) 40–50.

© (2012) Trans Tech Publications, Switzerland
doi:10.4028/www.scientific.net/AMM.238.26

A Review of Steel–polypropylene Hybrid Fiber Reinforced Concrete

Xiaoke Li[1,2a], Li Sun[1,b], Yiyi Zhou[2c] and Shunbo Zhao[1,d]

[1]North China University of Water Resources and Electric Power, Zhengzhou 450011, China

[2]School of Civil, Environmental and Chemical Engienering, RMIT University, Melbourne, Victoria 3001, Australia

[a] lixk@ncwu.edu.cn, [b] sunli627101421@163.com, [c] yiyi.zhou@rmit.edu.au, [d]sbzhao@ncwu.edu.cn

Keywords: steel-polypropylene hybrid fiber reinforced concrete; strengthening principle; mix proportion design; mechanical behavior; durability.

Abstract. The steel-polypropylene hybrid fiber reinforced concrete can take full advantages of macro-scale crack resistance and toughening effect on the concrete matrix of steel and polypropylene fibers. The shortcomings of concrete are improved and there is a wide prospect application in engineering. This paper summarizes the enhancement theories of hybrid fiber reinforced concrete to explain its strengthening mechanism. The research status is reviewed including mix proportion design, working performance of fresh concrete, mechanical behaviors, durability (impermeability, shrinkage and others), and engineering applications etc. Some further researches are forecasted. It would be very useful to apply and popularize steel-polypropylene hybrid fiber reinforced concrete.

Introduction

The concrete performance will be improved by mixed fibers with high tensile strength, excellent toughness, short length and slender shape. It has proved that the fibers with high elastic modulus could effectively enhance the tensile strength and toughness of concrete [1]. The long-term strength of concrete has not significantly improved by mixing fibers with low elastic modulus. But this type of fiber is beneficial to restraining the early plastic shrinkage crack and reducing the drying shrinkage deformation. To improve crack resistance and mechanical behavior during the whole operation life, a new type of concrete, hybrid fiber reinforced concrete is applied, which mix various fibers in different elements and structures. The size and performance effects of different fibers will give their play in the right time and suitable place. Thus all components and materials can make their best of mechanical behaviors.

Now more study on hybrid fiber reinforced concrete is about the hybrid of high elastic modulus fiber such as steel fiber, carbon fiber and glass fiber, with low elastic modulus high ductility synthetic fiber such as polypropylene fiber and polyethylene fiber, among them the hybrid of steel fiber and polypropylene fiber is widely applied. A lot of research revealed that the hybrid of steel fiber and polypropylene fiber in concrete could make use of the composite advantages of two fiber material properties, effectively improve the interface condition between cement and aggregate, constraint the occurrence and development of concrete crack, and enhance material medium continuity of the concrete [1-3]. The concrete is mainly used in underground waterproof projects, road and bridge engineering and seismic structures. It has bright application prospect in the future. In this paper a general review of literature on steel-polypropylene hybrid fiber reinforced concrete would be given according to Fig. 1. Some questions and unclear points about the study are summarized. It is very useful for the researchers who want to do more works about this material.

Hybrid Fiber Reinforced Theory

There are mainly two theories to explain the strengthening mechanism of hybrid fiber reinforced concrete. One is composite material mechanics theory based on composite material mixed rate law; the other is fiber spacing theory based on elastic fracture mechanics [4].

Composite Material Mechanics Theory. Fiber reinforced composite material is considered as a multiphase system in composite material mechanics. The strength and elastic modulus can be obtained by superimposing the corresponding values in each phase when it is in the elastic stage. Fiber reinforced concrete strength is advised, considered the fiber bonding force with different concrete matrix and length-diameter ratio. The synergistic effect from fiber continuity, scattered uniformity and direction of distribution are also taken into account [5].

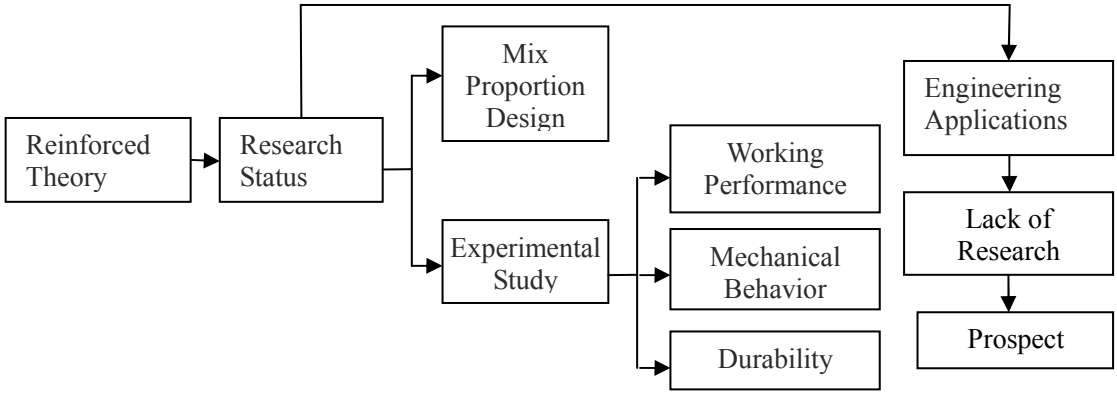


Fig. 1 Flow Chart

Composite material mechanics theory is built on condition that fibers are extracted from the matrix, this is, the bond failure between fibers and matrix happen. In the meanwhile, the effective fiber volume proportion of the composite along the direction of tensile stress and the length of discontinuous short fibers should be revised to coincide with the fact as nearly as possible.

Fiber Spacing Theory. Fiber spacing theory is based on elastic fracture mechanics theory. The theory shows that there are inherent defects in concrete. With structural forces increasing, the cracks will be widened and expanded, more cracks occur, penetrating cracks would be gradually formed and structural deflection would be increased till to rupture failure. The mixed fibers could improve the concrete inherent defects, enhance concrete toughness, reduce stress concentration at end of cracks and prevent internal cracks occur and expand. That is, the concrete will be strengthened. In certain fiber volume content, tensile strength of fiber reinforced concrete is approximately proportional to fiber spacing [5].

It is assumed in fiber spacing theory that the bond between fiber and matrix is in good condition, however there must be some weak parts existed. The fiber spacing is involved with the effect of different fiber length, fiber diameter and mix proportion. The corresponding formula has been put forward. But when it exceeds the concrete proportional limit, fiber reinforced mechanism wouldn't be described objectively with this theory.

Research Status

Mix Proportion Design. Orthogonal design is a popular method to deal with hybrid fiber reinforced concrete mixture design, which the level of various factors usually bases on the experience and the fiber content are decided by additive method. Wang [6] studied mix proportion design of hybrid fiber reinforced concrete by selecting six factors such as water-binder ratio, sand ratio, steel fiber content, polypropylene fiber content, unit water and the fly ash content. With interaction between steel fiber content and polypropylene fiber content, the parameters of six factors were optimized to seek the optimum proportion of hybrid fiber reinforced concrete. Liu [7] designed mix proportion and studied the strength and toughness of hybrid fiber reinforced concrete by different steel fiber type, volume ratio, steel fiber length, steel fiber diameter ratio and polypropylene volume ratio. The results showed polypropylene fiber volume ratio had great influence on compressive strength, tensile strength and ratio of tensile strength to compressive strength. The steel fiber appearance and steel fiber volume ratio is the second and steel fiber length, steel diameter ratio is the least. Researchers in China who applied orthogonal test method to design mix proportion also include Chen [8], Wang [9], Singh et al [10] applied fixed benchmark mix

proportion on the tests of strength and flexural toughness of steel-polypropylene hybrid fiber reinforced concrete, which fiber content were decided by additive method. The hybrid ratio of two kinds of fibers was discussed and the advised value was given. Luca Sorelli [11] also used similar mix proportion design method in uniaxial test of hybrid fiber reinforced concrete.

The code about synthetic fiber reinforced concrete have been added into the newly revised technical specification [12] and part of steel fiber reinforced concrete also been revised. But it was still vacant in hybrid fiber reinforced concrete and there are not the detailed specifications and technical documents about applying hybrid fiber reinforced concrete to guide engineering design.

Wu [13] in his study about mechanical behavior of basalt fiber reinforced concrete mentioned that when basalt fibers were put into the mixture and then were split into very fine flocculent filaments, these filaments would been packaged with a lot of cement mortar and the mix fluidity was weakened. Gao Danying [14] mentioned that steel fiber surface should be full of mortar to ensure the quality of steel fiber reinforced concrete. But research of hybrid fiber reinforced concrete considering mortar thickness to design mixture proportion has not been reported.

Working Performance of Fresh Concrete. The added fibers could increase the viscosity of fresh concrete. The fine fibers which usually have great specific surface area need a lot of grout to wrap around them and thick fibers would "hold" concrete component. Thus the viscosity of fresh concrete will be increased, the segregation and weeping will be reduced and the fluidity will be decreased.

The hard works from Wang [15] showed that there was great influence on working preference of fresh concrete by mixing fiber. The slump was proportional to the specific surface area of fiber, the slump flow was declined obviously and fluidity was also decreased. All these proved that the fibers which were distributed uniformly in the concrete would play a “hold” function and concrete cohesiveness was improved. B.Babal [16], Yang[17] also got the similar results.

Mechanical Behavior-Compressive Strength. As one of basic mechanical behaviors to evaluate concrete, compressive strength of steel-polypropylene hybrid fiber reinforced concrete will be changed by fibers with different physical and mechanical performance, fiber hybrid ratio and fiber total content. Yao Wu [18] studied mechanical behavior of high performance concrete with low volume content (fiber total volume content was 0.5%). It showed that compressive strength of normal concrete reached 44.3MPa. Compressive strength of hybrid fiber reinforced concrete with steel fiber (0.2%) and polypropylene fiber (0.3%) was 45.3MPa, only 2.23% higher compared with benchmark concrete. That is, there was hardly any influence to compressive strength of fiber reinforced concrete.

Sun [19] carried out mechanical behavior tests of steel-polypropylene hybrid fiber reinforced concrete and the results showed that the overall increase of compressive strength was greater 10% ~ 31% than C30 benchmark concrete. Wang [20] studied the effect on strength and toughness of low content steel-polypropylene hybrid fiber reinforced concrete. It suggested that the lower dosage of hybrid fiber could not bring the obvious enhancement of compressive strength, compared with its normal concrete, only increased 10.5% or so. However because of mixing fibers, the ductility would be increased when concrete was compressed to failure. The sudden decreasing and collapse of concrete compressive strength would never happen. After it reached peak value, compressive strength would reduce gradually and the damage signs could be observed. It showed that hybrid fiber reinforced concrete would be ductile damage. Other literatures [21-23] also showed that the hybrid of steel-polypropylene fiber had little effect on compressive strength like the former. Compressive strength would be decreased with the increasing of polypropylene fiber content.

Mechanical Behavior-Tensile and Flexural Strength. It is not obvious to enhance concrete compressive strength by mixing steel-polypropylene hybrid fiber. But it is one of effective ways to improve the toughness, crack resistance and other concrete performances [1]. Literature [20] and [21] showed that hybrid fiber was beneficial to promoting concrete tensile and flexural strength and revealed the superimposition effect caused by mixing different fibers. Steel fiber and polypropylene fiber together formed three dimensional unordered supporting net. To some certain extent, it made up for the initial concrete defects and tensile strength of concrete matrix would be improved. “Fiber

Chain" effect caused by steel fiber and polypropylene fiber winding together would increase the flexural strength of the specimens more. M.I.El-Hamrawy, A.M.Saba [24] studied the fracture energy of hybrid fiber reinforced concrete. The results showed that the smaller synthetic fiber would bridge micro-cracks, control crack propagation and delay micro-cracks to be merged. Then tensile strength was improved. The bigger steel fiber would restrain main cracks expansion and then fracture toughness would be enhanced. S.Eswari, P.N.Raghunath[25] analyzed flexural strength and toughness model of hybrid fiber reinforced concrete with regression method. The results showed that flexural strength and flexural toughness could been increased 81.0% and 31.42% respectively compared with normal benchmark concrete and could been increased 22.22% and 12.15% respectively compared with same dosage of end curved hooked steel fiber reinforced concrete. All studies proved that concrete mixed with steel-polypropylene hybrid fiber could boost tensile and flexural strength significantly because of cracking resistance by fiber.

Durability-Impermeability. It is less relatively to study the durability of steel-polypropylene hybrid fiber reinforced concrete. The most achievements focused on crack resistance, seepage control and frost resistance etc., especially on anti-permeability. However, it is regretful that the study about anti-permeability of hybrid fiber reinforced concrete doesn't have yet to agree on.

Wang [15] carried out a serial of tests about anti-permeability of hybrid fiber reinforced concrete and the results showed that it would be a good way to improve anti-permeability with one type of fiber mixed in the concrete. But there would be more effective to improve the concrete impermeability with two or three type of fibers mixed in concrete. Sun [2] studied the physical properties of cement base mixed with different scale level of steel and polypropylene fibers. It revealed that hybrid fiber could improve concrete anti-permeability significantly. More scale levels of hybrid fibers could improve anti-permeability more. The fundamental causes are the graduated cracking resistance and performance complementation with different scale level and different type of fibers used in the corresponding structures. Marijan Skazlić[26] proved that tensile and flexural strength of steel-polypropylene hybrid fiber reinforced concrete are higher than the concrete mixed with same dosage of steel or polypropylene fiber. The durability (gas permeability and water permeability) is better than the concrete mixed with single type of fiber. However, Huang [17] indicated that steel-polypropylene hybrid fiber had less effect on anti-permeability of concrete and it was different with the view of majority researchers who believed that hybrid fibers could improve the impermeability. The phenomenon might be interpreted as in the following. When fiber was mixed into the concrete, the interface area would be increased and concrete porosity would be promoted. The quantitative grout could package more aggregates and fibers. It was more fragile than the interface only packaged aggregates. So it was easier to cause micro-crack and anti-permeability might be reduced. Sun [27] got the similar results and proved that hybrid proportion of fibers would produce positive and negative effects on permeability.

Durability--Shrinkage. A lot of works have been taken to study the shrinkage of steel-polypropylene hybrid fiber reinforced concrete. Sun [2] tested the shrinkage performance and analyzed the limited shrinkage and anti-permeability mechanism of hybrid reinforced cement base composite materials by changing steel fiber size mixed with low elastic modulus polypropylene fiber. The results showed that concrete shrinkage performance would be improved by mixing fiber. Concrete mixed with a variety of elastic modulus fibers was better than concrete with single elastic modulus fiber. But more interfaces would be found in the internal of cement base with mixed more hybrid fibers and it might not be benefit to the shrinkage, that is, there should be an optimal content for the fiber. Liu [28] proved that the limited shrinkage of concrete could be improved significantly by mixing hybrid fiber and then the cracks caused by concrete drying and shrinkage would be reduced. There was an optimal hybrid dosage to reduce drying shrinkage when low elastic modulus of polypropylene fiber mixed with high elastic modulus of steel fiber. Low elastic modulus fibers benefited to early-age shrinkage and high elastic modulus fibers, on the contrary, benefited to long-term concrete shrinkage. Marijan Skazlić [26] also got the similar conclusion.

Other Durability: The research on durability of steel-polypropylene hybrid fiber reinforced concrete also includes freezing resistance, corrosion resistance and abrasive resistance etc. Hua Yuan [29] revealed that the effects on freezing-thawing resistance, anti-permeability, sulfate corrosion resistance and bending strength with water immersion were better significantly than a single fiber reinforced concrete. Huang [30] showed that compressive and flexural strength of hybrid fiber reinforced concrete which were corroded in sulfate solution about 200d could increase 10.7% and 6.1% respectively, compared with the 28d strength and the brittleness was also improved. The similar conclusion was proved by Ma [31]. The toughness of hybrid fiber reinforced concrete was declined less than the concrete mixed with single type of fiber. Because of mixing fiber, air content in concrete was increased, crack extension was restricted and then concrete freezing-thawing resistance would be improved. Don Wimpenny [32] found hybrid fiber had obvious advantages on improving fire resistance, abrasion resistance, sea water corrosion resistance of plain concrete and reinforced concrete. And the ductility also could be improved after cracks happened. Vassou [33] proved that the type of fiber could affect the abrasion resistance of concrete significantly. In the same fiber volume content, the abrasion resistances of polypropylene fiber reinforced concrete, steel fiber reinforced concrete and hybrid fiber reinforced concrete would be increased 86%, 75% and 73%, compared with ordinary concrete. N. Banthia [34] showed that hybrid fiber reinforced concrete could effectively reduce early shrinkage and improve anti-permeability under pressure.

Engineering Applications

Based on the excellent nature of hybrid fiber reinforced concrete, it is widely applied in civil engineering. The main applications are summarized as in the following:

Road and Bridge Engineering. The material properties of hybrid fiber reinforced concrete such as high flexural strength, crack resistance and abrasive resistance etc. can be taken full advantages. Because of mixing hybrid fiber in concrete, steel reinforcement can be replaced, thickness of bridge deck pavement can be reduced. Then the engineering quality will be improved, costs of engineering maintenance will be reduced and project service life could be extended.

Industrial and Civil Building. The bearing capacity, crack resistance, seismic resistance and durability of high-rise or large-span buildings, common pre-fabricated elements and precast pipe etc. could be improved significantly if hybrid fiber reinforced concrete is applied.

Coastal Engineering. Because fiber reinforced concrete could provide the excellent crack resistance and anti-permeability performance, the corrosion such as steel reinforcement corrosion by chlorine ion in the sea, concrete erosion by sulfate and magnesium ions can be delayed. And the wave and weight in wharf impact resistances will be improved. The fiber reinforced concrete is successfully applied to Oslo Port in Norway and Naval Port of United States in Panama and the actual results are perfect.

Conclusions

The complete set has been not established in the research field of mix proportion design for steel-polypropylene hybrid fiber reinforced concrete. Most of research based on orthogonal design method to deal with mix proportion design by mixing fiber directly. The level of various factors usually bases on the experience. The accurate and reliable engineering calculation method for mix proportion design is lack. More details need be given in the corresponding codes and specifications.

The part of hybrid fiber reinforced concrete is vacant in the newly revised Technical specification for fiber reinforced concrete structures.

It is dispersive to the experimental results of hybrid fiber reinforced concrete and is deficient to the theoretical research. The micro mechanics analysis of hybrid fiber reinforced concrete is lack. The effect of hybrid different type of fiber in concrete is not clear. And most of works based on macro composite material theory and fiber interface theory.

The study about the durability of hybrid fiber reinforced concrete is less and some conclusions are not consistent with each other. Most tests were taken in an ideal environment and there are too much different with the actual engineering.

According the former, there are still a lot of problems need to solve during the design and construction periods, such as the insufficient test data accumulation in mechanical behaviors and physical properties, the inconsistent research conclusions of concrete durability and the difference between theory and application etc. although large quantities of work have been done successfully. As a new potential material used in civil engineering, the steel-polypropylene hybrid fiber reinforced concrete would be widely applied to many fields. It is urgent to establish a new simple method of mix proportion design to meet the requirements of actual engineering and overcome the shortcomings of mix proportion design results vary from person to person. The inconsistent research conclusions should be resolved and the research of concrete durability should be enhanced. All these works are the base for the application of steel-polypropylene hybrid fiber reinforced concrete.

References

[1] Z. Xu, Technology and Application of Fiber Reinforced Concrete, China Building Industry Press, Beijing, 2003.

[2] W. Sun, H. Qian, H. Chen, The effect of the combination of hybrid fibers and expansive agent on the physical properties of cementitious composites, Journal of the Chinese Ceramic Society, 2 (2000) 95-99.

[3] W. Yao, J. Cai, B. Chen, Study of high performance concrete reinforced hybrid fibers, Journal of Three Gorges University (natural science edition), 1 (2002) 21-23.

[4] G. Zhao, Steel Fiber Reinforced Concrete Structure, China Building Industry Press, Beijing, 1999.

[5] W. Cao, Talking about the characteristics and development prospect, Cement and Concrete, 6 (2008) 24-27.

[6] H. Wang, Experimental Study of Hybrid Steel-Polypropylene Fiber Concrete, Thesis for Master Degree, Northwestern Polytechnical University, 2005.

[7] F. Liu, Study on strength and composition of new patter reinforced high performance concrete, Concrete, 6 (2010) 112-133.

[8] J.Chen, Study on optimization of proportion of C40 pumping hybrid fiber reinforced concrete, Concrete and Cement Products, 6 (2006) 38-42.

[9] Z.Wang, An Orthogonal Experimental Study on High Performance Concrete of Steel- Propylene Hybrid Fiber, Journal of Engineering Institute of Jiaozuo, 1 (2003) 15-20.

[10] S. P. Singh, A.P. Singh and V. Bajaj, Strength and flexural toughness of concrete reinforced with steel-polypropylene hybrid fibers, Asian Journal Of Civil Engineering (Building and Housing), 4 (2010) 495-507.

[11] Information on http://scholar.google.com.

[12] CECS38:2004, Technical Specification for Fiber Reinforced Concrete Structures, China Plan Press, Beijing, 2004.

[13] Z. Wu, Study on Mechanical behavior and Applications of Basalt Fiber Reinforced Concrete, Thesis for Master Degree, Wuhan University of Technology, 2009.

[14] D. Gao, J. Zhao, H. Zhu, Design and Application of Steel Fiber Reinforced Concrete, China Building Industry Press, Beijing, 2002.

[15] H. Wang, Y. Chen, Q. Ding, S. Hu, The effect of hybrid fibers on the mechanical properties and impermeability of high-performance concrete, Concrete, 11 (2003) 33-35.

[16] B. Babal, T. Nurnbergerova, Hybrid fiber-reinforced concrete under repeated loading. Nuclear Engineering Design, 156 (1995) 195-200.

[17] C. Yang, C. Huang, Y. Che, B. Wang, Mechanical properties and impermeability of hybrid fiber reinforced concrete, Journal of Building Materials, 1 (2008) 89-93.

[18] W. Yao, L. Jie, Keru Wu, Mechanical properties of hybrid fiber-reinforced concrete at low fiber volume fraction, Cement and Concrete Research, 33 (2003) 27-30.

[19] H. Sun, Z. He, A. Gong, The effect of hybrid fiber-reinforced concrete on mechanical properties and crack resistances, Concrete and Cement Products, 2 (2009) 48-51.

[20] K. Wang, Y. Zhang, X. Wang, Effect of smaller volume S-P hybrid fibers on mechanical properties of high performance concrete, Journal of Harbin Industry of Technology, 10 (2003) 1209-1211.

[21] C. Jiao, W. Sun, H. Qin, Experimental study on bending performance of high-strength concrete of steel-propylene hybrid fiber. Architectural Technology, 1 (2004) 48-50.

[22] C. Jiao, Z. Zhan, Experimental study on compressive strength performance of concrete of steel-propylene hybrid fiber, Journal of Guangzhou University, 4 (2007) 70-73.

[23] J. Zhao, X. Cai, H. Jiao, The effect of hybrid fibers on the early-age shrinkage of concrete. Journal of Harbin Industry of Technology, 2 (2007) 232-234.

[24] M. I. El-Hamrawy, A. M. Saba, Fracture energy of hybrid fiber reinforced concrete, Regional Conference on Civil Engineering Technology, 3 (2007) 232-234.

[25] S. Eswari, P. N. Raghunath, Regression modeling for strength and toughness evaluation of hybrid fiber reinforced concrete. Journal of Engineering and Applied Sciences, 5 (2011) 1-8.

[26] Marijan Skazlić, Development and application of hybrid fibre reinforced concrete, Second International Conference on Sustainable Construction Materials and Technologies, 2010.

[27] J. Sun, The performance study of polypropylene hybrid fiber concrete, Concrete, 11 (2003) 16-20.

[28] Y. Liu, W. Qiu, D. Li, The Shrinkage of steel-polypropylene hybrid fiber reinforced concrete, Materials Technology and Applications, 33 (2003) 27-30.

[29] Y. Hua, Y. Ceng, The durability experimental study of hybrid steel-polypropylene fiber concrete, Low Temperature Building Technology, 3 (1998) 18-20.

[30] G. Huang, Experimental study on resistance of sulfate and chlorine salt erosion performance about hybrid fiber concrete, Anhui University of Technology, 2010.

[31] X. Ma, Crack and freezing-thawing resistance of high performance concrete of steel-propylene hybrid fiber, Dalian University of Technology, 2006.

[32] Information on http://scholar.google.com.

[33] Information on http://cipremier.com/100030056.

[34] Information on http://www.claisse.info/specialabstracts.htm.

© (2012) Trans Tech Publications, Switzerland
doi:10.4028/www.scientific.net/AMM.238.33

Experimental Study on Flexural Toughness of SFRC

Changyong Li [a], Lisha Song [b], Li Sun[c], Chenjie Cao [d] and Tong Xing [e]

School of Civil Engineering and Communication, North China University of Water Resources and Electric Power, Zhengzhou 450011, China

[a] lichang@ncwu.edu.cn, [b] songlisha0202@163.com, [c] sunli627101421@163.com,

[d] 624377384@qq.com, [e] 281838622@qq.com

Keywords: steel fiber reinforced concrete (SFRC); flexural toughness; flexural strength; fraction of steel fiber by volume; thickness of cement paste.

Abstract. This paper introduces the test results of the flexural performance of CF40 steel fiber reinforced concrete (SFRC) designed by the binary superposition mix design method. The flexural strength and flexural load ~ deflection curves were got from the test SFRC specimens with the different fraction of steel fiber by volume and the different thickness of cement paste wrapping steel fibers. The effects of the fraction of steel fiber by volume and the thickness of cement paste on the flexural strength and toughness of SFRC are analyzed. It is demonstrated that the flexural toughness of SFRC increases with the increase of the fraction of steel fiber by volume, the reasonable thickness of cement paste wrapping steel fibers is 1.0mm.

Introduction

The flexura strength and toughness are the important properties of steel fiber reinforced concret (SFRC) to evaluate the effectiveness of SFRC structures resisting deformation and earthquake [1, 2], which are influenced by many factors compositing in SFRC [3]. In order to overcome the anthropic factor in mix design of SFRC, the authors of this paper studied the direct mix design methods such as considering the steel fiber as the replacement of aggregate included into the calculation of sand ratio [4], adding additional cement paste wrapping steel fibers by binary superposition method [5, 6]. To further demonstrate the binary superposition mix design method for SFRC, the experimental study of flexural performances of CF40 SFRC was carried out in accordance with the current standard test method for fiber reinforced concrete [7], the effects of the fraction of steel fiber by volume and the average thickness of cement paste wrapping steel fibers are analyzed in this paper.

Experimental

Raw Materials. The ordinary silicate cement of grade 42.5 with qualified stability, the natural river sand of 3.3 fineness modulus, the crushed limestone of series 5mm-20mm were used. The steel fiber is plate shearing type with rectangular section and end-hooks, the equivalent diameter is 0.87mm, the average length is 40mm. The high-performance water reducer is FDN-1 type about 15% of water reducing rate. The water is tap-water.

Mix Proportion of Concrete. The mix proportion of concrete was design as grade of CF40. As list in Table 1, the parameters were considered such as the fraction of steel fiber by volume (ρ_f) and the thickness of cement paste wrapping steel fibers (t_{cp}).

Table 1 Mix proportion of SFRC

Grade	m_c/m_w	β_s (%)	ρ_f (%)	t_{cp} (mm)
CF40	0.45	0.41	0/0.5/1.0/1.5/2.0	1.0
	0.45	0.41	1.0	0.8/1.0/1.2

Test Method. The tests coincide with the standard test method specified in CECS13:2009, the specimens were the beams of 100mm×100mm×400mm [3]. The MTS servo-type hydraumatic test machine was adopted to exert the load, the load sensor was added between the load distribution beam and the upper plate of test machine to measure the loads on specimen. The deflection was

measured by the displacement sensor fixed on the bottom plate of the machine. All the data were automatically recored by the data acquisition system SI35951B IMP, the acquisition frequency is one time each second. Fig. 1 shows the picture of the test view.



Fig. 1 Picture of test equipments

Analyses of Test Results

Flexural Tensile Strength of SFRC. As shown in Fig. 2, the flexural tensile strength of SFRC increases with the increase of fraction of steel fiber by volume, which is the same as that of SFRC designed by the former method specified in CECS38:2004, the reason has been thoroughly explained by many researches. Compared with the reference concrete without steel fiber, the maximum increment of the flexural strength of SFRC reaches 51%. It can be concluded that the bridge-like effects of steel fiber were increased by the space-frame structure of steel fiber in concrete, which improved the stress distribution of base concrete across the cracks, i. e. the confinement of steel fiber on the prolongation of cracks enhanced the ability for elasto-plastic deformation, the steel fibers across the crack spiry and the inherent defects of concrete reduced the stress concentration and postponed or restrained the elongation of internal cracks [3, 6].

As the same as the former study [6], the flexural strength of SFRC increased with the increase of the thickness of cement paste wrapping steel fibers. It is also illustrated that the interface between steel fiber and cement paste in concrete should be guaranteed by adding certain amount of cement paste on the basis of the reference concrete to eliminate the internal defects of cement paste and enhance the interface between steel fibers and cement paste.

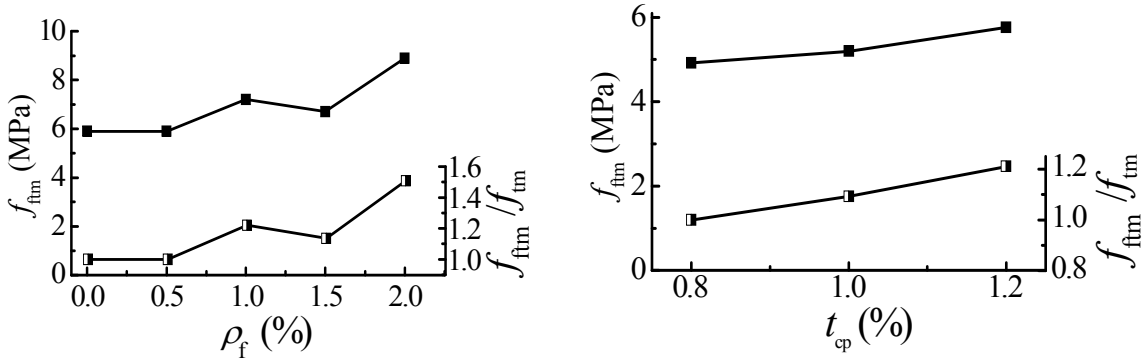


Fig. 1 Variation of flexural tensile strength

Based on the current design specification in CECS38:2004, the splitting tensile strength of SFRC can be computed as follows [1],

$$f_{ftm} = f_{tm}\left(1+\alpha_{tm}\lambda_f\right). \tag{1}$$

Where, f_{ftm} is the flexural tensile strength of SFRC, f_{tm} is the flexural tensile strength of reference concrete, α_{tm} is the effect coefficient of steel fiber on flexural tensile strength of SFRC, λ_f is the characteristic value of steel fiber, which equals to the fraction of steel fiber by volume multiplying the ratio of length (l_f) to diameter (d_f) of steel fiber.

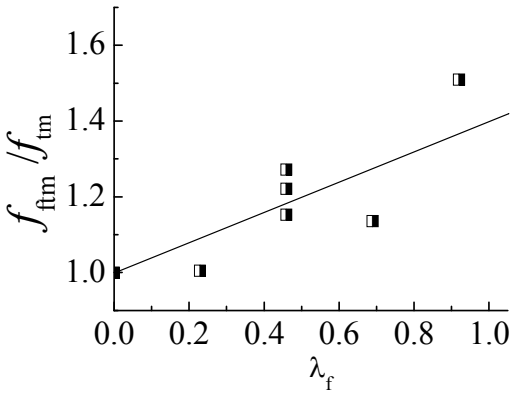


Fig. 3 Statistical analysis of flexural tensile strength

Draw the scatter points of test results in Fig. 3, the statistical value α_{tm}=0.42, the scatter coefficient is 0.175.

Flexural Toughness of SFRC. The curves of mid-span deflection vs load of SFRC beams are drawed in Fig. 4. Based on the method specified in CECS13:2009, the first-crack strength, the flexural strength (f_{ftm}), the flexural toughness indexes I_5, I_{10} and I_{20}, the equivalent flexural strength (f_e) and the flexural toughness ratio (R_e) of SFRC are calculated and listed in Table 2.

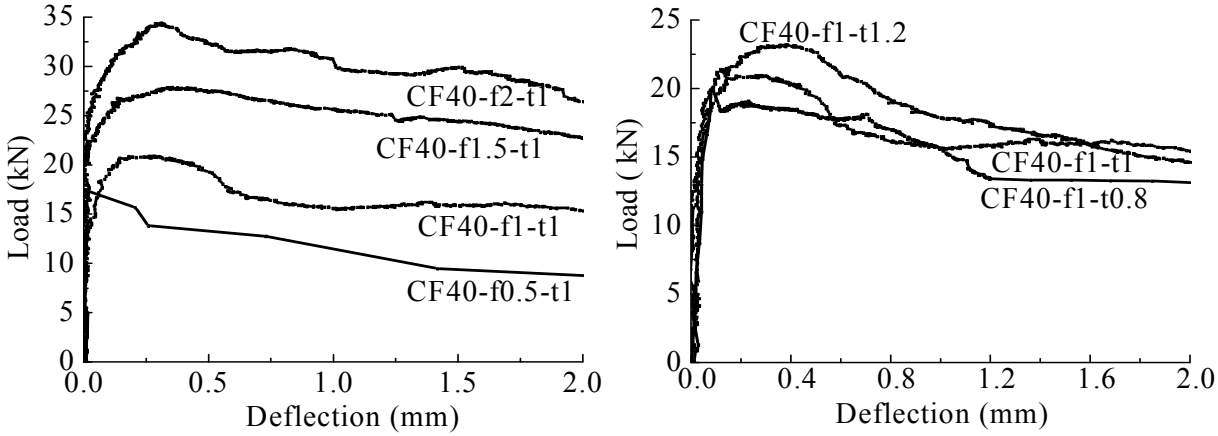


Fig. 4 Curves of mid-span flexural deflection vs loads

Table 2 Test results of flexural toughness of SFRC

Grade	ρ_f (%)	t_{cp} (mm)	First-crack strength (MPa)	f_{ftm} (MPa)	I_5	I_{10}	I_{20}	f_e (MPa)	R_e
CF40	0.5	1.0	4.35	4.48	4.82	9.14	17.26	2.74	0.63
	1.0	0.8	4.75	4.92	4.89	9.67	18.70	3.86	0.81
	1.0	1.0	4.36	5.20	5.13	10.70	22.50	4.22	0.97
	1.0	1.2	4.85	5.76	5.16	10.66	22.14	4.56	0.94
	1.5	1.0	5.49	6.81	5.20	10.86	22.76	6.22	1.13
	2.0	1.0	6.67	8.52	5.30	10.82	23.24	7.17	1.07

It can be seen that with the increase of the fraction of steel fiber by volume, the first-crack load and the ultimate load on SFRC beams increased, the deformation corresponding to ultimate load also increased, the load ~ flexural curves tended to much more full with flat desending segment and larger resident load, the beams presented much more deformation-holding ability, and the failure turns to more and more ductility from brittleness. In numerical, the fraction of steel fiber by volume increased from 0.5% to 2.0%, the first-crack strength of SFRC increased 53%, the flexural strength increased 90%, the equivalent flexural strength increased 162% from 2.74MPa to 7.17MPa, and the flexural toughness ratio increased 70% from 0.63 to 1.07.

With the increase of thickness of cement paste wrapping steel fibers, the first-crack strength of SFRC changed little but the ultimate flexural strength increased obviously, the fullness of the load ~ flexural deflection also increased. However, the resident loads corresponding to deformation larger than 2.0mm changed a little.

At the same time, the toughness indexes increased and reached the ideal flexural toughness indexes I_5=5, I_{10}=10 and I_{20}=20 of elasto-plastic materials. Therefore, the better and better flexural toughness of SFRC is resulted from the increase of fraction of steel fiber by volume.

For the SFRC with the 1.0mm and 1.2mm thickness of cement paste wrapping steel fibers, their I_5, I_{10} and I_{20} were all larger than that of elasto-plastic materials. The first-crack strength and the flexural strength of SFRC with 1.2mm thickness were higher than those of SFRC with 1.0mm thickness, but its flexural toughness I_{10} and I_{20}, and the flexural toughness ratio were lower. Therefore, the thickness is relatively reasonable taken as 1.0mm considering the cost of cement.

Conclusions

The flexural strength and flexural toughness of SFRC were tested to further verify the validity of the binary superposition mix design method. The factors such as the fraction of steel fiber by volume varying from 0.5% to 2.0% and the average thickness of cement past wrapping steel fibers varying from 0.8mm to 1.2mm were considered. The results show that:

The flexural strength of SFRC increased with the increase of the fraction of steel fiber by volume and the thickness of cement paste wrapping steel fibers. Meanwhile, the flexural toughness indexes of SFRC reached to the values of ideal elasto-plastic materials, the loading capacity in large deformation of steel fiber reinforced concrete beams also increased.

The flexural strength of SFRC increased with the increase of the thickness of cement paste wrapping steel fibers, while the flexural toughness did not constantly increased. Comprehensively analysis the flexural strength, flexural toughness of SFRC and the cost of cement, the reasonable thickness of cement paste wrapping steel fibers may be taken as 1.0mm.

Acknowledgement

The study was supported by the Scientific and Technical Leader Raising Plan of Zhengzhou City, China; the Natural Science Research Plan of the Education Department of Henan Province, China.

References

[1] CECS38:2004, Technical Specification for Fiber Reinforced Concrete Structures, China Plan Press, Beijing, 2004.

[2] ASTM C1550-02, Standard Test Method for Flexural Toughness of Fiber Reinforced Concrete (Using Centrally Loaded Round Panle), ASTM International, USA, 2002.

[3] S. Zhao, X. Sun and C. Li, Flexural toughness of steel fiber reinforced high-strength concrete, Journal of Building Materials, 1 (2003) 95-99.

[4] S. Zhao, H. Du and X. Qian, C. Li, Study on direct mix design method for steel fiber reinforced high-strength concrete, China Civil Engineering, 7 (2008) 1-6.

[5] S. Zhao, H. Huo, C. Song, L. Song, Binary superposition mix design method for SFRC Part I: principle and evaluation, Advanced Materials Research, Vols. 168-170 (2011) 2186-2190.

[6] H. Huo, S. Zhao, L. Song, C. Song, Binary superposition mix design method for SFRC Part II: flexural strength and toughness, Advanced Materials Research, Vols. 168-170 (2011) 2191-2194.

[7] CECS13:2009, Standard Test Method for Fiber Reinforced Concrete, China Plan Press, Beijing, 2010.

© (2012) Trans Tech Publications, Switzerland
doi:10.4028/www.scientific.net/AMM.238.37

Constitutive Model Based on Damage Mechanics of Fiber Reinforced Concrete (FRC): A Review

Duoxin Zhang [a] and Qingyun Wang [b]

School of Civil Engineering and Communication, North China University of Water Recourses and Electric Power, Zhengzhou 450011, China

[a]dxzhang@ncwu.edu.cn, [b]wqy@yeah,netl

Keywords: fiber reinforced concrete(FRC); continuum damage mechanics (CDM); anisotropic damage; micro-micromechanics.

Abstract. In order to study the constitutive model of fiber reinforced concrete (FRC) for future, this paper emphasizes on three aspects. FRCs constitutive model based on damage mechanics has been reviewed. The knowledge and development of constitutive models is discussed based on its historical developments and logical relations. Damage model of FRCs which has been developed in recent years is summarized at macro and micro levels. The development trends of constitutive modeling for FRCs are suggested on the basis of our understanding of essential physical properties of FRC, e.g. its nonlinearity

Introduction

The high strength and damage resistance of FRC are very important for a number of practical applications. In order to predict the strength and other properties of composites, a number of mathematical models of deformation, damage and failure of FRC have been developed, which include plasticity, CDM, fracture mechanics, elastic-damage, and combined plasticity and damage mechanics.In order to study the constitutive model of FRC for future, a brief review has been made, in which main features as well as limitations of models are pointed out. The focus here is only the behavioral features of the constitutive models based on damage mechanics.

Continuum Damage Mechanics Based Models

The growth of micro cracks, fiber breaks and interface debonding in FRCs can be described in the framework of CDM as long as the problem size can be assumed to be sufficiently larger than the defect/microcrack size. A number of models of failure behavior of FRC are based on the methods of CDM with internal variables, formulated in the framework of the thermodynamics of irreversible processes. This approach includes the introduction of corresponding internal state variables (ISV) to characterize damage modes, and derivation of the damage growth laws on the basis of thermo-dynamical analysis of the system. So, Hild et al. [1] introduced the ISV, describing the matrix cracking and interface debonding and sliding and employed this model to analyze the fiber and matrix breakage in FRC. From the formula for the total free energy density, Hild and colleagues derived equations for the overall stress, energy release rate density, and other parameters. Matzenmiller et al. [2] developed a constitutive model, relating the effective elastic properties and damage of the material. The authors introduced a set of phenomenological internal variables, and a potential function, and derived kinetic equations for these variables. The rate equation for damage variables was presented as a sum of local damage parameters multiplied by scalar growth functions, given as power functions of state variables. For the analysis of both active and passive damage, they introduced separate damage states for tension and compression. The authors considered the damage evolution under uniaxial tension in fiber direction, and analyzed the dependencies of the stress-strain diagrams on the material parameters. Voyiadjis and Kattan [3] developed a continuum damage model of fiber FRC, in which two local damage tensors allow for nucleation and growth of voids in the ductile matrix, and for the fracture of fibers, respectively. The authors suggested representing the debonding and delaminating problems in terms of the combination of these two tensors.

In those models, the plasticity and damage in the deformation process did not have to achieve strong coupling [4]. Have aimed at nonlinear mechanical behavior and failure characteristics of the FRC, the coupling of anisotropic damage and plasticity constitutive modeling for FRC material has been established within the framework of thermodynamics. The weighted impact functions of the all kinds of fibers related damage models were proposed, meanwhile, the fibers related damage variables has been analyzed here to interpret the effect of all combined damage models, furthermore, the evolutionary relationship of fibers related damage variables , take into account of characteristic parameters of fibers, has been put forward. Adoption of three kinds of damage mechanisms, fibers related damage, tensile and shearing damage, to describe the FRC damage mechanism. The fibers related damage variables was been introduced into FRC damage mechanism through in form of power on tensile and sharing damage tensor, the fourth-order damage effect tensor has been reconstructed simultaneously, the coupling mechanism of fibers damage with tension and shearing damage has been realized. The plastic model is introduced from an effective stress space point of view in this study, and with an aim to decode the relative fibered damages on the basis of energy released rate, the damage model has also been established in damage configuration. Consequently, this creative damaged model has succeeded in reconstructing a fourth-ordered damaged tension in view of a given relationship between configurative damages and its functions. Created the plastic potential and damage potential functional, using the maximum principle, the plastic and damage hardening effect variables evolution have been given. Furthermore, a combination coming from the plastic-yielded surface and damage-loaded surface is adopted to make this evolutionary formula of plastic flow and damage evolution into full play. The stress-strain incremental constitutive relation has been established through derivation of elastoplastic damage tangent stiffness tensor. Finally, based on the experiments, material parameters were calibrated, and the predictive performance of constitutive model was assessment, to prove the correctness and validity of this study. Summarize the governing equations of elastic-plastic anisotropic constitutive relation as follows:

(1)The relationship between the damage configuration and effective configuration

$$\bar{\boldsymbol{\sigma}} = \mathbf{M} : \boldsymbol{\sigma} \tag{1}$$

$$\mathbf{E}(\mathbf{D}) = \mathbf{M}^{-1} : \bar{\mathbf{E}} : \mathbf{M}^{-\mathrm{T}} \tag{2}$$

(2) Plasticity criteria and plastic potential in the effective configuration

$$f^{\pm} = \sqrt{\frac{3}{2}\left(\bar{\mathbf{S}}^{\pm} - \bar{\mathbf{X}}^{D\pm}\right) : \left(\bar{\mathbf{S}}^{\pm} - \bar{\mathbf{X}}^{D\pm}\right)} + \alpha \bar{I}_1 + \beta\left(\varepsilon_{eq}^{+}, \varepsilon_{eq}^{+}\right) H\left(\tilde{\bar{\sigma}}_{\max}\right) \tilde{\bar{\sigma}}_{\max} - \bar{R}^{\pm}(\varepsilon_{eq}^{\pm}) = 0 \tag{3}$$

$$F^{\pm} = f^{\pm} + \frac{3}{4}\gamma \bar{\mathbf{X}}^{\pm} : \mathbf{C}^{-1} : \bar{\mathbf{X}}^{\pm} \tag{4}$$

(3) Damage criteria and damage potential damage in the configuration of damage

$$g^{\pm} = \sqrt{\frac{1}{2}\left(\mathbf{Y}^{\pm} - \mathbf{H}^{\pm}\right) : \mathbf{L} : \left(\mathbf{Y}^{\pm} - \mathbf{H}^{\pm}\right)} - K^{\pm}(r_{eq}^{\pm}) = 0 \tag{5}$$

$$G^{\pm} = g^{\pm} + \frac{d}{2}\mathbf{H}^{\pm} : \mathbf{A}^{-1} : \mathbf{H}^{\pm} \tag{6}$$

$$\dot{\boldsymbol{\varepsilon}}^{\mathrm{I}\pm} = \dot{\lambda}^{p\pm}\frac{\partial F^{\pm}}{\partial \boldsymbol{\sigma}} + \dot{\lambda}^{d\pm}\frac{\partial G^{\pm}}{\partial \boldsymbol{\sigma}} \tag{7}$$

$$\dot{\mathbf{D}}^{\pm} = \dot{\lambda}^{p\pm}\frac{\partial F^{\pm}}{\partial \mathbf{Y}^{\pm}} + \dot{\lambda}^{d\pm}\frac{\partial G^{\pm}}{\partial \mathbf{Y}^{\pm}} \tag{8}$$

(4) Evolution law of damage and plasticity variables

$$\dot{\mathbf{X}}^{\pm} = \frac{2}{3}\mathbf{C} : \left(-\dot{\lambda}^{p\pm}\mathbf{M}^{\pm} : \frac{\partial F^{\pm}}{\partial \bar{\mathbf{X}}^{D\pm}}\frac{\partial \bar{\mathbf{X}}^{D\pm}}{\partial \bar{\mathbf{X}}^{\pm}} - \dot{\lambda}^{p\pm}\frac{3}{2}\gamma \mathbf{C}^{-1} : \bar{\mathbf{X}}^{\pm}\right) \tag{9}$$

$$\dot{R}^{+} = h\dot{\varepsilon}_{eq}^{+} \tag{10}$$

$$\dot{R}^{-} = b\left(Q - R^{-}\right)\dot{\varepsilon}_{eq}^{-} \tag{11}$$

$$\dot{\mathbf{H}}^{\pm} == \mathbf{A} : \left(\frac{\partial g^{\pm}}{\partial \mathbf{Y}^{\pm}} - d\mathbf{H}^{\pm} \right) \dot{r}_{eq}^{\pm} \tag{13}$$

$$\dot{K}^{\pm} = \frac{K_0^{\pm}}{B^{\pm}} \exp\left[-B^{\pm} \left(1 - \frac{K^{\pm}}{K_0^{\pm}} \right) \right] \dot{r}_{eq}^{\pm} \tag{14}$$

$$\mathbf{Y}^{\pm} = -\frac{1}{2} \bar{\boldsymbol{\sigma}} : \left(\bar{\mathbf{E}}^{-1} : \mathbf{M} : \frac{\partial \mathbf{M}^{-1}}{\partial \mathbf{D}^{\pm}} + \frac{\partial \mathbf{M}^{-\mathrm{T}}}{\partial \mathbf{D}^{\pm}} : \mathbf{M} : \bar{\mathbf{E}}^{-1} \right) : \bar{\boldsymbol{\sigma}} \tag{15}$$

(5) Condition of Kuhn-Tucker

plastic: $f^{\pm} \le 0, \dot{\lambda}^{p\pm} \ge 0, \dot{\lambda}^{p\pm} f^{\pm} = 0, \dot{\lambda}^{p\pm} \dot{f}^{\pm} = 0$ (16)

damage: $g^{\pm} \le 0, \dot{\lambda}^{g\pm} \ge 0, \dot{\lambda}^{g\pm} g^{\pm} = 0, \dot{\lambda}^{g\pm} \dot{g}^{\pm} = 0$ (17)

Where the physical meaning of each symbol, see [4].

CDM and Micro-mesomechanics Based Models

Some ideas on the analysis of the mechanical behavior of unidirectional FRC on the scale level of laminates, based on combining the CDM and micromechanics, was suggested by Talreja. This idea was mainly applied for the modeling of transverse cracking of laminates. However, in some works the ISV approach and combined damage mechanics/micromechanics models were applied to the analysis of FRC at the level of fibers and fiber bundles. So, Megnis et al. utilized the ISV approach to develop thermodynamically consistent formulation for damageable FRCs. Fiber fracture was included into their model via the corresponding internal state variable. The damage tensor was determined using a unit cell model of a cracked fiber in the matrix. The stiffness degradation of the composite as a function of the applied strain was determined numerically, and compared with the experimental data.

Hassan and Batra [5] used CDM approach with three scalar internal variables to model damage evolution in polymer composites. The dependence of material parameters on the damage variables is determined using the mechanics of materials approach Hassan and Batra derived equations describing the damage evolution, and developed their own finite element code to model 3D damage evolution in the composite. In order to take into account the strain rate effect, the dependence of the damage variables on the reference transverse and shear strain rates was postulated. The authors studied the dependence the tensile strength of composites on the fiber orientation angle in tension, as well as time histories of damage variable evolution.

Raghavan and Ghosh [6] developed a CDM model of FRCs with damageable interfaces. The interface debonding was simulated using the cohesive zone models. The macroscopic damage variables and damage evolution laws were determined on the basis of the micromechanical analysis of representative volume elements with subsequent asymptotic homogenization of microscopic variables. The micromechanical analysis was carried out with the Voronoi cell finite element method.

CDM and Micro-mesomechanics Models Considered the Fiber Random Distribution

In these models, micromechanical models of composites are used to determine parameters of the damage growth law. Another way of combining micromechanical and CDM approaches is the incorporation of continuum damage models of the void growth or microcracking in the matrix are incorporated into continuum mechanical, finite element models of composites. Often, CDM based models for matrix are combined with either CDM or probabilistic models for fiber failure. Weigel et al. [7] developed a material law for ceramic matrix composites in the framework of CDM. Parameters of the model were determined from the micromechanical analysis of different damage modes: stochastic fiber failures under tensile loading, transverse cracking in longitudinal plies, fiber bundle micro-buckling under compression. Using the Weibull-type law for the failure probability of fibers and homogeneous load distribution, they derived the stress-strain relation for fiber bundle under axial loading. Further, the strain-stress relationships for the damageable longitudinal plies were obtained analytically. For the case of shear damage, stress-strain relations was derived using a model with two

damage variables, which takes into account the damage coupling between tension and shear, and the effective stress concept. To analyze the fiber micro-buckling under compression, they considered a half-wave of a fiber of sinusoidal shape. Using the conditions of force and moment equilibrium, and approximating the displacement field by sinusoidal function, they determined the critical force for the failure due to fiber buckling or interface debonding.

A simplified CDM model was proposed describing the inelastic behavior of concrete reinforced with randomly distributed short fibers [8]. The constitutive and damage behavior of such concrete usually involves anisotropic damage, unilateral effect, coupled volumetric and deviatoric inelastic deformation and complicated failure mechanisms due to its heterogeneous morphology. To avoid the analytical and computational complexity, a scalar damage variable is adopted, while the anisotropy and unilateral effect of damage corresponding to different states of stress and stress histories are described through introducing the Lode parameter μ_σ. The proposed model can take into account the effect of fiber content on damage development and the effect of volumetric stress on deviatoric inelastic response. The validity of the proposed model is demonstrated by comparing the theoretical and experimental results for plain and fiber-reinforced concrete subjected to triaxial stress histories.

Conclusions

When analyzing the strength, damage and fracture of FRC, a number of challenges have to be overcome, among them the problem of the correct representation of the load transfer and redistribution between fibers and matrix, taking into account the interaction between multiple fiber cracks, matrix and interface cracks, modeling the interface bonding mechanisms and their effects on the composite behavior.

The continuum mechanical models are most strictly justified, and have potentially no limitations in incorporating all the complex phenomena of damage evolution in composites. However, at the current stage of the development of modeling techniques, the incorporation of real or generic microstructures of composites into discrete models and including the emerging discontinuities still present challenges. Only recently, some numerical investigations of composite damage, based on 3D multifiber unit cells with random fiber arrangement have been carried out.

References

[1] F. Hild, A. Burr, F.A. Leckie, Matrix cracking and debonding in ceramic-matrix composites, International Journal of Solids and Structure, 33 (1996) 1209-1220.

[2] J. Matzenmiller, R. L. Lubliner, A. Taylor, Constitutive model for anisotropic damage in fiber-composites, Mechanics of Materials, 20 (1995) 125-152.

[3] G. Z. Voyiadjis, B. Deliktas, A coupled anisotropic damage model for the inelastic response of composite materials, Computation Methods Application Mechanical Engineering, 183 (2000) 159-199.

[4] D. Zhang, W. Qu, Q. Wang, et al, Research on the coupled anisotropic damage and plasticity constitutive model for quasi-brittle materials, Acta Mechanica Solida Sinica, 33 (2012) 199-208.

[5] R. C. Batra, N. M. Hassan, Blast resistance of unidirectional fiber reinforced composites, Composites Part B: Engineering, 39 (2008) 513-536.

[6] S. Ghosh, J. Bai, P. Raghavan, Concurrent multi-level model for damage evolution in microstructurally debonding composites, Mechanics of Materials, 39 (2007) 241-266.

[7] N. Weigel, B. Kröplin, D. Dinkler, Micromechanical modeling of damage and failure mechanisms in C/C–SiC Original Research Article, Computational Materials Science, 16 (1999) 120-132.

[8] X. Peng, C. Meyer, A continuum damage mechanics model for concrete reinforced with randomly distributed short fibers, Computers and Structures, 78 (2000) 505-515.

© (2012) Trans Tech Publications, Switzerland
doi:10.4028/www.scientific.net/AMM.238.41

Experimental Study on Full Stress-strain Curve of SFRC in Axial Tension

Hongyuan Huo [a], Chenjie Cao [b], Li Sun [c], Lisha Song [d] and Tong Xing [e]

School of Civil Engineering and Communication, North China University of Water Resources and Electric Power, Zhengzhou 450011, China

[a] huohongyuan@ncwu.edu.cn, [b] 624377384@qq.com, [c] sunli627101421@163.com,

[d] songlisha0202@163.com, [e] 281838622@qq.com

Keywords: steel fiber reinforced concrete (SFRC); stress-strain curve; fraction of steel fiber by volume; thickness of cement paste; axial tension.

Abstract. The tests were carried out to study the effects of the fraction of steel fiber by volume and the thickness of cement paste wrapping steel fibers on the axial tensile properties of steel fiber reinforced concrete (SFRC). The strength grade of SFRC was CF40 with the fraction of steel fiber by volume varying from 0.5% to 2.0%, and the thickness of cement paste wrapping steel fibers varying from 0.8mm to 1.2mm. The tests were conducted by WAW-600 electric-hydraulic servo-type test machine. The results show that the axial tensile properties such as the axial tensile strength, the fullness of stress-strain curve, the tensile energy and the axial tensile toughness ratio are all improved obviously by the adding of steel fiber in concrete. The reasonable thickness of cement paste wrapping steel fibers is 1.0mm. The formulas for stress-strain relationship of SFRC in axial tension are proposed.

Introduction

The successful tests were difficult for the full load ~ deformation curve of concrete under the axial tension [1-3], which attributed to the following factors: (1) specimens would be apt to damage by eccentric tension for it is different to confirm the accurate place of specimens; (2) as the stiffness of ordinary pressure testing machine was not sufficient, the stress curves after the peak is different to record. However, by means of the WAW-600 electric-hydraulic servo-type test machine, this paper successfully got the axial tensile stress-strain curves of steel fiber reinforced concrete (SFRC). Based on the test, the reasonable thickness of cement paste wrapping steel fibers and the constitutive relationships of SFRC in axial tension were proposed.

Experimental

The mixture of SFRC comprised ordinary silicate cement in 42.5 grade, crushed stone in 5~20mm particle size, natural sand with 3.3 fineness modulus, the thin-plate shearing steel fiber, high-performance water reducer with 15~25% water reducing ratio and tap-water. Their properties are listed in Table 1 to Table 4. Test combination parameters are listed in Table 5.

Table 1 Physical and mechanical properties of cement

Fineness (%)	Standard consistence (%)	Setting time (min)		Compressive strength (MPa)		Flexural strength (MPa)	
		Initial	Final	3d	28d	3d	28d
2.0	29.20	185	295	29.5	46.8	5.4	8.0

Table 2 Physical properties of cement

Particle size distribution	Fineness modulus	Apparent density (kg/m^3)	Bulk density (kg/m^3)	Closed-volume density (kg/m^3)	Mud content (%)
0.16～5	3.3	2600	1490	1620	1.6

Table 3 Physical properties of stone

Apparent density (kg/m^3)	Bulk density (kg/m^3)	Crushed index (%)	Mud content (%)
2720	1430	9	0.4

Table 4 Characteristic parameters of steel fiber

Average length (mm)	Average width (mm)	Average thickness (mm)	Equivalent diameter (mm)	Aspect ratio
40.02	0.92	0.57	0.87	46

Table 5 Test combination parameters

Strength grade	Fraction of steel fiber by volume (%)	Thickness of cement paste wrapping steel fibers (mm)	Water to cement ratio	Sand ratio (%)	Water reducer (%)
CF40	0.0/0.5/1.5/2.0	1.0	0.45	41	0.6
	1.0	0.8/1.0/1.2			

7 groups of specimens were cast, each group comprised 4 specimens. The size of specimens was 100mm×100mm×550mm. One deformed bar of 16 diameter was embedded at ends on center of the cross sections of each specimen as loading parts, the length of the deformed bar was 165mm embedded for 125mm [4].

The enforced puddle mixer with horizontal shaft was used to make steel fibers well-distribute in concrete. The feeding sequence of raw materials is as Fig. 1. Where steel fiber was added during the mixing, and the total mix time was kept less than 6min to avoid the aggregation of steel fibers. After 24 hours natural curing, the specimens were remodeled and put into standard curing room with (20±2) ^{o}C temperature and 95% relative humidity for 28 days.

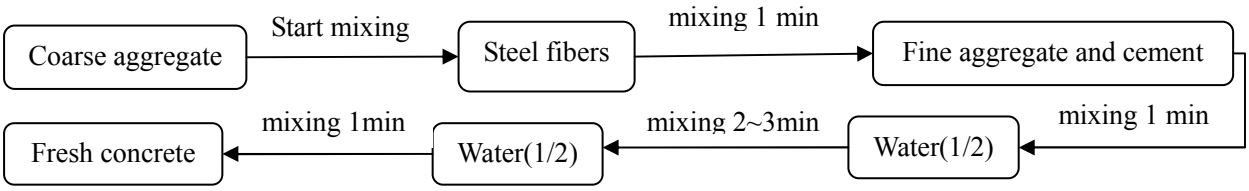


Fig. 1 Feeding sequence of raw materials

WAW-600 electric-hydraulic servo-type test machine was used in the experiment, which had several functions controlled by computer such as translation between different control modes smoothly, constant loading and constant rate of loading. Load and deformation mixed control system was used in the test. The loading speed was 0.4MPa/min until tensile load reached the peak, and after that, loading was controlled by the deformation as 0.1mm/min ~0.2mm/min. As shown in Fig. 2, dial indicators were fixed on the two contrast sides of the specimens, and the measure distance was 250mm. The embedded deformed steel bars were connected with chucks by spherical hinges, and the loading were tried several times to adjust the location before the formal test began。

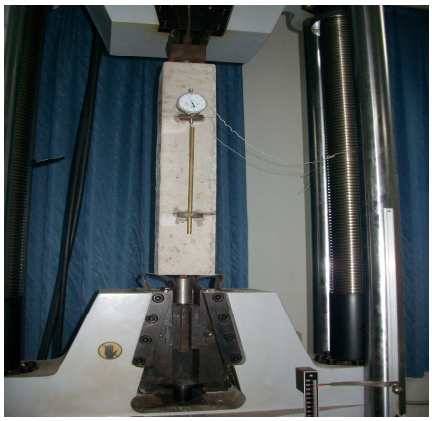


Fig. 2 Test equipment for axial tension

Analyses of Stress-strain Curves

Effect of the Fraction of Steel Fiber by Volume. As shown in Fig. 3, the stress-strain curves of SFRC in axial tension with the different fraction of steel fiber by volume may be divided into two segments: the upward segment and downward segment. The stress-strain curves have the similar

trends as linear relationships in upward segment and the different change rate in downward segment. With the increase of the fraction of steel fiber by volume, the axial tensile strength of SFRC increases, the downward curves become more and more flat. Compared with the axial tensile strength of reference concrete without steel fiber, the maximum increment of SFRC is 11.8%. The axial tensile strength of SFRC with 1.0% fraction of steel fiber by volume displays a little decrease due to the grate slump and slightly bleeding of the fresh mixture.

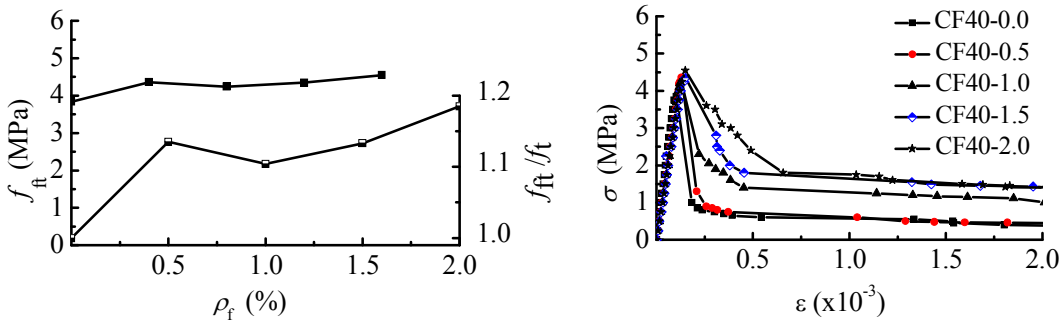


Fig. 3 Effect of the fraction of steel fiber by volume on the axial tensile strength and stress-strain curves

Effect of the Thickness of Cement Paste Wrapping Steel Fibers. With the constant fraction of steel fiber by volume of 1.0%, if the amount of cement paste is not sufficient, the steel fibers will not be wrapped effectively and the workability of fresh mixture may be bad, which finally result the reduction of the density and the bond between steel fiber and concrete. If the amount of cement paste is excessive, the superfluous paste shows no effect on the strength but will be adverse to the volume stability of the SFRC [5].

As shown in Fig. 4, with the increase of the thickness of cement paste wrapping steel fibers, the axial tensile strength and the stress-strain curves change a little.

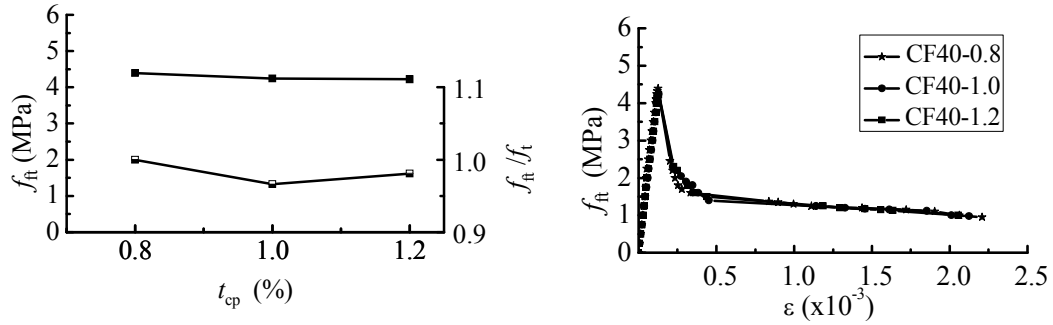


Fig. 4 Effect of the thickness of cement paste wrapping steel fibers on the axial tensile strength and stress-strain curves

Constitutive Relationship of SFRC in Axial Tension

There are several forms of equations describe the stress-strain curves of SFRC, the forms of mathematical equations [6] are used to simulate the stress-strain curves in this test:

$$y = 1.2x - 0.6x^6 \quad (0 \le x < 1) \tag{1}$$

$$y = \frac{x}{a_{ft}(x-1)^{1.7} + x} \quad (x \ge 1.0) \tag{2}$$

Where $x=\varepsilon/\varepsilon_{ft}$, $y=\sigma/f_{ft}$. f_{ft} is the axial tensile strength of SFRC corresponding to the strain ε_{ft}. $a_{ft} = \frac{a_t}{1+A\lambda_t}$, $a_t=0.312f_t^2$, f_t is the axial tensile strength of reference concrete (MPa); λ_t is the characteristic value of steel fiber; A is parameter determined by the test dates. A=4.9 in this paper.

Fig. 5 shows the calculated and test curves of SFRC with different fraction of steel fiber by volume, it can be seen that there are good fitness between them.

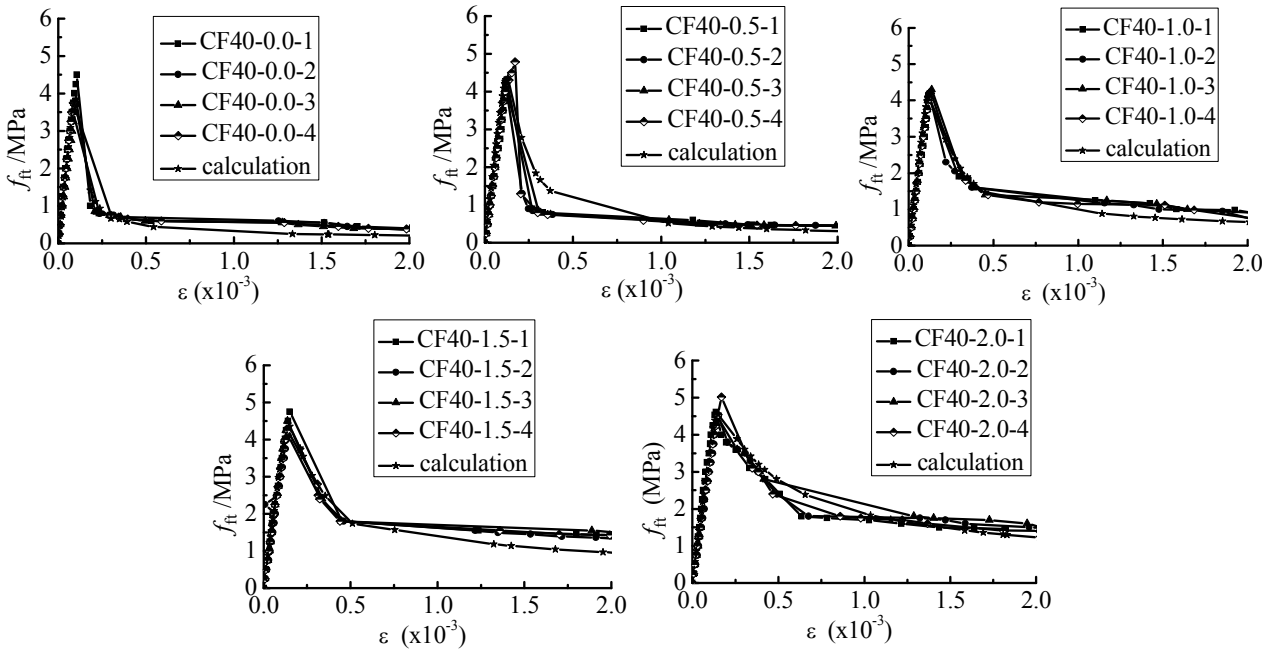


Fig. 5 Comparison of calculated and test curves

The Axial Tension Toughness Ratio of SFRC

The tension energy $W_{0.2}$ is the area under the axial tensile load-deformations curves corresponding to the deformation from zero to $0.002L_0$, here L_0 is the standard distance (mm). The axial tension toughness ratio $R_{e,0.2}$ is defined as follows [4]:

$$R_{e,0.2} = \frac{W_{0.2}}{F_{\max} \times L_0 \times 0.2\%} \tag{3}$$

Where $F_{\max}$ is the ultimate loads of load-deformations curves (N).

As shown in Table 6, the tension energy and the axial tension toughness ratio of SFRC increase significantly comparing with the reference concrete, the brittleness of reference concrete was improved obviously. The axial tension toughness ratio of SFRC increased with the increase of the fraction of steel fiber by volume, but no liner relationship is between the axial tension toughness ratio of SFRC and the thickness of cement paste wrapping steel fibers. The maximum axial tension toughness ratio of SFRC reached at the 1.0mm thickness of cement paste wrapping steel fibers.

Table 6 Tension energy and axial tension toughness ratio of SFRC

Strength grade	Fraction of steel fiber by volume (%)	Thickness of cement paste wrapping steel fibers (mm)	Tension energy $W_{0.2}$ (N·m)	Axial tension toughness $R_{e,0.2}$
40	0.0	1.0	3.88	0.202
	0.5	1.0	4.19	0.192
	1.0	0.8	6.74	0.307
		1.0	7.19	0.339
		1.2	6.87	0.326
	1.5	1.0	8.35	0.384
	2.0	1.0	10.14	0.446

Conclusions

With the increase of the fraction of steel fiber by volume, the axial tensile strength of SFRC increases, the stress-strain curves become more and more fullness, the axial tension toughness ratio increases and the brittleness of SFRC in axial tension has been improved.

The thickness of cement paste wrapping steel fibers affects a little on the axial tensile strength and the stress-strain curve. The reasonable thickness is 1.0mm to make the axial tensile toughness of SFRC reach the maximum.

The formulas for stress-strain relationship of SFRC in axial tension are given out, the calculated curves have a good fitness with the test curves.

References

[1] Z. Dong, J. Pan, Experimental study on stress-strain characteristics of steel fiber reinforced concrete under uniaxial tension, Journal of Hydraulic Engineering, 5 (2002) 47-50.

[2] M. Li, Experiment on steel fiber reinforced concrete axial tensile stress-strain curves, Jiangsu Construction, 2 (1995) 26-30.

[3] X. Liu, B. Wen, Description on the uniaxial tensile stress-strain relationship of concrete, Engineering Mechanics, A01 (1998) 8-18.

[4] CECS13:09, Standard of Test Method for Steel Fibers Reinforced Concrete, China Plan Press, Beijing, 2008.

[5] X. Lin, G. Yang, High-strength and Super High-strength Steel Fiber Reinforced Concrete, Science Press, Beijing, 2002.

[6] X. Zhang, Z. Wang, C. Li, Experimental study on axial-tensile properties of steel fiber reinforced concrete, Journal of North China Institute of water Conservancy and Hydroelectric Power, 3 (2007) 8-50.

© (2012) Trans Tech Publications, Switzerland
doi:10.4028/www.scientific.net/AMM.238.46

Study on Damage Evolution Mechanism of Concrete under Uniaxial Tension

Weifeng Bai[1, a], Ying Cui[2,b], Qian Wang[3,c],
Junfeng Guan[1,d] and Jianwei Zhang[1,e]

[1]North China University of Water Resources and Electric Power, Zhengzhou 450011, China

[2]Yellow River Engineering Consulting Co.,Ltd. , Zhengzhou 450003, China

[3]Jilin Province Water Resource and Hydropower Consultative Company, Changchun 130000,China

[a]yf9906@163.com, [b]cuiyingfangfang@163.com, [c]slwq3319@163.com,

[d]shuaipipi88@126.com, [e]zhangjianwei@ncwu.edu.cn

Keywords: concrete; damage mechanism; damage variable; uniaxial tension; statistical damage constitutive model.

Abstract. The damage and failure mechanism of quasi-brittle materials is the most fundamental research topic in Damage Mechanics. In this paper, the mesoscopic damage mechanism of concrete under uniaxial tension was discussed. The rupture and yield damage modes in meso-scale were introduced as the two basic parameters to define the damage accumulated variable. The results show that the proposed statistical damage model can accurately predict the whole deformation and failure process of concrete under uniaxial tension, including the two-stage deformation characteristics and the size effect.

Introduction

The quasi-brittle materials such as concrete, rock and some ceramics are heterogeneous aggregate materials in meso-scale which are weakened by countless randomly distributed microcracks of irregular shapes and random in size and orientation in the microstructure and exhibit non-linear constitutive behavior on macro scale under exoteric loads [1-2]. Since the failure of the quasi-brittle materials essentially attributes to the nucleation and growth of microcracks produced by local tensile strain, the uniaxial tension can be regarded as one of the most fundamental failure forms. The stress-strain entire curve of concrete in direct tension can reflect the tensile performance greatly, however, no reasonable test method for direct tension is available to appraise the tensile performance of concrete. The failure mechanism of concrete is still the controversial and challenging issue.

Characterization of Concrete under Uniaxial Tension

A typical nominal stress-strain curve under uniaxial tension is shown in Fig. 1. Signs *D* and *E* denote the peak nominal stress state and the critical state respectively. A denotes the limit elastic state, *B*, *C* denotes two states in strengthen segment, *F*, F' denotes two states in soften segment.

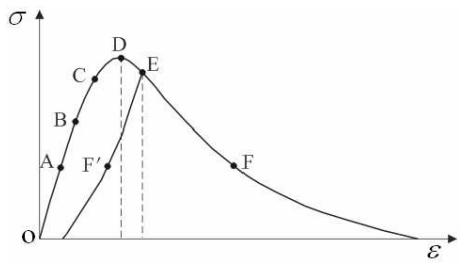


Fig. 1 Typical nominal tensile stress-strain curve of concrete

The nonlinear stress-strain curve is the macroscopic response of the mesoscopic heterogeneous damage evolution process. The mechanical properties can be summarized as follow:

(1) The whole specimen can be divided into two regions, the fracture process zone (FPZ) and the other region.

(2) The whole fracture process can be divided into two stages: the homogeneous damage phase, corresponding to the segment *OE* in Fig. 1, in which the whole specimen keeps the same damage state; the local breach phase, corresponding to the segment *EF* and *EF'*, in which the FPZ and the other region exhibit the different mechanical behavior, i.e. the FPZ exhibiting the softening process, meanwhile the other region exhibiting the unloading process.

(3) The irreversible deformation is produced during the damage process.

(4) The critical state *E*, at which macro-cracks start to develop in the FPZ of the test specimen and the damage process switches into local softening phase, lies in the softening region behind peak state *D*. It should be noted that the different of the two characteristic states *D* and *E* was almost neglected in traditional research.

Definition of Damage Variable

The definition of the damage variable is one of the basic problems in Damage Mechanics. The suitable damage variables must be able to reflect the influence of the mesoscopic defects on the macroscopic properties.

Traditional Definition Method. The hypothesis of equivalent strain and the PBS, regarded as the fundamental theory of Damage Mechanics, take the effective cross-section area and the elastic modulus to measure the damage degree. The expression can be written as

$$D = \frac{1-A}{A_0} = \frac{1-E}{E_0} \tag{1}$$

where A and E denote the effective cross-section area and the elastic modulus of the damaged material, respectively; A_0 and E_0 represent the initial values of the pristine material, respectively; D is the accumulated damage variable. It is assumed that the macroscopic effects of the decrease of the elastic modulus and the degradation of the effective cross-section on the damaged material are equivalent.

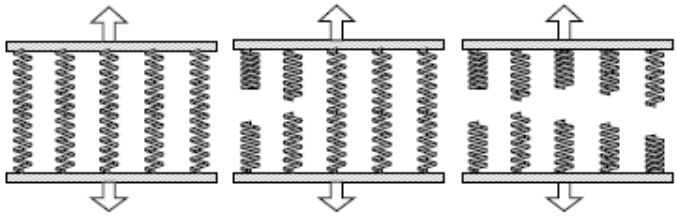


Fig. 2 Fracture process of equivalent springs

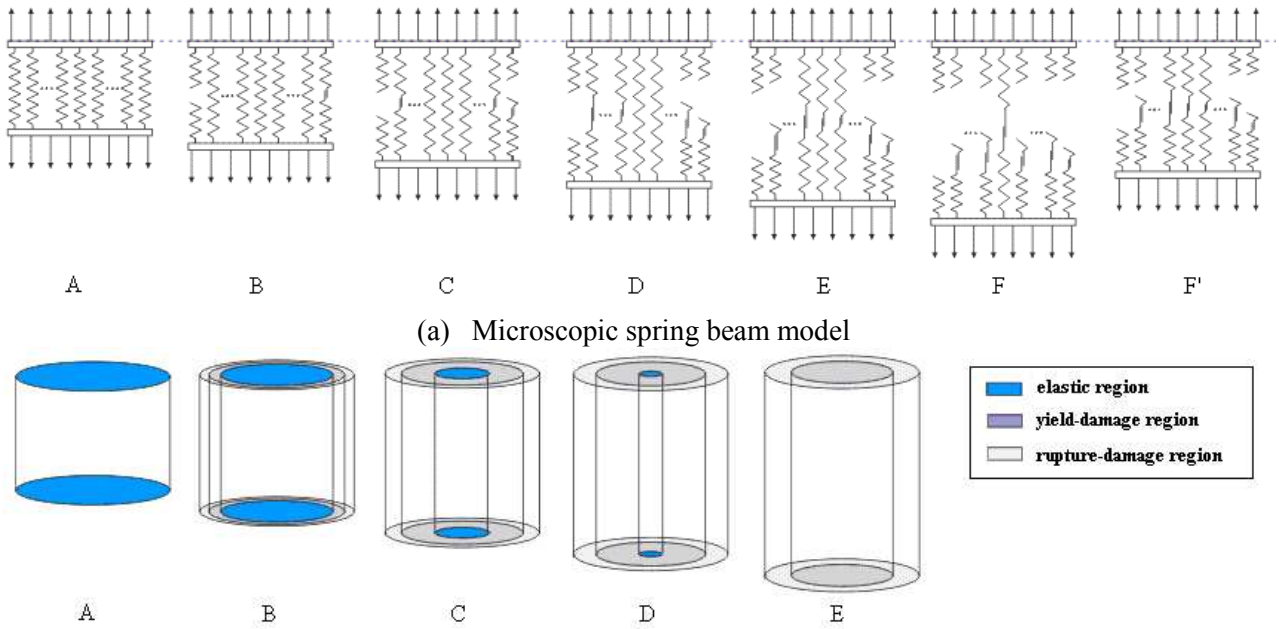
The damage mechanism could be described by the equivalent springs model in Fig. 2. The representative volume element (RVE) of concrete under uniaxial tension is regarded as a uniaxial link by a system with many vertical deformable springs connected by two rigid horizontal end-bars. The material disorder is introduced by the unequal rupture strain ε_R to each spring.

In fact, this kind of statistical damage model describes an ideal elastic-brittle damage process with microscopic heterogeneity, in which the whole deformation and failure is a uniform damage evolution course. However, there is a great gap between theoretical and practical damage processes, As Bazant [3] commented, PBS represents an unacceptable model for a material that is brittle on a large scale and it is not suitable for describing damage mechanisms of real materials.

Definition of Damage Variable. In this paper, the fundamental hypotheses of the proposed damage mechanism are given as follows [4]:

(1) The influence of the irreversible microchanges on the material macroscopic mechanical properties can be divided into two dominant aspects: the decrease of the effective cross-section and the degradation of elastic modulus in the effective region.

(2) The two damage modes can be simulated, respectively, by rupture and yield of the micro-element (bar); and the essence of failure can be interpreted as a continuous accumulation and evolution process of the two damage modes.



(a) Microscopic spring beam model

(b) Cylinder model

Fig. 3 Uniaxial tensile damage evolution process

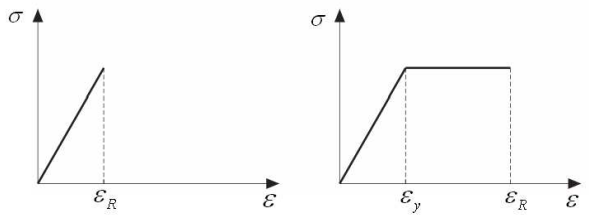


Fig. 4 Fracture modes of micro-bar element

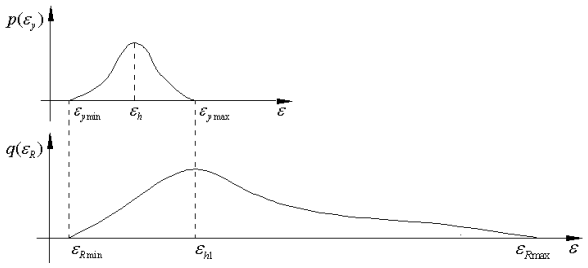


Fig. 5 Probability density function of yield strain and rupture strain

As shown in Fig. 3, the uniaxial tensile damage evolution process of concrete is simulated by the microscopic spring beam model and the cylinder model. The disorder is introduced by the unequal rupture strain ε_R and yield strain ε_y to each micro-bar, which are defined by the independent probability density function $q(\varepsilon_R)$ and $p(\varepsilon_y)$. The damage states A—F (F') correspond to the same characteristic states in Fig. 1.

In Fig. 3(a), the micro-bar has two kinds of failure modes, brittle-fracture and yield-fracture, as show in Fig. 4, A corresponds to the limit elastic state, where all the micro-bars remain elastic state. B, C, D correspond to the two states in strengthen segment and the peak nominal stress state, where some micro-bars are out of work due to fracture, some are yield, and the others remain the elastic state. E corresponds to the critical state, where all the residual bars are yield. F corresponds to the local breach phase in the FPZ, where the yielded bars continue to fracture, exhibiting the softening phenomenon. F' corresponds to the local breach phase in the other region, exhibiting the unloading phenomenon.

In Fig. 3(b), the specimen could be divided into three regions, the elastic region, the yield-damage region and the rupture-damage region during the damage process. With the growth of damage, the elastic region will gradually transform into the other two kinds of region. When reach the critical state E, the elastic region will disappear, the tensile traction will be fully borne by the yield-damage region, and then the damage of specimen will change into the local breach phase.

Damage variable D can be expressed as

$$D = 1-(1-D_R)(1-D'_y) \tag{2}$$

$$D'_y = \int_{\varepsilon_0}^{\varepsilon} p(\varepsilon_y)d\varepsilon_y - \frac{\int_{\varepsilon_0}^{\varepsilon} p(\varepsilon_y)\varepsilon_y d\varepsilon_y}{\varepsilon} \tag{3}$$

$$D_R = \int_{\varepsilon_0}^{\varepsilon} q(\varepsilon_R)d\varepsilon_R \tag{4}$$

Where D'_y is defined as the accumulated damage variable of elastic modulus due to the yield of the micro-bars; D_R is the accumulated damage variable of elastic modulus due to the rupture of the micro-bars.

In this paper, the yield and rupture strains ε_y, ε_R of micro-element are introduced as the fundamental random parameters, the damage variable D is defined by the independent probability density function $q(\varepsilon_R)$ and $p(\varepsilon_y)$ corresponding to the micro-elements.

In Fig. 5, $\varepsilon_{ymin}=\varepsilon_{Rmin}$ denotes the minimum values of the micro-bar yield and rupture strain, respectively. $\varepsilon_{ymax}=\varepsilon_{Rmax}$ denotes the corresponding maximum values. It assumes that ε_{ymax} represents the strain of critical state E, and ε_{Rmax} corresponds to the final failure state.

Constitutive relation of the statistical damage model. The constitutive relation [5] can be written as

$$\sigma_E = E_0(1-D'_y)\varepsilon \tag{5}$$

$$\sigma_N = E_0(1-D'_y)(1-D_R)\varepsilon \tag{6}$$

Where σ_E is the effective stress corresponding to the effective cross-section area A, σ_N is the nominal stress corresponding to the initial cross-section area A_0.

Examples and Verification

The macroscopic constitutive behavior of concrete specimen under uniaxial tension was simulated by the proposed damage model. The two probability density functions, $q(\varepsilon_R)$ and $p(\varepsilon_y)$ were introduced with triangular distribution.

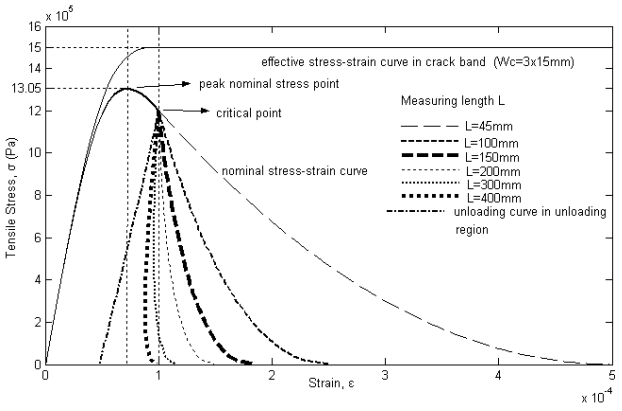


Fig. 6 Influence of the size effect on the master stress-strain curves

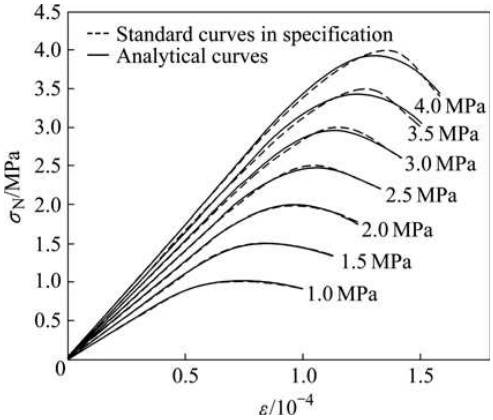


Fig. 7 Nominal stress-strain curves for concrete with different strength

In Fig. 6, the influence of the size effect during the local breach phase was discussed. W_c=3×15mm, denotes the width of the FPZ. L denotes the length of the specimen. After the critical state, the nominal stress-strain curves of the entire specimen exhibit a remarkable size effect. The slopes of these descendant curves become much steeper with the growth of the length L. Therefore, this softening segment of the nominal stress-strain curve obtained from a specific specimen cannot be considered as a pure material property.

In Fig. 7, the comparison between the analytical and the standard curves with different strength in specification [6] was conducted. Here, assume that the critical state corresponds to the location in the softening curves where the differential coefficient of second rank is zero.

Conclusions

The influence of the meso-damage evolution on material macroscopic properties could be classified into two dominant aspects: (1) decrease of effective cross-section and (2) degradation of elastic modulus of the effective framework. The two aspects can be modeled by rupture and yield of micro-bars.

The yield and rupture strains ε_y, ε_R of micro-element are introduced as the fundamental random parameters, the damage variable D is defined by the independent probability density function $q(\varepsilon_R)$ and $p(\varepsilon_y)$.

The proposed damage model could accurately describe the whole damage and fracture process of concrete under uniaxial tension, including the two-stage deformation properties and the size effect in the local breach phase.

Acknowledgements

This study was financially supported by the National Natural Science Foundation of China for Youth (51009020) and the High-level Personnel Research Project of North China Institute of Water Conservancy and Hydroelectric Power (201109).

References

[1] D. Krajcinovic, Damage mechanics: Accomplishments, trends, and needs, International Journal of Solids Structures, 37 (2000) 267-277.

[2] J. Lemaitre, R. Desmorat, Engineering damage mechanics: Ductile, creep, fatigue and brittle failures, Berlin: Springer, 2005.

[3] Z. P. Bazant, S. D. Pang, Mechanics-based statistics of failure risk of quasi-brittle structures and size effect on safety factors, Proceedings of the National Academy of Sciences, 103 (2006) 9434−9439.

[4] W. Bai, J. Chen, Z. Hu, Study on physical model of complete failure process of quasi-brittle materials in tension, Chinese Journal of Rock Mechanics and Engineering, 26 (2007) 670-681.

[5] W. Bai，J. Chen, G. Lin, S. Fan, The statistical damage model for quasi-brittle materials in uniaxial tension, Journal of Central South University of Technology, 16 (2009) 669-676.

[6] GB50010-2002, Specification for Design of Concrete Structure, China Building Industry Press, Beijing, 2002.

© (2012) Trans Tech Publications, Switzerland
doi:10.4028/www.scientific.net/AMM.238.51

Experimental Research on Sulfate Attack Resistance of Steel Fiber Reinforced Fly Ash Concrete

Lei Cui[1,a], Xiaodan Ge[2,b] and Qinyong Ma[2,c]

[1]Department of Civil Engineering, Zhejiang University, Hangzhou 310058, China

[2]College of Civil Engineering and Architecture, Anhui University of Science and Technology, Huainan 232001, China

[a]lcui@zju.edu.cn, [b]geshodan@163.com, [c]qyma_aust @ 163.com (corresponding author)

Keywords: SFRFAC; compressive strength; flexural strength; sulfate attack; concrete.

Abstract. Sulfate attack is one of the important factors affecting the durability of concrete. An experimental work had been carried out to investigate the behavior of steel fiber reinforced fly ash concrete (SFRFAC) exposed to sulfate attack in comparison with the plain concrete (PC), fly ash concrete (FAC) and steel fiber reinforced concrete (SFRC).The sulfate resistance of the SFRFAC, PC, FAC and SFRC under sodium sulfate attack of different concentrations were evaluated by measuring the compressive strength and flexural strength. The results show that the sulfate resistance of SFRFAC is higher than those of PC, FAC, and SFRC. With the increase of sodium solution concentration the compressive strength and flexural strength of SFRFAC, PC, FAC and SFRC decrease first, and then increase.

Introduction

Sulfate attack is one of the important factors affecting the durability of concrete and has been studied by many researchers, since Tuthill [1] noticed that the deteriorations of concrete structures caused by sodium sulfate attack in the 1930s. The effects of water cement ratio, cement sand ratio, specimen size, pre-storage method, solution concentration and temperature on the rate of concrete sulfate attack were investigated [2]. Shi et al [3] investigated resistance to sulfate salt crystallization of cement pastes containing ultra-fine fly ash and proposed that the breakage caused by sulfate salt crystallization corrosion on concrete was more severe compared to sulfate salt chemical corrosion. Bassuoni *et al.*[4, 5] investigated the durability of self-consolidating concrete to sulfate attack. Three different sulfate attack exposure regimes (full immersion, wetting-drying and partial immersion) were used to study the damage mechanisms and potential performance risks of self-consolidating concrete. Hartell et al [6] quantified the degree of sodium sulfate attack through the degradation of mechanical properties and found the surface disintegration caused by salt crystallization. Basista et al [7] proposed a micromechanical model under external sulfate attack to study the chemically assisted damage of concrete and to simulate the deformation of cementitious composites. Bonakdar and Mobasher [8] indicated that the sulfate resistance of cementitious materials was significantly influenced by the chemical composition and the transport properties of the system which could be improved by appropriate fly ash substitution. In another study, an improvement in accelerated testing as a way of predicting durability was proposed [9]. The researches of sulfate attack on concrete have also been addressed by a majority of references listed above, and also by the work of Sahmaran and Erdem et al [10], Monteiro and Kurtis et al [11] and Hekal et al [12]. It is debatable whether this form of sulfate attack is physical or chemical with physical consequences [13]. Mehta [14] and Haynes et al [15] referred to this type of attack as physical sulfate attack or salt hydration distress.

Based on these studies, in this paper, the study focuses on the sulfate resistance of the SFRFAC, PC, FAC and SFRC under sodium sulfate attack of different concentrations. The analysis on sulfate attack law of SFRFAC by comparing with SFRC, FAC and PC is presented.

Materials

Cement. Locally available ordinary Portland cement was used. The chemical composition of the cement is listed in Table 1.

Table 1 Chemical composition of the cement used in the study

Compound	SiO_2	CaO	Al_2O_3	Fe_2O_3	MgO	K_2O	SO_3	Na_2O	Loss on ignition
Content (%)	20.1	64.2	5.1	3.7	1.5	0.3	1.8	0.2	2.3

Coarse Aggregate and Fine Aggregate. The coarse aggregate used was crushed stone with good gradation. The size of the coarse aggregate was between 5 and 15mm. The fine aggregate used was natural silica sand. The sand had a fineness modulus of 2.957.

Fly Ash. The fly ash was obtained from the Tianjiaan power plant in Huainan and was shown in Fig. 1. The quality index of fly ash is listed in Table 2.

Table 2 Quality index of fly ash

Quality index (%)	WRR	LI	WC	FT	FCO	Fineness (45μm)
Testing Value	94	0.1	0.2	0.3	0.03	11

WRR=Water requirement ratio.LI= Loss on ignition.WC= Water content.FT= Fulfur trioxide.FCO= Free calcium oxide.



Fig. 1 Fly ash used in the test

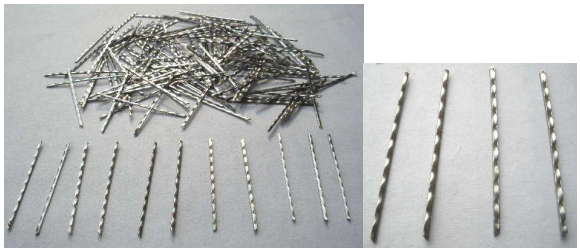


Fig. 2 Steel fibers used in the test

Steel Fiber. The corrugated steel fiber with 35mm long was supported by Yixing Junwei metal fiber Co., LTD in Jiangsu province and was shown in Fig. 2. The length-diameter ratio was 45 and the tensile strength is greater than 825MPa.The mechanical and physical properties of corrugated steel fiber are presented in Table 3.

Table 3 Mechanical and physical properties of corrugated steel fiber

Length (mm)	Tensile strength (MPa)	Elastic modulus (MPa)	Equivalent diameter (mm)	Length-diameter ratio	Incorporating volume percent (%)
35	825	2×10^5	0.8	45	1.2

Superplasticizer and Water. The NFsuperplasticizer was obtained from the Huainan synthetic materials Co., LTD. The water reducing rate can reach to 12% ~ 25%. Drinking water was selected.

Sodium Sulfate Anhydrous. The sodium sulphate anhydrous was produced by Wuxi Zhangwang chemical Co., LTD. Its physical properties and chemical composition are listed in Table 4.

Table 4 Sodium sulfate anhydrous

Compound	Na_2SO_4	Oxide	WI	LG	Phosphates
Content (%)	≥99.0	≤0.001	≤0.005	≤0.2	≤0.001
Compound	Ca	K	Fe	N	HM
Content (%)	≤0.002	≤0.01	≤0.0005	≤0.0005	≤0.0005

WI= Water insolubles. LI= Loss on ignition. HM= Heavy metal.

Mix Proportion. The mix proportions of SFRFAC, SFRC, FAC and PC were shown in Table 5.

Table 5 Mix proportions of SFRFAC, SFRC, FAC and PC

Type of concrete	SF (%)	FA (%)	W/C ratio	SR (%)	SP (%)	Materials (kg/m^3)						
						Cement	Water	Gravel	Sand	SP	SF	FA
PC	-	-	0.43	41	0.75	400	172	1037	721	3	-	-
FAC	-	30	0.43	41	0.75	400	172	1037	721	3	-	120
SFRC	1.2	-	0.43	41	0.75	400	172	1037	721	3	93.6	-
SFRFAC	1.2	30	0.43	41	0.75	400	172	1037	721	3	93.6	120

SF= Steel fiber. FA= Fly ash. SR= Sand ratio. SP= Superplasticizer.

Experimental

Specimens Preparation. The method of SFRFAC was first dry-mixing and then wet-mixing which was determined by many tests according to code for design of concrete structures (GB50010-2002), code for application technology of fly ash concrete (GBJ146-90) and test method of steel fiber reinforced concrete (CECS 13:89). The mixing procedure was cement, sand, gravel and fly ash were added in concrete mixer to stir in 3 minutes, and then added the steel fiber again to stir in 2 minutes, made its intensive mixing, finally added water and superplasticizer to stir in 2 minutes. The concrete specimens were 150 mm cubes in total of 12 groups with 36 specimens used to measure the reduction in compressive strength and 100×100×400mm concrete cuboids in total of 12 groups with 36 specimens used to measure the reduction in flexural strength. All specimens were demoulded after 24 hours and moist-cured at 20℃ and 95% RH for 28 days.



(a) Sulfate attacking (b) Airing (c) Drying (d) Sulfate attacking

Fig. 3 Accelerated erosion testing

Test Procedures. The sodium sulfate solution concentrations of 100 mg/L, 1000 mg/L and 10000 mg/L were used. Each group with 3 specimens of SFRFAC, SFRC, FAC and PC were put in the same sodium sulfate solution. An accelerated erosion testing as shown in Fig. 3 was the specimens attacked by sulfate at 21°C, dried in the air at 21°C and in the dryer at 60°C, and then attacked by sulfate at 21°C. The wetting–drying cycles were carried out 50 days at the end of the sulfate attack. The specimens were taken out of sodium sulfate solution and dried in air 4 hours before the test. The measurements of compressive strength were conducted with the continuous speed of 0.4MPa/s at TYE-2000C compression testing machine (Fig. 4). The measurements of flexural strength were conducted with the continuous speed of 0.01mm/s at RMT-150B multi-function automatic rock mechanics test system (Fig. 5).



Fig. 4 The test of compressive strength



Fig. 5 The test of flexural strength

Results and Discussion

Average Compressive Strength. Test results of average compressive strength of SFRFAC, SFRC, FAC and PC under the sulfate attack are listed in Table 6. The comparison of SFRFAC, SFRC, FAC and PC on average compressive strength under different sodium sulfate solution concentration is shown in Fig. 6. The average compressive strength of SFRFAC is higher than those of SFRC, FAC and PC, which are 17.4%, 12.4% and 21.0% respectively under the concentrations of 100 mg/L, and are 17.6%, 7.9% and 30.7% under the concentrations of 1000 mg/L and 19.0%, 9.7% and 21.7% under the concentrations of 1000 mg/L.

Fig. 6 indicates that with the increase of the concentration the average compressive strength of SFRFAC decreases 5.6% first, and then increases 2.2%, the SFRC decreases 5.7% first, and then increases 0.9%, the FAC decreases 1.7% first, and then increases 0.5%, and the PC decreases 1.7% first, and then increases 0.5%.

Table 6 Average strengths of SFRFAC, SFRC, FAC and PC under sulfate attack (MPa)

Type of concrete	Average compressive strength			Average flexural strength		
	100mg/L	1000mg/L	10000mg/L	100mg/L	1000mg/L	10000mg/L
PC	56.3	49.2	54.0	4.44	4.08	4.18
FAC	60.6	59.6	59.9	5.04	4.54	4.79
SFRC	58.0	54.7	55.2	5.40	5.04	5.14
SFRFAC	68.1	64.3	65.7	6.00	5.30	5.65

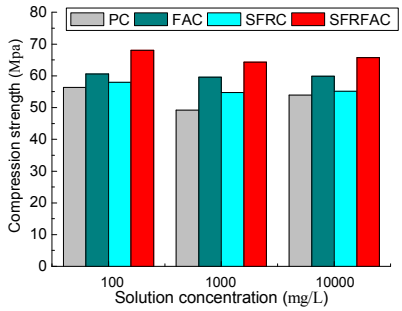


Fig. 6 Comparison of average compressive strength

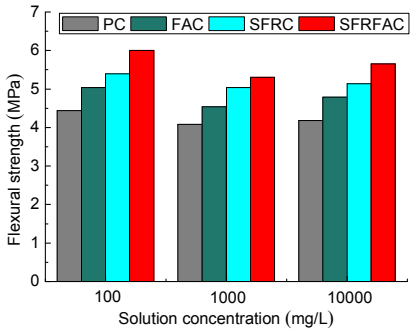


Fig.7 Comparison of average flexural strength

Average Flexural Strength. Test results of average flexural strength of SFRFAC, SFRC, FAC and PC under the sulfate attack are listed in Table 7. The comparison of SFRFAC, SFRC, FAC and PC on average flexural strength under different sodium sulfate solution concentration is shown in Fig.7. The average flexural strength of SFRFAC is higher than those of SFRC, FAC and PC, which are 11.2%, 19.0% and 35.3% respectively under the concentrations of 100 mg/L, and 5.0%, 16.6%, 29.7% under the concentrations of 1000 mg/L and 9.9%, 18.0%, 35.1% under the concentrations of 1000 mg/L.

Fig.7 indicates that with the increase of the concentration the average flexural strength of SFRFAC decreases 11.7% first, and then increases 6.7%, the SFRC decreases 6.5% first, and then increases 2.0%, the FAC decreases 9.9% first, and then increases 5.4%, the PC decreases 9.2% first, and then increases 2.4%.

The load-displacement curves of flexural strength test on SFRFAC, SFRC, FAC and PC are shown in Fig.8, Fig.9, Fig.10 and Fig.11. Fig.8 and Fig.9 indicate that the sulfate resistances of PC and FAC under the concentration of 1000 mg/L are lower than those under the concentrations of 100 mg/L and 10000 mg/L, and the PC and FAC have the traditional characteristics of brittleness.

Fig.10 indicates that the SFRC still has a good toughness after sulfate attack. There is a second peak in the Load-displacement curve, for the steel fibers of SFRC aren't completely corroded.

Fig.11 indicates that the sulfate resistance of the SFRFAC is higher than those of SFRC, FAC and PC, and the SFRFAC after sulfate attack still has high strength, good ductility and toughness.

Discussion. Sulfate ions enter into the SFRFAC, SFRC, FAC and PC by the capillary diffusion or penetration. The higher is the sodium solution concentration, the more distribution of sulfate ions is on the per unit area of specimens. Simultaneously, the more sulfate ions permeate into the concretes, the faster the concretes are damaged. Migration of sulfate ions into SFRFAC, SFRC, FAC and PC may cause the following chemical reactions:

$$Ca(OH)_2+Na_2SO_4+2H_2O\rightarrow CaSO_4\cdot 2H_2O+2NaOH \quad (1)$$

$$Ca(OH)_2+MgSO_4+2H_2O\rightarrow CaSO_4\cdot 2H_2O+Mg(OH)_2 \quad (2)$$

The strength and stiffness of the concretes are decreased by the formation of gypsum. Subsequently, when the concentration increases from100mg/L to 1000mg/L, the compressive and flexural strength of SFRFAC, SFRC, FAC and PC are reduced after sulfate attack.

When solution concentration continuesly increase, the damage would be reduced with the increasing of sodium solution concentration, as the sodium sulfate solution concentration is too high, a lot of sulfate ions permeates into the concretes at a very short time. The chemical reactions are:

$$3CaSO_4 \cdot 2H_2O + 3CaO \cdot A1_2O_3 + 26H_2O \rightarrow 3CaO \cdot A1_2O_3 \cdot CaSO_4 \cdot 32H_2O \quad (3)$$

$$6Ca^{+2} + 3SO_4^{-2} + A1_2O_6^{-6} + 32H_2O \rightarrow 3CaO \cdot A1_2O_3 \cdot CaSO_4 \cdot 32H_2O \quad (4)$$

There are amount of ettringite formation, which can increase the viscosity of the concretes and stop sulfate ions further infiltration and erosion reaction. Subsequently, when the concentration increases from1000mg/L to 10000mg/L, the compressive and flexural strength of SFRFAC, SFRC, FAC and PC are relatively increased after sulfate attack.

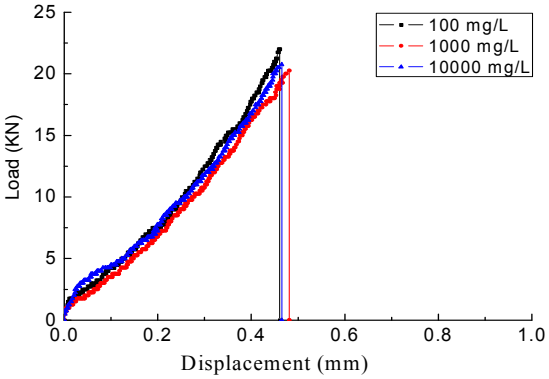


Fig. 8 Load-displacement curves of PC

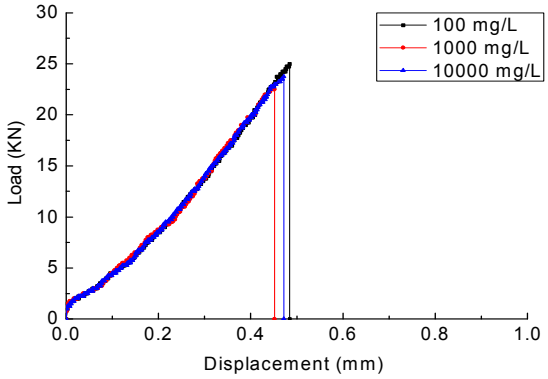


Fig. 9 Load-displacement curves of FAC

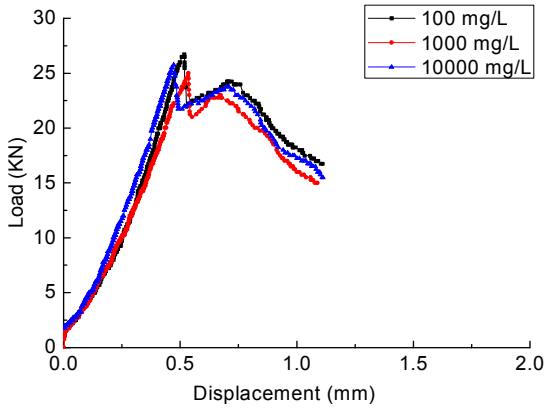


Fig.10 Load-displacement curves of SFRC

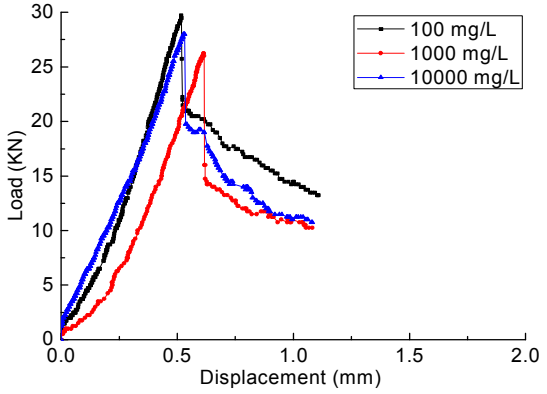


Fig.11 Load-displacement curves of SFRFAC

From above discussion it can be deduced that the sulfate resistant of FAC is higher than that of PC, for the fly ash could improve workability, increase the viscosity and reduce the bleeding and segregation of concrete. The sulfate resistant of SFRC is higher than that of PC, for the tensile strength, flexural strength and flexural toughness could be significantly improved by the steel fiber. The sulfate resistance of SFRFAC is higher than those of PC, FAC, and SFRC, for the sulfate resistant and the durability of SFRFAC are significantly improved by mixing appropriate amount of fly ash and steel fiber. Consequently, the SFRFAC presents many advantages in terms of good toughness, high strength, excellent durability, etc.

Conclusions

This study presents the results of the sulfate attack resistance of SFRFAC in comparison with SFRC, FAC and PC. Based on the results obtained from the study, the following conclusions can be drawn:

The compressive and flexural strength of SFRFAC are higher than those of SFRC, FAC and PC under sodium sulfate attack of different concentration， and still have high strength and good ductility and toughness.

With the increase of sodium solution concentration from 100mg/L to 10000mg/L, the compressive strength and flexural strength of SFRFAC, PC, FAC and SFRC decrease first, and then increase.

The sulfate attack resistant and the durability of SFRFAC are significantly improved by mixing appropriate amount of fly ash and steel fiber. SFRFAC presents many advantages in terms of good toughness, high strength, excellent durability, etc.

Acknowledgements

This work was supported by the Science and Technology Projects in 2007 the Ministry of Construction (2007-K2-27). The authors are grateful to Yixing Junwei metal fiber Co., LTD.

References

[1] L.H. Tuthill, Resistance of cement to the corrosive action of sodium sulfate solutions. ACI Journal, 33 (1936) 83-103.

[2] X. Fang, C. Shen, D. Yang, Investigations of influence factor on the rate of concrete sulfate attack, Journal of Building Materials, 10 (2007) 89-96.

[3] M. Shi, Y. Xie, B. Liu, Resistance to sulfate salt crystallization of cement pastes containing ultra-fine fly ash, Journal of Building Materials, 6 (2003) 350-355.

[4] M.T. Bassuoni, M. L. Nehdi, Durability of self-consolidating concrete to different exposure regimes of sodium sulfate attack, Materials and Structures, 42 (2009) 1039-1057.

[5] M.T. Bassuoni, M. L. Nehdi, Durability of self-consolidating concrete to sulfate attack under combined cyclic environments and flexural loading, Cement and Concrete Research, 39 (2009) 206-226.

[6] J. A. Hartell, A. J. Boyd, C. C. Ferraro, Sulfate attack on concrete: effect of partial immersion, Journal of Materials in Civil Engineering, 23 (2011) 572-579.

[7] M. Basista, W. Weglewski, Chemically assisted damage of concrete: A model of expansion under external sulfate attack. International Journal of Damage Mechanics, 18 (2009) 155-175.

[8] A. Bonakdar, B. Mobasher, Multi-parameter study of external sulfate attack in blended cement materials, Construction and Building Materials, 24 (2010) 61-70.

[9] F. Girardi, W. R. Vaona, D. Maggio, Resistance of different types of concretes to cyclic sulfuric acid and sodium sulfate attack, Cement and Concrete Composites, 32 (2010) 595-602.

[10] M. Sahmaran, T. K. Erdem, I. O. Yaman, Sulfate resistance of plain and blended cements exposed to wetting–drying and heating-cooling environments. Construction and Building Materials. 21 (2007) 1771-1778.

[11] P. J. M. Monteiro, K. E. Kurtis, Experimental asymptotic analysis of expansion of concrete exposed to sulfate attack, ACI Materials Journal, 105 (2008) 62-71.

[12] E. E. Hekal, E. Kishar, H. Mostafa, Magnesium sulfate attack on hardened blended cement pastes under different circumstances, Cement and Concrete Research, 32 (2002) 1421-1427.

[13] J. Skalny, J. Marchand, I. Odler, Sulfate Attack on Concrete. Spon Press, London and New York, 2002.

[14] P. K. Mehta, Sulfate attack on concrete: separating myths from reality, Concrete International, 22 (2000) 57-61.

[15] H. Haynes, R. O'Neill, P. K. Mehta, Concrete deterioration from physical attack by salts, Concrete International, 18 (1996) 63-68.

[16] W. Jin, Y. Zhao, Durability of Concrete Structures, Science Press, Beijing, 2002.

[17] ASTM C1012, Standard Test Method for Length Change of Hydraulic-cement Mortars Exposed to a Sulfate Solution. Am Soc Test Mater, 2004.

© (2012) Trans Tech Publications, Switzerland
doi:10.4028/www.scientific.net/AMM.238.57

Toughness of ECC Evaluated by Nominal Fracture Energy

Shuling Gao[1,2,a] Wei Shao[3,b] Jinli Qiao[1,c] and Ling Wang[1,d]

[1] School of Civil Engineering, Hebei University of Technology, Tianjin, China

[2] Civil Engineering Technology Research Center of Hebei Province, Tianjin, China

[3]China Qingdao International Economic & Technical Cooperation(Group) Co.,Ltd, China

[a]gsl200001@yahoo.com.cn, [b] hob_w_shao@hotmail.com, [c]qiaojinli@126.com,[d] wlark@sina.com

Keywords: bridge deck pavement; bridge deck negative moment zone; ECC; nominal fracture energy; multiple cracking.

Abstract. ECC (Engineered Cementitious Composites) has ultra-high toughness and can be used in the zone needing the ultra-high tensile strain and very high durability. In order to investigate the toughness of ECC, the normal fracture energy G_F is calculated and compared with ordinary concrete. The influence of the matrix (fly ash, silicon fume), the fiber (glass fiber, steel fiber and PVA fiber) and the fiber volume ratio on the G_F of ECC are analyzed. The research indicates that silicon fume and glass fiber, steel fiber are all not able to be used in ECC. But flash ash and PVA fiber are very suit for using in ECC, the toughness of ECC increases with the increase of their content.

Introduction

The fracture energy G_F of concrete is defined by the surface energy of crack expanding unit area. Concrete is a quasi-brittle material, the load drops quickly and strain begins softening after cracking and happens single crack cracking. So, the fracture energy can be used to evaluate the toughness of ordinary plain concrete.

ECC is the composites with naked strain-hardening phenomenon in uniaxial tension. Accompanying the strain-hardening phenomenon, the multicrack, the ultra-high toughness and the energy absorption ability are greatly different with ordinary concrete [1-2]. The strain-hardening character held by ECC is the source of unique toughness and the result of realizing stable cracking. The tensile strain is more than steel bar (2000με at yielding stress) and can easily reach 10000με.

There are multiple cracks occurring in ECC [3-4]. The long range plastic zones happen at the precut crack tip and the shape is like onion. The composites happen ductile fracture and can not directly use the linear elastic fracture mechanical theory to evaluate the toughness of the composites. In addition, not one fracture plane happen but many more fracture plane happen. So, the calculating results of fracture energy in fact are not the true fracture energy. But, it can be uses to approximately evaluate the toughness of the strain-hardening composites by Normal Fracture Energy. In this research, wedge splitting specimen is used to investigate the toughness of PVA-FRCCs [5-8].

Experimental Procedures

Materials. Superplasticizer, HPMC and defoamer are 0.8%, 0.15% and 0.08% of the mass of cement. Silicasand is 536 kg/m^3, and water is 450 kg/m^3.

Table 1 Mix proportions (kg/m^3)

Material	Cement	Silica fume	Fly ash	PVA	Glass fiber	Steel fiber
F-2	1070			26		
FA-2	962		108	26		
SF-2	962	108		26		
SF-1	962	108		13		
SF-0	962	108				
SF-GF	962	108			26	
SF-1-GF	962	108		13	13	
SF-SF	962	108				13

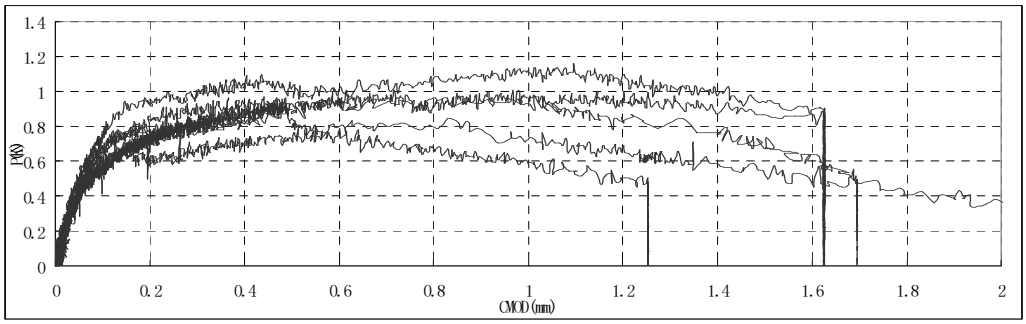
The matrix used in this study include cement (52.5R I ordinary Portland cement), silica fume (made in Elkem), fly ash (Grade I), silica sand, superplasticizer, defoamer (PRS-6E) and hydroxypropy l methyl cellulose(HPMC-60HD4000). The average particle size of silica sand is between 45 order and 75 order. The Discontinuous PVA fiber (REC15) is used in this research manufactured by Kuraray Co. Ltd. The mix proportions of each batch are shown in Table 1.

Composites Preparation. The composites are carefully prepared in a UJZ-15 mortar mixer. For each batch, at least five wedge splitting specimens (152 mm×157 mm×50 mm). The steps of manufacturing PVA-FRCCs by cast are similar to the steps of conventionally cast concrete, except some little differences [8].

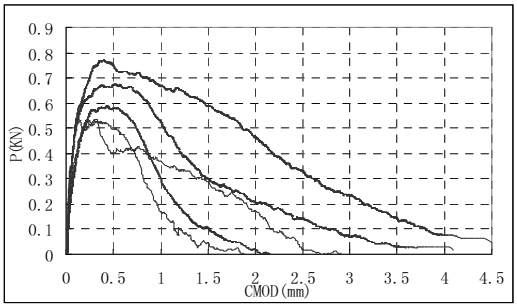
When the fresh mix was ready, the wedge splitting specimens were made in already wooden molds, with a table vibrator. Twenty-four hours after casting, specimens were demolded and placed in water tank at normal temperature for 28 days.

Results and Discussions

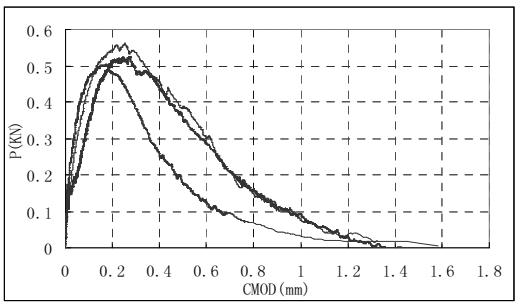
PSH (*P-CMOD*) Curves



(a)F-2-65

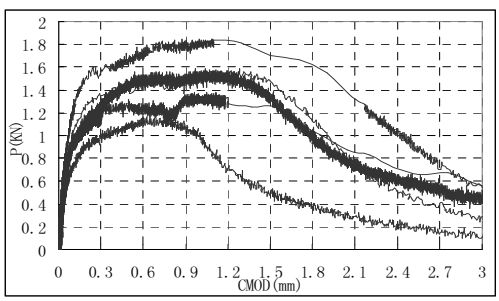


（b）SF-1-GF-65

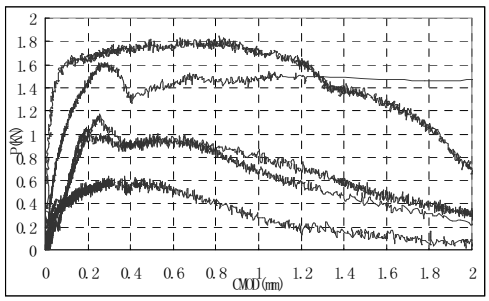


（c）SF-GF-65

Fig.1 *P-CMOD* curves of all kinds of cementitious composites (initial crack length=65mm)



(a)FA-2-50



(b)F-2-50

Fig.2 *P-CMOD* curves of all kinds of cementitious composites (initial crack length =50mm)

Nominal Fracture Energy G_F.

$$G_F = \frac{W + mgCMOD_0}{A \cdot 2tg\alpha} \tag{1}$$

Where G_F is the fracture energy (N/m), W is the the area between the whole $P\sim CMOD$ curve and horizontal ordinate (N•m), $CMOD_0$ is the maximum crack mouth opening displacement (m), mg is the gravity of wedge loading devices (kN), A is the ligament area (m^2), $A=t(h-a_0)$, a_0 is the prenotched crack height (m), h is the specimen height (m), t is the specimen width (m).

The calculation results can be shown in Table 2. The peak load P_{max} of FA-2-50 is 1.6kN and is the 1.13 times of F-2-50 (1.419kN). The $CMOD_0$ of FA-2-50 is 1.113mm and is the 2.88 times of F-2-50 (0.387mm). The G_F of FA-2-50 series are the maximum and reach to 2154.97N/m, which is the 1.75 times of F-2-50 (1229.24N/mm). The fracture of PVA reinforced cementitious composites is even greater than steel fiber reinforced concrete. This suggests that the adding of fly ash is very favorable to the toughening. The G_F of steel fiber cementitious composites (SF-SF-50 series) is 223.15N/m more than SF-GF-50, which is same with high strength concrete. This indicates that the glass fiber is not suit to using in cementitious composites.

Table 2 Fracture energy of cementitious composites

No. of specimen	Initial crack length =50mm			No. of specimen	Initial crack length =65mm		
	P_{max} (kN)	$CMOD_0$ (mm)	G_F (N/m)		P_{max} (kN)	$CMOD_0$ (mm)	G_F (N/m)
F-2-50-1	1.052	0.192	746.01	F-2-65-2	1.123	1.086	1107.95
F-2-50-2	1.626	0.276	1449.35	F-2-65-3	0.915	0.468	1102.98
F-2-50-4	1.139	0.253	893.43	F-2-65-4	1.047	0.994	1072.63
F-2-50-5	1.86	0.828	1828.17	F-2-65-5	0.944	0.868	927.23
Mean	**1.419**	**0.387**	**1229.24**	Mean	**1.007**	**0.854**	**1052.7**
S.D	0.336	0.256	434.01	S.D	0.083	0.236	73.69
C.V	0.236	0.662	0.353	C.V	0.082	0.276	0.07
FA-2-50-2	1.582	0.967	1927.37	SF-2-65-1	0.336	0.513	562.68
FA-2-50-3	1.381	1.118	2431.46	SF-2-65-2	0.623	0.893	1607.85
FA-2-50-4	1.587	1.283	1788.07	SF-2-65-3	0.434	0.643	652.74
FA-2-50-5	1.848	1.086	2472.98	Mean	**0.464**	**0.683**	**941.09**
Mean	**1.6**	**1.113**	**2154.97**	S.D	0.119	0.158	472.9
S.D	0.166	0.113	301.66	C.V	0.257	0.231	0.503
C.V	0.104	0.101	0.14	SF-1.5-65-1	0.546	0.724	997.93
SF-SF-50-1	0.332	0.136	107.57	SF-1.5-65-2	0.376	0.616	843.98
SF-SF-50-2	0.535	0.123	159.16	SF-1.5-65-3	0.6	0.76	1282.95
SF-SF-50-3	0.732	0.204	281.16	Mean	**0.507**	**0.7**	**1041.62**
SF-SF-50-4	0.591	0.171	344.7	S.D	0.096	0.061	181.852
Mean	**0.548**	**0.158**	**223.15**	C.V	0.189	0.087	0.175
S.D	0.144	0.032	94.327	SF-1-65-1	0.453	0.515	630.91
C.V	0.262	0.2	0.423	SF-1-65-2	0.418	0.484	586.10
SF-50-0	0.426	0.095	61.166	SF-1-65-4	0.397	0.563	637.58
SF-GF-50-2	0.633	0.67	237.86	Mean	**0.423**	**0.521**	**618.2**
SF-GF-50-4	0.616	0.672	193.55	S.D	0.023	0.033	22.86
Mean	**0.625**	**0.671**	**215.71**	C.V	0.055	0.063	0.037
S.D	0.008	0.0009	22.16	SF-1-GF-65-3	0.535	0.589	413.3
C.V	0.013	0.0014	0.103	SF-1-GF-65-4	0.612	0.677	733.47
				Mean	**0.535**	**0.6**	**545.95**
				S.D	0.063	0.058	136.35
				C.V	0.117	0.097	0.25
				SF-GF-65-1	0.508	0.562	238.48
				SF-GF-65-2	0.457	0.526	226.14
				SF-GF-65-3	0.47	0.504	162.12
				Mean	**0.478**	**0.53**	**208.91**
				S.D	0.021	0.024	33.47
				C.V	0.045	0.045	0.16

The G_F of SF-2-65 is less than SF-1.5-65 and more than SF-1-65, the G_F of SF-1-GF-65 is less than SF-1-65. This indicates that extra glass fiber added can not improve the toughness of matrix. The G_F of SF-GF-65 only adding the 0.96% glass fiber is only 1/3 of SF-1-65 added 1% PVA fiber. This fully displays the advantage of PVA fiber in toughening the cementitious composites.By comparing the G_F of SF-2-65 and F-2-65, we can find that the silicon fume adding in the cementitious composites can decrease the toughness. But fly ash can increase the toughness of cementitious composites.

Conclusions

Nominal Fracture Energy G_F can be as a index to assess the toughness same with the strain-soften materials. PVA fiber can not only largely increase the Nominal Fracture Energy of cementitious composites but also influence the crack shape at precut crack tip. In fact, only one main crack expands along the precut crack tip of strain-softening composites. But, many microcracks occur surrounding the crack tip like onion except the main crack happening not always along the precut crack tip.

Through experiments, it is proved that PVA fiber has the best effect to toughen the cementitious composites. And the Nominal Fracture Energy of ECC is equal to steel fiber reinforced concrete. The toughness of steel fiber added in mortar is less than added in concrete. The toughness of glass fiber composites is less than steel fiber composites. PVA fiber is the relative best toughening materials.

The Normal Fracture Energy G_F as the other methods to assess the toughness of PVA-FRCCs is more twice to triple than that of ordinary concrete. The $CMOD_0$ value is from 7.4 and 10.6 times that of ordinary concrete. Those indicate the ultra toughness of PVA-FRCCs .

Acknowledgments

This work is sponsored by the National Science Foundation for Young Scientists of China (51108151), Jiangsu Province Civil Engineering Materials Key Laboratory Open Funded Projects, the State Key Development Program(973 Program) for Basic Research of China (2009CB623203), Natural Science Foundation of Hebei Province, China (E2012202097), the National Science Foundation for Post-doctoral Scientists of China (20100470046).

References

[1] Victor C Li, S. Wang, Cynthia Wu. Tensile strain-hardening behavior of polyvinyl alcohol engineered cementitious composite (PVA-ECC). ACI Materials Journal, 6 (2001) 483-492.

[2] Victor C Li, Engineered cementitious composites for structural applications innovations forum. Journal of Materials in Civil Engineering, 2 (1998) 66-69.

[3] Victor C. Li, On engineered cementitious composites (ECC) - A review of the material and its applications, Journal of Advanced Concrete Technology, 1 (2003) 215-230.

[4] S. Xu, S. Gao, Fracture and tensile properties of polyvinyl alcohol fiber reinforced cementitious composites, Journal of Wuhan University of Technology (Materials Edition), 1 (2008) 7-11.

[5] S. Gao, S. Xu, Toughness study on PVA fiber reinforced cementitious composites using total work done by horizontal load, Journal of Southeast University (Science and Technology), 2 (2007) 324-329.

[6] S. Xu, Y. Zhao, Z. Wu, The experimental study on the fracture energy of concrete using wedge splitting specimens, Journal of Hydroelectric Engineering, 4 (2003) 15-22.

[7] B. L. Karihaloo, H. Abdalla, Q. Xiao, Coefficients of the crack tip asymptotic field for wedge splitting specimens, Enigneering Fracture Mechanics, 70 (2003) 2407-2420.

[8] J. Xiao, Holger Schneider, Cindy Donnecke, Gert Konig, Wedge splitting test on fracture behaviour of ultra high strength concrete, Construction and Building Materials, 18 (2004) 359–365.

© (2012) Trans Tech Publications, Switzerland
doi:10.4028/www.scientific.net/AMM.238.61

A Review on the Connection of FRP Bars

Guoqing Yuan [a] and Nan Zhu [b]

School of Aerospace Eng. and Applied Mechanics, Tongji University, Shanghai 200092, China

[a] gqyuan@tongji.edu.cn, [b] anjikian@yahoo.com.cn

Keywords: FRP bar, coaxial connect, off-axis connect, research progress.

Abstract. Just like the steel bars, the connection of FRP bars is needed in engineering application. But most of the steel bars' traditional connection ways are not suitable for FRP bars because of the differences of the material properties. With the engineering application standards' appearing, it is becoming an urgent need that we should have one or some connection methods for FRP bars which can be selected and used by engineers. This paper presents a brief overview about the research progress of FRP bars' connections, gives the definition and the design principles of FRP bars' connection, emphatically introduces the research progress of coaxial connection of FRP bars, and discusses the off-axis connection ways. At last, we put forward some works that need to be further researched.

Introduction

Because using FRP(Fiber Reinforced Polymers) bars to replace steel bars can significantly improve the durability and reduce the life-cycle costs of the concrete structures, concrete structures reinforced with FRP bars, prestressed FRP bars and FRP anchor bolts are being more and more used in bridge, offshore structures, nuclear reactor engineering, airport pavement, underground constructions and coal mine tunnel structures with the promulgation and implementation of the design specifications [1-5]. Similar to steel bars constraining in transportation and production, the length of commercially produced FRP bars is limited by such constraints. This leads to the need of joining such bars when longer bars are required [6-8].

The splicing, which is suitable for steel bars, such as welding, pressed sleeve splicing of ribbed steel bars, tapered threaded splicing of bars, parallel thread rebar splicing with cold upsetting end, parallel thread rebar splicing with rolled thread end, molten metal filling the sleeve splicing, etc., are not suitable for thermosetting FRP composite bars. The thermosetting FRP bars do not have the solder ability and can't be cold-bended. Although thermoplastic FRP rebar can be welded, but its essence is the matrix welding, the fibers, which are the main role in load carrying, can't be welded. And FRP bars' strength and stiffness are anisotropic, bearing strength and lateral performances are weak. It is brittleness. The basic section of FRP bars is circular. To increase the adhesive ability between FRP bar (anchor bolt) and concrete (anchor solid), in practice, FRP bars (anchor bolt) are usually processed to thread shape and the surface is coated by sand or other granular materials or short fibers to make uneven form etc. The load FRP bar transferred in application is big and centralized and high reliability is needed. So the connection of FRP bars are obviously different from the connections, which are widely used in aviation, aerospace engineering composite material components and other composite structures, such as adhesively bonded joints and mechanically fastened joints. It should be specially researched. This paper will focus on the review about the study in the connection of FRP bars and give some further research suggestions.

Definition of FRP Bars' Connection

This paper mainly discusses the connection of two FRP bars, including coaxial connection and off-axis connection of FRP bars. The so-called coaxial connection means the axes of the connected two FRP bars are in the same line after they were connected. If not, we call it off-axis connection.

The generalized connection of FRP bars also includes the anchorage of FRP bars in concrete, the connection between FRP bars and test machine in performance test of FRP bars, etc. Such connection does not belong to the discussion scope in this paper.

Design Principles of FRP Bars' Connector

FRP bars connector design should meet the requirements of the joint strength, and should also keep FRP corrosion resistance, no magnetic predominant performance.

According to the specific requirements of the joint strength, the connector can be divided into different levels. For example, we can ask for Grade A connector its single tensile strength and repeated stretching strength in high stress level is not less than the connected FRP bars' corresponding performance, Grade B connector its tensile strength can be lower than 100% but should be higher than 70% (or other proportion) FRP bars' corresponding performance. The indexes and classification method need to further research.

Coaxial Connection of FRP Bars

Steel Sleeve/expansion Cement Coaxial Connection. The work of J. M. Lees [9] about FRP bars' coaxial connection is the earliest and systematic. J. M. Lees, Gruffydd-Jones and C. J. Burgoyne put forward the steel sleeve/expansion cement FRP bars coaxial connecting scheme based on the CFRP sleeve/expansion cement anchorage presented by Harada [10] and make some experiments.

This steel sleeve/expansion cement coaxial connection scheme provided by J.M.Lees is easily construction and low cost. But according to FRP bars' design principle, it is not an ideal connection method for FRP bars because the steel sleeve is easy to corrode and do not fit for the non-magnetic requirements. In addition J.M.Lees had not studied the fatigue property of the connection. However Harada's research on steel sleeve/expansion cement anchorage fatigue properties shows that it has good fatigue performance. Besides, the engineering implementation method based on the scheme also needs further research, especially horizontal pouring implementation methods.

Steel Sleeve/adhesive Coaxial Connection. Early in 1983, V.Navaratnarajah [11] had researched the epoxy sleeve connectors. J. K. Zhou [7] studied the design method of connection with steel sleeve and epoxy adhesive for GFRP bars in 2006. They measured the bond-slip relationship between GFRP bar and steel sleeve by pull out tests firstly, and got average bond strength. Thus the connection section length size can be calculated according to the average bond strength. But the paper didn't mention connector test, and didn't give any connector test data also.

This connector scheme is similar with the bonded anchorage, as one of anchoring methods of prestressed FRP bars [12]. It posses the following faults: long curing time, high requirements to adhesive properties, big creep, large sleeve size and steel sleeve easy to corrode. Its long-term reliability, environmental adaptability and the fatigue properties also require further study.

Pressed Steel Sleeve Coaxial Connection. Hughes Brothers Company has developed a pressed steel sleeve anchorage. Colin [13] applies it to the connection of CFRP bar. The CFRP tendons were only available in lengths up to 12 m because the 12-mm-diameter tendons cannot be coiled for transportation. In order to span a length of 18 m, the tendons were delivered with a Hughes Brothers anchor epoxied to one end, and two tendons were spliced together by using a threaded rod coupler.

In fact we found that the failure load is only about 70% FRP bar's load capacity itself in the tensile experiment we have done for GFRP bars with dry pressed steel sleeve anchorage ends. And all specimens broke at the entrance of the extrusion sleeve without exception. So the connector efficiency is suspect. And it's also facing easy corrosion, not degaussing problem.

The wet pressed steel sleeve anchorage put forward by Zhang [14] also can be used in connector for FRP bars. But Zhang pointed out that it needs high pressing process level. Certainly steel sleeve also exist corrosion problems.

FRP Sleeve/expansion Cement Coaxial Connection. Recognizing the shortcomings of steel sleeve/expansion cement connection schemes, Yuan, Dong etc. [15] put forward a modified method of FRP bars coaxial connection with FRP sleeve/expansion cement. By experiment[15], the connection scheme is effective, the strength of the joint are not less than the strength of FRP bars itself, the destruction position is located in the free section, as shown in Fig.1.

Because of FRP sleeves can be prefabricated, the quality is easy to control, and the expansive cement is low cost, this connection method has obvious advantages such as simple in construction, light weight, high strength, and corrosion resistance. And it can be used for a degaussing requirements structure and so on. But it still has the problem of big shape dimension. In addition the durability, resist fatigue properties, design method and so on also need to be studied further.



Fig. 1 Sample of FRP sleeve/expansion cement coaxial connection and tensile failure pattern

Coaxial Connection of FRP Bars with Winding Fiber Cloth

Yuan and Dong [16] also developed another coaxial connection method for FRP bars with winding fiber cloth. Fig.2 is the diagram of the connection scheme. The experimental results indicate that the connection method has the following characteristics: small size, light weight, high strength, corrosion resistance, easy to construction etc. Fig.3 is the destruction condition of the connection scheme. The destruction position occurred in the free section rather than connection parts.

The mechanism of load transfer in the connection scheme is adhesive/mechanical bite coupled transfer load. According to the characteristics of shear and peel stress in the adhesive layer, and the necessary circumferential direction constraint strength for effective bite, it is the key of the connection scheme that winding some fiber bundle/belt at the both ends and the middle of the connection. It has been proved effective in further CFRP bars connection study. Of course the mechanism of load transfer, resist fatigue properties, durability of the connection scheme still need to do more research.

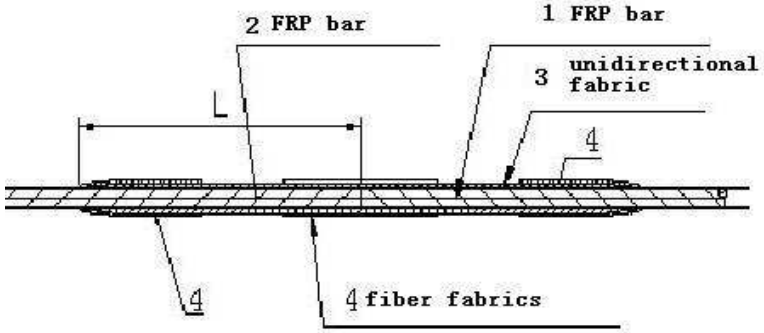


Fig. 2 FRP fiber cloth winding coaxial connecting scheme



Fig. 3 FRP bar tensile failure pattern with fiber cloth bound by coaxial connection

Other coaxial connections

Steel Sleeve with Female Thread Coaxial Connection for Full Thread FRP Bars /anchor Bolt. For two full thread FRP bars/anchor bolts, they can be connected together with a steel sleeve with female thread [17], in which a full thread FRP bar is anchored at the ends with nuts. But literature [17] also pointed out that the connection strength is only 60-80% strength of the bar itself because of the screw connection structure's defects (mainly resulting from thread forming process). Such connection efficiency cannot meet the performance requirement of Grade A connector.

Reversed Cone Connection. Y. L. Zhu [18] had studied the connection of pultrusion GFRP rod as early as 1981. He analyzed the bearing capacity of two connecting forms which are adhesive and reversed cone connections and gained the following results: the tensile strength of either adhesive connection or reversed cone connection is always less than the tensile strength of pultrusion GFRP round bar. Of course, although the FRP bars studied today is also belong to pultrusion product, but due to the introduction of the surface treatments, it is different from pultrusion round bar.

Off-axis Connection of FRP Bars

Lap Splice without Binding. For lap splice without binding, the two connected bars are parted before the concrete hardened. Load transfer is actually through the hardened concrete. The method given in ACI 440.1R-06 [19] is actually developed by Benmokrane 1997 [20], Mosley 2002 [21]. The splice length is advised to take 1.3ld (ld is the minimum development length). And ld is relevant to concrete strength, the type, size and surface morphology of FRP bars, spacing in concrete, concrete cover thickness and so on. But according to GB50010 [22] this lap splice has applicable scope. The connection of FRP bars can't wholly rely on such connection.

Compared with the coaxial connection, lap splice without binding has obvious advantages. It needn't special connection construction. But its shortcomings are also clear: material waste, size large, load transfer path changing. Especially it cannot be used in many cases.

Lap Splice with Binding. C.J. Fu and Z. F. Zhou [23] did a preliminary experiment research to lap splice with binding. G.Q. Yuan etc [24] also did some research about lap splice with binding.

This connection scheme is a high efficiency off-axial connection method, which it can be used when the coaxial connection is difficult to use. It still has good anticorrosion properties, and it is convenient in construction. Fig.4 is a tensile specimen with such connector. Preliminary tests show that the connection efficiency is about 80%.



Fig. 4 A tensile specimen with off-axis connector of FRP bars

Conclusions

The research about FRP bars' connection above is still preliminary. Most of the works are focused on the experimental study. The studies about the connection mechanism, design analysis method, strength prediction model, high stress repeated tension properties, fatigue performance, applicable condition of different connection mode, key points of construction quality control testing standards, classification method are lack. Facing the development of the engineering application in the future, the research of all these aspects is indispensable.

References

[1] Z. Zhou, J. Ou, Study on smart FBG sensors and their applications in civil engineering, Chinese High Technology Letters, 4 (2005) 23-28.

[2] Z. Lu, Application of high performance FRP and innovations of structure engineering, Journal of Architecture and Civil Engineering, 1 (2005) 1-5.

[3] L.C. Hollaway, A review of the present and future utilization of FRP composites in the civil infrastructure with reference to their important in-service properties, Construction and Building Materials, 24 (2010) 2419-2445.

[4] F. Peng, L. Ye, FRP structures and FRP composite structures in structural engineering, China Civil Engineering Journal, 3 (2006) 14-18.

[5] Q. Yue, Y. Yang, High performance fiber reinforced composite and modern civil engineering application, in: The 15th National Composite Materials Academic Conference, 2008, 31-36.

[6] Camille A. Issa, Antoine Nasr, An experimental study of welded splices of reinforcing bars, Building and Environment, 41 (2006) 1394-1405.

[7] J. Zhou, Q. Du, J. Lu, S. Chen, Experimental study of glassfiber reinforced polymer bar joint, Fiber Reinforced Plastics/Composites, 5 (2005) 24-27.

[8] B. Tighiouart, B. Benmokrane U, Phalguni Mukhopadhyaya, Bond strength of glass FRP rebar splices in beams under static loading, Construction and Building Materials, 13 (1999) 383-392.

[9] J. M. Lees, B. Gruffydd-Jones, C. J. Burgoyne, Expansive cement couplers-A means of pre-tensioning fiber-reinforced plastic tendons, Construction and Building Materials, 6 (1995) 413-423.

[10]T. Harada, T. Idemitsu, A. Watanabe, M. Khin, K. Soeda, New FRP tendon anchorage system using highly expansive material for anchoring. In: Modern Prestressing Techniques and Their Applications, Proceedings Volume II, FIP93 Symposium, Japan, 1993: 71 l-718.

[11]. V. Navaratnarajah, Splicing of reinforcement bars with epoxy joints, International Journal of Adhesion and Adhesives, 2 (1983) 93-99.

[12] Jacob W. Schmidt, Anders Bennitz, Bjőrn Täljsten, Per Goltermann, Henning Pedersen, Mechanical anchorage of FRP tendons-A literature review, Construction Building Materials (2012), doi:10.1016/j.conbuildmat.2011.11.049.

[13] Colin MacDougall, Mark Green, Lucio Amato, CFRP tendons for the repair of post-tensioned, unbonded concrete buildings, Journal of Performance of Constructed Facilities, 3 (2011) 149-157.

[14] J. Zhang, H. Zhu, Z. Lu, K. Zhao, Development of anchor devices of prestressed FRP tendon, Industrial Construction, add (2004) 259-262.

[15] G. Yuan, G. Dong, J. Ma, Study of coaxial FRP sleeve/expansion Cement connection of FRP rebers, 18th International Conference On Composite Materials, 2011, Jeju Island, Korea.

[16] G. Yuan, G. Dong, J. Ma, Luciano Feo, David Hui. Study of coaxial connecting methods of FRP rebars with winding fiber cloth composites. 19th Annual International Conference on Composites or Nano Engineering, July 23-28, Shanghai, China.

[17] W. Min, Finite Element Value Simulation of Composite Bolt Threaded Nut Contact and Experimental Study, Master Degree Thesis, Taiyuan University of Science and Technology, 2008.

[18] Y. Zhu. Connection of pultrusion GFRP rod, Fiber Reinforced Plastics, 2 (1981) 7-17.

[19] ACI 440.1R-06, Guide for the Design and Construction of Structural Concrete Reinforced with FRP Bars, American Concrete Institute (ACI), 2006.

[20] B. Benmokrane, Bond strength of FRP rebar splices, Proceedings of the Third International Symposium on Non-Metallic (FRP) Reinforcement for Concrete Structures (FRPRCS-3), Vol. 2, Japan Concrete Institute, Tokyo, Japan, 1997: 405-412.

[21] C. P. Mosley, Bond performance of fiber reinforced plastic (FRP) reinforcement in concrete, MS thesis, Purdue University, West Lafayette, Ind., 2002.

[22] GB50010-2010, Code for Design of Concrete Structures, China Building Industry Press, Beijing, 2011.

[23] C. Fu, Z. Zhou, B. Wang, Study of GFRP bar used in concrete, Fiber Reinforced Plastics/Composites, add. (2001) 254-257.

[24] G. Yuan, Research report about the performance testing and connection method of FRP bars, School of Aerospace Engineering and Applied Mechanics, Tongji University, 2009.

© (2012) Trans Tech Publications, Switzerland
doi:10.4028/www.scientific.net/AMM.238.66

A Novel Internal Model Control Method for Non-square System

Ling Quan [1,a], Hailong Zhang [2,b] and YangYang[3,c]

[1]Institute of Electric Power, North China University of Water Resources and Electric Power, Zhengzhou 450011, China

[2]School of Civil Engineering and Communication, North China University of Water Resources and Electric Power, Zhengzhou 450011, China

[a]goodluck136946@yahoo.com.cn, [b]zhlongql@yahoo.cn, [c]yangyang@ncwu.edu.cn

Keyword: non-square system; ENRG method; V norm decouple; internal model control.

Abstract. Multivariable non-square systems with time delays widely exist in the chemical production process. Owing to the matrix that is adopted to describe non-square system is not square, many classical multivariable control methods can be hardly applied in such system. In this paper, based on non-square effective relative gain (NERGA), a novel internal model control method is proposed. Firstly the input and output loops of the non-square system are paired using NERGA, and then V-norm internal model controller is designed based on the model of squared subsystem. Finally, simulation study is carried out for a non-square system. The results can demonstrate the effectiveness of the proposed method.

Introduction

In the actual chemical process, due to the change of working conditions, the model of the controlled object may be changed, system with unequal number of inputs and outputs occur frequently [1,2]. Because of the singularity of the process transfer function matrix, many control methods used for the square system are difficult to apply in such system. At present, only a few control methods have proposed for non-square system, such as generalized inverse method and main manipulated variable method ect. [3-5]. These control methods are designed based on the original model of the non-square system, although satisfied control effect may be obtained, the design is complicated, calculation amount is large.

In this paper, combining the NERGA law and V norm internal model control, an effective control method is proposed for non-square system. The NERGA for non-square system is derived, and then to square down the non-square systems by NERGA. Based on the squared system a strong robust V norm internal model controller is designed subsequently. The new control method has advantages of less calculation, simple design and easy to be understood by operators. Finally, this method is applied in a system with more inputs than outputs, the simulation results show that the proposed method has good control performance and robust performance.

The Derivation of the Non-square Effective Relative Gain

Non-square effective relative gain is the extension of effective relative gain [6], which is mainly applicable to analysis and pairing the loops of non-square system.

Consider a $n \times m$ ($n > m$) non-square system:

$$G(s) = \begin{bmatrix} g_{11}(s) & g_{12}(s) & \cdots & g_{1m}(s) \\ g_{21}(s) & g_{22}(s) & \cdots & g_{2m}(s) \\ \cdots & \cdots & \cdots & \cdots \\ g_{n1}(s) & g_{n2}(s) & \cdots & g_{nm}(s) \end{bmatrix} \tag{1}$$

Where $g_{ij}(s)$ is the transfer function of the loops with the i^{th} input and the j^{th} output.

While analysis the coupling of the system and loops pairing, to consider steady-state gain and response speed these two factors at same time, effective gain of the transfer function was adopted:

$$e_{ij} \approx g_{ij}(0)\omega_{ij} \qquad i, j = 1,2,\ldots,n \tag{2}$$

Where $\omega_{c,ij}$ is the critical frequency of $g_{ij}(s)$, which is determined by the frequency where the magnitude of frequency response reduced to $0.707g_{ij}(0)$.

The effective gain matrix can be calculated by the following matrix:

$$E = G(0) \otimes \Omega \tag{3}$$

Where, $\otimes$ is the Hadamard product, $G(0)=\begin{bmatrix} g_{11}(0) & g_{12}(0) & \cdots & g_{1n}(0) \\ g_{21}(0) & g_{22}(0) & \cdots & g_{2n}(0) \\ \cdots & \cdots & \cdots & \cdots \\ g_{n1}(0) & g_{n1}(0) & \cdots & g_{nn}(0) \end{bmatrix}$ and $\Omega=\begin{bmatrix} \omega_{11} & \omega_{12} & \cdots & \omega_{1n} \\ \omega_{21} & \omega_{22} & \cdots & \omega_{2n} \\ \cdots & \cdots & \cdots & \cdots \\ \omega_{n1} & \omega_{n1} & \cdots & \omega_{nn} \end{bmatrix}$ are the steady-state gain matrix and the bandwidth frequency matrix, respectively.

We define the effective relative gain Φ_{ij} between output variable y_i and input variable u_j as the ratio of two effective gains:

$$\phi_{ij} = \frac{e_{ij}}{\hat{e}_{ij}} \tag{4}$$

Where $\hat{e}_{ij}$ is the effective gain between output variable y_i and input variable u_j while all other loops are closed [6]. After calculated the effective relative gains of all the input and output combinations of a multivariable process, it results in an array which we call it non-square effective relative gain array (NERGA), the formula is:

$$\Phi = E \otimes (E^{+})^{T} = \begin{bmatrix} \phi_{11} & \phi_{12} & \cdots & \phi_{1m} \\ \phi_{21} & \phi_{22} & \cdots & \phi_{2m} \\ \cdots & \cdots & \cdots & \cdots \\ \phi_{n1} & \phi_{n1} & \cdots & \phi_{nm} \end{bmatrix} \tag{5}$$

Where, $E^{+}=E^{H}[EE^{H}]^{-1}$, $E^{+}$is the generalized inverse of E.

From Eq. (5), we can compute the sums of all elements in each row/column, then we have:

$$RS = [\sum_{j=1}^{n}\phi_{1j} \quad \sum_{j=1}^{n}\phi_{2j} \quad \cdots \quad \sum_{j=1}^{n}\phi_{nj}]^{T} \tag{6}$$

$$= [rs(1) \quad rs(2) \quad \cdots \quad rs(n)]^{T}$$

$$CS = [\sum_{j=1}^{n}\phi_{i1} \quad \sum_{j=1}^{n}\phi_{i2} \quad \cdots \quad \sum_{j=1}^{n}\phi_{im}]^{T} \tag{7}$$

$$= [cs(1) \quad cs(2) \quad \cdots \quad cs(m)]^{T}$$

Where, $rs(i)$ is the sum of the i^{th} row of NERGA, $cs(j)$ is the sum of the j^{th} column [7, 8].

The Loops Paring Criteria of NERGA for Non-square System

If $\Phi_{ij} \leq 0.5$, y_i should be avoided to paired with r_j. If Φ_{ij} is very close to 1, that means r_j and y_i have a large amount of interaction, loop r_j and loop y_i should be paired.

For non-square system, the sums of all elements in each row and in each column are not definitely equal to 1. For a $m \times n$ ($m \neq n$) non-square system, if $m>n$, each row are equal to 1, but each column are between 0~1. If CS is close to 0, shows that the input loop has little impact on the output loop, so this input loop can be removed. If $m<n$, the result is opposite.

Simulation Research

Consider the above non-square system, the model of this system is shown as:

$$G_p(s)=\begin{bmatrix} \dfrac{119e^{-5s}}{21.7s+1} & \dfrac{153e^{-1.59s}}{337s+1} & \dfrac{-2.1e^{-5s}}{11.36s+1} \\ \dfrac{37.0e^{-5s}}{500s+1} & \dfrac{76.7e^{-5s}}{28s+1} & \dfrac{-5.0e^{-5s}}{10s+1} \end{bmatrix}$$

From Eq.(1) ~ Eq.(7), non-square effective relative gain matrix, the sums of all elements in each row and in each column of NERGA can be obtained:

$$\Phi = E \otimes (E^{+})^{T} = \begin{bmatrix} 1.0023 & -0.00247 & 0.00044 \\ -0.00236 & 0.97035 & 0.032 \end{bmatrix} \qquad RS = [1 \quad 1]^{T}$$

$$CS = [0.999 \quad 0.968 \quad [0.032]]^{\mathrm{T}}$$

From *CS* matrix, we found that the third column is 0.032, so the third input loop has little impact on the output, it can be removed, and then the transfer function matrix of non-square system can be changed as:

$$G_p^S(s)=\begin{bmatrix} \dfrac{119e^{-5s}}{21.7s+1} & \dfrac{153e^{-1.59s}}{337s+1} \\ \dfrac{37.0e^{-5s}}{500s+1} & \dfrac{76.7e^{-5s}}{28s+1} \end{bmatrix}$$

Though above calculation, the effective relative gain matrix of $G_p^{\ s}$ is:

$$\Phi^{s} = E \otimes (E^{-1})^{T} = \begin{bmatrix} 1.002 & -0.002 \\ -0.002 & 1.002 \end{bmatrix}$$

From effective relative gain matrix, we can see that the input loops and output loops are correctly paired，there is no coupling between loops. So there is no need to decouple the system, the only job is to design internal model controllers based on the main diagonal elements. According to the design method of V norm internal model controller introduced in ref. [9], then we can obtained the expression of controllers are:

$$C_{11}(s)=\frac{21.7s+1}{119(\lambda_1 s+1)}, \quad C_{22}(s)=\frac{28s+1}{76.7(\lambda_2 s+1)}$$

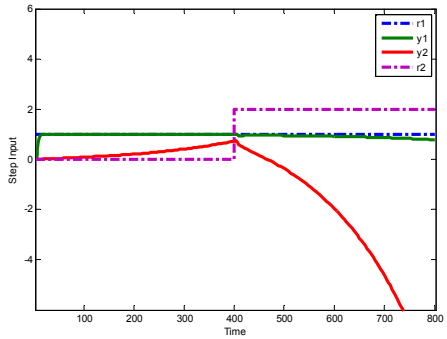


Fig. 1 Matched model: the control effect of subsystem consist of r_1-y_1 and r_3-y_2

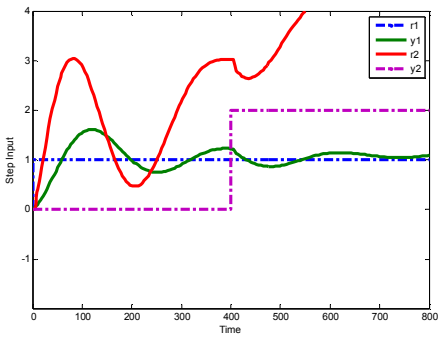


Fig. 2 Matched model: the control effect of subsystem consist of r_2-y_1 and r_3-y_2

In order to testify the effectiveness of NERGA in loop analysis and paring for non-square system, we will research the control effect of the other two loop paring programs which were not using NERGA loop paring method. This two loop paring programs are: loop r_1-y_1 with loop r_3-y_2, the

obtained square subsystem is $G_p(s)=\begin{bmatrix} \dfrac{119e^{-5s}}{21.7s+1} & \dfrac{-2.1e^{-5s}}{11.36s+1} \\ \dfrac{37.0e^{-5s}}{500s+1} & \dfrac{-5.0e^{-5s}}{10s+1} \end{bmatrix}$; Loop r_2-y_1 with loop r_3-y_2, then we get the square subsystem $G_p(s)=\begin{bmatrix} \dfrac{153e^{-1.59s}}{337s+1} & \dfrac{-2.1e^{-5s}}{11.36s+1} \\ \dfrac{76.7e^{-5s}}{28s+1} & \dfrac{-5.0e^{-5s}}{10s+1} \end{bmatrix}$, the simulation results were shown in Fig. 1 and Fig. 2.

From above simulation results, we can find that the outputs of this two square subsystem which were not paired by NERGA were divergent, that means the simulation results are consistent with the calculated results, NERGA is an effective method to pair the loops of system.

To testify if there is coupling between loops, assumed a step input with magnitude 1 was added to the input loop one at t=1s, a step input with magnitude 2 was added to the input loop two at t=400s, and the simulation result is shown as Fig. 3. Meanwhile, we compared the method introduced in ref.[10] with the method proposed in this paper in the same condition, the simulation result is shown as Fig. 3, where real line represent the output curve of the method proposed in this paper, the broken line represent the output curve of the other method [10]. In order to testify the disturbance-rejection capacity of the system, when the models are matched, a step input with magnitude 0.5 and -0.5 were added to the input loops at t=200s and t=600s, the simulation result is shown as Fig. 4.

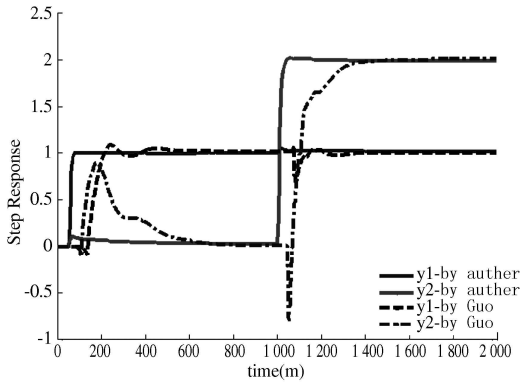


Fig. 3 Model matched: without disturbance

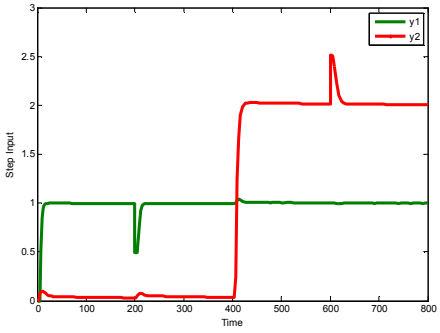


Fig. 4 Model matched: with disturbance

In order to testify the robustness of the system, all the time constant, gains and time delays of the controlled object are increased by 20% separately and simultaneously, the simulation results are shown in Fig. 5, Fig. 6, Fig. 7 and Fig. 8. We can see that the system has good tracking characteristics and decoupling characteristics. When the models were matched, a step disturbance was added to the system, the output can quickly track the set values. When the models were unmatched, the system still maintained good control effect, and almost has no coupling between loops.

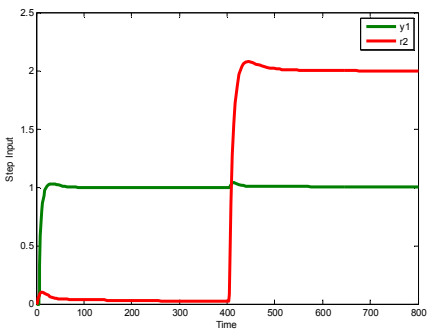


Fig. 5 Time constant increased 20%

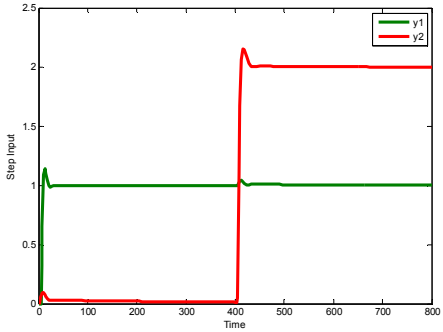


Fig. 6 Gain increased 20%

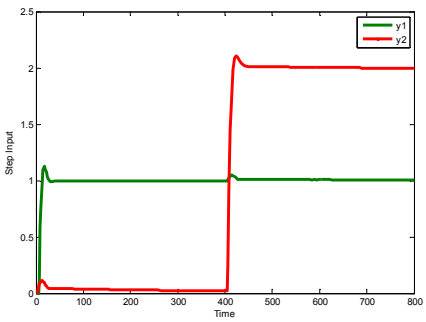


Fig. 7 Models unmatched: Time delay increased 20%

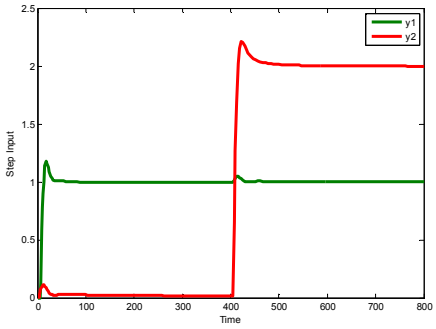


Fig. 8 Gain and Time constant decreased 20%, Time delay increased 20%

Conclusions

For the systems with unequal number of inputs and outputs are frequently encountered in process industries, we proposed a novel NERGA based on internal model control method for non-square system. This new method avoids the complex calculation, such as calculate the inverse of the matrix, the controller structure is simple, has a few tuning parameters, and is easy to be accepted by operators. Finally, the simulation results show that the proposed method has relatively good control performance and robust performance.

References

[1] K. L. N. Sarma, M. Chidambaram, Centralized PI/PID controller-for nonsquare systems with RHP zeros, Journal of the Indian Institute of Science, 22 (2005) 201.

[2] A.Seshagir, M. Chidambaram, Smith delay compensator for multivariable non-square system with multiple time delays, Computer and Chemical Engineering, 30 (2006)1243-1246.

[3] J. Pian, Application in Generalized Inverse of Singular Value Decomposition, Journal of Fuyang Teachers College, 22 (2005)16-20.

[4] E. J. Loh, M. S. Chiu, Robust decentralized control of nonsquare systems, Chemical Engineering Communications, 22(1997)157-160.

[5] S. Palankia, Juan C. Cockburnb, Soumitri N. Kolavennuc, Robust state feedback synthesis for control of non-square multivariable nonlinear systems, Journal of Process Control, 13 (2003) 623-626.

[6] X. Qiang, J. Wen, Effective transfer function method for decentralized control system design of multi-input multi-output processes, Journal of Process Control. 16 (2006) 773.

[7] J. Chang, C. Yu, The relative gain for non-square multivariable systems, Chemical Engineering Science, 45 (1990) 1309-1312.

[8] D.E. Reeves, Y. Arkun, Interaction measures for nonsquare decentralized control structure, AIChE J., 35 (1989) 603-606.

[9] Q. Fei, The simulation research on multivariable internal model control algorithm, Beijing University of Chemical Technology, Beijing, 2008.

[10] Q. Jing, Z. Liu, A. Song, Decoupling internal model control for non-square process with time delays, The proceedings of 2010 International Conference on Measuring Technology and Mechatronics Automation, 2010: 898-901.

© (2012) Trans Tech Publications, Switzerland
doi:10.4028/www.scientific.net/AMM.238.71

Ocean Engineering Concrete using High-volume GGBS

Keliang Li

School of Civil Engineering and Communication, North China University of Water Resources and Electric Power, Zhengzhou 450011, China

R&D High Technology CO., Nanjing Hydraulic Research Institute, Nanjing 210029, China

klli73@163.com

Key words: ocean engineering, concrete, slag, mechanical property, durability.

Abstract: To improve ocean engineering durability, concrete using high-volume ground granulated blast-furnace slag (GGBS) was prepared, its mechanical property and durability were investigated. 4% activator and 61% GGBS were used to replace 65% cement in cementitious material. Activator was used to improve workability, volume stability and early strength of high-volume GGBS concrete. Ocean concrete using high-volume GGBS has good impermeability with small gas diffusion coefficient and relative permeability coefficient. As the good property of resistance to chloride-ion penetration with a low effective diffusion coefficient, it can protect steel-bar from corrosions. Property of frost resistance is also favorable. Expansions caused by alkali-silica reaction and sulfate attack fall down markedly after using high-volume GGBS. It is proved that the high-volume GGBS concrete with good mechanical property and durability is applicable to the constructing of ocean engineering concrete.

Introduction

A lot of granulated blast-furnace slag is produced in China per year. It should be utilized to reduce circumstance pollution. In the meantime, cement industry releases more harmful gas and consumes large quantities of natural resources and energy sources. It has enormous environmental benefit to use ground granulated blast-furnace slag (GGBS) to replace cement in concrete. Chloride-ion concentration in seawater is very high, and it has a severe corrosion to steel-bar in ocean concrete under an alternate dry-wet condition. To enhance ocean engineering durability, durability and mechanical property of ocean concrete using high-volume GGBS were investigated.

Raw Material and Mix Proportion

Raw Material. Ordinary Portland cement of 42.5 class, GGBS and activator were used in cementitious material. Activity index of GGBS is 107% measured according to a Chinese standard named as Mineral Admixtures for High Strength and High Performance Concrete [1]. Activator was used to improve workability, volume stability and early strength of high-volume GGBS concrete, its main components were dihydrate gypsum, oxy-compound and surfactant. Particle size of crushed stone was from 5 mm to 40 mm. Fine aggregate was the medium sand. Admixture was the naphthalene-based superplasticizer.

Mix Proportion. Raw material dosages in a stere concrete are listed in Table 1. Water-cementitious material ratio of ocean engineering concrete with high-volume GGBS was taken as 0.35 in accordance with a Chinese specification named as Corrosion Prevention Technical Specifications for Concrete Structures of Marine Harbor Engineering [2]. Dosage of whole cementitious material was 441 kg/m. 4% of activator and 61% of GGBS were used to replace 65% of cement. Dosage of admixture was defined by initial slumps between 50 mm and 70 mm.

Table 1 Raw material dosages in a stere concrete

Cement (kg/m^3)	GGBS (kg/m^3)	Activator (kg/m^3)	Sand (kg/m^3)	Stone (kg/m^3)	Water (kg/m^3)	Admixture (kg/m^3)
154	269	18	696	1045	154.4	6.62

Concrete Property

Mechanical Property. Mechanical properties at 28 days are shown in Table 2. Fig. 1 shows the dry shrinkage rate at different ages. Ocean engineering concrete with high-volume GGBS cured in moist environment for 5 days has a slight expansion, which is beneficial to compensate dry shrinkage in the later stage. They are 297×10^{-6} and 594×10^{-6} at 28 days and 180 days in dry shrinkage room with relative humidity of 60%.

Table 2 Mechanical property of concrete

Compressive strength (MPa)	Axis tensile strength (MPa)	Elastic modulus (MPa)	Ultimate tensile strain
50.7	4.32	3.81×10^{4}	120×10^{-6}

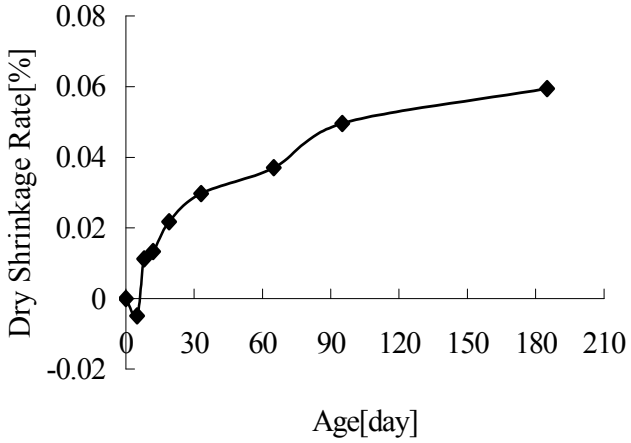


Fig. 1 Dry shrinkage rate at different ages

Impermeability. In the method of gas permeability, there were two testing tanks on the two sides of the concrete specimens respectively. One side opened to vacuum and the other side opened to air. For the action of the air pressure difference between the two sides of specimens, air accessed continuously from the side opening to air into the side opening to vacuum. Ventilation time was measured in the experiment when the gas pressure in vacuum changed from 0.056 MPa to 0.050 MPa. Gas diffusion coefficient was gotten according to ventilation time. Gas diffusion coefficients of ocean concrete with high-volume GGBS are 4.09×10^{-7} m^2/s and 2.83×10^{-7} m^2/s at 28 days and 56 days respectively.

In the method to test relative water impermeability, hydraulic pressure was controlled at 1.2 MPa for 24 hours. Then the water-penetrated heights were measured after specimens being split. The relative permeability coefficient was calculated by the water-penetrated height. The relative permeability coefficient of ocean concrete with high-volume GGBS is 510×10^{-8} cm/h.

Resistance to Chloride-ion Penetration. Natural soaking method was used to analyze the property of chloride-ion penetration resistance. Specimens were put into sodium chloride solution with a concentration of 3.5% for 5 months. Samples at different depths in concrete were gotten. Concentrations of water-soluble chloride-ion were measured in samples at different depths. Results are shown in Fig. 2. Concentrations of water-soluble chloride-ion reduced gradually with depths. Concentration of water-soluble chloride-ion was very small to 0.023% at the depth of 15 mm. When the depth was deeper than 15 mm, it was smaller. Based on the data in Fig. 2, an effective diffusion coefficient of chloride-ion was obtained by curve fitting, which adopted the minimum diplo-multiply method and Fick's second law [3]. Effective diffusion coefficient of ocean concrete with high-volume GGBS is 1.79×10^{-12} m^2/s. It is ok to say that ocean engineering concrete with high-volume GGBS has a good resistance to chloride-ion penetration.

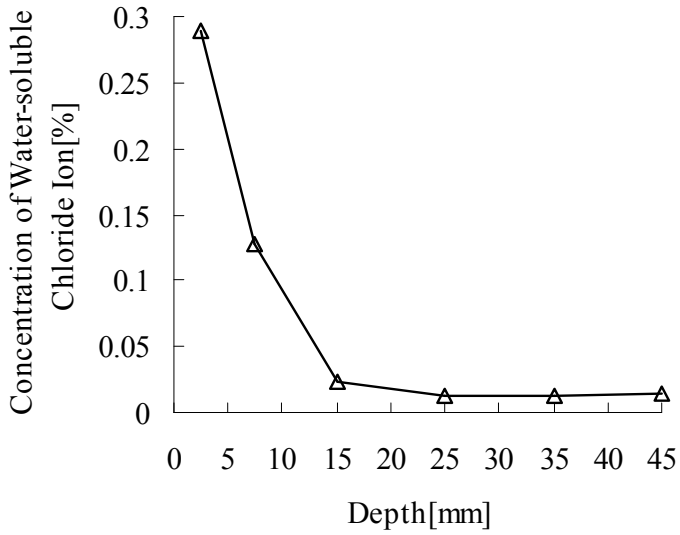


Fig. 2 Concentration of water-soluble chloride-ion at different depths

Alkali-silica Reaction. Sand was made from active quartz glass. Content of active SiO_2 in quartz glass was above 99.0%. Standard specimen used cement without GGBS and activator. Comparison specimen used 4% activator and 61% GGBS replacing 65% of cement. Specimens were put into sealed barrels and cured at 38 °C±2 °C for 14 days, then the expansion rate was measured. Expansion rate of standard specimen is 0.40%. Expansion rate of comparison specimen is 0.05%, which is only 12.5% of that of standard specimen. It shows that using 4% activator and 61% GGBS greatly reduce the expansion due to alkali-silica reaction.

Steel-bar Corrosion. Concrete cubes with 100mm dimensions were cured for 28 days before being put into oven to dry at 80 °C±2 °C for 4 days. They were soaked in sodium chloride water with a concentration of 3.5% for 24 hours, and then dried at 60 °C±2 °C for 13 days. A dry-wet cycle was 14 days. After 15 cycles, steel-bars in concrete were taken out. They did not rust. It is ok to say that ocean concrete with high-volume GGBS can protect steel-bars from premature corrosions.

Sulfate Resistance. Property of sulfate resistance was analyzed by measuring expansion rate of mortar bars in sulfate solution. 4% activator and 61% GGBS were used to replace 65% of cement. water-cementitious material ratio of the mortar was 0.35. Expansion was measured at different ages. Expansion rates shown in Fig. 3 are the result of mortar bars in the sulfate solution deducting the expansion rate of the mortar bars in the clean water, which present the expansion rate induced by sulfate corrosion. No expansion is produced in 360 days. It is to say that high-volume GGBS can greatly enhance the capacity of sulfate resistance.

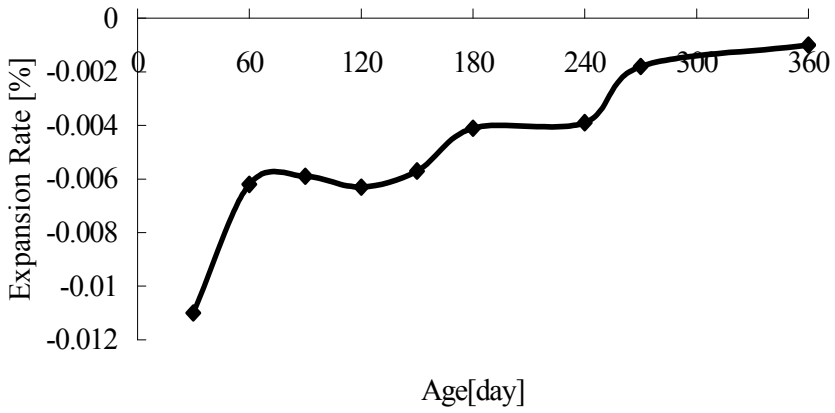


Fig. 3 Expansion rates of mortar bars in sulfate solution

Frost Resistance. Aggressive medium was seawater in frost resistance test. Mass loss rates of concrete are respectively 0.17% and 0.36% after 100 and 200 frosting-thawing cycles. The relative dynamic modulus of elasticity of concrete is respectively high up to 93.3% and 90.5% after 100 and 200 frosting-thawing cycles. Results of test prove that ocean engineering concrete with high-volume GGBS has a favorable property of frost resistance.

Conclusions

Ocean engineering concrete with high-volume GGBS has good strength, high ultimate tensile strain and low dry shrinkage rate. It has good impermeability with small gas diffusion and relative permeability coefficients. It has good property of resistance to chloride-ion penetration with small effective diffusion coefficient. It can prevent steel bars from premature corrosion. Its frost resistance is also favorable. High-volume GGBS greatly reduces expansion due to alkali-silica reaction.

Ocean engineering concrete with high-volume GGBS has good mechanical property and durability. It is applicable to the constructing of ocean engineering concrete.

References

[1] Chinese Code GB/T 18736-2002, Mineral admixtures for high strength and high performance concrete, China Building Industry Press, Beijing, 2002.

[2] Chinese Code JTJ275-2000, Corrosion Prevention Technical Specifications for Concrete Structures of Marine Harbor Engineering. China Communication Press, Beijing, 2000.

[3] P. S. Mangat, B. T. Molloy, Prediction of long term chloride concentration in concrete, Materials and Structures, 27 (1994) 338-346.

© (2012) Trans Tech Publications, Switzerland
doi:10.4028/www.scientific.net/AMM.238.75

Mechanical Behaviors and Chloride Permeability of Rice Husk Ash Concrete

Hailong Wang [a], Qiwen Peng [b] and Xiaoyan Sun [c]

Department of Civil Engineering, Zhejiang University, Hangzhou, China

[a]hlwang@zju.edu.cn, [b]pengqw414@zju.edu.cn, [c]selina@zju.edu.cn(corresponding author)

Keywords: concrete; rice hush ash; mechanical behavior; elastic modulus; chloride permeability.

Abstract. Rice husk ash (RHA) was used as a mineral additive in concrete and replaced the ordinary cement by 0-30% in this study. The fresh concrete properties, compressive strength, split tensile strength, and elastic modulus as well as the chloride permeability of concretes mixed with different RHA contents was tested. The experimental results reveal that the fluidity, the mechanical behaviors and the chloride ion resistance of rice husk ash concrete decrease with the increasing replacement rate of RHA. The particle size of RHA limits its pozzolanic activity, which indicates that the controlled burning temperature and the fineness of RHA have significant impact on the properties of rice husk ash concrete.

Introduction

The world production of rice paddy is huge and about 20% of dried rice paddy is made up of the rice husks. According to the statistics in reference [1], China has the largest production of rice paddy all over the world as agriculture is its foundation industry, leading to the generation of large volumes of rice by-products. Uncontrolled burning is often considered as the most cost-effective disposal method for such by-product [2], which has adverse impact on both nature and social environment. Nevertheless, properly treated ashes have been to be active within cement paste.

Rice husk ash is a very fine pozzolanic material. Its particle size and specific surface depend upon the burning condition under which it is produced [1, 3]. Two different kinds of RHAs from Uruguay and USA were compared in reference [4], which showed that the development of compressive strength of rice husk ash concrete was influenced by several factors such as fineness, replacement rate, water/(cement + RHA) ratio and age. Besides, lots of researches have been carried out to get high performance concrete with controlled burning condition in lab whereas they are difficult to accomplish in the real engineering because of the inconvenient application of certain condition and grinding methods.

In China, disposal of rice husk still is a problem and the research on RHA used in concrete is far not satisfying compared with the developed countries. This article attempts to discuss whether the RHA with simple burning condition can be used to obtain high performance concrete and get economical benefits.

Materials, Casting and Curing

The rice husk ash burned in modern electric furnace from Zhejiang province was used in this experiment. The inner temperature of burning rice husks can achieve above 1000℃. The untreated ash was sieved and 15.6% of ash particles passing the sieve with fineness of 80 μm.

A commercial 42.5 ordinary Portland cement was used in the experiment. River sand with a maximum particle size of 2.5mm was used as fine aggregate and natural gravel with a maximum particle size of 16mm was used as coarse aggregate.

The detailed mix proportions of concretes are listed in Table 1. The designed compressive strength of regular concrete is C40. When the rice husk ash added, the amount of RHA was included in the water-to-cement ratio as a cementing material. Rice husk ash was used as a substitution of 10%, 20% and 30% by the weight of cement. The desired workability of the different compositions was achieved with the aid of the water reducer SP8-CR. After mixing raw materials, the fresh concrete was cast into wooden molds by a vibrating table.

Table 1 Proportions of concrete mixtures

No.	Addition rate [%]	W/ (C+RHA)	The amount of raw concrete materials [kg/m^3]					SP8-CR [%]
			Cement	Rice husk ash	Water	Fine aggregate	Coarse aggregate	
O	0	0.43	512	0	220	561	1042	0
R1	10	0.43	461	51	220	561	1042	0.06
R2	20	0.43	410	102	220	561	1042	0.12
R3	30	0.43	359	153	220	561	1042	0.18

To examine the effect of RHA on the workability of concrete, slump tests were carried out for the fresh concretes. Three slump tests were done for each mixture and their average value was calculated. After 24 hours the concrete specimens were demolded and then stored in a standard curing room with the temperature of 20±2℃ and a relative humidity above 95%.

Experiments

The cubic compressive strengths of concretes, with dimensions of 150 ×150 ×150 mm^3, were measured at 3, 7 and 28 days. The split tensile strengths of cubic concrete specimens, with the same dimensions of 150 ×150 ×150 mm^3, were measured at 28 days. The elasticity modulus of concrete, with dimensions of 150 ×150 ×300 mm^3, were also tested at 28 days. The harden specimens were taken out of the standard curing room just before test and their surfaces were maintained wet during the test. Three specimens from each mixture were tested.

To determine the chloride ion diffusivity in concrete, a rapid testing method called RCM was used in the experiment. The cylinder specimens (100±1) mm in diameter and (50±2) mm in height were used for chloride permeability test. Three specimens from each mix were tested. All the tests were carried out following the standards [5, 6].

Results and Discussion

Fresh Concrete Properties. The slump value of fresh concrete is shown in Fig.1. It can be seen that the slump decreases with the increase of added RHA contents proportionally. According to these results, the use of RHA increases the water demand. When the RHA added to 30% of the cement material, the slump falls to 0 mm and the workability of fresh concrete mixture was bad though water reducer was added into the mixture.

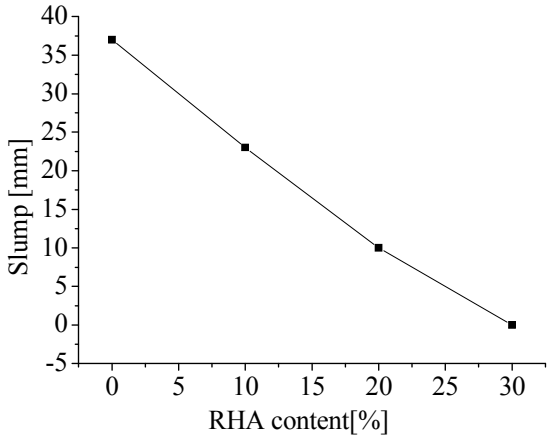


Fig. 1 Effect of RHA on the slump of fresh concrete

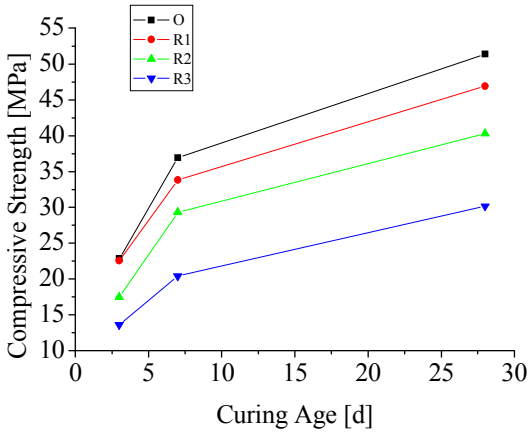


Fig. 2 Development of compressive strengths of various mixture proportions of concretes

Mechanical Behaviors. The compressive strengths of various proportions of concrete mixtures are shown in Fig. 2. All of the compressive strengths decrease with the increase substitution of cement by RHA, and the regular mixture achieved the highest strength. At 3 days, all the concretes

with and without RHA can achieve 43-48% of 28d compressive strength. It seems that the concrete with a replacement rate of 10% can achieve the highest 3d compressive strength. As shown in Fig. 2, the early development of compressive strength of concrete with higher percentage of RHA is slower than the regular concrete.

The split tensile strengths of concretes at various mixture proportions at 28 days are shown in Fig. 3. The split tensile strengths of concretes with added RHA decrease by 10-28.6% respectively. The decrease trend of split tensile strength is similar to that of compressive strength.

The elastic modulus of concretes at 0, 10%, 20% and 30% replacement rate of cement by RHA are shown in Fig. 4. Compared with the change of strength, the elastic modulus decreases slowly with the increase of replacement rate. The decline rate is 3.9%, 10.7% and 19.7% respectively.

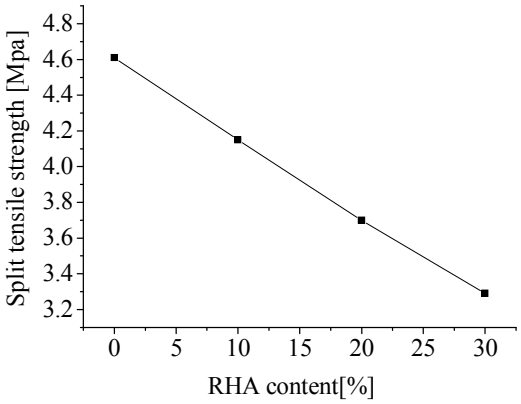


Fig. 3 Effect of RHA on the split tensile strength

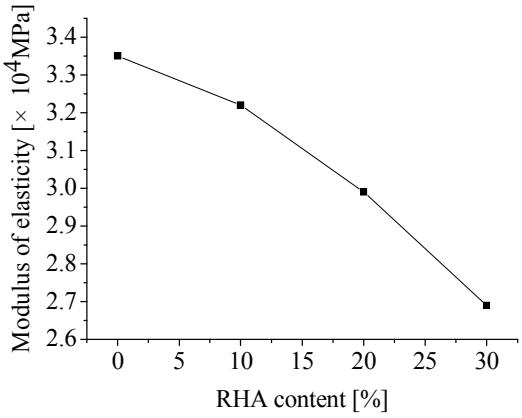


Fig. 4 Effect of RHA on the elastic modulus

Chloride Permeability. Chloride ion diffusivity was obtained to indicate the concretes' ability to resist the chloride penetration as the charge passed through the concrete under the application of an external electrical field during 24 hours. The values of chloride ion diffusivity calculated from experiment are shown in Fig.5. According to the results, chloride ion diffusivity increases with the increase of RHA content, in other words, the chloride resistance of concretes declines remarkably. The chloride permeability increased by 11.4%, 34.3% and 45.7% respectively compared with the reference concrete when the cement is partially replaced with 10%, 20% and 30% RHA.

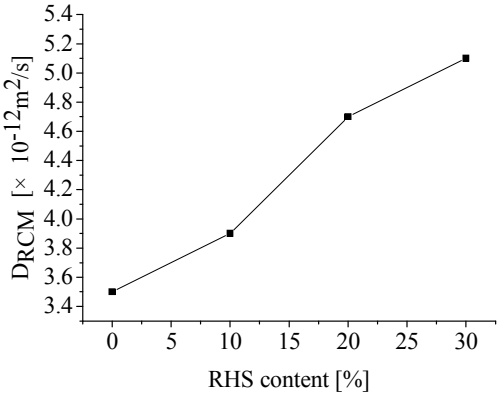


Fig.5 Effect of RHA on the chloride permeability of concrete

Discussion. The addition of RHA causes several changes in the properties of concrete. The apparent fluidity of fresh concrete is reduced mainly due to the high water absorption and porosity of rice husk ash molecules, which influences the mechanical behaviors and the chloride permeability of concrete.

The role of rice husk ash as a filler and pozzolanic additive has been reported by several authors. According to the researches [2, 7], the compressive strength would increase with the addition of RHA by certain grinding technology because of RHA particles' high pozzolanic activity. Article [8] compared two kinds of RHAs and figured out that the specific surface of RHA had a significant effect

on the compressive strength of concrete. The results from this experiment indicate that all of the compressive strength, the split tensile strength, the elastic modulus and the chloride resistance decline with the addition of RHA. The main reason is that the RHA used in this study is untreated, therefore the particle size is bigger than that of treated rice husk ash, which influences the pozzolanic activity of RHA and results in the decline of concrete properties. It can be surmised that the not well-pretreated RHA has low pozzolanic activity or the activity is not shown until certain age. The role of RHA here is mainly as a filler until a super fineness of RHA can be achieved for high pozzolanic activity.

Therefore, the available rice husk ash sold in the market is not suitable for concrete mineral additive for the reason that its comparative big particle size will lead to a low pozzolanic activity. It should be well grinded for a super fineness before utilization. Without grinding process, the presence of rice husk ash will become a weakness for concrete and decreases its performance.

Conclusions

The addition of RHA decreases the fluidity of fresh concrete due to its high porosity and water absorption.

The compressive strength, split tensile strength, elastic modulus and chloride resistance decrease with the increase of untreated RHA content in concrete.

The RHA concrete at 10% replacement rate of cement has a similar property with the regular concrete, which can make an economic benefit.

The available rice husk ash sold in the market should be grinded again for a super fineness to gain its pozzolanic activity.

Acknowledgements

This work was financially supported by the National Natural Science Foundation of China (51178417), the marine cross-guide research funds of Zhejiang University, and the fundamental research funds for the central universities.

References

[1] Satish Chandra, Waste Materials Used in Concrete Manufacturing, Noyes Publications, United States, 1997.

[2] M. Nehdi, J.Duquette, A. EI Damatty, Performance of Rice Husk Ash Produced using a Nnew Technology as a Mineral Admixture in Concrete, Cement and Concrete Research, 33 (2003) 1203-1210.

[3] Mehta, P. K., Rice Husk Ash-A Unique Supplementary Cementing Material, Proceedings of the International Symposium on Advances in Concrete Technology, ed. V. M. Malhotra, Athens, Greece, May 1992, pp 407-430.

[4] Gemma Rodriguez de Sensale, Strength Development of Concrete with Rice-husk Ash, Cement & Concrete Composites. 28 (2006) 158-160.

[5] GB/T 50081, Standard for Test Methods of Mechanical Properties of Ordinary Concrete, 2002.

[6] GB/T 50082, Standard for Test Methods of Long-term Performance and Durability of Ordinary Concrete, 2009.

[7] FENG Qing-ge , YANG Lv-feng, CHEN Zheng , YU Qi-jun , ZHAO San-yin, The Strength Property and Pore Distribution of Concrete with Highly Active Rice Husk Ash, Journal of Wuhan University of Technology. 27 (2005) 17-20.

[8] Andres Salas, Silvio Delvasto, Ruby Mejia de Gutierrez, David Lange, Comparison of Two Processes for Treating Rice Husk Ash for Use in High Performance Concrete, Cement and Concrete Research. 39 (2009) 773-778.

© (2012) Trans Tech Publications, Switzerland
doi:10.4028/www.scientific.net/AMM.238.79

Square-shaped $Nd_2Sn_2O_7$ Nanocrystals Prepared by Salt-assistant Combustion Method

Yuping Tong[1,a], Xi Chen[1,b], Shunbo Zhao[1,c] and Lude Lu[2,d]

[1] School of Civil Engineering and Communication, North China University of Water Resources and Electric Power, Zhengzhou 450011, China

[2] Key Laboratory Soft Chemistry and Functional Materials of Ministry Education, Nanjing University of Science and Technology, Nanjing 210094, China

[a]tongyuping@ncwu.edu.cn; [b]xixp1983@yahoo.com.cn; [c]sbzhao@ncwu.edu.cn; [d]lulude17@yahoo.com.cn.

Keywords*:* nanomaterials; ceramics; salt-assistant combustion method; X-ray.

Abstract. Ultrafine square-shaped pyrochlore-type $Nd_2Sn_2O_7$ nanocrystals were synthesized by a convenient salt-assisted combustion process using glycine as fuel. The products were characterized by X-ray diffraction (XRD), Fourier transform infrared spectroscopy (FT-IR), Raman spectroscopy, Transmission electron microscopy (TEM) and high-resolution transmission electron microscopy (HRTEM). The results indicate that the products are phase-pure nanocrystals with pyrochlore-type structure. TEM and HRTEM images reveal that the products are composed of well-dispersed square-shaped $Nd_2Sn_2O_7$ nanocrystals with the average size of 30 nm and the crystallite is structurally uniform and crystalline. The presented method provides a convenient and low-cost route for the synthesis of oxide materials nanostructures.

Introduction

The pyrochlore structure-type has a wide variety of compositions with a wide range of technologically important properties, such as the interesting thermal, optical, electrical, magnetic and cataltytic properties [1-4]. The pyrochlore oxides have the chemical composition $A_2B_2O_7$, and their basic framework is a three-dimensional corner-sharing network of BO_6 octahedra [5]. Among various pyrochlore oxides, lanthanide stannates ($Ln_2Sn_2O_7$ (Ln=Y, La-Lu), form a group of isostructural compounds. There has been an initial interest in stannate pyrochlores stemmed from their high efficiency for the oxidative coupling of methane and their potential use as high-temperature gas sensors or fast ion conductors [6], due to their high stability and melting points.

Great efforts have been made to devise versatile techniques to synthesize $Ln_2Sn_2O_7$, such as conventional solid state reaction [7], co-precipitation [8], sol-gel [9], hydrothermal technique [10] and so forth. Conventional solid state synthesis employs a solid-state reaction of SnO_2 with appropriate rare-earth oxides at high temperature (>1200^{o}C) for a long time (several days). The method is simple, nevertheless it inherits several drawbacks. As is well known, the high temperature in the preparation process can easily lead to nonuniform in part in chemical component and large sized particles. The present paper has shown that nanosized perovskite oxide powder can be prepared by glycine combustion synthetic method [11], and this may provide another possible method to synthesize $Nd_2Sn_2O_7$ nanoparticles. In many previous reports, it was shown that inert salt played an important role in the reaction process [12-14]. The emphasis of this work is to prepare and characterize $Nd_2Sn_2O_7$ nanocrystals via salt-assisted combustion method (SACM) using glycine as fuel.

Experimental

Preparation of $Nd_2Sn_2O_7$ Nanocrystals. All reagents were of analytical grade and used without further purification. The fabrication procedure of $Nd_2Sn_2O_7$ is illustrated as followed. $Nd(NO_3)_3 \cdot nH_2O$ obtained from Nd_2O_3 dissolved in HNO_3 and $SnCl_4 \cdot 5H_2O$ were used as the

precursors of Nd and Sn, respectively. Firstly, appropriate amount of glycine was dissolved in 60 ml deionized water. Then proper amounts of $Nd(NO_3)_3 \cdot nH_2O$, $SnCl_4 \cdot 5H_2O$ and KCl were added to above glycine aqueous solution in turn. The mixed solution was vigorously stirred for 2h at 60°C and evaporated at 110°C. At this stage, the viscous liquids swelled, followed by the evolution of gases, and self-propagating solution combustion slowly occurred, yielding loose powders. The obtained powders were calcined at 700°C for 5h in air. In order to remove salt, the as-calcined powders were filtered and washed with hot deionized water and ethanol. Finally, the product was dried in an oven at 80°C. For comparison, a parallel experiment was done in the absence of KCl.

Instrumentation. The crystalline phase structure was determined by Bruker D8 Advance X-ray diffractometer (XRD) using Cu Kα radiation. Raman spectra were run on a Renishaw in Raman microscope. Transmission electron microscopy (TEM) and high-resolution transmission electron microscopy (HRTEM) images were recorded on a JEOL JEM-2100 transmission electron microscope.

Results and Discussion

The XRD measurement of $Nd_2Sn_2O_7$ sample prepared by salt-assisted glycine combustion process is shown in Fig. 1, and all the diffraction data can be indexed to the cubic phase of $Nd_2Sn_2O_7$ crystals (JCPDS No: 13-0185). No peaks of impurity are detected in the XRD patterns, indicating that pure crystalline $Nd_2Sn_2O_7$ was fabricated by the presented procedures.

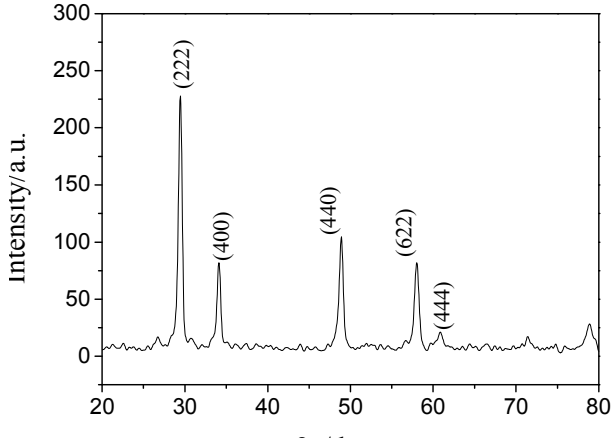


Fig.1 XRD pattern of the $Nd_2Sn_2O_7$ nanocrystals

The pyrochlore structure was also identified by Raman spectra. And the Raman spectrum of $Nd_2Sn_2O_7$ nanocrystals is shown in Fig. 2. The Raman bands at 302, 403, 497 and 671 cm^{-1} are all clearly visible, which is similar to that reported [13]. The band at 671 cm^{-1} is attributed to the stretching vibration of O-Sn.

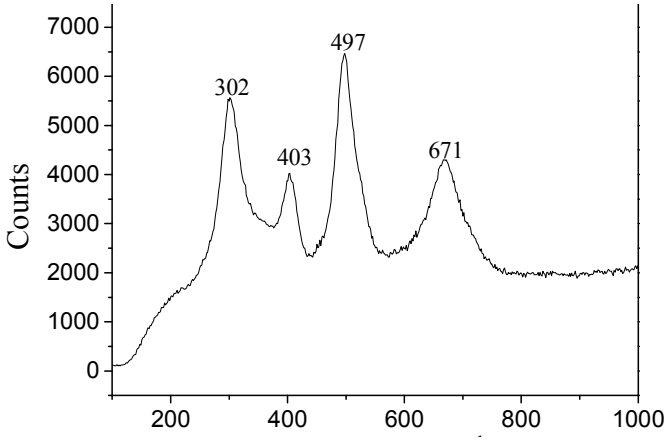


Fig. 2 Raman spectrum of $Nd_2Sn_2O_7$ nanocrystals

The direct information about the size, shape and agglomeration of the produced $Nd_2Sn_2O_7$ nanocrystals are shown in Fig. 3. As shown in Fig.3a, the samples obtained are inseparable three-dimensional network agglomerates with their particle size in the submicrometer range in the

combustion process without KCl. Fig.3b reveals that the products are composed of well-dispersed square-shaped $Nd_2Sn_2O_7$ nanocrystals with the average size of 30 nm. Compared with conventional combustion synthesis, the introduction of KCl in the solution combustion reaction process can effectively prevent nanocrystallites from sintering and forming inseparable three-dimensional network, which could result in the formation of well-dispersed nanoparticles. Also, a better dispersibility was shown than that reported similar series by hydrothermal method [11]. The corresponding HRTEM image (Fig.3c) shows the clear lattice orientation and the regular succession of the atomic planes, indicating that the crystallite is structurally uniform and crystalline. The lattice spacing of 0.301 nm is consistent with that of the (222) plane of $Nd_2Sn_2O_7$ nanocrystals.

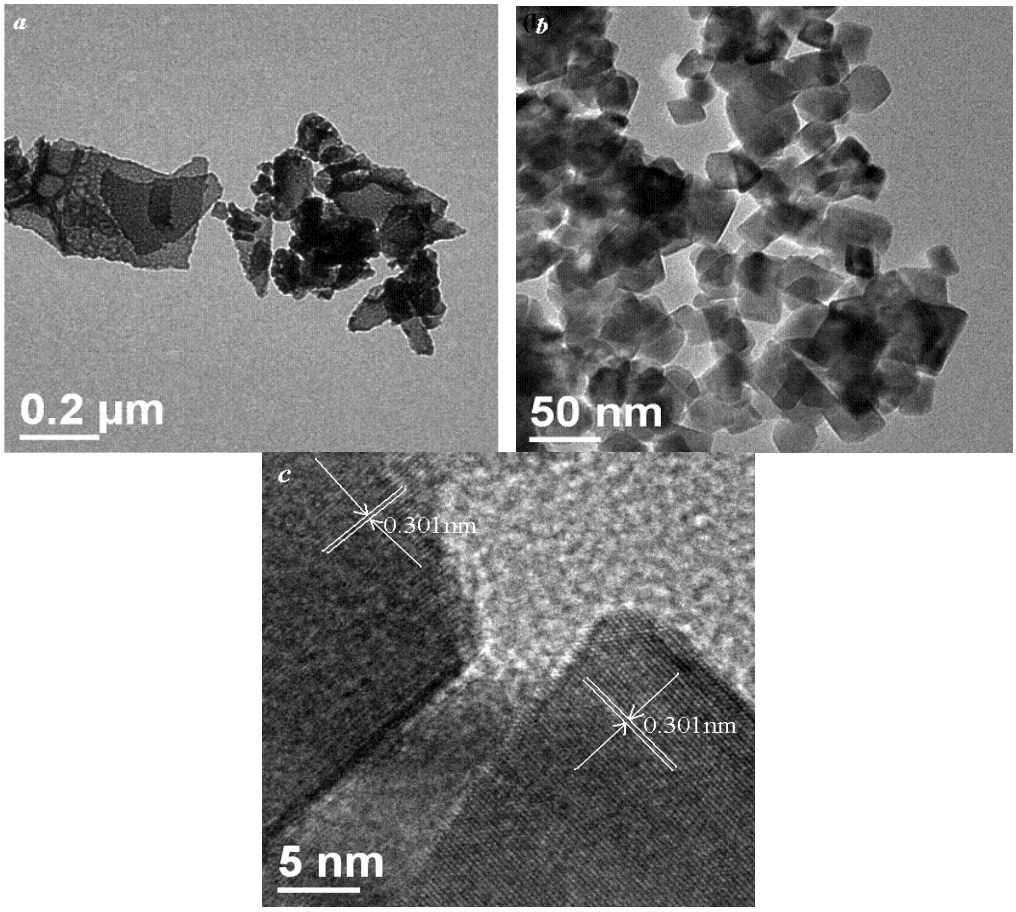


Fig. 3 Representative TEM images of $Nd_2Sn_2O_7$ nanocrystals: (a) TEM image in the absence of KCl; (b) TEM image and (c) HRTEM image in the presence of KCl.

The role of KCl in the formation process of well-dispersed $Nd_2Sn_2O_7$ nanocrysals was assumed as follows. As is well known, the self-propagating combustion reaction can release large amount of heat in a very short time and result in the instant high temperature of the reaction system, and the particles can be formed. Meanwhile, the salt precipitation in situ is completed in an instant to form a thin layer of salt crust on the surface of the newly formed nanoparticles. After the rapid cooling, the salt-coated $Nd_2Sn_2O_7$ particles are trapped in the salt matrix, which prevents the reagglomeration. And well-dispersed $Nd_2Sn_2O_7$ nanocrystals can be obtained eventually.

Conclusions

$Nd_2Sn_2O_7$ nanocrystals were successfully synthesized via this simple salt-assisted combustion method. Compared with conventional solid state reaction, the preparation temperature was lowered (from 1200°C to 700°C) and the procedure was simpler and milder. The control route was easily manipulative and well repeatable. It was expected to create other oxides nanocrystals using this method. The TEM results indicated $Nd_2Sn_2O_7$ nanocrystals were square-shaped with good dispersibility and its average size was 30nm. And $Nd_2Sn_2O_7$ nanocrystals obtained by this procedure showed the better dispersibility and uniformity than that reported similar series by other method. It was also expected to create other oxides nanocrystals using this method.

Acknowledgments

The work was supported by the Technological Leading Talent plan of Zhengzhou City (096SYJH23105), Natural Science Research Projects of Education Department of Henan Province (2010B430018) and Key Programs for Science and Technology Development of Henan Province (122102210239).

References

[1] K. J. Moreno, A. F. Fuetes, J. García-Barriocanal, et al, Mechanochemical synthesis and ionic conductivity in the $Gd_2(Sn_{1-y}Zr_y)_2O_7$ ($0\leq y\leq 1$) solid solution, Journal of Solid State Chemistry, 179 (2006) 323-330.

[2] D. W. Hwang, H. G. Kim, J. S. Lee, et al, Photocatalytic hydrogen production from water over M-doped $La_2Ti_2O_7$ (M=Cr, Fe) under visible light irradiation, Journal of Physics and Chemistry B, 109 (2005) 2093-2102.

[3] J. M. Sohn, M. R. Kim, S. Ihl Woo, The catalytic activity and surface characterization of $Ln_2B_2O_7$ (Ln=Sm, Eu, Gd and Tb; B=Ti or Zr) with pyrochlore structure as novel CH_4 combustion catalyst, Catalysis Today, 83 (2003) 289-297.

[4] H. G. Kim, D. W. Hwang, S. W. Bae, et al, Photocatalytic water splitting over $La_2Ti_2O_7$ synthesized by the polymerizable complex method, Catalysis Letters, 91 (2003) 193-198.

[5] K.W. Li, H. L. Li, H. M. Zhang, et al, Hydrothermal synthesis of Eu^{3+}-doped $Y_2Sn_2O_7$ nanocrystals, Materials Research Bulletin, 41 (2006) 191-197.

[6] B. J. Kennedy, B. A. Hunter, C. J. Howard, Structural and bonding trends in tin pyrochlore oxides, Journal of Solid State Chemistry, 130 (1997) 58-65.

[7] Ismunandar, B. J. Kennedy, B. A. Huner, et al, Bonding and structural variation in doped $Bi_2Sn_2O_7$, Journal of Solid State Chemistry, 131 (1997) 317-325.

[8] V. Ravi, S. Adyanthaya, M. Aslam, et al, Synthesis of tin bismuth pyrochlore, Materials Letters, 40 (1999) 11-13.

[9] Z. Lu, J. Wang, Y. Tang, et al, Synthesis and photoluminescence of Eu^{3+}-doped $Y_2Sn_2O_7$ nanocrystals, Journal of Solid State Chemistry, 177 (2004) 3075-3079.

[10] H. Zhu, D. Jin, L. Zhu, et al, A general hydrothermal route to synthesis of nanocrystalline lanthanide stannates: $Ln_2Sn_2O_7$ (Ln: Y, La-Yb), Journal of Alloys and Compounds, 464 (2008) 508-513.

[11] Y. Wang, J. Zhu, X. Yang, et al, Preparation and characterization of $LaNiO_3$ nanocrystals, Materials Research, 41 (2006) 1565-1570.

[12] Y. Tong, J. Zhu, L. Lu, et al, Preparation and characterization of $Ln_2Zr_2O_7$ (Ln = La and Nd) nanocrystals and their photocatalytic properties, Journal of Alloys and Compounds, 465 (2008) 280-284.

[13] Y. Tong, Y. Wang, Salt-assistant combustion synthesis of nanocrystalline $Nd_2(Zr_{1-x}Sn_x)_2O_7$ ($0\leq x\leq 1$), Materials Characterization, 60 (2009) 1382-1386.

[14] W. Chen, F. Li, J. Yu, Salt-assisted combustion synthesis of highly dispersed pervoskite $NdCoO_3$ nanoparticles, Materials Letters, 61 (2007) 397-400.

© (2012) Trans Tech Publications, Switzerland
doi:10.4028/www.scientific.net/AMM.238.83

Safe and Sustainable for the Structural Silicone Sealant in Ultra High-rise Building Curtains

Hailong Zhang[1, 2, a] and Ling Quan[3, b]

[1] School of Civil Engineering and Communication, North China University of Water Resources and Electric Power, Zhengzhou 450011, China

[2] Zhengzhou Zhongyuan Applied Technology Research and Development Co., Ltd. Zhengzhou 450007, China

[3] Institute of Electric Power, North China University of Water Resources and Electric Power, Zhengzhou 450011, China

[a]zhlongql@yahoo.cn, [b]goodluck136946@yahoo.com.cn

Keywords: structural silicone sealant; building curtains; safe; sustainable.

Abstract. The properties of the structural silicone sealant under standard condition and after aging conditions were characterized. The results showed that the structural silicone sealant had very good ability to resist the ultraviolet in the long time. In the other aging environment conditions, the different failure time for the structural silicone sealant were appeared. The value of the maximum strength under the different mechanical aging factors obviously existed in the structural silicone sealant with different compositions. The residual strength that the attenuation ratio is more than 75% standard strength would keep the ultra high-rise building curtains safe and sustainable.

Introduction

With the rapid development of economy in China, the Ultra High-rise building with over two hundred meters is very common in big cities. The building curtains for the building envelope structure also became more and more application owing to the lower weight than the main structure. Some new materials and new technologies were applied in building curtain, which made it form diversification and get very beautiful. The structural silicone sealant as the structural sealant glazing materials played an important role in building curtains with the structural bonding and transferring various loads [1], which could change displacement with good performance owing to itself belonging to elasticity.

As we know, the working life of the building curtains is more than 25 years in the design [2, 3]. The structural silicone sealant is one of the main raw materials in building curtains, but the cost is very low compared with other material, such as metal material, glass. As the polymer materials, the properties of the structural silicone sealant rapidly attenuated in the use of the processing [4]. Therefore, some performances need to be tested in the laboratory to simulate the aging conditions. The aging environment factors suffered in the using of the process, the various forces influenced the properties should be simulated in the laboratory, and the evaluation of the properties should be made.

The aging factors for the structural silicone sealant using in the building curtain were analyzed in this paper. The properties of structural silicone sealant with different standards were compared. So we propose the reasonable advices for the structural silicone sealant in the ultra high-rise building curtains, which could provide the safe and sustainable for the building curtains.

Experimental section

Materials. The structural silicone sealants with 25 years working life were coming from the Zhengzhou Zhongyuan Applied Technology Research and Development Co., Ltd. The other structural silicone sealants according to GB 16776 were purchased from the domestic market.

Preparation of Product. The test samples are assembled by the manufacturer or in accordance with their instructions used in the system. All the test samples are conditioned initially for 28 days after manufacture at a temperature of (23±2)°C and at (50±5)% relative humidity.

Characterization. The adhesive properties of the structural silicone sealants were tested according to the GB 16776-2005 and ETAG 002.

Results and Discussion

Environmental Factors. The tensile strength of the structural silicone sealant under the pure Ultraviolet (UV) was shown in Fig. 1. It can be seen that the tensile strength of the structural silicone sealant was not significantly changed in the about 0.90MPa with the increasing time. It was ascribed to the basic composition that was the polydimethylsiloxane with mainly silicone-oxygen chemical bonding, which had higher breakage bonding energy compared with the energy of the UV. The UV in the sun was different to decompose the silicone-oxygen chemical bonding. So the structural silicone sealant with the structural sealant glazing system could keep the longest elasticity and transfer external loads to ensure the safe and sustainable in the building curtains.

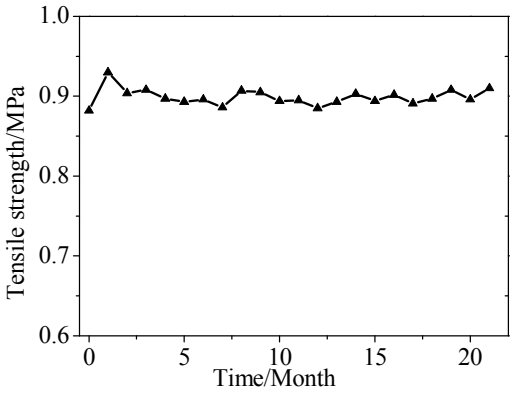


Fig. 1 Tensile strength of the structural silicone sealant under UV

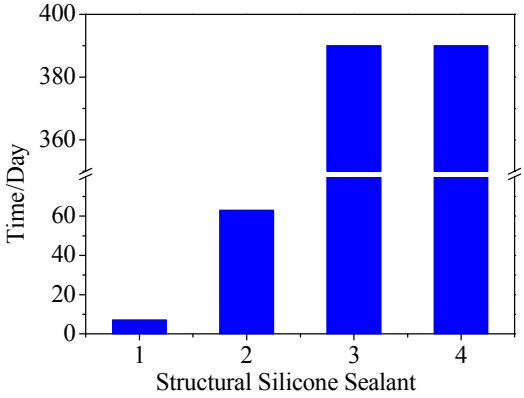


Fig. 2 Failure time of structural silicone sealant under water

Fig. 2 shows the failure time of the structural silicone sealant. The four Structural silicone sealants came from the different company with the different compositions. We could see that the failure time is 7 days under water for the brand 1, and the failure time is 63 days for the brand 2, but the brand 3 and brand 4 could keep well properties under water up to 390 days. The four brands with the same structural silicone sealant present the obvious failure time. This was explained that the aging conditions played an important role on the properties of the structural silicone sealant. The structural silicone sealant would often suffer from water to affect the working life in the building curtains. Therefore, we should simulate this aging condition in the laboratory.

For the polymer materials, the UV in the sun and the water is the main reasons on the properties of failure. Fig. 3 shows the different failure time of the structural silicone sealant under water-UV, we can see the brand four structural silicone sealant showed distinguish failure time. The brand 1 have the lowest failure time with 300 hours, and the failure time of the brand 2 is about 700 hours, but the brand 3 and brand 4 could up to 2500 hours. This is illustrated that the brand 3 and brand 4 would have the longest using time than brand 1 and brand 2.

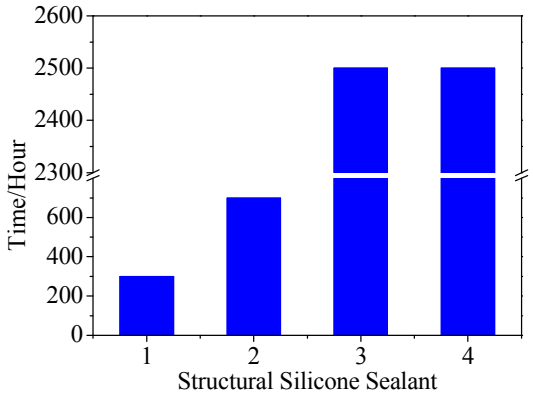


Fig. 3 Failure time of structural silicone sealant under water-UV

For the other environmental factors, such as salt spray, SO_2 atmosphere, façade cleaning products, high temperature, would the facing aging conditions. The salt spray test simulates the marine or saline wet climate environment according to the ISO 9227-atmosphere NSS maintained for 480 hours. The SO_2 atmosphere test simulates the acid rain environment according to EN ISO 3231 with 20 cycles. The façade cleaning products test simulates the properties of the structural silicone sealant that immersed in the cleaning product for 21 days. The high temperature test is carried out in according with the document EN ISO 8339 with the temperature of 100 °C and the 7 days.

Mechanical Factors. The structural silicone sealant as the structural adhesive materials used in the building curtains, which transferred wind load and the earthquake load, or other loads. So the structural silicone sealant would suffer very complicated forces in the use of the working life. In the laboratory, we should analyze all kinds of the force and simulate the adhesive property. Usually, the tensile force owing to the wind load was accepted by the building curtain designer. But, the weight of the glass that was large for the laminated-insulated glass caused the shear force which assumed by the structural silicone sealant. In some cases, owing to the displacement for the expansion coefficient caused by the different temperature, the cyclic load on the structural silicone sealant would make the fatigue force in the building curtains. Some gap on the structural silicone sealant would cause the stress concentration that was tested to simulate the mode of propagation of the force. The displacement of the long term shear force and tensile force was evaluated the creep properties, which conditions were the higher temperature with the (55±2)°C and the relative humidity with the (95±5)%. All of those need to be analyzed and tested to evaluate to the adhesive properties.

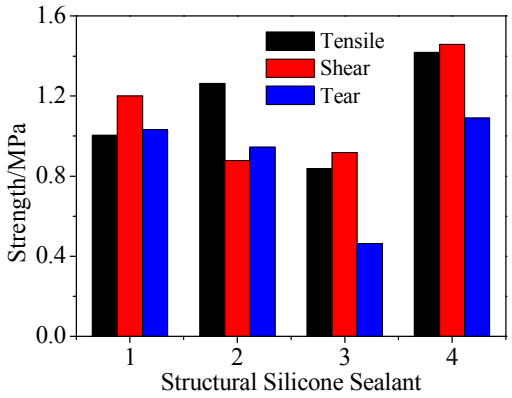


Fig. 4 Different mechanical factors for the structural silicone sealant

Fig. 4 shows the strength of the four structural silicone sealants under different forces. For the brand 1, the maximum strength is the shear force. The maximum strength is tensile force for the brand 2. The tensile strength and shear strength could satisfy the requirement of the standard for the brand 3, but the tear strength is less than 0.60MPa. For the brand 4, the value of strength is higher than other brands, but the tear strength is lower compared with the tensile strength and shear strength. These phenomenons illustrate that the maximum adhesive strength of the structural silicone sealant is different. Only testing the complicated forces for the structural silicone sealant used in the building curtains, the properties could have a very good evaluation.

The Attenuation Rate. The properties of the structural silicone sealant under the different aging factors were shown in Fig. 5. The structural silicone sealant with number 1 coming from the domestic market was satisfied with the tests of the GB 16776 <Structural silicone sealant for building>, and the structural silicone sealant with the number 2 coming from the Zhengzhou Zhongyuan Applied Technology Research and Development Co., Ltd. was satisfied with the tests of the ETAG 002<Guideline for European technical approval for the structural sealant glazing systems>. The residual strength is the value of aging strength and standard condition strength ratio.

For the brand 1, after different aging factors, the residual strength presented significant differences. After high temperature, the residual strength would have the 83% standard condition strength, and the residual shear strength only had the 43 percentage of the standard condition shear strength. After the artificial aging conditions, the residual strength of the brand 1 was 68% standard condition tensile strength in Water-UV environment, and was 58% standard condition tensile strength in salt spray

environment, and was 74% standard condition tensile strength in SO_2 environment, and 65% standard condition tensile strength in façade cleaning product. According to the ETAG 002, the residual strength with less than 75% is not the qualified product. So the brand 1 does not satisfy the requirements of the ETAG 002.

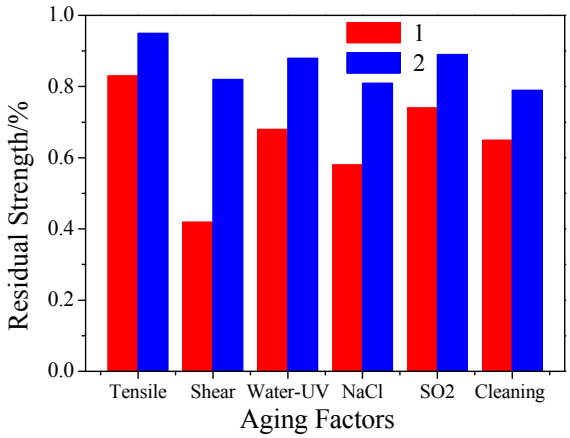


Fig. 5 The properties for the structural silicone sealant with the different aging factors

For the brand 2, after the processing of different mechanical forces and artificial aging conditions, the residual strength is more than 75% standard strength. The maximum value is 95% in tensile with the high temperature condition, and the minimum value is 79% in the façade cleaning product. So the comprehensive properties of the brand 2 are better than the brand 1.

For the materials, the attenuation ratio proportioned the working life in the using. The slower is the attenuation ratio, the longer is the working life. So, the brand 2 could make it safer and more sustainable than the brand 1 in the building curtains.

Conclusions

The structural silicone sealant has very strong ability to resist ultraviolet owing to the silicone-oxygen chemical bonding, which was used in the building curtain to play the adhesive property and transfer various loads. In the application, it would face many of aging factors including environment factors and mechanical factors. The influence of the adhesive properties on the aging factors should be analyzed and simulated in the laboratory. The methods that took the attenuation ratio evaluate the properties after aging are very scientific and rationality.

References

[1] Q. Ma, W. Liu, D. Zhang, et al, Structural Silicone Sealant for Building, Standardization Administration of the People's Republic of China, Beijing, 2005.

[2] X. Huang, X. Zhao, Q. Jiang, et al, Technical Code for Glass Curtain Wall Engineering, Ministry of Construction of the People's Republic of China, Beijing, 2003.

[3] M. Li, D. Hu, Z. Shi, et al, Unified Standard for Reliability Design, Ministry of Construction of the People's Republic of China, Beijing, 2001.

[4] M. A. Mendelsohn, R. M. Luck, F. A. Yeoman, et al, Sealants for solar collectors, Industrial & Engineering Chemistry Product Research and Development, 20 (1981) 508-514.

© (2012) Trans Tech Publications, Switzerland
doi:10.4028/www.scientific.net/AMM.238.87

Research on Comprehensive Utilization of the Tail Ore

Yingjie Chen [a] and Gen Li [b]

Department of Civil Engineering and Mechanics, Yanshan University, Qinhuangdao, China

[a]cyjysu@126.com, [b]ligen_hebut@126.com

Keywords: tail ore; particle gradation; easy grinding property; compressive strength; comprehensive utilization.

Abstract. A lot of tailings have been accumulated in China, which brought severe environmental pollution and took up the massive land, and even threatened the life safety of the people. By the experimental study, it is found that in the north area of China, the tail ore is easy to be grinded and burned, and may be used as the sand with good particle gradation. The ignition loss quantity of the tail ore and the compressive strength of concrete with different proportion of the tail ore are studied. It offers a new way for the comprehensive use of tail ore.

Introduction

Since the reform and opening up, along with the rapid development of the construction industry, the world each year to consume large amounts of cement, natural sand, etc. In resources shortage of today, energy conservation and environmental protection material urgently need to be people. If the goods can be mixed with a lot of concrete in fine grinding mineral admixtures, which can improve the performance of many of the concrete, and can reduce the dosage of cement clinker through, to some extent, inhibit large-scale construction period of strong demand for cement, so as to realize the precious resources saving country and energy to the target.

Our country is rich in mineral resources, in the full utilization of mineral resource service society construction at the same time; a large number of mineral resources exploitation also brought an incredible amount of tailings. Every year because of a large accumulation of tailings discharge by the cultivated land occupied, environmental pollution and casualty case for infinite in number. At present, all countries in the world into a lot of manpower material resources research tailings, as a secondary resources to treat, many industrial developed countries take utilization degree as a measure of tailings science and technology level and economic development level of the sign.

At present, although our country has large iron ore size tail made concrete products, instead of clay and pave the iron ore production, cement clinker, such as the shougang 2 million tons of production line to the project to move all by the Beijing institute of civil engineering and architecture and shougang mining company developed tailings sand concrete construction, but our country tailings comprehensive utilization of waste is only 7% or so, whether use scale, use value and economic benefit is not into full play.

Tailings form severe in north china. Such as Hebei cherry blossoms mining Co, LTD Luan county cherry blossoms in the crude ore processing of iron ore ore-dressing plant of about 500000 tons, annual output of about 330000 tons of tailings; MiaoGou iron ore concentrator for years production scale of 1.22 million tons of crude ore processing, tail mineral rate was 62.68%, with the annual production capacity of about 765000 tons of debris. Relevant government to reduce the accumulation of the ore containment, policy to encourage enterprise in the ready-mixed mortar process using made of tailings sand mechanism, if use enterprise line with the policy requirements, can enjoy preferential tax.

The Application of the Ore

Compared with other countries in the world, mineral resources in lean more characteristic is less rich deposits, half composite ore more, a single ore less, therefore, the comprehensive utilization of tailings is difficult, and specific questions to specific to specific analysis. Tailing experiment

showed that different mine tailings although mineral composition and content often changes, but the basic can be classified into three categories: acidic tailings (high silicon aluminum type), alkaline tailings (high calcium magnesium type), and high mud kind of tailings. In north China there are more acidic tailings.

Tail Ore Particle Grading. Particle grading refers to all size particles in aggregate the proportion of, this ratio adopt prescribed a group of aperture to sieve residue sieve to expression. Table 1 and Table 2 respectively is MiaoGou iron ore concentrator, Luan County cherry blossoms iron ore tailings concentrator grain size analysis form.

Table 1 MiaoGou iron ore tailings concentrator composition analysis table size

Mesh	Particle size（mm）	Production rate（%）	Cumulative yield（%）
80	+2	4.07	4.07
100	-2~+1.5	5.98	10.05
140	-1.5~+0.10	5.80	15.85
200	-0.10~+0.076	10.20	26.05
280	-0.076~+0.055	16.22	42.27
350	-0.055~+0.042	4.19	46.46
400	-0.042~+0.03	10.80	57.26
—	-0.03~+0.02	9.15	66.41
—	-0.02~+0.01	6.22	72.63
—	-0.01	27.37	100.00

MiaoGou tailings particle density 2.85 t/m^3, tailings pulp density 40%, tailing grain size 0.056mm on average, among them, -200 mesh is occupied 74%, to 400 yard accounted for 50%.

Table 2 Luan County cherry blossoms iron ore tailings concentrator grain size analysis form

Grain of level（mm）	+0.074	-0.074～+0.056	-0.056～+0.037	-0.037～+0.019	-0.019
Production rate（%）	31.04	19.47	17.04	14.60	17.85

Luan County cherry blossoms tailings tailing grain average particle size is 0.0978mm, tailings of median diameter of 0.028mm.

The rationale of particle grading is make ingredients obtain low porosity in a major way, particle gradation will influence the concrete close degree, the smaller the fineness modulus, the greater the water unit, the lower the concrete strength.

500g MiaoGou sampling tail ore screening, of which 5.0 sieve is 47g, 2.50 screens is 38g, 1.25 screen is 34g, 0.630 screen is 69g, 0.315 screen is 94g, 0.160 screen is 91g, 0.08 screen is 100g, remaining 22g. Compared with natural sand, the high density of tail ore, clay content, clay pieces content and the organic matter content is low, fineness modulus small, mostly less than 1.0, also is the tail ore generally fine than sand. Will more than 0.16 screens the tail ore instead of natural sand, 0.16 screens the following instead of cement, sand and with natural compound use, can change the size of the fine tailings partial defects.

Easy Grinding and Burning Properties of the Tail Ore. Easy grinding property is refers to the cement clinker grinding in powder ink the degree of difficulty. Cement is raw burned is to point to in kiln in practical operation, clinker to the difficulty of the firing. Real production, easy to burn and inherent hard to simultaneously optimize grinding, manufacturers often attend, if mixed with tail ore can simultaneously optimize easy grinding and burning properties, it will have great significance for production. Table 3 different material is easily grinding experiment results, Table 4 is easy burning experiment results. Experiments show that the configuration of the ore is raw material grinding sex and burn sex has improved.

Table 3 Easy ground experiment results

The raw material	Sandstone	Lime-stone	Mixed with tail ore (%)					
			0	20	40	60	80	100
Grinding function index Wi/(KWh/t)	16.7	10.2	12.4	11.7	11.2	10.4	8.2	7.6

Table 4 Easy burning experiment results

Serial number	Mixed with tail ore amount (%)	Clinker rate value			Fineness	f-Cao%			Reaction rate (1450℃)%
		KH	SM	AM	+80μm content	1350	1400	1450	
A-01	0	0.920	2.45	1.38	17.7	5.75	3.25	2.43	94.5
A-02	20	0.900	2.39	1.37	16.4	5.61	3.63	2.28	96.6
A-03	40	0.898	2.32	1.35	14.2	5.24	2.25	1.64	97.4
A-04	60	0.894	2.20	1.33	13.4	4.98	1.98	1.42	97.6

The Compressive Strength of Sand. Because the sand is an extremely the rules and amorphous aggregate species, and they compared with natural sand has high strength, have good bonding with concrete characteristics. But there is also the ability in swimming is poor, sliding low degree of the gradation, bad shortcomings. So in the concrete mixing tail ore to ensure that not only meet the concrete work performance, but also making a big liquidity, the slump losses small goals.

Will end by M7.5 mortar sand ratio, concrete block 28 days strength test results: slag mixed with 60%, 7.4 MPa, can reach 99%; Slag mixed with 70%, 6.5 MPa, can reach 87%; Slag mixed with 80%, 5.5 MPa, can reach 73%; Slag mixed with 90%, 6.0 MPa, at 80%. Choose high with 60% and 70% of the two groups, they were the 7d and 28d strength.

Table 5 Test the mortar material used

Serial number	Water	Cement	Sand	Tail ore	Stone
B-01	185	330	718	0	1172
B-02	269	330	304	414	1172
B-03	275	330	235	483	1172

Table 6 Tail ore concrete compressive strength and workability

Serial number	Tail ore replace rate (%)	Water cement ratio	Collapsibility (mm)	Compressive strength (MPa)		Concrete workability
				7d	28d	
B-01	0	0.56	80	27.2	30.1	Good liquidity and cohesiveness, no secrete water
B-02	60	0.86	80	26.6	37.4	A bit poor liquidity, common cohesiveness, secrete water
B-03	70	0.88	80	21.3	27.4	A bit poor liquidity, common cohesiveness, secrete water

The tail in the ore contains a certain amount of cement a reduced secrete water and the problem of segregation, and limestone and cement and water formed the paste, improve the concrete workability. But when the ratio of ore reached more than 60%, with the increase of the content of will make things too dry white concrete thick, liquidity becomes poor, appear secrete water and segregation phenomenon.

End of the Ore Ignition Loss Quantity. Ignition loss quantity and says alexa reduction, it is to point to in the blank burn out in the process of gesso, carbonate the separating CO_2, sulfate the separating SO_2, and organic impurity content quantity after been ruled out of the loss. Slag cement ignition loss determination of the characteristics of the countries have been no good way, virtue in countries such as specified in the national standards though slag ignition loss amount of determination method, but the test method trivial, instrument high cost.

Our country is now no slag ignition loss quantity determination of the specification, to MiaoGou tail ore cement specimens with reference to fly ash ignition loss quantity determination standards, sand mixed with 60% and 70% of the specimens are 6.585 and 5.409 respectively results, accord with fly ash ignition loss quantity secondary standard.

Conclusions

The experiment results are given in this can be directly applied in engineering practice, the content of the ore can satisfy normal mortar performance standards, its wide application can not only to conserve natural resources and protect the ecological environment, and can also be for enterprise to bring significant economic benefits.

References

[1] J. Wong, The development and production of iron in China tailings of building material present situation and prospect, Housing Materials & Applications, 4 (1998) 16-35.

[2] Q. Chia, J. Cheung, F. Li, Status and research of utilization of iron ore tailings, Mining Engineering, 4 (2006) 7-9.

[3] Z. Ho, C. Teng, Tailing in ready-mixed concrete application of the experimental research, Concrete, 9 (2009) 115-118.

[4] T. Wong, Slag cement ignition loss quantity determination method of the initial study, Building Materials Standardization and Quality Management, 1 (1990) 23-24.

[5] P. Tuan, Z. Cheung, Y. Miau, End in ordinary sand dry mortar of application, China Silicate Fittest Materials in 2006 to Branch Conference Proceedings, 10 (2006) 272-278.

[6] Q. Chiao, Y. Chu, X. Lau, Iron ore in cement production of the comprehensive utilization of research, Modern Mining, 9 (2009) 102-121.

© (2012) Trans Tech Publications, Switzerland
doi:10.4028/www.scientific.net/AMM.238.91

Experimental Study on Mechanical Behavior of Concrete Loading along Path (Constant Stress, Constant Strain, Increasing Strain)

Zhe Wang [1, a], Jing Li [1, b] and Renjie Shang [2, c]

[1] School of Civil Engineering Beijing Jiaotong University, Beijing 100044, China

[2] Central Research Institutes of Building and Construction, MCC Group; Beijing 100088，China

[a] zhwang@bjtu.edu.cn, [b] 314666466@qq. com, [c]shangrj2000@yahoo.com.cn

Keywords: normal concrete; constant stress; constant stress; strength; strain.

Abstract. Triaxial compressive experiments were performed with normal concrete by using the large triaxial test system. The loading process was divided into two stages: (1) Under the condition of keeping the three axial stresses equivalent, the compressive stress was increased to a specified value p, which was maintained for a period of time; (2) The strain in y direction was increased monotonously while the stress in x direction and the strain in z direction both remained constant. In this paper, the study on the experiments indicates: the minimum principal stress significantly influences the strength of concrete, i.e., the greater the minimum principal stress is, the greater the concrete strength is; the stress in y direction where the strain stayed constant is the middle principal stress; the constant strain influences the relationship between σ_2 and σ_1, they reach the peak values at the same time and approximate to linear relationships in much parts of their descending stage, curvature only appears at their ends; When ε_{13}>8, each relationship curve of τ_{13}-γ_{13} gradually becomes horizontal；Below a line AB in figure of coordinate system ε_x, ε_y the curves of ε_x-ε_y approximately parallel to each other; If the minimum principal stress is 15MPa or 20MPa, After ε_{kk} reaches the peak point, the volume gradually becomes stable after a transient decrease stage.

Introduction

Concrete constitutive models are generally based on the tests of strength and deformation, as a common state, plane strain state is an important and ancient subject [1, 2]. The tests of strength and deformation under plane strain state lay the foundations of damage theory researches of concrete dam and other large concrete structures, the characteristics of concrete in the stress state have been studied both at home and abroad by many people [3-5]. Due to the limitations of test conditions and equipments, the tests of strength and deformation under plane strain state are rarely implemented. Dalian University of Technology has already done some researches in this field, but the stress ratio only reached -0.2 in the tension -compression state [6, 7]. In some literatures, unconfined triaxial tests are reported, however, as there is no lateral deformation, the descending stage for axial stress-strain curve cannot be obtained during loading process, hence no triaxial strength [8] exists. In some other literatures, although the equivalent uniaxial strain model is studied and its stress-strain relationships are deduced correspondingly, it is only used for the biaxial compression in plane strain state [9]. In this paper, the self-developed triaxial test instrument was utilized in order to study the strength and deformation of concrete under complex stress-strain states.

Experimental Program

Material and Specimens. Table 1 shows the proportion of concrete, the details of these materials are described as follows: The cement used in this test is the ordinary Portland cement whose strength grade is 42.5. To meet the requirement of determining the proportion and consider the workability of the mixture, both artificial sand and natural sand are used. Artificial sand is made of stone powder, whose particle gradation is Gradation II and the fineness modulus is 2.5, so it is a intermediate sand. Natural sand is ordinary river sand, whose fineness modulus is low thus it is categorized to the fine sand.

The fine sand can not only improve the local mobility of the mixture slurry and the quality of the specimens, surface, but also increase the cohesive performance of the mixture. Artificial sand is able to ensure the sand lies in the normal gradation range and the strength of concrete.

Stone is limestone rock with 5 ~ 10 mm particle. Using the solid defoamer produced in Beijing Construction Engineering Research Institute.

Table 1 Proportion of concrete

Proportion of concrete (cement, sand, stone, water)	Material dosage in 1^3(kg)				Defoamer(%)	water cement ratio	slump (cm)
	Cement	Sand	Stone	Water			
1:1.89:3.06:0.618	364	688	1123	225	0.1	0.618	8

The specimens with the dimensions of 100mm×100mm×100mm, were cast in steel molds and then demolded after 24-hour curing in the constant temperature room, then the specimens were moved into water at the temperature of 40°C to cure for 28 days, finally stored in the room.

Loading Equipments and Methods. Servo-hydraulic true triaxial testing machine of the state key laboratory of Coastal and Offshore Engineering, Dalian University of technology, was used in this experiment. Displacement and load feedback control in three directions were applied, the details can be seen in literature [10].

On the basis of experimental data, Fig. 1 and Fig. 2 were obtained in order to exemplify the loading method. The entire loading process consisted of two phases, the first phase was corresponding to the part A-B-C in Fig. 1, during which the three axial stress curves coincided with each other. For part AB, the three axial stresses increased with the ratio of 1:1:1 until reaching the specified value $\sigma_x=\sigma_y=\sigma_z=P$, then the stresses were maintained constantly for a period of time (part BC). After passing the point C, the test reached the second phase, the strain in y direction increased monotonously with the constant stress in x direction and the constant strain in z direction. Apparently, the state of second stage is similar to plane strain state.

The test was grouped into four categories according to the value of P, which were 5 MPa, 10 MPa, 15 MPa and 20 MPa, two specimens for each group. When analyzing and processing data of the second stage, the strain in the three directions should minus the strain of point C in Fig.1 respectively, at which, the strain was considered as zero.

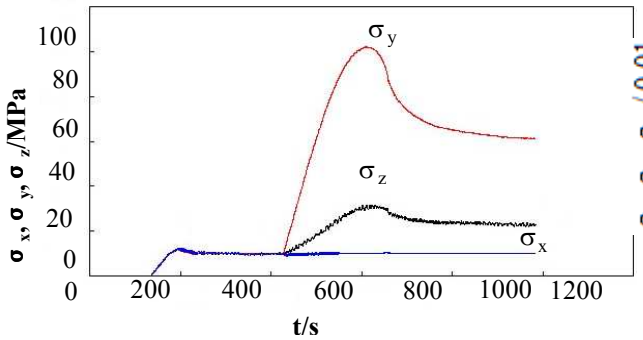


Fig. 1 Relationship curves of $\sigma_x,\sigma_y,\sigma_z$ with t

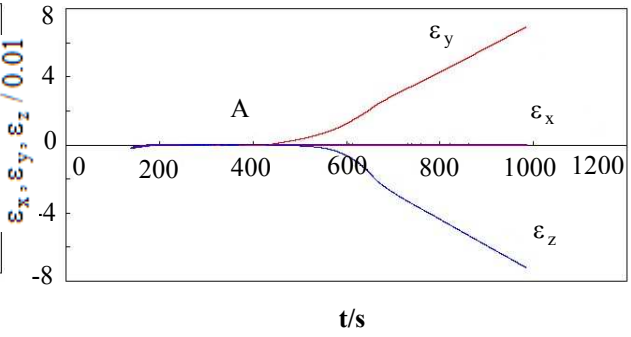


Fig. 2 Relationship curves of $\varepsilon_x,\varepsilon_y,\varepsilon_z$ with t

Results and Analysis

Failure Modes. As the result of the constant strain in z direction and constant stress in x direction in the loading process, when compressed in y-direction, the specimen merely expanded in x direction. All the specimens failed in a wedge-shaped pattern. It is observed that failure surface is covered with a certain thickness of powder and traces of sliding are also found. According to these failure modes, it is deduced that the failure was caused by shearing along with compressive stress.

Strength Property. Table 2 gives the peak strength of concrete, Fig. 3 gives the relationship between the maximum principal stress σ_1 and the middle principal stress σ_2 In order to emphasize the order of magnitude, σ_1,σ_2 and σ_3 are used instead of $\sigma_y\,\sigma_z$ and σ_x, i.e. $\sigma_1\geq\sigma_2\geq\sigma_3$.

In Table 2, the minimum principal stress significantly influences the strength of concrete, the greater the minimum principal stress is, the greater the concrete strength is; In figure 1, the stress in Z direction is always smaller than that in y direction, So the principal stress in z direction where strain is a constant value is the middle principal stress. Lu De-chun [11] and Li Guang-Xin [12, 13] have studied the principal stress of soil in plane strain condition, one of their loading paths is similar to the one mentioned here.

Table 2 The triaxial strength of concrete

Types of concrete	*P*(MPa)	$\sigma_3=\sigma_x$ (MPa)	$\Sigma_2=\sigma_z$ (MPa)	$\Sigma_1=\sigma_y$ (MPa)
B_1	5	5	19.13760	78.78055
B_2	10	10	31. 68158	102. 167
B_3	15	15	40. 56758	119. 4514
B_4	20	20	46. 20129	131. 6682

Fig. 3 illustrates the relationship between σ_2 and σ_1. It can be observed that, all the curves have both transcending stage and descending stage, $\sigma_2$and σ_1 increase, fall and reach the peak value in the same pace. In the transcending stage, their relationship trends in curvature; but most parts of the descending stages approximate straight line segments, curvature appears at their ends ,which is a rare phenomenon in the literature of non-proportional loading triaxial test. In addition, this phenomenon does not exists in the experiment of keeping the stress in z direction as well as the strain rate ratio between x and y direction remained constant [14]. It is concluded that constant strain influences the relationship between σ_2 and σ_1.

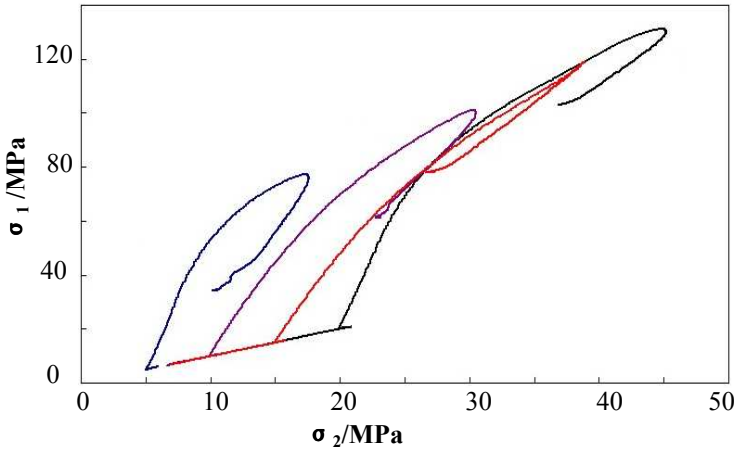


Fig. 3 Relationship curves of $\sigma_1-\sigma_2$

Deformation Property. Here we mainly research the relationship of shear stress and shear strain as shown in Fig. 4, the stains of x axis and y axis as shown in Fig. 5, as well as the relationship between the shear strain and volume strain as shown in Fig. 6.

In Fig. 4, when $\tau_{13}\leq$50MPa, all curves coincide except the curve of σ_3=20MPa; the curve of σ_3=5MPa has an obvious peak point, but a relative "stress-stable region" occurs in other curves, the greater the peak stress is , the wider the "stress-stable region" stays; then there comes the descending stage, when γ_{13}>8, all these curves gradually become horizontal, at this stage, the cracks near the shear belt of concrete gradually interconnected, finally, the failure surface was formed.

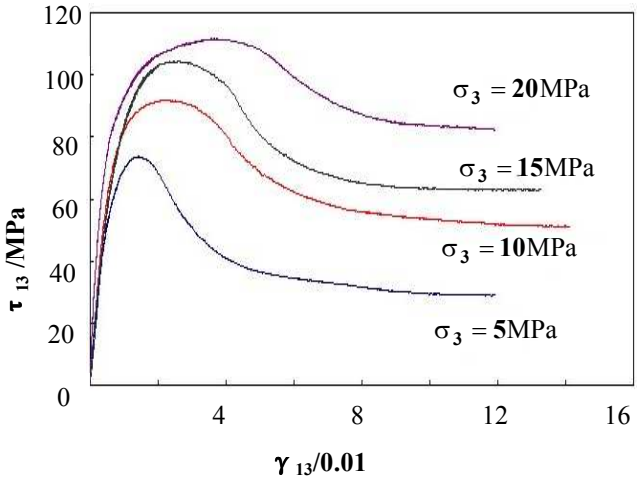


Fig. 4 Relationship curves of τ_{13} -ε_{13}

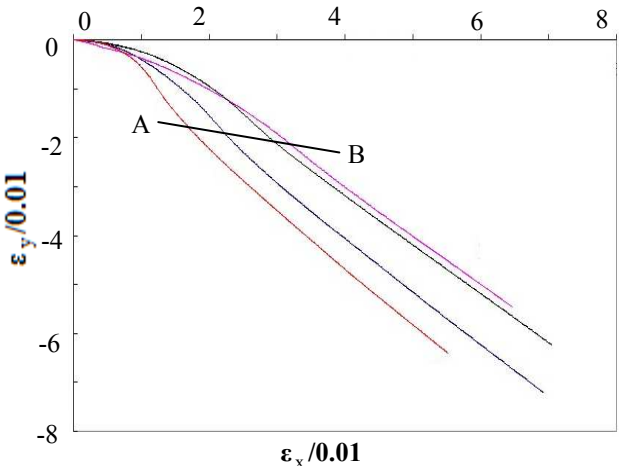


Fig. 5 Relationship curves of ε_x - ε_y

In Fig. 5, it is found that ε_y increases monotonously with the increase of ε_y. Above the line AB, their relationship trends in curvature; below the line AB, the relationship becomes liner, on the basis of the experimental data, the slope for lines of B_1, B_2, B_3 and B_4 are 1.1221, 1.0707, 0.996, 0.982 respectively. Obviously, all these line segments approximately parallel to each other.

In Fig. 6, if the minimum principal stress is 5 MPa or 10MPa, After ε_{kk} reaches the peak point, it begins to decrease with the increase of γ_{13}. The phenomenon of dilatancy constantly appears in the descending stage; if the minimum principal stress is 15 MPa or 20MPa, after ε_{kk} reaches the peak point, the volume gradually becomes stable after a transient decrease stage.

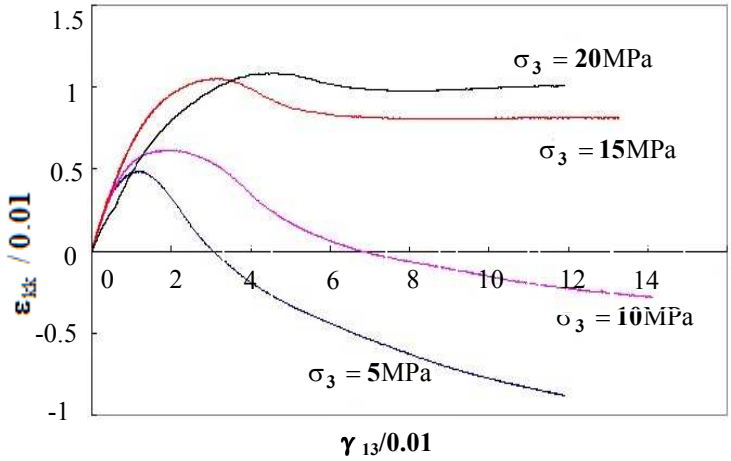


Fig. 6 Relationship curves of ε_{kk}-γ_{13}

Conculsions

The minimum principal stress significantly influenced the strength of concrete, the greater the minimum principal stress is, the greater the concrete strength is; the stress in z axis where the strain was a constant value is the middle principal stress.

When γ_{13}>8, each relationship curve of τ_{13}-γ_{13} gradually become horizontal.

In figure 5, above the line AB, their relationship trends in curvature; below the line AB, the relationship becomes liner, all these line segments approximately parallel to each other.

If the minimum principal stress is 15 MPa or 20MPa, after ε_{kk} reaches the peak point, the volume gradually becomes stable after a transient decrease stage.

Acknowledgments

This study was supported by the National Natural Science Foundation of China (51078024, 50879004). Thanks are due to Changfan Wei, Jin Zhao and Li Li for their assistance in the test.

Reference

[1] D. H. Cornforth, Some experiments on the influence of strain condition on the strength of sand, Geotechnique, 14 (1964) 143-167.

[2] A. W. Bishop, Sixth Rankine lecture: the strength of soil as engineering material, Geotechnique, 16 (1966) 89-130.

[3] H. Kupfer, & K.H. Gerstle, Behavior of concrete under biaxIal stresses, ASCE, 99 (1973) 353-869.

[4] N. Gardner, Triaxial behavior of concrete. J. ACI. 66 (1969) 139-146.

[5] C. Wang, Z. Guo, X. Zhang, Experimental investigation of concrete strength under biaxial and triaxial compressive stresses, China Civil Engineering Journal, 2 (1987) 15-27.

[6] Y. Song, G. Zhao, The character of deformation and strength of concrete under plane strain state, Journal of Hydraulic Engineering, 5 (1990) 22-28.

[7] Y. Song, G. Zhao, Strength criterion of concrete under plane strain state with tension-compression lateral stresses, Journal of Dalian University of Technology, (1997) S104-S109.

[8] T. Gabet, Y. Malecot and L. Daudeville, Triaxial behavior of concrete under high stresses: Influence of the loading path on compaction and limit states, Journal of Cement and Concrete Research, 38 (2008) 403-412.

[9] J. Wang, H. Zhu, H. Wang, Equivalent uniaxial constitutive model of concrete in plane strain, Journal of Hohai University, 30 (2002) 6-l0.

[10] M. Li, Y. Liu, Q. Zhang, J. Wang, Research and implementation of digital control technology on motor servo system, Computer Measurement & Control, 18 (2010) 15-26.

[11] D. Lu, Y. Yao, A. Zhou, Relationship between principal stresses of soil mass under plane strain condition, Chinese Journal of Rock Mechanical and Engineering, 25 (2006) 2320-2326.

[12] G. Li, Q. Zhang, Y. Huang, Study on transforming of principal stresses in constant stress ratio plane strain tests, Rock and Soil Mechanics, 27 (2006) 1867-1872.

[13] G. Li, Y. Huang, Q. Zhang, The principal stress of soil in the direction of plane strain, Chinese Journal of Rock Mechanical Engineering, 23 (2001) 358-361.

[14] Z. Wang, X. Ma, Mechanical behavior of concrete under triaxial compression - Loaded along paths in (stress, train, train) pace, Electric Technology and Civil Engineering, (2011) 2358-2361.

© (2012) Trans Tech Publications, Switzerland
doi:10.4028/www.scientific.net/AMM.238.96

Robust Statistics Analysis of Proficiency Test Result of Cement Chemical Composition

Yan Jia[1, a], Xiaotian Cheng[1, b] and Dong Wei[2, c]

[1]Henan Institute of Product Quality Supervision and Inspection, Zhengzhou 450004, China

[2]Henan Provincial Communications Planning Survey & Design Institute Engineering Test & Consultation Co., Ltd. Zhengzhou 450052, China

[a]huangh12345@sohu.com, [b]xiaotain0126@126.com, [c]wd19841212@yahoo.com.cn

Keywords: cement; chemical composition; proficiency test; robust "Z-score".

Abstract. Test result of cement chemical composition was obtained from the participating laboratory through organizing and performing the cement proficiency test plan. After performing the robust statistical analysis to the result, the test proficiency of the laboratory is evaluated, the proficiency of each laboratory on chemical composition analysis and test is objectively reflected.

Introduction

Proficiency test is a effective method to finally evaluate test proficiency of laboratory and ensure the laboratory technical capacity and management level being improved constantly through the comparison between laboratories as per the comparison principle specified in advance which is carried out by several test laboratories who organize, perform the test of the same sample (parameter).

In order to analyze and evaluate the analyzing and test proficiency of laboratories which participate the cement chemical composition analysis and test, this proficiency test of laboratory of cement chemical composition analysis and test is organized. On the significant 0.05 level, firstly ensure the sample is well-proportioned; send the sample to the laboratory for independent test on the basis of meeting the proficiency test requirement; then perform the robust statistical technique to the all the results of participated laboratories; as per the conformity of each laboratory result and other laboratories results andrefer to the test result distributing situation of each participated laboratory, minimize the influence to statistics from abnormal value; evaluate the satisfaction degree of each cement laboratory test result and evaluate the professional skill on test of each cement laboratory.

Homogeneity Test of Proficiency Test Samples

As the homogeneity and stability of cement samples, which are used in the laboratory proficiency test, is the basis for performing the proficiency test plan, as per the specifications of CNAS-GL03：2006 Evaluation Guideline of Homogeneity and Stability of Proficiency Test Samples, all cement samples must be completely well-proportioned and reliable & stable to ensure that any doubtful, unsatisfied results comes from the comparison result are not caused by the differences between the samples.

Preparation of Laboratory Proficiency Test Sample

During the cement sample preparing process, as per GB/T176-2008 *Method for Chemical Analysis of Cement* and GB/T12573-2008 *Sampling Method for Cement*, the factors that influence homogeneity and stability of cement samples should be considered and prepared, such as preparing process of samples, sampling quantity, sealed packing materials, storage condition, time and test method; the less additives added portland cement or common portland cement should be selected for the cement proficiency test sample.

Two groups of common portland cement are selected in this comparison; mixed sieve for three times by using 0.08 mm square hole sieve and all samples must pass the 0.08 mm square hole sieve; completely and evenly mix respectively; seal with polypropylene bottles to avoid the influence to the sample stability from the packing container. During the whole test period, avoid the influence to the analysis result of cement chemical composition due to the tightness of the polypropylene bottle. The samples are a sample group recorded as sample A and sample B, with proficiency test mark and number labelled at the outside of the polypropylene bottle.

Homogeneity Test of Samples

As per CNAS-GL03：2006 *Guidance on Evaluating the Homogeneity and Stability of Samples Used for Proficiency Testing,* test the homogeneity of sample by using single factor variance analysis method; test the obtained data with F test method; when the F value is not more than the critical value Fα（f_1,f_2）（α=0.05）, then each cement sample is well-proportioned when they are at the 0.05 significant level.

Tested even value of sample $\overline{x}_i = \sum_{j=1}^{n} x_{ij} / n_i$

Total tested mean value of all samples $\overline{\overline{x}} = \sum_{i=1}^{m} x_i / m$ Total times of test $N = \sum_{i=1}^{m} n_i$

Sum of squares among samples $SS_1 = \sum_{i=1}^{m} n_i \left(\overline{x}_i - \overline{\overline{x}}\right)^2$ Mean square $MS_1 = \frac{SS_1}{f_1}$

Sum of squares within samples $SS_2 = \sum_{i=1}^{m}\sum_{i=1}^{m} \left(x_{ij} - \overline{x}_i\right)^2$ Mean square $MS_2 = \frac{SS_2}{f_2}$

Degree of freedom $f_1 = m-1$ $f_2 = N-m$ Statistics $F = \frac{MS_1}{MS_2}$

Select 10 bottles of sample from the plastic bottles of A, B groups prepared cement samples. Take one group of sample homogeneity test as example: take two test pieces from different part of the same sample; as per the requirement of GB/T176-2008 Method for Chemical Analysis of Cement, under the same test environment, time and reagent conditions, the loss on ignition and sulfur trioxide are tested by the same test personnel and homogeneity test is performed by the same test personnel as well. The homogeneity test result and the statistic analysis are shown in Table1.

Table 1 The homogeneity test result and the statistic analysis

Sample No.	Loss on ignition (%)		Sulfur trioxide (%)	
	1	2	1	2
A-1	1.85	1.83	2.89	2.85
A-2	1.8	1.81	2.82	2.86
A-3	1.79	1.83	2.85	2.87
A-4	1.78	1.82	2.81	2.85
A-5	1.82	1.8	2.86	2.81
A-6	1.83	1.86	2.83	2.85
A-7	1.8	1.79	2.85	2.87
A-8	1.87	1.85	2.83	2.87
A-9	1.83	1.85	2.85	2.89
A-10	1.86	1.83	2.82	2.85
Total mean value	1.825		2.849	
Variance source	Among samples	Within sample	Among samples	Within sample
Degree of freedom	9	10	9	10
Sum of squares	0.005542	0.0034	0.00408	0.00630
Mean square	0.000615	0.00034	0.000453	0.00063
F	1.80		0.719	
F critical value	$F_{0.05(9,10)}$=3.02			

The statistics F of homogeneity data are respectively 1.80 and 0.719, both of which are less than the critical value $F0.05$（9,10）=3.02. It indicates that at the 0.05 significant level, the loss on ignition and sulfur trioxide are well-proportioned, which meets the requirement on proficiency test sample homogeneity.

Stability Test of Sample

As this laboratory proficiency test is within Henan Province, sampling is done by the participating unit itself, and the test and result report are done within one week after sampling, therefore the time from cement preparation to delivery is short; in the condition that the samples are packed tightly and sealed with good condition, the samples are stable (verified by cement proficiency test of China National Accreditation Service for Conformity Assessment). If the time for transportation is long, considering the influence to samples from transportation, the stability of cement loss on ignition can be tested.

The Necessity of Preparing Two Groups of Samples

At first, after homogeneity of proficiency test samples has been determined and the differences between samples are reduced to the lowest degree, then the differences among the proficiency test results are mainly from the differences among laboratories and the differences within the same laboratory. The organizer prepared two groups of A and B to make a sample pair to enable the participating laboratories perform twice tests, in such way, differences among laboratories and the differences within the same laboratory can be both found through data statistics.

In order to ensure the objective fairness, data communication among laboratories, data tampering and data falsification should be avoided. While it is difficult to avoid data communication among laboratories with only one group of samples, consequently it will make the statistics results distorted and the proficiency test job meaningless.

Therefore with the data difference between chemical composition of prepared A and B samples, robust "ZB-score" among laboratories and robust "ZW-score" within the laboratory can be calculated; the purpose is that not only differences among the participating laboratories can be evaluated but also can avoid data communication among laboratories and result falsification.

Statistics Analysis Design of Laboratory Comparison Result Data

The robust statistical method is adopted to process the test result，that is, use the robust total statistics based "Z-score", adopt the median to estimate the total mean value of samples and adopt the NIQR to measure the level of dispersion of sample data. The "Z-score" of laboratory should be calculated as per the Formula 1:

$$Z = [X - \text{median}(X)] / \text{Normal IQR}(X). \quad (1)$$

Wherein, X is the test data of each participating laboratory; median(X) is the median of all test data; Normal IQR (X) is the NIQR of all test data.

As the differences among samples provided to each laboratory have been reduced to the lowest degree, the variation of the results is mainly from: the variation among laboratories and variation within laboratory; robust "Z-score" is divided into "ZB-score" among laboratories and "ZW-score" within laboratory; in doing the robust statistics analysis, evaluate the each participating laboratory's proficiency as per the "Z-score" (including ZB and ZW).

In this comparison test, each laboratory gets two samples of A and B for test, that is, by using sample pair, sum up the test results (the participating laboratories are required to provide the original record of test) of participating laboratories (each laboratory is assigned a lab code and gets the sample pair randomly), comparison statistics "Z-score"(including ZB and ZW) and make them into a table for convenient of statistics and analysis.

Statistics Result of Proficiency Test of Cement Chemical Composition

The evaluation rule of robust "Z-score" results (including ZB and ZW) of the laboratories that participate the proficiency test of cement chemical composition: $|Z|\leq 2$ is the satisfactory result; $2<|Z|<3$ is the doubtful result, which relevant laboratories are encouraged to analysis the reason of the problem result; $|Z|\geq 3$ is the unsatisfactory result (or it can be called the outlier result).

Marks "+"and"-"of "*Z*" indicate the result deviation direction from the median. "+"indicates the result is more than the median, and "-" indicates the result is less than the median. ZB indicates the differences among laboratories and reflects the system error of the test result; ZW indicates the differences within laboratory and reflects the random error of the test result. The smaller the *Z* value, the deviation degree is less and the laboratory proficiency is stronger, vice versa. The following is an example of sulfur trioxide of cement chemical composition analysis, on which the statistics result analysis is done. See Table 2:

It can be seen from Table 2 that the absolute values of ZB among laboratories of No. 06 and No. 18 laboratories are higher than 3, which are the unsatisfactory result (outlier); the absolute value of ZW within laboratory of No. 10 is higher than 3, which is also the unsatisfactory result (outlier) and it indicates that there is system error in the result and it is necessary to find the reasons in terms of personnel, equipment, test condition, chemical reagent, etc., after that, the effective solutions should be adopted to correct the deviation. While the absolute value of ZB among laboratories of No. 14 laboratory is $2<|Z|<3$, which is the doubtful result; the absolute values of ZB among laboratories of No. 06, 14, 18 laboratory are $2<|Z|<3$, which are the doubtful results and indicates that there is random error and it is necessary to analyze the reason for error and eliminate the deviation.

Table2 The statistics result analysis of the sulfur trioxide of cement chemical composition analysis.

Lab code	"Z-score" among laboratories (ZB)	"Z-score"among laboratories (ZW)	Lab code	"Z-score" among laboratories (ZB)	"Z-score" among laboratories (ZW)
01	0.34	0.34	11	0.87	0.00
02	0.67	-0.34	12	0.00	1.01
03	-0.34	1.01	13	1.04	-0.34
04	0.00	-0.34	14	-2.89	2.74
05	1.37	0.35	15	-0.34	1.01
06	-3.06ξ	2.40	16	0.34	-0.34
07	1.54	-0.67	17	-0.51	0.00
08	0.00	-0.34	18	-3.23ξ	2.74
09	-0.67	-0.34	19	1.54	-0.67
10	-0.84	3.41ξ			

Conclusions

In this laboratory proficiency test of cement chemical composition, the test level and management capacity on chemical composition of laboratory are objectively and actually evaluated. Through the quality control method of proficiency test, laboratories can actively search for problems from test equipments, working environment, test personnel, etc. In this way the laboratory will keep the high test proficiency and keep improving its quality management capacity, as well as improving the quality management level of the whole cement test industry.

References

[1] Guidance on Laboratory Accreditation. Beijing. China National Accreditation Service for Conformity Assessment. CNAS-GL01, 2006.

[2] Guidance on Evaluating the Homogeneity and Stability of Samples Used for Proficiency Testing. Beijing. China National Accreditation Service for Conformity Assessment. CNAS-GL03, 2006.

[3] Guidance on the Application of Testing and Calibration Laboratory Competence Accreditation Criteria. Beijing. China National Accreditation Service for Conformity Assessment. CNAS-CL01, 2006.

[4] Method for Chemical Analysis of Cement. 176 (2008).

[5] C. Wang, The proficiency testing by inter laboratory comparisons and robust statistical techniques. Lecture 5 Robust Statistical Techniques I. Physical and Chemical Test—Physics Fascicule, 40 (2004).

[6] C. Wang. The Proficiency Testing by Inter Laboratory Comparisons and Robust Statistical Techniques. Lecture 5 Robust Statistical Techniques II. Physical and Chemical Test-Physics Fascicule, 40 (2004).

[7] China Building Material Test & Certification Group Co., Ltd. National Quality Test Center of Cement. Cement Laboratory Work Book. China Building Materials Press, Beijing, 2009.

© (2012) Trans Tech Publications, Switzerland
doi:10.4028/www.scientific.net/AMM.238.101

Influence of Sludge Content on Compressive Strength of Sintering Sludge-shale Bricks

Bangbiao Huang [1,2, a] Xianghua Zhang [3, b] and Jizhen Zhu [3, c]

[1]Department of Continuing Education, Guangxi University of Technology, Liuzhou 545006, China
[2]Department of Civil Engineering, Huazhong University of Science&Technology, Wuhan 430000, Wuhan, China
[3]Department of Civil Engineering, Guangxi University of Technology, Liuzhou 545006, China

[a]61394936@qq.com, [b]752359768@qq.com, [c]815348222 @qq.com

Key words: sintering sludge-shale brick; sludge; the content; compressive strength.

Abstract. Sintering sludge-shale brick is a new kind of environmental protection and energy saving material. In order to study the different sludge content on the influence of compressive strength of sintering sludge-shale bricks, through the experiment and comparison to the finished products of the five groups of the sludge content with the method of contrast test, the reasonable content is found. The result shows that the compressive strength of the brick decreases sharply with the increase of the sludge content in the same experimental condition. In order to realize the greatest degree of sludge utilization, the best sludge content of sintering sludge-shale brick is 30%.

Introduction

With the improvement of people's living standard and the dramatically increasing of city population, the issues that sludge treatment development rapidly and urban sludge processing difficult appeared in China. According to the survey, at the end of 2010, national urban sludge treatment reached 34.3 billion cubic meters, dry sludge of them are 22 million tons, and 80% are not properly handling. Disposal of sewage sludge cannot be reasonably has become the restricting yoke on urban development. According the "Twelve-Five" planning of building materials industry of China, it advocates that to devoting major efforts to develop energy-saving materials. Municipal sludge mixed with shale powder making and burning to form bricks, not only can achieve reasonable handling of sludge, saving the land required for dumping sludge, eliminating the pollution, but also can be made to treasure, to create certain economic benefits. This article in order to make full use of sewage sludge as a starting point, to research the content of sludge on the influence of sintering sludge-shale bricks' compressive strength, to improve sludge utilization, reduce product cost, produced the bricks which can meet the requirements [1].

Physical and Chemical Analysis of Raw Materials

The sludge what is collected in a sewage treatment plant in Liuzhou. Make physical and chemical analysis on the sludge, the result as shown in Table 1. Put the sludge which moisture content is in 70~80% into sedimentation tank, make the sludge's moisture content reduced to about 12% by precipitation and dewatering treatment.

Table 1 The chemical composition of sludge in a sewage treatment plant of Liuzhou

Composition	SiO_2	MgO	CaO	Fe_2O_3	Al_2O_3	K_2O	Na_2O
Weight (%)	36.52	3.83	7.02	4.97	8.50	0.65	0.67

The shale is another raw material used in brick production. And the actual collection of shale is located near the village of Peace in Liuzhou for the experimental. Make physical and chemical analysis on the shale, the result as shown in Table 2. Put the shale in the blower drying, then use of ball mill grinding grain size ≤ 0.3mm shale powder alternate. Using the diameter of shale above, not only in making mixing and sludge fully mixed evenly, but also improves the density of brick after pressing [2].

Table 2 The chemical composition of shale for brick production in Liuzhou

Composition	SiO_2	MgO	CaO	Fe_2O_3	Al_2O_3
Weight (%)	51.3	1.47	1.19	10.42	24.26

Experiment and Data Processing

According to research the content of sludge mixed with sintered Shale Brick strength of this experimental purpose, put the sludge and shale powder as Table 3 divided into five groups marked A, B, C, D, E. Under the same experimental conditions, respectively, plus a small amount of water in the mixer sufficiently mixing (the raw material of total moisture content does not exceed 15%). Vacuum mixing raw materials by the machine. Turn the raw materials into the mud. Then cut bricks by brick making machine, sample specifications for 240mm×115mm×90mm. After drying the five groups of the wet body in the drying room under the same conditions, placed into high temperature furnace burning into finished products under the range of 900~1050 ^{o}C.

Table 3 Weight of all kinds of raw materials in the sintering sludge-shale bricks (Dry weight)

Group	A	B	C	D	E
Sludge (%)	0	10	20	30	40
Shale (%)	100	90	80	70	60

Make the five groups with different content of sludge burning into bricks, then choose 5 bricks which have the good and flat surface in the production in every group to start the compression experiment. First place the smooth glass on the platform preparing the specimen, place a sheet of tissue paper on the glass so that moist the tissue paper evenly. Then spread a layer of cement paste which has suitable Consistency and the Thickness under 5mm above the paper, placing the compressive test block on a wire rack after soaking in water for 10min-20min and dripping into dry for 3min-5min. Lets the torsion side of the block places on the cement paste, on the opposing pressure surface add little pressure. After the cement paste turning solidification, together with glass and the blocks shop turned in another platform repeat the above steps. After the production is completed, conserving at the temperature more than 10 for 3 days, then start the compressive strength test. Put the block into the test machine, load until the block destruction step by step, and read pressure value. According to the length and width of each test block, calculate the compressive strength [3]. The result are shown in Table 4.

We can draw that the compressive strength of brick increasing obviously with the content of sludge increases. When the percentage of sludge content is 10%, the sintering sludge-shale bricks' average compressive strength is the maximum, which reached 21.1MPa. When the content increases to 40%, the sintering sludge-shale bricks have the lowest average compressive strength, which is 4.52MPa, the average compressive strength declined by 78%, the test result consistent with the findings of the Central South University. It also can be seen from table 4 that the size of blocks changing small with the increasing of sludge content. After considerable analysis, because the sludge contains large amounts of organic matter, when roasting the bricks under high temperature so that the organic matter combustion and left a large number of holes in brick body. With the

content of sludge increase, the number of the holes of the sintering sludge-shale brick is also increase, this situation will reduce the capacity of the material particles bond with each other in the process of the brick body drying and sintering, which brings the increase of contraction and deformation of the brick, thereby greatly affects compressive strength of the brick [4].

Table 4 The experimental results of the compressive strength

Group	No.	Length× width (mm)	Pressure value (MPa)	Compressive strength (MPa)	Mean
A	A1	242×115	670.7	24.1	24.4
	A2	241×114	692.3	25.2	
	A3	240×115	670.6	24.3	
	A4	242×116	688.2	24.5	
	A5	240×116	659.8	23.7	
B	B1	241×115	568.2	20.5	21.1
	B2	240×117	606.5	21.6	
	B3	240×115	574.1.	20.8	
	B4	239×116	598.8	21.6	
	B5	241×116	593.2	21.2	
C	C1	240×115	328.4	11.9	12.0
	C2	239×114	335.1	12.3	
	C3	239×116	371.5	13.4	
	C4	241×114	318.7	11.6	
	C5	240×116	306.2	11.0	
D	D1	238×114	257.7	9.5	9.22
	D2	238×113	220.5	8.2	
	D3	237×113	286.5	10.7	
	D4	239×114	261.6	9.6	
	D5	238×112	215.9	8.1	
E	E1	238×113	180.2	4.7	4.52
	E2	237×113	155.3	4.5	
	E3	236×114	166.8	5.2	
	E4	238×114	132.9	4.2	
	E5	237×113	147.3	4.0	

Conclusions

Under the same test conditions, the compressive strength value of brick increases obviously along with the content of sludge increase. When the percentage of sludge content is 10%, the mean compressive strength of sintering sludge-shale bricks is the maximum and the compressive strength of sintered product meet the requirements

In order to achieve the maximum extent of sludge resources utilization and in conformity with the relevant provisions of the sintering sludge-shale bricks, the best sludge content of sintering sludge-shale brick is 30%.

References

[1] W. Chao, T. How, J. Chen, Production of synthetic lightweight aggregate using reservoir sediments for concrete and masonry. Cement & Concrete Composites, 33 (2011) 292–300.

[2] T. Joo-Hwa, Bricks Manufactured From Sludge. Journal of Environmental Engineering, 6 (1987) 278-284.

[3] N. Okuno, S. Takahashi. Full scale application of manufacturing bricks from sewage, Water Science and Technology, 36 (1997) 243-250.

[4] J. Luan, A. Li, T. Su, X. Cui, Synthesis of nucleated glass-ceramics using oil shale fly ash, Journal of Hazardous Materials, 173 (2010) 427–432.

© (2012) Trans Tech Publications, Switzerland
doi:10.4028/www.scientific.net/AMM.238.105

Preparation of PZT Material with Different Zi/Ti Ratio by Sol-Gel Method

Xi Chen

School of Civil Engineering and Communication, North China University of Water Resource and Electric Power, Zhengzhou 450011, China

chenxi@ncwu.edu.cn

Keywords: PZT; sol-gel method; Zi/Ti ratio.

Abstract. Lead zirconate titanate powders (PZT) with different Zi/Ti values 52/48, 53/47, 54/46 and 55/45 were prepared by sol-gel technique. The sol was prepared by mixing stable solutions of Zr-nitrate, Pb-acetate and Ti $(OC_4H_9)_4$ precursors. The decomposition of precursors above 773 K, 923 K and 1073 K for Zi/Ti value equls to 52/48, 53/47 and 54/46 respectively. The value 55/45 leads to the formation of pure perovskite phase. X-ray diffraction analysis was carried out to confirm the phase formation of PZT. The relationship of synthesis temperature and Zi/Ti ratio value is disscused. It is found that higher synthesis temperature is needed to prepare pure PZT with the increase of Zi/Ti ratio.

Introduction

$Pb(Zr_xTi_{1-x})O_3$ (PZT), a solid solution of $PbZrO_3$ (PZ) and $PbTiO_3$ (PT) posses perovskite-type ABO_3 structure, is a material of high technological importance. It has high piezoelectric and dielectric constant (piezoelectric constant d33 150–250 mm/V; dielectric constant at room temperature 500–700), which can be used in electronic devices, such as nonvolatile memories, infrared sensors, optical shutters, modulators etc [1, 2, 3]. The dielectric characteristics of PZT change with its stoichiometry. Dai et al. [4] reported an enhancement in dielectric constant from 10000 to 14000 in PZT, with change in Zr/Ti ratio from 95/5 to 55/45 also the Curie temperature changed from 523 to 653 K. As so far, there are main two solution synthesis techniques for the preparation PZT ceramics: metallorganic decomposition route [5] and solution-based methods [6]. There are essentially three different kinds of sol–gel process such as: colloidal sol–gel processes; derivation of inorganic polymeric gels from organometallic compounds and gel routes involving formation of an organic polymeric complex (polymeric precursor method).

In this work, we have studied the preparation and characterization of piezoceramics PZT 52/48, 53/47, 54/46 and 55/45 obtained by the sol-gel method and revealed the relationship between the preparation temperature and Zi/Ti ratio.

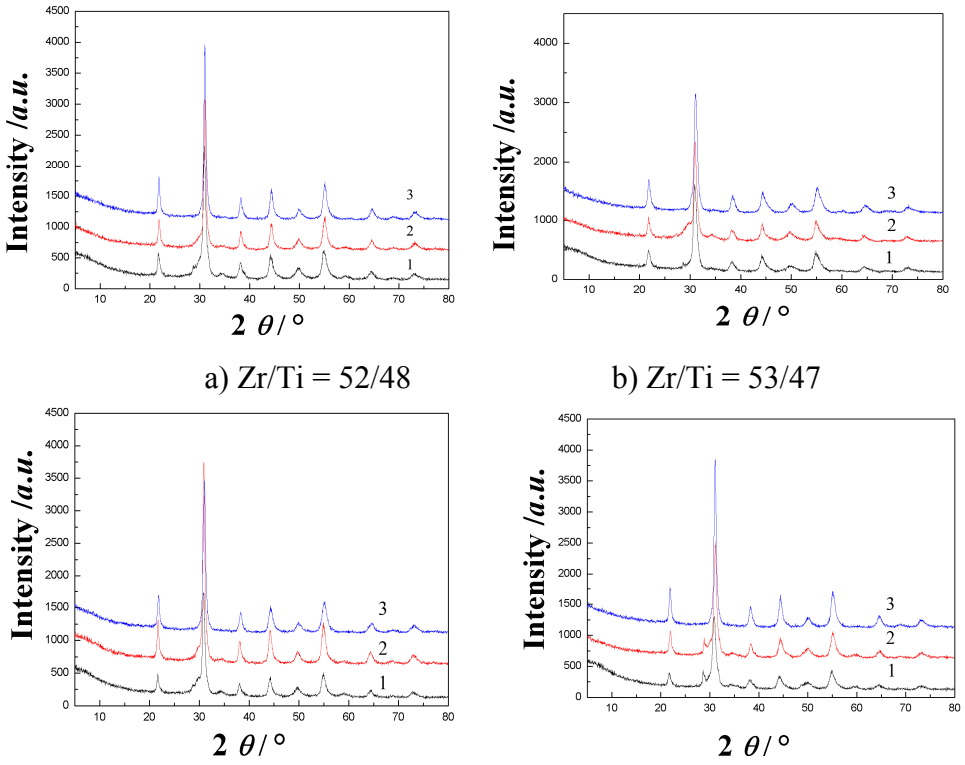
Experimental Procedure

The solutions of PZT 52/48, 53/47, 54/46 and 55/45 ($Pb(Zr_xTi_{1-x})O_3$ when $x = 0.52$，0.53，0.54，0.55) were prepared by polymeric precursor method. Considering the loss of lead component during the annealing process, the molar ratio of raw material was chosen as Pb:Zr:Ti=1.1: x:(1-x).First, 50 mL 0.01 x mol/L $Zr(NO_3)_4 \cdot 5H_2O$ aqueous solution and 50 mL 0.01(1-x) mol/L $Ti(OC_4H_9)_4$ anhydrous ethanol solution were mixed in the beaker. And then 50 mL 0.011 mol/L $Pb(CH_3COO)_2 \cdot 3H_2O$ was dissolved in the anhydrous ethanol to add to the mixture slowing during stirring continuously. The mixture was then hydrolised (to activate the hydrolisis reaction distillated water was used) and a colloid solution were formed. In few minutes, the sol-gel system was formed. The so-obtained sol-gel derived powder was ground in a mortar and preannealed at 653K for 0.5h. Finally the powers were obtained followed by annealing the precursors at 773K, 923K and 1073K, respectively.

All X-ray diffraction (XRD) patterns were collected on a Philips X'Pert MPD diffractometer with X'Celerator detector using Cu-$K\alpha$ radiation. The room temperature XRD data of PZT over the region of 5~80° (2θ) used to determine the crystal structures were collected using continues mode and indexed using the PowderX software suite.

Results and Discussion

The Structure of PZT with Same Zi/Ti Ratio at Different Annealing Temperatures. Fig. 1 shows the XRD patterns of PZT with Zr/Ti ratio equaling to 52/48, 53/47, 54/46 and 55/45 annealing at 773K, 923K and 1073K, respectively. It can be seen that when annealing at 773K, there is other phase in all samples, i.e., the precursors do not transfer to pure PZT phase in this situation. The powers can be indexed with the perovskite structure when heating at 923K for 2h expect for Zr/Ti = 55/45. Comparing to the ref. [7], no peaks attributed to others phase appear. Therefore, it can be deduced that the final products are pure PZT when Zr/Ti ratio equals to 52/48, 53/47 and 54/46. When the sintering temperature increased to 1073K, all precusors transform to perovskite structure with fine XRD peaks, and it is well fit to the standard pattern of PZT(JCPDS-PDF: 14-0031). The sol-gel process of PZT preparation experiences two steps: the hydrolysis of the precursor; and the polycondensation reaction for the formation of metal elements in order to coordinate with ethylene glycol. Finally, it results in the system containing polymer chain or network. From different products obtained at different temperatures, it can be known that the system in which the distribution of metal ion is uniform after heating at 653K, and the metal ions rearranged and crystallized into the perovskite structure when annealing the power at high temperature. The activation energy is needed during this process so higher temperature is benefit to the formation of well crystallized pure phase. Take Zr/Ti = 55/45 for example, when the product obtained heating at 773K for 2h, it can be seen from Fig. 2 which shows the XRD pattern of the sample that the final product is the mixture of ZrO_2 and PZT. It reveals that Ti ion is easier to form perovskite structure than Zr ion. The reason will be discussed in section 3.2.



a) Zr/Ti = 52/48 b) Zr/Ti = 53/47

c) Zr/Ti = 54/46 d) Zr/Ti = 55/45

Fig. 1 The XRD of PZT powers obtained at different annealing temperature (line 1: 773 K-2h; line 2: 923 K-2h; line 3: 1023 K-2h)

The Structure of PZT with Different Zi/Ti Ratio at Same Annealing Temperatures. Fig.3 shows the XRD patterns of products with different Zr/Ti ratios 52/48, 53/47, 54/46 and 55/45 obtained annealing 2h at same temperature. As can be seen, well crystallized PZT(Zr/Ti=52/48, 53/47 and 54/46) ceramics can be obtained heating the precursors at 773K or 923K , whereas in the XRD pattern of PZT(Zr/Ti=55/45) obtained at the same condition, there is peaks attributed to ZrO_2 phase. With increasing Zr/Ti ratio, the intensity of ZrO_2 peaks becomes more and more higher, which

indicated that PZT with high Zr/Ti ratio is much difficult to sinter than that of low Zr/Ti ratio. And at the low annealing temperature, there is remained ZrO_2 after the transformation. Both $PbZrO_3$ and $PbTiO_3$ have the same structure and all of them belong to perovskite structure (ABO_3). Because of the similar property of Ti^{4+} and Zr^{4+}, B site in the cell can be Ti^{4+} or Zr^{4+} ion. By comparing the ion radius, it can be seen that the radius of Zr^{4+}(0.77Å) is bigger than that of Ti^{4+}(0.64Å), it will result in that Ti^{4+} is much easier to occupy B site of ABO_3 than Zr^{4+} during the process of metal ions rearrangement and crystallization into the perovskite structure. The higher Zr/Ti ratio, the higher sintering temperature needed. It can be proved by the fact that there is only peak of ZrO_2 but no peaks attributed to TiO_2.

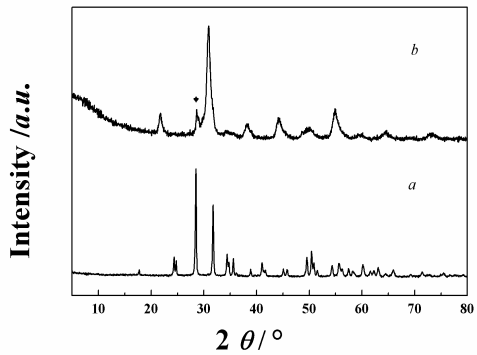
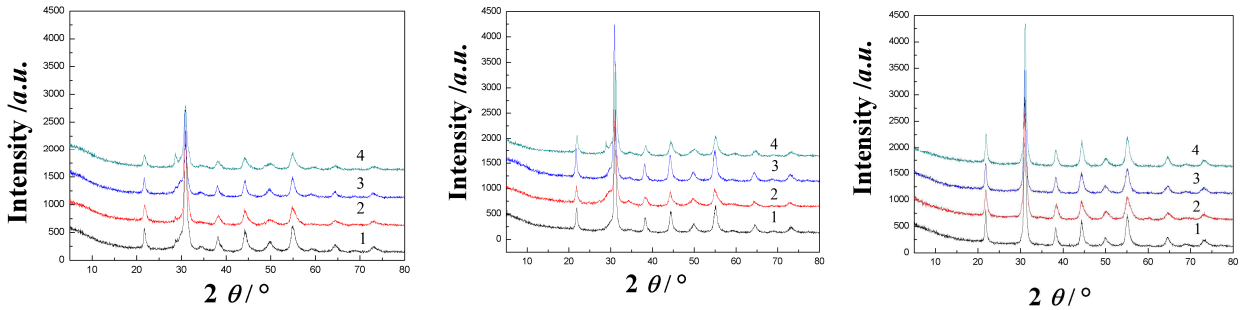


Fig. 2 The comparison of the sample annealiing at 723K for 2h for Zr/Ti = 55/45(*a*) with ZrO_2(*b*)



a) 773 K-2 h *b*) 923-2 h *c*) 1073-2h

Fig. 3 The XRD of PZT powers with different Zr/Ti ratio obtained annealing 2h at same temperature (line 1: Zr/Ti = 52/48; line 2: Zr/Ti = 53/47; line 3:Zr/Ti = 54/46； line 4: Zr/Ti = 55/45)

Conclusions

A sol gel method was used to synthesize lead zirconate titanate powders with different Zi/Ti values 52/48, 53/47, 54/46 and 55/45. Using X-ray diffraction analysis, it can be known that pure PZT ceramic can be otained when Zi/Ti ratio equals 52/48, 53/47 and 54/46 heating at 923K for 2h, whereas when Zi/Ti ratio is 55/45, the pur PZT only can be obtained sintering at 1073 K for 2 h.

The products with different Zi/Ti values were compared, it is deduced that higher Zi/Ti ratio, higher synthesis temperature is needed to prepare pure PZT. And the best preparation temperatures are decided: 773 K for Zi/Ti 52/48, 923K for Zi/Ti 53/47 and 54/46, and 1073K for Zi/Ti 55/45.

References

[1] C. O. Paiva-Santos, C. F. Oliveira, W. C. Las, et al, Effect of niobia on the crystal structure and dielectric characteristics of $Pb(Zr_{0.45}Ti_{0.55})O_3$ prepared from polymeric precursor, Materials Research Bulletin, 35 (2000) 15-24.

[2] M. S. J. Nunes, E. R. Leite, F. M. Pontes, et al, Microstructural and ferroelectric properties of $PbZr_{1-x}Ti_xO_3$ thin films prepared by the polymeric precursor method, Materials Letters, 49 (2001) 365-370.

[3] Z. C. R. Cho, L. F. Francis, D. L. Polla, Ferroelectric properties of sol–gel deposited Pb(Zr, Ti)O_3/$LaNiO_3$ thin films on single crystal and platinized-Si substrates, Materials Letters, 38 (1999) 125–130.

[4] X. Dai, Z. Xu, D. Viehland, Effect of oxygen octahedron rotations on the phase stability, transformational characteristics, and polarization behavior in the lead zirconate titanate crystalline solution series, Journal of America Ceramic Society, 78 (1995) 2815-2827

[5] M. Okada, K. Tominaga, Preparation and properties of (Pb,La)(Zr,Ti)O_3 thin-films by metalorganic chemical vapordeposition, Journal of Applied Physics, 71 (1992) 1955–1959.

[6] D. S. Hagberg, D. A. Payne, Sol–gel Optics, Processing and Applications, Kluwer, Boston, 1994.

[7] N. Tohge, S. Takahashi, T. Minami, Preparation of $PbZrO_3$－$PbTiO_3$, ferroelecteic thin films by the sol-gel process, Journal of America Ceramic Society, 74 (1991) 67-71.

© (2012) Trans Tech Publications, Switzerland
doi:10.4028/www.scientific.net/AMM.238.109

Toughness Properties of Concrete Modified with Water-borne Polyurethane

Bei Ding[1, a], Xia Zhang[2, b], Dongling Zhou[2, c] and Chanwen Miao[3, d]

[1]Jiangsu Research Institute of Building Science, Nanjing, China

[2] Jiangsu Bote New materials Co., Ltd., Nanjing, China

[3]The National Key Laboratory of High Performance Building Materials, Nanjing, China

[a]dingbei@cnjsjk.cn, [b]zhangxia@cnjsjk.cn, [c]zhoudongliang@cnjsjk.cn, [d]mcw@cnjsjk.cn

Keywords: water-borne polyurethane; concrete toughness; fracture energy; early plastic cracking resistance; impact resistance.

Abstract. A novel kind of block polymer with characteristics of rod-like chain conformations, water-borne polyurethane (PUA), was synthesized by incorporate polyacrylate (PA) into the PU chain to prepare an aqueous polyurethane-polyacrylate (PUA) hybrid emulsion with core-shell structure. The influence of water-borne PUA on workability and mechanical performance of concrete were investigated experimentally. PUA had minimal harmful effect on the compressive strength whereas the flexural strength was increased by 23.2% with dosage of 0.5% and 23.3% with dosage of 1.0%, respectively. The fracture energy ratios of concrete with a dosage of PUA less than 1% are greatly improved more than double with the decreasing of concrete strength less than 10%. The water-borne PUA also enhances the early plastic cracking resistance and the impact resistance of concrete. The impact energy consumption of samples with PUA increase nearly three times more than reference samples, also better than samples with PP fiber. And PUA can refine the crack from 2-4mm to 0.2-0.5mm of the main distribution, decreasing total area of crack greatly.

Intorduction

Concrete is a highly brittle material. The ratio of tensile strength to compressive strength is about 1 to 10. Poor fracture toughness of concrete is one of the most important reason for problems of concrete durability currently [1]. Many ways to improve the toughness of concrete resulted in the expense of other important properties of concrete such as workability and mechanical performance, etc. [2-4].

Previous research reported that polymer-modified concrete was the key in improving the toughness of concrete; it changed the properties of concrete via the formation of consequential films in concrete [5-7]. Since the 1920s, researchers have been adding polymer latex into concrete in order to improve its adhesive properties, impermeability, toughness, and so on [8]. This additive enhanced the toughness of concrete in that it increased its flexural strength [9, 10]. However, severe problems were also produced. One was the sharp decrease in compressive strength, which was fundamental to concrete, and the other was the high cost attributed to the high additive content, which was usually above 10 wt% of the cementing material [11-13]. Therefore, in China, polymer emulsions were mainly used in mortar for modification and for several special concrete engineering tasks such as repair engineering or for improving concrete durabilities [14, 15]. The development of a new polymer-modified concrete that required less additive, had greater toughness improving effects, and did not affect the compressive strength was urgently required.

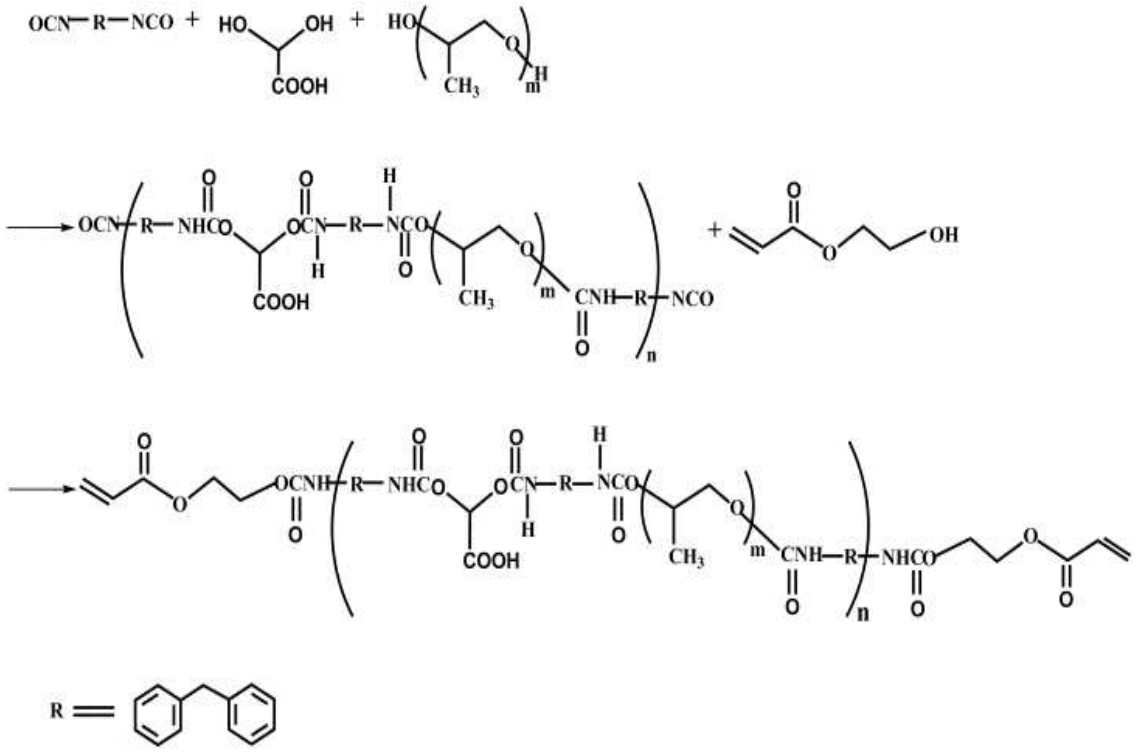
The frequently reported polymer latexes that were utilized to modify concrete focused on acrylic emulsions [8, 16], styrene butadiene rubber emulsions, and vinyl acetate-ethylene emulsions. They proved to be impractical as a concrete additive for common engineering. However, waterborne polyurethane (PU), which also existed in the form of small particles dispersed in water, has seldom been studied in terms of the modification of concrete, with the exception of several studies on PU foam concrete.[17, 18].As a high-performance material that is comparable with acrylic emulsions, styrene butadiene rubber emulsions, and vinyl acetate-ethylene emulsions, waterborne PU has better mechanical strength and higher chemical and solvent resistance [19, 20]. Given this, the effect of waterborne PU utilized as a concrete additive in improving the toughness of concrete is of interest.

In this study, we hypothesized that waterborne PU dispersions could improve the toughness of concrete with very small additive amounts by reacting with cement particles during cement hydration rather than the fill effect of concrete via the formation of films such as conventional polymer emulsions [8]. In order to maintain a comparatively stable conformation in the strong alkaline media of concrete, it was necessary to incorporate polyacrylate (PA) into the PU chain to improve alkali resistance. The set of PU and acrylic-polyurethane (PUA) water dispersions were prepared via the acetone method to synthesize pure PU and through emulsion polymerization to synthesize PUA. Polymer structure was investigated by infrared spectroscopy. The fracture energy of concrete as a comprehensive characterization of toughness revealed that the designed PU plays a notable role in improving the toughness of concrete. The early plastic cracking resistance and impact resistance of concrete modified with PUA also improvement because of better toughness.

Experimental

Synthesis of PU Dispersion. 60g of MDI was melted in a glass reactor equipped with a mechanical stirrer and a condenser at 60°C. Next, 13.8g of DMPA, 72g of PPG1000, 50g of acetone, and 0.12g of DBTD were added and reacted for 3 hours to obtain NCO-terminated prepolymer. Subsequently, 0.66g of 1, 4-BG was added and maintained for 30 min. Next, 6.68g of HEA was added and reacted for 2 hours. Afterwards, the reaction mixture was cooled to room temperature and 10.4g of TEA was slowly dropped in for 10 min. A stable and translucent dispersion named S was obtained after 400g of water was added to the prepolymer solution at 400 rpm. Acetone was removed at 50°C under reduced pressure. The S dispersion was used to prepare the PUA dispersion in the next operation. The synthesis scheme is presented in scheme 1.

Apure PU dispersion named PU was synthesized in strict accordance with the method except for the absence of HEA.

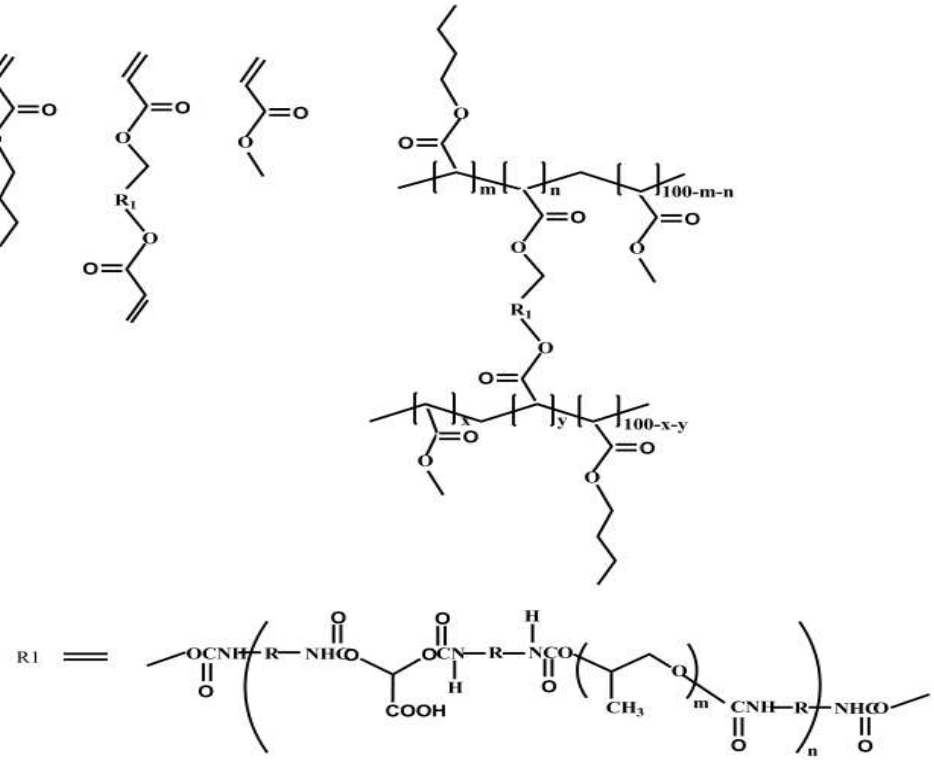


Scheme 1 Synthesis of PUA water dispersion

Synthesis of PUA Dispersion. The mixture of BA and MMA was slowly added to the emulsifier solution by dissolving SDBS, AES, and OP-10 in water under constant stirring. The obtained monomer pre-emulsion was then stirred for an additional 0.5 hours.

The reactor vessel was charged with the prepared S dispersion, K-90, and 50g of water. The initiator solution and monomer pre-emulsion were then slowly dropped in for 3 hours while stirring at 80°C. After the dropping, the reaction was maintained at 80°C for 2 hours. Finally, the reaction

mixture was cooled to room temperature. PUA dispersions were named A, B, and C according to the weight ratio of acrylic composites (PA). For example, the weight ratio of acrylic composites of sample B is 21%, which equals $m_1/(m_1+m_2)$ (m_1 is the amount of acrylice monomer, m_2 was the amount of S dispersion). The synthesis scheme is presented in scheme 2.



Scheme 2 Synthesis of PUA water dispersion

For comparison with PU and PUA, a pure polyacrylate dispersion (named PA) was also synthesized following the above operations. The basic formulations of the polymer dispersion series are presented in Table 1.

Table 1 Basic formulations of the polymer dispersion

Sample	PU dispersion (g)	MMA (g)	BA (g)	Solid content (%)
PUA (A)	563	68	34	29
PUA (B)	563	102	51	31
PUA (C)	563	204	102	35
PA	0	68	34	45

Concrete Mixing. The following materials and mix proportions were utilized to form concrete.

Binders: type II Portland cement with 52.5 grades from the Nanjing Jiangnan Cement Company plant was utilized.

Class I fly ash: came from Nanjing Thermoelectrical Plant. The chemical and physical properties of the binders are listed in Table 2.

Fine aggregate: river sand with fineness modulus of 2.65 and density of 2650 kg/m^3 was used.

Coarse aggregate: 5–25mm continuous graded crushed basalt and density 2700 kg/m^3 was used.

Admixtures: polycarboxylic acid superplasticizer and polyether defoaming agent were purchased from Jiangsu Bote New Materials Co., Ltd., China.

The concrete mix proportion is presented in Table 3. The polymer dispersions were added to concrete in accordance with the mass percentage of cement.

Table 2 Chemical and physical properties of the binder

Name (symbol)	Chemical composition (%)							Density (kg/m^3)	Specific Area (m^2/kg)
	SiO_2	Al_2O_3	CaO	MgO	Fe_2O_3	SO_3	Loss		
Cement	20.60	5.03	64.11	1.46	4.38	1.72	1.18	3150	450
Fly ash	49.39	33.36	4.13	0.85	4.92	1.96	2.49	2200	615

Table 3 Concrete mix proportion (kg/m^3)

Cement	Fly ash	Water	Coarse aggregate	Fine aggregate	*W*/*B*
350	87.5	122.5	1072.5	720	0.35

Characterization

Fourier Transform Infrared (FTIR) Spectroscopy. Casting films prepared as mentioned above were utilized in the analysis. The chemical structure of polymer was analyzed using a Nicolet IS-10 infrared spectrophotometer employing the attenuated total reflectance method.

Concrete Fracture Energy. The mechanical properties of hardened concrete were tested through the methods based on the Chinese general technical standard GB/T 50081-2002 (a standard for test methods of mechanical properties of ordinary concrete). Concrete fracture energy was utilized to characterize the toughness of concrete. Concrete fracture energy was determined by the wedge splitting method based on the Chinese testing standard DL/T 5332-2005 (the norm for the fracture test of hydraulic concrete), and calculated according to the method published by Sh. L. Xu [22]. The fresh concrete was set into modules of 100 mm × 100 mm × 100 mm and 100 mm × 100 mm × 400 mm to test compressive strength and flexural strength. Concave-shaped modules (shown in Fig. 1) were utilized to test the fracture toughness of the hardened concrete. The specimens were 200 mm long, 100 mm wide and 170 mm high. The relative notch depth of the specimens was 30 mm. All concrete specimens were cured under standard conditions with 20 ± 3℃ and relative humidity above 90% for 28 days.

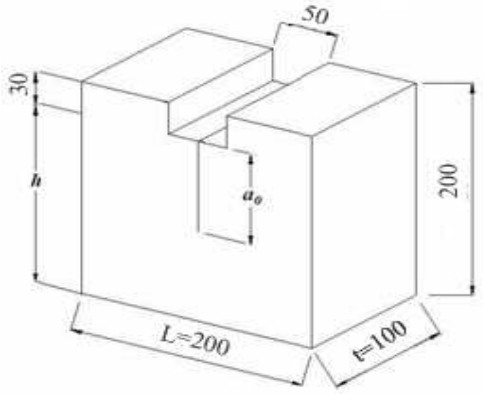
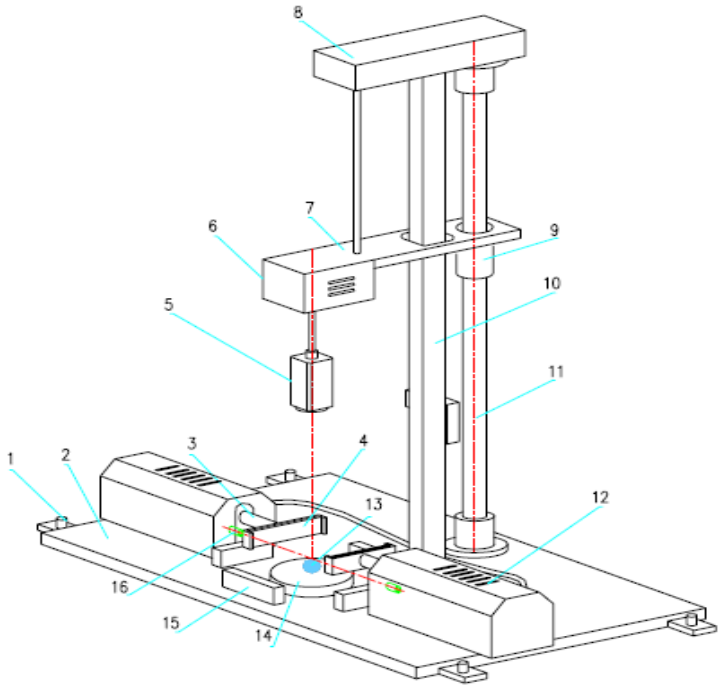


Fig. 1 Concave-shaped mold

Concrete Impact Resistance. The impact resistance of hardened mortar was tested by the methods of synthetic fibre used in concrete and mortar (GB/T21120-2007). The testing apparatus is shown in Fig. 2.

Concrete Early Plastic Shrinkage. According to the test methods of early plastic shrinkage crack of mortar and concrete proposed by Soroushian and Kraai [21], and Chinese building material industry standard - experimental methods for the cracking resistance of cement mortar, a set of experimental mold for the mortar plastic shrinkage crack was designed, which can be seen in Fig. 3. The mold is 300mm×150mm with the wooden baseboard of water-proof surface and film. The peripheral plates of angle iron were fixed by bolts. The restrain comes from the vertical steel bar at each end. With the cooperation of the bump for stress concentration in the middle, the tiny crack in the middle zone could become larger and easier for determination for quantifying the cracking resistance performance of the functional material.

The temperature and humidity of the chamber for the experiment were well controlled (31℃, RH 30%). The mixed mortar was cast into the mold under the iodine-tungsten lamp of 1000W with the wind of 3~3.2 m/s by electric fan to evaluate the improvement of the fiber on the mortar in severe environment. During the period, the surface water of the mortar will evaporate by heat and wind. When the evaporation rate is greater than the bleeding rate, there will be plastic shrinkage stress caused by water losing in the capillary of the cement paste which could lead to plastic crack. The initial time and cracks in 6 hours should be observed and recorded.



1-anchor bolt, 2-baseboards, 3-pneumatic cylinder, 4-falling dart clip, 5-falling dart, 6-falling dart delivering device, 7-crossbeam, 8-support base, 9-Base- oriented, 10-stand, 11-orientation, 12-device prevent second impact, 13-steel ball, 14-specimens, 15-board, 16-photoelectric switch.

Fig. 2 Apparatus for impact resistance test

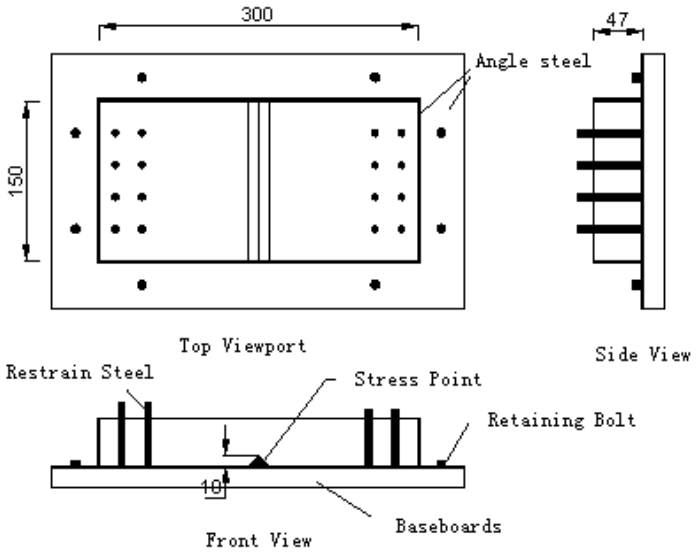


Fig. 3 Mould design drawing for cracking resistance test (mm)

Results and Discussion

Characterization of Polymer Dispersion. PU was first synthesized through the conventional acetone method and PUA was then prepared through emulsion polymerization to obtain a hybrid polymer. Polymers existed in latex particles in water. Figure 4 presents the IR spectra of the polymer. The absorption peaks at 3318 cm^{-1} were due to -NH stretching vibration. Double peaks at 2940 cm^{-1} were due to alkane -CH stretching vibration, and peaks at 1720 cm^{-1} were due to C=O stretching. The peaks at 1597–1529 cm^{-1} were due to aromatic ring stretching, and the peak at 1142 cm^{-1} was due to C-O stretching. There was no apparent difference in the absorption peaks of different polymers. However, as is evident in Fig. 2, PU had the strongest -NH stretching vibration whereas samples A, B, and C decreased in sequence because the increase of PA formed a shell that covered the PU, which may have resulted in the weak stretching of –NH groups.

Also, C=O stretching of samples A, B, and C was stronger than that for PU, which was attributed to the overlap of C=O stretching of urethane and acrylate groups. The IR spectra confirmed the formation of PU and PA structure.

Pure PU contained several hydrophilic COO^- groups in the polymer chain that enabled it to self-assemble into micelles in water, whereas the PUA dispersion formed micelles under the cooperation of COO^- groups and the emulsifier. Both PU and PUA dispersions were sensitive to media that contained a high concentration of ions, especially the strong alkaline from concrete slurry. In consideration of this problem, the primary requirement of polymer water dispersions is to maintain a comparatively stable conformation when added to concrete slurry until the concrete has set. Given this, it is necessary to study the aggregation behavior of polymer dispersions in alkaline media.

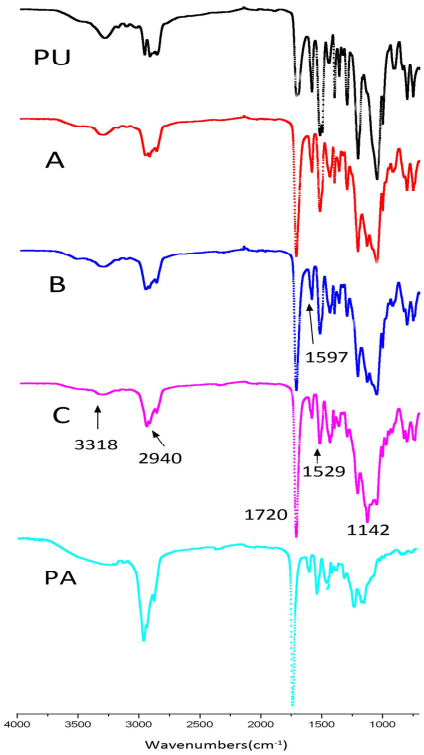


Fig. 4 IR spectra of polymer dispersion: PU, samples A, B, and C, PA

Concrete Properties

Concrete Fracture Energy. The properties of fresh concrete are shown in Table 4. PUA was added to concrete in order to improve the toughness while having minimal harmful effect on concrete strength, especially compressive strength. In the experiments, Polymer was added to concrete in 0.5 wt% and 1.0 wt% of cement. Blank concrete was designed to have a highly plastic state with slumps of 20 cm. PUA additives improve the workability of concrete to a certain extent. The higher dosage of polymer additives results in better fluidity and water retention.

Table 4 The properties of fresh concrete

Sample (%)	Slump (cm)	Air content (%)	Compressive strength (MPa)		Flexural Strength (MPa)	
			7d	28d	7d	28d
0	16.7	2.0	50.1	67.7	4.85	5.30
0.5	16.9	2.3	47.7	58.0	5.41	6.53
1.0	18.9	1.6	49.2	59.6	5.17	6.93

The fracture behavior was calculated, as shown in table 5. The fracture energy of concrete modified by PUA was improved to 231 $N \cdot m^{-1}$, which was double that of blank concrete (97 $N \cdot m^{-1}$), when a dosage of additives is 0.5%. This demonstrated that the toughness of concrete could be improved drastically and the strength could also be maintained. It is of note that only 0.5 wt% of

cement additive was used. It can be concluded there was no direct relationship between the tensile properties of polymer films and the concrete properties under our experimental conditions. It is assumed that when the designed polymer in our study was used at only 1 wt% of cement additive, it was very difficult to form consequential films in hardened concrete [12] and other chemical reactions may take place with the cement particles and form a toughness C-S-H gel. This assumption will be explored in future research.

Table 5 Fracture energy of concrete

Sample (%)	P_{Hmax} (KN)		K_{IC} (MPa·$\sqrt{m}$)		G_F ($N \cdot m^{-1}$)	
	7d	28d	7d	28d	7d	28d
0	3.26	4.04	0.81	1.00	96	115
0.5	3.96	4.70	0.98	1.16	179	231
1.0	3.82	5.22	0.94	1.29	213	213

The stress-strain curve of hardened concrete is shown in figure 5 and figure 6. The shape of curve is still a typical characteristc of brittle materials, whether modified by PUA or not. But the stress curve decreases more slightly, and the maximum stress in concrete failure is geater than blank concrete. It's the reason of fracture energy improvement.

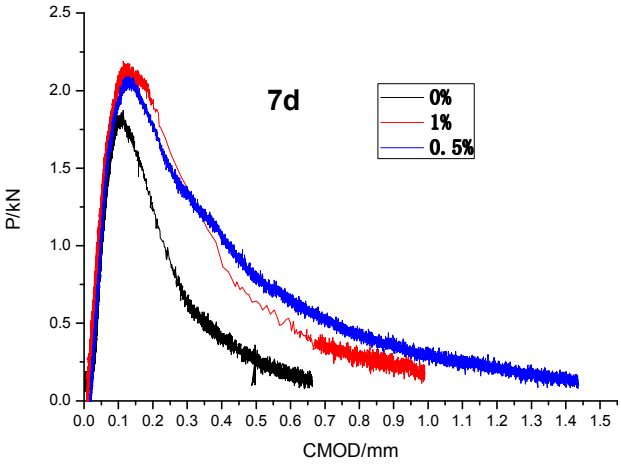


Fig. 5 Stress-strain curve of 7d concrete

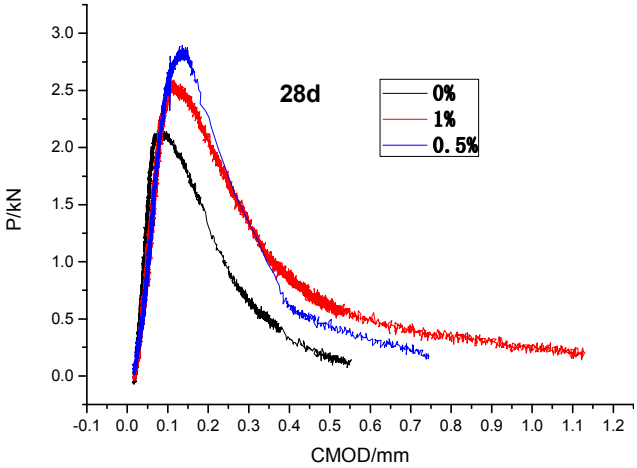


Fig. 6 Stress-strain curve of 28d concrete

Concrete Impact Resistance. The influence of the toughening material on the impact resistance of the mortar was evaluated by drop weight test. The experiment results of the reference sample and PP fiber sample are listed in Table 6. it can be found that the impact resistance of the mortar is improved significantly by the PUA. The impact energy consumption of 28d samples increase nearly three times more than reference samples, also better than samples with PP fiber. Due to the discreteness of the impact resistance test, a large amount of tests have been repeated, different dosages of the PUA have been tested. It can be concluded that the reinforcement of concrete toughness improves the concrete abilities of resistance external load.

Table 6 Concrete impact resistance

Sample	Impact times		Impact energy consumption	
	7d	28d	7d	28d
reference	14	15	308	352
PUA (0.5%)	34	27	748	946
fiber(0.9kg/m^3)	31	29	682	726

Concrete Early Plastic Shrinkage. Fig. 7 is the concrete early plastic shrinkage image. The photo makes the modification of early plastic shrinkage by PUA more visually, the crack width of concrete with PUA reduced more narrow.

Table 7 shows that the maximum crack width, average crack width and the total area of crack of mortar could be reduce by the PUA. By the distribution of the crack width, as showed in figure 8, it could be concluded that the PUA can refine the crack from 2-4mm to 0.2-0.5mm of the main distribution to improve the plastic crack resistance of the material.

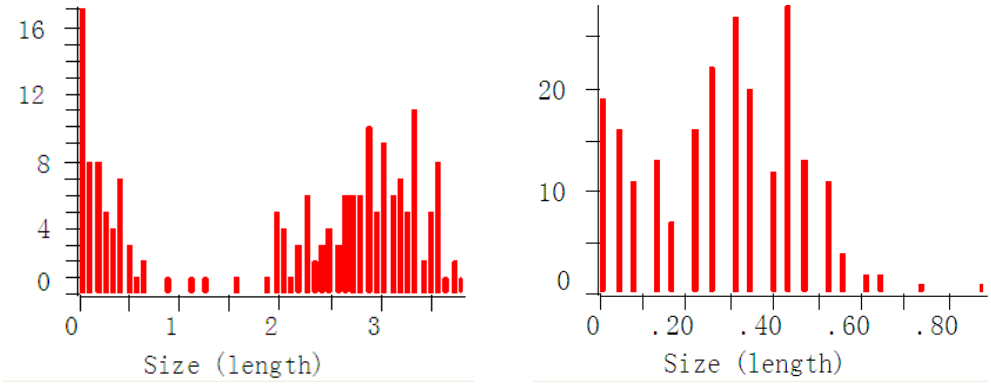


Blank concrete Extracted crack Concrete modified with PUA Extracted crack

Fig. 7 Concrete early plastic shrinkage image

Table 7 Crack calculation

NO.	maximum crack width (mm)	average crack width (mm)	total area of crack (mm^2)
1	3.83	2.08	450
2	0.88	0.29	67.4



Blank concrete Concrete modified with PUA

Fig. 8 Width distribution of crack

Conclusions

A polyurethane water dispersion named PUA was synthesized by incorporating polyacrylate (PA) into the PU chain to prepare an aqueous polyurethane-polyacrylate (PUA) hybrid emulsion with core-shell structure.

PUA had minimal harmful effect on the compressive strength whereas the flexural strength was increased by 23.2% with dosage of 0.5% and 23.3% with dosage of 1.0%, respectively. The fracture energy ratios of concrete with a dosage of PUA less than 1% are greatly improved more than double with the decreasing of concrete strength less than 10%. The water-borne PUA also enhances the early plastic cracking resistance and the impact resistance of concrete. The impact energy consumption of samples with PUA increase nearly three times more than reference samples, also better than samples with PP fiber. And PUA can refine the crack from 2-4mm to 0.2-0.5mm of the main distribution, decreasing total area of crack greatly.

Acknowledgements

We are grateful to the National Basic Research Program of China (2009CB623205) and the Science and Technology Support Program of Jiangsu Province (BE2010009) for their support of this work.

References

[1] Alina Badanoiu, Jonas Holmgren et al, Cementitious composites reinforced with continuous carbon fibers for strengthening of concrete structures, Cement and Concrete Composites, 25 (2003) 387-394.

[2] A. E. Naaman, H. W. Reinhardt, High performance fiber reinforced cement composites HPFRCC-4: International workshop Ann Arbor, Michigan, Cement and Concrete Composites, 6 (2004) 757-759.

[3] Andrzej M. Brandt, Fibre reinforced cement-based (FRC) composites after over 40 years of development in building and civil engineering, Composite Structures, 86 (2008) 3-9.

[4] Yoshihiko Ohama, Recent progress in concrete-polymer composites, Advanced Cement Based Materials, 5 (1997) 31-40.

[5] H. Hashimoto, Y. Ohama, Polymer modified mortars, The Journal of the College of Engineering of Nihon University, Series A, 19 (1978) 113-117.

[6] J. M. Gao, C. X. Qian, B. Wang, K. E. Morino, Experimental study on properties of polymer modified cement mortars with silica fume, Cement Concrete Res., 32 (2002) 41-45.

[7] J. G.Wang, S. X. Zhang, et al, Reinforced polymer concrete: Physical properties of the matrix and static/dynamic bond behaviour, Cement Concrete Comp., 27 (2005) 934-944.

[8] Y. Ohama, Polymer-based admixtures, Cement Concrete Comp., 20 (1998) 189-212.

[9] S. Pascal, A. Alliche, P. Pilvin, Mechanical behaviour of polymer modified mortars, Mater. Sci. Eng.: A, 380 (2004) 1-2.

[10] C. T. Sumathy, M. Dharakumar, M. Sarojadevi, S. Saccubai, Modification of cement mortars by polymer latex, J Appl. Polym. Sci., 63 (1997) 1251-1257.

[11] L. K. Aggarwal, P. C. Thapliyal, S. R. Karade, Properties of polymer-modified mortars using epoxy and acrylic emulsions, Constr Build Mater., 21 (2007) 379-383.

[12] S. Zhong, Z. Chen, Properties of latex blends and its modified cement mortars, Cement Concrete Res., 32 (2002) 1515-1524.

[13] H. Wang, E. H. KO, Y. S., J. K. Jeon, J Ind. Eng. Chem., 26 (2008) 265-271.

[14] T. Sebök, O. Stráněl, Wear resistance of polymer-impregnated mortars and concrete, Cement Concrete Res., 34 (2004) 1853-1858.

[15] J. Y. Do, Y. S. Soh, Performance of polymer-modified self-leveling mortars with high polymer–cement ratio for floor finishing, Cement Concrete Res., 33 (2003) 1497-1505.

[16] Y. Ohama, Recent progress in concrete-polymer composites, Adv. Cement Base Mater., 5 (1997) 31-40.

[17] L. Verdolotti, E. D. Maio, M. Lavorgna, S. Iannace, L. Nicolais, Polyurethane-cement-based foams: Characterization and potential uses, J Appl. Polym. Sci., 107 (2008) 1-8.

[18] J. Nascimento, H. O. Martinelli A.E., D. M. A. Melo, A. C. V. Nóbrega, D. M. H. Martinelli, Pinto E.N.M.G. Polymers, Nanocomposite Systems with Photo-Electro-Ionic Properties and Applications, Mater. Sci. Forum., 591 (2005) 423-429.

[19] O. Lorenz, F. Haulena, O. Klebon, Rubber elastic behavior of polyurethane ionomers, Angew. Makromol Chem., 33 (1973) 159-165.

[20] O. Lorenz, H. Hick, Investigation of the particle surface of anionic polyurethane dispersions with COO-groups, Angew Makromol Chem., 72 (1978) 115-117.

[21] Z. P. Bazant, M. T. Kazemi, Determination of fracture energy, process zone length and brittleness number from size effect with application to rock and concrete, Int. J Fract., 44 (1990) 111-131.

[22] S. L. Xu, Y. H. Zhao, et al, The experimental study on the fracture energy of concrete using wedge splitting specimens, J. Hydroelectric Eng., 4 (2003) 15-17 (in Chinese).

© (2012) Trans Tech Publications, Switzerland
doi:10.4028/www.scientific.net/AMM.238.118

Soil Stabilizer Prepared with Saline Soil and Industrial Solid Wastes

Xufang Zhang [1, a], Jing Wang [2.b] and Wen Ni [2 c]

[1]North China University of Water Resources and Electric Power, Zhengzhou 450011, China

[2] University of Science and Technology Beijing, Beijing 100083, China

[a]zhangxufang@ncwu.edu.cn, [b] whaleking@126.com, [c]niwen@ces.ustb.edu.cn

Keywords: saline soil; industrial solid waste; solidification; stabilizer.

Abstract. A soil stabilizer was prepared by mixing saline soil, slag, desulfurization gypsum and clinker. The compressive strengths of samples is up to 6.11MPa when the mixing amount of slag, desulfurization gypsum and clinker at 14% after 7 days curing. Results show that the stabilizer can meet the sub-base engineering applications, is an ideal stabilizer.

Introduction

The saline soil were widely distributed in China from the coast to the mainland [1-2], a large number of roads through the saline soil area with the rapid development of road transportation network. Saline soil contains large amounts of soluble salt ions, the phase and number of salts in the soil will changed with the effect of water and temperature, salt expansion, corrosion, frost heave and many other diseases will occurred [3-4]. Saline soil can not be directly used in highway, must take some measures, such as set fault, improve the roadbed, lower the groundwater level and chemical treatment [5], which increased the road construction costs, and strong, over-saline soil can not be used as roadbed filler according to the specification for design of highway subgrads, it was necessary to transport roadbed fill from other area, the cost will increased significantly. Soil stabilizer can be directly cemented soil particles at room temperature, and reacted with clay mineral generate the cementitious material [6]. The advantages of soil stabilizer technology were wide range of applications, simple construction, short construction period, low cost, etc., have been successfully used in water conservancy projects, the highway grass-roots level and sub-base, soft foundation treatment. The disadvantages water stability and salting will occurred in the consolidation process, so the consolidation response was more complex, and the effect was not easy to control, saline soil consolidation problems has been a civil problem. The consolidation mechanism of saline soil was studied adding slag, desulfurization gypsum and clinker in this paper, made the compressive strength to be able to meet the highway roadbed requirements, can not only solve some diseases of the subgrade in saline areas, saving land resources, reduce the cost of road construction in the saline soil area, but also use of solid waste, turning waste into wealth, reduce pollution. Provide a new approach to saving resources and energy; maintain the ecological balance.

Raw Materials and Experimental Methods

Materials The slag was obtained from capital steel Company, Beijing, desulfurization gypsum was obtained from the Shijingshan Power Plant, Beijing, and the chemical composition of the slag and desulfurization gypsum was listed in Table 1.

Table 1 The chemical composition of furnace slag and desulfurization gypsum (wt%)

Raw materials	SiO_2	Al_2O_3	Fe_2O_3	MgO	CaO	TiO_2	Loss	MnO	SO_3
Slag	32.70	15.40	0.40	8.97	38.79	0.65	0.76	0.015	
Desulfurization gypsum	2.84	0.78	0.25	0.47	40.13	0.06			33.21

The clinker was obtained from Jidong Cement Plant in Tangshan, Hebei Province, the chemical composition and XRD analysis were listed in Table 2 and Fig. 1.

Table 2 The chemical composition of the clinker

Chemical composition	SiO_2	Al_2O_3	Fe_2O_3	CaO	MgO	SO_3	TiO_2
Content(%)	22.50	4.86	3.43	66.30	0.83	0.31	0.83

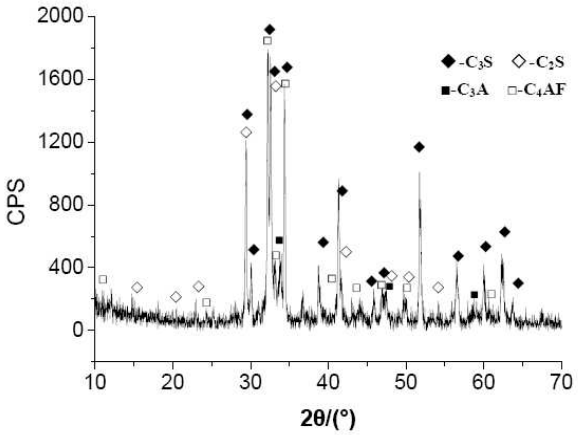


Fig. 1 The XRD of the clinker

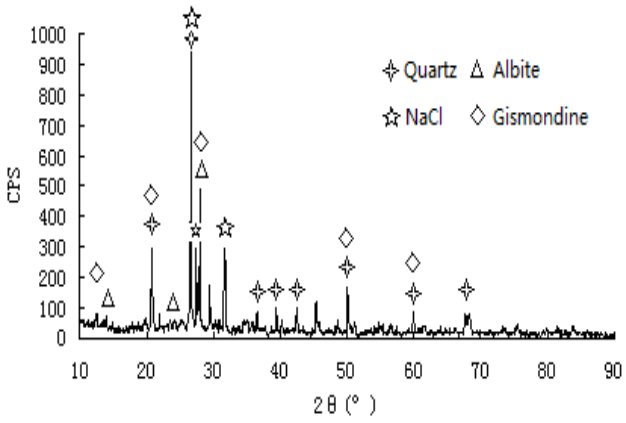


Fig. 2 The XRD of the saline soil

It can be seen from Table 2 that the main chemical composition of clinker are CaO, SiO_2 and a small amount of Al_2O_3 and Fe_2O_3. It is shown in Fig 1 that the main mineral composition of clinker are tricalcium silicate ($3CaO•SiO_2$), dicalcium silicate ($2CaO•SiO_2$), tricalcium aluminate ($3CaO•Al_2O_3$) and tetracalcium aluminoferrite ($4CaO•Al_2O_3•Fe_2O_3$).

The saline soil was obtained from a highway construction site in Dagang, Tianjin, the chemical composition of soluble slat and XRD analysis of the saline soil were listed in Table 3 and Fig. 2.

Table 3 The chemical composition of soluble slat in saline soil

Soluble slat ions	K^+	Na^+	Ca^{2+}	Mg^{2+}	Al^+	Fe	Cl^-	NO_3^-	HCO_3^-	SO_4^{2-}	Total
Content（mg/kg）	387	19049	1089	63	4	2	42966	118	54	4589	68321

It can be seen from Table 3 that the total ion content of the saline soil used in this experiment was 6.8%, and the mole ratio of $Cl^-$and SO_4^{2-} was (Cl^-/35.5) / (SO_4^{2-}/ 96) = 25.32> 2, so the saline soil used in this experiment was a strong chlorine saline soil according to the classification criteria of the saline soil.

The liquid limit W_L=34.82%, plastic limit W_p=18.69%, and plasticity index I_p= W_L-W_p=14.95%, the maximum dry density 1.97g/cm^3, and the optimum water content of the saline soil was 14.07% according to the soil test and test methods of materials stabilized with inorganic Binders for High way Engineering.

Test Methods. Cylindrical specimens were prepared with diameter of 50 mm, high 50 mm, and the volume was 100 cm^3 according to specification for construction and acceptance of fly ash-lime-stabilized materials for road base. Calculated for each block of total quality for 224.72 g (including dry salted soil for 197 g, water 27.72 g) according to test methods of materials stabilized with inorganic binders for high way engineering. Firstly, weighed dry saline soil 200g, mixed 3 ~ 5 min with a certain percentage of waste, activator and water. (The actual of water calculated with optimum water content of soil). Then samples were prepared with the mixed soil samples 224.72g, curing at a temperature of 20±2°C, humidity at 95%. Compressive strength was tested after 24 hours immersion.

Results and Analysis

After the samples were cured for 7d, 28d, 60d and 90d, compressive strength was tested. The results of consolidated saline soil were listed in Table 4. It can be seen from Table 4 that the effect of stabilizer which prepared with slag, desulfurization gypsum and clinker was significant. The compressive strength of cured for 7d up to 6.11 MPa when the mixing amount at 14%.

Table 4 The results of consolidated saline soil

Saline soil (g)	Clinker (%)	Desulfurization gypsum (%)	Slag (%)	Compressive strength(MPa)			
				7d	28d	60d	90d
200	2.1	2.1	9.8	6.11	10.01	11.23	11.82

In engineering applications, the road construction costs and economic benefits were affected by the mixing amount of stabilizer, and therefore as little as possible mixed with soil stabilizer. The consolidated test results of saline soil with different use level of stabilizer were listed in Table 5.

Table 5 The consolidated test results of saline soil with different use level of stabilizer

No.	Saline soil (g)	Content of the stabilizer (%)	Compressive strength(MPa)			
			7d	28d	60d	90d
1	200	13	5.31	8.97	9.14	9.32
2	200	14	6.11	10.01	11.23	11.82
3	200	15	6.71	11.38	12.07	12.98
4	200	16	7.47	13.56	14.77	15.09

Powdery soil stabilizer can improve and enhance the technical performance of soil which prepared with inorganic salt powder, cement, lime and fly ash. Stabilizer used in this experiment was a mixture made from slag, desulfurization gypsum and clinker, and therefore should belong to the powdery soil stabilizer. The data in this paper were laboratory data, laboratory data were different with engineering practice, so we can not take the laboratory data directly to do with the strength of the GB standards. According to literature, the strength of the laboratory should be discounted, and reduction factor of about 0.5 [7]. So the laboratory strength data were twice more compared to the standard. The application of stabilizer aimed for the consolidation of the road subgrade, and the 7 d compressive strength of cementitious materials up to 3~4 MPa according to soil stabilizer (CJ/T3073-1998), so the strength data of laboratory should in 6~ 8Mpa. It can be seen from Table 5 that the compressive strength of cured for 7d up to 6.11 MPa when the mixing amount at 14%, which means a mixture of 9.8% slag, 2.1% clinker and 2.1% desulfurization gypsum. The 7d consolidated soil compressive strength of stabilizer can meet the primary soil, and the strength of sub-base was lower than primary soil, so the stabilizer can meet the sub-base engineering applications, was an ideal stabilizer.

Acknowledgements

This study was financially supported by National High Technology Research and Development Program (SS2012AA062404); Key Science and Technology Project of Henan Province (112102310689)

References

[1] F. Li, B Li, J. Chen, et al, Highway-related dividing scheme of salty soil, Journal of Chang'an University, 6 (2006) 12-14.

[2] J. Yang, Development and prospect of the research on salt-affected soils in China, Acta Pedologica Sinica, 5 (2008) 837-845.

[3] X. Wang, H. Zhang, M. Xue, et al, Road disease and treatment in saline soil area, Journal of Tongji University, 10 (203) 1178-1181.

[4] Q. Lin, C. Li, B. Huo, et al, Engineering application of saline soil after modification, Journal of University of Science and Technology Beijing, 5 (2007) 456-460.

[5] X. You, Modern Roadbed and Pavement Engineering, Beijing, 2004.

[6] M. Wang, The application of soil solidifier in irrigation work, Water Resources and Hydropower of Northeast China, 155 (1997) 35-39.

[7] T. Yue, Performance Appraisal and Mechanism Investigation of the Soil Stabilized by Waste Residue Gel Material, Beijing, 2006.

© (2012) Trans Tech Publications, Switzerland
doi:10.4028/www.scientific.net/AMM.238.121

An Improved Method to Calculate the Direction and Weight in Microplane Constitutive Model

Mingxiao Jia [a], Zujun Liu [b] and Wei Xie [c]

North China University of Water Resources and Electric Power, Zhengzhou 450011, China

[a]jmxwish@163.com, [b]lishushan@ncwu.edu.cn, [c]xwei@ncwu.edu.cn

Keywords: microplane constitutive model; orientation; weight; numerical discrete; spherical geometry.

Abstract. This paper analyzes the calculation method on microplane direction and weight in current literature based on introducing numerical discretization algorithm in the microplane model. The characteristics and disadvantages of current methods are given out. In response to the issue that the orientation of microplane is not enough uniform and the shape and physical meaning of microplane is not clear, it is given out a kind of method that carrying out projection on the spherical surface after dividing the surface grid of regular polyhedron to calculate the orientation of microplane, then using the knowledge of spherical geometry to calculate the weight of microplane. Comparing and selecting the dividing scheme of microplane that obtained by different regular polyhedron and the grid levels, the optimization objective of fitting macroscopic elastic stiffness matrix is given out. The calculation results indicate that the method provided in this paper can obtain the dividing scheme that the shape and size of microplane are fully uniform, and the calculation result is more accurate than the optimal solution in the literature.

Introduction

The microplane module is a kind of multi-scale constitutive model. It describes the macro mechanical property through setting up constitutive relation on the microplane. The basic idea of microplane model can be traced to 1938 when Taylor given out metal slip theory during studying on plastic property of metal material. B. P. Bažant improved the plastic slip theory and initially proposed the microplane model for concrete in 1983 [1]. Later the microplane model has experienced 5 generations after continuous improvement and development [2-9]. This model directly establishes constitutive relation on the microplane in vector form, the concept is simple and can reflect various mechanic behavior of concrete, it has significant advantages compared to the constitutive module in tensor form.

The improvement of successive microplane model from M1 to M5 is mainly reflected on the selection of strain component and determination of stress-strain relation on the microplane, but there is less study on the orientation of microplane model and the calculation method of weight. The microplane orientation and the determination method of weight is the main reason to affect the calculation accuracy of module. Therefore, this paper has given out a kind of new microplane orientation and weight calculation method based on analyzing the method in current literature.

Introduction of Microplane Model and Integral Discrete Method

It is different from the constitutive model of macro tensor form, the basic concept of microplane model is to use the simple stress-strain relation of vector form on various microplanes to describe the complex mechanical characteristic of concrete, and its calculation process is shown in Fig. 1.

Firstly, the macro strain is projected on the microplane through dynamic constraint to obtain the microplane strain components on a certain orientation. As shown in Fig. 2, the microplane includes one normal component N and two shear components L and M,the normal micro strain ε_N and shear micro strain ε_L and ε_M are : $\varepsilon_N = N_{ij}\varepsilon_{ij}$, $\varepsilon_L = L_{ij}\varepsilon_{ij}$, $\varepsilon_M = M_{ij}\varepsilon_{ij}$ .Where $N_{ij} = n_i n_j$, $L_{ij} = \left(l_i n_j + l_j n_i\right)/2$, $M_{ij} = \left(m_i n_j + m_j n_i\right)/2$, n_i, l_i and m_i indicate the angle cosine between the normal component N, two shear components L, M and whole axis x_i respectively. ε_{ij} denotes macro strain tensor.

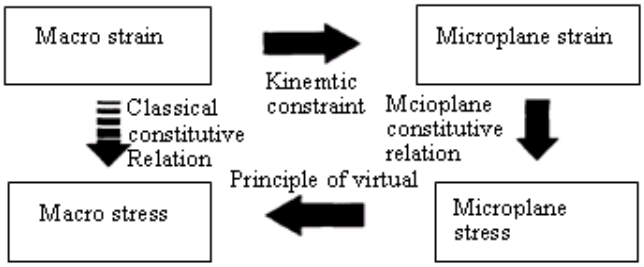


Fig. 1 Calculation flow chart of microplane model and traditional model.

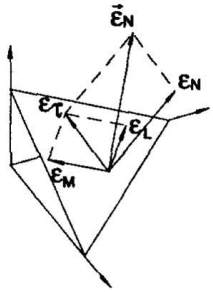


Fig. 2 The strain components on single microplane

After defining the stress-strain relation on the microplane, integrate the microplane stress into macro stress based on the principle of virtual work:

$$\sigma_{ij} = \frac{3}{2\pi}\int_{\Omega}\left(\sigma_N N_{ij} + \sigma_L L_{ij} + \sigma_M M_{ij}\right)d\Omega = \frac{3}{2\pi}\int_{\Omega} S_{ij}\,d\Omega \tag{1}$$

Where, $S_{ij} = \sigma_N N_{ij} + \sigma_L L_{ij} + \sigma_M M_{ij}$.

Further discrete the above formula on the hemisphere surface to obtain the approximation calculation formula of above integral expression on the hemisphere surface:

$$\sigma_{ij} = \frac{3}{2\pi}\int_{\Omega} S_{ij}\,d\Omega \approx 6\sum_{\mu=1}^{N_m} w_\mu S_{ij}^{\mu} \tag{2}$$

Where, w_μ indicates the weight related to the integration point; μ indicates a series of integration points indicated by direction that defined by unit vector n_i^{μ}; $\sum_{\mu} w_\mu = 0.5$ for each hemisphere surface. The integral of infinite number of directions on the hemisphere surface Ω can be approximately expressed as the sum on microplane in finite number of directions.

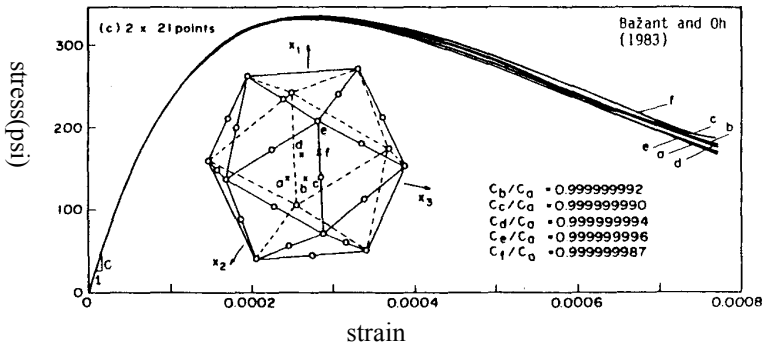


Fig. 3 21 microplanes

The method to set microplane orientation in the model M1 is to select some special points to represent the direction of microplane on the regular polyhedron. Take the icosahedron in figure 3 as an example, select the vertex and the midpoint of all edges, the vector from the centre of icosahedron to these special points can be expressed as the normal vector of one microplane, there are total 21 microplanes.Then use the method of optimization approach to obtain the weight of microplane, the objective of optimization is to make all microplanes do rigid rotation in case of no change on the loading direction of overall axis and macroscopic uniaxial ,of which the deviation of macroscopic uniaxial stress-strain curve obtained under different rotation positions is the smallest.

The above method to determine the orientation of microplane is clear and the weight distribution obtained through optimization calculation can satisfy the calculation accuracy required by engineering application. But it is still found that there are some shortages in the method of M1 through analyzing the above calculation process, which include the following points:

(1) The selection method of orientation make the distribution of microplane on the space is not enough uniform.

(2) The calculation process of weight need to be obtained through optimization calculation method, the calculation process is relatively complex and the specific shape of microplane is not clear, therefore the physical meaning represented by weight is not intuitive on the geometry.

(3) The optimization objective of using uniaxial stress-strain curve as microplane orientation and weight is insufficient. As a triaxial constitutive model for concrete, the optimization objective of microplane model should be able to fully reflect the stress-strain characteristics of triaxial.

Improving Method

In face with the shortage of above M1, this paper has improved the integral discrete method on the microplane through three aspects such as orientation selection method, weight calculation method, the optimization objective on orientation and weight calculation. The specific methods are as follows:

(1) Divide the each face on the regular polyhedron in uniform, use the vector from the centre of regular polyhedron to the centre of each dividing grid to indicate the orientation of one microplane. The advantage of this kind of handling method is to make the orientation distribution of microplane becomes uniform as far as possible, so as to further refine the grid and improve the accuracy of integral discrete.

(2) The grids on the polyhedron is projected on the external sphere to obtain the sphere grids on continuously dividing sphere, the ratio of the area of each spherical polygon accounting for spherical area is the weight on the corresponding microplane. Such calculation method of weight is simple and direct, the intuitive physical meaning of geometry on the microplane is very clear.

(3) It is proposed to use elastic stiffness matrix as the optimization objective of orientation and weight, which is better than the uniaxial stress - strain curve to fully valuate the accuracy of discrete model. Fig. 4 is the general framework of comparison on two kinds of method calculation procedures and characteristics.

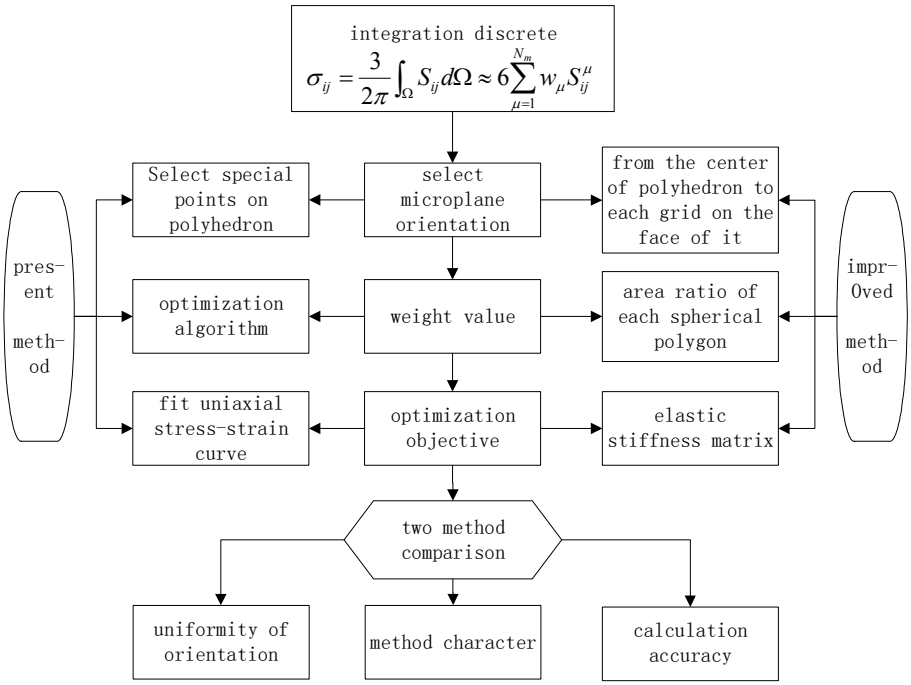


Fig. 4 Framework and comparison of two calculation methods

Improved Orientation and Weight Calculation Method

After dividing in uniform of grids on all faces of regular polyhedron, the centre coordinate of one of the grid is known as:

$$r_i = (x_i, y_i, z_i) \tag{3}$$

Then it can be known according to the knowledge of geometry, the point represented by centre is projected onto the unit sphere to obtain the unit normal vector of corresponding microplane as follows:

$$\bar{r}_i = \frac{r_i}{|r_i|} \tag{4}$$

Let a certain spherical triangle on the corresponding unit sphere of microplane to be ΔABC, record the area of ΔABC as S_{ABC} ,then the weight of such microplane is

$$w_i = \frac{S_{ABC}}{2\pi} \tag{5}$$

It can be seen according to the knowledge of geometry, the area of ΔABC is

$$S_{ABC} = A + B + C - \pi \tag{6}$$

Where A, B and C indicate the interior angles of three vertexes in ΔABC respectively. Its calculation method is introduced as follows.

Let a, b, c respectively indicate the position vectors of three vertexes A, B, C in the unit spherical triangle, i.e. $\mathrm{a} = \overrightarrow{OA}, \mathrm{b} = \overrightarrow{OB}, \mathrm{c} = \overrightarrow{OC}$, they are all unit vectors. It can be seen from the knowledge of spherical trigonometry (Wuyi Xiang, 2004):

$$\begin{aligned} b \cdot c &= \cos l_{BC} \\ c \cdot a &= \cos l_{CA} \\ a \cdot b &= \cos l_{AB} \end{aligned} \tag{7}$$

Where l indicate the length of a side of spherical triangle, and

$$\begin{aligned} \sin l_{BC} &= |b \times c| \\ \sin l_{CA} &= |c \times a| \\ \sin l_{AB} &= |a \times b| \end{aligned} \tag{8}$$

It can be seen from the cosine law of spherical triangle:

$$\begin{aligned} \sin l_{CA} \sin l_{AB} \cos A &= \cos l_{BC} - \cos l_{CA} \cos l_{AB} \\ \sin l_{AB} \sin l_{BC} \cos B &= \cos l_{CA} - \cos l_{AB} \cos l_{BC} \\ \sin l_{BC} \sin l_{CA} \cos C &= \cos l_{AB} - \cos l_{BC} \cos l_{CA} \end{aligned} \tag{9}$$

Therefore, A , B and C can be obtained and indicated respectively as

$$\begin{aligned} A &= \arccos \frac{\cos l_{BC} - \cos l_{CA} \cos l_{AB}}{\sin l_{CA} \sin l_{AB}} \\ B &= \arccos \frac{\cos l_{CA} - \cos l_{AB} \cos l_{BC}}{\sin l_{AB} \sin l_{BC}} \\ C &= \arccos \frac{\cos l_{AB} - \cos l_{BC} \cos l_{CA}}{\sin l_{BC} \sin l_{CA}} \end{aligned} \tag{10}$$

Then the weight of all microplanes can be obtained by simultaneous equation 5, 7, 8 and10.

Dividing Program of Microplane

The model of dividing microplane adopts the method based on dividing grids of regular polyhedron. Fig. 5 is respectively octahedron, dodecahedron and icosahedron; Fig. 6 is grid dividing model of octahedron and icosahedron, Fig. 7 is the dividing method of dodecahedron, which can divide the each face in the polyhedron into grids with different grid sizes.

For octahedron, the 2 kinds of dividing methods shown in Fig. 6 can respectively obtain 16 and 36 microplanes, for icosahedron, it can obtain 40-90 microplanes respectively ; two kinds of dividing methods shown in Fig. 7 can divide the dodecahedron into 40-90 microplanes.

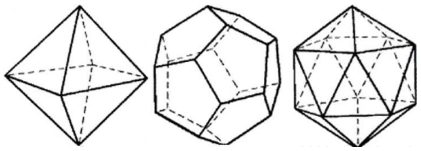


Fig. 5 Regular polyhedron

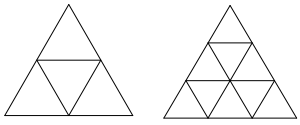


Fig. 6 Triangle grid dividing

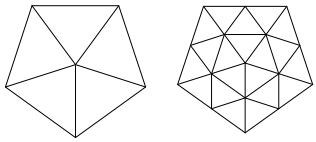


Fig. 7 Pentagon grid dividing

According to the calculation method in this paper, firstly determine the vertex coordinates of polyhedron, the normal vector of microplane can be determined after knowing of the vertex coordinates, and then the weight of microplane can be calculated.

Calculation Results Analysis

Uniformity of Weight and Orientation. The distribution of microplane should divide the sphere in uniform as far as possible to enable the stress process on different orientation can be fully captured after the integral discrete. Therefore it is necessary to carry out assessment on the orientation uniformity of microplane to compare the uniformity of various microplane dividing scheme.If the shapes of all microplanes are the same and the weights are equal, it indicates that the microplane has divided the sphere in uniform; the orientation uniformity of such kind of dividing scheme is the most optimum. In case of the microplane shape and weight are not equal, it can be seen according to the knowledge of mathematical statistics, and the concept of variance can be used to describe the change situation of the value of one set of data around the mean value. The larger the variance is, the poorer uniformity shall be. On the contrary,the smaller the variance is, the better uniformity shall be. Therefore, use the variance of microplane weight as the indicator to evaluate the uniformity of orientation, which is defined as follows

$$D(\omega_i) = E(\omega_i^2) - [E(\omega_i)]^2 \tag{11}$$

Where $E(\omega_i) = \frac{1}{n}\sum_{i=1}^{n}\omega_i$, $E(\omega_i^2) = \frac{1}{n}\sum_{i=1}^{n}\omega_i^2$.

The evaluation indicators of orientation uniformity based on various microplane dividing methods are shown in table 1.It can be seen from the data in the table, on the aspect of microplane orientation uniformity, it is the most uniform of dividing hemisphere surface into 30 microplanes based on dodecahedron, the variance of weight is zero, the size of spherical triangle of each microplane that formed on each sphere is the same; the weight variance obtained by using icosahedron to divide microplane has less difference than those of 21 microplanes in the module M1;divide microplane by projecting octahedron onto sphere, its weight discrete is large and the uniformity is relatively poor.

Table 1 Evaluation indicator comparison on the microplane orientation uniformity

Regular Polyhedron	Number of microplane	Weight variance
Octahedron	16	0.20
	36	0.37
Dodecahedron	30	0.00
	120	0.29
Icosahedron	40	0.07
	90	0.12
M1 model	21	0.10

Fit the Elastic Stiffness Matrix. It is different with the method of data calculation accuracy after evaluating the integral discrete in the model M1. This paper has given out the optimization method based on elastic stiffness matrix as its objective. It has mainly considered the following two points: firstly the microplane model is three-dimensional constitutive relation for concrete, the indicator used to evaluate the integral discrete mode should be able to reflect the multi-axis nature; secondly take the uniaxial loading condition as an example, the linear elastic stage and early softening stage has played an important role in the actual engineering application. Therefore selecting elastic stiffness matrix as the optimization objective shall have the real meaning.

In microplane model, the macroscopic elastic stiffness matrix is expressed as follows:

$$D = D_V + D_D + D_T$$

$$= \frac{1}{30}\begin{bmatrix} 10E_V+8E_D+12E_T & 10E_V-4E_D-6E_T & 10E_V-4E_D-6E_T & 0 & 0 & 0 \\ 10E_V-4E_D-6E_T & 10E_V+8E_D+12E_T & 10E_V-4E_D-6E_T & 0 & 0 & 0 \\ 10E_V-4E_D-6E_T & 10E_V-4E_D-6E_T & 10E_V+8E_D+12E_T & 0 & 0 & 0 \\ 0 & 0 & 0 & 6E_D+9E_T & 0 & 0 \\ 0 & 0 & 0 & 0 & 6E_D+9E_T & 0 \\ 0 & 0 & 0 & 0 & 0 & 6E_D+9E_T \end{bmatrix}$$

Where,

$$D_V = \frac{1}{30}\begin{bmatrix} 10E_V & 10E_V & 10E_V & 0 & 0 & 0 \\ 10E_V & 10E_V & 10E_V & 0 & 0 & 0 \\ 10E_V & 10E_V & 10E_V & 0 & 0 & 0 \\ 0 & 0 & 0 & 0 & 0 & 0 \\ 0 & 0 & 0 & 0 & 0 & 0 \\ 0 & 0 & 0 & 0 & 0 & 0 \end{bmatrix} \quad D_D = \frac{1}{30}\begin{bmatrix} 8E_D & -4E_D & -4E_D & 0 & 0 & 0 \\ -4E_D & 8E_D & -4E_D & 0 & 0 & 0 \\ -4E_D & -4E_D & 8E_D & 0 & 0 & 0 \\ 0 & 0 & 0 & 6E_D & 0 & 0 \\ 0 & 0 & 0 & 0 & 6E_D & 0 \\ 0 & 0 & 0 & 0 & 0 & 6E_D \end{bmatrix} \quad D_T = \frac{1}{30}\begin{bmatrix} 12E_T & -6E_T & -6E_T & 0 & 0 & 0 \\ -6E_T & 12E_T & -6E_T & 0 & 0 & 0 \\ -6E_T & -6E_T & 12E_T & 0 & 0 & 0 \\ 0 & 0 & 0 & 9E_T & 0 & 0 \\ 0 & 0 & 0 & 0 & 9E_T & 0 \\ 0 & 0 & 0 & 0 & 0 & 9E_T \end{bmatrix}$$

The value calculation results after the integral discrete should be able to express the form of above elastic stiffness matrix as far as possible, according to the previous data results, the program of dividing the pentagon into five triangles before projecting on the sphere based on dodecahedron can divide the sphere into 30 microplanes. The weights of microplanes are equal, the distribution is the most uniform.Therefore, this section has compared the elastic stiffness matrixes obtained by calculating the data in 21 and 30 microplane schemes, the data calculation results are as follows.

$$D_{21} = E_V \begin{bmatrix} 0.3333 & 0.3333 & 0.3333 & 0.0000 & 0.0000 & 0.0000 \\ 0.3333 & 0.3333 & 0.3333 & 0.0000 & 0.0000 & 0.0000 \\ 0.3333 & 0.3333 & 0.3333 & 0.0000 & 0.0000 & 0.0000 \\ 0.0000 & -0.0000 & 0.0000 & 0.0000 & -0.0000 & -0.0000 \\ 0.0000 & 0.0000 & 0.0000 & 0.0000 & 0.0000 & 0.0000 \\ -0.0000 & 0.0000 & 0.0000 & 0.0000 & 0.0000 & 0.0000 \end{bmatrix}$$

$$+ E_d \begin{bmatrix} 0.2497 & -0.1262 & -0.1234 & 0.0000 & 0.0000 & -0.0028 \\ -0.1262 & 0.2469 & -0.1207 & 0.0000 & 0.0000 & 0.0056 \\ -0.1234 & -0.1207 & 0.2411 & 0.0000 & 0.0000 & -0.0028 \\ 0.0000 & 0.0000 & 0.0000 & 0.2016 & 0.0000 & 0.0000 \\ 0.0000 & 0.0000 & 0.0000 & 0.0000 & 0.2182 & 0.0000 \\ -0.0028 & 0.0056 & -0.0028 & 0.0000 & 0.0000 & 0.2099 \end{bmatrix}$$

$$+ E_T \begin{bmatrix} 0.4114 & -0.2016 & -0.2099 & 0.0000 & 0.0000 & 0.0000 \\ -0.2016 & 0.4198 & -0.2182 & 0.0000 & 0.0000 & 0.0000 \\ -0.2099 & -0.2182 & 0.4281 & 0.0000 & 0.0000 & 0.0000 \\ 0.0000 & 0.0000 & 0.0000 & 0.2943 & -0.0042 & 0.0000 \\ 0.0000 & 0.0000 & 0.0000 & -0.0042 & 0.2859 & 0.0000 \\ 0.0000 & 0.0000 & 0.0000 & 0.0000 & 0.0000 & 0.2901 \end{bmatrix}$$

$$D_{30} = E_V \begin{bmatrix} 0.3333 & 0.3333 & 0.3333 & 0.0000 & 0.0000 & 0.0000 \\ 0.3333 & 0.3333 & 0.3333 & 0.0000 & 0.0000 & 0.0000 \\ 0.3333 & 0.3333 & 0.3333 & 0.0000 & 0.0000 & 0.0000 \\ 0.0000 & 0.0000 & 0.0000 & 0.0000 & -0.0000 & -0.0000 \\ 0.0000 & 0.0000 & 0.0000 & 0.0000 & 0.0000 & 0.0000 \\ -0.0000 & 0.0000 & 0.0000 & 0.0000 & 0.0000 & 0.0000 \end{bmatrix}$$

$$+ E_d \begin{bmatrix} 0.2667 & -0.1333 & -0.1333 & 0.0000 & 0.0000 & -0.0000 \\ -0.1333 & 0.2667 & -0.1333 & 0.0000 & 0.0000 & 0.0000 \\ -0.1333 & -0.1333 & 0.2667 & 0.0000 & 0.0000 & -0.0000 \\ 0.0000 & 0.0000 & 0.0000 & 0.2000 & 0.0000 & 0.0000 \\ 0.0000 & 0.0000 & 0.0000 & 0.0000 & 0.2000 & 0.0000 \\ -0.0028 & 0.0056 & -0.0028 & 0.0000 & 0.0000 & 0.2000 \end{bmatrix}$$

$$+ E_T \begin{bmatrix} 0.4000 & -0.2000 & -0.2000 & 0.0000 & 0.0000 & 0.0000 \\ -0.2000 & 0.4000 & -0.2000 & 0.0000 & 0.0000 & 0.0000 \\ -0.2000 & -0.2000 & 0.4000 & 0.0000 & 0.0000 & 0.0000 \\ 0.0000 & 0.0000 & 0.0000 & 0.3000 & -0.0000 & 0.0000 \\ 0.0000 & 0.0000 & 0.0000 & -0.0000 & 0.3000 & 0.0000 \\ 0.0000 & 0.0000 & 0.0000 & 0.0000 & 0.0000 & 0.3000 \end{bmatrix}$$

In order to judge the similarity between the elastic stiffness matrix obtained by using two kinds of value calculation scheme and the exact solution obtained by integral calculation, which can be expressed by the ratio of sum of absolute value of corresponding element difference and corresponding modulus of elasticity in the value solution and exact solution of three component

stiffness matrixes, i.e. $\sum_{i=1}^{6}\sum_{j=1}^{6}\left(D'_{ij}-D_{ij}\right)\Big/E$. Where D'_{ij} indicate the value calculation result, D_{ij} indicates exact value, $i, j = 1,2,\cdots,6$ is the subscript of matrix element. Table 2 has listed out the specific calculation results.

It can be seen from the table that the sum of absolute value of all element difference in scheme 2 is zero, the calculation results has indicated the following 2 points.

(1) Generally the elastic stiffness matrix and exact solution obtained from two kinds of schemes has little difference with the exact solution, where the error in scheme 2 is zero, which indicate that it can accurately simulate the macroscopic elastic stiffness matrix, so it has more higher accuracy than scheme 1.

(2) Because the scheme 2 is obtained based on projecting dodecahedron onto the sphere, this method has carried out uniform dividing on the sphere, the shape and size of microplane are equal, it has obtained uniform orientation distribution .When the direction of macro load is unchanged and the sphere do rigid rotation, the weight of microplane keeps unchanged, the orientation also keeps unchanged basically, therefore it shall have less influence on the macro calculation results.

Table 2 Calculation result comparison of elastic stiffness matrix

Dividing scheme	Volumetric	Deviatoric	shear
Scheme (21)	0.0000	0.1737	0.1568
Scheme (30)	0.0000	0.0000	0.0000

Conclusions

According to the methods provided in this paper, including improvement of microplane dividing model, improvement of orientation and weight calculation method, improvement of microplane optimization objective etc. it can obtain the following conclusions:

The calculation result indicates that the 30 microplane programs obtained by using dodecahedron projection of which the accuracy on the elastic stiffness matrix fitting is better than the 21 microplane programs in M1, and it has obtained the orientation dividing program distributed in uniform.

By adopting the method of projecting to the sphere based on regular polyhedron, the microplane dividing method is flexible and various in forms, it can obtain microplane in any grid size level;

The method of calculating microplane weight based on spherical geometry knowledge is simple and clear, it has eliminated the trouble in current method to determine weight through iterative optimization algorithm, also the shape of microplane obtained by dividing sphere surface is very intuitive.

Acknowledgements

This research is supported by Science and Technology Project of Henan Province (122300410185), Science and Technology Development of Zhengzhou (0910SGYG23261-1) and North China Institute of Water Conservancy and Hydropower funded projects to introduce high level personnel (40154).

References

[1] Z.P. Bažant, B.H. Oh, Microplane model for fracture analysis of concrete structures. Proc., Symp. On the Interactions of Non-Nuclear Munitions with Structure. U.S. Air Force Academy, Colorado Springs, Colorado, 1 (1983) 49-53.

[2] Z.P. Bažant, B.H. Oh, Microplane model for progressive fracture of concrete and rock. Journal of Engineering Mechanics, 114 (1985) 559-582.

[3] Z.P. Bažant, P.C. Prat, Microplane model for brittle plastic material: I. Theory, Journal of Engineering Mechanics, 114 (1988) 1672-1688.

[4] Z.P. Bažant, P.C. Prat, Microplane model for brittle plastic material: II. Verification, Journal of Engineering Mechanics, 114 (1988) 1689-1702.

[5] Z.P. Bažant, Y. Xiang, P.C. Prat, Microplane model for concrete. I. Stress-strain boundaries and finite strain, Journal of Engineering Mechanics, 122 (1996) 245-254.

[6] Z.P. Bažant, M.D. Fellow, ASCE, C.C. Ferhun, et al, Microplane model M4 for concrete: I. Formulation with work-conjugate deviatoric stress, Journal of Engineering Mechanics, 126 (2000) 944-953.

[7] Z.P. Bažant, C.C. Ferhun, Microplane Model M5 with Kinematic and Static Constraints for Concrete Fracture and Anelasticity I: Theory, Journal of Engineering Mechanics, 131 (2005) 31-40.

[8] Z.P. Bažant, C.C. Ferhun, Microplane Model M5 with Kinematic and Static Constraints for Concrete Fracture and Anelasticity II: Computation, Journal of Engineering Mechanics, 131 (2005) 41-47.

[9] I. Carol, P.C. Prat, Z.P. Bažant, New explicit microplane model for concrete: Theoretical aspects and numerical implementation, International Journal of Solids and Structures, 29 (1992) 1173-1191.

[10] W. Xiang, Basic Geometry, People's Education Press, Beijing, 2004.

© (2012) Trans Tech Publications, Switzerland
doi:10.4028/www.scientific.net/AMM.238.129

Experimental Study on Long-term Exposure of Concrete in Magnesium Sulfate Solution

Fenglan Li [a], Xinxin Ding [b] and Lihui Jin [c]

School of Civil Engineering and Communication, North China University of Water Resources and Electric Power, Zhengzhou 450011, China

[a] sbzhao@ncwu.edu.cn, [b] 1034515716@qq.com, [c] jinlihui@ncwu.edu.cn

Keywords: concrete; magnesium sulfate attack; compressive strength; tensile strength; sulfate-ion content.

Abstract. Tests were carried out to study the concrete attacked by magnesium sulfate solution. The concrete specimens were exposed in the magnesium sulfate solution with three different concentrations for 360 days. At the exposure times of 90 days, 180 days, 270 days and 360 days, the properties of concrete such as the mass change, the compressive strength and the tensile strength were measured, and the contents of sulfate-ion diffusing into different depths of concrete were determined. Their changes with the solution concentration and the exposure time are analyzed in this paper, which could be used as reference for the protecting of concrete against the attack of magnesium sulfate.

Introduction

Sulfate attack is one of the important factors which are harmful to the durability of concrete structures. It would make concrete expansion and deformation, and result in strength degradation. As sulfate widely exists in the saline soil, ocean, groundwater, interior lake and industrial wastewater, serious sulfate attack on concrete has been found in some infrastructure projects such as hydroelectric engineering, highway and railway [1].

The types of sulfate inducing concrete deterioration are sodium sulfate, magnesium sulfate, ammonium sulfate and calcium sulfate. As calcium sulfate has a low solubility (1400mg/L) and ammonia sulfate general exists in agricultural soil, the sulfate attack on concrete is common from sodium and magnesium sulfates [2]. The ion in sodium sulfate solution that attacks concrete is sulfate-ion, while both the magnesium-ion and the sulfate-ion in magnesium sulfate solution have erosion effects on concrete.

At present, some researches of magnesium sulfate attack on concrete have been conducted [3-7]. However, most of them were tested on the cement slurry sample or the mortar sample [8]. The macroscopic tests mainly included the apparent phenomenon, the mass change, the dynamic elastic modulus and the expansion rate, the microscopic tests mainly applied SEM, XRD and other technology on the microstructure and phase analysis. No research about magnesium sulfate attack on concrete was found on the content of sulfate-ion at different depth of concrete.

Therefore, tests of long-term exposure of concrete in magnesium sulfate solution were carried out. The main results are introduced in this paper.

Experimental

The raw materials included the cement in 42.5 strength grade with the chemical compositions as shown in Table 1, the river sand with 2.71 fineness modulus and the crushed limestone with maximum grain size of 20 mm as well as the tap water.

The proportion of concrete is listed in Table 2, which corresponds to the strength grade of C40. The specimens were cubes with 100mm dimension. After 24 hours natural curing, they were demoded and put into the standard curing room with (20±2) ^{o}C temperature and 95% relative humidity for 28 days. After that, the specimens were steeped into the magnesium sulfate solution as Fig. 1. The sulfate-ion content in magnesium sulfate solution were 800mg/L, 6000mg/L and 50000mg/L, marked by B, C and D respectively. During tests, to keep solution concentration constant, the solution was sealed by plastic membrane and refreshed once every month.

Table 1 Chemical composition of cement (%)

SiO_2	CaO	Al_2O_3	Fe_2O_3	SO_3	MgO	f-CaO	Na_2O	K_2O	Loss on ignition	Alkali
31.43	41.28	12.43	3.34	3.22	4.25	0.76	0.43	0.80	1.09	0.97

Table 2 Mix proportion of concrete

W/C	Cement (kg/m^3)	Water (kg/m^3)	Sand ratio (%)	Sand (kg/m^3)	Crushed stone (kg/m^3)
0.44	457	201	33	591	1201

In order to avoid disturbance of multi-directional sulfate attack, two parallel surfaces of specimen perpendicular to the casting-surface were exposed in magnesium sulfate solution, others were sealed by paraffin. The mass of specimens at dry surface state was weighed every 60 days. The strength and the sulfate-ion content were measured at the exposure time of 90 days, 180 days, 270 days and 360 days respectively.

The test methods of compressive and tensile strengths were in accordance with the Chinese Standard GB/T50081-2002. The chemical titration method for measuring the sulfate-ion concentration of sand was improved to measure the sulfate-ion concentration of concrete expressed by the content of SO_3 [10]. The samples were made as follows: a core with diameter of 20 mm was drilled in the central area of attacked surface of every specimen by drilling machine, and accurately divided into several layers by diamond cutting machine. The thickness of the first layer was 1.5 mm, the second was 2 mm and the followings were all 5 mm. When the layered samples were air dried, they were ground into powder which could be passed through a sieve with an aperture of 0.08 mm. The small aggregates were sorted out during the grinding.

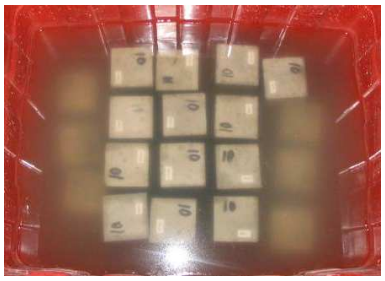


Fig. 1 Picture of concrete in magnesium sulfate solution



Fig. 2 Specimens sealed by paraffin

Results and Discussion

Mass of Concrete. As shown in Fig. 3, the mass of concrete increased slowly with the exposure time, which is different from the alternatively ascent-descent change of mass of concrete exposed in sodium sulfate solution [10]. Observing the surface of specimens, no peeling off was taken place on concrete exposed in magnesium sulfate solutions.

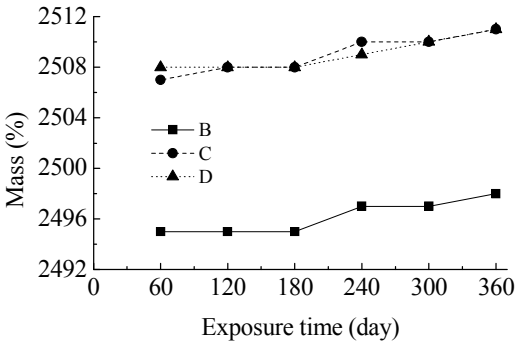


Fig.3 Mass changes of concrete

Strength of Concrete. Fig.4 and Fig. 5 show the changes of compressive and tensile strengths of concrete in different magnesium sulfate solution, in which the ratio is the strength at each exposure time relative to the initial strength. The changes of compressive and tensile strengths of concrete are not regular with the increase of exposure time and the concentration of solution. Relatively, the change of tensile strength is larger than the change of compressive strength while the concrete was exposed in solutions with higher concentrations. However, the reduce of concrete strength in some exposure times should be taken attention.

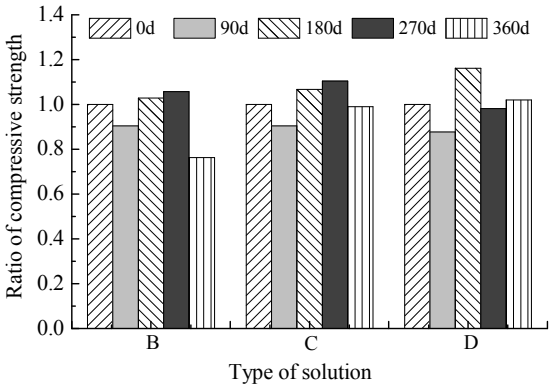


Fig. 4 Changes of compressive strength of concrete

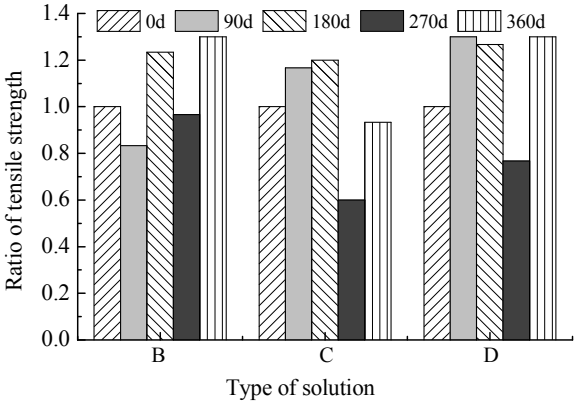


Fig. 5 Changes of tensile strength of concrete

Sulfate-ion content in Concrete. Fig. 6 shows the changes of sulfate-ion content in different depth of concrete exposed in the three magnesium sulfate solutions, in which the depth of concrete is the distance measured from the exposed surface. It can be seen that the sulfate-ion content drops from 0.75mm to 2.5mm depth, and almost keeps constant at interior concrete. Therefore, the diffusion of sulfate-ion into concrete was shallow within the test exposure time, the depth does not relate to the concentration of solution. Obviously, the large gradient of content is due to the gather of sulfate-ion near the surface of concrete. The reasons of above results could be analyzed as follow: when specimens long-term exposed in the magnesium sulfate solution, a cover of magnesium hydroxide formed on the concrete surface [5, 11]. Although magnesium hydroxide is also an attack product, its solubility into water is small. So that, the pores of concrete were blocked by the cover, the diffusion of sulfate-ion was confined.

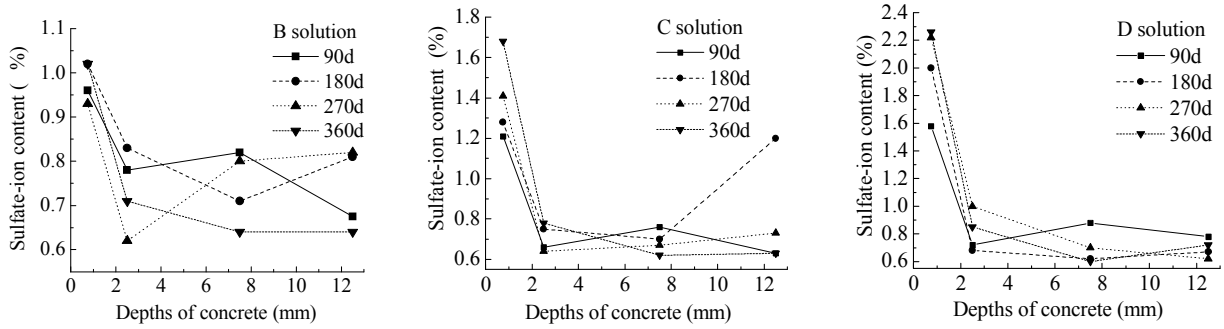


Fig. 6 Changes of sulfate-ion content in concrete

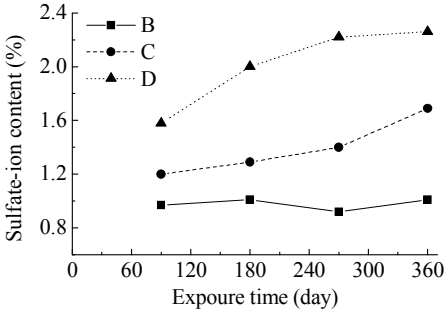


Fig. 7 Sulfate-ion content in the 0.75mm depth

Fig. 7 shows the sulfate-ion content of the 0.75mm depth of concrete in the three different solutions. The sulfate-ion content of the 0.75mm depth in B solution changes a little with the exposure time, while it changes largely in C and D solutions. At the same exposure time, the sulfate-ion content of concrete in C solution was about 25%~65% increment than that in B solution, while it was about 31%~57% increment in solution D relative to in solution C. Therefore, the gather of sulfate-ion near concrete surface relates to the concentration of solution.

Conclusions

The concrete was long-term exposed in magnesium sulfate solution with different concentration. The test results show that with the increase of exposure time, the mass of concrete increased in some extent, the compressive and tensile strengths had no significant change, the content of sulfate-ion in concrete was larger near the surface of specimen and increased with the concentration of solution. The diffusion of sulfate-ion into concrete was shallow during the test exposure time. The peeling off of concrete surface did not take place while the concrete was exposed in magnesium sulfate solution.

Acknowledgement

The authors thank to the financial supports of the Scientific and Technical Leader Raising Plan of Zhengzhou City, China (096SYJH23105); the Technical Plan Project of Education Department of Henan Province, China (2010A560011).

References

[1] J. Kang: Concrete, 3 (1995) 9-18.

[2] F. Zheng and G. Qin: Journal of Xuzhou Institute of Technology (Natural Sciences Edition), 3 (2010) 21-28.

[3] X. Gong: The Experimental Research of Sulfate Attack Resistance of Concrete, Thesis for Master Degree of Dalian University of Technology, Dalian, China, 2008.

[4] L. Yang, H. Yu and H. Ma: Journal of Bulletin of the Chinese Ceramic Society, 30 (2011) 764-769.

[5] Y. Liang and Y. Yuan: Journal of the Chinese Ceramic Society, 35 (2007) 504-508.

[6] E. E. Hekal, E. Kishar and H. Mostafa: Cement and Concrete Research, 9 (2002) 1421-1427.

[7] M. Santhanam, M. D. Cohen and J. Olek: Cement and Concrete Research, 4 (2002) 585-592.

[8] R. Gao: Micro-Macro Degradation Regularity of Sulfate Attack on Concrete under Complex Environments, Thesis for Ph.D Degree of Tsinghua University, Beijing, China, 2010.

[9] S. Zhao, J. Chen and R. Gao: Port Engineering Technology, 3 (2008) 31-33.

[10] X. Sun: Experiment on Concrete Long-term Steeped in sodium sulfate Solution, Thesis for Master Degree of North China University of Water Resources and Electric Power, Zhengzhou, 2009.

[11] Y. Jin and S. Zhou: Journal of East China Jiaotong University, 5 (2006), p. 4-8.

© (2012) Trans Tech Publications, Switzerland
doi:10.4028/www.scientific.net/AMM.238.133

Experimental Research on the Influence of Grain Size of Coarse Aggregate on Pebble Concrete Compressive Strength

Wei Xie [a], Yanan Jin [b] and Shushan Li [c]

North China University of Water Resources and Electric Power, Zhengzhou 450011, China

[a]xiewei@ncwu.edu.cn, [b]JYNjin@126.com , [c]lishushan@ncwu.edu.cn

Keywords: pebble concrete; coarse aggregate; gradation; maximum diameter; compressive strength.

Abstract. To discuss the influence of coarse aggregate size, water cement ratio and ages on the concrete compressive strength，the compressive strength tests were carried out by 54 cubic specimens of pebbles concrete in dimensions of 150mm, 18 cubic specimens with dimensions of 200mm and 72 specimens with size of 150mm×150mm×300mm. The results show that the maximum size of coarse aggregate rises with the decrease of the concrete compressive strength; Concrete compressive strength of coarse aggregate size affects more apparently as the ratio of water-cement decrease; with the increasing of age, concrete compressive strength of the aggregate size effect has no significant changes.

Introduction

Aggregate is an important component of concrete, generally accounts for 60% to 80% of the volume of concrete, which accounts for more than 40% of the aggregate [1]. Under pressure load, coarse aggregate concrete through between the heritability, not only enhance compressive strength of concrete but also improve concrete deformation property [2]. It is found that the size of coarse aggregate have certain effects on the concrete property [3-5]. On one hand, when the workability and dosage of cement is constant, the coarse aggregate size is larger; when the cement paste content of mixture is less, the concrete strength is higher; On the other hand, the specific area and the bond strength reduce with the increasing of coarse aggregate size, and subsidiary stress as a result of the large coarse aggregate increasing drag changes of water mud cause concrete strength to be decreased. This effect is more apparent in the rich concrete. Wu Libin [6] thinks that in certain amount of cement and sand-ratio content, concrete strength exist coarse aggregate's maximum grain-size effect that it is optimal max-diameter 20mm. Wu Keru and others research [7] the influence of coarse aggregate size distribution on the mechanics properties of concrete by acoustic emission technology, concrete compressive strength rising with the improvement of coarse aggregate maximum size, but the concrete strength decreasing slightly when the size exceed 15mm.

The size of coarse aggregate has more complicated effects on the concrete strength. But previous research achievements are mostly localized in gravel aggregate, while the pebble aggregate have been vacant systemic study. Therefore, based on many model tests, under the same volume fraction of the pebble aggregate, here are three factors that we should think about when we analyze the rules of effect on concrete compressive strength on pebble coarse aggregate grading. These will provide test data as a reference for the engineering application.

Overview of the Test

The cement used in this test is P.O 42.5 grade ordinary Portland cement manufactured by Zhengzhou TianRui cement limited company. Its physical and mechanical properties are shown in Table 1. Natural sand with the fineness modulus of 3.1 is fine aggregate. The additives used in this test is the improved high efficiency FDN-1 water reducer produced by Henan Province building material institute and other additives used in this test is the new air entraining agents ZY-99 of Hangzhou ZhongYe nature plants Technology limited company. The specific designed concrete mixing ratios are shown in Table 2. The coarse aggregate is pebble aggregate. The continuously

graded coarse aggregate carry on artificial screening for 4 pebble aggregate interval diameter: 5-10mm,10-20mm, 20-40mm, 40-60mm. The mix ratio of aggregate gradation is shown in Table 3. The physical properties of pebbles aggregate are shown in Table 4. Its grain diameter is 5~60mm and specific area is 0.157m^2/kg. Its grain diameter is 5~60mm and specific surface area is 0.157m^2/kg. When the diameter of grain is between 5mm to 40mm, 5mm to 20mm and 5mm and 10mm, the respective specific surface areas are 0.201m^2/kg, 0.378m^2/kg and 0.696m^2/kg. The specific surface area is respectively increased by 28.0%, 140.7%, 343.3%.

Table 1 Physical and mechanical properties of cement

Test items	Initial setting	Final setting	Compressive strength (MPa)		Flexural strength (MPa)	
			3d	28d	3d	28d
Test value	135min	195min	27.0	48.3	5.2	9.1

Table 2 Parameters of pebble concrete mixing ratio design in each cubic meter

No.	W/C	Aggregate	Dosage of materials of concrete in each cubic meter (kg)					
		Size (mm)	Water consumption	Cement	Sand	Cobblestone	Air entraining agent	Water reducer
PC05-10	0.5	5~10	148	296	733	1196	0.06	1.5
PC05-20		5~20	148	296	733	1196	0.06	1.5
PC05-40		5~40	148	296	733	1196	0.06	1.5
PC05-60		5~60	148	296	733	1196	0.06	1.5
PC04-10	0.4	5~10	146	365	689	1214	0.06	3.65
PC04-20		5~20	146	365	689	1214	0.06	3.65
PC04-40		5~40	146	365	689	1214	0.06	3.65
PC04-60		5~60	146	365	689	1214	0.06	3.65

Table 3 Mix ratio of pebble aggregate gradation

Aggregate size (mm)	Mix ratio of cobblestone (%)			
	5-10mm	10-20mm	20-40mm	40-60mm
5~10	100	-	-	-
5~20	40	60	-	-
5~40	16	24	60	-
5~60	12	18	30	40

Table 4 Physical properties of pebble aggregate

Aggregate size (mm)	Apparent density (kg/ m^3)	Bulk density (kg/m^3)	Void content	Specific area (m^2/kg)
5~10	2710	1523	43.8%	0.696
5~20	2722	1540	43.4%	0.378
5~40	2730	1577	42.2%	0.201
5~60	2730	1589	41.8%	0.157

Testing Results and Analysis

Slump. The relation curve between the slump of concrete mix and the maximum coarse aggregate size is shown in Fig. 1. Experiment result shows that under the same conditions, with changing the size of coarse aggregate, the larger size of coarse aggregate, the larger slump of fresh concrete is. After analyzing the reasons, under the same consumption of coarse aggregate, the size of coarse aggregate rises with the decrease of tiny particle and total specific surface area in the aggregate, which could lead to reduce cement paste content on the surface, and then the cement paste content of the ubrication and liquid flow are increased. It raises the slump of mixture as a result. It is difficult to form the test specimen that the slump of concrete mix that maximum aggregate size is 10mm which is less than 25mm.

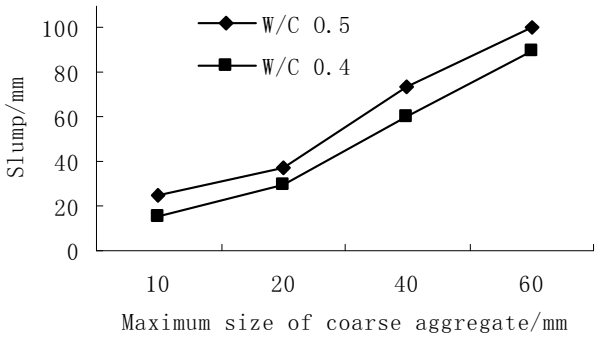


Fig. 1 Influence of pebble aggregate size for slump of fresh concrete

Compressive Strength. The variation of concrete compressive strength and aggregate size is shown in Fig. 2 to Fig. 5. With the increase of the curing period, the concrete compressive strength increased gradually. When the water-cement ratio and coarse aggregate quantity is constant, it shows a certain law that the compressive strength of concrete increases with the aggregate size decreases.

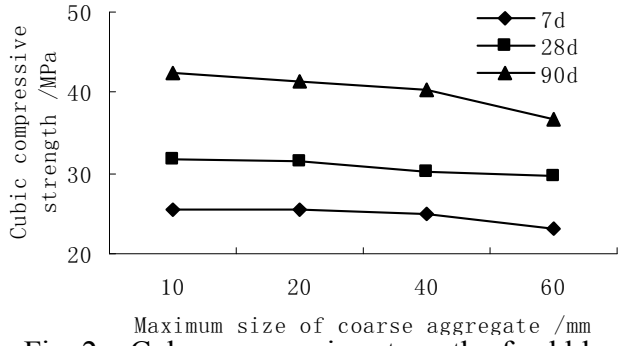


Fig. 2 Cube compressive strength of pebble concrete with water cement ratio of 0.5.

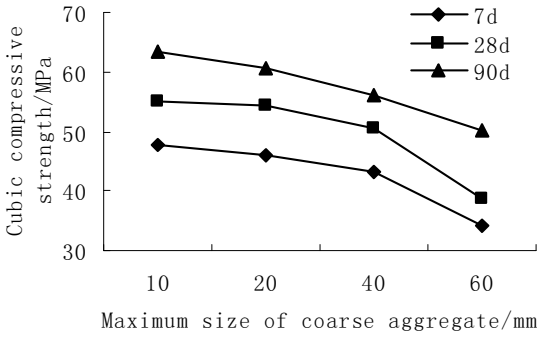


Fig. 3 Cube compressive strength of pebble concrete with water cement ratio of 0.4.

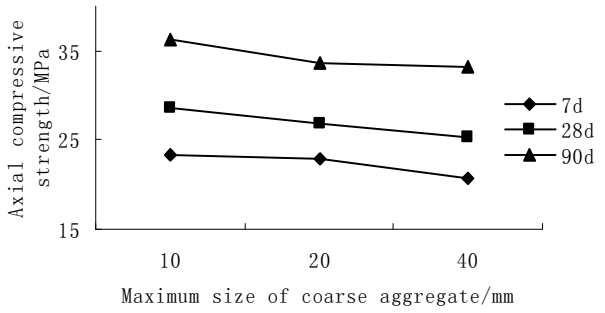


Fig. 4 Axial compressive strength of pebble concrete with water cement ratio of 0.5.

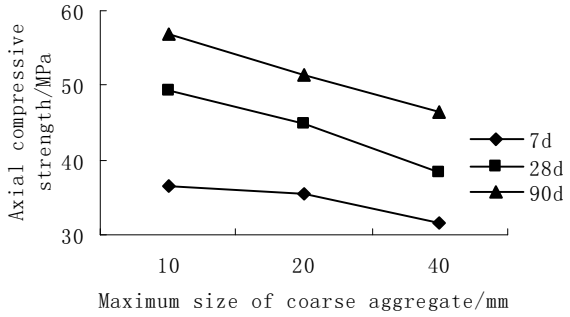


Fig. 5 Axial compressive strength of pebble concrete with water cement ratio of 0.4.

Fig. 2 and 3 show that the larger the specific surface area in the aggregate amount of the same case, the higher the interfacial strength and the interfacial region is more uniform by force, the higher the compressive strength of concrete. In addition, the smaller the size of aggregate, the smaller the pore is the lower part of the formation of aggregates in concrete, the less at the same time the smaller the interfacial region due to the hardening of cement paste shrinkage cracks, the less these are to improve concrete the compressive strength of advantage [8]. Pebbles the size effect of the compressive strength of concrete values in Fig. 5 shown the gravel concrete compressive strength by the particle size more significant impact, especially for the axial compressive strength. Aggregate size effect of concrete compressive strength is also affected by the water-cement ratio, with the lower water-cement ratio, the use of smaller aggregate size to obtain high strength .When the value of concrete's cement ratio is 0.5, the maximum particle size of coarse aggregate is 30~40mm; If the value of concrete's cement ratio is 0.4, the maximum particle size of coarse aggregate is 20mm.

Mechanism Analysis

Hardened concrete is a multiphase porous composite material with a high degree of heterogeneity and complexity of internal structure. Microstructure of the concrete is divided into hardening slurry-based phase, aggregate phase, and the transition zone between cement paste and aggregate interface. The strength of the transition zone is lower than the cement paste body, it is the weakest link in the three-phase. When the hydration gel has fundamental effect on the strength, the dense packing of the particles fill the space is very important for the formation of high strength.

The influence on concrete compressive strength of the coarse aggregate gradation can also be considered from its impact on the quality of the interfacial transition zone [9]. On the premise that the coarse aggregate has the same mineral composition, the quality of the transition zone depends on the cementing materials consumption of surrounding aggregates, especially at the bottom of the trend of the bleeding and that wrapped in the

In Fig. 2 and Fig. 4, because of the large water-cement ratio of concrete, and less cementing materials on the smaller particle size of coarse aggregate concrete, in addition to its large internal surface area of coarse aggregate, the consumption of cementing materials is small, thus, weakening the quality of the interface transition zone and reduce the strength of the concrete. In Fig. 3 and Fig. 5, the water-cement ratio of concrete is small, and the consumption of cementing materials is large, the amount of coarse aggregate visible cementing materials is no longer a factor restricting the quality of the interface transition zone, but due to the larger size coarse aggregate, especially around the bottom of the bleeding trend is enhanced, thereby, weaken the quality of the interface transition zone and reduce the strength of the concrete.

The larger aggregate particles cause a large stress concentration with the pressure load, and the aggregate particles' strength will be reduced. The larger aggregate particles increases the resistance of the volume change of cement paste, it will cause additional stress in the cement paste cause additional stress, and weakening the strength of concrete.

There are four aspects [10]. On the mechanism of the effect of the particle size of coarse aggregate: (1) with the aggregate size increased, weakening the bond of coarse aggregate and cement, increasing the discontinuity of concrete internal structure, resulting in a lower concrete strength. (2) The coarse aggregate in concrete restricts cement contraction. The modulus of elasticity between Coarse aggregate and cement paste are different, and thus it come into being tensile stress in the other interior, this internal stress with increasing aggregate size increases, resulting in lower strength of concrete. (3)As the aggregate size increases, the aggregate interfacial transition zone of $Ca(OH)_2$ crystal orientation degree increases, so that the interface structure weakened, then the strength of the concrete is reduced. (4) As the aggregate size increases, the characterization of concrete under different loading of elastic / plastic ratio is decreased.

Conclusions

There is a significant influence on the fresh concrete when the coarse aggregate size is changing.

When the water-cement ratio is great, the coarse aggregate size have less effect on concrete compression strength; When the water-cement ratio is small, the coarse aggregate size have great effect on concrete compression strength.

The maximum coarse aggregate size rises with the reduction of pebble concrete compression strength. Pebble concrete compression strength reduces with the increasing of the maximum coarse aggregate size.

The smaller is the water-cement ratio, the more obvious is the coarse aggregate's grain-size effect of the concrete compression strength; it has no significant change for the aggregate's grain-size effect of the concrete compression strength when we rise the age time.

The pebble aggregate size is decreased. This not only increased bonding area between pebbles and cement mortars, in the course of vibrating the concrete, but also improved pebble's uniformity in the concrete. At the same time, this also reduced the harmful pore of the bottom of pebble and reduced hydrophilic membranes wrapping pebbles and so on. Finally, it will improve effectively concrete compression strength.

References

[1] N. Feng, High Performance Concrete, Chinese Architecture and Building Press, Beijing, 1996.

[2] A.M. Neville, Translated by S. Liu, Concrete Property, China Architecture and Building Press, Beijing, 2011.

[3] Z. Wu, H. Lian, High Performance Concrete, China Railway Press, Beijing, 1999.

[4] Y. Wang, H. Kui, J. Tong, et al, Influence factor of adhesion interface of cement concrete, Jilin University Journal (liberal arts ed.), 33 (2003) 56-59.

[5] M. Sidney, J. F. Young, D. David, Translation of K. Wu, Concrete, Chemical Industry Press, Beijing, 2005.

[6] L. Wu, Study impacts of aggregate for mechanical property of high performance concrete, Tongji University, Shanghai, 2001.

[7] K. Wu, B. Chen, Y. Wu, et al, Effect of coarse aggregate type on mechanical properties of high-performance concrete, Cement and Concrete Research, 31 (2001) 1421-1425.

[8] J. Han, P. Yan, Influence of aggregate gradation for concrete strength on the development history, Concrete, 1 (2008) 62-63.

[9] M. S. Medeah, Z. Salim, B. Sa, Effect of content and particle size distribution of coarse aggregate on the compressive strength of concrete, Construction and Building Masteries, 2009.

[10]Y. Sun, C. Zhong, Z. Gu, et al, Material Selection of Concrete in the Control of the Cracks, Chemical Industry Press, Beijing, 2009.

© (2012) Trans Tech Publications, Switzerland
doi:10.4028/www.scientific.net/AMM.238.138

Basic Mechanics Properties Test of Fly Ash Concrete

Wei Xie [a], Haijuan Zhang [b] and Shushan Li [c]

North China University of Water Resources and Electric Power, Zhengzhou 450011, China

[a]xwei@ncwu.edu.cn, [b]zhanghaijuanz@126.com, [c]lishushan@ncwu.edu.cn

Keywords: fly ash concrete; the amount of fly ash; mechanics properties; influence mechanism.

Abstract. By the test study of basic mechanics properties of concrete with different fly ash content, the influence of the content of fly ash on the compressive strength, flexural strength, splitting tensile strength and static compressive elastic modulus of concrete are analyzed with the explaining of the influence mechanism of fly ash. The test results show that, comparing with the normal reference concrete, the early age strength of fly ash concrete enhances slowly, while the late strength develops rapidly, even overpasses the strength of normal reference concrete.

Introduction

Fly ash is the emissions of thermal power plant. With no proper disposal solutions, it will pollute atmospheric air, groundwater and impacts on the environment adversely, so it has important social significance to increase the comprehensive utilization rate of fly ash. Fly ash utilization in China mainly has 3 aspects, first it is used in the production of the construction materials, such as cement, fly ash concrete; second it is used for road building; third it is applied in agriculture, which can be used for producing magnetic fertilizer and microbial fertilizer, etc [1]. We can recycle amount of fly ash with above measures, but the utilization rate of fly ash in our country is still low [2]. In addition, a large number of resources and energy are consumed for producing concrete which is the main material of modern building. According to the policy of our country about the environment protection and resources saving, the main future trend of concrete development is the research and application about the Green High Performance Concrete (GHPC) [3]. The big focus of construction researchers is how to mix the admixture with concrete reasonably, which can not only improve the performance of concrete, but also reduce environmental pollution. Fly ash concrete is one of the kinds of the Green High Performance Concrete, it not only can prevent the environmental pollution caused by fly ash, but also improve the performance of concrete, therefore, it is very significant to research and apply fly ash concrete. This article was written mainly about the influence of different fly ash content and trial ages on concrete performance, has made comparison research with reference concrete and studied the rule of strength development, which can be used as reference for the future study of fly ash concrete.

Overview of the Test

Properties of Materials. There is a grade 42.5 ordinary Portland cement supplied by Zhengzhou Shangjie Cement Plant, the physical mechanics property is shown in table 1.The gradation of cobble stone is from 5mm to 25mm. Xinyang sand is used, and its modulus of fineness is 2.9. A grade Ⅱ fly ash from Zhengzhou Thermal Power Plant is used as mineral admixture, the physical property is listed in Table 2. Tap water is used for the test water. JKH-1 superplasticizer is made by Henan Jiancai, optimal mixing content is 0.5% ~ 1%.

Test Design. The mix proportion of concrete is designed in terms of the literature [4]. Concrete without fly ash is used as reference concrete. In the fly ash concrete, the percentage of fly ash as partial replacement of cement is respectively 10%, 20%, 30%, 40%. The mixture ratio of concrete is listed in table 3.In the compressive strength test, 3 concrete specimens with the size of 100mm×100 mm×100mm each group have been made. In the bending strength test, the specimen size is 100 mm×100mm× 400mm, there are 3 specimens in each group. Besides, 3 concrete specimens with the size of 150mm × 150mm×150mm for the splitting tensile strength test and 6 concrete specimens with the size of 150mm×150mm×300mm for the static compressive elastic modulus test have been made. Standard curing period is 28 days. Trial ages are respectively 7, 28, 90, 180 days. [5]

Table 1 Physical mechanics property of cement

Fineness [%]	Standard consistency [%]	Setting time [min]		Compressive strength [MPa]		Flexural strength [MPa]	
		Initial set	final set	3-day	28-day	3-day	28-day
3.7	28	170	230	25.0	51.3	4.7	8.9

Table 2 Physical property of fly ash

Fineness [%]	Water requirement ratio [%]	Ignition loss [%]	Water content [%]	SO_3 content [%]
14	98	7	0.6	2.5

Table 3 The mixture ratio of concrete

Control . No.	W/C ratio	Sand ratio [%]	Fly ash percentage [%]	Water [kg/m^3]	Cement [kg/m^3]	Sand [kg/m^3]	Cobblestone [kg/m^3]	Water reducing agent [kg/m^3]
F-0	0.5	38	0	148	296	733	1196	1.5
F-10	0.5	38	10	148	266.4	733	1196	1.5
F-20	0.5	38	20	148	236.8	733	1196	1.5
F-30	0.5	38	30	148	207.2	733	1196	1.5
F-40	0.5	38	40	148	177.6	733	1196	1.5

Results and Discussion

Compressive Strength. A graph of relationship between fly ash content and compressive strength is drawn in accordance with test results, as shown in Fig. 1. The 7-day value of concrete compressive strength becomes smaller and smaller, while the rate for replacement cement by fly ash is higher and higher. The 28-day value of concrete compressive strength is also reduced along with the increasing of the fly ash content, while the extent of the decrease is weaker than that of 7-day. At 90 day, the strength of 10% fly ash content is the largest, 20% fly ash content is the second among the groups, which have exceeded the reference concrete strength, while the strength of 30%and 40% content is still lower than the reference one; At 180 day, the strength of concrete with fly ash content is lower than 30% all have been more than the strength of benchmark concrete. The results of the present investigation indicate that, the early age strength of concrete is lower and lower with the increasing percentage of fly ash as partial replacement of cement, While the later strength of fly ash concrete increases rapidly, and the quantity of fly ash is 40 percent of total binder by weight, the strength of fly ash concrete is higher than that of reference concrete.

Bending Strength. The relationship between fly ash content, trial ages and bending strength is measured, as is shown in Fig. 2. At 7 day, it has been shown that, the bending strength of concrete decreases with the increasing of fly ash content; At 28 day, bending strength reaches its highest point at the percentage of 30%, the bending strength increases with less than 30% fly ash content increasing, but decreases with the fly ash content exceeded 30%; At 90 day and 180 day, the law of the bending strength development are similar to that of 28 days.

Splitting Tensile Strength. The influence of fly ash content and trial ages to splitting tensile strength is discussed, which is shown in Fig. 3. The splitting tensile strength of concrete decreases with the increase of the fly ash content on the 7th and the 28th days; At 90 day, the test indicates splitting tensile strength increases with the adding fly ash content below 30%, and the biggest strength is at 30%, but decreases with the fly ash content exceeded 30%; At 180 day, the trend of the splitting tensile strength development are similar to that of 90 days, but the extent of the growth is weaker.

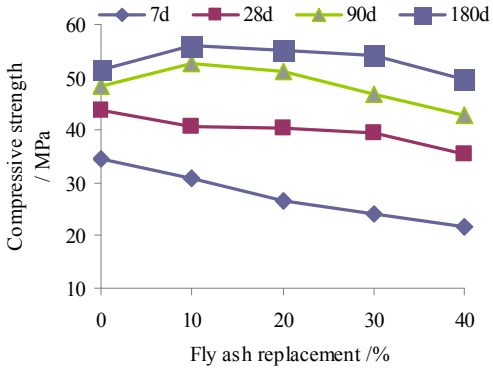


Fig. 1 Relationship between compressive strength and percentage replacement of fly ash

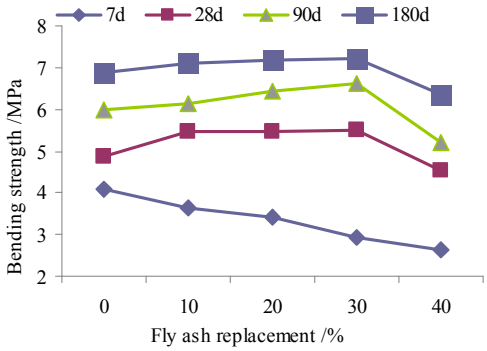


Fig. 2 Relationship between bending strength and percentage replacement of fly ash

Static Compressive Elastic Modulus. Fig. 4 shows the relationship of fly ash content and elastic modulus of concrete. The 7-day elastic modulus of concrete decreases with the increasing of the fly ash content; the maximum value of 28-day elastic modulus of concrete is obtained at 10% replacement level; At 90 day, elastic modulus of concrete with the percentage from10% to30 % is more than that of reference concrete, and the peak value is at 30% level. The 180-days elastic modulus almost follows the same trend as that of 90 days.

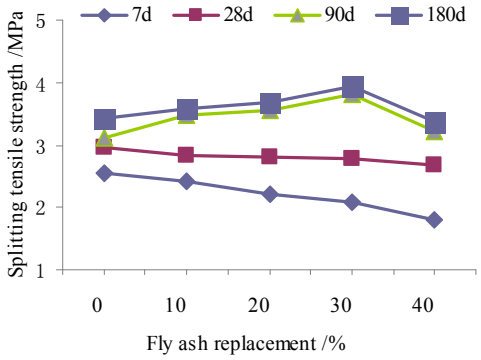


Fig. 3 Relationship between splitting tensile strength and percentage replacement of fly ash

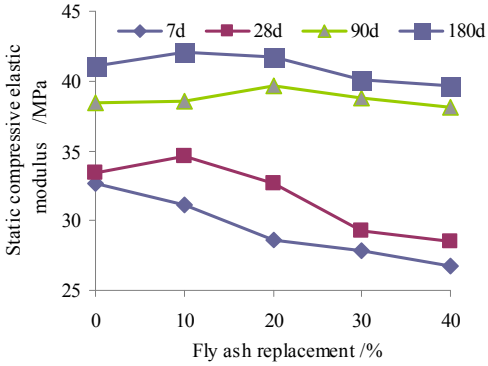


Fig. 4 Relationship between static compressive elastic modulus and percentage replacement of fly ash

Influence Mechanism

Pozzolanic Reaction of Fly Ash. Cement reacts with water to produce calcium hydroxide which has good activation to fly ash, then fly ash reacts with calcium hydroxide to form C-S-H gel, which is called the secondary reaction. It can not be found that clear fibrous crystal is in the surface of fly ash granule until 90 days, and the crystal can improve the bonding strength of fly ash and cement paste. In addition, the secondary hydration reaction products can further fill the capillary of concrete, which makes concrete more compacting [6].

Micro-aggregate Effect. The fly ash particles dispersing in the concrete reduce the adhesion between cement particles, make the cement particles become more dispersed, which is to the hydration reaction's advantage. What 's more, fly ash particles constitute reasonable micro gradation with cement, improve stacking density .In addition, it plays an important role in workability of flesh concrete, and makes the micro structure of harden concrete more dense [7].

Interaction Effect. There are physical or chemical interactions among fly ash, cement, water reducing agent. For example, $Ca(OH)_2$ is generated by the cement hydration is the reactive activator of fly ash which can reduce fluid alkalinity after hydration and make further hydration of unhydrated cement. Since the time of fly ash hydration reaction is slow, the high range water reducing agents on fly ash will not work in a short period of time, then can be gradually released with the fly ash hydration , so the loss of flesh fly ash concrete slump constant is low [8].

Conclusions

The early age strength of fly ash concrete is low and develops slowly; the late strength increases rapidly, which can catch up with and even surpass the strength of reference concrete. It is suitable for long term strength to design fly ash concrete, so it can be used in concrete for hydraulic structure.

To meet the strength of concrete, the percentage of grade II fly ash as partial replacement of cement is up to 30%.

It is possible to allocate high strength concrete, when grade II fly ash and water reducing agent is in a reasonable range.

Fly ash used in concrete not only saves the cement and reduces the cost of concrete, but also improves the utilization of fly ash, and it has numerous economic benefits and environmental benefits.

Acknowledgements

This work was supported by Innovation Scientists and Technicians Troop Construction Projects of Zhengzhou City (112PLJRC354) .

References

[1] G. Liu, Discussion on the present situation and development perspective of comprehensive utilization of fly ash, Sci-Tech Information Development & Economic, 20 (2010) 167-170.

[2] Q. Huang, Analysis of development prospects and status quo of comprehensive utilization of fly ash at home and abroad, China Well and Rock Salt, 42 (2011) 41-43.

[3] Z. Wu, Green high performance concrete-development trend of concrete, China Concrete and Cement Products, 1 (1998) 3-6.

[4] DL/T5330-2005, Code for Mix Design of Hydraulic Concrete, China Waterpower Press, Beijing, 2005.

[5] DL/T5150-2001, Test Code for Hydraulic Concrete, China Waterpower Press, Beijing, 2006.

[6] Y. Zhen, Application of Fly Ash in Hydraulic Concrete, China Waterpower Press, Beijing, 1992.

[7] S. Shen, Fly Ash concrete, China Railway Press, Beijing, 1989.

[8] D. Li. Application of fly ash and ore powder in concrete, Scientific and Technical Information, 21 (2010) 302-303.

© (2012) Trans Tech Publications, Switzerland
doi:10.4028/www.scientific.net/AMM.238.142

Bond-Slip Relation of Plain Steel Bar in Concrete with Machine-made Sand

Shunbo Zhao [a], Xinxin Ding [b] and Changyong Li [c]

School of Civil Engineering and Communication, North China University of Water Resources and Electric Power, Zhengzhou 450011, P. R. China

[a]sbzhao@ncwu.edu.cn, [b]1034515716@qq.com, [c]lichang@ncwu.edu.cn

Keywords: machine-made sand concrete (MSC); plain steel bar; bond-slip relation; pull-out test.

Abstract. To meet the requirement of machine-made sand application in concrete structures, experimental studies were carried out on the bond of plain steel bar with Machine-made Sand Concrete (MSC) by the central pull-out test method. Three specimens were cast as one group, 14 groups were tested considering the influence of concrete strength, bond length and stone powder content in machine-made sand. Based on the experimental research, the characteristic values of bond-slip curve such as the initial-slip and ultimate bond stresses with corresponding slips are statistically analyzed, the bond-slip constitutive relations between plain steel bar and MSC were obtained.

Introduction

With the supply of natural sand face the exhausted situation in recent years in China, The replacing products especially the machine-made sand has successively occupied the sand market [1]. However, machine-made sand has many characteristics different from natural sand, and the design codes for concrete structures in china are made on the basis of natural sand concrete. Many fundamentals researches have not realized that the machine-made sand would affect the properties of concrete[2~5]. One of them is the bond properties of steel bar with MSC. The experimental studies of plain steel bar with MSC are carried out by the authors of this paper.

Experimental

The mixture of MSC comprised ordinary silicate cement in 42.5 grade, crushed stone in 5~31.5mm particle size and zone 2 continuous particle grading, machine-made sand of crushed limestone with different content of stone powder, high-performance water reducer and tap-water. Their properties are listed in Table 1 to Table 3. The MSC in three strength grades were designed to cast the specimens, their mix proportions are listed in Table 4.

Table 1 Main properties of cement

Strength grade	Fineness (%)	Standard consistence (%)	Setting time (min)		Compressive strength (MPa)		Flexural strength (MPa)	
			Initial	Final	3d	28d	3d	28d
42.5	359	27.8	166	232	27.1	46.3	5.3	8.4

Table 2 Main properties of stone

Apparent density (kg/m^3)	Closed-volume density (kg/m^3)	Bulk density (kg/m^3)	Crushed index (%)	Needle-pieces content (%)	Mud content (%)
2723	1624	1456	8.0	3.5	0.6

Table 3 Main properties of machine-made sand

Content of stone powder (%)	Fineness modulus	Apparent density (kg/m^3)	Bulk density (kg/m^3)	Closed-volume density (kg/m^3)	*MB* (g/kg)
6.75/9/13	3.03/2.88/2.62	2744	1550	1750	0.75

Table4 Mix proportion and mechanical properties of MSC

No. of concrete	Water to cement ratio	f_{cu} (MPa)	f_t (MPa)	Sand ratio (%)	Water (kg/m^3)	Cement (kg/m^3)	Stone (kg/m^3)	Sand (kg/m^3)
JA	0.56	41.4	4.18	42	170	303	1117	809
JB	0.44	49.6	4.27	32	180	409	1265	595
JC	0.32	69.2	5.48	28	175	547	1244	484

The plain steel bar of 16mm diameter was PHB310 with 303.3MPa yield strength, 419.4MPa ultimate strength and 42.5% elongation after fracture.

14 groups of test specimens as shown in Fig. 1 were cast, each group comprised 3 specimens. The plain steel bar was placed at the center of the cross section. To eliminate the influences of non-uniform restraining of free-ends concrete on the bond properties, the unbounded lengths of 35mm of these bars were enclosed by PVC tubes at the ends of specimens. The total length of each plain steel bar of tensile side was determined by the arrangements of slip measure, load sensor and loading jack. The cross section of specimens was 150mm×150mm, the length L of specimens comprised the bond length l_a and the total unbounded length of 70mm, as listed in Table 5. Meanwhile, the standard cubes in 150mm dimensions accompanied the specimens to value the strength grade of MSC.

Table 5 List of specimens

No. of specimens	Ratio of cement to stone power	Content of stone powder (%)	l_a (mm)	L (mm)
JA80/JA160/JA240/JA300	5.55	6.75	80/160/240/300	150/230/310/370
JB80/JB160/JB240/JB300	10.18	6.75	80/160/240/300	150/230/310/370
JC80/JC160/JC240/JC300	16.74	6.75	80/160/240/300	150/230/310/370
$JB80_1$/ $JB80_2$/$JB80_3$	10.18/7.64/5.28	6.75/9/13	80	150

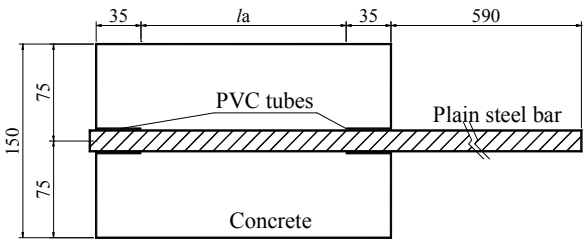


Fig. 1 Side view of specimen

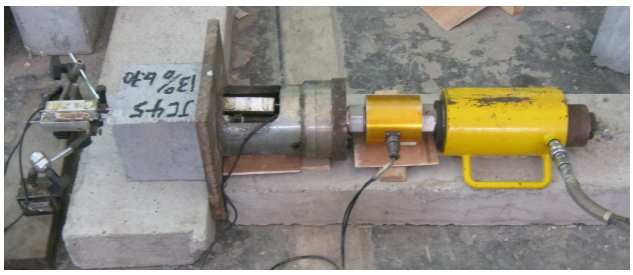


Fig. 2 Picture of Pull-out test

The tests were conducted according to the central pull-out method [6]. As shown in Fig. 2, the plain steel bar was centrally pulled out of the concrete by the oil-pressure jack. The load was measured by the sensor. The slip at free-end of plain steel bar was measured by two displacement sensors respectively corresponding to the end of plain steel bar and the surface of concrete. The slip at tensile-side of plain steel bar was measured by one displacement sensor fixed on the bar touching the concrete surface, in which the elastic elongation of plain steel bar in segment from the section fixing sensor to the bond section at tensile side was measured. All the data were automatically recorded by the computer.

Discussion of Test Results

As tensile load reached ultimate load, all of plain steel bars in the MSC were pulled-out, in which the plain steel bar yielded in the groups JB300, JC160, JC240 and JC300.

The bond stress is calculated by using the tensile load divided the bond surface area of plain steel bar. Average the ultimate bond strength of 3 specimens of one group to get the characteristic strength of each group. Slips at free end and tensile side of plain steel bar corresponding to the ultimate bond strengths are got by the same way. The bond stress-slip curves of JA, JB and JC are drawn in Fig. 3, where the groups of which bond lengths are 80mm, 160mm, 240mm and 300mm corresponded to the

horizontal abscissa value of starting points are 0.0, 0.5, 1.0 and 1.5.The measured values of characteristic strength and slips are listed in Table 6, in which $\tau_{u,a}$ is the average ultimate bond stress, $s_{f,a}$ and $s_{t,a}$ are the average of slips at free end and tensile side of plain steel bar corresponding to the ultimate average bond stress respectively.

Table 6 Characteristic values of bond-slip curves of specimens in different bond length

No.	JA80	JA160	JA240	JA300	JB80	JB160	JB240	JB300	JC80	JC160	JC240	JC300
$\tau_{u,a}$ (MPa)	1.55	1.40	1.48	1.23	1.97	2.38	2.32	3.51	3.25	4.74	4.32	3.49
$s_{f,a}$ (mm)	0.24	0.38	0.36	0.37	0.46	0.71	1.11	0.24	0.57	0.99	0.19	0.36
$s_{t,a}$ (mm)	0.23	0.48	0.44	0.57	0.60	0.83	1.26	2.46	0.61	1.46	1.17	3.59

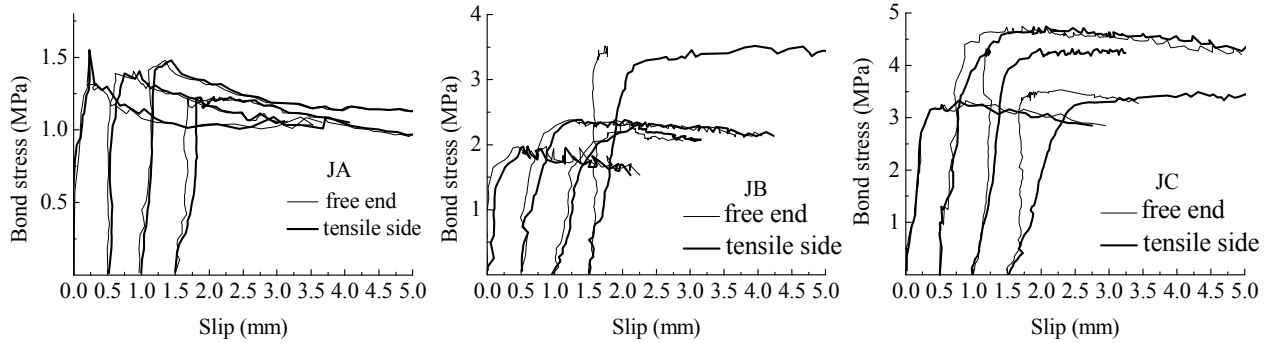


Fig. 3 Bond stress-slip curves of specimens with different bond length

In groups of JA, with the bond length increase, the shapes of the average bond stress-slip curves become more and more flat and the bond strength shows a slightly lower trend. Moreover, the slips at tensile side of plain steel bar corresponding to the ultimate bond strength have a few increase, while which at free end have a slower change. The bond strength and slips of JB have not significant changes except JB300, which has higher bond strength. In the groups of JC, the bond strength reduced dramatically with the bond length increase except JC80. So we have reasons to believe that the bond strength will become higher when the plain steel bar yield and the bond strength would have a few reduce with the bond length increased no matter the plain steel bar yield or not.

The average bond stress-slip curves of JB1/JB2/JB3 are drawn in Fig. 4. The stone powers contents of them are 6.75%, 9% and 13% corresponded to the horizontal abscissa value of starting points are 0.0, 0.5 and 1.0.The actual values of characteristic strength and slips are listed in Table 7. With the stone power content increasing, the ultimate bond strength and residual strength reducing obviously, the slips at free end and tensile side of plain steel bar corresponded to the bond strength become small and the decline parts of bond-slip curves become steep.

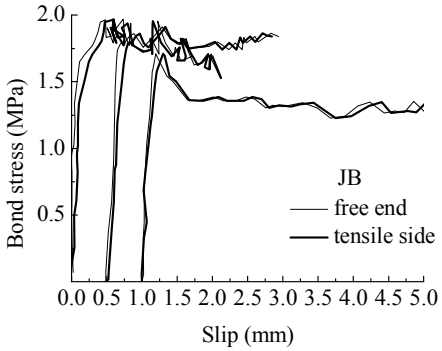


Fig. 4 Influence of stone powder in machine-made sand on bond behavior

Table 7 Test characteristic values of bond-slip curve in different content of stone powder

No.	Content of stone power (%)	τ_u (MPa)	s_f (mm)	s_t (mm)	$\tau_{u,0}$ (MPa)	$s_{f,a}$ (mm)	$s_{t,a}$ (mm)
JB	6.75	1.86/2.07/1.97	0.61/0.34/0.47	0.73/0.42/0.60	1.97	0.48	0.59
	9	1.55/2.07/1.96	0.32/0.59/0.24	0.38/0.65/0.38	1.86	0.39	0.47
	13	1.33/1.68/2.12	0.17/0.24/0.18	0.34/0.30/0.26	1.71	0.20	0.30

The cement to stone power ratios in MSC are calculated by the mix proportion of MSC (Table4), the cement to stone power ratio reduces with the content of stone power increases. The stone power mainly has the filling effect in MSC [7], the cement played the cohesive action will reduce in per unit bond area as a result. Moreover, as the cement content per unit volume has no change, the paste content increases with the content of stone power increase. With growth of the stone power content, elastic modulus of MSC reduces [7-9] and bond strength reduces too.

Considering the test date listed in Table 6 and the tensile strength f_t of MSC calculated by the formula [10]

$$f_{t,c} = 0.207 f_{cu,0}^{0.734} \tag{1}$$

The statistical results of characteristic values are listed in Table 8.

The ratio of bond strength to tensile strength increases with the growth of strength grade. As shown in Table 4, when the content of stone power is 6.75%, the ratio of cement to stone power would reduce with the strength grade of MSC increase. It also shows that the stone power has a negative effect on the bond properties between plain steel bar and MSC.

Table 8 Statistical results of characteristic values of bond-slip curves

Strength grade of concrete	$\tau_u/f_{t,0}$		$\tau_u/f_{t,c}$		Mean value
	μ	δ	μ	δ	$\bar{\mu}$
JA	0.467	0.153	0.356	0.153	0.412
JB	0.742	0.296	0.632	0.296	0.687
JC	0.822	0.145	0.696	0.145	0.759

Based on the test result, the bond-slip constitutive relation between plain steel bar and MSC is proposed as follows

$$\tau = \frac{2x^{0.05 f_t} - 1}{x^{0.03 f_t}} \tau_u \qquad (0 < x \le 1) \tag{2}$$

$$\tau = \frac{x^3}{(0.1 f_t)^3 \cdot (x-1)^3 + x^3} \tau_u \qquad (x > 1) \tag{3}$$

While $x=s/s_u$, s is the slip, s_u is the slip corresponding to ultimate bond strength, here it is the average of the slips between free end and tensile side of plain steel bar. τ_u is the ultimate bond strength and f_t is the concrete tensile strength.

Corresponding to the concrete strength grade of JA, JB and JC, the values of τ_u are $0.412f_t$, $0.687f_t$ and $0.759\,f_t$, the values of s_u are $0.0018l_a$, $0.005l_a$ and $0.0088l_a$.

τ~s relation curves calculated by bond-slip constitutive relation are drawn in Fig. 5 (the thick real line），while tensile strength is averaged by measured data $f_{t,c}$ and calculated date $f_{t,0}$.The measured τ~s curves are also drawn in Fig. 5.

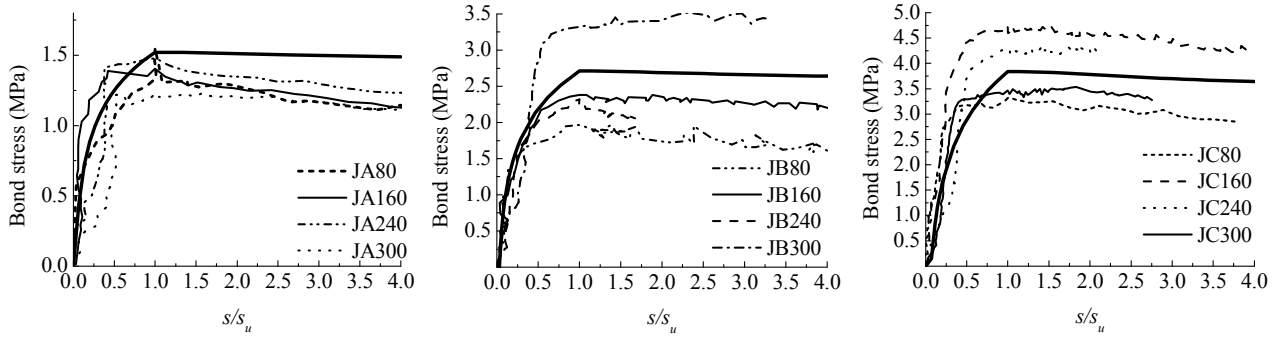


Fig.5 Comparison of constitutive relationship of bond-slip

Conclusions

The bond properties are studied by the central pull-out test, considering the influence of bond length and the stone powder content in machine-made sand. With bond length increasing, ultimate bond strength has no significant change, slips at tensile side of plain steel bar corresponding to ultimate bond strength has some growth ,while which at free end has a slower growth.

With the content of stone power in machine made sand increases, ultimate bond strength and residual bond strength reduces to some extent, the slips at free end and tensile side of plain steel bar decreases, the decline parts of bond-slip curves become steep.

Acknowledgements

The authors thank to the financial supports of the Scientific and Technical Leader Raising Plan of Zhengzhou City, China (096SYJH23105); the Technical Plan Project of Education Department of Henan Province, China (2010A560011).

References

[1] Chinese Standard GB/T14684-2001: Sand for Building. China Building Industry Press, Beijing, 2001.

[2] S. Zhao, M. Xia and C. Liu: Journal of Railway Science and Engineering, 2 (2006) 15-20.

[3] S. Zhao, C. Liu, J. Ren and C. Li: Central-south Highway Engineering, 2 (2006) 37-41.

[4] X. Zhang, X. Ding, S. Zhao and Z. Ge: Applied Mechanics and Materials. Vols. 71-78 (2011) 4361-4364.

[5] F. Li and Q. Zhu: Advanced Materials Research, Vols. 152-153 (2011) 1479-1482.

[6] Chinese Standard GB50152-92: Standard of Test Method for Concrete Structures, China Building Industry Press, Beijing, 1992.

[7] F. Li, Q. Zhu and Y. Xu: Concrete, 2 (2010) 84-86.

[8] F. Li, Q. Zhu and Y. Xu. Water Resources and Hydropower Engineering, No. 7 (2010) 76-78.

[9] F. Li, Q. Sun and Q. Zhu: Journal of Yangtze River Scientific Research Institute, 8 (2010) 66-69.

[10] F. Li, Y. Zeng and C. Li: Advanced Materials Research, Vols. 418-420 (2012) 441-444.

© (2012) Trans Tech Publications, Switzerland
doi:10.4028/www.scientific.net/AMM.238.147

Influence of Aggregate Gradation of Coarse Aggregates on Concrete Strength

Wei Xie [a], Dengkui Yuan [b] and Shushan Li [c]

North China University of Water Resources and Electric Power, Zhengzhou 450011, China

[a] xiewei@ncwu.edu.cn, [b] yuandengkui2010@126.com, [c] lishushan@ncwu.edu.cn

Keywords: concrete; maximum aggregate size; compressive strength; flexural strength.

Abstract. Concrete is widely used in engineering construction, and studying how to improve the strength of concrete is particularly important. The coarse aggregate is one of the elements in concrete, its property affects the strength of concrete prominently. The effect of coarse aggregate size distribution on the development process of concrete strength was studied, while keeping the constant content of coarse aggregate and altering the size distribution of coarse aggregate and the water to cement ratio. The experimental results show that when the maximum aggregate size is 10mm, 20mm and 30mm respectively, the compressive strength of concrete will be increased, and the flexural strength of concrete will be reduced.

Introduction

Concrete is the backbone of the development of modern civilization, with the rapid development of engineering construction, the amount of concrete will be increased year by year, therefore, the concrete strength requirements are also increasing.

The strength of concrete depends on three main parts, cement, aggregate and interface transition zone. In order to improve the strength of concrete, we must consider the three factors. The aggregate as the concrete skeleton, accounting for about three-quarters of the concrete volume, is the very important composition of concrete. In this paper, the mechanical properties of concrete test analyzes the impact of the concrete compressive strength and flexural strength， while altering the coarse aggregate size distribution, It can guide the mix proportion design in project.

Overview of the Test

Properties of Materials. There is a grade 42.5 ordinary Portland cement supplied by Zhengzhou Tianrui Cement Plant, the physical mechanic property is shown in table 1. The gradation of gravel stone is from 5mm to 30mm, configuration in accordance with a certain proportion. Xinyang river sand is used as the fine aggregate, and its modulus of fineness is 2.9. The Zhengzhou city tap water is used as Test water. JKH-1 superplasticizer is made by Henan Jiancai, appropriate mixing content is 0.5%~1%. The optimal mixing content is making the concrete slump between 10~50mm.

Table 1 Physical mechanics property of cement

Fineness [%]	Standard consistency [%]	Setting time [min]		Compressive strength [MPa]		Flexural strength [MPa]	
		Initial set	final set	3-day	28-day	3-day	28-day
3.7	28	170	230	25.0	51.3	4.7	8.9

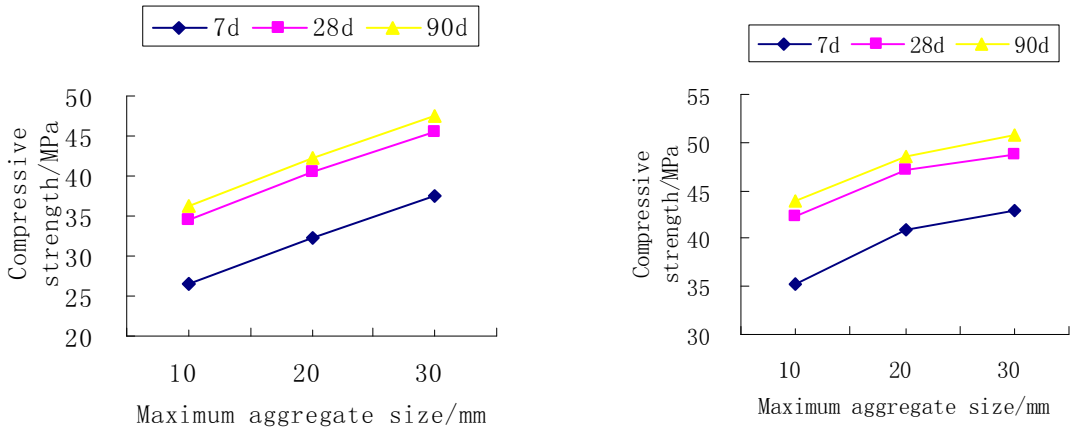
Test Design. In the compressive strength test, three concrete specimens with the size of 150mm×150mm×150mm each group have been made. In the bending strength test, three concrete specimens with the size of 100mm×100 mm×400mm each group have been made. All specimens are conserved in the standard curing conditions. By artificial screening，we have three particle size rangesranges 5-10mm, 10-20mm, 20-30mm. The proportion of aggregate size and the mixture ratio of concrete are listed in Table 2.

Table 2 The mixture ratio of concrete

Strength grade	W/C ratio	Maximum aggregate size (mm)	Materials consumption（kg /m^3）							
			Water	Cement	Sand	5-10	10-20	20-30	Sand ratio	Super plasticizer
C30	0.5	30	148	296	733	191.36	287.04	717.6	38%	1.5
	0.5	20	148	296	733	478.4	717.6	——	38%	1.5
	0.5	10	148	296	733	1196	——	——	38%	1.5
C40	0.4	30	146	365	689	194.24	291.36	728.4	36%	3.65
	0.4	20	146	365	689	485.6	728.4	——	36%	3.65
	0.4	10	146	365	689	1214	——	——	36%	3.65

Results and Discussion

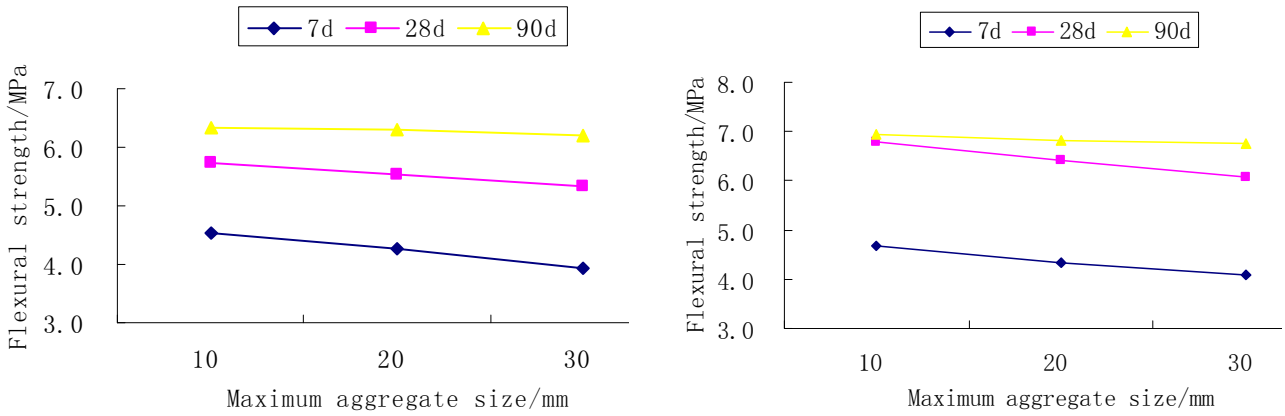
Compressive Strength. Water cement ratio, age, the maximum aggregate size of the three factors on the cube compressive strength is shown in Fig. 1. With the increasing of age, the concrete strength growth trends have been basically completed before 28 days, there have less growth after 28 days. When the water-cement ratio is 0.5, the maximum aggregate size of 10mm, 20mm, 30mm, the ratio of compressive strength is 1:1.18:1.32 in 28 days; When the water-cement ratio is 0.4, the maximum aggregate size of 10mm, 20mm, 30mm, the ratio of compressive strength is 1:1.11:1.15 in 28 days. From figure (a), the water-cement ratio is larger, its internal surface area will make the smaller particle size of coarse aggregate concrete's visible cementitious materials reduce, resulting in appearing the weak interfacial transition zone, so the compressive strength of concrete will be reduced; From diagram (b), the water-cement ratio is smaller, the amount of cementitious materials is relatively large, but the interfacial transition zone is still a factor restricting the concrete compressive strength, only the rate of increase is smaller. When the water-cement ratio is 0.5 and 0.4, both of them should adopt the maximum particle size of coarse aggregate is 30mm.



(a) water-cement ratio is 0.50 (b) water-cement ratio is 0.40

Fig. 1 Relationship between compressive strength and maximum aggregate size

Flexural Strength. Water cement ratio, age, the maximum aggregate size of the three factors on the flexural strength is shown in Fig. 2. With the increase of age, the concrete strength growth trends have been basically completed before 28 days, there have less growth after 28 days. With the maximum aggregate diameter increasing, keeping water-cement ratio constant, the flexural strength of concrete will be decreased. Because the gravel particle size increases the surface area of a single block of particles, it is easy to appear segregation and bleeding, so the adhesive force of interfacial transition zone will be reduced. The concrete structures are more likely to crack, most of the specimen fracture will run along the interface failure. When the water-cement ratio is 0.5 and 0.4, the maximum particle size of coarse aggregate is 10mm.



(a) water-cement ratio is 0.50 (b) water-cement ratio is 0.40

Fig. 2 Relationship between flexural strength and maximum aggregate size

Conclusions

The strength of concrete depends primarily on the size of the water-cement ratio. The smaller is water-cement ratio, the bigger is concrete compressive strength and flexural strength. The concrete strength growth trends have been basically completed before 28 days, there have less growth after 28 days.

The maximum aggregate size has greater impact on the strength of concrete. Through the analysis of experimental data, a reasonable choice of maximum aggregate size can improve the compressive strength and flexural strength of concrete. But for different water-cement ratio, the maximum aggregate size for the strength magnitude is different.

This article only study that when the water-cement ratio is 0.5 and 0.4, the maximum aggregate size have the impact on strength, lacking of experimental study on the mechanical properties of high strength concrete, so it still need to study the concrete strength in the case of small water-cement ratio.

Acknowledgements

This work was supported by Innovation Scientists and Technicians Troop Construction Projects of Zhengzhou City (112PLJRC354) .

References

[1] SL 352-2006, Test Code for Hydraulic Concrete, China Waterpower Press, Beijing, 2006.

[2] T. Y. Lyubimove, E. R. Pinus, Crystallization structure in concrete contact zone between aggregate and cement in concrete, Cement and Concrete Research, 24 (1962) 491-498.

[3] B. Dannys, C. G. Andre, B. Gerard, et al, Contribution to the formation mechanism of the transition zone between rock-cement paste, Cement and Concrete Research, 23 (1993) 335-346.

[4] P. K. Mehta, P. J. M. Monteiro, Concrete microstructure, properties and materials, Indian Concrete Institute, Indian, 1997.

© (2012) Trans Tech Publications, Switzerland
doi:10.4028/www.scientific.net/AMM.238.150

Influence of Surface Treatment of Testing Specimens on Spacing Factor

Michaela Kostelecká[1, a] and Jiří Kolísko[2, b]

[1]Klokner Institute, Czech Technical University in Prague, Czech Republic

[2]Klokner Institute, Czech Technical University in Prague, Czech Republic

[a]michaela.kostelecka@klok.cvut.cz, [b]jiri.kolisko@klok.cvut.cz

Keywords: spacing factor; microscope Lext OLS3000; surface treatment.

Abstract. The measurements of spacing factor on different surfaces are demonstrated. Using of the confocal laser raster microscope Lext OLS 3000 for the spacing factor measurement is described. The different surface treatments and their influence to the spacing factor determination are discussed.

Introduction

The spacing factor value greatly influences frost resistance of materials.
The spacing factor is determined on the basis of standard ČSN EN 480 – 11 [1], which defines method of testing for determining the structure of air void in specimen of aerated hardened concrete. Air void structure is described by the following parameters: total air content, paste content, specific surface of air void system, spacing factor, air void distribution and micro air content.

The article deals with comparison of spacing factor results on polished and unpolished surface of specimens, which are measured with confocal laser microscope.

Measuring Equipment

The value of spacing factor was determined using the confocal laser raster microscope Lext OLS3000.

The Olympus company has developed the Lext OLS3000 microscope (see Fig. 1) — a new confocal laser scanning microscope for ultra-precise measurement and observation with the highest levels of reliability. No vacuum pump down or special sample preparation are required, and the sample can be placed directly on the microscope stage as it is. Both 3D observation and high-precision 3D measurement are possible in real time. With much higher resolution than conventional optical devices but just as many different observation methods, every user can make quicker, more accurate specimen analyses all based on a strict traceability system. The Lext microscope, as a next-generation analysis device, is ideally suited for the ultra-fine surface observation and measurements required for micro fabrication devices like MEMS (Micro Electro Mechanical System), for new materials development, and for today's thinner devices, with more compact surface mounting requirements.

The microscope Lext works with magnification from 120x to 14400x. The basic principle of imaging by the microscope is that the image is not created at once, but it is scanned in lines as point by point. It is used for imaging in XY plane. For creation of 3d images the precise displacement resp. shift of the lens along the Z axis is used.

Measuring Method

The concrete bodies were cut out of load-bearing elements produced on vibration pressing machine. They were used for measuring and the maximum grain of stone was 16 mm. Size of testing specimens are given in Table 1. Two sets of measuring were carried out on the same specimens. The difference was in surface treatment. We used polished surface in the first set, and unpolished surface in the second set of measuring. The second set of measuring was carried out on the specimens from the first set, but their surface was grinded while wet. After that, surfaces were cleaned with a brush and then they were polished according to the standard ČSN EN 480 – 11 [1] until dry lustreless shine was

created. The purpose of this preparation is to created a surface suitable for microscopic structure examination of air void in concrete. The actual measuring of spacing factor was conducted so that a system of measuring lines was marked on the specimens. The lines were parallel with distance of 6 mm. The total minimal length of measuring lines must be 2400 mm. These measurements were used to determine initial values for calculations – the total length of chords over air voids and the total length crossing solid state. The sum of these lines crossing the air voids and the solid states represents the total length of the system of measuring lines (2400 mm).

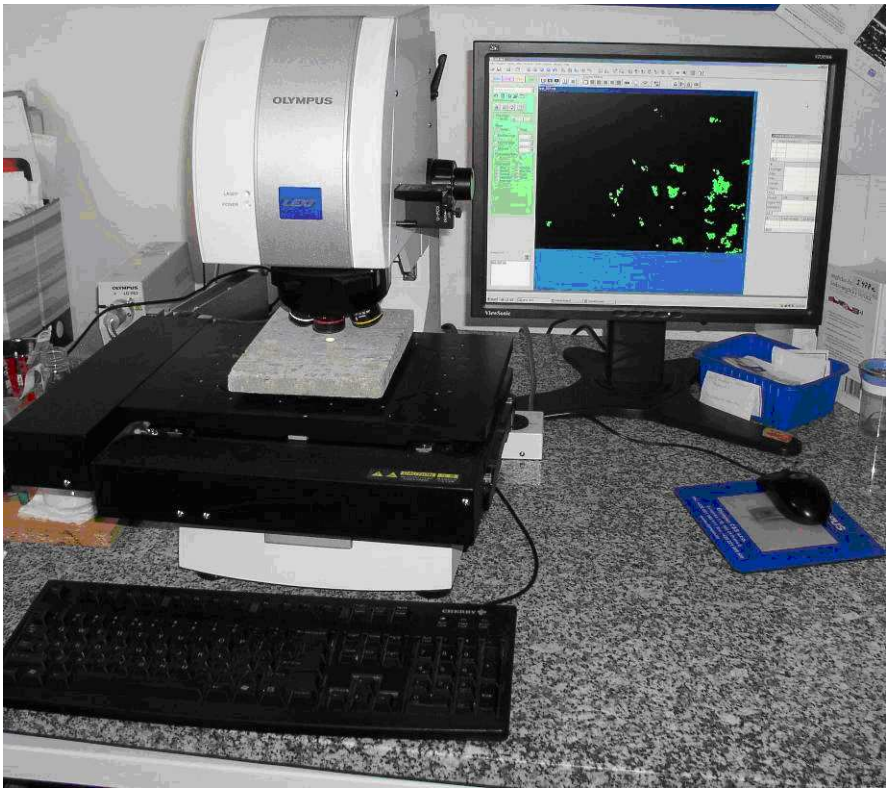


Fig.1 Setup of testing

Table 1 Dimensions and volume weights of samples

Label of specimens	Size			Weight of specimens [g]	Volume weight [kg/m^3]
	length [mm]	width [mm]	thickness [mm]		
1	190	150	22	146,7	2340
2	192	149	21	138,6	2310
3	190	150	23	148,1	2260
4	191	151	22	135,8	2140

Results of Measuring

The results of measuring are stated in Table 2. The measured values of spacing factor on unpolished surface of specimens are in the first column. The second column shows values measured on polished surface of specimens.

Table 2 Comparison of coefficients of the spatial distribution of the air pores

Label of specimens	Unpolished surface [mm]	Polished surface [mm]
1	0,23	0,23
2	0,14	0,13
3	0,17	0,21
4	0,16	0,16

The article presents measuring of spacing factor on four testing specimens, the focus was on the influence of surface treatment on spacing factor. The results measured by confocal microscope Lext on specimens with polished and unpolished surface are very similar. The difference is only in the result of specimen 3 (see Table 2). The reason of different result could be caused by irregular distribution of air voids in specimen 3. The above mentioned shows that it is not necessary to polish a testing specimen when using the Lext microscope, which is caused by the fact that we work with planar, not voluminal air voids when determining the value of spacing factor. Nevertheless, the standard [1] requires surface treatment of specimen by grinding and polishing. The Lext microscope works on the principle of scanning so that the range between the highest and the lowest scanned place is divided into several optical cuts, which are later connected in one unit. The testing specimens were cut from parts intended for load-bearing wall. The parts were made by vibrating; it is therefore not common aero concrete. The presented results may be influenced by this fact. That is why another comparative measuring will be conducted on specimens of aero concrete.

Organisation of the interlaboratory testing could bring another interesting comparison.

Conclusions

The article deals with spacing factor measurement. It is written for help of students and industrial workers. Spacing factor is pores distribution in system, i.e. size, shape and connection of pores. It has mainly influence on frost resistance, absorbability and permeability of silicate composites, i.e. concrete and mortar. For example sufficient content of micro-pores for frost resistance of concrete is to 300 micrometer. Check of size and distribution of pores in concrete is carried out according to Czech and European standard ČSN EN 480-11.

Measurements were carried out on four identical test specimens. First unpolished specimen surface was measured and in the second step polished surface of tested specimens was observed. Modern 3D confocal laser microscope Lext OLS3000 (see Fig. 1) was used for observation of all tested specimens. From the experimental results follow, spacing factors for polished and unpolished surface has practically same values. These parameters are listed in Table II. Only third specimen take the different value (see Table II). In homogeneity distribution of air pores in test specimen No. 3 can be occasion above mentioned difference. Other reason of differences it can be sampling. Test specimens were cut-off from element given for retaining wall. Elements were produce by vibro-pressing. This mean the specimens are not made from commonly aerated concrete. This fact can influence accuracy of these experimental results.

Acknowledgements

The research has been supported by Grant P105/12/GO59.

References

[1] ČSN EN 480 – 11, Admixtures for concrete, mortar and grout – test methods – Part 1: Reference concrete and reference mortar for testing. (in Czech)

[2] M. Kostelecká, J. Kolísko, Application of Confocal Scanning Microscope LEXT OLS3000 to Determine of Porosity of Materials, International Conference Construmat , Brno, Czech Republic, pp. 121, ISBN 97880-214-3660-2.

© (2012) Trans Tech Publications, Switzerland
doi:10.4028/www.scientific.net/AMM.238.153

Investigation of Corrosion of Cement-Based Materials by Using of Rotating Disc Method

Daniel Dobiáš [a]

Czech Technical University in Prague, Klokner Institute, Šolínova 7, 166 08 Prague 6, Czech Republic

[a]daniel.dobias@klok.cvut.cz

Keywords: corrosion resistance; cement-based materials; rotating disc method; flowing environment.

Abstract. The paper introduces the rotating disk method, its features and the scope of application. It also describes the application of this technique in the research of corrosion of cement-based materials caused by aggressive liquid solutions and the effect of flow of solutions on the corrosion rate.

Introduction

Rotating disc shows a number of advantages compared to other systems. Disc rotating in a liquid represents a system with a three-dimensional axially symmetric flow. The most important feature is the definability of hydrodynamic conditions, as for the rotating disk system there exists a precise solution of Navier-Stokes equations. For the two-dimensional flow along a flat plate or in a tube only approximate calculation is possible. From the solution of these equations follows, that in a newtonian liquid the mass flow to the disc surface as well as the diffusion boundary layer are invariable along the surface of disc. Therefore the mass transport proceeds with invariant rate in every point of disc surface. On the flat plate or in the tube the diffusion layer changes with the distance from leading edge [1, 2].

The rotating disc method can be successfully used for the investigation of properties of silicate systems, for instance the investigation of chemical reaction between the inorganic binder such as cement or gypsum and the surrounding aggressive liquid environment. In the concrete sphere, processes occurring in this interaction are according to analogy with metals called corrosion. In natural conditions and mainly in industrial sphere (use of concrete in chemical industry) most frequently the corrosion of type I and II occurs. These types of corrosion consist in dissolution of some concrete components by aqueous solutions with very low salt content and also with the action of some acids and salt solutions, such as NH_4Cl etc.

Concrete is not completely dense. The mass is filed with a capillaries and pores of different shape and sizes. During the action of substances causing the corrosion of type I and II the corrosion front moves towards the inside of material. On the surface a layer of reaction products begins to form, through which the dissolved compounds pass towards the surface (so called internal diffusion) and then to the bulk solution (external diffusion).

In the contact zone between the solution and the hydrated cement chemical reactions take place. The corrosion rate is apparently controlled by the speed of the slowest process, which is either the speed of mass transport or slowest chemical reaction.

If the process occurs in the range of external diffusion, it is possible to determine the characteristics of external diffusion, diffusion flow and diffusion coefficient.

During the transition to the internal diffusion range, when the process is controlled by the transport of mass in the pore structure of the hardened cement paste or a layer of reaction products, it is possible to calculate the internal diffusion coefficient as well as a diffusion flow. These characteristics determine the properties of hardened cement paste or concrete.

The rotating disc method enables one to determine which process is the decisive one, and based on the experimental quantitative data it is possible to determine characteristics of investigated materials in the early stages of corrosion.

Experimental Apparatus Description

Experimental setup (Fig. 1) for the rotating disc testing usually consists of three main parts:

- Unit that brings the disc into rotation,
- Suitable disc specimen,
- Working vessel.

To maintain the conditions required by theoretical basis, the experimental setup must fulfil some elemental requirements.

The unit that keeps the disc spinning must:

- Keep the rotating speed constant during the experiment,
- Enable one to choose within a wide range of revolution count,
- Be equipped with a precise revolution counter,
- Make it possible to fasten the disc to the machine without any radial or axial vibrations.



Fig. 1 Experimental setup in detail

There are also some requirements for the disc holder. Several precise measurements were made from which followed that a bell-shaped holder or a shape of infinite cylinder give the results nearest to those presumed by theory (Fig. 2). Non-willing additional disturbing flows occur when using other holder shapes, which causes the results to vary more or less from the theory.

Experimental Procedure for Testing the Corrosion Resistance

In the pilot testing of building materials corrosion resistance a paste made of Portland cement CEM I 42,5 was chosen for the preparation of specimen. The water to cement ratio was set to 0,35. Series of rounded plates - discs were prepared from a tested binder. The discs were cast in plastic forms of suitable dimensions (diameter and thickness). Specimens were left in the forms for 24 hours in damp environment. Then they were demoulded and put in back in wet environment. In a specified moment the specimens were brought out and fixed in a holder, the shape of which should comply the above mentioned requirements (Fig. 3). A silicone putty was used for gluing and sealing the disc to the holder.

After fixing the disc, the holder was fastened to the apparatus and the rotation in the liquid environment started. Four different rotation counts were chosen: 250, 590, 900, 1370 rpm.

Short-term tests (the rotation duration: 8 hours, the experiment duration: 24 hours) as well as long-term tests (the rotation duration: 35 hours, the experiment duration: 194 hours) were performed in the course of experimental works.

Distilled water (water with a low salt content) was chosen as a corrosive liquid then a solution 0,03 % of HCl (acid environment) and a solution of ammonium sulphate in the concentration 2000 mg/l NH_4^+ (a corrosion by ammonium salts) were used, too. In specified time intervals a small amount of the liquid solution was taken out and analyzed by a proper method. The differences of the chemical concentration of the investigated material in the bulk solution, the amount of the eluted material, were noticed.

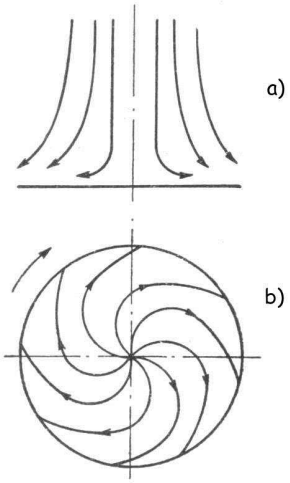


Fig. 2 Liquid flow around the rotating disc [3]
a) under the disc b) close to the surface



Fig. 3 Rotating disc holder

Results and Discussion

The results of short-term experiments show that the rate of a cement paste dissolution (in four different flowing regimes were used - 250, 590, 900, 1370 rpm) does not fulfil the common dependence on the square root of an angular velocity. In the faster flowing regimes the dissolution speed was slower than what was expected from this theoretical relation.

The results of long-term experiments show that with the graduation of a corrosion process towards the inside of a material the corrosion rate slows-down as well as the influences of flowing regimes to the speed of the corrosion process. The process started to be limited by the speed of an inner diffusion between a solid-liquid interface and a corrosion rate. The affected layer made a protective barrier decreasing the corrosion rate. This effect is well illustrated by an increasing progress of a released amount of Ca^{2+} (Fig. 4).

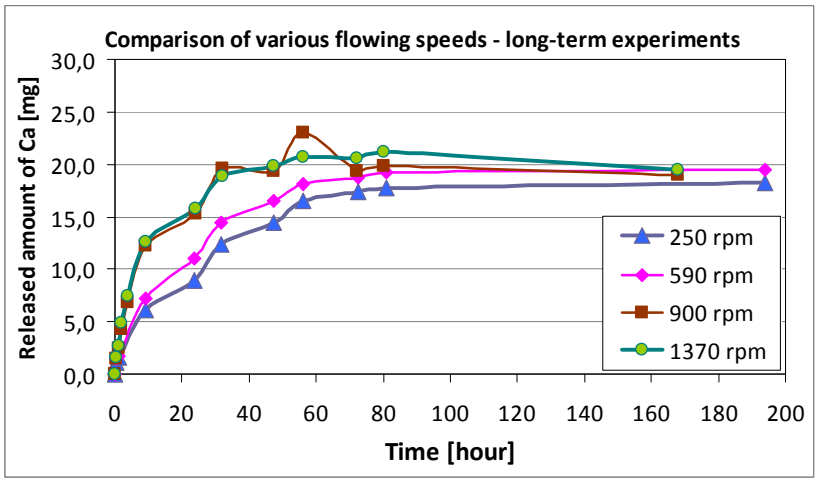


Fig. 4 Comparison of time progress of released amount of Ca^{2+} for various flowing speed

The curves gradually come together in various flowing regimes and growths of an amount of ions in the liquid solution are almost independent on the flowing speed of the media.

The above mentioned effect is highlighted in case of using an aggressive solution as an aggressive media (both solution of 0,03 % HCl and solution of ammonium sulphate in the concentration 2000 mg/l NH_4^+). In this case decreasing of a process happened by an inner diffusion even earlier. It was thanks to the aggresivity of the solution which accelerated a process of a corrosion towards the inside of a material. Then was found out that with an accelerating aggressivity of a media increases an impact of the inner diffusion which otherwise affects a process in an initial stages of a corrosion. The released amount of monitored cations is in case of using an aggressive liquid media almost one order higher than in case of using a distilled water (Fig. 5).

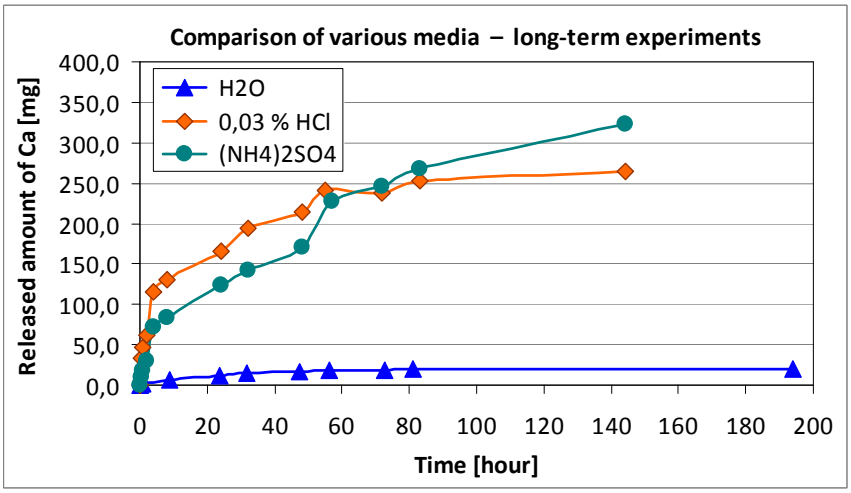


Fig. 5 Comparison of time progress of released amount of Ca^{2+} for various corrosion media

After 365 days, it was also taken out a sample of a hydrous solution from the specimen which was all time left in a non-flowing stable environment of a distilled water. The released amount of calcium ions approximately corresponded to the repeating of 3-5 cycles applied in long-term experiments in a flowing environment.

The dissolution speed of the hardened cement paste specimens that were exposed to a flowing environment was one order higher than of those placed in a non-flowing stable environment. It can be concluded that at least in the initial stages of a corrosion the effect of a flow of a liquid media is very significant.

Acknowledgements

This paper was elaborated with the financial support by the Grant Agency of the Czech Republic in the frame of grant project No. 103/09/1935

References

[1] K. Lund, H.S. Fogler, C.C. Mc Cune Acidization I. The dissolution of dolomite in hydrochloric acid, Chem. Engn. Sci., 30 (1975) 825-835.

[2] H. Schlichting, Boundary-Layer Theory, Mc Graw-Hill, New York, 1968.

[3] A. N. Zelikman et al, Theory of process hydrometallurgy, Metallurgija, Moscow, 1975

© (2012) Trans Tech Publications, Switzerland
doi:10.4028/www.scientific.net/AMM.238.157

Effect of Silica Fume on Workability and Water Impermeability of Concrete

Fuhua Wang [a] and Sen Li [b]

China Road & Bridge Corporation, Beijing 100011, China

[a]wangfuhua123@163.com, [b]li.gu.qiao@163.com

Keywords: workability; water impermeability; concrete; silica fume.

Abstract. A designed experimental study has been conducted to investigate the effect of silica fume on workability and water impermeability of concrete, a large number of experiments have been carried out in this study. The results indicate that the addition of silica fume has adverse effect on the workability of concrete composite. The slump and flowability of the concretes containing silica fume is less than that of the concrete without silica fume, and a considerable decrease for the slump and flow of the concrete was observed by increasing the dosage of silica fume. Besides, the addition of silica fume can improve the water impermeability of the concrete composite evidently, and the water impermeability is becoming better and better as the silica fume content is increasing gradually.

Introduction

Pozzolanic materials are generally able to combine with the hydrated calcium hydroxide $Ca(OH)_2$ forming the hydrated calcium silicate (C-S-H), which is responsible for the strength of hydrated cement pastes. Also an increase in bulk density of concrete results as the mixture voids is filled with very small admixture particles (micro filler effect) [1]. Silica fume is a byproduct of the smelting process in the silicon and ferrosilicon industry. Silica fume consists of very fine vitreous particles with a surface area between 13,000 and 30,000 m^2/kg. Its particles are approximately 100 times smaller than the average cement particle [2]. The silica fume can produce both chemical and physical effects, which cause meaningful changes in the microstructure of concrete. Because of its extreme fineness and high silica content, silica fume is a highly effective pozzolanic material. It has been found that silica fume improves compressive strength, bond strength, and abrasion resistance, and therefore helps in protecting reinforcing steel from corrosion.

Lee conducted the experimental work on both mechanical properties and durability of concrete or mortar incorporating silica fume to investigate the effect of replacement of silica fume on the performance of hardened concrete or mortar [3]. Park et al. studied the effects of the amount of silica fume on the mechanical characteristics of the fluidity, compressive strength, elastic modulus and flexural strength and on the micro structure of UHPC by means of SEM and MIP, and the results revealed that adequate amount of silica fume is improving the fluidity and strength [4]. Zhang et al. [5-7] studied the effect of silica fume on the mechanical properties, flexural properties, fracture properties of fiber reinforced concrete composites containing fly ash. Workability and water impermeability of concrete composite is so important in the mix design and application of concrete composite, especially when the concrete composite is used in underwater environment. However, so far, there is little report about workability and water impermeability of concrete composites containing silica fume. This article reports the investigation of workability and water impermeability of concrete composites containing silica fume.

Experimental Details

Raw Materials. Ordinary Portland cement (Class 42.5R) and silica fume were used in this work. The cement and silica fume properties are given in Table 1. Coarse aggregate with a maximum size of 30 mm and fine aggregate with a 2.82 fineness modulus were used in this experiment. A high range water reducer agent was used to adjust the workability of the concrete mixture. Silica fume was mixed in concrete composites by replacing the same quantity of cement, and the content of silica fume content (by mass) is from 3% to 12%. Mix proportions are given in Table 2.

Table 1 Properties of cement and silica fume

Chemical compositions									Physical properties	
Composition (%)	SiO_2	Al_2O_3	Fe_2O_3	CaO	MgO	Na_2O	K_2O	SO_3	Specific gravity	Specific surface (cm^2/g)
Cement	20.17	5.58	2.86	63.51	3.15	0.12	0.57	2.56	3.05	3295
Silica fume	93.72	0.82	0.48	0.34	1.44	0.40	1.22	0.47	2.30	-

Table 2 Mix proportions of the concrete mixtures

Mix no.	Cement (kg/m^3)	Silica fume (%)	Silica fume (kg/m^3)	Coarse aggregate (kg/m^3)	Fine aggregate (kg/m^3)	Water (kg/m^3)	Water reducer agent (kg/m^3)
1	494.0	0	0	1151	647	158	4.94
2	479.2	3	14.8	1151	647	158	4.94
3	464.4	6	29.6	1151	647	158	4.94
4	449.5	9	44.5	1151	647	158	4.94
5	434.7	12	59.3	1151	647	158	4.94

Experimental Method. The workability of the fresh concrete composites can be evaluated by the parameters of slump and slump flow. The values of slump and slump flow can be measured using a standard slump cone made of thin steel sheet, the height, the diameter of upper open mouth and the diameter of the bottom of which are 300 mm, 100 mm and 200 mm, respectively. After the slump cone was lifted vertically, it should be placed on the flat plate alongside the fresh concrete composite slumped from the slump cone. The difference of the maximum height of the fresh concrete composite and the height of the slump cone was measured as the value of slump. The final maximum and minimum diameters of the spreading fresh concrete composite were measured to calculate the value of slump flow. The larger values of slump and slump flow indicate that the fresh concrete composite has better workability.

A series of frustum specimens with the size of Φ175×150×Φ185 mm were used to determine the water impermeability of concrete composite. The water impermeability of concrete composite can be evaluated by the length of water permeability of the specimen under the action of pressure water. The shorter length of water permeability indicates that the concrete composite has better water impermeability. Before testing, the specimens were cured for 28 days at 100% relative humidity and controlled temperature (21±2 ^{o}C). The tests of water impermeability of concrete composite were carried out by water impermeability instrument in accordance with the Chinese Standard [8]. The side face of the specimens were adhered a layer of sealant, which was made of grease and cement by mixing. The sealant can ensure the tightness between the side face of the specimen and the inwall of the specimen sleeve. The water pressure was controlled at 3.5 MPa, and the floating pressure did not exceed 0.05 MPa. The test should last 24 h before the specimens were taken off from the water impermeability instrument. After the test finished, the specimen was split in half along the longitudinal section on the pressure testing machine. Finally, the average length of water permeability of the specimen can be measured.

Results and Discussion

Effect of Silica Fume Content on Workability. Fig. 1 and 2 show that the varying rules of the slump and slump flow of concrete composite with the increase of silica fume content, respectively. As can be seen from the figures, in general, the addition of silica fume can decrease the slump and slump flow of the concrete composite, which indicates that the addition of silica fume has adverse effect on the workability of concrete composite. Compared with the concrete composite without silica fume, the decrease of the slump and slump flow were determined as 14% and 33.3% for the concrete composite with 12% silica fume content respectively. With the increase of silica fume content, both of the slump and slump flow are decreasing gradually, however, the effect of silica fume on the slump

is not obvious when the silica fume content is less than 6%. There is great decrease in the slump when the silica fume content increases from 6% to 9%, and the decrease rate in the slump becomes smaller after the silica fume content exceeds 9%.

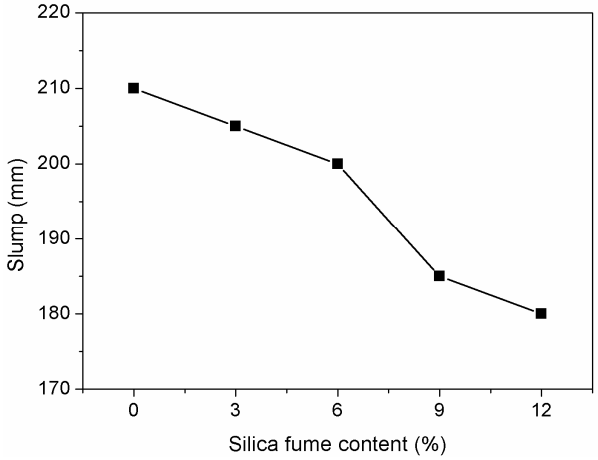


Fig. 1 Effect of silica fume content on slump

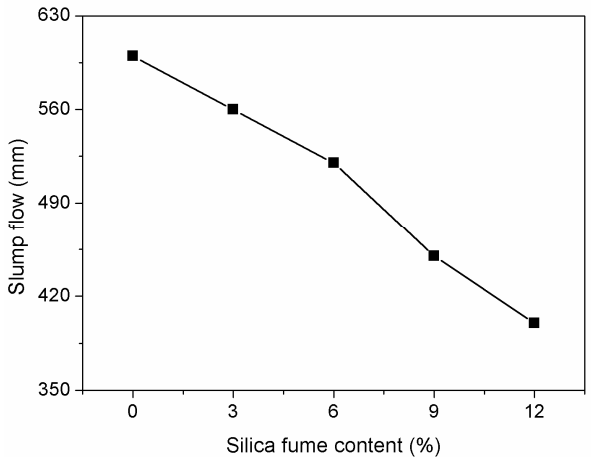


Fig. 2 Effect of silica fume content on slump flow

Effect of Silica Fume Content on Water Impermeability. The variations of the length of water permeability of concrete composite versus silica fume content of the water permeability specimen are illustrated in Fig. 3. A considerable decrease for the length of water permeability of the concrete was observed by increasing the content of silica fume. Compared with the mix without silica fume, the decrease was determined as 63% for 12% silica fume content. As seen from the variation curve, the decreasing speed of the length of water permeability is very high before the silica fume content is less than 3%, and the decreasing speed of the the length of water permeability becomes lower with the silica fume content increasing beyond 3%. The main reason of silica fume can improve the water impermeability of concrete composite is that silica fume can take part in hydration reaction to produce more hydrate and decrease the porosity of concrete composite in the early hydration of cement. Therefore, the addition of silica fume can improve the water impermeability of concrete composite evidently.

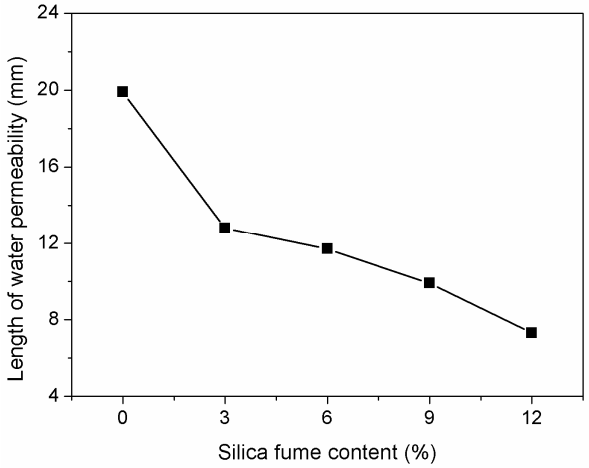


Fig. 3 Effect of silica fume content on the length of water permeability

Conclusions

In order to investigate the effect of silica fume on workability and water impermeability of concrete, a large number of experiments have been carried out in this study. On the basis of the experimental results of the specimens of five sets of mix proportions, the mechanism of action of silica fume on workability and water impermeability has been analyzed in details. The results indicate that the addition of silica fume has adverse effect on the workability of concrete composite. The slump and slump flow of the concretes containing silica fume was less than that of the concrete without silica

fume, and a considerable decrease for the slump and slump flow of the concrete was observed by increasing the dosage of silica fume. Besides, the addition of silica fume can improve the water impermeability of the concrete composite evidently, and the water impermeability is becoming better and better as the silica fume content is increasing gradually.

References

[1] H. Song, S. Pack, S. Nam, J. Jang, V. Saraswathy, Estimation of the permeability of silica fume cement concrete, Constructions and Building Materials, 24 (2010) 315-321.

[2] M. L. Khan, R. Siddique, Utilization of silica fume in concrete: Review of durability properties, Resour, Conservation and Recycling, 57 (2011) 30-35.

[3] S. T. Lee, S. H. Lee, Mechanical properties and durability of cement concrete incorporating silica fume, Journal of the Korean Ceramic Society, 47 (2010) 412-418.

[4] J. J. Park, G. S. Ryu, S. T. Kang, S. W. Kim, The influence of the amount of silica fume on the mechanical property of ultra-high performance concrete, Key Engineering and Materials, 385-387 (2008) 701-704.

[5] P. Zhang, Q. Li, H. Zhang, Combined effect of polypropylene fiber and silica fume on mechanical properties of concrete composite containing fly ash, Journal of Reinforced Plastics and Composites, 30 (2011) 1851-1860.

[6] P. Zhang, Q. Li, Z. Sun, Influence of silica fume and polypropylene fiber on fracture properties of concrete composite containing fly ash, Journal of Reinforced Plastics and Composites, 30 (2011) 1977-1988.

[7] P. Zhang, Q. Li, Z. Sun, Effect of polypropylene fibre on flexural properties of concrete composites containing fly ash and silica fume, Proc. Inst. Mech. Eng. Part L, Journal of Materials Research Applications 226 (2012) 177-181.

[8] JTJ E30-2005, Test methods of cement and concrete for highway engineering test methods of materials stabilized with inorganic binders for highway engineering, China Communications Press, China, 2005.

© (2012) Trans Tech Publications, Switzerland
doi:10.4028/www.scientific.net/AMM.238.161

Effect of Silica Fume on Mechanical Properties and Carbonation Resistance of Concrete

Qinglong Wang [a] and Junchao Bao [b]

China Road & Bridge Corporation, Beijing, 100011, China

[a]wql.fly@gmail.com, [b]bjch2005@126.com

Keywords: mechanical property; carbonation resistance; concrete; silica fume.

Abstract. A designed experimental study has been conducted to investigate the effect of silica fume on mechanical properties and carbonation resistance of concrete, a large number of experiments have been carried out in this study. The results indicate that the addition of silica fume has improved the compression strength and elastic modulus of concrete. A considerable increase for the compression strength and elastic modulus of the concrete was observed by increasing the dosage of silica fume. Besides, the addition of silica fume can improve the carbonation resistance of the concrete composite evidently, and the carbonation resistance is becoming better and better as the silica fume content is increasing gradually.

Introduction

Silica fume consists of very fine particles about 100 times smaller than the average cement particles. The extreme fineness of the silica fume particles allows it to fill the microscopic voids between cement particles. Silica fume is among one of the most recent pozzolanic materials currently used in concrete. It was first used in 1969 in Norway but only began to be systematically employed in North America and Europe in the early 1980s. Since then, the use of silica fume in concrete has been increasing rapidly; it has been used either as a partial replacement for cement or as an additive when special properties are desired [1]. The rapid increase in the use of silica fume is attributed to its positive effects on the mechanical properties of cementitious composites. During the last decade, considerable attention has been given to the use of silica fume as a partial replacement of cement to produce high-strength concrete. Khatri and Sirivivatnanon [2] indicated that the addition of silica fume to Portland cement concrete marginally decreased the workability of concrete but significantly improved its mechanical properties.

Bhanja et al. investigated the isolated effect of silica fume on concrete and suggested the optimum content of silica fume with regard to the compressive strength of concrete [3]. Zain et al. investigated the possibility of developing high performance concrete (HPC) using silica fume (SF) at relatively high water-binder ratios. The test results indicated that concrete under water curing offers the best results, and it is possible to produce HPC at relatively high water-binder ratios under controlled curing conditions [4]. Smith proposed several models to estimate the chloride ion ingress into portland cement concrete and silica-fume-enriched concrete under different exposure conditions, and the results indicated that small amounts of silica fume were sufficient as long as appropriate concrete covers to reinforcement are maintained and chloride exposure to the concrete is correctly assessed [5]. Zhang et al. [6-8] studied the effect of silica fume on the mechanical properties, flexural properties, fracture properties of fiber reinforced concrete composites containing fly ash. Carbonation of concrete has great negative impact on durability of concrete. The main harm of concrete carbonation is that it can increase PH of concrete, which will weaken the alkaline protection of the reinforcing rebar in concrete. As a result, the reinforcing rebar has larger possibility of corrosion, and the reinforced concrete is likely to be damaged. However, so far, there is little report about carbonation resistance of concrete composite containing silica fume. This article reports the investigation of mechanical properties and carbonation resistance of concrete containing silica fume.

Experimental Details

Raw Materials. Ordinary Portland cement (Class 42.5R) and silica fume were used in this work. The cement and silica fume properties are given in Table 1. Coarse aggregate with a maximum size of 30 mm and fine aggregate with a 2.82 fineness modulus were used in this experiment. A high range water reducer agent was used to adjust the workability of the concrete mixture. Silica fume was mixed in concrete composites by replacing the same quantity of cement, and the content of silica fume content (by mass) is from 3% to 12%. Mix proportions are given in Table 2.

Table 1 Properties of cement and silica fume

Chemical compositions									Physical properties	
Composition (%)	SiO_2	Al_2O_3	Fe_2O_3	CaO	MgO	Na_2O	K_2O	SO_3	Specific gravity	Specific surface (cm^2/g)
Cement	20.17	5.58	2.86	63.51	3.15	0.12	0.57	2.56	3.05	3295
Silica fume	93.72	0.82	0.48	0.34	1.44	0.40	1.22	0.47	2.30	-

Table 2 Mix proportions of the concrete mixtures

Mix no.	Cement (kg/m^3)	Silica fume (%)	Silica fume (kg/m^3)	Coarse aggregate (kg/m^3)	Fine aggregate (kg/m^3)	Water (kg/m^3)	Water reducer agent (kg/m^3)
1	494.0	0	0	1151	647	158	4.94
2	479.2	3	14.8	1151	647	158	4.94
3	464.4	6	29.6	1151	647	158	4.94
4	449.5	9	44.5	1151	647	158	4.94
5	434.7	12	59.3	1151	647	158	4.94

Experimental Method. The 150-mm concrete cubes were cast for compression strength, and 150×300 mm quadruple prisms were used for elastic modulus. The tests of compression strength were carried out by hydraulic pressure universal testing machine according to the Chinese Standard [9]. Before testing, the specimen was put onto the pad of the elevating platform of the test machine. The loading rate of compression strength test was controlled between 0.5 MPa/s and 0.8 MPa /s. Elastic modulus test was also carried out by hydraulic pressure universal testing machine according to the Chinese Standard [9]. During the course of loading and unloading, the deformation of the specimen was measured using two micrometers with dial indicators, which were supported by dial holders on the two symmetrical sides of the specimen respectively. To keep the deformation changing equably, the loading rate of elastic modulus test was controlled between 0.2 MPa/s to 1 MPa/s.

A series of cube specimens with the size of 100×100×100 mm were used to determine the carbonation resistance of concrete composite. The carbonation resistance of concrete composite can be evaluated by carbonation depth of the specimen under the action of CO_2 pressure. The shorter carbonation depth indicates that the concrete composite has better carbonation resistance. For carbonation resistance of concrete composite test, each set of per composition includes 15 specimens, and the average value of the 15 data was computed as the final result. Before testing, the specimens were cured for 28 days at 100% relative humidity and controlled temperature (21 ± 2 ^oC). The test of concrete carbonation was carried out in concrete carbonation box in accordance with the Chinese Standard [10]. Before carbonation test, the specimens were baked for 48 h in the oven under the temperature of 60 ^oC. In the concrete carbonation box, the CO_2 concentration should be controlled at 20 ± 3%, and the humidity and temperature should be controlled at 70 ± 5% and 20 ± 5 ^oC, respectively. The carbonation test should last 24 days. After the test finished, the specimen was split in half, and the fracture surface was sprayed phenolphthalein alcohol solution with the level of 1%. Finally, the average carbonation depth of the specimen can be measured.

Results and Discussion

Effect of Silica Fume Content on Compression Strength. Fig. 1 shows the variation of compression strength of silica fume concrete mixes with 3%, 6%, 9% and 12% cement replacement with silica fume at 28 days, the compression strength of concrete containing silica fume is increasing gradually with the increase of silica fume content. Compared with the concrete without silica fume, the compression strength increases from 61.5 MPa to 68.3 MPa, and increases by 11% with 12% cement replacement with silica fume.

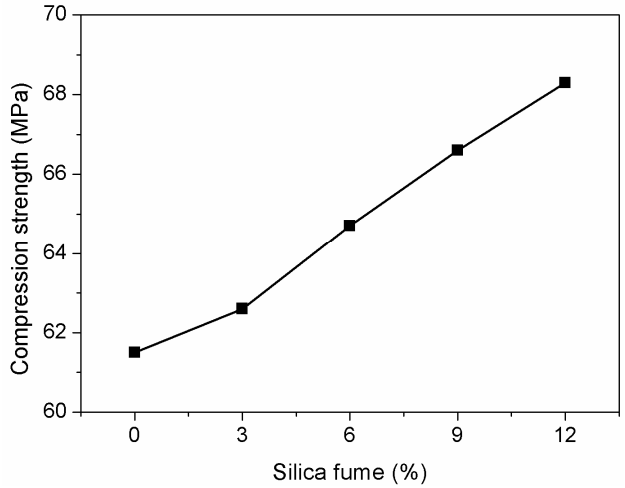


Fig. 1 Effect of silica fume content on compression strength

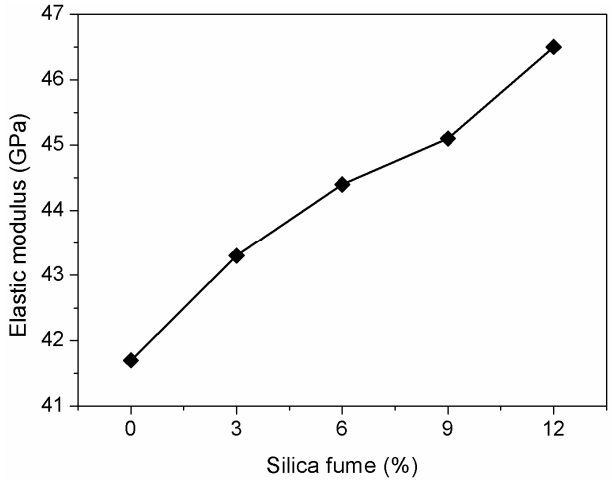


Fig. 2 Effect of silica fume content on elastic modulus

Effect of Silica Fume Content on Elastic Modulus. The variations of elastic modulus of silica fume concrete mixes with 3%, 6%, 9% and 12% cement replacement with silica fume at 28 days curing are illustrated in Fig. 2 From the test results, it can be seen that the elastic modulus of silica fume concrete with different percentages cement replacement was higher than the control mix, and a considerable increase for elastic modulus was observed by increasing the content of silica fume. The results indicate that the addition of silica fume makes the concrete more brittle.

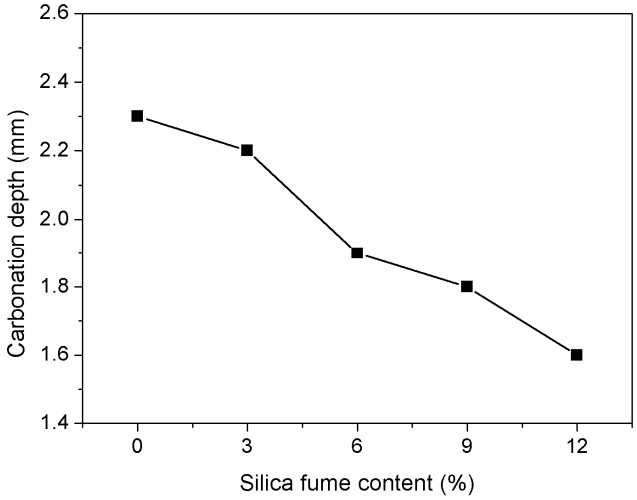


Fig. 3 Effect of silica fume content on carbonation depth

Effect of Silica Fume Content on Carbonation Resistance. The variations of the carbonation depth of concrete composite versus silica fume content of the carbonation specimen are illustrated in Fig. 3. A considerable decrease for the carbonation depth of the concrete was observed by increasing the content of silica fume. Compared with the mix without silica fume, the decrease was determined as 30% for 12% silica fume content. The main reason of silica fume can improve the carbonation resistance of concrete composite is that the grain size of silica fume particle is smaller than that of the cement. As a result, the silica fume particles can fill the interspace around the cement particles to

make the hardened concrete much more compact. Besides, in the early hydration of cement, silica fume can take part in hydration reaction to produce more hydrate and decrease the porosity of concrete composite. Therefore, the anti-permeability of concrete composite was improved evidently, and it can be difficult for the CO_2 in the atmosphere to permeate into concrete.

Conclusions

In order to investigate the effect of silica fume on mechanical properties and carbonation resistance of concrete, a large number of experiments have been carried out in this study. On the basis of the experimental results of the specimens of five sets of mix proportions, the mechanism of action of silica fume on mechanical properties and carbonation resistance has been analyzed in details. The results indicate that the addition of silica fume has improved the compression strength and elastic modulus of concrete composite. A considerable increase for the compression strength and elastic modulus of the concrete was observed by increasing the dosage of silica fume. Besides, the addition of silica fume can improve the carbonation resistance of the concrete composite evidently, and the carbonation resistance is becoming better and better as the silica fume content is increasing gradually.

References

[1] A. T. Houssam, E. Tahar, The influence of silica fume on the compressive strength of cement paste and mortar, Cement and Concrete Research, 25 (1995) 1591-1602.

[2] A. A. Almusallam, H. Beshr, M. Maslehuddin, O. S. B. Al-Amoudi, Effect of silica fume on the mechanical properties of low quality coarse aggregate concrete, Cement and Concrete Composites. 26 (2004) 891-900.

[3] S. Bhanja, B. Sengupta, S. K. Kaushik, P. Kumar, Optimum silica fume content and its mode of action on concrete, ACI Materials Journal, 101 (2004) 327-328.

[4] M. F. M. Zain, M. Safiuddin, H. Mahmud, Development of high performance concrete using silica fume at relatively high water-binder ratios, Cement and Concrete Research, 30 (2000) 1501-1505.

[5] B. G. Smith, Durability of silica fume concrete exposed to chloride in hot climates, J. Mater. Civ. Eng. 13 (2001) 41-48.

[6] P. Zhang, Q. Li, H. Zhang, Combined effect of polypropylene fiber and silica fume on mechanical properties of concrete composite containing fly ash, Journal of Reinforced Plastics and Composites, 30 (2011) 1851-1860.

[7] P. Zhang, Q. Li, Z. Sun, Influence of silica fume and polypropylene fiber on fracture properties of concrete composite containing fly ash, Journal of Reinforced Plastics and Composites, 30 (2011) 1977-1988.

[8] P. Zhang, Q. Li, Z. Sun, Effect of polypropylene fibre on flexural properties of concrete composites containing fly ash and silica fume, Proc. Inst. Mech. Eng. Part L, Journal of Materials Research Applications, 226 (2012) 177-181.

[9] JTJ E30-2005, Test methods of cement and concrete for highway engineering test methods of materials stabilized with inorganic binders for highway engineering, China Communications Press, Beijing, 2005.

[10] GB 11974-1997, Test method for carbonation of aerated concrete, Standards Press of China, Beijing, 1997.

© (2012) Trans Tech Publications, Switzerland
doi:10.4028/www.scientific.net/AMM.238.165

Effect of Silica Fume on Dry Shrinkage and Freezing-thawing Durability of Concrete

Feng Li [a] and Zaipeng Cui [b]

China Road & Bridge Corporation, Beijing 100011, China

[a]aaronlifeng@yahoo.com.cn, [b]cuizp1987@126.com

Keywords: dry shrinkage; freezing-thawing durability; concrete; silica fume.

Abstract. An experimental study has been conducted to investigate the effect of silica fume on shrinkage and freezing-thawing durability of concrete, a large number of tests have been carried out in this study. The results indicate that the addition of silica fume has adverse effect on the dry shrinkage property of concrete. The dry shrinkage strain of the concrete containing silica fume is more than that of the concrete without silica fume, and a considerable increase for the dry shrinkage strain of the concrete was observed by increasing the dosage of silica fume. However, the addition of silica fume can improve the freezing-thawing durability of the concrete evidently, and the freezing-thawing durability is becoming better and better as the silica fume content is increasing gradually.

Introduction

Silica fume has been defined as "very fine non-crystalline silica produced in electric arc furnaces as a by-product of the production of elemental silicon or alloys containing silicon" by the American Concrete Institute (ACI). The addition of silica fume to concrete mixtures is a common practice in construction with high-performance concrete, which is accepted and regulated by all official standards and [1]. Silica fume is an amorphous mineral material composed of extremely small, chemically active, particles of SiO_2 that appear as a by-product in silicon or ferrosilicon industries. It can be considered a supplementary cementing material that improves the mixture particle (aggregate, cement) packing and the compactness of the concrete. Its great specific surface area results in a high chemical activity with the calcium hydroxide released as a consequence of cement hydration (pozzolanic activity), which is considered responsible for the significant increase of the compressive strength of the silica fume added concrete [2]. Many extensive experiments were carried out by many researches around the world indicated that the usage of silica fume in concrete increases the concrete strengths, modulus of elasticity, chemical and abrasion resistance, in addition to enhancing mechanical properties.

Bhanjaa and Sengupta [3-5] studied the effect of silica fume on the tensile and compressive strength of high performance concrete; they developed mathematical model using statistical methods to predict the 28-day compressive strength of silica fume concrete with water-to-cementitious material (w/cm) ratios ranging from 0.3 to 0.42 and silica fume replacement percentages from 5 to 30. Zhang et al. [6-8] studied the effect of silica fume on the mechanical properties, flexural properties, fracture properties of fiber reinforced concrete composites containing fly ash. The dry shrinkage property and freezing-thawing durability are so important in the mix design and application of concrete composite, especially when the concrete composite is used in the severe cold region and in dry environment. However, so far, there is little report about dry shrinkage property and freezing-thawing durability of concrete composites containing silica fume. This article reports the investigation of dry shrinkage and freezing-thawing durability of concrete containing silica fume.

Experimental Details

Raw Materials. Ordinary Portland cement (Class 42.5R) and silica fume were used in this work. The cement and silica fume properties are given in Table 1. Coarse aggregate with a maximum size of 30 mm and fine aggregate with a 2.82 fineness modulus were used in this experiment. A high range

water reducer agent was used to adjust the workability of the concrete mixture. Silica fume was mixed in concrete composites by replacing the same quantity of cement, and the content of silica fume content (by mass) is from 3% to 12%. Mix proportions are given in Table 2.

Table 1 Properties of cement and silica fume

Chemical compositions									Physical properties	
Composition (%)	SiO_2	Al_2O_3	Fe_2O_3	CaO	MgO	Na_2O	K_2O	SO_3	Specific gravity	Specific surface (cm^2/g)
Cement	20.17	5.58	2.86	63.51	3.15	0.12	0.57	2.56	3.05	3295
Silica fume	93.72	0.82	0.48	0.34	1.44	0.40	1.22	0.47	2.30	-

Table 2 Mix proportions of the concrete mixtures

Mix no.	Cement (kg/m^3)	Silica fume (%)	Silica fume (kg/m^3)	Coarse aggregate (kg/m^3)	Fine aggregate (kg/m^3)	Water (kg/m^3)	Water reducer agent (kg/m^3)
1	494.0	0	0	1151	647	158	4.94
2	479.2	3	14.8	1151	647	158	4.94
3	464.4	6	29.6	1151	647	158	4.94
4	449.5	9	44.5	1151	647	158	4.94
5	434.7	12	59.3	1151	647	158	4.94

Experimental Method. The tests of dry shrinkage properties of concrete composite were carried out in accordance with the Chinese Standard [9]. A series of beam specimens with the size of 100×100×400 mm^3 were used to determine the shrinkage properties of the concrete composite. For the shrinkage properties of concrete composite test, each set of per mix includes 6 specimens, and the average value of the 6 data was computed as the final result. After the specimens were cast, the moulds should be removed the next day, and the specimens were put into the standard and curing room to be cured at 100% relative humidity and controlled temperature (20±2^{o}C). After the specimens were cured for two days, the initial lengths of the specimens should be measured, and then they were put into the shrinkage room to be further cured at 60±5% relative humidity and controlled temperature (20±2^{o}C). There are 10 curing periods, and the length variation of the specimen should be measured by the dial indicator at the end of each period to calculate the dry shrinkage strain.

Freezing-thawing durability of concrete composite can be measured referring to the standard of ASTM [10]. The freezing-thawing durability of concrete composite was evaluated by the relative dynamic elastic modulus of the specimen after 300 freezing-thawing cycles. The higher relative dynamic elastic modulus indicates that the concrete composite has better freezing-thawing durability. On the contrary, the material has worse freezing-thawing durability with lower relative dynamic elastic modulus. Relative dynamic elastic modulus of concrete composite can be measured referring to the standard of ASTM [11]. A series of prism specimens with the size of 100×100×400 mm were used to determine the relative dynamic elastic modulus of concrete composite. For freezing-thawing test of concrete composite, each set of per composition includes 3 specimens, and the average value of the 3 data was computed as the final result. Before testing, the specimens were cured for 28 days at 100% relative humidity and controlled temperature (21±2 ^{o}C), and the specimens have been soaked in saturated lime water in the last 4 days of the curing period. One freezing-thawing cycle should be carried out in 2 h to 5 h, and the thawing time should not be less than a quarter of the total time of one cycle. At the end of freezing and thawing, the temperature of the specimen centre should be controlled at -18^{o}C and 5^{o}C, respectively.

Results and Discussion

Effect of Silica Fume Content on Dry Shrinkage. Dry shrinkage tests can provide necessary information on how the drying shrinkage stresses develop although they can not offer sufficient information on the behavior of concrete structure. Dry shrinkage with curing age is shown in Fig. 1

for different concretes with different silica fume content. It can be seen that the shrinkage values yielded approximately comparable values at early ages of drying period. However, a clear distinction was observed for different concretes after about ten days. From Fig. 1, it can be seen that the dry shrinkage strain in the concretes containing silica fume was more than that in the concrete without silica fume, and a considerable increase for the dry shrinkage strain of the concrete was observed by increasing the dosage of silica fume. As the silica fume content is increased from 0 to 12%, the maximum dry shrinkage strain of 90 days ages increases 22% from 693 microstrain to 845 microstrain. In other words, the addition of silica fume may have adverse effect on the anti-dry-shrinkage cracking property of concrete composite. This adverse effect appeared to be more pronounced with increasing replacement level of silica fume.

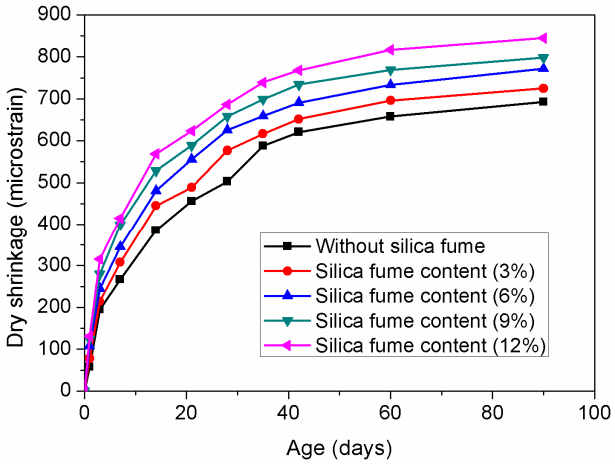


Fig. 1 Effect of silica fume content on dry shrinkage

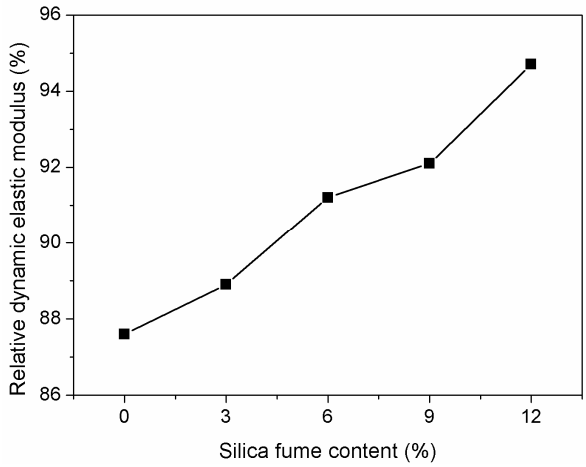


Fig. 2 Effect of silica fume content on relative dynamic elastic modulus

Effect of Silica Fume Content on Freezing-thawing Durability. The variations of the relative dynamic elastic modulus of concrete composite versus silica fume content are illustrated in Fig. 2. A considerable increase for the relative dynamic elastic modulus of the concrete was observed by increasing the content of silica fume. Compared with the mix without silica fume, the increase was determined as 8.1% for 12% silica fume content. The particles of silica fume can react with $Ca(OH)_2$ generated from cement hydration to produce C-S-H, which can be filled into the interspace around the cement particles. With the addition of silica fume, the bubble structure in the concrete composite was improved for the number of little bubbles and gel holes was increased, and the number of large bubbles was decreased. As a result, the space between two bubbles was reduced, which has positive contribution on the freezing-thawing durability of concrete. In addition, the pozzolanic effect of silica fume can improve the compactness of concrete. So the amount of free water permeating into the concrete composite is less, and the amount of water likely freezing is less. Therefore, the addition of silica fume can improve the freezing-thawing durability of concrete composite evidently.

Conclusions

In order to investigate the effect of silica fume on shrinkage and freezing-thawing durability of concrete, a large number of experiments have been carried out in this study. On the basis of the experimental results of the specimens of five sets of mix proportions, the mechanism of action of silica fume on shrinkage and freezing-thawing durability has been analyzed in details. The results indicate that the addition of silica fume has adverse effect on the dry shrinkage property of concrete composite. The dry shrinkage strain in the concretes containing silica fume was more than that in the concrete without silica fume, and a considerable increase for the dry shrinkage strain of the concrete was observed by increasing the dosage of silica fume. Besides, the addition of silica fume can improve the freezing-thawing durability of the concrete composite evidently, and the freezing-thawing durability is becoming better and better as the silica fume content is increasing gradually.

References

[1] V. T. Giner, F. J. Baeza, E. Zornoza, B. Ferrer, Silica fume admixture effect on the dynamic properties of concrete, Construction and Building Materials, 25 (2011) 3272-3277.

[2] J. Xie, A. E. Elwi, J. G. MacGregor, Mechanical properties of three high-strength concretes containing silica fume, ACI Materials Journal, 92 (1995) 135-143.

[3] S. Bhanjaa, B. Sengupta, Influence of silica fume on the tensile strength of concrete, Cement and Concrete Research, 35 (2005) 743-747.

[4] S. Bhanjaa, B. Sengupta, Investigations on the compressive strength of silica fume concrete using statistical methods, Cement and Concrete Research, 32 (2002) 1391-1394.

[5] S. Bhanjaa, B. Sengupta, Modified water-cement ratio law for silica fume concretes, Cement and Concrete Research, 33 (2003) 447-450.

[6] P. Zhang, Q. Li, H. Zhang, Combined effect of polypropylene fiber and silica fume on mechanical properties of concrete composite containing fly ash, Journal of Reinforced Plastics and Composites, 30 (2011) 1851-1860.

[7] P. Zhang, Q. Li, Z. Sun, Influence of silica fume and polypropylene fiber on fracture properties of concrete composite containing fly ash, Journal of Reinforced Plastics and Composites, 30 (2011) 1977-1988.

[8] P. Zhang, Q. Li, Z. Sun, Effect of polypropylene fibre on flexural properties of concrete composites containing fly ash and silica fume, Proc. Inst. Mech. Eng. Part L, Journal of Materials Research Applications, 226 (2012) 177-181.

[9] JTJ E30-2005, Test methods of cement and concrete for highway engineering test methods of materials stabilized with inorganic binders for highway engineering, China Communications Press, China, 2005.

[10] ASTM C666 1997, Standard test method for resistance of concrete to rapid freezing and thawing, Annual Book of ASTM Standards, 04.02: 310-315, 1997.

[11] ASTM C215 1997, Test method for fundamental transverse, longitudinal, and torsional frequency of concrete specimens, Annual Book of ASTM Standards, 2 (1997) 119-124.

© (2012) Trans Tech Publications, Switzerland
doi:10.4028/www.scientific.net/AMM.238.169

A Kind of Simple Method for Mesh Generation of Concrete at Meso Level

Juan Wang[1, a], Longbang Qing[2,b] and Junfeng Guan[3,c]

[1]College of Water Conservancy and Environment Engineering, Zhengzhou University, China

[2]State Key Laboratory of Hydroscience and Engineering, Tsinghua University, Beijing, China

[3]North China Institute of Water Resources and Electric Power, Zhengzhou, China

[a]wangjuan@zzu.edu.cn, [b]qlongbang@126.com, [c]shuaipipi88@126.com

Keywords: concrete; meso-structure; mesh generating; random aggregate.

Abstract. The paper proposed a method to generate the finite element mesh of concrete at meso level semi-automatically. And an aggregate meshing computer program, AggMesh, was developed by C++ language. Since it avoids the judgment of node coincidence in contact surface between aggregates and mortar through meshing process, the approach can greatly increase the finite element meshing capability for concrete mesostructure and improve meshing efficiency. The study shed light on preparation for simulating concrete strength at meso level.

Introduction

Mesh generating is one of the most difficult work for meso-simulting of concrete in 3D [1-2] because of the complex structure of concrete. Therefore, most specimen for simulating concrete are relatively small or simulating in 2D in the existing research literature [3-5]. To avoid the difficulty of mesh, unit element is used for concrete model just modifying the element properties according to their location [6-8]. Although the mesh is easy to generate, they are not agreement with the real structure. Furthermore, the element depth of interfacial transition zone (ITZ) is more thick than it is[9-11]. In order to reveal the mechanism of concrete strength, the model should be builded as close to real structure as possible.

It is well known that automatic subdivision for mesh of aggregates and mortar matrix separately are easy and efficient. The main difficulty in the generation of meso-structure mesh is the coincident nodes generation in the aggregate and mortar contact surface. In the current commercial FE software, the more aggregates there are, the more curved surfaces will be generated. When the number of aggregate comes to a limitation, the meshing work exceeds the capacity of computer or the FE software. Therefore, it is necessary to study the meshing method for meso-structure of concrete.

Geometry Model

Aggregates are assumed as spherical particles, and the grading are determined according to Fuller aggregate grading curve shown as Formula (1) [12].

$$P_t = \sqrt{d/d_{\max}} \tag{1}$$

Where d is the diameter of target aggregate; P_t is the cumulative density function which is the mass fraction of the aggregates which diameter are less than d to total aggregates; $d_{\max}$ is the maximum aggregate diameter.

The aggregate (particles) generation process is as follows:

(1) Define the geometric parameters such as the specimen size, aggregate volume fraction, aggregate diameter range, etc;

(2) Divide the subinterval of aggregate diameters and calculate each volume fraction according to the grading;

(3) Generate aggregates location (X,Y, and Z coordinate location of shpere center) and diameters randomly in each aggregate diameter subinterval;

(4) Calculate the distance between adjacent particles, find ones the distance away from another particles being shorter than the given allowed value shown as formula (2), and mark the aggregates;

(5) Adjust the marked aggregates position and diameter slightly until the distances between all particles are permitted;

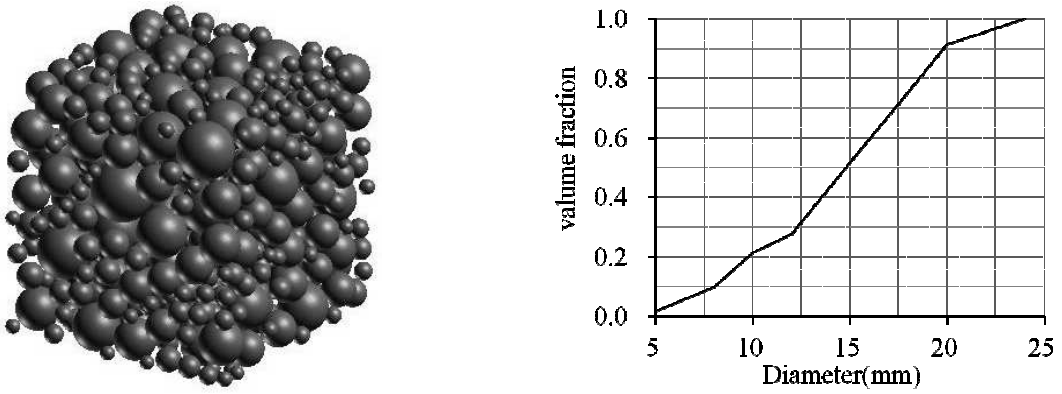
(6) Calculate aggregates volume and compare to the predefined value, if the former is larger or equal the later then finish the work of particle generating, otherwise repeat the steps (3)-(5);

(7) Output the information of aggregate coordinate locations and size.

$$\Delta d_{\min} = \left(D_1 + D_2\right)/10 \tag{2}$$

Where D_1 and D_2 are the diameter of the two adjacent particles; $\Delta d_{\min}$ is the allowed minimal distance between the adjacent aggregates.

The cube sample with 100mm side-length was generated by the above method and the distribution of aggregate is shown as Fig. 2. In the cube sample, coarse aggregate volume fraction is about 42%. Aggregate gradation curve is shown as Fig. 3.



(a) The 3d aggregates model (b) The coarse aggregate grading curve

Fig. 1 Aggregates distribution generated by computer

Mesh Generating

Mesh Process. Mesh generating in three dimensional is always one of the most difficult issue in concrete mesoscale computational mechanics. In this paper, both aggregate and mortar are meshed by solid elements, while the interface discreted into zero-thickness spring elements[13]. It is required that the nodes in the interface between aggregates and mortar are coincident which increase the difficulty of mesh generateing. The steps of mesh generating are as follows.

(1) Meshing mortar by free manner with tetrahedral element;

(2) Generate the nodes on the surfaces of aggregates according to the nodes of the same location in the mortar;

(3) Produce the spring elements at the coincident nodes in the interface between aggregates and mortar;

(4) Generate the interior nodes of aggregates at the location of aggregate center;

(5) Generate the elements of aggregate by the nodes of the interior of the aggregates and the nodes of the interface nodes, which will be described detailedly in the following section.

Mesh of aggregate. On the basis of the existing mortar element information, the meshing program AggMesh for aggregates is developed. The program compiled by C++ language, and the results stored in a text file.

The program flow is described as the following steps.

(1) Determine the contact with the mortar unit and surface nodes for a given aggregate particles;

(2) Generate a new node in the aggregate center position for each aggregate;

(3) Add a new node between the ball center to the surface node if the aggregate diameter R lager than given length l considering elements accuracy;

(4) Generate tetrahedral element directly by connecting three nodes adjacent to the center node if $R<l$, otherwise add new node at the mid position between surface node and center node, then connect them with surface nodes to generate prism elements and connect them with center node to generate tetrahedral element;

(5) Iterate over all aggregate.

The elements of aggregates are shown as Fig 2.



(a) Elements of all aggregates;… …..(b) Enlarged drawing of a single-aggregate elments

Fig. 2 Aggregate elements schematic drawing

Mesh of ITZ. Zero-length spring elements are employed to model ITZ, which connect aggregates and mortar matrix by non- perfect bonding way. The spring elements are generated automatically by the program compiled based on the APDL language provided by ANSYS. The detailed steps are as follows.

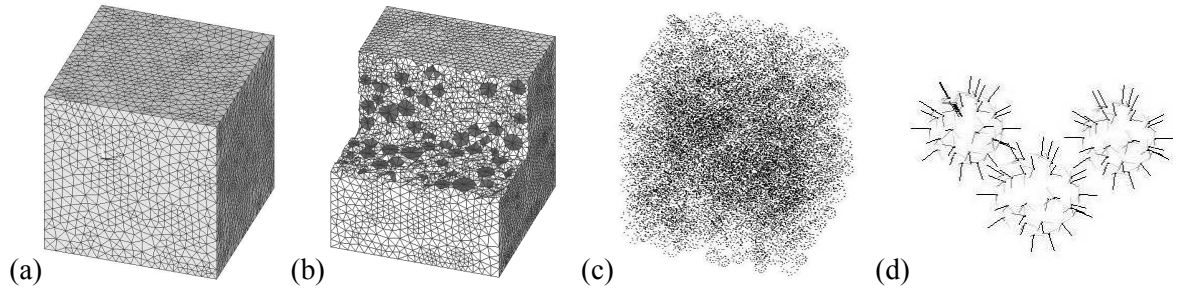
(1) Establish node sets of aggregate surfaces according to the existing aggregate node information;

(2) Compose node-pair for each surface node of aggregates with mortar node at the same location;

(3) Generate three orthogonal spring elements with each node-pair, one of them along aggregate surface normal direction and the other two elements along the tangential directions;

(4) Rotate coordinate system of all surface nodes to spherical coordinate which coordinate origin at center of aggregate.

(5) The FE model of whole structure is shown as Fig. 3(a) and Fig. 3(b). The ITZ elements are shown as Fig. 3(c). The spring directions are shown as Fig. 3(d).



(a) (b) (c) (d)

Fig. 3 FE model of concrete: (a) The whole model (b) Inner elements schematic drawing, where dark elements are aggregate and the other are mortar elments; (c) Elements of ITZ; and (d) The schematic drawing of spring directions

Conclusions

It is hard work for FE simulating to mesh the mesostructure of concrete in 3D because of the high costs of memory led by the complicated composition of concrete at meso level. In this paper, concrete was considered as three-phase composite material consisting of coarse aggregate, mortar matrix and ITZ, and a semi-automatic meshing method was put forward, which meshed each phase

of concrete separately. Accordingly, the aggregate meshing program AggMesh was developed by C++ language and ITZ meshing program was compiled based on the APDL language provided by ANSYS. This approach can improve meshing efficiency as it avoids the nodes coincidence judgments when mesh the contact surface between the aggregates and mortar.

Acknowledgments

This study was financially supported by Research Center on Levee Safety and Disaster Prevention of Ministry of Water Resources (201202) and the High-level Personnel Research Project of North China Institute of Water Conservancy and Hydroelectric Power (201064).

References and Notes

[1] J. Wang. Doctoral Dissertation of Tsinghua University, Beijing, 2011.

[2] P. K. Mehta, J. M. Monteiro, Concrete: microstructure, properties and materials. China electric power press, Beijing, 2008.

[3] G. Lilliu, J.G.M. van Mier, Engineering Fracture Mechanics, 70 (2003) 927.

[4] R. Mohamed, W. Hansen, ACI Materials Journal, 96 (1999) 196.

[5] A. Caballero, C.M. Lopez, I. Carol, Computer Methods in Applied. Mechanics and Engineering. 195 (2006) .

[6] X. Tang, C. Zhang, Journal of Tsinghua University of Science & Technology, 3 (2008) 48.

[7] F. Dang, W. Han, W. Tian, Journal of Xi'an University of Technology, 2 (2006) 22.

[8] G. Liu, Z. Wang, Journal of Tsinghua University (Science & Technology), 1 (1996) 36.

[9] J. P. Ollivier, J. C. Maso, B. Bourdette, Advanced Cement Based Materials, 2 (1995) 30.

[10] K. Liao, P. Chang, Y. Peng, et al, Cement and Concrete Research, 34 (2004) 977.

[11] K. Wu, Doctoral Dissertation of Tsinghua University, Beijing, 2010.

[12] S. Hafner, S. Eckardt, T. Luther, et al, Computers & Structures, 7 (2006) 84.

[13] J. Wang, Q. Li, L. Qing and J. Guan, Advanced Materials Research, 243 (2011) 291.

© (2012) Trans Tech Publications, Switzerland
doi:10.4028/www.scientific.net/AMM.238.173

Orthogonal Test on Large Content of Solid Waste in Building Binder

Huanqiang Liu

School of Civil Engineering and Communication, North China University of Water Resources and Electric Power, Zhengzhou 450011, China

liuhuanqiang@ncwu.edu.cn

Keywords: solid waste; building binder; orthogonal test; activator.

Abstract. With the compound system of fly ash and aluminum slag as the main material, activated through ordinary activator, a type of building binder in which wastes is more than 80 percent is studied in the paper. The ratio of the activator is optimized through orthogonal test. Experimental results show that the active component in the solid wastes can be greatly activated under the mixture proportion as following: 10% lime, 4% gypsum, 0.5% sodium carbonate and 0.5% sodium sulfate. The cementing medium has enough strength to meet the requirements in construction engineering. Material of the cementing medium has the advantage of easy availability, low cost and high rate of waste utilization. It will be a kind of green building materials with a great expect.

Introduction

With Continuous improvement in quality of cement products, its strength grade is higher and higher when preparing low-grade mortar the small content high strength grade leads to poor and affect the quality of construction. To resolve this problem, general to meet the requirements of the construction performance of the mortar with a certain amount of mineral admixture is added. The incorporation of mineral admixtures generally use only a single effect (such as improving the workability), rather than effectively use the "combined effect". The so-called combined effect of mineral admixture means that all or most of the effects of the admixture mineral can be taken. Currently miner admixtures, such as fly ash, slag, silica fume are widely used. They are wastes of other industrial waste, if you do not take advantage of, will result in large degree it not properly used, more over It will pollutes environment, there is active ingredient in the wastes ,if they are effectively used, it will be economical and environmental. Building Binder with large content of solid waste, with 28d compressive strength of 21.4MPa, is prepared using small amount of cement with high content of fly ash and aluminum slag.

Material and Methods

Raw Materials. Cement is produced by Tianrui cement plant production of 42.5 ordinary Portland cement, Aluminum slag is a commercially available ultra-fine powder of aluminum slag. Fly Ash is winnowing Class I gray from Luoyang Power Plant. Lime, gypsum, sodium sulfate and sodium carbonate are commercially available. Sand is from Xinyang river with fineness modulus of 2.6, and the apparent density 2.59g/cm^3.

Table 1 Physical properties of cement and admixture

norm / variety	Degree of fineness 45μm (%)	Moisture content (%)	Loss on ignition (%)	Density (g/cm^3)	Specific surface area (m^2/kg)	Water demand radio (%)
Cemnent	20.6	—	2.63	3.10	330	—
Fly ash	15.4	0.17	—	2.16	303	96.6
Aluminum lag	7.2	0.12	—	2.85	484	—

Test Methods. The composition ration of the fly ash and aluminum slag in the composite system is determined according to its flexural and compressive strength.

The effect of the activator on the mineral admixture and fundamental properties of the binder is also studied.

40mm × 40mm × 160mm specimen that at room temperature has conserved for 24 hours and then are mould and then sent immediately to the curing room and conserved under the condition of environment a relative humidity of greater than 95% and temperature of 22 ± 1°Cor 28 days the compressive and flexural strengths are measured according to GB/17671-1999 normal consistency of setting time is tested in accordance with GB/1346-2011.

Orthogonal test, the activator of component ratios. The specific test parameters to determine the following: L9 (3^4) orthogonal table were investigated the effects of lime, gypsum, Na_2SO_4, Na_2CO_3 on the strength of fly ash and slag composite system excitation effect. The level of each component to determine the basis of relevant information [1-3] is determined.

Results and Discussion

The Determination of Ratio of the Composite System. It is showed with increasing content of aluminum slag 7 and 28 days strength is increasing without clinker, indicating that the composite system has a certain cementitious property. According to the study reported when the aluminum slag content exceeds a certain degree, the bleeding of the binder and the increased shrinkage values results in the poor performance and post-cracking. It is generally believed that the content of the slag should be not exceed 40% of the total amount of cementitious material [4~5]; In the same time, thinking of lowing the cost of materials the ratio 40:60 of the slag and fly ash is selected. And the content lime and gypsum, Na_2SO_4 + Na_2CO_3 content are 10%, 4% , 1% of the total (slag + fly ash) respectively.

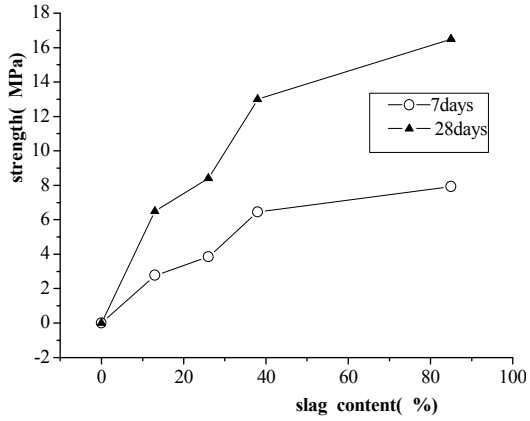


Fig.1 Compressive strength

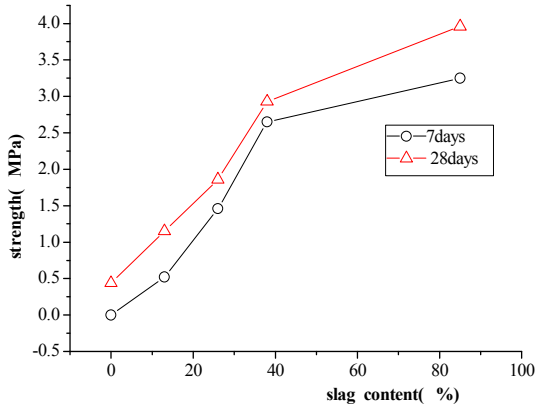


Fig. 2 Flexural strength

Table 2 Orthogonal test results and data processing

Lime Plaster Na_2CO_3 Na_2SO_4 Flexural Compressivestrength strength						
1	1 (5%)	1(0%)	1(0%)	1(0%)	2.34	8.19
2	1	2(4%)	2(0.5%)	2(0.5%)	2.13	10.53
3	1	3(8%)	3(1%)	3(1%)	2.02	7.32
4	2(10%)	1	2	3	2.73	10.3
5	2	2	3	1	1.85	9.02
6	2	3	1	2	2.54	8.73
7	3(15%)	1	3	2	2.18	8.25
8	3	2	1	3	2.54	7.25
9	3	3	2	1	2.05	6.92
I flexural II III range $\overline{R}$	6.49 7.12 6.77 0.63	7.25 7.52 6.61 0.91	7.42 6.91 6.16 1.26	6.24 8.85 6.8 0.61	3>2 >1>4	
I compressive II III range $\overline{R}$	26.04 28.05 22.42 5.63	26.74 26.8 22.97 3.83	24.17 27.75 24.59 3.58	24.13 27.51 25.1 3.38		1>2 >3>4

Optimization of the Composite Activator. In order to further reduce the cost of the cementitious material, are chosen several common products of the industrial level for as activator. Activator such as i.e. components: lime, gypsum, Na_2SO_4 and Na_2CO_3 mentioned above. And L9 (3^4) orthogonal test is performed, the results are shown in Table 2. It is seen that the sort result of the significant factors on the flexural strength is 3> 2> 1> 4. And corresponding respectively level are 0% Na_2CO_3, 4% gypsum, 10% lime and 0.5% Na_2SO_4. The significant effect order on the compressive strength factors 1> 2> 3> 4 corresponding to the levels are 10% lime, gypsum, 0.5% Na_2CO_3 and 0.5% Na_2SO_4 respectively. To ensure both compressive and flexural strength of cementitious material, the activators are chosen as 10% lime, 4% gypsum, 0.5% Na_2CO_3 and 0.5% Na_2SO_4.

The Determination Cementing Material of the Component. According to the testing it is can be seen that the strength of the binder which composed of aluminum mineral slag and fly ash and activated by above compound activator cannot meet the needs of engineering projects. This has unfavorable effect on construction because of its early low strength. So a certain amount of clinker or cement should be added to improve its early strength. So experiments are made to find the appropriate content of the cement. The content of cement in the cementitious materials are 10%, 15%, 20% and 25% respectively. The ratio of compound system is chosen according to the results of the orthogonal test. They are listed in Table 3.

Table 3 Basic properties of the specimen under different cement

	Compressive strength (MPa)		Flexural strength (MPa)		Setting time	
	7d	28d	7d	28d	Initial setting	final setting
1(10%)	7.08	16.65	1.95	3.24	8：08	11：20
2(15%)	7.33	18.20	2.33	3.87	7：35	10：48
3(20%)	8.98	21.38	2.37	4.35	6：55	9：33
4(25%)	9.77	23.43	2.83	4.87	6：28	7：56

Conclusions

The building binder with the waste utilization rate more than 80% can be prepared by using simple activator as 10% lime, 4% gypsum, 0.5% Na_2CO_3 and 0.5% Na_2SO_4. The early and late strength of the binder is feasible. As late activity of slag and fly ash continues to be excited, its strength is still growing, which is beneficial for long-term performance of the project. The construction binder with different intensity levels can be prepared, it can reduce the project cost (compared with the same intensity level of ordinary Portland cement, save cost by 15%), it is a certain "green building."

Acknowledgement

The work was supported by Science and Technology Research Projects, Zhengzhou, China (083STRF40344-5).

References

[1] J. Peng, F. Lin, Fly ash and slag, clinker, cement and mortar, Silicate Building Products, 5 (1995) 30-33.

[2] S. Manjit, G. Mridul, Cementitious binder from fly ash and other industrial wastes, Cement and Concrete Research, 3 (1999) 309-314.

[3] Y. Pu, M. Clinker, Blast furnace slag cement compressive strength, Journal of Yanbian University, 12 (2002) 288-290.

[4] H. Qin, W. Gang, G. Zhang, Such as doped slag powder dry mortar performance and application, New Building Materials, 2 (2004) 7-9.

[5] Q. Niu, N. Feng, J. Yang, Superfine slag powder mechanism, Building Materials, 3 (2002) 84 -89.

© (2012) Trans Tech Publications, Switzerland
doi:10.4028/www.scientific.net/AMM.238.176

Numerical Simulation of Bond Properties of Steel Bars in Concrete with Machine-made Sand

Shunbo Zhao [a], Xinxin Ding [b] and Shiming Liu [c]

School of Civil Engineering and Communication, North China University of Water Resources and Electric Power, Zhengzhou 450011, China

[a] sbzhao@ncwu.edu.cn, [b] 1034515716@qq.com, [c] sokd_0@163.com

Keywords: machine-made-sand concrete (MSC); plain steel bar; deformed steel bar; bond properties; complete bond-slip curves; numerical simulation.

Abstract. Based on the experimental studies, finite element models were built using ANSYS software to simulate the bond properties of steel bars in machine-made-sand concrete (MSC), which considered the nonlinear bond behavior of interface between steel bar and MSC. The concrete strength and the bond length of steel bar are considered as the main parameters for calculation. The complete bond-slip curves of plain and deformed steel bars are well simulated comparing those obtained from the experimental studies. The study gives an theoretical method to analyze the bond properties of steel bar in MSC.

Introduction

As a replacing product of the natural sand, machine-made sand has been widely used in infrastructure at present. However, there are some different properties between machine-made-sand concrete (MSC) and natural sand concrete in proportion, application, mechanical properties, durability, and bond properties [1]. In view of lack of theoretical analysis on the bond properties between steel bars and MSC, the numerical simulation of the bond properties is necessary.

It is a common method to simulate bond properties of steel bar and concrete by ANASYS software. The concrete model is built by SOLID65 element, the steel bar model is simulated by LINK8 element and the bond properties of steel bar with concrete is simulated by the spring element COMBIN39. Based on the bond-slip constitutive relations summed from the experimental studies, the force-deflection curves of the spring element are determined [2]. The bond properties of steel bars in MSC are calculated.

Finite Element Model

The concrete element SOLID65 is a linear element. Close the extra displacement option in the calculation for a best result. The steel bar element LINK8 is a uniaxial tension-compression element, which can be used to model trusses, sagging cables, links, springs, etc. As in a pin-jointed structure, no bending of the element is considered. Plasticity, creep, swelling, stress stiffening and large deflection capabilities are included. To simulate the nonlinear bond behavior between steel bar and concrete, the spring element COMBIN39 is used in concrete model and steel bar model respectively. COMBIN39 is a unidirectional element with nonlinear generalized force-deflection capability that has longitudinal or torsional capability in 1-D, 2-D, or 3-D applications.

The real constants of the concrete elements were set as the default settings, where the real constants of the steel bar elements should set the area of cross-section. The spring element COMBIN39 is defined by two (preferably coincident) node points and a generalized force-deflection curves that are determined by bond-slip constitutive relations. The points on this curve (D1, F1, etc.) represent force (or moment) versus relative translation (or rotation) for structural analyses.

The bond-slip constitutive relations between plain steel bars and MSC could be divided into upward and downward stages, as formulas (1) and (2) shows. The bond-slip constitutive relations of deformed steel bars and MSC included initial slip stage, slip stage, internal splitting stage and descending stage, shown as formulas (3) to (6).

$$\tau = \frac{2x^{0.05f_t} - 1}{x^{0.03f_t}}\tau_u \qquad (0 < x \le 1) \tag{1}$$

$$\tau = \frac{x^3}{(0.1f_t)^3 \cdot (x-1)^3 + x^3}\tau_u \qquad (x > 1) \tag{2}$$

$$\tau = \tau_s \sqrt[4]{\frac{s}{s_s}} \qquad (0 < s \le s_s) \tag{3}$$

$$\tau = \frac{\tau_{\mathrm{cr}}\left(\sqrt[4]{s} - \sqrt[4]{s_{\mathrm{s}}}\right) - \tau_{\mathrm{s}}\left(\sqrt[4]{s} - \sqrt[4]{s_{\mathrm{cr}}}\right)}{\sqrt[4]{s_{\mathrm{cr}}} - \sqrt[4]{s_{\mathrm{s}}}} \quad (s_s < s \le s_{cr}) \tag{4}$$

$$\tau = \tau_{\mathrm{u}}\left[1 - \frac{\left(s - s_{\mathrm{u}}\right)^2}{\left(s_{\mathrm{u}} - s_{\mathrm{cr}}\right)^2}\left(1 - \frac{\tau_{\mathrm{cr}}}{\tau_{\mathrm{u}}}\right)\right] \quad (s_{cr} < s \le s_u) \tag{5}$$

$$\tau = \frac{\tau_u}{0.1\left[f_{\mathrm{t}}\left(1 - \frac{s_{\mathrm{u}}}{s}\right)\right]^{2\alpha_{\mathrm{sr}}} + 1} \qquad (s_{\mathrm{u}} < s \le d) \tag{6}$$

The mathematical expression of the force-deflection curves is $F=\tau(D, X_{\mathrm{i}})A_{\mathrm{i}}$. As the bond stress is approximated to well distribute along the length direction, the mathematical expression can simplified as, where is the bond area corresponding to a spring element.

Table1 List of input parameters for MSC

No.	Elastic modulus E_{c} (MPa)	Poisson ratio	Axial compressive strength f_{c} (MPa)	Tensile strength f_{t} (MPa)	Typical shear transfer coefficients	
					ShrCf-Op	ShrCf-Cl
JA	47082	0.24	35.5	3.18	0.5	1
JB	50852	0.24	42.1	3.63	0.5	1
JC	58463	0.23	58.0	4.64	0.5	1
EA2	48348	0.2	37.5	3.32	0.5	1
EB2	51208	0.2	42.6	3.66	0.5	1
EC2	55194	0.2	51.1	4.22	0.5	1
ED2	57522	0.18	57.1	4.59	0.5	1

Table 2 List of input parameters for steel bars

types	d (mm)	Elastic modulus E_{s} (MPa)	Poisson ratio	Yield strength f_{y} (MPa)	Ultimate tensile strength f_{u} (MPa)
Plain steel bars	16	2.0e5	0.28	303	420
Deformed steel bars	12	2.0e5	0.28	463	554

Isotropic linear elastic constitutive relationship was chosen for concrete element, which was realized by entering a uniaxial compressive stress-strain curve. The stress-strain curve is simplified to a polyline and the corresponding key points were input then. The compressive stress-strain curve is based on the China code GB50010-2010, where the value of elastic modulus, axial compression strength and tensile strength are shown as following formulas [3]

$$E_{c,0} = \frac{10^5}{1.17 + \frac{37.4}{f_{cu,0}}} \tag{7}$$

$$f_{c,0} = 1.97 + 0.81 f_{cu.0} \tag{8}$$

$$f_{t,0} = 0.207 f_{cu,0}^{0.734} \tag{9}$$

Where $f_{cu,0}$ is the test value of cubic compressive strength of concrete (MPa), $E_{c,0}$ is the test value of elastic modulus of concrete (MPa), $f_{c,0}$ is the test value of axial compressive strength of concrete (MPa), $f_{t,0}$ is the test value of tensile strength of concrete (MPa).

The input parameters of SOLID65 are shown in table 1. Bilinear kinematic hardening of material (BKIN) was considered for steel bars models, the input parameters are listed in Table 2. The banding element COMBIN39 needs no materials parameters.

Finite Element Models

The size of finite element models should match the true size of the specimens as far as possible. Considering appropriate mesh density at the same time, the cross section of the concrete model that perpendicular to the axis of steel bar is 154mm×154mm. The steel bar model is placed on the center of concrete model. The bond length of the plain steel bar pull-out specimens are 80mm, 160mm, 240mm and 300mm respectively, where the band length of the deformed steel bars pull-out specimens are all 60mm.

Models were established in accordance with “top to bottom” method. Considering symmetric properties of specimens, the1/2 of structure was modeled. Concrete models were established by mapped meshing. Steel bar elements were formatted from steel bar nodes that generated by copying the concrete nodes. COMBIN39 were generated by bonding steel bar nodes and the corresponding concrete nodes. In order to simulate the bond behavior between steel bar and MSC , [KEYOPT (3)] of the spring element was set as displacement along nodal X axes.

Both the length of concrete elements and steel bar elements that along the length of the steel bar were 5mm, where the length of concrete elements that perpendicular to the axis of steel bar were set at 11mm. Spring elements were set at every 5mm of the bonding parts between concrete and steel bar. finite element model of the specimens is shown in Fig. 1.

As the finite element models were established considering the symmetry, symmetry constraint should be used on the symmetric surface. In addition, according to the true physical constraints in tests, the concrete surface that perpendicular to the steel bar and close to the tensile-side should applied the fixed constraints. Constraints of specimen are shown in Fig. 2.

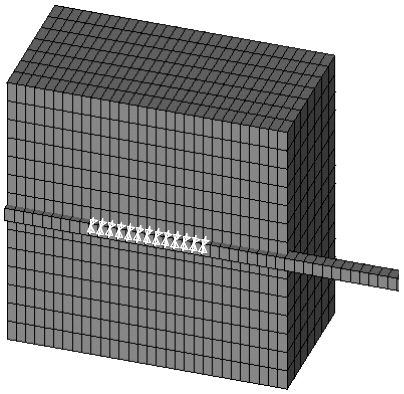


Fig. 1 Finite element model of specimen

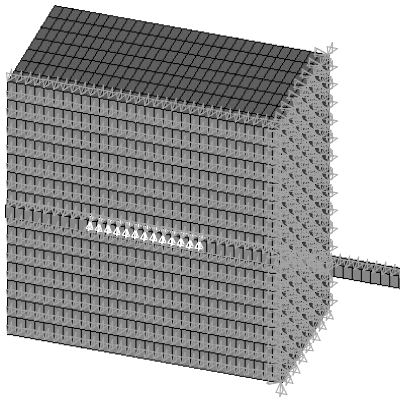


Fig. 2 Constraints of specimen

Calculation

The biggest difficulty in the calculation of the finite element model is normal convergence. In order to solve the convergence problem ,many factors need to be considered, such as the KEYOPT options of SOLID65,analysis model, mesh density, number of sub steps, convergence criteria and precision, solution settings and so on. In this paper, the multi-step displacement loading was applied for achieving convergence; the displacement load was imposed gradually along the positive direction of the X axis. At the same time, the values of force-deflection curves of the spring element were adjusted reasonably in different load steps. Massive trial calculation had carried out to ensure the convergence of simulation results.

Results of the Plain Steel Bars

As shown in Fig.3, with the increasing slip, the average bond stress became larger and larger until reached the largest. Then the entire plain steel bar turned to slip while the bond stress became to decrease. The difference values of slips at free end and tensile side of plain steel bar increased with the load increases, while which had a little decreases as the load decrease after the load peak. When the bond lengths were identical, as the concrete strength grade increases, the bond failure load increased and the slips at free end and tensile side increased significantly. While the concrete strength grades were identical, as the bond length increases, the bond failure load could be increased and the slips at free end and tensile side also be increased

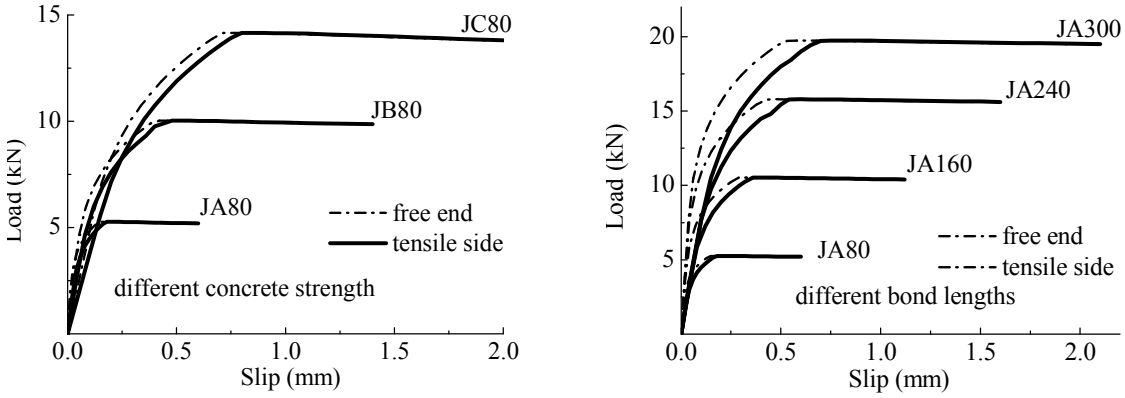


Fig. 3 Load-slip curves

The bond-slip curves of the JA groups obtained from numerical simulation and which obtained from experiments are drawn in Fig.4. They have a good fit. The bond lengths of JA groups are 80mm, 160mm, 240mm and 300mm corresponded to the horizontal abscissa value of starting points are 0.0, 0.2, 0.4 and 0.6. When the concrete strength grade were identical, with the bond lengths increases the bond strength had a little change, the slips at free end and tensile side of plain steel bar corresponding to the bond strength had a linear increases. In addition, the difference values of slips at free end and tensile side of plain steel bar increased with the bond length increases.

The bond-slips curves obtained from numerical simulation and which obtained from formula is shown in Fig. 5. The bond-slip at free end curves obtained from numerical simulation almost coincidence with the formula curves, where the bond-slip at tensile side curves obtained from numerical simulation had a little difference in displacement with the formula curves.

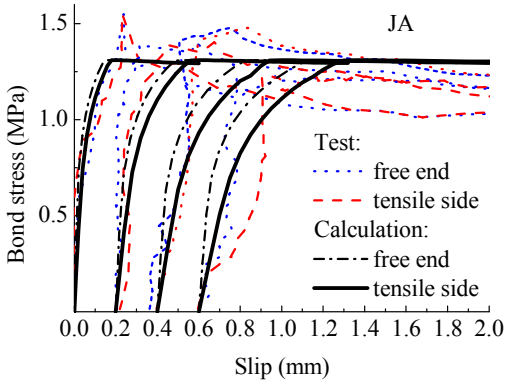


Fig.4 Bond-slip curves of JA

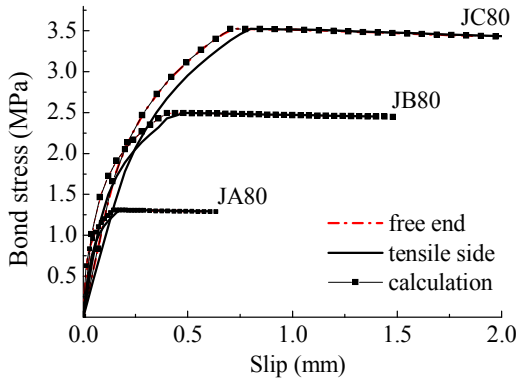


Fig.5 Bond-slip curves of concrete in different grades

Results of Deformed Steel Bars

The bond-slip curves of deformed steel bar obtained from numerical simulation, formula and experimentations are drown in Fig.6, the bond failure strength and corresponding slips are listed in Table3. Considering the slips were measured at the free end of deformed, the slips of simulation curves and formula curves are all use slips of the free end. Simulation curves have a good fit with

formula curves. There are few fluctuation near the peaks in the simulation curves, which is influenced by the unstable calculation that caused by spring stiffness changes. In a word, It is feasible that use finite elements method to simulate bond behavior of deformed steel bar and MSC.

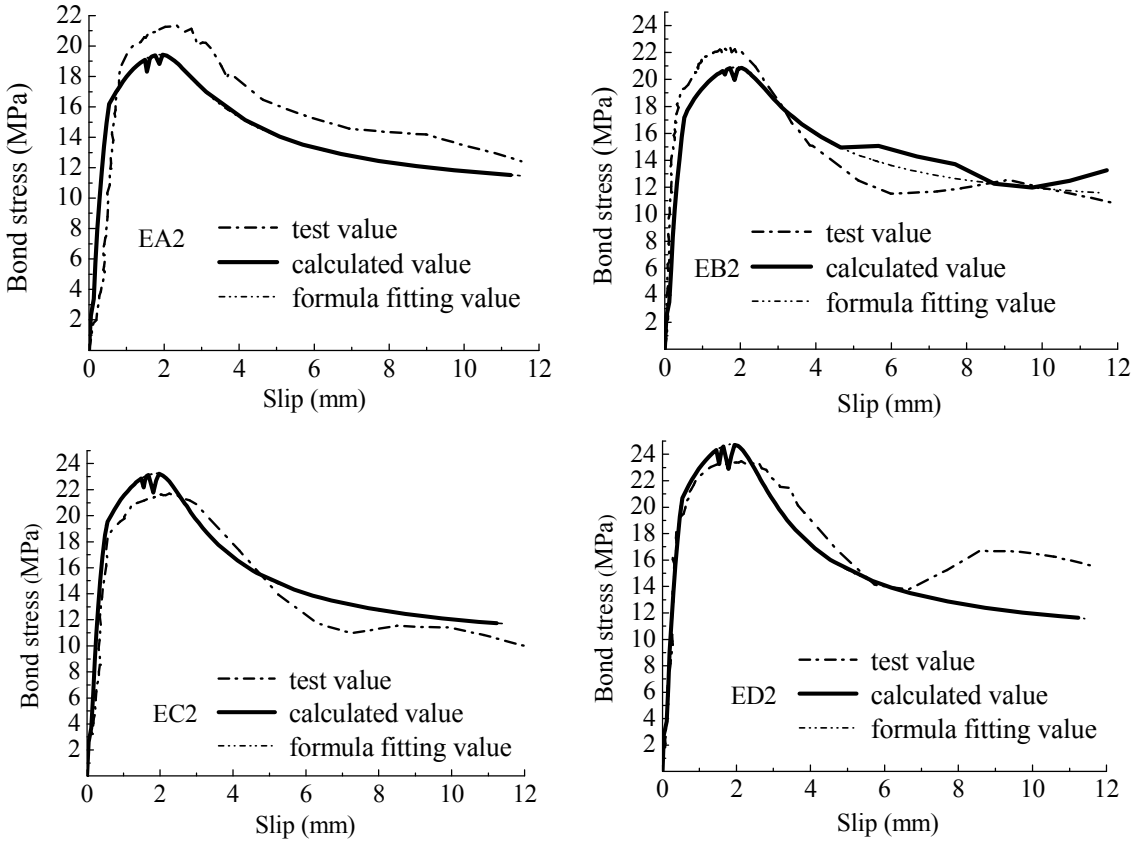


Fig. 6 Bond-slip curves

Table 3 Comparison of characteristic values of bond-slip

No.	Test values		Calculated values		
	τ_u (MPa)	$s_{f,a}$ (mm)	τ_u (MPa)	$s_{f,a}$ (mm)	$s_{t,a}$ (mm)
EA2	21.37	2.19	19.38	1.76	2.2
EB2	22.40	1.74	20.86	2.03	2.5
EC2	21.74	2.24	23.23	1.98	2.5
ED2	23.44	1.90	24.72	1.94	2.5

Conclusions

Nonlinear spring element COMBIN39 is used to simulate the bond properties of steel bar in MSC. It is feasible both about deformed steel bar and plain steel bar in MSC. In the calculations, the appropriate element type, mesh density and convergence criteria ,and the proper loading can obtain reasonable results.

References

[1] F. Li, Y. Zeng and C. Li: Evaluation of relations among basic mechanical properties of concrete with machine-made sand. Advanced Materials Research, Vols. 418-420 (2012) 441-444.

[2] X. Ding, Bond Properties of Plain Steel Bar with Machine-made Sand Concrete, Thesis for Master Degree, North China University of Water Resources and Electric Power, Zhengzhou, China, 2012.

© (2012) Trans Tech Publications, Switzerland
doi:10.4028/www.scientific.net/AMM.238.181

Brief Analysis on Crack of Unbonded Partially Prestressed RPC Beam

Qiang Fu[1, a], Bingfeng Lv[1,b], Xia Cao[1,c], Lingzhi Jin[1,d] and Ning Deng[2,e]

[1]GuangXi Key Laboratory of Constructional Engineering Test, Guilin University of Technology, Guilin 541004, China

[2]Guangxi Institute of Building Research and Design, Nanning 530011, China

[a]0331fuqiang@163.com, [b]lbf_7@163.com, [c]caoxia6510@163.com, [d]jlz-5904@163.com, [e]chmdgg@163.com

Keywords: reactive powder concrete; unbonded prestressing; experimental study; crack.

Abstract. Reactive Powder Concrete (RPC) has excellent properties such as high toughness and high durability. In this paper, based on the experimental research of the different unbonded prestressed tendons of the unbonded partially prestressed RPC beams, the crack calculation of prestressed RPC beams is analyzed. The results show that the crack regulation is special in some extent of the unbonded partially prestressed RPC beams. It is suggested that the crack width of unbonded partially prestressed RPC beams calculated in accordance with the specification for unbounded partially prestressed concrete structure should multiply the reduction factor of 0.7.

Introduction

Crack is the main factor affects durability of structure. Unbonded prestressing technology has improved the cracking load of concrete structures greatly. However, due to the prestressing tendons and concrete do not bond; the crack width limit depends mainly on the role of non-prestressed tendons. In this experiment mix reactive powder concrete with the steel fiber, the adhesion stress between concrete and reinforcing tendon than ordinary concrete, reduced the bond-slip between the tendon and concrete, which lower the average strain of tendon and make the average tensile strain in the main cracks of the steel fiber reinforced concrete higher than ordinary concrete, so reduces the main crack width [1].The computational method of ordinary concrete beam crack is also suitable for high-strength concrete and steel fiber reinforced concrete, which has been confirmed by many experiments [2]. So the computational method of reactive powder concrete crack width can refer to the common concrete, and combine the characteristic of reactive powder concrete for further research. According to experimental results, based on the theory of the prestressed concrete beam, this thesis explore the calculation method of crack width and crack load in unbonded partially prestressed reactive powder concrete beam.

General Situation of Experiment

The experiment comprises eight unbonded prestressed reactive powder concrete beams. According to different conditions of non-prestressed tendons can be divided into 4 groups, as shown in table1. Adopt one root diameter of 15.2 mm, strength for 1860 MPa linear prestressed tendon is shown in Fig 1. Clip and anchorage is produced by Liuzhou OVM Company. The construction of the anchorage in the component the tension side and the fixed end are the same. The control stress of prestressed tendon $\sigma_{con}=0.7f_{ptk}=0.7\times1860=1302$MPa and the test tension control force $F_l=\sigma_{con}A_p=0.7\times1860\times140=182$kN. At the one end of the beam adopted graded tension and then anchored. The pre-tensioning force is $10\%F_l$, then in ten stages, with each stage $10\%F_l$ to stretch.

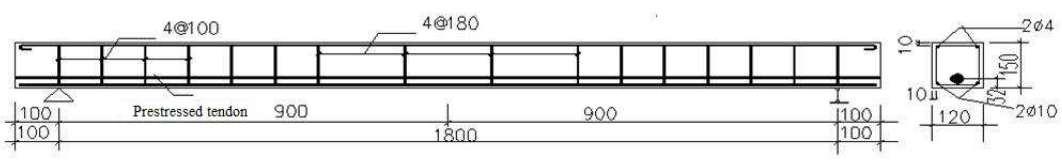


Fig. 1 Reinforcements of prestressed RPC beam

Table 1 Design of prestressed beams

No.	Non-prestressed tendons located in the upper part	Non-prestressed tendons located in the lower end	Stirrup	Prestressed tendon	Number of beams	Length of the beam (mm)
L1	None	None	None	one with 15.2mm diameter, 1860MPa, linear tendon	L1-1, L1-2	2000
L2	2φ4	2φ10	φ4@100/180		L2-1, L2-2	2000
L3	2φ10	2φ4	φ4@100/180		L3-1, L3-2	2000
L4	2φ4	2φ4	φ4@100/180		L4-1, L4-2	2000

Third point loading sees Fig. 2. Loading process is divided into preload and formal loaded. Preload [3]: Carried out three times, each taking the theoretical calculation of 20% of the calculated cracking load, and then three times to finish unloading. After each time load (or unload), pause for 10 minutes and then load the next level. Formal loaded: Before the load is added to 90% of the calculated cracking load, each load to take a 10% standard load. After the load is added to 90% of the calculated cracking load, each load to take a 5% standard load, until the first crack appears. When the first crack appears, each stage loading taken take a 10% standard load; to experimental load calculation value of 90%, each stage loading values of standard load value is5%; each with one stage, resting10min. After the load is added to 90% of bearing capacity of beams, each load to take a 5% standard load, pause for 10 minutes and then load the next level.

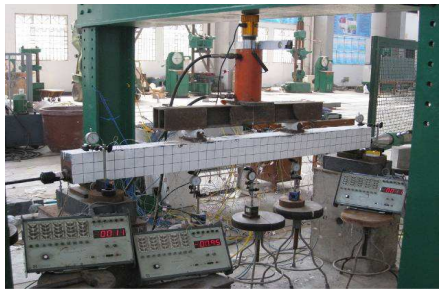


Fig. 2 Picture of the Test

Analysis of Experimental Result

Analysis of Stress. In the calculation of the crack width, the deformation, or the ultimate bearing capacity, the stress of prestressed tendon in unbounded partially prestressed concrete are indispensable parameters. Through the axial force sensor and bar measure strain, draw the load–stress curve of steel stranded wire diagram, as shown in Fig. 3 (select only one beam from each group).

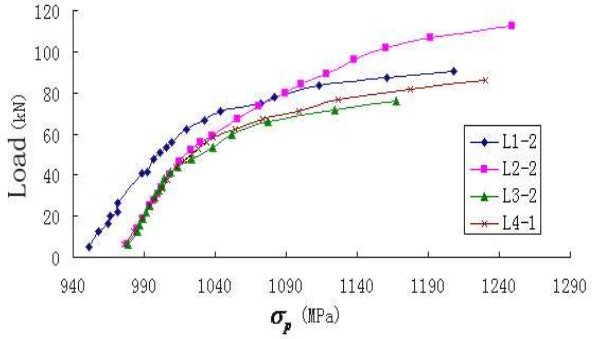


Fig. 3 Load with stress of prestressed tendon

Before the beam crack, the stress of prestressed tendons of L2, L3, and L4 are slightly different. Due to the effective prestresse of L1 is smaller than others', so in the same load state its stress is small. After the beam crack, the stress of L3, L4 is bigger than L2. This is due to at the lower end of L2 beam configure two diameter of 10 non-prestressed tendons, reducing the force of the prestressed tendons. Then the stress of L2 is bigger than the other three in the failure stage. In view

of this, quantity of non-prestressed tendons and effective stress of the steel stranded wire is the main factors of influence stress of steel stranded wire, as with ordinary concrete member, the stress performance of the partially prestressed beams is better.

Analysis of Crack Spacing. According to the Chinese code GB50010-2010, the calculation method and formula of the average crack spacing [4]: $l_{cr} = \beta(1.9c + 0.08d_{eq} / \rho_{te})$, the calculated and measured results are shown in Table 2.

Table 2 L2 crack spacing's measured and calculated results under normal loads

No.	ρ_{te}	d_{eq} (mm)	c (mm)	$c_{cr,m}$ (mm)	$t_{cr,m}$ (mm)	$c_{cr,m}$/ $t_{cr,m}$
L2-1	0.0174	14.28	20	103.6	83	6.35
L2-2					74	6.88

Comparison of the data can be seen from table, the calculated average crack spacing value of L2 beam according to specification is larger than the measured value. In calculation of the average crack spacing for reactive powder concrete beam, can be coupled with a reduction factor in the formula of the above specification to consider the influence of steel fiber on the average crack spacing effect: $l_{cr} = \beta(1.9c + 0.08d_{eq} / \rho_{te})\alpha$. According to the measured values of the average crack spacing of the beams, $\alpha \approx 0.7$ is more reasonable.

Analysis of Crack Width. The non-uniformity coefficient of longitudinal tendons in this experimental less affected by the steel fibers, so this paper calculate the non-uniformity coefficient ψ of tensile tendons based on the Chinese code GB50010-2010. The characteristic coefficients of loaded members include a variety of the effects of parameters, can be expressed as $\alpha_{cr} \equiv c_p c_t c_c c_f$. The value of the reactive powder concrete members should be smaller than the specified value due to the limitations of this test, according to the specification is taken as 1.7. Bring Measured data in this experiment into the above formula can be obtained the calculated value of crack width are shown in Table 3.

Table 3 Calculating and measured values of the crack width of L2

No.	α_{cr}	ψ	σ_s^t (σ_s^c) (MPa)	w_{max}^c (mm)	w_{max}^t (mm)	w_{max}^c / w_{max}^t
L2-1	1.7	0.4(0.4)	304.92(604.26)	0.10(0.2)	0.08	1.25(2.5)
	1.7	0.4(0.44)	359.1(685.75)	0.12(0.25)	0.16	0.75(1.56)
	1.7	0.4(0.5)	407.19(748.61)	0.14(0.31)	0.2	0.7(1.55)
L2-2	1.7	0.4(0.4)	267.12(644.36)	0.09(0.22)	0.1	0.9(2.2)
	1.7	0.4(0.47)	330.12(722.98)	0.11(0.28)	0.18	0.61(1.55)
	1.7	0.4(0.55)	409.92(817.5)	0.14(0.38)	0.25	0.56(1.52)

As can be seen from the above table, when the stress reaches yield strength or so , the crack width calculated value is relatively accurate; when the stress exceeds the yield limit, crack width Calculated by the measured values of steel stress is smaller than the actual measuring value. The crack width calculated by steel stress in accordance with the specification has a larger gap with the measured values, largely because the calculation of the steel stress did not consider the tensile strength of reactive powder concrete.

According to the above analysis, in calculation of crack width of the RPC structures, the calculation of steel stress is the main factor affecting its accuracy. According to actual internal force diagram of cracking section calculation of steel stress is more accurate and reasonable. But for engineering design, it is more complicated and difficult to be achieved. Therefore, suggest that by experimental research on steel stress modify the formula in specification and take into account of the reactive powder concrete tensile effect to modify the crack width.

Conclusions

Taking unbounded partially prestressed concrete beam for the study, crack resistance and crack width are carried out experimental study and theoretical analysis. The result of the experiment conform theoretical calculations basically, experimental results and conclusions which have certain practical reference value.

Experiment phenomena and the experimental data indicate that the measured value of crack spacing is less than the values calculated by the formula in " code for design of concrete structures" and suggest that modify the calculated values. The experiment results show that the reduction coefficient is 0.7.

At the same time, it should explain that , according to the formula of "technical specification for concrete structures prestressed with unbonded tendons" ,there is a large discrete to calculate crack width and recommend to modify the formula.

Acknowledgements

Thanks for the support by GuangXi Key Laboratory of Constructional Engineering Test(11-cx-04) , Guangxi science and technology development project(No.0995004) and Innovation Project of Guangxi Graduate Education(2011105960814M11).

References

[1] T. Lin, Research on bending performance of steel fiber high-strength concrete beam, Thesis for Master degree, Dalian University of Technology, Dalian, 2002.

[2] C. Huang, G. Zhao, Z. Wang, Simplified analysis on flexural member’s crack width of steel fiber high-strength concrete beam, Journal of Dalian University of Technology, 5 (1993) 373-376.

[3] GB 50152-92, Standard Methods for Testing of Concrete Structures. China Building Industry Press, Beijing, 1992.

[4] D. Gao, Q. Zhang, Q. Guan, Simplified analysis on cracking moment of steel fiber high-strength concrete beam, Journal of Zhengzhou University, 4 (2005) 34-38.

© (2012) Trans Tech Publications, Switzerland
doi:10.4028/www.scientific.net/AMM.238.185

Experimental Research for Flexibility Properties of RC Beams Strengthened with Steel Wire-Polymer Mortar

Chiyun Zhao [1, a], Shimin Huang[2,b], Qiulai Yao[2,c] and Yajing Chen[1,d]

[1]Beijing Higher Institution Engineering Research Center of Structural Engineering and New Materials, Beijing University of Civil Engineering and Architecture, Beijing, China

[2]China Academy of Building Research, Beijing, China

[a]zhaocy@bucea.edu.cn, [b]hsmcabr@yahoo.com.cn, [c]come-ql@sina.com, [d]chenyajing0345@126.com

Keywords: flexural performance; reinforced concrete beam; polymer mortar; strengthening; experiment; interfacial bond strength.

Abstract. This paper presents the results of the experimental investigation on the flexural performance of beams strengthened with steel wire-polymer mortar. A total of five rectangular doubly RC beams were constructed and tested to failure. The test variables were numbers of reinforcement layers and configuration. A new accurate method to measure elongation of steel wire was proposed. Then the interfacial bond strength between concrete and polymer mortar was tested. The failures of the specimens were all bending failures and polymer mortar layer debonded from beam was not occurred. Only a few wires were pulled off in failure. The polymer mortar and concrete has a better bonding effect. Steel wires play the more effective tensile roles of themselves. After strengthened, the RC beams improve their bending bearing capacity and bending stiffness, delay the cracks occur and crack development.

Introduction

Steel wire-polymer mortar strengthening existing reinforced concrete structures is a new method, which uses steel wire as strengthening material and polymer mortar as matrix to compose a thin-layer structure. Generally the thickness of one steel wire reinforcement layer ranges from 25 mm to 30 mm. Steel wire has advantages such as high strength, no rust, convenient for transportation and construction. Polymer mortar is inorganic materials and has good properties of bonding with concrete material. This technology also has the following advantages: the resistant of corrosion, high temperature and aging. Because of such characteristics, steel wire-polymer mortar has a broad application prospect. In recent years, scholars around the world have developed numerous experiments and theoretical studies in the field of mortar strengthened structures. In China, the research by Nie [1,2], Cao [3, 4], Liu [5] et al. are to adopt polymer mortar to strengthen RC beams, columns and frame joints. In other countries, Logan [6], Basaunbul [7] et al. use mortar strengthening technology to study RC beam cracks behavior.

In this paper, a total of five rectangular doubly RC beams were constructed, strengthened with steel wire-polymer mortar and then tested to failure to study flexural performance such as bending bearing capacity and bending stiffness, crack distribution and development, ductility of strengthened beam and steel wire stresses. During the failure tests, a new accurate method to measure elongation of steel wire is proposed.

Experimental Program

Experimental Purpose. The experimental purpose is to explore the bending performance of strengthened RC beams by using steel wire-polymer mortar method, such as bending bearing capacity, failure type, bending stiffness, crack distribution, crack development and bond strength between old concrete and new polymer mortar layer.

Experimental Materials and Related Parameters. There were 5 reinforced concrete beams in the test. The cross section of each specimen was 200 mm wide and 300 mm deep. The span and clear span of the specimens were 3400 mm and 3000 mm, respectively. There were 3 longitudinal steel

bars of diameter 20 mm at the bottom of the specimens, and 2 bars of diameter 14 mm at the top of them. The steel grade of bars was HRB335. Single loop of diameter 10 mm were placed 80 mm on center in nearby the end of the specimens and 150 mm in the middle of them, respectively. The steel grade of stirrups was HPB235. Concrete strength grade was C20, and the concrete cover was 25 mm. The specifications of steel wire were 6 × 7 + IWS, the mesh of diameter 3.05 mm were placed 30 mm on center. The nominal tensile strength, elastic modulus of steel wire was 1870 MPa and 134 GPa, respectively. The compressive and tensile strength of polymer mortar were 24 MPa and 4.8 MPa, respectively.

BF-1 was the compared member that unstrengthened. BF-2 and BF-3 were strengthened with one layer steel wire-polymer mortar of depth 25 mm, while BF-4 and BF-5 were strengthened with two steel wire layers of depth 30 mm. Especially at the end of beam BF-2 and BF-4 were strengthened with U-shaped reinforcement layer to enhance the anchor of steel wire at the bottom, as shown in Fig. 1. The details of the specimens were shown in Fig. 2.

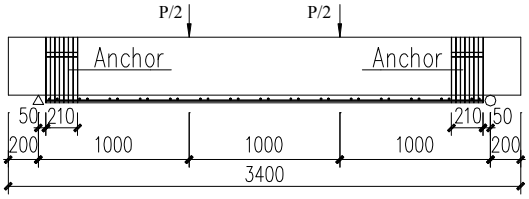


Fig. 1 Sizes of Strengthened beams and loading

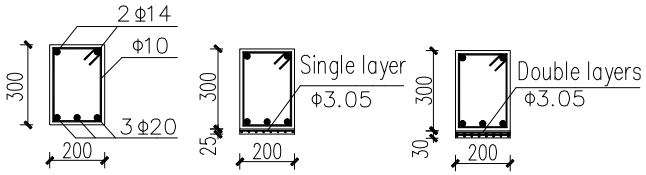


Fig. 2 Beam section before and after strengthened

Loading Equipment and Test Measurement Contents. Loading equipment in the tests was shown in Fig. 3. Measurements of the tests were load value, steel strain, concrete (mortar) strain, the displacement of support point, mid-span and loading point, the elongation of steel wire and so on. All of the contents and methods of measurements were in Table 1.

Concrete strain gauges, which standard was 100AA, were pasted along the high direction of the mid-span of the beam to measure concrete strain, as shown in Fig. 4. Steel strain gauges, which standard was 3AA, were pasted the longitudinal bars to measure the steels strain, as shown in Fig. 5. In each steel wire connect stroke lead extensometer, which lead is 200mm, to measure the elongation of steel wire, as shown in Fig. 6. In the mid-span, loading point and support point install displacement meter to measure the vertical displacement of the five-point, as shown in Fig. 4.

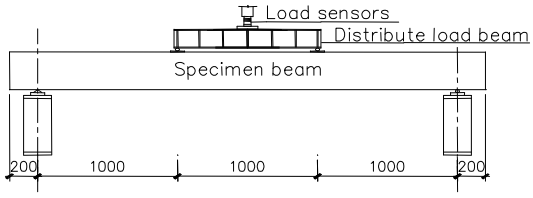


Fig. 3 Loading equipment

Table 1 Instruments and measurement contents

Instruments	Measurement contents
load sensors	load value[kN]
concrete strain gauge	concrete strain
displacement meter	deflection[mm]
steel strain gauge	steel strain
instrument for deforming	steel wire elongation[mm]

The more accurately mechanical behavior of steel wire can be measured, the more correctly strengthened effect by steel wire-polymer mortar may assess. In this paper, a new method for measuring the elongation of steel wire was proposed. Two Z-shaped steel rods, which have so larger diameters that could be assumed as rigid body comparing to the steel wire, were inserted into the clamps preinstalled in steel wire of the beam, and the steel rods were parallel to the tested steel wire, so the displacement of steel rod was equal to the elongation of steel wire. The proposed testing method was shown in Fig. 7.

Results and Discussion

Bending Bearing Capacity of the Specimens. To increase the bearing capacity of strengthened specimens was one of the main purposes, steel wire-polymer mortar strengthened concrete structures equivalent to the reinforcement of itself in vitro. During the test, the bending bearing capacity of the 5 beams are shown in Table 2, It can be seen that the bending capacity of single-layer strengthened

beams BF-2 and BF-3 are increased by 9.8 % and 7.9% than the BF-1 contrast component, the double-layer strengthened BF-4, BF-5 are increased by 21.8% and 17.8% than BF-1. It illustrates that RC beams strengthened with steel wire-polymer mortar can significantly increase their bending capacity.

The 5 test beams failure in the form of bending damage, after the longitudinal bars yielded; the compression zone concrete was crushed.

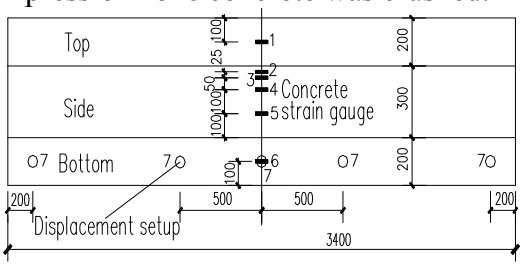


Fig. 4 Measured points layout at specimens

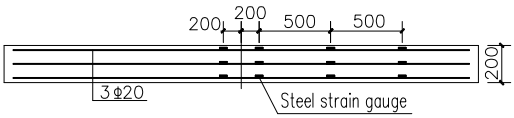


Fig. 5 Measured points layout at steel bars

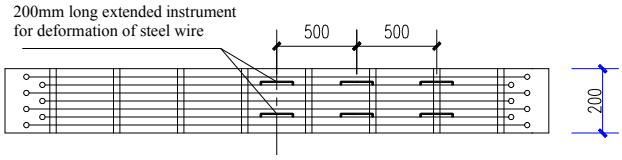


Fig. 6 Measured points layout at steel wires

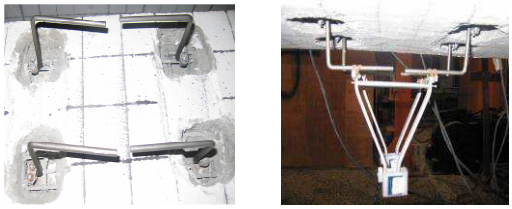


Fig. 7 Method of measuring the elongation of steel wire by the test

Beam Deflection. The mid-span deflection comparison of 5 beams was shown in Fig.8, it can be seen from the chart that, before the reinforcement layer cracks, the load and mid-span deflection were of linear relationship basically, and the slop of beam BF-4 increased significantly than BF-1 which illustrate that beams after strengthened can improve their stiffness, but other reinforcement increased level of rigidity was not obvious; with the load increasing, the reinforcement layer cracks at first, then the pull district concrete cracks, after the cross-section cracked, stiffness reduced, deflection with rapid growth than cracks occur before, load-deflection curve appear turning point. However, due to the existence of steel wire, the increasing rate of the deflection with the load is smaller than the contrast beam.

Table2 Bearing capacity of the specimens

specimen	Bearing capacity [kN]
BF-1	165.6
BF-2	181.8
BF-3	178.7
BF-4	201.7
BF-5	195.1

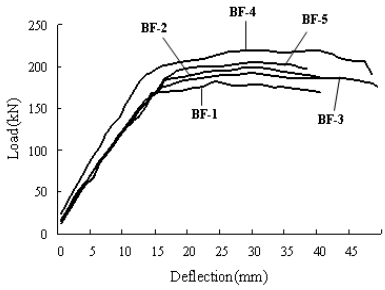


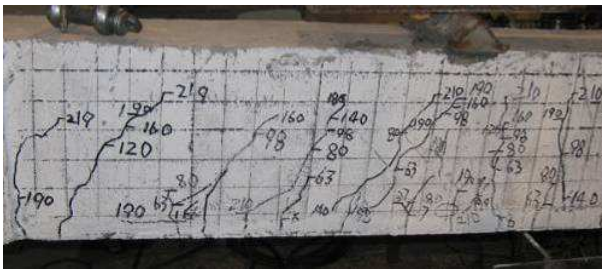
Fig. 8 Load-deflection curve of the specimens

Beam Cracks. In beam BF-1, cracks first occur at the beam side when the load was 18kN, the crack width was 0.02 mm, then the beam bottom also cracks; when the load was 108 kN, the crack width of beam bottom and beam side was 0.2 mm, and the crack width was 0.4 mm with the load of 170 kN.

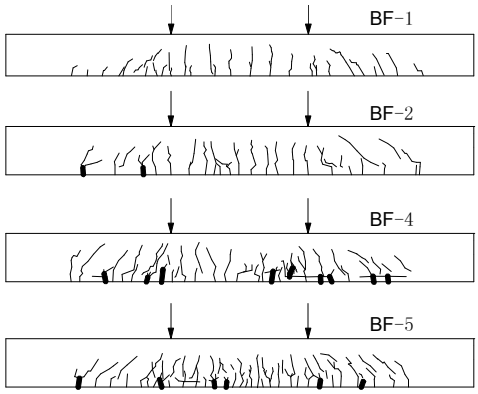
In beam BF-5, cracks first occur at the beam bottom polymer mortar layer when the load was 22.5 kN, the crack width of concrete crack was 0.06 mm, the crack width of mortar layer was 0.16 mm with the load of 51.9 kN. and the width was 0.2 mm with the load of 69.37 kN, at this time the crack width of concrete was 0.02 mm; then the cracks of concrete and mortar develop together.

The cracks development of the other strengthened beams were almost the same with beam BF-5, were not depict.

From the record above and the phenomenon during the experiment we can see that, steel wire mesh-polymer mortar strengthened components have good crack resistance, the crack width and pitch of strengthened component is smaller than the compared component, the crack form of strengthened components are more closer and disorder than the compared specimen. Cracks of some of the test beam damage are in Fig. 9.



(a) photo for cracks disdribution in BF-4 in failure



(b) cracks disdribution in failure

Fig. 9 Sketch for cracks distribution in the specimens

Analysis of the Longitudinal Bar Yielding. During the test, each beam was measured the strains values of longitudinal steel bars at 12 points, in order to analysis the role of longitudinal bar act and study longitudinal bar yielded at which load, now list the load value of the longitudinal bars yielding, as shown in Table 3, where load 1 is the value of bottom steel bar which first yield, and load 2 is the value of bottom longitudinal bar are all yield.

It can be seen from Table 3 that, longitudinal bars at beam bottom bending section all yield before the beams reached their ultimate bending bearing capacity, it shows that the vertical bars played the full role and we also see that strengthened beams yield load value has increased than the compared beam, which fully proved the reinforced effect.

Steel Wire Strains. As already mentioned, the elongation of the steel wire was measured during the test, the experimental results in accordance with steel wire measured length and the elasticity modulus(134 GPa) can calculate the stress of steel wire stress, as shown in Table 4.

The tensile strength of steel wire is 1870MPa, it can be seen from Table 4 that, when the components achieved the ultimate bearing capacity, the steel wire stress spend more than 75% except beam BF-2 is 60%, illustrates that steel wire played a full role but carbon fibre strain play the role in the amount of 40% [6]. Only a few wires within beam BF-5 were pulled off, other components do not occur such situation, since during the test the beam bottom longitudinal tendon bars first yield then concrete crushed, and the steel wire damage at last, so this is why only a few wires were pulled off.

Table3 Loading analysis of longitudinal bars yielding

specimens	load1[kN]	load 2 [kN]
BF-1	109	145
BF-2	124	158
BF-3	120	167
BF-4	127	170
BF-5	118	162

Table 4 Steel wire stress analysis

specimens	steel wire stress σ	σ/1870
BF-2	1123	0.60
BF-3	1397	0.75
BF-4	1561	0.83
BF-5	1671	0.89

Conclusions

By the experimental process and analysis of the test results for the bending performance of specimens strengthened with steel wire-polymer mortar, some significant conclusions for can be got:

Experiments show that steel wire-polymer mortar strengthened reinforced concrete beams, can obviously improve the bending bearing capacity of the beam. The bending bearing capacity of single strengthened beam BF-2 and BF-3 has increased about 9% than the BF-1 contrast component, double strengthened beam BF-4 and BF-5 has improved about 20% than BF-1.

Steel wire mesh-polymer mortar strengthened RC beams can delay the beam cracks occur and cracks development, after strengthened the beam cracks are in the form of more closer and disorder.

The final failure form of 5 test beams are all of bending damage, domestic polymer mortar and concrete bond well with each other, does not appear polymer mortar layer falling off from the beam during the test.

Steel wires play the more effective tensile roles of themselves. Beam BF-2 played the stress value of 60%, other components are played more than 75%, but carbon fiber strain play the role in the amount of 40%.

Acknowledgments

This research is supported by Institute of Earthquake Engineering, China Academy of Building Research. This research is also supported by Doctoral Scientific Research starting Foundation in Beijing University of Civil Engineering and Architecture.

References

[1] J. Nie, H. Wang, T. Zhang et al: Experimental study on flexural behavior of RC beams strengthened with stainless steel wire mesh and permeability polymer mortar, Journal of Building Structures, 26 (2005) 1-9.

[2] J. Nie, Q. Cai, T. Zhang, H. Wang et al: Experimental study on shear behavior of RC beams strengthened with stainless steel wire mesh and permeability polymer mortar, Journal of Building Structures, 26 (2005) 10-14.

[3] Z. Cao, A. Li and Y. Wang: Experimental study on beam-column connections strengthened with high-strength steel wire mesh and polymer mortar, Journal of Building Structures, 27 (2006) 10-15.

[4] Z. Cao, A. Li and Y. Wang: Experimental study on beam-column joints with floor slab and transverse beams strengthened with high strength steel wire mesh and polymer mortar, Journal of Building Structures, 28 (2007) 130-136.

[5] B. Liu, G. Xing and T. Zhu: Experimental investigation and finite element simulation about RC T-beams strengthened with wire cable mesh and polymer mortar, Journal of Xi'an University of Architecture & Technology, 38 (2006) 103-108.

[6] D. Logan and S. P. Shah: Moment capacity and cracking behaviour of ferrocement in flexure, Journal of the American Concrete Institute, 70 (1973) 799-804.

[7] I. A. Basaunbul, A. Gubati, Al-Sulaimani et al: Repaired reinforced concrete beams, ACI Material Journal, 87 (1990) 345-354.

© (2012) Trans Tech Publications, Switzerland
doi:10.4028/www.scientific.net/AMM.238.190

Calculation Method of Crack Width of Steel Fiber Reinforced High-strength Concrete Beams under Fatigue Load

Danying Gao [a] and Ming Zhang [b]

Zhengzhou University, Zhengzhou 450002, Henan, China

[a]gdy@zzu.edu.cn, [b]zhangmingzzu@126.com (corresponding author)

Keywords: calculation method; steel fiber; high-strength concrete; fatigue.

Abstract: Based on the fatigue test, 8 steel fiber reinforced high-strength concrete beams are studied, the influencing factors of crack width are discussed in the paper, and the calculation method of crack width under fatigue load is investigated. Based on the analysis of test results, the formulas are put forward. The results show that adding steel fiber into the high-strength concrete beams can prevent the development of the fatigue crack, fatigue crack widths are decreased by 26.0%~121.0% and the calculated values have good agreement with test date.

Introduction

Steel fiber reinforced concrete is a complex material which is made up by doping steel fiber into concrete. Recently years, steel fiber concrete is widely researched and applied.Previous experimental studies and theoretical analysis [1-3] show that steel fiber in the concrete can decrease the stress concentration of concrete crack tip, hinder the development of concrete cracks, reduce the steel stress in the concrete structure, increase the binding power between steel and concrete at the same time, and reduce crack width. In recent years, with the development of high performance concrete, the study on crack of high-strength concrete structures under fatigue load become more important. In the paper, through the fatigue tests of 8 steel fiber high-strength concrete beams, the influence just like steel fiber volume ratio, steel fiber type and the range of steel fiber adding into beams on crack width are studied, the calculation method of crack width of steel fiber reinforced high-strength concrete under fatigue load are discussed ,and the formulas are put forword.

General Situation of Tests

According to technical specification for concrete structures and fiber reinforced concretestructures [4-6], 8 beams are designed, made up and divided into 3 series. In the first series, the steel fiber volume ratio parameter are included 0.5% , 1.0% , 1.5%. In the second series, steel fiber types are changed. These changes include end-hook steel fiber, milled steel fiber and waved steel fiber. The third series alter the range of the steel fiber adding into beams to ansys the fatigue performance of steel fiber reinfored partly concrete beams.

Design of Specimens. The beams have a cross-section of 15 cm ×30cm and are 300 cm long. All the beams were the same size. The detailed dimension and form of reinforcement are displayed in Fig. 1 and the number and main parameter of specimens are displayed in Table 1.

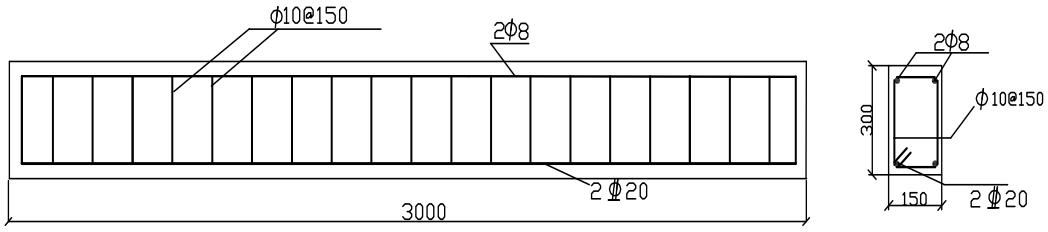


Fig. 1 The dimension and reinforcement

Table 1 Specimens parameters

Numbers	Geometric parameter $b\times h$ (mm)	Steel fiber type	Adding range of steel fiber	Volume ratio	Compressive strength of the cube (MPa)
F0	151×302	-------	h	0	76.5
F1	151×301	end-hook steel fiber	h	1.0%	69.5
FSF1	149×304	end-hook steel fiber	h	0.5%	79.7
FSF2	150×301	end-hook steel fiber	h	1.5%	82.2
FST1	148×298	milled steel fiber	h	1.0%	78.3
FST2	152×297	waved steel fiber	h	1.0%	78.9
FH1	151×301	end-hook steel fiber	1/3h	1.0%	73.1
FH2	147×303	end-hook steel fiber	1/2h	1.0%	73.1

Testing Program. The beams were tested in one-point bending configuration with a simply supported span of 2700 mm. In order to simulate the actual work, the beams bearings use rubber bearing. The beams should keep geometrical centering, and steel plate should be placed under the bearings in order to prevent the occurrence of concrete crush. Based on situation of the test equipments and practical applications, fatigue-loading frequencies of 5 Hz is used and fatigue load ranges: $0.15M_u$~$0.5M_u$ is applied. According to standard for test methods of concrete structures [7] , The test procedure is divided into three steps: static load test, fatigue test and damage test. For the fatigue tests, the beams are initially loaded beyond the cracking load up to the maximum level of the associated fatigue load range before starting the fatigue load cycles. Loads should be regulated again and again in the process of test in order to limit error not more than ±3%. When the cycling number reaches 10000, 50000, 100000, 150000, 200000, 500000, 1 million, 1.5million and 2 million times, fatigue load was terminated to perform static response. Fatigue test was terminated either at about 2 million cycles to perform static test utill beams damage. The test unit and specimen in position are displayed in Fig. 2.

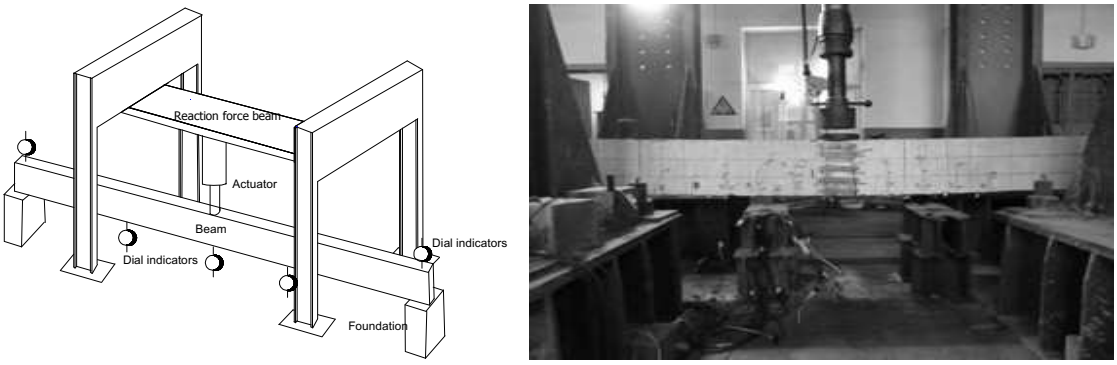
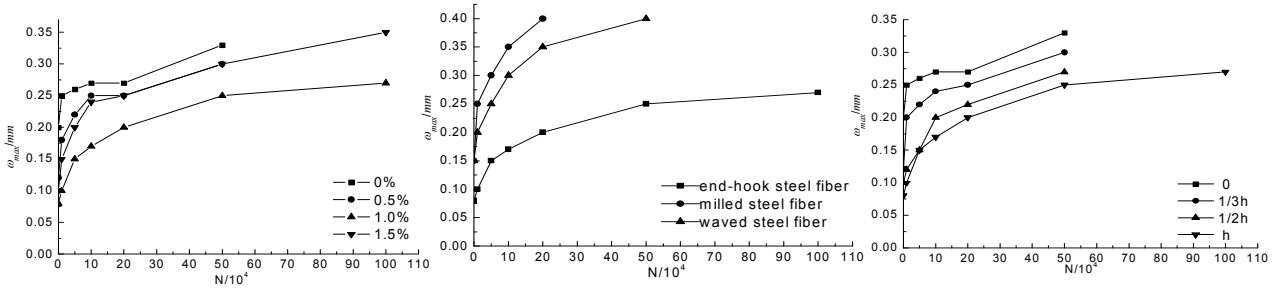


Fig.2 Test equipments and loading



(a) (b) (c)

Fig.3 The development curves of fatigue crack width

Analysis of Test Result

The development curves of maximum crack width ω_{max} along with the fatigue cycles are shown in Fig. 3. Fig. 3a shows the development curves of maximum crack width ω_{max} of different steel fiber volume ratio parameter included 0%, 0.5% , 1.0% , 1.5%. It is showed that accompanied with the fatigue cycles, crack width of all the specimen becomes bigger and has a non-linear upward tendency primarily. Compared with reinforced concrete beam without steel fiber, beams joined steel fiber can effectively reduce the crack width, the reduction of steel fiber reinforced concrete beams crack width are 52%~ 121% under different fatigue cycles. But the beam with 1.5% steel fiber volume ratio don't conform to the rules beacuse that the phenomenon of steel fiber is caking in the beams when steel fiber volume ratio is high. The analysis of actual measured steel fiber distribution can prove the phenomenon of caking. Steel fiber types can influence the bond behavior between steel bar and concrete, so the steel fiber types is also a key influence factor on the cracking moment of steel fiber reinforced concrete beams. 3 types of steel fiber include end-hook steel fiber, milled steel fiber and waved steel fiber. In the Fig. 3b, it is shown that beams with end-hook steel fiber got the most remarkable effect, the reduction of fatigue crack width are 38%~110% compared with other two types of steel fiber. The anti-cracking property of milled steel fiber and waved steel fiber shows little difference. Fig. 3c shows the development curves of maximum crack width of different range of the steel fiber adding into beams. The reduction of maximum crack width are 26%~87% following with the range growth of the steel fiber adding. Fig. 3a~c also show that fatigue crack width increases rapidly in initial 200000 fatigue cycles, then the speed of increase of fatigue crack width becomes slow, the development of fatigue crack width enters a relatively stable stage.

Calculation Model and Formulas

Based on the Chinese Code [5] and analysis of various influence factors on the steel fiber high-strength concrete beam fatigue crack width, the calculation formulas of crack width of the steel fiber high-strength concrete beam under fatigue load is put forward. According to the bond-slip theory, considering various influence factors to the parameters in above formulas, the formula derivation is shown in paper.

The Bond-slip Theory. Based on the theory of bond-slip and previous studies, the crack width could be considered as value of differece between steel and concrete elongation in a crack section, so the formulas of crack width can be written as：

$$\omega = (\overline{\varepsilon_s} - \overline{\varepsilon_c})\ l_m \approx \varphi \frac{\sigma_s}{E_s} l_m \tag{1}$$

Stress Distribution in Cracked Section. Stress distribution in the cracked section of steel fiber reinforced high-strength concrete beams is shown in Fig. 4.

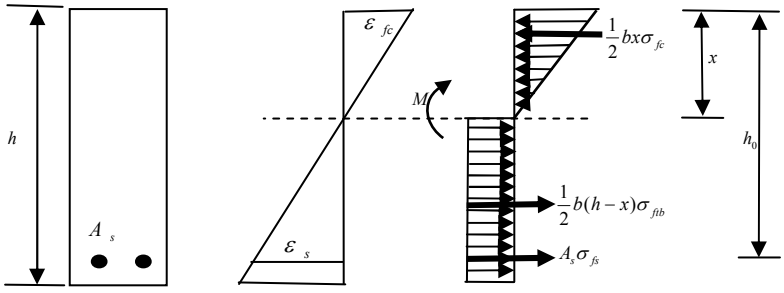


Fig.4 The stress distribution on the section

In the stage of static load test, according to moment balance, the Eq. 2 can be got:

$$M = \sigma_{ftb}(b-x)\left[h - \frac{h-x}{2} - \frac{x}{3}\right] + \sigma_{fs} A_s (h_0 - \frac{x}{3}) \tag{2}$$

The reinforced stress σ_{fs} can be calculated according to Eq. 3:

$$\sigma_{fs} = \left[M - \sigma_{ftb}(b-x)\left[h - \frac{h-x}{2} - \frac{x}{3} \right] \right] \Big/ A_s(h_0 - \frac{x}{3}) \tag{3}$$

According to stress distribution of normal high-strength concrete beams, the stress σ_{sk} is:

$$\sigma_{sk} = M \Big/ A_s(h_0 - \frac{x}{3}) \tag{4}$$

Substituting σ_{sk} into Eq. 3, the reinforced stress σ_{fs} can be written as Eq. 5:

$$\sigma_{fs} = \sigma_{sk} - \sigma_{ftb}(b-x)\left[h - \frac{h-x}{2} - \frac{x}{3} \right] \Big/ A_s(h_0 - \frac{x}{3}) \tag{5}$$

Based on the Chinese Technical Specification [6], the tensile stress of steel fiber concrete is $\sigma_{ftb} = \beta_{tb} f_t \lambda_f$, After n times of fatigue cycles, concrete stress reduction factor is applied as θ_f, the stress of steel fiber concrete after n times of fatigue cycles can be written as $\sigma_{nftb} = \theta_f \beta_{tb} f_t \lambda_f$. According to Eq. 5, the tensile stress of steel bars after n times of fatigue cycles is:

$$\sigma_{ns} = \sigma_{nsk} - \theta_f \beta_{tb} f_t \lambda_f (b-x)\left[h - \frac{h-x}{2} - \frac{x}{3} \right] \Big/ A_s(h_0 - \frac{x}{3}) \tag{6}$$

σ_{nsk} is the tensile stress of steel bars of normal high-strength reinforced concrete beams after fatigue cycles. Applied η_f as amplifying coefficient of tensile stress of steel bars, so σ_{nsk} can be written as $\sigma_{ns} = \eta_s M \Big/ A_s(h_0 - \frac{x}{3})$. The formula of the tensile stress of steel bars can be put forward.

$$\sigma_{ns} = \eta_s \sigma_{sk} - \theta_f \beta_{tb} f_t \lambda_f (b-x)\left[h - \frac{h-x}{2} - \frac{x}{3} \right] \Big/ A_s(h_0 - \frac{x}{3}) \tag{7}$$

Non-uniform Coefficient of Steel Stress. Non-uniform coefficient of steel stress φ is the ratio of the average strain and maximum strain of steel bar. The maximum steel stress is reduced because of adding steel fiber cracked section, and steel fiber also increses the bond of concreste and steel bar. Two effect cause the non-uniform coefficient of steel stress has little change with steel fiber. This law is still applicable under fatigue load. So the non-uniform coefficient of steel stress φ can be calculated based on Chinese Code [5].

Crack Spacing. Experiment results show that average of steel fiber reinforced high-strength concrete beams is less than normal concrete beams, and after certain fatigue cycles(10×10^4), crack spacing will become stable. For simplified calculation the formula of crack spacing can be written as:

$$l_{fcr} = \kappa(1.9c + 0.08\frac{d}{\rho_{te}}) \tag{8}$$

κ is the fatigue crack spacing coefficient considering the influence of steel fiber, according to the analysis of the test data in this paper: κ=0.78.

Force Characteristic Parameters. The force characteristic parameter is probably relative to various factors. According to previous research achievements, the influence of adding steel fiber into beams to the parameters is not significant; this law is still applicable under fatigue load. The force characteristic parameter can take the value according to specification regulated value.

For all these reasons to sum up, a calculation model for crack widths of steel fiber reinforced high strength concrete beams is put forward.

$$\omega_{nfmax} = \alpha_{cr} \varphi \kappa (1.9c + 0.08\frac{d}{\rho_{te}}) \times \frac{\eta_s \sigma_{sk} - \theta_f \beta_{tb} f_t \lambda_f (b-x)\left[h - \frac{h-x}{2} - \frac{x}{3} \right] \Big/ A_s(h_0 - \frac{x}{3})}{E_s} \tag{9}$$

Because reduction coefficient of tensile stress of concrete θ_f and amplifying coefficient of tensile stress of steel η_f are all probably relative to Fatigue cycles (N), setting $\theta_f = \zeta_1\gamma(a+b\lg N)$, $\eta_f = \zeta_2\gamma(a+b\lg N)$, the calculation formula for fatigue crack width can be written as:

$$\omega_{nfmax} = \alpha_{cr}\varphi\frac{\sigma_{sk}}{E_s}(1.9c+0.08\frac{d}{\rho_{te}})\kappa\gamma(a+b\lg N)\times\left[1-\frac{\zeta_1\beta_{tb}f_t\lambda_f(b-x)\left[h-\frac{h-x}{2}-\frac{x}{3}\right]}{\zeta_2\sigma_{sk}A_s(h_0-\frac{x}{3})}\right] \quad (10)$$

Considering the linking up with the current ordinary concrete structures and steel fiber concrete component calculation formula, and for convenient calculation, according to calculation model, the calculation formula for crack width of steel fiber high-strength concrete beams is simplified as:

$$\omega_{nfmax} = \nu(a+b\lg N)\omega_{max}(1-\beta_{cw}\lambda_f) \quad (11)$$

In the formula, ν is the comprehensive correction factor for fatigue crack width of steel fiber reinforced high-strength concrete beams, according to the test data by regression analysis , ν=1.4, a=-1.2518, b=0.5458; ω_{max} is the maximum crack width not considering the effect of steel fiber, λ_f is the represent parameter of steel-fiber, β_{cw} is crack width influence coefficient of steel fiber concrete beams which could be determine through the test.

The results are show in Table 2. The calculated results are in good accordance with the experiment results.

Table 2 Calculated value and the measured value of fatigue crack widths

Number	Fatigue cycles	Calculated w_{nfmax} (mm)	Experimental w_{nexp} (mm)	w_{nexp} / w_{nfmax}
F0	$1*10^4$	0.2608	0.18	0.959
	$5*10^4$	0.3676	0.22	0.699
	$10*10^4$	0.4136	0.25	0.653
	$20*10^4$	0.4596	0.25	0.896
	$50*10^4$	0.5204	0.33	0.634
FSF1	$1*10^4$	0.1565	0.18	1.150
	$5*10^4$	0.2206	0.22	0.997
	$10*10^4$	0.2482	0.25	1.007
	$20*10^4$	0.2758	0.25	0.907
	$50*10^4$	0.3123	0.30	0.961
F1	$1*10^4$	0.1043	0.10	0.959
	$5*10^4$	0.1470	0.15	1.020
	$10*10^4$	0.1654	0.17	1.003
	$20*10^4$	0.1838	0.20	1.088
	$50*10^4$	0.2082	0.25	1.201
	$100*10^4$	0.2266	0.27	1.192
FSF2	$1*10^4$	0.1304	0.15	1.150
	$5*10^4$	0.1838	0.20	1.088
	$10*10^4$	0.2068	0.24	1.160
FSF2	$20*10^4$	0.2298	0.25	1.088
	$50*10^4$	0.2602	0.30	1.153
	$100*10^4$	0.2832	0.35	1.236
FST1	1*104	0.1956	0.25	1.278
FST2	1*104	0.1956	0.20	1.023
	$5*10^4$	0.2757	0.25	0.907
FH1	$1*10^4$	0.1565	0.20	1.278
	$5*10^4$	0.2206	0.22	0.997
	$10*10^4$	0.2482	0.24	0.967
	$20*10^4$	0.2758	0.25	0.907
	$50*10^4$	0.3123	0.30	0.961
FH2	$1*10^4$	0.1304	0.12	0.920
	$5*10^4$	0.1838	0.15	0.816
	$10*10^4$	0.2068	0.20	0.967
	$20*10^4$	0.2298	0.22	0.957
	$50*10^4$	0.2602	0.27	1.038

Conclusions

Adding steel fiber into the high strength concrete beams can prevent the development of the fatigue crack, reduce the crack widths effectively.

Crack widths of steel fiber reinforced high-strength concrete beams are decreased by 26%~121% under fatigue load.

Calculation model for fatigue crack width of steel fiber reinforced high-strength concrete beams is put forward. The fatigue crack widths can be computed according to Eq. 11 in the paper. The calculated results and the test results are closely coincide.

References

[1] O. T. Ibrahim, A. R. Luxmoore, Control of cracks in reinforced concrete using steel fibers, In: R N Swamy et al eds. Developments in Fiber Reinforced Cement and Concrete, Rilem symposium, Sheffield England, Lances: R L Wagstaffe, (1986) 241-247.

[2] Shao-Bin D, Ming-Hai S, Jun H, Influence of characteristics on bending strength of layered steel fiber reinforced concrete, Wuhan University Journal of Natural Sciences, 5 (2005) 883-889.

[3] C. Huang, G. Zhao, K. Liu, Method for calculating crack width of steel fiber reinforced concrete members under axial tension, Journal of Building Structures, 3 (1997) 2-10.

[4] J. Jiang, W. Sun, Y. Zhang, et al, Cracking resistance performance of super vertical-distance pumped SFRC, Frontiers of Architecture and Civil Engineering in China, 2 (2008) 179-183.

[5] GB50010-2002, Technical Specification for Concrete Structures, China Architecture and Building Press, Beijing, 2002.

[6] CECS38:2004, Technical Specification for Fiber Reinforced Concrete Structures, China Planning Press, Beijing, 2004.

[7] GB 50152-1992, Standard for Test Methods of Concrete Structures, China Architecture and Building Press, Beijing, 1992.

© (2012) Trans Tech Publications, Switzerland
doi:10.4028/www.scientific.net/AMM.238.196

Testing Researches on Mixing Proportion of Consolidator-mixed Pile Composite Foundation

Guozhi Zhang[a], Dongliang Xun[b], Fuquan Ji[c] and Zhao Yang[d]

CCCC Second Harbour Engineering Co., Ltd., Wuhan 430040, China

[a]452762256@qq.com, [b]277507986@qq.com, [c]jifuquan_geo@163.com, [d]yangzhaolp@126.com

Keywords: mixed pile; mixing proportion; consolidator; silt; composite foundation.

Abstract. By the laboratory tests of mixing proportion, this paper contrastively analyzes the consolidation instances of silt with HEC, HAS and cement, also emphatically discusses the influence regularities of the unconfined compression strength of solidified silt with the following factors such as the dose of consolidators and the curing time, which provide reliable data for situ tests. According to the test results in site, the optimum mixing proportion for consolidator-mixed pile is HAS with 12% dose. The result can be used as reference for the optimum mixing proportion design of consolidator-mixed pile composite foundation.

Introduction

Currently, mixed pile has been widely used as a method for foundation treatment [1-3]. However, there are a lot of problems among the reinforcement mechanism, design calculation method and construction technology. Especially, the choose of consolidators, wet method, dry method and the dose should be further studied, which is based on the laboratory test of mixing proportion and situ test of bearing capacity [4-6]. According to the Chinese Code JGJ79-2002, laboratory test of mixing proportion should be done before the design of mixed pile composite foundation. For the silt layer in the area of Ningbo, China, this paper contrastively analyses the consolidation instances of silt with HEC [7], HAS [8] and cement soil consolidators, so as to provide the parameters of dose and curing time for the design of mixing proportion in consolidator-mixed pile composite foundation.

Test Methods

Through the laboratory tests of mixing proportion and a series of situ tests, the consolidation instances of silt with HEC, HAS and cement are contrastively analyzed, so as to make the optimum mixing proportion. The laboratory samples come from Cai riverbank, Ningbo, China. The scheme of mixing proportion is shown in Table 1. In site, situ tests include the coring test , bearing capacity of single pile test , bearing capacity of composite foundation test.

Table 1 Laboratory test of mixing proportion

Consolidator	Wet method		Dry method	
	dose/meter (kg)	test	dose/meter (kg)	test
HEC	40	unconfined compression strength for 7 d and 28 d	40	unconfined compression strength for 7 d and 28 d
	43		43	
	53		46	
HAS	40		40	
	43		43	
	53		46	
cement	55		55	
	65		60	
	71		65	

Test Contents and Results

Laboratory Tests of Mixing Proportion. Test of mixing proportion with wet method are listed in Table 2. It shows that the unconfined compression strength increases with the increase of the dose of soil consolidator. Under the same dose, the unconfined compression strength increases significantly with the curing time.

Table 2 Test of mixing proportion with wet method

consolidator	dose/meter (kg)	unconfined compression strength test	values (MPa)			average (MPa)
cement	55	7d	0.46	0.41	0.44	0.44
		28d	0.91	0.87	0.97	0.92
	65	7d	0.60	0.62	0.61	0.61
		28d	1.18	1.27	1.22	1.22
	71	7d	0.90	1.01	0.91	0.94
		28d	1.29	1.31	1.32	1.31
HAS	40	7d	0.26	0.28	0.32	0.29
		28d	0.62	0.56	0.64	0.61
	43	7d	0.32	0.34	0.40	0.35
		28d	1.15	1.19	1.18	1.17
	53	7d	0.80	0.87	0.83	0.83
		28d	1.21	1.28	1.25	1.26
HEC	40	7d	0.50	0.50	0.49	0.50
		28d	0.90	0.87	0.94	0.90
	43	7d	0.49	0.53	0.53	0.52
		28d	1.19	1.25	1.22	1.22
	53	7d	0.60	0.62	0.63	0.62
		28d	1.28	1.28	1.27	1.28

Test of mixing proportion with dry method are shown in Table 3.

Table 3 Test of mixing proportion with dry method

Consolidator	Dose/meter (kg)	Unconfined compression strength test	Values (MPa)			Average (MPa)
HAS	40	7d	0.33	0.26	0.42	0.34
		28d	0.46	0.49	0.42	0.46
	43	7d	0.59	0.51	0.56	0.55
		28d	1.10	1.12	1.12	1.11
	46	7d	0.41	0.40	0.32	0.38
		28d	1.18	1.15	1.18	1.17
HEC	40	7d	0.54	0.58	0.57	0.56
		28d	0.98	1.18	0.97	1.04
	43	7d	0.63	0.61	0.71	0.65
		28d	1.15	1.14	1.17	1.15
	46	7d	0.55	0.44	0.50	0.50
		28d	1.27	1.20	1.18	1.21
cement	55	7d	0.38	0.44	0.59	0.47
		28d	1.16	1.18	1.27	1.20
	60	7d	0.54	0.59	0.55	0.56
		28d	1.16	1.10	1.19	1.15
	65	7d	0.68	0.66	0.69	0.68
		28d	1.21	1.24	1.27	1.24

Table 2 and Table 3 show that the change laws of unconfined compression strength is the same between the dry method and the wet method. What's more, the wet method is a little better than the dry method.

Situ Tests. While the piles had been formed for 7 days, the coring tests were done, so as to measure the diameter of piles. The results of coring tests are shown in Table 4.

The results of coring test of deep mixed piles are listed in Table 5, which shows that the strength of pile increases with the increase of the dose of soil consolidator. When the dose of HEC or HAS soil consolidator is 12%, its effect on the strength of pile is the same as cement dosing 16%.

Table 4 Diameter of pile

Order	Diameter of pile (cm)	Order	Diameter of pile (cm)	Order	Diameter of pile (cm)
HAS-1-s1	61	c-1-s1	50	HEC-1-s1	57
HAS-1-s2	60	c-1-s2	57	HEC-1-s2	58
HAS-1-s3	55	c-1-s3	57	HEC-1-s3	57
HAS-1-s4	56	c-1-s4	58	HEC-1-s4	57
HAS-1-s5	60	c-1-s5	54	HEC-1-s5	57
HAS-1-s6	60	c-1-s6	54	HEC-1-s6	57
HAS-1-s1	41	c-1-s1	55	HEC-1-s1	55
HAS-1-s2	55	c-1-s2	59	HEC-1-s2	55
HAS-1-s3	57	c-1-s3	56	HEC-1-s3	55
HAS-1-s4	60	c-1-s4	59	HEC-1-s4	55
HAS-1-s5	56	c-1-s5	57	HEC-1-s5	55
HAS-1-s6	60	c-1-s6	55	HEC-1-s6	55
HAS-3-s1	52	c-3-s1	55	HEC-3-s1	54
HAS-3-s2	55	c-3-s2	57	HEC-3-s2	54
HAS-3-s3	55	c-3-s3	57	HEC-3-s3	54
HAS-3-s4	56	c-3-s4	60	HEC-3-s4	53
HAS-3-s5	56	c-3-s5	59	HEC-3-s5	53
HAS-3-s6	55	c-3-s6	56	HEC-3-s6	53

Table 5 Coring results of mixed pile

Material	Dose (%)	Order	Strength of pile (MPa)			Average (MPa)
			1~5m	5~10m	10~15m	
HAS	9	S5	/	/	/	/
	12	S2	0.72	1.06	1.45	1.07
HEC	9	S5	0.62	0.58	0.33	0.51
	12	S1	0.87	1.01	1.52	1.13
cement	12	S5	0.35	0.47	0.69	0.74
	16	S2	1.29	0.99	/	1.14
	20	S3	/	/	1.65	/

Bearing Capacity of Pile. According to the Chinese code JGJ79-2002, the static loading tests of single pile have been done in site. From the above, the results of unconfined compression strength test and coring test show that there is little relationship between the strength of pile and the species of soil consolidators. In fact, the dose of soil consolidator determines the strength of pile. Then the tests of bearing capacity of piles have been done, which are mixed with different doses and species of consolidators. The results are shown in Table 6, and the typical *Q-S* curve is shown in Fig. 1.

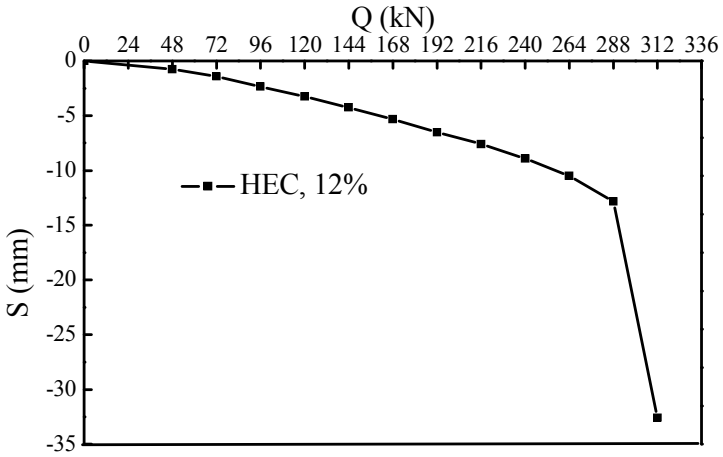


Fig. 1 $Q - S$ curve of single pile

Table 6 shows that, along with the increase of the dose of soil consolidator, the bearing capacity of single pile increases. When the dose of HEC soil consolidator is 12%, its effect on the ultimate bearing capacity of single pile is the same as cement dosing 16%.

Table 6 Bearing capacity of single pile

Consolidator	Dose (%)	Ultimate bearing capacity (kN)	Characteristic value of bearing capacity (kN)
HAS	9	192	96
cement	16	288	144
HEC	12	288	144

Bearing Capacity of Composite Foundation. According to the Chinese code JGJ79-2002, the static loading tests of single pile composite foundation have been done in site, then the results of bearing capacities of composite foundation are shown in Table 7.

Table 7 Bearing capacity of composite foundation

consolidator	dose (%)	maximum load (kN)	settlement (mm)	ultimate bearing capacity (kN)	characteristic value of bearing capacity (kN)
HEC	9	320	52.10	240	120
	12	400	60.07	320	160
cement	16	400	61.66	320	160
HAS	9	320	60.13	240	120
	12	400	69.53	320	160

With different doses and species of consolidators, the typical Q-S curves of the loading test of composite foundation are shown in Fig. 2.

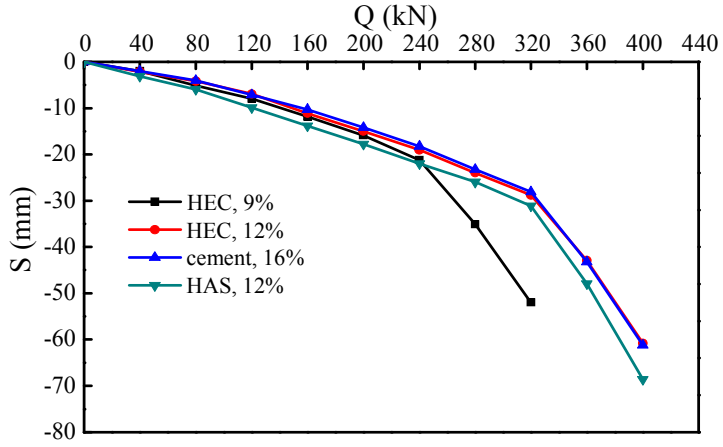


Fig. 2 Q-S curves of composite foundation with different doses and species of consolidators

Fig. 2 shows that there is little relationship between bearing capacity of composite foundation and the species of soil consolidators. But along with the dose of soil consolidator increases, the bearing capacity of composite foundation increases too. When the dose of HEC or HAS soil consolidator is 12%, its effect on the ultimate bearing capacity of single pile composite foundation is the same as cement dosing 16%, then the choose of HAS dosing 12% may be the optimum mixing proportion economically.

Conclusions

For HEC, HAS and cement soil consolidators, the influence laws of the unconfined compression strength and bearing capacity are the same. Along with the increase of soil consolidators, the unconfined compression strength of solidified soil sample increases, and the bearing capacity of single pile composite foundation increases too.

When the dose of HEC or HAS soil consolidator is 12%, its effect on the unconfined compression strength and ultimate bearing capacity is the same as cement dosing 16%, then HEC and HAS soil consolidators may take the place of cement in the design of mixed pile composite foundation.

References

[1] J. Zhou, D. Feng, H. Zheng, Finite element analysis for compound foundation of deep mixing piles, Rock and Soil Mechanics, 2 (1997) 44-50.

[2] Z. Gu, G. Gao, K. Cui, The experimental study on the optimal ratio of added lime in expansive soil of He-Xu expressway, Geotechnical Engineering Technique, 5 (2003) 286-288.

[3] C. Hong, X. Gong, X. Wen, Probability analysis of the bearing capacity of deep mixing composite foundation, Chinese Journal of Geotechnical Engineering, 3 (2000) 279-283.

[4] X. Huang, T. Hu, On stabilization of soft soil with waste gypsum and cement, Chinese Journal of Geotechnical Engineering, 5 (1998) 72-76.

[5] Dobie, Terrence R., Ng, Smuel Y., and Henning, Norman E. A laboratory evaluation of lignite fly ash as a stabilization additive for soils and aggregates, Report Prepared for North Dakota State Highway Department and Federal Highway Administration, Jan., 1975.

[6] T. Y. Chu, D. T. Davidson, W. L. Geocker, Z.C. Moh, Soil stabilization with lime-fly ash mixture: studies with silty and soils, Bulletin No.108, HRB, 1995, pp.102-112.

[7] T. Chen, J. Zhou, M. Sun, Influence of solidfying agent HEC on loess permeability, Agricultural Research in the Arid Areas, 4 (2004) 192-194.

[8] L. Zhang, Application of HAS curing agent in the hardening of overwet earth subgrade, Western China Communications Science and Technology, 4 (2006) 27-31.

© (2012) Trans Tech Publications, Switzerland
doi:10.4028/www.scientific.net/AMM.238.201

Analysis on Load Stress of Asphalt Pavements with Different Crack States

Yan Wang [a] and Zhifeng Liu [b]

Jinling Institute of Technology, Nanjing 211169, China

[a]wangyan.seu@gmail.com, [b]lzf@jit.edu.cn

Keywords: highway engineering; asphalt pavement; crack states; load stress.

Abstract. Semi-rigid base asphalt pavement has well load-bearing capacity if no cracks occur. But cracks appear inevitably at the weak part of the structure. Models under different working conditions are set up with the finite element method (FEM) to analyze the stress distribution in the structure while the cement-stabilized macadam-base asphalt pavement encounters different crack states and interface conditions. The analysis indicates that the interlayer cohesion is the key factor affecting the spread of cracks. When the cohesion between the surface and base is weak, the tensile and shear stresses at the bottom of the surface course increase rapidly and both transverse cracks from the bottom to the top and longitudinal cracks in traffic direction come into being in the asphalt surface even though the base doesn't crack; those transverse cracks which haven't spread through the base in depth direction will reflect to the surface course under load. The reflected cracks can be reduced and stayed if the surface course is covered after the shrinking cracks in the base course have fully spread and been cured.

Introduction

Certain transverse shrinking cracks appear inevitably at the weak part of the base course in cement-stabilized macadam base due to water loss and temperature reduction. After the covering of the surface course, the cracks in the base course keep growing into the lower and upper parts of the structure due to repeating vehicle load and the environmental factors.

More researches have been done on the reflective cracks and the top-down cracks in the surface of the asphalt pavement, which includes theoretical analysis [1, 2], indoor and outdoor experiments [3, 4], trial pavements [5], etc. However, even under the same temperature condition and vehicle load, the internal stress of the structure differs greatly if the interlayer cohesion state is different or the cracking state in the base is different. It isn't analyzed which state is the least favorable and how the correspondence between the different cracking state and the internal stress of the structure is. Hence, pavement structure models under different working conditions are set up with the finite element software ABAQUS to analyze how the stress in asphalt pavements with different base states changes under vehicle load, and determine which the unfavorable state of the asphalt surface stress is. This can help establish reasonable designing and constructing methods, avoid or reduce the existence of the unfavorable state and provide suggestions on how to control the producing and spreading of transverse crack in the base.

Selection of Model Parameters

The FEM Parameter Determination. The finite element method is adopted to analyze the stress of asphalt pavements with different base under vehicle load.

The calculated result of finite element method and those of the elastic layered system theory are compared to validate the model, and determine the suitable model size, element type and meshing density. By adopting different model sizes to do the pilot calculation, the model's plane size is determined to be 5m×5m [6], the sub-grade is 8m in depth. The element is the three-dimensional eight-node incompatible entity element (3D8I).

In the model, direction 1, 2 and 3 are along the traffic direction, the structure depth and the structure width respectively. The corresponding tensile and shear stress directions are defined with mechanics norms, e.g. σ_1 indicates the tensile stress in direction 1, and τ_{12} indicates the shear stress in direction 2 inside the surface whose normal direction is direction 1.

Load Selection. The vehicle load includes the standard axle of BZZ-100 and the 0.7MPa tire pressure. The influenced sphere of the single tire pressure is 18.9cm×18.9cm, the tire tread is 32cm and the space between the two side wheels is 182cm [6], shows in Fig. 1. While considering the horizontal loading effect, the horizontal loading coefficients are taken as 0.1, 0.3, 0.5, 0.7 and 1.0.



Fig.1 Sketch map of load size (cm)

The Structure Selection. A lot of structure data used in Jiangsu province was investigated, the typical highway structure type is employed as the basic analyzing structure. The relevant parameters are shown in Table 1.

Table 1 Parameters of pavement structure

Layers of structure	Depth (cm)	Modulus (MPa)	Poisson Ratio
Asphalt surface	18	1800	0.30
Cement-stabilized base	30	4000	0.15
Graded Macadam subbase	30	1000	0.25
Subgrade	800	60	0.35

Calculation and Analysis. After the confirmation of the parameters, finite element models under different working conditions can be set up to analyze the stress distribution in the structure of asphalt pavements with different cement-stabilized macadam-based courses under load. Two different states of the base states are chosen: ① there are cracks in the base, ② there are cracks in the pavement surface. Furthermore, several factors were considered in these two states.

There are Cracks in the Base

The cement-stabilized base course badly cured or exposed outside in cold seasons will inevitably cause certain amounts of transverse shrinking cracks, which will spread up and downwards in the structure under the vehicle load after the surface course has been covered.

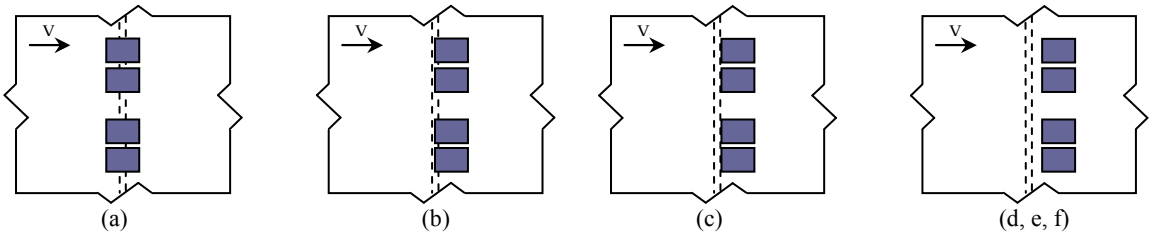


Fig. 2 Sketch maps of the load Position

Symmetrical load and some eccentric loads at different positions are chosen to analyze how the stress of the structure changes under different interlayer cohesion conditions with the transverse shrinking cracks forming through the base course. The positions of load are marked as Fig. 2: a—symmetrical load; b—the wheel side is in the crack center; c—the wheel side is at the edge of the crack; d, e and f—the wheel side is 1cm, 5cm and 10cm away from the edge of the crack respectively.

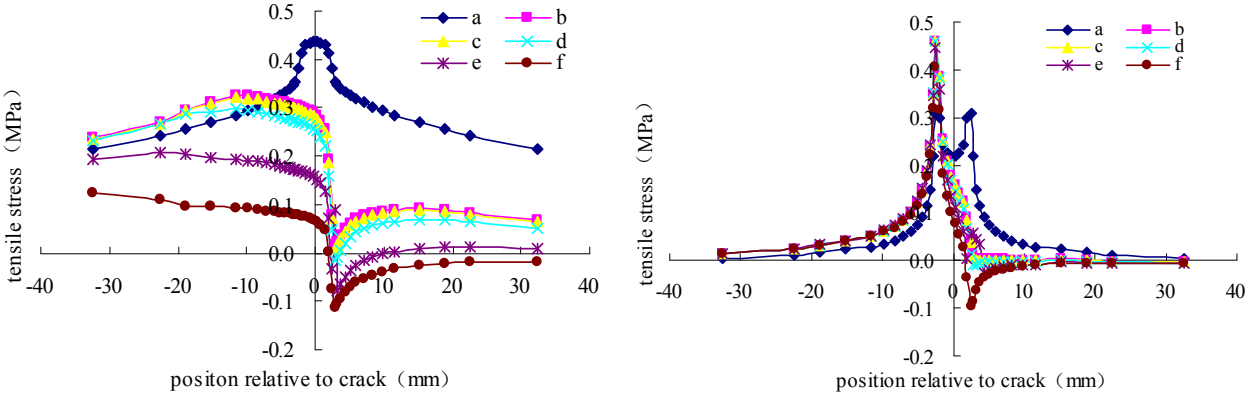
The Layer Continuous State. The bottom of the surface course is being pressed whether under the symmetrical load or under the eccentric load, the compressive stress under the inner wheel is higher than that of the outer wheel. The maximum shear stress in the surface course is shown in Table 2. The shear stress is the largest at load position b, which is at the crack position on the pavement surface. Therefore, after transverse shrinking cracks come into being in the base, they will gradually meet the shearing cracks in the surface of the pavement due to the repeated vehicle load.

After the formation of cracks in the base course, the symmetrical load brings more damage than the eccentric load does. The bottom of the base course is in tensile constantly, which results in further opening of the cracks and large crack opening displacement. This, plus the cycle of motion of temperature and load, keeps the cracks in the base course repeatedly open and close, which will cause fatigue cracking at the bottom of the surface course and hence form reflective cracks.

Table 2 Calculated stresses for different load position

Stress (MPa)	Positions					
	a	b	c	d	e	f
τ_{max} of asphalt surface	0.2778	0.3516	0.3338	0.2927	0.2808	0.3166
σ_1 in base bottom	0.2083	0.1885	0.1876	0.1832	0.1626	0.1338

The Layer Smoothness State. Different layers in the pavement structure cannot be totally continuous due to layer-by-layer construction, stage-by-stage construction and other reasons. Fig. 3 indicates how the tensile stress at the bottom of the surface course changes under loads of different loading positions when it is smooth between layers.



(a) surface-base interlayer smoothness (b) base-sub-base interlayer smoothness

Fig. 3 σ_1 in surface bottom when interlayer smoothness

When it is smooth between the surface course and the base course, large tensile stress turns on the side bearing the wheel load. With change of the position of wheel load, the maximum tensile stress appears somewhere with certain distance from the edge of the crack rather than in the middle of the crack. When the load is 10cm away from the edge of the crack, the maximum tensile stress at the bottom of the surface course appears somewhere 3.5cm away from the edge of the crack and even farther. It is worth noting that the tensile stress only appears at the bottom of the surface course, the value brought from the eccentric load is much higher than the strength by being 0.44MPa, located at the middle of the crack. The position the maximum tensile stress shows that when the cohesion between the surface course and the base course is weak, the crack will reflect to the surface of the pavement and form one or two close transverse cracks, the reflective crack position may not be in accord with the crack in the base course.

When it is smooth between the base course and the sub-base course, the tensile stress brought by the load at the bottom of the surface is higher. The least favorable loading position can lead to a tensile stress of 0.463MPa at the bottom of the surface course. Considering the temperature effect, the bottom of the surface course can be easily ripped by a single loading process under the low temperature in winter. As to the position where the maximum tensile stress occurs, it occurs at the edge of the crack on one side of the loading effect under the eccentric load, while under the symmetrical load it occurs at the edge of the cracks on both sides of the loading effect. The reflective cracks formed this way are all corresponding cracks.

By comparing the cohesion state between different layers, it is clearly seen that an important factor leading to the formation of reflective cracks is the weak interlayer cohesion. It is the least favorable when the cohesion between the upper and lower base courses or between the base and sub-base courses is weak.

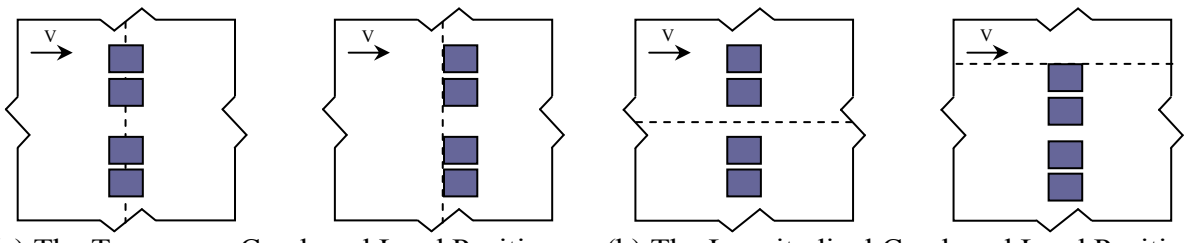
Different Depth and Width of Cracks. To different kinds of cement-stabilized macadam base structure, the displacement of the crack opening is different even under the same temperature and load. Moreover, regardless of the effect of water loss or temperature, the maximum shrinking and warping stress always occurs at the top of the base course and rips the top. With the aggravation of the water loss and the day-night temperature difference, the cracks spread towards the inner part of the base course. Hence, there might be some transverse cracks through or not through the base course. For this reason, the change of the structure's internal stress under the load should be considered when analyzing the difference in the cracks' depth and width in the base course.

According to above analyses, the state when it is smooth between the base and sub-base courses and the loading position c is adopted for analysis. Calculated results revealed that the bottom of the surface course is compressed before the cracks cut through the base. With the increase of the width of the base course cracks, the tensile stress at the bottom of the surface course decreases due to the open-close motion of the cracks absorbed by the distortion of the asphalt mixture in a large range at the bottom of the asphalt surface course, which results in the distortion decrease in each scale and relatively weakness of the concentration of the stress. The tensile stress at the bottom of the surface course obviously decreases when the crack is 1cm wide than it is less than 1cm. The shear stress in the surface course is not much affected by the depth of the crack, it decreases rapidly with the increase in the crack width. This indicates that the micro-cracks formed at weak points by the shrinking of the base course are the key factor leading to the damage to the surface course structure.

The tensile stress in the base course gradually increases with the spreading down of the cracks while the bottom of the base course is pulled under the load. While the stress is distributed again after the cracks cut through the layer, the tensile stress at the bottom of the base course decreases. The tensile stress decreases slightly with the increase of the crack width. The shear stress in the base course decreases with the increase of the crack depth and width. The tensile and shear stresses are both large before the cracks cut through the layer. The cracks grow rapidly downwards until they cut through the base course. During the time the shear stress in the base course is far lower than the tensile stress, the width of the transverse cracks in the base course keeps increasing.

There are Cracks in the Pavement Surface

Vehicle load works on the pavement surface directly, two shapes were used to divide the surface crack. The transverse crack is along the structure width direction, while the longitudinal crack along the traffic direction. Both symmetrical load (normal load) and partial load were applied. Crack directions and load positions were shown in Fig. 4. According to the calculation, if asphalt pavement cracks, on condition that the interlayer is successive, surface layer bottom still pressed no matter under the symmetrical or partial load. The place away from the load at a distance will produce tensile stress, but the stress is far less than the mixture of tensile strength, can be neglected.



(a) The Transverse Crack and Load Position (b) The Longitudinal Crack and Load Position

Fig. 4 Sketch maps of the different surface crack

Table 3 Load stress for the different load location and crack direction

Working conditions		τ_{12} in pavement surface	σ_1 in the base bottom
Transverse crack	Normal load	0.2172	0.1424
	Partial load	0.1973	0.1484
Longitudinal crack	Normal load	0.1588	0.05954
	Partial load	0.1224	0.07269

As list in Table 3, regardless of the surface transverse or longitudinal crack, the shear stress in surface layer is larger under normal load, while the base bottom tensile stress slightly big under partial load. In view of the base bottom tensile stress is small due to load effects, the shear stress in the surface layer should be served as the control index. Therefore, the symmetrical load was used to analysis load stress in the structure with surface transverse and longitudinal crack below.

Different Contact Conditions. Table 4 shows the load stresses with surface cracks in the structure for different layers contact conditions. The load stresses in surface and base layer reach the maximum when the contact condition between the base and sub base is smooth for both the surface transverse and longitudinal crack. As for the transverse crack in surface, the surface shear stress index grows approximately 24% comparing to the continuous layer condition, while the base tensile stress increases 2.3 times than the continuous. On the surface longitudinal crack, the surface shear stress indicator is not very different for all the smooth conditions, than the continuous growth of 5%.

Table 4 Load stresses for different layer conditions

Working conditions		τ_{12} in surface	τ_{max} in surface	σ_1 in base bottom
Transverse crack	Continuum	0.2172	0.6905	0.1424
	Smooth between surface and base	0.1292	0.4120	0.1687
	Smooth between base and sub-base	0.2644	0.8561	0.3294
Longitudinal crack	Continuum	0.1588	0.2527	0.05954
	Smooth between surface and base	0.1661	0.4062	0.07706
	Smooth between base and sub-base	0.1661	0.4139	0.1383

It can be seen that the layer's bonding state is important to improve the stress in structure. Therefore, napping and spraying adhesive oil to enhance the bonding state of layers is good methods to make the pavement stress condition better.

Conclusions

The stressing state of the asphalt pavement with cement-stabilized macadam base with different types of transverse shrinking cracks and without cracks in the base course is analyzed.

If the cohesion between the surface and the base courses is weak, the bottom of the surface course will be pulled instead of being pressed, which will cause the vertical shear stress at the bottom of the surface course. As a result, cracks will be formed from the bottom to the top in the surface course even though no cracks are found in the base course.

Interlayer contact conditions have great impact on the load stress. Especially when the bonding is not good, stress in the structure is particularly bad.

After transverse shrinking cracks formed through the base course, if the cohesion between the upper-lower base courses or base-subbase courses is weak, the tensile stress at the bottom of the base course under loading process may reach the materials' strength. By adding the temperature loading effect, the cracks in the base course will rapidly reflect to the surface of the pavement.

As for the containing base crack structure, when the vehicle load position changes, the position of the surface bottom where caused by the stress concentration does not correspond exactly to the base crack. When loads deviate from the crack edge 10cm, the maximum tensile stress of the surface bottom located at a distance of 3.5cm or even farther from the crack. Therefore, the upward reflection of the base cracks to the surface layer may do not correspond.

Acknowledgements

The research was supported by the Youth Fund of Jinling Institute of technology (jit-n-201008).

References

[1] J. Wang, X. Zhu, Dynamic analysis of asphalt pavement with reflective cracking on the soft clay ground, China Journal of Highway and Transport, 1 (2004) 1-6.

[2] H. Wang, X. Huang, Z. Fu, Influence factors on surface crack of semi-rigid base course, Journal of Traffic and Transportation Engineering, 2 (2005) 38-41.

[3] C. Chen, Y. Cheng, D. Sun, J. Li, W. Qin, F. Ni, Research on use of low cement content stabilized material base to prevent reflection cracking in thin asphalt pavement, Journal of Highway and Transportation Research and Development, 9 (2005) 48-51.

[4] F. Ni, Y. Ying, M. Gao, Lab simulation study on reflective cracking resistance of treatment with fiberglass-polyester paving mat, Journal of Southeast University (Natural Science Edition), 1 (2007) 128-131.

[5] Y. Jiang, J. Dai, Application of geotextile in preventing reflection cracks in asphalt pavement, Journal of Chang'an University (Natural Science Edition), 4 (2007) 18-22.

[6] Y. Wang, Research on the mechanism and design method of cracking in cement-treated base asphalt pavements, Southeast University, Nanjing, 2008.

CHAPTER 2:

Innovation in Civil and Hydraulic Engineering

© (2012) Trans Tech Publications, Switzerland
doi:10.4028/www.scientific.net/AMM.238.209

Research Progress of Diffusion Absorption Refrigeration Technology

Xiuhong Ren [a] and Yingying Tan [b]

Planning & Architectural Engineering Institute, Henan University of Science & Technology, Luoyang, China.

[a]xiuhongren@126.com, [b]yingyingtan@yeah.net.

Keywords: diffusion absorption refrigeration cycle; bubble pump；operation parameter; low-grade thermal energy; working medium.

Abstract. Compared with the gas-compressed refrigeration system, the diffusion absorption refrigeration cycle has no moving part and the associated noise and vibration. It can be operated without any electric input and driven by various energy sources, has no the problem of the substitute of CFC, furthermore it has positive significance in energy conservation, off peak, environmental protection, and promoting the use of gas. So it has broad application prospects as a kind of absorption refrigeration mode. In the development of diffusion absorption refrigeration technology, the performance of diffusion absorption refrigeration system has been improved and enhanced continuously. The paper presents and discusses the recent research progress of diffusion absorption refrigeration which contains design of bubble pump, adjustment and optimization of operation parameters, utilization of low-grade thermal energy and selection of working medium. The research direction of diffusion absorption refrigeration in the future is suggested.

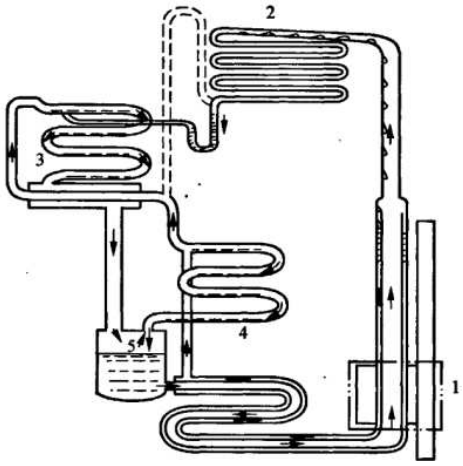
Introduction

Nowadays, along with the deterioration of the world environment and the enhancement of people's green awareness, the problem of the substitute of CFC has become urgent, which has aroused the depletion of the ozone and the other effects such as "greenhouse effect". Ammonia-water absorption refrigeration system has no damage to the ozone layer and no greenhouse effect. It can be driven by waste heat or other heat sources to energy conservation effectively. So it has become an important research direction in refrigeration industry. As one kind of absorption refrigeration cycles, the diffusion absorption refrigerator uses the auxiliary gas to equalize the system pressures. Three-component working medium is adopted in diffusion absorption refrigeration system (DAR), ammonia as a refrigerant, water as absorbent, and hydrogen gas (or helium) as a secondary balance gas. Compared with conventional ammonia-water absorption refrigeration cycle, the unique feature of this technology is that the introduction of the auxiliary gas provides pressure equalization throughout the cycle. The entire system is in the same pressures, there are no solution pump and expansion valve, no moving part and valve. So the system's maintenance, noise, and vibration are at minimum. It can be operated without any electric input and driven by various energy sources. In addition it has long life, low cost and no leak problem. The DAR technology has good reliability, durability, minimum maintenance costs, and operates without chlorofluorocarbons. Based on these features, the DAR can be widely used in hotels, hospitals, office buildings, family, etc, where quiet is important. In addition electric heating, combustible gas such as coal gas, liquefied petroleum gas, and marsh gas, waste heat can be used to driven it. Thus they are widely applied in some countries and regions which electric power shortages.

Working Principle

Schematic diagram of diffusion absorption refrigeration cycle is showed in Fig.1.The rich solution arriving to the generator (1) is heated by the heat flux applied in the bottom of the bubble pump which causes the evaporation of some refrigerant. The resulting poor solution leaves the generator toward the absorber (4) via the solution heat exchanger while the vapor rises toward the condenser (2) through the rectifier. The purified ammonia vapor condenses in the condenser releasing

condensation heat to the surrounding air. The resulting condensate flows to the evaporator (3). At the evaporator entrance, the partial pressure of the liquid ammonia reduced due to mixing with the hydrogen gas returning from the absorber. As a result, the liquid ammonia begins evaporating. The resulting cold and heavy ammonia–hydrogen gas mixture leaves the evaporator, falls down in the reservoir (5) and flows upward the absorber in counter current to the weak solution arriving from the absorber's top. Along the absorber the weak solution absorbs the ammonia vapor. As low density, hydrogen upward into the evaporator continually, complete cycle of pressure balance gas.



1. generator 2.condenser 3. Evaporator 4. absorber 5. Reservoir.

Fig. 1 Schematic diagram of diffusion absorption refrigeration cycle

Research Progress of Diffusion Absorption Refrigeration Technology

The Design of Generator and Bubble Pump. The bubble pump is the motive force and critical component of the absorption diffusion refrigeration cycle. The performance of the diffusion absorption cycle depends primarily on the efficiency of the bubble pump. Scholars have taken on a lot of research work for it.

An experimental study has been made for the air-lift pumps with different riser tube diameters and submergence ratios by Peng Yicuan (1989). Based on the theory of air-liquid two phase flow, a formula for predicting air-lift pump performance is presented. The calculating results showed a reasonable agreement with those by experiments and indicated that the efficiency of air- lift pump will be improved, provided that a small riser tube diameter and large submergence ratio can properly be selected [1]. A study by J.Chen et al. (1996) concerned with performance enhancement of a diffusion-absorption refrigerator was performed. They developed a new generator configuration that increased the COP of the cycle by 50%.The generator consists of heating elements, a bubble pump and a coaxial heat exchanger. Heating losses was reduced by this configuration thus increasing the efficiency of the heating process and the COP [2]. Based on the principle of air-lift pump, Delano (1998) developed an analytical model to evaluate the bubble pump performance. Using the analytical model, the influence of heat input, tube diameter and submergence ratio on bubble pump performance were investigated. He found that increasing the heat input to the bubble pump for a fixed submergence ratio will increase the flow rate of the liquid through the bubble pump to a maximum and then further increase in the heat input will decrease the liquid flow rate. It was found that it can achieve optimum efficiency when the bubble pump operates at slugflow regime. This research conclusion provided important basis for the design of bubble pump with ammonia-water as working medium group [3]. Based on this, Schaeffer (2000) used a turbulent single-phase friction factor to substitute experience values, and analysed the relation between diameter, submergence ratio, the flow rate of the liquid and heat input. It provided an important theory evidence for optimization designing of bubble pump [4].

Based on the special structure for lunate channel can efficiently accelerate the boi1ing of heat transfer, enhance heat and mass transfer, Zheng Hongfei(2003) put forward a conceptualization which used lunate channel solution riser in thermosiphon pump. He made a experimental research

on many lunate channel risers solution. Researches indicted that lunate bubble pump had better upgrading effects [5].Fang Liguo(2005) advanced a triple-for-wrap thermal diffusion absorption refrigerator, in which thermosiphon pump was triple-pipe Thermosiphon pump. It enhanced thermal utilization factor of thermosiphon pump. Lu Leiying (2007) designed a diffusion-absorption refrigerator with a rectifier. She made an experimental research, in which indicated that the riser structures, heat temperature, ammonia concentrations, air pressure can had some impact on refrigeration appliances. Furthermore she determined the selection of structural parameters for a riser [6]. Koyfman used R22—DMA, Uli Ja kou used NH_3—H_2O, Saravanan R used LiBr-H_2O made research and analysis. They found that the performance of bubble pump was independent of motive head and the bubble pump's heat input. A set of visual pump bubble experimental device was designed by Tang Chengwei(2009) ,he made a research on the bubble pump performance in different kinds of working conditions, in which used ammonia water as the research object. The experimental results showed that the startup time of the bubble pump decreased with the increase of beginning pressure, the liquid delivery of the bubble pump exhibited the periodicity, which decreased with the increase of heating power and immersion ratio. In this experiment, we also found that the bubble pump liquid flow increased with the rising of heating power and immersion ratio. The stability of the bubble pump also related to heating power and immersion ratio, which indicated that the stability of the bubble pump became better with the decrease of heating power and the increase of immersion ratio [7].

Low Temperature Heating Source Utilization. Low temperature heating source has a great variety and enormous amount. The use of low temperature heating source not only can relieve the tense issues of fossil, but also helps to reduce the emission of harmful substances, reducing environmental pollution. Compared with direct current, alternating current, liquefied petroleum gas, Lin L. adopted automobile exhaust act as driven heat of diffusion absorption refrigeration system. The experimental result showed that automobile exhaust temperature above 200^{o}Ccan act as the heating source of diffusion absorption refrigeration system. Automobile load less than 25%, no cooling effect due to automobile exhaust temperature less than 200^{o}C.When automobile load is 50%, 75% and 100%, diffusion absorption refrigerator can operate normally due to exhaust temperature greater than 200^{o}C. The result shows that automobile load is 75% has the maximum Coefficient of Performance, the minimum temperature difference of evaporator inlet and outlet, best system performance [8].

Chen Fujin (Henan agricultural university) adopted a biomass energy act as driven heat source of diffusion absorption refrigeration system. The experimental result showed that the internal pressure in water jacket is 200kPa can reach the generating temperature of generator. Furthermore he indicated that input power optimum value of system is 0.2 kW. Not only does this can open a new way for biomass energy, but also find a solution to resolve the problem of refrigeration in remote rural areas [9].

The Study of Working Medium. The conventional diffusion absorption refrigerator used ammonia as a refrigerant, water as absorbent, and hydrogen as a secondary balance gas. Thermal conductivity and thermal capacity of hydrogen is greater, so it cause a lot of energy was wasted in cycle process. Some scholars advanced that we can carry on theoretical analysis and experimental research with helium instead of hydrogen. J． Chen compared COP, the relation between refrigerating capacity and input power as hydrogen and helium act as secondary balance gas respectively. System performance differences are not significant when used helium act as secondary balance gas [2].

The water generated by generator must be removed by way of rectification, as the difference is a little between boiling point of ammonia and water. At the same time the heat generated by rectification also reduces system performance. So some scholars proposed that we can add lithium bromide to ammonia solution to enhance system performance.

Wang Handong used ammonia-sodium thiocyanate as working medium. The result showed the COP of ammonia-sodium thiocyanate system is greater than ammonia solution system. But ammonia-sodium thiocyanate crystallize readily, which effects the operation of the system [10]. Koyfman A． used DMA and R22 to carry on research, the COP is 0.35 by theoretical analysis[11].

Re-adjust and Optimize Operating Parameter. Li Huazhi gaved theoretical analyses in which ambient temperature, pressure, concentration and pressure balance gas may affect COP. The result showed that COP may increase with decreasing ambient temperature, but raise margins of COP fluctuation is very minimal. The COP of system may decrease with increasing system pressure and the amount of pressure balance gas. The higher concentration of rich ammonia water solution or the lower concentration of weak ammonia water is, the higher COP of the system [12]. Wu Yongqiang established simulation program about diffusion absorption heat pump, in which he analyzed generating temperature, evaporation temperature, pressure and concentration affect system performance [13]. Based on the diffusion absorption refrigerator produced by Dometic Company of Sweden, A.Zohar established a thermodynamic model of DAR system. The performance of the system was examined parametrically by computer simulation. Investigation of cycle performance under different conditions indicated that the best performance was obtained for a concentration range of the rich solution of 0.2~0.3 ammonia mass fraction and the recommended concentration of weak solution was 0.1.The COP of DAR unit working with helium was higher by up to 40% than a cycle working with hydrogen as the auxiliary insert gas. A.Zohar found that the DAR cycle without condensate sub-cooling showed higher COP of 14–20% in compare with the DAR cycle with the condensate sub-cooling, but it occurs at higher evaporator temperature of about 15^{o}C [14].

Conclusions

In recent years, we pay more attention to the diffusion absorption refrigerator due to it using a variety of low temperature heating source and working medium without damage to environment and the ozone layer. But the diffusion absorption refrigeration technology involves three-component working medium to work cooperatively, which making the operating conditions and system architecture is more complex than conventional systems. Configuration design of generator, bubble pump and rectifier, adjustment and optimization of operating parameters become the focus of the study[15]. In addition to improve system performance, development of the diffusion absorption refrigerator using different energy also caused manufacturers' interesting. At present, there are many problems to be studied and resolved in enhancing system performance, selecting working medium, operating parameter optimization and the development of useful products.

References

[1] Y. Peng, Z. Xiao, A Theoretical and Experimental Study on Air-Lift Pump Phenomena, Journal of Northeast University of Technology, 3 (1989) 111-117.

[2] J.Chen, et al, Performance enhancement of a diffusion-absorption refrigerator, International Journal of Refrigeration, 3 (1996) 208-218.

[3] A. Delano, Design Analysis of the Einstein refrigeration cycle, Georgia Institute of Technology, Atlanta,1998.

[4] L. Schaefer, Single Pressure Absorption Heat Pump Analysis, Georgia Institute of Technology, Atlanta, 2000.

[5] H. Zheng, Study on enhanced heat transfer of lunate channel in solar energy air-conditioning system, Refrigeration, 1 (2003) 18-22.

[6] L. Lu, H. Zhang, Experiment of Diffusion-Absorption Refrigeration, Cryogenics Cryo. & Supercond, 35 (2007) 79-83.

[7] C. Tang, D. Liu, Experimental Study on the Performance for Pump Bubble Single Pressure Absorption Refrigeration System, Fluid Machinery, 8 (2009) 49-53.

[8] L. Lin, Y. Wang, T. Shemmeri, et a1, Characteristics of the diffusion absorption refrigerator driven by the waste heat from engine exhaust, Journal of Process Mechanical Engineering, 3 (2006) 139-149.

[9] W. Li, Y. Cheng, et al, The latest research results concerning the absorption refrigeration cycle driving by low temperature heat source and its development trend, Energy Conservation, 11 (2009) 21-23.

[10]H. Wang, L. Hu, Experimental research on ammonia-sodium thiocyanate diffusion absorption refrigeration system, Refrigeration, 1 (1999) 9-13.

[11]A. Koyfman, M. Jelinek, A. Levy, I. Borde, An experimental investigation of bubble pump performance for diffusion absorption refrigeration system with organic working fluids, Applied Thermal Engineering, 23 (2003) 1881-1894.

[12]H. Li, S. Cui, Thermodynamic parameters analysis about affecting the COP of diffusion absorption refrigerator, Low Temperature and Specialty Gases, 6 (2000) 12-14.

[13]Y. Wu, The heat and mass analyses of the diffusion-absorption heat pump system-research on the generator, Master thesis of Shanghai Jiaotong University, China, 2004.

[14]A. Zohar, M. Jelinek, A. Levy, I. Borde, The influence of diffusion absorption refrigeration cycle configuration on the performance, Applied Thermal Engineering, 27 (2007) 2213-2219.

[15]X. Xue, D. Liu, et a1, Research progress of single pressure absorption refrigeration technology, Refrigeration and Air-Conditioning, 5 (2008) 30-34.

© (2012) Trans Tech Publications, Switzerland
doi:10.4028/www.scientific.net/AMM.238.214

A Practical Technique for Generating Hexahedral Meshes

Xinli Bai [a], Bing Ma [b] and Jiangyan Li [c]

North China University of Water Resources and Electric Power, Zhengzhou 450011,China

[a]baixinli@ncwu.edu.cn, [b]mabwater@126.com, [c]ljywater@126.com

Keywords: finite element method; preprocessing; automatic meshing; hexahedron; tetrahedron.

Abstract. A practical technique for generating hexahedral meshes automatically is proposed in this paper. The technique is accomplished by secondary subdivision of a tetrahedron. The implementation method from tetrahedron to hexahedron through secondary subdivision is discussed. The method and treatment of boundary condition formula are derived, and the simple and practical load processing method is given. Finally a tetrahedron-based hexahedron automatic meshing program is developed. Engineering examples shows that the calculation accuracy of the method is comparatively high. The proposed method can be applied to any entity.

Introduction

The development of finite element preprocessing technology [1] has experienced three stages as follows: (1) manual data input stage; (2) semi-automatic (interactive) data input stage; (3) fully automatic meshing stage.

Fully automatic meshing method is benefited from the development of three-dimensional molding and surface modeling system and the rapid development of computer software. Although this method has some shortages, it has received many scholars' attention after it is put forward, because its usage is simple, performance is reliable and the element quality is better. At present, the technology of fully automatic meshing tetrahedron has become increasingly mature [2-5].

Compared with the tetrahedron element, hexahedron element has better mechanical properties. In order to achieve the same precision, the numbers of hexahedron nodes and elements are far less than those of tetrahedron elements. So hexahedron elements in finite element analysis field have higher value. But technically speaking, hexahedral meshing is much more difficult than the tetrahedron meshing, this is because the theory of hexahedral meshing is still not fully established. So, for any complex objects, it has been a difficult problem to obtain reliable and high quality hexahedral finite element mesh in the field of CAE. Although a lot of methods has put forward, but these methods are not fully resolved the automatic meshing problems, some methods are only suitable for a certain condition.

Based on the tetrahedron, conversion method (secondary subdivision method) is adopted to realize the fully automatic hexahedron meshing for an arbitrary 3-d entity.

Implementation of the Automatic Hexahedral Subdivision

Method from a Tetrahedron to Hexahedrons through Secondary Subdivision. The method converting a tetrahedron to hexahedrons is shown in Fig. 1. The vertices of a tetrahedron are represented by nodes (1,2,3,4), nodes (5,6,7,8,9,10) are respectively the middle points of edges (1,2), (1,3), (1,4), (2,3), (3,4) and (4,2) , and nodes (11,12,13,14) are respectively the centers of four surface triangles (1,2,3), (1,3,4), (1,4,2) and (2,4,3) of the tetrahedron. From geometrical knowledge we know that, the planes (13,5,11), (11,6,12), (12,7,13), (11,8,14), (12,9,14), (14,10,13) passing through the central lines of the edge nodes (5,6,7,8,9,10) must intersect at the center node 15 of the tetrahedron, the plane will divide the tetrahedron into four hexahedral elements, i.e. element No. 1, No. 2, No. 3, No. 4 in Fig. 1.

For example, when generate four 8-node hexahedron elements from a tetrahedron, the first element local node numbers are:

Element No. 1: 1, 6, 12, 7, 5, 11, 15, 13.

When generate four 20-node hexahedron elements, the first element local node numbers are:

Element No. 1: 1, 6, 12, 7, 5, 11, 15, 13, 16, 17, 18, 19, 20, 21, 22, 23, 24, 25, 26, 27.

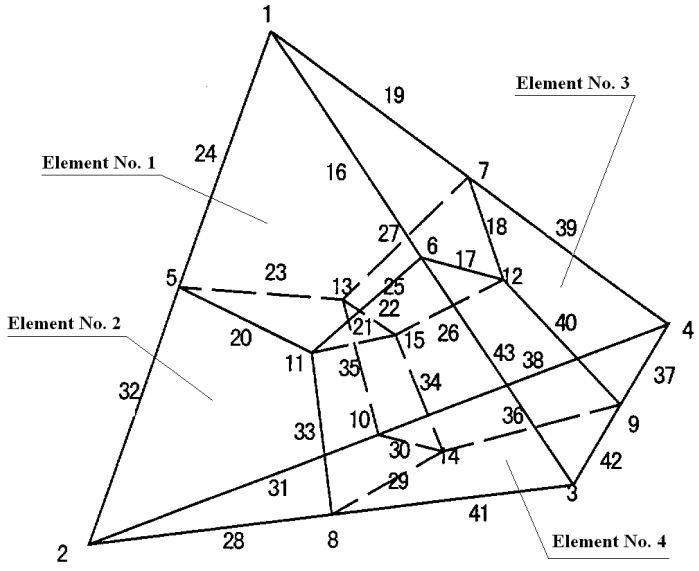


Fig. 1 Local node numbers of a tetrahedron into four hexahedrons

Treatment of Boundary Conditions. In Fig. 1, the nodes (1, 2, 3, 4) are the four nodes (vertices) of the original tetrahedron, 5-43 for new generated nodes. In order to conveniently programming, the node numbers used the certain numbers rules, namely: the top 15 nodes are used to form four 8-node hexahedron elements; Then adding the side middle node in the four 8-node hexahedron elements, it can form the four 20-node hexahedron elements, namely 16 to 43 node is the element side middle nodes.

Fig. 2 separately shows node local numbers of Element No.1 in Fig. 1 (8-node and 20-node element). The node numbers are same to those in Fig. 1. In order to observe conveniently, the element No. 1 in Fig. 1 is mapped to a hexahedron.

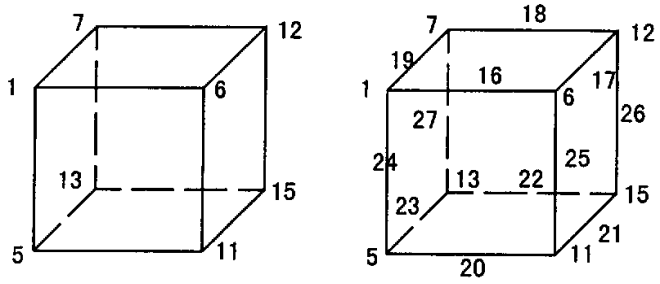


Fig. 2 Local node numbers of a hexahedral element

The following rules are adopted in the boundary constraint conditions processing:

The constraint conditions of the original four nodes (1, 2, 3, 4) keep unchanged. The middle nodes on each edge, namely nodes (5, 6, 7, 8, 9, 10) in Fig. 1, are decided by the constraints of both end nodes. For example, the constraint condition of node 5 is determined by node 1 and node 2. Suppose constrained node (direction) is marked as 1, unconstrained node (direction) is marked as 0, the constraint condition of node 5 can be determined according to the following principle:

When the constraint marks of the two end nodes are all 1 (i.e. constrained in both ends), the middle node constraint mark in that direction is 1; otherwise the mark is 0. Considering the integer division rule in computer, the above principle can simply described as follows:

$$C(5) = [C(1) + C(2)]/2 \tag{1}$$

where, $C(\cdot)=1$, means constrained in a certain direction; $C(\cdot)=0$ without constraint. Similarly, to the node on a surface, such as node 11, there is

$$C(11)=[C(1)+C(2)+C(3)]/3 \tag{2}$$

For center node 15, there is

$$C(15)=[C(1)+C(2)+C(3)+C(4)]/4 \tag{3}$$

Treatment of Loads. There are two kinds of methods for treatment of loads. The first method is that, mark each element load in the beginning of forming tetrahedral elements and keep them, and then process the loads during the following hexahedral subdivision. This method has a high precision, and can deal with lots of load types. But its defect is difficult, and the program structure is complex, especially for complex surface force. The second approach is that, adopt the nodal loads on the original tetrahedron element, do not allocate load on the new generated node. The precision of the second method is not as high as the first method, but in accordance with the Saint-Venant principle, the result is acceptable. The second method is used in this paper.

Application

In the abovementioned method, a program [6] has developed to mesh a tetrahedral element into four hexahedrons automatically. It can be used to mesh any entity into tetrahedral elements, the coordinates, constraints, loads etc of the obtained tetrahedrons can be cut into hexahedrons through secondary subdivisions. Dozens of example analysis show that this method is simple and effective, and the precision is higher. Now two engineering examples are listed below.

Stress Calculation of Mars Oil Pump Isolation Tank. Mars oil pump isolation tank is the main parts used for discharging dust of the mortar pump in power plant. The tank is made of material 16MnR. The subjected load is internal pressure of 8.00MPa. High precision 20-node hexahedral elements are adopted, and the element shape after subdivision is shown in Fig. 3. The obtained the maximum equivalent stress (Von Mises stress) is 281.23MPa, its position is in intersection of the wall and the pipe.

Compared to calculation results (272.81MPa) in reference [7], the error is 3.09%.

Compared with ANSYS calculation results, the error is -3.06%. In ANSYS calculation, the adopted element is 10-node tetrahedral element (Fig. 4). The maximum stress obtained is 290.10MPa, and the position of maximum equivalent stress is the same to in this paper. But the calculation scale (number of degree of freedom, i.e. DOF) is much smaller in this paper.

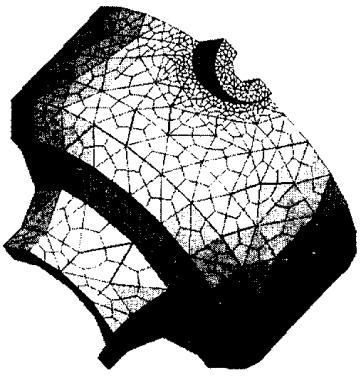


Fig. 3 Mesh in this paper

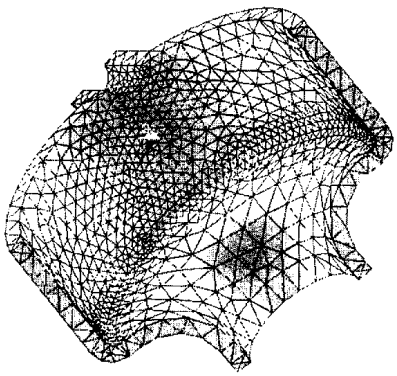


Fig. 4 Mesh in ANSYS

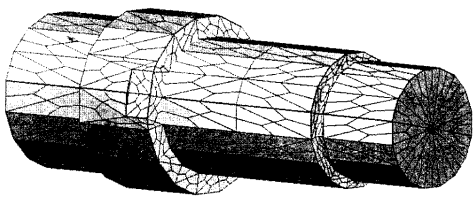


Fig. 5 Mesh of the crank shaft

Stress Calculation of a Crank Shaft (oil field). The crank shaft is an important component of the drilling equipment, by 45# steel. The simplified mechanical model of the shaft is: one end is fixed and another end subjected to pure torque, with the torque moment of 3.00kN·m. The 20-node hexahedral elements (Fig. 5) are used. As compared with theoretical solution, the maximum error of the equivalent stress in several key sections is 4.12%.

Conclusions

From the above analysis, the following conclusions can be drawn:

(1) By the secondary subdivision technology, 8-node and 20-node hexahedral element automatic subdivisions are realized on the basis of tetrahedron division. Not only the meshing speed is fast, but also the operation is simple, the method is suitable for all kinds of levels of finite element analysis.

(2) Through the comparison of theoretical solution and engineering examples, the results show that the proposed hexahedral mesh algorithm is feasible, and the programming is correct. The computation precision and efficiency of the meshed hexahedral element is higher than tetrahedral element.

Acknowledgements

This work was financially supported by the Development fund of Mechanical industry technology (2006 JXA0101); Construction funds (2011-2012) of Engineering Mechanics Discipline of North China University of Water Resources and Electric Power.

References

[1] J. Liu, Research and Implementation of Finite Element Preprocessing, Beijing Univ. of Aeronautics Press, Beijing, 1991.

[2] W. Dai, Z. Cao, J. Xie, The automatic division method of finite elements and its application in engineering, J. of Changchun Institute of Technology, 10 (2009) 61-64.

[3] E. Nie, C. Chao, Application of VB and TrueGRID software to 3-D FE mesh division of lock heads, Port & Waterway Engineering, 19 (2009) 138-142.

[4] M. Li, J. Zhou, The FE mesh automatic division with high quality of arbitrary planar region, J. of Applied Mechanics, 21 (2004) 125-128.

[5] T. Luo, Z. Hua, A. Peng, Applications of AutoCAD-based FE preprocessing, J. of Hubei University of Technology, 23 (2008) 59-62.

[6] X. Liang, et al, ZRIME CAE Technology Report, Zhengzhou Research Institute of Mechanical Engineering, Zhengzhou, 2001.

[7] Z. Jiang, X. Yang, Strength of Pressed Parts in Boiler and Pressure Vessel, Mechanical Industry Press, Beijing, 1999.

© (2012) Trans Tech Publications, Switzerland
doi:10.4028/www.scientific.net/AMM.238.218

Three-dimensional Two Material Transportation Method Based on the Volume Fractions Interface Algorithm

Jilin Wu[a], Zeyu Wu[b], Yuping Tong[c] and Peirong Du[d]

School of Civil Engineering and Communication, North China University of Water Resources and Electric Power, Zhengzhou 450011, China

[a]wujilin2012@163.com, [b]wuzeyu@ncwu.edu.cn, [c]tongyuping@ncwu.edu.cn, [d]dupr2005@126.com

Keywords: numerical simulation; Eulerian method; material interface.

Abstract. In order to solve the problem of three-dimensional two medium transportation problems of fluid dynamics, the transportation principles of a metal ball moving in constant velocity fields were given. The space district was dispersed into some cuboid Euler cells in the directions of three coordinate axes, along which mediums were transported by turns. The continuous boundary condition was adopted to simulate infinite boundary. The interface reconstruction method in the mixture cells was the volume fractions method. The numerical simulation result indicates that the shape and size of the medium cuboid can keep unchanged basically during the medium transportation. The overspeed transportation problem of the volume fractions method in the course of transportation is pointed out. The research may provide certain reference and guidance for solving the multi-material fluid dynamics problems.

Introduction

Eulerian method faces a great difficulty when it is applied to dispose of three-dimensional multi-material mixed cell. How to calculate various quantities that are transported from donor cell to acceptor cell? Where is the position of interface? These problems restrict seriously the development and application of Eulerian method. With the improvement of interface disposal technique of multi-material Eulerian method gradually and with the introduction of interface tracking technique with high-order algorithm and arithmetic of transport quantities [1-3], we pay more attention to the study and the application of Eulerian method.

Research on two-dimensional hydro-elastoplastic problems, which is obtained through simplification of the actual problems, is more mature at present [4-8], but there is a certain error between the calculation result and the actual one. In recent years, great progress has been made in the three-dimensional study, but the depth of its research is a far cry from the two-dimensional in comparison. Three-dimensional approach has no limitations of geometric configuration, so it can truly reflect the physical processes compared to two-dimensional one. To solve the problems really, in-depth and careful studies on three-dimensional problems have to be made.

The Volume Fractions Interface Algorithm

The interface disposal technique used in the majority of three-dimensional computer programs is VFIA (the Volume-Fractions-Interface-Algorithm) method, in which the volume share of each medium in a cell is represented by the ratio of its volume size to the total volume of the cell to describe the so-called volume ratio method. The physical quantities in a cell and the transportation quantities between two cells are calculated through the volume share. According to the volume share of each medium in a donor cell and acceptor cell, the distribution of material is speculated in order to determine the order in which every kind of material is transported. Donor-Acceptor Cell Technic widely used is adopted in the method. The mixed cells itself are considered the material interfaces. This method is relatively simple, the exact location of the interface in a mixed cell isn't defined. In this paper, some exploration about this point is made.

The space district is dispersed into some rectangle Euler cells in three coordinate directions. The number of a cell is defined (i, j, k), and the length of the cell is respectively $\Delta x_i, \Delta y_j, \Delta z_k$:

$$x_i = \sum_{l=1}^{i-1} \Delta x_l + \frac{1}{2}\Delta x_i \ , \ y_j = \sum_{l=1}^{j-1} \Delta y_l + \frac{1}{2}\Delta y_j \ , \ z_k = \sum_{l=1}^{k-1} \Delta z_k + \frac{1}{2}\Delta z_k \ , \tag{1}$$

where (x_i, y_j, z_k) are the coordinates of the cell center.

Initial and boundary condition include the initial evaluating method and the boundary processing. The continuous boundary condition has been adopted. On each side of the boundary of calculation field the virtual cell technique is adopted, that is, on the front and last boundary there are a row virtual cells in order to compute the physical quantity on the boundary according to the boundary condition:

$$u_{i+1} = u_i \ , \quad u_{j+1} = u_j, \ u_{k+1} = u_k \ , \tag{2}$$

Where = is assignment symbol.

Take x axial direction as an example, when the velocity $u_{i+1/2,j,k}$ of right side of the cell (i, j, k) is greater than zero, the cell (i, j, k) is a donor cell, and the cell (i+1,j,k) is a acceptor cell. The transportation volume of material ΔV is:

$$\Delta \mathrm{V} = \Delta \mathrm{t} \cdot \mathrm{s} \cdot \mathrm{ui+1/2,j,k} \ , \tag{3}$$

Where $\Delta t \cdot$ is time step and s is transportation area of the donor cell.

When there is a kind of material in a donor cell, material transportation is accomplished with the transportation volume of material ΔV. There is decrease of the transportation volume of material ΔV in the donor cell, and there is accordingly increase of the transportation volume of material ΔV in the acceptor cell .

When there are two kinds of material in a donor cell, we have

$$\Delta V_\theta = \beta_\theta \Delta V \tag{4}$$

$$\beta_\theta = \frac{1}{2}\left((\eta_\theta)_{\mathrm{DC}} + (\eta_\theta)_{\mathrm{AC}}\right) \tag{5}$$

$$\eta_\theta = \frac{V_{ijk(\theta)}}{V_{ijk}} \tag{6}$$

$$V_{ijk} = \Delta x_i \times \Delta y_j \times \Delta z_k \tag{7}$$

Where ΔV_θ is the transportation volume of θ material, and $V_{\mathrm{ijk}(\theta)}$ is the volume of θ material in the (i, j, k) cell, and DC ,AC stand for donor cell and acceptor cell accordingly. If there is a kind of material in a acceptor cell, β_θ=1, and the material contained in the acceptor cell is transported firstly. When the volume of the material is less then ΔV, the supplementation of another kind of material is again transported . If there are two kinds of material in a acceptor cell, the first material is transported firstly. When the volume of the first material is less then ΔV, the supplementation of the second material is again transported .

Along x, y, z direction, material transportation is accomplished by turns. The calculation time step satisfies the CFL condition (Courant-Friedrichs-Lewy). Here CFL condition ensures the convergence of the adopted difference scheme.

$$\Delta t^n = k_0 \cdot \min\left\{ \min\left[\frac{\Delta x_i}{\left|u_{ijk}^n\right| + C} \right], \min\left[\frac{\Delta y_j}{\left|v_{ijk}^n\right| + C} \right], \min\left[\frac{\Delta z_k}{\left|w_{ijk}^n\right| + C} \right] \right\} \ , \tag{8}$$

Where C and k_0 are adjusting coefficient, and Δt^n is time step.

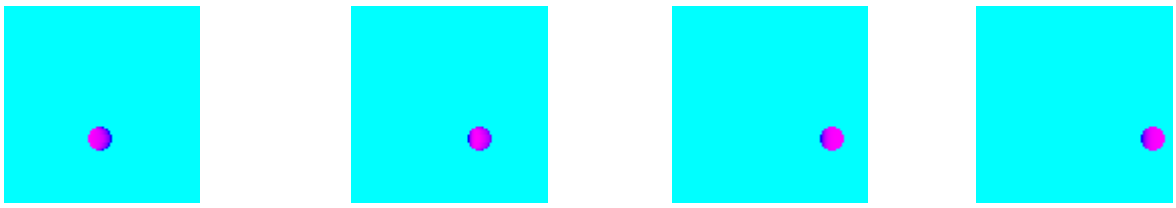
The Numerical Simulation of Material Transportation

Applying the structured programming method and the idea of software engineering, based on the numerical method above, the code is developed by FORTRAN. By adopting the code, some transportation problems have been numerically simulated. There are two kinds of material of air and metal in the field of calculation mode(25m×25m×20m),which is divided 100×100×80 meshes. The numerical results are shown in Figures 1-7, where (u_x, v_y, w_z) are velocity components in the (x, y, z) coordinate directions, and D_{eltt} is time step, and n is the number of numerical calculation cycles. The Figures 1-7 are perpendicular to the z axis. The initial coordinates of ball center are (8, 8, 2), and the coordinates of ball center during transportation process are shown in Table 1.



n=300 *n*=600 *n*=900 *n*=1200

Fig. 1 The transportation figure of ux=wz=400(m/s) and Deltt=1.0E-5(s)



n=100 *n*=200 *n*=300 *n*=350

Fig.2 The transportation figure of ux=wz=400(m/s) and Deltt=1.0E-4(s)



n=10 *n*=20 *n*=30 *n*=35

Fig. 3 The transportation figure of ux=wz=400(m/s) and Deltt=1.0E-3(s)



n=100 *n*=200 *n*=300 *n*=350

Fig. 4 The transportation figure of vy=wz=400(m/s) and Deltt=1.0E-4(s)



n=10 *n*=50 *n*=100 *n*=150

Fig. 5 The transportation figure of ux=1000(m/s),wz=400m/s and Deltt=1.0E-4(s)



n=4 *n*=24 *n*=40 *n*=60

Fig. 6 The transportation figure of u_x=2000(m/s), w_z=400m/s and D_{eltt}=1.0E-4(s)



n=10 *n*=50 *n*=100 *n*=150

Fig. 7 The transportation figure of u_x=v_y=w_z=400(m/s) and D_{eltt}=1.0E-4(s)

Table 1 Coordinates of ball center during transportation process

Calculation cycles *n*	Coordinates of ball center						
	Fig. 1	Fig. 2	Fig. 3	Fig. 4	Fig. 5	Fig. 6	Fig. 7
n=4	—	—	—	—	—	9.00,8,2.25	—
n=10	—	—	12.00,8,6.00	—	9.00,8,2.50	—	8.50,8.50,2.50
n=20	—	—	16.00,8,10.00	—	—	—	—
n=24	—	—	—	—	—	13.00,8,3.00	—
n=30	—	—	20.25,8,14.25	—	—	—	—
n=35	—	—	22.25,8,16.25	—	—	—	—
n=40	—	—	—	—	—	16.00,8,3.75	—
n=50	—	—	—	—	13.00,8,4.25	—	10.25,10.25,4.25
n=60	—	—	—	—	—	20.00,8,4.50	—
n=100	—	12.00,8,6.00	—	8,12.00 ,6.00	18.25,8,6.25	—	12.25,12.25,6.25
n=150	—	—	—	—	23.00,8,8.00	—	14.50,14.50,8.50
n=200	—	16.00,8,10.00	—	8,16.00 ,10.00	—	—	—
n=300	9.25,8,3.25	20.25,8,14.25	—	8,20.25 ,14.25	—	—	—
n=350	—	22.25,8,16.25	—	8,22.25 ,16.25	—	—	—
n=600	10.5,8,4.50	—	—	—	—	—	—
n=900	11.75,8,5.50	—	—	—	—	—	—
n=1200	13.00,8,7.00	—	—	—	—	—	—

Conclusions

The numerical simulation result indicates that the shape and size of the medium cuboid can keep unchanged basically during the medium transportation. The overspeed transportation problem of the volume fractions method in the course of transportation is pointed out. Several examples of numerical simulation illustrate that the adopted numerical method is effective and stable. The code is fit for computing three-dimensional Hydro-elastoplastic problems, and can show clear material interface. However, these are only preliminaries. It needs to be study further so as to be consummated and applied.

Acknowledgments

This work was supported by the Science and Technology Fund of Training the High-level Talents of North China University of Water Resources and Electric Power.

References

[1] Rich M, A method for Eulerian Fluid Dynamics, Los Alamos Scientific Lab. Report, LA-2826, 1963.

[2] R. A. Gentry, R. E. Martin, B. J. Daly, An Eulerian differencing method for unsteady compressible flow problems, J. Comp. Phys., 1 (1966) 87-118.

[3] J. D. Kershner, C. L. Mader, A two-dimensional Continuous Eulerian Hydrodynamic Code for Computing Multi-component Reactive Hydrodynamic Problems, Los Alamos Scientific Lab. Report, LA-4846, 1972.

[4] G. Xu, Z. Yu, Z. Liao, An Eulerian numerical method for the multi-material compressible fluid dynamics. Journal of Numerical Methods and Computer Applications, 3 (1980) 163-172. (in Chinese)

[5] W. Wen, S. Yun, Y. Zhang, An algorithm for tracking interfaces in two-dimensional Eulerian code, Journal of Numerical Methods and Computer Applications, 3 (2000) 161-170. (in Chinese)

[6] H. Tu, S. Yun, J. Ding, Numerical simulation 2D explosion field for hazard evaluation. China Safety Science Journal, 2 (1994) 1-6. (in Chinese)

[7] J. Ning, Z. Wang, H. Zhao, et al, Study on the flow of the explosive shock wave around the wall numerical simulation, Journal of Beijing Institute of Technology, 5 (1999) 543-547. (in Chinese)

[8] T. Ma, High Velocity Multi-material Dynamic Computation and Software, Beijing Institute of Technology, 2007. (in Chinese)

© (2012) Trans Tech Publications, Switzerland
doi:10.4028/www.scientific.net/AMM.238.223

Numerical Simulation of Rural Brick Buildings Strengthened with CFRP under Flood Actions

Yongjun Liu[1, a], Xingtao Ma[2, b] and Yongmei Sun[1, c]

[1] School of Civil Engineering, Shenyang Jianzhu University, Shenyang 110168, China

[2]Liaoning Hydrology and Water Resources Bureau, Shenyang 110003, China

[a]liuyongjun66@hotmail.com, [b]maxt1975@163.com, [c]sunyongmeigirl@163.com

Keywords: flood hazard, rural building, CFRP, numerical simulation.

Abstract. In China, floods often cause life and property losses due to heavily damage and collapse of rural buildings. It is very important to conduct comprehensive research on flood behavior of rural buildings. In this paper, formula of hydrodynamic load imposed on building by flowing flood is derived based on conservation of momentum and test results firstly. Secondly, the finite element analysis of rural brick buildings strengthened with CFRP under flood actions is conducted using ANSYS software to check the effect of CFRP. Simulation results demonstrate that the formula of hydrodynamic pressure and the numerical model of rural buildings are of high accuracy, and can be referenced for further study and applied in engineering practices.

Introduction

Flood disaster has a significant influence on social progress and economic development, and it is one of the worst natural disasters in the world. China is a flood prone country, and flood poses a great threat on people's lives because of its high frequency, and ferocious destructive power [1]. Especially in towns and villages where economic level is relatively low, and a large number of rural buildings were damaged even collapse in floods, for examples, 5.24 million houses collapsed in famous Henan 75.8 flood disasters, and 187, 200 houses collapsed in 2003 Huaihe River flood [2, 3].

Under the support of National Key Technology R&D Program of P. R. China, the authors of this paper conducted a serial studies on structural behaviors of rural building under flood actions with emphasis on GIS-based flood forecasting system, test and numerical simulation of failure mechanism of rural building in flood, retrofitting and strengthening technologies for rural building under flood action, developing finite element software for analysis of flood resistant behavior of rural building, and so on. In this paper, the calculation method of hydrodynamic pressure and numerical simulation technology of CFRP strengthened rural brick building under flood actions is presented.

Flow Pressure of Flood on Rural Buildings

Hydrodynamic Actions. Flood actions on a building can be classified in the following categories: hydrodynamic actions, hydrostatic actions, hebris actions, huoyancy action, hrosion actions, non-physical actions [3]. Here, we discuss how to calculate hydrodynamic actions with emphasis. In general, when the velocity of flowing water is more than 0.9m/s, the hydrodynamic actions on building should be take into account [3, 4]. Test studies conducted by authors demonstrated that hydrodynamic actions on walls from flowing flood water is uneven on the upstream surface of the walls, and the actual distribution of hydrodynamic actions depends on several factors [4].

In this paper, it is assumed that flood water is steady incompressible non-viscous flow. Based on conservation of momentum in a non-viscous flow, following formulation of hydrodynamic actions on upstream surfaces of walls from flood water can be derived

$$P_{\mathrm{d}}(x,y)=\frac{1}{2}C_{\mathrm{D}}(x,y)\rho(x,y)\,v(x,y)^2 \tag{1}$$

Where, $P_D(x, y)$ is the hydrodynamic pressure (N/m^2); C_D (x, y) is the drag coefficient fall in 1.0 and 2.0 depending on such factors as shape, width, and depth of water; ρ (x, y) is the fluid mass density (kg/m^3); $v(x, y)$ is the flow velocity of flood water (m/s).

Resultant force of hydrodynamic pressure acting upon upstream surface of a wall is

$$F_d = \int_{\Omega} \frac{1}{2} C_D \rho v^2 d_A \tag{2}$$

Where, F_d is the resultant force of hydrodynamic pressure; Ω is the region of a wall under hydrodynamic pressure.

Equation (2) is formulation to calculate hydrodynamic pressure in integral form, which is inconvenient to use and needs to be simplified. In most cases, F_d is supposed to be a constant on whole region. After adjusting drag coefficient according to the width depth ratio of upstream surface of a wall, resultant force of hydrodynamic pressure acting upon upstream surface of a wall can be calculated using following equation

$$F_d = \frac{1}{2} C_A \rho_A v_A^2 A \tag{3}$$

Where, C_A is the average value of drag coefficient; ρ_A is fluid average mass density; v_A is the average flow velocity of flood water (m/s); A is the area of upstream surface of a wall (m^2).

Numerical Simulation of Rural Building under Flood Actions

Basic Assumptions. In order to cut computational cost, following assumptions are made: (1) Hydrodynamic actions are simplified as equivalent distributed load. (2) CFRP sheet is an ideal elastic material and remains elastic throughout process. (3) Brick walls and CFRP sheets are bonded together perfectly and no slip happens before bricks break.

Element type. The wall of which is made of brick and mortar is treated as a homogeneous materials, and element Solid65 in ANSYS is used to model the wall. Materials properties is determined according to that of brick and motar. CFRP sheet is modeled using element Shell63 which is especially suitable for modelling CFRP sheet.

Principles of Failure. Two Principle of failure are adopted. Firstly, if first principal stress in a wall element is more than 11.25MPa or shear stress is more than 0.27MPa then the element is treated as a failed element. Sceondly, if node's displacement perpendicular to a wall exceed 0.06m the the wall is taken for failure.

Materials Properties. The elastic modulus of brick is 1.3×10^4N/mm^2, axial compressive strength of brick is 19.5N/mm^2, tensile strength is 1.54N/mm^2, Poisson's ratio of brick is 0.1. The elastic modulus of motar is 1×10^4N/mm^2, axial compressive strength of motar is 5N/mm^2, Poisson's ratio of brick is 0.25. Material properities of CFRP sheet are shown in Table 1.

Table 1 Material properities of CFRP sheet

Effective thickness (mm)	Tensile strength (MPa)	Elasticity modulus (MPa)	Ultimate strain (mm/mm)	Unit weight (kg/mm^2)
0.111	2100	2.35×10^5	0.015	0.300

Finite Element Mesh. Numerical simulation and model test is based on a 1:5 reduced scale model of representative rural resident building in Northeast part of China [4]. Size of the building model is 180cm×100cm×60cm. The unstrengthened model is termed as model 1, and the strengthened one is termed as model 2. The comparison of structural behavior in flood shall be conducted in this paper. Fig. 1 illustrates the finite element mesh without hidden lines of model 2.

Boundary Conditions and Loads. It is assumed that all nodes at bottom surface of walls are fixed in three directions. The values of hydrodynamic actions are converted into equivalent hydrostatic loads according to eqution (4). The load from roof is represented as equivalent even distribution load on the top surface of walls.

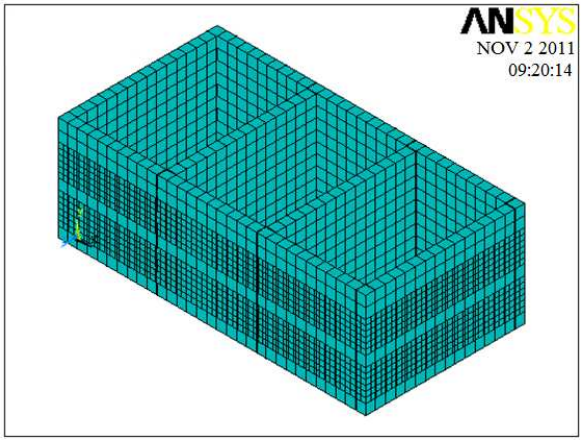


Fig. 1 Finite element mesh without hidden lines

Compration and Analysis of Results from Numerical Simulation

Stress Distributions in Model 1 and Model 2. Because the walls facing to water flow are impacted by flowing water, the displacement of and stress in those walls are bigger than displacement of and stress in other walls. When the rate of flow and the deep of the flood approach 1.2m^3/s and 0.6m respectively, model 1 failed. Instead, model 2 did not fail and can continue to work.

Fig. 2 and Fig. 4 show the first principal stresses distributed in model 1 and model 2 respectively. From Fig.2, we can find that maximal first principal stress occurs in the area where lognitudinal and transverse walls joint. In addition, maximal first principal stress occurs in the bottom of walls too. In model 2 which is strengthened with CFRP sheets shown in Fig. 3, we can find that first principal stress is reduced significantly.

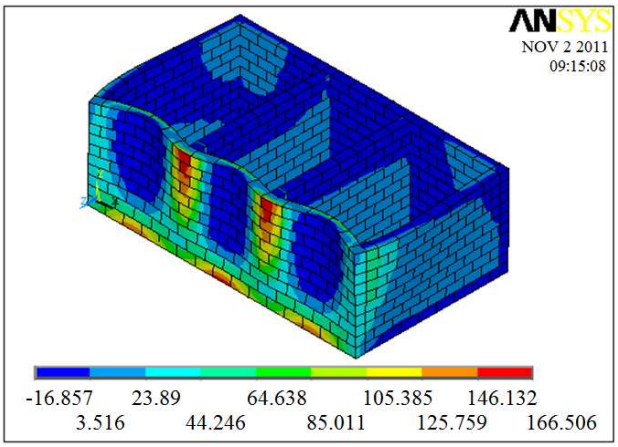


Fig. 2 First principal stress in model 1

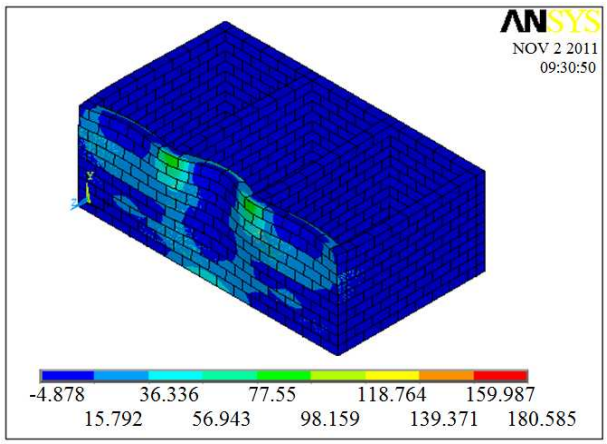


Fig. 3 First principal stress in model 2

Displacements in Model 1 and Model 2. Fig. 4 and Fig. 5 illustrate the displacements of two models along the directions of water stream. When the rate of flow and the deep of the flood approach 1.2m^3/s and 0.6m respectively, the maximal displacements in model 1 and model 2 are 10.24mm and 6.35mm respectively. As a result, it can be concluded that CFRP sheet can improve the stiffness of a brick building effectively.

Fig. 6 shows maximal displacement-load curves of model 1 and model 2. It can be seen that the realtionships between maximal displacement and load are nonlinear, and the CFRP sheets can reduce the maximal displacement in rural brick buildings obviously.

Conclusions

Flood water may impose considerable lateral impact force at the upstream walls, as a result, flood water may damage rural buildings even make them collapse.

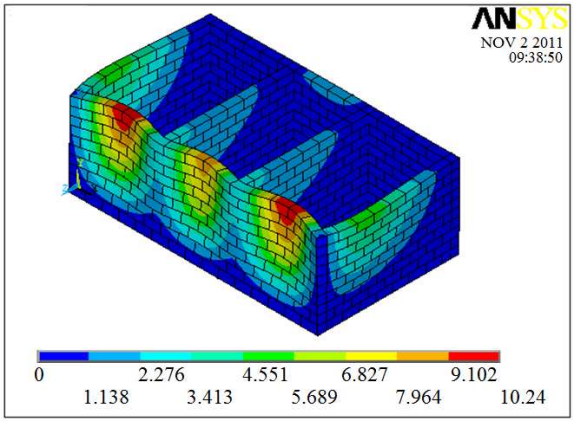


Fig. 4 Displacement of model 1

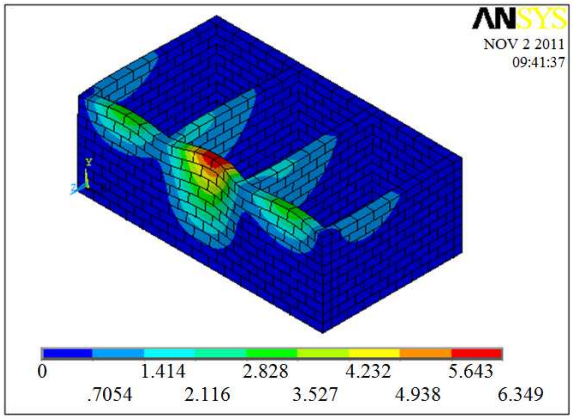


Fig. 5 Displacement of model 2

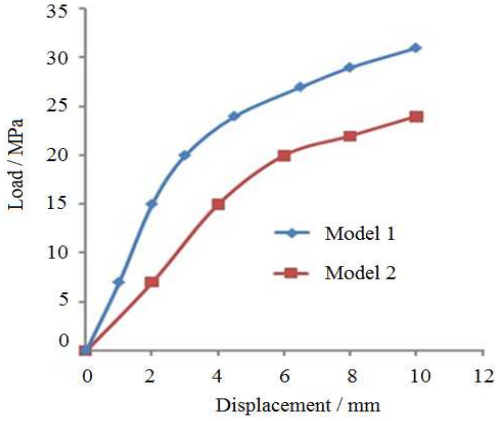


Fig. 6 Maximal displacement-load curves

CFRP strengthened rural brick buildings have improved anti-impact ability, and the displacement of and stresses in rural buildings can be reduced at a large extent.

The element Solid65 and Shell63 of ANSYS are useful for simulating the bahaviors of CFRP sheets strengthened rural brick buildings under flood actions.

Acknowledgments

This work is supported by National Key Technology R&D Program in the 11th Five Year Plan of P. R. China (2008BAJ08B014).

References

[1] X. Tan, W. Zhang, J. Ma, and Z. Su, Journal of China Institute of Water Reources and Hydropower Research, 2 (2004) 50-55

[2] Y. Liu, J. Zhou and X. Meng, Journal of Information Technology in Civil Engineering and Architecture, 3 (2011) 57-64.

[3] I. Kelman, Spence R. Engineering Geology, 73 (2004) 297-309.

[4] Z. Yin, Y Ren, J. Zhou, Y Liu, X. Meng, Journal of Catastrophology, 25 (2010) 127-130.

© (2012) Trans Tech Publications, Switzerland
doi:10.4028/www.scientific.net/AMM.238.227

Research of Viscous-spring Artificial Boundary in Dynamic Analysis

Hongyang Zhang[1, a], Liwei Han[1,b], Zongtao Tao[2,c], Liang Yao[3,d], Songping Li[4,e] and Xiangdong He[4,f]

[1] North China University of Water Resources and Electric Power, Zhengzhou 450011, China

[2] Guilin University of Technology, Guilin 541004, China

[3] Construction and Administration Bureau of South-to-North Water Diversion Middle Route Project, Beijing 100038, China

[4] Henan Hydraulic Research Institute, Zhengzhou 450003, China

[a]1694440@qq.com, [b]14634281@qq.com, [c]502262740@qq.com, [d]48582695@qq.com, [e]706309212 @qq.com, [f]66350363@qq.com

Keywords: dynamic artificial boundaries; wave input; displacement time histories.

Abstract. Some dynamic artificial boundaries were summarized, including the local boundary and the global boundary. The viscous-spring artificial boundary is introduced in dynamic analysis, and the wave input method is analyzed. Finally, the precision and stability of visco-spring artificial boundary is proved by the example.

Introduction

In 1968, Alterman firstly put forward the concept of artificial boundary conditions (artificial boundary condition) [1]. The artificial boundary can be classified into two aspects as the global artificial boundary and the local artificial boundary. There are boundary element method [2, 3], infinite element method [4, 5] and thin layer method [6, 7, 8], which are the global artificial boundaries. Global artificial boundary usually has higher precision, but it is space-time relative and increases the computational complexity. At present, global artificial boundary is used in homogeneous medium about problems of infinite domain. Viscous boundary [9], viscous-spring boundary [10], side the shaft approximate boundary [11, 12], stacked boundary [13, 14] and transmitting boundary [15] are commonly used as the local artificial boundary. Viscoelastic artificial boundary is proposed in 1994 by Deeks [16], which is simple and absorbs wave and scattering energy by a series of springs and dampers [17]. It is widely used because of implemented easily and good regularity and high stability.

The Viscous-spring Artificial Boundary

In polar coordinates system, the equation of out-plane cylindrical wave is

$$\frac{\partial^2 \omega}{\partial t^2} = c^2 \left(\frac{\partial^2 \omega}{\partial r^2} + \frac{1}{r} \frac{\partial \omega}{\partial r} \right) \tag{1}$$

Where $c = \sqrt{G/\rho}$ is the shear velocity in medium, ω is the out-plane displacement, G is the shear modulus, ρ is the density, r is the distance to coordinate center.

The stress expression at the radii of r_b is

$$\tau(r_b, t) = -\frac{G}{2r_b} \omega(r_b, t) - \rho c \frac{\partial \omega(r_b, t)}{\partial t} \tag{2}$$

It can be seen, imposing spring ($C_b = \rho c$) and damper ($K_b = G/(2r_b)$) at the radii of r_b can eliminate the reflection in the truncated boundary by scattered waves.

Method of Wave Motion Input

At the viscoelastic artificial boundary, the essence of wave input is realized by imposing equivalent load with equal displacement and stress as original wave field in boundary. The movement at artificial boundary is composed of incident wave and scattered wave [18].

The displacement and stress of any point P at the artificial boundary by original wave field can be divided into the displacement and stress by incident wave field and scattering wave field.

$$\sigma_{\mathrm{m}} = \sigma_{\mathrm{f}} + \sigma_{\mathrm{s}} \tag{3}$$

$$u_{\mathrm{m}} = u_{\mathrm{f}} + u_{\mathrm{s}} \tag{4}$$

The stress by scattering wave field is

$$\sigma_{\mathrm{s}} = -\alpha \frac{G}{R} u_{\mathrm{s}} - \rho c u_{\mathrm{s}} \tag{5}$$

Imposing the stress F_{p} on point P at boundary, then on which the stress is

$$\sigma_{\mathrm{m}} = -\alpha \frac{G}{R} u_{\mathrm{m}} - \rho c u_{\mathrm{m}} + F_{\mathrm{p}} \tag{6}$$

Combining the equations, the equivalent nodal stress imposed on point P at boundary is:

$$F_{\mathrm{p}} = \alpha \frac{G}{R} u_{\mathrm{f}} - \rho c u_{\mathrm{f}} + \sigma_{\mathrm{f}} \tag{7}$$

Example of Verification

The calculation area, which is half infinite space, is shown in Fig. 1, impact load is imposed at point A. The density ρ is 2500kg/m^3, the elastic modulus E is 0.02GPa, the poisson ratio μ is 0.25 and the shear velocity in medium is 57m/s.

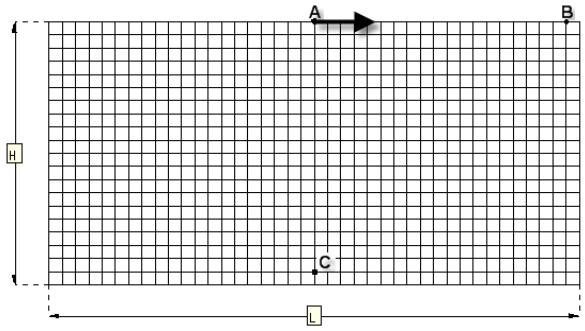


Fig. 1 Schematic diagram of calculation area

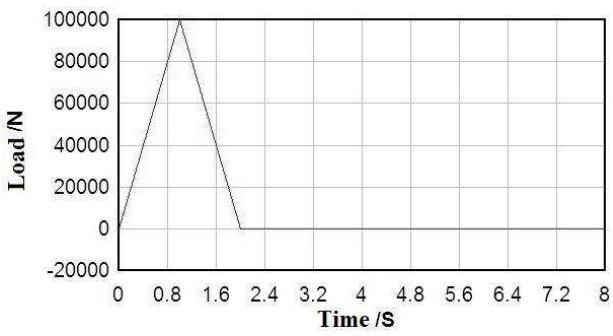


Fig. 2 Time-history curve of impact load

Selecting three different boundaries, which are viscous-spring artificial boundary, fixed boundary and large size foundation boundary, to verify accuracy and superiority of the viscous-spring boundary.

Model 1: In Fig. 1, L=400m, H=200m, imposing viscous-spring boundary on two side and bottom of calculating area, and the top is free surface.

Model 2: In Fig. 1, L=400m, H=200m, imposing fixed boundary on two side and bottom of calculating area, and the top is free surface.

Model 3: In Fig. 1, L=960m, H=480m, imposing fixed boundary on two side and bottom of calculating area, and the top is free surface. Truncation border is far enough from the interesting area, in order to ensure the impact load does not reflect during calculation time and get the quasi-exact result.

Imposing impact load shown in Fig. 2 at point A for all three models, time step of calculation is 0.01 seconds and the time lasting 10 seconds. The time-history curves of displacement at point A (0, 0), B (190, 0) and C (0, 190) are got and shown from Fig. 3 to Fig. 5.

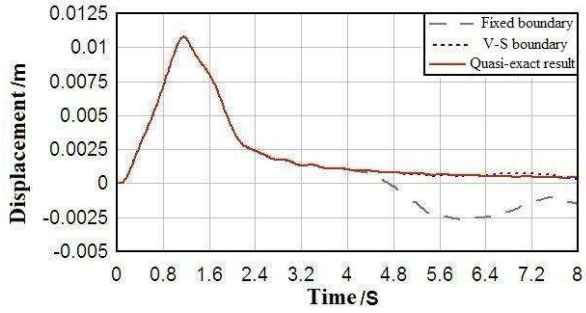


Fig. 3 Time-history curves of displacement at A

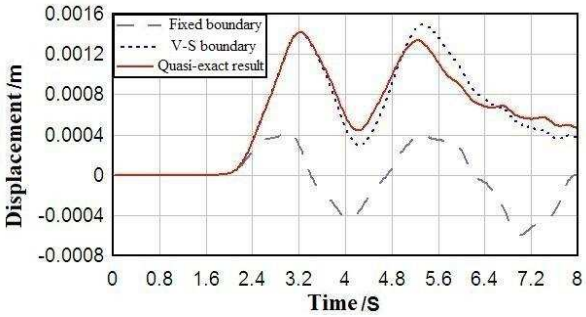


Fig. 4 Time-history curves of displacement at B

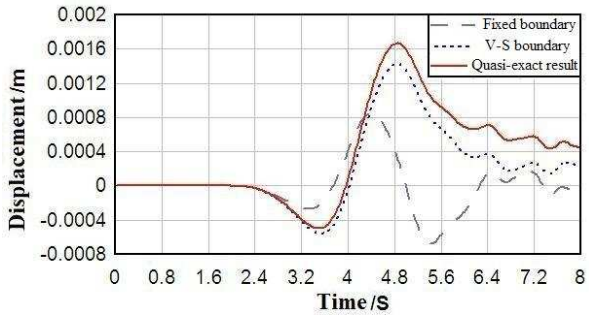


Fig. 5 Time-history curves of displacement at C

From the figures, it is known that the calculation of fixed boundary is distorting due to the reflecting on the boundary. The scope of boundary is the same as model 2, but the calculation of viscous-spring boundary has good agreement with which of model 3 (quasi-exact result). The results show that the viscous-spring boundary is effective and accurate in dynamic analysis.

Conclusions

The viscous-spring artificial boundary is introduced in dynamic analysis. The principle and the wave input method are analyzed. The precision and stability of visco-spring artificial boundary is proved by the example.

The foundation is considered as elastic and single phase medium in dynamic analysis by viscous-spring artificial boundary. In fact, the foundation material is a kind of porous media. It is meaningful about study on artificial boundary of porous media in wave problems.

References

[1] Alterman Z. S., Karal F. C, Propagation of elastic waves in layered media by finite-difference methods, J. Bull. Seism. Soc. Am., 58 (1968) 367-398.

[2] Givoli D, Numerical Methods for Problems in Infinite Domains, third ed., Elsevier, Amsterdam, 1992.

[3] Banerjee P K, The Boundary Element Methods in Engineering, second ed., McGraw-Hill, London, 1994.

[4] Bettess P, Zienkiewica O C, Diffraction and refraction of surface waves using finite and infinite elements, J. Int. J. for Num. Meth. Ineng., 11 (1977) 1271-1290.

[5] C. Zhao, C. Zhang, G. Zhang, Simulation of semi-infinite plane elastic foundation using infinite elements, J. Tsinghua University (Science and Technology), 26 (1986) 51-64.

[6] Lysmer J, Lumped mass method for Rayleigh waves, J. Bulletin of the seismological Society of America, 60 (1970) 89-104.

[7] Kausel E, J M Rossess, G Wags, Dynamic analysis of footings on layered media, J. Engineering Mechanics, ASCE, 101 (1975) 679-693.

[8] Manolis G D, D E Beskos, Boundary Element Methods in Elastodynamics, first ed., Unwin Hyman, London, 1988.

[9] Lysmer J, Kulemeyer R L, Finite dynamic model for infinite media, J. Engng. Mech. Div., ASCE, 95 (1969) 859-877.

[10] Dominguez J, Maeso O, Model for the seismic analysis of arch dams including interaction effects, 10th World Conference of Earthquake Engineering, Madrid, 8 (1992) 4601-4606.

[11] Clayton R, Engquist B, Absorbing boundary conditions for wave-equation migration, J. Geophysics, 45 (1980) 859-904.

[12] Clayton R, Engquist B, Absorbing boundary conditions for acoustic and elastic wave equations, J. Bull. Seism. Soc. Amer., 76 (1977) 1529-1540.

[13] Smith W, A non-reflecting plane boundary for wave propagation problems, J. Comp. Phys., 15 (1973) 492-503.

[14] Kunar R. R, Marti J, A non-reflecting boundary for explicit calculations, J. Computational methods for infinite domain media-structure interaction, ASME, 46 (1981) 183-204.

[15] Z. Liao, K. Huang, B. Yang. Transmitting boundaries to transient wave, J. Scientia Sinica Mathemation, 26 (1984) 50-56.

[16] Deeks A. J., Randolph M. F., Axisymmetric time-domain transmitting boundaries, J. Engineering Mechanics, 120 (1994) 25-42.

[17] G. Gu, Earthquake Engineering for Earthrock Dams, second ed., China WaterPower Press, Beijing, 2009.

[18] J. Liu Jingbo, Y. Lv, A direct method for analysis of dynamic soil-structure interaction, China Civil Engineering Journal, 31 (1998) 55-64.

© (2012) Trans Tech Publications, Switzerland
doi:10.4028/www.scientific.net/AMM.238.231

Study on Design Method for Scale and Layout of Road Passenger Station

Zhicheng Li[1, 2, a], Quanxin Sun[1, b] and Shunbo Zhao[2, c]

[1] School of Traffic and Transportation, Beijing Jiaotong University, Beijing 100044, China

[2] School of Civil Engineering and Communication, North China university of Water resources and Electric Power, Zhengzhou 450011, China

[a] shixing1980@163.com, [b] sunquanxin@jtys.bjtu.edu.cn, [c] sbzhao@ncwu.edu.cn

Keywords: scale design; road passenger station; volume of station; bi-level programming model.

Abstract. On basis of summarizing the traditional design methods on road passenger station, this paper discusses the influence of road passenger station layout on scale design. Combined with the analysis of layout design method for road passenger station, a bi-level programming model is proposed taking into account the overall optimization design problem of the scale and the location of the road passenger station. Through a numerical example analysis, an optimized station layout plan and an optimum volume allocation of the station are given out.

Introduction

In the field of road passenger station planning, the station scale and location are two very important aspects of the entire process, with a direct impact on the effectiveness of the investment and operation of the entire station. Recently a lot of people carried out the research work of the station scale and station location, but which are respectively analyzed, and the relationship between them was ignored. The method for determining the scale of the station, commonly considered combination of qualitative analysis and quantitative analysis, include regression analysis, the five-factor method, the gravity model, etc., which are basically based on the Volume of the forecast of each traffic zone, and then combine with various socio-economic urban transport factors to estimate the design scale value of the station. The station location is a classic problem in the station planning, commonly used mathematical-physical model, operations research methods, flow decision model, bi-level programming model, etc., the focus of these models consider different. The application has some limitations, must be combined with qualitative factors to make a decision.

Overall, the current theories and methods about the scale of the road passenger station design and location problem, with little regard for the intrinsic link between the two ones, we should consider the two combined for analysis. In the current design specifications of road passenger terminal building, the scale of the road passenger station is generally decided in its Average Passenger Delivery Volume Periderm In A Year, and station-scale level is divided according to the Average Passenger Delivery Volume Periderm In A Year, and the corresponding station facilities are set up according to the specification, so the Average Passenger Delivery Volume Periderm In A Year should be relatively accurately predicted. In fact, based on accurately prediction of the volume of each traffic zone, how to reasonably allocate the volume to the road passenger stations, which can make the lowest overall construction costs, and inspire ability to attract of each passenger station, has become key consideration of the road passenger stations construction sector in the practical application. Of course, the location plan is considered by the government related to passenger transport authorities and funding departments, but the difference between the actual location plan will affect passenger travel choice, and passengers certainly hope that the cost of travel reaches the lowest level. So in this paper, we consider the variables of the road passenger station location as decision ones, establish the upper model regarding the lowest total cost and the maximum services capabilities to be used as the optimization targets, establish the lower model regarding the lowest total passenger travel cost as the optimization targets, obtain the optimal station layout plan through the bi-level programming model, and finally obtain the corresponding design volumes of road passenger station scale.

Establishment of the Bi-level Programming Model on Scale and Location Layout of Road Passenger Station

Bi-level Programming Model. The bi-level programming model has unparalleled advantages compared with traditional single-model approach, embodied in:

1) It can simultaneously analyze two different and conflicting goals in the decision-making process;

2) Decision-making method of the multi-value criteria is closer to the actual situation;

3) It can make it clear that the interaction of the higher level policy-making departments and the public. Passenger station location problem related to the decision makers of the two distinctly different objective function-site planners and users, therefore, the use of bi-level programming model is appropriate to describe this relationship.

Model Definition and Assumptions. Set the object area is divided into m traffic zones, select the suitable site for k road passenger stations, in which k is predicted qualitatively given by the total Volume of the city as the maximum value of the options, the actual selection of sites for the number may less than k. So we can make the following assumptions about the model:

1) Presumption is given that k road passenger station location has been selected, now we consider how to select the appropriate ones in the k election sites.

2) The road passenger station can fully complete each other, and the volume generated in every traffic zone may be shared by k road passenger stations.

3) Through the passenger survey in stations, we find that travelers out of the city choose public transport to the passenger station, with the public transport service costs and lines been relatively fixed, so we can assume that a unit cost of travel out of town visitors is relatively fixed for a certain rate.

Define a few basic symbols: s_j is (0,1) variable for location of the station, bj is the per establishmenting and operating costs of k station which is selected, the value can be determined by the land use of the status quo or the future at the selected location, economic development conditions, traffic conditions and other factors.

The Bi-level Programming Model on Road Passenger Station Scale and Location Layout. The land and construction costs of the construction of road passenger stations in the whole object area is

$$C_1 = \sum_{i=1}^{m} \sum_{j=1}^{k} S_j x_{ij} b_j \tag{1}$$

The attractiveness of the passenger station can be reflected by the aggregation of passenger traffic, as follows:

$$C_2 = \sum_{i=1}^{m} \sum_{j=1}^{k} x_{ij} \tag{2}$$

Therefore, the location problem of the passenger station can be described by the following model

$$\text{U: } \min C(S) = C_1 - \lambda C_2 \tag{3a}$$

$$s.t.\ s_j = 0 \text{ or } 1,\ 1 \le j \le k \tag{3b}$$

λ is correction factor, $x=(x_1, x_2, \cdots, x_a)$ is the solution of the lower-level mathematical programming model.

Lower-level programming (L) describes the allocation patterns volume of every traffic zone among different stations on the condition of the existence of a number of elected passenger stations, which are committed to the lowest cost of each passenger travel. The passengers from each traffic zone always consider the unit cost between the home and the station, when they make the choice of one station. The proportion of traveler who selected the bus way is accounted for about 78%, based on the travel survey. In city traffic organization, the unit cost of bus travel and travel time costs are relatively fixed, so we assume that the paths can be choose by the inter-city travelers are limited, and the unit costs are relatively fixed. The lower-level problem can be described as follows

$$\mathrm{L}: \quad \min F(x) = \sum_{i=1}^{m}\sum_{j=1}^{k} x_{ij} p_{ij} \tag{4a}$$

$$s.t. \quad \sum_{j=1}^{k} x_{ij} = A_i \quad , \quad \forall i = 1,\cdots,m \tag{4b}$$

$$x_{ij} \leq M \quad s_j \qquad \forall i = 1,\cdots,m \quad \forall j = 1,\cdots,k \tag{4c}$$

$$x_{ij} \geq 0 \quad \forall i = 1,\cdots,m \quad \forall j = 1,\cdots,k$$

Where x_{ij} is the volume assigned from i traffic area to j passenger station; p_{ij} is unit cost spent by the passengers who arrive at j road passenger station from i traffic zone; A_i is the volume of i traffic zone; While j passenger station is selected, s_j is taken as 1, and 0 otherwise; M is arbitrarily large positive number.

This is a bi-level programming model, the upper model is to make construction and operation cost of the passenger station reach lowest level, and service capabilities are fully utilized, which is the result of policy makers hope to achieve; while the lower is a user-service model, is intended to make total travel cost of the lowest customers on the basis of the higher managers decision-making.

Model of the Solution. Algorithm idea: 0, 1 variable in the upper model, Enumeration method or the branch and bound method can be used to solve, because the passenger station options are generally very limited, so we can use an enumeration method to solve. All cases of the entire passenger station layout will be listed. Find every C(s) of the location program, the minimum is the optimal location program.

It can be seen from model L, the constraints (4c) has expressed that the relationship between the distribution of demand and the location program of the passenger station. So on the terms of the underlying problem, s_j is known, If $s_j = 0$, then $x_{ij} = 0$, this constraint can be removed; if $s_j = 1$, then $x_{ij} \leqslant M$, M is an arbitrarily large number, so this constraint is naturally satisfied, which can be removed. That is, for a fixed s_j, lower-level problem constraints may be omitted. But in order to get the specific form of the response function, the constraints (4c) can be transformed into a form of the following (but not added to the model)

$$x_{ij} = Ms_{ij} - \theta_{ij} \quad , \quad \forall i = 1,\cdots,m \quad \forall j = 1,\cdots,k \tag{5}$$

Where θ_{ij} is slack variables, while $s_{ij} = 0$, x_{ij} and θ_{ij} can be directly obtained; while $s_j = 1$, L can be soluted by the existing method, then the demand x'_{ij} for the equilibrium distribution of customers in all distribution centers can be obtained, and use formula (5) to calculate the value of the slack variable θ'_{ij}. So get all reaction function can be written as

$$x_{ij} = Ms_j - \theta'_{ij} \tag{6}$$

These relations be taken into the upper objective function, available existing methods can be used to solve the optimal problem. Once again soluting the lower-level problem, we can get the allocation of customer demand at each passenger station，repeating the above ideas, but also can get a new set of location of the program. Such double counting, the last is expected to converge to the optimal solution of the bi-level programming model. The solution algorithm is actually a heuristic algorithm based on equation (6). The specific calculation steps are as follows:

Step 1: Setting an initial solution s_j^0, and setting the number of iterations $r = 0$;

Step 2: For a given s_j^r, solving the underlying problem, getting x_{ij}^r;

Step 3: according to equation (13), computing θ_{ij}^r, and $x_{ij} = M_{sj} - \theta_{ij}^r$ will be into the upper objective function, solving the top problem, getting a new set of values;

Step 4: If $|F^{r+1} - F^r| \leq \varepsilon$, stopping cycle; otherwise, so, turn to Step 2. In which ε is the iterations precision.

Examples of Analysis. Supposing a city carry on layout planning of the road passenger stations, location selection and design scale will be determinate on the basis of the 2020 Volume which is predicted. There 5 traffic zones, which are respectively numbered as {1, 2, 3, 4, 5}, in which only

No.1, No.2, and No.3, with construction conditions will be selected, therefore n=3. The location of two stations will be selected. m=5, k=2, λ=1, M=100×10^3. The volume of the passenger station in each traffic zone, the unit cost of each selected station, the travel rates among the selected station locations and different traffic zone are showed in Table 1, Table 2 and Table 3.

Table 1 Volume of traffic zone (10^3 passengers/day)

Traffic zone	1	2	3	4	5
A_i	22	15	20	25	30

Table 2 The unit cost of the passenger station in each selected station site (10^4 ¥/ person.)

Station site	1	2	3
b_{ij}	1	2	3

Table 3 Travel rates between the traffic zone and the selected location (¥ /person)

	Station site 1	Station site 2	Station site 3
Traffic zone 1	3	3	5
Traffic zone 2	3	2	4
Traffic zone 3	5	4	1
Traffic zone 4	3	2	3
Traffic zone 5	2	5	3

The Calculation Steps. The upper model can be solute through enumeration; the lower model can be used Matlab optimization toolbox for solving linear constrained optimization problem. Which are calculated as follows:

Step1: Initializing. Assuming that three passenger stations will be constructed, then S=(1,1,1), and the number of iteration steps r=0.

Step2: Solving the underlying problem, and obtaining the respective volume assigned to each passenger station based on the minimum of the cost of travel from every traffic zone, the result is that x'_{11}, x'_{12}, x'_{13}, x'_{21}, x'_{22}, x'_{23}, x'_{31}, x'_{32}, x'_{33}, x'_{41}, x'_{42}, x'_{43}, x'_{51}, x'_{52}, x'_{53} are respectively 11, 11, 0, 0, 15, 0, 10, 0, 0, 25, 30, 0, 0. Further it can be obtained that θ_{ij}' is respectively equal to 89, 89, 100, 100, 85, 100, 90, 100, 90, 100, 100, 75, 70, 100, 100. So we can obtain response function, the other and so on.

Step 3: Taking the linear relationship into the upper model, using the enumeration method, we can obtain a new location program S=(1, 1, 1) of the upper model, which is the best location program. If we choose a program which does not meet the convergence condition，then continue to return to the first step in solving.

Solving Until the Election of the Scale of the Station Site. Known by solving the above model, only three sites to be selected will be all constructed to meet the goal of the optimization model, then the volume of them can be respectively obtained as shown in Table 4.

Table 4 The volume assigned to the corresponding passenger station (10^3 passengers/day)

	Station site 1	Station site 2	Station site 3
Traffic zone 1	11	11	0
Traffic zone 2	0	15	0
Traffic zone 3	10	0	10
Traffic zone 4	0	0	25
Traffic zone 5	30	0	0
Total	51	26	35

It can be seen, the first station will have to bear the larger amount of the passengers, carrying on a large-scale planning and construction is clearly necessary, the third station the scale should be correspondingly greater than the second station.

Conclusions

The scale and location design of the road passenger station is a complex issue, influenced by many factors, of course, should be combined with quantitative and qualitative analysis. Combination of the proposed bi-level programming model , taking into account the selection of station locations and the design of the station scale, we can get the most suitable location of the passenger stations to be selected, with the cost of establishment station, service capacity, passenger travel costs been in the optimal conditions, and consider the station-scale design problems by calculating the volume assigned to corresponding station on the optimal conditions, undoubtedly it is a good idea for the current plan of road passenger station. Of course, the model built in this paper set several assumptions, ignoring some actual factors, so it can be further consideration on the actual conditions of the model correction.

References

[1] X. Liu, S. Qiu, F. Ren, Research on road freight distribution center the best location method, China Journal of Highway and Transport, 5 (1992) 84-89.

[2] X. Liu, L. Shen, X. Yang, Urban passenger transport hub in the evaluation index system, China Journal of Highway and Transport, 8 (1995) 97-102.

[3] G. Rui, H. Pan, Golden Phoenix Court Highway main hub general layout of the site, China Journal of Highway, 13 (2000) 89-92.

[4] G. Bi, Consider the routing of the logistics distribution center location two-tier regulatory Ge II model and solution algorithm, China Journal of Highway and Transport, 16 (2003) 115-119.

© (2012) Trans Tech Publications, Switzerland
doi:10.4028/www.scientific.net/AMM.238.236

Variation Rules of Warping Effect with Respect to Parameters of Cylindrical Helical Spring

Ying Hao [a] and Junfeng Guan [b]

North China University of Water Resources and Electric Power, Zhengzhou 450011, Henan, China

[a] haohao517112@tom.com, [b] shuaipipi88@126.com

Keywords: warping effect; natural frequency; cylindrical helical spring.

Abstract. The effect of warping deformation on the natural frequencies of the cylindrical helical spring with non-circle cross section, based on naturally curved and twisted beam theory, is analytically investigated in this paper. The purpose of this article is to discuss the variation rules of the warping effect with respect to the parameters of springs. The numerical simulations show that the results of the present model demonstrate a good agreement with those of ANSYS when the warping effect is included. Additionally, the effect of warping on the natural frequencies is more obvious as the parameters of the spring increase.

Introduction

Helical springs are important parts of industrial production. In order to improve the carrying capacity of the springs and meet the various requirements of installation space, a large number of special-shaped helical springs with their variability in cross-sectional shapes, helical shapes and material properties, are used in engineering practice in recent years. The cylindrical helical spring with non-circle cross section is the simplest of the special-shaped helical springs.

The problem of free vibration of cylindrical helical springs has been reported by many researchers [1-4], but the shapes of wire cross section for these springs are mostly circular. Recently, Yu et al. [5] worked out the effect of warping behavior in the formulation on the free-vibration characteristics of naturally curved and twisted beams. Yu and Hao [6, 7] derived the differential equations of motion for cylindrical helical springs with non-circular cross sections including the warping effect at the first time. The vibrational parameters, which influence the natural frequencies, are chosen as the helix pitch angle, the number of coils, the diameter of the cylinder, and the shape of cross-section and the arrangements of the cross section. The warping effect on natural frequencies of cylindrical helical springs with non-circular cross sections is pronounced, which should be taken into consideration in the free vibration analysis of the springs [6, 7].

But the effect of warping isn't discussed systematically [6, 7]. Based on the research results [6, 7], the variation rules of the warping effect on natural frequencies with respect to the parameters of the spring are expounded in detail in this paper. The purpose of this article is to answer when the warping deformation should be considered and when it can be ignored.

Free Vibration Equations of Springs

Similarly, $u_s(s)$, $u_\xi(s)$, $u_\eta(s)$ are the three translations, and $\varphi_s(s)$, $\varphi_\xi(s)$, $\varphi_\eta(s)$, are the three rotations, and $\alpha(s)$ is a generalized warping coordinate, respectively. The differential equations of motion of the cylindrical helical springs are simplified as follow, the coefficients can be got from [6, 7]. The natural frequencies of cylindrical helical springs are solved analytically by applying the automated Muller root search method and the bisection method, and detailed discussions are carried out.

$$(D^2-\lambda_{A1}+\lambda_{A2})u_\xi(\beta)-(\lambda_{A3}+\lambda_{A4})Du_\eta(\beta)+\lambda_{A5}Du_s(\beta)-c\lambda_{A6}\varphi_\xi(\beta)-cD\varphi_\eta(\beta) +c^2(\lambda_{A7}D-\lambda_{A8})\alpha(\beta)=0 \tag{1}$$

$$(\lambda_{B1}+\lambda_{B2})Du_\xi(\beta)+(D^2-\lambda_{B3}+\lambda_{B4})u_\eta(\beta)+\lambda_{B5}u_s(\beta)+cD\varphi_\xi(\beta)-c\lambda_{B6}\varphi_\eta(\beta) +c^2(\lambda_{B7}D+\lambda_{B8})\alpha(\beta)=0 \tag{2}$$

$$\lambda_{C1}Du_{\xi}(\beta)-\lambda_{C2}u_{\eta}(\beta)-(D^2-\lambda_{C3}+\lambda_{C4})u_s(\beta)-c\lambda_{C5}\varphi_{\eta}(\beta)-c^2(\lambda_{C6}D-\lambda_{C7})\alpha(\beta)=0,$$
$$\lambda_{D1}u_{\xi}(\beta)+\lambda_{D2}Du_{\eta}(\beta)-c(D^2-\lambda_{D3}+\lambda_{D4})\varphi_{\xi}(\beta)+c\lambda_{D5}D\varphi_{\eta}(\beta)-c\lambda_{D6}D\varphi_s(\beta)-c^2(\lambda_{D7}D^2$$
$$+\lambda_{D8}D-\lambda_{D9}+\lambda_{D10})\alpha(\beta)=0 \tag{3}$$

$$\lambda_{E1}Du_{\xi}(\beta)-\lambda_{E2}u_{\eta}(\beta)+\lambda_{E3}u_s(\beta)+c\lambda_{E4}D\varphi_{\xi}(\beta)+c(D^2-\lambda_{E5}+\lambda_{E6})\varphi_{\eta}(\beta)+c\lambda_{E7}\varphi_s(\beta)$$
$$-c^2(\lambda_{E8}D^2-\lambda_{E9}D-\lambda_{E10}+\lambda_{E11})\alpha(\beta)=0 \tag{4}$$

$$\lambda_{F1}D\varphi_{\xi}(\beta)-\lambda_{F2}\varphi_{\eta}(\beta)-(D^2-\lambda_{F3}+\lambda_{F4})\varphi_s(\beta)+c(\lambda_{F5}D+\lambda_{F6})\alpha(\beta)=0 \tag{5}$$

$$(\lambda_{G1}D+\lambda_{G2})u_{\xi}(\beta)+(\lambda_{G3}D-\lambda_{G4})u_{\eta}(\beta)+(\lambda_{G5}D+\lambda_{G6})u_s(\beta)-c(\lambda_{G7}D^2-\lambda_{G8}D$$
$$-\lambda_{G9}+\lambda_{G10})\varphi_{\xi}(\beta)+c(\lambda_{G11}D^2+\lambda_{G12}D-\lambda_{G13}+\lambda_{G14})\varphi_{\eta}(\beta)-c(\lambda_{G15}D-\lambda_{G16})\varphi_s(\beta)$$
$$-c^2(D^2+\lambda_{G17}+\lambda_{G18})\alpha(\beta)=0 \tag{6}$$

Applications

Some numerical results are given in this section. As the example, a spring with the rectangular cross section and clamped-clamped ends, and with material and geometry properties: ρ=7900kg/m^3, E=2.06×1011N/m^2, μ=0.3, the diameter of the cylinder R, the helix pitch angle α, the number of active turns n, the rectangular cross section of width 2a in the ξ-direction and height 2b in the η-direction.

Example 1. R=5mm, α=8.5744^o, n=7.6.

Table 1 Variation of warping effect with aspect ratio(a/b) of the rectangular cross section

Mode No. (Hz)		1	2	3	4	5
2a=1mm 2b=0.4mm	FEM	228.42	228.68	274.89	527.26	535.11
	Warping ignored	256.17	264.32	400.20	593.58	608.63
	Error (%)	12.15	15.59	45.58	12.52	13.74
	Warping included	242.67	246.35	329.22	568.10	573.48
	Error (%)	6.24	7.73	19.26	7.75	7.17
2a=1mm 2b=0.6mm	FEM	320.97	328.43	382.32	606.39	728.90
	Warping ignored	335.48	339.41	435.69	599.77	773.53
	Error (%)	4.46	3.34	13.96	1.09	6.12
	Warping included	328.72	330.5	412.88	599.54	753.63
	Error (%)	2.41	0.63	7.99	1.13	3.39
2a=1mm 2b=0.8mm	FEM	390.67	392.48	464.14	596.23	875.01
	Warping ignored	396.77	397.18	480.34	599.59	886.80
	Error (%)	1.56	1.20	3.49	0.56	1.35
	Warping included	393.98	394.94	475.36	598.68	881.25
	Error (%)	0.85	0.63	2.41	0.41	0.71
2a=0.8mm 2b=1mm	FEM	395.76	399.49	465.37	479.62	849.93
	Warping ignored	400.41	404.33	479.82	482.76	861.35
	Error (%)	1.18	1.21	3.11	0.66	1.34
	Warping included	395.48	400.18	470.31	480.51	853.42
	Error (%)	0.07	0.17	1.06	0.19	0.41
2a=0.6mm 2b=1mm	FEM	329.77	335.29	367.04	387.87	681.45
	Warping ignored	343.22	348.61	365.45	438.88	690.25
	Error (%)	4.07	3.97	0.43	13.15	1.30
	Warping included	329.48	335.51	362.22	396.05	680.58
	Error (%)	0.08	0.07	1.31	2.11	0.13
2a=0.4mm 2b=1mm	FEM	230.92	240.91	246.75	276.88	456.38
	Warping ignored	239.66	271.45	276.33	403.51	468.80
	Error (%)	3.78	12.68	11.98	45.73	2.73
	Warping included	236.04	247.72	249.85	294.66	463.51
	Error (%)	2.22	2.83	1.26	6.42	1.56

Example 2. α=8.5744°, n=7.6, 2a=0.7mm, 2b=1mm.

Table 2 Variation of warping effect with diameter of the cylinder

Mode No. (Hz)		1	2	3	4	5
R=4mm	FEM	569.71	577.31	653.90	665.40	1196.0
	Warping ignored	583.49	589.67	659.11	715.25	1225.83
	Error (%)	2.42	2.14	0.80	7.49	2.49
	Warping included	570.07	578.16	657.44	679.28	1208.71
	Error (%)	0.06	0.14	0.54	2.09	1.06
R=6mm	FEM	252.81	256.16	290.62	295.36	531.08
	Warping ignored	260. 22	262.79	293.70	319.17	546.22
	Error (%)	2.93	2.59	1.06	8.07	2.85
	Warping included	253.88	257.35	292.46	303.18	538.23
	Error (%)	0.42	0.47	0.63	2.64	0.54
R=8mm	FEM	142.25	144.01	163.30	165.80	298.23
	Warping ignored	146.90	148.33	165.60	180.21	307.45
	Error (%)	3.26	3.01	1.41	8.70	3.09
	Warping included	142.93	144.89	164.64	170.85	303.09
	Error (%)	0.48	0.61	0.82	3.05	1.63
R=10mm	FEM	90.90	92.10	104.56	106.22	191.01
	Warping ignored	94.75	95.24	106.67	115.89	197.51
	Error (%)	4.23	3.40	2.02	9.11	3.41
	Warping included	91.59	92.82	105.43	109.47	194.04
	Error (%)	0.76	0.77	0.83	3.06	1.59

Example 3. R=5mm, n=7.6, 2a=0.7mm, 2b=1mm.

Table 3 Variation of warping effect with helix pitch angle

Mode No. (Hz)		1	2	3	4	5
α=5°	FEM	422.13	436.13	483.51	493.93	815.88
	Warping ignored	422.44	460.53	487.88	500.67	818.32
	Error (%)	0.07	5.60	0.91	1.36	0.30
	Warping included	420.89	437.80	480.91	492.77	815.96
	Error (%)	0.29	0.38	0.54	0.23	0
α=7.5°	FEM	394.09	403.04	427.42	435.19	792.68
	Warping ignored	400.86	408.75	429.19	462.42	801.97
	Error (%)	1.72	1.42	0.41	6.26	1.17
	Warping included	391.16	401.17	425.80	440.24	794.93
	Error (%)	0.61	0.46	0.38	1.16	0.28
α=10°	FEM	330.68	334.25	416.46	422.68	729.75
	Warping ignored	337.24	340.88	417.51	454.76	747.90
	Error (%)	1.98	1.98	0.25	7.59	2.49
	Warping included	328.66	333.25	416.43	431.69	732.72
	Error (%)	0.61	0.30	0	2.13	0.41
α=12.5°	FEM	276.13	279.48	406.21	410.77	644.40
	Warping ignored	280.95	284.78	409.82	446.61	660.34
	Error (%)	1.74	1.89	0.89	8.72	2.48
	Warping included	273.11	277.94	408.68	424.14	644.32
	Error (%)	1.09	0.55	0.61	3.26	0.01

Example 4. R=5mm, α=8.5744°, 2a=0.7mm, 2b=1mm.

Table 4 Variation of warping effect with number of coils

Mode No. (Hz)		1	2	3	4	5
n=6	FEM	497.93	522.49	522.76	565.27	998.30
	Warping ignored	517.95	533.66	539.13	595.32	1025.97
	Error (%)	4.02	2.14	3.13	5.32	2.77
	Warping included	505.90	528.67	529.09	572.94	1021.81
	Error (%)	1.60	1.18	1.21	1.36	2.36

Table 4(continue) Variation of warping effect with number of coils

Mode No. (Hz)		1	2	3	4	5
n=8	FEM	332.81	336.81	394.35	408.44	725.55
	Warping ignored	345.60	348.33	399.85	437.34	747.72
	Error (%)	3.84	3.42	1.40	7.07	3.06
	Warping included	337.42	340.28	398.41	416.07	733.16
	Error (%)	1.39	1.03	1.03	1.87	1.05
n=10	FEM	231.88	232.88	316.48	324.28	533.52
	Warping ignored	240.40	240.68	320.46	348.33	550.37
	Error (%)	3.67	3.35	1.22	7.42	3.16
	Warping included	235.03	235.29	319.53	330.60	539.18
	Error (%)	1.36	1.03	0.96	1.95	1.06
n=12	FEM	169.12	169.45	263.66	263.66	404.35
	Warping ignored	175.53	176.82	267.45	289.94	418.77
	Error (%)	3.79	4.35	1.44	7.71	3.57
	Warping included	171.07	172.04	266.56	274.83	409.44
	Error (%)	1.15	1.53	1.10	2.10	1.26

From Table 1, the effect of warping on the natural frequencies is more obvious as the cross section is narrower. When the spring's cross section areas keep fixed, the different arrangements of the cross section have significant influences on the effect of warping on the third and the fourth natural frequencies.

From Tables 2 to Table 4, as expected, the effect of warping on the natural frequencies increases with the diameter of the cylinder, the helix pitch angle, the number of coils increasing.

Conclusions

The purpose of this article is to present the variation rules of the effect of warping on natural frequencies with respect to the parameters of the spring. The warping effect increases with the aspect ratio, the diameter of the cylinder ,the helix pitch angle, the number of coils increasing, in which the biggest effects is the aspect ratio.

References

[1] D. Pearson, International Journal of Mechanical Engineering Sciences, 24 (1982) 163-171.

[2] V. Yildirim, International Journal for Numerical Methods in Engineering, 39 (1996) 99-114.

[3] J. Lee, Journal of Sound and Vibration, 302 (2007) 185- 196.

[4] V. Yıldırım, International Journal of Mechanical Sciences, 41 (1999) 919-939.

[5] A. Yu, C. Yang, G. Nie, Journal of Sound and Vibration, 329 (2010) 1376-1389

[6] A. Yu, Y. Hao, Journal of Sound and Vibration, 330 (2011) 2628-2639.

[7] Y. Hao, A. Yu, Chinese Journal of Theoretical and Applied Mechanics, 43 (2011) 561-569.

© (2012) Trans Tech Publications, Switzerland
doi:10.4028/www.scientific.net/AMM.238.240

Calculation of Shear Capacity of Continuous Compound Spiral Hoop Reinforced Concrete Column

Junfeng Guan[1, a] and Juan Wang[2, b]

[1] North China University of Water Resources and Electric Power, Zhengzhou 450011, China

[2] College of Water Conservancy and Environment Engineering, Zhengzhou University, Zhengzhou 450001, China

[a]shuaipipi88@126.com, [b]wangjuan@zzu.edu.cn

Keywords: continuous compound spiral hoop; concrete column; shear capacity; anti-seismic performance.

Abstract. High-ductility stirrups, which yield strength standard value is great than 1100MPa, are usually employed as a horizontal reinforcing steel bar of continuous compound spiral hoop reinforced concrete column to improve the anti-seismic performance of the short column. In this paper, a method is proposed to calculate the shear capacity of the continuous compound spiral hoop reinforced concrete column by regression analysis on the existing test data. Furthermore, the engineering application of the proposed method was illustrated in a specific case. This study provides supports for engineering projects of continuous compound spiral hoop reinforced concrete columns.

Introduction

As we all known, short reinforced concrete (RC) columns are usually of large stiffness, but their deformability and energy dissipation capacity performance of RC short columns are poor. The failure mode of RC short column is generally occurrence of shear or bond failure. Lots of previous earthquake damage investigation results showed that the damage of short column was an important factor for the structural failure or even collapse of structure. So from the point of view of engineering application, it is of great importance to improve the anti-seismic performance of RC short columns by improving their structural forms.

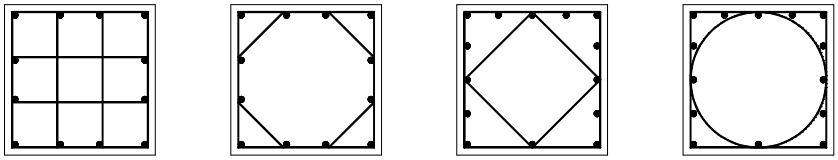
Conventional compound hoop cannot completely bind with concrete under pressure and has low hoop strength. In addition, the hoop can easily yield and lose its binding force to the concrete when the concrete under pressure expands or shear slips. Meanwhile, high-strength stirrup has been used for the continuous compound spiral hoop, and small limb can provide effective constraint for concrete, resulting in an increased bearing capacity of the components and resistance to deformation. Continuous compound spiral hoop cancels the 135°C hook at the end of a single hoop, thus, preventing the problem of hoop ineffectiveness during earthquake, and the constraint effect to concrete close to circular stirrups, even better than square tubes. The stirrup is made by a whole reinforcing steel bar, so its spatial continuity can be effective to overcome the phenomenon of loose buckle for ordinary hoops under repeatedly seismic forces. Thus, the purpose to enhance and improve the seismic performance of concrete short columns can be achieved. In addition, the continuous compound spiral stirrup is steel-saving, and its use of modern machinery production can enhance the construction quality, speed up the construction progress and improve the traditional behindhand production of it. It can solve the problem of "fat columns, short columns" by using the confined concrete.

Some scholars [1-5] have carried out relevant tests for confined concrete columns, showing that high-strength stirrup can be effective in delaying the shear failure and beneficial for the bearing capacity and deformation of beams or columns; in addition, it is necessary to use slenderer and denser high-strength stirrups to get better effect of the constraints of concrete. But up till now, systematical experiments on shear capacity of continuous compound spiral hoop RC columns are very scarce, and the existing test data is dispersive, a mature and unified method of calculation has not yet been

proposed. So it is of great value in both engineering application and research significance to accomplish the method for calculating shear capacity of the continuous compound spiral hoop RC column.

Calculation Methods

Fig. 1 shows the shapes of the cross-section layout of continuous compound spiral hoops in engineering projects.



(a) (b) (c) (d)

Fig. 1 Cross-section shapes of continuous compound spiral hoops

The related test data in Table 1 for confined concrete columns are given by the early scholars [1-5]. The calculation formulae i.e. formula (1) to (6) for calculating shear capacity of continuous compound spiral hoop RC column is proposed by regression analysis on the test data and consideration on some limits of the safety factor.

Table 1 Test data of continuous compound spiral hoop RC columns

Sectional width b/mm	Sectional depth h/mm	Compressive strength of concrete f_{cu}/MPa	Yield strength standard value of Stirrup f_{yk} /MPa	Reinforcement Volume ratio of stirrups ρ_v	Axial compression ratio n_0	Spacing of stirrups s/mm	Measured value of shear force V_u /kN
200	200	92.6	732.63	0.0021	0.80	70	207
200	200	92.6	732.63	0.0014	0.80	100	108
250	250	69.1	1430	0.0182	0.26	50	555
250	250	76.7	1430	0.0182	0.47	50	617
250	250	77.2	1430	0.0176	0.23	35	549
250	250	77.4	1430	0.0307	0.47	30	650
250	250	78.0	1430	0.0303	0.46	30	698
250	250	80.7	1430	0.0182	0.67	50	561
250	250	83.1	1430	0.0303	0.65	30	706
250	250	92.8	1360	0.016	0.35	40	417
250	250	92.8	1360	0.016	0.35	40	467
250	250	92.8	1360	0.016	0.52	40	441
250	250	101.5	789.2	0.015	0.35	60	400
250	250	101.5	789.2	0.022	0.35	40	430
250	250	101.5	1148.2	0.015	0.35	60	410
250	250	101.5	789.2	0.015	0.35	30	400
250	250	101.5	873.8	0.014	0.35	60	410
250	250	101.5	789.2	0.015	0.35	30	380
250	250	101.5	789.2	0.022	0.35	40	400
250	250	107.2	1430	0.0303	0.28	30	754
250	250	114.3	1430	0.0303	0.52	35	785
250	250	118.8	1355	0.01	0.30	44	859
250	250	118.8	1355	0.01	0.50	44	891

Calculation of Shear Capacity of Frame Column and Box Pillars Considering Combined Seismic Load. (1) Shear cross-section shall match the following conditions:

Shear span ratio $\lambda>2$ of the frame column:

$$V_c \le \frac{1}{\gamma_{RE}}(0.2\beta_c f_c b h_0) \tag{1}$$

Shear span ratio $\lambda\le 2$ of the frame column and box pillars:

$$V_c \le \frac{1}{\gamma_{RE}}(0.15\beta_c f_c b h_0) \tag{2}$$

Where, V_c—design value of shear force; β_c—the influence coefficient of strength of concrete; f_c—design values of axial compressive strength of concrete; b—sectional width; h_0—effective sectional depth; γ_{RE}—seismic adjustment factor of bearing capacity; $\lambda=M/(Vh_0)$,when their inflection point within the storey, $\lambda=H_n/(2h_0)$, H_n is clear height of the storey.

(2) Shear capacity shall match the following conditions:

When $\rho_w f_{yv} \le 4.2N/mm^2$:

$$V_c \le \frac{1}{\gamma_{RE}}[\frac{0.105}{\lambda+1} f_c b h_0 + \rho_w f_{yv} b h_0] \tag{3}$$

When $\rho_w f_{yv} > 4.2N/mm^2$:

$$V_c \le \frac{1}{\gamma_{RE}}\left\{\frac{0.105}{\lambda+1} f_c b h_0 + [4.2+0.3(\rho_w f_{yv}-4.2)] b h_0\right\} \tag{4}$$

Where, ρ_w—area ratio of reinforcement of stirrups; f_{yv}—design values of tensile strength of stirrups;

When $\lambda<1$, $\lambda=1$; When $\lambda>3$, $\lambda=3$; N—design values of axial compression forces corresponding the design values of shear forces V_c , when $N>0.3f_cA$, $N=0.3f_cA$, A is sectional areas of members.

Method for Calculating Shear Capacity of Confined Short Concrete Column. When longitudinal reinforcement of confined short concrete column ($1<\lambda\le 2$) is deformed steel, in addition to should be formula (3) and (4), still in accordance with the following formula for checking the bonding shear capacity:

$$V_c \le \sum(f_{bt}\psi)h_e + \left[0.52 f_c - \frac{2\sum(f_{bt}\psi)}{b_e}\right]\frac{bh^2}{4H_n} \tag{5}$$

$$f_{bt} = \left[(0.35\alpha_1+0.6)+40A_{sv}\frac{1+0.85(n-2)}{sN_s^2 d_s}\right] f_t \tag{6}$$

Where, Ψ—Circumference of longitudinal reinforcement, $\Psi=\pi d_e$, d_e—the nominal diameter of longitudinal reinforcement; h_e—the longitudinal reinforcement centroid distance along depth direction of the outer edge h-2c; b_e—the longitudinal reinforcement centroid distance along width direction of the outer edge b-2c; c—thickness of concrete cover; b—sectional width, h—sectional depth; f_c—design value of compressive strength of concrete; f_{bt}—bond strength of concrete and deformed steel; H_n—column height between layers; α_1—the ratio between column width deduct the sum of the bar diameter and the sum of the bar diameter, $\alpha_1=(b-N_s d_s)/(N_s d_s)$; d_s—diameter of longitudinal reinforcement; N_s—the number of longitudinal reinforcement on section side; f_t—design value of concrete tensile strength; A_{sv}—cross-section area of stirrup; S—spacing of stirrups; n—the number of stirrups limb, when $n>4$, $n=4$.

Engineering Applications

A reinforced concrete column has been designed, with square cross-section, to meet the seismic requirements. $b=h=550$mm, $H_n=1800$mm. the design value of axial force is $N=3600kN$, and the design value of shear force is $V=800$kN.The direction of shear force and the x-axis angle $\theta=0°$, the inflection point of moment was in range of height of storey. 20Φ 25 of longitudinal reinforcement along the quads uniform configuration, each side arranged six steels, $d_e=25$mm, $d_s=27$mm, $c=40$mm.

The strength grade of concrete is C60, standard value of yield strength of stirrup f_{yk}=1100MPa, stirrups diameter of 8mm, design value of tensile strength of stirrup f_{yv}=900MPa, γ_{RE}=0.8, the stirrups forms can be shown as the Fig. 1(a).

(1) Check the cross-section:

$$\lambda = 1800/2\times(550-40-25/2) = 1.81$$

$$V_c = 800 < \frac{1}{0.8}\times(0.15\times 0.933\times 27.5\times 550\times 497.5) = 1316kN$$

The size of cross section can meet the requirements.

(2) Check the shear capacity:

The number of stirrups limb is 4, $p_w f_{yv} = 4.2N/mm^2$, spacing of stirrups is 80mm.

$$\frac{1}{0.8}\times\left[\frac{0.105}{1.81+1}\times 27.5\times 550\times 497.5 + 4.2\times 550\times 497.5\right] = 1788kN > 800kN$$

Shear capacity can meet the requirements.

(3) Check the bonding capacity:

$$f_{bt} = \left[(0.35\times 2.4+0.6) + 40\times 50.24\times\frac{1+0.85\times 2}{80\times 6^2\times 27}\right]\times 2.04 = 3.1N/mm^2$$

$$6\times(3.1\times 3.14\times 25)\times 470 + \left[0.52\times 27.5 - \frac{2\times 6\times(3.1\times 3.14\times 25)}{470}\right]\times\frac{550\times 550^2}{4\times 1800} = 873kN > 800kN$$

Bonding capacity can meet the requirements.

Conclusions

In this paper, a method was proposed to calculate the shear capacity of continuous compound spiral hoop reinforced concrete column by regression analysis of the existing test data. Furthermore, a case of engineering applications was given to illustrate the calculation of shear capacity of continuous compound spiral hoop reinforced concrete column. The shear capacity formulas derived by regression was used in a 480,000 square meter mall project in Baoding, Hebei province.

It should be noted that the range of the section height of existing experimental data is still relatively small, so the application of the method to a broader range needs further more experiment verification. In addition, due to the widespread application of the ultra-high strength concrete in the ultra-high-rise buildings, the next step of research can be the tests of the small shear span test rather than the constraints of the shear capacity of concrete columns in the compressive strength of 100MPa or more.

Acknowledgements

This study was financially supported by the High-level Personnel Research Project of North China Institute of Water Conservancy and Hydroelectric Power (201064) and Research Center on Levee Safety and Disaster Prevention of Ministry of Water Resources (201202).

References

[1] P. Guan, Q. Guan, Journal of Dalian University, 20 (1999) 56-58.

[2] S. Yan, X. Xiao and Y. Zhang, Journal of Shenyang Jianzhu University, 22 (2006) 7-10.

[3] Q. Shi, K. Yang and L. Bai, China Civil Engineering Journal, 44 (2011) 9-17.

[4] L. Bing, R. Park and H. Tanaka, ACI Structural Journal, 98 (2001) 395-406.

[5] H. S. Chung, K. H. Yang and Y.H. Lee, Canadian Journal of Civil Engineering, 29 (2002) 820-830

© (2012) Trans Tech Publications, Switzerland
doi:10.4028/www.scientific.net/AMM.238.244

Research on Regional Dividing Technology for Liquefaction-induced Lateral Spreads Based on MAPGIS

Chengcheng Li[1, a], Weiming Wang [1, b], Rui Sun[1, c] and Yurun Li[2,3, d]

[1]Key Laboratory of Earthquake and Engineering Vibration, Institute of Engineering Mechanics, China Earthquake Administration, Harbin 150080, China

[2]College of Civil Engineering, Hebei University of Technology, Tianjin 300401, China

[3] Technology Research Center of Hebei Province, Tianjin, 300401

[a]lichengchegn113@126.com, [b] wswwml1983@163.com, [c] iemsr@163.com,

[d] emlyr7888@163.com

Keywords: MAPGIS; regional dividing; liquefaction-induced lateral spreads; Tangshan

Abstract: A simplified empirical statistical regression method for liquefaction-induced lateral spreads is stated in this paper. It is used to determine the corresponding calculation parameters for Tangshan city and its south region where 36 borehole data were collected. Using two multiple linear regression formulas, the free face model and the ground slope model are developed to calculate the lateral spread at each filed survey point in the region. The liquefaction-induced lateral spreads map was divided into hazard zones according to the calculated horizontal displacement at each borehole based on MAPGIS.

Introduction

China is a marked earthquake active country and has much experience of historical earthquakes with great loss of the lives and properties of the people. Due to the complex mutable soil condition and widespread weak soil in many regions, the research of rock-soil seismic damage prediction and liquefaction-induced lateral spreads based on MAPGIS technique should be vigorously developed as it has great significance of guiding the site selection in national construction. Lateral spreading occurs when a soil liquefies and blocks of intact, surficial soil move downslope or towards a free face during earthquake shaking, which is an permanent deformation caused by missing shear strength of the layers of soil. As lateral spreading has caused substantial damage during several major earthquakes, many researchers have developed empirical, analytical and numerical methods to estimate the amount of horizontal displacement from lateral spreading [2].

It is well known that the most important feature of MAPGIS is validate using date from actual erthquakes. Some case validations show that the key problem is with plotting the liquefaction-induced lateral spreads map, more information sources are necessary to improve current systems .

Lateral Spreads Computing Method

Various methods of estimating liquefaction-induced, ground failure displacement from sliding block analysis have been developed. Such as empirical estimation-method obtained from earthquake field survey and empirical prediction method with parameters deserved from standard penetration test or in suit test and so on. In the past, liquefaction-induced lateral spreads was overlooked by the statisticians according to the aerial images before and after the earthquake, and then built the regression formula (1)

$$D_H = 0.75H^{1/2}\theta^{1/3} \tag{1}$$

Where H is the thickness of liquefied layer, θ is the ground slope or the slop of liquefied layer.

After that, a popular method for producing ground failure maps was the Liquefaction Severity Index (LSI) of Yond and Perkins (1987), which provides an estimate of the maximum amount of horizontal ground displacement in gently sloping, highly susceptible deposits as a function (2) of earthquake magnitude and source distance

$$\log LSI = -3.49 - 1.86\log R + 0.98M_w \tag{2}$$

Where LSI is the maximum, permanent, horizontal displacement in inches, R is the horizontal distance from the energy source in kilometers, M_w is the earthquake moment magnitude.

Recently, it was recognized that the thickness, density and fines content of the liquefiable layer and the surrounding topography play significant roles in affecting the amount of horizontal displacement of lateral spread. A multiple linear regression (MLR) model (S.F. Bartlett and Yond, 1992) was built and subdivided into an equation for a situation with a free-face nearby (3) and an equation for the situation of gently sloping terrain (4) [3].

$$\begin{aligned}\log(D_H) = &-16.358 + 1.1782M - 0.9275\log R - 0.0133R + 0.6572\log W \\ &+ 0.3483\log T_{15} + 4.5270\log(100 - F_{15}) - 0.9224D50_{15}\end{aligned} \tag{3}$$

$$\begin{aligned}\log(D_H) = &-15.7870 + 1.1782M - 0.9275\log R - 0.0133R + 0.4293\log S \\ &+ 0.3483\log T_{15} + 4.5270\log(100 - F_{15}) - 0.9224D50_{15}\end{aligned} \tag{4}$$

Where D_H is the amount of lateral spread predicted (m), M is the moment magnitude of earthquake anticipated, R is the horizontal distance to the fault (km), W is the ratio (%), S is the ground slope (%), T_{15} is the thickness (m) of the spreadable layer with $(N1)_{60}$ less than 15, F_{15} is the average fines content (%) of the spreadable layer, $D50_{15}$ is the mean grain size (D_{50}) in the layer.

Table 1 Lateral spread state

Lateral spread state	Intac	Slight	Moderate	Severe
Lateral spread value（m）	0	0～0.1	0.1～0.3	≥0.3

The MAPGIS Regional Dividing Technology

Take Tangshan city and its south region for example, the statistics for thickness, density and fines content of the liquefiable layer according to the 36 born hole data are showed in Table 2.

Table 2 Calculation results for lateral spread

Born number	Magnitude	Epicentre (km)	Ground ratio (%)	Clay contents (%)	Mean grain size (mm)	Thickness of layers (m)	Lateral spreads (m)	Lateral spread state
1	7.8	16.6614	1.27	6.71	0.621	2.925	0.106	moderate
2	7.8	19.69175	35.21	19.82	0.246	3.075	0.543	severe
6	7.8	15.7613	28.02	4.4	0.256	1.1	0.675	severe
7	7.8	14.90725	29.28	1.2	0.318	0.8	0.607	severe
8	7.8	19.79946	15.11	8.5	0.533	6.075	0.474	severe
10	7.8	17.74568	1.47	14.44	0.270	8	0.236	moderate
11	7.8	15.2601	10.71	2.90	0.197	3.05	0.760	severe
12	7.8	13.51121	1.27	2.41	0.197	8.4	0.414	severe
13	7.8	16.94211	20.9	10.51	0.175	4.85	0.910	severe
14	7.8	10.4236	6.85	0	0.309	2	0.386	severe
15	7.8	12.3238	10.5	0.66	0.552	2.675	0.332	severe
18	7.8	3.170391	3.88	4.40	0.214	1.1	0.093	slight
19	7.8	6.122333	0	3.04	0.274	6.7	0.054	slight
22	7.8	4.658839	0	0	0.945	1.4	0.021	slight
23	7.8	4.653188	0	4.95	0.203	4.9	0.123	moderate
24	7.8	6.539927	5.15	0	0.184	0.85	0.234	moderate
25	7.8	9.991651	3.44	24.72	0.096	1.85	0.118	moderate
26	7.8	6.762223	0	0	0.194	1.95	0.156	moderate
27	7.8	6.605801	4	10.33	0.109	4.3	0.267	moderate
31	7.8	6.663762	0	4.99	0.152	2.15	0.138	moderate
32	7.8	6.451665	0	0.95	0.584	2	0.063	slight
33	7.8	8.718878	1	9.06	0.525	2.9	0.070	slight
34	7.8	9.939723	2.73	3.9	0.152	0.8	0.214	moderate
35	7.8	4.891049	8.55	28.68	0.591	5.3	0.040	slight

The horizontal distance to the fault and the ground slope are measured through the geographic relationship of born holes position from the epicenter (Fig. 1) and the contour plots (Fig. 2) based on MAPGIS. The final lateral spreads are calculated by the MLR method, and given the states in Table 1, in which the borns numbered 3, 4, 5, 9, 16, 17, 20, 21, 28, 29, 30 and 36 are intac. Then the liquefaction-induced spreads distinct map is formed with MAPGIS (Fig. 3).

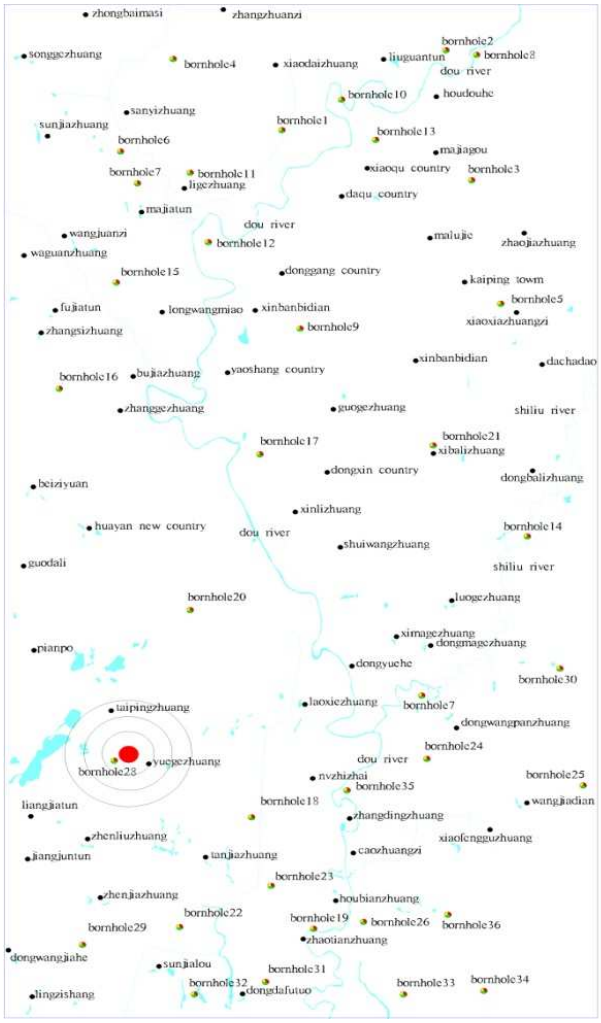


Fig. 1 Born holes position

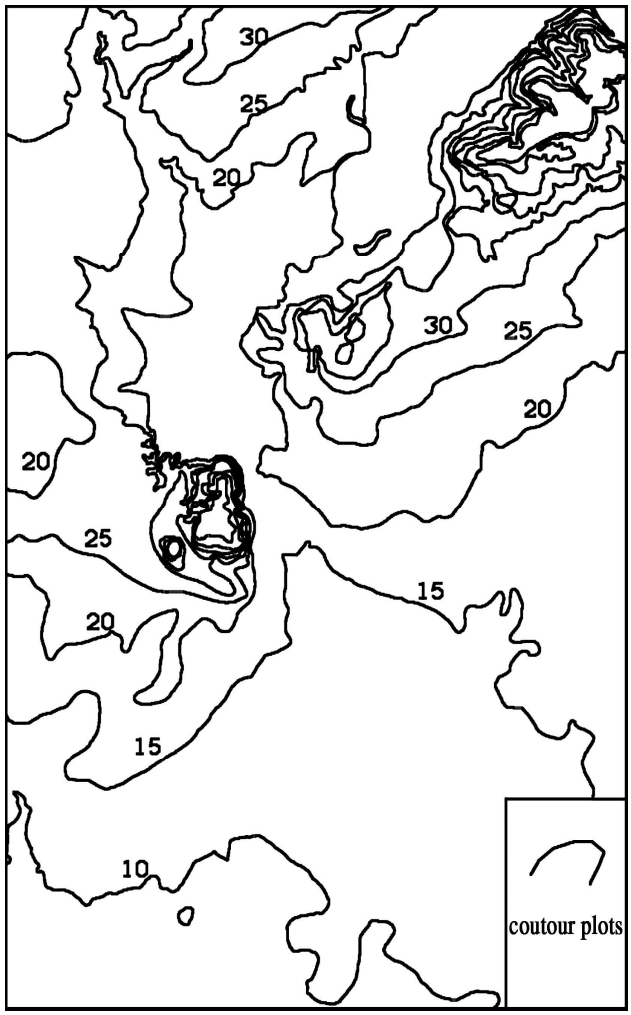


Fig. 2 Contour plots for Tangshan and its south region

Conclusions

Reasearches on lateral spreads usually focus on the deformation mechanism and estimation method, few think of liquefaction-induced lateral spreads for the seismic zoning work plotted with GIS technologis.

In order to adjust the influence of topogapical and soil factors, MLR method is applied to formulate a more comprehensive empirical modle for predicting lateral spread displacement.

According to the thickness, silt content and mean grain-size of the liquefied layer, the horizontal distance to the fault and the ground slope for each born hole, the lateral spread displacement states map based on MAPGIS is completed.

Acknowledgements

This research was jointly supported by Fundamental Research Funds of Institute Engineering Mechanics and Earthquake (200708001), and National Natural Science Foundation of Youth Fund (51008110).

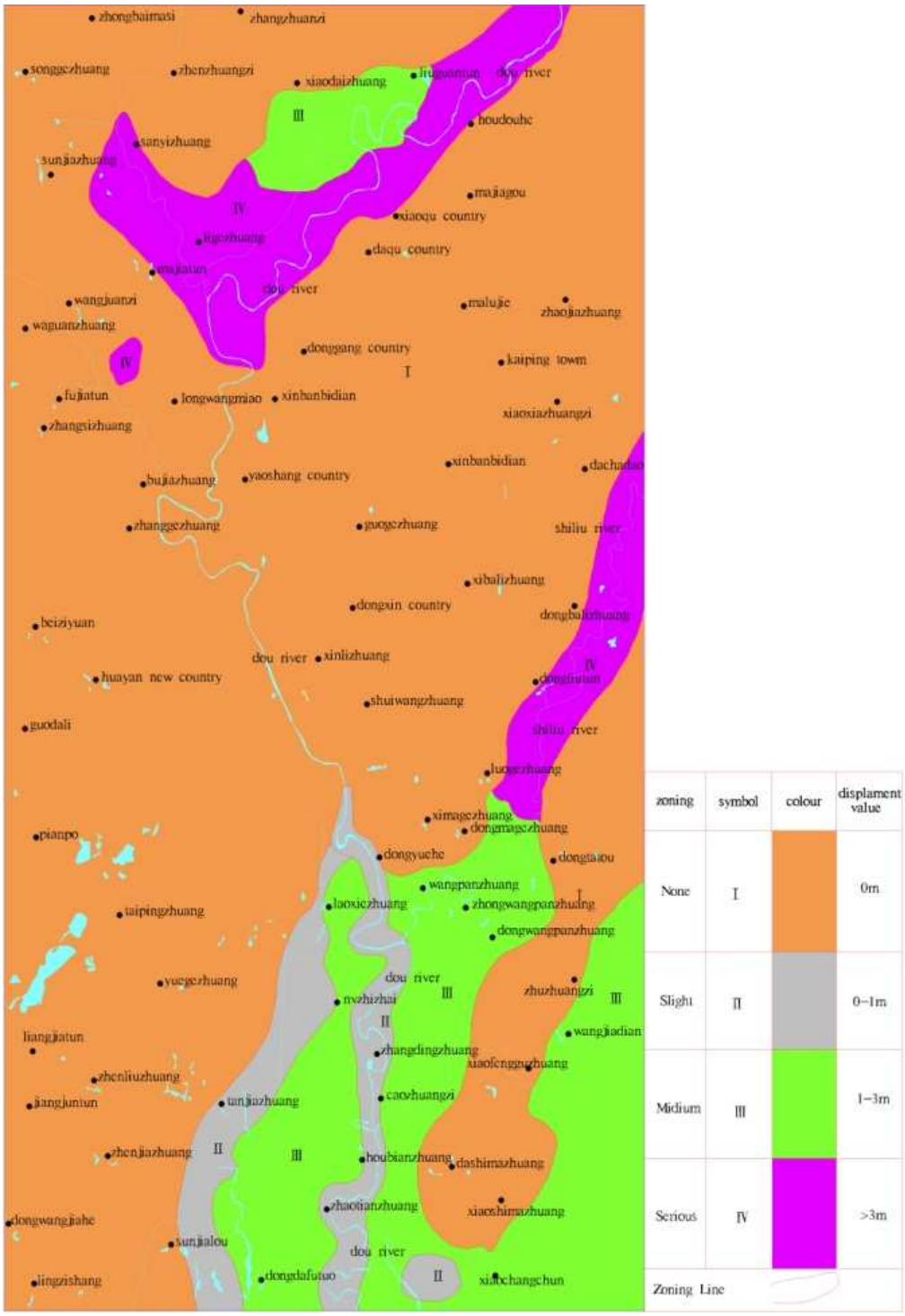


Fig. 3 Regional dividing of liquefaction-induced lateral spreads

References

[1] Daniel W. Hinckley, Liquefaction-induced Ground Displacement Mapping for The Salt Lake Valley, Utah. Salt Lack City: The University of Utah, 2010.

[2] Michael J. Olsen, Steven F. Bartlett, Barry J. Solomon, Lateral Spread Hazard Mapping of Northern Salt Lake Valley, Utah for a M7.0 Scenario Earthquake, Developing the Next Generation, Salt Lack City: The University of Utah, 2010.

[3] Bartlett S.F, Yond, Empirical Analysis of Horizontal Ground Displacement Generated by Liquefaction-induced Lateral Spreads, Doctoral Dissertation, Department of Civil Engineering, Brigham Young University, Provo, Utah, Technical Report CGE-92-1.

© (2012) Trans Tech Publications, Switzerland
doi:10.4028/www.scientific.net/AMM.238.248

The Dynamic Response Analysis on Train Liquid Storage Tanks under Harmonic Excitation

Qinghua Zhang

North China University of Water Resources and Electric Power, Zhengzhou 450011, China

z_q_h@sohu.com

Keywords: liquid storage tank; dynamic response; harmonic excitation; ANSYS.

Abstract. This paper take the typical train liquid storage tank as research object, the fluid-solid coupling dynamic responses of the tank are analyzed under the track irregularities using finite element software ANSYS. The research indicates that the difference of the liquid volume in tank has great influence to the structural stress and strain. When the tank is not filled with liquid, the liquid has large-scale amplitude sloshing, and the stress and strain are much bigger than the static condition. But if the tank is full of the liquid, the stress and total amount of deformity of the tank can be obviously reduced.

Introduction

The liquid storage tank is one kind of vessel of widespread application in petroleum, chemical industry and other professions, mainly used in the storage and transport inflammable, explosive and high risky liquid or gas. At present, domestic and foreign scholars have done a lot of work for the earthquake resistance research to the anchor and non-anchor liquid storage tank, and have formed the more perfect theoretical system [1-3]. But, for the train liquid storage tank, the research of its solid-fluid interactive vibration are few, the existing research much is also centralized in the modal analysis of coupled structure, train liquid storage tanks to the response characteristics and vibration mechanism research is still relatively lack.

China fuel oil transportation of 60%~70% [4] is completes by the railroad, especially with the speed increasing of the train in recent years, the storage tanks will suffer a stronger dynamic loading. Large-scale amplitude sloshing of liquid, on the one hand will have the remarkable additional dynamic pressure to the vessel, causes structural damage, on the other hand, the coupled vibration of liquid and structure will have great influence to the train's movement stability. Once the accident happens, it will cause big casualties and property losses, produces secondary disasters and also causes serious effect and harm to natural environment. It is necessary to the fluid structure interaction dynamic response analysis.

The harmonic excitation is one of train system common excitation modes. Many reasons can cause the periodic harmonic excitation, for example, the local damage of train wheel created by the soldering, the deviation of the wheel gravity and geometric center, and so on. This article takes the typical cylindrical tank as the research object, liquid-solid coupling dynamic response of the tank are calculated and analyzed under the track irregularities using the finite element software ANSYS.

Excitation and Finite Element Calculating Model

Harmonic Excitation. Selecting the vertical rail harmonic irregularities as the model of excitation, the vehicle system responses are calculated and analyzed. Fig. 1 is the track irregularity schematic drawing. The specific calculation conditions as follows [5]:

Table 1 Simulation condition of the vertical model

Vehicle	Wavelength [λ]	Depth of Wave [a]
tanker	500 mm	2 mm



Fig. 1 Track irregularity

So, the harmonic excitation for the vehicle system is simplified along the z axis direction a continuous support movement, the displacement excitation can be expressed as: 0.02sin ϖt, where ϖ is the circular frequencies of excitation,

$$\varpi = \frac{2\pi}{\lambda} v \tag{1}$$

Because of the differences of vehicle speed v, the circular frequencies ϖ of the displacement excitation is a range of value. And the rail tankers speed usually is less than 100 km/h, then the range of ϖ is about 0~350 rad/s. Table 2 gives the harmonic excitation circular frequencies under the different vehicle speed.

Table 2 The circular frequencies of system

Vehicle speed (Km/h)	20	40	60	80	100
Circular frequencies of excitation(ϖ) (rad/s)	69.81	139.63	209.44	279.25	349.07

The vibration of the train storage tank system belongs to the forced vibration induced by the movement of foundation under the track irregularities. The damping effect of train system itself will have great influence to the deformation, stress, cannot be neglect. The simplified diagram of the train system is as Fig. 2. The damping effect of vehicle would be considered, and the system damp is regarded as viscous damp. According to literature [6], take tank vehicle spring stiffness K = 10.5 × 106 N/m, damping coefficient ξ = 0.256.

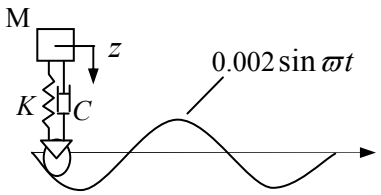


Fig. 2 Model of the tanks

Finite Element Calculating Model. This paper selects the cylindrical liquid storage tank (the design pressure: Positive pressure 0.15 MPa, negative pressure 0.1 kPa, the nominal capacity of 60 m^3) as the main research object, its physical dimension sees table 3 [7]. The materials of tank's barrel is Q235, its elastic modulus E = 206 GPa/m^2, Poisson's ratio μ=0.3, density is 7800 kg/m^3. Supposed the Liquid is water in the liquid storage tank, water density is 1000 kg/m^3.

Table 3 Structural parameters of the cylindrical tank

Volume (m^3)	Barrel (m)			Shell cover (m)			
	Inner diameter	Length	Thickness	Spherical radius	Ruffled radius	Height	Thickness
60	2.6	11.2	0.005	2.6	0.39	0.588	0.005

In order to fully accurate analysis for the fluid-solid coupling train storage tank, the three dimension finite element model of system should be applied. The finite element mesh result of the liquid storage tank is as shown in Fig. 3, and the shell of the tank uses 4 node shell element (shell 63) simulation. In view of the structural symmetry, the shell of the storage tank is divided by the mapped meshing, altogether has divided 3866 units. Note that the dynamic responses of vehicle system focus on the stable state forced vibration, did not consider the transient situations in the harmonic analysis.

Calculations and Analysis of Responses

Conditions of Responses Calculation. The static response and dynamic response of liquid storage tank under the harmonic excitation are calculated and analyzed for the storing liquid ratio h = 0, 0.5, 0.75, 1 (h = storing liquid volume/ tank volume). Harmonics response analysis of the system uses the full method, and selects the stepped load. Considering actual trail speed < 100 Km/h, when it through the wavelength λ, the maximum frequency f_{max} < 60 Hz, then the solution of the frequency is range from 0 to 60 Hz.

Results of Static Analysis. The main concern for static analysis of different value of storing liquid ratio h is structural total displacement and principal stresses which are given in table 4. The calculating results show that the structural principal stresses become larger with the mass increasing

because of the increase of the liquid volume in the tank. But, when $h = 1$ (tank filled with the liquid), the liquid has outwards even hydrostatic pressure to the entire shell of the train tank, instead can reduce the structural maximum total deformation.

In addition, because the material of the liquid storage tank is Q235, its yield strength $\sigma_s \geq 235$ MPa, tensile strength $\sigma_b = (375 \sim 460)$ MPa, it can be seen from the static calculating results of liquid storage tank that the principal stress obviously is smaller than the yield strength and tensile strength, so the structural system is absolutely safe from the static analysis point of view.

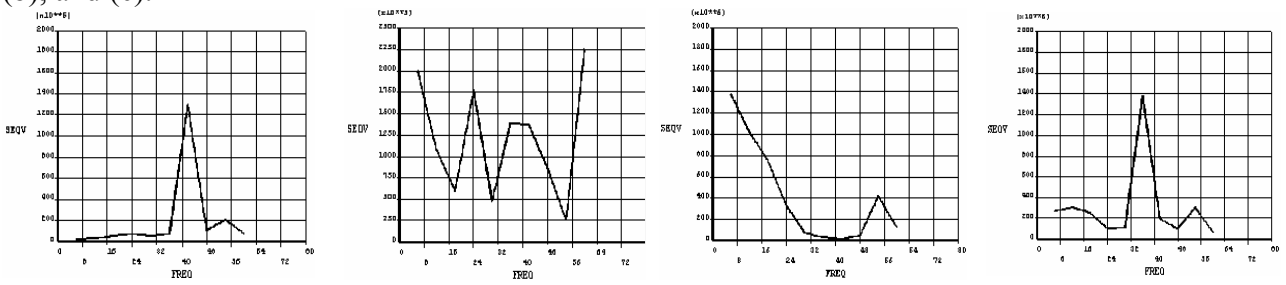
Table 4 The stress and displacement values of tanks with different height fluid

h	1st principal normal stress (MPa)	2nd principal normal stress (MPa)	3rd principal normal stress (MPa)	Total deformation U_{sum} (m)
0	-0.039~7.81	-4.52~5.72	-10.4~0.020	0.385×10^{-3}
0.5	-0.491~80.7	-59.3~45.7	-116~0.320	0.405×10^{-3}
0.75	-0.616~110	-85.2~87.8	-152~0.399	0.932×10^{-3}
1	-0.613~131	-71.6~96.9	-168~0.336	0.652×10^{-3}

The Dynamic Response analysis Under Harmonic Excitation. According to the failure mode of the plastic material, the fourth strength theory stress (von Mises SEQV) is applied to analyze the stress of the liquid storage tank. The maximum deformation node of the tank (according to the static analysis results obtained) are selected as key node to discuss the dynamic response under the harmonic excitation. The relationship diagram between the stresses, strain calculated by ANSYS with the frequency sees Fig. 4 and Fig. 5.

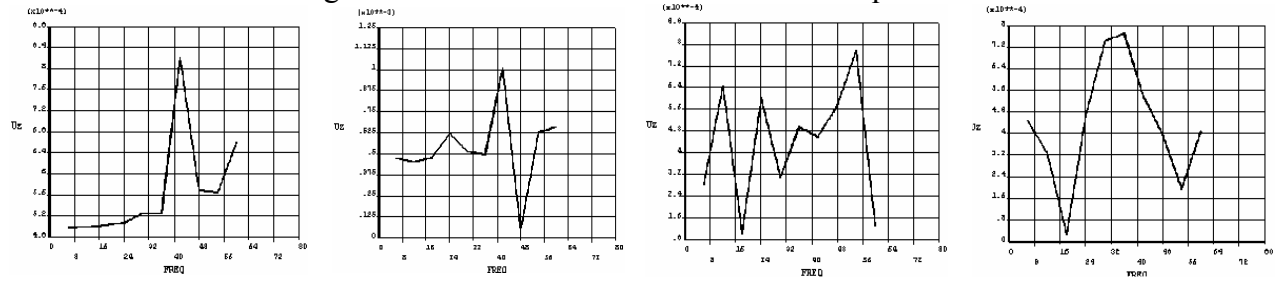
In Fig. 4(a), 5(a), the stress and displacement of the key node have a rapid increase when the excitation frequency is about 42Hz (the corresponding speed is about: 76 Km/h), and the storing liquid ratio $h = 0$. Only that the frequency of excitation approach the trail system natural frequency will lead to this kind of phenomenon, when $h = 0$, the 27th order natural frequency of the structure is 41.9Hz, So vertical vibration of the train storage tank system is most easily generating resonance with high order natural frequency of the tank, and for the typical liquid storage tank the natural frequency before the 27th order natural frequency is not produced by vertical vibration.

In addition, when the tank doesn't be filled with fluid, a liquid shaking space would be exist, if the train is running, the liquid sloshing in the tank will make the vessel deformation and stress continuous oscillation because of the track irregular excitation. Especially in the train has just started, the additional force applied by the liquid sloshing will be very large, and the stress in tank sometimes may even beyond the material can withstand, as shown in Fig. 4 (b), and (c) and Fig. 5 (b), and (c).



(a) $h=0$ (b) $h=0.5$ (c) $h=0.75$ (d) $h=1$

Fig. 4 The relations between stress and frequencies



(a) $h=0$ (b) $h=0.5$ (c) $h=0.75$ (d) $h=1$

Fig. 5 The relationship between strain and frequencies

When the storage tank filled with fluid (h = 1), its stress (Fig. 4 (d)) shape is similar to the empty tank. Because the tank is full of the fluid, the deformation (Fig. 5 (d)) of the shell of tank is oscillation when the train is running, but the value of deformation is small. So the liquid storage tank filled with fluid is more security.

Conclusions

Based on the finite element software ANSYS, the static and dynamic response under the track irregularity are analyzed for the typical train liquid storage tank. The harmonic excitation calculating results show that:

(1) With the increasing of the liquid volume in the tank, and the structural principal stress growing larger through the static analysis. But, when h = 1 (tank filled with the liquid), the liquid has outwards even hydrostatic pressure to the entire shell of the train tank, instead can reduce the structural maximum total deformation.

(2) When the tank doesn't be filled with fluid, the liquid sloshing in the tank will make the vessel deformation and stress continuous oscillation because of the track irregular excitation. The additional force applied by the liquid sloshing will be very large, and the stress in tank sometimes may even beyond the material be able to withstand.

(3) When the storage tank filled with fluid (h = 1), the deformation of the shell of tank is oscillation when the train is running, but the value of deformation is small.

References

[1] S. Mitra, K. P. Sinhamahapatra, 2D simulation of fluid-structure interaction using finite element method, Finite Elements in Analysis and Design, 45 (2008) 52-59.

[2] M. Utsumi, K. Ishida, Vibration analysis of a floating roof taking into account the nonlinearity of sloshing, Journal of Applied Mechanics, 75 (2008) 41008-41009.

[3] T. Matsui, Sloshing in a cylindrical liquid storage tank with a single-deck type floating roof under seismic excitation, Journal of Pressure Vessel Technology, 131 (2009) 21303-21306.

[4] D. Yan, Oil-gas Storage and Transportation Engineering, China Petrochemical Press, Beijing, 2003.

[5] H. Li, Simulation on dynamic performance of wagon and analysis of derailment accident, Master Dissertation in Dalian Railway Institute, 2003.

[6] T. Wang, Vehicle Dynamics, China Railway Publishing House, Beijing, 1981.

[7] G. Guo, Oil Storage and Transportation, China Petrochemical Press, Beijing, 2003.

© (2012) Trans Tech Publications, Switzerland
doi:10.4028/www.scientific.net/AMM.238.252

Stability Analysis of Concrete Gravity Dam

Zhonghua Wen [a] and Juan Zhou [b]

School of Civil Engineering and Communication, North China University of Water Resources and Electric Power, Zhengzhou 450011, China

[a]wzhzhonghua@126.com, [b]zhoujuan@ncwu.edu.cn

Keywords: concrete gravity dam; stability; rigid body limit equilibrium method; finite element technique.

Abstract. The safety is first-class important event of the dam. The crash for the gravity dam usually causes due to slid, the slippery stable is a key problem of big dam. This paper checks the stability of one dam by rigid body limit equilibrium method and finite element technique. Rigid body limit equilibrium method is a kind of traditional stable analytical method, which is confirmed by factual engineering, the safe coefficient is always used to judge the big dam safety degree. The finite element technique is a method which is quickly developed in the calculator science and the basic theories of the rock soil mechanics. The paper compares the two methods and makes sure the fact that the finite element is more reasonable than rigid body limit equilibrium method for analyzing the stability of gravity dam.

Introduction

One reservoir lies in Yellow River tributary Luo river midstream, its important function is flood controlling, and doubling as irrigation, generating electricity, providing water and so forth. Reservoir building consists of dam, powerhouse of power station and closed conduit .The type of dam is solid gravity dam. The highest part of dam is 125m, the elevation of dam top is 553m,the length of dam top is 315m,The dam is consist of 21 dam section, the width of normal dam station is 16.5m,the biggest width is 19m,the least width is 13m.The upper gradient of dam is 1:0.2,the elevation of slope point is 510m,the lower gradient is 1:0.8. The sliding resistance of this concrete dam is computed by rigid body limit equilibrium method and FEM in this paper.

Anti-sliding Stability Analysis of Gravity Dam.

Primary loads on gravity dam are self-weight, hydrostatic pressure, uplift pressure, sediment pressure. The paper mostly researches Sliding stability of gravity dam on basic loads of what is mentioned.

Rigid Body Limit Equilibrium Method

The formula of stability coefficient is computed by rigid body limit equilibrium method has two style: shear formula, shear strength formula. Shear strength formula considered the cementation of dam and bedrock, friction and cohesion is included in, it is conformed to the real working conditions and physical concept is also distinct [1].But the result of experiment indicated that the on-the-spot inspection values is not stability in most cases and the adhesion forms of specimens are not exactly in line with the fact. The safety factor which is set in criterion would be reduced because of the development of trial technology and the increase in daming experience. Therefore, shear strength formula is more reasonable on condition that the dam has good foundation and reliable shear strength parameter by detail investigations. Taking thought of the case of gravity dam, shear strength formula is adopted to calculate stability coefficient in the paper [2, 3].

The base parameter of material as follows: concrete density γ_c=2400Kg/m^3,water density γ_0=1000kg/m^3, sediment buoyant density γ_c=900Kg/m^3.

Self-weight of dam: $\boldsymbol{W}=v\gamma_s$=[15×15+ (15+37.4)×28/2+(37.4+119.4)×82/2]×1×24

= (225+733.6+6428.8)×1×24=7387.4×1×24=177297.6kN/m

Sydrostatic pressure on the surface of dam: $\boldsymbol{P}_1$=24.8×24.8×10/2=3075.2 kN/m, $\boldsymbol{F}$=(24.8×10+106.8×10)×83.6/2=55008.8 kN/m, $\boldsymbol{P}$=53956 kN/m, $\boldsymbol{W}_1$=10791.2 kN/m.

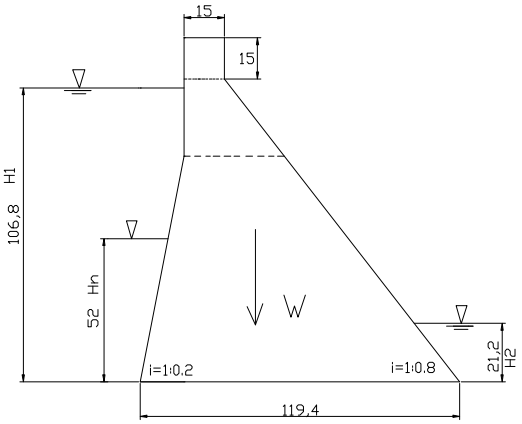


Fig. 1 Section of gravity dam (m)

Uplift pressure: U_1=H$_2\gamma_0$ l=25312.8kN/m^3, U_2=Hγ_0/2 l=51103.2kN/m^3, U=U_1+U_2=76416kN/m^3.

Sediment pressure: Sediment weight can be neglected because the engineering has bigger upper gradient. By correlative criterion, buoyant weight of Sediment as follows:

$$\gamma_c = 9.0,\ \Phi_n = 12^o,\ P_n = \frac{1}{2}\gamma_n h_n^2 \mathrm{tg}(45^o - \frac{12^o}{2}) = 7983.42\mathrm{kN/m}$$

Anti-sliding stability safety factor k (f'=1.0 c'=0.7MPa)

$$W_3 = W_1 + W_2 + W = 10791.2 + 1797.8 + 177297.6 = 189886.8\mathrm{kN/m}$$

$$P_3 = P_1 + P + P_n - P_2 = 3075.2 + 53956 + 79833.42 - 2247.2 = 62767.4\mathrm{kN/m}$$

$$K = \frac{f(W_3 - U)}{P} = 1.27 \qquad K' = \frac{f'(W_3 - U) + c'A}{P} = 3.14$$

Table 1 Safety factor of anti-sliding stability

Safety factor	load combination	grade of dam		
		1	2	3
K	basic combination	1.10	1.05	1.05
	(1)especial combination	1.05	1.00	1.00
	(2)especial combination	1.00	1.00	1.00
K'	basic combination	3.0		
	(1)especial combination	2.5		
	(2)especial combination	2.3		

The results indicate that sliding stability of the dam is enough by comparing it is safety factor of anti-sliding stability with above table.

Finite Element Method

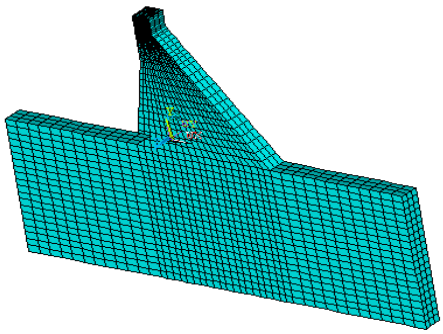


Fig. 2 Mesh of gravity dam

The research object is an integrated dam section here, the scope of calculation include length along stream direction which is the same with the width of dam foundation and dam foundation depth which as big as the height of dam. Normal constraint is set on the boundary of the upper and lower of dam section, the boundary of bottom is fixed end [4, 5].the dam model of FEM as shown in Fig. 2.

Calculation of Dam Foundation Stability Coefficient by FEM

The general solution method about stability analysis of concrete dam is calculating dam stress first and comparing it with foundation rock's, then checking whether the foundation rock would distorted by strength ,at last analyzing the safety of the whole dam. A plane is cut out according to two-dimensional analysis and the model is calculating by plane strain, the computational result of shear stress along dam foundation surface as shown in Fig.3 and Fig.4.

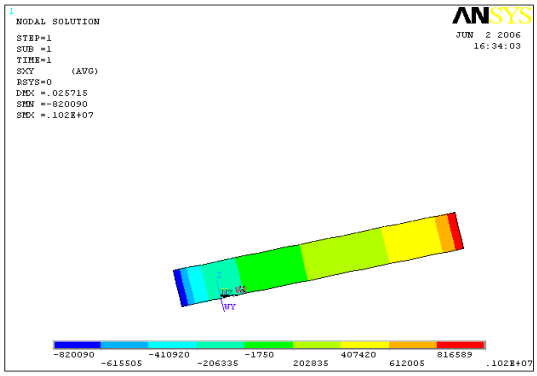


Fig. 3 *yx*-direction shear stress on dam foundation surface

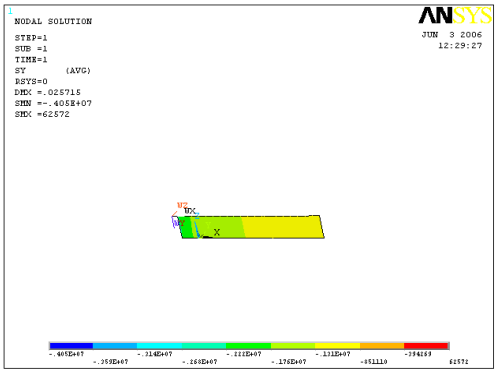


Fig. 4 *y*-direction shear stress on dam base foundation surface

For some point, the Safety factor of different direction is different, so $K_p=f(\theta)$, θ indicate direction angle, the minimum safety factor K_{pmin} must satisfied:

$$\mathrm{d}K_P/\mathrm{d}\theta = 0$$

So the minimum safety factor is as follows:

$$K_{P\min}=\frac{c+tg\varphi[\frac{\sigma_1+\sigma_2}{2}+\frac{\sigma_1-\sigma_2}{2}\cos 2\alpha]}{\frac{\sigma_1-\sigma_2}{2}\sin 2\alpha} \tag{1}$$

$$\alpha=\frac{1}{2}\cos^{-1}\frac{(\frac{\sigma_1-\sigma_2}{2})tg\varphi}{c+(\frac{\sigma_1+\sigma_2}{2})tg\varphi} \tag{2}$$

Where, c, φ — cohesion and internal friction angle of rock, σ_1, σ_2—maximum and minimum normal stress of the calculational point.

The result is c =0.7MPa, σ_1=3.62MPa, σ_2=3.62MPa, α=15°,

$$K_{P\min}=\frac{0.7+tg15[\frac{3.62+0.72}{2}+\frac{3.62\text{-}0.72}{2}\times 0.303]}{\frac{3.62\text{-}0.72}{2}\times 0.9592}=1.02$$

The stability coefficient of the project ranges from 1.0 to 1.3 [6] by correlative criterion, so the stability of creativity dam is enough according to the above result.

Conclusions

From above calculating result about anti-sliding stability safety factor of the gravidity dam by rigid body limit equilibrium method and FEM, we can get conclusions as follows: the safety factor from rigid body limit equilibrium method is bigger than that from FEM, it signals that rigid body limit equilibrium method is more safe and conservative than FEM. the result from FEM is closer to the gravity dam because it accord with the project fact by considering uneven material. FEM provides more reasonable theory and method for the resolution of gravity dam and more powerful guarantee for reliability of gravity dam.

References

[1] Y. Duan, Y. He, Study on failure process of gravity dam along interface between dam and foundation with theory of real shear strength, Journal of Wuhan University of Hydraulic and Electrical Engineering, 32 (1999) 13-18.

[2] G. Zhang, F. Jin, Comparison of stability of gravity dams by discontinuous deformation analysis and finite element method, Journal of Hydroelectric Engineering, 23 (2004) 10-14.

[3] J. Liu, The anti–sliding stability numerical analysis of gravity dam with weak interralated layer in foundation, Thesis for Master Degree, Dalian University of Technology, 2005.

[4] W. Hao, ANSYS Civil Engineering Application Example, China WaterPower Press, Beijing, 2005.

[5] L. Li, ANSYS Finite Element Analysis Practical Course, Tsinghua University, Beijing, 2005.

[6] SL319-2005, Design Specification for Concrete Gravity Dams, China WaterPower Press, Beijing, 2005.

© (2012) Trans Tech Publications, Switzerland
doi:10.4028/www.scientific.net/AMM.238.256

Stress Calculation of Gravity Dam Based on Elastic Mechanics

Haibo Cui [a], Haitang Zhu [b] and Jinchao Yue [c]

College of Water Conservancy and Environment, Zhengzhou University, Zhengzhou 450001, China

[a]cuihaibo109@163.com, [b]htzhu@zzu.edu.cn, [c]yuejc@zzu.edu.cn

Keywords: gravity dam; elastic mechanics; stress calculation; dimensional analysis.

Abstract. Based on the elastic mechanics theory, combined with Saint-Venant principle and the superposition principle, the calculating method for the stress of gravity dam in arbitrary storage water lever were put forward by means of the equivalent stress method and the dimensional analysis method through the conversion between a Cartesian coordinate system and Polar coordinate system. The method not only offers a new idea for calculating the stress of gravity dam, but also presents research bases for evaluating synthetically the strength of gravity dam.

Introduction

Strength is deemed to a very important aspect of the building safety, while stress analysis is the precondition of strength checking. Not only the gravity dam stress analysis is to determine whether the serving phase and construction phase to meet the strength and stability requirements, but also provide basis for the design and construction-related research and other issues. Now the materials mechanics and the linear finite element analysis are common ways to figure out the dam stress. The paper presents a new method for solving dam stress at any water level based on the elastic mechanics, namely from link of three aspects of statics, deformation of coordination and material of physical relationship, the basic equations of elastic mechanics are established [1].

Equivalent Transformation of Dam Loading

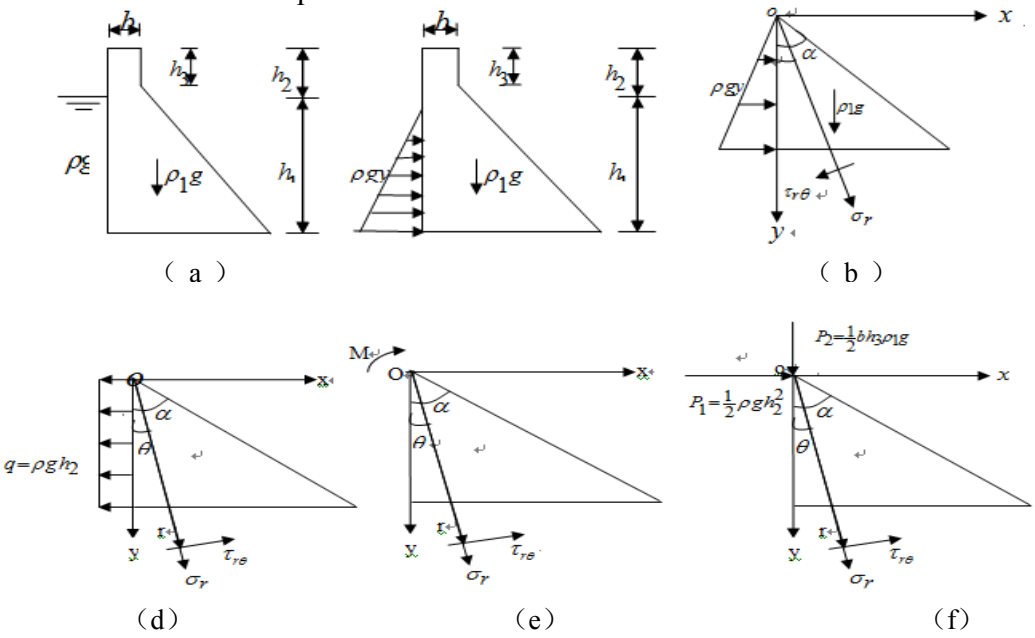
In normal circumstances, for the entity gravity dam, the upstream slope ratio is 1:0~1:0.2 and the downstream slope is 1:0.6~1:0.8 [2]. In the reasonable case, some appropriate simplification may be made in order to give a formula taking into account of the weight of the dam and the internal stress generated by the upstream water pressure as shown in Fig. 1(a), that is 1:0 as upstream and 1:0.75 as downstream slope, the downstream water level and soil pressure are not taken into account. If considering other loads, the same simplified computational model may be made. Fig. 1(a) shows the force of the dam, the water level h_1 for any height, b is the width of dam crest, ρ represents the density of water and ρ_1 represents the density of dam. It could be concluded that the force of the Fig. 1(b) is equal to the result of superposition of Fig. 1(c), (d), (e) and (f) using superposition principle.

Internal Stress Calculation of Dam Using Elastic Theory

Stress Analysis under Simplification. As shown in Fig. 1(c), the dam is under the water pressure and its own weight, the density of water and dam are ρ and ρ_1 respectively. Within the scope of linear elastic mechanics, stress is bound with their dimensionless proportionally, at the same time its dimensionless is NL^{-3}. Assuming that the problem has polynomial solution, their functional forms must be $\rho g N_1$ and $\rho_1 g N_2$, wherein N_1 and N_2 are the function of x, y and θ, as well as they must be the first degree function. Because the power of x and y in stress function must be higher 2 times than the stress components, so the stress function φ must be a cubic polynomial function and can be assumed that:

$$\varphi = \frac{A}{6}x^3 + \frac{B}{2}x^2 y + \frac{C}{2}xy^2 + \frac{D}{6}y^3 \tag{1}$$

Eq. 1 meets the biharmonic equation:



（a） （b）

（d） （e） （f）

Fig. 1 Load simplification of entity gravity dam

$$\left(\frac{\partial^2}{\partial r^2}+\frac{1}{r}\frac{\partial}{\partial r}+\frac{1}{r^2}\frac{\partial^2}{\partial\theta^2}\right)\left(\frac{\partial^2\varphi}{\partial r^2}+\frac{1}{r}\frac{\partial\varphi}{\partial r}+\frac{1}{r^2}\frac{\partial^2\varphi}{\partial\theta^2}\right)=0 \tag{2}$$

While the physical component is F_x=0, F_y=$\rho_1 g$, and the corresponding stress components could be obtained by the formula, as follows:

$$\begin{aligned}\sigma_x&=\frac{\partial^2\varphi}{\partial^2 y}=Cx+Dy\\ \sigma_y&=\frac{\partial^2\varphi}{\partial^2 x}-\rho_1 gy=Ax+By-\rho_1 gy\\ \tau_{xy}&=-\frac{\partial^2\varphi}{\partial x\partial y}=-Bx-Cy\end{aligned} \tag{3}$$

Boundary conditions for

$$\begin{aligned}&(\sigma_x)_{x=0}=-\rho gy\ ;\ (\tau_{xy})_{x=0}=0\\ &l(\sigma_x)_{x=y\tan\alpha}+m(\tau_{yx})_{x=y\tan\alpha}=0\\ &l(\tau_{xy})_{x=y\tan\alpha}+m(\sigma_y)_{x=y\tan\alpha}=0\end{aligned} \tag{4}$$

Put Eq. 3 into Eq. 4, the stress components can be obtained as follow:

$$\begin{aligned}\sigma_x&=-\rho gy\\ \sigma_y&=(\rho_1 g\cot\alpha-2\rho g\cot^3\alpha)x+(\rho g\cot^2\alpha-\rho_1 g)y\\ \tau_{xy}&=-\rho gx\cot^2\alpha\end{aligned} \tag{5}$$

According to the stress components of coordinate transformation formula [3]:

$$\begin{aligned}\sigma_r&=\sigma_x\cos^2\theta+\sigma_y\sin^2\theta+2\tau_{xy}\sin\theta\cos\theta\\ \sigma_\theta&=\sigma_x\sin^2\theta+\sigma_y\cos^2\theta-2\tau_{xy}\sin\theta\cos\theta\\ \tau_{r\theta}&=(\sigma_y-\sigma_x)\sin\theta\cos\theta+\tau_{xy}(\cos^2\theta-\sin^2\theta)\end{aligned}$$

In order to facilitate the calculation result integration, the Eq.5 results conversion to polar coordinate, the converted the results are as follows:

$$\begin{aligned}\sigma_r&=-\rho gy\cos^2\theta+[(\rho_1 g\cot\alpha-2\rho g\cot^3\alpha)x+(\rho g\cot^2\alpha-\rho_1 g)y]\sin^2\theta-\rho gx\cot^2\alpha\sin 2\theta\\ \sigma_\theta&=-\rho gy\sin^2\theta+[(\rho_1 g\cot\alpha-2\rho g\cot^3\alpha)x+(\rho g\cot^2\alpha-\rho_1 g)y]\cos^2\theta+\rho gx\cot^2\alpha\sin 2\theta\\ \tau_{r\theta}&=[(\rho_1 g\cot\alpha-2\rho g\cot^3\alpha)x+(\rho g\cot^2\alpha-\rho_1 g)y+\rho gy]\sin\theta\cos\theta-\rho gx\cot^2\alpha\cos 2\theta\end{aligned} \tag{6}$$

Calculate Method for Internal Stress of Dam. Based on the preceding detailed answers, the other specific computing and graphics are similar to the fig.1(c), so the solution process omitted here and the stress expression under other figures will be given directly as follows:

$$\begin{aligned}
\sigma_2 &= \frac{\tan\alpha\sin^2\theta+\sin\theta\cos\theta+\theta-\alpha}{\tan\alpha-\alpha}q \\
\sigma_\theta &= \frac{\tan\alpha\cos^2\theta-\sin\theta\cos\theta+\theta-\alpha}{\tan\alpha-\alpha}q \\
\tau_{r\theta} &= \frac{\tan\alpha\sin\theta\cos\theta-\sin^2\theta}{\tan\alpha-\alpha}q \\
q &= \rho g h_2
\end{aligned} \tag{7}$$

$$\begin{aligned}
\sigma_{\mathrm{r}} &= \frac{2M}{r^2}\frac{\tan\alpha\cos 2\theta - \sin 2\theta}{\alpha - \tan\alpha} \\
\sigma_\theta &= 0 \\
\tau_{r\theta} &= \frac{M}{r^2}\frac{\tan\alpha\sin 2\theta - 2\sin^2\theta}{\alpha - \tan\alpha}
\end{aligned} \tag{8}$$

$$\begin{aligned}
\sigma_r &= \frac{2[P_1\sin^2\alpha\cos\theta+P_2(\sin\alpha\cos\alpha-\alpha)\cos\theta-P_1(\sin\alpha\cos\alpha+\alpha)\sin\theta+P_2\sin^2\alpha\sin\theta]}{r(\alpha^2-\sin^2\alpha)} \\
\sigma_\theta &= 0 \\
\tau_{r\theta} &= 0
\end{aligned} \tag{9}$$

As mentioned the stress in the calculations of the Fig. 1(c)~(f), then repeated addition, stress calculation formula could be obtained which is in polar coordinates as follows:

$$\begin{aligned}
\sigma_{\mathrm{r}} &= \frac{2[P_1\sin^2\alpha\cos\theta+P_2(\sin\alpha\cos\alpha-\alpha)\cos\theta-P_1(\sin\alpha\cos\alpha+\alpha)\sin\theta+P_2\sin^2\alpha\sin\theta]}{r(\alpha^2-\sin^2\alpha)} - \\
&\quad \rho g y\cos^2\theta + \frac{2M(\tan\alpha\cos 2\theta-\sin 2\theta)}{r^2(\alpha-\tan\alpha)} + \frac{q(\tan\alpha\sin^2\theta+\sin\theta\cos\theta+\theta-\alpha)}{(\tan\alpha-\alpha)} + \\
&\quad [(\rho_1 g\cot\alpha-2\rho g\cot^3\alpha)x+(\rho g\cot^2\alpha-\rho_1 g)y]\sin^2\theta-\rho g x\cot^2\alpha\sin 2\theta \\
\sigma_\theta &= [(\rho_1 g\cot\alpha-2\rho g\cot^3\alpha)x+(\rho g\cot^2\alpha-\rho_1 g)y]\cos^2\theta+\rho g x\cot^2\alpha\sin 2\theta-\rho g y\sin^2\theta+ \\
&\quad \frac{q(\tan\alpha\cos^2\theta-\sin\theta\cos\theta+\theta-\alpha)}{\tan\alpha-\alpha} \\
\tau_{r\theta} &= [(\rho_1 g\cot\alpha-2\rho g\cot^3\alpha)x+(\rho g\cot^2\alpha-\rho_1 g)y+\rho g y]\sin\theta\cos\theta-\rho g x\cot^2\alpha\cos 2\theta+ \\
&\quad \frac{q(\tan\alpha\sin\theta\cos\theta-\sin^2\theta)}{\tan\alpha-\alpha}+\frac{M(\tan\alpha\sin 2\theta-2\sin^2\theta)}{r^2(\alpha-\tan\alpha)}
\end{aligned} \tag{10}$$

Effect Analysis of Water Level on Dam Stress

Stress Values Change in the Same Position of Dam under Same h_1 and Different θ. Take "Gushan Lake Reservoir gravity dam design" as an example, take the normal water level to calculate, when r=50m, h_2=9m, y=40m, b=9m, $H=h_1+h_2$=84m, h_1=75m, h_2=9m, h_3=12m, n_1=1:0, n_2=1:0.75 (i.e. θ=37°), γ=24kN (i.e. ρ_1g=24kN/m^3), ρg=10kN/m^3. When x=0, 5m, 10m, 15m, 20m, 25m and 30m, the relationship chart as shown in the Fig. 2: Curves 1, 2 and 3 represent the relationship between σ_γ, σ_θ, $\tau_{\gamma\theta}$ and x respectively, that is the stress change trend in different point under any water level.

From Fig. 2, when the water level is constant, the farther from the upstream face, the smaller of the data of σ_{r}. At first change quickly, gradually be more stable. About σ_θ, first increased and then decreased, mainly because of the results of the stress added, While $\tau_{\mathrm{r}\theta}$ is continuously increasing quickly and then slowly. At such situation, the stress value and trend accord with the actual situation.

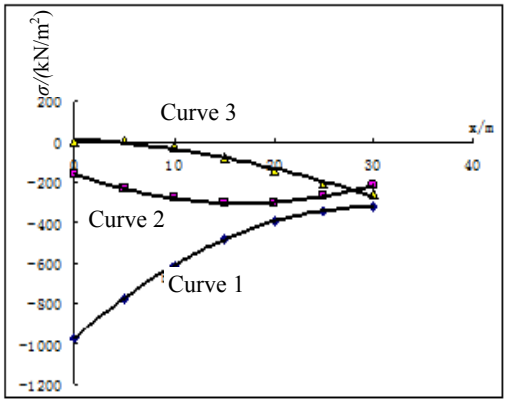


Fig. 2 Stress values change under different θ

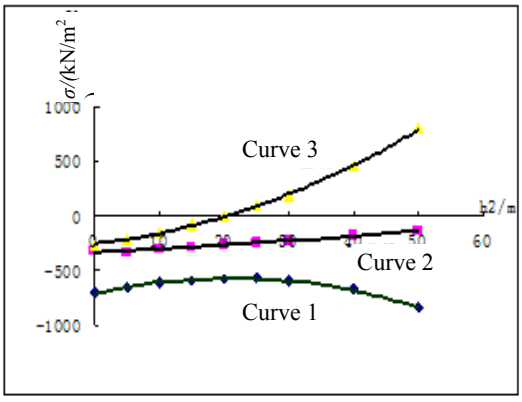


Fig. 3 Stress values change under different water level

Stress Values Change in the Same Position of Dam under Different h_2. Basic calculating parameters in this case as above example, and taking the point r=50m, θ=20° for study. According to the actual situation of project and control requirements on the dead water level and silt elevation, the h_2 must be less than 52m, the control points are taken as h_2=0, 5m, 10m, 15m, 20m, 25m, 30m, 40m, 50m, the diagram as shown in Fig. 3: Curves 1, 2 and 3 represent the relationship between σ_r, σ_θ, $\tau_{r\theta}$ and h_2 respectively, that is to say, it reflects the relationship between the stress of a point within the dam and the water level. It is shown From Fig. 3 that the stress calculating results given by elastic mechanics method are real appropriately, the stress trend at the same point shows σ_r from decrease to increase and the stress direction is invariable because of the superposition by the triangle principle. At the same time the change of σ_θ and $\tau_{r\theta}$ are originated from the superposition of dam self-weight and water weight, the value of $\tau_{r\theta}$ could be equal to zero. According to the results, $\tau_{r\theta}$ changes obviously when h_2 varies and needs to be paid more attentions.

Conclusions

The strength and stability requirements of gravity dam need to be meet whether in the serving phase or the construction phase, so the stress analysis is a very important aspect for the safety of gravity dam. In this paper, a new reference method for calculating the gravity dam stress is presented based on elastic mechanics method. This method can accurately calculate the stress at any position in the gravity dam, and have strong extensibility which can solve the strain and displacement of gravity dam by means of physical equations and geometric equations.

References

[1] P. Londe, M. Lino, The Faced Symmertrical Hardfill Dam: a New Concept for RCC, J. International Water Power & Dam Construction, 2 (1992) 19-24.

[2] J. Lin, Hydraulic Structures, Third Edition, China WaterPower Press, Beijing, 2007.

[3] H. Liu, Elastic-plastic Mechanics Brief Tutorial, China Economy Press, Beijing, 2011.

[4] Z. Xu, Elastic Mechanics Brief Tutorial, Third Edition, Higher Education Press, Beijing, 1990.

[5] X. Sun, X. Fang, T. Guan, Material Mechanics, Higher Education Press, Beijing, 2010.

[6] J. Pan, Gravity Dam Design, China WaterPower Press, Beijing, 1995.

[7] DL/T5108-1999, Design Code for Concrete Gravity Dam, China WaterPower Press, Beijing.

[8] L. Xiao, Y. He, P. Li, Stress Analysis of Hardfill Dam by Elasticity Theory, Engineering Journal of Wuhan University, 1 (2008) 38-45.

[9] B. Qian, Q. Hu, Stress Function in Gravity Dam, Journal of Xichang College (Natural Science Edition), 2 (2007) 50-52.

© (2012) Trans Tech Publications, Switzerland
doi:10.4028/www.scientific.net/AMM.238.260

Dynamic Analysis of Face Rockfill Dam Based on Finite Element Theory

Yu Zhao [a], Shengzhao Cheng[b] and Jianwei Zhang[c]

North China University of Water Recourses and Electric Power, Zhengzhou 450011, China

[a]zhaoyu@ncwu.edu.cn,[b]chengshengzhao@yahoo.com.cn,[c]zhangjianwei@ncwu.edu.cn

Keywords: face rockfill dam; dynamic response; slab movement; seismic wave.

Abstract. Concrete face rockfill dam is an important type of dam. Dynamic analysis of the dam under seismic conditions is important for researching the safety degrees of face rockfill dam under unusual conditions. This paper takes practical engineering project, Henan Tianchi pumped storage power station, as an example, makes dynamic calculation under seismic conditions, and analyzes the dynamic response of the face slab. This paper has reference meaning for face rockfill dam's design and construction.

Engineering Situation

Tianchi pumped storage power station is located in Mashiping Township, Henan province. This hydro-junction is composed by upstream reservoir, downstream reservoir, water conveyance system and powerhouse. The gradient of the upstream dam slope is 1:1.40, the gradient of the downstream dam slope is 1:1.35. First-order berms are set at the downstream elevation of 1045m, 1025m, 1005m and 985m, the berm's width is 2.0m, the composite gradient of downstream slope is 1:1.40. Clay blanket is set at the upstream of the slab, under the elevation of 1000m. The clay blanket can play a role in auxiliary seepage proof. The width of the top of the clay blanket is 3m, the gradient of the upstream slope is 1:1.6. Coverage weight area of stone ballast is set at the upstream of clay blanket, the width of the top is 6m, the gradient of the upstream slope is 1:2.

Calculation Model

In the finite element calculation, Duncan EB nonlinear elastic model is used to simulate the dam material(including cushion material, transition material, main rockfill material and secondary rockfill materials) [1-3]. The face slab and toe slab are made of reinforced concrete, linear elastic model is used to simulate them. Linear elastic model is also used to simulate rock mass of dam foundation.

Duncan EB Model. In Duncan EB model, tangent elastic modulus and tangent bulk modulus can be expressed as

$$E_t = \left[1 - \frac{R_f(1-\sin\varphi)(\sigma_1-\sigma_3)}{2c\cos\varphi + 2\sigma_3\sin\varphi}\right]^2 Kp_a\left(\frac{\sigma_3}{p_a}\right)^n \tag{1}$$

$$B_t = K_b p_a\left(\frac{\sigma_3}{p_a}\right)^m \tag{2}$$

According to Duncan EB model, unloading condition can be discriminanted as follows: when $(\sigma_1-\sigma_3)<(\sigma_1-\sigma_3)_0$ and $S<S_0$, elements are under unloading condition, E_{ur} is used, or E_t is used.

For unloading condition, elastic modulus can be calculated as:

$$E_{ur} = K_{ur} p_a\left(\frac{\sigma_3}{p_a}\right)^n \tag{3}$$

Where, c is material cohesion; φ is material internal friction angle; P_a is standard atmospheric pressure, R_f, K, n, K_b, K_m, K_{ur} are model parameters.

For coarse-grained materials (such as rockfill material), cohesion c is 0, internal friction angle φ can be calculated as:

$$\varphi = \varphi_0 - \Delta\varphi \lg\left(\sigma_3 / p_a\right) \tag{4}$$

Duncan EB model is a typical representative of earth rock material nonlinear elastic model. Its elastic modulus is function of stress state, it can describe the nonlinearity and barotropy of the soil's stress-strain relationship. The model uses different modulus in loading and unloading conditions, so that elastic-plastic of material can be reflected to some extent.

Constitutive Model of Concrete. The concrete slab is usually in three-dimensional pressure state. Strictly speaking, under complex stress state, stress-strain relationship of concrete is not linear relationship. When the stress is in the compressive strength of 30% ~ 50%, stress-strain relationship of concrete can be regarded as linear relationship; plastic strain takes a small proportion, when the stress level is more than 0.5, the proportion which plastic strain takes increases. In the analysis of medium and low concrete face fockfill dam, concrete slab usually uses linear elastic model.

Material Calculation Parameters

According to the material Duncan EB model of some domestic rockfill dams[4-6], analogy to take the dynamic parameters of the dam as follows:

Tables 1 Dynamic Parameters

Dynamic parameters	Main rockfill	Secondary rockfill	transition material	cushion material
k_2'	2336	2205	1997	1216
n	0.625	0.575	0.5	0.5

In the calculation, the relationship of G/G_{max}-γ and λ-γ uses the curves which are summarized by Xianjing Kong. The curves are shown in Fig 1 and 2. Seismic time-history curve is shown in Fig 3.

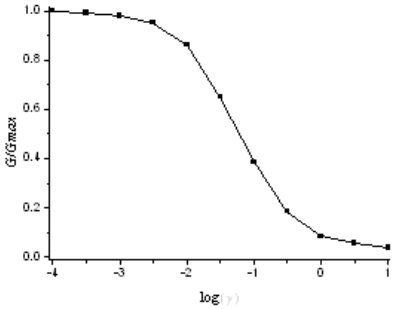


Fig 1 G/G_{max}-γ curve

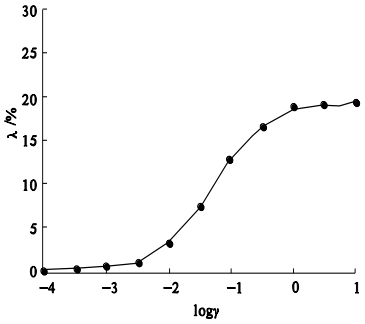


Fig 2 λ-γ curve

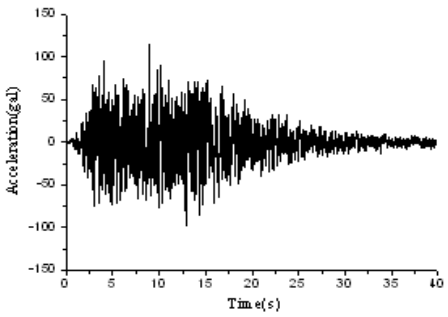


Fig 3 Seismic time-history curve

Finite Element Model

Three-dimensional finite element mesh is shown in Fig 4. It mainly uses hexahedron elements, locally uses prism units to transit, the peripheral joints and contacts between slabs and cushions uses contact elements to simulate. The model considers basic geology and real terrain of material partition and ground. The foundation extends from the dam to upstream, downstream, bottom and transverse river direction. The finite element model has 15367 elements and 16623 nods.

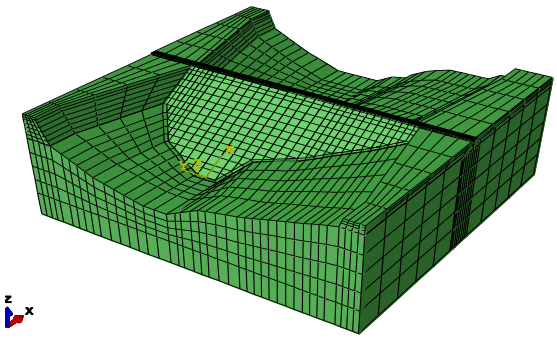


Fig.4 Finite element model

Result of Dynamic Finite Element Analysis

Dynamic calculation of the face rockfill dam is made with large general-purpose finite element analysis software ABAQUS. Contour maps of along slope deflection peak value, along slope tensile stress, along slope compressive stress，are shown in Fig 5-10.Then, we can get the following results.

(1) Under seismic condition, the upside along slope maximum displacement presents to 1/6 of dam height, 1/3 of dam width, the value of maximum displacement can reach 34.4cm. In contrast, the downside along slope displacements is small, the maximum displacement presets to 1/3 of dam width, and the value is 3.8cm.

(2) The along slope maximum tensile stress 3.4MPa, it presents to 1/2 of dam height, 1/2 of dam width; besides, there is high tensile stress area presents to 1/3 of dam height, 1/4 of dam width. The transverse river direction maximum tensile stresses are low, the value is 0.2MPa, they are distributed along the toe of slope.

(3) The along slope maximum compressive stress reaches 3.4MPa, it presents to 1/2 of dam height, 1/2 of dam width. The transverse river direction maximum compressive stresses are low, the value is 0.2MPa, and they are distributed along the toe of slope.

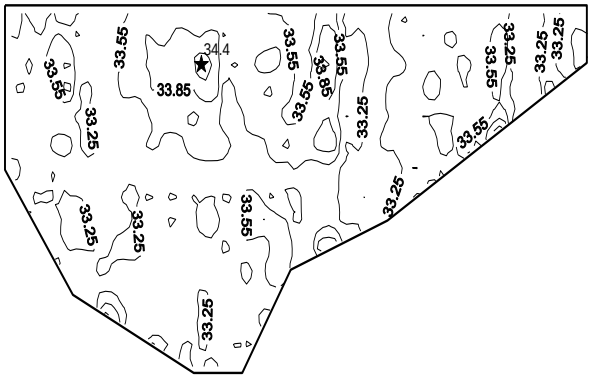


Fig 5 Upside along slope displacement contour map

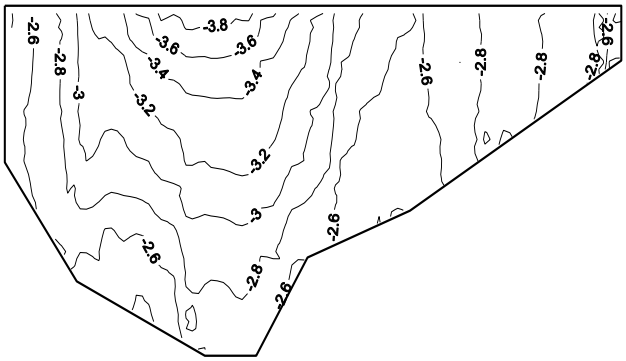


Fig 6 Downside along slope displacement contour map

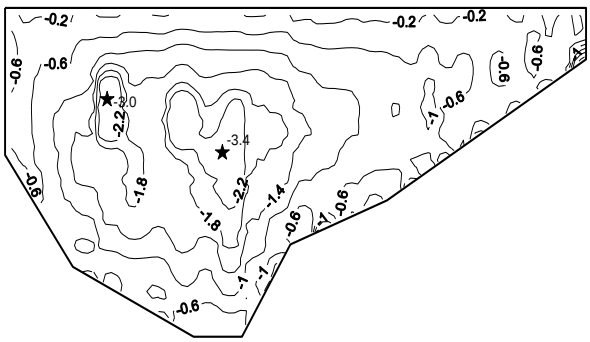


Fig 7 Along slope tensile stress contour map

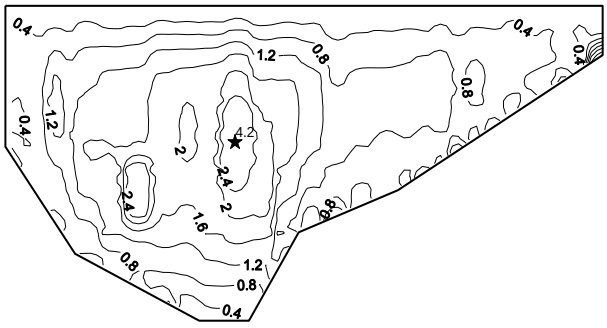


Fig 8 Along slope compressive stress contour map



Fig 9 Transverse river direction tensile stress contour map

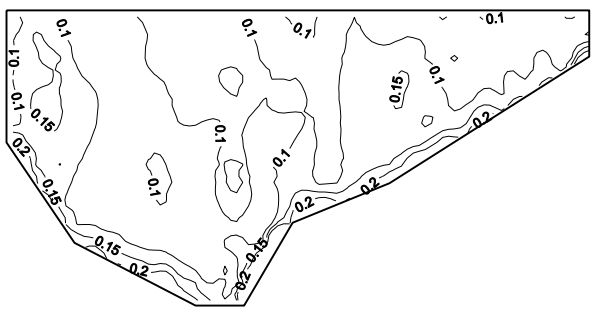


Fig 10 Transverse river direction compressive stress contour map

Conclusions

This paper uses large general-purpose finite element analysis software ABAQUS to make a calculation of a practical engineering project, Henan Tianchi pumped storage power station, and analyzes the maximum displacement, tensile stress and compressive stress of the slab. The analysis shows that at the middle of the slab, there is a area of high tensile stress. During operation, this area should be paid attention to. Under seismic condition, local areas appeal high tensile stress, the value can reach more than 2MPa. During construction, steels should be set at these parts of slab. This paper has some reference meaning for face rockfill dam's design and construction.

Acknowledgements

The work was financially supported by the High-level talents of North China University of Water Resources and Electric Power.

References

[1] X. Wu, M. Luan, X. Zhou, Comparison of computational results of different dynamic analysis methods for concrete faced rockfill dam, Journal of Hydraulic Engineering, 3 (2004) 15-21.

[2] J. Dong, D. Zhu, L. Cheng, Research on contact surface and dynamic characteristics of panel in facing rockfill Dam, Water Resources and Power, 29 (2011) 93-96.

[3] B. Wang, T. Liu, Dynamic analysis of face rockfill dam based on MSC Marc, Computer Aided Engineering, 15 (2006) 414-416.

[4] X. Xie, Finite element simulation model of statics and dynamics in concrete faced rockfill dam and its application, Thesis for Master degree, Hehai University, 2007.

[5] S. Chi, Influence of different seismic input on dynamic response of concrete faced rockfill dam, World Information on Earthquake Engineering, 18 (2002) 69-74.

[6] J. Li, H. Ma, Research on the dynamic property of CFRD in the period of water storage, Chinese Journal of Geotechnical Engineering, 17 (1995) 20-27.

© (2012) Trans Tech Publications, Switzerland
doi:10.4028/www.scientific.net/AMM.238.264

3D Finite Element Analysis of Concrete Face Rockfill Dam

Jianwei Zhang[a], Shengzhao Cheng[b], Shufang Yuan[c] and Yu Zhao[c]

North China University of Water Resources and Electric Power, Zhengzhou 450011, China

[a]zjwcivil@126.com, [b]chengshengzhao@yahoo.com.cn,

[c]226yuanshufang@163.com, [c]zhaoyu@ncwu.edu.cn

Keywords: concrete face rockfill dam; three-dimensional finite element; static analysis.

Abstract. Concrete face rockfill dam has the certain superiority in the construction of dam. Duncan-Chang nonlinear elastic model is selected as the dam materials in ABAQUS, which is an nonlinear finite element analysis software. Stresses and deformations of the concrete face rockfill dam are analyzed during its completion, operation and water level drawdown periods. Study shows that all results meet the requirements of the project, and have referenced value for other similar engineering.

Introduction

A pump-storage hydropower station is located in Henan province. The water control project consists of the upper reservoir, the lower reservoir, conveyance system and the power plant. This hydroplant has regulation performance. Total installed capacity is 1200 MW, and the reservoir storage is 1.518×107 m^3. Concrete face rockfill dam is located in the upper reservoir bed. The followings are the dam parameters such as the crest elevation of 1068.4m, the dam top width of 10.00m, the maximum dam height of 118.40m, the dam axes of 412 m, the rate of uppers dam lope of 1:1.40, the rate of lower dam lope of 1:1.35. The river valley of dam is "V" shape, and the altitude of the valley is between 937m and 975m. The lithology of the dam site is mainly of granite and diorite. The rock is hard and dense, and its mechanics strength is high.

In this paper, by nonlinear finite element analysis software ABAQUS, the stresses and deformations of the face rockfill dam have been analyzed during its completion, operation and water level drawdown periods. This paper analyzes the stress of the dam and the face, and the deformation of the periphery chink. This provides reliable theoretical analysis for the design of concrete face rockfill Dam.

Calculation Conditions

Material Model and Parameters. In the finite element computation, Duncan-Chang nonlinear elastic model is used with dam materials[1-4]. Material parameters are shown in Table 1. With the linear-elastic model, the material of the face and toe slab is the reinforced concrete. The elastic modulus of the concrete face is 22 GPa, and the elastic modulus of the concrete toe slab is 18 GPa. The poisson ratio is 0.17, and the density is 0.25g/cm^3. The linear-elastic model is used with the rock body of the dam face[5-7]. Because of the large difference between the face material and toe slab material, there probably occurs the discontinuous displacement.

Where c is the rial cohesion, φ_0 is the rial inner friction angle, $\Delta\varphi$ is the variation of inner friction angle, R_f is the destruction rate, K is the coefficient of elastic modulus, n is the index of elastic modulus, m is the index of bulk modulus.

Table 1 Parameters of dam material

Materials	ρ [g/cm3]	c [kPa]	φ_0 [°]	$\Delta\varphi$ [°]	R_f	K	n	K_b	m
Cushion	2.18	0	44.5	4.5	0.75	800	0.38	220	0.18
Transition Region	2.15	0	48.8	4.3	0.71	710	0.34	290	0.24
Main rock-fill zone	2.11	0	48.8	5.2	0.74	1000	0.26	300	0.20
Downstream rock-fill zone	2.07	0	46.5	5.3	0.65	640	0.27	280	0.19

Duncan-Chang model is the typical model of nonlinear elastic soil and rock model. Its elastic modulus is the function of the stress state, and can describe the nonlinear and the stress hardening of the stress-strain relationship of soil. Difference moduli for the load and unload are chosen in this model, and reflect material elastio-plastic to a certain extent.

In the Duncan-Chang model, tangent elastic modulus and tangent bulk modulus are expressed as the follow equations

$$E_t = \left[1 - \frac{R_f(1-\sin\varphi)(\sigma_1-\sigma_3)}{2c\cos\varphi + 2\sigma_3\sin\varphi}\right]^2 Kp_a\left(\frac{\sigma_3}{p_a}\right)^n \quad (1)$$

$$B_t = K_b p_a\left(\frac{\sigma_3}{p_a}\right)^m \quad (2)$$

On the unloading condition, the elastic modulus is expressed as the follow equation.

$$E_{ur} = K_{ur} p_a\left(\frac{\sigma_3}{p_a}\right)^n \quad (3)$$

Where P_a is the standard atmospheric pressure, σ_1 and σ_3 are the maximum and minimum principal stress. K_{ur} is the coefficient of elastic modulus at load and unload.

Load Calculation and Working Conditions. In the finite element simulation, there 20 steps load are calculated. From dam body to dam top, 17 steps load are calculated in process of construction. The face is completed as the 18th load. The load from storage water level to normal is used as the 19th load. The load is considered as 20th load at water level drawdown. Working conditions include completion, operation and water level drawdown conditions. The load of the completion condition is the gravity. The load of the operation and water level drawdown conditions include the gravity, hydrostatic pressure and silt pressure.

Calculation Results and Analysis

Calculation Model. Three-dimensional finite element meshes are shown in Fig. 1, which mainly uses the hexahedron elements and local prism transition elements. The contacts of the face to cushion and between periphery chinks were simulated by the contact element. The FE model was totally divided into 15367 elements and 16623 nodes, including 5352 elements of the dam.

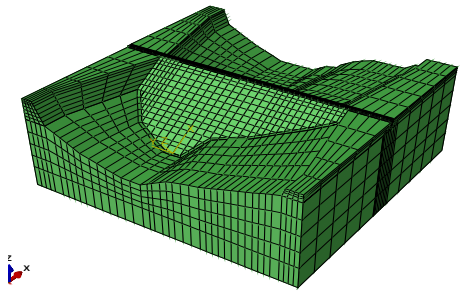


Fig. 1 Meshes

Stress and Displacement Analysis of the Dam. The maximum stresses and displacements of the dam body in completion, operation and water level drawdown conditions are shown in Table 2.

Table 2 The maximum stress and displacement of rock-fill

Working condition	Along the river (cm)		Vertical (cm)	Major principal stress (MPa)	Minor principal stress (MPa)
	Upstream	Downstream	Downward		
Completion	22.8	23.1	82	1.8	0.45
Operation	10.0	30.5	84.4	2.5	0.8
Water level drawdown	20.9	25.7	81.9	1.6	0.42

The dam body displacements in completion condition and stress in operation condition are shown in Fig 2 to Fig 5 at the dam 0+000 section.

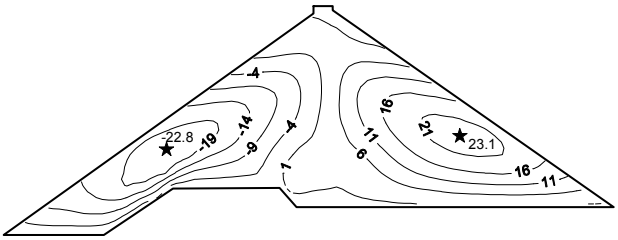


Fig 2 Completion of horizontal displacement contour (cm)

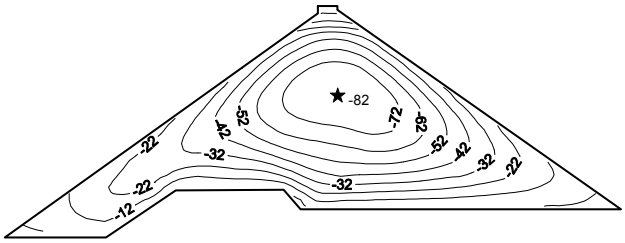


Fig 3 Completion of vertical displacement contour (cm)

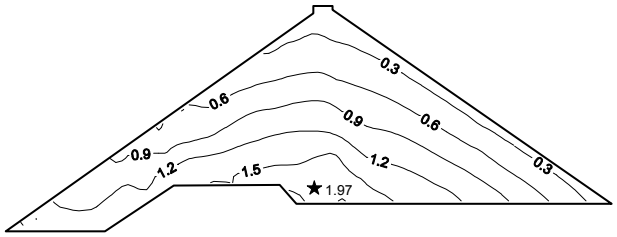


Fig 4 Operation of major principal stress distribution (MPa)

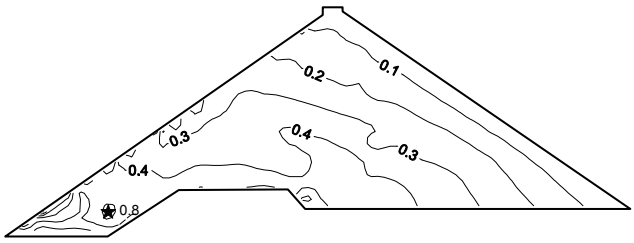


Fig 5 Operation of minor principal stress distribution (MPa)

Face Displacement and Stress Analysis. It is completion, operation and water level drawdown conditions that the maximum stresses and displacements of face are shown in Table 3.

Table 3 Maximum stress and displacement of the face

Working conditions	Face deflection(cm)		The slope-direction stress (MPa)	
	dam inside	dam outer	Pressure stress	Tensile stress
Completion period	2.0	/	0.32	0.0
Operation	21.6	/	2.45	1.27
Water level drawdown	11.6	10.5	2.4	0.0

The face vertical deflections in operation and the water level drawdown condition are shown in Fig 6 and Fig 7.

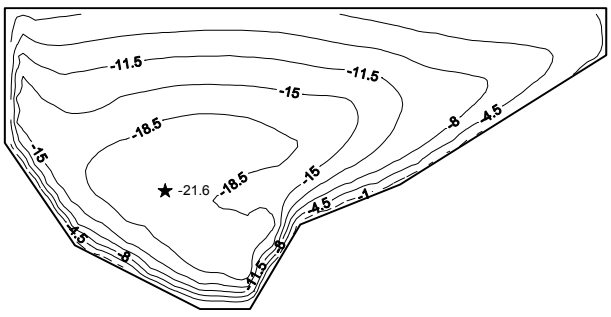


Fig. 6 Operation of the face vertical contour

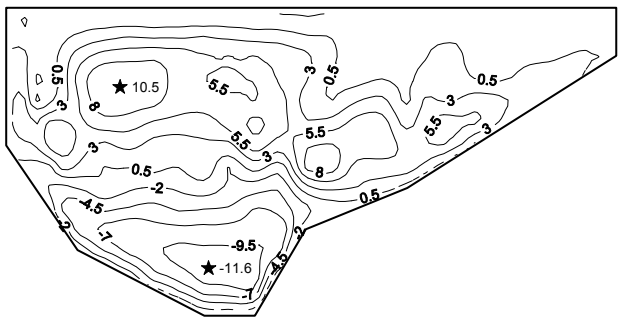


Fig 7 Water level drawdown of the face vertical contour

Conclusions

Stress and deformation of the face rock-fill dam is normal, and deformations are within permitted. The maximum sedimentation is 84.4cm, only the maximum dam height of 0.74%. The results are consistent with the completed project observations. In the calculation, the reverse pressure acted on inside the face in the normal design of water level altitude, and the water pressure acted on outside face in the dead storage level. Hence, that reverse deflection occurred in the face. Tensile stress had no significantly increase in the face.

Acknowledgements

It is a project jointly supported by Chinese National Natural Science Foundation (51009066), Basic and Advanced Technology Projects in Henan Province (102300410037) and Scientific and Technological Project of Zhengzhou city (0910SGYG21201-5, 10PTGS507-6).

References

[1] DL5077-1997, Load Design Criterion on Hydraulic Structure, China Waterpower Press, Beijing, 1997.

[2] Z. Fu, J. Feng, Concrete Face Rock-fill Dam, Huazhong University of Science and Technology Press, Wuhan, 1993.

[3] Z. Xu, Study on Stress and Deformation of Concrete Face Rock-Fill Dam, The Yellow River Water Conservancy Press, Zhengzhou, 2005.

[4] J. Qian, Z. Yin, Principle and Calculation of Soil, second edition, China Waterpower Press, Beijing, 1996.

[5] W. Song, Deformation and stress analysis of Sanbanxi concrete face rockfill dam, Journal of Hydroelectric Engineering, 6 (2006) 34-38.

[6] X. Kong, S. Lou, D. Zhou, The equivalent dynamic shear modulus and equivalent damping ratio of rockfill material for dam, Journal of Hydraulic Engineering, 8 (2001) 20-23.

[7] H. Jiang, The Modern Computational Method and Program of Hydraulic Structure Engineering and Geotechnical Engineering, Hehai University Press, Nanjing, 1992.

© (2012) Trans Tech Publications, Switzerland
doi:10.4028/www.scientific.net/AMM.238.268

Temperature Character Analysis of RCC Based on Stepwise Regression Model

Yuqing Zhao

North China University of Water Resources and Electric Power, Zhengzhou 450011, China

bqyj925@163.com

Keywords: RCC; stepwise regression analysis; temperature monitoring; raw data.

Abstract. The basic principles and ways of stepwise regression analysis is explained, taking the case of Jiangya gravity dam. On the basis of the temperature monitoring data, the optimal regression equation of the dam temperature is established gradually by the dam bedrock temperature, air temperature and reservoir water temperature and other related factors. It is proved that stepwise regression analysis model is reasonable and the simulation is fairly well with high precision. The stepwise regression model can be used to analyze the concrete temperature. The work provides the practical calculation basis for the monitoring of dam safety running.

Introduction

Stepwise regression analysis is one of the important contents in regression analysis, it is also one of primary means in statistics and modeling, it's essential thinking is founding the regression equation by selecting the distinct effected variables to y which is relate to the these variables . Stepwise regression analysis not only can make the factors which inflecting the dependent variable comprised but also can stick out some primary factors.

Multiple Regression Analysis Modeling

Some effect $y(t)$ of dam may be looked as a kind of multiple sequential random variable which follows Gaussian distributions ($x_n(t)$), Mathematical expectation is E, variance is σ, environmental effect factors which have been determined denotes $x_1(t)$, $x_2(t)$, $x_{n-1}(t)$,when y and these factors are linear correlated, there exist following relationship between $E\{y(t)/\ x_1(t),\ x_2(t),\ x_{n-1}(t),\}$ and environmental independent variables:

$$E\left\{y(t)/x_1(t),x_2(t),\cdots,x_{n-1}(t)\right\}=\beta_0+\sum_{i=1}^{n-1}\beta_i x_i(t) \tag{1}$$

equation (1) is theory regression equation about Mathematical expectation of variable $y(t)$, $x_i(t)$ is general variable, $\beta_i$is coefficient. according to the limited m times measured value between $y(t)$ and $x_i(t)$, regression equation is founded:

$$\hat{y}_t=b_0+\sum_{i=1}^{n-1}b_i x_i(t) \tag{2}$$

$\hat{y}_t$ is the regression value of dependent variable. it is the agonic estimate of average when $y(t)$ is in correlation factor combined; b_i(i=1, 2, … n-1) is regression coefficient, they are the estimation of materity parameter. Variance $\sigma^2$is estimated by residual variance of equation S^2.Residual sum of square between regression value and measured value is:

$$Q=\sum_{t=1}^{m}\left[x_n(t)-\widehat{x_n}(t)\right]^2=\sum_{t=1}^{m}\left\{[x_n(t)-\overline{x_n}]-\sum_{t=1}^{n-1}b_i[x_i(t)-\overline{x_i}]\right\}^2 \tag{3}$$

the normal equation of b_i(i=1, 2, … n-1) is shown as:

$$\sum_{i=1}^{n-1} S_{ij} b_i = S_{nj} \quad (j = 1, 2, \cdots, n-1) \tag{4}$$

Equation (5) becomes normal equation, number n-1, b_i may be solved by combining number n-1 equation, then constant term is obtained.

$$b_0 = \overline{x_i} - \sum_{i=1}^{n-1} b_i \overline{x_i} \tag{5}$$

b_i (i=1, 2, … n-1) is the least squares estimation of β_i (i=0, 1, 2, … n-1), they make Q becoming into the minimum value, so equation(2) is the optimum fitted equation when number n-1 factors is in m times value.

$$d_i = b_i \sqrt{S_{ii} / S_{nn}} \qquad (i = 1, 2, \cdots, n-1) \qquad r_{ij} = \frac{S_{ij}}{\sqrt{S_{ii} S_{jj}}} \qquad (i = 1, 2, \cdots, n) \tag{6}$$

Brought in Equation (5) :

$$\sum_{i=1}^{n-1} d_i r_{ij} = r_{nj} \qquad (i, j = 1, 2, \cdots, n-1) \tag{7}$$

Stepwise Regression Analysis Modeling Step

Stepwise regression analysis is a kind of method that chooses the optimal regression equation.It derives from one independent variable, independent variables will be inducted into regression equation step by step . In the light of visibility which acts on dependent variable. there is varying correlativity between independent variables .So it maybe make the previous inducted variables becoming indistinctively because of the induction of the later variables. here, the previous inducted variables will not be kept, they may be eliminated from regression equation at any moment. so, every step of Stepwise regression analysis should carry out statistic inspection(F inspection) to ensure the regression equation only contain obvious factors, until obvious factors will all be contained into regression equation.

Solving the Stepwise Regression Equation. Every step of stepwise regression analysis need to solve the normal equation set and carry out the significance test, this can be achieved by correlation matrix transformation. correlation coefficient is augmented into (n-1)×(n-1) matrix ,it is called correlation matrix.

$$r = (r_{ij}) = \begin{bmatrix} r_{11} & r_{12} & \cdots & r_{1(n-1)} & r_{1n} \\ r_{21} & r_{22} & \cdots & r_{2(n-1)} & r_{2n} \\ \cdots & \cdots & \cdots & \cdots & \cdots \\ r_{(n-1)1} & r_{(n-1)2} & \cdots & r_{(n-1)(n-1)} & r_{(n-1)n} \\ r_{n1} & r_{n2} & \cdots & r_{n(n-1)} & r_{nn} \end{bmatrix} \tag{8}$$

This matrix is also called step 0 correlation matrix, $r^{(0)} = (r_{ij}^{(0)})$ 。

Supposing independent variables that are contained into equation is $x_{k1}(t)$, $x_{k2}(t)$, …$x_{kl}(t)$ after correlation matrix is alternated step h. it is called h step variable. the equation is following:

$$x_n(t) = b_0^{(h)} + \sum_{i=1}^{l} b_i^{(h)} x_{k_i}(t) \tag{9}$$

The number of h step variable $l \le h$.

Step h correlation matrix: $r^{(h)} = [r_{ij}^{(h)}]$(i, j=1, 2, ⋯, n). It can be solved by "well-knit variation method" by use of the element $r^{(h-1)}$,the formula is following:

$$\begin{cases} r_{(ij)}^{(h)} = r_{ij}^{(h-1)} - r_{ik}^{(h-1)} r_{kj}^{(h-1)} / r_{kk}^{(h-1)} & (i \ne k, j \ne k) \\ r_{(ik)}^{(h)} = -r_{ik}^{(h-1)} / r_{kk}^{(h-1)} & (i \ne k) \\ r_{(kj)}^{(h)} = r_{kj}^{(h-1)} / r_{kk}^{(h-1)} & (j \ne k) \\ r_{(kk)}^{(h)} = 1 / r_{kk}^{(h-1)} \end{cases} \tag{10}$$

The Choice of Importing and Eliminating Factors. At first, the biggest factor in $r_{in}^{(0)}$ is inducted into regression equation as the first factor, then new factors are sort out to enter regression equation from the rest of factors. When choosing inducted factors at step h,for all factors $x_i(t)$, standard regression quadratic sum to dependent variables $x_n(t)$, is calculated:

$$V_i^{(h)} = [r_{in}^{(h-1)}]^2 / r_{ii}^{(h-1)} \tag{11}$$

Offal standards i=1~n-i,factor number which have enter regression equation is not inside of the offal standards, the biggest one of the $V_i^{(h)}$ is solved:

$$V_{i_0}^{(h)} = \max V_i^{(h)} \tag{12}$$

Factor $x_{i_0}(t)$ becomes the possible object which maybe be inducted the equation., in order to examine whether the effect to $x_n(t)$, is prominent ,statistic is calculated:

$$F_t = V_{i_0}^{(h)}(m-l-2)/[r_{nn}^{(h-1)} - V_{i_0}^{(h)}] \tag{13}$$

Then $F_l^* = F^{\alpha}{}_{f_1,f_2}$ is solved, it is the critical value of F test in $f_1 = 1$, $f_2 = m-l-2$ and conspicuous level is α. If $F_l \geq F_l^*$, it denotes the variance of $x_{i0}(t)$ is prominent. Leading it to the equation; if $F_l \leq F_l^*$, it denotes the variance of $x_{i0}(t)$ is not prominent, it cannot be lead into the equation. From the second step, factors that have entered equation should be inspected on every step, judging whether exist the factors which in not prominent to variance .if correlation matrix transform h step ($h \geq 2$),

Factors $x_{k1}(t)$, $x_{k2}(t)$, …$x_{kl}(t)$ have been imported into the regression equation. the standardized partial regression quadratic sum that these factors correspond to $x_n(t)$:

$$V_{k_i}^{(h)} = [r_{k_i n}^{(h)}]^2 / r_{k_i k_i}^{(h)} \tag{14}$$

k_i is the superscript of every factors that have entered regression equation. the minimum of partial regression quadratic sum is following:

$$V_{k_i^*}^{(h)} = \min V_{k_i}^{(h)} \tag{15}$$

$x_{ki}(t)$ is possible be eliminated. In order to explore $x_{ki}(t)$ is significant to $x_n(t)$ or not. statistic is obtained

$$F_2 = V_{k_i^*}^{(h)}(m-l-1)/r_{nn}^{(h)} \tag{16}$$

$$F_{l,m-l-1} = \frac{U/l}{Q/m-l-1} = \frac{U}{lS^2} \tag{17}$$

According to free degree $f_1 = 1$, $f_2 = m-l-1$, F test critical value $F^{\alpha}{}_{f_1,f_2}$ is found out on the condition ofprominent level is α by mathematical statistics. A usually takes 0.10,0.05,0.01. if $F \geq F^{0.01}$,regression is highly significant; if $F^{0.05} \leq F < F^{0.01}$, regression is significant; if $F < F^{0.10}$, regression is not significant.

Engineering Project

JiangYa hydraulic complex is full face RCC gravity dam. On the basis of temperature monitoring data of 5# dam , monitoring data on some representative locations- bottom of dam are selected to carry out regression analysis calculation. The result may turn into reference for dam safe running, 30 months temperature monitoring data is selected .The data of Air temperature ,rock temperature and water temperature is monthly average. monitoring data is shown on Table 1.

Bottom of Dam Temperature Regression Analysis. By calculation, temperature of rock is the primary factor, the second factor is air temperature, the temperature of water is rejected.The first time ,coefficient of determination of regression model R=0.975; the second time, coefficient of determination R=0.979. furthermore, coefficient of air temperature and rock temperature all pass

two-tailed test (p<0.05), these variables may exist model as explanatory variables. They can explain the variation of concrete temperature on bottom of dam. The standardized stepwise regression equation is y=-73.282+0.013x_1+3.618x_2, the comparison is shown in Fig. 1.

Table 1 The temperature monitoring data of RCC dam

item	date	Temperature on bottom of damy (°C)	Temperature on the center of damy (°C)	Temperature on the top of dam y (°C)	Temperature of air x_1 (°C)	Temperature of the rock x_2 (°C)	Temperature of water x_3 (°C)
1	2000-1-1	26.66	26.30	25.01	7.96	27.56	14.94
2	2000-2-1	26.55	26.12	24.07	10.00	27.53	12.60
3	2000-3-1	26.30	25.93	23.45	13.00	27.50	12.49
⋮	⋮	⋮	⋮	⋮	⋮	⋮	⋮
⋮	⋮	⋮	⋮	⋮	⋮	⋮	⋮
34	2002-10-1	23.53	22.49	20.20	17.50	26.71	12.73
35	2002-11-1	23.43	22.36	19.95	15.67	26.74	12.87

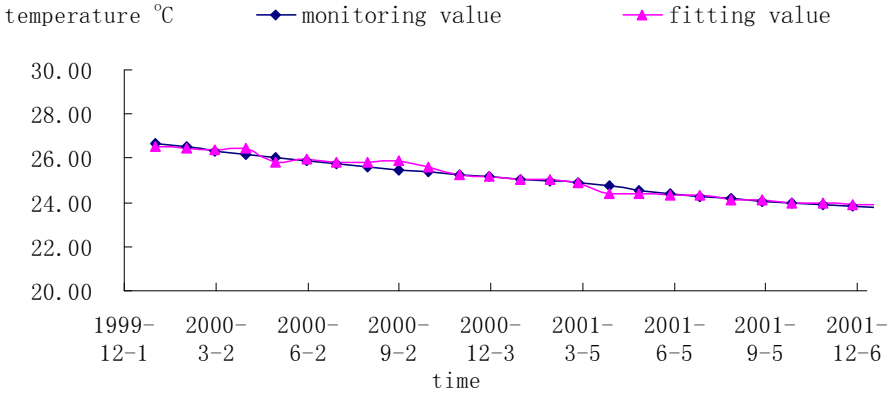


Fig. 1 Comparison between measured data curve and fitting curve of concrete temperature

Conclusions

Stepwise regression analysis theory is studied in this paper, principal and step of stepwise regression analysis modeling is discussed. Stepwise regression analysis model of dam concrete temperature is founded on the basis of analysis principal. The engineering project calculation indicates that calculated variables of Stepwise regression analysis method is few ,model precision is high, modeling found is successful, the emphasis of monitoring work should be put on the rock temperature, scientific basis will be provided for safe running and management of dam.

References

[1] H. Wang, Partial Least Square Regression Method and Application, National Defense Industry Press, Beijing, 1999: 202-206.

[2] R. Ren, H. Wang, Multivariate Statistical Data Analysis-Theory, Method, Example, National Defense Industry Press, Beijing, 1998: 56-59.

[3] Miles, Classical and Modern Regression with Applications, Academic Press, Beijing, 2006: 51-52

[4] H. Zhang, Z. Dang, F. Yu, Application of Grey Linear Regression Model on calculating resistance coefficient of pipe, Journal of North China Institute of Water Conservancy and Hydroelectric Power, 1 (2009) 12-14.

© (2012) Trans Tech Publications, Switzerland
doi:10.4028/www.scientific.net/AMM.238.272

Temperature Control of RCC Dam in Yongding Project

Xiangdong Xu[1,2,a] and Jinchao Yue[1,b]

[1]Zhengzhou University, Zhengzhou 450001, China

[2]Henan Technical College of Construction, Zhengzhou 450002, China

[a] 2861570348@qq.com, [b] yuejc@zzu.edu.cn

Keywords: roller compacted concrete (RCC); dam; construction during hot season; temperature control.

Abstract. Yongding RCC gravity dam with large project scale is in the construction all over the year, and the big temperature stress is a key factor for construction quality and progress. The temperature of the RCC dam in typical season with and without control conditions was analyzed by FEM, the temperature situation in typical season of RCC dam was controlled by the embedded cooling water pipes by practical method. Key points in concrete temperature control during high temperature season are found out, the counter measures and issues to be noticed are put forward.

Introduction

Yongding bridge reservoir roller compacted concrete gravity dam is level 2 building, by retaining dam, spillway, diversion dam etc. crest length of 181.00m, the maximum dam height is 123m, concrete content is 478900m3, it is a large volume of high RCC dam, Complex construction technology, and the requirements of the construction all over the year. So the dam temperature control design is a key factor for construction quality and construction progress.

In this paper, by means of numerical simulation technology in the diversion dam, for example (Fig. 1), the construction and operation period of the temperature field and temperature stress field under different temperature control scheme of the simulation, analysis of a variety of solutions and the temperature stress distribution law.

Calculation Principle

Temperature Field Finite Element Simulation Principle. Finite element simulation analysis of dam concrete is according to the boundary conditions such as concrete initial temperature, lift thickness, intermittent time, outside temperature changes, if buried inside the concrete cooling pipe. By the finite element simulation method, the simulation analysis of the dam during construction and operation condition, the concrete temperature and temperature stress development status, the impact of concrete temperature and the stress of the adverse factors can be done, which may provide a theoretical basis to determine the concrete construction method and temperature control method.

By outside temperature and hydration heat of concrete, concrete dam body either the spatial distribution or time variation process is not uniform. Concrete structure stress is the uneven temperature distribution caused by concrete, heat flow obey Fourier law experiment, the temperature field of heat conduction equation [1]:

$$\frac{\partial T}{\partial \tau} = a\left(\frac{\partial^2 T}{\partial x^2} + \frac{\partial^2 T}{\partial y^2} + \frac{\partial^2 T}{\partial z^2}\right) + \frac{\partial \theta}{\partial \tau} \tag{1}$$

Where α is concrete thermal conductivity; and θ(t)is the adiabatic temperature rise of concrete function.

Initial conditions : When $t = 0$, $T(x, y, z, 0) = T_0(x, y, z)$

Boundary conditions:

$$\lambda \frac{\partial T}{\partial n} = -\beta(T - T_c) \tag{2}$$

Where β is Surface heat transfer coefficient; λ is thermal conductivity; and Tc is Ambient temperature.

The cooling water pipe cooling correction equation of heat conduction for:

$$\frac{\partial T}{\partial \tau} = a(\frac{\partial^2 T}{\partial x^2} + \frac{\partial^2 T}{\partial y^2} + \frac{\partial^2 T}{\partial z^2}) + (T_0 - T_w)\frac{\partial \phi}{\partial \tau} + \theta_0 \frac{\partial \psi}{\partial \tau} \tag{3}$$

Where T0 is concrete placement temperature, and Tw is the cooling water temperature.

Creep Stress Field Finite Element Simulation Principle. Assume that in every period Δτi, the stress is linearly, even stress to the time derivative is constant, also in Δτi; the stress curve is a polygonal approximation to the true stress curve, if $\frac{\partial \sigma}{\partial \tau} = \xi_i = \text{Constant}$, the n of a unit time increment of strain is{Δεn}, strain increment includes the elastic strain, creep strain increment , temperature strain increment, Then:

$$\{\Delta\varepsilon_n\} = \{\Delta\varepsilon_n^e\} + \{\Delta\varepsilon_n^c\} + \{\Delta\varepsilon_n^T\} \tag{4}$$

Where {Δεen} is the elastic strain increment array; {Δεcn} is the temperature weight creep deformation incremental array; {ΔεTn} is the temperature strain increment array.

In creep, temperature and external loads, Creep stress is:

$$\{\Delta\sigma_n\} = [\bar{D}_n]\left([B]\{\Delta\delta_n\} - \{\omega_n\}(1 - e^{-s\Delta\tau_n}) - \{\Delta\varepsilon_n^T\}\right) \tag{5}$$

Where $[\bar{D}_n] = [D_n] \Big/ \left[1 + C_n(1 - f_n e^{-s\Delta\tau_n}) \cdot E(t_{n-1} + \frac{1}{2}\Delta\tau_n)\right]$; [B] is the strain and displacement transformation matrix; {Δδn} is the period N node displacement matrix.

By virtual work principle

$$[K]\{\Delta\delta_n\} = \{\Delta P_n^c\} + \{\Delta P_n^T\} + \{F\} \tag{6}$$

Where K is the structural stiffness matrix, Δδn is the nodal displacement increment, ΔpTn is the temperature load increment, Δpcn is the creep deformation of equivalent load increments, F is the unit of force; by formula (4) determined displacement increment can be calculated, substitution (6) can be calculated.

RCC Dam Temperature Control Simulation

Temperature Control Simulation Boundary Conditions and Initial Conditions for Determination. Basic boundary temperature according to the first kind boundary treatment, and water contact boundary as the first kind boundary condition, the crest and downstream surface according to third kinds of boundary treatment [3]. Prior to the pouring of concrete, according to the surface temperature and deep and stable temperature was calculated on the basis of the base portion of the initial temperature field.

Calculation Model. According to the research of contract and task, considering the dam and the dam joint structure arrangement, work characteristics and other factors, selection the diversion dam for modeling calculation, Selection the foundation depth is 1 times direction of dam height. Up and down stream length respectively take 1 times of maximum dam width, Left and right bank foundation of the dam is about 1 times dam length. Cell division mainly use hexahedral elements, five elements supplemented, The size of unit is base on the construction progress and the layer thickness, the left and right abutment direction as Z axis, right direction as positive, flow direction as X axis direction, dam elevation direction as y axis positive.

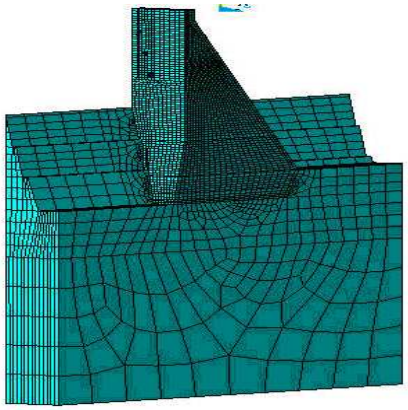


Fig.1 The model of diversion

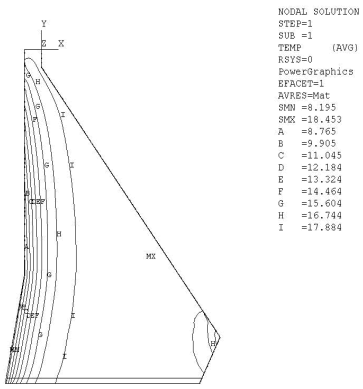


Fig.2 The steady temperature field of diversion dam

The elements of the three-dimensional diversion dam of finite element model is 29022, the node number is 33014.According to the construction plan and construction progress, the dam pouring begins from the first year of October 1st to January of third year, which lasts16 months, elevated 123m.

The calculation meshes of stress field finite element is the same as temperature simulation computing grid, which considering gravity, water pressure and temperature load, simulation of roller compacted concrete by temperature, weight, heat of hydration, creep and other auto antibodies and outside the complex change of dam temperature field and stress field.

Stable Temperature Field Calculation. Steady temperature field of dam during operation period is defined during construction control of concrete temperature and preventing the base foundation temperature difference, appear through out the important basis of crack.

In this paper, use the 3D finite element method to calculate diversion dam steady temperature field (Fig. 2), Calculation boundary conditions is the average temperature of many years, up and down stream of reservoir water temperature. Range the bedrock surface to 20m, initial temperature takes the average temperature of 17.8 oC of many years, Yongding bridge engineering rock is dolomitic limestone, is hard rock, The depth increases 50m, the temperature increases 1 oC.

According to the dam temperature, water temperature and water temperature in front of dam at different water depth change, seek the dam temperature field change over the month after impoundment, get stable temperature field for steady temperature field, Based on the temperature distribution analysis, near the upstream face temperature affected by reservoir water temperature effect, dam lower part is 8~10 oC, the upper 10~16 oC, the middle part of the dam is about 17.8 oC, While the downstream surface belongs to the influence by outside temperature, the average temperature of 17.8 oC about for years.

Different Temperature Control Calculation. Diversion dam is calculated with 8 kinds of temperature control scheme (the calculation results shown in Fig. 3 and 4),The time of Simulation calculation span from the start to achieve steady temperature field of dam. Temperature units: oC .

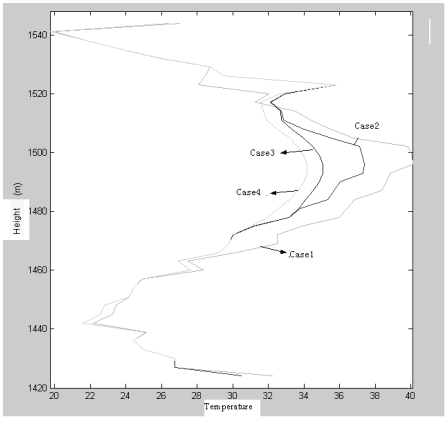


Fig.3 Temperature field in Case 1~4

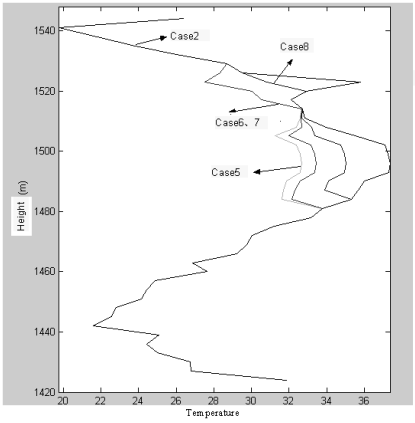


Fig.4 Temperature field in Case 1~4

Case1, The pouring temperature of concrete in different month natural pouring temperature;
Case 2, 3, 4 and 5, concrete temperature control from July to August, the highest pouring temperature is 24oC, 20oC, 18 oC and 24oC respectively.
Fig 4 is Case 1~ 4 high temperature envelope diagram along the dam. Along dam appeared 2 peak of temperature, the first temperature peak position bases on normal concrete cushion, Occurrence time is fifth days after the start pouring, as a result of normal concrete hydration heat relatively large, Began construction the 4-7 days dissipate most heats, the highest temperature appears. Second temperature peak position appear the elevation of 1500.0m, occurrence Time of is the summer, mainly affected by environment temperature and pouring temperature effect. Case 4 temperature field accords with the standard.
In June ~August pouring dam using water cooling scheme, water cooling schedule is as follows: The cooling water pipe made of high density polyethylene PVC tube, outer diameter 32mm, diameter 28mm, length 200m, pipe spacing 1.5m×1.5m, the cooling water pipe shall be vertical flow direction, the vertically space of cooling water pipe is the same as pouring thick layer, water tube is generally arranged in each block at the bottom. After pouring,12℃cold water cooling, water time is 15 days, water cooling temperature range should not be too large, general daily reduce temperature should not exceed 1℃,monthly temperature decreased by 5 ~10℃ control, In order to make concrete uniform cooling, the cooling process, should be constantly changed back and forth water import and export orientation.
Case 6, 7 and 8, Concrete temperature control from July to August, the highest pouring temperature is 24 oC, the temperature of cooling water is 12 oC. The pipe spacing is 1.5m×2.0m in Case 6 and 8 while it is 1.5m×1.5m in Case 7. The water time is 15 days in Case 6 while it is 11 days in Case 7 and 8.
The dam maximum temperature is 32.61oC in Case 5, 35.23 oC in Case 6, 33.89 oC in Case 7 and 33.89 oC in Case 8 respectively. Recommend a water cooling scheme using Case 6 scheme with pipe spacing of 1.5m×2.0m, water temperature 12 oC, water time 15 days from June to August pouring temperature peak.

Stress Field Calculation Results. Based on the calculation results of the temperature field, the calculation results of temperature stress field in Case 4 and 6 are shown in Fig. 5 to Fig. 8. Diagram of principal stress were S1, S3, the tensile stress is positive, the pressure stress is negative.

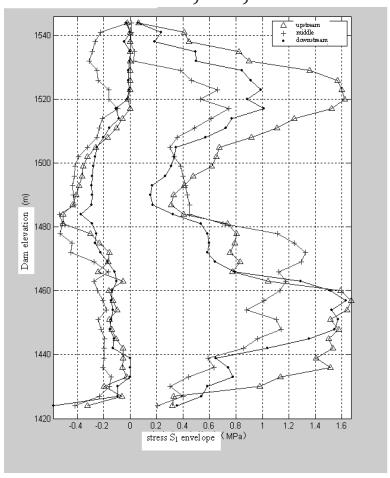


Fig. 5 Envelope diagram of S1 of Case 4

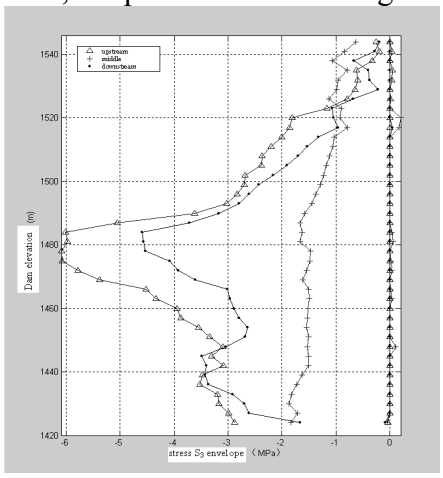


Fig. 6 Envelope diagram of S3 of Case 4

Case 4 highest pouring temperature control at 18oC, the dam on the lower temperature difference, strongly constrained region of temperature difference, Weakly constrained region of temperature difference, the highest temperature does not exceed the standard of dam, the maximum tensile stress is1.66MPa,the maximum compressive stress -4.0MPa, dam body temperature and temperature stress comply with regulatory requirements.
Due to the low air temperature in winter, there is big temperature difference inside and outside dam, the dam will appear larger tensile stress, the temperature stress in January 2010, 2011, 2012 and 2013 are analyzed in detail, the results are shown in Table 1.

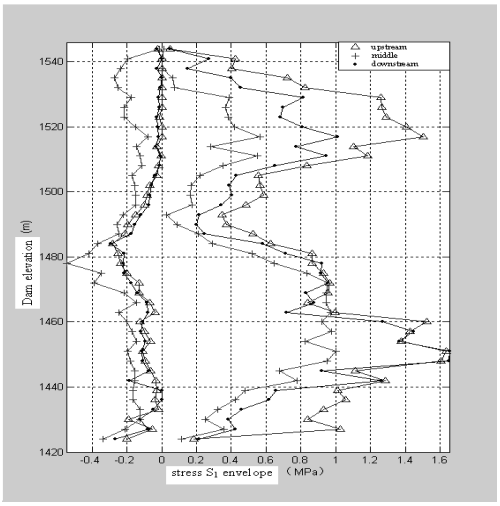


Fig. 7 Envelope diagram of S1 of Case 6

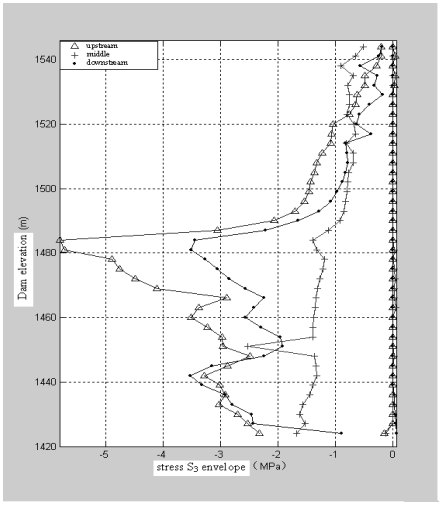


Fig. 8 Envelope diagram of S3 of Case 6

Table 1 Statistics of diversion dam Case 4 stress components

Time	σx (MPa)		σy (MPa)		σz (MPa)	
	Max	Min	Max	Min	Max	Min
Jan. 2010	0.52	-0.49	0.00	-1.37	0.52	-0.17
Jan. 2011	0.70	-0.42	0.21	-0.94	0.32	-0.46
Jan. 2012	0.14	-0.75	0.43	-0.76	0.23	-1.13
Jan. 2013	0.12	-0.80	0.00	-0.98	0.07	-0.87

Flow direction normal stress over time has the tendency of reduction, maximum tensile stress value of 0.70MPa, appear January 2011. Dam height direction (Y direction) σy the height of the main direction of compressive stress, the maximum tensile stress value is 0.43MPa, occurred in January 2011. The dam axis direction normal stress over time are decreased, maximum tensile stress value is 0.52MPa, appeared in January 2010.

Case 6 with water pipe cooling, dam on the lower temperature difference, strongly constrained region of weakly bound zone temperature and the highest temperature does not exceed the standard, the maximum tensile stress was 1.68MPa, the maximum compressive stress - 5.5MPa, dam body temperature and temperature stress specification. Table 2 gives the condition of 6temperature stress analysis table.

Table 2 Statistics of diversion dam Case 6 stress components

Time	σx (MPa)		σy (MPa)		σz (MPa)	
	Max	Min	Max	Min	Max	Min
Jan. 2010	0.53	0.93	0.00	-1.28	0.51	-0.40
Jan. 2011	0.28	-1.00	0.00	-0.85	0.05	-0.79
Jan. 2012	0.00	-1.0	0.00	-1.18	0.06	-0.81
Jan. 2013	0.10	-1.14	0.03	-1.07	0.10	-0.73
Jan. 2014	0.14	-0.99	0.00	-0.91	0.14	-1.04

Flow direction normal stress over time are decreased, maximum tensile stress value is 0.53MPa, appeared in the January 2010 operation period. Dam height direction (Y direction) along the dam height direction is mainly compressive stress, tensile stress and the maximum value is 1.28MPa, occurred in January 2010.The dam axis direction normal stress over time are decreased, maximum tensile stress value is 0.51MPa, appeared in January 2010.The main stress is mainly composed of X and Z direction tensile stress generated, but because their value is relatively small, will not have a greater impact on dam surface.

The Dam Allowed Temperature

Based on the FE simulation of dam, according to Chinese Code SL319-2005 and already built projects [2, 3], the maximum allowable temperatures of dam concrete are listed in Table 3.

Table 3 Maximum allowable temperature of the dam

Position	Upstream dam heel zone	Upstream facing water	Foundation restraint area			Other pouring zone
			Normal concrete	RCC		
			Cushion	Restraint	Weak restraint	
Max. allowable temperature (oC)	27	28	32.5	30.5	33	35

Conclusions

By using the finite element method of Yongding bridge of roller compacted concrete dam temperature field and stress field simulation calculation, the inside maximum temperature, temperature difference between internal and external concrete and concrete creep stress calculation analysis shows that: in each summer high temperature pouring concrete, is to produce larger horizontal tensile stress region; if we do not adopt temperature control measures of high temperature season, the pouring concrete temperature will exceed the limit value or design permissible value; winter concrete surface without insulation, appears extremely likely surface crack, elimination approach is lowered the maximum pouring temperature, two is on the concrete surface to take surface heat preservation measures.

References

[1] B. Zhu: Mass Concrete Temperature Stress and Temperature Control, China Electric Power Press, Beijing, 1999.

[2] Chinese Code SL314-2004: Design Specification for Roller Compacted Concrete Dam, China Water Power Press, Beijing, 2005.

[3] Y. Zhu, J. He and Y. Liu: Water Power, 11 (2002) 32-36.

© (2012) Trans Tech Publications, Switzerland
doi:10.4028/www.scientific.net/AMM.238.278

Study on Fundamental Frequency of Runway based on Winkler Model

Xianmin Zhang[1,a], Liang Liang[1,b] and Wei Zhang[2,c]

[1]Airport College, Civil Aviation University of China, Tianjin 300300, China

[2] Yunnan Airport Group Co., Ltd., Yunnan 650000, China

[a]cauczxm@126.com, [b]515806540@qq.com, [c]weizhang1101@163.com

Keywords: pavement; finite element; Winkler foundation; fundamental frequency.

Abstract. The change mechanisms of fundamental frequency of runway under different conditions are discussed in this paper. A full scale cement concrete slab finite element model is built to analyze the relationship between foundation modulus and the fundamental frequency of runway. The results show that the coupling effect of runway plates can not be neglected. The minimum area affecting the fundamental frequency of runway is 45m in longitudinal and 15m in transversal according to the analysis of fundamental frequency of different size runway. The fundamental frequency of runway ranges from 7.5Hz to 23.6 Hz when the foundation modulus increases.

Introduction

Domestic and foreign scholars have done a lot of researches on the frequency of rigid pavement, Kantorovich [1] got the analytical solution of frequencies of thin plate on elastic foundation, Xiaoping Zheng [2] got the approximate solution of dynamic response of rectangular plate on viscoelastic foundation under moving Loads, Yang Zhong [3] got the analytical solution of vibration problems of four-sides-free rectangular sheet with Kantorovich method. However, the results are got by only one pavement, and multi-block pavement answers have not been got. The fundamental frequency of runway is discussed in this paper according to a full scale 30 cement concrete slab finite element model, and the finite element results coincide well with the theoretical results. A new method of runway evaluation is put forward.

Structural Analysis Methods of Runway

The pavement structure analysis methods include analytical method and finite element method. Analytical method has already been used in elastic layered system and Winkler foundation model. However, the analytical method applies to two layers of pavement structure and couldn't be applied to complex three-dimensional boundary constraint, the method has certain limitations[4]. The runway is analyzed with finite element method in this paper. Multi-layer pavement finite element model is built, and three-dimensional runway of the boundary conditions is taken into account, which makes the results more realistic.

Establishing and Solving of the Finite Element Model

Material Parameters The finite model is created by concrete surface layer and cement crushed stone base, and the structural layer under stabilized macadam base is simplified with Winkler model. The foundation is simulated by spring unit. The spring stiffness is got by Allocation Area Method [5]. Each structure and its corresponding parameters are list in Table 1, and different locations of spring and the corresponding stiffness when the foundation modulus is 70MN/m³ are list in Table 2.

Model Parameters. The finite element model is built by the actual parameter of an airport pavement. Single plate size of the pavement is 5m×4.5m×0.3m. Concrete surface layer and cement crushed stone base are simulated by solid45 unit. The foundation is substituted by a series of discrete and vertical spring, and the spring is simulated by combine14 unit. The dowels between pavements do little to the fundamental frequency of the runway according to the previous calculations. The dowels are ignored in the finite element model and the pavements are thought coupled well.

Table 1 Model Structure and Parameters

Structure	Thickness *h* (m)	Resilient modulus *E* (MPa)	Poisson's ratio	Flexural tensile strength (MPa)
Concrete surface layer	0.3	30000	0.167	4.5
Cement crushed stone base	0.33	1500	0.25	--

Table 2 Spring Stiffness (MN/m)

Location	Spring Stiffness
Center	3.5
Edge	1.75
Corner	0.875

The secondary unit gets the better results under coarse grid condition (*h*/*e*=2, *h* is the thickness of the pavement, *e* is the cell size). Quadratic hexahedron units are selected when the test accuracy and computing speed are under consideration. The mesh size is 0.5m×0.5m×0.3m.

Boundary Conditions The concrete surface layer and the cement crushed stone base are fully in contact. The nodes on the contact surface take the same freedom. In the finite element model *X* represents horizontal direction, *Y* represents longitudinal direction, *Z* represents vertical direction. The boundary conditions: the underside of the foundation springs is fully constrained, the four sides of the underside of the cement crushed stone base are constrained. The four sides of the concrete surface layer are free. Fig. 1 shows the structure of the pavement.

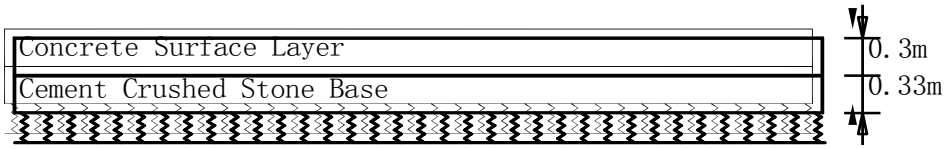


Fig. 1 Structure of the pavement

Dynamic Response Analysis of the Pavement

Accuracy Verification of the Model The finite element model is compared with the theoretical solution of flexible space model to verify the accuracy of the model. According to the transforming relationship between the resilient modulus of the foundation E_0 and the foundation modulus *K* which proposed by Zhang [6]. The resilient modulus of the foundation E_0 is 184MPa when the foundation modulus *K* is 70MN/ m³ corresponds. Table 3 shows the compared vertical displacement of Winkler model and flexible space model.

Table 3 Vertical displacement of Winkler model and flexible space model

	vertical displacement (μm)			
Distance away from the loading area (m)	0	0.5	1	1.5
Winkler model	355	288	197	131
Flexible space model	367	296	203	137
Error (%)	-3.38	-2.78	-3.05	-4.58

The Frequencies of the Pavements of Different Sizes. Different sizes of finite element models are built to analysis the impact of law when the size of the pavement changes. The foundation modulus is 70 MN/m³.

Fig. 2 shows the frequency curve when the lateral dimensions ranges from 4.5m to 45m while the vertical size is 5m. The figure shows that the fundamental frequency reduces when the lateral dimensions increase. When the lateral dimensions range from 4.5m to 22.5m, the rate of change of frequency is 34.1%; the lateral dimensions range from 22.5m to 45m, the rate of change of frequency is 4.7%. At last the lateral dimension is identified for 45m.

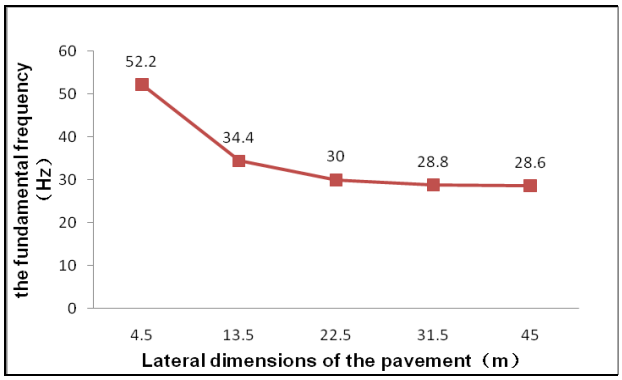


Fig. 2 Fundamental frequency curve 1

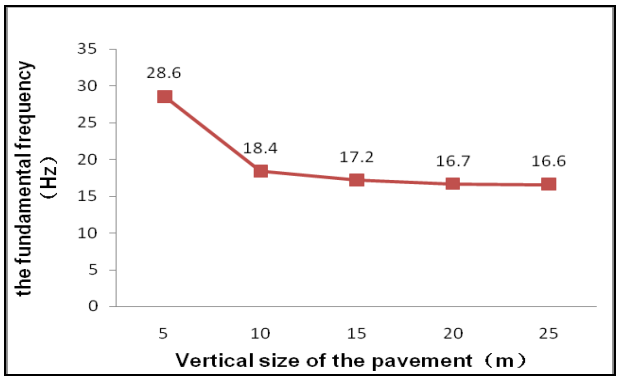


Fig. 3 Fundamental frequency curve 2

Fig. 3 shows the frequency curve when the vertical dimensions range from 5m to 25m while the lateral size is 45m. The figure shows that the fundamental frequency reduces when the vertical dimensions increase. When the vertical dimensions range from 5m to 15m, the rate of change of frequency is 39.9%; the vertical dimensions range from 15m to 25m, the rate of change of frequency is 3.4%. At last the vertical dimension is identified for 15m.

The coupling effect of runway plates couldn't be neglected, and the effect reduces gradually while the dimensions of the pavement increase. The final dimension of the pavement is identified for 45m×15m.

Frequencies on Different Foundation Modulus. The changes of the foundation modulus are simulated according to the changes of the foundation spring stiffness. Fig. 4 shows the changes of the fundamental frequencies on different foundation modulus.

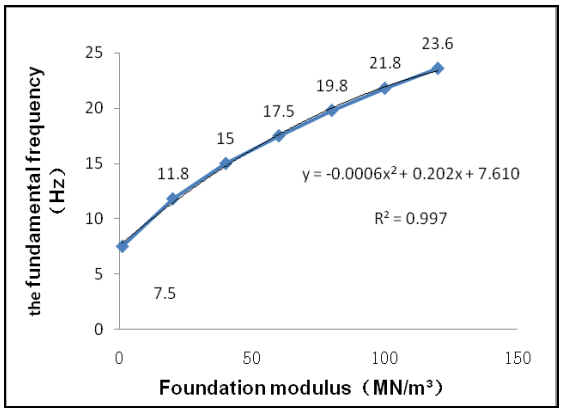


Fig. 4 Changes of the fundamental frequencies

Fig. 4 shows that the fundamental frequency increases when the foundation modulus increases. The fundamental frequencies range from 7.5Hz-23.6 Hz when the foundation modulus ranges from 0 MN/m³ to 120 MN/m³. The trend line shows that the relationship between fundamental frequency and foundation modulus is $y=-0.0006x^2+0.202x+7.610$, and the correlation coefficient is 0.997.

Conclusions

The fundamental frequency is analyzed by different dimensions and foundation modulus according to the finite element models. The appropriate conclusions are finally got:

The coupling effect of runway plates can not be neglected. The minimum area that affects the fundamental frequency of runway least is horizontal 45m and vertical 15m.

The fundamental frequency increases when the foundation modulus increases. The fundamental frequency ranges from 7.5Hz-23.6Hz according to two kinds of extreme conditions. The relationship between fundamental frequency and foundation modulus is $y=-0.0006x^2+0.202x+7.610$, and the correlation coefficient is 0.997.

Acknowledgements

This work is financially supported by the National Natural Science Foundation (51178456).

References

[1] Kantorovich L V, Krylov V I, Approximate Methods of Higher Analysis, Noordhoff Groningen, the Netherland, 1964.

[2] X. Zheng, S. Wang, Dynamic Response Analysis of Airport Pavement, Acta Aeronautica et Astronautica Sinica, 3 (1990) 35-38.

[3] Y. Zhong, F. Zhou, Y. Zhang, Vibration analysis of a thin plate on Winkler foundation with completely free boundary by Kantorovich method, Journal Of Vibration Shoct., 3 (2007) 53-57.

[4] C. Yang, L. Liu, Dynamic response analysis of cement concrete pavement under different vehicle speed, Journal of Hebei University of Technology, 3 (2010) 63-66.

[5] Z. Zhou, J. Ling, J. Yuan, 3D finite element analysis of the load transfer efficiency of joints of airport rigid pavement, China Civil Engineering Journal, 2 (2009) 22-25.

[6] J. Zhang, X. Zhang, A simple way of estimating load-carrying capacity of airport pavement, Journal of Northwestern Polytechnical University, 1 (2004) 19-22.

© (2012) Trans Tech Publications, Switzerland
doi:10.4028/www.scientific.net/AMM.238.282

S-transform Analysis on Pulsating Water Pressure Acting on the Stop Log Gate

Hu Huang[a], Xinyong Xu[b] and Jianwei Zhang[c]

College of Water Resources, North China University of Water Resources and Electric Power, Zhengzhou 450011, China

[a]huanghu@ncwu.edu.cn, [b]xuxinyong@ncwu.edu.cn, [c]zhangjianwei@ncwu.edu.cn

Keywords: pulsating water pressure; stop log gate; S-transform; time frequency transform; phase distribution.

Abstract. The vibration of sluice gate may lead to the damage of the hydraulic structure, based on the S-transform, the frequency and the phase distribution of the pulsating water pressure. The results show that as the water level increases, the frequency of the pulsating water pressure is small, the pulsating power acting on the bottom of the gate is decreasing, the components of frequency are rich, the power is wide, although the amplitude of frequency is decreasing, the whole power of pulsation is not changed; there is an obvious wave about the phase as the time changes, the phase distribution map is symmetry and periodically changes, and the velocity of wave may increase as the frequency increases.

Introduction

The vibration of sluice gate is a common problem in hydraulic engineering, which may cause the fatigue rupture and the deformation of metal constructions, sometimes, the vibration may lead to the damage of hydraulic structures. The main external cause of vibration is pulsating water pressure, so the study of the pulsating water pressure is very important.

The mechanism of pulsating water pressure is very complex. Many researches has been down, and different results are attained. The characteristics of pulsating water pressure can be described as the amplitude, spectrum and duration time, the amplitude can express the intension of the pulsating power, the spectrum can express the frequency distribution characteristics of the pulsating pressure, and the duration time can describe the pulsating power distribution during a segment time.

Signals of frequency field are consist of two components: amplitude and phase. Amplitude spectrum contains power information of each frequency component and phase spectrum contains relative location information of each frequency component.

Most of the result about the pulsating pressure just concentrate on amplitude characteristics and neglect the phase. S-transform is a new windowed fourier transform, its windowed function is an expansion Gaussian function which is changing as the frequency, so the resolution of s-transform depend on the frequency, S-transform keeps intimately in touch with Fourier transform, the core of which does not meet the compatibility condition. In this paper, S-transform program based on MATLAB was applied in analyzing of the pulsating water pressure, which can explain the distribution characteristics of pulsating pressure by considering the relation between time and frequency field. By researching on phase distribution patterns,basic characteristics comprehensively considering frequency and phase can be demonstrated.

S-transform Method

The thoughts of S-transform origin from the thoughts of windowed Fourier transform and the ideas that the window can be adjusted for wavelet transform. Beginning from the windowed Fourier transform, the basic principles are shown as follow:

For continuous time signal $x(t)$, it can be conducted such a windowed Fourier transform:

$$S(\tau, f, \sigma) = \int_{-\infty}^{+\infty} x(t) w(\tau - t, f) \exp(-i2\pi f t) dt \tag{1}$$

In the formula, τ is the center of the time window function, f is frequency, σ is regulatory factor, i is imaginary unit, $w(\tau\text{-}t, f)$ is window function.

$$w(\tau - t, f) = \frac{|f|}{\sqrt{2\pi}} \exp\left[\frac{-f^2(\tau - t)^2}{2}\right] \tag{2}$$

The windowed function is an alterable Gaussian windowed function, the width of the window changes with the frequency inversely and meets the normalization conditions:

$$\int_{-\infty}^{+\infty} w(\tau - t, f) d\tau = 1 \tag{3}$$

One dimension continuous S-transform of time signal $x(t)$ is:

$$x(t) = \int_{-\infty}^{+\infty}\int_{-\infty}^{+\infty} S(\tau, f, \sigma) \exp(i2\pi f t) d\tau df \tag{4}$$

By S-transform, frequency analysis of time sequence is conducted and always the disperse pattern of S-transform is adopted. The below demonstration is calculating formulas of one dimension disperse S-transform and one dimension generalized S-transform can be mimetically deduced.

First, the calculating formulas of one dimension continuous S-transform can be transformed as below, making it into the function of $X(t)$ which is Fourier transform of $x(t)$:

$$S(\tau, f) = \int_{-\infty}^{+\infty} x(t) w(\tau - t, f) \exp(-i2\pi f t) dt = \int_{-\infty}^{+\infty} X(\alpha + f) \exp(-\frac{2\pi^2\alpha^2}{f^2}) \exp(i2\pi\alpha\tau) d\alpha \tag{5}$$

$$(f \neq 0)$$

Second, signal $x(t)$ is sampled, disperse time sequence of $x[k\ T]$ (k=0,1,2,…,N-1) is attained, sampling interval is T, the number of total sampling spots is N, so disperse Fourier transform is:

$$X[\frac{n}{NT}] = \frac{1}{N}\sum_{k=0}^{N-1} x[kT] \exp(-\frac{i2\pi nk}{N}) \tag{6}$$

$$(n = 1, 2, \ldots, N-1)$$

In the formula (4), $f \rightarrow n/NT$ and $\tau \rightarrow kT$, using formula (5) in formula (4), one dimension disperse S-transform of disperse time sequence $x[k\ T]$ is attained:

$$S[kT, \frac{n}{NT}] = \sum_{m=0}^{N-1} X[\frac{m+n}{NT}] \exp(-\frac{2\pi^2 m^2}{n^2}) \exp(\frac{i2\pi mk}{N})$$

$$(m = 0,1, 2, \ldots, N-1) \tag{7}$$

Especially, when n=0 the S-transform definition of time sequence is:

$$S[kT, 0] = \frac{1}{N}\sum_{m=0}^{N-1} x[\frac{m}{NT}] \tag{8}$$

From the deducing process, the S-transform result of signal $x[kt]$ is a complex time frequency matrix (S matrix), column vectors contain time signals which are changing and distribution information of amplitude and phase for a certain moment for different frequency components, row vector contain time signal which reflects change and distribution of amplitude and phase in some frequency for different time.

Pulsating Pressure Experiment and Results

Basic Data of Model and Distribution of Measuring Points. The background of the model experiment is stop log gate of water intake in some hydropower station. The interaction of flow and gate structure is simulated and the model is designed by gravity similar criterion. Undistorted model

is adopted so the similarity of water flow regime and geometry boundary conditions is guaranteed. The model geometry scale λ_L is 30.8. The whole sluice gate is comprised of three components and according to the characteristics of sluice gate, measuring points are arranged on two sides: upstream and downstream of the sluice gate, in the central line. There are 8 measuring points in each component, totally 24 measuring points. The distribution of measuring points can be seen in Fig. 1. The relative location of sluice gate and water intake can be seen in Fig. 2.

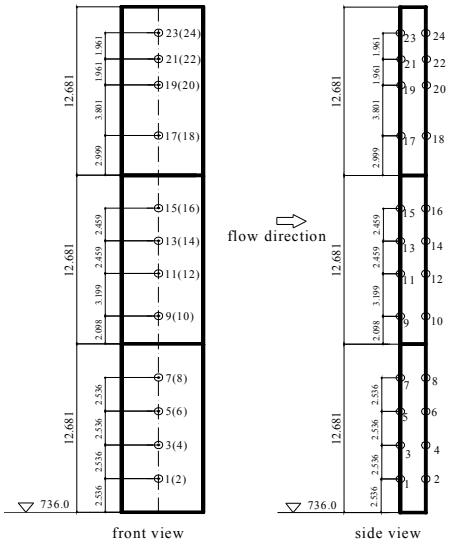


Fig. 1 Measuring Points Distribution

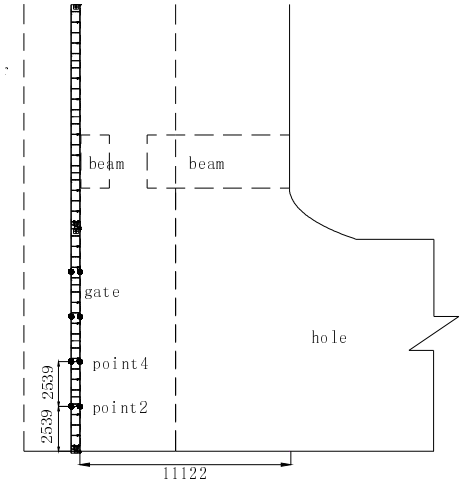


Fig. 2 Sluice gate and Water Intake Relative Location

Experiment Scheme. Based on characteristics of stop log gate and the confine of the reservoir characteristic water level, 3 schemes for the experiment are selected:

(1) In scheme 1, intake water from 3rd layer, 1 layer stop log gate retains water, the water level of the reservoir is 777.7m;

(2) In scheme 2, intake water from 2nd layer, 2 layers of stop log gates retain water, the water level of the reservoir is 790.4m;

(3) In scheme 3, intake water from 1st layer, 3 layers of stop log gate retain water, the water level of the reservoir is 803.0m;

Experiment Results. According to experiment results, the pulsating pressure of measuring point 2# has good representativeness. So measuring point 2#, which is on the downstream side of 1st stop log gate, is selected as research object. By measuring point 2#, when intake water the pulsating water pressure can be demonstrated. Measuring point 2# pulsating pressure time history curves of different schemes are shown in Fig. 3. The values in the figure are all converted into values of prototype by gravity similar law.

Analysis of Pulsating Pressure Signal Based on S-transform

Pulsating Pressure Signal Frequency Analysis. By S-transform, time and frequency analysis of pulsating pressure signal for different schemes are conducted and time domain and frequency distribution can be attained. Fig. 4~ 6 shows the change of pulsating pressure amplitude with the variation of time and frequency. The brightness of the figure reflects the power (amplitude) of corresponding time and frequency, higher brightness means more power and the time and frequency of pulsating represent distribution laws of the pulsating power. After S-transform, better time frequency expression for pulsating signal can be attained and time frequency resolution changes as the variation of frequency. Time domain and frequency are directly connected, the pulsating signal distributions of time domain and frequency are compared and the pulsating characteristics are revealed.

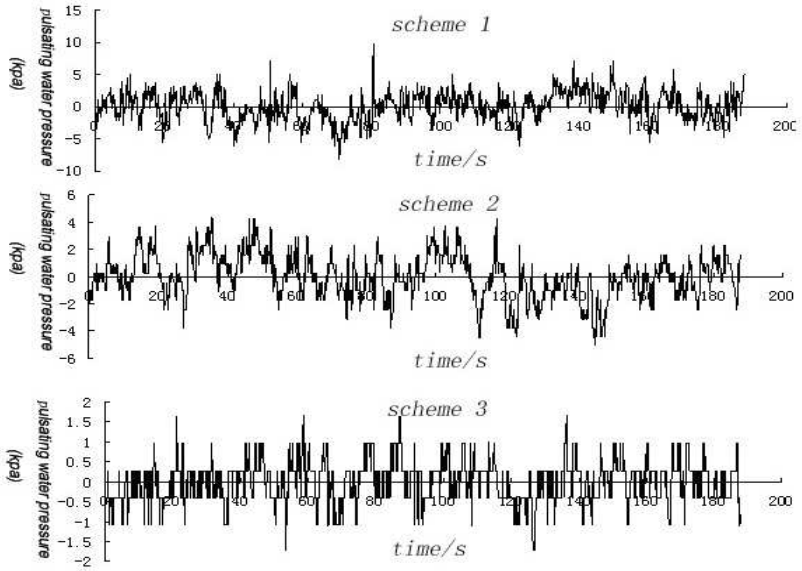


Fig. 3 Measuring point 2 # pulsating water pressure time history for 3 different schemes

Based on pulsating pressure signals S-transform analysis for different water intake schemes, it can be concluded that for each scheme, the pulsating pressure signal dominant frequency is smaller. For scheme 1, pulsating pressure dominant frequency is obvious, the maximum dominant frequency is 0.35Hz, the frequency is broad and the happening time is about 50s.

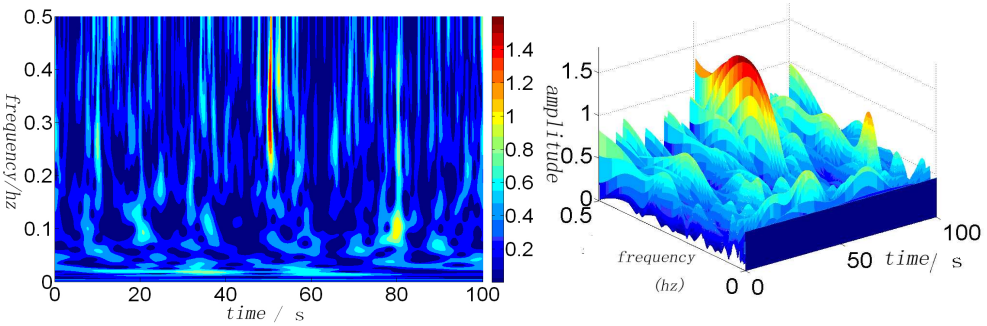


Fig. 4 Pulsating signal S-transform results of measuring points for scheme 1

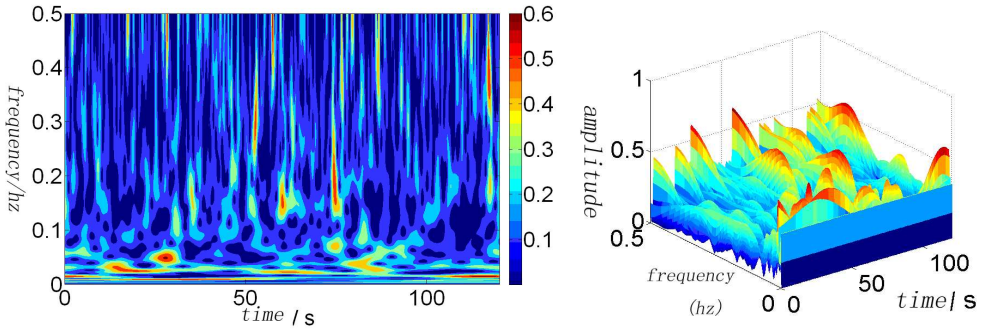


Fig. 5 Pulsating signal S-transform results of measuring points for scheme 2

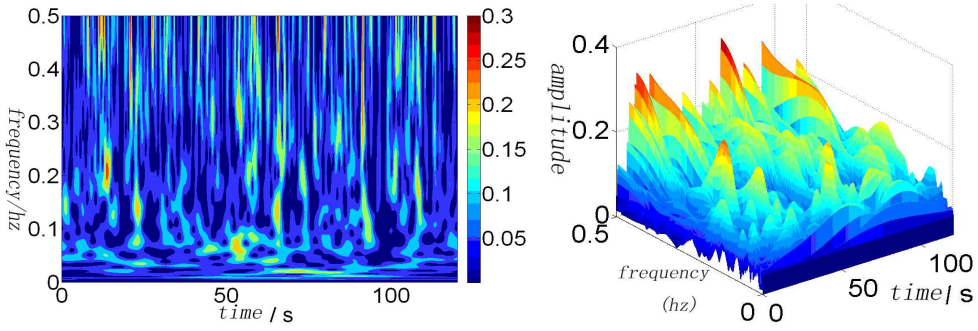


Fig. 6 Pulsating signal S-transform results of measuring points for scheme 3

According to Fig. 4 for time frequency distribution, the amplitude of dominant frequency is obviously bigger than the amplitude of the frequencies for other segments. The dominant frequency of the whole vibration signals is centralized so the pulsating power is large and centralized. Pulsating pressure dominant frequency for scheme 2 is relatively dispersive, the dominant frequency decreases, the frequency for maximum amplitude is 0.05 Hz, the happening time is about 30s. The frequency varies distinctly and after 50s, four obvious dominant frequencies bands occur, in which the maximum is 0.4Hz and it happens after 11.5s. According to the distribution and frequency in Fig. 5, the distribution of pulsating dominant frequencies is broad but the amplitude of corresponding dominant frequencies is small. So the distribution of pulsating power is broad. Pulsating pressure frequency band for scheme 3 is distributed more broadly but the distribution of dominant frequency band is not obvious. The dominant frequency is mainly about 0.2Hz. From Fig. 6 for time frequency distribution, the extreme points for pulsating pressure increase but the amplitude decreases. The frequency of pulsating water pressure has a fluctuation change with time and the frequencies and different periods vary largely. It can be seen that distribution of pulsating power is not continuous and centrally distributed.

From the analysis results, the pulsating pressure frequency is small and the maximum frequency is within 0.5Hz. As the height of water intake increases, pulsating pressure power is gradually dispersed. The components of pulsating signal are rich and power is broadly distributed. Though the amplitude decreases but pulsating pressure power is not reduced.

Pulsating Pressure Signal Phase Analysis. For the integral signal, the spectrum of signal is composed of amplitude spectrum and phase spectrum so phase characteristics are also important. In order to thoroughly understand pulsating pressure signal information, the amplitude spectrum and phase spectrum should be both considered. According to S-transform theory, through self-compiling program, S-transform of pulsating pressure is attained and joint time frequency analysis can be conducted. Local phase characteristics of pulsating pressure can be acquired.

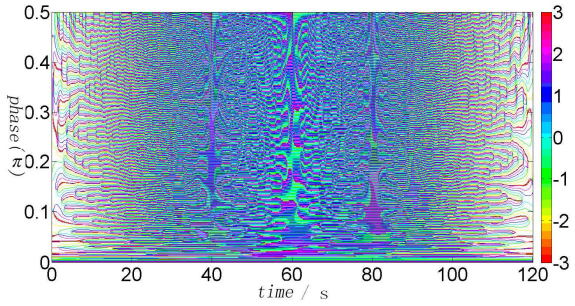


Fig. 7 Pulsating signal phase for scheme 1

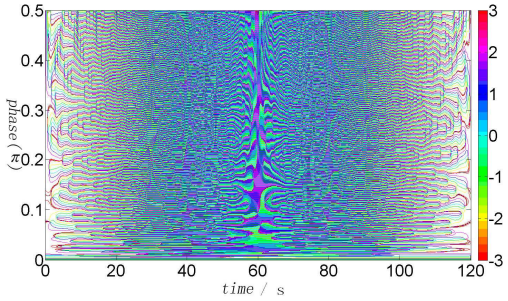


Fig. 8 Pulsating signal phase for scheme 2

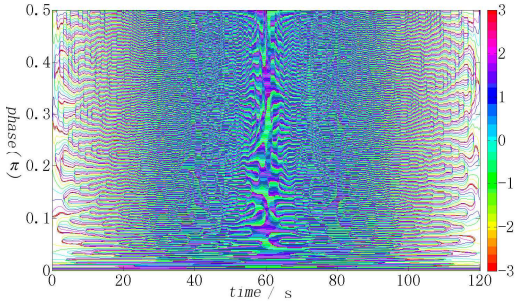


Fig. 9 Measuring points pulsating signal phase for scheme 3

Fig 7~ 9 shows local phase characteristics of measuring points for different schemes (sine signal phase for different frequencies). It can be seen that different measuring points in different schemes have different phase distribution characteristics. On the whole, phase mainly range from $-\pi$ to π. Phase distribution obviously fluctuates as changing of time. As viewed from time, phase is symmetrically distributed and can be divided into 4 time segments: starting time segment, medium time segment (two sides of symmetrical axis), symmetrical axis center time segment, ending time segment. In starting time segment and ending time segment, the vibrating of each frequency is the most slowly. The symmetrical axis center time segment is a little faster and the medium time

segment is the fastest. Phase fluctuation changes as the frequency periodically. The periodicity of symmetrical axis center time segment is not distinct and phase vibrating velocity increases as the increasing of frequency. In inner sides of starting time segment and ending time segment, there is phase dense distribution region and phase changes fast. Under the same frequency difference, the phase difference is large. As viewed from local portion, the phase in different time segments differs as changing of time and frequency. For starting time segment and ending time segment, the phase distribution is relatively disperse, changing gradient of phase is large, for coinstantaneous equal frequency difference, the phase difference is large. For symmetrical axis center time segment, the changing gradient of the phase is small as frequency changes. In a certain range of frequency, the phases are basically identical and exhibit good texture. In other time segments, this phenomenon does not exist. For phase dense distribution region, phase changes fast and exhibits obvious volatility.

Conclusions

By use of S-transform, the information hidden in pulsating pressure signal can be attained, frequency, power, and phase distribution characteristics are understood. For further researching on pulsating pressure mechanism, a certain basis is supported.

According to S-transform results, pulsating pressure frequency is small, belonging to low frequency pulsatile. As the changing of time, frequency of pulsating water pressure has distinct variation and frequencies of different time have obvious differences. It can be concluded that the pulsating power distribution is centralized, not continuous. As the water intake height increases, the frequency components of pulsating signal become richer and power distribution frequency is broad. Pulsating pressure power for a certain characteristic frequency gradually reduces; as time is changing, phase distribution express distinct volatility and as viewed from, time it is symmetrically distributed. Phase fluctuating changes periodically as frequency and phase fluctuating velocity has an increasing tendency as frequency increases.

Reference:

[1] R.G. Stockwell, L. Mansinaha, R.P. Lowe, Localization of the complex spectrum the S-transform, IEEE Transactions on Signa Processing, 44 (1996) 998-1001

[2] R.G. Stockwell, A basis for efficient representation of the S-transform, Digital Signl Processing, 17 (2007) 371-393.

[3] K.A. Jones, P. Bernice, C. David, et al, S-transform time-frequency analysis of P300 reveals deficits in individuals diagnosed with alcoholism, Clinical Neurophysiology, 117 (2006) 2128-2143.

[4] W. Qu, S. Liu, J. Wang, et al, HHT analysis of stochastic fluctuant pressure for flow-induced vibration in radial gate, Journal of Wuhan University of Technology, 28 (2006) 68-71.

[5] Y. Lei, L. Liu, X. Wei, et al, Analysis on determining maximum amplitude of model fluctuation pressure on training stoplogs gate with varying elevation intake, Journal of Hydrodynamics (A) 22 (2007) 273-277.

[6] X. Peng, H. Guo, R. Zhang, Wavelet analysis on flow fluctuating pressure acting on plunge pool slope, Journal of Hydraulic Engineering, 8 (2003) 26-31.

[7] G. Li, Z. Shen, C. Zhou, et al, An experimental study on impact pressure characteristics of self-resonant cavitating jets, Journal of Hydrodynamics (A), 9 (2003) 570-575.

[8] J. Zhang, J. Lian, H. Wang, Progress of research on backward problems of hydraulic structure dynamics induced by flow exciation, Journal of Hydraulic Engineering, 40 (2009) 1326-1322.

[9] S. Zhang, H. Huang, J. Niu, et al, Pulsating water pressure features of a stop log gate based on S-transform, Journal of Vibration and Shock, 30 (2011) 145-147.

© (2012) Trans Tech Publications, Switzerland
doi:10.4028/www.scientific.net/AMM.238.288

A Multiobjective Decision Framework for River Basin Management

Xueqing Zhang [1,a], Hui Gao [1,2,b] and Xiang Yu [1,c]

[1]Department of Civil and Environmental Engineering, The Hong Kong University of Science and Technology, Hong Kong, China

[2]Department of Engineering Economics and Management, Hohai University, Nanjing, China

[a]zhangxq@ust.hk, [b]cekohii@ust.hk, [c]xyuac@ust.hk

Keywords: river basin network, flood management, water quality management, water resources management, multi-objective decision.

Abstract. A decision support system (DSS) for the purpose of obtaining optimal operation strategies of various hydraulic structures is needed to achieve effective and efficient management of a river basin network. The core of such a DSS is a multiobjective decision model that can optimally schedule operation strategies of different hydraulic structures to fulfill the requirements on flood management, protection of water quality, and utilization of water resources. In this paper, we develop a framework of this multiobjective decision model to discuss its decision horizon, rules, variables, objectives, constraints and solving algorithm. This framework can be used to further establish the DSS for a river basin network.

Introduction

The effective and efficient management of a river basin network is important to the regions' social sustainability, economic development and environmental protection. Commonly, the major management works of a river basin network are flood management [1, 2], water quality management [3, 4] and water resources management [5, 6]. To fulfill these management works, it is necessary to develop a computer-based decision support system (DSS) to simulate the changes of hydrology, hydrodynamics and water quality over time and to obtain optimal operation strategies of different hydraulic structures (e.g., reservoirs, dams, weirs, sluice gates and pumping stations) in the network.

DSSs have been developed since the 1970s. However, the development of a success DSS for a river basin network is not promised due to the complexity of involved hydraulic structures, uncertainties in estimating hydrological and hydrodynamic variables, and stakeholders in the decision process. The simulation models usually are nondeterministic and decision models are nonlinear. Many computerized decision-support tools have been developed to help solve these complicated problems. For example, the genetic algorithm was introduced by U.S. Department of Agriculture's Soil and Water Assessment Tool for single objective evaluations, and a Strength Pareto Evolutionary Algorithm has been integrated with SWAT for multiobjective optimization [7]. Furthermore, Muleta and Nicklow improved it with the artificial neural network using a hybrid of evolutionary programming and the back propagation algorithms [8]. The application of the artificial neural network in flood control can be found in Shim et al. [2].

A DSS for a river basin network is a complex system involving many components to fulfill various functions, such as the flood forecasting, water quality investigation, and water resources allocation [9]. The foundation of a success DSS is the knowledge of hydrology, hydrodynamics, and hydraulic structures of the river basin network. In this paper, we first briefly introduce the development of an integrated hydrology-hydrodynamics-water quality model. Then, the framework of a multiobjective decision model for a river basin network is discussed. The further development of a DSS is presented in the following section.

Integrated Hydrology-Hydrodynamics-Water Quality Model

Modeling the changes of hydrology, hydrodynamics, and water quality over time is the basis to understand the operation conditions of a river basin network. For example, a distributed hydrology model with the grid as the most basic simulation unit can be formulated to account for varied

rainfall-runoff generation processes in different meteorological and environmental conditions, such that the hydrological boundaries of the river basin network can be known for the operation of hydraulic structures [10]. The dynamic simulations with deterministic or stochastic processes on these correlated systems can be integrated into a multi-dimensional multi-variable model to evaluate the relationship of these correlated systems and to further analyze major management works of the river basin network. Based on geographic information system and remote sensing system, spatial analysis can be done for (1) flood forecasting and control; (2) water quality investigation; and (3) water resources allocation [2, 11]. The developed spatial database and integrated hydrology-hydrodynamics-water quality model provide the initial inputs of the decision model.

Framework of a Multiobjective Optimization Model

The framework of a multiobjective decision model for a river basin network is shown in Fig. 1.

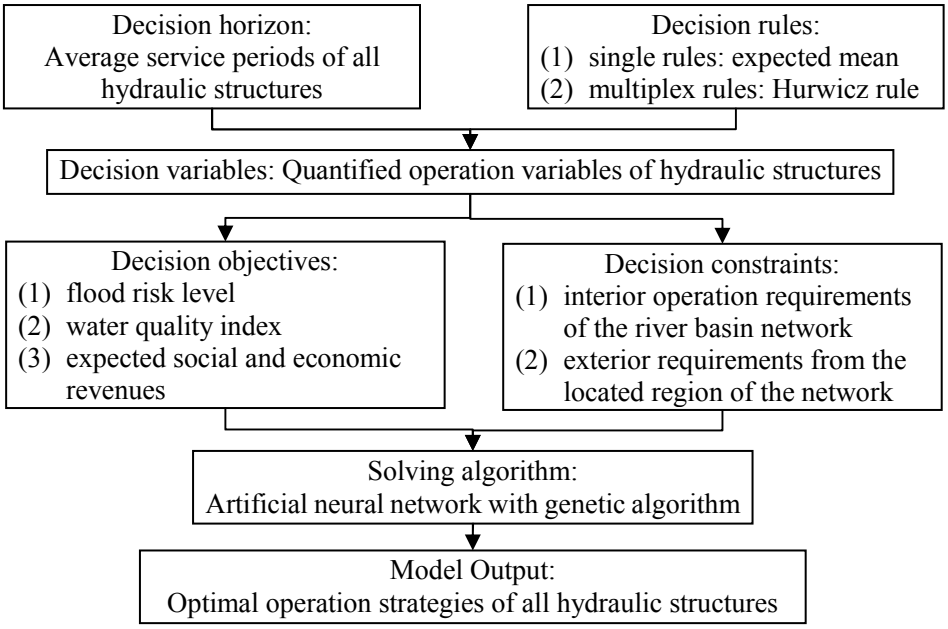


Fig. 1 Framework of a multiobjective decision model for a river basin network

Decision Horizon and Decision Rule. The decision horizon usually is the average service periods of all hydraulic structures of a river basin network, i.e., the average life cycle of a river basin network. The decision rule is the criteria to justify the decision objectives. The commonly used decision rules are the expected average or discounted values of decision objectives, e.g., the life-cycle operation costs of a reservoir. Considering some special needs in measuring decision objectives, some statistical values (e.g. variance and covariance) and multiplex rules (e.g., max min rule, max max rule, and Hurwicz rule) are also commonly used [12]. For example, when risks of decisions are concerned, it is better to use variance rule instead of mean rule. Also, when uncertainties of one or several parameters are considered in a Robust decision, the max min rule can be used if the uncertainties are negative to the objective while the max rule is used if the uncertainties are positive to the objective. The Hurwicz rule can allow the attitude of decision makers on the uncertainties (i.e., judgments on whether uncertainties are negative or positive) to be involved in the decision [13].

Decision Variables, Objectives and Constraints. The decision variables are operation strategies of various hydraulic structures over the decision horizon. These operation strategies can be embodied with some quantitative variables. For example, the reservoir operation strategy can be quantified as the storage volume and target release volume [6]. An operation strategy influences the performance of a river basin network on various decision objectives which, in this paper, are described as (1) flood risk level, (2) water quality index, and (3) expected social and economic revenues. The flood risk level is expressed as the product of the probability and consequence of flood inundation. The water quality index is described as the combination of several water quality variables (e.g. organic carbon,

ammonia nitrogen, nitrate chlorine, organic/inorganic phosphorus, dissolved oxygen and pH value). The expected social revenues are the industrial/agricultural/commercial/residential incomes of located region of the river basin network due to water resources allocation. The expected economic revenues are the life cycle operation costs and operation incomes of the river basin network, such as the hydropower incomes. The multiobjective decision model can be written as follows:

$$\text{Min } \{F(t), Q(t), -R_1(t), -R_2(t)\} \quad (1)$$

Where $F(t)$ = the flood risk level at time t; $Q(t)$ = the water quality index at time t; $R_1(t)$ = the social revenues at time t; and $R_2(t)$ = the economic revenues at time t. The first two objectives should be minimized and the revenues should be maximized. The objective function of each single objective can be formulated by different programming methods (e.g., linear programming, dynamic programming and quadratic programming) [4]. The decision constraints are expressed as the interior requirements on the operation of the river basin network (e.g., reservoir capacity, sluice discharge and operation budgets) and exterior requirements from the located region of the river basin network (e.g., industrial demands of water, irrigation needs and flood protection standards).

Solving Algorithm of Multiobjective Decision. The multiobjective decision is to find tradeoff solutions between competing objectives. The Pareto optimal solutions can be obtained by many methods, such as the traditional aggregation method which transforms the multiobjective problem into single objective and the minimum distance method which finds the minimum distance between the Pareto optima and the target values of each objective [14]. However, these methods need multiple search runs and may not find the global Pareto optimal solution. This makes them unsuitable for solving multiobjective decision of a river basin network which has large decision spaces. The artificial neural network, an adaptive method learning knowledge from a training algorithm, is more feasible to find the global Pareto optimal solution for the multiobjective decision of a river basin network [2, 8]. The genetic algorithm can be used as the training algorithm to design the hierarchy and weights of the artificial neural network [15].

Development of a Decision Support System

A properly designed DSS of a river basin network is an interactively computer-based information system with user-friendly interfaces. The useful information, e.g., historical rainfall data, topography, pollutant distribution, are compiled and stored in a spatial database to help decision makers identify and solve problems and make decisions. The changes of hydrology, hydrodynamics and water quality of the river basin network are simulated over time and all impacting factors in these changing processes are parameterized in the DSS. In terms of the simulation and parameterization processes, a multi-dimensional multi-variable model integrating hydrology, hydrodynamics and water quality is established in the DSS to provide initial inputs of a multiobjective decision model formulated to fulfill the major management objectives of the river basin network. Then, based on the sensitivity analyses and adaptive control methods, the obtained operation strategies of different hydraulic structures from the decision model can dynamically feed back to the integrated hydrology-hydrodynamics-water quality model and the multiobjective decision model to evaluate the management performance of strategies and to further improve the optimal operation strategies.

Conclusions

In this paper, we develop a multiobjective decision framework for a DSS of a river basin network to optimally schedule operation strategies of different hydraulic structures and to effectively fulfill the requirements on flood management, water quality management and water resources management. The decision horizon, rules, variables, objectives, constraints and solving algorithm of the multiobjective decision model are discussed for further development of a DSS.

Acknowledgment

This study is sponsored by the Public Benefit Special Research Fund of the Ministry of Water Resources of China (Project Number: 201201017).

References

[1] S. Ahmad, S.P. Simonovic, An intelligent decision support system for management of floods, Water Resour. Manage., 20 (2006) 391-410.

[2] K. Shim, D.G. Fontane, J.W. Labadie, Spatial decision support system for integrated river basin flood control, J. Water Resour. Plann. and Manage., 128 (2002) 190-201.

[3] S. Murray, M. Ghazali, E.A. McBean, Real-time water quality monitoring: assessment of multisensor data using Bayesian belief networks, J. Water Resour. Plann. and Manage., 138 (2012) 63-70.

[4] K.S. Westphal, R.M. Vogel, P. Kirshen, Steven C. Chapra, Decision support system for adaptive water supply management, J. Water Resour. Plann. and Manage., 129 (2003) 165-177.

[5] J. Mysiak, C. Giupponi, P. Rosato, Towards the development of a decision support system for water resource management, Environmental Modelling & Software, 20 (2005) 203-214.

[6] D. Koutsoyiannis, G. Karavokiros, A. Efstratiadis, N. Mamassis, A. Koukouvinos, A. Christofides, A decision support system for the management of the water resource system of Athens, Physics and Chemistry of the Earth, 28 (2003) 599-609.

[7] J.G. Arnold, R. Srinivasan, R.S. Muttah, J.R. Williams, Large-area hydrologic modeling and assessment. I: Model development, J. Am. Water Resour. Assoc., 34 (1998), 73-89.

[8] M.K. Muleta, J.W. Nicklow, Decision support for watershed management using evolutionary algorithms, J. Water Resour. Plann. and Manage., 131 (2005) 35-44.

[9] R. Q. Grafton, K. Hussey, Water Resources Planning and Management**,** Cambridge University Press, Cambridge, 2011.

[10] L. Feyen, R. Vazquez, K. Christiaens, O. Sels, J. Feyen, Application of a distributed physically-based hydrological model to a medium size catchment, Hydrology and Earth System Sciences, 4 (2000) 47-63.

[11] C. K. Makropoulos, D. Butle, C. Maksimovic, Fuzzy logic spatial decision support system for urban water management, J. Water Resour. Plann. and Manage., 129 (2003) 69-77.

[12] Y. Xu and Y. Tung, Decision rules for water resources management under uncertainty, J. Water Resour. Plann. and Manage., 135 (2009) 149-159.

[13] C. Revelle, E. Whitlatch, J. Wright, Civil and Environmental Systems Engineering, Prentice Hall, Upper Saddle River, 1997.

[14] H. Gao, X. Zhang, Developing a road maintenance optimization model considering social costs: submitted to Computer-Aided Civil and Infrastructure Engineering, (2011).

[15] M.K. Muleta, J.W. Nicklow, Evolutionary algorithms for multiobjective evaluation of watershed management decisions, J. Hydroinformatics, 4 (2002) 83-97.

© (2012) Trans Tech Publications, Switzerland
doi:10.4028/www.scientific.net/AMM.238.292

Finite Element Analysis of Complicated Sedimentation Basin

Xiaoyan Zhang[1, a], Xuchao Liu[2, b], Shunqun Yang[2, c] and Lili Dong[2, d]

[1]North China University of Water Resources and Electric Power, Zhengzhou 450011, China

[2]Yellow River Engineering Consulting Co.Ltd., Zhengzhou 450003, China

[a]zxyanzi@ncwu.edu.cn, [b]56406923@qq.com, [c]22803816@ qq.com, [d]54024690@qq.com

Keywords: complicated sedimentation basin; 3D FEM; static force; dynamic force; spectrum.

Abstract. Due to the larger workflow, more complex foundation and special structure and with the 8° design seismic intensity, it is necessary to analyze this sedimentation basin in the static and dynamic by 3D finite element method. This paper describes the structural model and the selected parameters for calculation of static and dynamic properties, and states the stress analysis results under the various conditions.

Introduction

The sedimentation basin is one part of the large power station located in South America. Its design flow is 222m^3/s, and the comparative complex foundation with the cover layer thickness of 70m is located in the staggered parts between covers and bedrock, 8 degrees of seismic design intensity in the engineering region. The sedimentation basin is divided into six chambers, and there are three jointed parts which consist of two chambers in the every part and is divided into upper and lower parts, and the purpose of the upper chamber is to diverse water and settle sand, while the lower corridors is designed to wash the settled sand [1]. Therefore, it is necessary to conduct some analysis for complicated sedimentation basin in order to study the stress and displacement of various structure parts, foundation settlement, and the optimization of sedimentation basin body.

Calculation Model and Calculation Scheme

Calculation Model. The longitudinal length of sedimentation basin is 120m, which consists of four segments divided by settlement joint and the length of every segment is 30m. As to the horizontal layout, the sedimentation basin is divided into six chambers, and there are three segments which consist of two chambers in each segment with relatively independent operate functions, single-cell box clear width 13m, wall thickness 1.5m. The general arrangement of sedimentation basin is shown in Fig. 1. Therefore, the calculation model with 30m longitudinal width is selected. Calculation model includes the sedimentation basin structure and foundation (about three times as high structure). Fixed constraints are adopted at the bottom of the foundation and the lateral sides of foundation are constraint along the normal direction. The coordinate system of the calculation model is set as follows: the x direction is perpendicular to the direction of the sedimentation basin, and the *y* direction is the direction of gravity acceleration, then the *z* direction is along the flow direction. The hexahedral elements are used during the calculation.

Calculation Parameter. The selected material parameters of the model are shown in Table 1, the strength grade of concrete of the basin structure is C30 with density of 2500kg/m^3.

Table 1 Material Parameters

Material Partition	Static elasticity modulus	Poisson's ratio	Thermal conductivity (J/(m·h·^{o}C))	Linear expansion coefficient (1/^{o}C)
Sedimentation basin structure	30.0GPa	0.167	10600	1×10^{-5}
Silty soil	14.0MPa	0.33		
Sand and Gravel	33.0MPa	0.26		
Backfilled Carbide Slag	70.0MPa	0.26		

Calculation Loads. The main calculated loads are as follows: (1) concrete weight of the sedimentation basin (2) the exterior and interior hydrostatic pressure of the sedimentation basin (3) the earth pressure generated by backfilled carbide slag (4) the hydrodynamic pressure (5) seismic load (seismic intensity 8 degrees, the design intensity 9 degrees) [2]. The concrete weight is added according to inertia loads, then the external and internal hydrostatic pressure is exerted according to the water level, and earth pressure is considered in terms of the internal friction angle of 30 degrees ,and the vibration of water pressure is not only added to the finite element model in the form of a mass element but also the role of the force direction is considered, and earthquake inertia force is simulated according to the response spectrum method recommended by specifications accordingly [3].

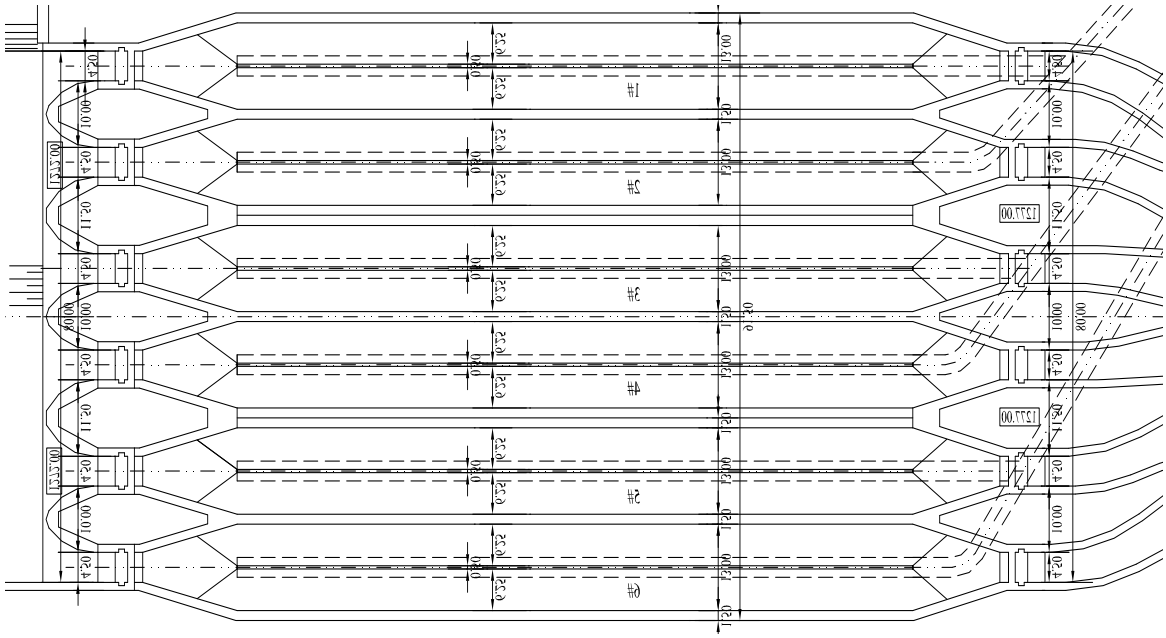


Fig. 1 Layout of Sedimentation basin

Load Conditions. The calculation conditions and load combinations of the static and dynamic analysis are shown in Table 2.

Finite Element Static Analysis

Structural Model Impact Analysis of the Bar. It is necessary to the reasonability of the structural arrangement and the better structure form

Table 2 The calculation conditions and load combinations

Calculation Conditions				Load Combinations
Static Analysis	Basic Combinations	Design 1	the whole sedimentation basin is filled to the operational water level, groundwater level 1265.71m	①+②+③
		Design 2	the single chamber is filled to the operational water level, groundwater level 1265.62m	①+②+③
	Special Combinations	Check 1	the whole sedimentation basin is filled to the operational water level, groundwater level 1261.81m	① +②+③
		Maintenance1	the whole sedimentation basin is no water, groundwater level 1267.20m	①+②+③
Dynamic Analysis	Earthquake Conditions	Earthquake 1	the whole sedimentation basin is filled to the operational water level, groundwater level 1265.71m	①+②+③+④+⑤
		Earthquake 2	the single chamber is filled to the operational water level, groundwater level 1265.62m	① +②+③+④+⑤

In order to improve the load conditions of the structure due to the relatively special complex structure and large horizontal and vertical span, the stress state analysis of both the model with bar set on the top of the sedimentation basin and the model without bar are analyzed under the normal operation conditions (the whole sedimentation basin is filled to the operational water level). Models are shown in Fig. 2 and Fig. 3. The results of analysis are as follows:

(1) Comparison of Structural Displacement. In the model without bar, the horizontal displacement of the structure is about 17mm, and vertical displacement is about 160mm. After the bars are set in the model, the great impact of the structural displacement (maximum lateral displacement is reduced to about 3mm) because of the bar limit, while the vertical displacement is affected less. This is in line with the general law.

(2) Comparison of Structural Stress. As to the model without bar, the maximum horizontal stress appears at the rim of the sediment hole and the value is about 5.53MPa, but a large range of tensile stress zone lies in the interior of the side slope board and the maximum value is approximate 3.77MPa, and the maximum axial tensile stress is around 4.65MPa. The maximum of the vertical stress appears at the interior of the bottom plate, and the value is about 2.72MPa, in the meanwhile, there is also vertical tensile stress zone at the interior of the side slopes board and the maximum value is around 1.25MPa. The maximum longitudinal stress zone also appears in the interior of the side slopes board and the maximum is about 1.0MPa. Therefore, the interior of the side slope board is the weakest parts in terms of the structural stress state in the model without bar.

As to the model with bar, the maximum horizontal stress appears at the bar and the value is about 4.59MPa. In addition to the stress of the bar, the maximum transverse tensile stress is also at the rim of the sediment hole, but the maximum tensile stress value was significantly reduced and the value is about 1.8MPa. The maximum of the vertical stress appears in the lateral side walls and the value is about 2.27MPa.

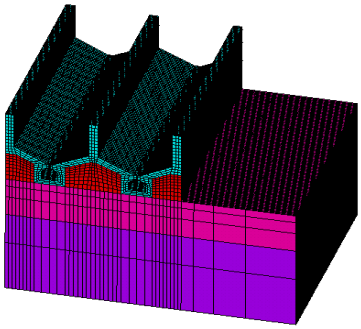


Fig. 2 The Model without Bar

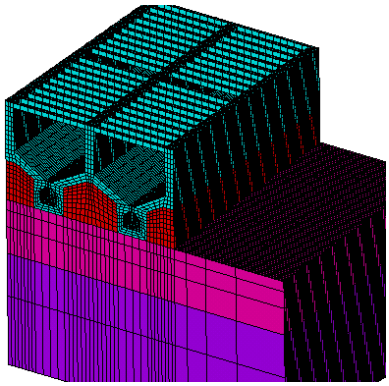


Fig. 3 The Model with Bar

(3) Comparison of Structural Reinforcement. The control section of the model without bar is in the slope board, while the control section of the model with bar is at the lower part of vertical section of the structure. According to the comparison of the stress reinforcement for the two control section, structure reinforcement volume of the model without bar is 6923mm^2 , while the amount of reinforcement for the model with bar is 3059mm^2 [4].

According to Comprehensive comparative analysis, the model with bar is more favorable in terms of comparison of the stress state of the structure or the comparison of the maximum amount of reinforcement bar. Furthermore it is recommended that additional bar should be set at the top of the sedimentation basin to improve the stress state of the structure.

Analysis of the Static Calculation Result. The static analysis is based on the model of the bar set on the top of the sedimentation basin, and model is shown in Fig 3. By this way, the conditions of design I, design II, check I, and check II are analyzed in static calculation respectively.

(1) Structural Displacement. Due to the differential settlement of foundation caused by the single chamber full of water in design II, the maximum lateral displacement δ_x is about 4.13cm, and the vertical displacement δ_y of the left and right chambers are 15cm and 13cm respectively. And because of the foundation settlement, the maximum vertical displacement δ_y of the sedimentation basin is about 20cm, which is appeared in the check I.

The extreme values of lateral and vertical displacement in each condition are summarized in Table 3, and the distributions of the lateral and vertical displacement are shown in Fig. 4 and Fig. 5 respectively.

(2) Structural Stress. According to the calculation result, the extreme values of stress in each condition are gathered in Table 4, and the distribution s of the lateral and vertical stress are shown in Fig. 6, Fig. 7 and Fig. 8 respectively.

The statistic states that, the maximum values, include the lateral tension stress σ_x, vertical tension stress σ_y and longitudinal tension stress σ_z, are all happened in the check I. The extreme value of lateral tension stress σ_x in each condition, are all occurred at the upper part of the both ends of the bar, which is 5.38MPa, meanwhile, the tension stress also took place at the bottom of the midspan and around the sediment hole, and the extreme value of the extension stress around sediment hole is 3.24MPa. The longitudinal tension stress σ_z in each condition, are all taken place around the sediment hole or at the inner side of the slope board or at the under part of the outside of the sidewall, which is 0.8MPa, and it also found at the bar and around the sediment hole. The extreme value of the principle tension stresses in each condition is always occurred at the under part of the outside of the sidewall, which is 4.35MPa, the principle tension stress also occurred around the sediment hole and at the bar, sometime it is up to 5.46MPa.

Table 3 The summary of the extreme displacement of the sedimentation basin (cm)

Items \ Conditions	Design I	Design II	Check I	Service II
Lateral dis δ_x	0.04	4.13	3	0
Vertical dis δ_y	17	15	20	

Table 4 The summary of the extreme stress of the sedimentation basin (MPa)

Items \ Conditions	Design I	Design II	Check I	Service II
Lateral tension stress σ_x	4.59	4.01	5.38	1.98
Vertical Tension stress σ_y	2.27	2.75	3.24	
Longitudinal tension stress σ_z	0.6	0.54	0.8	
Principal stress σ_1	2.27	2.84	5.46	

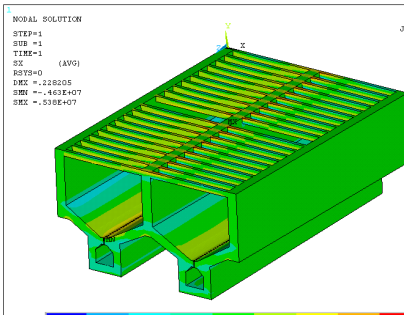


Fig. 4 Lateral displacement δ_x(check I)

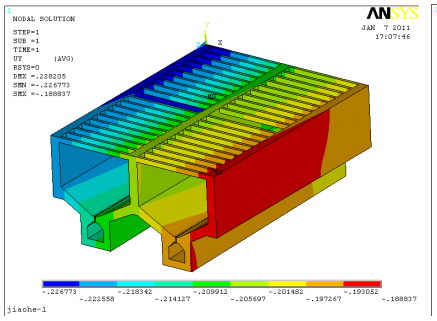


Fig. 5 Vertical displacementδ_y (check I)

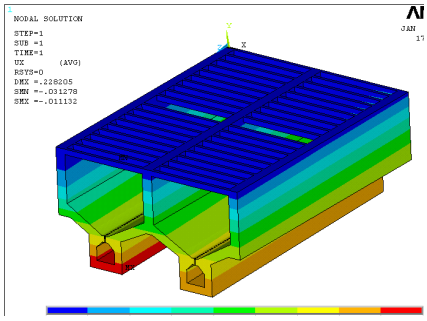


Fig. 6 Lateral stress σ_x (check I)

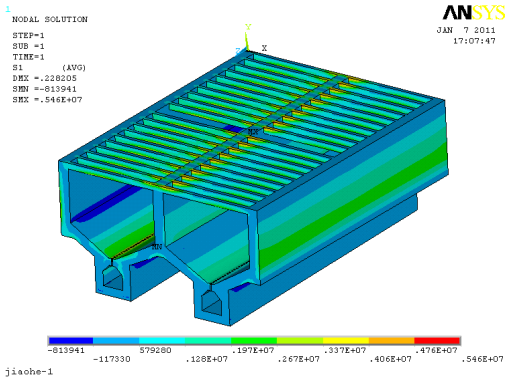


Fig. 7 Vertical stress σ_y (check I)

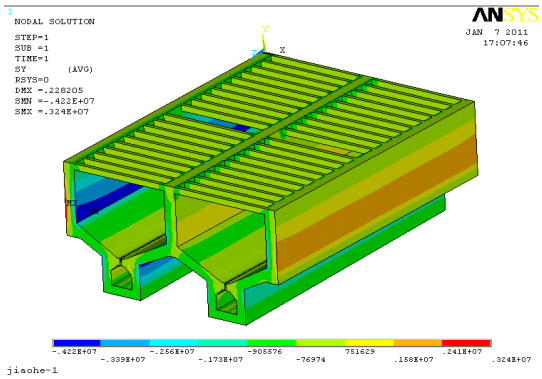


Fig. 8 Principal σ_1 (check I)

Dynamic Analysis

Calculation Method. Seismic effect is calculated in method of the Response Spectrum in dynamic analysis, the natural vibration period and corresponding vibration mode of the structure is analyzed, then the maximum dynamic response of each vibration mode are solved directly in the standard design response spectrum recommended in the standard.

Select Parameter. Spectral analysis applied the standard spectrum in accordance with the standard, because the design intensity is 8^o, the corresponding maximum representative value β_{max} of design response spectrum is 2.25, and the site classification is belonged to 2, therefore the characteristic period T_g of the site is equal to 0.3s; the value of horizontal earthquake acceleration α_h=0.2g, and the vertical earthquake acceleration α_v =2/3α_h. During the seismic effects of three direct are analyzed, the horizontal seismic effect is combined with the vertical seismic effect multiplied with the coefficient 0.5.

Modal Analysis. According to the method of 3d finite element dynamic analysis, through the dynamic finite element of the sedimentation basin, the self-vibration characteristic of three conditions are calculated respectively, which are empty, full of water in single chamber and full of water of 3 chambers, at the same time, the participation factor and mass of each modal are analyzed as follows:

(1) Due to the interaction of the chamber and the inside water has impact on the natural frequency of vibration, therefore, the inside water-chamber structure interaction should be considered when the dynamic characteristic and response of sedimentation basin is analyzed.

(2) According to the analysis of the vibration mode and participation factor, it is proved that the vibration modes of the structure in all directions are all controlled by the low order type of vibration.

(3) According to the calculation results of the self-vibration characteristic for each condition and the calculation results analysis of the participation factor and mass of each modal, , it has met the accuracy requirement if the order is 10 in the calculation of the Response Spectrum.

Dynamic Analysis Results. All the three chambers full of water and single chamber full of water encounter with the earthquake (earthquake I and II) are analyzed in the dynamic analysis. According to the calculation results, the extreme values of dynamic stress are summarized in Table 5. The stress distributions are shown in the Fig. 9, Fig. 10 and Fig. 11.

The calculation results show that, the single chamber full of water encountered with earthquake (earthquake II) is the control condition, the extreme values of the lateral tension stress in the two conditions are occurred at the end of the bar, which is 7.14MPa, meanwhile, the comparative lateral tension stress also took place at the bottom of the midspan and around the sediment bare, the maximum value is 4.82MPa. The extreme value of the vertical tension stresses σ_y in each condition is always occurred at the under part of the outside of the sidewalls and the middle wall, which is 3.81MPa. The longitudinal tension stress σ_z in each condition, are all taken place at the inner side of the slope board or at the under part of the outside of the sidewall and the middle wall, which is 0.88MPa.

Table 5 The summary of the extreme dynamic stress of the sedimentation basin (MPa)

Condition / Items	Earthquake I	Earthquake II
Lateral tension stress σ_x	6.53	7.14
Vertical Tension stress σ_y	3.32	3.81
Longitudinal tension stress σ_z	0.76	0.88

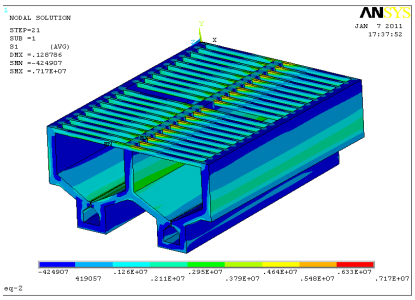


Fig. 9 Lateral stress σ_x (earthquake II)

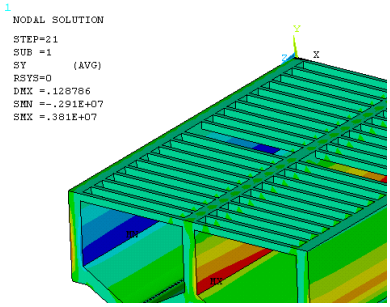


Fig. 10 Vertical stress σ_y (earthquake II)

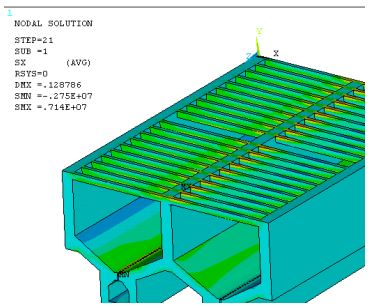


Fig. 11 Principal stress σ_1 (earthquake II)

Conclusions

Through the comparison of with and without bar, it can be seen that the bar can reduce the cantilever effect of the side walls and the slope board efficiently, and can improve the integrity strained condition, therefore, in order to improve the stress state of the structure, the bars are recommended to set on the top of the sedimentation basin.

These are, by the modal analysis, the dynamic effect of water in the chamber and the structure has impact on the self-vibration characteristic; meanwhile, according to the analysis of the vibration mode, the three directions seismic response of the structure are all controlled by the low order vibration mode.

On the basis of the static and dynamic analysis, the relative large tension stress will be occurred at the outside of the sidewalls, around sediment holes, at the bottom of the midspan and the bar, furthermore, the maximum value exceeds the ultimate tension 2.18MPa of the C30, which makes it become the weakness of the sedimentation basin.

References

[1] DL 5077-1997, Specifications on Designing Sand Basin of Hydropower and Water Conservancy Projects, China Electric Power Press, 2000.

[2] DL 5077-1997, Specifications for Load Design of Hydraulic Structures, China Electric Power Press, 1998.

[3] SL203-97, Specifications for Seismic Design of Hydraulic Structures, China WaterPower Press, 1998.

[4] SL 191-2008, Design Code for Hydraulic Concrete Structures, China WaterPower Press, 2009.

© (2012) Trans Tech Publications, Switzerland
doi:10.4028/www.scientific.net/AMM.238.298

Study on Settling Efficiency of Sedimentation Basin of Coca Codo Sinclair Hydropower Station in Ecuador

Xuanying Guo[1, a], Songwei Chen[2, b] and Dongpo Sun[1, c]

[1]North China University of Water Resources and Electric Power, Zhengzhou 450011, China

[2]Yellow River Engineering Consulting Co.,Ltd., Zhengzhou 450003, China

[a]guoxuanying@126.com, [b]chensongwei_x@163.com, [c]sundongpo@ncwu.edu.cn

Keywords: sedimentation basin; quasi-hydrostatic; unsaturated sediment discharge method; settling velocity; volcanic ash.

Abstract. Ecuador is located in South America, and sediment of CCS hydropower station is mainly volcanic ash. This paper makes a study on settling efficiency of sedimentation with the quasi-hydrostatic settlement method and unsaturated sediment discharge method. The result shows that settling efficiency of the two methods are close to each other. Further more, the paper makes a study on settling velocity in different calculation methods, including the method of hydraulic engineering design manual, Zhang Ruijin calculation method and method of the United States Army Corps of Engineers. The settling velocity of volcanic ash under the weak alkaline condition and the influences of temperature on settling velocity are studied by testing. It can provide a reference for design of hydropower station in the surrouding area of South America.

Introduction

Coca Codo Sinclair Hydropower Station Project is a diversion type station, located on the border of Napo and Sucumbios in northern Ecuador in South America. The total installed capacity of the Project is 1500MW. Eight impulse turbine units are installed. Main structures include head complex (including principal spillway, secondary spillway, sedimentation basin, and water intake), headrace tunnel, compensating reservoir, penstock, underground powerhouse, etc.

The sedimentation basin is located close to the intake. There are six chambers in all with a total length of 264.5m. It mainly consists of upstream connecting section, service section, downstream connecting section, side spillway and flushing gallery system. The service section has an effective service length of 150m.

According to layout and dimension of sedimentation basin and basic design data, we make a settlement calculation of sedimentation basin. It shows that one dimension unsaturated sediment discharge method is adequate for the project, and it provides valuable reference for other projects.

Settlement Calculation Method for Sedimentation Basin

Quasi-hydrostatic Settlement Method (Method One). According to *Design of Sand Basin of Water Conservancy and Hydropower Projects*, quasi-hydrostatic settlement method is the earliest method of settlement calculation used for sedimentation basin. As the settling velocity of sediment is modified by velocity in quiescent water, it is called 'quasi-hydrostatic settlement method'. It is assumed that the vertical distribution of sediment concentration is uniform, and the basic formula is as follows:

$$S_i = S_{0i}(1 - \frac{\omega_i L}{KVH}) \tag{1}$$

Where, S_i is the sediment concentration of group i at the outlet section (kg/m^3); S_{0i} is the sediment concentration of group i at the inlet section (kg/m^3); ω_i is the average settling velocity of group i sediment (m/s); L is the calculated length of sedimentation basin (m); V is the average flow velocity of sedimentation basin (m/s); H is the average water depth of sedimentation basin (m); and K is a coefficient.

When the sediment is nonuniform, Eq. 1 means longitudinal variation of grouping sediment concentration. Through accumulating the grouping sediment concentration, we can get the formula of longitudinal variation of total sediment concentration:

$$S = \sum_{i=1}^{n} S_i = \sum_{i=1}^{n} S_{0i}\left(1 - \frac{\omega_i L}{KVH}\right) \tag{2}$$

Where, S is the total sediment concentration at outlet section (kg/m^3); and n is the number of group of sediment. In accordance with the requirement for analysis of sediment passing through turbines, n is 9.

By definition, when the sedimentation basin is calculated piecewise, the sedimentation rate of a certain basin segment is:

$$\eta_{ki} = 1 - \frac{S_{ki}}{S_{0ki}} \tag{3}$$

Where, S_{ki} is the sediment concentration of group i at the outlet section of basin segment k; S_{0ki} is the sediment concentration of group i at the inlet section of basin segment k.

We can get the following equation by substituting Eq. (1) into Eq. (3):

$$\eta_{ki} = \frac{\omega_i L_k}{KV_k H_k} \tag{4}$$

Where η_{ki} is sedimentation rate of group i sediment in a certain calculated basin segment, which is generally expressed as percentage but expressed as ratio in this formula; ω_i is average settling velocity of group i sediment (m/s); L_k is the length of calculated basin segment (m); V_k is average flow velocity of calculated basin segment (m/s); H_k is average water depth of calculated basin segment (m); K is coefficient and the numerical value is 1.2 according to reference book [3].

One Dimension Unsaturated Sediment Discharge Method (Method Two). According to *Design of Sand Basin of Water Conservancy and Hydropower Projects*, on the operation of the sedimentation basin, sediment will be in a depositing process and the sediment concentration of each section is in a supersaturated state. It is applicable to adopt equation of continuity of sediment with characteristics of unsaturated sediment discharge. On the non-uniform flow condition, assuming water depth and sediment carrying capacity vary linearly, the formula of one dimension unsaturated sediment discharge is as follows:

$$S = S_* + (S_0 - S_{0*})e^{-\frac{\alpha\omega_s x}{q}} + (S_{0*} - S_*)\frac{q}{\alpha\omega_s x}\left(1 - e^{-\frac{\alpha\omega_s x}{q}}\right) \tag{5}$$

Where S_0, S_{0*} are the average sediment concentration and average sediment carrying capacity at inlet section (kg/m^3), respectively; S, S_* are the average sediment concentration and average sediment carrying capacity at outlet section (kg/m^3), respectively; x is the length of calculated basin segment (m); q is the discharge per unit width [m^3/(s·m)]; ω_s is the sediment settling velocity (m/s); and α is the coefficient of saturation recovery.

If the calculated basin segment is very short, the flow can be regarded as uniform flow. Then average sediment carrying capacity of inlet section is equal to that of outlet section, and the last term of the formula will be removed. On the condition that flow velocity is very small and sediment carrying capacity can be ignored, the above formula will be converted to:

$$S = S_0 e^{-\frac{\alpha\omega_s x}{q}} \tag{6}$$

Then longitudinal variation of grouping average sediment concentration can be expressed with the following formula:

$$S_i = S_{0i} e^{-\frac{\alpha_i\omega_i x}{q}} \tag{7}$$

Where S_{0i}, S_i are the grouping sediment concentration of inlet section and outlet section, respectively (kg/m^3); ω_i is the average settling velocity of grouping sediment (m/s); α_i is the saturation recovery coefficient of grouping sediment; x is the length of calculated basin segment (m); and q is the discharge per unit width [m^3/(s·m)].

The sedimentation basin can be divided into several segments while doing settlement calculation. Symbolizing the segment number with letter "k", we can get the sedimentation rate of grouping sediment at a certain basin segment in a calculation interval.

$$\eta_{ik} = 1 - e^{-\frac{\alpha_{ik}\omega_i\chi_k}{q_k}} \tag{8}$$

Comparison of Two Methods. Relevant studies show that calculation formula of these two methods can be transformed under a certain condition. Quasi-hydrostatic settlement method can estimate the variation of sediment concentration in the sedimentation basin if an appropriate calculated length is selected. According to the calculation method mentioned above, the value of sedimentation rate of grouping sediment calculated with the two methods is listed in Table 1

Table 1 Value of sedimentation rate of grouping sediment calculated with two methods

Group of particle size (mm)	Sedimentation rate of grouping sediment (%)	
	Quasi-Hydrostatic settlement method	Unsaturated sediment discharge method
0.002~0.01	42.8	44.1
0.01~0.04	43.4	44.4
0.04~0.05	45.8	46.0
0.05~0.06	47.3	47.3
0.06~0.07	49.1	48.9
0.07~0.10	52.9	52.7
0.10~0.25	70.3	72.8
0.25~0.50	96.0	98.1
0.50~2.00	100.0	100.0

We can see that the calculation results of the two methods are close to each other. Unsaturated sediment discharge method not only considers sediment-laden flow with characteristics of extra-saturation sediment transportation, but also considers the effect of upwards turbulence under a certain extent. It can reflect hydraulic factors with sediment and the theory is more advanced. Consequently, one dimension unsaturated sediment discharge method is applied to computational analysis for the settlement calculation of the sedimentation basin in current design.

Calculation Method of Settling Velocity

Sha Yuqing Formula. According to *Specification for Design of Sedimentation Basin of Water Conservancy and Hydropower Engineering*, Sha Yuqing formula is used to calculate settling velocity if the sediment particle diameter is between 0.062mm and 2.0 mm.

$$(\lg S_a + 3.790)^2 + (\lg\varphi - 5.777)^2 = 39.00 \tag{9}$$

$$S_a = \frac{\omega}{g^{1/3}(\frac{\rho_s}{\rho_w} - 1)^{1/3}\nu^{1/3}} \tag{10}$$

$$\varphi = \frac{g^{1/3}(\frac{\rho_s}{\rho_w} - 1)^{1/3} D}{10\nu^{2/3}} \tag{11}$$

Where S_a is the discrimination number of settling velocity; φ is the discrimination number of particle diameter; ω is the settling velocity of sediment (cm/s); D is the particle diameter of sediment (mm); ρ_s is the density of sediment (g/cm^3); ρ_w is the density of clear water (g/cm^3); g is acceleration of gravity (cm/s^2); and ν is kinematic viscosity coefficient of water (cm^2/s).

Zhang Ruijin Formula. According to *Specification for Design of Sedimentation Basin of Water Conservancy and Hydropower Engineering*, for the transition region, we select the formula as follows:

$$\omega = -13.95\frac{\nu}{d} + \sqrt{(13.95\frac{\nu}{d})^2 + 1.09\frac{\gamma_s - \gamma}{\gamma}gd} \tag{12}$$

Where, ω is settling velocity of sediment (cm/s); d is particle diameter of sediment (cm); γ_s is the density of sediment (g/cm^3); γ is the density of clear water (g/cm^3); g is acceleration of gravity (cm/s^2); and ν is kinematic viscosity coefficient of water (cm^2/s).

Method of the United States Army Corps of Engineers. Fig. 1 shows the relationship between sediment particle diameter and settling velocity for naturally worn quartz particles falling alone in quiescent distilled water of infinite extent recommended by U.S. Interagency Committee on Water Resources, Subcommittee on Sedimentation. The figure shows the variation of settling velocity with temperature and sand shape factor. It can be calculated that settling velocity of sediment with 0.25 mm particle diameter is 3.19 cm/s when the temperature is 20°C and the sand shape factor is 0.7.

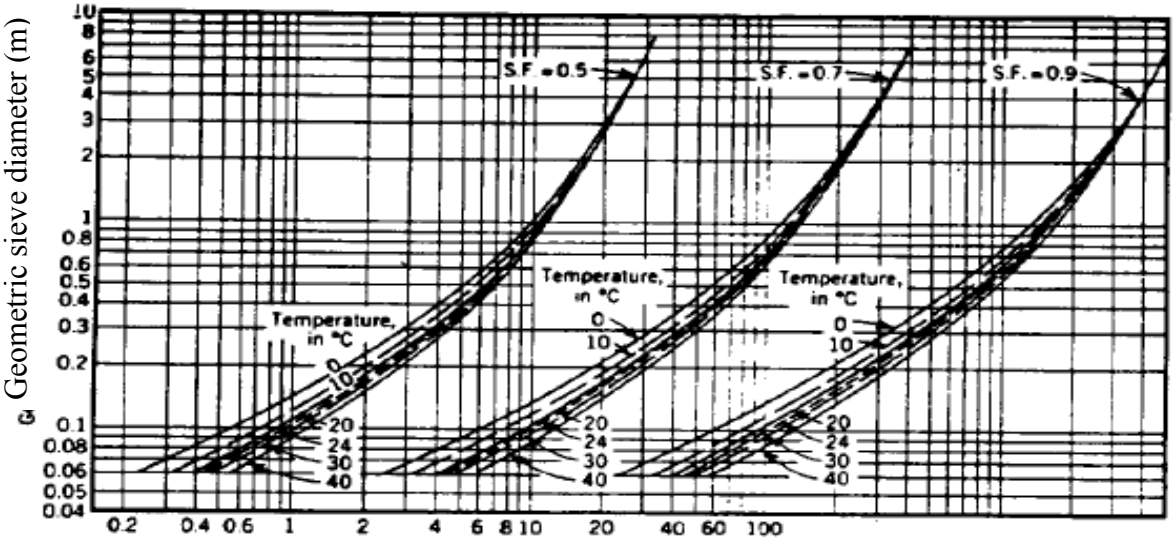


Fig. 1 Relationship of sieve diameter and settling velocity

For the sediment of 0.25 mm particle diameter, we can calculate the settling velocity with above three methods, respectively. The results are listed in Table 3.

Table 3 Settling velocity of sediment of 0.25mm diameter

Temperature (°C)	Water kinematic viscosity coefficient (cm^2/s)	Settling velocity (cm/s)		
		Sha Yuqing formula	Zhang Ruijin formula	Method of US Army Corps of Engineers manual
10	0.01306	2.09	2.57	3.00
15	0.01139	2.27	2.84	3.08
20	0.01003	2.43	3.09	3.19

Experimental Study on Sediment Settling Velocity. Under the environment that water temperature is 13.9°C and 20°C, we measure settling velocity of sediment of 0.25 mm particle diameter with 2 m standard sedimentation cylinder by local sand samples. The measured result is listed in Table 4. The experimental results show that average settling velocity is 3.14 cm/s and 3.39 cm/s, respectively when the water temperature is13.9°C and 20°C.

Comprehensive Evaluation and Adopting the Calculation Method of Settling Velocity. Based on the above analysis and experimental study, we can see that the settling velocity of local sand samples by test is maximum. When the water temperature is 20°C and the particle diameter is 0.25 mm, the measured settling velocity is 3.39 cm/s. The settling velocity calculated by Zhang Ruijin

formula is between the experimental result and Sha Yuqing formula calculation result and the value is 3.09 cm/s. The settling velocity calculated by Sha Yuqing formula is minimal and the value is 2.43 cm/s. The settling velocity calculated by method of the United States Army Corps of Engineers is 3.19 cm/s. By comprehensive consideration, the calculation result of Zhang Ruijin formula is close to the experimental result as well as that of method of the United States Army Corps of Engineers, so the method of Zhang Ruijin formula is adopted in basic design.

Table 4 Experimental results of settling velocity

No.	Settling velocity (cm/s)	
	Water temperature at 13.9°C	Water temperature at 20°C
1	3.28	3.54
2	3.13	3.39
3	3.11	3.35
4	3.34	3.61
5	2.98	3.21
6	3.11	3.35
7	3.16	3.42
8	3.21	3.46
9	3.02	3.26
10	3.10	3.34
Average	3.14	3.39

Analyzing Influence of Acceleration of Gravity on the Sediment Settling Velocity. According to settling velocity calculation formula of Zhang Ruijin, we can get that the local acceleration of gravity has little influence on sediment settling velocity. The sediment settling velocity under different acceleration of gravity at a normal temperature is listed in Table 5.

Table 5 Influence of acceleration of gravity on the sediment settling velocity

No.	Acceleration of gravity (m/s^2)	Settling velocity (cm/s)	Remarks
1	9.78	3.09	(1) Temperature is 20°C, and kinematic viscosity coefficient of water is 0.01003cm^2/s. (2) Sediment particle diameter is 0.25 mm.
2	9.79	3.09	
3	9.80	3.09	
4	9.81	3.10	
5	9.82	3.10	
6	9.83	3.10	

Calculation Method of Coefficient of Saturation Recovery

There are different explanations about coefficient of saturation recovery. It is considered by Wuhan Institute of Hydraulic and Electric Engineering that the coefficient is a variable and it is related to settling velocity of sediment, water depth, and friction velocity of flow. Chengdu Investigation and Design Institute (CHIDI) established the calculation methods for the coefficient of saturation recovery based on measured data and flume experiment data of sedimentation basin such as Yuzixi, Nanyahe, Qingshuihe, etc. According to *Specification for Design of Sedimentation Basin of Water Conservancy and Hydropower Engineering*, the coefficient of saturation recovery is expressed as

$$a_{ik} = K\left(\frac{\varpi_i}{u_{*k}}\right)^{0.25} \tag{13}$$

$$u_{*k} = \sqrt{g\overline{R}_k\overline{J}_k} \tag{14}$$

Where ϖ_i is average settling velocity of sediment size groups (m/s); u_{*k} is friction velocity of flow in basin segment k (m/s); $\overline{R}_k$ is average hydraulic radius of basin segment (m); $\overline{J}_k$ is average hydraulic gradient of basin segment k; and K is empirical coefficient and the value is 1.2.

According to the settlement calculation method of sedimentation basin mentioned above, we make a settlement calculation of sedimentation basin by one dimension unsaturated sediment discharge method. From inlet section to the end of the sedimentation basin, the basin is divided into 6 chambers. The sedimentation rate of total sediment is 62.2%, and the sedimentation rate of sediment particle diameter greater than 0.25 mm is 98.62%. It shows that the design of sedimentation basin can meet the requirement of the project.

Conclusions

According to the paper, we can see that the unsaturated sediment discharge method not only considers sediment-laden flow with characteristics of extra-saturation sediment transportation, but also considers the effect of upwards turbulence under a certain extent. It can reflect hydraulic factors with sediment and the theory is more advanced than quasi-hydrostatic settlement method. Consequently, one dimension unsaturated sediment discharge method is applied to computational analysis for the settlement calculation of the sedimentation basin.

For settling velocity, the calculation result of Zhang Ruijin formula is close to the experimental result, so the method of Zhang Ruijin formula is adopted.

One dimension unsaturated sediment discharge method is adequate for Coca Codo Sinclair Hydropower Station Project, and it provides valuable reference for other projects.

References

[1] East China Institute of Water Conservancy and Hydroelectric Power, C. Zhang, Hydraulic Engineering Design Manual, Water Resources and Electric Power Press, Beijing, 1984.
[2] Teaching and Research Section of River Sediment Engineering of Wuhan Institute of Hydraulic and Electric Engineering, J. Xie, River Sediment Engineering, Water Resources and Electric Power Press, Beijing, 1983.
[3] Y. Li, J. Yang, J. Zhang, Design of Sand Basin of Water Conservancy and Hydropower Projects, China Water Power Press, Beijing, 2004.
[4] W. H. Graf, E. R. Acaroglu, Settling Velocities of Natural Grains, Bulletin of the International Association of Scientific Hydrology, 4 (1966).
[5] W. W. Rubey, Settling velocities of Gravel, Sand, and Silt Particles, American Journal of Science, 25 (1933) 325-338.
[6] E. F. Schulz, R. H. Wilde, M. L.Albertson, Influence of Shape on the Fall Velocity of Sedimentary Particles, MRD Sediment Series, 5 (1954).
[7] W. L. Graf, Hydraulics of Sediment Transport, McGraw-Hill, New York, 1971.
[8] E. W. Lane, A. A. Kalinske, Engineering Calculations of Suspended Sediment, Transactions of the American Geophysical Union, 1941.
[9] V. A. Vanoni, Transportation of Suspended Sediment by Water, Transactions of the ASCE, 111 (1946).
[10] D. B. Simons, F. Senturk, Sediment Transport Technology, Water Resources Publications, Fort Collins, Colorado, 1977.
[11] S. Goldstein, The Steady Flow of Viscous Fluid Past a Fixed Spherical Obstacle at Small Reynolds Number, Proceedings of the Royal Society of London, Series A, 123 (1929.
[12] H. Rouse, Fluid Mechanics for Hydraulic Engineers, chapter XI, Dover, New York, 1938.
[13] U. S. Bureau of Reclamation, Design of Small Dams, Denver, Colorado, 1987.
[14] V. A. Vanoni,. Sedimentation Engineering, ASCE Task Committee for the Preparation of the Manual on Sedimentation of the Sedimentation Committee of the Hydraulics Division, ed. 1975, Reprinted 1977.
[15] C. T. Yang, Incipient motion and Sediment Transport, Journal of the Hydraulics Division, ASCE, 99 (1973), HY10, Proceeding Paper 10067.
[16] Chih Ted Yang. Sediment Transport Theory and Practice.

© (2012) Trans Tech Publications, Switzerland
doi:10.4028/www.scientific.net/AMM.238.304

Application of MIKE21 MODEL on Flood Routing in the Lower Yellow River from Gaocun to Sunkou

Xiaolei Zhang[a], Shaolei Guo[b]

North China University of Water Resources and Electric Power, Zhengzhou 450011, China

[a]zhangxiaolei@ncwu.edu.cn, [b]guoshaolei@ncwu.edu.cn

Keywords: the Lower Yellow River; flood routing; MIKE 21; numerical simulation.

Abstract: The 2-D water flow mathematical model based on MIKE 21 software which reflects flood routing in the reach from Gaocun to Sunkou has been developed in this paper. Through the numerical simulation of the "96.8" typical flood, the simulating results in the condition of present topography are agreement with the measured ones. It shows that this model is basically reasonable in the selection aspects of river terrain, boundary treatment, roughness and water flow parameters, and the model has a reference value for simulating flood routing in the Lower Yellow River.

Introduction

The reach from Gaocun to Sunkou in the Lower Yellow River shown in Fig. 1 is a transitional reach [1]. It's about 126km from Gaocun to Sunkou. On the both sides of the channel in the reach from Gaocun to Sunkou in the Lower Yellow River, local farmers have built some small scale dykes in order to protect the farmlands from flood, and the dikes are called productive dikes. The dikes affect water and sediment exchange between floodplains and channel. If the productive dikes are stationed there for a long time, it would make the channel shrinking and the bankfull discharge decreasing, so it would decrease the capacity of flow conveyance and endanger the river health. At present, in the reach of the lower Yellow River, a lot of such productive dikes significantly influent the flood propagation, overflow and inundation on the floodplains and the fluvial process. In addition, the distribution of a number of residential places, irrigation canals, roads, and other controlling works also greatly limits the flooding range. Therefore when the peak discharge is very large, the flood is prone to resulting in productive dikes bursting, which will greatly endanger the lives of residents in flood plains [2].

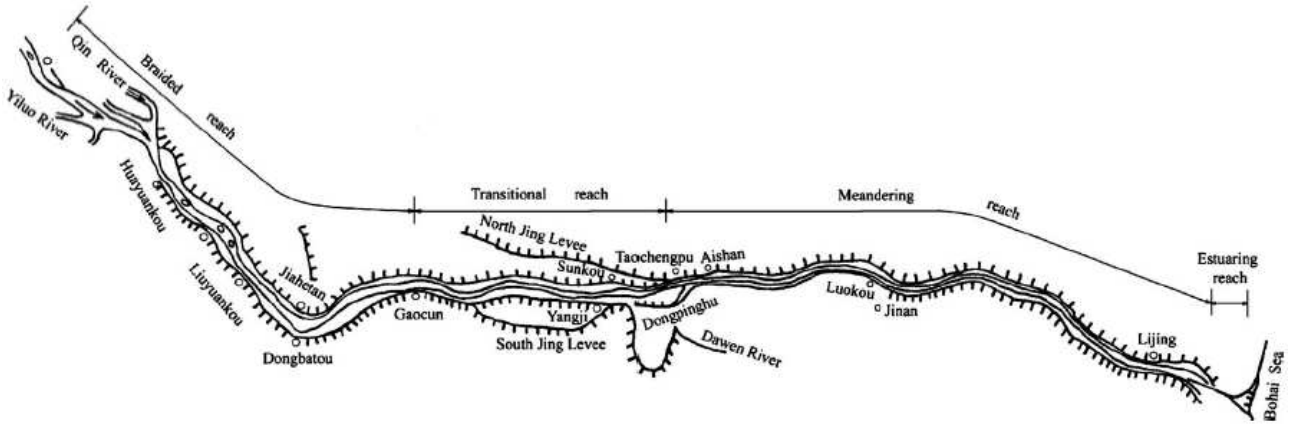


Fig. 1 Sketch of the Lower Yellow River

MIKE 21 HD is the basic computational hydrodynamic module of the entire MIKE 21 system providing the hydrodynamic basis for other MIKE 21 modules such as advection-dispersion (AD), water quality (ECOLab), sand transport (ST) and mud transport (MT). MIKE 21 HD simulates the water level variation and flow in response to a variety of forcing functions in lakes, estuaries, bays and coastal areas. The water levels and flows are resolved on a rectilinear grid, a curvilinear grid, a triangular element mesh or any combination hereof covering the area of interest. MIKE 21 HD can be applied to a wide range of hydraulic and related phenomena. This includes modeling of tidal

hydraulics, wind and wave generated currents, storm surges and flood waves [3].It is a general hydraulic model that easily can be set up to describe specific hydraulic phenomena. So the application of Mike 21 software in China develops rapidly. In this paper based on the measured data in the hydrological stations from Gaocun to Sunkou in the Lower Yellow River, the two-dimensional hydrodynamic mathematical model in this reach is established for the simulation on flood propagation by making use of MIKE 21 software.

Set of Mike21 Model

Basic Governing Equations. Hydrodynamic governing equations consist of a continuity equation and two momentum equations as follows:

Continuity equation:

$$\frac{\partial \zeta}{\partial t} + \frac{\partial p}{\partial x} + \frac{\partial q}{\partial y} = S \tag{1}$$

Momentum equation in X direction:

$$\frac{\partial p}{\partial t} + \frac{\partial}{\partial x}\left(\frac{p^2}{h}\right) + \frac{\partial}{\partial y}\left(\frac{pq}{h}\right) + gh\frac{\partial \zeta}{\partial x} + \frac{gp\sqrt{p^2+q^2}}{C^2h^2}$$
$$-\frac{1}{\rho}\left[\frac{\partial}{\partial x}\left(h\tau_{xx}\right) + \frac{\partial}{\partial y}\left(h\tau_{xy}\right)\right] - \Omega q - fVV_x + \frac{h}{\rho}\frac{\partial}{\partial x}\left(p_a\right) = S_{ix} \tag{2}$$

Momentum equation in Y direction:

$$\frac{\partial q}{\partial t} + \frac{\partial}{\partial y}\left(\frac{q^2}{h}\right) + \frac{\partial}{\partial x}\left(\frac{pq}{h}\right) + gh\frac{\partial \zeta}{\partial y} + \frac{gq\sqrt{p^2+q^2}}{C^2h^2}$$
$$-\frac{1}{\rho}\left[\frac{\partial}{\partial y}\left(h\tau_{yy}\right) + \frac{\partial}{\partial x}\left(h\tau_{xy}\right)\right] + \Omega q - fVV_y + \frac{h}{\rho}\frac{\partial}{\partial y}\left(p_a\right) = S_{iy} \tag{3}$$

Where ζis water level, h is still water depth; and p, q is the flux in x and y direction respectively, $\Omega(x,y)$ is Coriol parameter which has a value of $2\omega\sin\psi$, $\omega$is rotational angular velocity of the earth, ψ is latitude of a calculation point which generally has a value of $0.7249\times10^{-4}s^{-1}$, $f(V)=\gamma_a^2\rho_a$ is wind friction factor function, γ_a^2 is wind stress parameter, S is source item, ρ_a is the air density, and V is the wind speed, g is acceleration of gravity, and τ is viscous shear stress.

Solution Method. In space, because the adopted grid belongs to unstructured grid, the original equations are discretized by second-order central difference scheme in finite volume method, and the overall calculation region is divided into lots of non-overlapping cells. In time, explicit integration method is employed to solve the governing equations.

Model Range. According to the characteristics of morphologies of river channels in the Lower Yellow River reaches and other factors such as controlling hydraulic engineering, production dikes and embankments, the model scope is selected. The upper boundary is chosen in Gaocun station, and the lower boundary is chosen in Sunkou station. The total length of the reach is about 100.3km. The 3-D topography of the simulated reach from Gaocun to Sunkou is shown in Fig. 2. The computational mesh of the simulated reach from Gaocun to Sunkou is shown in Fig. 3.

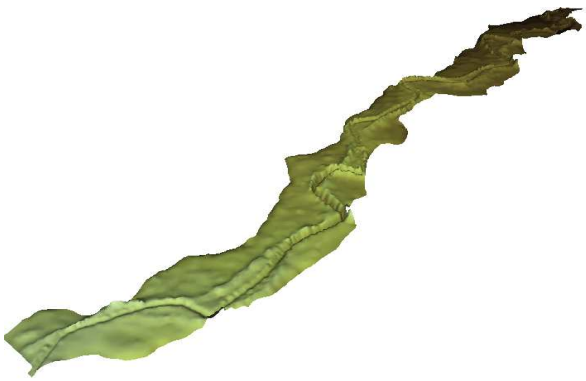


Fig. 2 3-D topography of the simulated reach

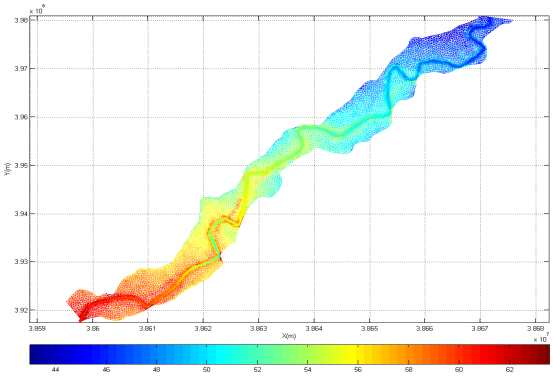


Fig. 3 Computational mesh

Boundary Conditions. Beach terrain adopts the river course topographic map in 1999 with consideration of productive dikes. The main channel take the cross-section conditions measured in 2004 for reference. The upstream entrance of the open boundary adopts flood flow process, controlled by the given frequency flood process line. If there is the measured hydrological and cross-section data, the downstream open boundary, namely, the river outlet cross-section adopts the relationship between water level and discharge as the controlling open boundary condition. If there isn't the measured hydrological and cross-section data, we adopt the natural open boundary based on the local river gradient and terrain conditions [4].

Simulation Results and Analysis

The simulating calculation adopts the actual measured water level of the flood in August 1996, with the peak flow at Gaocun station is 6810m^3/s, which is hereinafter called "96.8" flood for short. The floodplain terrain uses 1/10000 river course topographic map, and the river course topography is amended according to the measured cross sections before flood season. "96.8" Flood belongs to the medium flood. As the flood is flooding and out of slots, it can reflect the situation of the flood discharge and the resistance status of the river course and the beach in some extent. "96.8" flood discharge process at Gaocun station is shown in Fig. 4. The distribution of measured cross sections and observed points are shown in Fig. 5. The observation data of flooding potential and flood peak flow and the measured points are shown in Table 1.

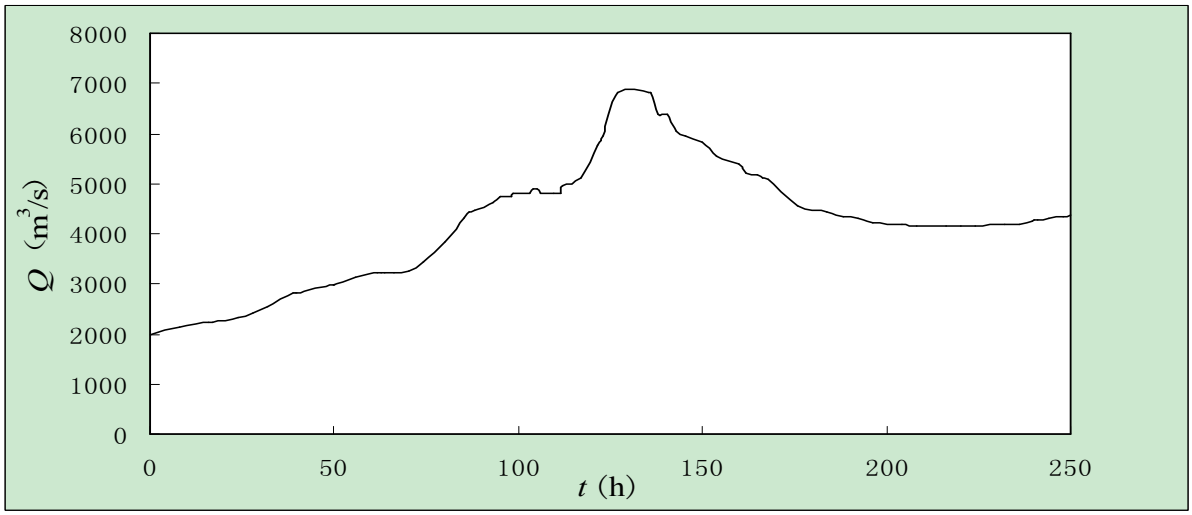


Fig. 4 Discharge process of "96.8 flood" at Gaocun station

The model uses different roughness of the beach and slot to simulate the flow field resistance. The river channel roughness generally chooses 0.010～0.015 by comparison, and the beach roughness chooses 0.025～0.035. In order to simulate the resistance effect of the village reasonably, the elevation of the grid is 0.5m higher than the locality, and its roughness is set to 0.06.

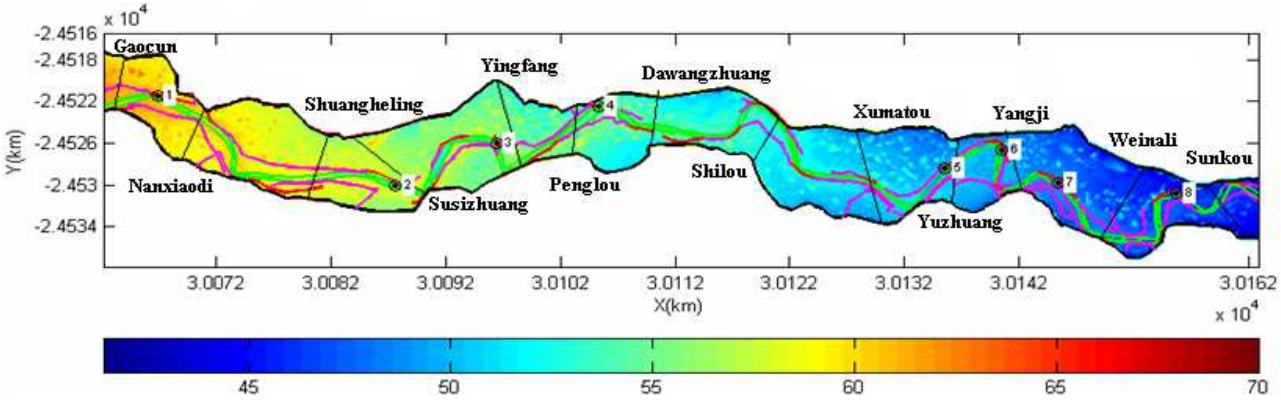


Fig. 5 Distribution of measured cross sections and observed point in the simulated reach

Table 1 Comparison between simulated value and measured value of water level

Serial number	Observed points	Measured value [m]	Simulation value [m]	error [m]
1	Nanshangyan	62.03	62.29	0.26
2	Lianshansi	58.77	59.00	0.23
3	Mazhangzhuang	57.72	57.93	0.21
4	Penglou	56.1	56.32	0.22
5	Yanglou	51.44	51.73	0.29
6	Sunlou	51.65	51.69	0.04
7	Hanhutong	49.95	50.02	0.07
8	Lianglukou	48.27	48.39	0.12

In order to verify the accuracy of the 2-D mathematical model, the simulated values are compared with the measured data at the flood peak of “96.8” flood. The water level measured at the flood peak of “96.8” flood and the simulated values are compared with the measured data, which is shown in Table 1. We can see good agreement between the two from the table. Most of the errors are controlled below 0.2m. The results above show that the chosen flow field roughness and other parameters are appropriate, and the river flood routing simulation based on Mike21 HD is credible.

Conclusions

Flood modeling based on MIKE 21 can better simulate the flood propagation in the reach from Gaocun to Sunkou in the lower Yellow River. According to the calculation results of “96.8” flood, the simulated values are in basic agreements with measured values. And the flow fields of "96.8" flood in this reach basically reflect the flood characteristics of historical flood, horizontal distribution of velocity, river regime and over-bank features. So the 2-D water flow model based on MIKE 21 is appropriate in aspects of the processing method of river terrain and boundary condition, the chosen roughness and the parameters of water flow. The model on the basis of Mike21 software has a reference value for the flood forecasting in the Lower Yellow River flood in the future.

References

[1] G. Wang, J. Xia and B. Wu. Journal of Hydraulic Engineering, 9 (2008) 1064-1078.

[2] Codification of the Yellow River Conservancy Committee, Expert forum on a General Plan for Lower Yellow River Management, Yellow River Water Conservancy Press, Zhengzhou, 2004, 112-116.

[3] D. Sun, G. Jin, X. Li, Yellow River, 11 (2009) 27-28.

[4] D. Sun, X. Liao, P. Wang, Journal of Hydrodynamics, 1 (2007) 24-30.

© (2012) Trans Tech Publications, Switzerland
doi:10.4028/www.scientific.net/AMM.238.308

Analysis of Influence Factors of Irrigation Method in Detecting Compactness of Canal Bank

Yingbin Kang [a], Kun Huang [b] and Abdurxt Rjap [c]

North China University of Water Resources and Electric Power, Zhengzhou 450011, China

[a]kyb123@163.com, [b]351232607@qq.com, [c]abdurxt@gmail.com

Keywords: canal bank; irrigation method; detection of compactness; influence factors.

Abstract. This paper introduces the actual operation method of detection of the degree of compaction of the canal bank by using irrigation method and summarizes the project experience of detection of the degree of compaction of the canal bank. Taking a channel engineering as an example, some influencing factors of the irrigation method to detect the density of gravel soils are analyzed, and the application of irrigation method in dry density test of the gravel soils is discussed.

Introduction

In water conservancy engineering quality test, the main control index of canal bank project is filling material compactness. There are mainly direct method and indirect method two kinds of the method to detect the degree of compaction of filling material in engineering. The direct method is mainly trial pit replacement method (irrigation method or sand filling method) and the indirect method including compaction settlement observation method, vibration grinding outfit accelerometer method, control of the rolling parameters method, static elastic modulus method, move mode method, surface wave method, a nuclear density method and additional quality standard, etc. The replacement method of trial pits is most original and commonly used. Especially irrigation is most commonly used of trial pits replacement method. However, in the irrigation method during the test, many factors will affect the accuracy of test results, or even come to the unreasonable result, so it is necessary to analyze and propose measures to reduce or eliminate the impact of influencing factors.

The Basic Principles of Irrigation Method

Excavating a test pit at the measuring point and weighing the quality of the filling material-M from the test pit dug, weighing the quality of the irrigation, translated the volume V of the digging of trial pits, at the same time, get the filling material moisture content ω. The filling density is calculated by the following formulas:

Filling material wet density $\rho = M / V$ (1)

Filling material dry density $\rho_d = \rho/(1+ \omega)$ (2)

Filling material Porosity $n = 1 - \rho_d / G_s \cdot \rho_w$ (3)

Where G_s is the density of filling material, ρ_w is the water density.

Irrigation Test on Site

The channel project starts in the Xihuaishu village and end at the White Village in Cixian country. It is between mark 14+330 and 16+280 and the total length is 13.866km. The length of the channel is 13.37km and the length of the building is 0.496km. All kinds of 28 cross structures are needed in all, including an inverted siphon culvert, six drainage inverted siphon on the left bank, an outlet gate, three canal cross seats, ten highway bridge and seven production bridge. The channel use open channel artesian water conveyance scheme and its flow section is trapezoid. The design bottom width is from 22.5m to 24.5m. The canal embankment is filling with gravel soil, and the volume is about 1.2 million m^3.

In the detection of the canal embankment, taking six groups of filling soil samples in total, according to the specification for soil testing, irrigation test should be carried out according to the following steps:

(1) Finding a relatively flat ground on site randomly, then detect whether the site meets the formation requirements with a horizontal ruler and remove loose soil on the surface. The diameter D of pilot hole is depending on the maximum particle size d_{max} of the filling material. Draw contour lines of the pilot hole in accordance with the determined diameter of pilot hole. The size of pilot hole is depending on the maximum particle size of the filling material and determined according to Table 1. And select the appropriate diameter of steel ring. The maximum value of gravel soil particle size is less than 40mm in this project. The test pit excavation diameter is 200mm, and the depth is 250mm.

Table 1 Trial pit size and the corresponding maximum diameter

Maximum diameter of sample (mm)	Trial pit size	
	Diameter (mm)	Depth (mm)
5(20)	150	200
40	200	250
60	250	300
200	800	1000

(2) Place the steel ring on the ground and fixed. Before digging test pits, to prevent dug trial pit wall collapsed, dig deep within 2~5cm at the site along the steel ring. When the steel ring is smooth, cover along the ground and inner wall of steel ring with plastic film, lay films flat as possible, then start irrigation. Irrigation is controlled in the steel ring all swamped the ground, and then placed wooden on the steel ring. An iron nail is nailed in the middle of the wooden, Stop irrigating when the nail tip just faces the water surface and make a sign in the steel ring where the wooden is placed. Then weigh the irrigation water and take out the film.

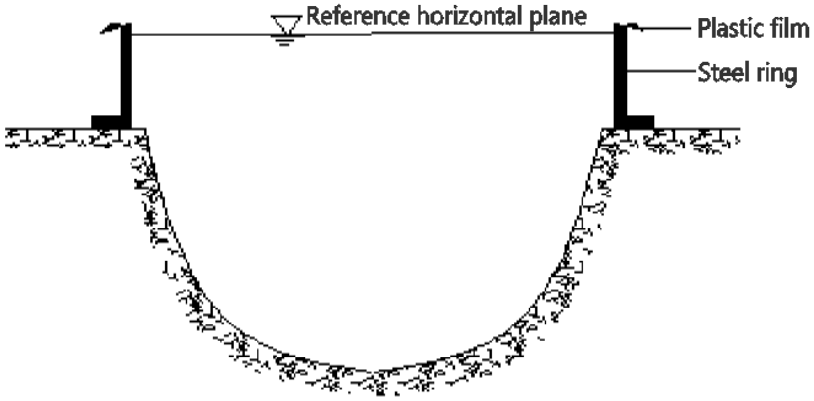


Fig. 1 Schematic diagram of the irrigation density test

(3) Excavate test pit. Points for attention of excavating: 1) At the beginning, dig out the filling material inside the contour line of the steel ring carefully. Do not make the material loss or move the steel ring. Pay attention to keep the ambient coarse particles not loose and try to make the pit dug into shape rules in the context of steel ring during the excavation process. 2) Get out the loosened particles by hand carefully. After the pit was dug, check out whether the sides and bottom of pit around have sharp corners or not. If there is, knock gently smoothed with a small hammer. Sweep out loosening particles on the wall or bottom of the pit gently by brush, and weighing. 3) In order to stop the evaporation of moisture and not affect the accuracy of the data, all the filling material which is removed from the pit should be weighed immediately.

(4) The plastic film which is thin and tough should be paved along the wall and bottom of pit closely. The film should be out of steel ring and pressed by some pieces of small stone. Before the film is paved, check that there is no sharp corner in the wall and bottom of the pit around carefully, lest the film will be punctured, and make the film be closed to inner wall of the hole.

(5) Irrigation. Weigh quality of the empty bucket M_t, and then weigh quality of the bucket which is bottled with water M_{t+w}. When the water level is up to the pithead position, put the wood on the location again that is determined in the previous steps. Observe carefully and make the water level is substantially parallel with the nail. In the irrigation process, the water should not be sprinkled to the outside of the pit. When the water level is close to the steel ring, observe and water carefully, the residual water of the final bucket is M_r.

(6) Organize the data record, and then seal a part of the filling material that is dug out by a plastic bag in order to prevent the water evaporating. Take the bag back to the laboratory and measure the moisture content-ω.

Test Results and Analysis

Data obtained on site are arranged as follows:

(1) Total mass M. Including all the filling materials that dug out from the test pit, there must not be any omission.

(2) Water content ω. Based on the test of indoor measurement, weighted average.

(3) Volume of trial pit V. Convert the volume of trial pit water to the volume of trial pit. The total weight of poured water is $G_w = N(M_{t+w}-M_t)-M_l$. N is frequency, the weight of poured water $G=G_w-G_{1w}$, the corresponding volume $V_w=G/\rho_w$. V_f is obtained by use of vernier caliper to measure 10 layers of the film thickness. The pit volume V is equal to the volume of water and the film $V=V_w+V_t$.

(4) According to formula (1) and (2), calculate the filling density ρ and dry density ρ_d.

Table 2 Gravel soil filling density calculation

Stake number	Elevation (m)	Quality of wet soil in the trial pits M (g)	Test pit volume V (mL)	Wet density ρ (g/cm^3)	Moisture content ω (%)	Dry density ρ_d (g/cm^3)
208+940	65.20	8840	4465	1.98	10.4	1.79
208+950	65.20	9351	4177	2.24	5.0	2.13
208+960	65.20	8452	4276	1.98	7.0	1.85
207+200	64.10	8941	4301	2.08	7.5	1.93
207+210	64.10	9024	4286	2.11	9.4	1.92
207+220	64.10	7863	4511	1.74	8.6	1.61

Table 2 shows that dry density of the gravel soil is in the range of 1.61~2.13g/cm^3 in the method of irrigation. A wide range of dry density that shows there is a big error when measuring dry density of cohesionless soil material in the use of irrigation method. Combined with practical engineering, we can obtain the influence factors of the precision of irrigation method as follows.

Analysis and Control of the Factors Affecting the Accuracy of the Test in Digging Process. (1) The size of rock fill material is large and very uneven and the rolling surface is difficult to reach the precision that the test required, so we usually modify the surface with a grommet on the surface in the irrigation experiment. We need a reference horizontal plan, which will show a strong effect on the whole experimental results when it changes. In order to prevent the movement of grommet that will change the reference horizontal plan. So after the grommet is fixed, it is not allowed to be moved in the process of experiment. That is to say, digging is done in the interior of the grommet which should pay special attention in the process. The grommet should be compressed or fixed firmly before digging. In the process of digging, it requires that the filling material should be dug out from the center to the edge. In case of large pieces of stone, get them out by rod. If the stone is too big to remove, it may be taken out by dissolution after measurement. The gross weight will be taken into the residual volume of the rock particle, so it can efficiently avoid the disturbance and shift of the steel grommet.

(2) The regular degree of pit wall has a great influence on the joint degree between the pit wall and film, thus it would affect the precision of the test pit volume measurement. When the distribution of stone affecting the shape of pit, and the pit wall is very irregular or beyond the outer steel grommet, the pit should be abandoned. When digging to the bottom, pick up the loose material and make the bottom surface roughness as far as possible. The pit should be dug into a hemispherical. The pit wall should be radian as possible and avoid angular.

Error Analysis and Control of the Trial Pit Volume Measurement. (1) In the irrigation method test, plastic film is used for measuring the volume of water. The film has a great impact on the accuracy of the test. If the film is too thick, its compliance is poor, and it would affect the fitting degree between the film and the pit wall, which may produce the cavity between the film and the pit wall, so that the measurement volume is smaller, and the measured density is bigger. In addition, if the film is too thick, it will have large volume itself, it also affects the volume measurement accuracy of test pit. If the film is too thin and it will be easily broken, which will cause water leakage and test failure. If there is water leakage, the test must be begun over again. Therefore, make a good choice of medium thickness, good toughness, compliance of the film. The film should also be carefully paved and the wrinkle should be extended. Pour water and at the same time emptying the gas at the bottom of the film, and avoid air entrainment between the film and pit wall.

(2) In the process of rock fill density detection, the pit volume tended to have relatively large and the amount of injected water is large, too. So the measurement accuracy of water volume is also an important factor to the test results. We should choose pure water, use high precision flow meter for measuring the volume of water or use bench scale weighing the quality of water. The water storage tank can also be used to measure the volume of injected water.

(3) In the course of irrigation method test, the determination of the reference level also influent the accuracy of the test. The needle fixed on the edge of the steel grommet which is lifting and rotating can be more accurate and faster to find the horizontal plane. The needle should be thin and sharp as possible, and it should be easily observe the contact points between the tip and the surface, keep the reference horizontal plane consistency. In the process, when the water needle tip contacts the reference surface, the two visual errors will affect the accuracy of test. In order to reduce the error in each of irrigation, it should be kept the same person with a view and subjected to the pinpoint just touching the surface to form convex.

Weighing Error Analysis on Trial Pit Soil. The main factor of effects on weighing error is weighing accuracy, times and human factors. Bench should be adjusted to level, check point, reduce movement during the experiments. The more times of weighing, the bigger the accumulated error is. Human factors are mainly to prevent the leakage or repeated weighing, so weigh carefully as much as possible. In addition, when the water content of the pit is relatively large, the soil loading frame wall will stick with a small amount of soil sample, it should be always paid attention to.

Conclusions

As one of the most basic and direct density detection method, irrigation is widely used in water conservancy engineering such as quality testing on rock fill dam, embankment compactness of the sand and gravel, crushed stone, but it also has some limitations. The efficiency of the detection method is low, and it is time-consuming, laborious and it has some destructive. In the peak stage of dam body filling, it does not only affect the construction progress, but also caused the loss of the machinery of the filling system, and the higher the frequency of detecting is, the greater the interference on construction is. The size of the rock fill is large and irregular and it is inconvenient to dig out, which makes the sample pit irregular. In the process of taking sample, it is extremely easy to destroy the original structure. Sometimes there would be reverse slope, empty, sampling pit border is unclear, volume calculation is uncertain and so on, which will have seriously impact on the accuracy of the rock fill density test. During the test, the operator should have a highly responsibility, careful operation, take measures, minimize or even eliminate the factors which have effect on dry density.

References

[1] SL237-1999, Specification for Soil Test, China Water Conservancy and Hydropower Press, Beijing, 1999.

[2] SL260-98, Specification for Levee Project Construction, China Water Conservancy and Hydropower Press, Beijing, 1998.

[3] DL/T5129-2001, Technical Specification for Rolled Earth-Rock Dam Construction, China Water Conservancy and Hydropower Press, Beijing, 1999.

[4] D. Xia, X. Zheng, Error analysis and control of dry density of rockfill dam for the detection of irrigation method, Water Conservancy and Hydropower Construction, 3 (2008) 80-82.

© (2012) Trans Tech Publications, Switzerland
doi:10.4028/www.scientific.net/AMM.238.313

Numerical Simulation of Excavation of Abutment Slope at Left Bank in Dagangshan Hydropower Station

Kun Yang [a], Zhichao Ma [b] and Hao Han [c]

Key Laboratory Mining Disaster Prevention and Control, Ministry of Education, Shandong University of Science and Technology, Qingdao, China

[a]kunyang11@163.com, [b]496315037@qq.com, [c]hanhao1013@qq.com

Keywords: Dagangshan hydropower station; abutment slope; numerical simulation; excavation.

Abstract. The abutment slope at left bank in Dagangshan hydropower station has complex geological conditions with deep fractures, developed faults and unloading crack. The excavation will influence the stability of the slope. To evaluate the slope stability, the finite element model of this abutment slope was built in this paper to study the deformation, stress and plastic zone distribution of the slope during the excavation. The potential failure location of the slope is forecasted, some suggestions are proposed to be helpful to keep the stability of the slope.

Introduction

Dagangshan hydropower station is located in Shimian, Sichuan Province of China. It is one of the large-scale hydropower projects to be developed on Daduhe River recently. Dam area has complex geological conditions with deep fractures, developed faults and unloading crack. The rock mass in engineering area will form a series of high and steep slopes during the excavation. As the strike of most weak structural surfaces is parallel to the river, and the dip is steep, the problem of slope stability is rather serious. It mainly involves abutment high slope at left and right bank. If no reinforcing measures are taken during excavation, large-scale landslides or mountain deformation will be caused, which would bring huge damage to engineering construction.

Numerical simulation is performed in this paper to analyze the deformation, stress and plastic zone distribution of the abutment slope at left bank during excavation, which provides a reference for reasonable optimizing excavation scheme and supporting measures [1, 2].

Calculation Method

Finite Element Model. The selected model is a section of abutment slope at left bank in Dagangshan hydropower station [3]. The geological conditions and topography in this section are very complex, the weathering and unloading on the excavation slope are very serious. In the finite element model, 16 faults and 18 dykes are simulated. 8436 elements including 1224 excavation elements with 13011 nodes are divided. The finite element models around the excavation are shown as Fig. 1 and Fig. 2.

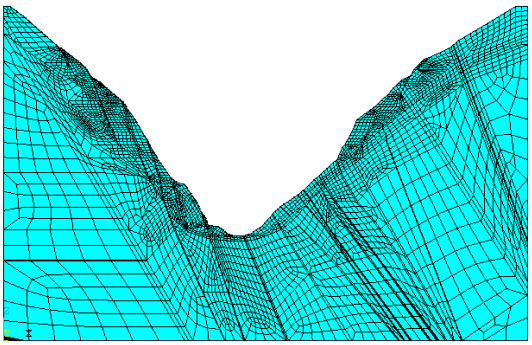


Fig 1 The model before excavation

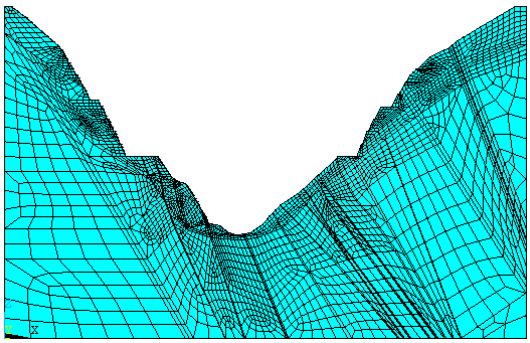


Fig 2 The model after excavation

Rock Mechanical Parameters. On the basis of geo-mechanical classification of the rock mass, 13 kinds of materials are determined finally and the parameters are shown in Table 1.

Table 1 Rock mechanical parameters

Name	Quality level	Material number	E (MPa)	μ	c (MPa)	f
Fault	Ⅱ	1	14500	0.23	2.0	1.3
	Ⅲ	2	8000	0.25	1.25	1.1
	Ⅳ	3	3000	0.27	0.7	0.8
Dyke	Ⅱ	4	14500	0.225	2.0	1.3
	Ⅲ1	5	8500	0.235	1.5	1.2
	Ⅲ	6	8000	0.245	1.25	1.1
	Ⅲ2	7	7500	0.255	1.0	1.0
	Ⅳ	8	3000	0.265	0.7	0.8
	Ⅴ	9	800	0.275	0.1	0.4
Rock mass	Ⅱ	10	14500	0.22	2.0	1.3
	Ⅲ	11	8000	0.24	1.25	1.1
	Ⅳ	12	3000	0.26	0.7	0.8
	Ⅴ	13	800	0.27	0.1	0.4

Simulation of Excavation Process. The excavation process was divided into 8 steps, as shown in Fig. 3.

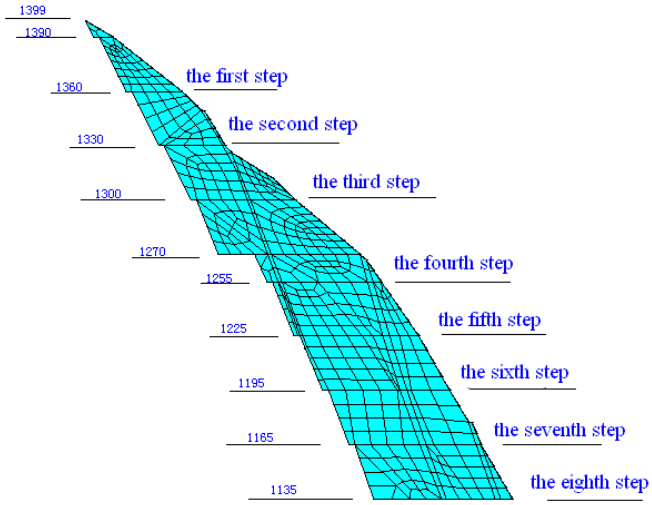


Fig. 3 The excavation steps of abutment slope at left bank

Results Analysis

Displacement. The displacement vector diagrams, total displacement isoline maps of abutment slope at left bank during excavation are shown in Fig. 4 and Fig. 5.

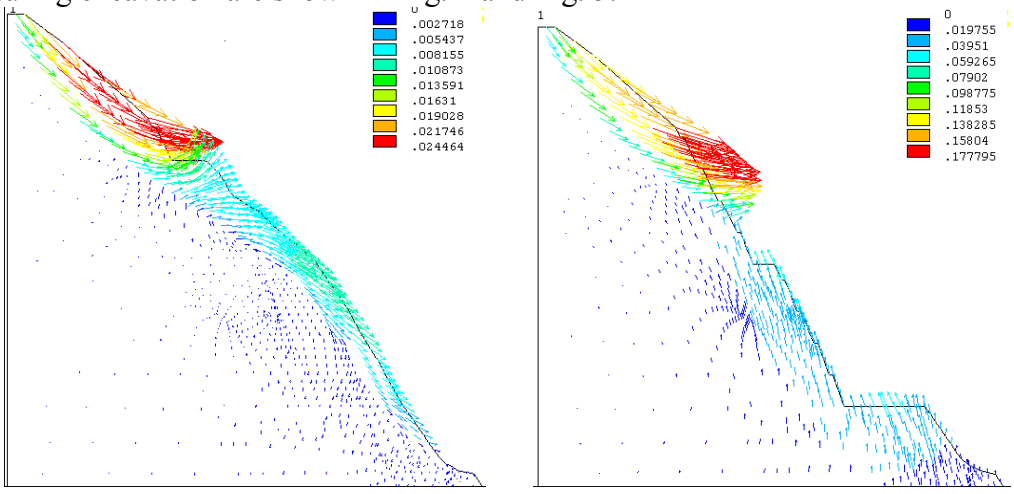


Fig. 4 The displacement vector of the first and eighth excavation step

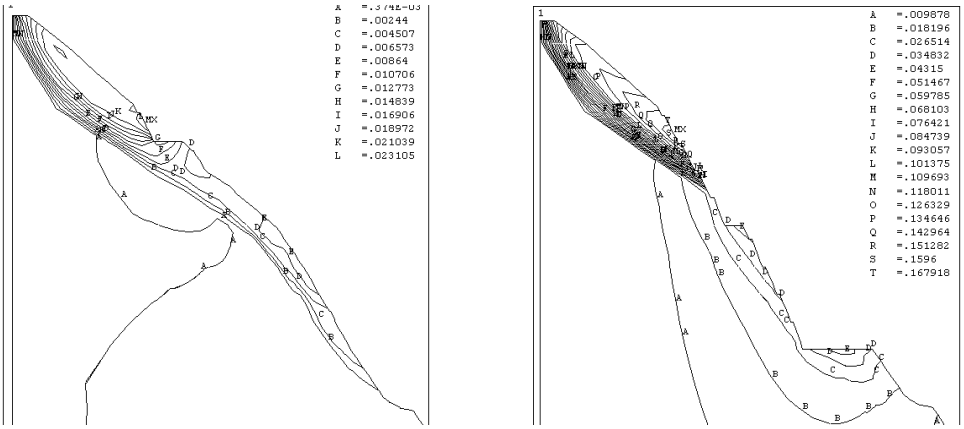


Fig. 5 Total displacement isoline of the first and eighth excavation step

In views of the process of deformation and excavation, the range of rebound deformation caused by excavation gradually increases. The displacement increment by every excavation step is relevant to the excavation volume. The bigger is the excavation volume, the larger is the deformation.

From the displacement vector diagram, the direction of displacement paralleled to the river in some places pointed in the hill. The reason of this rebound deformation lies in stress state of the rock mass on the slope. If the slope is steep and the first principal normal stresses of rock mass on the slope is zero or low tensile stresses, this rebound deformation pointed in the hill will be caused.

Stress. The isolines of the first and third principal normal stresses during excavation are shown in Fig. 6 and Fig. 7. The influence of slope excavation is small on the first and third principal normal stresses. The third principal normal stresses are mainly in the state of compression and change little with excavation, which is helpful to slope stability. Most of the first principal normal stresses are also compressive and many places on slope are in the state of biaxial compression, which is helpful to shallow stability of the slope.

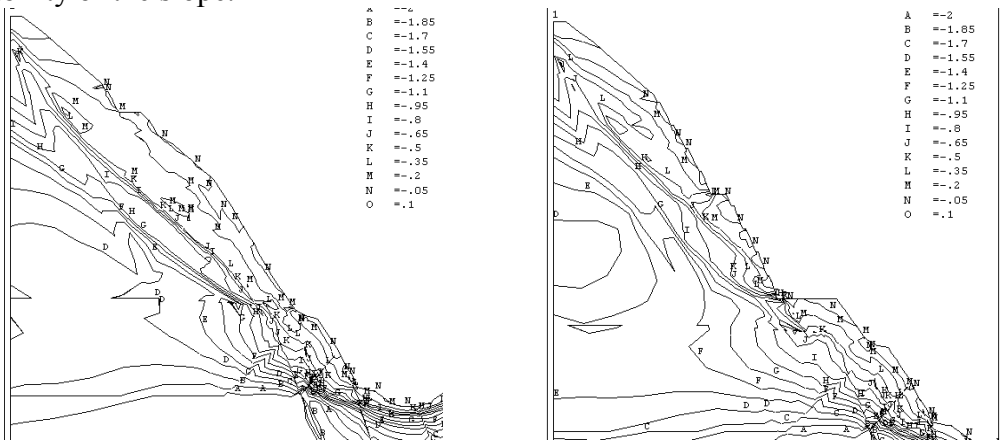


Fig. 6 Isolines of the first principal normal stresses for the first and eighth excavation step

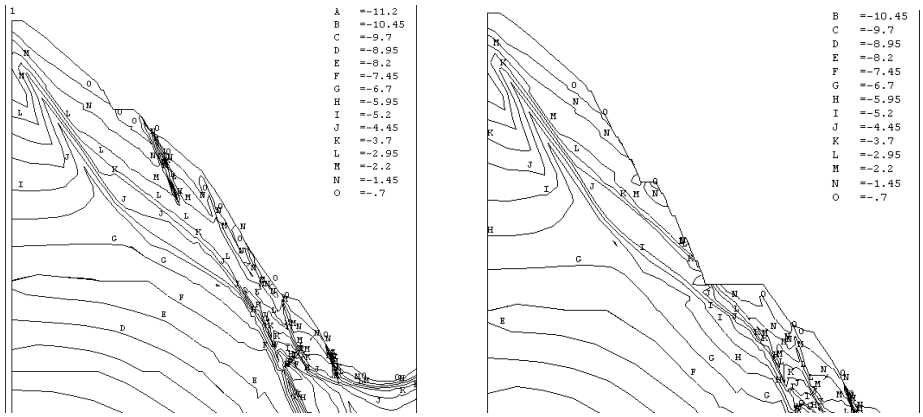


Fig. 7 Isolines of the third principal normal stresses for the first and eighth excavation step

Plastic Zone Distribution. The plastic zone distribution during slope excavation is shown in Fig. 8. The first step excavation just reached the plastic penetration zone, which caused a new outcropped plastic penetration zone. The equivalent plastic strain was large in this zone. The plastic range was located at 20-60m distant from slope face and an obvious slipping tendency was formed. During excavation, as timely support and other measures were not done, the maximum equivalent plastic strain gradually increased with the excavation, from 0.000824 at the first excavation step to 0.005456 at the last.

With the slope excavation, the plastic penetration zone in rock mass gradually moved towards slope face. The reason is that slope excavation causes relaxation zone around the slope face and the mechanical parameters are reduced, which influence the local stability on the slope.

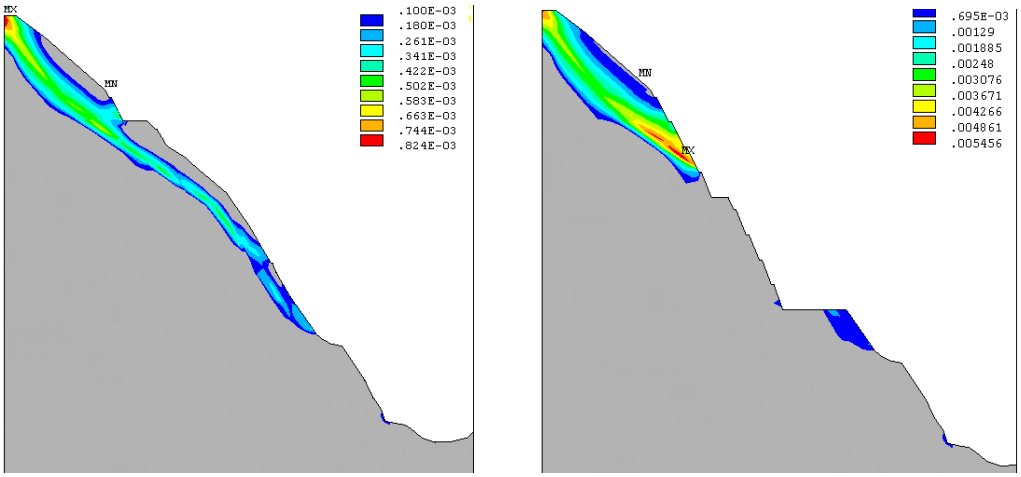


Fig. 8 Contours of plastic zone distribution for the first and eighth excavation step

Conclusions

Numerical simulation method is adopted in this paper to study the excavation course of abutment slope at left bank in Dagangshan hydropower station. The following conclusions are presented:

After the first step excavation, an obvious plastic penetration zone is formed at left bank. For keeping the slope stability during excavation, the arrangement of anchor cable before excavation is suggested and the depth of the anchor is about 65m.

The slope deformation failure was mainly shallow landslide gradually forming with the excavation, relaxation zone around the slope face. To control the local stability of slope, the supporting of slope during excavation should be adopted.

Acknowledgements

This work was financially supported by the Chinese National Natural Science Foundation (51109124), the National Special Research Program of China (973 Program) (2011CB411906) and SDUST Research Fund (2010kytd106).

References

[1] Z. Qi, Z. Tang, Q. Jiang, Finite element simulation of excavation and support of abutment slope at Dagangshan Hydropower Project, J. Rock and Soil Mechanics, 29 (2008) 161-165.

[2] P. Zhang, R. Hu, Finite element simulation of excavation and support of slope at right bank in Dagangshan Hydropower Station, Water Resources and Power, 27 (2009) 122-125.

[3] C. Zhou, W. Lu, Y. Chen, The report of slope stability and support measures in Dagangshan hydropower station, Wuhan University, Wuhan, 2007.

© (2012) Trans Tech Publications, Switzerland
doi:10.4028/www.scientific.net/AMM.238.317

Application of High Pressure Jet Grouting Technology in Seepage Prevention of ChuLou Reservoir

Shibao Zhang[1,a] and Jie Wen[2,b]

[1] North China University of Water Resources and Electric Power, Zhengzhou 450011, China

[2] Beijing IWHR Technology Company, China

[a]zhangshibao@ncwu.edu.cn, [b]wenjie1985imau@163.com

Keywords: high pressure jet grouting; Impermeable wall; quality detection; Chulou reservoir.

Abstract. In view of the existing permeable sand layer and the leakage risk which threaten the earth dam foundation of Chulou reservoir, the high pressure jet grouting measure was applied to block leakage passage to solving the leakage problems of earth dam foundation. This paper mainly describes the high pressure jet grouting impermeable wall construction, including construction equipment, technological process, construction parameters and method, and wall quality detection. The test results show that the indexes such as wall depth, continuity, compressive strength, permeability coefficient meet the design requirements. The quality of impermeable wall is accepted.

Introduction

ChuLou reservoir locates in 2 km southwest of the city of Xingyang of Henan province, it is 25 km east to Zhengzhou city, it is one of the three medium reservoirs of the upstream cascade development of Jialu River's branch, Suo River, which locates in Huai River basin. The controlled drainage area is 44.5 km^2, with a total capacity of 18.85 million m^3, its main function is flood control, and as the comprehensive utilization of the medium reservoir, it also has other functions like agricultural irrigation, urban water supply, aquaculture, tourism development. The main structure of the reservoir is the water retaining earth dam, the spillway on bank, the tunnels underground. Running for many years, the exploration of the dam foundation showed seepage channel dangers. Considering the dam foundation's water permeable sand layer and the leakage position, takes high pressure jet grouting measure to stock the leakage passage therefore solving the leakage problems of earth dam. High pressure jet Impermeable is designed as rotary dowel joint form, the grouting hole has two rows, the whole distance of the first sequence (I) hole is 1.6m, shaping the "column" wall by applying the high pressure jet grouting method, and then shape the second (II) hole with the hole distance 0.8m, then the two holes connect as an integrated Impermeable curtain structure [1].

The grouting axis coincide with ∇143.10 riding track axis, and the grouting range from 0 + 050 to 0 + 278, the total length of based grouting is 228 m, setting up 286 jet grouting drilling hole, and its total length is 4001.1 m, the total grouting length is 2077.5 m. The design drilling extend into the fifth bottom liquid limit clay layer 2 m, up stretch into the dam 1.5 m. Wall quality inspection standards: the compressive strength R28 = 3.0 ~ 5.0 MPa; Wall design permeability parameter is less than 1 x 10-6 cm/s.

High Pressure Jet Grouting Construction Technology

Construction Equipment. According to the high pressure jet grouting's quantities, schedules and other specific characteristics, through analysis and screening, the needed construction technology are:

(1) The drilling machine. XY-2, GQ-80 hydraulic pressure rotary drilling machine, it applies to the clay layer, sand layer and sand soft stone layer.

(2) High pressure jet grouting equipment:ZL-400 high speed pulp machine;TV-6/8 air compressor; 3D2-S series high pressure pump; BW150 grouting pump.

(3) High spraying trolley. Using GYP-5 high spraying trolley, hoisting height up to 15 m, hoisting weight 2 ~ 3 t, and the hoisting speed 6 ~ 25 cm/min.

High Pressure Jet Grouting Construction Parameters. The project adopts high pressure rotary dowel joint seepage control program, divide the grouting process into two sequences, the construction parameters of high pressure jet grouting determines to some extent whether the grouting is success or not. According to the interval value of the various grouting construction parameters given by design company, detect the construction parameters like filling slurry density, wind pressure, hydraulic pressure, slurry pressure and also apply the ground grouting test [2], and collaborating with the design company and supervisor company, eventually determine the related grouting construction parameters: water pressure is 38MPa, gas pressure is 0.7MPa, slurry pressure is 1.0MPa, slurry is gravity 15.8kN/m^3, the lifting speed is 12cm/min, the rotating speed is 10 r/min, back slurry gravity is 13.0 kN/m^3,the drilling aperture is 100 mm.

Main Construction Program. The grouting construction is divided into two sequences, the main construction procedure of single hole is: machines in place-drilling-put into the grouting tube-slurry grouting injection and ascension-flush piping-orifice back injection, etc [3].

(1) Drilling. Apply the hydraulic rotary drill with alloy aiguille of diameter arrange from 110mm to 150 mm, after drilling emplacement, aiming the drill pipe to the design hole, calibrating horizontal balance level of the body and fastening the base and frame of the machine. The hole deviation should be less than 50 mm. To ensure that the borehole partial slope is not more than 1% of the design requirements, the single length of the drill pipe is 20m, use the detection instrument KXP-1 to measure the hole inclination and rectify timely, In the process of the porous, if meeting the abnormal phenomenon such as drills drop or block, corresponding measures adopted timely, and need to make record. Takes the design hole deep as the construction reference value and adopts below 2.0 m of the relatively impermeable layer as the end hole depth. After the drilling, detecting hole deviation, grouting into mud to fasten the wall, in order to avoid the case of hole collapse and prevent mud enter into the hole smoothly.

If the hole deviation failed to meet the requirement, effective measures should be taken as rectification until it is available. Supervisor need to examine the hole deep and hole deviation and confirm the qualification is up to standard, and then sign the certification to grant to the next procedure construction.

(2) Grouting experience. Locate the high pressure jet grouting vehicle, connect the water, gas, mud pipe and check the injection direction and swing angle, switch on the machine to examine the mechanic and pipeline operation, and accurate the injection direction and swing angle.

(3) Enter into the jet tube. To prevent mud flow backward and block tube nozzle, covered the nozzle with rubberized fabric, then slowly enter into the hole until arrived the bottom.

(4) Pulp making. Pure cement mud adopted as the grouting pulp, PO 42.5 ordinary Portland cement is chosen to meet the requirement, the mixture ratio is 1:1, the corresponding proportion of the slurry is not less than 15.0 ~ 16.0 kN/m^3, adopting high speed pulping mechanism to make the pulp. Measuring the slurry proportion during the pulping process, if it is relatively lower, increase the cement to ensure the slurry mixed well.

(5) Jet grouting. According to design rotary jet grouting method and construction parameters to send high pressure water, compressed air and water mud. When the pump pressure, wind pressure, hydraulic pressure meet the design setting value, firstly high pressure rotary jet grout the situ hole bottom for 1～3 min, when grout return ratio exceed 13 kN/m³, ascend the jet tube according to the design rate, from the bottom-up, jet continuously until reach the design rotary jet grouting elevation, then again situ rotary jet for 1 ~ 2 min, after that, can stop water supply, air supply and mud sending and pull out the jet tube from the grouting hole. In the process of spraying, the ascending speed should be continuous and well-distributed, accurate measuring, ensures the cement mixed quantity not less than the design, and takes the construction record.

To ensure the quality of wall body, if have any abnormal or special situations during the construction process, the follow method should be taken [4]:

(1) testing the in and out cement mud, when the error exceed 0.1 to the allowed one, immediately stop spraying, and readjust the slurry cement ratio to meet the requirements.

(2) Any case interrupt injection (including remove nozzle), restore injection, if the interrupt time is short, the lap length should be not less than 0.5 m; if need to interrupt for a long time (more than 30 min), the lap length should be not less than 1.0 m.

(3) During the jet process, the spill mud go beyond (more than 20% of the grouting quantity) or completely no spill is the abnormal situation, the corresponding measures are: for overwhelming spill, improving the injection pressure or improve speed and rotate speed in order to reduce the spill; for no spill situation, to increase grouting quantity, to slow down the increase speed and static spray until the orifice appear return mud to use the normal injection method.

Static pressure backfill grouting: After the whole hole injection process, make use of the return slurry or the dense cement mud, backfilling the vacancy hole formed by water separating as it is sinking until the slurry no longer sinking.

Impervious Wall Quality Testing [5]

The Core-Drilling Depth Detection. High pressure jet grouting water pressure test is applied after finishing grouting 28 d. The detection hole should be located in the complex layout or in thebe of the quality defect. The detection hole number should be less than 10% of the whole grouting number, at least a check hole needed for a unit project. Check the hole position, according the construction record, among the stake number of 0+160～0+245, more cement is used, reaching 245 kg/m～255 kg/m, and other grouting part average cement consumption is about 210 kg/m. The final volume should consult with design and supervision department. This project has 6 detection hole: 0+120, 0+121, 0+160, 0+170, 0+240, 0+260/. From the view of drilling depth, meet the design depth requirements.

The Wall Body Continuity Test by GPR. GPR test work takes continuous measurement methods, the measuring line arranges near the top of the wall.

Combined with detection range of GPR and practical project, the detection range 0 + 050～0 + 130 section, round-trip twice detection. From the gained image analysis, there is no abnormal in the wall among the GPR detection rang; from local wall GPR detection result, in the radar detection range the wall continuity is better, no apparent discontinuous and empty phenomenon appear.

The Compressive Strength Test of Wall Body. Chose core sample which drilling from different elevation and its size meet the experiment requirement, 3 samples are chosen in every 5 m. The total groups are 12 and the core samples are 36. After maintenance processing and the indoor test, the results show that the no lateral restraint compressive strength value of intact core samples range from 3.7 to 5.1 MPa.

The Water Injection Test. Drilling water pressure test applies a single-point method by divided into several segmentations. The project places 31 water injection check hole, 54 water injection test section, the total length of the section is 197.9 m. Water injection test micro permeable test 15 groups, the permeability coefficient range 1.22 x 10-6 ~ 5.12 x 10-6 cm/s, accounting for 27.8% of the number of practical groups; Water injection test of microscopic permeable test 39 groups, the permeability coefficient value range 5.05 x 10-7 ~ 9.75 x 10-7 cm/s, accounting for 72.2% of the total groups, the permeability coefficient of impervious wall is less than the design requirements value.

Conclusions

According to the unit engineering quality assessment standards made by supervisor, make a comprehensive evaluation to the high pressure jet grouting construction technique, the total unit projects are 12, and the results all meet the requirement.

By core drilling, laboratory test, water injection test, as well as using GPR to detect the special part of the wall, the core sample of impervious wall is integrated, with little clip mud phenomenon, no faultage, and the wall continuity is fine, the core sample unconfined compression strength test and the permeability coefficient comply with the design requirements, the impervious wall quality is qualified.

High pressure jet construction practice shows that applying high pressure jet technology in the part of thick wall and the stratum complicated part, it has fast speed in construction and the technique and experience are grown to be perfect, the related index meet the design requirement, so the technique has been further applied in dam foundation seepage prevention.

References

[1] L. Dong, The reinforcement project preliminary design report of Chulou reservoir in Xingyang City, Zhengzhou Water Conservancy Construction Survey and Design Institute, Zhengzhou, 2008.

[2] X. Li, High pressure jet grouting technology in the application of a impervious wall construction, Yellow River, 12 (2010) 217-219.

[3] DL/T5200-2004, The High Pressure Jet Grouting Technology Standard of Water Conservancy and Hydropower Engineering, China Electric Power Press, Beijing, 2005.

[4] L. Zhang, Q. Xiao, The high pressure rotary jet impervious wall construction of Xixia reregulating reservoir, Yellow River, 7 (2006) 57-58.

[5] Z. Lv, K. Bian, The grouting quality inspection report of reinforcement project of Chulou reservoir in Xingyang city, Henan KeYuan water conservancy project detection Co., LTD, Zhengzhou, 2010.

© (2012) Trans Tech Publications, Switzerland
doi:10.4028/www.scientific.net/AMM.238.321

Reservoir Operating Policies Analysis by Using Genetic Algorithm

Shibao Zhang[a] and Jie Wen[b]

North China University of Water Resources and Electric Power, Zhengzhou 450011, China

[a]zhangshibao3655@163.com，[b]wenjie1985imau@163.com

Keywords: water resources; NSGA-II; optimal operation; multi-objective optimization.

Abstract. The target of this paper is to look for the optimal program in reservoir operation by using Simple Genetic Algorithm and NSGA-II (Non-Dominated Sorting Genetic Algorithm- II) in Matlab 2009a, and then make a comparison with the operation model's operation results in MODSIM, which is a generic river basin management decision support system.

Introduction

The use of evolutionary algorithms (EA) for optimizing reservoir operation has been gaining in popularity since the 1990s [1, 2], and the algorithm has been improved as the development of the computer technology, from Simple Genetic algorithm [3] to NSGA (Non-dominated Sorting Genetic Algorithm) [4] and then to the improved NSGA-II [5], which can be used to solve multi-objective problems.

The optimization theory of the MODSIM, the SGA and the NSGA-II

MODSIM simulates water allocation mechanisms in a river basin through sequential solution of the following network flow optimization problem for each time period $t = 1,...,T$:

$$Minimize \sum_{l \in A} C_l Q_l \tag{1}$$

subject to：

$$\sum_{l \in Q_i} Q_l - \sum_{k \in I_{iq}} Q_k = b_{it}(Q) \tag{2}$$

For all nodes i∈N

$$L_{lt}(Q) \le Q_l \le U_{lt}(Q) \tag{3}$$

For all links $l \in A$, where A is the set of all links in the network; N is the set of all nodes; O_i shows the set of all links originating at node i (i.e., outflow links); I_i shows the set of all links terminating at node i (i.e., inflow links); bit is the (positive) gain or (negative) loss at node i at time t; Q_l means flow rate in link l; C_l are costs, weighting factors, or water right priorities per unit flow in link l; and L_{lt} and U_{lt} are lower and upper bounds, respectively, on flow in link l at time t. As L_{lt}, U_{lt} and b_{it} are functions of Q, non-network constraints are introduced into the problem. Esq. 1-3 is then solved with the Lagrangian relaxation algorithm RELAX-IV. Lagrangian relaxation algorithm focus on the lower bound of a problem, which is different from many algorithms and its basic principle is to absorb the constraints which makes the problem difficult into the target function, meanwhile, keep the objective function remain linear, thus making the problem easier to solve [6].

The Simple Genetic Algorithm is based on the Darwinism, which select the superior and eliminate the inferior during the evolution procedure. It can find the better solution by select, cross, mutation process; The NSGA-II has following Improvement: It has a better sorting algorithm, and possess incorporates elitism, and no sharing parameter needs to be chosen a priori [7]. NSGA-II can handle conflicted problems, and find all the Pareto solutions for the decision makers to choose the suited one to set up the operation rules. Its flow chart can be seen in Fig. 1.

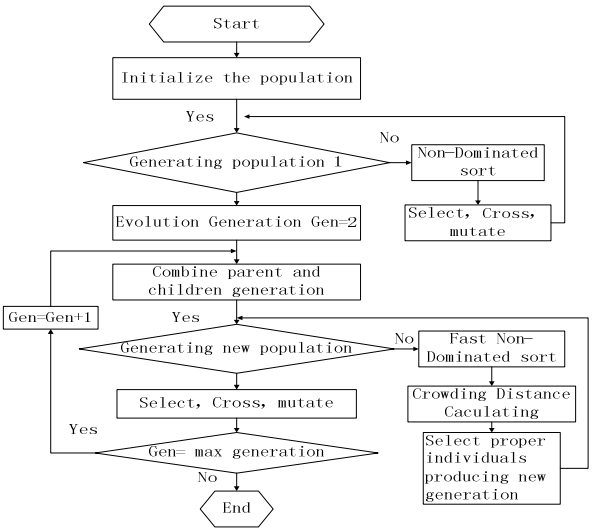


Fig 1 The flow chart of the NSGA-Ⅱ

Model formulation

Set up the model in MODSIM. The data is extracted from a reservoir which located in Inner Mongolia，China, and its main water consumption department. In order to simplify the model, the data we use are monthly time series of the typical year with largest inflow volume, and we just choose the reservoir as the storage nodes, and design only a non-storage point and a demand node as upstream inflow and downstream demand. Fig. 2 shows the MODSIM of the reservoir. In the figure, the red triangle stands for the reservoir, the blue round is the upstream inflow, and the purple square means downstream demand. As the needed data was imported into the MODSIM, it can calculate the value of different target, then give the result of water distribution, and export the result into Microsoft Access database.

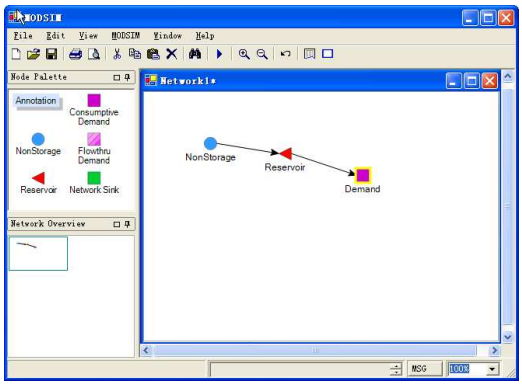


Fig. 2 MODSIM of the Reservoir

Set up the objective function. The main target of reservoir operation is to generate strategy to allocate water to meet the demand of downstream and the target storage. So the model contains two objectives, the first one is to minimize the squared difference value of the downstream demand and the water released from the reservoir, the function can be shown as follows, among the equation, R(t) is the monthly release from the reservoir, and D(t) is the demand of the downstream,

$$Minimize \quad (Y)_1 = \sum_{t=1}^{12} (D(t) - R(t))^2 \tag{4}$$

The second is to minimize the squared difference of the reservoir's storage and the target storage after releasing. That is,

$$Minimize \quad (Y)_2 = \sum_{t=1}^{12} (T_r(t) - T_t(t))^2 \tag{5}$$

Where $T_r(t)$ refers to monthly target storage, and $T_t(t)$ is the storage after water release.

Import the data. As the description in former paragraph, the data used is shown in Table 1.

Table 1 The extracted data from the watershed status (m^3)

Date(typical year)	Inflow	Downstream Demand	Target storage
1st January	9493.667	30710.5	152202
1st February	12006.2	48236.3	152043.3
1st March	12567.13	35119.9	152256
1st April	28203.8	53593.1	157901.3
1st May	54204.07	31009.5	177539.9
1st June	56084.8	59903.3	191852
1st July	45973.6	43852.6	197751.3
1st August	38715.4	63271.8	206361.3
1st September	32220.07	60453.2	203737.3
1st October	21708.73	46167.7	201128
1st November	21849.27	55491.3	193127.3
1st December	13290.4	69013.3	178749.3

Running the models in Modsim and Matlab . We imported the data with upstream inflow, reservoir target storage and capacity constraint and downstream demand into MODSIM, then run it and got the result of 12 months' solution of release water and the storage in the reservoir. After that we run the single model in Matlab Genetic Algorithm Pattern Research, and get another array of solution. As there are two objective functions, we use the weighted means method, in order to make the two objective function values in the same order of magnitude, we give the first weight coefficient 0.8, and second 0.2. So the objective function is

$$Minimize(Y)=0.8\sum_{t=1}^{12}(D(t)-R(t))^2+0.2\sum_{t=1}^{12}(T_r(t)-T_t(t))^2 \tag{6}$$

Since the objective function is based on the reservoir releases in each time step, releases should be the decision variable on which the GA is based. Therefore twelve decision variables are considered. The storage can be calculated by initial volume in the reservoir add inflow from the upstream then reduce the release, random number Generation, crossover and mutation probability is carried out to run the model.

Lastly, same data and the two objective functions model were solved in NSGA-II. When given initial value of 3000 as the start point, it can get the solution set quickly. We designed the population size as 80 and the parameter of Pareto fraction as 0.4. Then we got the solution set with solutions of 40 in the Pareto front. Fig.3 shows the Pareto front from NSGA-II.

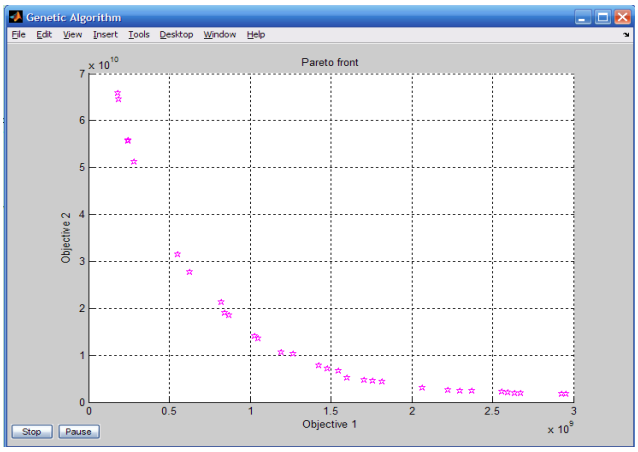


Fig. 3 The Pareto fronts of the NSGA-II

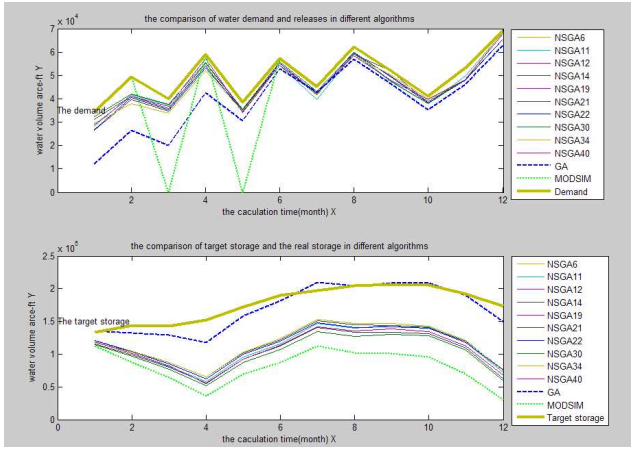


Fig. 4 Comparison of the solutions of 3 algorithms

Comparing the result of the different methodologies. We used the Matlab plot function to compare the result from different algorithms. As when given different priority value to different target in MODSIM, we could gain different results. The comparison result also divided into three figures, which show the common result, the result with demand having the priority, and the result

with the storage having the priority. The solutions from NSGA-II were chosen according to different emphasis. Fig. 4 to Fig. 6 illustrate the different situation. We can see that in Fig. 4, the result of the water release solution from the Modsim can just meet the demand except March and May, but in meeting the target storage of the reservoir; its performance is the worst. The result from GA shows its profit in meeting the reservoir's target storage, but in meet the water demand of the water consumption department of the downstream flow, it works not that well, especially in the early half year. The results which extract from the Pareto front of the NSGA-II show its strengthen in meeting the downstream water demand, and it is also works better than Modsim in fulfill the storage target. Correspondingly, in Fig. 5 and Fig. 6, GA and NSGA-II all show their better performance, especially when the storage given priority, the solutions from NSGA-II performance are quite good in compromise the two objectives.

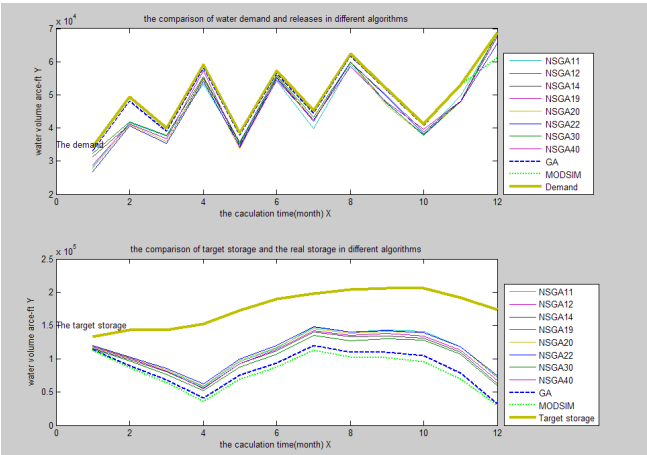


Fig. 5 Comparison of the solutions from three algorithms with the demand having priority

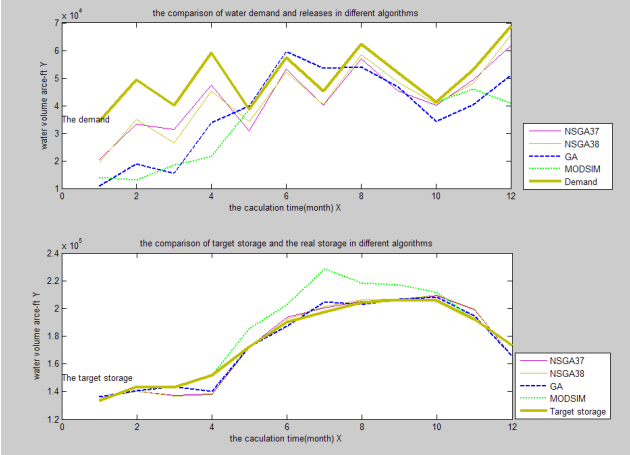


Fig. 6 Comparison of the solutions from three algorithms with target storage having priority

Conclusions

The MODSIM, which is based on Lagrangian relaxation method, can find out many exact points when given proper priority, but it neglects other points. The solution in GA can get similar results when given proper weighted number, and can also give consideration to other points. In meeting the two objectives, it works not very well. The NSGA-II can neglect the defect of GA, some solution in Pareto Front puts up satisfied performance in finding solution and considering two objectives.

References

[1] John W. Labadie, MODSIM decision support system for integrated river basin management, Colorado State University, 1999.

[2] A. Augugliaro, L. Dusonchet, E. Riva Sanseverino, Evolving non-dominated solutions in multi-objective service restoration for automated distribution networks, Electric Power Systems Research, 59 (2001) 185–195.

[3] V. Jothiprakash, S. Ganesan, Single reservoir operating policies using genetic algorithm, Water Resources Management, 20 (2006) 917–929.

[4] A. Augugliaro, L. Dusonchet, M. G. Ippolito, E. Riva Sanseverino, Multiobjective design of distributed reactive power production in a deregulated electric market, Electrical Power and Energy Systems, 27 (2005) 205–214

[5] X. Jin, J. Zhang, J. Gao, W. Wu, Multi-objective optimization of water supply network rehabilitation with non-dominated sorting genetic algorithm-II, Zhejiang Univ. Sci., A3 (2008) 391-400.

[6] J. M. Ngundam, F. Kenfack, T. T. Tatietse, Optimal scheduling of large-scale hydrothermal power systems using the Lagrangian relaxation technique, Electrical Power and Energy Systems, 22 (2000) 237–245.

© (2012) Trans Tech Publications, Switzerland
doi:10.4028/www.scientific.net/AMM.238.325

Thermal Stress Analysis of Large Scale U-Shaped Aqueduct

Jianhua Zhang

North China University of Water Resources and Electric Power, Zhengzhou 450011, China

yuluem@sina.com

Keywords: U-shaped aqueduct; thermal stress; steady thermal; transient thermal.

Abstract. The aqueduct is one of large scale water conservancy project across river, which is the first level of anti-cracking structure with rigorous control of cracks. At present, the thermal analysis of aqueduct structure most borrows ideas from box-girder bridge structure without considering their difference. As the thermal stress of large-scale concrete structure during construction and operational process is redoubtable, the U-shaped model of a practical aqueduct of South-to-North Water Diversion is established to do the steady and transient thermal analyses. The result shows that the structure of U-shaped aqueduct is reasonable, it is not necessary to take special measures to control the temperature during the construction and operational process.

Introduction

The aqueduct is one of large scale water conservancy project across the river, is the 1th level of anti-cracking structure, the cracks demanding is rigorous, once the cracks appears, it will cause large economic loss. At present, the thermal stress analysis of aqueduct is less, most temperature analysis draw lessons from box girder temperature, but they are different. First, it is flowed liquid in aqueduct but it is flowed gas in box girder bridge; Secondly, the Box girder flange is longer, and sunshine is less impact on the web, the aqueduct is shorter, solar can directly radiate to the web, it is much impact. So the method of box girder thermal stress can only draw lesson not copy. Temperature stress of large-scale concrete structure during the construction and operational process can not be ignored resulting from uneven temperature.

Steady State Thermal Analysis

The ultimate limit state of operation is taken to design during the thermal stress analysis, temperature load coefficient is 1.254, the equivalent temperature method is adopted in stress analysis of concrete structure, that is the temperature is transformed to equivalent temperature,

$$T^* = \rho T \tag{1}$$

Where T is the actual temperature, ρ is the stress relaxation coefficient, which is taken as 0.3 in this calculation.

Transient Thermal Analysis

Temperature Distribution of the Aqueduct during Construction. Calculation conditions of construction are: Warehousing temperature of Concrete is 14 ^{o}C, and air temperature is 14 ^{o}C.

Hydration heat calculation expression is taken from the Specifications for Hydraulic Concrete Construction1 during the construction, it is

$$Q_t = Q_0[1 - \exp(-m t^n)] \tag{2}$$

Where Q_t is the accumulated heat of hydration of t age (kJ/kg); Q_0 is the final heat of hydration (kJ/kg); t is concrete age (d); m and n are the heat transfer coefficient of cement.

Concrete elastic modulus calculation formula is taken from the Specifications for Hydraulic Concrete Construction1 during the construction, it is

$$E_c(t) = 1.44E_c(28)[1-\exp(-0.41t^{0.34})] \tag{3}$$

$E_c(28)$ is 28 days of the elastic modulus of concrete; $E_c(t)$ is t of the elastic modulus of concrete.

It emits heat due to the hydration heat during the hardening of concrete, the differential equation of heat conduction in actual working conditions is

$$\frac{\partial T}{\partial t} = a\nabla^2 T + \frac{\partial \theta}{\partial t} \tag{4}$$

In which $\nabla^2 = \frac{\partial^2}{\partial x^2} + \frac{\partial^2}{\partial y^2} + \frac{\partial^2}{\partial z^2}$

Internal heat source expression of concrete structure is

$$\frac{W}{c_p \rho} = \frac{\partial \theta}{\partial t} \tag{5}$$

Where $\theta(t)$ is the hydration heat emitted heat all used to raise its temperature; t is age; W is the heat emitted by Unit volume per time; c_p is Mass heat capacity at constant pressure.

Boundary Value Condition of Temperature Field

The heat conduction differential equation containing time coordinate variables and spatial coordinate variables. In order to solute the function of temperature field T, two kinds of boundary value conditions must be considered, they are time boundary value conditions(also known as initial conditions) and spatial boundary value conditions(also known as Boundary conditions).

Initial Conditions. At the beginning transient, temperature distribution of the whole object is known;

$$T\big|_{t=t_0} = T_0(P), \qquad [P \in (V, s)] \tag{6}$$

$P = P(x, y, z)$ is the point in space or space coordinate variables.

Boundary Conditions. Generally it is divided into three categories.

The first kind boundary condition: the instantaneous temperature distribution are Known on boundary s_1.

$$T\big|_s = T_b(P,t) \qquad (P \in s_1, t > t_0) \tag{7}$$

The second kind boundary condition: The instantaneous heat flux density is known on boundary s_2.

$$q_n\big|_s = -\lambda \frac{\partial T}{\partial n}\ \Big|_s = q_b(P,t), \quad (P \in s_2, t > t_0) \tag{8}$$

Where n express the Outer normal direction, (8) express the outward heat flux density. If a surface is heat flux symmetry plane, then q_n=0 on the surface, that is adiabatic boundary.

The third kind boundary condition: the convection heat exchange are Known on boundary s_3. If the object is contact with the fluid, in accordance with the law of heat convection

$$q_n\big|_s = -\lambda \frac{\partial T}{\partial n}\ \Big|_s = \beta(T - T_a), \quad (P \in s_3, t > t_0) \tag{9}$$

Where β is convection heat transfer coefficient, its dimension is $\mathrm{MT^{-3}\Theta^{-1}}$, its company is $\left(\frac{\mathrm{W}}{\mathrm{m^2 \cdot ^o C}}\right)$. T_a is fluid temperature, β is related to the velocity of the fluid, flow pattern and viscosity. When β is very small, $q_n \to 0$, it is close to adiabatic boundary condition; When β is very large, because q_n is limited value, $(T\text{-}T_a) \to 0$, the boundaries temperature T of objects is close to the fluid temperature T_a.

Engineering Example

The shahe aqueduct is combination building, that is dry aqueduct of acrossing Shahe, Jiangxianghe, Dalanghe and the swale zonary, and that is arrounding the lushan sloping flowing aqueduct. Interior rad of U-shaped aqueduct is 4 m, side thickness is 0.35m, the width of gutter pier is 1m, the height is 8.6m, singly slit lateral width is 10.4m, single span length is 45m.

The thermal structure coupled analysis method is adopted to have Thermal analysis to seek aqueduct temperature field, then to have structure analysis, that is making the temperature field of thermal analysis as a load of the structure, then result the displacement and the stresses distribution of aqueduct.

The thermal analysis of U-shaped aqueduct considers eight conditions in all. Aqueduct water is the turbulent state, the temperature of aqueduct in the water is water temperature; The part in the air exerts the air temperature. The outer surface temperature of side wall is 32^{o}C during the thermal analysis in summer, water temperature is 24^{o}C; The outer surface temperature of side wall is 1^{o}C during the thermal analysis in winter, water temperature is 9^{o}C, Temperature difference is 8^{o}C. The inside and outside surface of aqueduct is the first boundary condition, the both ends are Adiabatic boundary condition.

The Stress Summary Table of U Shape Aqueduct Steady Temperature Analysis. The stress summary table of U shaped aqueduct steady temperature analysis is listed in Table 1.

Table 1 The stress summary table of U shaped aqueduct steady temperature analysis

conditions	σ_x,place and reason(MPa)	σ_y, place and reason(MPa)	σ_z,place and reason(MPa)
Empty slot in the summer	0.05	0.03	0.09
	Bearing	Bearing	Bearing
	External constraint	External constraint	External constraint
Empty slot in the winter	0.02	0.01	0.06
	Bearing	Bearing	Bearing
	External constraint	External constraint	External constraint
Half cell in the summer	1.04	0.94	0.56
	Inner wall of Two ends	the inner wall of Both sides	the inner wall of Both sides
	Self constraints	Self constraints	Self constraints
Half cell in the winter	0.92	0.84	0.51
	outer surface of the central and end	outer surface of aqueduct bottom	outside surface of both sides
	Self constraints	Self constraints	Self constraints
Designed water in the summer	1.18	0.90	0.59
	Inner wall of Two ends	inner wall of Both sides	the inner wall of Both sides
	Self constraints	Self constraints	Self constraints
Designed water in the winter	1.08	0.85	0.57
	outer surface of both ends	outer surface of aqueduct bottom	The outside surface of both sides
	Self constraints	Self constraints	Self constraints
Groove in the summer	1.10	0.87	0.58
	inner wall of both ends and middle part	inner wall of both ends	the inner wall of Both sides
	Self constraints	Self constraints	Self constraints
Groove in the winter	1.52	0.82	0.58
	outer surface of both ends	outer surface of aqueduct bottom	outer surface side of both ends
	Self constraints	Self constraints	Self constraints

U-shaped aqueduct has the advantage being richly endowed by nature under temperature difference, because it has smooth surface and lightweight structure, the value of Stresses are small, and no stress concentration. Because the stress is less than the tensile strength design value of C50 concrete, there isn't cracking, and it is not necessary to take measures to control temperature, the prestress in the structure can avoid the whole tensile stress, and it also plays a better effect to prevent temperature crack for aqueduct.

The Temperature Distribution of the Aqueduct in Construction. The pouring of aqueduct is divided into two stages, the first pouring is to the neutral axis of cross section, and the second pouring is to the top, the time interval is 10 days between the two pouring, the calculation is 30 days in all. The concrete strength grade of aqueduct is C50, elastic modulus of 28 days is $3.45\times10^4 N/mm^2$, construction conditions is transient thermal analysis, The boundary condition is the third, it is considered that the stress relaxation because of concrete creep during the calculation of temperature stress of construction.

Due to limited space the calculation of image is no longer gusher. During the first pouring stages condition the temperature reached a maximum on second day T_{max}=20.666 ^oC, the body temperature fell daily from the third day, the highest temperature fell down to 15.428 ^oC. The second pouring stages is finished on the eleventh day, the highest temperature appears on the top of middle wall. Thereafter, the temperature is falling with time, and the highest temperature falls down to 15.552 ^oC on the sixteenth days.

It can be seen that Hydration heat dissipates soon, the body temperature of concrete tends to be steady in a week and is close to the air temperature.

The Thermal Stress Distribution of Aqueduct in Construction. Confined to length, the computing cloud is omitting. The stresses $\sigma_x\sigma_y\sigma_z$ exceed 1MPa in the fifth day, but early concrete elastic modulus is small, there is no major effect on aqueduct. The σ_x maximums of the tenth days, the fifteenth days and the twentieth days gradually reduce to 0.50MPa, 0.28MPa and 0.27MPa; The σ_y maximums are 0.39MPa, 0.38MPa and 0.37MPa; The σ_z maximums are 0.43MPa, 0.41MPa and 0.54MPa.

Conclusions

The maximum stress is 1.52MPa under the summer and winter temperature difference, and it is less than the tensile strength designed value of C50 concrete, then it cannot appear the cracking on U-shaped aqueduct during the operation, and it is not necessary to consider the stresses resulting from temperature change, the prestress in the structure can avoid the whole tensile stress, and it also plays a better effect to Prevent temperature crack for aqueduct.

U-shaped aqueduct for hydration heat has large temperature change in a short period of time (a few days) during construction pouring, but because the wall thickness is smaller, and the temperature drops more quickly, then it results in smaller temperature gradient in aqueduct and the stress is not great. So temperature stress can be regardless.

Therefore, U-shaped aqueduct has superiority on the stress; it should be given priority in the structural design.

References

[1] SDJ 207-1982, Specifications for Hydraulic Concrete Construction, China Electric Power Press, Beijing, 2002.

[2] B. Zhu, Temperature Stress and Temperature Control of Large Volume Concrete, China Electric Power Press, Beijing, 1999.

© (2012) Trans Tech Publications, Switzerland
doi:10.4028/www.scientific.net/AMM.238.329

Analysis on Axial Stresses of Crossbars on Aqueduct

Xinli Bai [a], Jiangyan Li [b] and Bing Ma [c]

North China University of Water Resources and Electric Power, Zhengzhou 450011, China

[a]baixinli@ncwu.edu.cn, [b]ljywater@126.com, [c]mabwater@126.com

Keywords: aqueduct; crossbar; axial stress; height-width ratio; water depth.

Abstract. By use of finite element method, the axial stresses of crossbars on the top of a simply supported rectangular-sectioned aqueduct were calculated in this paper. Three factors were considered, namely height-width ratio, water depth and crossbars spacing. The results show that, most crossbars are in compression when the height-width ratio of aqueduct cross-section is small, and with the height-width ratio increasing, the axial forces of crossbars change from compression to tension; Under a certain height-width ratio, when water depth is relatively small, most crossbars are in compression, and with the increase of water depth, axial forces of crossbars change from compression to tension; big axial tensile force is harmful to the rectangular cross-section floor (mid-span), but favorable to the side wall bottom. The obtained change rules of axial force and the influence of axial force on aqueduct body stress can be referenced to aqueduct design.

Introduction

Aqueduct is one of the indispensable interchanges buildings and key structural [1] in South- to-North Water Transfer Project.

According to aqueduct cross-section, rectangle and U-shaped cross-section aqueducts are widely used. According to whether crossbars are set on the top of an aqueduct, they can be divided into the aqueduct with crossbars and the aqueduct without crossbars. The spacing of crossbars is decided by the height and width of aqueduct cross section.

Crossbars on the top of rectangle aqueduct play a very significant role in improving its transverse stress conditions. It not only can reduce the maximum principal stress of some important area of the cross section, but also can make tensile stress of some area changing into compressive stress [2]. Therefore, it is necessary to analyze the forces of crossbars, finding out their mechanical rules, in order to make the crossbars favorable to the aqueduct.

Computation Model

In order to find the variation rule of axial forces of crossbars (in tension or in compression), the aqueduct body alone is taken as calculation model and analyzed by finite element method [1, 3-7]. Only the dead weight and water weight are considered in the analysis. Because of symmetry, only half a span is taken and the crossbars are numbered (1) ~ (6) from end section to the mid-span cross section, as shown in Fig 1.

The key dimension of beam-type aqueduct is its span [8], and the height-width ratio (H/B) has certain effect on the axial forces of crossbars. So three factors are considered in the calculation:

(1) Influence analysis of different height-width ratio. Six different height-width ratios were considered: 0.6, 0.8, 1.0, 1.2, 1.4 and 1.6.

(2) Influence analysis of different water depths. Five different water depths were considered.

(3) Influence analysis of different spaces on the axial force.

Calculation Result Analysis

By use of general finite element software, calculation was carried out for the axial forces of crossbars under the action of dead weight and water weight, considering the different height-width ratio, different water depths and different spacing of crossbars. Tensile force is defined as positive and compressive force as negative.

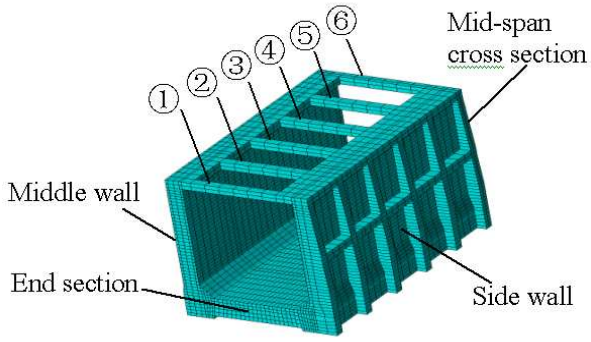


Fig. 1 Calculation model and crossbar numbers

Influence Analysis of the Different Height-width Ratio. Axial forces of crossbars under different height-width ratios are listed in Table 1.

Table 1 Axial forces (kN) of crossbars under different height-width ratios H/B

Height-width ratio H/B	Crossbars Number					
	No.1	No.2	No.3	No.4	No.5	No.6
0.6	11.9	5.43	-28.8	-55.1	-66.3	-68.9
0.8	80.4	101.4	80.9	61.4	52.9	51.1
1.0	75.7	90.8	79.4	67.9	62.5	61.3
1.2	111.8	140.2	135.3	131.1	126.7	125.6
1.4	154.3	193.8	197.6	196.3	194.7	194.3
1.6	267.5	266.7	266.3	263.5	254.9	205.0

It can be seen from Table 1 that, when aqueduct height-width ratio is comparatively small, most crossbars are in compression and they should be called columns. Only the end crossbars (bar (1) and bar (2) are tensile, can be called draw bars.

With height-width ratio increases, the axial forces are growing. Height-width ratio becomes the main influence factor, and other factors (such as the basic constraint, the distance of mid-span to the cross-section, etc.) become less obvious.

The greater the axial forces (in tension) are, the more harmful to the aqueduct floor (mid-span), and more favorable to the side wall bottom.

Influence Analysis of the Different Water Depths. After calculation, the axial forces under different water depths are obtained. And now the axial force results under the height-width ratio of 1.0 are listed in Table 2.

From Table 2 we can see that, for a given height-width ratio rectangle aqueduct, when aqueduct is empty or water depth is small, most crossbars are in compression, and should be called columns. When the water depth changes from 0.0 m to 2.5 m, most crossbars' axial forces increase gradually, and achieve maximum value when water depth reaches to 2.5 m. Then the axial pressure decreases gradually and finally become axial tensile force. Because the aqueduct is constrained at the end by the foundation, the bar (1) at the end section is in tension.

When aqueduct water depth changes from 2.5m to 7.5m, most crossbars changes from in compression to in tension. Because the static water pressure has a push to aqueduct side wall, the axial pressure became smaller even started in tension. If the water depth continues to increase, the axial tensile force grows significantly.

The larger axial tensile forces of crossbars are harmful for floor bottom surface of rectangle aqueduct, and the water is disadvantageous effect on the floor bottom surface, therefore, in the aqueduct design, the design level should have certain height from the top, that is, don't design into full tank water depth.

Influence Analysis of the Different Spacing of Crossbars. The influence of spacing of crossbars on the axial forces is obvious, the greater the spacing is, the bigger the axial force of every crossbar will be. The spacing of crossbars is also restrained by other factors. The smaller is the spacing; the better will be the aqueduct body stress.

Table 2 The axial forces (kN) of crossbars under different water depths (H/B = 1.0)

water depths (m)	Crossbars number					
	①	②	③	④	⑤	⑥
0.0	1.8	-6.1	-14.6	-20.3	-22.5	-23.0
2.5	4.0	-9.3	-23.2	-32.6	-36.5	-37.3
5.0	31.6	26.9	12.4	1.3	-3.8	-4.9
6.5	75.7	90.8	79.4	67.9	62.5	61.3
7.5	122.0	159.9	152.5	140.8	134.9	133.5

Conclusions

Under the dead weight and the water weight, from the above analysis, the following conclusions can be drawn:

(1) When aqueduct height-width ratio is comparatively small, most crossbars are in compression; with height-width ratio increases, the axial forces are changing from compression to tension; the greater the height-width ratios, the greater the tensile forces.

(2) Under a certain height-width ratio, when water depth is relatively small, most crossbars are in compression, and with the increase of water depth, axial forces of crossbars change from compression to tension; the greater the water depths, the greater the tensile forces will be.

(3) Big axial tensile force is harmful to the rectangular cross-section floor (mid-span), but favorable to the side wall bottom.

Acknowledgements

The followings are gratefully acknowledged: Fund- research and application of key technologies of the construction of South-to-North water transfer project (JGZXJJ2006-10); Construction funds of Engineering Mechanics Discipline of North China University of Water Resources and Electric Power.

References

[1] X. Bai, at el: Research and application of key technologies of the construction of South-to- North water transfer project: research reports on dynamic tracking, temperature loads and dynamic analysis of large-scale aqueduct, North China University of Water Resources and Electric Power, Zhengzhou, 2007.

[2] J. Li, S. He, Influence of crossbars spacing on aqueduct body stress, J. of Water Conservancy & Hydropower Developments, 33 (2005) 34-36.

[3] B. Zhu, Principle and Application of Finite Element Method, China Water Conservancy and Hydropower Press, Beijing, 1998.

[4] R. Ji, Y. Chen, Research on static structure computational method of large rectangle aqueduct with multi-longitudinal beams, J. of Hydroelectric Power, 35 (2005) 80-84.

[5] G. Chao, T. Li, U-shaped thin-shell aqueduct stress analysis based on strain element with the assumption of noncompatible hardening, J. of China rural hydropower, 46 (2005) 50-53.

[6] Y. Zhao, X. Bai, Stress analysis of aqueduct support structure in Dong-Shen water supply reconstruction project, J. of Irrigation and Drainage Water, 21 (2002) 53-56.

[7] X. Bai, H. Huang, Finite element analysis on a continuous prestressed U-shaped thin-shell aqueduct, J. of North China Univ. of Water Conservancy and Electric Power, 22 (2001) 1-4.

[8] H. Zhu, D. Chen: Aqueduct, China Water Conservancy and Hydropower Press, Beijing, 2005.

© (2012) Trans Tech Publications, Switzerland
doi:10.4028/www.scientific.net/AMM.238.333

Design Analysis of Shuangji River Drainage Aqueduct Body with Large Flow

Guangwei Feng [a] and Ying Gao [b]

Henan Water&Power Engineering Consulting CO., LTD., Zhengzhou 450016, China

[a] hpdwfgw@hnsl.gov.cn, [b] gaoying1971@yahoo.com.cn

Keywords: Middle Line of SNWTP; aqueduct; structure style; mechanical behavior; construction scheme; construction cost.

Abstract. On the basis of summarizing the completed structural types of aqueduct both at home and abroad, combined with the structural design of Shuangji River drainage aqueduct in China South-to-north Water Transfer Project (SNETP), the aqueduct body structural form was selected. The analysis and discussion has been done with three typical structure forms of Shuangji River aqueduct, the two mechanical construction schemes by aqueduct-making machine and aqueduct-installing machine have been researched. The results show that the aqueduct with the character of large flow, big section, large loads and gentle gradient should be comprehensive analyzed on the mechanical behavior, construction scheme and construction cost to select the appropriate structural style for improving the quality and efficiency. The results provide valuable reference for designing the similar aqueduct.

Introduction

Shuangji River aqueduct project is one of the key projects of the Middle Line of SNWT. The aqueduct has large flow, big section and gentle gradient, which is different from the many previous aqueducts. So the structural types of the aqueduct body directly affect the quality, safety and cost of the aqueduct. So it is very necessary to research type-selecting of Shuangji River aqueduct, and this has important guiding significance on the structure design of large aqueduct.

Basic Facts of Aqueduct

Shuangji River aqueduct is the 4 spans prestressed concrete structure, each span is 7.0m, the cross section of drainage flume is width of 7.0m and height of 7.9m, the design water depth is 0.14m. The design discharge is 305m^3/s, the maximum discharge is 365m^3/s. Thin-wall hollow pier and cast-in-place piles were used. The diameter of single pile is 1.8m. The condition of Shuangji River aqueduct subsoil is not favorable, whose bearing capacity is about 60~120 kPa [1].

Optimum Design of Aqueduct Body

Preliminary Design. Large flow, big section, large loads and gentle gradient is the character of Middle Line Project of South-to-North Water Conservancy. The flow of Shuangji River aqueduct is 365m^3/s, but the design water depth is 0.14m, the cross section of drainage flume is width of 28.0m, the loads per meter can be reached to 220t, and the distance between the bottom of the aqueduct and the river flood water level is about 4m.The valley arched aqueduct is not suitable for the aqueduct whose character of low clearance and broad. And do the many large longitudinal beams flume structures [2-4]. The girder flume is not suitable for Shuangji River aqueduct, too.

The transverse clear width is too large when integral structure was used for the aqueduct. So do the double line aqueduct with double troughs whose transverse clear width is 14m. And it is not economic for separate structure whose foundation is also separated. So the double line aqueduct with four troughs was selected to compare the designs.

Structure Design Projects

30m Prestressed Rectangular Flume with Single Partition Wall and without Rib. The cross sectional shape and dimensions of superposed aqueduct is shown in Figure 1, the cross section of drainage flume is width of 7.0m and height of 7.9m. The thickness of side walls, middle walls and bottom plate is 0.6m, 0.75m and 0.55m, respectively. Each cross linking component is set on the top of the flume with distance of 2.0m along the span. Thin-wall hollow pier and cast-in-place piles were used. The top of the pier is 19.3m long and 4.5m wide, the bottom of the pier is 20.55m long and 5.75m wide. the diameter and length of single pile is 1.8m and 35~54m, respectively. Full space supports cast-in-place construction technology or aqueduct-making machine can be used in the flume construction.

30m, 40m Prestressed Rectangular Flume with Single Partition Wall and Bottom Rib. Compared with the flume without rib, each bottom rib in height of 1.0m is set with distance of 2.95m along the span in the structure; the cross section is shown in Fig. 2. And the thickness of bottom plate is 0.4m. The side wall and middle wall in height of 9.5m are also used as longitudinal beam. The length of single pile of the 30m span and 40m span is 36~53m and 44~66m, respectively. Full space supports cast-in-place construction technology or flaming machine can be used in the flume construction, too.

30m U-shape Prestressed Aqueduct. The diameter and height of each flume is 8m and 7.6m, respectively. Two flume bodies are supported on a support pier. The common thickness of the U-shaped aqueduct wall is 0.35m, and the local bottom plate was thickened to 0.9m. The cross section is shown as Fig.3. Thin-wall hollow pier and cast-in-place piles were used. The top of the pier is 19.3m long and 4.5m wide, the pier is 21.0 m long and 5.6m wide. the diameter and length of single pile is 1.8m and 35～52m, respectively. Flaming machine is widely used in the 30m span flume construction.

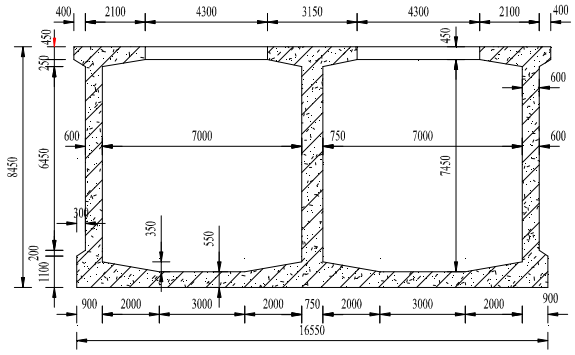


Fig. 1 Cross section of prestressed rectangular flume without rib (mm)

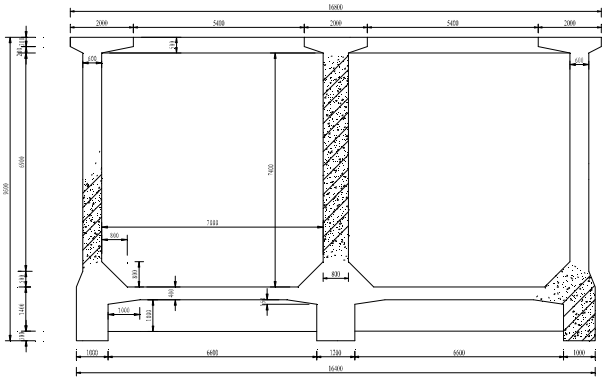


Fig. 2 Cross section of prestressed rectangular flume without rib (mm)

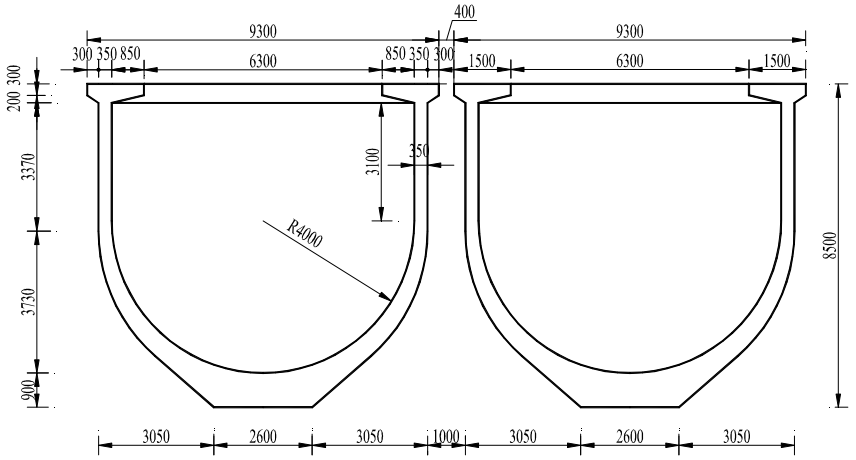


Fig. 3 The cross section of U-shape prestressed aqueduct (mm)

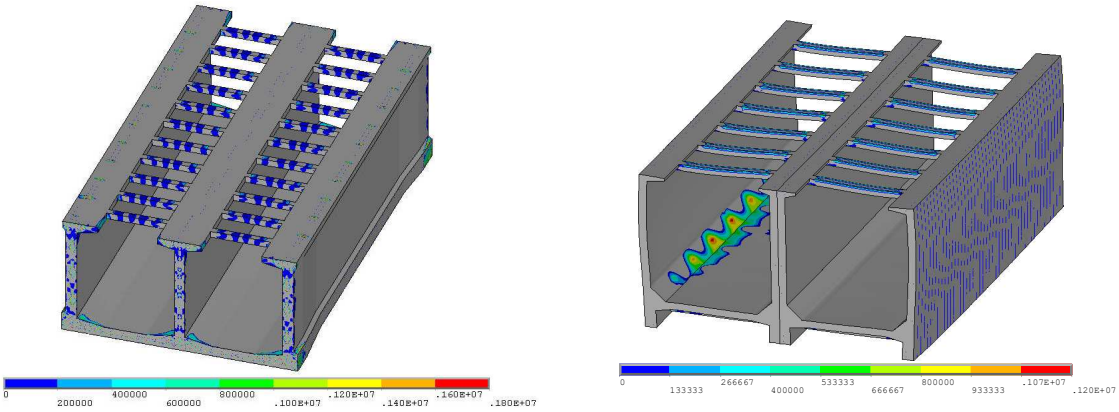
Engineering quantity and investment of each structure styles is shown in Table 1, in which the connecting section of U-shape prestressed aqueduct was set to connect the U-shape aqueduct and lock chamber, all structure style are the same total length.

Table 1 Main engineering quantity and investment of each structure styles

Structure style		30m prestressed rectangular flume without rib		30m prestressed rectangular flume with bottom rib		40m prestressed rectangular flume with bottom rib		30m U-shape Prestressed Aqueduct
		Support	Flaming machine	Support	Flaming machine	Support	Flaming machine	aqueduct-installing machine
Concrete (m^3)	C50 flume	44226	44226	50264	50264	51060	51060	41293
	C30 pier	59331	59331	56623	56623	44268	44268	60122
	C25 pile foundation	57326	57326	58360	58360	54444	54444	55955
Steel bar (t)	Steel bar	13043	13043	13700	13700	12572	12572	13523
	steel strand	2103	2103	2124	2124	2531	2531	1381
the entrance and exit section of Aqueduct (40m)	C30 rectangular flume (m^3)	/	/	/	/	/	/	8575
	Steel bar (t)	/	/	/	/	/	/	951
construction fee of open-channel (million yuan)		213	213	213	213	213	213	/
construction cost budgetary (million yuan)		20169	19578	19959	20307	19959	19959	22887
Construction Cost		978	4200	1095	4200	1095	1095	5110
Total invest		21147	23778	21054	24507	21054	21054	27997

Schemes' Contrast

Integral Forced Features and Construction Safety. The structures have a good integrity and high stiffness. All of them can be used for load bearing structural. So they are technically feasible as to the integral forced features and construction safety.



a) aqueduct without rib） b) aqueduct with bottom rib

Fig. 4 Stress concentration degree of the aqueduct without rib and bottom rib under the summer temperature rise and flume with full water

The lines of U-shape prestressed aqueduct are smooth and there are basically no concentrating stress phenomenon，the upstream face of flume were in pressured state. But the longitudinal and horizontal frames which were constructed by bottom ribs and bottom longitudinal beams of

rectangular flume have local stress concentration, and the tensile stress of nearly 1~2MPa appears in the upstream face of flume. Comparing with the flume with rib (Fig. 4), the thickness of the bottom plate of the rectangular flume without rib and longitudinal beam is increased and cast corners are used for reinforcement at the point of stress concentration between the wall and bottom of the flume. So the concentrating stress were reduced，the upstream face of flume were in pressured state and the result of stress analysis is similar to the U-shape prestressed aqueduct.

Construction Schemes Analysis. Full space supports cast-in-place construction technology is widely used, whose features are: big workload of formwork and scaffold, greatly influenced by flood in flood season. It is suitable for the structures which have less weight, firm foundation and rather smaller structure height. The condition of Shuangji River aqueduct subsoil is not favorable, whose bearing capacity is about 60~120 kPa. The deformation of support and foundation are difficult to control, so the risk of construction safety is big.

Flaming machine is not affected by alluvial soil foundation and waters flow, so the large cost of ground treatment and ground support are saved, and the construction will go on in flood season. The structural deformation during construction can be controlled by aqueduct-making machine stiffness, which can guarantee quality of pouring concrete easily. But the equipment cost is large.

Construction Cost Analysis. The cost of casting yard, conveying and lifting the equipment is large. So the total invest is still large although the superstructure investigation decreasing. The cost of equipment is small, so 2000~3000 million Yuan of total invest of full space supports cast-in-place construction will be saved than other methods. The total invest of the 30m prestressed rectangular flume without rib constructed by flaming machine is the least than the other structure types.

Conclusions

The mechanical behavior of 30m prestressed rectangular flume without rib is similar to the U-shaped prestressed aqueduct, the concentrating stress were reduced，the upstream face of flume were in pressured state, it can be constructed by flaming machine, the total invest is small. Through comparisons, 30m prestressed rectangular flume without rib was select for Shuangji River aqueduct, which can be constructed by aqueduct-making machine.

The aqueduct with the character of large flow, big section, large loads and gentle gradient should be comprehensive analysis the mechanical behavior, construction scheme and construction cost to select the appropriate structural style to improve quality and efficiency.

References

[1] Preliminary design report of Shuangji River of the Middle Route of South-to-North Water Transfer Project, Henan water & power engineering consulting CO., LTD, 2009.

[2] G. Niu, H. Yuan, Z. Wang, Selection and demonstration for structure of Caohe River Aqueduct, Water Resources and Hydropower Engineering, 4 (2005) 41-43.

[3] H. Zhu, D. Chen, F. Guan, Aqueduct, China WaterPower Press, Beijing, 2004.

[4] Y. Wang, L. Zhang, Q. Song, Research and optimization of Shahe aqueduct construction scheme in the Middle Route of South-to-North Water Diversion Project, South-to-North Water Diversion and Water Science & Technology, 3 (2011) 13-16.

© (2012) Trans Tech Publications, Switzerland
doi:10.4028/www.scientific.net/AMM.238.337

Study on Lateral Dynamic Response of Pile Foundation in Liquefiable Soil by Using FBG Method*

Yurun Li[1,2 a], Yan Liang[3 b], Xing Wei[1 c], Yunlong Wang[4 d] and Zhenzhong Cao[4, e]

[1]College of Civil Engineering, Hebei University of Technology, Tianjin 300401, China

[2]Civil Engineering Technology Research Center of Hebei Province, Tianjin 300401, China

[3]Tianyi architecrural design CO.,LTD, Tianjin 300384, China

[4] Institute of Engineering Mechanics, China Earthquake Administration, Harbin 150080, China

[a]iemlyr7888@163.com, [b]lyan_0305@126.com, [c]weixing1988@yahoo.cn,

[d]email:wyl_ys@yahoo.com.cn, [e] iemczz@163.com

Keywords: liquefiable soil; pile foundation; lateral dynamic response; FBG; peak acceleration.

Abstract. The study on lateral dynamic response of pile foundation in liquefiable soil is a significant part about seismic damage. In this paper, a new data acquisition system of FBG and calculation methods is used in the small shaking table test. The results show that FBG method used in this test is proved to be efficient and acceptable in both time characteristics and precision characteristics, it may be widely applied in the future doubtlessly. What's more, the characteristics of *p-y* curves in different peak accelerations are discussed. And varying of maximum stress and displacement by corresponding acceleration is discussed. A contrast about p-y curve between dry sand and saturate sand is related, which provides a new direction in research about *p-y* curve.

Introduction

Study on the characteristics of pile foundation under lateral loads, especially pile foundation located in liquefiable soil, is a key issue about the study in earthquake damage. Both in real-time monitor field and in experimental study field, accurate date is the most significant factors. As we know, large numbers of geo-materials are nonlinear and non-homogeneity, so it's particularly important in acquiring accurate test dates.

In design of pile foundation, including offshore platform pile foundation, nonlinear p-y curve method is used in determining the lateral character of piles widely. So how to determine the parameters of p-y curve in liquefiable soil under earthquake action is the key point of objective evaluation to earthquake action about lateral character [1]. So the accuracy of strain directly affects the facticity of p-y curve. In order to get accurate data, many methods are developed, such as strain gages [2]. As the existing research results show, although the strain gages are widely used, its frequency applicability still needs further studies. What's more, the result may drift and it cannot be neglected while in data processing, especially when using numerical integral.

In this test, a new data acquisition and processing method based on FBG has been put forward. In different vibration conditions, a large number data are obtained. By analyzing the data of dry sand and saturate sand, some conclusions are drawn, by which a deeper understanding about p-y curve of pile foundation can be got.

Measuring Method of FBG

Fiber Bragg Grating (FBG) can be applied to the structure of the low frequency vibration to measure the strain response [3], so it's widely used in test measuring and structure safety monitoring. In geotechnical test common measuring ways are limited. however FBG is based on optical interference, by which the influence of water can be neglected.

As shown in Fig. 1, in the test, there are five grants attaching to the pile to measuring the strain of the pile, by which displacement and press can be calculated.

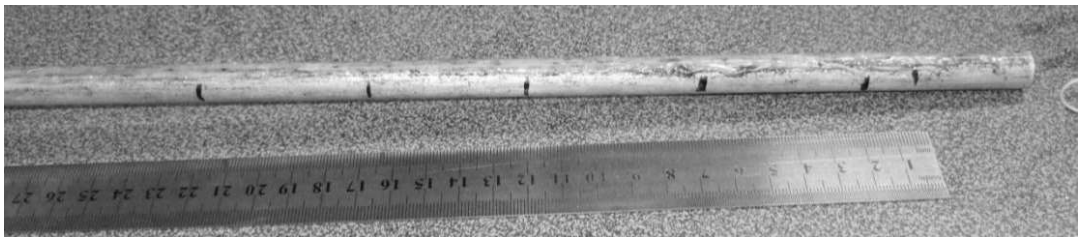


Fig. 1 Diagram and photo of FBG

Test of Shaking Table

Shaking Table and Test Box. The shaking table used in the test is developed by Institute of Engineering Mechanics, CEA. It's derived by hydraulic pressure. Its maximum load is 100 kg, maximum amplitude is 20 mm, and maximum acceleration is 0.5 g on vibration direction. The adapted working frequency is 1~10 Hz [4]. The test box is a rigid container made by aluminum. Its volume is 504mm×340mm×278mm. Two pieces of organic glass are put on both sides, and rubber blanket in the bottom. Show in Fig. 2.

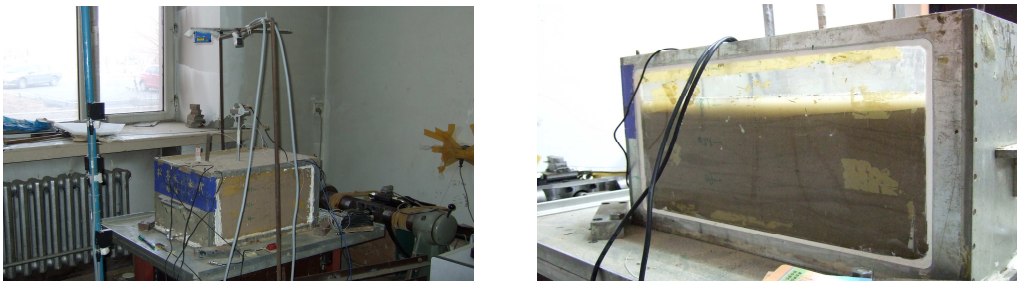


Fig. 2 Shaking table and test box

Test Condition. In the test, three different sine waves are input to the shaking table. The sine waves are shown in Fig. 3. The sine wave's frequency is 5 Hz, and its peak acceleration is 0.05g, 0.1g, 0.15g respectively. The relative density of dry sand is 0.3, and the saturate sand is 0.4.

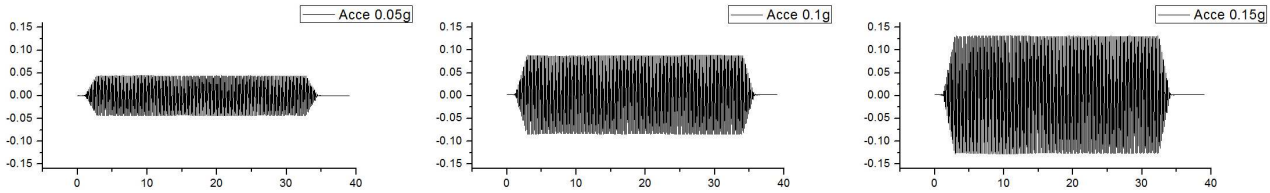


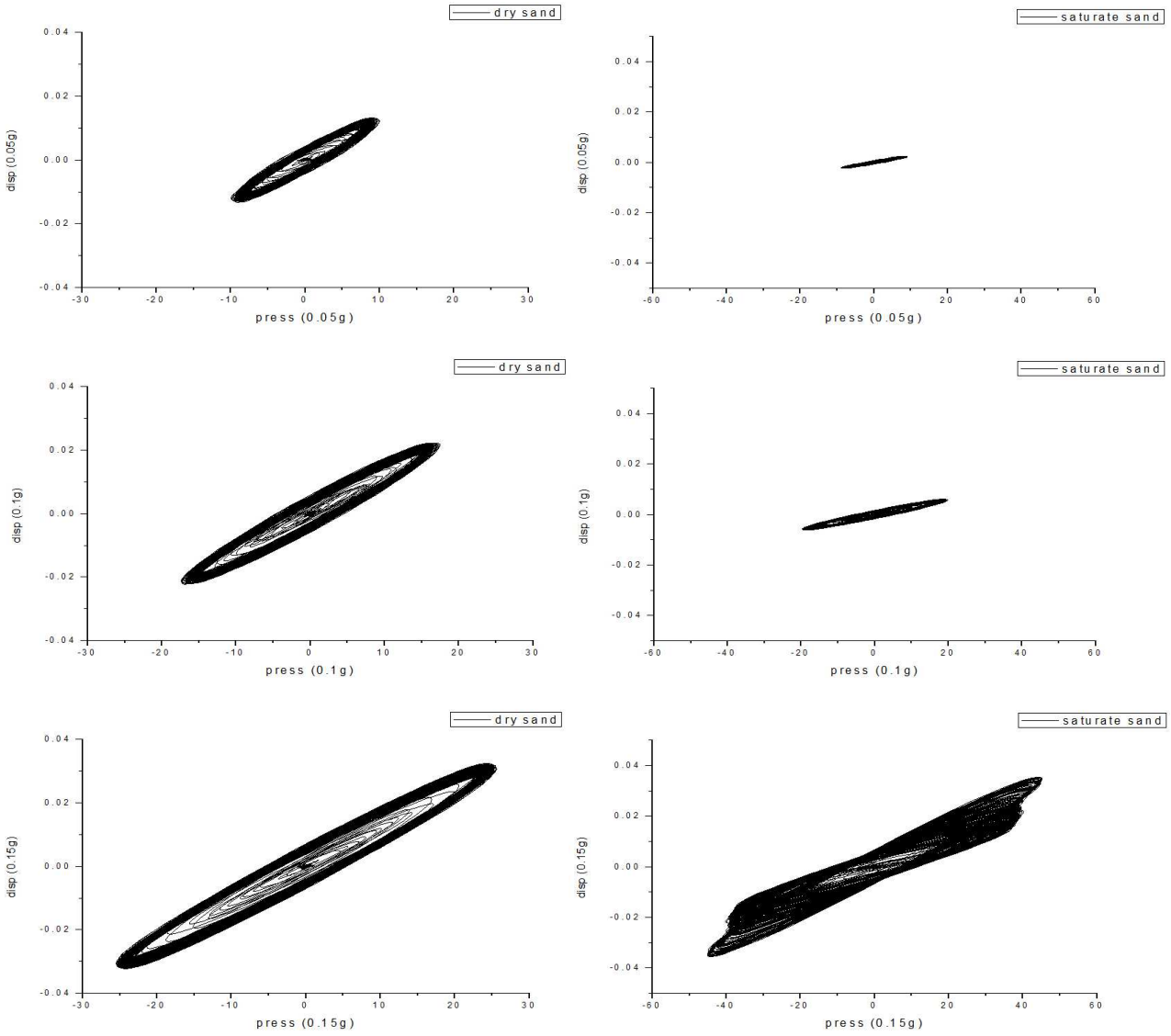
Fig. 3 Time-history of shaking table acceleration

Test Result and Analysis

The value of pile strain is acquired by FBG. And by mechanical and geometry calculation, using curve fitting and integral method, the press and displacement curve along the pile can be obtained. The calculation is completed by the software of Matlab.

Analysis of *p-y* Curve. Fig. 4 shows *p-y* curves of different peak accelerations. In dry sand test, *p-y* curves of different peak accelerations are similar, but the peak values are different. The peak value of both press and displacement increases by the increase of input acceleration. The conclusion also suggests that FBG has very good applicability to different accelerations. In saturate sand test, the change of pile stress and displacement with the peak acceleration is very sensitive; according to the increase of the peak value of acceleration, the pile stress and displacement are increased.

***p-y* Curve of First 3 Second.** Because of the limited space, we only display the result and the analysis for the first 3 second of 0.15g, as shown in Fig. 5. The figure indicates that, compared to the dry sand, the press of saturate sand is obviously bigger. In dry sand test, the shapes of *p-y* curve in every cycle are regular elliptic, while in saturate sand, the shape appeared deformation. The reason is the soil liquefaction affects, too.



(a) dry sand (b) saturation sand

Fig. 4 *p-y* curve of dry sand and saturate sand

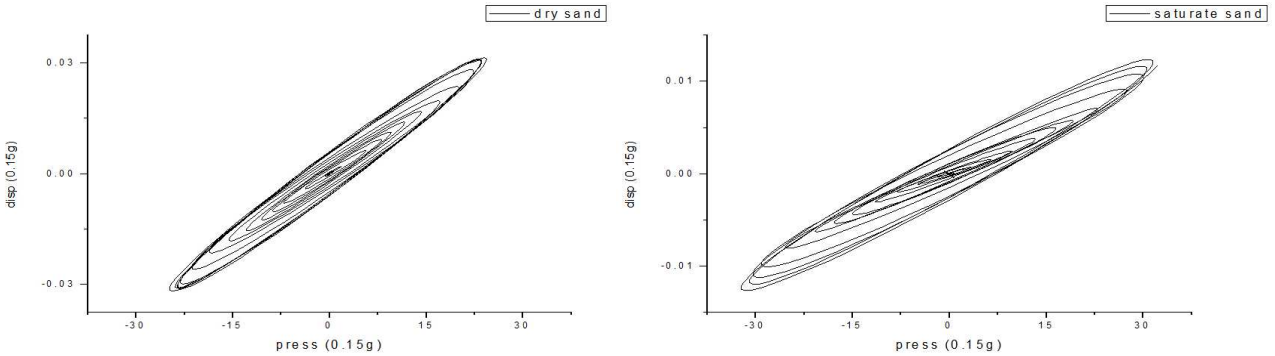


Fig. 5 *p-y* curve of the first 3 second

Peak Value of Different Acceleration. While the input wave is stable, the relationship between press and displacement under different accelerations is shown in the following, as shown in figure 6. In dry sand test, the variation of both the press and displacement is almost linear, but in the saturate sand test, it's exactly not. The reason is that soil liquefaction affects the lateral confinement to the pile, and leads the lateral confinement to decrease.

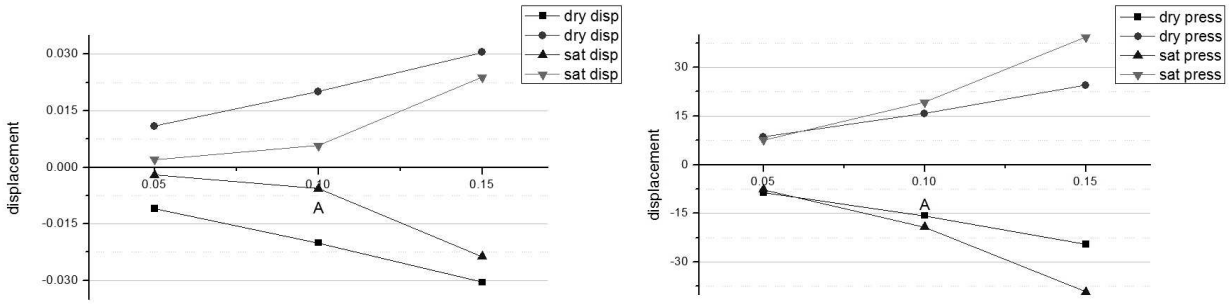


Fig. 6 Peak value of different acceleration

Conclusions

In this paper, a shaking table test on study the lateral response of soil-pile foundation for dry sand and saturation sand is completed in which three peak acceleration sine waves are input and FBG is used to collect data. A new method of mechanics theory calculation is referred to in order to calculate the press and displacement. The phenomenon and result are acceptable; here are some new understandings on the research:

FBG is based on optical interference, which makes it have a broad prospect. The measured results show that it is reliable completely, which indicate that FBG can be well applied in the study on lateral dynamic response of Pile foundation in liquefiable soil.

The displacement and the press of pile are related to the peak acceleration, while the peak acceleration increases, the displacement and press increase correspondingly. In dry sand test, the variation is linear ship, but in saturate sand test, it's not.

In dry sand test, the shapes of p-y curve in every cycle are regular elliptic, while in saturate sand, the shape appeared deformation. Especially after the soil liquefaction, the hysteresis loop area change greatly.

Acknowledgements

National Natural Science Fund Projects (No. 51008110)

References

[1] J. Wang, S. Feng, Rock and Soil Mechanics, 10 (2005) 1598-1601.

[2] Y. Li, Study on Lateral Dynamic Response of Pile Foundation in Liquefiable Soil, Ph.D. Thesis, Institute of Engineering Mechanics, China Earthquake Administration, 2006.

[3] L. Sun, H. Li, T. Zhu, L. Ren, R. Dong, Journal of Vibration and Shock. 3 (2006) 29-34.

[4] R. Sun, X. Yuan, Y. Li, Z. Cao, L. Chen, Northwestern Seismological Journal, 1 (2009) 8-14.

© (2012) Trans Tech Publications, Switzerland
doi:10.4028/www.scientific.net/AMM.238.341

Research on Temperature Control and Cracking Prevention on Pier by Installing Expansion Reinforcing Bands during Construction

Hongmei Li [a], Shushan Li [b] and Wei Xie [c]

North China Institute of Water Resources and Electric Power, Zhengzhou 450011, China

[a]lihongmei2002@163.Com , [b]lishushan@ncwu.edu.cn , [c]xwei@ncwu.edu.cn

Keywords: gate pier; cracks; expansion reinforcing band; temperature stress; temperature differences inside and outside.

Abstract. The mechanism of crack formation on the concrete structure of gate piers during the construction period is analyzed. The temperature control and cracking prevention technique which combines surface heat preservation and the installation of expansion reinforcing bands is proposed. Based on the calculation principle of temperature fields and stress fields of concrete structures, simulated calculation analysis is conducted on the gate pier structure during the construction process by using the finite element method. The results show that the crack prevention effect of this temperature control measure is positive, and this measure has a certain reference value to similar engineering designs and constructions.

Introduction

A gate pier is a structural style which has been widely used in hydraulic projects. Compared with concrete dams and other massive structures, a gate pier is relatively thin and vulnerable to cracking. The problem of cracking has not yet been solved. Some research [1] has shown that cracks on gate piers are caused by many factors, including structural load, concrete temperature, creep, etc, but the main cause of cracking during the construction period is the temperature stress on the concrete. By taking a gate pier as an example and on the basis of existing literature, the cracking mechanism of the pier-wall is illustrated. The crack prevention effect on the gate pier during the construction period using two techniques, surface heat preservation, and the installation of expansion reinforcing bands will be analyzed.

Cracking Mechanisms and Crack Prevention Techniques on Gate Pier Structures

Crack Forming Mechanism during the Construction Period. A lot of engineering practices have proved that the formation of cracks on the gate pier during the construction period is mainly related to the temperature difference inside and outside the gate pier and the external constraints [2]. Shortly after the pouring of the gate pier, the temperature of concrete rises continuously due to the hydration reaction in cement. Heat dissipation at the surface of the gate pier is faster than that found inside, so the surface temperature is lower than the internal temperature. This forms a temperature difference inside and outside. If the temperature difference between the inside and the outside is too great, it will lead to a relative deformation between the inside and the outside of the structure, and tensile stress will be formed on the surface. If the tensile stress exceeds the immediate tensile strength of the concrete, cracks will begin to generate [3]. However, during the cooling phase, the shrinkage deformation of the concrete in the freshly poured pier wall will be restricted by the constraints of the old concrete in the soleplate; therefore tensile stress will be generated. The larger the gap is between the new and old concretes, the larger the temperature drop amplitude will be, and the constraints will be more obvious. The dimension at the length of the concrete structure of the gate pier is much larger than that in the width direction, so the tensile stress exhibited due to the integral shrinkage of the structure is large. Once the cracks appear, they will be penetrating cracks.

Crack Prevention Technique. From the cracking mechanism of the concrete structure of the gate pier, we can see that to prevent cracks from generating, the temperature difference inside and outside the concrete structure should be reduced. Furthermore, concrete shrinkage should be compensated for at the length of the gate pier structure to reduce the integral shrinkage deformation.

The ways reduce the temperature difference inside and outside include reducing the adiabatic temperature rise of the concrete and the preservation of surface heat. The measures to reduce the rise of adiabatic temperature include the use of low heat cement, mixing with a suitable amount of fly ash, and the pre-cooling of the aggregate to achieve the purpose of controlling the placement temperature of concrete. Surface heat preservation can prevent the fast dissipation of heat at the structural surface and the formation of temperature differences inside and outside. It can also prevent attacks on the concrete surface by cold waves and temperature differences between day and night.

The installation of an expansion strengthening belt [4] in the new concrete can reduce the integral shrinkage deformation of the structure. After the installation of an expansion strengthening belt, expansion concrete will expand appropriately during the hardening process of the structural concrete. Due to the restraints of reinforcing bars and adjacent objects, certain self-stressing will occur within the concrete. The self-stressing, which is established at the expansion strengthening belt, will compensate for the temperature shrinkage stress and prevent the (relative) cracking of long structures.

Calculation Principles and Methods of Finite Element

Basic Theory of Unstable Temperature Field and Finite Element Method. The concrete structure of gate piers is usually poured layer by layer and block by block. Assume that the volume of concrete poured in the batch i is R_i (i=1, 2, …, n), the unstable temperature field T(x, y, z, t) in the concrete in R_i should meet the heat conduction equation [2]:

$$\frac{\partial T}{\partial t} = a(\frac{\partial^2 T}{\partial x^2} + \frac{\partial^2 T}{\partial y^2} + \frac{\partial^2 T}{\partial z^2}) + \frac{\partial \theta_i}{\partial \tau} \tag{1}$$

Where, T represents the temperature, °C; a represents the coefficient of temperature conductivity, m^2/h; θ_i represents the adiabatic temperature rise of the concrete poured in the batch i, °C t represents the time, d; τ represents the age, d.

According to the functional variation principle, disperse the region R_i by a finite element, and take the temperature mode of each unit as:

$$T = \sum_{i=1}^{m} N_i T_i \tag{2}$$

Adopt the time domain differential to equations (1) and (2), after introducing the initial conditions and the boundary conditions, the finite element calculation and recurrence equation of temperature field in backward difference can be obtained:

$$\left([H] + \frac{1}{s\Delta t_n}[R]\right)\{T_{n+1}\} + \left(\frac{1-s}{s}[H] - \frac{1}{s\Delta t_n}[R]\right)\{T_n\} + \frac{1-s}{s}\{F_n\} + \{F_{n+1}\} = 0 \tag{3}$$

Where, [H] represents the heat conduction matrix; [R] represents the supplement heat conduction matrix; $\{T_{n+1}\}$ and $\{T_n\}$ represents the node temperature array; $\{F_n\}$ and $\{F_{n+1}\}$ represents the node temperature load array; n represents the time ordinal; and Δt represents the time step.

Basic Theory of Stress Field and Finite Element Method. The stress increments of concrete under complex stress state include elastic stress increment, creep stress increment, temperature stress increment, drying shrinkage stress increment and autogenous volume stress increment [1], therefore,

$$\{\Delta\varepsilon_n\} = \{\Delta\varepsilon_n^e\} + \{\Delta\varepsilon_n^c\} + \{\Delta\varepsilon_n^T\} + \{\Delta\varepsilon_n^s\} + \{\Delta\varepsilon_n^0\} \tag{4}$$

Where, $\{\Delta\varepsilon_n^e\}$ represents the elastic stress increment; $\{\Delta\varepsilon_n^c\}$ represents the creep stress increment; $\{\Delta\varepsilon_n^T\}$ represents the temperature stress increment; $\{\Delta\varepsilon_n^s\}$ represents the drying shrinkage stress increment; $\{\Delta\varepsilon_n^0\}$ represents the autogenous volume stress increment.

The finite element governing equation in region R_i at any time section Δt_i can be expressed as:

$$[K_i]\{\Delta\delta_i\} = \{\Delta P_i^G\} + \{\Delta P_i^c\} + \{\Delta P_i^T\} + \{\Delta P_i^s\} + \{\Delta P_i^0\} \quad (5)$$

Where, $\{\Delta\delta_i\}$ represents the increment of node displacement in region; $\{\Delta P_i^G\}$, $\{\Delta P_i^c\}$, $\{\Delta P_i^T\}$, $\{\Delta P_i^s\}$ and $\{\Delta P_i^0\}$ represent the increment of equivalent node caused by external load, creep, temperature change, drying shrinkage, and autogenous volume deformation.

Engineering Applications

Project Overview. The structural shape of a gate pier of a large (II) reservoir spillway is an inverted T-type. The net width of the gate pore is 20m; the length, height and thickness of the gate pier reach to 24m, 14m and 1.8m, separately; the thicknesses and lengths of the gate soleplate are 2m and 28m, separately. The pier wall of the gate pier is long, so 2 expansion concrete strengthening belts are installed along the length of the central pier, as shown in Fig.1. The mix proportions of concrete for the gate pier are listed in Table 1.

Table 1 Mix proportions concrete for gate pier

Location	Level	Dosages in 1m^3 concrete /kg							
		Cement	Sand	Water	10~20mm stone	20~40mm stone	40~80mm stone	Fly ash	Additives
Gate pier and soleplate	C25	218	687	151	383	383	510	73	5.83 (water reducer)
Expansion belt	C30	376	644	188	515	630	0	0	42 (swelling agent)

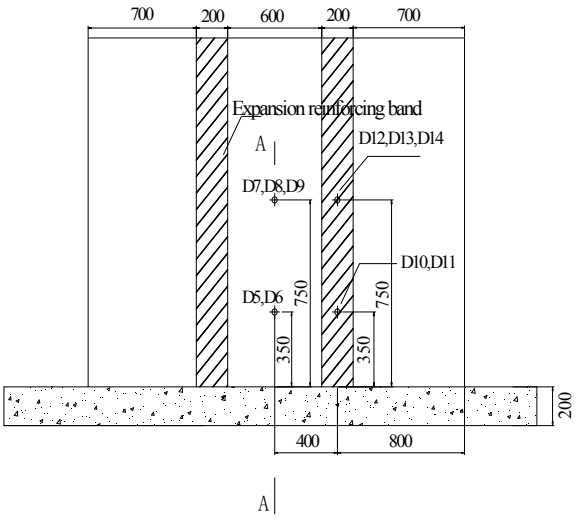


Fig. 1 Arrangement of temperature measuring points on pier

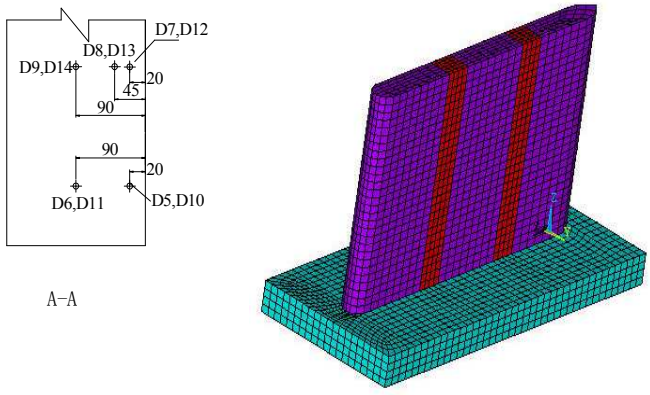


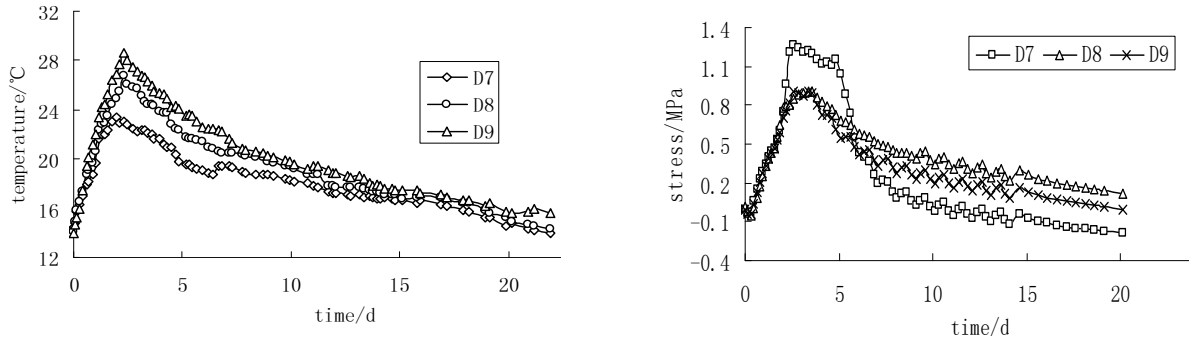
Fig. 2 The calculation grids of the finite element

Calculation Model. In view of the structural shape of gate pier projects, the pier wall and soleplate structure are calculated. The established calculation model should be consistent with the engineering practice as much as possible. During the construction period, the temperature near the surface of the gate pier is greatly affected by the ambient temperature. The temperature gradients and stress gradients are large. They are important when studying the temperature control and crack prevention in the concrete of the gate pier structure. Meanwhile, to simulate the layered pouring process, the unit thickness of the computing grid height is taken as 0.5m, which is the thickness of one layer of pouring. Spatial hexahedral and pentahedral isoparametric unit models are used for grid

division. The total number of units and nodes in the calculation model are 9584 and 11998. The gate pier structure and the arrangement of typical points are shown in Fig.1. The calculation grids of the finite element are shown in Fig.2.

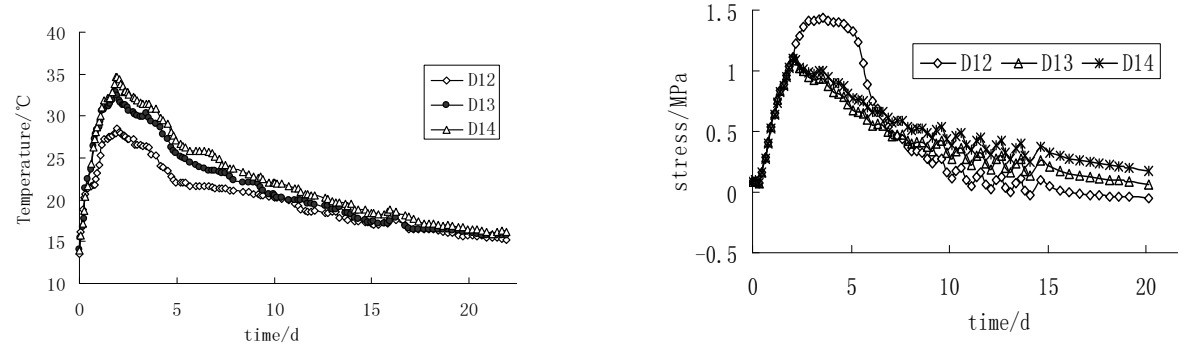
Analysis of Crack Prevention Measures. The temperature control and crack prevention measures which target the causes of cracks include: in the quality of raw materials, optimizing the mixing ratio of concrete through experiment, adding a suitable amount of fly ash, using additives to reduce the dosage of cement and lowering the rise in temperature caused by concrete hydration heat and the shrinkage of autogenous volume. After the pouring of soleplate concrete, preserve the heat by covering it with straw bags. For the pier wall, the crack prevention measures include adopting suitable surface heat preservation and installing an expansion strengthening belt. That is to say, the pouring of the gate pier should utilize a steel template, and its outside should be pasted with a thin plastic film for heat preservation. The pier wall of the gate pier is long, so 2 expansion concrete strengthening belts are installed along the length of the central pier.

The calculation results of the simulation are shown in Fig.3 and Fig.4, and the arrangement of typical points is shown in Fig.1.



(a) Temperature variation curve (b) Stress duration curve

Fig. 3 Temperature and stress duration curve of measuring points at D7, D8 and D9



(a) Temperature variation curve (b) Stress duration curve

Fig. 4 Temperature and stress duration curve of measuring points at D12, D13 and D14

From the calculation results we can see that the values of early surface tensile stress at the middle of the gate pier and the latter internal tensile stress are small due to the reasonable selection of raw materials. The adoption of the new temperature control and crack prevention measures with the combination of suitable surface heat preservation and the installation of an expansion strengthening belt during the construction stage. In terms of crack prevention, no cracks were found out on the poured water gate soleplate or the gate pier. This indicates that this crack prevention scheme is reasonable.

Conclusions

Due to the adoption of an inverted T-type gate pier structure, the constraint of the soleplate is obvious. The rate of cracking is high due to the early temperature difference inside and outside, and the later temperature drop shrinkage;

Selecting the best raw materials for concrete and surface heat preservation is an effective way to prevent cracks on the inverted T-type gate pier structure. Suitable surface heat preservation can help to prevent early cracking. The installation of expansion strengthening belts can compensate for the shrinkage deformation of concrete during the cooling process, and it can also reduce the temperature stress of the concrete. Practices prove that this crack prevention measure provides desirable results at low cost, so it is promising in application.

Acknowledgements

This work was supported by Innovation Scientists and Technicians Troop Construction Projects of Zhengzhou City (112PLJRC354) .

References

[1] Z. Zhao, Cracks and prevention measures on gate piers, Advances In Science and Technology of Water Resources, 4 (2003) 62-65.

[2] B. Zhu, Temperature stress and temperature control for large volume concrete, China Electric Power Press, Beijing, 1998.

[3] Z. Wang, Study on temperature control and crack prevention of Inverted T-shaped concrete structures during construction, Journal of Hydraulic Engineering, 6 (2007) 200-204.

[4] W. Xie, Thermal Analysis for Shishankou Reservoir Pier during the Construction Period, Water Power, 4 (2010) 30-33.

© (2012) Trans Tech Publications, Switzerland
doi:10.4028/www.scientific.net/AMM.238.346

Application of BOTDA in Mass Concrete Temperature Monitoring

Juhua Xiong[1, 2,a], Lujie Wang[1, 2,b], Wenyong He[3,c] and Haofeng Xing[1, 2, d]

[1] Department of Geotechnical Engineering, Tongji University, Shanghai 200092, China

[2] Key Laboratory of Geotechnical and Underground Engineering of Ministry of Education, Shanghai 200092, China

[3] Technical Center, Guizhou Transportation Planning Survey & Design Academe Co. Ltd, Guiyang 550001, China

[a]xiongjuhua2005@126.com, [b]2008jie2008@163.com, [c]490376638@qq.com, [d]hfxing@tongji.edu.cn

Keywords: mass; concrete temperature monitoring; hydrate heat; BOTDA.

Abstract. In order to study the application of distributed optical fiber in temperature monitoring of mass concrete, monitoring instruments are embedded in pile cap to carry out the field experiment. The results show that the distributed temperature fiber which is based on brillouin optical time-domain analysis (BOTDA) has the superiority of anti-jamming, corrosion resistance, high precision and continuous measurement. It can accurately reflect the temperature change, effectively guide the construction, and play a positive role in preventing the emergence of concrete cracks caused by temperature change. What's more, optical fiber has small volume and less influence on engineering, which make it have a good application prospect.

Introduction

With the development of the transportation, mass concrete is widely applied in bridge engineering. As the cast-in-situ concrete harden, it releases a lot of heat, which makes the temperature of the center rose rapidly, and the temperature of the surface and boundary is lower influenced by the surrounding environment. The difference of temperature between the inside and outside usually causes cracks which will reduce the bearing capacity of the pile cap and the durability of concrete. Therefore, we must make a scrutiny into the temperature monitoring of mass concrete. Liu Shanhong used the copper thermal resistance temperature sensor to measure the temperature of the mass concrete pile cap, and found that the heat dissipation relies mainly on the exposed surface; the cooling capacity of the bottom is very small, measures should be early implemented to strengthen the dissipation of internal temperature and superficial heat preservation to protect the concrete from cracking caused by the difference in temperature between the inside and outside [1]. Xu Jian points out that the variation in temperature of the center and surface have a hysteresis phenomenon, the maximum temperature difference is not the simple subtraction of the highest temperature [2]. Zhang Yong calibrated ten different single-mode optical fibers' temperature coefficients under different stress state and emplaced, and analyzed the impact model of temperature from temperature circle and emplaced ways [3]. Yang Xianyuan found that the optical fiber has the advantages of high precision, good real-time and high reliability by comparing with existing methods [4].

The distributed optical fiber temperature sensor which was produced by OZ Company was adopted to monitor the temperature in this paper. Feasibility research on application of the distributed optical fiber on Mass Concrete Temperature Monitoring was done for further exploration, and the law of the variation and development of hydration heat was attained by space arrangement of the distributed optical fiber. The research in this paper is expected to provide helpful reference for the mass concrete design and construction in other piers and abutments.

BOTDA Testing Principles

BOTDA (brillouin optical time-domain analysis) technology is the combinations of spectral analysis and optical time-domain reflection (OTDR), the incident light of one end is short pulse light, and the other is continuous spectrum. When the frequency difference is equal to the brillouin

frequency of the optical fiber, the stimulated brillouin scattering (SBS) will be strengthened, and the energy transferred between the two beams [5, 6]. It is known to all that the brillouin frequency shift is linear with temperature and strain. So the data can be obtained from one end of the optical fiber while continuous adjusting the laser frequency, and get the temperature and strain information by analyzing the data. The linear expressions as Eq. 1 shows:

$$\nu_B(\varepsilon, T) = \nu_B(0) + (T - T_0) \times C_T + (\varepsilon - 0) \times C_\varepsilon \quad (1)$$

Where $\nu_B(\varepsilon, T)$ means the brillouin frequency shift when strain is ε and temperature is T, $\nu_B(0)$ means the brillouin frequency shift when strain is 0 and temperature is T_0, C_T is the temperature effect coefficient, C_ε is the strain coefficient.

Engineering Example

The main bridge pier of Heizhang super highway bridge from Bijie city in Guizhou province to Weining is 195m, the design value of axial force is 62000 ton located on a pile cap which is about 27m×23m×6m. In the process of construction, the concrete pouring volume will exceed 4000m^3. In order to control the temperature difference between the inside and outside, some cooling pipes are embedded in the pile cap. The distributed optical fiber temperature sensor produced by OZ Company was adopted to monitor the temperature. The pulse width is 10ns, and sampling interval is 5 cm. The layout of distribute optical fiber as figure 1 shows, space distribution as shown in Fig. 2.

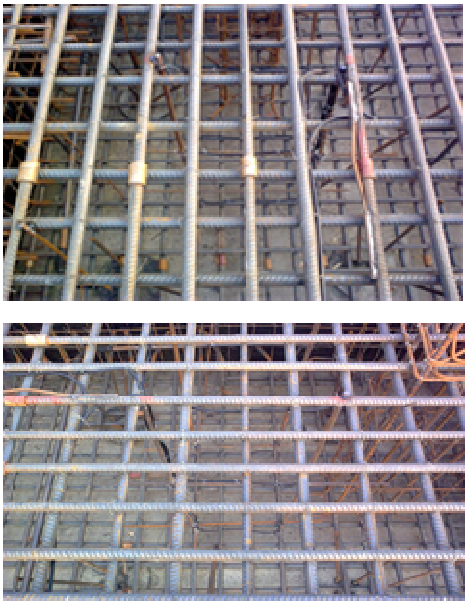


Fig. 1 Site layout of distribute optical fiber

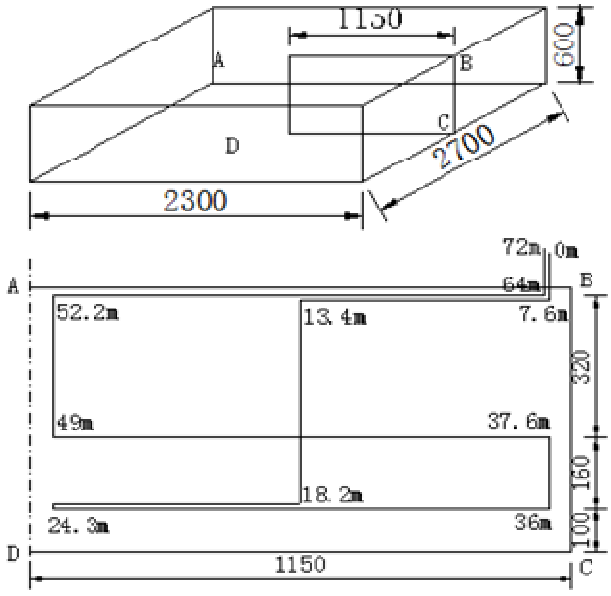


Fig. 2 Spatial arrangement of distribute optical fiber

Test Results and Discussion

Date acquisition start with pile cap is completed, and the result as shown in Fig. 3. As shown in the Fig. 2, the optical fiber between 0 to 13.4 m and 58.3 to 72 m were located in the same position, the difference is that the latter is more close to the surface in the space, but the difference is not big, and can be supposed on the same floor. Results in Fig. 3 show that the changing trends and the highest temperature are consistent. Its own contrast in this paper has also proved the validity of the test method. In Fig. 3, the highest temperature has reached 92.5 degrees after the pile cap completed. But for the surface of the pile cap, the temperature increases firstly and then decreases, it means that the hydration heat has been completed two days after pouring for mass concrete, and also reflects the temperature dissipation process from inside to outside. The average temperature near 50m is lower, because the fiber was arranged along the cooling pipes.

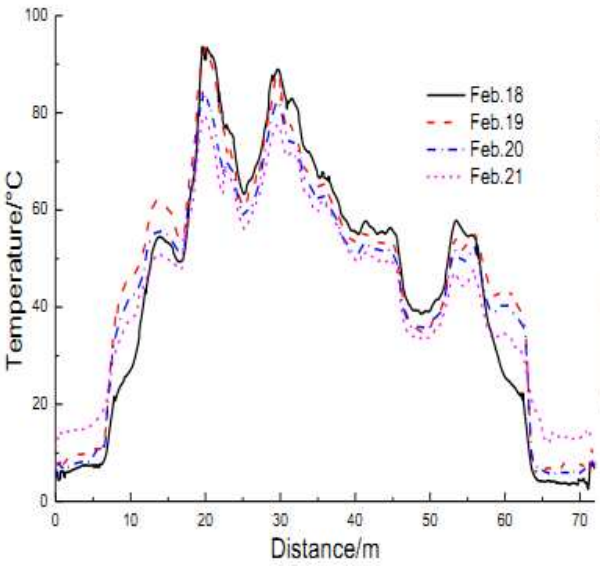


Fig. 3 The temperature cave along the distance over time

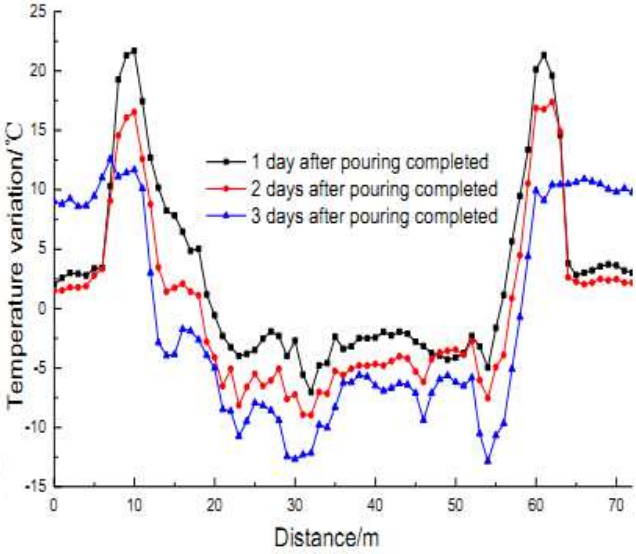


Fig. 4 Temperature variation curve along the distance over time

With the purpose of having an obvious temperature variation curve, the method of differencing is put forward to process the test data, all data subtracts the initial value, and the temperature variation as shown in Fig. 4. The optical fiber between 0 to 7.6 m and 64 to 72 m were designed to test the ambient temperature around the pile cap. The fluctuation of each temperature variation curve is not big, and can be regarded as straight line, but with the increase of monitoring days, temperature increased significantly. This mainly caused by the dissipation of the internal hydration heat and the heat preservation protective layer which prevent the temperature from dissipating.

The segment from 7.6 to 13.4m was along the horizontal buried in a certain depth below the surface from the edge to the center of the pile cap. For each curve, the temperature is linear increasing, but with the increase of monitoring days, the temperature variation is smaller. Through the lateral comparison, the conclusion can be concluded that the temperature difference between internal and external is the biggest at initial stage, and gradually decreases with the increase of monitoring days. The main reason caused the temperature increases rapidly can be ascribed to the slower abreaction of the hydration heat. The closer to the surface, the bigger exposed surface is, and natural convection is strengthened. But with the increase of monitoring days, the heat gradually spread to surface, so measures should be early implemented to strengthen the dissipation of internal temperature and superficial heat preservation to protect the concrete from cracking caused by the difference in temperature between the inside and outside. The maximal segment of temperature variation is not the center of the pile cap.

The part from 13.4 to 18.2m was along the vertical buried from top to bottom for longitudinal comparison. The temperature all increased one day after casting, but the increment in not much especially at the center of the pile cap. Two days later, the temperature increment already reduced significantly, and in an average of 3 degrees. The temperature increment is negative 3 days later, which means that the hydration heat has been completed two days after pouring for mass concrete, and in the process of temperature dissipating.

The optical fiber from 18.2 to 58.3 m was designed to test the center and bottom of the pile cap. In Fig. 4, the increment is negative, and as time increases, the temperature is in a process of scattered away on an average of 3 degrees each day. The temperature variation curve changed gently at the center and bottom of the pile cap which can reflect the concrete is a poor conductor of heat transfer. So measures should be done to strengthen the surface heat preservation and reduce the internal temperature gradient to avoid cracking.

Conclusions

For mass concrete, measures should be early implemented to strengthen the dissipation of internal temperature and superficial heat preservation to protect the concrete from cracking caused by the difference in temperature between the inside and outside. The middle and bottom of pile cap's temperature changed smooth, but the temperature of the edge and surface changed greatly. The segment of maximal temperature range is not the center of the pile cap, and has a lagging effect.

The distributed optical fiber which based on BOTDA technology can accurately reflect the temperature changes, effective guide the construction, and play a positive role in preventing the emergence of the temperature cracks. What's more, optical fiber has small volume and less influence on engineering, which make it have a good application prospect.

Acknowledgements

The work was supported by National Natural Science Funds (41172247) and Funds of GuiZhou Provincial Department of Transportation (2010-122).

References

[1] S. Liu, Q. Huang, X. Fu, Analysis of temperature monitoring for massive concrete in bridge pile-cap at normal temperature, Journal of Wuhan University of Technology, 8 (2009) 55-57

[2] J. Xu, Z. Liu, L. Lv, Pile cap mass concrete hydration heat temperature monitoring analysis, Gansu Science and Technology, 3 (2011) 97-98.

[3] Y. Zhang, G. Wei, B. Shi, Study on temperature effect of BOTDR-based optical fibers, Journal of Electronic Measurement and Instrument, 10 (2010) 929-934.

[4] X. Yang, Y. Li, D. Huang, Application of distributed optical fiber temperature measurement system to hydraulic concrete, Water Resources and Power, 2 (2010) 106-108.

[5] K. Kishida, C-H Li, Pulse Pre-pump-BOTDA technology for new generation of distributed strain measuring system, Structural Health Monitoring and Intelligent Infrastructure, 5 (2006) 471-477.

[6] J. Zhang, A. Lv, B. Li, Advances in the development of BOTDA-based distributed fiber sensing technology, Study on Optical Communications, 4 (2010) 25-28.

© (2012) Trans Tech Publications, Switzerland
doi:10.4028/www.scientific.net/AMM.238.350

Australian Seaport Infrastructure Resilience to Climate Change

Daniel Kong [a], Sujeeva Setunge [b], Tom Molyneaux [c],
Guomin Zhang [d] and David Law [e]

School of Civil, Environmental & Chemical Engineering, RMIT University, GPO Box 2476, Melbourne VIC 3001, Australia

[a]daniel.kong@rmit.edu.au, [b]sujeeva.setunge@rmit.edu.au (corresponding author),

[c]tom.molyneaux@rmit.edu.au, [d]kevin.zhang@rmit.edu.au, [e]david.law@rmit.edu.au

Keywords: seaport; climate change; concrete; deterioration.

Abstract. A research project continuing at RMIT University is exploring the resilience of port structures in a changing climate. Research completed to date comprises of identifying types of port infrastructure vulnerable to climate change, establishing materials and exposure conditions, developing deterioration models based on current knowledge to simulate the effect of climate change on key port infrastructure and modeling the selected elements of infrastructure to derive outcomes which will aid in decision making in port infrastructure management. A considerable effort has been concentrated on identifying input climate data most appropriate for the models developed.

The modeling approach is presented in this paper for quantitative projections of damage probability on port infrastructure taking into account the variability of material type, design considerations and environmental exposures with a changing climate. This paper provides a summary of the research undertaken in the development of material deterioration models and their responses to a changing climate load. Using climate information drawn from historical weather records and future climate projections, existing deterioration models were refined to include climate data into modeling runs in order to analyze changes to deterioration rates of different materials when impacted by a change in climate variables. Outputs from this modeling process will assist port authorities in making informed decisions on maintenance and capital budget planning allowing for impacts of climate change.

Introduction

There is a lack of reliable models to predict deterioration as a function of time. To address this deficiency, numerical models involving simultaneous transient diffusion and long term deterioration reactions for various construction materials are being developed. These are derived from existing models and include the effects of variations in 'climate properties' such as humidity, temperature, atmospheric carbon dioxide concentrations and chemical reaction rates as a function of time.

Different port structures consist of a range of construction materials; predominantly concrete, steel and timber. To provide a structure for deterioration assessment, the port assets were categorised into material types. A probabilistic approach using material and dimensional data (provided by port authorities) is used to simulate runs on a yearly increment from baseline up to 2070. These models evaluate the likelihood and probability of deterioration initiation and damage to seaside port infrastructures. They aim to study the potential effects of climate change on reinforced concrete corrosion, timber attacked by marine borers and steel corrosion. Concrete deterioration modeling has been selected for discussion and will be highlighted in this paper as concrete is a key material used in construction of ports.

Fig. 1 depicts the overall framework adopted to assess climate change impacts. Further, the deterioration predictions from the models are in a quantified form and therefore the output can be used for risk management, cost-optimised design, development of good practice manuals and establishing a durability design guide to accommodate a changing climate.

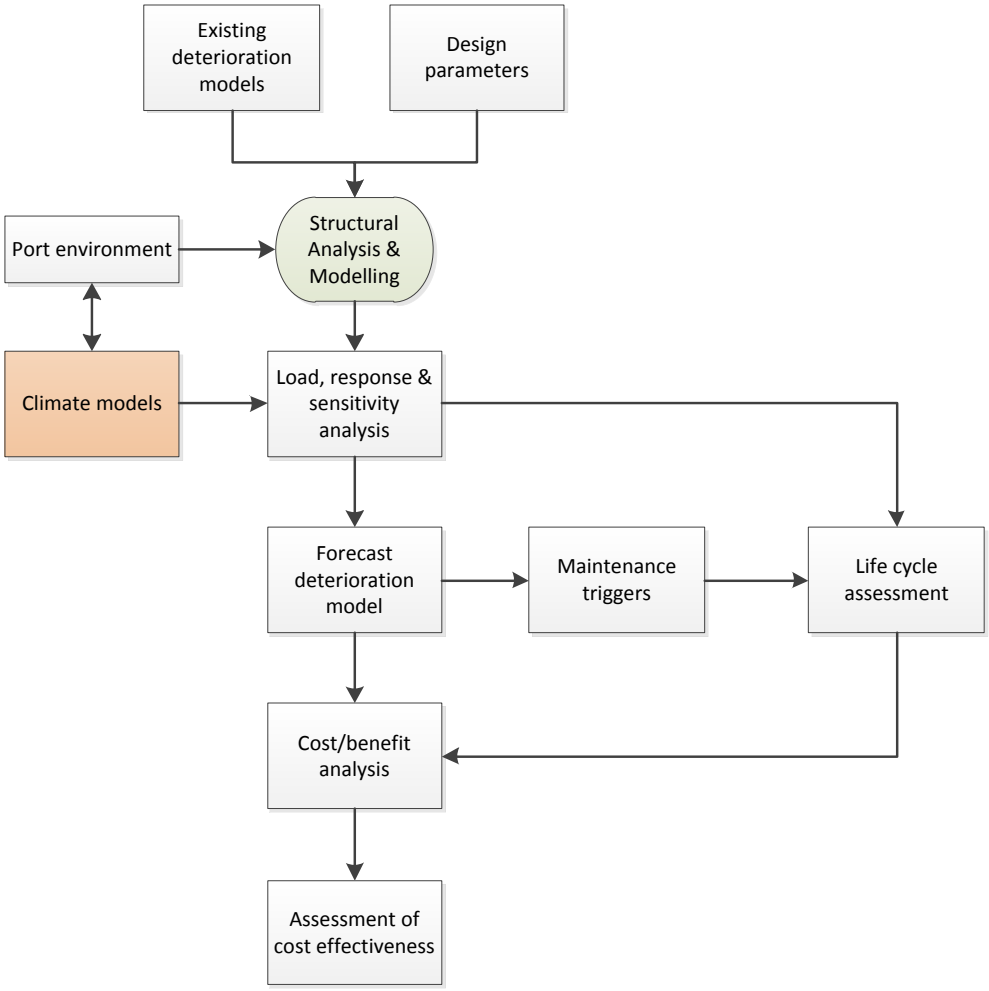


Fig. 1 Climate change impacts on seaport infrastructure assessment framework

Adaptation response, in the form of structural maintenance and retrofitting management, will vary depending on the level of vulnerability exposure, which can be quantified from the models developed. Once the level of vulnerability exposure is established, modeling can be repeated with a simulation of standard durability improvement responses to quantify their effectiveness towards a changing climate. Relevant maintenance and retrofitting options are currently being investigated.

Climate Models

In developing the climate model for this study, changes to temperature, carbon dioxide concentrations, relative humidity levels, sea surface temperatures and sea surface salinity were considered, as these are likely to have the most direct effect on material deterioration. Rainfall affects erosion/abrasion of structural surfaces, as well as diffusion of pollutants into the structural subsurface. However, the actual effects of rainfall on structures are highly site specific, as rainfall, surface temperatures and surface impact depend on the orientation of the site as well as any shelter provided to the surface. Therefore, rainfall is taken into account but simplified using a parameter to represent the frequency of wetting and drying cycles.

The IPCC has produced 40 emission scenarios based on population, energy, technology, land use and economic models. Two emission scenarios have been chosen for this research as they represent a high (A1FI) and a moderate (A1B) greenhouse gas emitting scenario respectively. The information for the future climate projections for this project was obtained using the CSIRO Climate Futures program and OzClim. All climate futures are defined in relation to a baseline climate and the results are expressed as a percentage of change with the exception of temperature. Multiple atmospheric-ocean global climate models (AOGCMs) were used to project climate variables (as opposed to just one model) to overcome shortcomings of individual models (IPCC 2007). As such, 18

AOGCMs (Table 1) were selected to project three possible climate futures: a 'most likely' climate, a 'hotter & drier' climate and a 'hotter & wetter' climate. The outputs of the projected values are provided in three time slices: 2030, 2050 and 2070.

Table 1 AOGCMs selected for climate projections

Models	Developers
BCCR-BCM2.0	Bjerknes Centre for Climate Research, Norway
CCSM3	National Center for Atmospheric Research, USA
CGCM3.1(T47) CGCM3.1(T63)	Canadian Centre for Climate Modelling and Analysis, Canada
CNRM-CM3	Météo-France/Centre National de Recherches Météorologiques, France
CSIRO-Mk3.0 CSIRO-Mk3.5	Commonwealth Scientific and Industrial Research Organisation, Australia
ECHAM5/MPI-OM	Max-Planck Institute for Meteorology, Germany
ECHO-G	Meteorological Institute of the University of Bonn Meteorological Research Institute of the Korea Meteorological Administration Model and Data Group, Germany/Korea
FGOALS-g1.0	National Key Laboratory of Numerical Modeling for Atmospheric Sciences Geophysical Fluid Dynamics (LASG)/Institute of Atmospheric Physics, China
GFDL-CM2.0 GFDL-CM2.1	Geophysical Fluid Dynamics Laboratory, US
IPSL-CM4	Institut Pierre Simon Laplace, France
MIROC3.2(hires) MIROC3.2(medres)	Center for Climate System Research (University of Tokyo) National Institute for Environmental Studies Frontier Research Center for Global Change (JAMSTEC), Japan
MRI-CGCM2.3.2	Meteorological Research Institute, Japan
UKMO-HadCM3 UKMO-HadGEM1	Hadley Centre for Climate Prediction and Research/Met Office, UK

The CSIRO Climate Futures program uses a 5 geographical grid and groups the individual AOGCM projections into a cluster of possible climate futures. This allows a better understanding of the likelihood of a particular climate future based on the number of models showing a similar future. One AOGCM was selected to represent each of the climate futures chosen in this study. AOGCM selection was governed by the availability of the climate variables required by each deterioration model. Results of the climate variable projections are depicted in Figures 2-6. These projections are subsequently applied to the baseline climate data as described in the next section.

Baseline climate information was extracted from current and historical databases maintained by the Bureau of Meteorology (BoM). A 30-year statistical data for a given site (e.g. Port Kembla) was used to establish the baseline. From this a statistical mean was derived as a baseline to apply changes projected from climate futures discussed earlier. Table 2 provides a summary of the climate data used as a baseline.

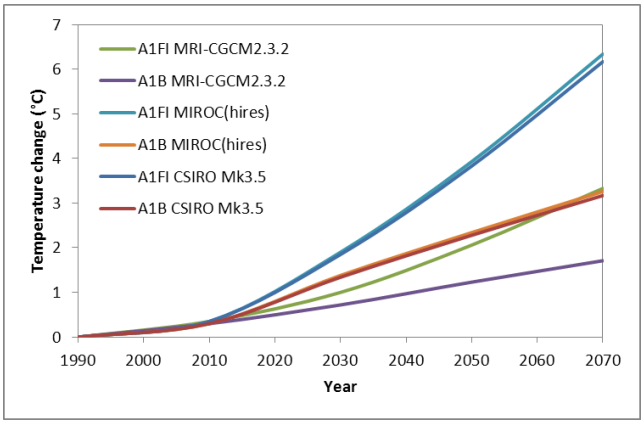


Fig. 2 Surface temperature change projection for Port Kembla region

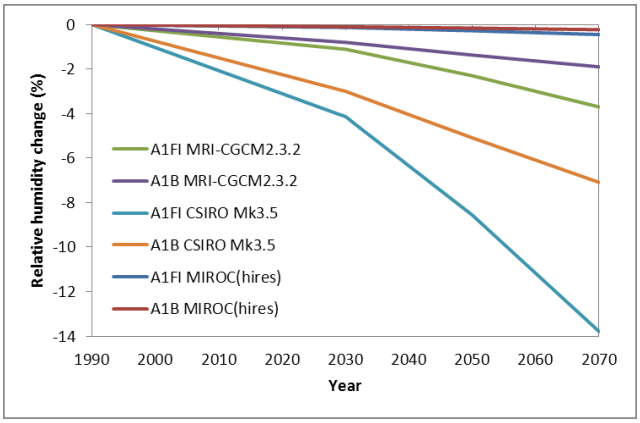


Fig. 3 Humidity change projection for Port Kembla region

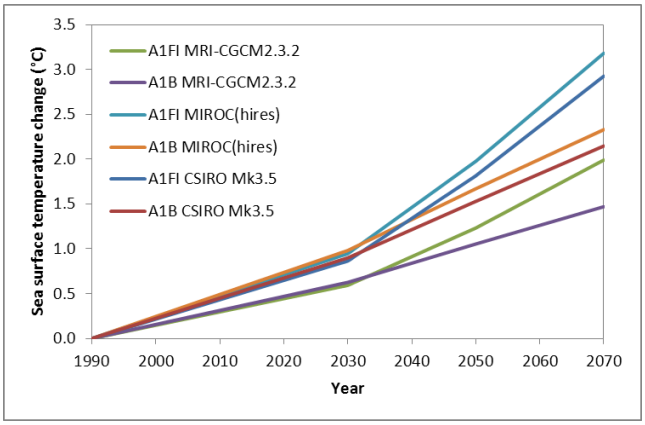


Fig. 4 Summer sea surface temperature change projection for Port Kembla region

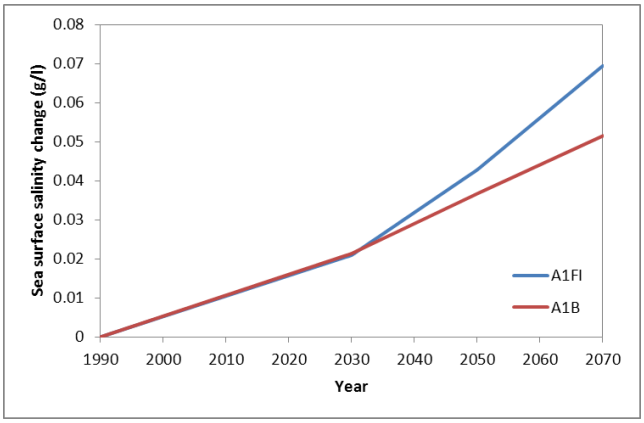


Fig. 5 Sea surface salinity change projection for Port Kembla region (MIROC-hires only)

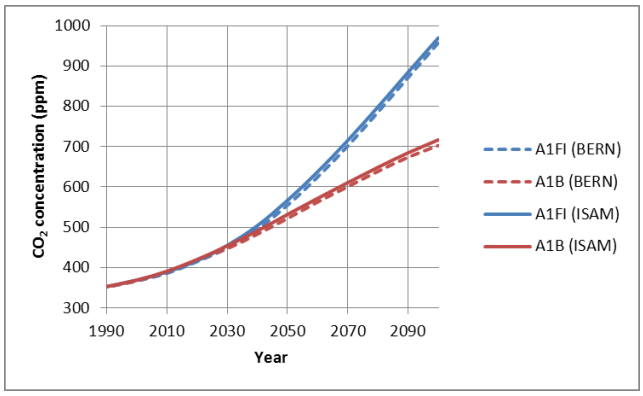


Fig. 6 Atmospheric CO_2 concentration projection for Port Kembla region

Table 2 Baseline climate data for Port Kembla

Model	CO_2		Mean temp		Mean RH		Summer Sea Temp		Salinity	
	ppm		°C		%		°C		g/l	
	A1FI	A1B	A1FI	A1B	A1FI	A1B	A1FI	A1B	A1FI	A1B
MRI-CGCM2.3.2	352.5	352.5	19.1	19.1	62.5	62.5	22.13	22.13	35.57	35.57
CSIRO Mk3.5	352.5	352.5	19.1	19.1	62.5	62.5	22.13	22.13	35.57	35.57
MIROC(hires)	352.5	352.5	19.1	19.1	62.5	62.5	22.13	22.13	35.57	35.57

Deterioration Models

Concrete structures deteriorate mostly on account of a combination of stresses generated by cycles of heating and cooling, wetting and drying and corrosion of the reinforcing steel. With reinforced concrete structures, the electrochemical phenomenon of corrosion of embedded steel is always associated with the cracking and spalling of the concrete cover. The mechanisms for corrosion that are driven by factors such as temperature, humidity and carbon dioxide and chloride concentration could be exacerbated by a changing climate. Changes attributable in the initiation probability for corrosion will depend on the climate change scenario, local environmental exposure (i.e. arid, temperate or tropical climatic conditions, together with the distance to coast etc.) and the standard that is applied to the structure.

For ports, increased corrosion hazards attributable to sea-level rise may also become significant as a result of splash and tidal zone shifts. This may potentially compromise the existing corrosion protection measures, such as cathodic protection.

The degradation of concrete is commonly modeled as occurring in two stages - initiation and propagation. During ‘initiation’, changes begin to take place within the concrete as a result of interaction with the exposure environment, until a limit is reached where damage occurs. During ‘propagation’, a certain defined event occurs, e.g. cracks appear, until a specified limit state is reached.

An explanation of two concrete deterioration mechanism models (i.e. deterioration due to carbonation and deterioration due to chlorination ingress) is provided in this section. These models are necessary to predict the deterioration of reinforced concrete structures due to climate change. Both models focus on reinforcement corrosion.

Carbonation-ingress model. The impact of carbonation has been the subject of many previous studies [1-3]. Carbonation depth depends on many parameters: concrete quality, concrete cover, relative humidity, ambient carbon dioxide concentration [4].

The carbonation depth model by Yoon et al. [1] considers a wide range of influencing parameters, namely aging of diffusion process, reduction in diffusion due to the increase of cement and calcium oxide content, reduction in diffusion due to increase of water-to-cement ratio and non-linear factor of diffusion processes under different environments in relation to time. The carbonation depth is predicted as a diffusion process based on Fick's 1st law and defined as follows:

$$x_c(t) = \sqrt{\frac{2D_{CO_2}(t)}{a} C_{CO_2}(t)} \left(\frac{t_0}{t}\right)^{n_m} \quad (1)$$

Where x_c is the carbonation depth (cm) of concrete at time, t (years), D_{CO2} is the CO_2 diffusion coefficient (cm^2/yr), $C_{CO2}(t)$ is the time-dependent mass concentration of ambient CO_2 (kg/m^3) and n_m is the age factor for microclimatic conditions associated with the frequency of wetting and drying cycles (n_m = 0 for sheltered outdoor and n_m = 0.12 for unsheltered outdoor). The amount of CO_2 for making completely carbonated concrete, a, has a function of CO_2 binding capacity. This can be calculated from the relationship between CaO in the cement and the degree of hydration in atmospheric condition as defined in Eq. 2.

$$a = 0.75 C_e \cdot \mathrm{CaO} \cdot \alpha_H \frac{M_{CO_2}}{M_{CaO}} \quad (2)$$

Where C_e is the cement content (kg/m^3), CaO is the calcium oxide (0.65), α_H represents the degree of hydration and M represents the molar masses of CO_2 and CaO respectively. The degree of hydration [5] is estimated as:

$$\alpha_H = 1 - e^{-3.38 W/C} \quad (3)$$

Where W/C is the water-to-cement ratio.

Eq. 1 is a point-in-time predictive model and assumes that $CO_2(t)$ is constant for all times up to time t. This will overestimate carbonation depth as the CO_2 concentration will gradually increase over time to the peak $CO_2(t)$. Therefore the carbonation depths are recalculated to factor in atmospheric CO_2 concentration conditions using the average CO_2 concentration over the time period as suggested by Stewart [6]. As such, it can be rewritten as:

$$x_c(t) = \sqrt{\frac{2\beta_T(t) D_{CO_2}(t)}{a} k_{urban} \int_{t_0}^{t} C_{CO_2}(t) \mathrm{d}t} \times \left(\frac{1}{t - t_0}\right)^{n_m} \quad (4)$$

The temperature factor, β_T, can be obtained using the Arrhenius-type equation given as:

$$\beta_T(t) = e^{\left(\frac{E}{R}\left(\frac{1}{293} - \frac{1}{T_{av}(t)+273}\right)\right)} \quad (5)$$

Where E is the activation energy of the diffusion process (kJ/mol) given in Table 3 and R is the gas constant (kJ/mol K). And the average temperature over a period is given as:

$$T_{av}(t) = \sum_{t_0}^{t} T(t) \times \frac{1}{t - t_0} \quad (6)$$

Where T(t) is the temperature at time t.

Table 3 Activation energy for typical w/c ratio [7]

W/C	E (kJ/mol)	W/C	E (kJ/mol)	W/C	E (kJ/mol)	W/C	E (kJ/mol)	W/C	E (kJ/mol)
0.3	49.3	0.4	41.8	0.5	44.6	0.6	32.0	0.7	29.7

The sample results below (Figures 7 and 8) are for analysis conducted on Pile No 243 at the AAT terminal at Port Kembla. This is a typical concrete bulkhead pile that is found in Berth 107. These two figures reports the probability of carbonation related corrosion due to climate change. Changes in carbonation depths due to climate change are another output from this study and this is presented in Figures 9 and 10.

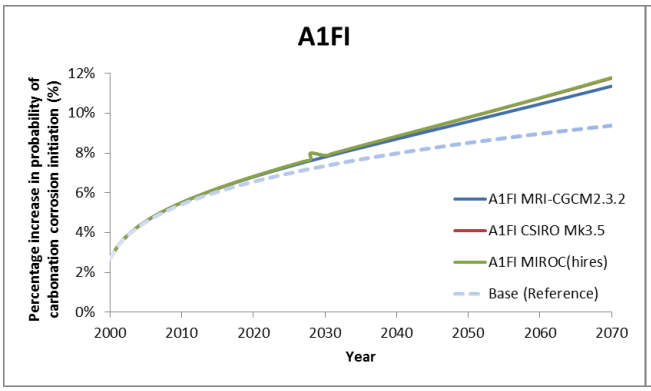


Fig. 7 Probability of carbonation-induced corrosion in concrete due to high emissions (Pile 243/107)

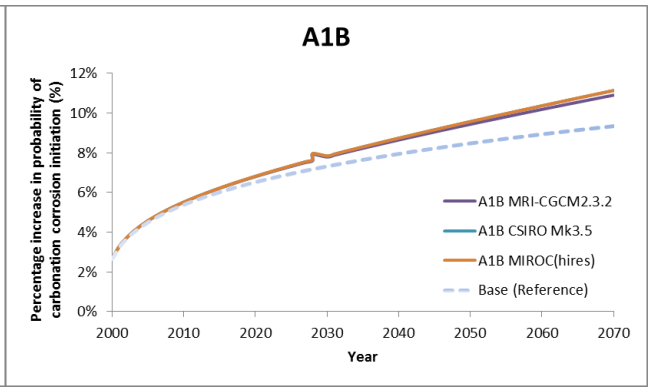


Fig. 8 Probability of carbonation-induced corrosion in concrete due to moderate emissions (Pile 243/107)

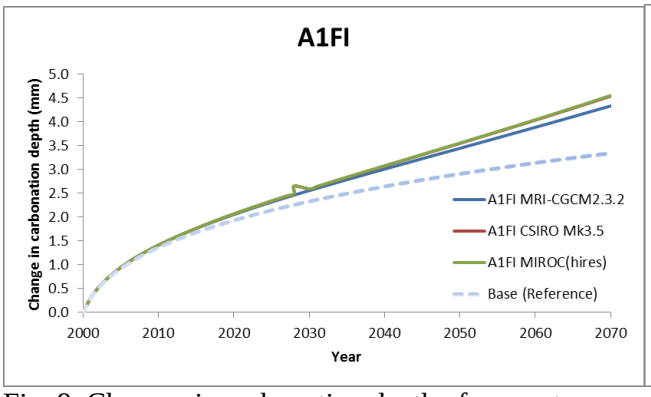


Fig. 9 Changes in carbonation depth of concrete due to high emissions (Pile 243/107)

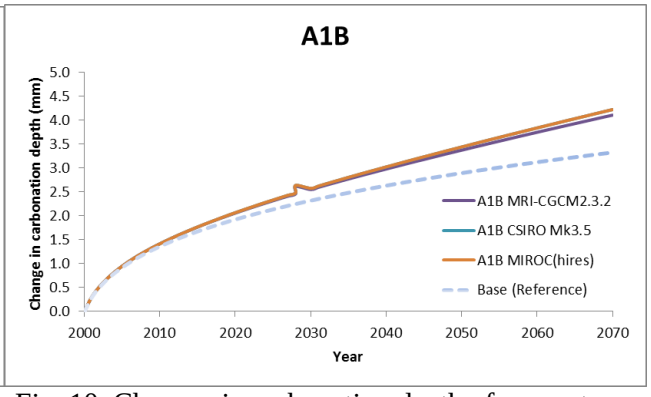


Fig. 10 Changes in carbonation depth of concrete due to moderate emissions (Pile 243/107)

Chloride-ingress model. One model to describe the chloride ingress-process in concrete was presented by Mejlbro [8]. The model, rewritten in a convenient form for design purposes, can be mathematically represented as follows:

$$C(x,t) = C_0\left[1 - erf\frac{x}{2\sqrt{D_c k_e k_t k_c \left(\frac{t_0}{t}\right)^n t}}\right] \tag{7}$$

Where C_0 is the chloride concentration at the surface (kg/m^3) provided in Table 4 and erf denotes the standard error function. D_C is the effective diffusion coefficient at a defined execution and environmental condition measure at time t, n is a factor which considers the influence from the material and environment on time-evolution of D_C (Table 5), k_c is a factor that considers the curing influence, k_e considers the differences between different exposure environments, k_t is a factor that considers the test-method and x is the depth.

Table 4 Surface chloride concentration in relation to various types of environment exposures [9]

Environment	Type	Mean (kg/m^3)
tidal/splash	E1	7.35
atmospheric (coast)	E2	2.95
atmospheric (>1km fr coast)	E3	1.15

Eq. 7 was modified to include a surface temperature variable and therefore can be expressed as:

$$C(h,t) = C_0 \left[1 - erf \frac{x}{2\sqrt{D_c k_e k_t k_c \beta_T \left(\frac{t_0}{t}\right)^n t}} \right] \quad (8)$$

Where h is the depth at cover and β_T is given as the temperature factor as previously established (Eq. 5).

Table 5 Environmental exposure factor

Environment	n		k_e	
	mean	SD	mean	SD
atmospheric	0.65	0.07	0.676	0.114
tidal	0.37	0.07	0.924	0.155
splash	0.37	0.07	0.265	0.045
submerged	0.3	0.05	1.325	0.223

The effect on ingress due to drying-wetting cyclic exposures will be considered in the next phase of chloride ingress modeling. The chloride boundary condition at the exposed side was such that the free chloride concentration during wetting phases will be 30.3 kg/m^3 and a chloride conductivity of 5.79x10^{-12} m^2/s as suggested by Meijers et al. [10].

The sample results below (Figures 11 and 12) are for analysis conducted on Pile No 243 at the AAT terminal. These figures show the probability of chloride initiation while Figures 13 and 14 depict the change in chloride concentration for the given pile.

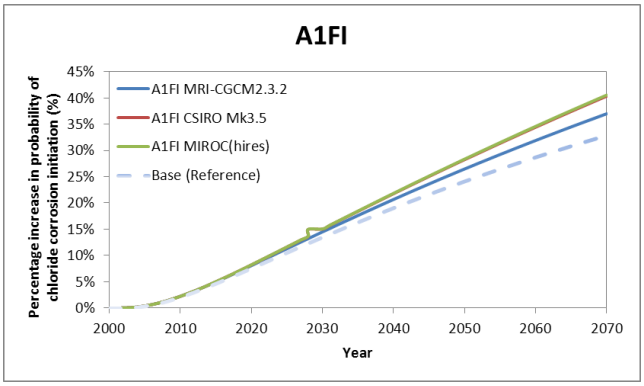


Fig. 11 Probability of chloride-induced corrosion in concrete due to high emissions (Pile 243/107)

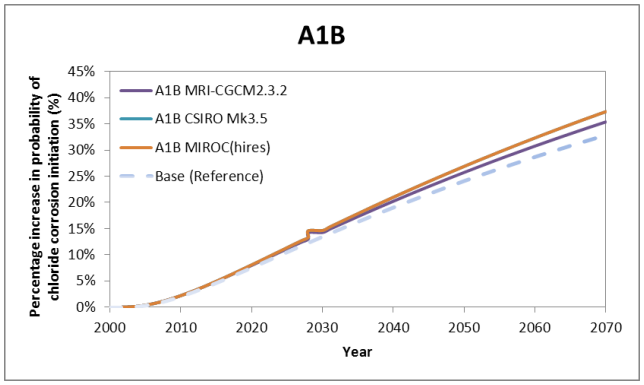


Fig. 12: Probability of chloride-induced corrosion in concrete due to moderate emissions (Pile 243/107)

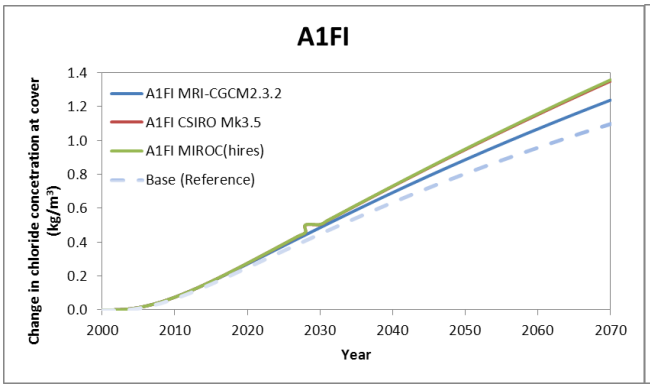


Fig. 13 Changes in chloride concentration at cover of concrete due to high emissions (Pile 243/107)

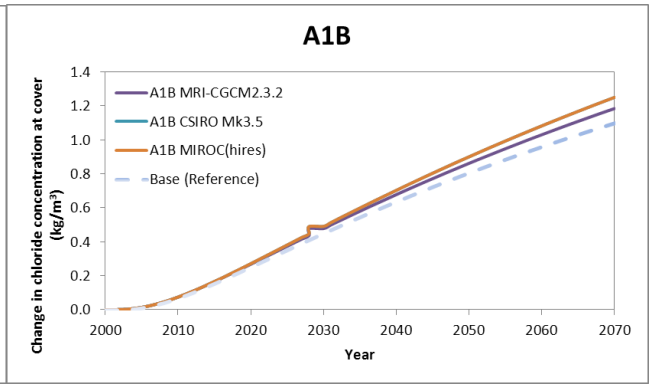


Fig. 14 Changes in chloride concentration at cover of concrete due to high emissions (Pile 243/107)

Conclusions

The modelling completed to date indicate the proposed approach can be used to forecast material degradation allowing for impacts of climate change, provided that reliable climate data are available as input to the models.

There are some limitations to the climate change data generated. For instance, the climate futures can only generate projections up to 2070. This has substantially hampered the ability to ascertain the impacts of climate change on port structures over a longer service life. There is also high uncertainty in climate change modeling and carbon emission scenarios which brings more complexity when applied to the less flexible nature of most engineering models. Gaps exist in climate parameters for some emission scenarios and AOGCM combinations. This has been addressed with assumptions made within the models which will in turn decrease the reliability of the models.

Some records of legacy structures are not available due to poor record keeping practices; thereby some assumptions have to be made based on engineering standards at the period of construction. This approach is believed to provide the most informed assumptions given the circumstances.

These models intend to prepare port authorities for risks that may severely impact the port's long term capabilities and resources. The climate and material modeling methodology developed here are generic and transferable for use with other ports. The next phase of development will evaluate the socio-economic impacts of the projected degradation.

References

[1] I.-S. Yoon, O. Copuroglu, K.-B. Park, Effect of global climatic change on carbonation progress of concrete, Atmospheric Environment, 41 (2007) 7274-7285.

[2] W. P. S. Dias, Reduction of concrete sorptivity with age through carbonation, Cement and Concrete Research, 8 (2000) 1255-1261.

[3] Li, G., et al, Influences of environment climate conditions on concrete carbonation rate, in: 2nd International Conference on Manufacturing Science and Engineering, ICMSE 2011, April 9-11, 2011, Guilin, China: Trans Tech Publications.

[4] Y. F. Houst, F. H. Wittmann, Depth profiles of carbonates formed during natural carbonation, Cement and Concrete Research, 12 (2002) 1923-1930.

[5] de Larrard, F.o., Concrete Mixture Proportioning: A Scientific Approach, Spons Press, London, 1999.

[6] M. G. Stewart, X. Wang, M. Nguyen, Deterioration of concrete structures in Australia under changing environment, in: 11th International Conference on Applications of Statistics and Probability in Civil Engineering, ICASP, August 1-4, 2011, Zurich, Switzerland: Taylor and Francis Inc.

[7] A. V. Saetta, R. V. Scotta, R. V. Vitaliani, Analysis of chloride diffusion into partially saturated concrete, ACI Materials Journal, 5 (1993) 441-451.

[8] L. Mejlbro, The complete solution of Fick's second law of diffusion with time-dependent diffusion coefficient and surface concentration, in: Durability of concrete in saline environment, 1996. Danderyd, Sweden: Cementa AB.

[9] D. V. Val, M. G. Stewart, Life-cycle cost analysis of reinforced concrete structures in marine environments, Structural Safety, 4 (2003) 343-362.

[10] S. Meijers, et al, Computational results of a model for chloride ingress in concrete including convection, drying-wetting cycles and carbonation, Materials and Structures, 2 (2005) 145-154.

© (2012) Trans Tech Publications, Switzerland
doi:10.4028/www.scientific.net/AMM.238.358

Study on the Inwall Crack Extension and Fatigue Life Evaluation for Deep-sea Steel Catenary Riser under Wave and Current Action

Bingjun Si[1, a] and Qiao Jin[2,b]

[1]Vibration & strength testing center Co, Ltd, Dalian University of Technology, Dalian, China

[2] School of Civil Engineering, Shenyang Jianzhu University, Shenyang, China

[a]sibingjun@yahoo.com.cn, [b]goldenfss@163.com

Keywords: deep-sea steel catenary riser; crack extension; fatigue life; touchdown zone; transportation for CO_2.

Abstract. Aimed at deep-sea steel catenary risers(SCRs) transporting supercritical or dense CO_2, this paper uses the macroscopic pipeline-transporting finite element model and the microscopic pipewall crack growth model to numerically simulate corrosive-inwall-defect-induced crack extension along radial direction for the deep-sea riser which is subjected to wave and current loads. Meanwhile, based on linear elastic fracture mechanics and fatigue crack extension theory, the effect of wave height on the fatigue life of the pipewall at touchdown zone is discussed. The above-mentioned study in this paper is expected to give a good reference to the similar study for oil&gas SCRs.

Introduction

Geological sequestration for anthropogenic carbon dioxide(CO_2) by injection into deep-sea basalt, as a part of sea-based carbon capture and storage(CCS) techniques, provides an alternative answer for reducing emissions of green house gases in worldwide range[1]. Under the high-pressure and low-temperature conditions of deep ocean, carbon dioxide in liquid state can easily be combined with water molecules to produce a hydrate which is denser than water and can be stably kept on or below the seafloor. One of the key issues involving in CCS is pipeline transportation of supercritical or dense CO_2. Since steel catenary risers(SCRs) have been a potential solution for deep and ultra deepwater production applications[2], it is of important significance to develop the fatigue damage evolution rules for the SCRs transporting CO_2 in the deep-sea environment.

In this paper, a defect-induced crack growth process of the pipe wall is studied, which is in the touchdown zone of a deep-sea SCR subjected to wave and current loads. To perform the analysis, the macroscopic pipeline-transporting finite element model and the microscopic pipewall crack growth model are built. And hence the alternating stress range due to environmental loads can be obtained. Thus, by using the two numerical models, the effect of wave heights and current directions on the fatigue life of the SCR is further evaluated based on the linear elastic fracture mechanics and the fatigue crack extension theory.

FEM Modelling

Integral FE Model of SCR. In order to analyze the stress state in the touchdown zone of SCR systems under environmental loads(seeing Fig. 1), a nonlinear integral FE model of the SCR is constructed using the finite element package ANSYS. The immersed pipe element, PIPE59, is used to simulate the riser into the ocean while the nonlinear spring, COMBIN39, is to simulate the soil-riser interaction along the touchdown zone. The ANSYS FE model of the target SCR is shown in Fig. 2. And the main parameters of the SCR is illustrated in Table 1, which is also used in the following analysis. In Table 1, the working inner pressure is set as 10 MPa , larger than the minimum pressure limit, 7.38 MPa, of supercritical or dense CO_2 transported through pipelines. Meanwhile, the inner fluid density is set as 800 Kg/m^3 though there exists a wide range of density variety for dense CO_2 under small pressure differences. Another critical issue in the numerical modeling of SCR systems is the riser-seafloor interaction in the touchdown zone (TDZ), which highly determines the fatigue

damage level of SCRs. Recent research [3, 4] indicates that the fatigue damage is sensitive to seafloor stiffness, which is characterized by non-linear *P-y* relationship of seafloor-riser interaction. In this paper, a non-degradating *P-y* curve proposed by Aubeny et al [5], is adopted to describe the riser-soil interaction (seeing Fig. 3) . The riser-seafloor spring model, shown in Fig. 4, is simulated by using the COMBIN39 element in ANSYS.

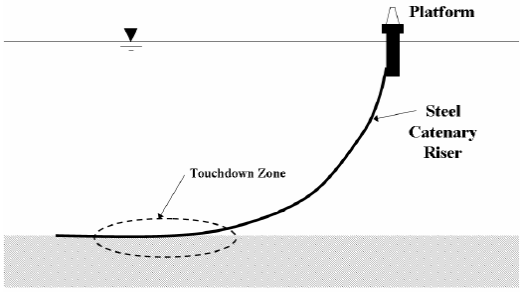


Fig. 1 Schematic of the SCR system

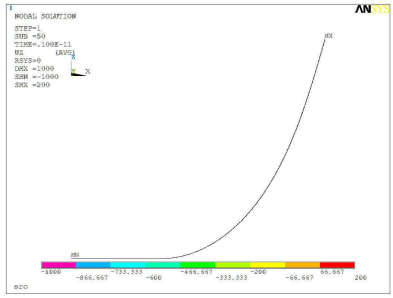


Fig. 2 The FE model of SCR

Table 1 SCR specification data and environmental condition

Pipe specifications	Values	Environmental conditions	Values
Total length of pipe(m)	2300	Water depth(m)	1000
Length of the overhung section(m)	1800	Maximum wave height(m)	Case1: 3.5 Case2: 7
Length of the horizontal section(m)	500	Associated wave period to max height(sec)	Case1: 9 Case2: 14
Pipe outer diameter(m)	0.320	Current speed(m/sec)	0m-300m:2m/s 300m-600m:1m/s 600m-1000m:0.4m/s
Wall thickness(m)	0.010	Lift force coefficient	0
Inner CO_2 pressure(MPa)	10	Drag force coefficient	1.2
Inner fluid density(Kg/m^3)	800(for dense CO_2)	Inertia force coefficient	2

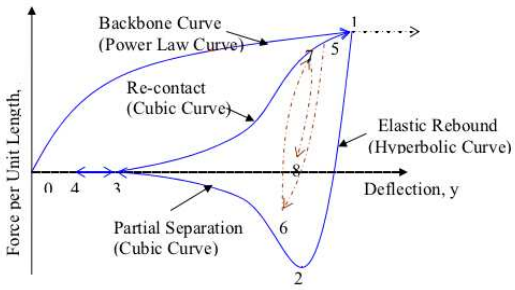


Fig. 3 Non-degradating P-y model

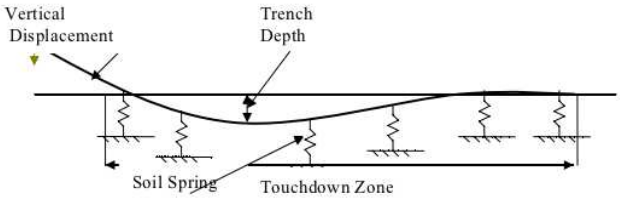


Fig. 4 Seafloor spring model

Localized Pipewall Crack Growth Model. In order to study the effect of environmental loads(wave, current, etc.) on the crack extension of the pipe wall in the vicinity of the touchdown zone, a two dimensional FE model of the SCR pipe wall is built and only Mode-I crack(tension crack) is considered(ignoring Mode Ⅱ, Ⅲ). Meanwhile, only the crack propagation life, not the crack nucleation one, is included in the following fatigue life analysis. And the allowable crack propagation range along the radial orientation was assumed to be from 0.1mm to 8.1mm (seeing Table 2). Considering structural symmetry and loading symmetry in this study, one half of the pipeline section is modelled and the half-symmetric boundary conditions are loaded according to the deflection compatibility. In this study, the crack advance has been simulated using the remeshing technique performed by FRANC2D software. All regions of this model is meshed with the bilinear four sided meshing algorithm. The location of the inner defect and the crack in the pipe wall, and meshing details around the crack tip are shown in Fig. 5 and Fig. 6, respectively.

Table 2 Parameters for crack growth analysis

Steel Type	X65
Min.yield stress(MPa)	448
Inner working pressure (MPa)	7.5
Radii of predefined semicircle defect(mm)	0.25, 0.5, 1
Initial crack size(mm)	0.1
Final crack size(mm)	8.1

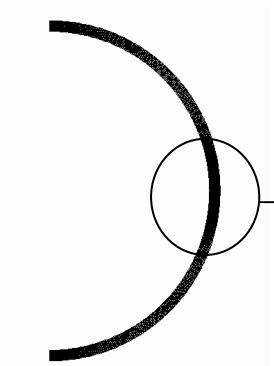


Fig. 5 The 2D model of one half pipeline section

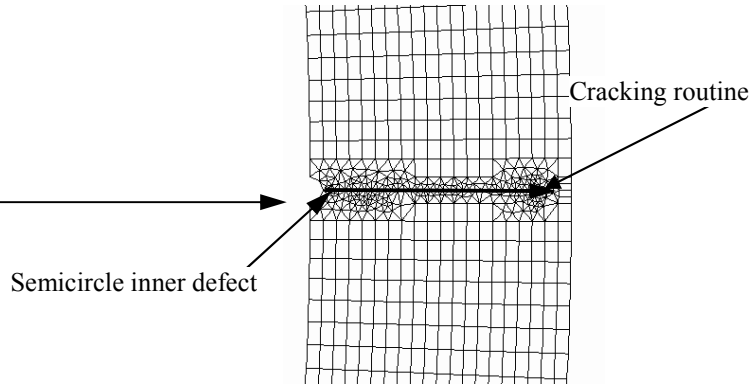


Fig. 6 Closeup of the cracked zone

The fatigue crack growth life of the SCR is calculated by the experimental equation presented by Huang [6], which is given as follows,

$$Da/dN=1.414\times10^{-11}(\Delta K_E^{2.88}-5.4^{2.88}) \quad (1)$$

Analysis of the Numerical Results

Based on the above FE models for the SCR system, the influence of wave height on the fatigue life of the pipeline is analyzed, which is particularly meaningful for structural durability evaluation of the pipeline transporting high corrosive CO_2 mixture.

For convenience of study, the corrosion topology of inner wall of the pipeline is simplified into semicircle shape and its dimension is measured by radius of the semicircle. Meanwhile, only wave fluctuations are used as cyclic loads which act on the riser.

Under the inner pressure of 7.5MPa, i.e. the almost lower limit for transportation of supercritical or dense CO_2, the SIFs(stress intensity factor), K, of the crack, induced by the inner defects of radii(0.25mm, 0.5mm and 1mm), are shown in Fig. 7, compared with that without inner defect. Similarly, the SIF increments , $\triangle K$, are varied as shown in Fig.8. The variation trend of k and $\triangle K$ in Fig.7 and Fig.8 indicates that with the increase of defect size, the value of K and $\triangle K$ grows larger. While the latter, as a crack driving force, determines the crack propagation speed under cyclic loads and hence the fatigue life of the pipeline.

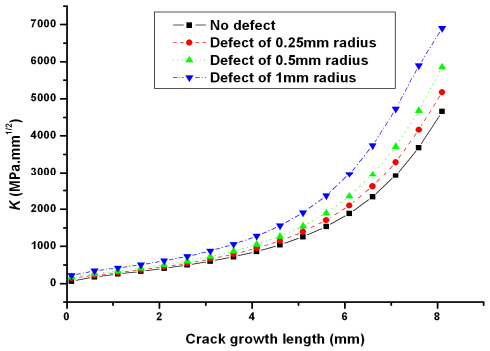


Fig. 7 SIF variation with crack growth length

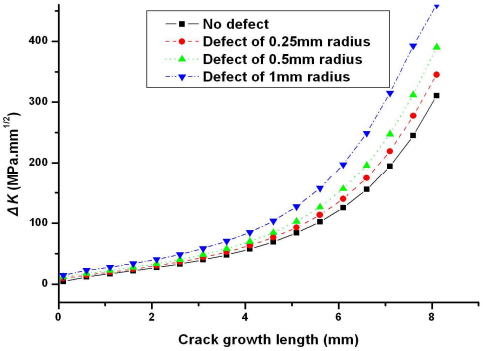


Fig.8 SIF increment variation with crack growth length

For fatigue crack growth problems due to cyclic loads, the plastic zone before the crack tip is small and linear elastic fracture mechanics is applicable. Therefore, the SIF, K and its variance, $\triangle K$, are proportional to the stress fluatuation resulted from cyclic loads. And hence, the fatigue life of the weakest point in the touchdown zone under different wave heights can be calculated by a integral of Eq.1,as shown in Table 3.

These data in Table 3 indicate that the number of stress cycles which represents the fatigue life of the pipeline always decreases with the increase of the wave height. Meanwhile, the fatigue lives of the pipeline with a defect of 1mm radius drops largely, compared with those of the pipeline with no inner defect. This result comparison implies great influence of defect sizes on fatigue crack growth life of the pipeline.

Table 3 Fatigue life values varied with wave fluctuation ranges [cycles]

Wave heights(m)	No defect	Defect of 0.25mm Radius	Defect of 0.5mm Radius	Defect of 1mm Radius
3.5	2347000	1952610	1515140	672210
7	1736780	1444931	1121203	497435

Conclusions

In this paper, we develop two FE models to initiatorily study the influence of environmental loads and defect sizes on the fatigue life of anthropogenic CO_2 SCRs. The following conclusions can be drawn:

(1) A defect-induced crack in pipe wall has a more rapid propagation rate, easily causing premature fatigue failure for pipelines, especially for anthropogenic CO_2 pipelines , because unavoidable impurities of carbon dioxide transported help to form these defects in the inner wall of pipelines.

(2) As for a pipeline with an birth or acquired defect, fatigue durability of the pipeline will decrease dramatically once crack nucleation happens at the vicinity of the defect. Therefore, the internal corrosion status of pipelines transporting corrosive medium ought to be inspected and monitored periodically, or evaluated preliminarily.

Acknowledgements

This work was financially supported by the Natural Science Foundation for the Youth (51008049).

References

[1] F. Peter. Carbon capture and sequestration (CCS): a primer. CRS report 42532, 2012.

[2] A. H. Stephen, W. Neil. Steel catenary risers for deepwater environments. The offshore Technology Conference. OTC8607, Houston,1998.

[3] C. Bridge, H. Howells, N. Toy, G. Paker. Full scale model tests of a steel catenary riser. Fluid Structure Interaction. 2003, p.107.

[4] C. Bridge, K. Laver, E. Clukey. Steel catenary riser touchdown point vertical interaction model. OTC, 2004.

[5] C. P. Aubeny, G. Biscontin, J. Zhang. Seafloor interaction with steel catenary risers. Texas A&M University, 2006.

[6] X. Huang, G. Jia, W. Cui, E. Qi. Unique crack growth rate curve model for fatigue life prediction of marine steel structures. Journal of ship mechanics. 15 (2011)118.

© (2012) Trans Tech Publications, Switzerland
doi:10.4028/www.scientific.net/AMM.238.366

System Identification Applications in Pavement Permittivity Back-calculation

Meili Meng[1, 2, a], Yingchun Cai[1,b] and Bei Zhang[1,c]

[1] Zhengzhou University, Zhengzhou 450001, China

[2] North China University of Water Resources and Electric Power, Zhengzhou 450011, China

[a] mmlgmx@163.com, [b]yccai@zzu.edu.cn, [c]zhangbei@163.com

Keywords: homogeneous clay dam, bridge, dam slope stability, seepage flow.

Abstract. The Ground Penetrating Radar (GPR) has been widely used in the road quality control of construction, maintenance management and deterioration investigation for its rapid, nondestructive and high efficient advantages. Whereas, the pavement layer thickness accuracy measured by GPR is not satisfied under any conditions, and the coring calibration must be done. Based on System Identification (SI) theory, sensitivity analysis method and the singular value decomposition of matrix technology, an inverse method is presented to back-calculate pavement permittivity and analyze layer thickness used the GPR waveform reflected by pavement structure. The experiments show the algorithm is faster, more stable and more accurate in thickness calculation. When it is used in GPR data analysis, the traditional coring calibration will be reduced or avoided.

Introduction

Dielectric properties of pavement materials can be evaluated according to the incident wave and reflection wave information that have gotten from the detected road by Ground Penetrating Radar. Then the pavement performance and condition can be inferred. This is basic principle of Ground Penetrating Radar (GPR) in pavement structure nondestructive detection. Therefore, the back-calculation of dielectric characteristic parameters is the one of key technology of this research project. In order to solve this problem, Newton iterative method and genetic algorithm are applied to calculate material dielectric constant [1-5]. Some achievements have been obtained and the precision is to be improved. In this paper, system identification is applied to calculate layers complex dielectric constant and layers thickness, combined with the sensitivity analysis technology and the singular value decomposition of matrix method. The results showed that the method is stable and can get higher precision and faster convergence rate.

Radar Wave Transmission Characteristics in Layer Pavement Structure System

When electromagnetic wave propagates in the layer medium, reflection and refraction will happen at the medium interface that electromagnetic characteristics are different.

When the radar pulse wave propagates in the pavement structure layer, assuming incident angle is 90° and Z is pavement structure depth, it can meet the following field's Maxwell equations:

$$\frac{\partial^2 E}{\partial z^2} = -\left(\omega^2 \mu\varepsilon - j\omega\mu\sigma\right)E \tag{1}$$

Where, $E = \mathrm{Re}\left[E_0 \exp\left(jwt\right)\right]$ is the electric field vector, E_0 is the amplitude of E; ω is the angular frequency, z is the direction of propagation, μ is the magnetic permeability, ε is the dielectric constant, σ is conductivity.

The equation (1) can be reduced to the following forms:

$$E = E_0 e^{-jkz} \tag{2}$$

Where k is propagation constant and is defined as follow:

$$k = \sqrt{\omega^2 \mu\varepsilon - j\omega\mu\sigma} = \omega\sqrt{\mu\left(\varepsilon - j\frac{\sigma}{\omega}\right)} \tag{3}$$

When the ground penetrating radar pulse wave propagates perpendicularly in multilayer road system, reflection coefficient $R(n)$ and transmission coefficient $T(n)$ respectively are:

$$R(n) = \frac{k_n - k_{n+1}}{k_n + k_{n+1}} \tag{4}$$

$$T(n) = \frac{2k_n}{k_n + k_{n+1}} \tag{5}$$

In general, the road medium conductivity is approximately equal, namely $\mu_n \approx \mu_{n+1}$. Relative complex dielectric constant is defined as $\tilde{\varepsilon}_r = \varepsilon_r - j\frac{\sigma}{\omega\varepsilon_0}$. At this time, formula (4) and formula (5) can be expressed as:

$$R(n) = \frac{\sqrt{(\tilde{\varepsilon}_r)_n} - \sqrt{(\tilde{\varepsilon}_r)_{n+1}}}{\sqrt{(\tilde{\varepsilon}_r)_n} + \sqrt{(\tilde{\varepsilon}_r)_{n+1}}} \tag{6}$$

$$T(n) = \frac{2\sqrt{(\tilde{\varepsilon}_r)_n}}{\sqrt{(\tilde{\varepsilon}_r)_n} + \sqrt{(\tilde{\varepsilon}_r)_{n+1}}} \tag{7}$$

When the GPR detects the actual pavement structure layers, the pavement medium complex dielectric constants are unknown. The dielectric constants need be calculated by type (6) according to reflection coefficient which is defined as the ratio of the measured reflection wave to the incident wave. This process is called dielectric constant back-calculation. According to the calculation of the dielectric constants and the information of measured reflection wave, each actual layer working condition can be inferred. Some methods are applied [6-9].In this paper system identification algorithm is used in pavement dielectric constant calculations. Examples show that this algorithm both converges fast and steadily and has high precision.

The Basic Principle of System Identification

In System identification method, the scientific and reasonable mathematical model is used to describe and simulation an unknown system. According to the input and output of the system, related parameters of the model are adjusted constantly to achieve an acceptable accuracy of error between the calculated output and the actual system output. At this time, the calculated parameters are assumed to be the true parameters of the practical system parameters [10].It can be seen that there are three key factors to determine the effective identification method: (1) the accurate measurement of the unknown system output data; (2) scientific and reasonable mathematical model; (3) the rapid convergence parameters adjustment method. If the measured data and the model are reliable, the algorithm is mainly depends on the parameters adjustment algorithms.

In this article, the sensitivity analysis is adopted as a parameters adjustment method, namely by establishing and calculating of the parameters adjustment that are obtained from the sensitivity matrix, then iterative calculating until the adjustment precision meets certain requirements. If a system has n parameters, we can establish mathematical model as following formula:

$$f = f(P_1, P_2, \cdots, P_n, x, t) \tag{8}$$

Where f is output function; P_1, P_2, …, P_n is model parameters, x and t are independent space and time variables. Written in Taylor series at $f_k(P_1, P_2, \ldots, P_n, x_k, t_k)$ and only class parts reserved, it is:

$$f_k(P + \Delta P) = f_k(P) + \nabla f_k \cdot \Delta P \tag{9}$$

Set parameters vector $P=[P_1, P_2, \ldots, P_n]^T$, if $f_k(P+\Delta P)$ is assumed as the actual system output. The actual radar reflection signals, $f_k(P)$ is the simulation system output using latest parameters: the radar simulation signals. The error between the actual and the simulative signals can be defined:

$$e_k = f_k(P+\Delta P) - f_k(P) = \nabla f_k \cdot \Delta P = \frac{\partial f_k}{\partial P_1}\Delta P_1 + \frac{\partial f_k}{\partial P_2}\Delta P_2 + \cdots + \frac{\partial f_k}{\partial P_n}\Delta P_n \tag{10}$$

Where ΔP is the parameters adjustment quantity. If $m(m \geq n)$, equations of dimensionless can be written as follows:

$$\left.\begin{aligned} &\frac{e_1}{f_1} = \frac{\partial f_1}{\partial P_1}\cdot\frac{P_1}{f_1}\cdot\frac{\Delta P_1}{P_1} + \frac{\partial f_1}{\partial P_2}\cdot\frac{P_2}{f_1}\cdot\frac{\Delta P_2}{P_2} + \cdots + \frac{\partial f_1}{\partial P_n}\cdot\frac{p_n}{f_1}\cdot\frac{\Delta P_n}{P_n} \\ &\cdots\cdots \\ &\frac{e_m}{f_m} = \frac{\partial f_m}{\partial P_1}\cdot\frac{\partial f_1}{f_m}\cdot\frac{\Delta P_1}{P_1} + \frac{\partial f_m}{\partial P_2}\cdot\frac{P_2}{f_m}\cdot\frac{\Delta P_2}{P_n} + \cdots + \frac{\partial f_m}{\partial P_n}\cdot\frac{P_n}{f_m}\cdot\frac{\Delta P_n}{P_n} \end{aligned}\right\} \tag{11}$$

Assuming:

$$r = \left[\frac{e_1}{f_1}, \frac{e_2}{f_2}, \cdots\cdots, \frac{e_m}{f_m}\right]^T, F_{ki} = \left[\frac{\partial f_k}{\partial P_i}\cdot\frac{P_i}{f_k}\right], \alpha = \left[\frac{\Delta P_1}{P_1}, \quad \frac{\Delta P_2}{P_2}, \quad \cdots \quad \frac{\Delta P_n}{P_n}\right]^T; (k = 1,2,\cdots,m; \quad i = 1,2,\cdots,n)$$

The equations (11) can be expressed as:

$$F\alpha = r \tag{12}$$

Where r is the error vector, F is the sensitivity matrix, α is the parameters adjustment vector. The singular value decomposition method is used to get parameters adjustment vector and new parameter is input and calculate again until the precision meet the requirement.

$$P^{k+1} = P^k(1+\alpha) \tag{13}$$

Where P^{k+1} is the k+1 iteration of model parameters, P^k is the k iteration of model parameters, α is the k iteration of model parameters adjustment vector.

Dielectric Parameters Back-calculation using System Identification Method

Based on the above the electromagnetic wave propagation model in the road surface layer medium, simulation reflected signals can be calculated using the incident signals and compared with the actual reflection signals. System identification and sensitivity analysis can be used to adjust system parameters until the precision meets the requirements. Specific steps are shown in Fig. 1.

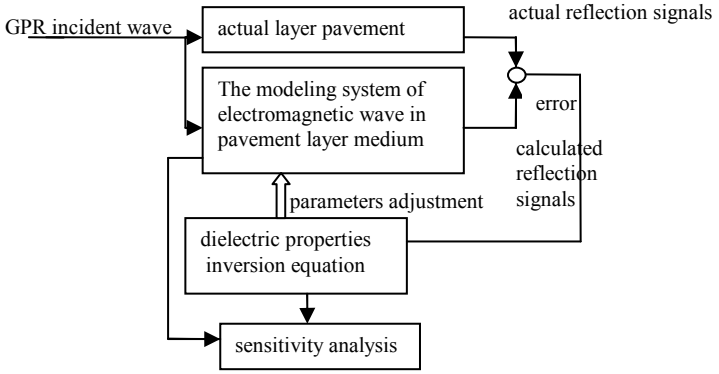


Fig.1 System identification procedure for back-calculating dielectric properties of layer structures

Assessment of System Identification Algorithm in Theory. In order to verify the effectiveness of the back-calculation algorithm, the theoretical assessment is indispensable. System parameters are back-calculated according to the simulation response that is calculated in view of known system parameters. Whether the algorithm is effective and how fast the algorithm converges can be tested by error analysis.

Table 1 Theory evaluation results of system identification algorithm

Design parameters of pavement structure			Back-calculated parameters					
Dielectric constant		Thickness (cm)	Dielectric constant				Thickness(cm)	
Real part	Imaginary part		Real part	Error (%)	Imaginary part	Error (%)	Back-calculated value	Error (%)
10.00	-2.00	16.00	9.89	1.10	-1.97	1.50	15.90	0.62
15.00	-2.00	16.00	14.97	0.20	-1.97	1.50	16.00	0.00
5.00	-2.00	16.00	4.74	5.20	-1.92	4.00	16.10	0.62

The ground penetrating radar receiving waveform that is reflected from the material properties known pavement (the dielectric constant and thickness as is shown in table 1) can be calculated and simulated according to the incident wave and then it is applied to back-calculate the related parameters using system identification principle. The algorithm quality in theory can be evaluated by comparing the calculated value with the real value. Evaluation results are listed in Table 1, it can be seen that the system identification inversion method can achieve good convergence to the real value.

Applications of the System Identification Algorithm. The layers thicknesses of a new built asphalt concrete pavement are detected by ground penetrating radar in the construction site. In the laboratory, the each layer dielectric constant is computed respectively using system identification algorithm according to the receiving reflection wave. Based on each layer dielectric constant, its thickness can be calculated and is compared with the drilling core actual thickness. The results are shown in Table 2, it can be seen that the thickness calculations have high precision using system identification algorithm. For example, surface layer errors are within 3% and base layer errors within 5%. Both of them can satisfy the precision requirement of engineering.

Table 2 Thickness comparison table

Point Numbers	Back-calculated results using system identification method				Actual thickness	
	Surface layer	Error (%)	Base layer	Error (%)	Surface layer	Base layer
1	6.90	2.82	30.50	1.61	7.10	31.00
2	7.60	1.29	31.60	4.24	7.70	33.00
3	7.10	2.74	38.80	3.00	7.30	40.00
4	7.80	2.50	35.50	1.43	8.00	35.00
5	8.10	0.00	35.40	1.12	8.10	35.80
6	15.70	1.26	31.50	3.96	15.90	32.80

Conclusions

Based on the basic principle of the road surface radar, pavement materials dielectric properties parameters are back-calculated successfully and accurately by the use of system identification method both in theory and in practice. Assessment in Theory shows the method can effectively converge to the real value and Application in practice make it clear that the method improves layer thickness detecting precision by ground penetrating radar. System identification method should be expanded and studied further.

References

[1] Y.Cai, Inverse Analysis of Dielectric Properties for Layered Inhomogenous Media—Study on Applied Technology of Ground Penetrating Radar. Dalian University of Technology, 2008.

[2] Timo Saarenketo, Tom Scullion. Road evaluation with ground penetrating radar, Journal of Applied Geophysics, 43 (2000) 73-88.

[3] B. Zhang, System Identification Method for Backcalculating the Dielectric Property and Thickness of Pavement Structures—Study on Applied Technology of Ground Penetrating Radar, Chongqing University, 2003.

[4] Fernando Emmanuel, Liu Wenting, Dietrich Bruce, Computer program for network level determination of pavement layer thicknesses, Proceedings of SPIE -The International Society for Optical Engineering, 2000, V4084:194-199.

[5] Y. Cai, F. Wang, H. Kang, Research and application of backcalculation for pavement permittivity by Genetic Algorithm. Journal of Wuhan University of Technology (Transportation Science & Engineering), 34 (2010) 542-544.

[6] Amara Loulizi, Development of Ground Penetrating Radar Signal Modeling and Implementation for Transportation Infrastructure Assessment, U.S. the Virginia Polytechnic Institute and State University, 2001.

[7] X. Dong, W. Wang, Parameter inversion of stratified media based on time domain reflection data, Acta Electronica Sinica, 9 (1999) 59-62.

[8] M. Meng, Simulation of Ground Penetrating Radar Echo Waves in Pavement Layers, Zhengzhou University, 2002.

[9] X. Tao, Research on the Application of Road Radar Technology, Zhengzhou University, 2002.

[10] F. Wang, R. L. Lytton, System Identification Method for Backcalculating Pavement Layer Properties, TRB.1993, V1384,pp. l-7.

© (2012) Trans Tech Publications, Switzerland
doi:10.4028/www.scientific.net/AMM.238.371

Calculation of Saturation Line of Groundwater under Reservoir Water Table Uniform Falling

Youyi Zhang

School of Civil Engineering and Architecture, Southwest University of Science and Technology, Mianyang, China

youyzh@126.com

Keywords: groundwater; saturation line; aquifer.

Abstract. It has been proved that the groundwater plays a key role in the stability of slope. It is important to determine the position of saturation line in the calculation of slope stability. Based on the basic differential equation of one dimension unsteady seepage flow, the calculation model is created with the uniform falling of reservoir water table, the counting equation by Laplace's transform is deduced. It is easy to use the equation which is fitted by polynomial expression to get simplified formula. Simplifying the formula can satisfy the engineering precision requirement.

Introduction

Changes in reservoir water level and rainfall will lead to the decline of stability of the slope. Stability calculation downhill in these condition, we must first determine the location of the saturation line, and be based on the saturation line to determine the seepage pressure, then do the stability analysis. The saturation line mostly based on experience and man-made to determine the stability calculation, which may case unsafe of regulation project. Therefore there is a need for further study about the calculation of the saturation line. The derivation of calculation formula of bank slope in the water level constant velocity decreases groundwater infiltration line.

Base Hypothesis and Calculation Model

Base Hypothesis. (1)The aquifer is isotropic, homogeneous, lateral unlimited extension, and which have a horizontal impermeable layer; (2) diving flow is one-dimensional flow, the original water table is level before the water level to drop; (3) water level decline in v_0 isokinetic.

According to the above assumptions, we can get the basic differential equations of the available one-dimensional unsteady seepage in isotropic soil moment [1]:

$$\mu\frac{\partial h}{\partial t}=k\frac{\partial}{\partial x}(\mathrm{H}\frac{\partial h}{\partial \mathrm{x}}) \tag{1}$$

The equation is the second-order nonlinear partial differential equations, finding the analytical solution usually use a simplified method, and linearization, and then solving. The simplified method is generally treating the thickness of the aquifer H as a constant, instead of which with the beginning and ending of the average thickness of the flow of diving, can get a simplified equation of motion:

$$\frac{\partial h}{\partial t}=\frac{kh_m}{\mu}\frac{\partial^2 h}{\partial \mathrm{x}^2} \tag{2}$$

Let be $a=\frac{kh_m}{\mu}$,then (2) can be recorded as:

$$\frac{\partial h}{\partial t}=a\frac{\partial^2 h}{\partial \mathrm{x}^2} \tag{3}$$

Where K is the coefficient of permeability (m/d), h_m is the average thickness of aquifer (m), μ is the specific yield or the storage rate, t is the duration of water lowering (d).

Calculation Model. The Calculation diagram is shown in Fig. 1. At the initial moment, t=0, as the assumptions, the initial water level is $h_{0,0}$ in the area.let the Groundwater level amplitude that the place is x faraway from bank slope is $\mu(x,t) = h_{0,0} - h_{x,t}$, at the t moment. When t=0 the water level amplitude is $\mu(x,t)$ =0 by assumptions. When the water level drop to the uniform, in the place of x=0, the water level amplitude is $u(0,t)= v_0 t$ at the t moment, the water level did not change in the place of x=∞,so u(∞,t).

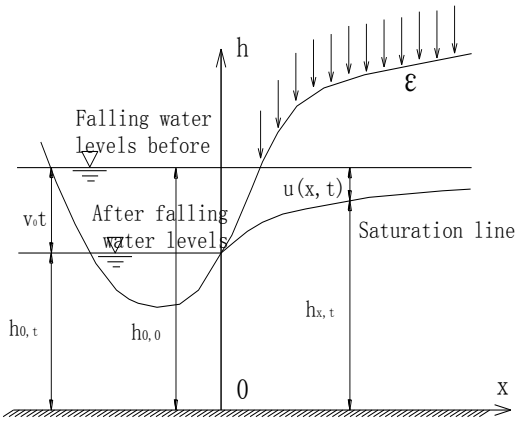


Fig. 1 Calculation sketch of phreatic surface

According to the above boundary and initial conditions, the above the water level dropped a semi-infinite aquifer unsteady groundwater seepage can come down to the following model equation:

$$\begin{cases} \dfrac{\partial u}{\partial t} = a\dfrac{\partial^2 u}{\partial x^2} & (0 < x < \infty,\ \ t > 0) \\ u(0,t) = v_0 t & (0 < x < \infty) \\ u(+\infty,t) = 0 & (t > 0) \\ u(x,0) = 0 & (t > 0) \end{cases} \tag{4}$$

Make all kinds of t Laplace (the Laplace) integral transformation in Equations (4), let $\bar{u} = \int_0^{+\infty} u e^{-st} dt$ .the first equation of Equation (4) same square e^{-st} and integral at two ends:

$$\int_0^{+\infty} \frac{\partial u}{\partial t} e^{-st} dt = \int_0^{+\infty} a\frac{\partial^2 u}{\partial x^2} e^{-st} dt \tag{5}$$

By the integration by parts of the definite integral shows that the left of (5):

$$\int_0^{+\infty} \frac{\partial u}{\partial t} e^{-st} dt = u e^{-st}\Big|_0^{+\infty} + s\int_0^{+\infty} u e^{-st} dt = s\bar{u} \qquad (u(x,0) = 0)$$

The right of （5）: $a\int_0^{+\infty} \dfrac{\partial^2 u}{\partial x^2} e^{-st} dt = a\dfrac{\partial}{\partial x^2}\int_0^{+\infty} u e^{-st} dt = a\dfrac{\partial \bar{u}}{\partial x^2}$

So: $s\bar{u} = a\dfrac{\partial \bar{u}}{\partial x^2} \Rightarrow \qquad \dfrac{d^2\bar{u}}{dx^2} - \dfrac{s}{a}\bar{u} = 0$ (6)

The second equation of Equation (4) same square e^{-st} and integral at two ends:

$$\int_0^{+\infty} u(0,t) e^{-st} dt = \int_0^{+\infty} v_0 t e^{-st} dt = \frac{-v_0}{s} t e^{-st}\Big|_0^{+\infty} \quad + \frac{v_0}{s}\int_0^{+\infty} e^{-st} dt = \frac{v_0}{s^2} \tag{7}$$

Thus by the above transformation can transform the model equations (4) into the following equations:

$$\begin{cases} \dfrac{d^2\bar{u}}{dx^2} - \dfrac{s}{a}\bar{u} = 0 \\ \bar{u}(0,s) = \dfrac{v_0}{s^2} \end{cases} \tag{8}$$

To Second order constant coefficient differential equation of the odd $\dfrac{d^2\bar{u}}{dx^2} - \dfrac{s}{a}\bar{u} = 0$, the general solution is: $\overline{u_0} = \alpha_1 e^{\sqrt{\frac{s}{a}}x} + \alpha_2 e^{-\sqrt{\frac{s}{a}}x}$.By the boundary conditions $\bar{u}(+\infty, s) = 0$, we can see $\alpha_1 = 0$; by the boundary conditions $\bar{u}(0,s) = \dfrac{v_0}{s^2}$, $\alpha_2 = \dfrac{v_0}{s^2}$ can be obtained. Therefore, we can calculate the linear differential equations of second order non-odd general solution is:

$$\bar{u} = \frac{v_0}{s^2} e^{-\sqrt{\frac{s}{a}}x} \tag{9}$$

Make Laplace (the Laplace) integral transformation in Equation (9):

$$u = L^{-}\left(\frac{v_0}{s^2} e^{-\sqrt{\frac{s}{a}}x}\right) = v_0 t * L^{-}\left(e^{-\sqrt{\frac{s}{a}}x}\right) = v_0 t\left[(1+2\lambda^2)erfc(\lambda) - \frac{2\lambda}{\sqrt{\pi}}e^{-\lambda^2}\right] = v_o t R(\lambda) \tag{10}$$

Where $\lambda = \dfrac{x}{2\sqrt{at}}$; $R(\lambda) = (1+2\lambda^2)erfc(\lambda) - \dfrac{2\lambda}{\sqrt{\pi}}e^{-\lambda^2}$.

The remaining symbols are the same of the front of the formula. Eventually get the drawdown versus time equation for the saturation line:

$$h(x,t) = h_{0,0} - u(x,t) \tag{11}$$

The above equation is the rainfall intensity of infiltration ε, the water level to the decline of v_0 by constant velocity, the saturation line in slope formula. The numerical of R(λ) can be obtained by $R(\lambda) = (1+2\lambda^2)erfc(\lambda) - \dfrac{2\lambda}{\sqrt{\pi}}e^{-\lambda^2}$, the change curve shown in Fig. 2.

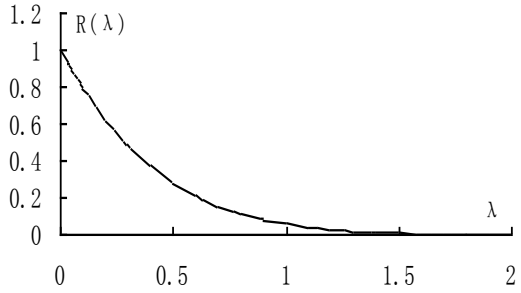


Fig. 2 λ and $R(\lambda)$ relation curve

From the calculation formula can be seen that the $R(\lambda)$calculation is very complicated, and need to integral, which is not conducive to engineering applications. In order to get the facilitate application of the expression, the curve polynomial fitting shown in Fig. 2, polynomial fitting the proposed formula is as follows:

$$R(\lambda) = \begin{cases} 0.1106\lambda^4 - 0.75\lambda^3 + 1.9175\lambda^2 - 2.2203\lambda + 1 & (0 \le \lambda < 2) \\ 0 & (\lambda > 2) \end{cases} \tag{12}$$

The Simplified formula of the saturation line calculated can be get when the water level draw down, and its expression is:

$$h_{x,t}=\begin{cases} h_{0,0}-v_0 t(0.1106\lambda^4-0.75\lambda^3+1.9175\lambda^2-2.2203\lambda+1) & (0\le\lambda<2) \\ h_{0,0} & (\lambda>2) \end{cases} \tag{13}$$

Simplified Formula to Verify the Analysis

In order to verify the applicability of the simplify formula, in this section we use the 3D-Mod flow to verify the foregoing formula. Visual-Mod flow was developed by the Canada Waterloo hydrogeology company based on the Mod flow, which uses the Modern visualization techniques, and is currently the world's most accepted and unanimously accepted by national counterparts visualization software system. The system was public offering in the international research and rural development in many areas of construction environmental protection, urban and rural development planning for the first time in August 1994. Water use was in a wide range of applications [3-5], late through continuous improvement, which has become the most popular groundwater flow simulation program.

In order to facilitate the verification, use Visual-Mod flow analysis software to verify the analysis compared the effects of different permeability coefficients, the water level drops speed and water supply, and other factors, as follows.

Effect of Permeability Coefficient. Bank slope rock mass is homogeneous vertical slope, with the same permeability coefficient in each direction, the value of 0.25m/d, the water level drawdown height of 30m, the down speed of 1m/d, the specific yield of 0.03, the porosity of 0.25, the average aquifer thickness of 40m in the lift before and after , the scope of the model of 400m×60m×60m, the length is 400m by Procedures and simplify the formula of the calculation to predict the change of the groundwater, the predicted time for 30 days, according to 0.05m/d, 0.1m/d, 0.5m/d, 1.0m/d, 2.0m/d to calculate the permeability coefficient, Contrast curve of water level change calculations shown in Fig. 3.

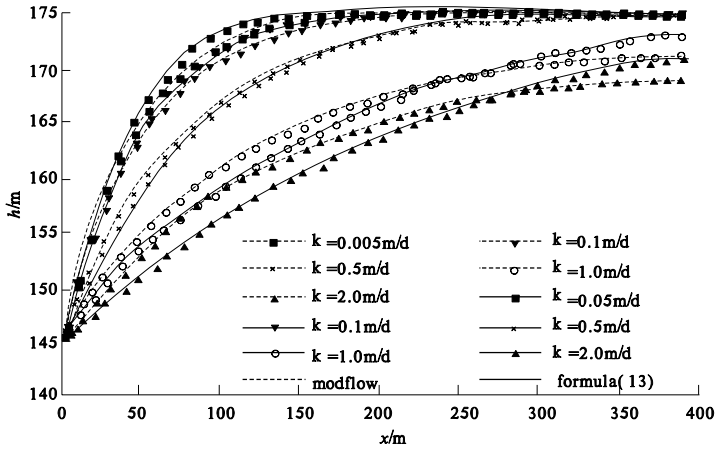


Fig. 3 The computational solution of V-M program and simplification formula

The comparative analysis shows that when the decline of the reservoir water level constant velocity, if the permeability coefficient is smaller, both of the prediction of the saturation line will have smaller difference; on the contrary, if the permeability coefficient is greater, now, the prediction of the saturation line will have small difference in the front of the slope, but they have more obvious differences in the rear of the slope. The simplified formula of the calculation is high, however, both of which fit better totally.

Effect of Drawdown Speed. Parameter settings same with the former, the water level drawdown speed according to 0.25m/d,0.5m/d,1.0m/d,5.0m/d calculated, the results shown in Fig. 4.the calculated results show that the two higher goodness of fit ,the deviation is large only in the rear of the slope.

The Effect of the Water Supply Rate. Parameter setting is same with the former, the specific yield according to 0.005, 0.008, 0.03,0.12 calculated, the results shown in Fig. 5.

The calculated results show that the calculation is Coincide. Increases with the specific yield forecast results with the simplified formula results deviation lower.

Comprehensive known, simplified formula meet the computing requirements of accuracy, and the application of computing convenience.

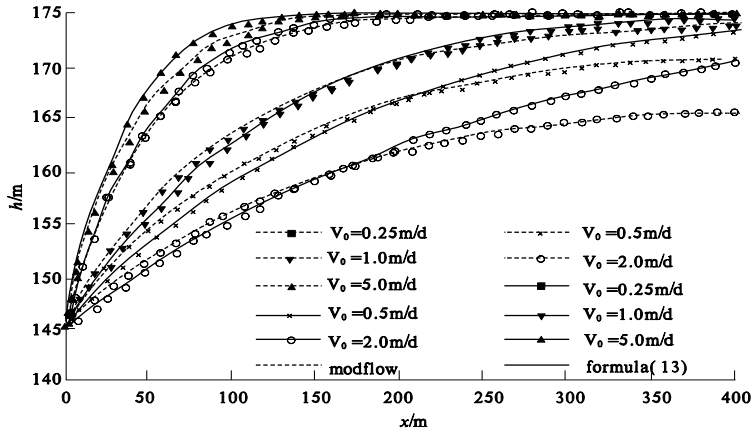


Fig. 4 The computational solution of V-M program and simplification formula

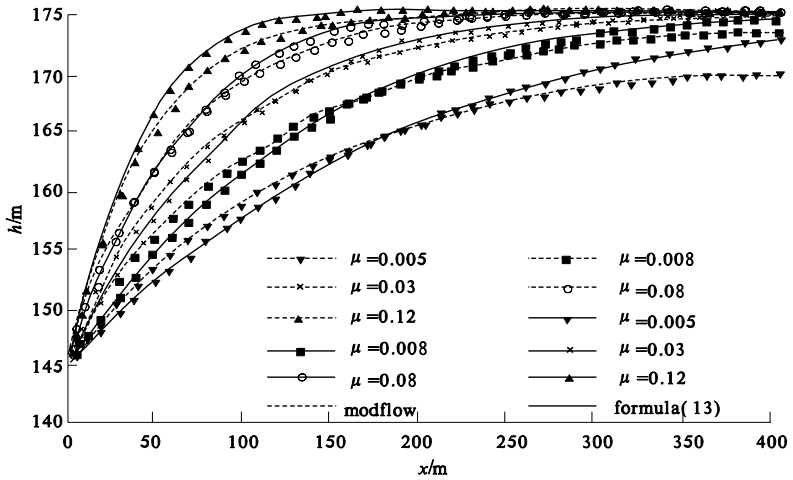


Fig. 5 The computational solution of V-M program and simplification formula

Infiltration Line of Impact Factors

From the above analysis, let the height of decline in water level is $\Delta h=v_0 t$, $t=\Delta h / v_0$, then:

$$\lambda = \frac{x}{2\sqrt{at}} = \frac{x}{2}\sqrt{\frac{\mu}{kh_m t}} = \frac{x}{2}\sqrt{\frac{\mu \Delta h}{kh_m v_0}} \tag{14}$$

From Fig. 2, with λ the increasing, the value of $R(\lambda)$ is smaller, $R(\lambda)$ is a decreasing function. That is, the value of λ is the smaller, the faster the free surface of the slope decreased. On the contrary, the value of λ is the greater the free surface of the slope decreased more slowly. When $\lambda=0$, $R(\lambda)=1$, free surface of water synchronized with the reservoir water level in the body lift;when $\lambda=\infty$, $R(\lambda)=0$, freedom in the slope of the water without the effects of reservoir water level fluctuation. When $\lambda \geq 2$, $R(\lambda)$ is very close to 0, then the impact of water level changes on groundwater seepage line can be ignored. so, we Can as the water level fluctuation of groundwater seepage line impact on the level range, namely:

$$x = 4\sqrt{\frac{kh_m v_0}{\mu \Delta h}}.$$

Determine the Specific Yield and Aquifer Thickness

Calculation of the previous analysis, the saturation line slope coefficient of permeability, specific yield, the average thickness of the aquifer, the water level speed and water level height is closely related. In the calculation of slope saturation line, these factors determined is every important.

The Determination of Specific Yield. The specific yield is a very important hydrogeological parameters, its size should be determined by actual tests. We usually define a unit of depth for falling water able, extending from the groundwater level to the unit level of the surface area of geotechnical cylinder, the volume of water released by gravity. When there is no experimental data in practical work, we should learn from empirical formula. Shensi Ji (1960) based on sand and gravel soil samples (the smallest particle size, d=0.25cm, minimum permeability coefficient=1.87×10-2cm/s), test results analysis to come to the water supply simple empirical formula is $\mu=0.117(k)^{1/7}$, where: permeability coefficient is k and (m/d)), this type is only suitable for coarse grained soil, not for particles smaller than fine sand soil.

The water supply behalf the rock mass' Excretion of water capacity, the size of which is not only closely related with the permeability coefficient, but also closely related with the density of the soil, that is closely related with the porosity. Literature [2] according to the experimental data of domestic and foreign sand and gravel and clay, analysis and obtained the empirical formula of specific yield:

$$\mu = 1.137n(0.0001175)^{0.607^{(6+\lg k)}}$$

Where: n--Porosity; k-- Coefficient of permeability (cm/s).

When we didn't have the experimental data, this Formula can be used to determine the size of the specific yield.

The Determination of the Thickness of the Aquifer. From the previous analysis, In order to solve the basic differential equations of unsteady seepage, flow with water table Usually we instead h_m of H, (h_m is the average of the beginning and the last paragraph of the thickness of flow with water table), This assumption applies to the station of lower lifting height, but it will cause Large errors when comes to higher lifting height. To this end the following methods can be used to determine the average thickness of the aquifer.

Impervious to Water Level. Under seepage analysis of research results, the phreatic line in the slope can be simplified as a parabolic (Parabolic equation:$y^2= ax + b$). This assumption applied to the analysis of the dam. In order to obtain the average thickness of the phreatic line, Parabola model can be used to determine the phreatic aquifer flow average thickness. Fig.6-a is a reservoir water level down and up two cases aquifer thickness calculation diagram, A case study of water goes down, we assume the initial thickness of aquifer is h_0,Water level drop height is h, Influence Scope is s,to substitute 0（0,0），$P(s,h)$ into parabolic equation and get decreased phreatic line equation：

$$y^2 = \frac{h^2}{s}x \tag{15}$$

Area of osp ： $\int_0^s \frac{h^2}{s}xdx = \frac{2}{3}sh$.Transforming aquifer into rectangle whose area is s, h_m can be available：

$$h_m = \frac{\frac{2}{3}sh}{s} + (h_0 - h) = h_0 - \frac{1}{3}h \tag{16}$$

Similarly we can derive the average thickness of the aquifer in the reservoir water level rises：

$$h_m = h_0 + \frac{1}{3}h \tag{17}$$

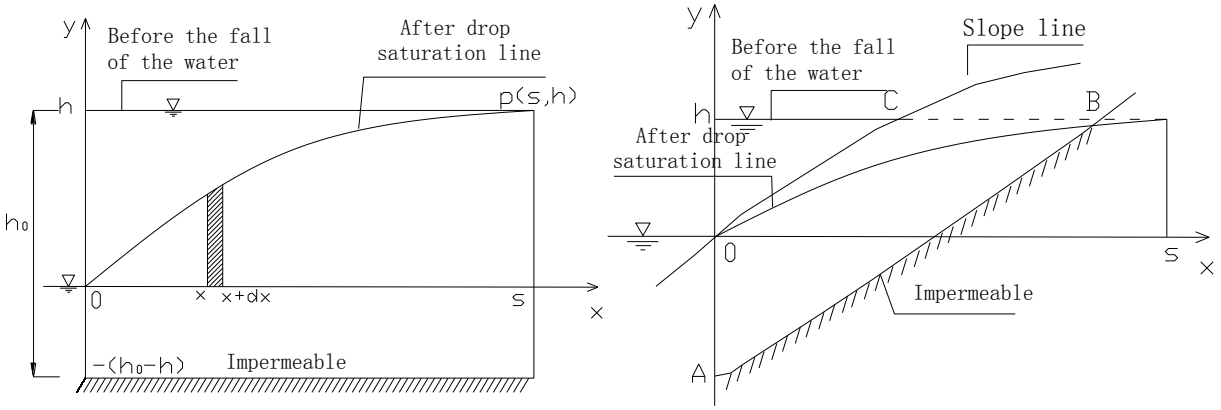
Where: h-- height of water level

From the resulting formula can be shown that the average thickness of the aquifer only have related to the water level fluctuation and the height of the initial thickness of the aquifer.

Impermeable for Irregular Surfaces. In practical engineering, the shape of impermeable is often Irregular surface.（Fig. 6-b）. The average thickness of the aquifer generally can use the following formula to approximately calculate：

$$h_m = \frac{S_{oABC}}{OS} \tag{18}$$

Generally, Geological profile is often drawn with AutoCAD, To determine the area of OABC is very easy, Therefore, to calculate the average thickness of aquifer will become very simple.



a、Impermeable torwater level　　b、Impermeable for irregular surfaces

Fig. 6　Calculation sketch of aquifer thickness

Conclusions

According to the basic differential equations of unsteady seepage movement and boundary conditions, to derive the reservoir water level declining in constant speed conditions for downhill line of the body infiltration formula, and its polynomial fits simplified formula to facilitate the practical application.

Through Visual-Mod flow in forecasting the results compared with the predictions of the simplified formula analysis, the simplified formula taking many factors case into account , the finite element simulation results have a certain bias, but in most cases it is very small deviation, indicating that the application of the simplified formula is feasible. But taking the effect of the combined effects of various factors into account, the application should require its appropriate amendments.

References

[1] W. Gu, Principle and Application of Seepage Calculation, China Building Materials Industry Press, Beijing, 2000.

[2] C. Mao, Analysis and Control of Seepage Flow Calculation (Second Edition), China Water Conservancy and Hydropower Press, Beijing, 2003.

[3] Y. Wei, M. Xu, J. Feng, Yangtze River Three Gorges engineering simulation of groundwater seepage field analysis of reservoir bank slope, Acta Geologica Sichuan, 23 (2003) 18-22.

[4] P. Li, W. Lu, Application of Visual MODFLOW in groundwater numerical simulation, Engineering Survey, 3 (2006) 24-27.

© (2012) Trans Tech Publications, Switzerland
doi:10.4028/www.scientific.net/AMM.238.378

Research on the Relationship between Effective Porosity and Ratio of Cement to Stone of Non-sand Concrete Well Pipe

Chaojun Yan

Anhui Water Conservancy Technical College, Hefei 230000, China

Chaojuny@qq.com

Key words: non-sand; concrete well pipe; effective porosity; ratio of cement to stone; study.

Abstract. Non-sand concrete well pipe is widely used in dewatering construction of deep foundation pit, the running effect of water-filtration well pipe have a close relationship with casting-pipe porosity, material ratio and casting-pipe time. With a long term test, the indicators' critical values of casting-pipe based on maximum porosity is proposed, which is under a condition of ensuring the adequate strength of non-sand pipe and different proportion of limestone cement and stones. The critical values have a great significance to improving non-sand pipe effective porosity, reducing permeation resistance and increasing infiltration capacity, and also can provide a reference for the design and constriction of similar projects.

Introduction

Non-sand concrete well pipe is widely used as deep well dewatering or decompression treatment materials for its low cost, long life and easily being closed after completion of processing. Usually, non-sand concrete well pipe is used for construction dewatering, relief wells or observation wells and so on. In the hydraulic engineering field, it is proved that deep well dewatering method is especially suitable for the projects with high permeability coefficient and deep dewatering, which has been used in Conservancy Engineering Construction in recent years, and is a practicable method for dewatering construction, in other fields it is also used more and more widely. The effective porosity and strength of non-sand concrete pipe are related to infiltration capacity (effects of dewatering or decompression) and working life, how to decide the parameter of casting a non-sand concrete pipe to guide the construction is a problem the engineers and technicians have been explored for a long time. Therefore, under the premise of ensuring the safety of seepage foundation to study the relationship between effective porosity and infiltration capacity or dewatering effect, the parameter of casting a non-sand concrete pipe is significant.

With years of prefabricated pipe-well construction experience and reference to Specification of Pumping test in Borehole for Hydropower and Water conservancy Engineering (SL320-2005), the author conducted a monographic study on non-sand pipe effective porosity ~ ratio of cement and stone ~ pipe casting time, and through arrangement analysis and practical test, under the condition of ensuring the safety of projects the critical value of casting non-sand concrete pipe based on maximum porosity is proposed. Through a series of engineering test of practice, all of the parameters achieved intended purpose.

Experimental Research

Effective porosity and strength values of non-sand concrete are a contradiction. The greater the effective porosity, the smaller the resistance of penetration through pipe wall, precipitation or decompression the better; while the greater the effective porosity is, lower the strength of the pipe, the more easily damaged during installation or in the case of compressive stress. Meanwhile, the porosity is too large to be incompatible with the steady seepage of foundation, would be impact on stability of the foundation. Therefore, according to the pending geological conditions of the foundation, selecting the porosity and the strength index of non-sand concrete pipe must be seriously study on in the construction program.

Into the Pipe Process and Control Factors. The main raw materials of prefabricated non-sand concrete pipe are cement, gravel and water. Cement often chooses ordinary Portland cement PO42.5, stones with limestone as raw materials after mechanical crushing screening diameter of 12 ~ 15mm artificial gravel. The preparation process of filtration well pipe: Cement and stones uniformly mixed, then add water and stir modulation into a semi-solid, then pour the mixing material into the pipe mold, finally, put on the pipe shaking table vibration into the pipe.

Determination of Effective Porosity. The porosity of skeleton filter in hydro geological exploration is through the percentage of the hole area accounted for the pipe side area manufactured in the production process, while the porosity of non-sand concrete pipe can not be determined in the manufacturing process. It's influenced by the non-homogeneous material and processes, the above prepared process of the non-sand concrete pipe inner and outer surfaces are irregular and pore a lot. The inside and outside of some pores are connected. The first one called as the effective porosity, while the other called as the blind gap, blind gap permeable meaningless. Since the appearance of non-sand concrete pipe is irregular, its effective porosity can not be directly measured. In engineering applications, the effective porosity is determined by two types of pipe penetration of Comparative Law. The specific method is: under the same boundary conditions, taking two types of pipe with the same diameter and long into penetration test. One pipe is a steel-framed filters of known porosity, the other pipe is for be measured non-sand concrete pipe. Inject the same volume of water and raise the same high degree of water head to the two pipes, and calculate the time when two pipe infiltrations finished respectively. Adjust the pores of the steel skeleton filter, so that the time of seepage equal to the be measured one finish leak the water, at this time the porosity of steel skeleton filter is equivalent to effective porosity of the be measured non-sand concrete pipe.

Test Data. According to"4.1.2 The porosity of pumping hole filter skeleton is not less than 30%; The porosity of observation hole is not less than 15%."technical provisions require of<Code of pumping test in borehole for water resources and hydropower engineering>(SL320—2005),and considering in the condition of ensuring the safety of foundation seepage, conducted a total of Seven groups tests with different ratio of lime and gravel in order to obtain the maximum porosity of tube,at the same time,in order to meet a certain tube strength, Conducted a total of 21 groups tests with different tube time. The results summarized in Table 1.

Table 1 Different ratio of lime and gravel~porosity~compressive strength

Ratio of lime and gravel	Porosity (%)	Vibration time (s)	Microvessel density (kN/m^3)	Compressive strength (kPa)	Well safety depth (m)
1:3.5	5	50	16.5	≥1150	≤70
	10	45	16.3	≥1050	≤65
	15	40	16.1	≥1000	≤60
1:4.0	10	50	16.3	≥1050	≤65
	15	45	16.1	≥1000	≤60
	20	40	15.9	≥900	≤55
1:4.5	15	50	16.1	≥1000	≤60
	20	45	15.9	≥900	≤55
	25	40	15.7	≥800	≤50
1:5.0	20	50	15.9	≥900	≤55
	25	45	15.7	≥800	≤50
	30	40	15.5	≥700	≤45
1:5.5	25	50	15.7	≥800	≤50
	30	45	15.5	≥700	≤45
	35	40	15.3	≥650	≤40
1:6.0	30	50	15.5	≥700	≤45
	35	45	15.3	≥650	≤40
	40	40	15.1	≥550	≤35
1:6.5	35	50	15.3	≥650	≤40
	40	45	15.1	≥550	≤35
	45	40	14.9	≥450	≤30

Test Results. Table 1 description:

(1) For the same group of ratio of lime and gravel,the longer vibration time of tube, The greater tube density, the larger compressive strength, the smaller porosity. On the contrary, the shorter vibration time of tube, The smaller tube density, the smaller compressive strength, the greater porosity.

(2) For the different ratio of lime and gravel,the same vibration time of tube, the larger ratio of lime and gravel, the larger porosity, the smaller compressive strength, the smaller porosity. On the contrary, the smaller ratio of lime and gravel，the smaller porosity，the larger compressive strength, the larger porosity.

(3) At the same ratio of lime and gravel, the longer vibration time of tube, the higher tube quality, the larger compressive strength.

The above test is based on the largest porosity, and take into account on the basis of the compressive strength and quality of the well pipe. Tests found that, in the condition of meeting the stability of foundation seepage, in order to obtain maximum porosity and tube quality, in the condition of certain ratio of lime and gravel, the vibration time of tube is not less than 40s. So this paper proposed: The porosity, tube density, compressive strength and no sand tube into the well safety depth in the 40s vibration time of tube as the critical test data, in Table 2.

Table 2 Non-sand pipe porosity ~ critical value of ratio of lime and gravel

porosity	ratio of lime and gravel	vibration time	tube density	compressive strength	Well safety depth
(%)		(S)	($kN/m^{3)}$	(kPa)	(m)
15	1:3.5	40	16.1	≥1000	≤60
20	1:4.0	40	15.9	≥900	≤55
25	1:4.5	40	15.7	≥800	≤50
30	1:5.0	40	15.5	≥700	≤45
35	1:5.5	40	15.3	≥650	≤40
40	1:6.0	40	15.1	≥550	≤35
45	1:6.5	40	14.9	≥450	≤30

Therefore, according to the construction site required depth, select on the table closest to the depth of the value of “Well safety depth”, from the line, investigation to take no sand tube optimal porosity, ratio of lime and gravel, vibration time,as tube technical parameters.

Application Examples

Shanxi zhuang check gate is one of the pivotal projects of continued hydraulic structures in Huaihong river. It is located in Dawei, Wuhe conty where the Wuhe to Guzhen highway meets the Xinhui River. There are seven holes in the check gate which designed with a 1150m3/s flood discharge capacity. The designed elevation of check gate is 10.87m and riverbed's elevation is about 13.0m before the construction, the elevation of deep foundation pit is about 7.5m and the designed center dewatering water level of foundation pit is around 6.5m (exceed down about 1.0m), and length and width of the designed deep foundation pit excavation is about 96m and 32m。According to the hydrogeological conditions, construction of foundation should adopt deep pipe dewatering and the depth is no more than 30m . For this, the foundation dewatering is not only the key nodes in projects construction period, but also important to the success of foundation construction. According to table 2, we adopt parameters that the proportion of limestone cement and stones is 1:6.5 and vibration time is 40 seconds for manufacturers to produce the non-sand pipe. It is indicated in construction that the non-sand concrete pipe produced according to the adopted parameters with a large effective porosity, its strength meets the requirements and there is no damage of foundation, which successfully solved the technical problem in construction.

Soon after, this technology achievement is effectively used in the deep pipe dewatering construction which is the early project of Zhaowang river check gate construction, one of the Wo river management projects, and the deep pipe dewatering construction in Yingtaizi pumping station reconstruction project pre-works, Huainan City, it all achieved the desired results.

Conclusions

The casting-pipe strength and effective porosity of non-sand concrete pipe have a close relationship with material ratio and casting-pipe time. It is proved in tests and engineering applications that the parameters in table 2 can not only meet casting-pipe strength but also achieve the best effect of dewatering. In the future, the author will further her research. In the condition of non-sand pipe's strength is strong enough, she plan to raise the cement grade to reduce the proportion or improve artificial gravel psephicity and add cement enhancer and so on to raise the non-sand pipe's effective porosity, and reduce blind porosity to improve the overall quality of water-filtration pipe.

References

[1] W. Shen, The application of well pipe dewatering in foundation pit construction, Science & Technology Economy Market, 3 (2011) 34-35.

[2] Y. Xu, The application of non-sand pipe well dewatering technology in the Shanghai ShiBoZhou Project, Jiangsu Construction, 4 (2009) 78-80.

[3] F. Xu, D. Xiao, Research on mix proportion of no-fines and porous concrete, Journal of Water Resources and Architectural Engineering, 4 (2005) 24-26.

[4] J. Chang, Specification of Pumping Test in Borehole for Hydropower and Water Conservancy Engineering, China Water Power Press, Beijing, 2005.

[5] B. Wu, Determine of non-sand pipe effective porosity, Geotechnical Investigation & Surveying, 1 (2010) 852-853.

© (2012) Trans Tech Publications, Switzerland
doi:10.4028/www.scientific.net/AMM.238.382

Study on Influencing Factors of the Elderly Population Crossing Speed

Chun'e Yin[1,2,a] and Xiaona Song[2, b]

[1] Chang'an University, Xi'an 710064, China

[2] North China University of Water Resources and Electric Power, Zhengzhou 450011, China

[a]yce@ncwu.edu.cn, [b]songxiaona@ncwu.edu.cn

Keywards: elderly population; crossing speed; influence factors; investigation and analysis.

Abstract. With China's entering aging society, the traffic problem of the elderly population has become the focus of public attention. Taking the elderly population of Zhengzhou as the study object, the speeds of the elderly population crossing the street was investigated. Based on the study, the differences in age and sex, traffic environment and signal control affect the speed of the elderly population crossing the street.

Introduction

According to the calculation method of the United Nations about the elderly population coefficients, aged 60 or older accounted for the total number of proportion reaches 10% called the "old" country. The data of 2007 of China shows that elderly population had increased to 153,000,000, accounting for11.6% of the total population which expected that in 2020 will reach 240,000,000 people, accounting for 17.17% of the total population, so China aging is very obvious. The aging trend, on one hand, marks the development and progress of social economy and medical conditions of our country, on the other hand it brings about pressure. Traffic is one of the important problems caused by it. Especially to old people walking across the street is the focus of our concern.

This paper mainly in elderly population in Zhengzhou city as the research object, investigated and analyzed the characteristics of the elderly crossing speed to provide important basis for the study of elderly pedestrian facility design and the elderly pedestrian safety and improving the elderly pedestrian environment and traffic facilities.

Subjective Factors Influencing the Elderly Crossing Speed

The Influence of Sex. Difference sex of the elderly has the different crossing speed. Table 1 shows that the elderly male's crossing speed, maximum, minimum, average and median is higher than elderly women's. This is mainly determined by its physical and physiological factors.

Table 1 Elderly population's crossing speed of different sex

Sex	Crossing speed (m/s)					Sample Capacity (a)
	average	standard deviation	median	minimum	maximum	
Male	1.15	0.26	1.12	0.89	1.50	770
Women	1.13	0.28	1.07	0.84	1.44	720

The Influence of Age. Table 2 shows the crossing speed characteristics of different age of elderly population. It can be seen that along with older age, its crossing speed significantly is reduced because along with the growth of the age, the elderly in flexibility, strength, reaction ability drops.

Table 2 The different age crossing speed

Age	Crossing speed (m/s)					Sample Capacity (a)
	average	standard deviation	median	minimum	maximum	
60~65	1.23	0.18	1.12	0.63	1.60	285
65~70	1.14	0.21	1.19	0.89	1.48	277
>70	1.00	0.24	1.00	0.69	1.30	300

Objective Factors Influencing the Elderly Crossing Speed

The Influence of Intersection Control Mode. From Table 3, we can see that the elderly population's crossing speed of signalized intersection is higher than no signal . This is mainly due to in no signal control intersection, the elderly feel security threat from motor vehicle, so the delay is longer and the speed is slower. while in the signal control condition, because the vehicle and the elderly has basically been separated, the elderly feel from the motor vehicle security threats very small, their speed are higher.

Table 3 Elderly crossing speed of no signal and signal intersection control

Control mode	Crossing speed (m/s)					Sample Capacity (a)
	average	standard deviation	median	minimum	maximum	
Signal	1.13	0.10	1.22	0.79	1.64	115
No signal	1.02	0.14	1.07	0.84	1.57	113

The Influence of Pavement Length. Table 4 shows that the pedestrian crossing is longer and the elderly speed is higher . This because that in a pedestrian crossing, if older people stay on the sidewalk in a long time, this can cause them feel insecurity, so the elderly will as soon as possible to walk faster to cross the safe area. But in short pedestrian crossing, it will not take too much time for the elderly to reach the opposite safety zone, so they are always showing an unhurried condition and walking slowly.

Table 4 Elderly crossing speed of different length of the pedestrian crossing

The length of pedestrian crossing (m)	7-10	10-15	15-20	20-25	25-30	30-35	35-40
Average speed (m/s)	0.88	0.91	0.96	0.99	1.04	1.08	1.12
15%speed (m/s)	0.78	0.79	0.80	0.83	0.86	0.90	0.92
80%speed (m/s)	1.00	1.03	1.06	1.13	1.17	1.21	1.21

The Influence of the Number of Pedestrians. As shown in Table 5, single elderly people crossing crosswalk average speed up to 1.18 m/s, 2 people together is the second of 1.15 m/s, more than 3 is 1.12 m/s. This phenomenon is mainly caused by psychological factors. The more people to cross pedestrian, the more security and more relax they feel, so their speed is a little lower.

Table 5 Elderly population's crossing speed of different numbers of pedestrians

People' number	Crossing speed (m/s)					Sample Capacity (a)
	average	standard deviation	median	minimum	maximum	
1	1.18	0.19	1.19	0.63	1.50	185
2	1.15	0.11	1.12	0.89	1.44	185
>=3	1.12	0.09	1.10	0.69	1.51	303

The influence of different time. The elderly in different time periods to cross the street, the physical and psychological have a different state, thereby influencing the elderly crossing speed. As you can see from Fig. 1 that in the morning peak period, older crossing average speed of is 0.98m/s, mainly due to the large flow of people and vehicle. In the morning peak time, traffic is relatively large, the older line of sight and the psychological pressure has certain effect, so the crossing speed slow.

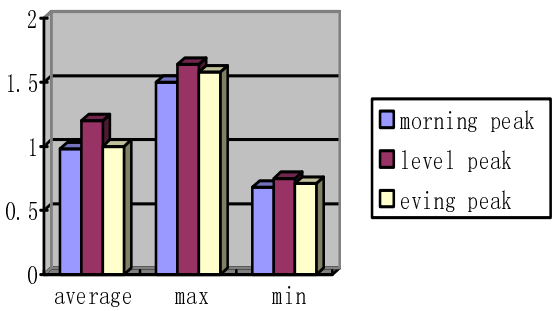


Fig. 1 The influence of different time

The Influence of Different Crosswalk Length. Fig. 2 shows that the longer is the crossing, the faster is the walk of old people. This is because in a crosswalk, older people stay on the sidewalk in a long time, which caused them to a sense of insecurity, the elderly will as soon as possible through the safe area, walk faster; in short a crosswalk, not take too much time, the elderly can reach the opposite safety zone, so the old man always showed an unhurried condition, walking slowly.

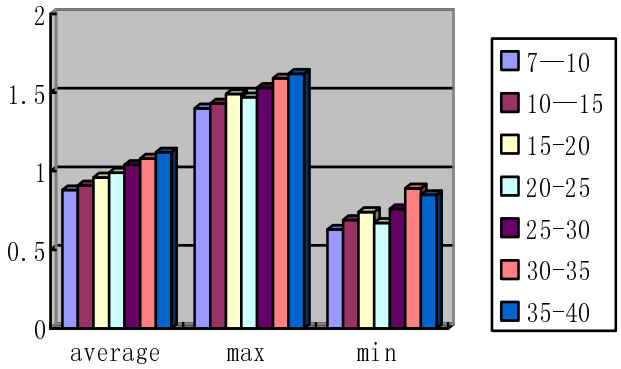


Fig. 2 The influence of different crosswalk length

Conclusions

Based on the survey of old person's crossing speed, we can learn that different sex and different age of older people's crossing speed is different which caused mainly by their physiological factors ; but in the objective factors, the crossing speed characteristics of older population is mainly related to their psychological factors. Through the study of crossing speed characteristics of the elderly population in different situations, we want to provide important reference to improve the elderly pedestrian crossing facilities and crossing safety.

Reference

[1] S. S. Bailey, Issues of Elderly Pedestrians, Transportation Research Record, 1375 (1992) 68-73.
[2] Z. Zhang, B. Mao, M. Liu, Beijing elderly people 's travel behavior analysis, Journal of Transportation Systems Engineering and Information, 6 (2007) 11-20.
[3] G. Liu, K. Li, Y. Ni, Intersection pedestrian's psychology and traffic behavior analysis, Traffic Science and Technology and Economy, 5 (2008) 58-61.

© (2012) Trans Tech Publications, Switzerland
doi:10.4028/www.scientific.net/AMM.238.385

Determination Optimum Pipe Diameter Method of Tree Path Heating Pipe Network

Meijie Wang[1,a], Weimin Di[2,b] and Yanke Wang[1,c]

[1]School of Environment & Municipal Engineering, North China University of Water Resources & Electric Power, Zhengzhou 450008, China

[2]Zhengzhou University, Zhengzhou 450001, China

[a]wmjdwm@126.com, [b]diweimin@126.com, [c]wangyanke.1@163.com

Keywords: tree path pipe network; optimum pipe diameter; objective function; hydraulic calculation; life cycle cost.

Abstract. Economy and hydraulic stability of piping network which has a fixed structure depend on the matching ability of pipe diameter. In order to improving the matching ability and maneuverability of selecting pipe diameter, a new design method is presented. A real case study shows that the piping network which is designed with the new method has excellent technical quality and the least life cycle costs, and can achieve saving more than 7 percent against the original design.

Introduction

Piping network is an important part of district heating system and has a significant share on the total costs (investment cost, operational cost and so on). Therefore optimization of piping network is vital important for the economical viability of the whole system. So far studies on piping network are mostly focused on two aspects. One is focused on the synthesis optimal design which includes structure and parameters optimization [1-4]. The other is focused on the parameters optimization [5-6]. In practice the structure and parameters optimization at the same time is difficult to achieve because their coupling. So the structure and parameters optimal design is essentially a step-wise, namely determine the optimal parameters of any a given feasible structure of tree path piping network, then calculate the total costs of the feasible piping network and compare all kinds of feasible piping networks, the one which has the least total costs is the optimal layout structure of piping network. Therefore pipe diameter optimization is the basis and directly affects the optimization design results of heating pipe network. Although optimal design of pipe diameter already has some researches [5-6], but must be with the help of modern optimization algorithm and require the designers have high ability of programming. The vast majority of designers are difficult to do this. Moreover, using the methods of recommended specific frictional resistance (RSFR) or economic flow rate to determine the diameters only satisfy the needs of the technology but dissatisfy the needs of the economy. Therefore it is an urgent need to find an economical and practical method for pipe diameter optimization. Based on the above reason, the following design method is proposed.

Mathematical Model

Objective Function Establishment. For a given central heating area, if the piping network can achieve the same economic benefits at less life cycle costs (LCC), then the piping network is better. So the design objective of heating pipe network is to minimize the LCC of distributed piping network, denoted here by Z. The LCC are defined as the sum of investment costs, depreciation and maintenance costs, running costs and heat loss costs of piping network. Due to the heat load calculation has included 5% heat loss, so the heat loss costs have been implied in the construction costs and operation costs. In addition, for a given central heating system, network operation maintenance costs depend mainly on the size and capacity of the heating area, rather than the network's initial investments. For a given central heating area, the heating demands and capacity are limited, so the maintenance costs can be as constant, which has no affect to the minimal LCC.

Therefore the LCC depend on the investment costs and running costs. If the selecting pipe diameters are large, investment costs of the pipelines increase, while operational costs decrease. On the other hand, when the selecting pipe diameters are small, the investment costs decrease, but operational costs increase. So there exists the optimum diameters to make the LCC of piping network are the least. To consider the time value of capital, here adopts terminal value method, namely determine pipe diameters to make the LCC of piping network to be the least when it has the same income. So the objective function is as the following equation [7]:

$$\text{Min } Z = (1+\text{i})^N \bullet \sum_{\text{j=1}}^{\text{n}} f\left(\text{d}_\text{j}\right) \bullet L_\text{j} + \left(\frac{(1+\text{i})^N - 1}{\text{i}} \right) \bullet 2.78 \times 10^{-8} \frac{GH}{\rho \eta_p} \tau \cdot c_e \tag{1}$$

Where Z is the LCC of piping network, 10^4 RMB/a; i is the interest rate; N is the life cycle; n is the number of pipe section; $d_\text{j}$is the pipe diameter of j pipe section, mm; L_j is the pipe length of j pipe section, km; $f(d_\text{j})$ is the unit length cost of j pipe section, 10^4 RMB/km; $G$is the design flow of circulating pump, t/h; H is the total resistance loss of piping network, p_a; ρ is the density of heat water, kg/m^3; $\eta_\text{p}$is the electrical and mechanical efficiency of circulating pump, τ is the annual running hours of circulating pump, h; $C_\text{e}$is the local electricity price, RMB/kW h; 2.78×10^{-8} is the unit conversion constant. For a certain district heating system, the represented numbers of the symbol i, N, ρ, τ, $\eta_{p,,}$ and C_e are the known constant, So $(1+i)^N$and $2.78\times10^{-8}\bullet\left(\left((1+\text{i})^N-1\right)/\text{i}\right)\bullet\left(\tau c_e/\rho\eta_p\right)$ are also constant, denoted here by C_1 and C_2 respectively. Then the equation (1) can be rewritten as:

$$\text{Min Z} = \text{C}_1 \bullet \sum_{\text{j=1}}^{\text{n}} f\left(\text{d}_\text{j}\right) \bullet \text{L}_\text{j} + \text{C}_2 GH \tag{2}$$

Heat supply network is composed of main line and branch lines. So the pipeline investment costs can be denoted with the trunk line investment costs and branch pipeline investment costs. Number the pipe section of the piping network. If pipe sections of the main line are sequentially recorded as1, ... , j, ... , n along the flow direction which starts from the heat source. The total pipe section number of branch line which collect with j pipe section of main line is denoted here by m_j. The total resistance of piping network is equal to the sum of each pipe section of main line. Then equation (2) can be rewritten as:

$$\text{Min Z} = C_1 \sum_{\text{j=1}}^{\text{n}} f(\text{d}_\text{j}) L_\text{j} + \text{C}_1 \sum_{\text{j=1}}^{n\text{-1}} \sum_{\text{k=1}}^{\text{m}_\text{j}} f(\text{d}_\text{k}) L_\text{k} + C_2 G \sum_{\text{j=1}}^{n} H_\text{j} \tag{3}$$

Where H_j is the total resistance loss of the j pipe section of main line.

According to the flow balance and pressure balance, the equation (3) can be rewritten as (derivation process is omitted):

$$\begin{aligned} \text{Min } Z &= \sum_{\text{j=1}}^{n} \left[\text{C}_1 f(\text{d}_\text{j}) L_\text{j} + \text{C}_2 G_\text{j} H_\text{j} \right] + \sum_{\text{j=1}}^{n-1} \left[\text{C}_1 \sum_{\text{k=1}}^{m_\text{j}} f(\text{d}_\text{k}) L_\text{k} + \text{C}_2 \left(G_\text{j} - G_{\text{j+1}} \right) \sum_{\text{j=j+1}}^{n} H_\text{j} \right] \\ &= \left(\text{C}_1 f(\text{d}_1) L_1 + C_2 G_1 H_1 \right) + \sum_{\text{j=1}}^{n-1} \left\{ \left(C_1 f(\text{d}_{\text{j+1}}) L_{\text{j+1}} + C_2 G_{\text{j+1}} H_{\text{j+1}} \right) + \left[C_1 \sum_{\text{k=1}}^{m_\text{j}} f(\text{d}_\text{k}) L_\text{k} + C_2 \left(G_\text{j} - G_{\text{j+1}} \right) \sum_{\text{j=j+1}}^{n} H_\text{j} \right] \right\} \end{aligned} \tag{4}$$

Where G_j and $G_{\text{j+1}}$ is the j and j+1 pipe section flow of main line respectively. In the equation (4), $C_1f(d_1)L_1+C_2G_1H_1$ are the total costs of the first pipe section of main line, and we can easily determine the Standard diameter to make the total costs are the least;$C_1fd_{\text{j+1}}L_{\text{j+1}}+C_2G_{\text{j+1}}H_{\text{j+1}}$ are the total costs of the j+1 pipe section of main line; and $C_1\sum_{\text{k=1}}^{m_\text{j}} f(\text{d}_\text{k}) L_\text{k} + C_2\left(G_\text{j} - G_{\text{j+1}}\right)\sum_{\text{j=j+1}}^{n} H_\text{j}$ is the total costs of branch line which collect with j pipe section of main line. In the conditions of velocity constraint and network structure constraint, we also can easily find the standard diameters to make the sum of the two section costs is the least. So the costs of the whole piping network are the least. Therefore these pipe diameters which can meet the above requirements are the optimal pipe diameters.

Constraint Conditions. The constraint conditions include flow balance constraint, velocity constraint, pipe diameter limit and pressure equilibrium constraint. The flow balance constraint means that the flow into the node is equal to the flow out the node; Velocity constraint means that pipeline of maximum velocity is generally not more than 3.5m/s; Pipe diameter limit means that standard diameter is discrete pipe diameter, and outdoor pipe network engineering available maximum diameter is DN1400, the smallest diameter is DN50; Pressure equilibrium constraint means that in any node branch line pressure drop should be equal to the pressure drop of main line. In the actual engineering design，the pressure drop is not often equal because the discrete pipe diameter. To ensure the user's operation in accordance with the design, we must reduce the unbalance rate, namely selecting pipe diameters to make the branch line pressure drop is less than or equal to and closest to the parallel main line pressure drop.

From the above, making the whole network has the least total cost is converted to making a branch node cost is the least, thus can greatly reduce the calculation.

A Real Case Analysis

This heating supply network lies in Henan province of China. It consists of one heat source and fourteen thermal power substations. The pipeline is two-pipe mode directly buried installation along the road with no compensation, the insulation materials is polyurethane foam, and the protective layer is the polyethylene plastic. The structure of district heating pipe network is shown in Fig. 1.

Basic Data. In this project, there are one heat source and fourteen substations indirect connection, and the flows of substation R1 to R14 are 30.5, 38.2, 64.3, 62.1, 37.2, 38.7, 40.4, 42.3, 69.8, 49.68, 38.85, 26.47, 31.11 and 25.79t/h respectively. The design supply and return temperature of heated water is 120-70^{o}C. The local resistance equivalent length ratios are main pipe of 0.2 and branch pipe of 0.3. Pipeline inner wall equivalent roughness is 0.5mm. The heating period is 100 days in a year. The local average electricity fee is 0.7 RMB/kW h, the life cycle is 20 years, the interest rate is about 10%, and the efficiency of pump is 0.6 and so on.

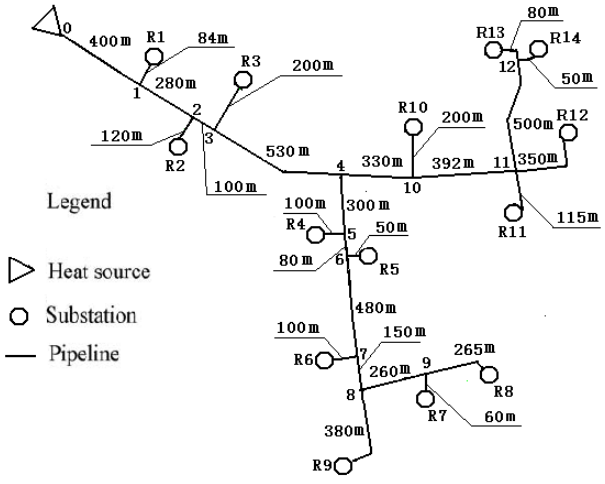


Fig. 1. Sketch map of the district heating pipe network

The heating pipeline total costs per unit length can be obtained by the National Municipal Engineering Investment Estimation Index, the Henan province construction project quantity list of comprehensive unit price, and recent price inquiry of pipeline. The results show in Table 1

Table 1 Investment per unit length of pipeline.

Dia. [mm]	Investments [10^4RMB/km]	Diameter [mm]	Investments [10^4RMB/km]	Diameter [mm]	Investments [10^4RMB/km]	Diameter [mm]	Investments [10^4RMB/km]
80	53.36	200	120.99	400	268.81	700	511.88
100	64.01	250	146.45	450	311.46	800	631.99
125	77.77	300	186.19	500	348.05	900	700.68
150	90.28	350	234.59	600	420.6	1000	840.01

The relationship between investment per unit length and pipe diameter can be obtained according to the method of least squares. The result can be written as:

$$f(d_i) = 0.0003d_i^2 + 0.522d_i + 7.1934 \quad (5)$$

Hydraulic Calculation. Determine the trunk line of piping network, number the heating substation and network node, show in Fig. 1. Calculate the design flow of any pipe section based on the user design heat flow and node flow balance.

In order to improve the hydraulic stability of piping network, the branch pipeline pressure drop must be less than or equal to and closest to the parallel main pipeline pressure drop, so the hydraulic calculation should start from the last node, then counter the flow direction, select optimal diameters to make the costs of each node and the main pipe section which connects to the heat source are the least respectively according to formula (4), then the optimal diameters of piping network are determined, at the same time the least LCC of the piping network is calculated.

Calculation Results. According to the above design method and the hydraulic calculation of Fig. 1, the optimal diameters of piping network are determined, and all kinds of costs of piping network are calculated, the results of hydraulic calculation with Excel soft are shown in Table 2 and Table 3 respectively.

Table 2 Optimal diameters of the piping network

Pipe section	New design	Original design	Pipe section	New design	Original design
	Diameter[mm]			Diameter[mm]	
0-B1	400	350	B7-B8	200	250
B1-R1	70	150	B8-B9	150	200
B1-B2	400	350	B9-R7	100	200
B2-R2	80	150	B9-R8	125	150
B2-B3	350	350	B8-R9	150	200
B3-R3	100	200	B4-B10	200	300
B3-B4	350	350	B10-R10	125	200
B4-B5	300	300	B10-B11	200	250
B5-R4	100	150	B11-R11	100	150
B5-B6	250	250	B11-R12	125	150
B6-R5	70	150	B11-B12	150	200
B6-B7	250	250	B12-R13	125	150
B7-R6	100	150	B12-R14	125	150

Note: the original design refers to the design of a henan design institute, in China.

Table 3 Costs Compare of piping network with different design methods [10^4RMB]

Design method	Network investment cost	Operation cost	Total cost
New method	5388.762	1353.791	6742.553
Original method	6111.669	1154.334	7266.003

The Table 2 shows that the pipe diameters which determined with new design method are larger than these determined with original design method in the beginning of the trunk line, and are smaller in the branch pipeline and the end of the trunk line. So the new design method can improve the parallel loop resistance balance rate, reduce the hydraulic disorder. Therefore the new method can improve the hydraulic stability.

The Table 3 shows that design with the new method can reduce piping network initial investment greatly, but the operation cost increase is not very significant. That should be attributed to the high hydraulic balance rate of the new piping network. The table 3 also shows that the LCC of the new piping network can achieve saving about 7.2 percent against the original design.

Conclusions

The above example shows that the new method can improve the matching ability of pipe diameters, hydraulic stability and economy of piping network.

The new methods can get the design results rapidly using Excel soft or modern optimization algorithm, and can reduce the amount of calculation. So the new method has the advantages of simple operation, easily making the majority of engineering designers understand and use.

The new method is a generally applicable method to the tree-shaped piping network with one heat/cold source, and has an important reference value to piping network optimal design of related specialty areas.

Acknowledgment

This work is supported by the Natural Science Research Project of Education Department of Henan Province of China (No.2009B560006).

References

[1] S. Li, M. Su, Optimal thermo-economic synthesis design of heat piping, Journal of Chemical Industry and Engineering, 53 (2002) 842-846.

[2] D. Dobersek, D. Goricanec, Optimization of tree path pipe network with nonlinear optimization method, Applied Thermal Engineering, 29 (2009) 1584–1591.

[3] N. Yildirim, M.Toksoy, G. Gokcen, Piping network design of geothermal district heating systems: Case study for a university campus, Energy, 35 (2010) 3256-3262.

[4] H. I. Tol, S. Svendsen, Improving the dimensioning of piping networks and network layouts in low-energy district heating systems connected to low-energy buildings: A case study in Roskilde, Denmark, Energy, 38 (2012) 276-290.

[5] Y. Kalinci, A. Hepbasli, I. Tavman, Determination of optimum pipe diameter along with energetic and exergetic evaluation of geothermal district heating system modeling and application, Energy and Buildings, 40 (2008) 742–755.

[6] X. Li, D. Lin, H. Shu, Optimal design of district heating and cooling pipe network of seawater-source heat pump, Energy and Buildings, 42 (2010) 100–104.

[7] M. Wang, H. Xiong, Y. Wang, Optimal design method of heating pipe diameter based on life cycle, HV&AC, 41 (2011) 44–47.

[8] X. Fu. Fluid Transmission and Distribution Network, second edit., China Building Industry Press, Beijing, 2006.

© (2012) Trans Tech Publications, Switzerland
doi:10.4028/www.scientific.net/AMM.238.390

Rural Drinking Water Security Evaluation and Simulation Based on MATLAB Digital and Vector Processing Technology

Hongwei Pan [1,2,a], Beidou Xi [2,b], Hongjun Lei [3,c], Zimin Wei [4,d], Xiaosong He[2,e] and Yonghai Jiang [2,f]

[1] College of Hydraulic & Architecture, Northeast Agricultural University, Harbin 150030, China

[2] Laboratory of Water Environmental System Engineering, Chinese Research Academy of Environmental Science, Beijing 100012, China

[3] College of Hydraulic, North China University of Water Resources and Electric Power, Zhengzhou 450011, China

[4] Life Science College, Northeast Agricultural University, Harbin, 150030, China

[a]phw103@163.com,[b]xibeidou@263.net, [c]hj_lei2002@163.com, [d]weizm691120@163.com, [e]hexs82@126.com, [f]jyhai203@126.com

Keywords: MATLAB; Fuzzy-AHP; vector; simulation; rural drinking water safety.

Abstract. MATLAB software is widely used in scientific computation and simulation area, and has also been increasingly used in the water science and related fields. In this paper, the FUZZY-AHP toolbox was developed based on MATLAB digital and Image processing technology. As an example the rural drinking water safety assessment was tested by the use of FUZZY-AHP toolbox. This study could also provide some new ideas for rapid assessment in drinking water safety & other related issues and a visualization method for evaluation results exhibition.

Introduction

MATLAB (Matrix Laboratory) software is one of the three best-known mathematical softwares with Mathematic and Maple. It was explored by the American mathworks company devoted to the mathematical analysis and mapping of scientific software. It is not merely widely used in sociology, economics and other general science, such as statistical analysis, forecasting and decision-making, but also widely used in genetics, molecular science, materials science, spectroscopy, aerospace, transportation and electronics. Some better results have been achieved in simulation, system identification and complex biochemical environment analysis. As a mathematical tool, MATLAB software does not require users to write complex programs, and it can be easily used by calling the corresponding functions, making it easy to spread. In addition, MATLAB also has a friendly interface, object-oriented, it is necessary not only allows the operator to prepare, call the function, tool and GUI, and with the demand of users' need, a series of advanced tools boxes was developed, such as the current more advanced optimization toolbox (GA-toolbox, NN-toolbox, PSO-toolbox, etc.) and other professional toolbox, which makes it easier to develop and apply. Meanwhile, MATLAB can provide better visualization capabilities, and the digital technology combined with image processing, which can be used for dynamic simulation and visualization.

Presently, MATLAB software has been widely received in the field of water science, e.g. The evaluation of water resources carrying capacity and sustainability, forecasting of the water resources, the water demands and the groundwater table, the optimal allocation of water, the reservoir operation, the irrigation systems and so on. The current systematic research on water resources is mostly math-based, but little studies have been conducted in the direct visualization. In this study the panel data of safety drinking water in rural areas of Henan Province-based was used to explore the rural drinking water resources system safety evaluation and simulation by MATLAB software.

Mathematical Model and Theory.

There are many methods used for system evaluation. The commonly used methods includes the Delphi method, AHP, fuzzy comprehensive evaluation method, entropy method, set pair analysis, principal component analysis, projection pursuit algorithm and the combination of these methods. The Delphi method and AHP are subjective weights methods, while entropy method, set pair analysis, principal component analysis and projection pursuit algorithm are known as the objective weights methods. As we all know, fuzzy comprehensive evaluation method belongs to a comprehensive weights method which is different to combination weights method. Objective weights method is based on the panel data without human interference, but the drawback is this method depending on the variation of the data itself, while the relative importance of things may be at odds with reality; while subjective weights method depends on the personal experience, and the evaluation results may be different in respect to different person with the lake of uniform standards. The current combination weights method are generally a combination of two objective weights method, however, which can't improve its weaknesses fundamentally. On the one hand, the comprehensive evaluation method has the advantage of enabling one to judge things by subjective comparison; on the other hand, the objective weight could be obtained by the membership function. But this method also has disadvantage condition, which is the determining of the relative importance of things lays on the operator's knowledge and experience. But overall, comprehensive weights method is relatively more scientific and reasonable.

AHP to Determine the Lateral Weight. Scale matrix is named by comparing the relative importance between two things, which is divided into three scales and nine scales. The importance of things is determined by the eigenvector corresponding to the maximum eigenvalue of scale matrix. Usually, the consistency of the scale matrix should be tested. The text method as follows:

A hierarchy structure contains a target layer A, a criterion layer C and a solution layer P, while a complex hierarchy structure may include multiple criterion layers. Consistency test includes the target layer, criterion layer and the overall system consistency check. Supposing the maximum eigenvalues of criterion layer C{i} is $\lambda_{max}\{i\}$, then the consistency index of the criterion C{i} is determined by the following formula.

$$CR\{i\}=CI\{i\}/RI\{i\} \quad (1)$$

Where $CI\{i\}=[\lambda_{max}\{i\}-n]/(n-1)$, $RI\{i\}$ is determined by the size of the matrix scale. If $CR\{i\}$ is less than 0.1, the consistency test of the criteria is not satisfied, and the scale matrix should be adjusted until the consistency test of the criteria is satisfied [1-3].

The test method of overall system consistency index is as follows.

$$CR_s=CI_s/RI_s \quad (2)$$

Where $CI_s=W_c\cdot CI$, $RI_s=W_c\cdot RI_c$, W is the evaluation layer weight, C is on behalf of the target layer.

When the consistency test are all satisfied, the weight of the corresponding layer is determined by the eigenvector (normalized after treatment) corresponds to the maximum eigenvalue. Assuming that the target layer weight vector is W_c, and the criterion layer weight vector is $W\{i\}$, then the solution layer's weight vector W could be obtained by the multiplication of the two layers' weight.

Entropy Method to Determine the Objective Weight. Shannon entropy is used to calculate the objective weight [4]. By entropy method the target layer weight vector $W'\{i\}$ and the criterion layer weight vector W' can be determined.

Combination Weight. The Lagrange least squares method is used to get the best combination of subjective and objective weights. The formula is as follows.

$$w_s=(w_c w_c')^{0.5}/\sum(w_c w_c')^{0.5} \quad (3)$$

Where w_c and w_c' are the objective weight and the subjective weight of the criteria layer respectively. w_s is combination weight of criteria layer. The combination weight of solution layer is calculated by the same way.

Membership Matrix. Membership function reflects the fuzzy properties of thing which means it belongs to both A and B. Membership function is logical representing the significant changes to traditional in understanding of the things property. The commonly used membership functions are trapezoidal, triangular, Gaussian and so on. Membership matrix *R* can be determined by the Membership function.

Comprehensive Weight. Fuzzy Computation of the combination weights *W*s and *R* receives comprehensive weight, which has multiplication, maximum and minimum, and other operations. Multiplication is more commonly used. According to the results of operations, evaluation could be made by the maximum degree of membership. Refs [5, 6] give the improved methods of evaluation.

Framework of Simulation Evaluation on MATLAB

The fuzzy comprehensive evaluation method was used to evaluate the sample data [7]. Fig. 1 shows the analytical hierarchy process (AHP) modules, Fig. 2 shows the fuzzy comprehensive evaluation modules, and Figure 3 shows the vector processing and database module.

There were 12 indicators and the evaluation unit was 17. These modules are all related to high-dimensional data cycle, such as in module 1, the operations of the target layer and criteria layer matrix; in module 2, the multi index, multi cells, multi layer data storage and the iteration of the membership function of multi cells; in module 3, the memory of vector data in sub-unit, These complex data in MATLAB software can be conveniently stored, recalled and operations using cell tissue method., The main function used in module 1 is 'xlsread', which is to read excel data format file, in addition, there are 'for' and 'if' recycling operations aim to test the consistency, and adjust the scale matrix. The core and difficult of the simulation program is module 2, it consists of three sub-modules, the first is the matrix calculation attached to each unit, the second is the entropy's calculation, the third is the operation of combined weights. In the sub-module 1, firstly the indicators properties, that whether it belong to benefit indicators or not was determined, then the membership of all layers were calculated, and operate the cycle of various indicators and the evaluation units. The core of module 3 is the vector map reading as well as the evaluation unit cell's results linking with the vector map, where the cell array method still used. First of all, correspond the order of the evaluation data and shape files (vector maps), after the comprehension evaluation, then, keep the target layer, criteria layer of evaluation unit respectively store in the form of cell array under a different name to shape file database, finally, set corresponding color with different security levels through the 'makesymbolspec' function, while the safety distribution map of rural drinking water of each evaluation cell can be displayed through the 'geoshow' function.

Results and Analysis

Through the modular design, a toolbox was developed to evaluate the Henan rural drinking water safety. The overall condition of rural drinking water safety of Henan Province was showed in Fig. 4. From Fig. 4a, more insecure and unsafe area accounted for two thirds of Henan province, indicating the serious situation of overall drinking water security in rural areas, from the view of the spatial distribution, unsafe drinking water mainly located in the eastern region, it is consistent with the evaluation safety of drinking water survey period. From Fig. 4b, it can be seen that northwest and central areas are showed poor water quality, because the groundwater was the dominants drinking water source in these rural areas, while the native groundwater pollution was more serious, mainly caused by geological processes, and therefore, it was necessary to deepen the depth of groundwater, or to find a reasonable source of water points or take other measures, to obtain relatively better quality water. Fig. 4c represents the status of water amount security, in the figure, the region's water situation is better, because in these areas groundwater resources are more abundant, water amount problem is not so prominent. In Fig. 4d, it can be seen that southeastern and southern regions are showed poor security situation in municipal water supply, which may be related to the level of local economic development; therefore, it's necessary to strengthen the supporting of drinking water facility construction in these areas.

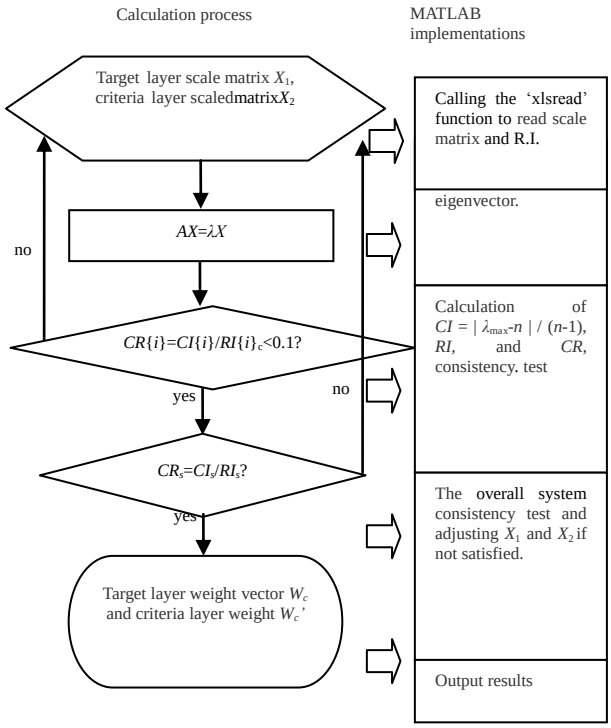


Fig. 1 The AHP modules

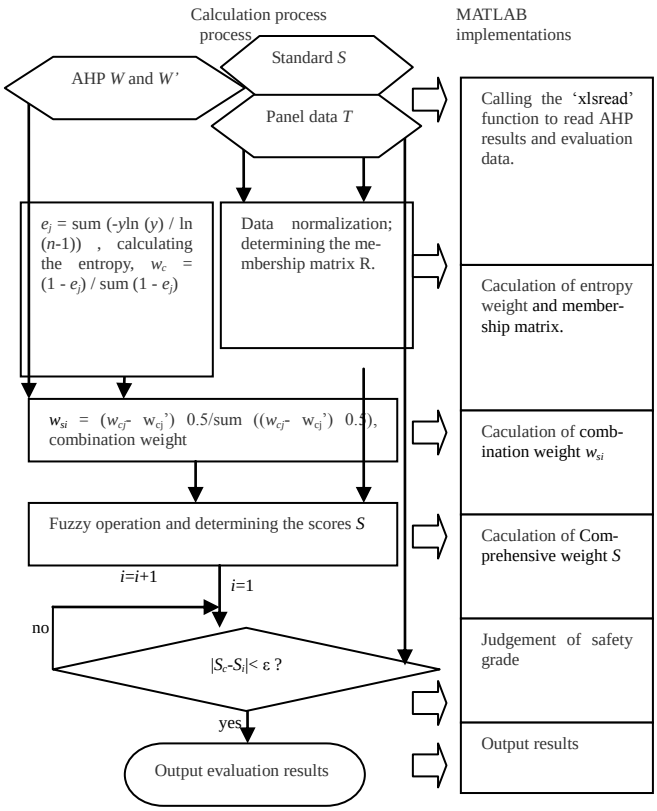


Fig. 2 The fuzzy comprehensive evaluation modules

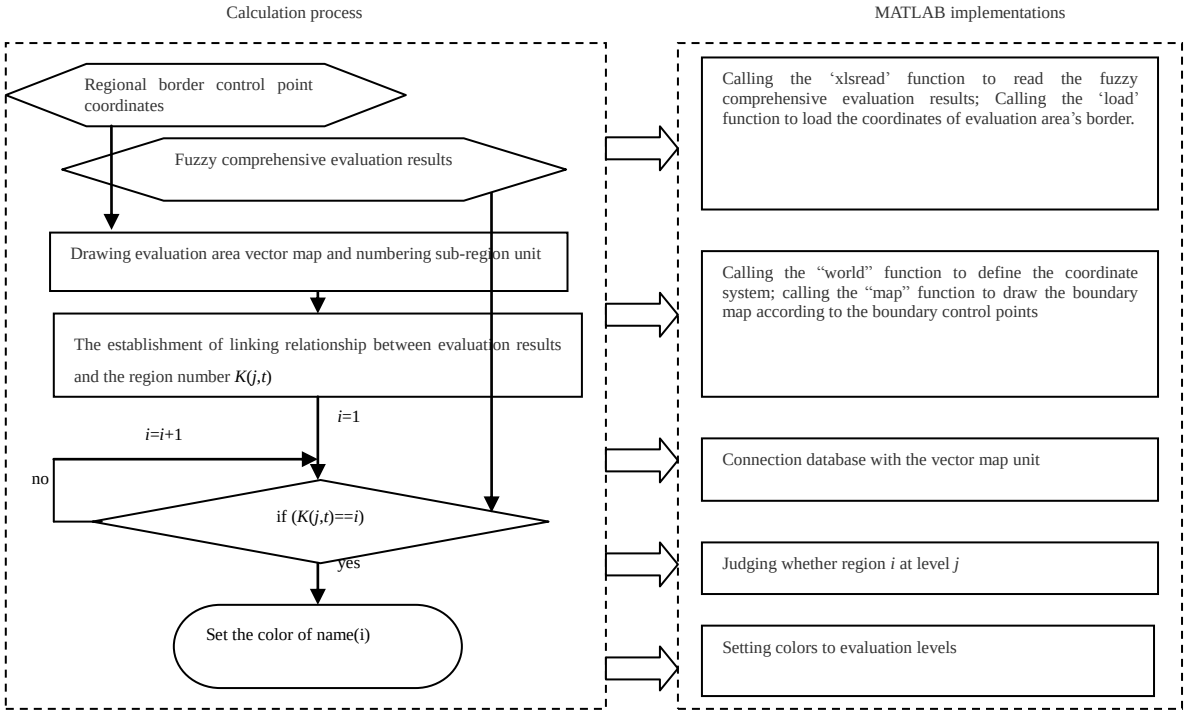


Fig. 3 The interface between Vector interface and evaluation results

Conclusions

Through the simulation drinking water safety in rural areas of Henan Province, on the one hand, it has a significance guide for the scientific understanding of the safety drinking water and decision-making of rural drinking water safety construction by the regional assessment of the situation of rural drinking water safety; on the other hand, a simulation platform to quickly evaluate

the object by fuzzy comprehensive evaluation method was established in this study, which has good versatility, while the research is based on MATLAB platform using vector image processing technology, combined with evaluation of results display, which can provide a consult for current research related to certain fields.

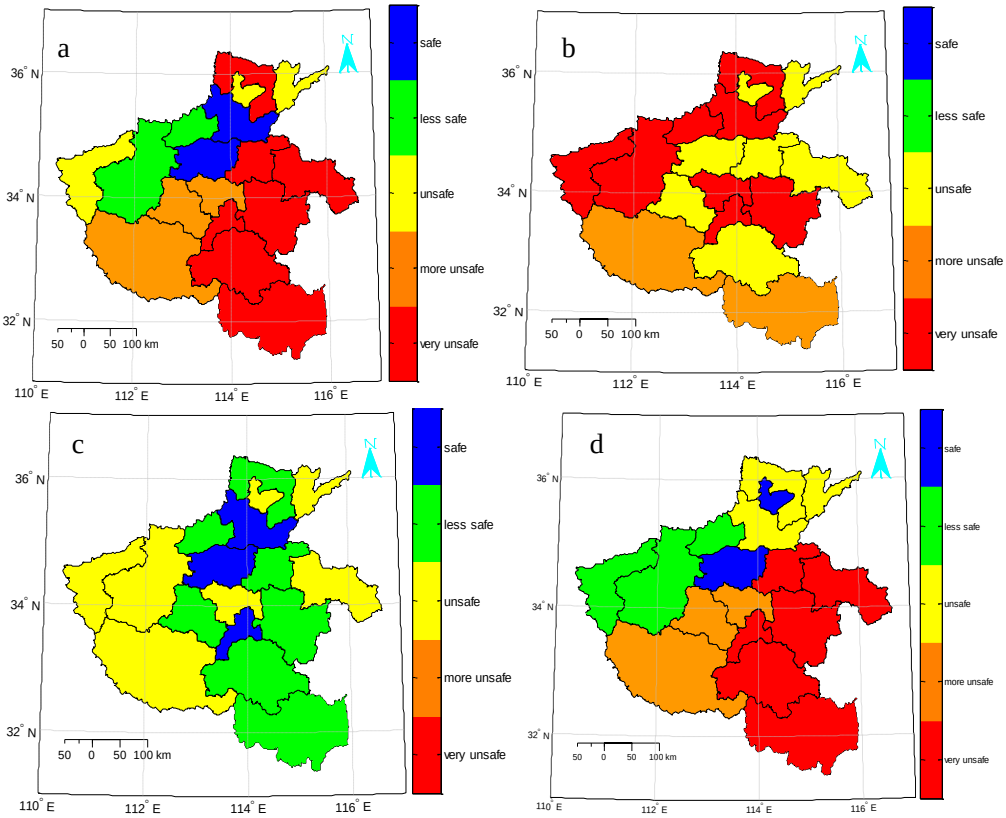


Fig. 4 Results of rural drinking water safety evaluation of Henan province

Acknowledgements

This work was financially supported by the National Natural Science Foundation of China (No.51078340), the National Public Benefit (Environmental) Research Foundation of China (No.201109009), and the Science and Technique Foundation of Henan Province during the 11th Five-Year Plan Period (No.092102110032) in China.

References

[1] T. L. Saaty, The Analytic Hierarchy Process, Priority, Resource Allocation. New York, 1980, pp. 287-305.

[2] T. L. Saaty, J. P. Bennett, A theory of analytical hierarchies applied to political candidacy, Behavioral Science, 22 (1997) 237-245.

[3] L. A. Zadeh, Fuzzy Sets. Information Context, 8 (1965) 338-358.

[4] L. A. Zadeh, Similarity relation and fuzzy orderings, Information Sciences, 3 (1971) 177-200.

[5] Z. Xu, Level analysis of the new scale method, Systems Engineering Theory and Practice, 18 (1998) 74-77.

[6] J. Jin, K. Wu, R. Li, Information entropy and fuzzy AHP coupling to improve regional water security evaluation model, Hydropower, 26 (2007) 61-66.

[7] C. Yuan, H. Lei, H. Wang, H. Pan, Evaluation of safety of drinking water in rural areas of Henan Province, Irrigation and Drainage, 28 (2009) 59-63.

© (2012) Trans Tech Publications, Switzerland
doi:10.4028/www.scientific.net/AMM.238.395

Analysis of the City Waterfront Landscape Design in Central Plains Economic Zone

Jingxia Liu [1 a] and Zengqiang An [2 b]

[1]North China University of Water Resources and Electric Power, Zhengzhou 450011, China

[2]Henan Water & Power Engineering Consulting Co.Ltd, Zhengzhou, China

[a]liujingxia@ncwu.edu.cn, [b]anzengqiang@163.com

Keywords: city waterfront; ecological landscape design; ecological restoration; Jialu river; Central Plains Economic Zone.

Abstract. The modern city waterfront construction is an important part of the city landscape environment design, many city put it as an important part of city development strategy. The article combines the ecosystem manage engineering case of Zhengzhou Jialu river, take out the course of river manage principle and important points in the process of designing under the background of Henan Central Plains Economic Zone construction.

Introduction

As an old saying goes: "The wise find joy in water; the benevolent find joy in mountains". "Water is the source of everything ", As the life line of the city, Waterfront area supports continuing of life in the city, not only load water body circulation, water and soil conservation, store water to adjust the flood, fluid matter self-restraint and support the operation function of atmosphere composition stability, but also regulate degree of humidity, purify air, absorb the dust to reduce the noise and improve the city climate, effectively regulate the ecoenvironment of city, urge the city keep on to develop healthily.

The modern city waterfront construction is an important part of the city landscape environment design, many city put it as an important part of city development strategy.《Circular of the State Council concerning support for Henan province to accelerate the building of area of Central Plains economy guidance》put forward to strengthen resource conservation and environmental protection, Vigorously promote the construction of ecological civilization. For the Central Plains Economic Area, How to construct the city waterfront landscape has important realistic meaning in the city develops.

Waterfront Landscape Design Ideas Under the Background of Central Plains Economic Zone

From the Global View, Construction of Waterfront Area Ecosystem Network Architecture. The river is an eco-system for exercising, including the physical structure of river soil, hydrological and biological, the material exchanges and chemical reaction, material flow among biological community, energy flow and information flow of the dynamic process of the unification of ecology. If we want to build up to be a have ego organization, ego maintenance and ego design ability of river eco-system in the city, we must respect this ecosystem rule of a river.

The landscape ecology thinks that the landscape is a piece of differences land district, constitute of form likeness, repeat a kind of eco-system structure and form of interaction of emergence constitutes and has values such as economy, ecosystem and esthetics etc.. River in the city is a switching important gallery of city landscape to carry on a logistics, can flow, the information flow, to ensure the keep on development of the city ecosystem, society and economy, to the safety of city, it also playing the role of unreplacement of the nature adjust to control and landscape function. We must follow headstream ecosystem regulation and imitating the nature river ecological structure in landscape designing, the square can develop esthetics value, history culture and city of harmony, city that the river appears a city and nature to the ecosystem service function of city and to total of comprehensive personal status.

Make Use of An Ecosystem Repair Technique, Strengthen a Resources to Economize Intensive Exploitation. The ecosystem repair is the in common use method that improves river water in the city, and it has already widely applied at present. Use a technical application of ecosystem engineering to combine the control of polluting the source on the one hand, effectively improve course of river fluid matter to make it attain the request of view water body fluid matter; on the other hand, we make use of the waterfront design of plants and water landscape to beautify the river landscape and makes it act in cooperation, merge into an integral whole mutually with urban and rural other functions. For example the ecosystem protect shore can promotes the commutation of earth's surface water and groundwater, retains the flood and regulates the water level, resumes the growth of animals and plants in the river, purify the water quality by make use of the function of animals and plants oneself. This kind of protecting shore can stabilize river bed, and can improve ecosystem and beautification environment, avoided the negative function that the concrete structure brings.

Develop Image Function and Practical Function of Waterfront Landscape. Waterfront resources in city are close connected with the city life, because diverse sex of water resources and permit sex, the waterfront area in city is a natural ecosystem resource, and plays multiple role in the city, therefore, the design of waterfront view also wants to pay attention to function, satisfy various needs of city.

Recreational function: Waterfront view wants to provide the space of a waterfront recreation for citizen and set up a view and open of get close to water sex humanities movable space, satisfy people and get close to water recreational demand.

Transportation function: Make use of a waterfront resources in city, perfect assistance transportation means, abundant city function, can also as a part of view in the city, draw on visitor's sightseeing.

Travel function: Much waterfront resources has very high appreciate value, or have deep history cultural bottom Yun. The design of waterfront in the city view, match with the demand of tour development in the city, provide a necessary tour kit at the same time facilities, satisfy the demand that the visitor develops to travel an activity in waterfront area.

Set Up the Harmony Waterfront Area Between Water and People. Although we are carrying on the view design of modern type, can not completely escape from local original culture and local humanities history to precipitate down, either of appreciate beauty wit and humor, cannot split into pieces a tradition. Actively construct a good waterfront hydrology and turn a view to a city, prosper a waterfront hydrology and turn business, develop an abundant and colorful waterfront hydrology and turn an activity, provide an excellent waterfront hydrology and turn facilities, actively develop waterfront square and follow a river park, build and get close to water facilities, get close to water and construct and art essay etc., can promote personal status in the city and layer, also be advantageous to waterfront area view environment that sets up harmony.

The Design Points of Waterfront Area Landscape

Design on Water Shape. Water view design is the importance of waterfront view to constitute part, water of the appearance is different, then constitute of the view is also different. The modern view design is in the outstanding landscape of at the same time, have to also maintain headstream original ecosystem as far as possible, is similar to river shore and wet, flushing of bottom of river and silt up, the performance of these natural vitalities should is allowed their existence and is rich with diverse sexual environment condition for living creature creation.

Design on Plant Landscape. To waterfront area, the plant is the corpus that its view main factor constitutes, the importance of waterfront area eco-system to constitute part, but for have already been subjected to water of the pollution and breakage, plant still as to it's carry on the emollient measure of ecosystem repair. Plant and water are the main factors that constructs a waterfront area in city natural ecosystem, combine together hydrophyte and waterfront area in city, construct a natural ecosystem type course of river, become the latest design principle of modern waterfront area ecosystem in city reformation.

Design on Water Facilities. Currently, we didn't have a clear definition of water facilities, Japanese river manages《Design of waterfront region water facilities》of plait Zhao in the center in like descend related definition: So-called "get close to water activity" means that people pass in waterfront space to carry on a stroll, exercise, drama water, angle for fish an amusement recreational activity of etc. and in the appreciating of scenery in the process acquire mentally with the satisfying of spirit activity of feeling. Therefore, "get close to water facilities" means to used for all facilities that develop to get close to water an activity.BE with get close to water activity for corpus of get close to water the ducting of facilities.

Case analysis

Project Circumstance The Jialu river ,also called small yellow river, belong to the Huaihe river system, originates from Shengshuiyu in Mi county, flow through Zhengzhou, Zhongmou, Wei Shi, E Ling,Fu Gou, Xi Hua, mingle in The Sha Ying river in Zhou Kou .The overall length is 256km, the drainage area is 5895 km^2.The river length in Zhengzhou is 137km, the drainage area is 2750 km^2, the river is the most important river in Zhengzhou except The Yellow River, almost undertake all flood control tasks of Zhengzhou.

Ecological Landscape Node Design. Through the arranging of waterfront area of Jia Lu river,the project The final landscape structure system is "one gallery, one core and 5 areas".

One gallery, is the ecosystem gallery along The Jialu River.

One core, is the ecosystem repairs core in the area of the Suoxu river mingle in the Jialu river.

5 areas, are 5 typical ecological landscape area along The Jialu river, the specific as follows: Zhongzhou Bridge ecological landscape area, the ecological landscape area of the Suoxu river mingle in the Jialu river, the New 107 national road ecological remediation area, the ecological remediation area of the old Suoxu river mingle in the Jialuzhi river, the resettlement residential landscape area.

The Layout and Profile, Cross-sectional Design of River. In order to better embody function in the city of the Gu Lu waterfront river in the river city ecosystem gallery, the outstanding course of river ecosystem manages of principle, the engineering will combine in satisfying the foundation of course of river flood control cross section course of river present condition to carry on appropriate adjustment to the Gu Lu river lord river slot flat surface appearance. Design lord river slot to consider the present conditions pool ground condition, such as fish pond, marsh land and Woodland...etc. that makes use of a ground as far as possible under the situation that promise the course of river flood control cross section width and swing in the dike feet line scope inside the cross-straits. Since protected an existing pool ground Woodland, again well made use of pool ground fish pond, marsh land, reduced course of river soil square to open to dig quantity.

On the course of river cross section in addition to lord river slot, course of river two grounds don't carry on soil as far as possible the square dig to fill and only make use of existing geography at course of river soil the square carry on a tiny geography sorting to the pool ground after the engineering completion of work and enrich the signing of course of river pool ground noodles appearance.

Ecological Bank Revetment Design. Survey a report according to the engineering geology, the Gu Lu river present condition geology takes sand Rang soil as a lord, for protect course of river lord slot appearance and refute shore, need in the crest blunt part to refute to consider in the shore design that the ecosystem protects to carve. The engineering totally designs five kinds of ecosystems to protect to carve a way: Natural vegetation protects shore and imitate a wooden post to protect shore, ecosystem bag to protect shore, the space guest stone cage net to protect shore and natural stone to protect shore.

Design on Plants. Including two parts, the arranging of present woodland along the river and hydrophyte design.

There have a lot of woodland along the river shore at present, the area adds up to about 51.6 hm^2.While satisfying the premise that the course of river goes a Hong cross section and course of river flat surface appearance, the wood who designs to the present condition brings in to go protection with comb. The wood who goes Hong to the baffling lord river slot takes to carry on chopping down with some trees of old tree, disease; Bring in a line of to fell to the wood of pool ground, the tree trunk 3 ms Be as follows carry on paring a processing; In order to promise the natural appearance of Woodland of partial ecosystem node, play chess a wood to bring in combing of a line of cluster form. Pass ground existing what wood took protect and comb to the pool, will to raise course of river of lead Hong ability, protect the living of existing course of river birds interest ground and promise course of river living creature diverse sex etc. s to will have the bigger improvement the function.

The hydrophyte programming is the importance of water ecosystem protection and repair to constitute part, is also improve fluid matter and increase one of the paths that the course of river livings the territory most effective type. Manage the characteristics of segment according to the river of Gu Lu, combine the difference that the hydrophyte lays particular emphasis on a point in the function of different location at the same time, will combine the river of Gu Lu to manage a segment to carry on a concrete programming respectively. Among them, the programming of general course of river segment hydrophyte lays particular emphasis on its ecosystem function, the important ecosystem node then needs to give attention to both certain function.

The species that the hydrophyte allocation of important ecosystem node can choose lotus flower, water lily, Spiked Loosestrlfe, Acorus calamus Linn, Monochoriamorsakowii, Typha orientalis Presl ,Monochoriamorsakowii and Arundo donax var. versicolor etc.

Drawing on birds is another, definitely recruit a bird wood (infuse a cluster) on programming of ground in the pool, the species of choice has mulberry, Lonicera maackii(Rupr.)Maxim, and Rhamnus parvifolia Bunge, and Dwarf apple...etc. of leaf, can provide various fruit of birds pleased food. The herbs can choose grain undergraduate course plant categories, such as Echinochloa crusgalli(barnyard grass), Setaira viridis(L.)Beauv , broomcorn millet ,...etc., can provide various corn food, suitable win small scaled birds especially the Qiao form eyes birds to build nest and take to eat an activity.

Pass the implementation of above engineering measure, will consumedly raise the eco-system that the Jialu river ecosystem manages a river segment integrity, the abundant course of river livings territory diverse sex and draws on more water to living, six living, amphibious living creature come to this dwells for rest, breeds and promises the integrity of waterfront district vegetative chain system.

Conclusions

The waterfront area landscape design in city differs from other general park designs, it needs more engineering techniques to prop up , such as ecosystem, economy and hydraulic engineering etc…and it loaded more compound function in the cities. Depends on the case of Jialu River landscape design, the article carried out a preliminary analysis and we hope it can provide some references for the waterfront landscape construction under the background of Central Plains Economic Zone.

References:

[1] Q. Kang, A study on urban riverfront green space design, Beijing Forestry University, Beijing, 2009.

[2] J. Gao, Near natural control: torrent control engineering based on the landscape ecology, Journal of Beijing Forestr University, 21 (1999): 80-85.

[3] X. Chen, X. Li, The eco-functions of ecological protection techniques of riverbank .Acta Ecologica Sinica, 27 (2007) 1168-1174.

[4] Z. Dong, Protect and resume river appearance diverse sex, China's Water Conservancy, 6 (2003)169-376.

[5] X. Li, The wood grows and plays to substitute regulation on Jialu River, Journal of Henan Normal University, 8 (1988) 49-97.

[6] D. Yuan, et al, Study on purified efficiency of phosphorus and nitrigen from domestic swage by several macrophytes in vertical flow constructed wetlands. Journal of Soil and Water Conservation. 18 (2004), 77-92.

[7] J. Xia et al, Study progress and development trend of ecological riverfront, Journal of Hehai University (Natural Sciences). 3 (2004)

[8] W.J. Mitsch, S.E. Jorgensen, Ecological Engineering and Ecosystem Restoration. Published by John Wiley&Sons, Inc., Hoboken, New Jersey, 2004, pp. 134-137.

[9] Civil Engineering and Planning Committee in Japan, Waterfront Landscape Design. Tokyo: Ji Bao Tang Publisher, 1988.

© (2012) Trans Tech Publications, Switzerland
doi:10.4028/www.scientific.net/AMM.238.400

Orthogonal Enumeration Method for Optimum Seismic Strength of Water Supply Network

Shuanghua He

School of Civil Engineering and Communication, North China University of Water Resources and Electric Power, Zhengzhou 450011, China

heshuanghua222@126.com

Keywords: water supply network; seismic reliability; discrete variable; seismic strength; orthogonal enumeration method.

Abstract. Considering the unit seismic reliability and node water head of the water supply network after the earthquake as control parameters, the method of optimum seismic strength is developed to make the system's nodal pressure shortfall or strengthening expense minimum. According to the function requirement and earthquake disaster character of the water supply network, the system's seismic strength is changed into optimum problem with fewer discrete varieties, and the difficulty of solving large nonlinear scheme can be avoided by adopting orthogonal enumeration method. The presented method is tested to be feasible and effective in optimum seismic strengthening of water supply network.

Introduction

For urban water supply network, some of the elements' damage under earthquake will cause part or all function's inactivation of the system. According to the function requirement and earthquake disaster characteristic of system, optimum mathematical model is established in this paper by restraining element's seismic reliability and nodal pressure of the network after earthquake and making minimum nodal pressure shortfalls and seismic strength input as the subject.

Optimum Seismic Strength Model of Water Supply Network

As pipeline's seismic reliability determines nodes' serviceability of the network after the earthquake, the system's seismic reliability can be improved effectively by strengthening or rebuilding the pipes with lower seismic reliability or the pipes that more important but difficult to repair.

Calculation of the Pipe's Seismic Reliability. The pipe's seismic reliability can be calculated by the method of statistic earthquake disaster with short of seismic reliability data [1].

Serviceability Analysis of the Water Supply Network after Earthquake. Assuming that pipe's leakage exist in the center of the pipe for the water supply network after earthquake, the leakage status can be simulated by adding a dummy leak node on the center position [2]. Nodal pressures and nodal flows of the water supply system after earthquake can be obtained by solving nodal pressure equations through hydraulic analysis.

Economic Indictor for the Network's Strength. Water supply network's strength cost can be calculated according to the strength program by giving system's fabrication cost [3].

Mathematic Model of System's Optimum Seismic Strength. According to the analysis of pipe's seismic reliability and network's strength cost and system's serviceability after earthquake, the mathematic programming can be established as follows,

$$\min \ \boldsymbol{C} = \sum_{j=1}^{J} \boldsymbol{C}_j\left(\varphi_j'\right) \text{ or } \min \ \Delta\boldsymbol{H}\left(A_{L1}', A_{L2}', \cdots A_{LJ}'\right) = \sum_{i=1}^{n} \Delta\boldsymbol{H}_i \tag{1}$$

$$\varphi_j' \geq \varphi_0 \ \left(j = 1, 2, \cdots J\right), \ \boldsymbol{H}_i' \geq \boldsymbol{H}_0 \quad \left(i = 1, 2, \cdots n\right)$$

Where, $\boldsymbol{C}$ is the system's fabrication cost, $\boldsymbol{C}_j$ is the pipe's fabrication cost, $\Delta\boldsymbol{H}$ is the nodal pressure shortfalls of the system after the earthquake (m), H_i' denotes the water head of the node after Optimum Seismic Strength (m); $\boldsymbol{H}_0$ shows urban minimum water head (m), φ_j' expresses pipe's seismic reliability after strengthening, φ_0 is the lower limit value of pipe's seismic reliability.

Orthogonal Enumeration Method for Optimum Seismic Strength of Water Supply Network.

Above mathematic model of system's Optimum Seismic Strength belongs to nonlinear programming problem. According to actual project, the network's strengthening program is discrete and limited, so the mathematic model can be inverted into discrete optimum model [4].

Selection Scheme for Pipe's Seismic Strength. Pipe's seismic reliability can be improved by changing pipeline materials, pipe diameters and employing seismic structural measures such as adopting flexible joint or adding covering layer. And adopting flexible joint is often selected as the strengthening scheme according to the design experience for earthquake disaster [5].

Orthogonal Enumeration Method for Optimum Seismic Strength of Water Supply Network. Orthogonal enumeration method will be adopted to simplify the calculation in order to seek not the optimum solution sedulously but the satisfactory solution. And existing and normalized orthogonal layout can be employed to enumerate few design schemes from many design scheme combinations to check and evaluate the object, and to determine the optimum design scheme. The few design schemes can represent all the possible design schemes selectively and skillfully, which greatly simplified the solution of challenging and multivariate nonlinear programming [6].

Case Study

As an example of the network shown in Fig. 1 [2], flexible joints are planned to adopted to improve pipe's seismic reliability(the required pipe's seismic reliability should not be less than 0.8), which will increase the pipe's unit cost of 12%. Try to carry out the optimum seismic strength of the water supply network with orthogonal enumeration method to satisfy the requirement of the network's minimum serviceability with the water head of 20m under earthquake intensity VII.

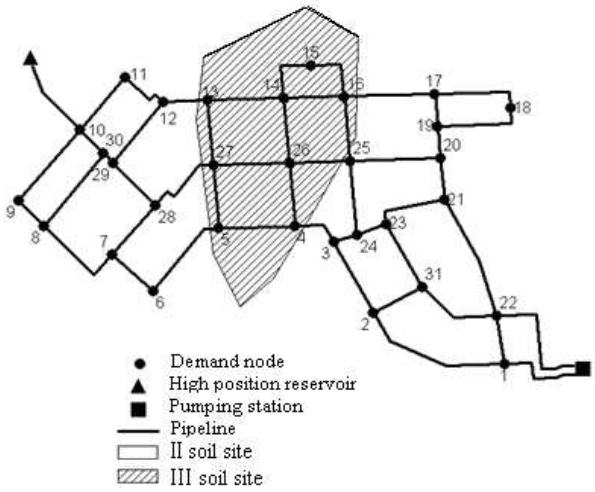


Fig. 1 The plan view of the ground condition and pipe network

Table 1 Nodal pressure of the network under earthquake VII

Node number	Nodal pressure /H(m)	Node number	Nodal pressure /H(m)	Node number	Nodal pressure /H(m)	Node number	Nodal pressure /H(m)
1	46.90	9	21.63	17	34.40	25	32.43
2	38.02	10	20.68	18	40.19	26	28.60
3	33.63	11	21.02	19	35.62	27	26.21
4	30.73	12	23.19	20	37.10	28	24.45
5	26.94	13	23.87	21	38.11	29	23.26
6	23.02	14	25.63	22	43.05	30	21.42
7	22.11	15	24.76	23	36.80	31	38.82
8	19.94	16	46.90	24	34.90		

It is calculated that all the pipes' seismic reliability are greater than 0.8 for this water supply network, but the water head of node 8 under earthquake intensity VII is less than the minimum water head (Table 1), so flexible joint connections for the pipes should be adopted to improve the network's

seismic reliability, that all the nodal pressures under earthquake intensity VII can satisfy the minimum water head requirement. We can select all the pipes with lower seismic reliability at the third site and part of the pipes at the second site to strengthen. By strengthening pipe 1, 4, 5, 6, 7, 8, 9, 10, 13, 14, 15, 16, 17, 30 and 47, select orthogonal layout $\boldsymbol{L}_{16}(2^{15})$ with 15 factors and 2 levels to perform strength test, the test results are shown in Table 2.

Pipes' strength cost and network's pressure shortfalls after earthquake for all the tests are shown in Table 3. According to the principles of minimum nodal pressure shortfalls after earthquake and minimum strength cost, better strength schemes in test 11 and 13 are selected by comparing the results in Table 3 one by one, and nodal pressures for these two schemes are shown in Fig. 2. In order to make the worst-case nodes' (node 6, 7, 8, 9) water head high enough, schemes in test 11 are selected as the optimum strength schemes, for which pipe 4, 5, 8, 9, 10, 13, 16 and 17 are of flexible joints, and schemes in test 13 are suboptimum strength schemes, for which pipe 6, 7, 8, 9, 10, 13, 14 and 15 are of flexible joints.

Table 2 Hydraulic analysis of water network with different strengthening schemes

Node number	Nodal pressure (m)							
	Test 1	Test 2	Test 3	Test 4	Test 5	Test 6	Test 7	Test 8
1	46.8982	47.6842	47.6760	47.7215	47.674	47.658	47.9282	47.7074
2	38.0175	39.1653	39.1743	39.2469	39.1197	39.1417	39.5439	39.2343
3	33.6275	35.0482	35.0786	35.1743	34.9621	35.0302	35.5347	35.1645
4	30.7219	32.5493	32.6588	32.8068	32.3258	32.5485	33.2225	32.8000
5	26.9399	28.9460	29.2625	29.2339	28.6855	28.9557	29.8840	29.2241
6	23.0210	24.9610	25.1662	25.1476	24.7844	24.9719	25.7991	25.1302
7	22.1143	24.0367	24.2106	24.1949	23.8824	24.0479	24.8468	24.1752
8	19.9366	21.7541	21.9012	21.8910	21.6242	21.7616	22.5200	21.8667
9	21.6290	22.9821	23.0502	23.0601	22.9201	22.9740	23.5354	23.0213
10	20.6825	21.6875	21.6946	21.7201	21.6775	21.6675	22.0752	21.6700
11	21.0248	22.9593	22.7866	22.9601	23.0906	22.8117	23.5708	22.7161
12	23.1874	25.8485	25.5406	25.8257	26.0840	25.6053	26.6243	25.4350
13	23.8670	26.8314	26.4276	26.7892	27.1402	26.5217	27.6412	26.3015
14	25.6264	28.8184	28.4688	28.7258	29.0557	28.3776	29.4145	28.0695
15	24.7559	28.4686	28.8238	28.3948	29.3730	28.0497	28.2295	27.8206
16	29.6525	32.3805	32.1049	32.2248	32.5859	31.8821	32.7426	31.8936
17	34.3993	36.3514	36.2061	36.2967	36.4591	36.1043	36.7365	36.1381
18	40.1919	42.0324	41.9063	41.9926	42.1255	41.8220	42.4206	41.8590
19	35.6171	37.3858	37.2719	37.3554	37.4697	37.1989	37.7764	37.2381
20	37.1017	38.6550	38.5782	38.6535	38.7108	38.5394	39.0524	38.5848
21	38.1090	39.4735	39.4189	39.4876	39.5080	39.3884	39.8432	39.4381
22	43.0510	43.9329	43.9163	43.9652	43.9323	43.8983	44.1988	43.9465
23	36.7977	38.1028	38.0815	38.1530	38.1047	38.0666	38.5107	38.1367
24	34.9040	36.3326	36.3150	36.3935	36.3310	36.3057	36.7927	36.3845
25	32.4338	34.4199	34.3549	34.4401	34.5036	34.4227	35.0751	34.4654
26	28.6012	30.9793	30.9481	31.0318	30.9118	31.0212	31.8013	31.0426
27	26.2094	28.4746	28.5813	28.5404	28.3723	28.5254	29.4316	28.5457
28	24.4451	26.6697	26.7690	26.7362	26.5716	26.7119	27.5904	26.7325
29	23.2600	25.3309	25.3905	25.3898	25.2721	25.3412	26.1645	25.3509
30	21.4240	23.2510	23.3077	23.3115	23.1960	23.2549	23.9892	23.2716
31	38.8207	39.9353	39.9194	39.9818	39.9310	39.9012	40.2821	39.9649

Table 2 (Cont) Hydraulic analysis of water network with different strengthening schemes

Node number	Nodal pressure(m)							
	Test 9	Test 10	Test 11	Test 12	Test 13	Test 14	Test 15	Test 16
1	47.7513	47.6904	47.9882	47.7329	47.9385	47.6507	47.6775	47.7045
2	39.2600	39.1602	39.6220	39.2394	39.5248	39.1024	39.1933	39.1911
3	35.1590	35.0258	35.6237	35.1405	35.4801	34.9561	35.1173	35.0766
4	32.6446	32.4422	33.3188	32.6549	33.0472	32.3702	32.7620	32.5737
5	28.9102	28.9088	29.8193	29.0857	29.4006	28.8683	29.2992	29.0225
6	24.9400	24.9600	25.6339	25.0097	25.4578	24.9392	25.1594	24.9590
7	24.0197	24.0455	24.6519	24.0599	24.5448	24.0299	24.1911	24.0128
8	21.7358	21.7650	22.3182	21.7642	22.2525	21.7540	21.8794	21.7202
9	22.9536	22.9851	23.3556	22.9726	23.3806	22.9839	23.0346	22.9405
10	21.6513	21.6844	21.9127	21.6630	22.0088	21.6907	21.6838	21.6401
11	22.7540	22.8532	23.2151	22.9055	23.6159	22.8892	22.8283	22.8564
12	25.5161	25.6652	26.1272	25.7729	26.7493	25.7237	25.6220	25.7043
13	26.4119	26.5890	27.0846	26.7511	27.8292	26.6612	26.5439	26.6729
14	28.4735	28.4305	29.2811	28.7347	29.7635	28.5556	28.1847	28.6513
15	27.5125	28.1893	29.7246	28.4352	30.0535	28.3235	27.1575	28.4105
16	32.3199	32.2785	33.1776	32.3104	33.2184	32.2966	31.8663	32.5022
17	36.4032	36.3330	36.9897	36.3722	36.9811	36.2971	36.0912	36.4274
18	42.1006	42.0263	42.6465	42.0665	42.6305	41.9825	41.8093	42.1016
19	37.4646	37.3875	37.9854	37.4285	37.9647	37.3386	37.1865	37.4507
20	38.7660	38.6807	39.2089	38.7237	39.1738	38.6164	38.5277	38.7069
21	39.5799	39.4971	39.9713	39.5423	39.9282	39.4355	39.3862	39.5165
22	44.0094	43.9450	44.2694	43.9865	44.2223	43.9003	43.9120	43.9571
23	38.2333	38.1345	38.6071	38.1934	38.5384	38.0599	38.0805	38.1377
24	36.4871	36.3748	36.8910	36.4403	36.8124	36.2871	36.3200	36.3694
25	34.7324	34.5855	35.1943	34.6216	35.1503	34.4202	34.3380	34.4758
26	31.2542	31.0193	31.6462	31.0287	31.7895	30.8815	30.8164	30.8498
27	28.5207	28.5822	29.0237	28.3697	29.2164	28.5901	28.4796	28.3288
28	26.7039	26.7646	27.2055	26.5692	27.3902	26.7727	26.6760	26.5282
29	25.3255	25.3872	25.8090	25.2489	26.0022	25.3977	25.3245	25.2078
30	23.2382	23.2914	23.6855	23.1888	23.8375	23.2992	23.2570	23.1512
31	40.0398	39.9549	40.3659	40.0090	40.3028	39.8944	39.9193	39.9648

Table 3 Optimization strength index values of the network system

Test number	Pressure shortfall $\Delta H(m)$	Strength cost （yuan）	Test number	Pressure shortfall $\Delta H(m)$	Strength cost （yuan）
1	236.9401	0	9	179.1362	257001.1
2	178.5602	230541.4	10	179.3713	263790.1
3	179.0180	250975.3	11	161.6545	174005.8
4	177.1618	278661.8	12	177.9865	267649.7
5	177.6238	251796.6	13	159.8026	153974.8
6	181.5012	226635.8	14	180.0400	231103.6
7	161.2302	190083.9	15	181.6839	229337.0
8	180.6790	271182.9	16	179.1961	237783.7

Conclusions

For the optimum strengthening of water supply network, orthogonal enumeration method are used to invert optimum variables into discrete variables by restraining element's seismic reliability and nodal pressure of the network after earthquake, and making minimum nodal pressure reduction and seismic strengthening input as the object in this paper, which is based on the principle of seeking not the optimum solution sedulously but the satisfactory solution. It can greatly decrease the amount of work, and lead to proper optimum strengthening schemes.

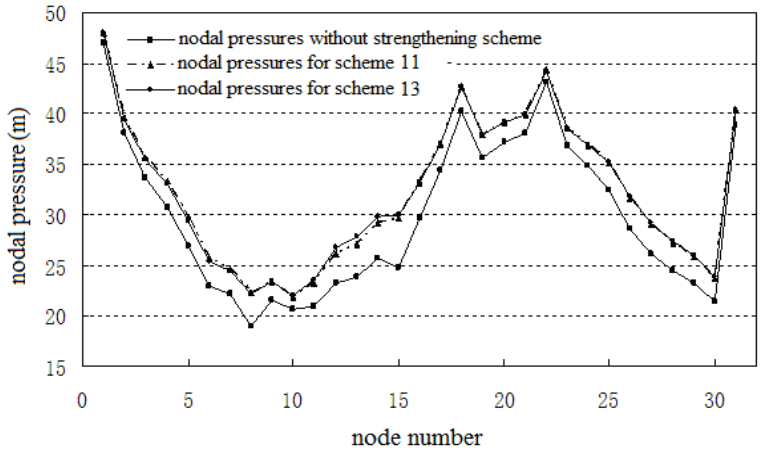


Fig. 2 Nodal water head of the network under earthquake intensity VII

References

[1] G. Wang, Practical Method for Seismic Optimum Design of Engineering Structure and System, China Architecture & Building Press, Beijing, 1999.

[2] C. Liu, A. Zhang, Seismic performance analysis on water supply network, Engineering Mechanics, 3 (2007) 142-146.

[3] M. Lu, F. Qu, F. Ding, Determination of factors a, b and alpha in cost function of pipeline, Water & Wastewater Engineering, 1 (1994) 9-11.

[4] Y. Chen, Y. Liang, X. Liu, Orthogonal enumeration method for the layout scheme optimization of road network, China Civil Engineering Journal, 7 (2003) 14-17.

[5] J. Li. Seismic Basic Theory and Application of Lifeline Engineering, Science Press, Beijing, 2005.

[6] K. Fang, C. Ma. Orthogonal and Uniform Experimental Design, Science Press, Beijing, 2001.

© (2012) Trans Tech Publications, Switzerland
doi:10.4028/www.scientific.net/AMM.238.405

Effect of Electrochemical Pretreatment and Flocculation on the Degradation of Pharmaceutical Wastewater

Xiao Mi

Department of Environmental and Municipal Engineering, North China University of Water Resources and Electric Power, Zhengzhou 450011, China

mixiao@ncwu.edu.cn

Keywords: electrochemical pretreatment; pharmaceutical wastewater; water treatment; flocculant.

Abstract. As it is not suitable for bio-treatment method, pharmaceutical wastewater is treated by physiochemical methods in this study. Besides, potassium permanganate oxidation, electrochemical pretreatment and the addition of $FeCl_3$ and $AlCl_3$ after potassium permanganate oxidation were compared. It is proved that electrochemical pretreatment had a little greater degradation efficiency compared with the other two flocculants. Electrochemical oxidation seems to be more cost-effective due to its ease of operation. Electrochemical pretreatment is expected to be a suitable method to assist the pharmaceutical wastewater treatment.

Introduction

A number of micro-pollutants such as pharmaceutical drugs are found in the natural waters and they become one of the great concerns around the world due to their influence on freshwater systems [1]. This is because the increased levels of micro-pollutants in surface and groundwaters may cause long term effects on aquatic ecology and human health. As a result, there is a great need to treat the pharmaceutical wastewaters effectively. Pharmaceutical wastewaters contain a large amount of drugs and their intermediates and they are characterized by high COD and comparatively low BOD. Besides, these pharmaceuticals are designed to treat and prevent diseases and bio-treatment methods are proved to be ineffective for these pharmaceutical wastewater.

A series of physicochemical methods and their combined technologies such as advanced oxidation processes (AOPs) are proved to be applicable before or after biological treatment [2-4]. In these treatment systems, Cl_2, ClO_2, ferrate (VI) and O_3 are frequently applied to oxidative treatments due to their high reduction potentials [5-7]. In this study, a pharmaceutical wastewater from a local pharmaceutical factory, which was not pretreated by any other methods before use, was employed for the degradation by potassium permanganate. The effect of electrochemical pretreatment and flocculation by $FeCl_3$ and $AlCl_3$ was comparatively investigated.

Materials and Methods

Materials. Potassium permanganate was obtained from Beijing Chemical Reagents Company. Other materials used in the test were of analytical grade. Deionized and doubly distilled water was used throughout the study.

Decolorization of Orange II by Hydrogen Peroxide Related Reactions. The pharmaceutical wastewater was obtained from a pharmaceutical factory in Zhengzhou, Henan province (China). Its initial pH value was measured to be 5.4. These reactions were carried out in a series of 200 mL beakers and 150 mL pharmaceutical wastewater was added. The solution was stirred vigorously by a magnetic stirrer.

Analyses. Shimadzu UVmini1240 UV-Vis spectrophotometer was employed to determine the absorbance at 254 nm. COD measurement was conducted by $K_2Cr_2O_7$ oxidation with the help of microwave irradiation and a subsequent titration with $(NH_4)_2Fe(SO_4)_2$.

Results and discussion

Effect of Reaction Time during Potassium Ermanganate Oxidation. Fig. 1 illustrates the effect of reaction time on the efficiency of COD removal by potassium permanganate. Typically, it was observed that the absorbance at 254 nm increased with an increase of reaction time. However, the COD removal efficiency was increased from 2.9% at 15 min to 48.8% at 30 min and then it declined to 17.4% at 60 min. It implies that there is an optimal reaction time for the pharmaceutical wastewater treatment. The reaction time was kept at 30 min in the following study.

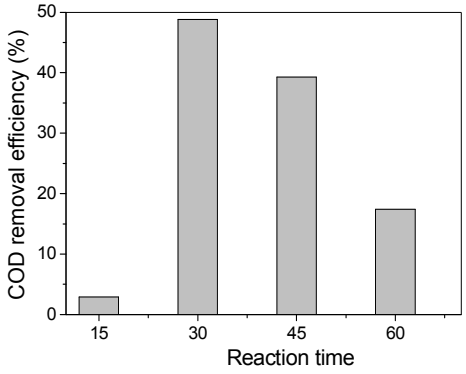


Fig. 1 COD removal efficiency as a function of reaction time during degradation by potassium permanganate (30 mg/L).

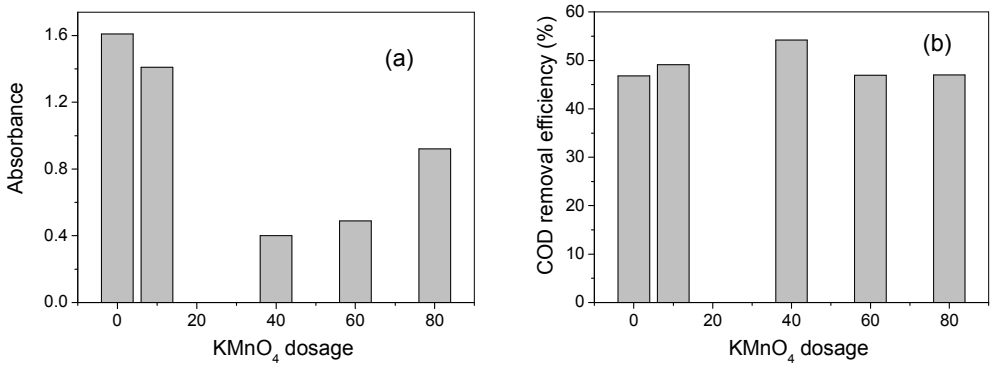


Fig. 2 The absorbance at 254 nm (a) and COD removal efficiency (b) as a function of potassium permanganate dosage for the degradation of pharmaceutical wastewater by 60 min of electrochemical pretreatment.

The pharmaceutical wastewater contains a number of aromatic intermediates and antibiotics. These aromatic rings are the most difficult to be degraded in organics and they have a characteristic absorption at around 255 nm [8]. The effect of potassium permanganate dosage on the degradation of pharmaceutical wastewater by of electrochemical pretreatment is illustrated in Fig. 2. The wastewater treated by 60 min of electrochemical oxidation was subjected to the potassium permanganate oxidation. It was observed that the absorbance at 254 nm decreased from 1.40 at 10 mg/L to 0.41 at 40 mg/L of potassium permanganate, while it achieved 0.49 and 0.92 at 60 and 80 mg/L, respectively. There was a peak value with an increase of potassium permanganate dosage. It indicated that the amount of potassium permanganate was comparatively cost-effective and powerful at 40 mg/L. Besides, the COD removal efficiency was also achieved the peak value of 54.2% at 40 mg/L of potassium permanganate and it decreased to 46.9% at 60 mg/L. The above proved that the optimal dosage of potassium permanganate was 40 mg/L and the concentration was kept in the following study.

Effect of Electrochemical Pretreatment Time. The effect of electrochemical pretreatment on the potassium permanganate degradation was also investigated as a function of pretreatment time, which is presented in Fig. 3. It can be observed that the absorbance at 254 nm decreased with an

increase of the pretreatment time, indicating that the longer the wastewater was pretreated, the more organics was degraded by the subsequent potassium permanganate oxidation due to the pretreatment process. Meanwhile, the removal of COD increased with the increasing pretreatment time which proved the effectiveness of electrochemical pretreatment as well. From Fig. 3, the COD removal efficiencies at pretreatment time of 60, 120 and 180 min reached 54.2%, 66.8% and 66.1%, respectively. Notably, there was an optimal electrochemical pretreatment time for the subsequent potassium permanganate.

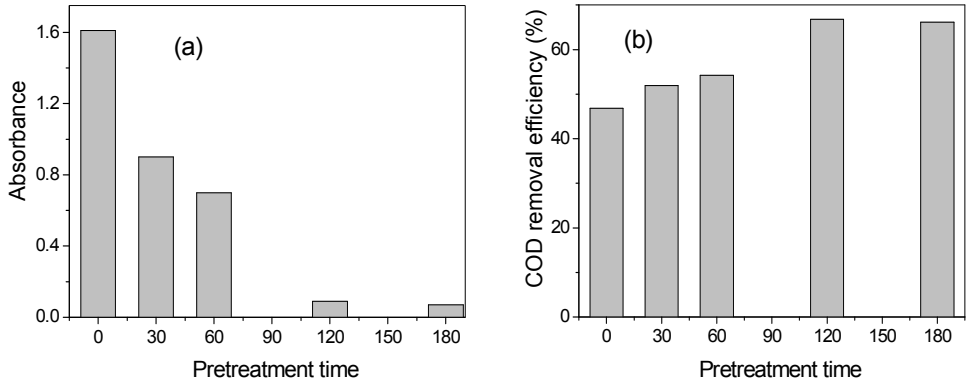


Fig. 3 Absorbance at 254 nm (a) and COD removal efficiency (b) as a function of electrochemical pretreatment time for the degradation of pharmaceutical wastewater by potassium permanganate

Effect of Ferric Chloride and Aluminium Chloride. In order to make clear if the electrochemical pretreatment is effective, the effect of flocculants such as $FeCl_3$ and $AlCl_3$ was also investigated. They were introduced into the reaction system after the pharmaceutical wastewater was treated by potassium permanganate. As presented in Fig. 4, the absorbance at 254 nm was decreased from 1.61 without $FeCl_3$ to 1.37 with 40 mg/L of $FeCl_3$, while it increased to 1.91 at 80 mg/L of $FeCl_3$. Similarly, the COD removal efficiency reached 63.9% at 40 mg/L of $FeCl_3$ which was also the highest efficiency. This indicates that there is an optimal $FeCl_3$ dosage in terms of both color removal and COD removal efficiency.

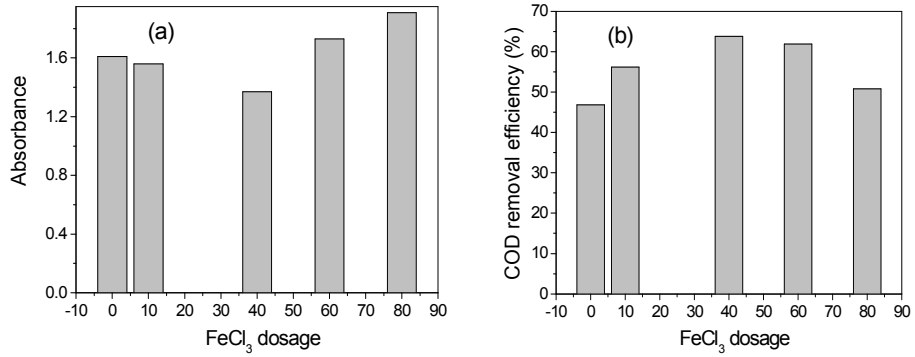


Fig. 4 The absorbance at 254 nm (a) and COD removal efficiency (b) as a function of $FeCl_3$ dosage for the degradation of pharmaceutical wastewater by potassium permanganate

Fig. 5 demonstrates the addition of $AlCl_3$ on the degradation of pharmaceutical wastewater by potassium permanganate. Differently, the absorbance at 254 nm for the $AlCl_3$ dosage of 10, 40, 60 and 80 mg/L achieved 1.43, 1.09, 0.87 and 1.13, respectively. The highest COD removal efficiency of 62.6% was observed at 60 mg/L of $AlCl_3$. These also suggest the existence of an optimal $AlCl_3$ dosage for the combined treatment of the pharmaceutical wastewater with potassium permanganate.

Compared with the highest COD removal efficiency of 54.2% for the potassium permanganate oxidation alone, the peak value for COD removal by electrochemical pretreatment, $FeCl_3$ and $AlCl_3$ treatment reached 66.8%, 63.9% and 62.6% respectively. The COD removal efficiency by electrochemical pretreatment is still a little higher than $FeCl_3$ and $AlCl_3$. Considering the easy operation of electrochemical oxidation and the addition of $FeCl_3$ and $AlCl_3$, electrochemical pretreatment becomes more cost-effective.

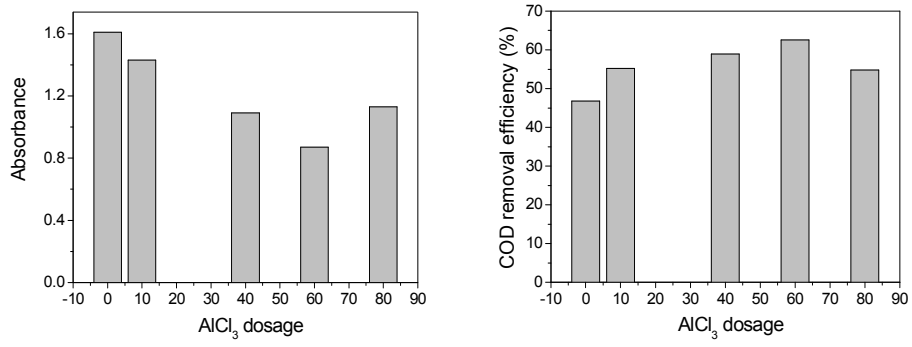


Fig. 5 The absorbance at 254 nm (a) and COD removal efficiency (b) as a function of $AlCl_3$ dosage for the degradation of pharmaceutical wastewater by potassium permanganate.

Conclusions

In order to enhance the treatment effectiveness of pure potassium permanganate oxidation, the pharmaceutical wastewater was pretreated by electrochemical oxidation, or by the addition of $FeCl_3$ and $AlCl_3$ after potassium permanganate oxidation. Both electrochemical pretreatment and flocculation were capable of help to reduce the organics efficiently. Electrochemical pretreatment has a great degradation efficiency and proved to be more cost-effective. Electrochemical pretreatment is expected to be a suitable method to assist the pharmaceutical wastewater treatment.

Acknowledgements

The authors would like to thank the support by the research programme from education department of Henan province (2010B610010).

References

[1] R. P. Schwarzenbach, B. I. Escher, K. Fenner, et al, Science, 313 (2006) 1072.
[2] V. K. Sharma, Chemosphere, 73 (2008) 1379.
[3] R. Andreozzi, L. Campanella, B. Fraysse, et al, Water Science and Technology, 50 (2004) 23.
[4] K. Ikehata, N. J. Naghashkar, M. G. El-Din, Ozone Science & Engineering, 28 (2006) 353.
[5] M. C. Dodd, M. O. Buffle, U. V. Gunten, Environmental Science & Technology, 40 (2006) 1969.
[6] J. Jiang, A. Panagoulopoulos, M. Bauer et al, Journal of Environment Management, 79 (2006) 215
[7] S. Esplugas, D. M. Bila, L. G. T. Krause, et al, Journal of Hazardous Materials, 149 (2007) 631.
[8] L. Huang, D. Yu, Application of UV-Vis Spectra in Organic Chemistry, Science Press, Beijing, 1988.

© (2012) Trans Tech Publications, Switzerland
doi:10.4028/www.scientific.net/AMM.238.409

Experimental Study of Ultrafiltration of Eutrophicated Source Water in Combination with Sand Filter and Biological Contact Oxidation

Fazhan Li [1,a] , Dong Chen [1,b] and Xiwu Lv [2,c]

[1]Institute of Environmental and Municipal Engineering, North China Institute of Water Resources and Electric Power, Zhengzhou 450008, China

[2]Department of Environmental Engineering, Southeast University, Nanjing 210096, China

[a]lifazhan2000@sina.com,[b]chendong@ncwu.edu.cn,[c]xiwulu@public1.ptt.js.cn

Keywords: ultrafiltration; water-dropping aeration; biological contact oxidation; eutrophication.

Abstract. The experiments of ultrafiltration of Taihu Lake water with sand filter and water-dropping aeration biological contact oxidation combinations were evaluated. The experiment results show that under the conditions of the average water temperature was 19.8°C and the HRT of the biological contact oxidation was 1.5h, the removal rates of turbidity, ammonia nitrogen, COD_{Mn} and algae by technological purification process were 99.1%, 85.2%, 53.6% and 98.7% respectively. As a comparison, the removal rates of turbidity, ammonia nitrogen, COD_{Mn}, algae, UV_{254} by routine purification process respectively were 96.6%, 16.3%, 35.8% and 95.5% separately in Wuxi Chongshan waterworks at the same water temperature. Under the conditions of approximately equivalent in investment and running expenditure by technological and economical analyses, the efficiency of technological purification process is higher than that of routine purification process.

Introduction

With the development of economy and accordingly the increase of pollution, water resource are being used widely both in range and degree. Absence of water resource is very severity, and water quality and ecology environment are gradually deteriorated. The water resources absence is correlative compactly with water ecology environment, and it becomes restricting impact of influencing the continuable development of economy. In Taihu lake, for example, algae bloom frequently occur and algal cells cover the entire body of water, this has led to the waterworks cease working and residents have no water to drink [1]. While eutrophication of Taihu Lake water, the water quality was serious deteriorate, especially dissolved small molecules organic matter. According to the reference, the ratio of dissolved organic matter DOC and total organic COD_{Mn} was 88% in Taihu Lake water [2]. The proportions of DOC and UV_{254} which molecular weight less than 4000 Daltons were 61% and 62% respectively. This was led by the slow removal of organic pollutants and ammonia nitrogen in routine purification process. Water chlorination process has not been effectively inactivated the source of parasite resistance but also formed pathogenic microorganisms of organic halides, this causes greater harm to human health, also the safety of drinking water becomes more difficult to be secured. The tap water was not compatible with the existing water quality standards and develop new purification process was exigent.

To replace the traditional purification process and to apply the membrane technology is a hot topic both in China and abroad. Membrane separation is smaller size, effluent quality is better and automation degree is higher. UF membranes can get rid of parasite eggs and polio virus -the smallest virus. This shows that removal turbidity and disinfection of drinking water can be fully realized with UF membranes. The UF membranes also have less sensitive to feed concentration fluctuations. The removal rate of soluble small molecules such as ammonia removal efficiency is not high in UF membrane unit. In order to ensure the safety of drinking water, taking corresponding measures is necessary. Biological treatment technology is the most effective and the most economical method to removal dissolved small molecules such as ammonia nitrogen in drinking water [3, 4].

Experiment

Water Quality. Water quality indexes of Taihu Lake (near Wuxi Chongshan plant) during experiment shown in Table 1.

Table 1 Water quality indexes of Taihu Lake

Water quality indexes	Range	Average	Water quality indexes	Range	Average
Temperature (^oC)	17.4~22.2	19.8	NH_3-N (mg/L)	1.86~4.79	3.27
pH	7.3~8.2	7.7	COD_{Mn} (mg/L)	3.33~5.87	4.24
DO (mg/L)	4.4~10.2	8.1	Algae (10^6/L)	8.0~9.8	9.0
Turbidity (NTU)	14.0~170.0	42.7	UV_{254} (cm^{-1})	0.084~0.126	0.103

Experimental Device. Choice "water-dropping aeration biological contact oxidation - sand filter - UF membrane " as pilot process.

Water-dropping Aeration Biological Contact Oxidation. Removal of dissolved organic matter and ammonia nitrogen on the role of microbial metabolism. In this experiment, the characteristics of the water itself dissolved oxygen is higher and pollutants concentration is lower. By way of water dropping to aeration is a bright spot in the test. Raw water was pumped to a higher level and then drop in three steps. This aeration manner not only satisfies the required oxygen of microbe, but also avoids to purchase aeration equipment, as a consequence, the power consumption and operating costs is reduced, and the operation becomes simple.

Sand Filter. Withholding the shedding biofilm, and removal most of the suspended solids and macromolecules organic from water, by doing this, the membrane flux can be improved. Filter media is quartz sand (size 0.5-1.2mm). The thickness of media layer is 0.7m and the thickness of support layer is 0.4m.

UF Membrane. The role of UF membrane was to retention small flocs and to remove residue suspended solids and part of organic, and further improve water qualities. The membrane in test was offered by Hainan Lisheng water purification technology company. The type of UF is LG0650× 1-B and the material of membrane is PVC alloy compression ultrafiltration membrane. The effective area of membrane is 13m2. And Cutting molecular weight is 100,000 Daltons. The type of filter is terminals and flux of production is 0.5-1m^3/h.

Technological Purification Process. The pilot test was carried in Wuxi Chongshan waterworks in the edge of Taihu Lake landscape. The results of experiment compared with the same period effluent quality of routine purification process. The purification process is divided as coagulation – flotation - filtration - disinfections.

Technological purification process is shown in Fig. 1. Taihu water was direct pumped to the Biological Contact Oxidation (BCO) and water was dropped from BCO in three steps. The height of water dropping was 0.5m, 0.4m and 0.4m respectively. The effluent of BCO flowed into middle-tank one, and then pumped into sand filter. Sand filtration column was carried with down flow manner. The effluent of sand filtration flowed into middle-tank two. The water in middle-tank two is the inflow of ultrafiltration membrane and the backwashing water of sand filter. The operation mode of membrane was carried with exterior pressure manner. It's means membrane surface water was filtered into the hollow fiber membrane and then outlet. Filtered water was flowed into production tank. And the tank is also the backwashing tank of membrane.

BCO was filled with elasticity-padding. The volume of filler were 0.53m^3, 0.51 m^3 and 0.53 m^3 respectively in three stages BCO. The total control of hydraulic retention time was 1.5h. The average effect of oxygen transfer to water was 0.46mg/L, 0.68mg/L and 0.47mg/L. The dissolved oxygen in BCO ranged of : 5.8~11.9mg/L, 4.5~11.4mg/L and 4.8~11.7 mg/L. And all are in aerobic conditions. BCO bottom was equipped with sullage trough. The sullage was discharged once every 2-3 days. Sand filter filtration rate was 6~7m/h and each 24 hours backwashing. The time of backwashing was 25min. Intensity was 5.7 L / (m^2.s). UF runs with dead-end and intermittent operation manner. Concentrated water discharges once every 40 minutes and every two hours for water backwashing. Backwashing flow was 1800L/h and lasted 2 ~ 3 min.

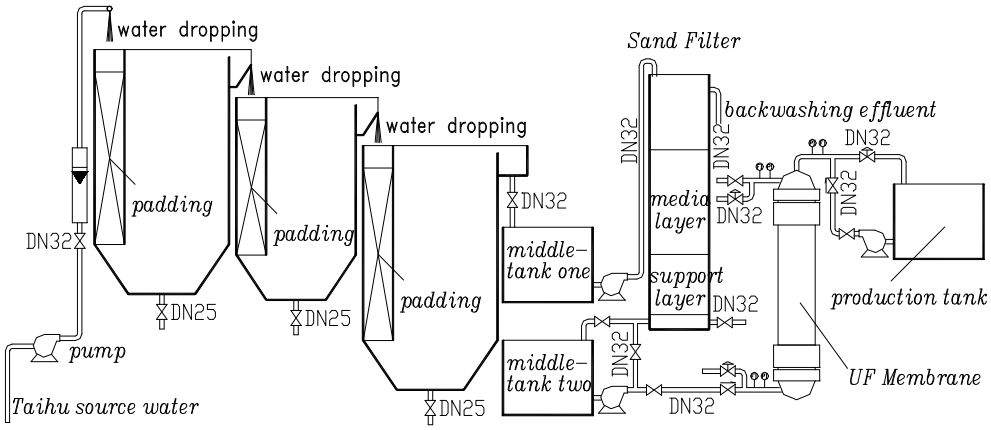


Fig. 1 Technological purification process

Experimental Results and Discussion

Removal Rate of Turbidity. As shown in Fig. 2 (where TPPE = technological purification process effluent, RPPE= routine purification process effluent), the turbidity of technological purification process effluent (TPPE) was consistently less than 0.5NTU. And the average removal rate of turbidity was 99.1%, while the turbidity of routine purification process effluent (RPPE) was range of 0.8~2.2NTU. The average removal rate of routine purification process reached 96.6%. This shows that the effluent turbidity of technological purification process is less than that of routine purification process. The results of experimental confirmed that the membrane filtration had superiority in turbidity removal.

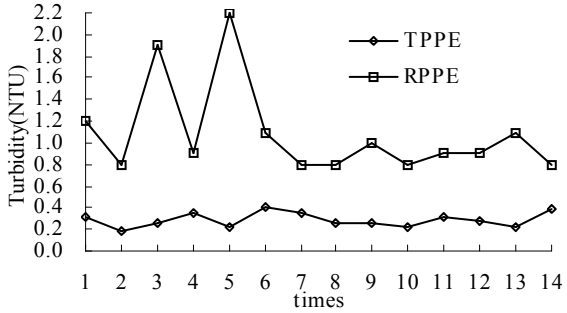


Fig. 2 Comparison of effluent turbidity between technological and routine purification processes

Removal Rate of NH_3-N. The concentration of ammonia nitrogen was higher and ranged from 1.86mg/L to 4.79mg/L in the raw water (RW). As shown in Fig. 3, the technological purification process effluent ammonia nitrogen was generally less 1.81mg/L, and the average was 0.56mg/L.The average removal rate was up to 85.2%. But at the same period the routine purification process effluent often is higher than 1.52mg/L, and the average was 2.75mg/L. The average removal rate was only 16.3%. This showed that the routine process was poor for ammonia nitrogen removal, which resulted the excessive use of disinfectants, and this has threatened water safety.

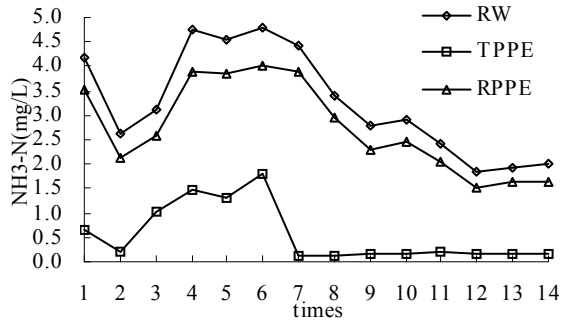


Fig. 3 Comparison of effluent NH_3-N between technological and routine purification processes

Removal Rate of COD_{Mn}. Organic matter, especially natural organic matter (NOM), has drawn great attention in water treatment throughout the world since the 1980s. Natural organic matter, defined as the complex matrix of organic material present in natural waters, significantly affects many aspects of water treatment, such as the performance of unit processes (i.e., oxidation, coagulation, and adsorption), application of disinfectants, and biological stability [5]. One fraction of NOM, humic substances, is widely known as strong disinfection by-product precursors [6].

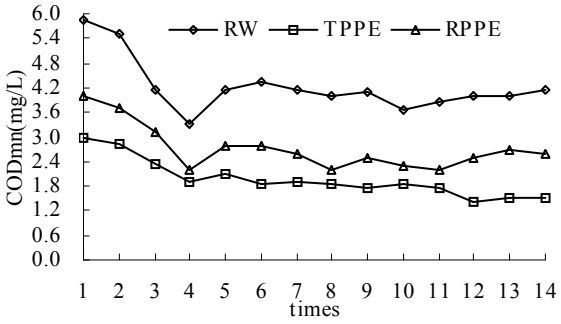


Fig. 4 Comparison of effluent COD_{Mn} between technological and routine purification processes

The concentration of COD_{Mn} was ranged of 3.3~5.9mg/L in period of experiment in Taihu Lake. Average COD_{Mn} was 4.2mg/L. As shown in Fig. 4, the removal rates of COD_{Mn} were not very high in effluent of technological purification process and routine purification process. The effluent COD_{Mn} of technological purification process was fluctuated in 1.4~3.0mg/L. The average removal rate reached 53.6%. In routine purification process, the effluent COD_{Mn} was fluctuated in 2.2~4.0mg/L, the average removal rate was only 35.8%. The effluents of the technological process could meet the "Drinking Water Sanitation Standards" which provides drinking water COD_{Mn} should less 3mg/L.

As being affected most by temperature, the removal of COD_{Mn} in technological process was not high. Another major influence was the moderating hydraulic in BCO and lower stirring intensity to the biofilm, this leads to a considerable number of inorganic particles attached to the surface of filler and serious impacted on the proliferation of biological and obstruction organic pollutants pervasion. It is advisable that to improve the hydraulic condition and to increase stirring intensity in BCO in the after test. The routine process, effluent COD_{Mn} was fluctuated in 2.2~4.0mg/L. To ensure that the effluent COD_{Mn} reaches drinking water standard in waterworks, a new water purification process shall be adopted. Pre-oxidation plus conventional process could provide higher removal rate of organic matter [7].

Removal Rate of Algae. The removal of algae by the drinking water industry as well as eutrophication had received dedicated attention in past three decades [8]. Algae is a low and contain chlorophyll plant, which includes visible with the naked eye and with microscope the tiny algae. There were microcystins in algae bodies. When algal cell death and breakdown, microcystins could be dissolved and would endanger the water safety. Lv Xiwu and others [9] in the test found that Paramecium quickly swallowed algae and when Paramecium were more and the removal rates of algae and microcystins were higher, this illuminated that the algae removal and microcystins removal were relativity.

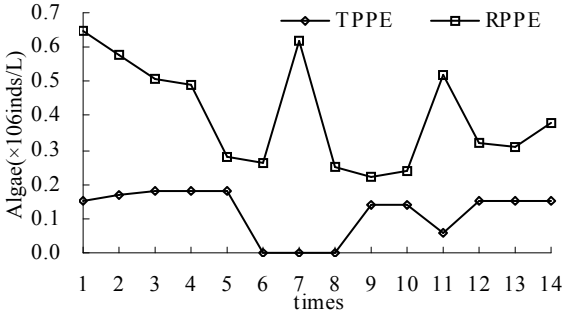


Fig. 5 Comparison of effluent algae between technological and routine purification processes

Removal algae could improve the drinking water safety (Fig. 5). In the raw water, algae concentration was 8.0~9.8×10^6 individuals /L (an average was 9.0×10^6 individuals/L). The effluent of the technological process were 0~0.18×10^6 individuals /L (an average was 0.12×10^6 individuals /L) and the routine process were 0.22~0.65 ×10^6 individuals/L (an average was 0.40 ×10^6 individuals /L). The removal rates were as high as 98.7% and 95.5% respectively.

Conclusions

The experiments of ultrafiltration of Taihu Lake water with sand filter and water-dropping aeration biological contact oxidation combinations were evaluated. The results showed that:

(1) The removal rates of turbidity, ammonia nitrogen, COD_{Mn}, algae, by technological process were 99.1%, 85.2%, 53.6%, 98.7% respectively under the conditions of the average water temperature was 19.8 ^oC and the HRT of the biological contact oxidation was 1.5h. While the removal rates of turbidity, ammonia nitrogen, COD_{Mn}, algae by routine purification process were 96.6%, 16.3%, 35.8%, 95.5% respectively at the same water temperature. The efficiency of technological process was higher than that of routine purification process;

(2) Water qualities of the technological process effluent could meet the Drinking Water Sanitation Standards, and Economic analysis showed that the investment and running costs were approximately equivalent about the two purification process with same scale.

Acknowledgements

The authors would like to thank the support by the starting fund for talents of North China University of Water Conservancy and Electric Power.

References

[1] L. Mu, C. Chen, S. Yu, et al, Investigation study on the content of microcystion in Tai lake and methods for microcystion treatment, China Public Health, 16 (2000) 803-804.

[2] B. Dong, D. Cao, J. Fan, et al, Examination of molecular distributions of dissolved organic compounds in natural water, Water & Wastewater Engineering, 26 (2000) 30-33.

[3] H. Ye, J. Xu, The problem of ammonia nitrogen in drinking water, China Water & Wastewater, 16 (2000) 31-34.

[4] K.H. Lim, H.S. Shim, Operating characteristics in aerated submerged biofilm reactor for drinking water treatment, Water Science and Technology, 36 (1997) 101-108.

[5] A. Matilainen, N. Lindqvist, S. Korhonen, et al, Removal of NOM in the different stages of the water treatment process, Environment International, 28 (2002) 457–465.

[6] P.C. Singer, Humic substances as precursor for potentially harmful disinfection by-products, Water Science and Technology, 40 (1999) 25-30.

[7] C. Chen, X. Zhang, W. He, et al, Comparison of seven kinds of drinking water treatment processes to enhance organic material removal: A pilot test, Science of the Total Environment, 382 (2007) 91-102.

[8] M.C. Steynberg, K. Adam, A.J.H. Pieterse, An algal monitoring protocol: The strategic link between reservoir and treatment process, Water Science and Technology, 37 (1998) 153-159.

[9] X. Lu, I. Yuhe, G. Ding, Degradation of microcystis viridis and microcystins with biological reactors, China Environmental Science, 19 (1999) 138-140.

© (2012) Trans Tech Publications, Switzerland
doi:10.4028/www.scientific.net/AMM.238.414

Research on the Effect of Gas Leaking and Gas-Supplementing Measurements of Air Cushion Surge Chamber

Guojie Luo[1,a], Yongsheng Hu[2,b] and Kun Huang [1,c]

[1]North China University of Water Resources and Electric Power, Zhengzhou 450011, China;

[2]Yellow River Engineering Consulting Co. Ltd. ,Zhengzhou 450003, China

[a] luogj2005@sina.com, [b] 964917998@qq.com, [c] 351232607@qq.com

Keywords: air cushion surge chamber; underground structure; hydropower design.

Abstract. Air cushion surge chamber is a water-engineering measurement different from the ordinary measurements and there is great development in 21th century in China. Aimed at the air leakage and supply measurements, the research of engineering layout, run-control methods and air-supplementing measurement are held in this paper, it can be the reference for the designer.

Introduction

In order to decrease the pressure of water hammer in the high-pressure tunnel, satisfy the requests of engine groups adjusting in the system of long pressure water channel, the pressure-adjusting room is usually built in the conjecture between the pressure leading tunnel and pressure tunnel. The basic type of pressure-adjusting room is divided to simple surge type, throttled surge type, water-chamber type, overflow type, differential type and air-cushion type.

For the diversion power station whose slope is from the top to the bottom of mountain, if the height of the mountain body is not satisfied, the measurement of air cushion surge chamber can be considered as the emphasis.

The air cushion surge chamber is formed by the high pressure air in the air room, using the closed gas compression and expansion characteristics to reflect the water hammer wave and water level fluctuations in the indoor inhibition.

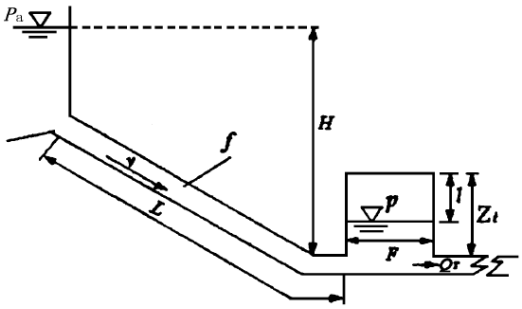


Fig. 1 Sketch map of the air cushion surge chamber

The air cushion surge chamber was first used in the Driva Water Station built in 1973 in Norway, and later was used by Jukla, Tafjord etc. 9 stations till 1989 in this country. But later, except Norway it is not used popularly, only one was used in a water station on Moose River in 1987 in US.

This technology is developed rapidly in China from the beginning of 21th century. There are 7 water stations on the operation which use this technology and other 2 are under construction. Table 1 shows the technical parameters of air cushion surge chamber on the operation or under construction at the end of 2011 in China.

Main advantages: ① not limited by the configuration of earth, it can be closed to the hydropower house as possible in order to decrease the pressure of water hammer pressure; ②compared to the ordinary surge shaft, the extent of fluctuation of water level of the air cushion surge chamber is relatively small, which can decrease the height of surge chamber to a great extent, and the period of fluctuation is short, which makes the engine group run smoothly; ③ according to the experience of Norway, bricks should not be used or used little in the air cushion surge chamber and water tunnel, so

the investment can be decreased; ④ the adjusting straight well and slope well of pressure tunnel are omitted, and the construction difficulty is decreased, the length of road is also reduced, the environment and plants are protected, finally the engineering cost decreases to a great extent.

Table 1 Main technical parameters of air cushion surge chamber in China

Name	Ziyili	Xiotiandu	Jinkang	Muzuo	Yinping	Jinping	Yesanhe	Gangquhe	Dagangou
Installed capacity (MW)	2×65	3×80	2×75	2×50	2×50	2×50	3×25	2×67.5	2×10
Rated head (m)	445	361	458	262.7	254.4	412	238	283	70
Design discharge (m^3/s)	32.44	77.7	37.4	43.02	53.7	27.72	24.24	53.92	33
Length of diversion tunnel (km)	9.37	6.03	14.49	12.10	8.99	8.37	8.49	11.24	5.14
Operation time	Dec. of 2004	Nov. of 2005	Apr. of 2006	Oct. of 2007	Jul. of 2009	Under-construction	Apr. of 2010	Under-construction	Jul. of 2000
Chamber size (m×m×m) (length × width × height)	112× 10× 13.9	80×16 ×16.5	80×9.6×15.9	69.6× 10.6× 16.8	98.6× 10.6× 16.3	112×10 ×13.9	Cylinder type φ14m×55m	110×11 ×15.5	Cylinder type φ10m×14m
Design pressure of chamber (MPa)	3.25	3.75	4.65	2.9	2.82	4.87	2.76	3.2	3.8
Surrounding rock classification	Two-Mica Granite (Class Ⅱ~Ⅲ)	Plagioclase granite	Quartz diorite (Class Ⅱ to Ⅲ)	Quartz phyllite (Class Ⅱ to Ⅲ)	Granite (Class Ⅱ to Ⅲ)	Limestones and dolomites (Class Ⅱ to Ⅲ)		Pyroclastic rock (Class Ⅱ to Ⅲ)	
Close gas type	High pressure grouting + water curtain		Sandwich type ladle + Equalizing pipe		Inside-hanging steel shell + flat-pressing chamber		Sandwich type ladle + Equalizing pipe	Reinforced concrete shell liner steel	High pressure grouting + concrete lining
Air leakage (Nm^3/min)	45/6.7	20	1.5	0.2	0.44				Air supply every year 7.5~10h

Main disadvantages: ① the request to the quality of earth is high, water and gas leakage is not permitted; ② air-compressor to supplement is needed, the cost of operation is high.

The harm of air-leaking in the air cushion surge chamber is great, when the amount of air leaked is big, the cost of air-compressor operation increases, which affect the smooth operation of water power generating system. When the leakage is huge, the amount of supplements provided by the air-compressor is not satisfied, the air-cushion room is completely filled with water, the function of pressure adjusting room will be lost totally, and the power station is not able to produce electricity.

Engineering Layout

The air cushion surge chamber is usually located to the height of 500-1000m upstream along the hydropower house. In the 2-D layout, it is flexible. In most stations of China, only one tunnel is built, but in Norway usually caves are built and they are connected with each other along the circle, for example, Kvilldal Water Station in the Fig. 2 and Fig. 3.

The air cushion surge chamber is a system, besides the air room there are also room communication cave, water curtain room, air room connection cave (well), power station, air compressor room, pump room and control room etc. The location of these rooms and plug take great effect to the air leakage of the air room.

According to the experience of the air cushion surge chamber on operation, the best location of these rooms and the air room are located along the two sides of the diversion tunnel. With the block of the high pressure water in the diversion tunnel, the air in the air room is blocked from leaking to the free surface of these caves and rooms. The distance between the free surface of these caves and rooms and air room should be long enough to extend the seepage tracking of the air room.

The width of the cave of the air cushion surge chamber is usually 8 to 12 meters, and the height is 12 to 16 meters, so the scale of the cave is not big. It is not a big issue to excavation, shotcrete, support and lining construction in the class I and II surrounding rock.

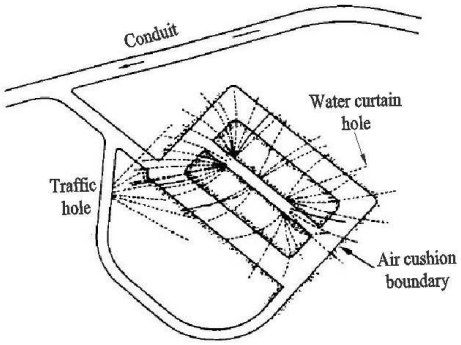
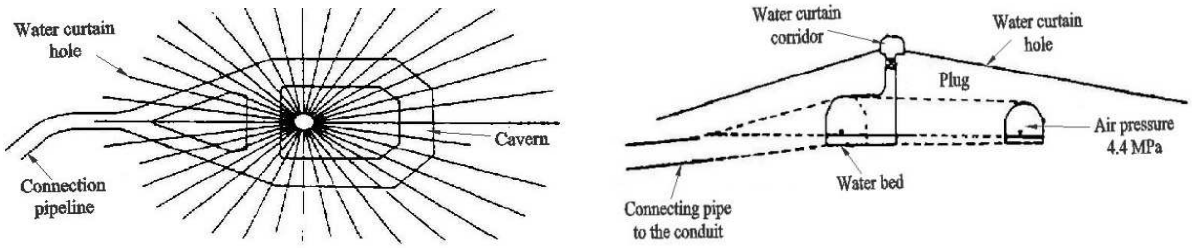


Fig. 2 Layout drawing of the surge chamber of Kvilldal hydropower station in Norway



(a) Planar graph (b) Elevation drawing

Fig. 3 Layout drawing of the surge chamber of Torpa hydropower station in Norway

The Closed Type and Air-leaking Operating of the Air Cushion Surge Chamber

When the power station runs, the air in the air room is request not leaking to the outside. But it is not possible that no absolute air leaks outside. There are 2 reasons, one is that the air dissolved in the lower layer of water under the air cushion, it consists 3 to 10 percentages loss of the compressed air, the effect of it is not obvious. The second is that the air leaks out from the cracks of the rock in the caves, the extend is determined by the soak property of the rock.

The relationship of the operation between the closing and leaking of air cushion surge chamber is that of prevention and adjusting. They develop along with each other, and the relative technology is developed continuously.

Because of the lack of the experience in the research and applicant of the air cushion surge chamber, although some gas-leaking measure is considered, some big problems happened in the operation of the projects either in China or Norway.

For example, the Kvilldal power station in Norway, when it ran in 1981, the gas leakage reached 4 Nm^3/min. The water curtain was installed in 1983, 47 water curtain caves were built in total, the diameter is 51cm, the pressure of the water curtain is 0.3 to 0.5 MPa higher than that of the air cushion, the leakage of gas almost disappeared. The principle of the water curtain is to manually increase the underground water pressure along the air curtain, i.e. to set up series of drilling holes connected to the water pumps, to fill with high pressure water to prevent the pressure gas in the air room from leaking outside.

The Ziyili Project in China, although at the beginning of design the high pressure concrete filling and water curtain were included, the effects of the application is not ideal due to the design experience and the earth conditions etc. The initial gas leakage reached 45 Nm^3/min. After research, the complicated measurements of remedy concrete filling technology were adopted. One is the ultra-fine concrete and epoxy resin are used to the concrete filling, and the other one is to operate high-pressure concrete filling with the water curtain holes, after the completion of concrete-filling, the water curtain hole were re-drilled, the gas leakage reduced obviously, but the leakage still reached to 6.7Nm^3/min.

The steel shell is tried being used in the Jinkang power station, the “Hamburger” type steel shell was adopted, the result is much better than that of the water curtain. The Muzuo power station also used this gas-closing type. But the engineering and projecting of “Hamburger” type steel shell is so complicated that leads the higher cost of building.

The "Hamburger" type steel type was updated in the Yinping power station, the inside-hanging steel shell and flat-pressing chamber were used, the cost of project decreased greatly, and the procedure of construction was also simplified to enough extent. The limitation of engineering experience was remedied, the big gas leakage problem in the environment of sophisticated zone of earth is resolved, the request of leakage property to the rock was decreased, which makes it possible to apply the air cushion surge chamber widely.

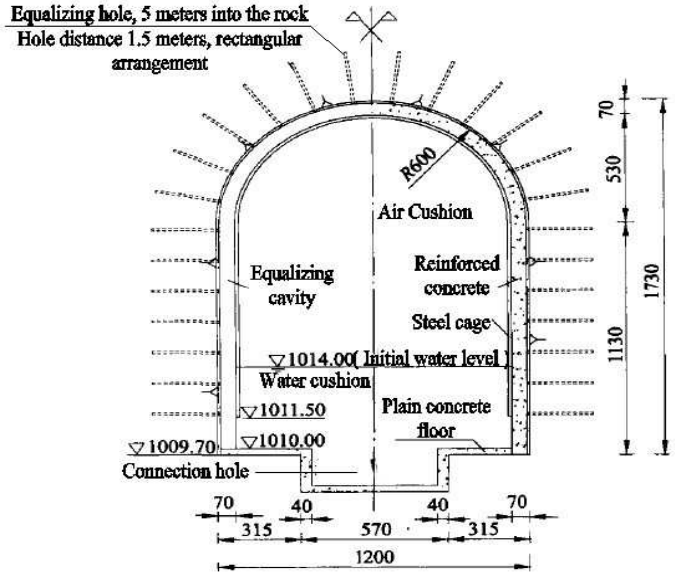


Fig. 4 Section of the air cushion surge chamber's of Yinping power station

The Remedy Measurement of Air-cushion Pressure-adjusting Room

The water level and gas pressure are usually controlled by three models :① equal water level, ② equal gas pressure, ③ equal PV valve. Although the former twos are equal to the third one within normal power-generating operation, the adaptability is poor to the different operation conditions, the air compressor and gas-expulsion vale are needed to operate constantly, which gives the big trouble to the operation control. While the third one considers all the water level and gas pressure variation, it can bring some advantages in the real operation control.

The Choice of Gas-supplementing Equipment in the Air Room

The Choice Rules of Gas-supplementing Air Compressor. At first, the following parameters are needed consideration:

(1) The gas leakage amount in the air-cushion pressure-adjusting room

(2) The gas amount needed to be supplemented.

(3) The continuous operation time and internal time of supplementing gas compressor.

The supplementing gas amount depends heavily on the initiating value of gas-supplementing gas compressor. All of the followings must be considered when the gas-supplementing gas compressor is chosen: the control mode of air-cushion gas-adjusting room, the continuous operation time and internal time of supplementing gas compressor.

The Determination of Gas-supplementing Gas Compressor. If the control mode in the air cushion surge chamber keeps constant i.e. PV keeps unchanging, the working time of the gas-supplementing air compressor is calculated according to the following formula:

$$T = \frac{P_0 V_0 - P_1 V_1}{10(Z\frac{Q_r}{K_h} - \sum q)} \tag{1}$$

In the formula, T is the working time of the gas compressor, h, usually 5 days are considered. P0 is the initial gas design pressure in the air cushion surge chamber, m water pole; V_0 is the initial gas volume in the pressure-adjusting room, mm^3; P_1 is the gas pressure of air cushion surge chamber when gas is supplemented, m water pole; V_1 is the gas volume when gas is supplemented, m^3; Z is the amount of the gas-supplementing gas compressors on the operation; Q_r is the gas-injecting ability of the gas-supplementing gas compressor, Nm^3/h; $\sum q$ is the leakage amount in the air cushion surge chamber, Nm^3/h; K_h is correction parameter of the height above sea level.

According to the above formula, the gas-injecting amount and gas pressure in the pressure-adjusting room are calculated, and the related gas-supplementing air compressor can be chosen. The Ziyili power station chose two $3m^3$/min, 4MPa gas-supplementing gas compressors. Two $3m^3$/min, 4MPa gas-supplementing gas compressors are used in Xiaotiandu power station.

Conclusions

Compared to the ordinary pressure-adjusting room, the air cushion surge chamber holds great unique advantages. It will be developed greatly in China with the development of conventional water power stations and water-pumping power-reserved stations. Especially with the big requests of the environments, the water power will be developed further in the future. The development and application of the air cushion surge chamber will bring more benefits to the economy and the society.

References

[1] D. Liu, L. Suo, etc. al, Hydraulic characteristics and operation control of air-cushioned surge tank of dagangou hydropower plant, Journal of Hydroelectric Engineering, 3 (2003) 95-100.

[2] J. Hu, J. Zhang, H. Wang, Review of application research on air cushion surge chamber in hydropower plant, Water Resources and Power, 25 (2007) 60-63.

[3] B. Wang , J. Zhang, X. Gong , X. Li, The Operating Characteristics of the Air Cushion Surge Chamber, Yellow River, 28 (2006) 23-27.

[4] W. Lu, G. Liu, C. Liu, Application of innovation and discussion of the air cushion surge chamber in China, Water Resources and Hydropower Construction, 6 (2011) 89-92.

© (2012) Trans Tech Publications, Switzerland
doi:10.4028/www.scientific.net/AMM.238.419

Study on Construction Technology of Geogrid Treatment for Slope of Swelling Rock

Ying Gao [1,a], Tinghua Zhao [2, b] and Jie Bao [3, c]

Henan Water&Power Engineering Consulting CO.,LTD.,Zhengzhou 450016,China

[a] gaoying1971@yahoo.com.cn ,[b] zhaotinghua@sina.com.cn, [c] baojie@hnsl.gov.cn ,

Keywords: geosynthetic reinforcement technology, channel slope, material, construction equipment and procedure; standards and testing for construction.

Abstract. Combined with the Luwangfen test section in the Middle Line of SNWT, the geosynthetic reinforcing technology which is an efficient treatment measure for channel slope in expansive soil region was studied by in-situ experiment. The raw material, operating sequences, standards and testing for construction were systematically researched and summarized. The results provide valuable reference for the similar project construction.

Introduction

As an effective way of slope reinforcement, geosynthetic reinforcement technology is widely used in the slope construction. One-way earthwork grille construction technique is widely used in canal slope construction. The earthwork grille has high modulus of elasticity, high tension strength, good coherence with soil and fine durability, so it has been used for reinforcing the retaining wall, steep bank slope, filter pack and geoweb-grass protection engineering. Combined with Luwangfen test section in the Middle Line of SNWT, the technical of earthwork grille was systematically studied in the paper. And a construction technology for the earthwork grille is introduced. It can provide referential experience to the same type of engineering [1-3].

Basic Facts of Test Section

Geotechnical grille and excavate material (expansive rock) were backfilled and compacted by layer, which is used to protect slope in Luwangfen test section. The backfilling thickness in the middle and weak expansive rock test section is respectively 2.0m and 1.5m. Pave a leveling layer with coarse sand which is about 5 mm thick on the geotechnical of water-carrying section under the firs berm. And then successively pave polystyrene board, compound geomembrane to anti-seepage and concrete lining. Spray sowing was used to the geotechnical grille above the firs berm.

Firstly, geotechnical grille was manually layered, which was filled by weak expansive rock. And then rolled and molded by bulldozer. Finally, local area was artificially compacted by earth-moving machinery-frog type compacting equipment. After roller compaction, each layer thickness is 50cm. The construction process is shown in Fig.1.

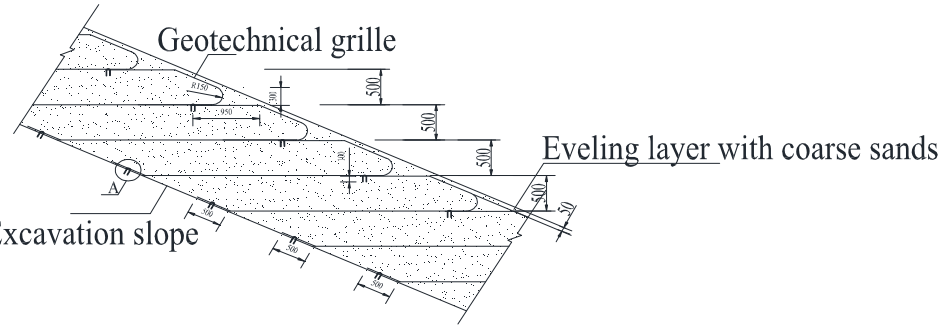


Fig.1 Construction process of geotechnical grille

Material and its Technical Indexes

Main materials: marl rock, geotechnical grille, medium coarse sand and so on.

Grid Material. One-way earthwork grille should be used, which has excellent endurance performance, good anti-temperature property, good workability. Its technical indexes are as follows: material, high density polyethylene; width, great than 1.0m; tensile strength, ≥80kN/m; elongation, ≤12%, strength corresponding the 2% strain, ≥23kN/m; strength corresponding the 5% strain, ≥44kN/m； Carbon black Content, ≥2.0%; creep strength (20^{o}C), ≥20kN/m.

Backfill Material. Marl rock was used for backfill material, whose maximum size should less than 100mm, the content of maximum size great than 5mm should less than 50%, and moisture content should be +1~2%.

Construction Equipment and Procedure

Main construction equipment: bulldozer, 18t vibratory rollers, sifting machine and so on. The procedures are shown in Fig. 2.

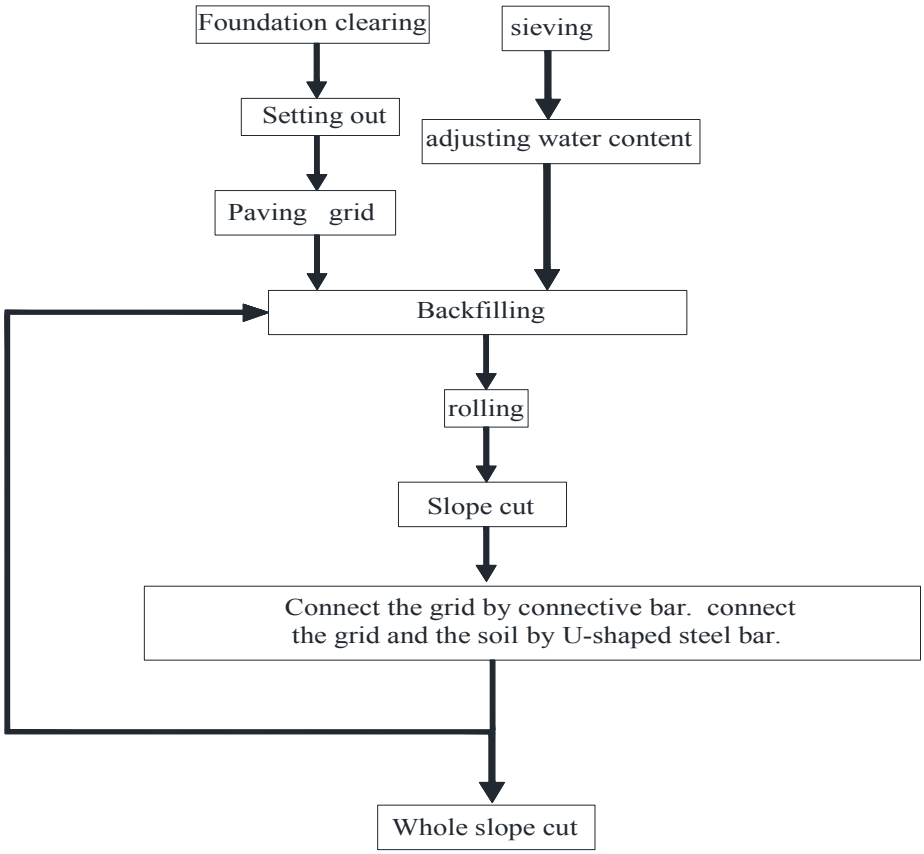


Fig. 2 Procedures of geosynthetic reinforcement technology

Foundation Clearing. The slope was excavated as working drawing requires, and the surface soils of slope and channel bottom were cleared. The base smoothness should less than ±5cm. The surface water should be drained, and the waterlogged soft soil should be replaced by cohesive soil to keep clean and dry.

Setting out. It should be done strictly as working drawing requires.

Paving Grid. Geotechnical grille was manually layered. The grid can be lapped by turn up lap method in slope and the turn up length should great than 100cm. And the grid can be also connected by connective bar. U-shaped steel bar was used for connecting the grid and the soil.

Sieving and Adjusting the Water Content. The water content and free swelling ratio of the soil should be test before backfilling. If the water content less than the allowed, sprinkle water by watering cart and mix well with excavator until the property meet above requirements. The soil should be timely encapsulated by geomembrane after adjusting the water content to prevent it varies again.

Backfilling and Compaction. Backfill and roughly level by bulldozer, and then fine manually level. The surface smoothness should less than ±5cm.

The vibratory roller should roll along the over filling soil in the outer-bank slope to ensure the compactness of backfilling slope after slope cut. And then repeat compact the backfilling. The required travel speed is about 2.0～3.0km/h. Vehicle and compaction machinery are not allowed to move on the grid. The field should be covered by rain cloth when the weather changes or overnight construction.

Standards and Testing for Construction

Raw material, compaction technology, compaction effect and grid tension effect are the key link of geosynthetic grid construction. The raw material should satisfy the request of the relevant technical indicator. Under the condition satisfying the compaction effect requirements, the roller compaction technology can be adjusted and optimized according to the actual need, the parameters of roller compaction construction control is shown in table 1. The slope surface smoothness should less than ±2cm. The relative compactness of leveling layer with medium coarse sand should great than 0.7. The control parameter for the compaction effect is shown in table 2.

Table 1 The parameters of roller compaction construction control

Backfilling material	Compaction technology	Spreading thickness	Water content (%)	Rollers machine	Number of rolling	Travel speed (km/h)
Marl rock	Vibratory Rollers	Advance method	+1~2%	18t vibratory rollers	12	2～3

Table 2 The control parameter for the compaction effect

Material	Maximum size (mm)	Optimum water content (%)	Compactness (%)	Thickness after compaction (cm)
marl rock	<100	+1~2%	95	≤50

Conclusions

The main difficulty of geosynthetic reinforcement technology is many operating sequences, excavated material sieving, adjusting water content, large work quantity of backfilling and slope cut. But the deformation monitoring result of canal slope shows the effect of preventing the deformation of canal slope is obvious, and the deformation is very small. So it can be used for the engineering in which the deformation of canal slope was strictly restricted.

References

[1] L. Miao, S. Liu, Engineering characteristics of expansive soil and engineering measures, Advances in Science and Technology of Water Resources, 4 (2001) 37-40.

[2] C. Bao, On slope stability of expansive soil canal of Middle Route Project of S-N Water Transfer and countermeasures, Yangtze River, 5 (2002) 4-6.

[3] S. Li, B. Shi, Y. Du. Study on the engineering geology of expansive soil in China, Nature Magazine, 2 (1997) 82-86.

© (2012) Trans Tech Publications, Switzerland
doi:10.4028/www.scientific.net/AMM.238.422

Study on Three-dimensional Reconstruction of Macro/meso-structure Evolution of Expansive Soils with CT-triaxial Apparatus

Xian Li [1,a], Shiji Wang [*1,2,b] and Zhenghan Chen [2,c]

[1] College of Engineering and Technology, Southwest University, Chongqing 400716, China

[2] Department of Architectural Engineering, Logistic Engineering University of PLA, Chongqing 400041, China

[a]haoyushi@swu.edu.cn, [b]shjwang@swu.edu.cn (*corresponding author), [c]chenzhenghan47@163.com

Keywords: computerized tomography (CT); three-dimensional reconstruction; structure evolution.

Abstract. A program is used to reconstruct the computerized tomography (CT) images of expansive soils in the manuscript. The physical and mechanical properties of expansive soils can be researched accurately and visually. In the experiment, the CT-triaxial apparatus is used to research the shearing strength of expansive soils with artificial holes in different conditions of suctions and net pressures. The three-dimensional reconstruction is successful and considerable. The principle of program is easy and convenient, and it can be learned fast and directly by those who are not major in computer. This technique will have a better prospect in geotechnical engineering.

Introduction

In tradition, all studies about physical and mechanical properties of soils are based on two dimensional planes [1-3]. But fissures and pores in reality are all three dimension [4]. It is very necessary to research macro/meso-structure in three dimensions, and the 3D model of soils in this article becomes the foundation of the next step of mechanical property.

We use some mathematical methods and a computer processing to deal with the projection data obtained by a physical quantity around objects. Through this process, we can reconstruct the two-dimensional images from surfaces of objects and gain the three-dimensional images which are based on a series of two-dimensional images. This technology is called 'Computerized Tomography', but the prerequisite of this technology is that we should not damage the object structure. Three-dimensional reconstruction of CT can be classified as the direct three-dimensional reconstruction and the three-dimensional reconstruction of two-dimensional CT image sequences. The direct three-dimensional reconstruction is gained by processing and reconstructing three-dimensional volume data (the data is obtained by planar detector), while the three-dimensional reconstruction of the two-dimensional CT image sequences is gained by the application of methods, such as computer graphics, image processing and image visualization.

This article mainly discuss how to do the triaxial testing under different conditions using the expansive soils and research the mechanical property, introduce the MATLAB program of three-dimensional reconstruction [5], and examine the three-dimensional reconstruction effect. There are two objectives: (1) Increasing the artificial holes in expansive soils can simulate the damage of the integrity of the soil, which is due to the organic raw in nature, such as the holes like plant rhizomes and earthworms existing in the soil. Then we research how the holes influence the physical properties and mechanical properties of the soils. CT-triaxial apparatus was applied to research the shearing strength, and it was different from the instrument, which was applied to research the saturated soil's property, in principal of designing and manufacture. A valve of suction and a valve of interior pressure chamber were added to the triaxial apparatus, because this apparatus was applied to research the unsaturated soil's property. (2) After the data of CT images which were from the CT apparatus were arranged and operated by writing a MATLAB program, we did some pretreatment of them, extracted the valuable information and discard that useless information. Then we could success the

three-dimensional reconstruction of CT scanning images which were filmed from different conditions, viewed and determined the physical change of artificial holes in three-dimensional view. Of course, some functions could be utilized properly and some parameters could be calculated and designed continuously by ourselves. Through analysis and comparison of suctions, net confining pressure, and axial strain rate, we concluded the change rule of these factors.

Experiment Summary

Before this experiment, there were various researches and discussions about physical and mechanical properties of the expansive soil, but these methods could only reflect the physical change from a planar, because those researches were based on two-dimensional CT images. If we want to research the physical properties and mechanical properties of the soil samples from the global, we must success the three-dimensional reconstruction of CT, especially for the soil samples with artificial holes.

In this experiment, expansive soils are from Nanyang, where is the beginning of divert water from the south to the north project. According to the geological data, Nanyang basin expansive soil is quaternary unification or updates the next update series and update tasseled different geological era sediments, sedimentary environment is more complex, and it comes from different medium environment. Its physical properties indicators are shown in Table 1.

Table 1 Physical property index of sample

Soil grain gravity	Dry density	Water ratio	Saturation	Void ratio
G_s	ρd	W_0 (%)	S_r (%)	e_0
2.73	1.5	24	80	0.82

The initial expansive soil using the soil broken machine became soil powder with less than 0.06 mm diameter after grinding and sieving, and they were put baking oven inside over eight hours. Then add proper water into the soil powder, and it became a soil sample with needed water ratio. The samples were put in moisturizing tanks after mixing. When we need them, we can get them from moisturizing tanks. The diameter of sample is 39.1mm, and height is 80mm. And the dry density is 1.7 g/cm^3, and water ratio is 20%. A special instrument was used to form five thick cylindrical specimens.

The instrument in this experiment is CT - triaxial apparatus for unsaturated soils from the scientific research station of Han Zhong, which is developed in the geotechnical engineering laboratory of Logistics engineering institute. It can be applied to various soil mechanics experiments of unsaturated soil, and we use ProSpeed AI type X-ray spiral CT machine to scan the soil sample. The biggest difference between unsaturated soil triaxial shear apparatus and saturated apparatus is that unsaturated soil triaxial shear apparatus has a double pressure chambers named ‘internal pressure chamber and external pressure chamber’. If internal pressure chamber and external pressure chamber are filled with distilled water, they can make sure that their stiffness will be approaching to infinite. Then the displacement and deformation will not have huge change due to the huge change of net confining pressure, and it can greatly reduce the error of test. This instrument is shown in Fig. 1.



Fig. 1 The CT - three workstation triaxial apparatus

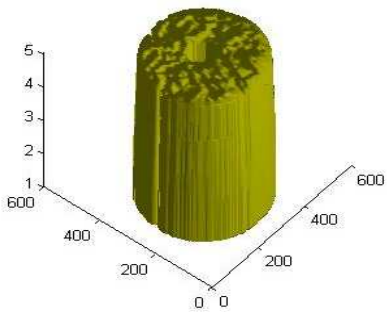


Fig. 3 Three-dimensional effect image

On the one hand, air enters the inside pressure room through the volume change tube and inner pressure valves, and it forms the confining pressure around the samples, on the other hand, the gas flows from the top to the bottom of pressure room through the suction valve. The difference value of confining pressure and suction pressure is called 'Net Confining Pressure'. In this experiment, keep the suction pressure 100kPa unchanged, make net confining pressure respectively as 50kPa, 100kPa and 200kPa, and it can constitute three groups of experiments. Then keep the suction pressure 200kPa unchanged, make net confining pressure respectively as 50kPa, 100kP and 200kPa, and it can constitute another three groups of experiments, a total 6 groups of test.

The important experiment equipment is the ProSpeed AI type X-ray spiral CT machine which locates at Nanzheng People' Hospital in Shanxi province and it is made by GE Corporation. This is an advanced high-resolution CT scanner, and has characteristics of good image quality, fast scanning speed, safety and a wide range of applications. A set of scanning parameters is shown in Table 2.

Table 2 The scanning parameters Settings

Voltage (kV)	Electric current (mA)	Time (s)	Thickness (mm)	Amplification coefficient
120	165	2	3	5

This equipment is used as a combination of an unsaturated soil triaxial shear apparatus of Logistics engineering institute, and it can scan six samples by the CT scanning equipment. Each sample can be scanned according to the scheduled labeled thread, and each layer is scanned four times. These four states are respectively 0, 5%, 10%, and 15% of axial deformation. Using scanning CT images and the matching measuring software, we can observe and measure the change of diameters of artificial holes of the samples, and make a three-dimensional reconstruction of these CT images using MATLAB program. Through data processing, further research the change rule of hole diameters in different conditions, and statistical analysis the changes of the average of 6 samples with scanning sequences are shown in Table 3.

Table 3 Average changes of aperture (mm^2)

Sequence / No.	1	2	3	4
1	69.578	68.218	67.67	67.622
2	68.348	65.864	64.642	61.114
3	69.314	59.164	58.348	56.368
4	68.17	57.578	56.108	55.138
5	69.802	56.33	55.18	53.67
6	68.43	54.622	53.208	49.7

Three-dimensional Reconstruction

CT Image Format Conversion. The original CT images are stored in the form of the standard DICOM3.0 and they cannot be recognized by MATLAB. In order to observe the CT images, we ought to translate the original CT images to 256-color BMP images, and use graphics software to do the necessary processes.

The Binary Image Processing. The binary image processing is to set the pixel gray value of the image as 0 or 255, and it also presents the obvious effect of black and white of the images. The 256 brightness levels of the grayscale images by selecting the appropriate threshold still can reflect the overall images and local characteristics. All the gray pixels which are equal or greater to the threshold are determined as attributing to a specific object whose gray value is 255; otherwise the pixels are excluded out from the area. The regional whose gray value is 0 denotes backgrounds or exceptions.

Image Enhancement. Histogram equalization is a non-linear stretching of the image and a re-distribution pixel value of the images, so that it has roughly the same amount within a certain gray-scale. The disadvantage is that the gray-scale of the transformed images reduces and some certain details have disappeared. For example, the histogram of some images has a peak, but the contrast ratio will increase after treated. Histogram equalization can be realized by using function 'histeq' in MATLAB. The soil CT images after equalization and histogram are shown in Fig. 2.

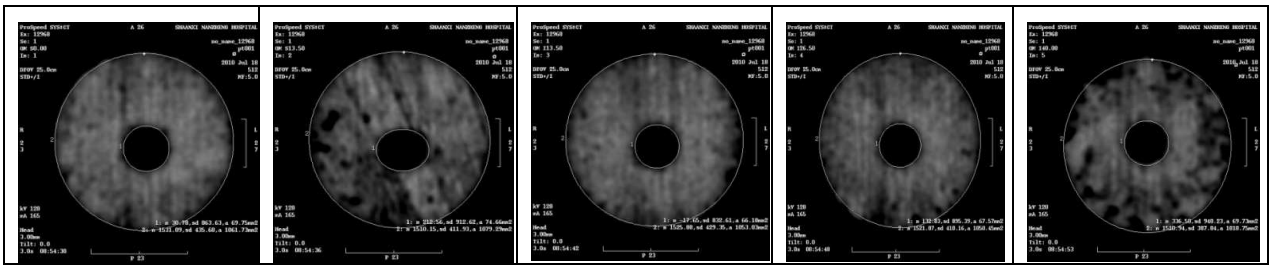


Fig. 2 The CT images after pretreatment

Three-dimensional Reconstruction of CT Images. (1) The collection of reconstruction data. Construct the N pieces of existing geotechnical data, and obtain a data set, which is named D. The matrix is denoted as $x \times y \times n$.

(2) Reconstruction of data pre-processing. The three-dimensional data set D conducted and adopted by the above methods has a large volume of data and decelerates in the processing of three-dimensional reconstruction, and it may be exceeded in the calculation of memory, so it can have a pre-process of the data set *D* and reduce the amount of data based on the actual situation. [*x y z D*] = reduce volume (*D*,[*a b c*]).

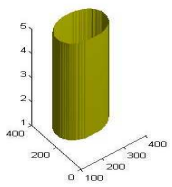
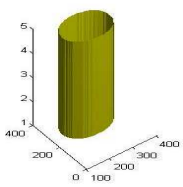
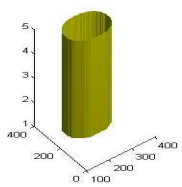
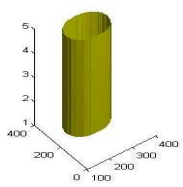
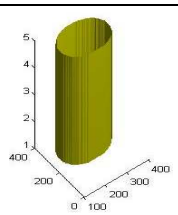
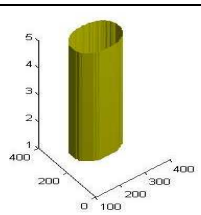
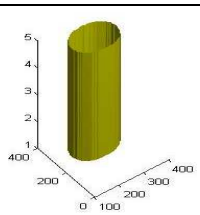
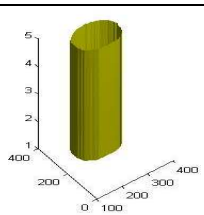
(3) To smooth the data with the "smooth ()" function, *D* = smooth3 (*D*).

(4) Calculate the accumulated data sets in the display plane projection, and use the "isosurface ()" function. To calculate the accumulated data sets in the display plane projection and the isovalue is self-definited based on the actual situation. fv = isosurface (*x*, *y*, *z*, *D*, isovalue). Use the patch () function to construct the debris about reconstruction of three-dimensional structure fragments , and the image's color and light are defined, where fv is the first (4) step to get. p = patch (fv, FaceColor', 'yellow', 'EdgeColor', 'none').

(5) To set the image's color, shadow and display results. Define the image color set using the "colormap()" function. The use of "view ()" function is defined to observe the perspective. The lighting function is used to define and display the image light shadow. Axis equal function is used to define and display the image axis. The daspect function is used to define and show the proportion of the *x*, *y*, *z*-axis. Reconstruct the three-dimensional according to the steps of the three-dimensional, and the result is shown in Fig. 3.

Each three-dimensional graph of the hole was independent extracted so that we could see the physical change of each hole in conditions of different confining pressures, suctions and axial deformations. Since the page was limited, only No.1 and No.2 were given. Their suctions were all 100kP, confining pressures were respectively 50kP and 100kP, and axial deformations were respectively 0, 5%, 10%, and 15%. The 3D reconstruction images of artificial holes are shown in Table 4.

Table 4 The relations of axial strain rate, suctions and net pressures in different samples

No.	Suction/ Net pressure (kPa)	Axial strain rate (%)			
		0	5	10	15
1	s=100 σ=50				
2	s=100 σ=100				

According to the above data and the MATLAB program, we success the 3D model, and these imagines reflect the relations of axial strain rate, suctions and net pressures in different samples.

Conclusions

Through above data and images, we can conclude that: (1) when the suctions and net confining pressure remain unchanged, the size of holes will be diminishing gradually when axial strain rate increases. (2) When the suctions and axial strain rate remain unchanged, the size of holes will be diminishing gradually when net confining pressure increases. (3) When net confining pressure and axial strain rate remain unchanged, the size of holes will be diminishing gradually when suctions increases. If suction, net confining or axial strain rate increases, the size of holes will be diminishing gradually. When the soil sample completed the concretion course, in the triaxial compression test, confining pressure around the sample is always larger than the suction in the sample, and the sample will be smaller with the holes contracted constantly in the diameter direction. (4) The change of the size of holes was not distinct through observing as the water ratio of sample was too small, so in order to gain distinct change, it is necessary to increase the water ratio of samples.

Using the technique, we can analyze 3D change rule quantitatively of the internal fissures and pores in the soils under the action of the external load. It is helpful for us to understand the internal meso-structure of different soils more clearly, especially for expansive soils and loess, and it is meaningful to research evolution of meso-structure, expanding of cranny and flow patterns of pore water. This technique will have a better prospect in geotechnical engineering.

Acknowledgment

The authors are grateful for the financial supports of Natural Science Foundation of China (NSFC) (10902091) and Natural Science Foundation Project of China SWU (SWU208010). The research is also supported by the Fundamental Research Funds for the Central Universities (XDJK2010C014).

References

[1] H. Chen, W. Ding, F. Dang, X. Yin, Journal of China Institute of Water Resources and Hydropower Research 4 (2006) 1-5.

[2] F. Dang, X. Yin, W. Ding, H. Yang, Chinese Journal of Rock Mechanics and Engineering, 24 (2005) 22-26.

[3] Z. Chen, Z. Lu, Y. Pu, Chinese Journal of Geotechnical Engineering, 23 (2001) 4-9.

[4] B. Schäffer, M. Stauber, T. L. Mueller, R. Müller, R. Schulin, Geoderma, 46 (2008) 183-189.

[5] Y. Xu, X. Wu, Y. Hu, Computer Engineering, 27 (2001) 12-16.

© (2012) Trans Tech Publications, Switzerland
doi:10.4028/www.scientific.net/AMM.238.427

The Influence of Concentration of Pore Water Solution on the Swelling Characteristics of Expansive Soils

Jingchao Jia [a], Huan Li [b] and Qingtao Bi [c]

School of Resources and Environment, North China University of Water Resources and Electric Power, Zhengzhou 450011, China

[a] jjcdut@yahoo.cn, [b] lihuan@ncwu.edu.cn, [c] bijingtao@ncwu.edu.cn

Keywords: expansive soils; bentonites; swelling pressure; swelling strain; concentration of pore water solutions.

Abstract. The influences of pore water solution concentration on the swelling properties of expansive soils were studied using the constant volume swelling pressure experiments and swelling ratio experiments under load. The results indicate that the swelling pressures decrease with the increase of solution concentration. Two specimens made by the same solutions concentration were immersed into solutions with two various concentrations to prepare specimen, one is smaller than the concentration of solution, and the other is same to that. The results showe that the swelling pressures and the swelling strains of two specimens are very close. The analysis on the exist state of the pore water shows that the experimental results are agree with the osmotic pressure theory.

Introduction

The study of influencing factors on the swelling behaviors of bentonites usually concentrated in the mechanical factors imposed on soils, for example the vertical load applied on the sample, and the physical character of soils, for example initial dry density, initial water content. Fewer works have been done on the effects of chemical characters of soil pore solutions. Alawaji[1]investigated in the solution concentration effects on the swelling potential, swelling pressure and swelling time.

In previous experiments, the solution concentration to prepare the soil sample is equal to that to inundate the samples. In praticle engineering, however, the rain and the ground water have certain concentration of ions, so the solution concentration in the expansive soils are various. Hence, the swelling characteristics of the expansive soil are studied when it experienced different solution concentration, with the solution concentrations to prepare the samples regarded as the previous concentraion, and the inundating solution concentration as the later concentration. Finally, the experimental results are analyed based on the osmotic theory.

Materials

The materials used in this investigation were obtained from Xirang Mine in Liaoning Province, China. The physical character index are determined and showed in Table 1.

Table 1 The characteristic indexes of XiRang bentonites

Liquid limit (%)	Plasticity index (%)	Optimum moisture content (%)	Maximum dry density (%)	PH
126.1	39.6	39.6	1.180	9.47

Because the exchangeable cations in the bentonites are mainly Ca^{2+}, the solutions to prepare and to inundate the sample are all $CaCl_2$ solutions, avoiding the influences of cation exchanging on the swelling.

Experimental Procedure

The solutions with various concentrations (0.001, 0.01, 0.1 and 1mol/L) were sprayed into the bentonites and mixing with a spoon until the desired water content of 40% was reached. Then the soils were placed in plastic bags and sealed to avoid water loss and allowed to cure in desiccator at room temperature for 24 h. Specimens were prepared by statically compacting the soils directly in the confining ring with diameter 60mm and height of 20mm at dry density of 1.1 g/cm^3 and moisture content of 40%. The experiments were conducted with the modified consolidation apparatus, on which a steel screw was installed to ensure that the constant volume swelling. Before the start of the experiments, the loading about 1 kPa was applied vertically on the sample to guarantee a better contact between permeable stone on the sample and screw. Then the solution was injected to the consolidation box.

Results and Discussion

The variations of swelling pressures of bentonites with time are shown in Fig.1. It can be seen that the primary swelling completed within about 2h. The influence of the solution concentration to the time is merely.

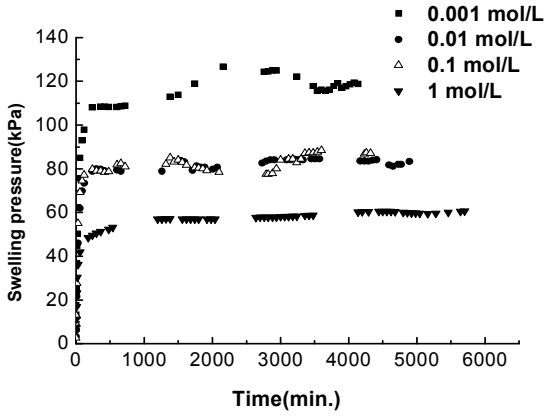


Fig. 1 Swelling pressures vs. time for Xirang bentonites inundated with various $CaCl_2$ concentrations

If the injection solution concentration is 0.001mol/L for each specimens prepared with various concentrations of solutions, the results are shown in Fig. 2. Similar to the results in Fig.1, the primary swelling in Fig. 2 also completed within 2h.

The variations of the swelling pressure with the solution concentration are showed in Fig. 3. The swelling pressures are decreased with the increasing of solution concentrations. It is similar to the results obtained by Alawaji[1]. It should be noted that if the inundating solution concentrations are lower than the ones to prepare specimens, the swelling pressures are not always larger than the ones that the concentrations of solutions to prepare and to inundate the specimens are equal to each other. It seems not coinciding with Gouy-Chapman double layer model[2-4]. Because according to the osmotic pressure theory, which is one of the theoretical fundamentals of the double layer model, the swelling pressure could be represented as[5].

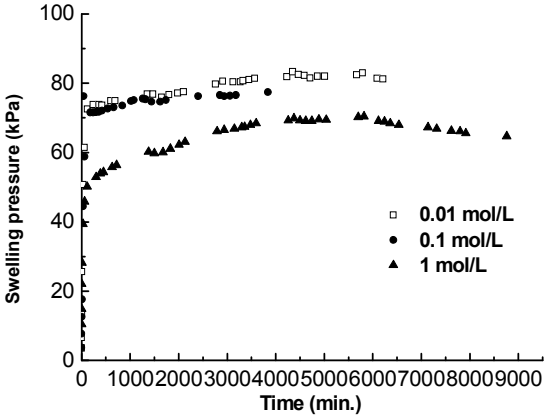


Fig. 2 Swelling pressure vs. time for Xirang bentonites prepared with various $CaCl_2$ concentrations inundated in 0.001 mol/L $CaCl_2$ solutions

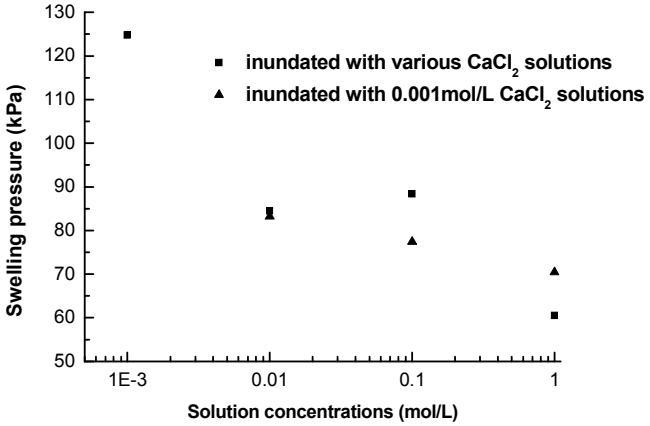


Fig. 3 Swelling pressure vs. CaCl2 concentration for Xirang bentonites

$$\pi = kT\sum\left(n_{iA} - n_{iB}\right) \tag{1}$$

Where k is the Boltzmann constant, T is the absolute temperature, n_{iA} and n_{iB} are the solution concentrations of the i type ion between and around the clay layers respectively, moreover, the n_{iA} has relation with the concentration of solution to prepare the specimens, and the n_{iB} is generally believed as the concentration of inundating solution. In the majority of investigations, the concentrations of solutions to prepare and to inundate the specimens are same.

From Eq.1 we can know that if the concentrations of inundating solutions are lower than the ones used to prepare the sample, the swelling pressure should be larger. But the experimental data indicate the predictions by Eq. 1 seem not correct. The reason for these results could be explained as follows: When preparing the specimens, the water molecules of the solution penetrate into the clay layers, and some solutions left out around the clay layers, shown as Fig. 4. Although the inundating solution, viz. bulk solution, is lower than the original solution to prepare the specimens, the concentrations of the solutions around the clay layers are not necessarily affected by the bulk solutions. So the swelling pressures in the circumstances that the inundating solution concentrations are lower than the ones to prepare the specimens are not always larger than the cases that the concentrations of solutions to prepare and inundate the specimens are equal to each other.

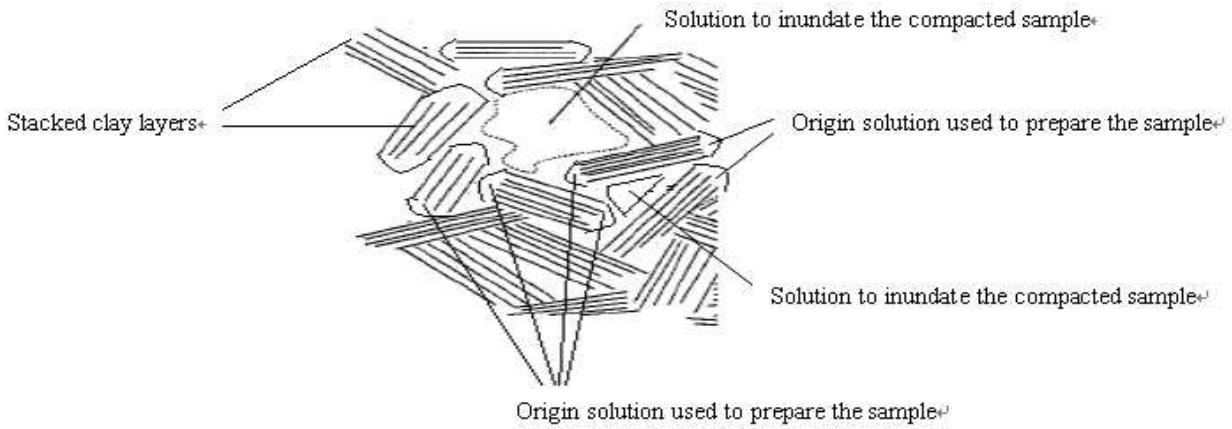


Fig. 4 Schematic representation of the bulk solution among the soil pores and the solution around the clay layers

Conclusions

In this paper, the effects of the concentrations of soil pore solutions on the swelling behaviors are studied. The emphasis is on the conditions that the concentrations of injected solution are lower than that used to prepare the sample. The results indicate that the swelling pressure will continue a long time, but the primary swelling completed within 2h. The swelling pressure decreases with the increasing of concentration of pore solution. If the concentrations of injected solution are lower than that used to prepare the sample, the swelling pressures are not always larger than the ones that the concentrations of solutions are same when used to prepare the sample and to inundate the sample.

Acknowledgments

The work was supported by NSFC (41140030), the Leading Talent Training Plan for the Innovative Scientific Talent, Zhengzhou (10LJRC185); SRF for ROCS, SEM; the Scientific Foundation for the High-level Talent of NCWU (001322).

References

[1] H. A. Alawaji, Swell and compressibility characteristics of sand-bentonite mixture inundated with liquids. Applied Clay Science, 15 (1999) 41-430.

[2] A. Sridharan, D. Choudhury, Swelling pressure of sodium montmorillonites, Geotechnique, 52 (2002) 459-462.

[3] S. Tripathy, A. Sridharan, and T. Schanz, Swelling pressures of compacted bentonites from diffuse double layer theory, Canadian Geotechnical Journal, 41 (2002) 437-450.

[4] H. Komine, N. Ogata, Prediction for swelling characteristics of compacted bentonite, Canadian Geotechnical Journal, 33 (1996) 11-22.

[5] J.K. Mitchell, Fundamentals of Soil Behavior, John Wiley & Sons, New York, 1976.

© (2012) Trans Tech Publications, Switzerland
doi:10.4028/www.scientific.net/AMM.238.431

Study on the Impact of Long-term Immersion on the Shear Strength of Compacted Lime Stabilized Expansive Soils

Yun Dong[1, 2, a], Weizhong He [1 b] and Baotian Wang [2,b]

[1] Faculty of Architecture and Civil Engineering of Huaiyin Institute of Technology, Huai'an , China.

[2] Key Laboratory of Ministry of Education for Geomechanics and Embankment Engineering, Hohai University, Geotechnical Research Institute, Hohai University, Nanjing, China.

[a] hadyun@163.com, [b] 944194836@qq.com, [c] btwang@hhu.edu.cn

Keywords: embankment; lime stabilized expansive soils; long-term immersion; shear strength.

Abstract. To offer or predict the shear strength of compacted lime stabilized expansive soils after long-term immersion for the slope analysis, the paper carried out direct shear test on the compacted stabilized expansive soils after different immersion time. The test results show that long-term immersion has significant impact on the shear strength of the lime stabilized expansive soils, the shear strength reduced sharply after soaking, but the shear strength tends to a stable value about 60%~70% normal strength while soaking is longer than 50 days. Logarithm model can well fitted the sketch of φ, c and immersion times within 50 days, which may be used to predict the shear strength of the stabilized expansive soils quickly.

Introduction

Many highways along the river were constructed on riverbank to reduce the cost. But many of these embankments need to be reconstructed for the deterioration of itself with the increasing of the using time. In these reconstruction projects, part of the embankment will always immerged, and that will cause shear strength attenuation of the filler especially in expansive soil areas. Furthermore, the attenuation may cause the failure of embankment. Therefore, the <Highway Subgrade Design Specifications> [1] in China explicitly stated that in the process of filling embankments along the river levee, we should take care of the effects on the intensity by long-term immersion. The specifications did not illustrate that long-term immersion has what effect on the strength, but clearly defines the minimum CBR strength of the filler, however the shear strength is more important than CBR in slope analysis.

Many scholars proceeded studies on the shear strength of expansive soils after long-term immersion [2-5], and most results considered that long-term immersion will cause shear strength attenuation, the compaction and water content has great effect on the shear strength etc. However, most studies were qualitatively, and were based on rainfall and focused on natural expansive soils but not compacted lime stabilized expansive soils. Therefore, the current results cannot clearly disclose the variation rules of shear strength with the immersion time, and directly used in practical slope analysis.

To explore the variation rules of shear strength of the compacted lime stabilized expansive soils with the immersion time, this paper carried out test study on the shear strength of the compacted lime stabilized expansive soils after long-term immersion, and established a prediction model which can be used to predict the shear strength quickly with the immersion time in practical slope analysis.

Test Scheme

The test scheme consists of stabilized programs of the expansive soils, specimen production and experimental conditions and so on.

Modified Programs. Based on the test results of lime-improved expansive soil, the physico-mechanical property indexes of 5% lime stabilized expansive soils can well meet the requirements as filler, so this paper carried out test study on 5% lime stabilized expansive soils after different immersion time.

Specimen Production. Mixed soil samples to achieve the best moisture content according to the compaction test results, then calculated and weighted the required quality soil sample according to the 96% compaction degree, as shown in formula (1). Finally, adopt static pile in molding the specimen one time.

$$m = 96\% \bullet \rho_{d\max}(1+\omega_{opt}) \bullet v \quad (1)$$

Where ρ_{dmax} is the maximum dry density, ω_{opt} is the optimum moisture content, v is the volume of the cutting ring.

Experimental Conditions. In order to simulate the condition of long-term immersion of the river levee, soaked the specimen entirely in the water (as shown in Fig. 1) after they were produced and curing, after 3days, 7 days, 14 days, 30days, 60 days and 180 days immersion, took the sample out and performed direct shear test according to the current test specifications (JTG E40-2007) [6].



a) moisture curing in a closed status b) soaked entirely in water

Fig. 1 Curing and immersion of specimen

Test Result and Analysis

The shear strengths of 5% lime stabilized expansive soil after different immersion time are shown in Table 1.

Table 1 Shear strength of lime stabilized expansive soil after different immersion time

Immersion time（day）	0	3	7	14	30	90	180
φ（deg）	30	26	25	24	23	23	23
c（kPa）	95	65	54	51	49	43	42

To facilitate data analysis, adjusted normal strength as the result of 0.01 days immersion, and drawn the sketch of φ, c and immersion time based on the test results as shown in Fig. 2.

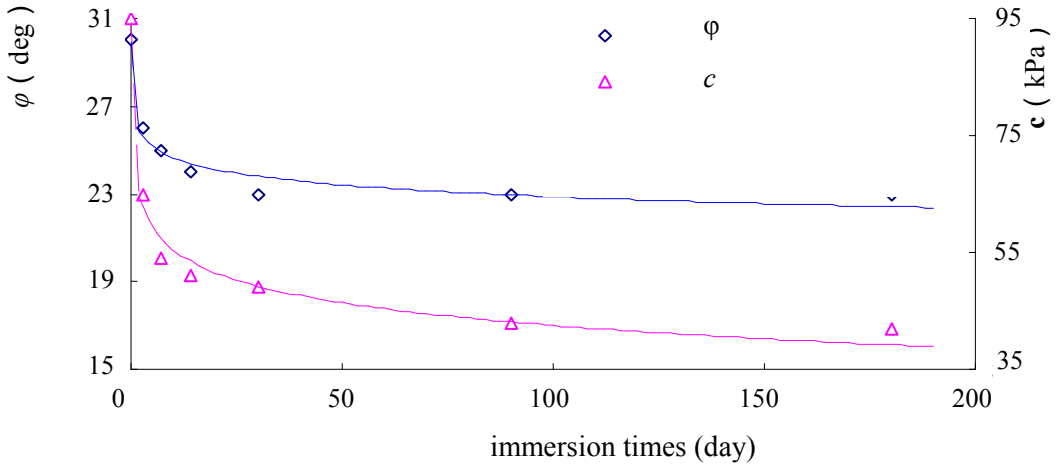


Fig. 2 Sketch of φ, c and immersion times

Test results shown, long-term immersion has significant impact on the shear strength of the compacted lime stabilized expansive soils, especially the first several days soaking. The internal friction angle (φ) dropped from 30° to 24°, a drop of 20%, while the cohesive strength dropped from 95 kPa to 54 kPa, fell more than 40% after soaking 14 days.

The main reason of the shear strength attenuation caused by immersion is the volume swell after water absorption, the specimen cracked in the process of swell, the water infiltrate into the specimen along the fracture, the integrity of the structure declined, further caused the strength attenuation.

But after soaking in water 14 days, the swell becomes smaller, and no more new fracture appeared, the shear strength trend to a stable value. The sketch of φ, c and immersion times shows that the stable value of the internal angle is about 75% while the cohesive strength is about 45% of the normal strength.

Prediction Model of Shear Strength after long-term immersion

In practical engineering, we always need the worst-case shear strength during the slope analysis. So, it is necessary to establish a prediction model of the shear strength. According to the test results, the logarithm model can well fit the sketch of φ, c and immersion times (while immersion times <50 days), the fitting curve was shown in Fig. 2.

The prediction model of the internal angle (φ) and immersion times can be expressed as:

$$\varphi = -0.78\ln(T)+k_1\varphi_0 \quad (2)$$

Where φ is the internal angle of the lime stabilized expansive soil (deg), T is the immersion times (day), k_1 is the test coefficient, it is 0.7~0.8 to lime stabilized expansive soils, the large the normal strength the smaller the k_1. φ_0 is the normal strength before immersion (deg).

The prediction model of the cohesive strength and immersion times can be expressed as:

$$c = -5.6\ln(T)+ k_2\, c_0 \quad (3)$$

Where c is the cohesive strength of lime stabilized expansive soil (kPa), T is the immersion times (day), k_2 is the test coefficient, it is 0.6~0.7 to lime stabilized expansive soils, the large the normal strength the smaller the k_2. c_0 is the normal strength before immersion (kPa).

The shear strength of the lime stabilized expansive soils after long-term immersion can be quickly predicted using the above models, especially after a few times immersion caused by rain or the water level change of the river, while the immersion time less than 50 days. For the shear strength trend to a stable value after long-term immersion, the internal angle should not less than 60% and the cohesive strength should not less than 50% of the normal strength while immersion time more than 50 days.

Conclusions

Long-term immersion has significant impact on the shear strength of the lime stabilized expansive soils.

The shear strength reduced sharply after soaking, but while soaking more than 50 days, the shear strength trends to a stable value which is about 60%~70% of the normal strength.

The sketch of φ, c and immersion times can be well fitted with logarithm model while immersion time less than 50 days, and the prediction models can be used to predict the shear strength of the stabilized expansive soils quickly.

Acknowledgements

This work was financially supported by the Jiangsu University Natural Science Foundation (10KJB170002).

References

[1] JTGD30-2004, Specifications for Design of Highway Subgrades, China Communications Press, Beijing, 2004. (in Chinese)

[2] H. Mi, H. Wang, C. Gao, Rock and Soil Mechanics,9 (2010) 2781-2785. (in Chinese)

[3] H. Hang, S. Chen, Chinese Journal of Geotechnical Engineering, 3 (2004) 422-424. (in Chinese)

[4] S. Chen, C. Zheng, G. Wang, Chinese Journal of Geotechnical Engineering, 6 (2007) 795-799.

[5] M. Yan, Test study on the mechanical properties of lime-treated soils in expansive soil roadbed, Institute of Rock & soil Mechanics Chinese Academy of Sciences, Wuhan, 2010. (in Chinese)

[6] JTG F10-2006, Test Methods for Highway Engineering, China Communications Press, Beijing, 2007. (in Chinese)

© (2012) Trans Tech Publications, Switzerland
doi:10.4028/www.scientific.net/AMM.238.435

Analysis on Collapsibility and Microstructure of Unsaturated Loess Using Fractal Geometry

Fuli Ma[1, a], Mei Wang[2,b], Jing Yang[1,3,c] and Xiaohong Bai[1,d]

[1] College of Architecture and Civil Engineering, Taiyuan University of Technology, Taiyuan 030024, China

[2] College of Mining Engineering, Taiyuan University of Technology, Taiyuan 030024, China

[3]Department of Civil Engineering, Taiyuan Institute of Electrical Engineering, Taiyuan 030013, China,

[a]mafuli0309@163.com, [b]wangmei3312@sohu.com, [c]yangjingd@126.com, [d]bxhong@tyut.edu.cn

Keywords: unsaturated soil; collapsible loess; microstructure; fractal.

Abstract. This paper studies the microstructure of 16 group samples from three different sites of North-west region in P. R. China. Pictures of microstructure were processed with imaging processing program to acquire the geometer parameter and fractal dimension of pores. The range of pores' fractal dimension is between 1.816~1.936. The pore distribution function of unsaturated soil is established based on fractal geometry theory. The pore water distribution of loess under natural moisture is analyzed. The relationships of collapsibility coefficient with fractal dimension and porosity of unsaturated pores are analyzed with the method of regression analysis. A larger fractal dimension represents a more complex pore-structure. The collapsibility coefficient of loess increases with the increase of fractal dimension and porosity of unsaturated pores.

Introduction

China has an extensive deposit of loess, which is mainly found in northwestern China, and sixty percent of which tends to settle uncontrollably due to its internal structural destruction when wetted. This phenomena is defined as water sensitivity, or collapsibility as it is often known in most literature, though, it has also been called 'hydro consolidation' [1]. Water is one of the factors that lead to the settlement of the loess when been wetted. Loess, which has high strength and low compression at natural low water content, will deform uncontrollably and the strength will decrease sharply when the water content increased or immersed in water [2]. The water sensitivity of loess has been the subject of investigation for many scholars [3-6].

Collapsible loess is a typical kind of unsaturation soil. Under the circumstances of low moisture, some pores are full up with water, while some are not. The unsaturated pores are easily to be broken when water immerges in. The focus of this paper is the distribution of the water in pores for collapsible soil at natural moisture. By using Scanning Electronic Microscopy and fractal geometry, the pore distribution of the soil and the relationship of the content of unsaturation pores and the collapsibility were analyzed.

Material and Methods

Soil Used in This Study. Undisturbed loess blocks were taken from three sites in two provinces of China, Huayin County, Tongguan County of Shaanxi Province and Lingbao County of Henan Province, shown in Fig. 1. The main parameters of the soil samples are listed in Table 2.

Preparation of Samples and Acquisition of Image. The specimens for microscopic analysis were taken from undisturbed loess samples, and after drying, the specimens were soaking with cementations material, hardening, cutting, polishing and gilding. The procedure outlined above is reported in literature [7]. The SEM images of the specemen were acquired by using the TM-1000 SEM (Hitachi, Japanese). The geometric parameters of pores, such as maximum diameter, minimum diameter, mean diameter, area and the proportion of the pores in the image, were measured by using the dimensional measurement function of the imaging processing system [8, 9].



Fig. 1 The location of the sites

Fractal Model for Pore Distribution. As a new theory that is mainly used to describe the nonlinear feature in nature, fractal is widely used in theoretical research of soil and rock mechanics and enjoys exceptional advantages in analyzing the mechanical property of unsaturated soil. In fractals, the fractal dimension is considered to be a continuously change fraction less than 3 [10,11]. The integral part of the fractal dimension provides a statement about the graphics in the space. Mandelbrot [12] suggested that fractal geometry could be quantified by measuring the fractal dimension through the following equation:

$$N(r) \approx br^{-D} \tag{1}$$

Where D is the geometry fractal dimension; b is a statistical constant; N(r) is the total number of parts with linear dimension r.

Hausdorff Dimension is the most common method of expressing the fractal dimension and is defined as following:

Let E be a set of points, $I_1, I_2, I_3, \ldots, I_n, I_{n+1}, \ldots$ are a series of open intervals to cover the point set E together, a is a real number greater than zero, δ is the extreme scale of the interval. The Hausdorff Exterior Measure of the points set E is described as Eq. (2).

$$H_\delta^a(E) = \inf\left\{\sum_{i=1}^{\infty} |I_i|^\alpha : \bigcup_{i=1}^{\infty} I_i \in E, |I_i| \le \delta\right\} \tag{2}$$

If there presents a number D_H that makes $H_\delta^a(E) \to 0$ become true where $0<\alpha<D_H$ gives a true statement. Then D_H is considered to be the Hausdorff Dimension of point set E.

A geometry could be divided into $N(\varepsilon)$ units which are self-similar with each other with the scale of ε. The dimension of this geometry is expressed as following:

$$D = -\lim_{\varepsilon \to 0} \frac{\ln N(\varepsilon)}{\ln \varepsilon} \tag{3}$$

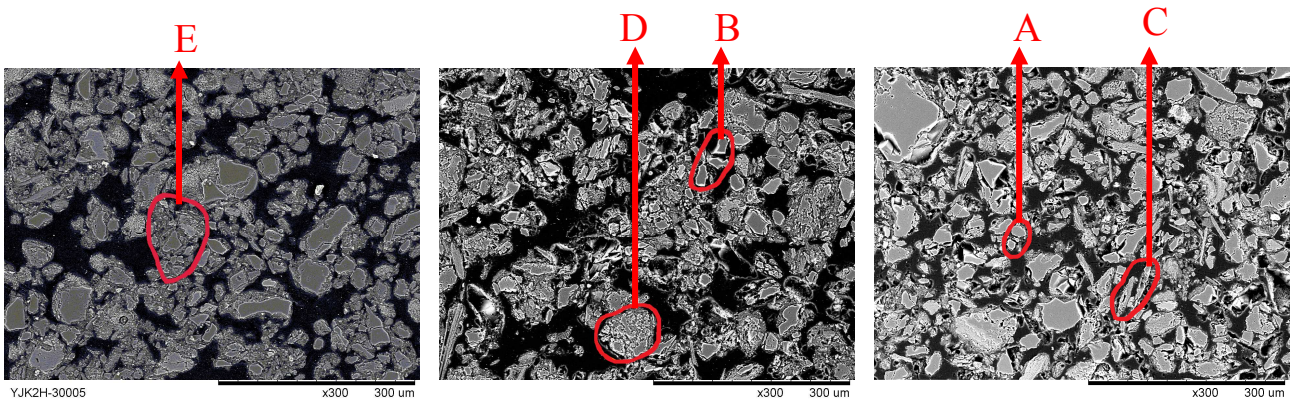
Where ε is calibration, $N(\varepsilon)$ is the result of the mensuration according to ε, D is the dimension of the subject studied [10].

Resulting

Characteristic of Loess Microstructure in Qualitative Analysis. In this study, 432 images were taken in total, 27image per specimen. The microstructural characteristic of the collapsible loess in this study could be summed as following:

(1) The skeleton particles can be classed as single particles and group particles which are cemented together called as domains. The single particles can be classified into three types according to the shape: rounded particles (marked with **A** in Fig. 2), sub-angular particles (marked with **B** in Fig. 2) and strips particles (marked with **C** in Fig. 2). There are two types of domains based on the composite aggregate pattern, one is consist of one large aggregate with many cement particles accumulating on the surface (marked with **D** in Fig. 2), the other is consist of many cement particles cementing together (marked with **E** in Fig. 2).

(2) The pores in the loess may be classified into pores between particles and pores within domain. When the size of the former type of pores is greater than that of particles and the cementation between the particles is weak, the microstructure of the loess would be instability. The loess with such kind of microstructure is easy to collapse when wetted.



(a)Lingbao Loess Magnification (×300)(b)Tongguan Loess Magnification (×300)(c)Lingbao Loess Magnification (×300)

Fig. 2 Microstructure of loess

Analysis of Distribution of Water in Soil. Young-Laplace Formula, that is $\psi=2T\cos\alpha/r$, established the relationship between matric suction ψ and the pore radius r of unsaturated soil. Where T is surface tension, α is the contact angle of water. The shrink film in the interface of water and soil is formed in pores with smaller radius. The matric suction generated by the shrink film is greater than that generated in larger pores. Due to the influence of the matric suction, the smaller pores with high matric suction absorbs more water per volume or even full-filled with water. The larger pores are usually unsaturated or moisture-free. The smaller pores are first saturated with water [13].

Soil pores distribution meets the fractal model Eq. (2) in terms of statistics. Assuming pores as spheres, and r is the radius, and b is the statistic constant, the total volume of pores in soil could be expressed as following:

$$V_V = \int_0^{d_{\max}/2} N \cdot 4\pi r^2 dr \tag{4}$$

Where $d_{\max}$ is the maximum diameter of the pore, substitute Eq. (1) into Eq.(5) could establish the express of the total volume of pores:

$$V_V = \int_0^{d_{\max}/2} br^{-D} 4\pi r^2 dr = \frac{4\pi b}{3-D}\left(\frac{d_{\max}}{2}\right)^{3-D} \tag{5}$$

The diameter of the pores fulfilled with water is different in soil with different water content. If the maximum diameter of pores fulfilled with water is expressed by d, the total volume of water in soil is

$$V_w = \int_0^{d/2} br^{-D} 4\pi r^2 dr = \frac{4\pi b}{3-D}\left(\frac{d}{2}\right)^{3-D} \tag{6}$$

Then, the saturation of soil could be expressed as following:

$$S_r = \frac{V_w}{V_v} = \left(\frac{d}{d_{\max}}\right)^{3-D} \tag{7}$$

So, the maximum diameter of saturated pores corresponding to the water content would be described as following:

$$d_0 = S_r^{\frac{1}{3-D}} \cdot d_{\max} \tag{8}$$

Measurement of Fractal Dimension. In order to calculate the fractal dimension, the target image obtained using the SEM was clipped into square with the size of 960×960 pixel using image processing system. Then the image was meshed by orthogonal line grids with decreasing size. The

number ($N(\varepsilon_i)$) of the meshes containing pores of the image was counted for each grid size ε_i and stored in a data list which could be met Eq.(3). Plot all the $\ln N(\varepsilon_i)$ and $\ln\varepsilon_i$ in double logarithmic coordinate and fit the plot into a straight line. (Shown in Fig.3) The slope of the fitting line will be K, the fractal dimension could be expressed as $D=-K$.

Table 1 Fractal dimension of the soil pore

Serior number		1	2	3	4	5	6
Huayin	D	1.850	1.936	1.888	1.875	1.831	1.842
	R^2	0.993	0.989	0.997	0.995	0.990	0.998
Serior number		7	8	9	10	11	
Tongguan	D	1.889	1.856	1.824	1.825	1.854	
	R^2	0.989	0.994	0.993	0.990	0.988	
Serior number		12	13	14	15	16	
Lingbao	D	1.834	1.834	1.823	1.816	1.834	
	R^2	0.995	0.989	0.989	0.993	0.995	

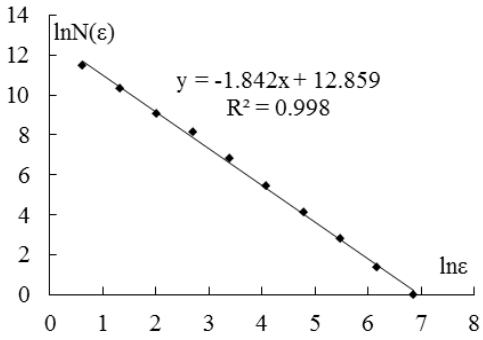


Fig. 3 $\ln N(\varepsilon)$~$\ln\varepsilon$ curve

Table 2 Main physical index of the samples and the parameters and results of the calculation

Sites	Serial number	G_s	Pore Ratio	ω %	ω_L %	ω_P %	I_P	S_r /%	δs 200(kPa)	D	d_{max} [μm]	d_0 [μm]	n(d>d_0)
Hua-yin	1	2.71	0.490	19.3	28.6	17.6	11	55	0.024	1.850	252	169	0.2133
	2	2.71	0.515	17.1	28.5	17.6	10.9	44	0.052	1.936	305	170	0.2713
	3	2.7	0.505	13	26.3	16.5	9.8	34	0.035	1.888	253	121	0.2206
	4	2.7	0.506	13.3	26.4	16.5	9.9	35	0.041	1.875	381	186	0.2602
	5	2.71	0.504	16.2	26.7	16.7	10	43	0.015	1.831	227	130	0.1952
	6	2.71	0.477	17.9	26.6	16.6	10	53	0.012	1.842	192	126	0.1433
Tong-guan	7	2.7	0.522	10.9	26.4	16.5	9.9	27	0.081	1.889	332	135	0.2711
	8	2.7	0.493	10.3	26.4	16.5	9.9	29	0.035	1.856	332	145	0.2631
	9	2.71	0.503	10.7	26.6	16.6	10	29	0.017	1.824	215	95	0.2017
	10	2.7	0.508	13	26.1	16.4	9.7	34	0.012	1.825	216	53	0.1452
	11	2.7	0.484	9.9	26.4	16.5	9.9	28	0.01	1.854	188	43	0.1460
Ling-bao	12	2.7	0.490	9	25.3	16	9.3	25	0.02	1.834	299	119	0.2290
	13	2.7	0.508	10	26.2	16.4	9.8	26	0.019	1.834	225	93	0.2196
	14	2.7	0.497	14.1	26.1	16.4	9.7	39	0.017	1.823	277	150	0.1711
	15	2.7	0.510	16.4	25.6	16.1	9.5	43	0.013	1.816	259	149	0.1719
	16	2.7	0.493	13.2	26.4	16.5	9.9	37	0.009	1.834	250	129	0.1356

Note: 1) $\delta_s=(h_1-h_2)/h_0$, where δ_s is coefficient of collapsibility, h_0, h_1 and h_2 are respectively the height of samples before consolidation, after consolidation and final height after the process of collapsibility comes to an end, If the coefficient of collapsibility of the loess is lower than 0.015, the soil is collapsible, otherwise is not [15]. **2)** G_s, Pore ratio, ω, ω_L, ω_P, I_P, S_r, δ_s are the main physical index of the samples, D, d_{max}, d_0, n(d>d0) are the parameters and results of the calculation.

The measured fractal dimensions are listed in Table 1. The fractal dimension of Huayin loess varies from 1.831~1.936, the average value is 1.870, and the variation range is 0.105. The fractal dimension of Tongguan loess varies from 1.824~1.889, the average value is 1.850, and the variation range is 0.065. The fractal dimension of Lingbao loess varies from 1.816~1.834, the average value is 1.828, and the variation range is 0.018. The SEM image analysis results in this program correlate well with the fractal dimension value 1. 6213~1.8971 obtained by Xu Y. [14] by analyzing SEM image of saturated soft soil.

Calculation of Maximum Diameter of Saturated Pores. The maximum diameters (d_{max}) of the pores of the 16 soil specimens were measured by using the imaging processing system. The maximum diameters of saturated pores (d_0) at natural water content of the 16 specimens were calculated by Eq. (8). The porosity $n(d>d_0)$ of unsaturated pores were determined, all the data are listed in Table 2. All of the maximum diameters of saturated pores are all larger than 100μm, the porosity of unsaturated pores for Huayin loess is the largest in the three types of loess.

Discussion

Relationship of Fractal Dimension and Coefficient of Collapsibility. Fractal dimension is used to describe the complexity of the fractal set and the filling degree of the geometric figure in space. The integer part of the fractal reflects the status of the image in space, non-integer dimension reflects the complexity of the system. The average fractal dimension of Huayin loess is the largest, which may imply that the pore marginal of Huayin loess is irregular, and the pore structure is more complex. Fig. 2 shows the microstructure image taken from Huayin loess and it proves the foregoing statement. Fig. 4 is the plot of the value of fractal dimension and coefficient of collapsibility and the data was fitted with a straight line. The coefficient of collapsibility increases with increasing of fractal dimension. The linear fitting equation could be expressed as δ_s=0.465D–0.834. The increase of fractal dimension means the pore structure is more irregular and unstable.

Relationship of Unsaturated Pores and Collapsibility. The unsaturated pore porosity at natural water content and the coefficient of collapsibility were plotted in Fig. 5. With the increase of porosity of unsaturated pores, the coefficient of collapsibility of loess increases nonlinearly. The fitting equation could be described as $n(d>d_0)$=0.073ln(δ_s) + 0.485. This may because the pores with smaller diameters are often saturated and that with larger diameters are unsaturated at natural water content. So, the larger $n(d>d_0)$ and the diameter of unsaturated pores are, the greater the possibility of collapse of loess.

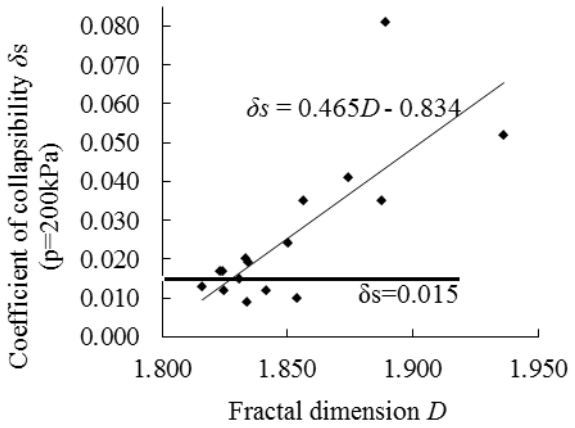


Fig.4 Curve of fractal dimension and collapsibility coefficient

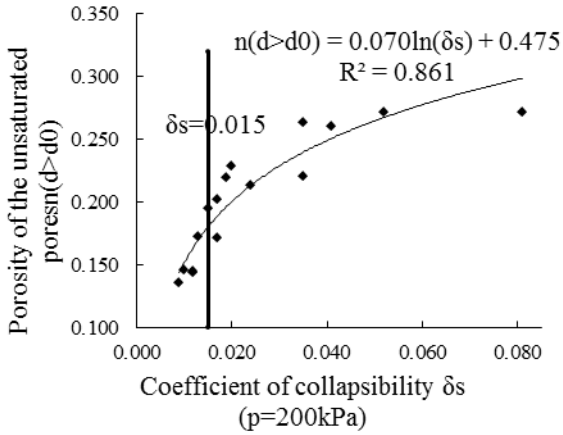


Fig.5 $n(d>d_0)$~δs curve

Conclusions

Based on the qualitative and quantitative analysis on the microstructure of the loess from the three cites, the following conclusions could be drawn. In our investigation, the characteristic of loess microstructure such as the pore characteristic influences the collapsibility of the loess. And the fractal geometry theory is proved to be proper to be used in analyzing the collapsibility of the loess. The relationship of coefficient of collapsibility and fractal dimension of the microstructure image could be described as a linear equation. The coefficient of collapsibility changes with the porosity of unsaturated pores nonlinearly.

Acknowledgements

Authors thank to Mr. Zhang W. for offering the undisturbed soil samples.

This research has been supported by the Project of Natural Science Foundation of China (51178287), Project of Natural Science Foundation of Shanxi Province of China (2010011029) and Research Project supported by Shanxi Scholarship Council of China (2011-026).

References

[1] A M Assallay, C D F Rogers, I J Smalley, Formation and collapse of metastable particle packing and open structures in loess deposits, Engineering Geology, 48 (1997) 101–115.

[2] D. Xie. Exploration of some new tendencies in research of loess soil mechanics, Chinese Journal of Geotechnical Engineering, 23 (2001) 3-13.

[3] M. Zhang, Y. Xie, B. Liu, Analysis of Compression Deformation Characteristics of Loess during Moistening and Demoistening Process, Journal of Hunan University of Science & Technology, 26 (2005) 50-55.

[4] M. Guo, S. Zhang, Y. Xing, Collapse deformation and pore pressure characteristics of unsaturated intact loess, Chinese Journal of Rock Mechanics and Engineering, 19 (2000) 785-788.

[5] M. Liu, Intermittence Moistening test of collapsible loess, Chinese Jounal of Geotechnical Engineering, 1 (1985) 47-54.

[6] X. Bai, P Smart, Engineering properties of Lucheng Loess in Shanxi, Chinese Journal of Geotechnical Engineering, 24(2002) 515-518

[7] M. Wang, X. Bai, J. Yang, Method of Specimen Preparation for Collapsible Loess Microstructure Research, Journal of Taiyuan University of Technology, 3(2010) 283-286

[8] Q. Xu, Y. Zhao; J. Fan, Application of Picture Analyses Technology in Soil Microcosmic Composition Research, Friend of Science Amateurs, 2 (2008) 147-148.

[9] N. K. Tovey, A digital computer technique for orientation analysis of micrographs of soil fabric, Journal of Microscopy, 120(1990) 303-325.

[10] J. Zhang, Fractal, Tcinghua University Press, Beijing, 2011.

[11] A. N. Anderson, A. B. Mcbratney, E. A. FitzPatrick, Soil mass, surface, and spectral fractal dimensions estimated from thin section photographs, Soil Science Society of America Journal, 60 (1996) 962-969.

[12] B. B. Mandelbrot, The Fractal Geometry of Nature, Freeman, New York, 1983.

[13] Y. Xu, D. Fu, Study on the structural strength of unsaturated soils, Engineering Mechanics, 16 (1999) 73-77.

[14] Y. Xu, J. Zhang, W. Li, Research on microstructure fractal features of the saturation soft soil, Rock and Soil Mechanics, 27 (2007) 49-52.

[15] Code for Building Construction in Collapsible Loess Zone, China Building Industry Press, Beijing, 2004.

© (2012) Trans Tech Publications, Switzerland
doi:10.4028/www.scientific.net/AMM.238.441

Study on Reasonable Feature of Compaction Loess with Air Porosities

Jing Yang[1,2,a], Linghao Wang[1,b], Fuli Ma[1,c] and Xiaohong Bai[1,d]

[1] College of Architecture and Civil Engineering, Taiyuan University of Technology, Taiyuan 030024, Shanxi, China

[2] Department of Civil Engineering, Taiyuan Institute of Electrical Engineering, Taiyuan 030013, Shanxi, China

[a] yangjingd@126.com, [b] bjwdxz@126.com, [c] mafuli0309@163.com, [d] bxhong@tyut.edu.cn

Keywords: compaction loess, degree of compaction, dry density, air porosity, water content.

Abstract. The degree of compaction is usually used as the compaction quality and control indicator of backfill in practical project. However, as the degree of compaction is affected by various internal and external factors, its accuracy is difficult to guarantee. In this paper, compacted loess samples were prepared under different compaction energies by normal compaction method. The curves of compression coefficient and dry density, the compression coefficient and porosity of compaction loess samples under different compaction energy are analyzed while the water content is constant. The air porosities of compaction loess samples under different compaction energy and water content are calculated and summed up. The air porosity of compaction loess samples under different compaction energy is more stable than the degree of compaction when the water content is exactly equal to the optimum water content. The rationality of using air porosity as the loess compaction quality control indicator is discussed. It is proposed using air porosity as additional indicator of compaction quality control on the condition of the loess compacted dry density meeting the requirements. The air porosity less than 6.5% is suggested as the additional quality control indictor for region backfill compaction.

Introduction

Filling is used widely in backfill foundation projects of buildings, railways, highways and other subgrades. Backfill usually refers to the stacked soil in human activities. Based on the material composition, density, water content controlled by the standard, backfill compacted in layer is called compacted backfill. The compaction quality of compacted backfill is directly related to the strength and stability of backfill foundation and subgrade. If the quality is not good, it will lead to inhomogeneous deformation, settlement or even destruction of superstructure and road, which will affect their regular service [1].

In current compaction code, the degree of compaction is usually applied as an indicator of testing and controlling the compaction quality of the backfill. Improving the quality of compacted fill by increasing the code of compaction degree has been accepted by the majority of researchers. In the new Code for Design of Highway Subgrade of Chinese Ministry of Transportation, the minimum compaction standards of upper and lower fill were increased by 1% and 3% from the original to ensure the quality of highway construction and reduce the disease of embankment. However, the degree of compaction is affected by various factors such as mechanical properties of soil, water content, compaction thickness, number of compactions, compacting machinery, test equipment, test operators and so on [1]. Such complex factors will inevitably make it difficult to guarantee the accuracy of the degree of compaction. In this paper, the engineering mechanical properties were researched and the air porosity is proposed to be used as an additional indicator for compaction quality control on the condition of the degree of compaction meeting the requirements, the rationality of air porosity is discussed.

Discussion of Degree of Compaction

Degree of compaction is the ratio of the dry density detected on site to the maximum dry density of the same kind of soil, which was obtained from the indoor standard compaction test. Namely that

$$K = \frac{\rho_{\mathrm{d}}}{\rho_{\mathrm{d\,max}}} \times 100\% \tag{1}$$

Where K is the degree of compaction (%), ρ_{d} is the dry density controlled on site (g/cm^3), ρ_{dmax} is the maximum dry density of soil sample detected by the indoor standard compaction test (g/cm^3).

K value is usually greater than 100% in quality inspection of practical project, which is customarily characterized as the phenomenon of the superdense degree of compaction [2]. By analyzing the reasons which lead to the superdense degree of compaction combining with indoor compaction test, the key is whether the calculative dry density will truly represent the maximum dry density during construction. Fig. 1 indicates the compaction curves of the same soil sample under different compaction energy, respectively including light compaction energy, heavy compaction energy and one between them. The three optimum water contents corresponding to different compaction energy (2684.9 kJ/m^3, 1208.2 kJ/m^3 and 592.2 kJ/m^3) are 11%, 13.4% and 15.8%. so that the maximum dry density of the same soil sample is different under different compaction energy. The maximum dry density obtained by the standard light compaction is 1.78 g/cm^3. However, the compaction energy used in construction is greater than the light compaction energy, taking the other two kinds of compaction energy for examples, the maximum dry density may reach to 1.87 g/cm^3 and 1.95 g/cm^3, the degree of compaction values are 105.1% and 109.6% calculated according to Eq. 1.

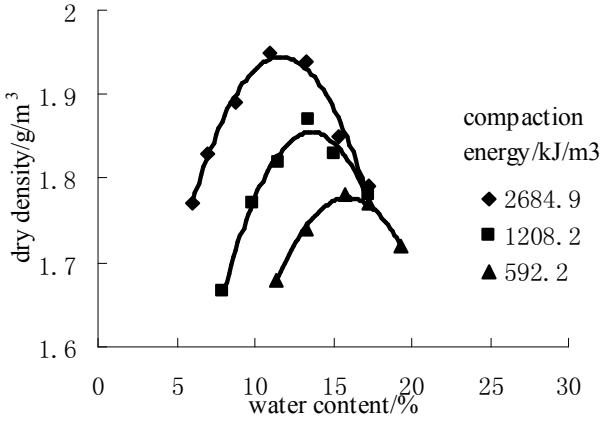


Fig. 1 Compaction curves of the same soil sample under three different compaction energy

Therefore, the degree of compaction is defined relatively to a kind of compaction energy. The standard of compaction energy of different backfill classification, structure type, and grade of buildings has not been stated clearly in current Chinese specifications [3, 4]. The compaction standard corresponding to the required degree of compaction is also unclear. These deficiencies will make the compaction standard difficult to determine during the quality inspection of backfill. Besides, the measured degree of compaction does not conform to the required degree of compaction, which makes the compaction quality of the backfill be ineligible.

Physical Properties of Test Soil Sample

Studies have shown that the compaction effect was strongly affected by soil quality. The compaction characteristics of fine-grained soil and coarse-grained soil are different, and the compaction effect of sandy soil is better than that of cohesive soil [5]. The loess is widely distributed in northern and northwestern regions of China, which is a kind of typical special soil. As the sediments are mainly silts, loess belongs to fine-grained soil. Loess is not the perfect filling material, but it was normally backfilled to reduce the project cost. The foundations or subgrades backfilled with loess are vulnerable to the impaction of rainfall, groundwater and surface water. The strength of backfill foundation or subgrade will be reduced when the water content increased.

Test soil samples were taken from the mountainous region of Fengshan Education Park, in Lvliang City, Shanxi Province. It can be known from the Table 1 that the test soil is silt-loess.

Table 1 Basic properties of soil sample

Granulometric composition (%)			Specific gravity	Liquid limit W_L (%)	Plastic limit W_P (%)	Plasticity index I_P (%)	Standard of compaction	Optimum water content (%)	ρ_{dmax} (g/m^3)
0.25~0.075	0.075~0.005	<0.005							
1.3	82.2	16.5	2.70	16.1	26.0	9.9	light	15.8	1.78
							heavy	11	1.95

Reasonableness of using Air Porosity as Judging Indicator for the Degree of Compaction

Definition of Air Porosity. In accordance with the three-phase theory of soil, assume that the total volume of soil equal to 1, V_s, V_w and V_a respectively represents the percentage of solid, liquid and gas phase in a unit volume of soil, then

$$V_s + V_w + V_a = 1 \tag{2}$$

$$\frac{\rho_d}{\rho_s} \times 100 + \rho_d \times w + V_a = 100 \tag{3}$$

Where ρ_d is the dry density of soil (g/cm^3), ρ_s is the density of soil particle (g/cm^3), w is the water content (%).

Air porosity refers to the proportion of air volume in the total volume, which is expressed as a percentage. It can be known from Eq. 3 that

$$V_a = 100 - \rho_d \times \left(\frac{100}{\rho_s} + w \right) \tag{4}$$

Analysis of Test Results. The samples were prepared with different water content of 11.5%, 13.5% and 15.5%. The samples with the same water content were compacted under different compaction energy of 671.2 kJ/m^3, 1208.2 kJ/m^3, 2013.7 kJ/m^3 and 2684.9 kJ/m^3 [6]. The compacted loess samples under different water content and different compaction energy were consolidated by laboratory confined consolidation test.

Fig. 2 and Fig. 3 are the curve of compression coefficient with dry density and the curve of compression coefficient with air porosity when the water content of soil sample is 11.5%. These two figures show that the compression coefficient of compacted loess decreases with the increase of dry density and the decrease of air porosity. Therefore, if the air porosity is used for the judging indicator of compacted loess quality, it will reflect the same regularity as dry density.

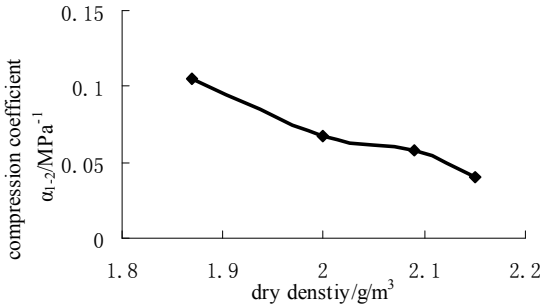


Fig. 2 Curve of compression coefficient with dry density

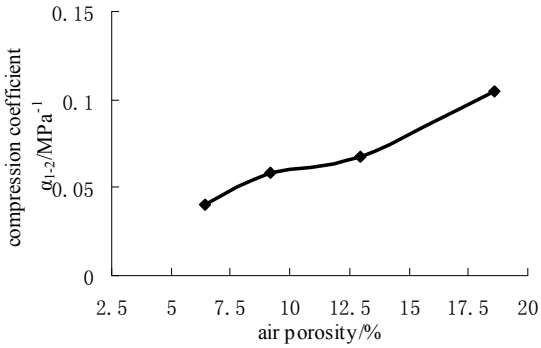


Fig. 3 Curve of compression coefficient with air porosity

The feature of the unimodal compaction curve indicates that compacted loess samples with similar dry density under the same compaction energy may have two different water contents, shown in Fig. 4. The regularities of compression coefficient of compacted loess in compaction water content state and saturation sate are researched in this paper. These compacted loess samples

have similar dry density and different water content, and the compaction energies are 1208.2 kJ/m^3 and 2684.9 kJ/m^3 respectively. The results are listed in Table 2, which show that the compacted sample with lower water content has the smaller compressibility, whether it is in initial state or in saturation state. It should be noted that the compression index varies within wide limits before and after the immersion saturation of compacted sample with low water content. The soil compression increases significantly, and its coefficient of collapsibility is greater than the soil sample with the higher water content. In contrast, the variation range of compressibility of soil sample with high water content is less than that of the sample with the lower water content before and after the immersion under water. By analyzing the reasons, the compacted soil has stronger water absorption power when its water content is lower, its air porosity is larger and its saturation is lower. All these reasons lead to the increase of deformation and compressibility of compacted soil after immersion under water.

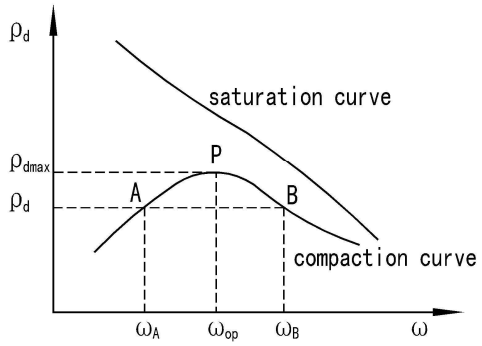


Fig. 4 Typical compaction curve

When the degree of compaction is used as the quality control indicator of compacted loess, the dry density of compacted soil should be controlled within a certain range according to the requirement of compaction degree. However, if the value of dry density would be only considered and the water content control be ignored, it may lead to a large deformation and subsidence of compacted loess when it encounters water. If the air porosity could be used as the indicator of compaction control at the same time, not only the dry density of compacted soil meet the required standard, the water content of soil during compaction can also be controlled. The saturation will be controlled lager, thus to reduce the water absorption power and control the deformation of compacted loess [7].

The air porosities of four compacted loess samples in initial state were calculated and listed in Table 2. Although the two compacted loess samples under the same compaction energy have similar dry density, their compressibilities are obviously different due to the difference of water contents. Thus, the control of water content is also important to the stability of compacted loess foundation or subgrade. When using air porosity as the indicator of compaction, the affection of water content may be considered at the same time.

The air porosities of compacted loess samples under three different water contents and four kinds of compaction energy are listed in Table 3. If the water content is constant, the air porosity will decrease with the increase of compaction energy. When the water content is lower, air porosity of compacted loess is strongly affected by the compaction energy. Air porosity is maintained at a certain level when the water content increases to a certain extent, and the influence of changes of compaction energy is not obvious at that moment.

Combining with the water contents of Table 3 and the optimum water content of compacted loess sample under different kind of compaction energy of indoor compaction test, the analysis shows that if the soil sample is compacted with exactly the optimum water content corresponding each kind of compaction energy, its air porosity will be in the range of 6.0%~6.5%. From this, whatever the compaction energy is, the air porosity of compacted loess sample will be very similar if water content is exactly the optimum water content. Thus, using air porosity as the index of the compaction quality will eliminate the effects of compaction energy to a certain extent. On the

promise that ensuring the dry density of compacted loess to the requirement of the controlled dry density requested by degree of compaction, if the air porosity reaches to a certain standard, the soil compaction quality is believed to be eligible.

Table 2 Compression of soil samples with similar dry density under different water content

Compaction energy (kJ/m^3)	Water content (%)	Dry density (g/m^3)	Saturation (%)	Compression coefficient (MPa^{-1})		Collapsibility coefficient (200kPa)	Porosity (%)
				initial	saturation		
1208.2	w_{A1}=10	1.78	55.7	0.04	0.08	0.0188	9.3
	w_{B1}=17		79.1	0.21	0.35	0.0125	7.6
2684.9	w_{A2}=8	1.87	47.2	0.07	0.15	0.0108	8.8
	W_{B2}=15		83.0	0.21	0.33	0.0089	5.6

Table 3 Air porosities of different compacted loess samples

Water content (%)	Compaction energy (kJ/m^3)	Air porosity (%)	Water content (%)	Compaction energy (kJ/m^3)	Air porosity (%)	Water content (%)	Compaction energy (kJ/m^3)	Air porosity (%)
11.5	671.2	18.6	13.5	671.2	11.2	15.5	671.2	6.5
	1208.2	12.9		1208.2	6.0		1208.2	5.5
	2013.7	9.2		2013.7	5.3		2013.7	5.6
	2684.9	6.4		2684.9	4.5		2684.9	5.1

Rationality of using Air Porosity as Judging Indicator for the Degree of Compaction

The air porosity has good stability. Although the maximum dry density and water content of the compacted loess are very dissimilar when the compaction energy is different, the value of air porosity of compacted loess is stable when the water content is exactly the optimum water content. It is stable and reliable by using air porosity to control the compaction of loess foundation or subgrade.

On the promise that ensuring the dry density of compacted loess meeting the requirements, if a smaller air porosity was used to control the compaction of loess foundation or subgrade, the influence of the water could be reduced. Thus it will help to prevent the large subsidence and deformation of loess foundation or subgrade, and eliminate the effects of compaction energy to a certain extent. It will also effectively prevent the superdense degree of compaction.

The convenience of calculation of air porosity. Only the dry density and water content on construction site are detected as calculating the air porosity of compacted loess.

Conclusions

On the promise of ensuring the dry density of compacted loess meeting the requirements, if air porosity is used to control the compaction quality of backfill foundation, the water content can be controlled close to the optimum for the compacted soil. The air porosity can reflect the compaction stability more truly and realistically, and adapt to the nature situation of inconstant soil and water content. According to the test results, the air porosity less than 6.5% is suggested as the additional compaction standard of silt-loess in this region. However, the above suggests are still remained to be tested by practice due to the limit of test conditions and the time.

Acknowledgements

The authors thank to the supports of National Natural Sciences Foundation of China (No.51178287) and Provincial Natural Sciences Foundation of Shanxi (No.2010011029).

References

[1] Z. Wang, H. Hu and W. Zou: Factors influencing road embankment compaction and requirements of compaction degree, Highway, 8 (2004) 91-94.

[2] J. Zhang: Discussion of superdense of compaction degree in highway engineering test, Highways and Transportation in Inner Mongolia, 2 (2006) 21-22.

[3] Chinese Code GB 50007-2002: Code for Design of Building Foundation, China Building Industry Press, Beijing, 2002.

[4] Chinese Code JGJ79-2002: Technical Code for Ground Treatment of Buildings, China Building Industry Press, Beijing, 2002.

[5] M. Li: Discussion of soil subgrade compaction standards and strength assessment, Technology Trend, 2 (2009) 163-165.

[6] Chinese Code GB/T50 123-1999: Standard for Soil Test Method, China Building Industry Press, Beijing, 1999.

[7] Y. Bao, J. Li and D. Li: Discussing the scientific feature of subgrade degree of compaction with porosity, Technology and Economy in Areas of Communications, 3 (2006) 14-16.

© (2012) Trans Tech Publications, Switzerland
doi:10.4028/www.scientific.net/AMM.238.447

Theoretical Solution to the Change of Site Predominant Period Caused by Soil Softening

Baorong Huang [a], Yongzhi Wang [b], Weiming Wang [c] and Xiaoming Yuan [d]

Key Laboratory of Earthquake Engineering and Engineering Vibration, Institute of Engineering Mechanics, CEA, Harbin 150080, China

[a]hbr_hfut@126.com, [b]yong5893741@163.com, [c]wswwm1983@163.com, [d]yxmiem@163.com

Keywords: soil softening, site predominant period, weak layer, theoretical solution.

Abstract. The site predominant period should be changed because of soil softening, which is an important parameter to reflect the dynamic characteristics of the site. In this paper, in order to acquire the theoretical solution to the site predominant period, the actual horizontal site has been simplified into two-particle system. And the influence that caused by the thickness and location of the weak layer on the site predominant period, has been analyzed.

Introduction

The seismic wave must be transmitted through the site under the building foundation before arriving at it, so it is very essential to determine the dynamic characteristics of the site, including the site predominant period, which is one of the most important parameter to reflect the dynamic characteristics of the site. The site predominant period is also one of the key parameters, which is needed to be considered in the seismic design of buildings.

According to the description of the Geotechnical Manual, the seismic waves of different period would be amplified by the surface soil, resulting in some periodic wave records would be more and particular in the seismograms, so it appears excellent. This period should be called the site predominant period [1].

There are three methods for solving the site predominant period at the present time: the first, it is acquired by the Fourier analysis on the records about this site; the second, it is determined by the micro-tremors testing method; the third, it is obtained based on the shear wave velocity of every soil layer according to Eq.1 [2].

$$T = \sum_{i=1}^{n} 4h_i / v_{si} \tag{1}$$

Where T is the site predominant period, h_i is the thickness of the layer i of the soil, v_{si} is the shear wave velocity of the layer i of the soil.

Model and Solution

The actual horizontal field can be simplified into a double-layer soil model, which can be further simplified into two-particle system (Fig. 1).

The parameters of two soil layers are shown in Fig. 1, G_1, ρ_1, h_1, v_{s1} are the shear modulus, density, thickness and shear wave velocity of the first soil layer, G_2, ρ_2, h_2, v_{s2} are the shear modulus, density, thickness and shear wave velocity of the second soil layer, m_1 is the weight of the first particle, m_2 is the weight of the second particle. K_1 is the average horizontal stiffness of the first soil layer, K_2 is the

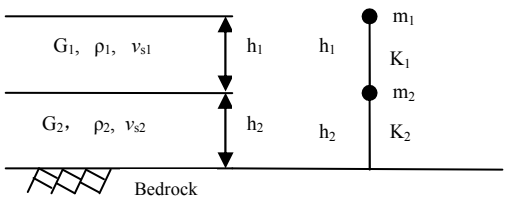


Fig. 1 The double-layer soil model and the two-particle system model

average horizontal stiffness of the second soil layer. Thus K_1, K_2 are defined as

$$K_1 = \frac{G_1}{h_1} \tag{2}$$

$$K_2 = \frac{G_2}{h_2} \tag{3}$$

The frequency of the first vibration mode of the two-particle system model is taken as the predominant frequency, it is computed as

$$\omega_1 = \left\{ \frac{1}{2} \left[\frac{1}{m_2} \left(\frac{G_1}{h_1} + \frac{G_2}{h_2} \right) + \frac{G_1}{m_1 h_1} - \sqrt{\left(\frac{1}{m_2} \left(\frac{G_1}{h_1} + \frac{G_2}{h_2} \right) + \frac{G_1}{m_1 h_1} \right)^2 - \frac{4 G_1 G_2}{m_1 m_2 h_1 h_2}} \right] \right\}^{\frac{1}{2}} \tag{4}$$

Where ω_1 is the predominant frequency. Suppose that the dendity of the first soil layer was equal to the second one, it is defined as

$$\rho_1 = \rho_2 \tag{5}$$

Beacuse of the shear modulus can be computed as

$$G = v_s^2 \bullet \rho \tag{6}$$

Thus the site predominant period is calculated as

$$T_1 = \frac{2\pi}{\omega_1} = 2\pi \Bigg/ \left\{ \frac{1}{2} \left[\frac{v_{s1}^2}{h_1 h_2} + \frac{v_{s2}^2}{h_2^2} + \frac{v_{s1}^2}{h_1^2} - \sqrt{\left(\frac{v_{s1}^2}{h_1 h_2} + \frac{v_{s2}^2}{h_2^2} + \frac{v_{s1}^2}{h_1^2} \right)^2 - \frac{4 v_{s1}^2 v_{s2}^2}{h_1^2 h_2^2}} \right] \right\}^{\frac{1}{2}} \tag{7}$$

Assume that the first soil layer is weak layer. When the weak layer was softened, its shear wave velocity defined as v'_{s1}, so the site predominant period after softening (T_1') can be expressed as

$$T_1' = \frac{2\pi}{\omega_1} = 2\pi \Bigg/ \left\{ \frac{1}{2} \left[\frac{v_{s1}'^{\,2}}{h_1 h_2} + \frac{v_{s2}^2}{h_2^2} + \frac{v_{s1}'^{\,2}}{h_1^2} - \sqrt{\left(\frac{v_{s1}'^{\,2}}{h_1 h_2} + \frac{v_{s2}^2}{h_2^2} + \frac{v_{s1}'^{\,2}}{h_1^2} \right)^2 - \frac{4 v_{s1}'^{\,2} v_{s2}^2}{h_1^2 h_2^2}} \right] \right\}^{\frac{1}{2}} \tag{8}$$

Where T_1' is the site predominant period of the model, whose weak layer was softened. So the rising rate of the site predominant period η can be defined as

$$\eta = \frac{T_1' - T_1}{T_1} = \frac{\left\{ \frac{1}{2} \left[\frac{v_{s1}^2}{h_1 h_2} + \frac{v_{s2}^2}{h_2^2} + \frac{v_{s1}^2}{h_1^2} - \sqrt{\left(\frac{v_{s1}^2}{h_1 h_2} + \frac{v_{s2}^2}{h_2^2} + \frac{v_{s1}^2}{h_1^2} \right)^2 - \frac{4 v_{s1}^2 v_{s2}^2}{h_1^2 h_2^2}} \right] \right\}^{\frac{1}{2}}}{\left\{ \frac{1}{2} \left[\frac{v_{s1}'^{\,2}}{h_1 h_2} + \frac{v_{s2}^2}{h_2^2} + \frac{v_{s1}'^{\,2}}{h_1^2} - \sqrt{\left(\frac{v_{s1}'^{\,2}}{h_1 h_2} + \frac{v_{s2}^2}{h_2^2} + \frac{v_{s1}'^{\,2}}{h_1^2} \right)^2 - \frac{4 v_{s1}'^{\,2} v_{s2}^2}{h_1^2 h_2^2}} \right] \right\}^{\frac{1}{2}}} - 1 \tag{9}$$

The following variables are defined as

$$\lambda = \frac{h_1}{h_2} \tag{10}$$

$$P_1 = \frac{G_1}{G_2} = \frac{v_{s1}^2}{v_{s2}^2} \tag{11}$$

$$P_L = \frac{G_1'}{G_1} = \frac{v_{s1}'^{\,2}}{v_{s2}^2} \tag{12}$$

Here λ is the thickness ratio between the first layer and the second layer of the site, P_1 is the shear modulus ratio between the first layer and the second layer of the site, P_L is the shear modulus ratio between the weak layer after softening and before softening.

An Weiping, Lan Qinglong (etc.1997) analyzed the relationship between the shear wave velocity and depth of the soil layer about the Taiyuan area [3], Chen Guoxing analyzed the relationgship about the Nanjing area [4]. They all considered that the ralationship was coincided well with Eq.13. Sun Rui considered that *b* should be valued between 0.2 and 0.45 [5]. In this paper, *b* is valued 0.2.

$$v_s = ah^b \tag{13}$$

Where *a* and *b* are parameters which should be valued. Thus P_1 is expressed as

$$P_1 = \frac{G_1}{G_2} = \frac{v_{s1}^2}{v_{s2}^2} = \left(\frac{a\left(\frac{2}{3}h_1\right)^{0.2}}{a\left(h_1 + \frac{2}{3}h_2\right)^{0.2}} \right)^2 = \left(\frac{\frac{2}{3}\lambda}{\lambda + \frac{2}{3}} \right)^{0.4} \tag{14}$$

Thus the Eq.9 is simplified as

$$\eta = \left[\frac{\left(\frac{\frac{2}{3}\lambda}{\lambda+\frac{2}{3}}\right)^{0.4} + \lambda + \left(\frac{\frac{2}{3}\lambda}{\lambda+\frac{2}{3}}\right)^{0.4} \frac{1}{\lambda} - \sqrt{\left(\left(\frac{\frac{2}{3}\lambda}{\lambda+\frac{2}{3}}\right)^{0.4} + \lambda + \left(\frac{\frac{2}{3}\lambda}{\lambda+\frac{2}{3}}\right)^{0.4} \frac{1}{\lambda}\right)^2 - 4\left(\frac{\frac{2}{3}\lambda}{\lambda+\frac{2}{3}}\right)^{0.4}}}{P_L\left(\frac{\frac{2}{3}\lambda}{\lambda+\frac{2}{3}}\right)^{0.4} + \lambda + P_L\left(\frac{\frac{2}{3}\lambda}{\lambda+\frac{2}{3}}\right)^{0.4} \frac{1}{\lambda} - \sqrt{\left(P_L\left(\frac{\frac{2}{3}\lambda}{\lambda+\frac{2}{3}}\right)^{0.4} + \lambda + P_L\left(\frac{\frac{2}{3}\lambda}{\lambda+\frac{2}{3}}\right)^{0.4} \frac{1}{\lambda}\right)^2 - 4P_L\left(\frac{\frac{2}{3}\lambda}{\lambda+\frac{2}{3}}\right)^{0.4}}} \right]^{\frac{1}{2}} - 1 \tag{15}$$

It is shown that the change of the site predominant period is mainly determined by two parameters, one is the thickness ratio λ, the other is the shear modulus ratio P_L .

Analysis of the Theoretical Solution

Fig. 2 is the Three-dimensional map of the rising rate of the site predominant period η, the thickness ratio λ and the shear modulus ratio P_L, which is obtained according to Eq.15.

According to Fig. 3, the rising rate of the site predominant period η should accrue with the increasing of the thickness ratio λ. Different values of the shear modulus ratio P_L have different influence on the rising rate of predominant period, the P_L is smaller, the influence is bigger.

The rising rate of the site predominant period η is decreasing with the accruing of the shear modulus ratio P_L according to Fig. 4, in other words, the softening of the site is more serious, the η values bigger.

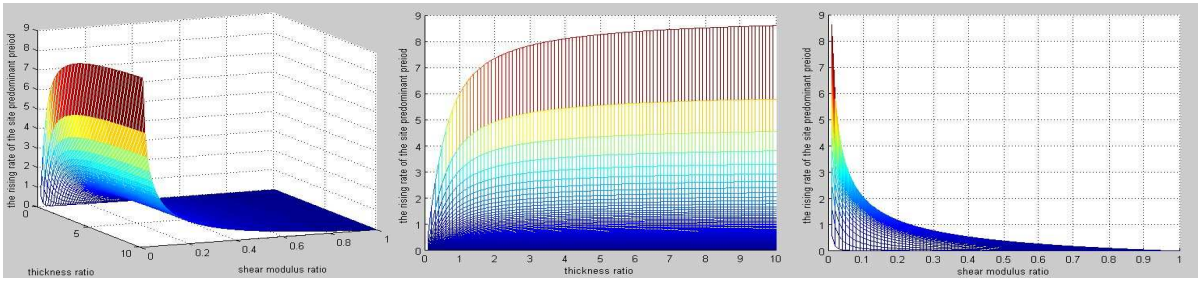


Fig. 2 Three-dimensional map of the rising rate of the site predominant period η, the thickness ratio λ and the shear modulus ratio P_L

Different Locations of the Weak Layer

In this paper, two work conditions are given (Fig. 5). The rising rate of the site predominant period and the site predominant period are computed (Table 1). Accroding to the Table 1, the rising rate of the site predominant period and the site predominant period should be different due to the different locations of the weak layer.

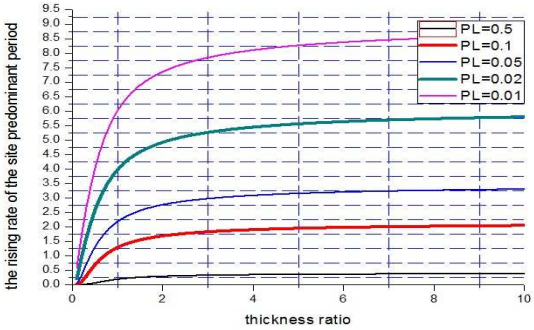


Fig. 3 The relationship between η and λ

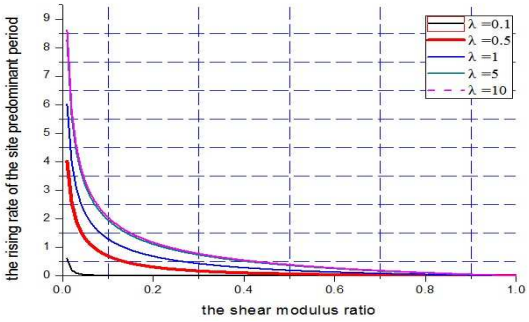


Fig. 4 The relationship between η and P_L

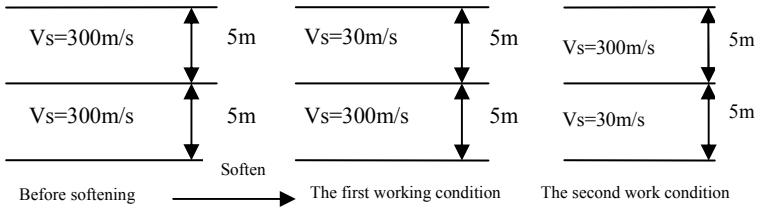


Fig. 5 Two given work conditions

Table 1 The site predominant period and the rising rate of the site predominant period

Work condition	Site predominant period before softening	Site predominant period after softening	Rising rate of the site predominant period
The first	0.17	1.05	5.18
The second	0.17	1.48	7.71

Conclusions

The theoretical solution to the change of site predominant period caused by soil softening is obtained, base on the simplification of the actual horzontial site into two-particle system, the results as fellows:

If the location of the weak layer is different, the rising rate of the site predominant period and the site predominant period will be different. The site predominant period is mainly determined by two parameters, one is the thickness ratio, the other is the shear modulus ratio. The rising rate of the site predominant period will increase with the increasing of the thickness ratio, and it will decease with the accruing of the shear modulus ratio.

Acknowledgements

This research is jointly supported by Fundamental Research Funds of Institute Engineering Mechanics and Earthquake (Grant No. 200708001).

References

[1] Geotechnical Engineering Manual Compilation Committee, Geotechnical engineering manual, China Architecture & Building Press, Beijing, 1994.

[2] G. Gao, S. Wu, J. Zhou, Dicussion and determination of the site predominant period, Geotechnical Investigation & Surveying, 5 (2000) 29-31.

[3] W. An, Q. Lan, The depth distribution of the shear wave velocity in Taiyuan region, Shanxi Seismic, 1 (1997) 88-94.

[4] G. Chen, J. Xu, L. Yuan, The ralationgship between the shear wave velocity and the depth of rock and siol in Nanjing, The transaction of Nanjing Architectural Engineering University, 2 (1998) 32-37.

[5] R. Sun. Study on seismic ground motion on liquefiable soil layer and site liquefaction detection, Institute of Engineering Mechanics, China Seismological Bureau, 2006.

© (2012) Trans Tech Publications, Switzerland
doi:10.4028/www.scientific.net/AMM.238.451

The Finite-element Analysis of Characteristics of Soil Slopeseepage Field Change in Continuous Rain Condition

Zhongming He [a], Wei Wu [b], ling Zeng [c] and Zhongxin Cai [d]

School of Traffic and Transportation Engineering, Changsha University of Science & Technology, Changsha 410014,China

[a]hezhongming45@126.com, [b]yswuwei5@163.com, [c]362491876@qq.com, [d] 273560113@qq.com

Keywords: rainfall infiltration; permeability coefficient; pore water pressure; seepage field.

Abstract. A numerical model is built by Finite Element Software, discussed the effect of rainfall on slope pore water pressure, volatile water content and depth of infiltration in continuous rain condition. The result indicated that when the rainfall intensity and rainfall duration reach a certain condition, the ground water table rises slowly, and mostly, the spill points of ground water locate in the foot of slope. The slope section appears three pore water pressure divisions: transient saturated zone, negative pressure region and hydrostatic pressure area after the rain.

Introduction

Because of the existence of the negative pore water pressure in soil, the mechanical properties have great change relative to the saturated soil. In continuous rain condition, the infiltration of the shallow rain which result in the negative pore water pressure changed due to the long time rainfall, and cause the mechanics parameters change, what's worse, it will cause the slope lose stability [1]. So, the characteristics analysis of unsaturated seepage field is the precondition of slope stability analysis [2]. The study at the moment in this field mainly focused on the analysis of slope seepage field in various rainfall intensity, duration and type and the changes of permeability coefficient, while there have not a lot of deep analysis of the characteristic of soil slope seepage field change under continuous rain condition [3]. Considering these reasons, in this paper the author adopted finite element software to build the numerical analysis model, and discussed the characteristics of slope seepage field in continuous rain condition, and provided reference for the engineering practice.

Calculation Model Building

Geometrical Model. A typical slope profile calculation model was established according to the actual situation. The X axis coordinate directs the slope inward at slope feet along the horizontal direction, and the length is 67 meters. Y axis direction is upward at slope feet along the vertical direction, and the height is 50 meters. The internal soil of the slope is presumed as clay layer, the slope has first degree excavation, and the gradient proportion is 1:1. Because in this article the main object of study is the seepage field in slope soil in continuous rain condition and the model area is relatively large, therefore, setting up the feature profile I-I~III-III along Y direction to study the seepage characteristics on slope in rainfall condition as shown in Fig. 1.

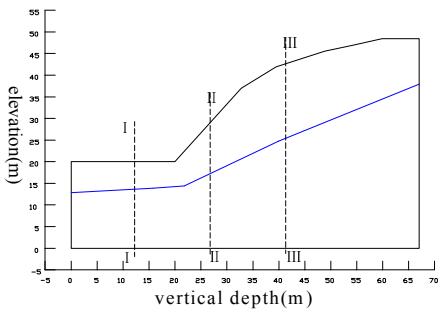


Fig. 1 Vadose model calculation section, feature points

Calculating Scheme and Boundary Conditions Design. According to National Weather Service's define of continuous rain by upper limits, the second scheme designs two rainfall intensity, such as 3.472mm/h and 5.556mm/h, and the rainfall duration is resumed for 72 hours. The analysis of the change of slope seepage field's characteristic and the effect of various rainfall intensities of the same rain type on seepage field can be received by numerical calculation.

Table 1 The calculating parameter of rainfall

Effect factor	Rain type	Rainfall intensity (mm/h)	Rainfall duration (h)	Rain capacity (mm)
rainfall	continuous rain	3.472	72	250
		5.556	72	400

During the calculating, the left, right and bottom side of soil slope are presumed as impervious boundaries, like Q=0, while the surface of slope was set as free infiltration border. If the rainfall intensity is smaller than the slope soil permeability, the unit speed of slope surface is equal to rainfall intensity, and the unit speed is:

$$q = i\cos\alpha \tag{1}$$

Where i is the rainfall intensity, a is the gradient rate of soil slope

When the rainfall intensity is larger than the slope infiltration capacity, non infiltration water on slope surface will form slope-runoff yield collect to the toe of slope, at this time, the boundary of the slope surface is set as the boundary of fixed water level, and the size is the level head of this point. Namely:

$$h=z \tag{2}$$

Where z is the level head.

When taking the finite-element analysis, V-G model is used to fit the permeability coefficient and volatile water content in unsaturated field [5]. During the calculating, the ratio of permeability between vertical direction and horizontal direction is k_y:k_x=1.2:1.

Results and Analysis

The Analysis of Distribution Characteristics of Pore Water Pressure after Rainfall. After analyzing from Fig. 2 and Fig. 3, we can know that the negative pore water pressure in the surface soil of slope in the condition of continuous rain takes big changes, and the underground water table can be seen in the earth's surface, which is the same with the distribution of pore water pressure in the condition of rainfall, but the surface water level on the top of slope is uncontinuous in the condition of continuous rain because the rainfall intensity is smaller than the slope soil permeability, which makes difficult for the slope surface to collect water. While the rain water of slope toe collect to slope toe, it shows the slope surface appears saturated conditions. Compared with rainfall condition, the infiltration depth makes a greater contribution to the rise of underground water. Because of infiltration, the underground water table of slope has a certain rise after rainfall, when it has certain rainfall duration, the rainfall intensity has an effect on the rising of underground water. Compare Fig. 2 and Fig. 3, we can know that the underground water table of slope toe has a certain rise after raining for 72 hours, while in Fig. 3, the increasing range is larger and the line of underground water table intersects with slope toe. The results show that the increasing range is controlled by rainfall intensity while all the other conditions remain unchanged, and prove that when the rainfall duration & rainfall intensity reach a certain condition, the underground water table will rise slowly, and mostly the spill points of ground water locate at slope toe.

After analyzing from Fig. 2 and Fig. 3, we can know that the negative pore water pressure in the surface soil of slope in the condition of continuous rain takes big changes, and the underground water table can be seen in the earth's surface, which is the same with the distribution of pore water pressure in the condition of rainfall, but the surface water level on the top of slope is uncontinuous in the condition of continuous rain because the rainfall intensity is smaller than the slope soil permeability, which makes difficult for the slope surface to collect water. While the rain water of

slope toe collect to slope toe, it shows the slope surface appears saturated conditions. Compared with rainfall condition, the infiltration depth makes a greater contribution to the rise of underground water. As infiltration, the underground water table of slope has a certain rise after rainfall, when it has certain rainfall duration, the rainfall intensity has an effect on the rising of underground water.

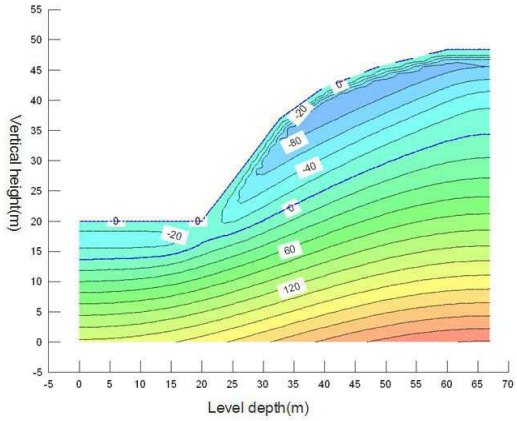


Fig. 2 The pore water pressure distribution when the rainfall intensity is 3.472mm/h after rainfall (kPa)

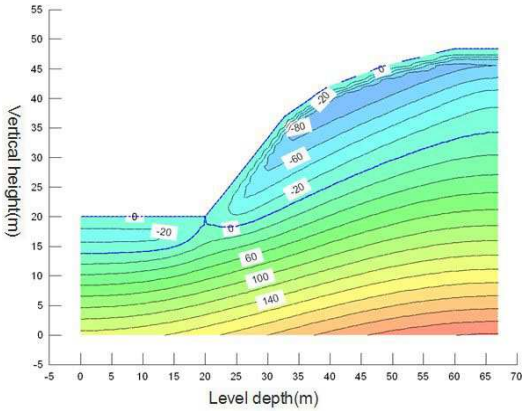


Fig. 3 The pore water pressure distribution when the rainfall intensity is 5.556mm/h after rainfall (kPa)

Compare Fig. 2 and Fig. 3, we can know that the underground water table of slope toe has a certain rise after raining for 72 hours, while in Fig. 3, the increasing range is larger and the line of underground water table intersects with slope toe. The results show that the increasing range is controlled by rainfall intensity while all the other conditions remain unchanged, and prove that when the rainfall duration and rainfall intensity reach a certain condition, the underground water table will rise slowly, and mostly the spill points of ground water locate at slope toe.

The Analysis of Relationship between Pore Water Pressure and Elevation when Rainfall. After analyzing from Fig. 5 to Fig. 9, we know that pore water pressure downward along the section elevation gradually became from 0 to negative value after rainfall infiltration in the slope, when reached the underground water level the pore water pressure became positive value again and presented the linear distribution and met $p=\gamma h$. For the different sections under the same rainfall intensity, because of the effect of rainwater in gravity collecting to slope toe on section I-I position the pore water pressure on this section was larger than section II-II and section III-III. The change trend of pore water pressure along the elevation direction shows that the area around the surface is a transient saturated zone, and the area between the surface and initial underground water table is unsaturated zone, the area under the underground water table is saturated zone, while the distribution of pore water pressure follows hydrostatic pressure.

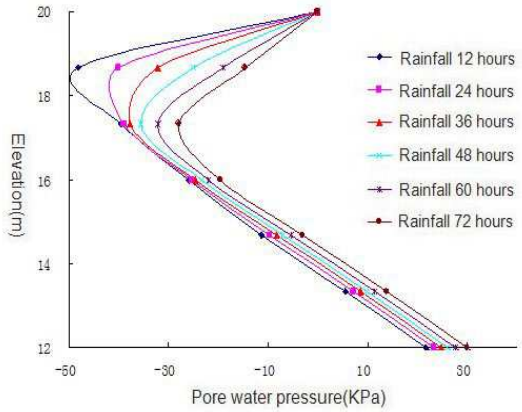


Fig. 4 The relationship between pore water pressure and elevation of section I-I when the rainfall intensity is 3.471mm/h

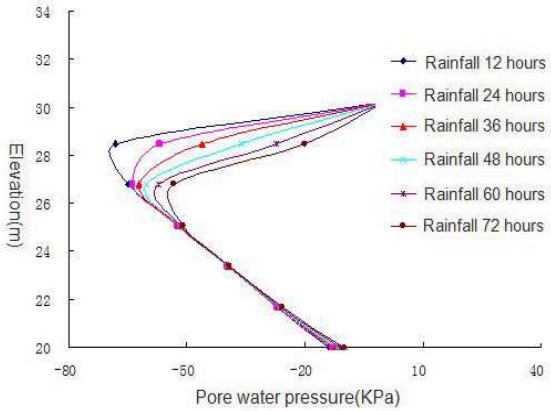


Fig. 5 The relationship between pore water pressure and elevation of section II-II when the rainfall intensity is 3.471mm/h

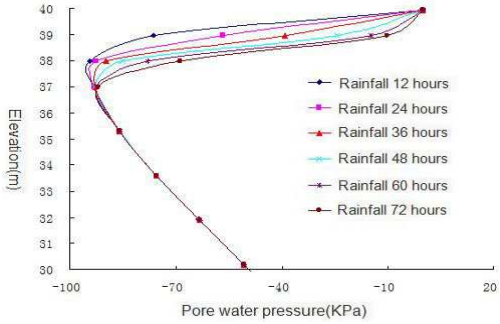


Fig. 6 Relationship between pore water pressure and elevation of section III-III when the rainfall intensity is 3.471mm/h

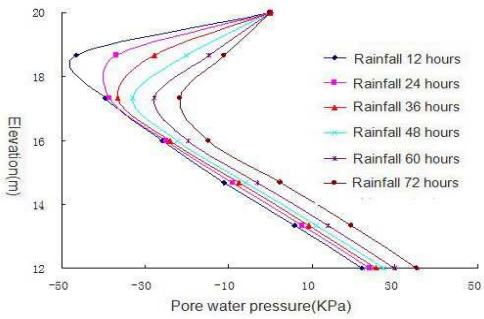


Fig. 7 Relationship between pore water pressure and elevation of section I-I when the rainfall intensity is 5.556mm/h

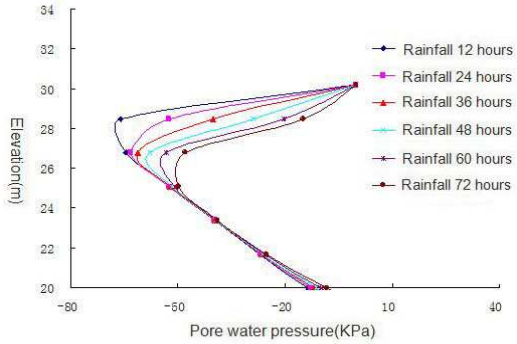


Fig. 8 Relationship between pore water pressure and elevation of section II-II when the rainfall intensity is 5.556mm/h

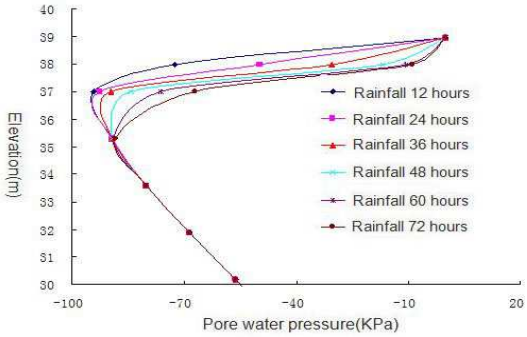


Fig. 9 Relationship between pore water pressure and elevation of section III-III when the rainfall intensity is 5.556mm/h

Conclusions

When the rainfall duration and rainfall intensity reaches a certain condition in continuous rain condition, the underground water table of slope will rise slowly, and mostly the spill points of underground water located at the slope toe.

In continuous rain condition, according to the change trend of pore water pressure in slope soil it can be divided into three zones: transient saturated zone, unsaturated zone and saturated zone, while the distribution of pore water pressure in saturated zone which located under the ground water table follows hydrostatic pressure.

Acknowledgements

This project obtained the funds of Hunan Traffic Science and Technology Plan Projects (2009003), Hunan Science and Technology Plan Projects (2011FJ3114).

References

[1] Z. Chen. Soil Slope Stability Analysis. China WaterPower Press, Beijing, 2003.
[2] G. Feng, X. Hu, G. Wu, et al, Rainfall infiltration mechanism of unsaturated soil in Enshi of Western Hubei Province, Geological Science and Technology Information, 5 (2010).
[3] W. Chen, H. Mou, L. Chen. Study on rainfall infiltration process and the biggest infiltration depth for unsaturated soil slope, Mining and Metallurgical Engineering, 6 (2009).
[4] G. Rong, W. Zhang, C. Zhou. Numerical analysis of saturated-unsaturated seepage problem of rock slope under rainfall infiltration. Rock and Soil Mechanics, 10 (2005).
[5] H. Liu, J. Zhang, H. Tumaerbai, Contrast analysis on soil water characteristic curve of VG model parameters, Journal of Xinjiang Agricultural University, 5 (2011).

© (2012) Trans Tech Publications, Switzerland
doi:10.4028/www.scientific.net/AMM.238.455

Influence of Compaction Density of Soil Mass to the Seepage Build Capacity of Rain and Drainage Design Parameter

Fangran Zhao[1, a], Ziliang Cai[1, b] and Tianwang Zhang[2, c]

[1]Airport College, Civil Aviation University of China, Tianjin, 300300, China

[2]Zhengzhou Xinzheng International Airport, Zhengzhou, 451163,China

[a]frzhao@cauc.edu.cn,[b]czliang08@163.com,[c]ztw71402@126.com

Keywords: soil surface area; compaction density; airfield drainage; seepage build capacity; soil infiltration rate.

Abstract. To reduce the pressure of rain efflux in the airport, and make full use of the resources of rain, the adjustment relationship between seepage build capacity of the soil surface area and rain convergence is studied. The condition of constraints between surface rain gradient and emissions is analyzed, according to airfield drainage design. The method to determine the ratio of the seepage area and non-seepage area is proposed to take full advantage of the rainwater seepage build capacity of soil surface area. Experiments have been performed to study the influence of infiltration rate of compaction density to clay and silty soil. The experimental results show that the soil infiltration rate decreases linearly with the increase of soil compaction, and reduces very fast at the first 30min of rainfall. It is recommended that the infiltration rate of rainfall on the first 30min can be used as the design parameter in the drainage design in the airfield. The influence coefficient reflecting the influence of compaction density to soil infiltration rate has been proposed.

Introduction

The improvement of water environment in airfield has become an urgent issue which can be settled by scientifically using of the regional precipitation. Because of the unbalanced regional precipitation, if the rainfall is quickly discharged, water resources will be difficult to reuse, and drainage facilities may be unbearable [1]. Hence, in order to achieve a reasonable topography optimization of airfield and make gradient deployment of the airfield rainwater between infiltration and drainage, reasonable technical characteristics of rainfall convergence have been discussed based on the permeability of the surface soil of the field area, and the surface soil permeability build parameters have been analyzed [2].

An Analysis of Soil Surface Rainwater Seepage Build Production Flow

The Flight Zone Landforms and Their Characteristics of Rainwater Seepage Build. Rainwater infiltration build capacity of different soil surface area of the airfield flight zone (as Figure 1) is usually quite different. In accordance with the relevant provisions, in order to meet the safety requirements, in case the aircraft may be missed or overran the runway, runway end safety area, both sides of the lift with the surface soil must reach a sufficient density in order to protect its adequate carrying capacity [3]; Typically, the mentioned regional soil density should above 75%~ 90 %, while in other regions of the soil density is about 75%. The difference of surface soil density leads to different rainwater seepage build capacity. In order to make the rain water convergence and its seepage build capacity of different regions to achieve a balance, the difference must be taken into account in the soil surface drainage to optimize the design work to ensure the smooth flow of surface drainage, and make the soil surface infiltration build capacity into full play [4]. Considering these factors, it is necessary to study different dense state infiltration rate and duration of continuous rainfall runoff changes in the field drainage design, as well as the rainwater seepage build requirements in light rain or showers.

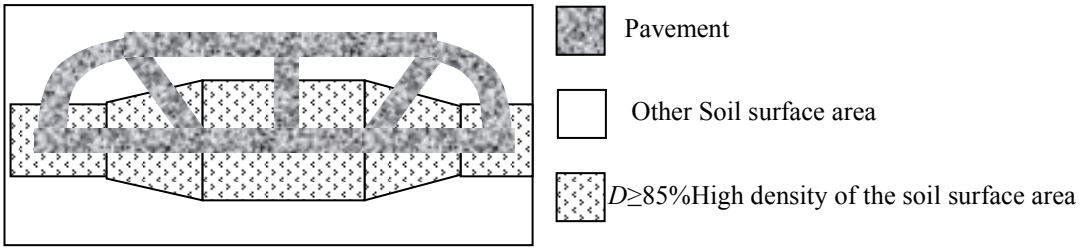


Fig. 1 Situation plan on the surface in an airfield

Soil Surface District Rainwater Flow Balance Analysis

Showers of the Soil Surface Area Runoff Balance. When comes to short periods rainfall of small and medium-sized scale, its per unit area of acceptance from other regions rain convergence can be calculated as follow.

$$I_1 = \int_{t_0}^{t_1} (f_p - i)dt \tag{1}$$

It is as shown in equation (1) [5], when the soil seepage water storage capacity is sufficient, and the infiltration rate larger than rainfall intensity ($f_p > i$),the soil surface area has the acceptance of rainwater convergence from other region; when the rainfall intensity is close to soil infiltration rate ($f_p = i$), $I_1=0$, the precipitation and infiltration of the region is in equilibrium; when the rainfall intensity exceeds the soil infiltration rate ($i > f_p$), $I_1<0$, then the soil surface District still need to outward discharge storm water flow and drainage t_0~t_1 period domestic demand $|I_1|$.

For non-seepage area, all rainfalls must be drained away, and the emission I_2 is shown as equation (2):

$$I_2 = \int_{t_0}^{t_1} idt \tag{2}$$

For the area with a smaller rainfalls, the rainfall intensity is typically less than the infiltration rate, ($f_p > i$). Therefore, it is necessary to set reasonable area ratio between penetrative soil surface area and corresponding the pavement area of non-water seepage.

For example, the penetrative soil surface area is A_1, and the adjacent impermeable area requiring rainwater drainage is A_2.The conditions that total rainfall of the two regions be absorbed by soil surface in time is:

$I_1A_1=I_2A_2$, or $A_1/A_2=I_2/I_1$

$$\text{if } R = A_1/A_2, \text{ then } R = I_2/I_1 = \int_{t_0}^{t_1} idt \Big/ \int_{t_0}^{t_1} (f_p - i)dt \tag{3}$$

It can be seen in equation (3), when the rainfall intensity needed to meet requirement is greater, the infiltrative soil surface area the flight area needs is larger. At the same time, when the infiltration rate of the soil surface area is smaller, the area which is used for in-situ permeability and storage is larger.

The Analysis of the Soil Surface Infiltration Rate in the Attenuation of the Production Flow Balance. For the larger rainfall, soil infiltration capacity starts from an initial maximum infiltration rate and reduces in exponential function until it reaches a stable value [6], namely:

$$f = f_c + (f_0 - f_c)e^{-kt} \tag{4}$$

The influence of infiltration rate attenuation is took into consideration, when the rainfall intensity is less than the soil infiltration rate and the quantity of infiltration rain does not exceed the soil storage capacity, per unit area of soil surface's acceptance to rain convergence from other regions is I'_1:

$$I'_1 = \int_{t_0}^{t_1} [f_c + (f_0 - f_c)e^{-kt} - i]dt \tag{5}$$

At this point, the area that per unit area of soil surface region can meet the requirement of other non-seepage drainage is:

$$R' = I_1' / I_2 = \int_{t_0}^{t_1} [f_c + (f_0 - f_c)e_{\mathrm{p}}^{-kt} - i]dt \Big/ \int_{t_0}^{t_1} idt \tag{6}$$

The Influence of Relative Density on the Infiltration and Build Capacity of the Soil Surface

The Influence of Density on Surface Drainage Capacity. Considering the density differences of each block of soil surface, the above formula needed to be amended, a parameter *Y* acting as a dense influence coefficient of water permeability in soil is introduced and equation (4) is amended as:

$$f' = Y[f_c + (f_0 - f_c)e^{-kt}] \tag{7}$$

The parameters are substituted into equation (6), when rainfall intensity exceeds the soil infiltration rate, the area that per unit area of soil surface region can meet the requirement of other non-seepage drainage after considering the soil density is shown as equation (8).

$$R'' = \int_{t_0}^{t_1} \{Y[f_c + (f_0 - f_c)e^{-kt_p}] - i\}dt \Big/ \int_{t_0}^{t_1} idt \tag{8}$$

In the same soil, the soil is more compact, lower infiltration rate. Obviously, the more dense is the soil, the low is the rainwater seepage build capacity.

The Compacting Effect of the Soil Infiltration Rate To make sure a reasonable ratio of impervious surface area, it is needed to know the density of the soil infiltration rate of rainwater. So the influence disciplines under different density are tested. The clay soil taken from the soil surface area of Zhengzhou international airport flight zone, silty soil taken from the soil surface area of Tianjin Binhai International Airport airfield, two soil particle size distribution shown in Table 1.

Table 1 Particle size distribution of the clay and silty soil (%)

Particle size (mm)	0.5~0.25	0.25~0.075	0.075~0.05	0.05~0.01	0.01~0.005	0.005~0002	<0.002
Clayey soils	0	0	5.4	14.2	14.5	68.2	43.5
Silty soil	0	25.8	35.2	32.1	2.4	4.5	3.6

Note: Experiment with clay soil C_u=2.25, C_c=1, I_p=16.4; Silty soil C_u=7.667, C_c=3.261, I_p =10.5. Heavy compaction experiments to determine the optimum moisture content and maximum dry density: Clayey soils respectively 14.85% and 1.77g/cm^3; Silty soils respectively: 13.76% and 1.69 g/cm^3.

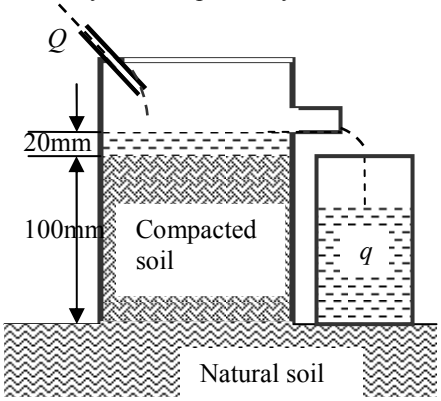




Fig.2 Experimental device testing soil infiltration rate

The seepage experiment testing soil infiltration rate with the improved experimental setup for the two types of soil, at the soil specimen relative density was reached 75% ~ 100% respectively. Depth of water on the soil surface at maintain about 20mm during testing, and volume *Q*, the volume of water flowing by the barrel opening *q* have been measured every 10min into the test barrel (Fig. 2) in water, and the density (*D*) state, time-varying infiltration rate (*K*) values have been calculated based on the measured dates, two types of soil relative density-infiltration rate curve is expressed as Fig. 3 and Fig. 4.

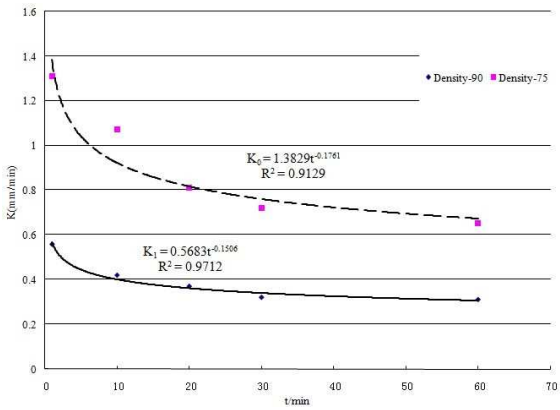


Fig. 3 The variation of clay soil infiltration rate

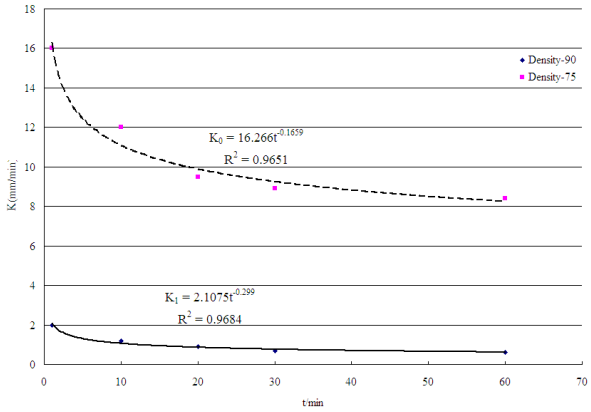


Fig. 4 The variation of silty soil infiltration rate

It is indicated that for the silty soil with density of 75% and 90% in the Fig. 3, both of their rainwater infiltration rates are the power function of the rainfall time:

$$K_0=1.3829t^{-0.1761} \tag{9}$$

$$K_1=0.5683t^{-0.1506} \tag{10}$$

It is indicated that for the silty soil with density of 75% and 90% in the Fig. 5, the power function which refers to soil infiltration and rainfall-way are:

$$K_0=16.266t^{-0.1659} \tag{11}$$

$$K_1=2.1075t^{-0.299} \tag{12}$$

Based on the change regular of the soil infiltration rate in the rainfall process(as Fig. 3, Fig. 4), it is indicated that the infiltration rate K tends to a steady when the rainfall process reaches 30min, and after then the K reduces not only very slowly, but also the reducing amount is very small. The rainwater infiltration rate at 30min in the rainfall process can be considered as the representative value, the infiltration rate have nearly constant value of the soil infiltration rate.

The Compaction Influence Coefficient of Different Soil. Different Rainwater seepage build capacity of different relative density and type of the soil is discussed, especially the satisfaction of the water permeability of the dense state soil under different rainfall time. A lower relative density of the soil infiltration rate is used as a reference based on the adjustment of infiltration rate compacting factor Y:

$$Y=K'/K_0 \tag{13}$$

Where K' is the certain density of the soil infiltration rate, K_0 is the density of 75% of the soil infiltration rate.

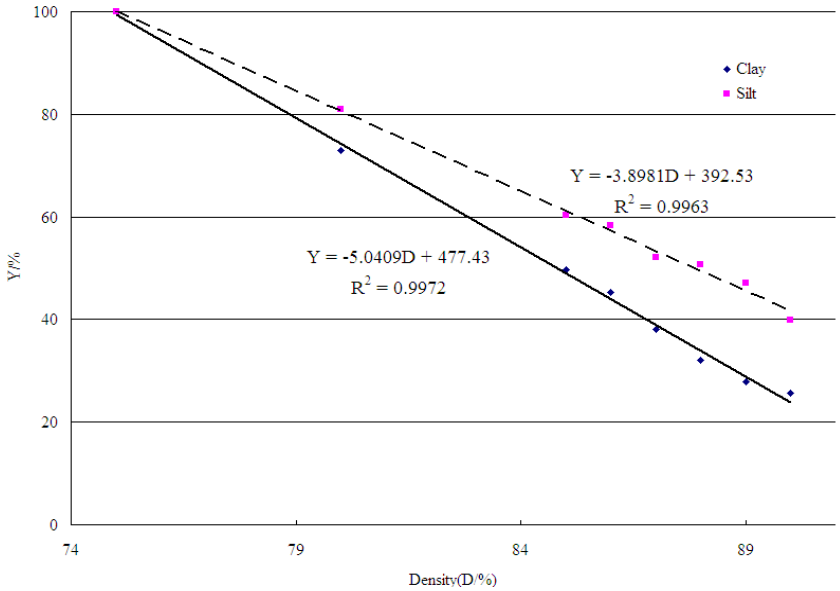


Fig. 5 Effect of relative density to the infiltration rate influence coefficients Y of clay and silty soil

As the representative values is rainwater infiltration rate under 30min, the infiltration rate relative density influence coefficient Y of clayey soils and silty clay can be got, according to the considerations of the relationship between infiltration rate and relative density of the two types of soil, the variation is expressed in Fig. 5.

It is indicated that the infiltration rate of soil reduces as the density increases in Fig. 5, and the reduction of the clay soil is more obvious. When the relative density increases, the regular reflect the attenuation of infiltration rate of the two type soils is expressed as follows:

$$\text{Clayey soils: } Y = 477.43 - 5.0409D \tag{14}$$

$$\text{Silty soil: } Y = 392.53 - 3.8981D \tag{15}$$

Conclusions

The regional storm water must be make full used, and gradient emissions as far as possible, to promote the water saving technology in airfield surface drainage design. In order that rainwater can be use and discharge gradiently, we ought to take the influences of soil type and relative density and other factors, as well as their effects into account in the regional rainwater flow direction distribution design.

In the distribution of regional flow of surface drainage, non-seepage area rain should be assigned to nearby the soil surface area for relatively small and short term rainfall, so that the rainwater held in the surface soil can improve regional surface and atmospheric water environment, and reduce the consumption of other water sources.

The area of seepage and impervious area involved in rain convergence deployment should in an appropriate proportion to keep the rainwater as much as possible in the soil surface. When the soil infiltration rate of soil surface area is small, the required seepage area with the proportion of non-seepage area is relatively large.

Soil infiltration rate is not only affected by the soil types, but also the soil relative density. The experiment results indicate that the silty soil infiltration rate is significantly higher than that of the clay soil, the trend of the soil infiltration rate decreased linearly with the relative density increase.

When the relative density of the soil from 75% to 90%, the infiltration rate will change significantly during the raining, which decreasing rapidly at first, and changing slower lately. Furthermore, when the raining keeps more than 30min, the entry infiltration rate is extremely slow. Therefore, we can take the rainfall infiltration rate in the presence of the drainage design, and assume the rain processes 30min as a design representative value.

References

[1] P. Deng, Urban storm water calculation in Chinese, Water Supply and Sewerage, 1998.

[2] J. Song, Regional urban rainwater utilization system of organic coordination in Chinese, China Water and Wastewater, 2010.

[3] F. Gao, The study of silt, clay compaction and the microscopic mechanism of infiltration in Chinese, Foreign Highway, 2010.

[4] G. Yue, T. Viraraghavan, Preliminary cost-effectiveness analysis of storm water drainage alternatives for an airport extension runway, Environmental Engineering Division, 10 (1985).

[5] A. J. R. Hartley, C. J. Evans, Birmingham International Airport drainage and pollution control works, Proceedings of the Institution of Civil Engineers, 5 (1996).

[6] Halm, Mark J, Managing storm water at airports, Pollution Engineering, 9 (1996).

© (2012) Trans Tech Publications, Switzerland
doi:10.4028/www.scientific.net/AMM.238.460

The Study on Rainfall Threshold Induced Landslides in Yucheng District by Binary Logistic Model

Youyi Zhang

Southwest University of Science and Technology, Mianyang, China

youyzh@126.com

Key words: landslide; binary logistic; rainfall threshold.

Abstract. Ya'an Yucheng District intituled "rain city" or "heavens poured" lies to the west of Sichuan Basin. Most of the landslides take place in the raining season with the shallow layer, small scale. This paper analyzes a great deal of dates of landslides and rainfall in the history in Yucheng District using binary logistic regression model. The results indicate that the rainfall of that day's and personnel 3 days' with landslide is closely related. Based on the analyses, the predict formula of landslide rate and the design formula of rainfall threshold are built, which is important to early warn and forecast the landslide in the research area.

Introduction

Landslide Hazard is the main types of geological hazard, the Landslide result from Rainstorm widely distributed and high frequency of occurrence which cause great harm to humans and great economic losses. According to the UNESCO survey showed that the annual loss of the United States, Japan, Italy and other countries reached to $1.5 billion due to rainstorm caused by landslides. It is estimated that every year china losses amounting to 20 billion yuan due to Landslide Hazard. So it is significant to build the statistical relation between Regional Landslide and Rainfall, determined the landslide rainfall critical value in different areas which will make great contributions to prediction and forewarning of Landslide Hazard in flood season .

Sketchy Circumstances in the Studied Area

Ya'anYucheng District lies to the west of Sichuan Basin. It has an area of 1067.31km^2. Yucheng is the transportation center in the west of Sichuan Province. It is also called "the barrier of Sichuan-Tibet and the window of Tibet". This area is in tropical humid climate with abundant rainfall, Average annual rainy days is 218d, average precipitation is 1805.4mm. Annual precipitation is concentrated in May-October, it reaches 1456.7mm. Accounting for 84.8% of the annual precipitation, the rainfall prominent in July-August, it reaches 868.2mm. Accounting for 48% of the annual precipitation. The heaviest reaches 339.7mm one day (1951~2005) in August 12, 1959. There are 43.7 days that annual precipitation is more than 10mm, 17 days' that more than 25mm, 6.7 days' that more than 50mm, which rains mostly at night. The precipitation happening at night (20:00—8:00) accounts for 60%.

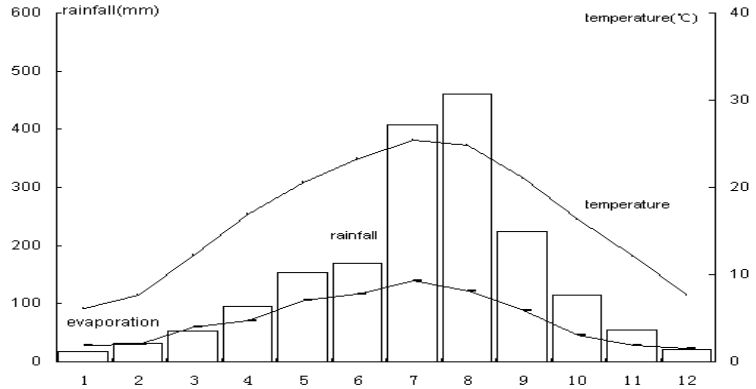


Fig. 1 Air temperature, evaporate quantity of average monthly rainfall

The river in the studied area is belongs to Qingyi river, which is the second order affluent of Min river, the first order affluent of Dadu river. It is 279km, the drainage area is 1.33 × 104km^2, region the length is 34.3km.

Landslide Characteristics in the Study Area

Relationship Between Rainfall Patterns and Landslide. The analysis about landslides and rainfall of the study area indicates the rainfall is mainly concentrated in July and August every year, the average monthly rainfall of many years in the same period also is the most, while the landslide disaster is mostly concentrated in July and August, the occurrence accounted for 79.7% of the total landslide (Fig. 2).

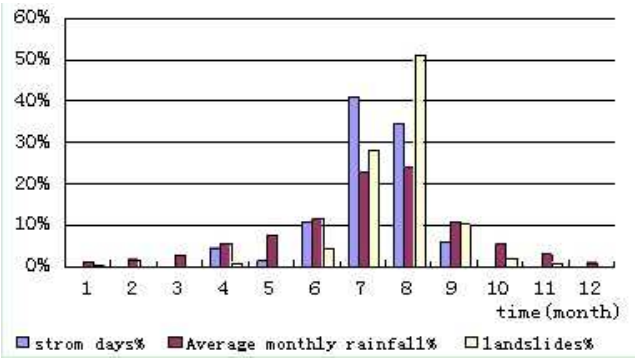
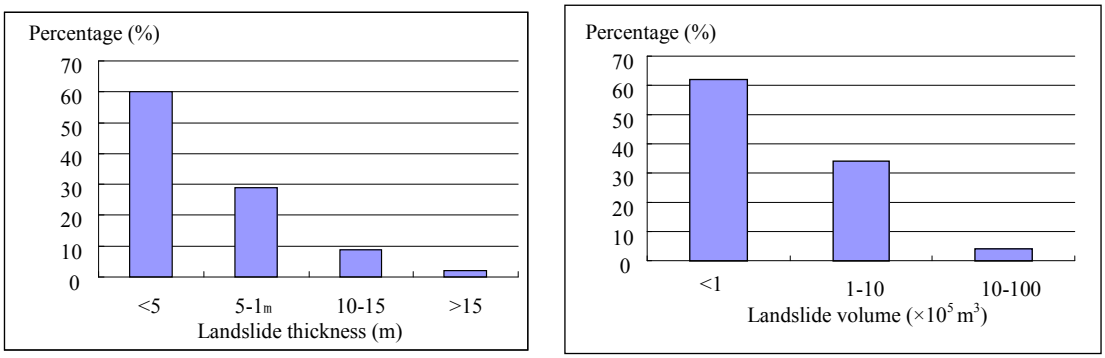


Fig. 2 Property relation between landslide times and rainfall

Characteristics of Rainfall-induced Landslide. According to the survey, study area has a total of 187 recorded landslides, among of this landslide occurrence time accurate to year and month has 162 landslides and accurate to date has 118 landslide, landslide main features are as follows:

(1) Landslide mainly for shallow landslide. Landslide thickness of less than 5m of landslides accounted for 60% of the total number of landslide, landslide thickness between 5-10m accounted for 29%, landslide thickness in 10-15m accounts for 9%, landslide thickness exceed 15m accounted for only 2% of the total number of landslides (Fig. 3a).



(a) (b)

Fig. 3 Property relation between landslide number and landslide (a) thickness, (b) size

(2) Landslides are mostly miniature and medium-sized landslide. Miniature landslide (<10×10^{5}m^3) accounted for 62% of the total landslide, medium-sized landslide（10×10^5 m^3~10×10^6 m^3）accounted for 34%, large-scale landslide（10×10^{6}m^3~10×10^7 m^3）accounted for 4% (Fig. 3b).

Study in Area Induced Landslide of Rainfall Threshold Strength

Data Sources and Screening. Access to historical landslide data in the study area, Mainly through the following channels: (1) government documents, publications, and Sichuan flood season briefing; (2) Ya'an survey of geological hazards study (1:500 000, 1995); (3) Flood season in 2002 and 2003 field investigation; (4) Use of network resources investigation.

Rainfall data of the study area, mainly through the following channels: (1) Ya'an City Bureau of Meteorology; (2) Sichuan Provincial Bureau of Meteorology; (3) laid rain gauge monitoring data.

Through the above channels, a total of landslide points 187, landslide occurrence time accurate to year and month has 162 landslides and accurate to date has 118 landslides.

Got data, there are two limitations:

(1) The distance between rain-gauge point and landslide point is too large, to some extent affected the accuracy of the analysis.

(2) The landslide occurred is inaccurate. A large part of the history of landslide does not have accurate time records, through visits to local people recalling the time of landslide occurrence, it is inevitable that the error.

The study found that landslide mass-occurrence in the study area is closely related to heavy rain Event. However, some monomer landslide occurred in a small rainfall or no rainfall case, analysis of the reasons, mainly due to irrational irrigation, artificial slope cutting. For accurate analysis of the relationship between rainfall and landslides occurred, we have chosen in three days (72 hours) the occurrence of landslides in the above two points as the analysis of samples. In this case, rainfall induced landslides, 85 landslide points to meet the requirements according to this principle.

The Model. Studies under a certain amount of rainfall, landslides occur or not. The problems independent variable is rainfall, the dependent variable has only two values: Landslides occur (1) or does not occur (0). Binary the logistic regression model can be used to predict the probability of two points of the characteristics of the dependent variable, in line with the modeling requirements.

Logistic Regression Model. Binary logistic regression model with one independent variable can be written as:

$$P = \frac{1}{1+e^{-p}} \tag{1}$$

Where $p = B_0 + B_1X_1 + B_2X_2 + \cdots\cdots + B_nX_n$, P is the concept of measuring the probability of occurrence relative to an event; B is the correlation coefficient.

The Logistic Regression Coefficient. In order to understand the meaning of the logistic regression coefficients, the equation can be re-write the ratio of the occurrence of an event, an event ratio is defined for its likelihood of occurrence and the likelihood ratio. Firstly, logistic equation can be written probability, named for the Logit P.

$$\text{Logit}P = \log\left(\frac{\Pr ob(event)}{\Pr ob(noevent)}\right) = B_0 + B_1X_1 + \cdots\cdots + B_nX_n \tag{2}$$

It can be seen that the logistic equation of the regression coefficients can be interpreted to change the value of the independent variable for a unit change in the probability of the number. As the understanding of probability is easier than the understanding of probability Logarithmic, so the logistic equation written as:

$$\frac{\Pr ob(event)}{\Pr ob(noevent)} = e^{B_0+B_1X_1+\cdots\cdots+B_nX_n} \tag{3}$$

When the i-th variable a unit of change, the probability of changes in value. Independent variable coefficient is positive, means that the probability of events will increase the value of a big one; if the independent variable coefficient is negative, means that the probability of events will be reduced, this value is less than 1; for 0, this value is equal to 1.

Evaluation of Model. Modeling, you need to judge the pros and cons of the fitting. In this paper, data are divided into two parts, part of the data to establish the regression equation, and then another part of the data into the equation to assess the model fits the data.

(1) Regression coefficients significance test. The regression coefficient significance test purpose is to individually test each explanatory variable in the model with the Logit P having a significant linear correlation, using the Wald test statistic. Wald test statistic degrees of freedom for a chi-square distribution, the value of the regression coefficients and their standard error of the ratio of the square.

(2) Goodness of fit test of the regression equation

① The Cox & Snell, R_2 statistic. Cox & Snell R_2 statistics are similar with an R_2 of the general linear regression analysis, it is also the equation interpreted variables reflecting the degree of variation to explain, its mathematical definition:

$$\text{Cox \& Snell R}^2 = 1 - \left(\frac{L_0}{L}\right)^{\frac{2}{n}} \tag{4}$$

② The Nagelkerke R_2 statistic. Nagelkerke R_2 is a modified Cox & Snell, R_2, and also reflects the equation for the explanatory variable degree of variation explained, and its mathematical definition:

$$\text{Nagelkerlke R}^2 = \frac{\text{Cox \& Snell R}^2}{1 - (L_0)^{2/n}} \tag{5}$$

Nagelkerke R_2 values in the range between 0 and 1, the closer to 1, the higher the degree of the goodness of fit of the equation; more close to 0, the lower the goodness of fit of the equation.

③ Misjudge the matrix. Misjudge the matrix is an extremely intuitive evaluation of the model of the merits of the method, through the matrix form of a table to show the predictive value and the actual value of the degree of agreement, the general form shown in Table 1. Table 1 is the actual value of 0 predicted values for the number of zero, is the actual value of 0 to predict for the number of the value of 1, is the actual value of a predictive value for the number of zeros, is the actual value of a predictive value for a number of columns, the correct rate can evaluate the quality of the model, the higher the correct rate means that the model the better.

Table 1 Erroneous judgement matrix

		Observed value		
		0	1	correct rate
Observed value	0	f_{11}	f_{12}	$\frac{f_{11}}{f_{11}+f_{12}}$
	1	f_{21}	f_{22}	$\frac{f_{22}}{f_{21}+f22}$
	General correct rate	$\frac{f_{11}+f_{22}}{f_{11}+f_{12}+f_{21}+f22}$		

Selection of the Model Data and Calculation Results

In order to determine the landslide occurred a few days ago the rainfall impact on the landslide, and the extent of impact, Special selected in August 2003, a continuous landslide concentration of development (a total of 32 landslide points) period of time data using a logistic regression model to strike a correlation coefficient of daily rainfall and landslides. Occurrence of daily rainfall before the landslide of the variable, select the date of rainfall, one day before rainfall, two days before rainfall, three days before the rainfall, four days before the rainfall, five days before rainfall as independent variables. To individually import the SPSS software, the calculated results with the relationship between statistical rainfall and landslides occurrence or not are shown in Fig. 4.

From the calculated results, As one by one to increase the number of variables, the number of rainy days to observe the landslide rainfall before the landslide. From the calculated results ,As one by one to increase the number of variables, the number of rainy days to observe the landslide rainfall before the landslide. We can see that when the independent variables to five days, the rainfall on the 6th, the correlation coefficient B becomes "0", indicating that the rainfall in the 5 days before the landslide occurred in the study area had no effect. It was concluded that the study area landslide occurrence is related to the former four days of rainfall, the date of rainfall and 3 days before the cumulative rainfall. In addition, we also can be seen that the day correlation coefficient of rainfall, and thus the impact of the landslide is also the largest.

Calculated variable coefficients (B) and constant, you can get:

$$p = 0.098R_1 + 0.065R_2 + 0.058R_3 + 0.033R_4 - 10.841$$

Get the study area landslide probability prediction formula:

$$P = \frac{1}{1 + e^{-(0.098R_1 + 0.065R_2 + 0.058R_3 + 0.033R_4 - 10.841)}} \tag{6}$$

Where P is the probability of landslide; R_1, R_2, R_3 and R_4, respectively, for the landslide on the 1st, 2nd, 3rd and 4th of rainfall.

Variables in the Equation

		B	Sig.
Step 1(a)	@1	.098	.044
	@2	.065	.007
	@3	.058	.019
	@4	.033	.038
	@5	.000	.998
	@6	.000	.998
	Constant	-10.840	.022

a Variable(s) entered on step 1: @1,

Model Summary

Step	-2Log likeihood	Cox & Snell R Square	Nagelkerke R Square
1	14.641(a)	.686	.931

a Estimation terminated at iteration number 10 because parameter estimates changed by less than .001.

Classification Table(a)

Observed			Predicted			
			Landslide		Percentage	Correct
			0	1		
Step 1	Landslide	0	51	0		100.0
		1	1	31		96.9
	Overall Percentage					98.8

a The cut value is .500.

Fig. 4 Result of computed

See from the above, the study area, landslide rainfall of the day and three days before the landslide will have a direct impact, which means you can use the day and three days before rainfall to express the critical rainfall.

Model Tests and Analysis. In order to test the accuracy of the prediction formula used to consider a formula to verify that all 53 landslide points in August 2003 outside the landslide occurrence probability of the rainfall on the 4th, landslide probability of occurrence of the landslide point of greater than 50% has 41, accounting for 77.4% of the total number. Very small probability of occurrence of the 12 landslide points, validation fails. The analysis shows that 12 landslide points that day rainfall and a combination of pre-rainfall is very small, and the landslide points is in more than 10 kilometers from the nearest rain gauge point, and some even over 20 kilometers. Validation failure was mainly due to the value of the rainfall inaccurate result.

Critical Rainfall Intensity to Determine. Landslide rainfall statistics based on the study area occurred in the past, excluding the point of validation failure, the choice of the remaining points on the day of rainfall and three days before the rainfall for the evaluation factor, making scatter plots, shown in Fig. 5.

The results show that, the study area landslides induced by rainfall critical value:

$$R_1 = \begin{cases} 250e^{-0.0238R_{L3}} & (R_{L3} < 65) \quad (a) \\ -32.851Ln(R_{L3}) + 190.35 & (R_{L3} \geq 65) \quad (b) \end{cases} \tag{7}$$

Where R_{L3} is 3 days before the cumulative rainfall, R_1 is the landslide occurred that day rainfall.

It can be seen from Fig. 5:

(1) The current three-day rainfall less than 65mm, the daily rainfall greater than 53mm, the daily rainfall landslide plays a dominant role, the available 7 (a) to determine; Day rainfall is less than 53mm, three days before rainfall at 65mm, the pre-rainfall dominant role in the occurrence of landslides and 7 (b) to determine.

(2) Early rainfall (RL3) with little or no pre-rainfall, daily rainfall (R_1) to reach 250mm, there will be landslides occurred; of rainfall (R_{L3}) of 200mm or above, even if the rainfall is very small，the study area will be a landslide occurred.

(3) The day and early rainfall (R_{L3}) of less than 118mm, the study area, there is no landslide; the day rainfall of more than 53mm, and three days before the cumulative rainfall of more than 65mm, the study area, a landslide occurred.

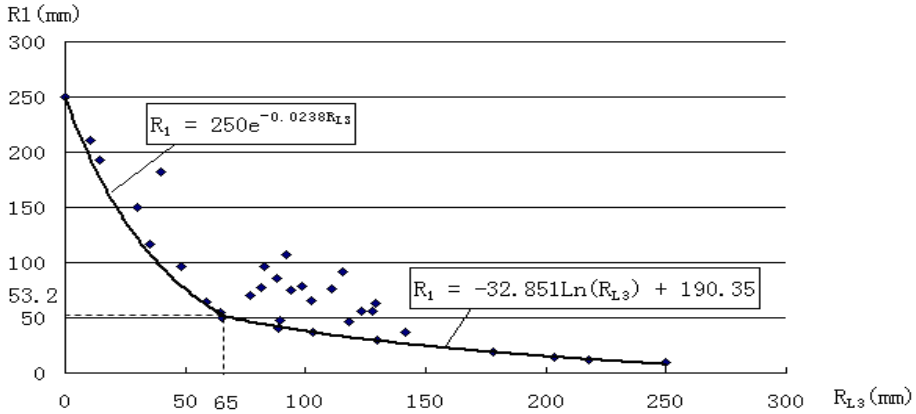


Fig. 5 The scatterplot of daily rainfall and earlier stage rainfall

Conclusions

The study area is mainly developed in small and medium-sized shallow landslide.

The study area landslide occurred not only closely related with the date of rainfall, but the cumulative rainfall of three days before.

The date of rainfall and accumulated rainfall on the 3rd of rainfall exceeds 200mm, the study area landslide occurred;-day rainfall of more than 53mm, the pre-rainfall exceeds 65mm, the study area landslide occurred .

References

[1] Y. Liu, Critical precipitation of rainstorm for cavsing landslide, Hydrogeoloty and Engineering Geology, 3 (1998) 43-45.

[2] J. Xu, K. Sun, Determination of landslide boundary by fluid inclusions, China Clvil Engineering Journal, 40 (2007) 69-73.

[3] E. W. Brand, J. Premchitt, H. B. Phillipson, Relationship between rainfall and landslide in Hongkong, Proceeding 4th International Symposium Landslides, Toronto, 1 (1984) 377- 384

[4] C. Liu, Y. Li, Study on early warning test field for geo-hazards in Ya an region, Sichuan Province of China, Hydrogeoloty and Engineering Geology, 31 (2004) 20-30.

[5] J. Xie, L. Liu, Study on the threshold valves of rainfall of landslide hazards for early-warning and prediction in Zhejiang province, Geological Science and Technology Information, 22 (2003) 101-105.

© (2012) Trans Tech Publications, Switzerland
doi:10.4028/www.scientific.net/AMM.238.466

Application of New Soil Consolidator in Road-construction Engineering

Hong Zhang[a], Dongliang Xun[b], Zhao Yang[c] and Fuquan Ji[d]

CCCC Second Harbour Engineering Co., Ltd., Wuhan 430040, China

[a]ming040416@163.com, [b]277507986@qq.com, [c]yangzhaolp@126.com, [d]jifuquan_geo@163.com

Keywords: soil consolidators; HEC; HAS; silt; experiments; road-construction engineering.

Abstract. This paper contrastively analyses the consolidation instances of silt with HEC and HAS soil consolidators, also emphatically discusses the influence regularities of the compressive strength of solidified soil with the following factors: the dose of consolidators and the curing time. Meanwhile, from the point of view of experiment, this paper studies the physical and mechanical properties of solidified soil. Case study shows that HEC and HAS soil consolidators behave as well as cement and lime in road-construction engineering, and even that filling subgrade independently. Also, this paper proposes the appropriate value 6% of HEC and HAS soil consolidators for solidifying silt layer, which can be used as reference for the similar geological conditions.

Introduction

From the early 1980s, as a new road material, solidified soil has been used in road-construction engineering and achieved remarkable economic and environmental benefits, which originates from Europe, America, Japan and Taiwan, China, etc. However, in many areas of China, the soft soil has characteristics of high water content and big void ratio, which result that cement is less living in dealing with the soft soil by oneself. Whatever, the structure of solidified soil mainly forms from two components of soil particle cementing and pore filling. But the growth of compression strength only comes from the gel sex of hydrates cementation generated by cement hydration, when using cement alone [1-3]. Ning and Huang [4] show that, for loose porous soft soil, the strength of solidified soil increases insignificantly, because there are some pore left, that the cement hydration products can't effectively filling the pore. For the silt layer in the area of Ningbo, China, this paper studies on HEC and HAS soil consolidators, discusses the physical and mechanical properties change of solidified soil, so as to provide beneficial reference for the theory and practice of road-construction engineering.

Test Materials and Methods

Soil Consolidators and Samples. HEC (High strength and water stability Earth Consolidator) is a hydrated kind of consolidator, which is high water-tolerant and solid-powder, belongs to rigid gelled material with inorganic water. The density is 2.90 g/cm^3, the specific surface area is 400 m^2/kg, the fineness is less than 4.0% with 80μm square hole, the content of MgO is less than 7.0%, and SO_3 is less than 4.0%, the time of initial set is more than 45min, and final set is less than 12 hours [5].

HAS is a high water-tolerant kind of soil consolidator, which is a new water-rigid gelled material produced from raw material containing industrial waste more than 80%. The density is 2.90 g/cm^3, the specific surface area is 372m^2/kg, the content of SO_3 is less than 4.34%, the time of initial set is more than 3.05 hours, and final set is less than 4.22 hours [6].

The silt samples are from Ningbo, China, the physical parameters of silt samples are shown in Table 1 shows that the silt can't satisfy the filling requirements, as its water content reaches 50%, so that its strength is lower.

Samples Preparation and Maintenance. HEC and HAS soil consolidators form with solid-powder shape, while prepare the samples, consolidators should be mixed with water and soil evenly under varying dose, and the whole process must be done in 3~4 hours. All samples should be maintained naturally until curing time in laboratory. The test plan is as follows: the dose of HEC and HAS soil consolidators is 4%, 6% and 8%; curing time is 1d, 3d and 7d.

Table 1 Physical parameters of silt samples

Depth (m)	Water content ω (%)	Proportion Gs	Liquid limit ω_L (%)	Plastic limit ω_p (%)	Liquidity index I_L	Plasticity index I_P	Organic content (%)
12~12.2	49.8	2.74	40.0	21.5	1.53	18.5	4.7
12.2~12.4	52	2.75	41.9	22.1	1.51	19.8	4.8
12.4~12.6	51.1	2.74	39.9	21.5	1.61	18.4	3.8

Test Results

Water Content and Dry Density. For soil samples, which have different dose of HEC and HAS soil consolidators, the curves between dry density and curing time are shown in Fig. 1. The curves between water content and curing time are shown in Fig. 2.

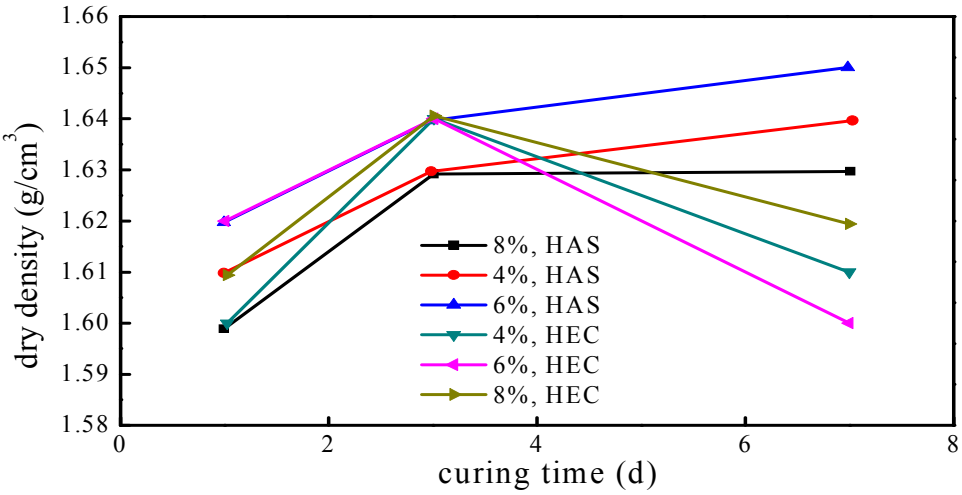


Fig. 1 Curves between dry density and curing time with different doses and species of consolidators

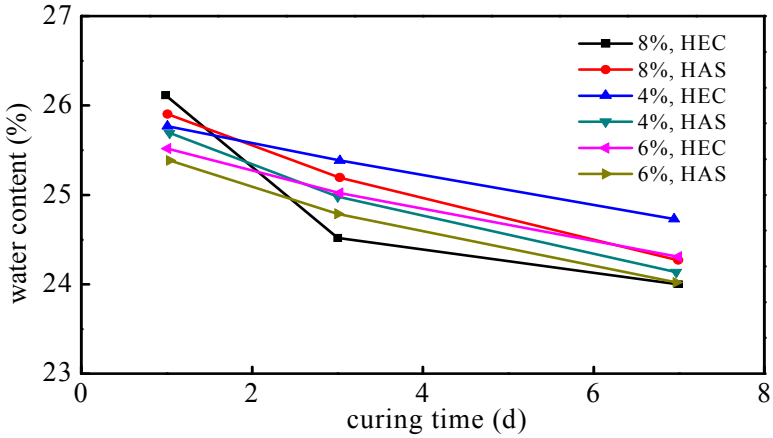


Fig. 2 Curves between water content and curing time with different doses and species of consolidators

Fig. 1 and Fig. 2 show that along with the increase of consolidators' dose, water content reduce, but dry density increase. For HEC consolidator, its dose has little influence on dry density, whatever the dose is 4%, 6% and 8%, the dry density reaches maximum at the 3d curing time. While the curing time reaches 5~7d, the water content and dry density of solidified silt samples change slowly.

Compaction Test. In order to explore the influence laws of dry density and water content with consolidators' dose, and then determine the maximum dry density and the optimum water content for each case of dose. This paper experiments on solidified soil samples according to the compaction design. The results are shown in Fig. 3 and Fig. 4.

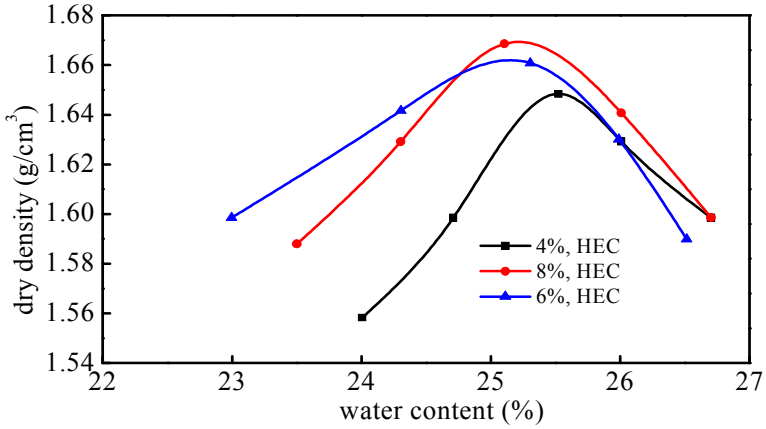


Fig. 3 Curves between dry density and water content with different dose of HEC

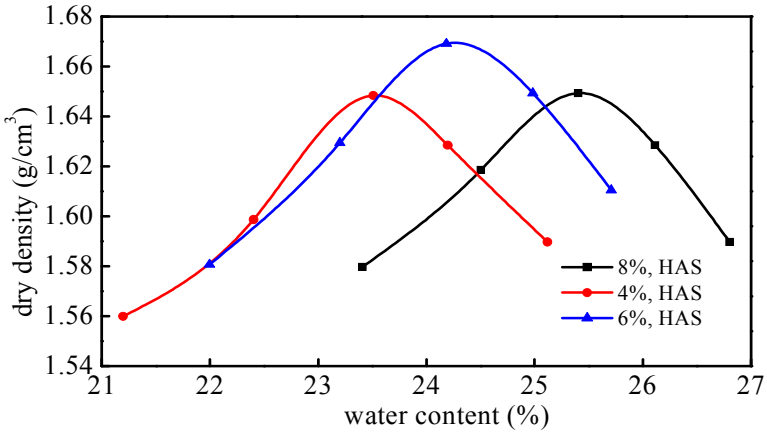


Fig. 4 Curves between dry density and water content with different dose of HAS

Fig. 3 and Fig. 4 show: (1) For the optimum water content, solidified silt samples have the following laws: 4% HEC > 6% HEC > 8% HEC; 8% HAS > 6% HAS > 4% HAS. Overall, HEC and HAS consolidators have improved the optimum water content at different degrees. (2) For the maximum dry density, solidified silt samples have the following laws: 8% HEC > 6% HEC > 4% HEC; 6% HAS > 8% HAS > 4% HAS. However, the dose has little influence on the maximum dry density, when it changes from 4% to 8%.

Unconfined Compression Strength. Unconfined compression strength determines the mechanical performance of solidified silt samples, which depends on the physical parameters of soil and consolidators' properties. For solidified silt samples, which have different dose of HEC and HAS consolidators, the curves between unconfined compression strength and curing time are shown in Fig. 5 and Fig. 6.

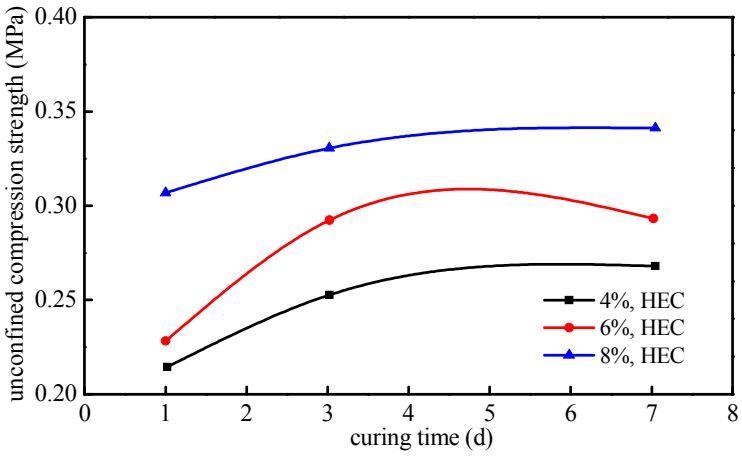


Fig. 5 Curves between unconfined compression strength and curing time with different dose of HEC

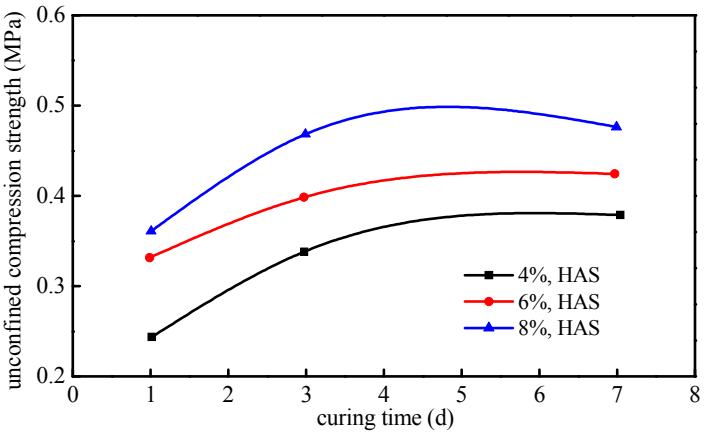


Fig. 6 Curves between unconfined compression strength and curing time with different dose of HAS

Fig. 5 and Fig. 6 show: (1) Along with the increase of curing time, unconfined compression strength increase; (2) Along with the increase of consolidators' dose, unconfined compression strength increase; (3) HAS is better than HEC. The unconfined compression strength can reach value of 0.49 MPa, when the dose of HAS is 8%.

Conclusions

The physical and mechanical properties of solidified silt samples have been improved effectively, which mix with HEC or HAS soil consolidator. As results, the solidified silt layer can be used as the filling material for road-construction engineering, which meets the design requirements.

The test shows that both HEC and HAS soil consolidators can solidify silt layer, and the advisable value of dose is 6%.

For unconfined compression strength, HAS is better than HEC. However, for dry density and water content, HAS is as well as HEC.

In site, the curing time of solidified silt should be 5~7d, then filling construction may proceed. In a word, the relationship between curing time and dose must be paid important attention, so that the best combination scheme is made in site.

References

[1] S. Saitoh, Y. Suzuki, K. Shirai, Hardening of soil improved by deep mixing method, Proc. of the 11th Int. Conf. SMFE, 1985: 1745-1748.

[2] F. G. Bell, Cement stabilization and clay soils, with examples, Environmental and Engineering Geoscience, 1 (1995) 139-151.

[3] M. Gotoh, Study on soil properties affecting the strength of cement treated soils, Proc. Conference, Tokyo, 1996: 399-404.

[4] J. Ning, X. Huang, Research on structure formation and the mechanism of strength increasing of stabilizing soil, Journal of Beijing University of Aeronautics and Astronautics, 1 (2006) 97-102.

[5] T. Chen, J. Zhou, M. Sun, Influence of solidfying agent HEC on loess Permeability, Agricultural Research in the Arid Areas, 4 (2004) 192-194.

[6] L. Zhang, Application of HAS curing agent in the hardening of overwet earth subgrade, Western China Communications Science and Technology, 4 (2006) 27-31.

© (2012) Trans Tech Publications, Switzerland
doi:10.4028/www.scientific.net/AMM.238.470

Study on Updating Design Pattern of Using Solar Energy Hot Water System in High-rise Residence

Junjie Zhang[1,a], Meibao Yu[2,b] and Qiang Liu[1,c]

[1]University of Jinan, No. 106 JiWei Road, Jinan 250022, China

[2]Shandong Lianchuang Architectural Design Co.,Ltd, No. 2000 Shunhua Road, Jinan 250022, China

[a] jj7212@126.com,[b] yumeibao@126.com,[c]cea_liuqiang@ujn.edu.cn

Keywords: high-rise residence; integration; design pattern; update.

Abstract. There are many problems on using solar water heating system in high-rise residence which mainly due to the traditional design method. By means of analyzing the design goal and principles of integration, this paper puts forward a new combinative idea, and meanwhile draws such conclusions as the updating planning design mode, the updating architectural design mode and the updating skin design mode.

Introduction

In order to solve the problem of tension of fossil energy and increasing use of building's energy consumption, the prospective trend within the world is more and more extensive use of renewable energy. The current consensus is that by 2020 renewable energy utilization ratio will reach 20%. China has good conditions for solar energy utilization, moreover, residential building is the biggest form. With the shortage of land resources and rapid process of urbanization, high-rise residence will occupy more and more proportion, so the design problem of high-rise residence based on solar energy utilization is more important and urgent.

Research Status Quo

The domestic research focus of using solar energy in residential building is the integration of solar hot water system and building. Representative researches: Zhong Jishou put forward integrated design method and principle between residence and solar hot water system [1]; Yuan Ying proposed the integrated idea based on solar collector component [2]; Song Dexuan funded by NSFC researched on the Shanghai ecological high-rise residential building using solar energy, and from the point of view of system theory and ecological view, his graduate Shi Jie put forward the integrated methods and approaches between solar hot water system and building external interface in her doctoral thesis [3]; through studies on high-rise residential building application of solar water heating systems in both North and South, Du Xiaohui proposed a combination of method and design variable from the roof and facade application in her dissertation [4].

Design Goals

It refers that the application of the solar water heating system should be integrated into the whole design process, especially in the early design phase, the design should comprehensive considered the building's basic conditions, characteristics, appropriate solar hot water system, building form, planar function, water heater position, and other related technology factors such as cohesive requirements. It should not only meet the requirements of high-rise residential style and function, but also to meet the requirements of high-quality supply of hot water.

Design Principles

Principles of Integrity. It refers that the high-rise residential building and solar hot water systems should be considered as a whole, in this way, systems design and architecture will be synchronized, so that the selection and application of systems should give full consideration to the building's geographical environment, layout, shape characteristics, local climate characteristics, life characteristics and other factors. The solar water heating systems based on the reasonable layout and high efficiency can organically be combined with the building, and can be a portion of building.

Principles of High Efficiency. It refers that we should take full advantage of the available area in the high-rise buildings when the solar water heating systems have been installed, solve the contradictions between the installation area and required. We also should consider the geographical environment, climate, economy and flat layout feature, and select the appropriate type of collector, installation angle and position, so that the efficiency of using solar water heating systems would be very high.

Principles of Conveniences. It refers that the installation of solar water heating systems should take full account of the special requirements of the location, and consider the conveniences of the installation, maintenance, clean, does not interfere with tenants, damaged the building, and can enhance the quality of public space.

Principles of Economy. It refers that the selection of solar water heaters type and system forms should synthetically consider of the system cost-effective. After determining the type of solar hot water system and its heating mode on the basis of the land natural conditions, operating requirements, and affordability, then the design can start.

Update the Design Mode

China's traditional planning and architecture design start from function, and less to consider the solar energy utilization but with the energy crisis and environmental pollution, the design starting from function, the environment and renewable energy use in the future is the inevitable choice, therefore, the traditional design patterns must be updated.

Update the Planning Design Mode. The planning layout are not only related to the quality of space, but also have a direct impact on solar energy utilization, especially in high-rise residential areas, As the reason of shading constructions, it is difficult to take full advantage of solar energy resources, so the planning design mode need to be fully taken into account. Foreign researchers have been studied solar application from an overall perspective. They think that the core of application of solar energy is compositive design, which is integrated design.

Therefore, in the planning stage, designers should analyze the impact on the utilization of solar energy not only including different architectural plan forms, correlation, and building height, but also according to different climatic characteristics, from the point of energy consumption for the year, study on the changes of planning, particularly the patterns of different architectural groups effecting on solar energy utilization, that has attracted the attention of more and more researchers. These papers such as references [5, 6] belong to this kind of research.

Update Architectural Design Mode. Current, when we designed, we considered high-rise residential building and solar energy as two independent treatments, almost didn't consider the impact on residential internal, which obviously can not make both the real combination. For example, the current solar hot water system on the high-rise residence is a distributed system installed on the balcony, but there are many problems in these aspects, such as installation, maintenance, collection efficiency, and have great impact on building structure, insulation, waterproofing, aesthetics, in order to solve these questions, we must change the traditional design mode of thinking, so that the improvement of residential function can closely combine with utilization of renewable energy.

Like the high-rise panel residential building, the conventional layout arranged the combination of elevators and stairs in the north, but this layout has many functional disadvantages and prejudices to the installation of solar water heaters. However, optimized residential units layout not only solve the

drawbacks of traditional, such as a good scale of indoor room , and indoor environment, but also solve the contradiction of the installation, maintenance, cleaning of solar water heaters on the south external walls.

Therefore, if the solar hot water system can become a fundamental element of building, it can combine with the optimized residential unit layout, the integration of them will be genuine.

Update the Design Mode of Building Skin. Traditional residential building shape is almost a reflection of the internal space, and then by the local shapes of the balconies, stairways, roofs, etc, material, and color changes to shape the architectural image. Clearly, this approach can not meet the use of solar energy, moreover, the post-accession of solar components will inevitably bring about the difficult coordination problems. According to the demand of solar energy utilization, the roof and south wall are the most appropriate parts of using solar energy, how to make full use of this site is the premise of combining with the building and increasing solar energy utilization efficiency. Therefore, a flexible, multi-functional, ecological building skin will be an essential shape element in the future high-rise residential building.

For example, if some frameworks were to set up on the building roof, the south facade and east-west part of the external walls, it not only can increase the utilization area of solar energy, provide installation area of solar water heater, photovoltaic system, the Solar-wall air heating, Trombe wall and the shadow role, but also solve the utilization problem of solar energy in lower portion of the high-rise residence. Moreover, through the initial program design and rhythmic solar component layout, it can also form a unique architectural technological aesthetics.

Conclusions

While sustainable development, ecological building, green building and construction conserves energy gradually have been the focus of the construction industry, it is the time that architects began to update the traditional design methods and mindset. Architects should establish a technical sense from the phase of program, regard the technology as the elements and contents of building, as the inspiration and source of architectural creation. It should be so for residential construction closely related to people's lives.

References

[1] China National Engineering Research Center for Human Settlements, Integration Design for Solar Water Heating System in Dwelling, China Architecture & Building Press, 2006

[2] Y. Yuan, G. Wang, Z. Wang, Solar collector components –only way of solar building integration, ACTA Energiae Solaris Sinica, 1 (2005) 44-48.

[3] J. Shi, The research on Solar energy Integrated Design With outside Surface in Shanghai High-rise Apartment, Doctoral Dissertation of Tongji University, 2008.

[4] X. Du, Design research of solar water heating system into high-rise residences, Doctoral Dissertation of Tianjin University, 2010.

[5] Z. Li, X. Li, P. Li, Influence of construction groups to solar thermal utilization on high-density and high-rise building facade, Construction Conserves Energy, 3 (2011) 29-32

[6] J. Zhao, Q. Wang, X. Wu, The simulation research on the energy consumption of semi-enclosed cluster residential building, Journal of Xi'an University of Architecture & Technology, 4 (2010) 579-582

© (2012) Trans Tech Publications, Switzerland
doi:10.4028/www.scientific.net/AMM.238.473

Application of Thermal Priority Strategy in Energy-saving Optimization Design of Low-cost Rural Residence

Meijun Lu[a] and Zhifeng Zheng[b]

School of Architecture, North China University of Water Resources and Electric Power, Zhengzhou 450011, China

[a]tumu1989@yahoo.com.cn, [b]8116590@qq.com

Keywords: thermal priority; low-cost; rural residence; energy efficiency optimization design; plane grid.

Abstract. In order to improve the indoor thermal environment of rural residences, on the basis of meeting the requirements of functionality, living habits and certain architectural modeling, the thermal priority strategy is put forward into the design. Aiming at the low cost, from the perspective of building layout and architectural monomer design, the thermal priority strategy is applied to energy saving design for rural residence to get the effective and reasonable comfort-type rural energy efficiency residence. Specific measures are adopted such as the selection of sunny and sheltered sites in north-south direction, the courtyard and main entrance location in south or south-east side to form the layout opening from east to west, the technical performance with low shape coefficient and energy-saving shape and taking solar radiation into account, and the reasonably settings of climate buffer layer, thermal comfort zone, plane grid, doors and windows.

Introduction

With the improvement of living standards in rural areas, more and more residences have been constructed in rural areas in China. Currently, rural construction area in China is about 24 billion square meters, which accounts for 60% of all buildings and continues to increase rapidly [1]. Therefore, building energy saving in rural areas must be put as the priority overall.

On the one hand, economy in rural areas is relatively backward and villagers' energy saving consciousness is weak. On the other hand, thermal performance of enclosure structure and air tightness of doors and windows in rural residence are poor, which results in poor rural residential indoor thermal environment and thermal comfort. Therefore, it is completely essential to explore a design strategy which is low in price, complying with the energy saving requirements and improving indoor thermal environment in rural residences.

Proposing Thermal Priority Strategy

Thermal priority means that when designing rural residences, it should meet the needs of villagers' use function and life habits, with certain architectural modeling, people should take the priority of thermal factors such as sun radiation and wind. Through rational optimization design of energy saving, not only more solar radiation heat in winter and less in summer solar radiation heat can be gained by external structure, but also cold air penetration can be reduced in winter and natural ventilation cool can be strengthened in summer.

Currently, in order to improve rural residential indoor thermal environment and thermal comfortableness, meet requirements of energy saving, considering low cost, people can relatively weaken use function and building modeling design in rural residence and strengthen energy saving design. From the perspective of building layout and residential building monomer design, people should apply thermal priority policies to energy saving optimization design in rural residence in order to devise effective and reasonable rural energy saving residence of comfortable type.

Application of Building Layout in Rural Residences

Building Location Facing the Sun and Sheltering. Building base should be selected in sunny and sheltered site, which will not be seriously blocked by other buildings around the building [2]. Main facade facing south in rural house can be selected, so that it is convenient for the main rooms gaining more solar radiation in winter, preventing the adverse effects of cold air infiltration in winter.

Selection of Building Orientation. All regions in China give the best and appropriate local orientation, which will make the main wall of building receive more solar radiation in winter, get less solar radiation in summer, so as to reduce energy consumption in winter heating and summer air conditioning [3]. Combining the best and most appropriate local buildings, north-south or near to north-south orientation is chosen in rural residence, Such measures not only will be conducive to fully gain solar radiation in winter, but also will improve indoor thermal environment of residence in summer and transitional season by the way of natural ventilation and further improve indoor thermal comfort.

Settings of the Layout of Building, Courtyard and Main Entry. In China northwest wind is prevalent in winter, and southeast wind is prevalent in summer. When layout of rural housing is designed, in order to save energy, on the one hand, building layout should be closed to northwest, which is in favor of reducing cold air permeability in winter, thereby reducing energy consumption for heating during the winter. On the other hand building layout should be open to southeast, which is in favor of natural ventilation organization in summer, thus reducing the energy consumption of air conditioning in summer. The courtyard and the main entrance is set in south or southeast of rural residence, building layout of opening the east side and closing the west side is formed, which not only will weaken adverse effects from northwester penetration in winter, improve thermal comfort of rural housing in winter, but also is conducive to introduce the southeaster into interior in summer, form natural ventilation, increase residential thermal comfort in summer [4].

Application of Building Monomer Design in Rural Residence

Application of Building Forms in Rural Residence. When people design residences, they often pursue changes in architectural forms. If thermal factors are given priority, reasonable building form design not only requires small shape coefficient, but also needs more radiant heat gaining in winter and less radiant heat gaining in summer. The architectural form through optimized portfolio will be the comfortable type of energy-saving houses in rural areas.

Reducing Shape Coefficient. The larger the building shape coefficient is, the greater the heat dissipation area of shared unit building space is, and the more energy consumption is. If the other conditions are same, building energy consumption will be increasing with the increasing of shape coefficient [5]. From the view of energy-saving, building shape coefficient should be reduced as much as possible.

At the present stage, typical rural residence is mostly one or two-story detached building, whose shape coefficient is larger and which is not conducive to energy saving. So, the on one hand, architectural shape whose flat and vertical surface form is flat and rule can be chosen in order to reduce the building shape coefficient. On the other hand, building layer number should be increased from one to two-layer or three-layer and architectural form should be adjusted from one independent household to a few row houses, in order to achieve small shape coefficient. In this way, indoor thermal comfort can be improved and heat loss in winter and summer can be reduced.

Energy-saving Shape Considering Solar Radiation. In Fig. 1, cube building models with the same volume are arranged into various shapes and orientations by the different ways. From the perspective of gaining solar radiation heat, the effect of building shape on thermal performance has been studied. Few conclusions can be drawn from Fig. 1: building shape A is one type which gains minimum radiant heat gain in winter; building shape D is one type which gains maximum radiant heat in summer; building shape E and D can gain more balanced radiation heat throughout the year; while building shape B with more appropriate length, width and height ratio has more heat gain in winter and less heat gain in summer [5].

It is essential to take thermal insulation in winter and heat in summer into account in rural housing in the cold and the hot-summer and cold-winter areas. So building shape B is relatively moderate in width, depth, and height. For one thing more solar radiation heat can be gained by larger metope in south in winter. For another less solar radiation heat can be gotten by smaller metope in east and west in summer. So it can be regarded as preferred rural residential energy-saving shape in cold and hot-summer and cold-winter region.

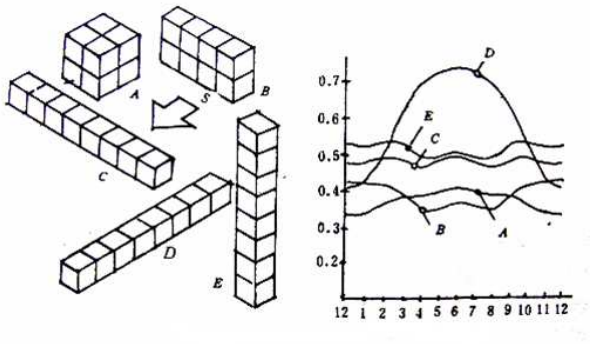


Fig. 1 Building radiant heat gain of different body with the same volume

Application of Plane Layout in Rural Residence

Reasonable Settings of Climate Buffer Layer. When rural residential apartments are designed in order to ensure the thermal comfortableness of main function rooms, thermal factor can be given top priority. The climate buffer layers can be set between indoor space and outdoor spaces of low temperature. Such buffer layers look like a lot of "Hot Gates", which not only can make the heat loss reduction from 40 to 50 per cent through external wall of room, but also can greatly reduce cold air infiltration of main function room.

Climate buffer layers can be achieved by arranging intensively the secondary room or traffic space in the north and west sides [3]. All variety of transitional space between internal and external architectural environment, such as gallery, platform, balcony, verandah and attached sunshine room can be designed reasonable, which can form climate buffering layer in north, west and south side in order to reduce heat consumption in winter [4]. Sketch of climate buffer layer is shown in Fig. 2.

Reasonable Settings of Thermal Comfort Partition. If giving priority to thermal factor, when rural residential style is designed, requirements for individual room temperature is not the same, such as stoves and refrigerators in kitchen can emit a certain amount of energy. Thus similar rooms of thermal requirement can be arranged intensively. The main function rooms in rural houses which are warmer spaces should be arranged in south side of residence, such as the master room, senior room, living room and dining room. So layout can not only be conducive to living space to meet the requirements of winter sunshine, but also be full access to solar radiation in winter. Therefore the energy consumption for heating during the winter can be effectively reduced. The auxiliary rooms in rural house which is colder space should be arranged in north and west side of residence, such as kitchen, bathroom, store room, garage or staircase, so as to form buffer layer of shielding climate. Bathroom can be arranged in the middle, by virtue of the surrounding room surrounded from the effects of adverse weather. Such thermal comfort partition can be conducive to get reasonable energy-saving type in rural residence [3].Sketch of thermal comfort partition is shown in Fig. 3.

Analysis of Planar Grids of Thermal Priority

It is necessary to take multi-factors into account to arrange each room layout in residential plane design. When rural residential plane is designed, based on low-cost, on the basis of meeting the needs of rural living habits, use function, and certain architectural modeling, priority can be given to thermal factors.

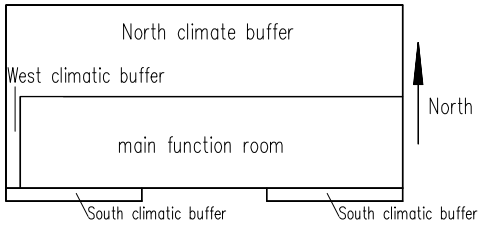


Fig. 2 Sketch of climate buffer layer

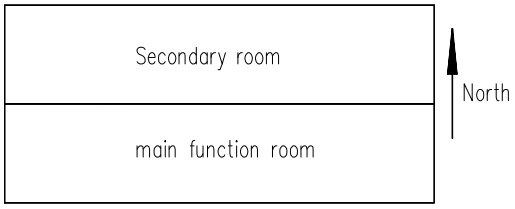


Fig. 3 Sketch of thermal comfort partition

At the present stage, typical rural residences are mostly two-storey detached buildings, whose form is three-bay and two-depth. Fig. 4 and 5 are respectively plane grid graph in one-layer and two-layer. Considering comprehensively thermal factors such as solar heat transfer surface, thermal analysis of priority in the plane grid can be given. Among Z stands for the main functional space and F stands for auxiliary space. For example, Z11 stands for the 1th grid main room in 1 floor and Z12 stands for the 2th auxiliary grid room in 1 floor. Locatives of each grid room and characteristics of thermal factor are shown in Table 1.

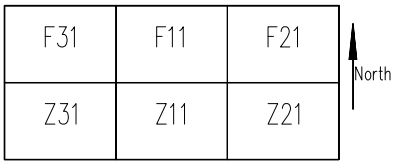


Fig. 4 Plane grid graph in one-layer

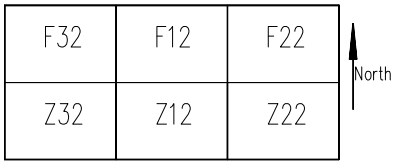


Fig. 5 Plane grid graph in two-layer

Table 1 Locatives of each grid room and analysis of thermal factors

Number	Locative	Analysis of thermal factor	Number	Locative	Analysis of thermal factor
Z11	1th main room grids 1 floor	one southern metope and one ground of heat transfer	Z12	1th main room grids 2 floor	one southern metope and one roof of heat transfer
Z21	2th main room grids1 floor	each south and east metope and one ground of heat transfer	Z22	2th main room grids 2 floor	each south and east metope and one roof of heat transfer
Z31	3th main room grids 1 floor	each south and west metope and one ground of heat transfer	Z32	3th main room grids 2 floor	each south and west metope and one roof of heat transfer
F11	1th secondary room grids 1 floor	one north metope and one ground of heat transfer	F12	1th Secondary room grids 2 floor	one north metope and one roof of heat transfer
F21	2th secondary room grids 1 floor	each north and east metope and one ground of heat transfer	F22	2th Secondary room grids 2 floor	each north and west metope and one roof of heat transfer

Considering thermal effects in winter and summer, thermal effect of building south is better than north and east is better than west, and thermal effect of one heat transfer metope is better than that of two and heat transfer ground is better than radiating roof [3]. Combining the character of thermal factors of each grid room, thermal effects can been seen: numbering area Z11> numbering area Z21> numbering area Z31> numbering area Z12> numbering area Z22> numbering area Z32> numbering area F11> numbering area F21> numbering area F31> numbering area F12>numbering area F22> numbering area F32.

When rural residential plane is designed, referring to conclusions of plane analysis of thermal priority, the main function room in southern side can select room location according to the length of sojourn time each room. From the sojourn time, living room>bedroom>dining-room, thus living room can be placed in the Z11 location, bedroom 1 can be placed in Z21 locations, dining-room can be located on the Z31.Bedroom 2 can be placed firstly in Z12 location, moreover in the Z22, finally in the Z23.

Application of Rural Residential Door and Window Layout

In winter, in order to make more solar radiant heat into building room, when rural housing is designed, no matter what house direction is, there are more and modest large open windows in south, sparingly and small open windows in north. In summer, in order to reduce solar radiant heat in east and west, there are no and small open windows in east and west. In order to prevent adverse influence on northerly and northwesterly penetration in winter and introduce southeast wind in summer, the main entrance of rural housing should be arranged in south or southeast as far as possible.

In summer and transitional season, in order to enhance natural ventilation and improve indoor thermal comfort of the main function room, on the one hand, it is very necessary to set reasonably the location of doors and windows in order to facilitate the formation of inlet and outlet, so as to organize effective natural ventilation. On the other hand, doors and windows setting can be combined with residential staircases and main entry and use staircase shaft drawing wind, strengthen the wind pressure and hot air ventilation, and thus improve indoor thermal comfort in summer.

Conclusions

Currently, in order to improve indoor thermal environment and comfort in rural areas, when rural housing is designed, on the basis of meeting use function and living habits, with certain architectural modeling, through relatively weakening rural residential use function and architectural modeling design, enhancing energy-saving design, thus thermal priority policy is put forward.

Rural housings should be constructed on the sunny side and leeside, direction should be south-north, and courtyard and main entrance of building are located in south-east or south side, so as to form the layout of opening west side and closing east side.

When rural housing forms are designed, low shape coefficient and energy-saving shape considering solar radiation should be selected.

Climate buffer layer, thermal comfort zone, planar grid and doors and windows should be designed rationally, so as to optimize rural residential layout.

Acknowledgements

This work was supported by Science and Technology Plan Projects of Zhengzhou City (0910SGYG21201-2), and College Student Innovative Experimental Project in 2011, North China University of Water Resources and Electric Power.

References

[1] Z. Zheng, Y. Li, X. Yang, Study on rural residential energy-saving in Beijing, Building Science, 1 (2008) 9~14.

[2] J. Liu, Building Physics, China Architecture and Industry Press, Beijing, 2010.

[3] C. Lin, Energy-saving Design and Construction of Residential Building in Small Towns, China Building Materials and Industry Press, Beijing, 2004.

[4] Housing Industrilization Promotion Center of The Ministry of Construction, Anthology of Works of National Energy-saving and Land-saving Housing Design Competition, China Architecture and Building Press, Beijing, 2007.

[5] Z. Xu, Practical Handbook for Building Energy Saving Technology, China Machine Press, Beijing, 2004.

© (2012) Trans Tech Publications, Switzerland
doi:10.4028/www.scientific.net/AMM.238.478

Simulation Study on Solar Collector— Air Source Heat Pump Combined System for Space Heating In Cold Region

Zhenqing Wang [a], Yan Chen [b] and Haixia Wang [c]

School of Civil Engineering and Architecture, Henan University of Technology, Zhengzhou, China

[a]hnzzwzhq@163.com, [b]chyan0371@yahoo.com.cn, [c]xthxwang@163.com

Keywords: ASHPS; space heating; solar collector; COP.

Abstract. An air source heat pump system (ASHPS) was set up, which provided space heating and cooling, as well as hot water for an office building in Tianjin. Its operating performance in winter was evaluated based on test data. Considering the local abundant solar radiation and the way to provide energy in an office building, a simulation study was carried out on the combsystem of ASHP and flat plate air collector (FPAC). The effects of collector area and its outlet parameters on the heating performance of ASHP were studied, and the favorable operating and matching mode were recommended. The results indicate that ASHPS is a technically viable method in Tianjin in winter, but not economically, and the air-solar combsystem should be taken into account for its massive replacement for conventional energy.

Introduction

In the north of China, coal is the mainly used fuel for space heating in winter. This results in great losses of primary energy and air pollution in city due to its low thermal efficiency (35%~58%) and emission of exhausted CO_2. With the rapid growth of social economy and public concerns of environmental protection, ASHPS for space heating, as a means of large-scale energy utilization, is getting more and more attention [1].

By inputting high-quality energy (electricity), ASHPS extracts heat (low-grade energy) from the air and increases its temperature for space heating or for hot-water production [2]. Compared with heating by electric radiator, this method has some features, such as rationality, cleanness and inexhaustibility. Therefore, it can offer a relatively sound solution for the degradation of energy utilization and air pollution of the burning of fuel. However, in winter, ASHPS used in most cities in north China were confronted with low COP, evaporator frosting that results in heating deterioration [3-5]. How to solve these problems is the key point that affecting its prevalent in application in the north in cold season. To this end, the effect of air temperature and humidity on its operation performance was analyzed and some reasonable defrosting parameters were presented. Some suggestions for its economical operating were made based on these analyses.

System Description.

The experimental system of ASHPS was installed in an office building in Tianjin for space heating and hot-water production in winter. The heated space includes six rooms on the top floor with a total area of 220m^2. This construction is made of reinforced concrete without any special insulation. Single layer of glass windows is on the south side with a mean area of 5 m^2 in each room. The heating load of unit area is 60W/m^2, including the part for preheating fresh air.

The operation mode of the experiment system is as follows: the target temperatures of the water box and the water supplying into the fan coil were set to be 50 ^oC and 40^oC respectively. The water in the tank would be heated by the condenser if its temperature below 50 ^oC. Simultaneously, the water circulation in the system for space heating would not be heated any more until the former reaching its target value. In the latter case, the heating would also be stopped if the water temperature was higher than 45 ^oC.

Simulation And Results.

According to the experimental results, heating by only ASHP isn't economically viable in Tianjin. Considering the abundant local solar radiation and the way to provide energy in an office building, this article developed a model of air-solar combisystem and a steady simulation study was made based on it. The combisystem includes two sub-models: ASHP and solar collector. The former consists of four parts, that is, compressor procedure, condenser procedure, capillary and evaporator procedures; the latter is flat-plate air collector (FPAC). In ASHP model, given an equal refrigerant mass flow at each interface, the four parts are interacted and connected organically. The refrigerant thermodynamic properties employed in four procedures are fitted in Origin7.5 according to NIST data. As to FPAC model, it is placed facing south with the slope of 45°and has a single glass cover and spectral selective coatings with the emissivity of 0.1, shown in Fig.1. The thickness of airflow and the distance between cover and absorber plate are 10mm and 20mm respectively. The convection heat transfer coefficient of air is 10W/（m^2•°C）.

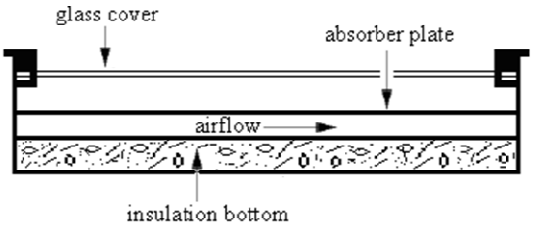


Fig.1 The schematic diagram of FPAC in the combisystem

The Operating Performance Of ASHP By Simulation. The curves in Fig.2 and Fig.3 correspond to different heating area and condensing temperatures, while the collector-to-room area ratios are all 20%. With an evaporating temperature rise or a condensing temperature drop of 5 °C, the system energy combustion decrease by 10% and 6% respectively, as shown in Fig.2. So increasing the ambient temperature is more effective for energy saving than decreasing the outlet water temperature.

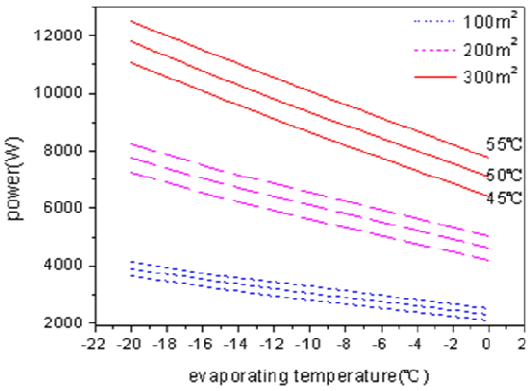


Fig.2 Evaporating temperature and input power of ASHP

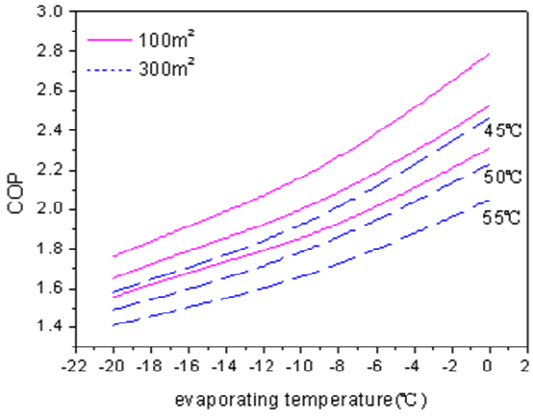


Fig.3 Evaporating temperature and COP of ASHP

Fig.3 shows the system COP and evaporating temperature under heating mode. With condensing temperature of 45 °C, the COP increments are 0.19, 0.21, 0.31 for 100m2 and 0.15, 0.18, 0.27 for 300 m^2 at every 5 °C rise in evaporating temperature; at the condensing temperature of 55 °C, the increments are 0.15, 0.15, 0.23 and 0.12, 0.13, 0.19 respectively. That is, the system COP grows faster when the evaporating temperature is raised and the favorable range is from -7 °C to 0 °C in view of roof area and investment. This should be taken into account when designing FPAC for better system performance.

Matching Parameters Of FPAC With ASHP. As shown is Fig. 4, given FPAC outlet temperature of -5 °C and 10 °C and with a same outlet water temperature rise of 10 °C, the system COP decrease by about 11% and 17% respectively. Namely, the higher the FPAC temperature, the sharper the system COP decline. Furthermore, with the heating area increasing from 100 m^2 to 300 m^2, the

system COP decrease by about 9.7% and 11.8% for the two FPAC temperatures, that is, if the heating capacity increases two times the system COP reduction is about 10%. This can also be seen from Fig.2 and Fig.3. Therefore, multi-system under parallel operating mode is more economically than single-system of the same capacity.

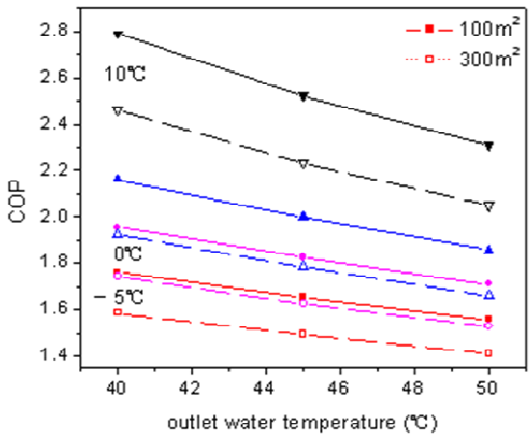


Fig.4 Heating area, outlet water temperature and system COP

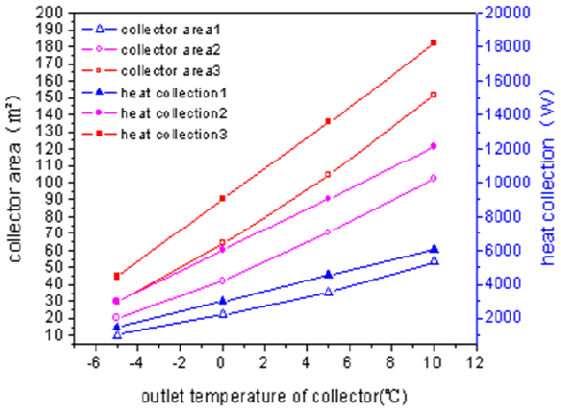


Fig.5 Aperture area, outlet temperature and heat collection of FPAC

Fig.5 shows the effects of different FPAC parameters on heating capacity under the ambient temperature of -10 °C. The collector area is proportional to the heating area at same FPAC outlet temperature. With the outlet temperature of -5 °C and 10 °C, the FPAC area is 10% and 50% of respective heating area. However, the collector area for every 5 °C rise in outlet temperature increase by 11.9%, 13.3%, 17.9% for 100 m2, 11%,14.2%,15.7% for 200 m2 and 11.4%, 13.3%, 15.8% for 300 m^2. Namely, with FPAC outlet temperature increasing, the necessary FPAC area grows faster.

As to the system COP, the benefits from expanded collector become weaker when the heating area expanding, as shown in Fig. 6. As the collector area increasing by 25%, the COP rise are 102%, 95%, 90% for the room of 100 m^2, 200 m^2, and 300 m^2 respectively under the same outlet water temperature of 45 °C.

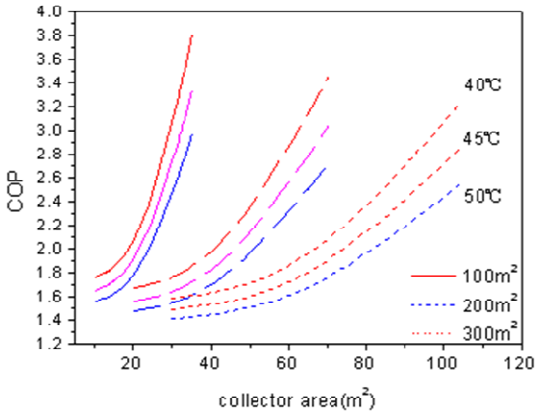


Fig.6 Aperture area of FPAC and system COP

Suggestions For Improving The Operation Performance.

Based on the inverse Carnot cycle, higher inlet air temperature of evaporator could lead to a higher COP and a better performance of ASHPS in winter [6,7]. So it is necessary to increase the air temperature and decrease its humidity in cold season to eliminating frost-forming factors.

According to the previous experimental results [8,9] and the combsystem simulation the flat plate solar collector with single glass cover is a good choice for preheating inlet air. The integrated solar collector-heat pump system is cost effective, but what should be emphasized is how to design the aperture area to get the optimal matching with the ASHPS. Moreover, the technical complexity and capital pay-back period should be taken into account as well [10].

Conclusions

According to the daily mean values of experiments, when ranging from -10 ^{o}C to 5 ^{o}C, the ambient temperature has a direct effect on the outlet and inlet water temperatures. Whereas, the difference of them and the overall system COP are mainly dependent on the heating load.

Simulation results indicate that system COP grows faster when evaporating temperature is raised and a favorable range is from -7 ^{o}C to 0 ^{o}C in view of roof area and investment, and the benefits from expanded collector become weaker when the heating area expanding. Moreover, the extra FPAC area needed for a same temperature rise grows with collector outlet temperature.

Heating by only ASHPS is not economically viable due to its low performance in winter. Considering the climate conditions, air-solar combsystem should be taken into account to benefit its application in the north of China.

Acknowledgment

This research was supported by Zhengzhou Leading Scientists Training Program Project (Grant No. 096syjh34104), and the project name is “Research and development of key technologies in green grain storage and silo building energy efficiency ” and supported by “Twelfth Five-Year” Plan for Science & Technology Support Project (Grant No. 2011BAD03B00).

References

[1] P. Lamp, F. Ziegler, European research on solar-assisted air conditioning, Int J Refrig, 21 (1998) 89-99.

[2] B. Xu. Y. Lu, Z. Ma, Heat Pump. China Architecture & Building Press, Beijing, 1988.

[3] M. Hosoz, M. Direk, Performance evaluation of an integrated automotive air conditioning and heat pump system, Energy Conversion and Management, 47 (2006) 545-559.

[4] D. L. O'Neal, Defrost cycle performance for an air-source heat pump with a scroll and a reciprocating compressor, Int J Refrig, 18 (1995) 107-112.

[5] T. Prud'homme, D. Gillet. Advanced control strategy of a solar domestic hot water system with a segmented auxiliary heater, Energy and Buildings, 33 (2001) 463-475.

[6] S. A. Kalogirou, Solar thermal collectors and applications, Progress in energy and combustion science, 30 (2004) 231-295.

[7] B. Huang, J. Chang, Performance characteristics of integral type solar assisted heat pump, Solar Energy, 71 (2001) 403-414.

[8] J. Zhao, Y. Ma, The xperimental study on solar-assisted heat pump system for hot water supply, Acta Energiae Solaris Sinica, 14 (1993) 30-34.

[9] J. Zhao, Investigation into the use of R134a in a direct expansion solar assisted heat pump, Journal of Tianjin University of Science and Technology, 33 (2000) 33-36.

[10] Z. Olympia, S. Anastassios. Effect of climatic conditions on the design optimization of heat pump systems for space heating and cooling, Energy Conversion and Management, 39 (1998) 609-622.

© (2012) Trans Tech Publications, Switzerland
doi:10.4028/www.scientific.net/AMM.238.482

Analysis on Waterproof and Drainage Systems of Pit House in the West of Henan Province

Guixiu Wang [a] and Hongguang Li [b]

School of Architecture, North China University of Water Resources and Electric Power, Zhengzhou 450046, China

[a]henanwangguixiu@sina.com, [b]lhg123ok@yahoo.com.cn

Keywords: Pit House; waterproof and drainage system; concept, design; structure.

Abstract. This paper analyzes on the unique concept, design and construction of waterproofing and drainage of Pit House in the west of Henan Province, China. The drainage design of Pit House concentrates on the water shutoff for controlling of catchment area and preventing rainwater flooding, the water drainage for draining water from roof, and the water seepage for draining off rain from underground courtyard. The waterproof mainly focuses on the protection to key waterproof parts of building materials and easy ways of building technology.

Introduction

Pit House is a specific form of the adobe building, characterized by specific environmental conditions. It is quiet and safe artificial microenvironment, and low cost, low energy, and easy to construct, and in favor of ecological balance [1]. This ancient and magical residential construction in the whole process, must pay special attention to water and drainage issues. Through investigation and study to Pit House in the west of Henan Province, we found that Pit House gradually formed a complete set of waterproof and drainage system, from sitting, design, construction, to maintenance repairs and so on.

Analysis of the Concept of Waterproofing and Drainage

Pit House in the west of Henan Province belongs to the sunken cave forms. It is completely hidden in the ground. It is formed by digging a big pit on the loess surface, then digging out the entrance of the horizontal-shaped cave and sloping ramp (or stairs), surrounded by vertical walls of the pit (Fig. 1). The water resistance is an important issue on Safety and durability of Pit House, because the whole building is formed by loess, and water intensity would be significantly reduced, with the extension of the soaking time, even prompted the cave collapsed as a whole.



Fig. 1 Pit House in western Henan



Fig. 2 Overall drainage of Pit House environment

By research, we found that the water drainage of Pit House in the west of Henan Province can be summed up taking draining water as the fundamental mode, taking the waterproofing as the secondary way, and Closely integrating drainage and waterproofing. The complete water drainage system is very favorable to safety, durability and Control of internal moisture of Pit House. We can focus on planning and site selection, kiln House design, and detailed structure.

Planning and Site Selection

Pit House in the west of Henan Province gathers together, taking the village as the unit. Location of village is the major consideration topography, soil, water, in addition to outside factors such as resources, location, agricultural land. The villages usually site in the higher ground, and Drainage using mainly original topography, to ensure the drainage edge of the village as a whole. The village depends mainly on the natural gully drainage (no artificial organization), and only digs some simple ditches, in places where local drainage is not smooth. (Fig. 2)

Overall, Pit House in the west of Henan Province on the village drainage considerations in planning and site selection is based on the original terrain, to rely on the natural gully drainage, partial drainage, at the organization.

Kiln House Design

On Kiln House, waterproof mainly to reduce the catchment area, and to prevent the intrusion of rain water; drainage is mainly reflected in drainage design of the roof and the courtyard ground.

Reduce the Catchment Area. Pit House has the unique characteristic on drainage. The courtyard catchment area differs from, the ground central courtyard construction. Ground courtyard drainage is roof (or part roof) rain row into courtyard, again by courtyard row into village public drainage system, but catchment area of pit courtyard include roof area (or part roof area) and courtyard area. Due to its special of forms, drainage of Pit House is divided into two part, one is roof rain which directly row into village public drainage system, the other is the rain of courtyard and entrance which is infiltrated by underground courtyard (Fig. 3). Due to the drainage of underground courtyard has its obvious disadvantages, so pit drainage design is mainly focused on controlling of catchment area, preventing rainwater flooding "interception", rowing roof rainwater and underground infiltrating courtyard rain. "Interception" was around the catchment area of Defense design, "Draining " is design that The kiln Top drainage is directly connected to the village as a whole drainage system, "leakage" is the use of the natural characteristics of loess to let the rain water seep.

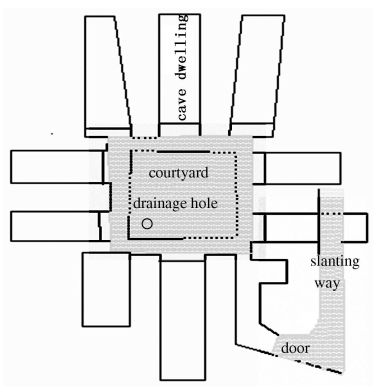


Fig. 3 Catchment area of pit courtyard



Fig. 4 Kiln roof drainage of Pit House

Kiln Roof Drainage Design. Kiln roof drainage of Pit House rely mainly on the construction of drainage slope, drains in the kiln top. Kiln top of the ground terrain, the construction of bulk water, slope reinforcement kiln top, the construction of the drainage slope of the kiln top, drains, such as main kiln terrain than other kiln terrain. To the airfield drainage slope from the bar horse wall around to find the slope of 5% is generally four weeks to do the gutter, rain to the cliff top row to the surrounding open space or farmland, and connected to the drainage system and the entire village (Fig. 4).

Entrance Ramp Design. The entrance of Pit House is very important to the entire water system (Fig. 5). Blocks the horse wall usually to construct in the pit mouth all around ， in order to prevent storm water flooding and people falling. Main kiln where the side bar horse wall height of about 50 cm, other the Trilateral height of about 35 cm, are one brick thick, and has a basis on both sides of the entrance ramp is generally assembled to brick. Adjust the drainage slope, the outside of the bar horse wall with brick paving pan of water. Aggregation, protection stopped the horse wall in order to prevent the clifftop rain gravitropism Pit House, the slope of the pan of water try to do a large number, about 15%, some as wide as possible, about 80 centimeters.



Fig. 5 Waterproofing details of entrance ramp



Fig. 6 Ground design of courtyard

Ground Design of Courtyard. Part of pit courtyard and entrance open part of the rain mainly rely on the courtyard itself to solve the penetration through the loess, so the courtyard ground design is very important. Combination of function and drainage needs of the courtyard ground general hospital ring channel and hospital heart of the ground of two parts. Hospital heart Yin bit additional infiltration wells, infiltration and storage of drainage the hospital heart loess ground infiltration and seepage wells completed (Fig. 6).

Detailed Structure

The water problems are important. Every detail in the construction pit house waterproofing measures reflected in several key parts of the cornice, the mouth of the cave, the plinth and the kiln surface package build with brick.

Cornice Structural Design. Around the Kiln House to set the brick cornice and surrounded by the bottom five groups of brick; the lowest level of a set of pull bricks, dog tooth brick, run in the third group of brick, and a fourth copy watts, and the fifth group of dripping eaves(Figure 7). At the four corners of the corner for more than downward for several groups of aesthetics and to prevent the corners of the eaves gutter fell into the role of wet cliff face. Cornice top finished with small green tiles, pick out 7-8 inches of the cliff face, the corners of roof drainage gutter, gutter corresponding kiln surface is often puzzle the horses tiles to be protected.

Cave Mouth of Structural Design. The kiln of the cave mouth at the surface often adduction 30-50 cm, forming a natural awning, the upper cave arch kiln face at 24 brick flat mounted, prominent part of the cross puzzle with 12 tiles, the role of decoration and protection of the cave

mouth. Can also be used to paste Qi level mounted outside the straw mud trowel, timely protection (Fig. 8). Fill the mouth of the cave wall lower part of the puzzle often have 90-centimeter-tall brick veneer, some of the external walls of the cave mouth lined with a layer of brick protection. Windows are with about 20 cm of bay windows, the natural slope of the drainage.

Plinth, Slope Protection Structure Design. The Kiln lower leg do the sharp shoulders wall, plinth, the locals also called "Genjiao", usually with brick masonry reinforcement kiln and legs to increase carrying capacity, but also to prevent rain protection kiln leg. Plinth main kiln where the cliff face about 60 cm, Le foot of the cliff face about 50 cm, 12 cm thick. The roots of the plinth There are 60 public and dispersed in the water, and some scattered water combined with hospital annular channel design, the use of brick or stone hardening and hardening measures (Fig. 9).



Fig. 7 Cornice



Fig. 8 Cave mouth



Fig. 9 Plinth, slope

Kiln Surface Structure Design. The main wall of the kiln surface commonly used paste “Huqi” solid, topical lime or straw mud smear layer, kiln surface protection from the rain and increasing the role of the beautiful, warm and rustic, thick and powerful, cost-effective. The whitewashed wall after three times smear generally, to facilitate the connection of the mud to strengthen the compactness. Enhance the waterproofing effect.

Conclusions

Pit House has the unique concept, design and structures in waterproofing draining water. In thousands of years of development history, Pit House gradually formed a complete set of waterproof and drainage system, from sitting, design, construction, to maintenance repairs and so on. As a vernacular style of the ancient and magical, Pit House is rich in culture, history and science, is the ancient wisdom of the working people. The building technique of Pit House is worth exploring, as non-material cultural heritage.

References

[1] The Formation and Characteristics of an Adobe Building; Architectural Design Data, sets 6, 1994.

[2] H. Yao, Chinese Cave, Henan Science and Technology Press, Zhengzhou, 1999.

[3] Left Full House, Giant White Constitution, The Henan houses, China Building Industry Press, Beijing, 2007.

[4] J. Min, Traditional Houses, Tianjin University Press, Tianjin, 1999.

© (2012) Trans Tech Publications, Switzerland
doi:10.4028/www.scientific.net/AMM.238.486

The Development of Low-Carbon Economy for Realizing Urban Sustainable Development: Taking the Example of Baotou

Ailin Zhang [1, a] and Haiyan Zhang [2, b]

[1]Architectural and Civil Engineering Institute, Inner Mongolia Scientific and Technical University, Baotou Inner Mongolia 014010, China

[2]Material Supply Campany of Baotou Steel (Group) Corp, Baotou Inner Mongolia 014010, China

[a]ellen1117@163.com, [b] daxianer0917@qq.com

Keywords: low-carbon economy, energy conservation and emission reduction, sustainable development.

Abstract. As the urban new developing strategy and mode, low-carbon economy meets the requirements for the sustainable development in the urban area. On the basis of development analysis for the low-carbon economy home and abroad, this paper illustrates the challenges that urban area meets in the process of low-carbon economy and sustainable development by taking the example of Baotou, as well as making proposals and suggestions accordingly.

Introduction

Under the big environment of global warming, the "Low-Carbon Economy" based on low energy consumption and low pollution has become a global hit. The Low Carbon Revolution cored with high power efficiency and low energy consumption that promoted by developed countries lays focus on developing the low carbon technology and has made a great adjustment to policies as industry, energy and technique to achieve the opportunities and industrial high ground. The battle for low carbon economy has begone quietly around the globe [1]. Under this kind of international environment, our country is also following the trend to develop low carbon economy positively and has put forward several proposals for the low carbon economy development. As a heavy industrial city, city Baotou has been influenced by traditional economical growth mode, which relies on the environment to a great extent. So the ecological environment has been affected and the energy conservation, emission deduction and the low carbon development will be a must choice for Baotou.

The Inherent Meaning and Development of Low Carbon Economy

Low carbon economy is the economic mode that based on low consumption, low emission and low pollution, which is another great leap following the agricultural civilization and industrial civilization, with the nature that can be summarized as issues as efficient utilization, clean energy development and the pursuit of Green GDP, and with the core of energy technology, energy conservation innovation, industrial structure and systematical innovation and the fundamental transfer for the concept of human living and development. The theoretical system was firstly proposed by the famous US scholar Royce in his "Eco-economic Revolution - Five Steps to Save the Planet and the Economy" in the year 1999. Currently, there has been an increasingly clear trend for low carbon economy to become the major energy in the future. Low carbon economy has also become the only choice for the world sustainable development. The developed countries are expanding a "New Industrial Revolution" cored as high power efficiency and low emission. While in our country, the state president Hu Jintao made clear the development of low carbon economy while attending the APEC meeting in the year 2007 and put forward several proposals to promote the low carbon economy development.

Low Carbon Economy is the Only Way for Economic Development in Baotou

Energy Supply and Consumption Structure Determines the Development of Low Carbon Economy in Baotou. Taking the perspective of energy production structure, coal is the major primary energy product in Baotou, and such energy varieties as Petrol and natural gas are mainly from internal redeployment. The energy supply has been relying on coal, which has put and will continue to put burden on environment and transportation. While looking from the energy-end consumption situation, coal and thermal power(mainly relying on coal consumption) are way higher than the consumption of other energy. The large amount of CO_2 produced in the combustion process of coal, which has been posing a certain impact on ecological environment, leaving the characteristics of high carbon consumption on the economic development [2]..

The Policy of Accelerating Industrial Restructuring and Building Environment-Friendly Society Determines the Development of Low Carbon Economy in Baotou. To achieve the scientific development, Baotou must lay focus on enterprises and industry, optimizing the industrial structure, promoting energy conservation and emission deduction, improving economic profit and promoting the coordinating development of economic society. The development of low carbon economy can efficiently address issues as heavy industrial structure, primary industrial issue, high energy consumption, high emission and high pollution, etc..Therefore, in the process of accelerating the transformation of development mode, the focus of our city should be laid on low carbon economy and accelerating the research on promoting the policies for low carbon economy and low carbon industries. It means a lot for our city to achieve harmonious development and to construct the environmental friendly society.

Important Strategic Decision for Confronting International Pressure and Challenges. Currently, the energy consumption and CO_2 emission in our country is attracting more attention of the world. Forceful actions must be taken to cope with the changes of international economic structure and trading rules. As a result, the low carbon economy is not only the necessity for the development mode transformation, industrial structure adjustment and ecological environment protection, it is also an important factor for the international stress to enhance the international competence of our country, to enlarge the export and ease the global green gas emission under the background of international financial crisis.

Hardships and Challenges for the Development of Low Carbon Economy in Baotou

Baotou is experiencing an important period for the rapid development of industrialization and urbanization now. The continuous promotion, the development of infrastructure construction in urban and rural area and the upgrading of civil consuming structure are all forming a great need for heavy industrial products, which turns into the vigorous need for energy consumption. Meanwhile, coal takes a large percentage in the energy consumption structure and the consuming structure centered with coal can maintain for a long time, bringing a large amount emission of CO_2.

On the other hand, the slow industrial structure adjustment in our city makes difficult for the realization of promoting the energy efficiency in short time. Though the industrial structure in Baotou has been adjusted and improved to some extent in recent years, the economic growth still relies on the second industrial and the industrial structure is still in an unreasonable situation.

In addition, the biggest limitation for Baotou's low carbon economy development is the lagged technological level and limited technique developing ability. So how to accelerate the development and introduction of low carbon technique is the key for realizing the leaping development in this whole area.

Proposals and Suggestions of Low Carbon Economy Development

The development of low carbon economy is a strategetic systematic project, where several measures should be taken simultaneously and promoted orderly. Combining with the actual situation in Baotou, the following measures should be taken orderly to promote the low carbon economy development in Baotou.

Establish and Perfect the Policies on Low Carbon Economy. The low carbon economy development is a systematic project, with a wide coverage, high working difficulties and high standard requirements. In order to coordinate the low-carbon economic development, the city's low-carbon economic development strategy and plan must be developed and the study on strategies promotion, international cooperation and technology introduction for low-carbon economy development should be carried out. The related departments should also perfect related polies on strategy developing, low-carbon technologies developing and promotion, low-carbon economy experimental demonstration and strengthen the exchanges and cooperation to form the well low carbon economy developing pattern as "To Promote with Policy, To demonstrate with Typical Examples and To Support with Projects [2, 3]".

Spur the Development and Promotion of Low Carbon Technology and Products. Technical innovation is a key factor for realizing the low carbon economy development and obtaining the goal of energy conservation and emission deduction. Baotou should lay focus on long term and mid-turn strategic technology reserve, establishing the governmental guiding as soon as possible, establishing the joint mechanism composed by higher education institutions and key enterprises, vigorously developing energy-saving and low-carbon technologies and products. Incorporate the market available energy saving and low carbon technologies and get them promoted and applied into practice. All levels of governments should take the perspective on strategetic level, establishing special fund to provide more support to the enterprises energy conservation and low-carbon technological innovation, encouraging the development and wide application of technique, equipment and processes on energy conservation.

Take Measures to Promote New Energy Industries. Coal has been the major consumption subject in recent years and this structure can not be fundamentally transformed in short time. Under this structure, the development of low carbon economy in Baotou should not only strengthen the technical innovation and structure upgrading in high energy consuming industries as iron and steel, coke, electricity, carry out the low-carbon and carbon-free treatment before the consumption, reducing the carbon emission from the combustion process, but also accelerate developing renewable energy as wind, solar and biomass, promoting the development of the new energy industry.

Establish Demonstration Sites for Low Carbon Economy and Recyclable Economy. Low carbon economy is a fresh technical revolution and should be continuously explored, summarized and perfected in practice no matter for products development or technical promotion. In order to seize the opportunity for the development of low carbon economy and recyclable economy, demonstration sites should be established first in such traditional pillar industries in Baotou as steel, aluminum, power, and high energy consuming and heavy polluting industries as transportation, construction, chemical industry and electrical power, locating them as key areas for exploring the low carbon economy development [4].

Increase the Propaganda on Low Carbon Economy and Energy Conservation, Strengthen the Energy Conservation Conscious and Cultivate the Low Carbon Conscious of Civil Citizens. The energy issue has become a significant factor for restraining the sustainable development of the economic society. The energy conservation and consumption deduction has been stretched to areas of production, circulation and consumption. The promotion and application of low carbon economy benefit nation and people, there should be more propaganda to make the general public understand the benefits of low-carbon economy, and let it become the conscious action of the whole society, forming the thick atmosphere of government promotion, market guiding and universal participation.

Conclusions

Low carbon economy is the only way to realize the urban development. The low carbon economy is suitable for the current and long-term interest of Baotou, is the necessity for economic and social development. The rapid development of low carbon economy will guide Baotou economy to the development orientation of resource conservation, environment protection and low carbon.

References

[1] K. Xia, The development of low carbon economy to realize sustainable development, Urban Area: Environment Protection, 3 (2008) 33-35.

[2] F. Wang, Researches on creative path of industrial enterprises energy conservation technology in inner mongolia from the low-carbon economy perspective, Scientific Management Research, 3 (2010) 40-46.

[3] X. Qin, S. Shen, C. Shi, Study on modern urban planning based on the concept of low carbon economy, Urban Development Research, 18 (2011) 92-96.

[4] Q. Wu, To promote the sustainable development of resources-based cities with circular economy, Resources and Industries, 6 (2008) 1-4.

[5] Y. Jin, R. Liu, Low-carbon economy and the transformation of China's economic developing mode, Economic Issues Exploration, 1 (2009) 84-87.

[6] Z. Xin, Y. Zhang, Low-carbon economy and low-carbon city, Urban Development Research, 15 (2008) 98-102.

© (2012) Trans Tech Publications, Switzerland
doi:10.4028/www.scientific.net/AMM.238.490

Research on Fire Prevention and Evacuation Design of Large Sports Facilities

Shaowei Zhang[1, a], Ling Song[1, b] and Zhimin Li[2,c]

[1]School of Architecture, North China Institute of Water Resources and Electric Power, Zhengzhou 450011, China

[2]School of Architecture, Xi'an University of Architecture and Technology, Xi'an 710055, China

[a]zhangshaowei@ncwu.edu.cn, [b]songling@ncwu.edu.cn, [c]lizhimin710055@yahoo.com.cn

Key words: large space; fire prevention; evacuation; process; borrow.

Abstract. The function of large sports facilities is complex as the space center of people assembling and the comprehensive displaying of city image and vitality, the importance is undoubted for the design of large sports facilities in fire prevention and safe evacuation. This paper puts forward the design process of fire prevention and evacuation and the method for reasonable division of fire partition. According to the special requirements of large space evacuation, the new idea of safety exit borrowing and setting the inner ring road is introduced, the design of building fire protection and smoke control area to open space is studied as the main characteristics of the large sports facilities.

Introduction

For the spatial pattern of the important node of city, the large scale sport facilities are the image of the city landmark building. In addition to undertake all types of games and training daily physical function, the large sports facilities often incorporates various other functional purposes, become the city complex. In this kind of enormous space, functional complex "giant", fire prevention and evacuation in relation to the audience and other kinds of people life safety and became one of the most important considerations must be. But because of the requirement of complexity such as its building qualitative, space layout, function partition and use, in building comprehensive fire prevention design of some aspects of the total exceeds standard conditions. According to this characteristic, designers should be based upon the existing fire technical specification, listening carefully to the local fire department comments and suggestions at the same time, effective reference and relevant stadiums fire control design, combined with the actual engineering creatively solve partial super standard knotty problems.

Process of Fire Prevention and Evacuation Design

The fire prevention and evacuation design of large sports facilities is not only related to the design scheme can meet the fire safety requirements, but the scheme is set up to produce major effect. Therefore it must be in the concept design stage in building fire evacuation considerations and runs through to the follow-up design stage of the whole process.

Scheme Design Stage. Building fire protection design and gymnasium buildings environment space overall arrangement, each building layout of peace, vertical, section design are inextricably intertwined, such as total plane road system, fire lanes, a large number of people in the general plane layout of distributed and obstacle to space layout, space and city and regional services road system and city fire fighting force relationship, stadium layout and design, are the needs of architects in the design must consider and properly solve the problem.

Preliminary Design Stage. This phase is to design the deepening, the optimization stage, at this stage there will be different levels of design modification and adjustment, fire protection design have also entered the practical operational stage, need undertakes to the project performance based

fire safety design and assessment, is the key stage involved in fire control design. At this stage many fire design problems will have basically been implemented, the close collaboration between each major is very important.

Construction Drawing Design Stage. This stage is the specific technical issues to resolve, especially need for construction and engineering to solve specific problems, at the same time the design of fireproof material application, fireproof construction practices, selection of fire fighting equipment and other aspects of the work.

Reasonable Division of Fire Partition

A large open area is the spatial structure of the significant features of large sports facilities, such as audience evacuation hall and audience lounge, there are less dangerous of fire in these regions. And the other regions such as the gymnasium floor along the spectator stand arranged around the commercial outlets, office space, warehouses, though fewer in number but higher risk of fire. The design of fire compartment, can be considered only for the fire danger high housing for fireproof isolation, automatic fire, smoke control key processing, so that the fire would not even on large spatial areas pose a threat, so in a large space, can not do the fire compartmentation, not only satisfy the sports games and watch activity of the functional requirements, but also can effectively ensure the fire safety, so as to achieve economic and effective.

Evacuation Design of Large Space

In the large sports facilities layout, plenty of function rooms unused by audience are usually arranged in close proximity to the central competition venues, including a variety of equipment room must be arranged nearby. Thus the area and depth of stadium in first floor or basement are so large, the problem of safety evacuation distance too long and exit quantity shortage are widespread.

Borrowing of Safety Exit. The larger and more fire district, at the same time, the amount of exit through external is limited, this condition often appeared in the stadium's basement. In order to increase the number of exit and shorten the safety distance, opening fire doors in the interface between fire proof partition is must be considered, so that the relevant requirements of the code for fire protection are meet in each fire district .

Setting Inner Ring Road. According to the physical process and the whole line layout requirements, there are a large number of sports function room and post-game operation room at the first floor of general stadium surrounding the central competition venues, and all is located under the audience distributed platform which is in the second floor. In order to ensure the safety of evacuation, besides setting a plurality of exits connected both inside and outside, internal annular channels can also be set up to strengthen the organization of internal function streamline, channel's width is 8-10m.(Fig .1)

The wall and roof and interior decoration materials of inner ring road are made of non combustible materials. All of the doors opening to the internal shall be used for first class fire door. The inner ring road should be installed with electric heat tracing of indoor fire hydrant fire system and the role of the automatic sprinkler system. At the same time also should be set to automatic fire alarm and detection system and emergency broadcast system and fire telephone line, fire emergency lighting system, evacuating indication system.



(a) (b)

Fig. 1 Stadium floor interior channel

Fire Protection Design of Building Structure

The static pressure box under the stand can be packed up with the fireproof board which fire-resistance limit is not less than 1 hour, it is completely separated between vertical lifting device and equipment warehouse through the super fire shutter. The tall lightweight wall is used as the separator of fire partition in the larger space. Because of the large space and unused of various fire-separated facilities sometimes, solid fire partition can be instead with the fireproof rolling curtain, water curtain and fireproof isolation belt.

Smoke Extraction Design

The natural smoke extraction solution should be considered firstly, and must be brought to the local fire department. It can be solved using the performance-based fire safety design and assessment method. The external facade of the building design and selection of materials directly affect the smoke exhaust effect, the following is Jinan stadium as an example to illustrate.

Jinan stadium design can be achieved by using steel structure canopy extending to the audience platform from the top, which is divided into two pieces, the canopy paved with sunshine plate and sheet metal is mainly used to block rain and shading. The lower part of the structure extending to the exterior facade of the canopy is higher opening ratio of perforated metal plate, which create not only the facade "willow leaves" styling detail texture, but also to create a good ventilation and lighting effects of the "gray space" for the enclosed interior space. Vertical canopy cover most of the audience distribution platform, if the gas generated from the other parts can adversely affect this area. That’s mainly considered in the fire protection design. Due to higher levels of safety requirements (to avoid the psychological panic generated), The limited gas must be excluded as quickly as possible by architectural treatment. In combination with vertical canopy structure design, with more than 30% perforation rate, ensure the ventilation effectiveness of perforated metal plate.

Conclusions

With the development of society and economy, the city builds change rapidly, as the foreign exchange and the display window. The large sport facilities have incomparable advantages, in the number and size of gained unprecedented development. At the same time, there are some new case and problem appeared in the fire evacuation safety design, which need to think seriously and study to designer, the idea and solution of the large space fire evacuation design have certain maneuverability, can provide guidance and reference for project practice now and in the future.

References

[1] Brenda Vale，Robert Vale, Green Architecture: Design for a Sustainable Future, Thames and Hudson, 2001.
[2] X. Liu, Ecology and architecture-the building of the road of sustainable development, Tianjin University Journal, 1 (2001) 85-89.
[3] People's Republic of China Ministry of Construction Green Building Rating Standard, China Building Industry Press, Beijing, 2006.
[4] L. Shi, Large space of eco-design of public buildings, Harbin Industrial University, Heilongjiang, 2007.
[5] International Olympic Committee. Olympic Charter, Beijing, 1996.

© (2012) Trans Tech Publications, Switzerland
doi:10.4028/www.scientific.net/AMM.238.493

Research of Highway Alignment Design Safety Evaluation using Curvature Change Rate

Shengneng Hu

North China University of Water Resources and Electric Power, Zhengzhou 450011, China

hushengneng@sina.com

Keywords: highway engineering, highway safety, curvature rate of change, highway alignment.

Abstract. Aiming at the disadvantages of traditional design method of highway alignment and existent problems including subjectivity, reliability index, comprehensive, applicability etcetera in highway alignment evaluation with running speed. On the basis of the "safety first" idea for highway design, the concept of change rate of curvature has been proposed. Curvature change rate is the clear factor impacting on road traffic safety. Road quality evaluation standard is established based on the curvature change rate and its application method in highway alignment design method. The method not only effectively evaluates highway alignment quality, but also may be used as the basis for the selection index of highway geometric design.

Introduction

Traditional highway alignment design method can meet the design speed to achieve the lowest flat, vertical alignment index, and the higher alignment index is not restricted. It is easy to let the alignment indicators meet the design requirements while the linear combination is not reasonable, the section of the traffic accidents has assemble forming the accident of black spot. To evaluate the quality of highway alignments design, there is no clear quantitative index except the general qualitative description. Implemented in certain arbitrariness, the author did the corresponding research for the safety of highway alignment design quality evaluation.

In recent years, running speed of highway alignment design quality inspection is the main research method [1-4]. In fact, this evaluation method has obvious deficiency. First, the measured sample size is limited, and other problems such as road conditions, traffic conditions and geographical constraints exist. In addition, as it is difficult to grasp the alignment elements on the running speed of the impact of weight, single variable will affect the precision of model, a plurality of variables exist in predicting error. The experience of model for prediction of V_{85} as the operating speed on highway alignment of inspection and evaluation, meant only to satisfy the 85% vehicle driving safety requirements, with 15% high-speed vehicles safety was not considered [5-7]. Therefore, based on the speed of operation guidance and evaluation of highway, alignment design is obviously insufficient.

Relations of CCR and Traffic Safety

Concept of CCR. Curvature rate of change (referred to as CCR), defines as plane curve road section unit length, the sum of angle change, through described a curve design element with the length of curve, radius and corner related curving process, the continuity of attribute plane curve curvature change. The research showed that for describing in path characteristic mostly has the practical significance parameter is to have transition curve single circular curve curvature rate of change CCRs (curvature changing rate of single circular curve), the formula is as follows:

$$CCR_s = \frac{200}{\pi}\left(\frac{Ls_1}{2R} + \frac{L_c}{R} + \frac{Ls_2}{2R}\right)\cdot L^{-1} \tag{1}$$

Where CCR_s is the curvature change rate of the single circular curve with transition curves (gon． km^{-1}), Ls_1, Ls_2 are the lengths head and end of transition curve (m), L_c is the length of circular curve (m), $L = L_c + Ls_1 + Ls_s$ is the length of curve (km), R is the radius of circular curve (m).

CCR and traffic accident loss degree. The latest study shows: the impact of vehicle operation safety is an important factor in the current section of the CCR value and the vehicle in different sections of the accident rate and accident severity is closely related with CCRs. Trapp believes that the road condition influence driving behavior's degree which may reflect by the CCRs value. Krebs research discovery, along with increase of CCRs value, incidence rate of traffic accidents increases, but the range is relatively small. High CCRs value of the traffic accident rate is for low values of CCRs sections of 2~3 times, but for special high section CCRs (CCRs > 500gon.km^{-1}), the traffic accident rate will be very high [2], as shown in Fig.1.

The traffic accident took place was a process of conversion of energy. The traffic accident under the difficult driving condition, automobile's kinetic energy is transformed as the mechanical energy, and the heat energy and vehicles are distorted. Obviously, if CCRs is higher in the accident occurrence process, the conversion of energy are also greater, the accident consequence is more serious [2]. Fig. 2 is the chart of research summarizes of Kloechner through the traffic accident loss factor and road section against CCRs change.

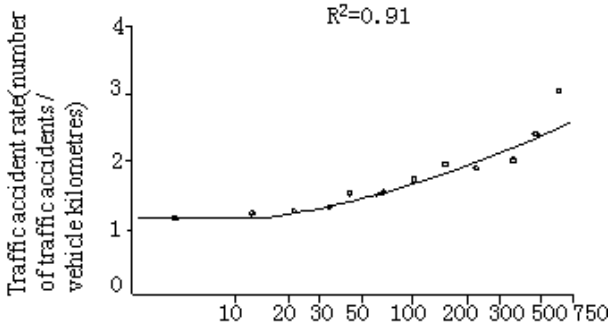


Fig. 1 Traffic accident rate and CCRs

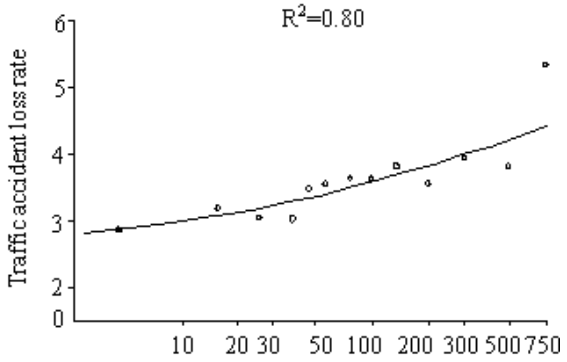


Fig. 2 Traffic accident loss rate and CCRs

Safety evaluation standard Based on CCR

Safety criterion I: Achieving Design Consistency. Because that plane curve design essential factor is complex, any sudden change in geometric design, will cause this position to have frequent traffic accidents, therefore, this standard of security mainly aims at the plane curve road section. For a curve, CCRs of design curve and curve average change rate should maintain in balance to guarantee the design uniformity. For the road section of poorer balance, the design variable must be adjusted to guarantee security. Safety criterion I contents see Table 1.

Table 1 Design consistency evaluation content and standard

Case	Evaluation index	Evaluation conclusion
Good	$\left\|CCR_s - \overline{CCR_s}\right\| \leq 180$ gon. km^{-1}	Does not need to change the design variable: May guarantee the design uniformity and security.
Fair	180 gon. km^{-1} < $\left\|CCR_s - \overline{CCR_s}\right\|$ <360 gon. km^{-1}	Does not need to redesign, may adjust through the revision design variable. When is unable to revise, should use the traffic safety facility.
Poor	$\left\|CCR_s - \overline{CCR_s}\right\| \geq 360$ gon. km^{-1}	1.cannot satisfy the design uniformity, the road section traffic accident took place frequently;
		2.should redesign, when terrain and other reasons cannot revise, must use the traffic safety facility to control the vehicle speed.

Safety criterion Ⅱ:Achieving Operation Speed Consistency. Criterion of operation speed consistency is adjacent the alignment elements of linear whether continuously, in order to prevent alignment from generating large fluctuation, which affects the automobile running safety. Safety criterion Ⅱ contents see Table 2.

Table 2 Operation speed consistency evaluation content and standard

Case	Evaluation index	Evaluation conclusion
Good	$\left\|CCR_{si}-CCR_{si+1}\right\|$ ≤180 gon. km^{-1}	May guarantee the running rate continuity and operational safety.
Fair	80 gon. km^{-1}< $\left\|CCR_{si}-CCR_{si+1}\right\|$ <360 gon. km^{-1}	Does not need to redesign, may adjust through the revision design variable. When is unable to revise, should use the traffic safety facility.
Poor	$\left\|CCR_{si}-CCR_{si+1}\right\|$ >360 gon. km^{-1}	1.cannot satisfy the design uniformity, the road section traffic accident took place frequently;
		2.should redesign, when terrain and other reasons cannot revise, must use the traffic safety facility to control the vehicle speed.

Safety criterion III: Achieving Comfort Consistency. Curve on a vehicle speed change significantly, because the brake drag reduction caused by traffic accident situation was more obvious. Therefore, in order to control the lateral force coefficient, ensure vehicle stability is obtained based on the driving stability. Safety standards, inspection contents and standards are as shown in Table 3.

Table 3 Comfort consistency evaluation content and standard

Case	Evaluation index	Evaluation conclusion
Good	CCR^{si} ≤180 gon. km^{-1}	Maximum effective lateral force coefficient of curves can guarantee the automobile safety comfort through.
Fair	180 gon. km^{-1}< CCR^{si} <360 gon. km^{-1}	Passengers can feel existence of curve, but does not need to redesign, may through the revision related design variable adjustment road section.
Poor	CCR^{si} >360 gon. km^{-1}	1.Centrifugal force of vehicles is more obvious after the corners,the vehicles are more unsafe,are easy to appear overturn a vehicle and run out of road and other accidents;
		2.should redesign, when terrain and other reasons cannot revise, must use the traffic safety facility to control the vehicle speed.

Application of CCR of highway route design method

Application of CCR's highway alignment design law steps are as shown in Fig.3. The dotted line frame is a new step, after using standard inspection revision and after CCR safety evaluation standard inspection revision. Highway alignment design method of CCR is in the present design method's foundation, increase is to check and modify the initially flat, longitudinal, transverse and geometric elements of technical index link. According to the design speed and topographical condition of designation, initially set the route even, vertical and horizontal technical specification according to the road technical standard request, application of CCR safety evaluation standard

conducts the geometric design inspection. Through the change technical specification, makes the highway alignment change continuously, balanced, coordinated, and as determining basis of other technical specification and design.

Conclusions

According to the limitation of current highway alignment evaluation method, it is presented for the first time in China based on CCR of highway alignment evaluation method and security evaluation criteria of CCR. The goal is to check and evaluate highway alignment design, targeted changes, so as to meet the alignment design of continuity, balance and coordination of the basic requirements, at the same time for effective control of speeding, improve the alignment design quality and guarantee the traffic safety. It has important significance and application value.

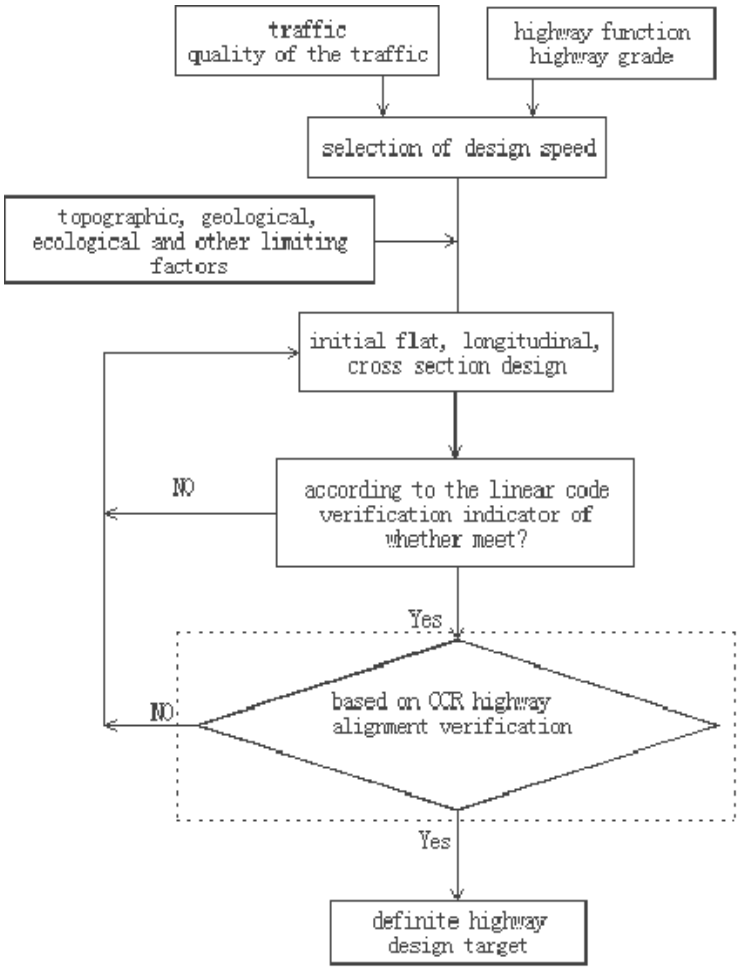


Fig. 3 Highway alignment design method with CCR

References

[1] Donnellet, K. L. Fitzpatrick, D. Elefterladou, J. Harwood, Speed Prediction for Two-lane Rural Highways, FHWA Transportation Research Record, 2000.

[2] Federal Highway Administration, Speed prediction for two-lane Rural Highways, Federal Highway Administration, Washington, 2000.

[3] S. Hu, Two-lane second-class road plane curve essential factor and traffic safety relations study, Chang'an University, 2006.

[4] S. Yang, F. Shi, B. Pan, Application of possible velocity in design for highway alignment, Journal of Chang'an University (Natural Science Edition), 3 (2004) 1-4.

[5] X. Meng, Z. Guan, L. Zheng, Safety evaluation of mountainous express way based on geometric alignment indexes, China Journal of Highway and Transport, 2 (2011) 103-108.

[6] J. Gao, Z. Guo, Evaluation of highway alignment design quality based on operation speed, Journal of Tongji university (natural science), 7 (2004) 906-911.

[7] Y. Pei, G. Cheng, Research on the relationship between discrete character of speed and traffic accident and speed management of freeway, China Journal of Highway and Transport, 1 (2004) 74-78.

© (2012) Trans Tech Publications, Switzerland
doi:10.4028/www.scientific.net/AMM.238.497

Cold Recycling Technology Application of Old Asphalt Pavement in Rural Road Alteration Engineering

Zhidong Guo[1,a], Jia Liu[2,b] and Cangbo Li[3,c]

[1] Hebei University of Technology, Traffic Bureau of Jixian County of Tianjin, China

[2] Hebei University of Technology, Tianjin, China

[3] Traffic Bureau of Jixian County of Tianjin, China

[a]jxxlbgzd@126.com, [b]674976275@qq.com, [c]janchojia@126.com

Keywords. old asphalt pavement; cold recycling technology; rural road; application.

Abstract. Cold recycling technology of old asphalt pavement is a relatively new technology which has important application in the road surface treatment. Combining with the application of the cold recycling technology in rural old asphalt pavement, this paper analyzes and elaborates its construction technology and experience approach. The existing old asphalt pavement material is used in accordance with the new design requirements to form a special pavement structure surface. On rolling forming sections, the test is conducted for compaction, smoothness, bending and sinking and drill-core sampling for compressive strength. The results show that this process meets the general requirements of pavement base, and the quality is good with the advantages of saving costs and reducing waste damaging the environment.

Introduction

With the rapid development of china's rural road construction in the 1990s, the rural road network has improved constantly, and the early part of the road is old and damaged. The focus of highway construction is excessing from the new to the renovation and overhaul. During the transformation process of the old road, the handling of the old road is a problem that the road builders have to face. The traditional approach of abandoning the old pavement materials is not only a waste of the available value, but also waste dumps occupy the cultivated land and space, at the same time it caused environment pollution [1]. To the end, in the process of rural roads transformation of Jixian, cold recycling technology is accepted widely. Cold recycling technology of the old asphalt pavement is using the existing old asphalt pavement material (old asphalt surface and some grass-roots), in accordance with the new design requirements, participating with the right amount of aggregate selectively, joining with binder material (such as cement, lime, fly ash) at some proportion and the right amount of water, using in-place cold recycling mixing plant, continuously completing planer milling, broken, adding materials, mixing, spreading, followed by leveling and compaction in old asphalt pavement and part of the grassroots at a natural room temperature. Ultimately form a construction technology of special pavement structure surface that the technology meets the required performance and quality [2, 3].

Jixian County Transportation Bureau has purchased two WB525 cold recycling machines in 2008 and 2010 which have worked at Liujiading Road, Sun Jin road, Tou-Xie road, Xiayong road, Yixianchuan road, Banghou road, Liu Wei road and so on. We have summed up a set of effective construction process and quality control method of cold recycling.

Project Overview

Liu Jiading road is in the Sangzi town of Jixian, from Bao Ping Road to Liujiading, a total length of 3.5km, width of 4m, four highway standards. The old road structure constitute 15cm lime soil grass-roots layer and 5cm asphalt concrete, which was built in 1999.After nine years' running, the road appears serious pavement rutting and trenches phenomenon locally, impacting on local traffic

travelling seriously. After purchasing cold recycling machine for the first time in 2008, we plan to overhaul for reconstruction. The design structure is 18cm cement cold regeneration grassroots and 5 cm asphalt concrete surface.

Cement Cold Regeneration Grassroots Gradation Design Requirements

According to the specification requirements, when using for the highway, the grassroots level of roads ,the secondary road and below, a single milling's maximum particle size is not more than 31.5mm, and greater than 4.75mm aggregate content accounted for more than 65% [4]. Regeneration mixture gradation shall meet with Table 1 with the scope of requirements.

Table 1 The mixture gradation scope of the cement stability recycled base

Sieve size(mm)	31.5	26.5	19	9.5	4.75	2.36	0.6	0.075
Through the quality percentage (%)	100	90-100	72-89	47-67	29-49	17-35	8-22	0-7

According to Liu jiading road pavement damage condition, select the general damaged section of 200 meters for testing section 1, and severely damaged sections of 200 meters for testing section 2. Field test and technical personnel conduce screening test with broken mixture, checking whether the recycled mixture gradation meet design requirements .The screening results are as Table 2 with the design requirements.

Table 2 Renewable materials gradation table of different sections

Section number	Section number (mm)	31.5	26.5	19	9.5	4.75	2.36	0.6	0.075
section1	Through the quality percentage (%)	100	93	80	53	34	24	13	2
	Cumulative retained percentage (%)	0	7	10	47	66	76	87	98
section2	Through the quality percentage (%)	100	96	91	75	58	36	24	99
	Cumulative retained percentage (%)		4	9	25	42	64	76	1

From Table 2, milling regeneration material from representative sections 1 meets grading conditions required by the design and specification requirements, so there is no need to add a new aggregate. Representative sections of 2 milling regenerative materials do not conform to the specification requirements and design gradation, thus still need to add the corresponding proportion of aggregate, so that more than 4.75mm's aggregates of the sections' mixture account for more than 65%, and ensure that the regeneration layer form skeleton close-grained structure, to meet the requirements of bearing capacity [4]. Added new aggregate shall meet Table 3's requirements:

Table 3 Recycled materials mixed with the aggregate technical requirements table

Quota	Unit	Standard value	Test method
Aggregate crushing value	%	≤30	T0316
Apparent relative density	kg/m^3	≥2.45	T0304
Flat-elongated particles content	%	≤20	T0312
Less than 0.6mm particle liquid limit index	%	＜28	T0354
Less than 0.6mm particle liquid limit index	%	＜9.0	T0354

This project adopts cement as a PS.A 32.5 level's slag silicate cement, its technical indicators and the experiment results are shown in Table 4, in which the cold regeneration combined with material require that cement initial setting time is over 3 hours, final setting time is over 6 hours, the measured results meet the requirements.

Table 4 PS.A32.5 slag silicate cement technical indicators and testing results

Quota	Fineness (%)	Setting time (min)		Compressive strength (MPa)		Bending strength (MPa)	
		Initial	Final	3d	28d	3d	28d
Standard value	≤10	≥45	≤600	≥10.0	≥32.5	≥2.5	≥5.5
Measured value	4	212	384	16.7	33.9	3.7	6.7

After cement with mixture by adding different dosage mold, in accordance with *the highway engineering inorganic matrix stabilized materials experimental regulation* conduct test for the 7d unconfined compressive strength to determine. Prepared with different proportion of the mixture by 4.5%, 5%, 5.5%, 6% of the dosage of cement, the measured each mixture maximum dry density, the optimum moisture content and the 7d unconfined compressive strength data are showed in Table 5, in which take the guarantee rate was 90%, *Z*a on 2-level and the following highway value is 1.282. *R* average value $\geq R_d/(1-Z_aC_v)$.

Table 5 Unconfined compressive strength average value of different solution

No.	Proportion of materials (cement: cold regeneration material)	Maximum dry density (g/cm^3)	Optimum moisture content (%)	7d unconfined compressive strength				
				Strength (MPa)			Coefficient of deviation C_v (%)	
				Test	Design	$R_d/(1-Z_aC_v)$	Test	Required
1	4.5:100	2.19	8.3	2.7	2.5	2.99	12.7	Not more than 20
2	5.0:100	2.19	8.3	3.1	2.5	3.03	13.6	
3	5.5:100	2.19	8.3	3.3	2.5	3.04	13.9	
4	6.0：100	2.19	8.3	3.4	2.5	3.05	14.1	

According to 7d unconfined compressive strength data showed by Table 5, the unconfined compressive strength from cement dosage of 4.5% cold recycled mixture can not meet the design requirements [5]. With the increase of cement content, strength index grows linearly; When the cement content reached more than 5%, the mixture of 7d unconfined compressive strength has reached the design requirement, combined with the four level of rural highway reality, select plan 2 as laboratory optimum mix ratio, namely cement :milling material = 5.0: 100.

Quality Control in Constructive Process

The Old Pavement Treatment. Professional persons organize staff to sweep the old pavement, the old pavement pothole is filled up with 80% 1-3cm stones and 20% lime soil fill with 12% lime. Control that its elevation is consistent with the designed one by measuring, leveling, rolling.

Paving Cement. Make grid in the old pavement, and pave cement with uniform width, and pay attention that spreading area from each bag of cement is equal, and no leakage or excessive centralization. According to the initial setting time of cement , determine the regeneration operation length. The regeneration length of four-level grade rural highway (non-stop) is 150-250 m generally, and we can select upper limit to reduce the transverse joints. Pre-setting width is greater than the design of renewable width of 10cm or more.

Milling Planning and Mixing. During the mixing process when cold recycling machine is pushing sprinkler, marching speed of cold recycling machine must adjust and control strictly according to the new added aggregate thickness and regenerated depth. The average marching speed of cold regeneration machine is 4-8 m/ min, and rotor speed is 100-200 r/ min in general, and the back scraper pressure is 500-1500kPa generally. The slope from the part of mountain road is steep and turn is urgent, part of serious net-shapes cracks should adjust marching speed and rotor speed reasonably according to mix-design parameters and construction situation of test section. In the process of milling and mixing, we should reduce downtime without reason, reduce and avoid the transverse joints as far as possible.

Recycling machine must be followed with professionals who check recycling depth, cement content and water rate at any time, and coordinate the machine operator to adjust the machine. Checking of recycling depth should be based on adjacent top surface from recycling structure layer or the old pavement, and stab the drill steel to the lower bearing layer top surface for measuring the penetration depth, and qualy its' depth. Detection position is on the both sides of which the cutting knife from recycling machine and every check time is 30-50 meter [6].

Precision. Use bulldozers to discharge pressure at the same time when cold recycling is mixing and forming,. We should recover Midline and Sideline quickly after preloading, and use the grader to precise. In the precision process, height material is scraped way out directly in order to avoid the

thin patch phenomenon. We should achieve the aim of required slope and way arch camber during the precision process, besides, paying attention to the accommodation flat seams especially. For local low-lying, we should rake surface above 5cm using tooth harrow, and use fresh mixture for leveling. The test people make sample check cement dosage and conduct unconfined strength test.

Rolling. Cement after mixing and plastic stabilizing can be cold recycled in-place stablely, and we should complete rolling before initial time of cement setting and during the delay time determined by test in order to satisfied with required compactness and no obvious wheel path. Finally, use wheel roller to close surface. In the process of rolling, surface of the recycled mixture should always be wet, in the condition of its rapid evaporation, should spray water in time. If water rate of the recycled mixture is too large, such as presenting *spring*, *loose* and *peeling* phenomenon, we should open that layer and add appropriate amount of cement to deal with. From penetrating the cement to rolling finished, we must guarantee that construction time is no more than 4 hours.

Treatment of Construction Joint. If the road width is less than 6 meters, it should choose the full width construction instead of half construction, in order to reduce the number of seams, improve construction efficiency; Overlapping width of longitudinal regeneration layer is not less than 15 centimeter, at the same time we must due to increase the dosage of cement in the joints. The position of longitudinal joint should avoid the slow, heavy vehicle wheel trace as far as possible; Transverse joint cohesion should lap a mixing, and leave 5-8 meters' no-rolling a while ago after mixing .The unpressed forepart should add cement to remix, and compacted with the followed one together at the time of following one that is constructing .

Curing. Rolling forming section should close traffic and water curing in time. Curing uses auto sprinkler nozzle type sprinkling vehicle, and during the curing time, it must always maintain the structural layer humidity. The marching speed of watering car keeps 20 kilometers per hour and can not turn over and brake and stay in curing section, besides that the curing time should not be less than 7d. Heavy vehicles are prohibited in this period [7].

Effect Analysis of Construction Technology

Effect Analysis of Structure Layer Quality. Construction of Cold-Recycled Base from Liu Jiading road has finished. On rolling forming sections, we conduct the test of compaction, smoothness, bending and sinking and core sampling drill compressive, the results are shown in Table 6~Table 9.

Table 6 Sampling results of cold-recycled base compaction

Serial No.	Pile No.	Located away from the midline (m)	Measured value of compaction degree (%)	Compaction standard (%)
1	K0+379	1.0	97.6	≥97
2	K1+585	1.1	98.1	
3	K2+387	0.9	98.5	
4	K3+288	1.2	97.9	

Table 7 Sampling results of cold-recycled base smoothness

Pile No.	Total number of feet	No. of unqualified ruler	Roughness average (mm)	Qualified rate (%)
K0+030-0+090	20	0	7	100
K1+150-1+210	20	2	6	90
K2+320-2+380	20	0	8	100
K3+230-3+290	20	1	6	95

Table 8 Sampling results of cold-recycled base bending and sinking

Pile No.	Deflection measuring points	Elimination of abnormal points	The average values of deflection (0.01mm)	Deflection value (0.01mm)	Deflection design value (0.01mm)	Conclusion
K0+320-0+820	20	2	22	31	67.2	qualified
K1+250-1+650	16	1	31	40	67.2	qualified
K2+350-2+950	24	2	35	44	67.2	qualified
K3+120-3+420	12	1	37	46	67.2	qualified

Table 9 Sampling results of cold-recycled base core boring sampling

Serial No.	Pill No.	Core sample thickness (cm)	Compressive strength (MPa)	Core sample surface quality
1	K0+350	19.8	3.17	Core sample integrity, compacting, the plate body is good
2	K1+270	18.5	3.06	
3	K2+380	18.9	3.10	

Through the experiment data, we can discover that the core sample is complete and compacting, slab entirety is strong, pavement thickness, regeneration after compaction, evenness and strength reach the designed index , meet the general requirements of pavement base, quality effect is good.

Economic Effect Analysis of Structure Layer . Take Liu Jiading road as an example (the old road structure is formed by 15cm lime soil grass-roots and +5 centimeters asphalt concrete), if the 15 centimeters lime soil and 5 centimeters oil surface which are excavated is according to the 1 square meter calculation: All excavation (Quota 2-3-2) Cost: $0.15m^2 \times 1m \times 14.5yuan/m^3 + 0.05 \times 1m \times 52.2yuan/m^3 = 4.79yuan$; the sub-base of 10% lime needs 12yuan; the grass-roots of 12% lime needs 15yuan. Three total per square grass-roots cost 31.8yuan.

The 18 centimeters base layer used by Cold recycling technology is calculated as one square meter: cold recycling mixing fee is 5.3yuan, leveling and rolling fee is 3yuan, cement and other materials fee is 7.5yuan, labor and other costs is 2yuan, per square meter cost of the above is 17.8yuan.

By comparison, we can find the save cost: 31.8-17.8 = 14.0yuan per square meter. According to the 4 meter wide of 4-level rural highway, the saved cost is 56,000yuan per kilometer.

At the same time traditional lime soil construction processes with taking and spoiling job disturbs the original flora and fauna's habitat, and destruct Ground vegetation, which can cause low-lying after soiling, change the existing drainage system and form local water; the soil structure is destructed after soiling, and fertility dropped, the soil productivity and erosion resistance decrease. The use of cold recycling process fully use of renewable resources of waste asphalt to avoid the generation of a large number of highway construction waste, to save considerable land resources, to effectively prevent soil erosion[8]. 1 kilometer and 4 meter width road can save earthwork $4.6m \times 1000m \times 0.3m = 1380m^3$, and avoid construction waste 1380 m3, so that more than 100 kilometers of transformed old asphalt pavement in Jixian County can be saved 414 acres of land annually (digging farming is computed as 50cm per acre) , Each year to avoid slag 138000 cubic meters, saving the special environmental governance cost of hundreds of thousands of dollars.

Conclusions

Through practice and effectiveness analysis of rural highway in Ji county in recent years, cold recycling technology of asphalt pavement can reach the technical standards of the new grass-roots level in quality and technical indicators , and balance a large number of construction funds, reduce the resources waste and damage to the environment that is considered not only solve the contradictions of highway construction and acquisition of farmland, but also it can accelerate the progress of the project, shorten the construction period, reduce earthwork, fully reflect the advantages of short construction period of cold recycling technology, using the original pavement materials to save the investment, clean construction site, not affecting the open of traffic, which has good economic and social benefits. Further strengthen the research and promotion of cold recycled asphalt concrete base is of great significance on rural road construction in China.

References

[1] JTG F80/1-2004, Inspection and Evaluation Standards for Highway Engineering, China Communication Press, Beijing, 2004.
[2] JTG B01-2003, Technical Standard of Highway Engineering, China Communication Press, Beijing, 2004.
[3] P. Guo, S. Shu, Old Asphalt Pavement of Cement Stabilizing and In-place Cold Recycling Base Construction Technology Guide in Shanxi Province, China Communication Press, Beijing, 2010.
[4] JTJ034-2000, Technical Specifications for Construction of Highway Subgrades, China Communication Press, 2000.
[5] X. Yang, S. Zhang, The old pavement material mixed with cold regeneration base construction technique and quality control, Highway, 2 (2004).
[6] A. Zhou, Y. Li, Y. Huang, The regeneration technology and application of asphalt pavement, Foreign Building Materials Science and Technology, 1 (2005).
[7] S. Jia, Survey of asphalt pavement cold regeneration technology, Master Thesis, Hebei University of Technology, 2007.
[8] Z. Wu, H. Wu, Construction technology and economic benefit analysis of cement base with in-place cold recycling, Highway Engineering, 4 (2011).

© (2012) Trans Tech Publications, Switzerland
doi:10.4028/www.scientific.net/AMM.238.503

Analysis of Dynamic Impedance Functions in Urban Traffic Flow Guidance System

Zhicheng Li [1, 2]

[1] School of Traffic and Transportation, Beijing Jiaotong University, Beijing 100044, China

[2] North China University of Water Resources and Electric Power, Zhengzhou 450011, China

shixing1980@163.com

Keywords: ITS; traffic flow guidance system; dynamic impedance functions.

Abstract. The successful application of Intelligent Transportation Systems (ITS) depends on the traffic flow at any time with high-precision and large-scale assessments, it is necessary to create a dynamic traffic network model to evaluate and forecast traffic. Dynamic route choice model sections of the run-time function are very important to the dynamic traffic network model. To simplify the dynamic traffic modeling, improve the calculation accuracy and save computation time, the flow on the section of the interrelationship between the exit flow and number of vehicles are analyzed, a run-time functions into the flow using the said sections are established.

Introduction

Intelligent Transportation Systems (ITS) effectively integrates advanced information technology, computer technology, data communication technology, sensor technology, electronic control technology, automatic control theory, operations research, artificial intelligence, into transport, service control and vehicle manufacturing, strengthens the links among the vehicles, road and users, thus forms a time, accurate, and efficient integrated transport system. The main objective of the intelligent transport systems than ever before in a broader form, is applying information technology to the highway transportation system, as well as applying the latest useful information to drivers, vehicles, road infrastructure to set synthesis of a wide range of integrated system. The development and application of intelligent transport systems improve the efficacy and safety of existing transportation equipment, and ease the transportation system's impact on the environment. In the terms of ITS, successful application depends on network conditions forecast in the plan and run strategy with advanced transport and network performance analysis. Many ITS subsystems, especially the advanced traffic management systems (ATMS), advanced passenger information system (ATIS), Advanced Public Transportation Systems (APTS), commercial vehicle operation (CVO) and the Emergency Management System (EMS) relies heavily on the traffic flow at any time, high-precision, large-scale assessment. Therefore it is necessary to establish the dynamic traffic network model to evaluate and forecast traffic information needs to meet these subsystems, and seek a help in the evaluation of the ITS traffic management and information systems. Dynamic traffic network model is different from the static traffic network model, because it is the time on the basis that the various traffic variables. It includes temporary traffic variables to better reflect the actual traffic conditions. If a trip can not be more than one hour to complete large-scale road network, the static traffic assignment model based on the hourly traffic demand will not be able to well reflect the real traffic conditions. Dynamic route choice model in the dynamic traffic network model impedance functions are particularly important.

Analysis of Road Impedance Function

In the static traffic assignment, the impedance function is a function of traffic volume and travel time (Fees), such as the BPR function, is the basis of one description of the balance of traffic online traffic flow. Static equilibrium distribution requirements of the increasing convex function as a single function. When the network congestion, low traffic can also result in low-speed and long

travel time. Since the static traffic assignment models in transportation planning to serve primarily the estimated accuracy of travel time do not ask. But in the dynamic case, improve the prediction accuracy is a basic requirement. Dynamic impedance functions, the dynamic path of the performance function in the dynamic user optimal (DUO) occupy a very important position. A good dynamic impedance functions, not only appropriate to reflect the actual situation but also good to meet the performance of mathematical algorithms. Dynamic impedance functions can be used free flow travel time and delay caused due to the clogging of the downstream section of said (of Ran et al 1997).

$$C_a(t) = C_{1a}(t) + C_{2a}(t) \tag{1}$$

In the above formula, $C_{1a}(t)$ is the free flow travel time, $C_{2a}(t)$ is the delay time caused by downstream sections of the blockage. $C_{1a}(t)$ and $C_{2a}(t)$ can be said to function of the enter flow $U_a(t)$, the exit flow $V_a(t)$, and the number of vehicles $X_a(t)$ in road a, then (1) can be written as:

$$C_a(t) = C_a(U_a(t), V_a(t), X_a(t)) \tag{2}$$

Regarding the Exit Flow as a Variable. Many researchers regard the exit flow as a function of the number of vehicles, $V_a(X_a(t))$, to a certain extent, on behalf of the real situation, but it also causes some problems in computing:

(1) Whenever the traffic flow enters the road, the exit flow of the road section is always immediately positive, that is $X_a(t)>0$, but if the link flow is initialized as 0, then this phenomenon is unreasonable. Because no matter how short road length is, traffic flow is always to spend some time through the whole road.

(2) If the sections of the exit flow are nonlinear, it is difficult to break down the sections of use to the end of exit flow. This will be difficult to model and solve multi-endpoint dynamic traffic network.

(3) So far, no one knows what the non-linear sections of the exit stream function are, of course, would not be able to calibrate it. If sections of exit flow as a variable and not a function of the method is very easy to solve the problems caused by the non-linear sections out to the stream function (Ran and Shimazaki 1989). This simplified many dynamic traffic network model would be very easy to model, and will reduce the calculation of the difficulty and time.

The Links among the Enter Flow, the Exit Stream, the Number of Vehicles. In dynamic road network, the enter flow, the exit stream, and the number of vehicles are considered to be three different variables in the same team. The concept of a two-node simple network is easy to demonstrate. Assumptions within the time interval t, the vehicle for the real road time $\tau_a(t)$. We will be very easy to define this team: the enter flow rate within the time period t, the number of vehicles between time t and $t+\tau_a(t)$ (excluding the later), and within the time period $t+\tau_a(t)$ the outflow flow rate. We can also say that sections of a given running time, it can determine the relationship of the enter flow, the exit flow, and the number of vehicles. Similarly, these three variables are interrelated, no one can be independent of the other two variables. In discrete dynamic route choice model, based on the three relationships, we can call it a variable instead of three.

First of all we can prove that the enter flow and the exit flow can replace each other. On a specific path P between r and s within the OD set in time period k, traffic flow propagation constraint is:

$$U_{apk}^{rs}(i) = V_{apk}^{rs}(i + \tau_a(i)) \qquad \forall r, s, a, p, k, i \tag{3}$$

Formula (3) shows that the enter flow is equal to the exit flow on a specific path P in time period $t+\tau_a(t)$. The exit flow in road a in time period $t+\boldsymbol{\tau_a(t)}$ may be composed by the enter flows in different time periods.

$$\sum_i U_a(i) = V_a(i + \tau_a(i)) \qquad \forall a, (i + \tau_a(i)) \tag{4}$$

Taking the formula (4-2) into (4-1), and then considering r, s, P, k, it can be the following formula:

$$\sum_{rs}\sum_{p}\sum_{k}\sum_{1}^{i}\sum_{i}U_{apk}^{rs}(i)=\sum_{rs}\sum_{p}\sum_{k}\sum_{1}^{i}V_{apk}^{rs}(i+\tau_a(i)) \quad \forall a,(i+\tau_a(i)) \tag{5}$$

Let t +$\tau_a(i)$, the above equation can be abbreviated as:

$$\sum_{i=t\ \tau_a(t)}U_a(i)=V_a(t) \quad \forall a,t \tag{6}$$

Taking characteristic variables into the formula (4-4):

$$V_a(t)=\sum_{i}U_a(i)\delta_{a1}(t) \quad \forall a,t \tag{7}$$

Where:

$$\delta_{a1}^{i}=\begin{matrix}1\\0\end{matrix}\quad\begin{matrix}\text{if i}+\tau_{\text{a}}(\text{i})=\text{t}\\\text{ot her si t uat i ons}\end{matrix}\quad \forall a,i,t \tag{8}$$

Now we can see from the formulas (7) and (8) that the exit flow is equal to the exit flow ($U_a(i)\leq t$) entering road a before the time t, and outflow sections of a time period t. The exit flow $V_a(t)$ and the enter flow $U_a(t)$ which can be interrelated by characteristic variables show that the exit flow at least in theory, can be instead by the enter flow. Equation (4-5) (4-6) (4-1) are obtained in considering the path P, the time period i, 0-point D on the basis of the rs and the starting time k. So you can clearly know, on the basis of the known road resistance time, the enter flow on the road a and the exit flow can be used interchangeably.

In the same example, the number of vehicles on road a can be expressed using the following formula:

$$X_{apk}^{rs}(t)=X_{apk}^{rs}(t\text{-}1)+U_{apk}^{rs}(t\text{-}1)\quad V_{apk}^{rs}(t\text{-}1) \tag{9}$$

the sum of available on the basis of R, S, P, k is:

$$X_a(t)=X_a(t\text{-}1)+U_a(t\text{-}1)\quad V_a(t\text{-}1) \tag{10}$$

The number of vehicles on the road a from a time period 1 added to the time period t-1, it can be obtained on the road a before time *t*:

$$X_a(t)=\sum_{i=1}^{t\ 1}U_a(i)\quad\sum_{j=1}^{t\ 1}[\sum_{j}U_a(j)\delta_{a1}^{j}(j)] \quad \forall a,t \tag{11}$$

Note that the known dynamic impedance functions based on the number of vehicles on the section can be expressed as a function into the stream. Formula (11) can be written as:

$$X_a(t)=\sum_{i}U_a(i)\delta_{a2}^{i}(t) \tag{12}$$

Where:

$$\delta_{a2}^{i}=\begin{matrix}1\\0\end{matrix}\quad\begin{matrix}\text{if i}+\tau_{\text{a}}(\text{i})=\text{t}\\\text{ot her si t uat i ons}\end{matrix}\quad \forall a,i,t \tag{13}$$

Conclusions

It can be seen from the above analysis that the enter flow, the exit flow, the number of vehicles can replace each other. Dynamic impedance functions can simply use the following formula:

$$C_a(t)=C(U_a(1),U_a(2)\cdots,U_a(t))$$

The dynamic impedance functions only showed by the entering flow function not only allows the modeling simple and can save a lot of time running on your computer and provide a basis for later analysis in the dynamic network traffic in large cities.

References

[1] W. Huang, Introduction of Intelligent Transport Systems (ITS), China Communications Press, Beijing, 1999.

[2] S. Lu, Q. Shi, Y. Yan, Dynamic traffic assignment theory Retrospect and Prospect, Highway and Transportation Research, Beijing, l996.

[3] Z. Yuan, Road model based on dynamic traffic assignment, China Journal of Highway, 3 (2002).

[4] H. Chen, Dynamic Travel Choice Models: A Variation Inequality Approach, Department of Civil Engineering of National Central University, 1999.

© (2012) Trans Tech Publications, Switzerland
doi:10.4028/www.scientific.net/AMM.238.507

Compensation Design of Highway Landscape

Shengneng Hu [1, a], Qindong Fan [1,b], Zhonghuang Hu [2,c] and Xinhua Xiao [1,d]

[1] North China University of Water Resources and Electric Power, Zhengzhou 450011, China

[2] CCCC Guangzhou Dredging Co. Ltd, Guangzhou 510221, China

[a] hushengneng@sina.com, [b]fanqindong@126.com, [c] 42970367@qq.com,[d] 420163716@qq.com

Key words: highway engineering; highway landscape; compensation design.

Abstract. By summarizing the landscape design situation at present in China and overseas, this paper analyzes the problems and defects existed in the Chinese highway landscape design. The compensation design method of highway landscape is put forward, which contains the road side slop, the central dividing strip, the intercommunication grade separation and the service area.

Introduction

With the continuous improvement of living standards, people are increasingly high demands on traffic. From the initial solution of basic travel problems gradually transformed into can provide comfortable, safe, efficient, fast and user-friendly traffic problem, requirement highway in satisfying their traffic function at the same time, pay more attention to appearance, comfort and spiritual level function. Therefore, attention should be paid to highway landscape design.

Domestic and Foreign Development Status of Highway Landscape

Foreign Development Status. Data shows, developed in the highway construction attaches great importance to the protection of the ecological environment around the road, some countries have even using a variety of mechanisms and incentives on highway greening to contribute to the group. The developed countries in highway landscape design can offer the experience that draw lessons from with [1, 2]:

(1)Different regions have different values, different area has its unique geographical position, topography features, climate and weather characteristics and social environment; living in different regions and groups have different cultural traditions, customs and aesthetic view.

(2)Special area, ecological environment sensitive areas and places of historic interest and scenic beauty should be please related experts to participate in the consultation and argumentation, according to the characteristics of road area, specializing in environmental design.

(3)Road and the surrounding environment is regarded as an aesthetic whole. In general, people on the surrounding environment in the psychological feeling, can produce a significant response, so the designers on the main engineering design at the same time, cannot be ignored in coordination with the surrounding environment.

(4)From the legal provisions of highway design and environmental protection simultaneously; it also provides residents along the representative participation to highway construction decision.

Insufficiency in Our Country Highway Landscape Design. The research of highway landscape design in China started relatively late, whether the design content and design method are in relatively low level. Existing studies only focused on Expressway land within the green afforestation and beautification of the discussion, a comprehensive system of highway landscape research did not receive the necessary attention and concern. Through to our country present highway landscape design were analyzed, it is not difficult to find in highway landscape design has some problems [3].

(1) Highway design only focuses on indicators selection, ignore road and the surrounding terrain coordinate. Design of high grade highway, often covers a very large area. In the construction of large cutting slope, excavation hill hillock, fill up the roads, the felling of forests, wetlands,

grasslands and other violations of occupation segmentation of natural landscape and ecological environment, and the surrounding environment, lack of fusion between coordination, add radiance and beauty to each other.

(2) Visual effect along highway is not well. Visual image is mainly from the human visual experience requirements, according to the aesthetic rule, using spatial entity objects, create a pleasant environment image. Must be on the freeway space environment within the visual features are studied, to find out the rules, which will be used as the basis of road landscape design. At present our country highway design to regional landscape resources without investigation and assessment and landscape planning and design requirements. In construction of high grade highway damage or destruction of landscape resources phenomenon it is often seen. and the influence is irreversible.

(3) At present our country high grade highway with high embankment in plain form, average filling high above of 3.15 m, mountainous area average filling higher, to regional geomorphology caused great destruction, but also denied the surrounding people's aesthetic vision.

(4) There are two species of road greening sustainable development tendency. One is the "emphasis on short-term effect, ignoring long-term effect", a direct result of the "one year, two years, three years, green yellow blight, four years death" phenomenon occurred; two is "too much emphasis on greening effect", such as the number of drought little rain in the western provinces also stressed that the vegetation coverage, even to plant trees, often in great, the effect is not ideal, it is neither scientific nor economic.

New Concept of Highway Design

United States Federal Highway Administration fully aware "in highway construction at the same time, strengthen the protection of natural ecological environment and landscape, cultural and historical resources and for the public to provide safe, efficient transportation services is that they face a huge challenge", therefore put forward the new idea of flexibility in highway design.

Flexibility in highway design is defined on the basis of existing regulations, standards, norms, in does not reduce the security of the premise, through reasonable choice standard and flexible use of design index, seeking to achieve more consistent with highway sustainable development needs and interests. Specifically, it is a reasonable choice of construction standard, flexible use of design index, from the architecture, aesthetics angle differential drain protection engineering structure and the feasibility of appearance, from the visitors view protection, green engineering rationality.

In 2004, "six adherence, six sets " highway design new concept has been put forward at china highway reconnaissance designs working conference which include" people-oriented, safety first; protect environment, natural harmony; conservation of resources, sustainable development; quality first, public satisfaction; indicators of appropriate, creative design; systems thinking, life cycle cost".

Highway Landscape Compensation Design Method

Compensatory design mainly from the local basic situation, gives a set of reasonable rehabilitation of the environment, and gradually transition to the environment sustainable development order section. At present, the highway landscape compensatory is designed mainly to solve highway green problems, including: landscape design of expressway slope compensation, central dividing strip landscape design of the septum with compensatory.

Landscape Compensation Design of Road Side Slope. With the mountainous area highway construction, there are the filling digging type subgrade slope everywhere. Increasingly serious damage to the environment, so in the highway landscape design should be considered firstly in compensatory slope landscape design. While the slope landscape compensatory design, the problem of first consideration is how to restore the damaged road ecological environmental problems.

Slope landscape design is compensatory in the local natural landscape based on, select the appropriate plant populations, on subgrade slope greening, and try to make the slope environment into the nature, form a continuous loop road region ecosystem. So in the landscape design of slope

greening design of compensation, we must first select some grass, choose a certain plants planted on the roadbed, taking into account the cultivated plants can be integrated into the natural environment. In general, the choice of plant is original, along the highway and easy to survival of plant population. This can make the slope in a very short period of time to establish a simple road ecological circulation system.

Landscape Compensation Design of Central Dividing Strip. Landscape compensation design of central dividing strip is one part in highway landscape design. Soil layer that because the medial strip is thin, soil to be barren, the plant growth condition of local growth is bad, simultaneously does not favor the construction and later period maintains, when because of this to the medial strip afforestation, must pay attention to choose the construction cost lowly, to raise protects the expense to be few, the growth rate slow, combats drought and bears, the anti-pollution, to bear the trim barrenly the tree seed as against dizzy plant, generally therefore selects the indigenous plant that is easy to transplant

Landscape Compensation Design of Intercommunication Grade Separation. Freeway interchange landscape design aims to enable interchange modeling beautiful, legibility, a guide to the driver's line of sight, to guarantee the safety of train operation and the ornamental effect. Interchange district greening layout should obey the traffic function, to ensure smooth running of sight, prominent green traffic sign. Located in the main city and resort in the entrance, can highlight the local landscape and historical connotation, make its construction can represent geographical features.

Intersection design is a key consideration does not affect the intersection visibility. Intersection layout reasonable and appropriate afforest, can improve the intersection recognition ability, but also to save land, obtain good ground structure modeling effect and create intersection visual landscape are good.

Landscape Compensation Design of Service Area. Because the service area location, landscape requirements are relatively high, green must be with the local background and landscape characteristics of integration, can use the trees and flowers to enhance the feeling of the season, and through the space division and plant configuration, using buildings as the main body, combined with modern architecture expression means, and to the lighting and landscaping embellishment and, to watch, to improve the environmental quality of the purpose of leisure. From the whole to create a peripheral green environment, a rich green atmosphere is formed.

Conclusions

Highway landscape compensation design is very major role for the regeneration of landscape, don't make overall modeling and the surrounding landscape apart, should cause the whole construction of road while satisfying esthetics and traffic safety request, but can also play to balance the function of road and natural landscape.

References

[1] R. S. James, L. P. Kimberly, C. L. Harlow, Guidelines for aesthetic design in freeway corridors, U.S. Department of Transportation Federal Freeway Administration, 2001.

[2] Landscape and Aesthetics Design Manual, Texas Department of Transportation, 2009.

[3] S. Hu, Study on the Freeway Landscape Planning and Design Technology, Chang'an University, Xi'an, 2011.

CHAPTER 3:

Innovation in Architecture and Building Construction

© (2012) Trans Tech Publications, Switzerland
doi:10.4028/www.scientific.net/AMM.238.513

Critical Risks Influencing the Application of EERTs in Australian Green Office Buildings

Guomin Zhang[1,a], Ibrahim Mosly[1,b], Sujeeva Setunge[1,c] and Xiao-Hua Jin[2,d]

[1]School of Civil, Environmental and Chemical Engineering, RMIT University, Melbourne, Australia

[2]School of Computing, Engineering and Mathematics, University of Western Sydney, Australia

[a]kevin.zhang@rmit.edu.au, [b]ibrahim.mosly@rmit.edu.au, [c]sujeeva.setunge@rmit.edu.au, [d]xiaohua.jin@uws.edu.au

Keywords: risk; stakeholders; lifecycle; energy efficient technology; renewable energy technology; green office buildings.

Abstract: This paper aims to explore the risks of applying energy efficient and renewable technologies (EERTs) in Australian green office buildings. An online questionnaire survey was conducted in several Australian states and territories to identify and evaluate the potential critical risks that may influence the implementation of EERTs. Consisting of architects, engineers, project managers, and contractors, participants of the survey were asked to evaluate the generic and some specific EERTs risks occurring in the implementation of a selected number of commonly used EERTs in Australian green office buildings. In addition, the participants were asked to pinpoint those stakeholders who were the most affected by the risks and the lifecycle stage of the technology or buildings at which these risks might mostly occur. The data analysis results shows that *uncertain governmental policies* were identified as the critical risk with the highest mean risk impact value, *Lack of access to funds* and *Presence of system constraints* were the most popular risks with influences on most of EERTs. It also identifies the EERTs owners as most affected stakeholders by EERTs risks and that the majority of these risks occur during the operation stage.

Introduction

Governmental rebates for the installation of energy efficient & renewable technologies (EERTs) are assessing its spread in both residential and commercial buildings in Australia. Taking part in transforming these buildings into what is so called nowadays by green buildings. True in some cases, the energy bill is decreasing but is that the case for all installed EERTs? Uncertainty and risk related to new green technology is widespread [1]. This is why general concerns exist when it comes to applying these technologies in practice. To reduce or eliminate this uncertainty and risk more research on risk management for new green technologies should be carried out.

Although green buildings address lots of attributes during its lifecycle such as, efficiency in energy consumption, water conservation, and providing a productive and healthy environment to its occupants [2], this research will only focus on the energy attributes of green office buildings in Australia. This is because other technologies related to other attributes such as enhancing water conversation might cause risks which are not shred or relevant to energy related technologies and thus should be studied separately.

The source of data collection in this study was an online questionnaire survey. It was circulated among different green building industry experts including architects, engineers, project managers, and contractors. The questionnaire survey was designed to answer four main questions, what are the critical risks associated with the implementation of EERTs?, Is there a difference in opinion of different expert groups when it comes to risk perception?, Who is the most affected stakeholder/s by each risk among the different stakeholders?, At which stage of the technology or building lifecycle is it most likely for each of these risks to occur?. The survey focal point was to evaluate a number of risks related to EERTs as part of a risk management process, in addition to investigating and identifying those stakeholders affected by these risks as well as identifying the technology or building lifecycle stage at which these risks might occur.

EERTS for Green Office Buildings

A total of nine energy efficient & renewable technologies (EERTs) formed the bases of this study. These EERTs were selected due to their popular usage in Australian green office buildings rated either five or six green stars by the Green Building Council of Australia. The EERTs were categorized under four groups, two being energy efficient technologies including, heat ventilation and air conditioning (HVAC) and lighting, and two being renewable energy technologies including, solar and wind [3].

HVAC and lighting were selected as the two groups for energy efficient technologies because they consume a major portion of energy in the Australian commercial buildings that is 70% for HVAC and 15% for lighting (Australian greenhouse office, 1999). For office buildings in particular, HVAC and lighting was found to consume 70% of the total building energy consumption in the Unites States of America, 72% in the United Kingdom, and 85% in Spain [4].

Renewable energy technologies can be classified into two types according to their supply, onsite and offsite supply options. Onsite supply options refer to technologies that use energy sources available onsite and offsite options refer to technologies that use energy generated from another location. Solar technologies like, photovoltaic panels and solar thermal heating are considered to be the most applicable onsite technologies. Other technologies like wind are applicable also but for limited applications [5]. Therefore solar and wind were selected as the two groups for renewable energy technologies because they can be feasibly implemented in office buildings without being concerned with the topography and location of the office building. The selected EERTs are illustrated in Table 1.

Table 1 Commonly implemented EERTs in Australian green office buildings (Source [3])

Category	Technology	Description
HVAC	Chilled beams (CB)	Chilled beam systems can be passive or active (Schultz, 2007). Passive chilled beam systems comprise of a coil with fins covered by the metal sheeting. In the cooling system, chilled water with temperatures of 13 ^{o}C to 17 ^{o}C passes through the coil, which in turn cools the air and force it to move down to the ground level. On the other hand, active chilled beam systems are considered to be more complex than passive chilled beam systems as they are equipped with an air supply that passes through the cooling coil and drop down to the building floor (Roth et al, 2007).
	Night ventilation (NV)	Night ventilation helps in reducing energy consumption by using natural or mechanical ventilation to let in the cool night air, which in turn reduces the inside temperature of the air, fabric and building slab (Kolokotroni and Aronis, 1999).
	Radiant system (RS)	Radiant cooling and heating systems depend on the mechanism of radiation heat transfer, where heat is transferred in straight lines by electromagnetic waves that can also be reflected. Basically heat transfer takes place between surfaces or between surfaces and a source of heat (ASHRAE, 2003).
	Underfloor air distribution (UFAD)	The UFAD system consists of a high induction swirl diffusers that circulate the air in an upward direction directly to the occupied zone. The air then returns by going through the ceiling grilles (Hui and Li, 2002).
Lighting	Energy efficient light bulbs (EELB)	Including the major types of energy efficient light bulbs such as, fluorescents, light emitting diodes (LED), high intensity discharge (HID), and halogen lightings.
	Motion sensors (MS)	Motion sensors or occupancy sensors are used to turn on lights when occupants are in a room or shut it off after they leave the room. There are three types of motion sensors and they are: passive infrared, ultrasonic and a hybrid of infrared and ultrasonic technology. The infrared motion sensor reacts to heat source, while ultrasonic sensor reacts to any movement that disturbs the ultrasonic waves emitted by the device (Stein and Reynolds, 2000).
Solar	Photovoltaic panels (PV)	Photovoltaic panels are used to generate electricity from sunlight (Turkenburg, 2000).
	Solar thermal heating (ST)	Solar thermal heating works by transferring sunlight into heat. The temperature of heat produced can reach up to 100 ^{o}C (Turkenburg, 2000).
Wind	Wind turbines (WT)	Wind turbines operate by converting kinetic energy from the wind into mechanical energy using its rotor. After that, the mechanical energy is converted into electrical energy by its electrical generator (Hau, 2006).

From Table 1, the nine technologies comprise of four technologies under HVAC, two under lighting and solar, one technology under wind. HVAC group has the most number of technologies implemented in the Australian green office buildings, which could be directly linked to the reason for it being responsible for the majority of energy consumption in buildings. On the other hand, only one type of wind technologies is commonly implemented in the Australian green office buildings due to limited application of this group.

Risks Associated with the Implementation of EERTs

Risk is the undesirable consequence of activities such as loss of human life, adverse health effects, loss of property and impacts to the natural environment that take place due to natural or human activities. Risk from an engineering viewpoint is associated with the exposure of recipients to hazards and can be articulated as the combination of probability and consequence of the hazard [6].

Risk identification is the first step in risk assessment. It aims to produce a broad list of risk triggers and events that could have an impact on the success of objectives initially identified in the context. The identification should include risks that can be or can't be controlled by the organization [7].

Table 2 Risks associated with EERTs and categories affected (Source: [8])

Risks	HVAC	Lighting	Solar	Wind
Aesthetically unpleasing	X	X	X	X
Birds collision				X
CO2 suffocation	X			
Dangerous emissions from unit production			X	
Draught & thermal discomfort	X			
Emerge of new, superior technology	X	X	X	X
Fire risk		X	X	
Future change in regional climate and weather fluctuation	X		X	X
Glare risk from collector sunlight reflection			X	
Headaches, skin rash and depression		X		
Hidden costs	X	X	X	X
Lack of access to funds	X	X	X	X
Lack of access to information about technology	X	X	X	X
Lack of access to necessary spare parts	X	X	X	X
Lack of access to the technology itself	X	X	X	X
Lack of availability of skilled personnel	X	X	X	X
Leakage of hazardous material	X	X	X	
Low consumer demand and acceptance	X	X	X	X
Low product and performance reliability	X	X	X	X
Misplaced incentives	X	X	X	X
Noise and building vibration				X
Operation failure	X	X	X	X
Physical degradation			X	X
Presence of system constraints	X	X	X	X
Slow response rate to temperature changes	X			
Surface condensation and mold growth	X			
Unauthorized building entrance	X			
Uncertain availability of incentives	X		X	X
Uncertain governmental policies			X	X
Uncertain payback period	X	X	X	X

The risks explored in this paper were obtained from various sources that investigated the risks of EERTs. Based on literature, this study has examined a total number of 66 research sources that investigated all nine EERTs listed in Table 1 were reviewed. The sources included books, journal articles, conference papers, reports and official internet websites. Authors of these sources used different methods for data collection, such as surveys, interviews, focus groups, and case studies. The outcome of the literature review process was the identification of 30 risks illustrated in Table 2. These risk factors can be grouped into two main types, generic and specific. The first type of risks is those

risks that can occur to technologies from more than one category and the second type is those risks that can occur to certain technologies in certain categories. An example of the first type is hidden costs, which can occur to any technology among all categories. An example of the second type is glare risk, which might only occur to technologies listed under the solar category [8].

One or more of the generic risks such as *lack of access to information about technology, lack of availability of skilled personnel,* and *low product and performance reliability* in addition to other risks were identified in many sources that investigated energy efficient technologies or renewable energy technologies or even both of them combined together in one study such as in [9, 10, 11, 12, 13]. On the other hand, other sources investigated one or more specific risks for HVAC technologies such as in [14, 15, 16] which investigated risks like *presence of system constraints* and *Surface condensation and mold growth* in radiant systems, chilled beams, and underfloor air distribution systems. More details on generic and specific risks and its sources identified in this study can be found in [8].

Research Methodology

An online questionnaire survey was used in this research to gather information on the risks associated with the implementation of EERTs. The questionnaire was piloted by two senior researchers and an engineer and as a result, a few constructive feedbacks were obtained to improve the understanding of questions included in the survey. An online questionnaire survey was then created and invitations to participants were sent by email to a sample size of 400 green building technology participants in the construction industry, mainly including architects, engineers, project managers, and contractors. A respond rate of 41.25% was achieved at the end of data collection period with approximately 94% of the respondents being Green Star Accredited Professionals by the Green Building Council of Australia.

The questionnaire was designed to answer four questions, 1) What are the critical risks associated with the implementation of EERTs?, 2) Is there a difference in risk perception among different industry practitioners?, 3) Who is the most affected stakeholder/s by each risk among the different stakeholders, 4) At which stage of the technology or building lifecycle is it most likely for each of these risks to occur?

Three different methods were used to analyse the data in this research. The statistical analyses were executed with the aid of SPSS software. Firstly, a risk matrix was used for identifying the critical risks of EERTs. Secondly, ANOVA test was undertaken to scrutinize the differences between different practitioners perception on the risks of EERTs. Finally, Chi square test was used to identify the most affected stakeholder/s by the risks as well as pinpoint at which lifecycle stage/s the risks will most likely occur.

Questionnaire Data Analysis and Results

Participants Profile. A total of 165 practitioners have participated in this questionnaire survey. This included 40 architect, 67 engineers, 42 project managers, and 16 contractors. Their level of education varied from secondary school to postgraduates and included three secondary school certificates holders, 80 undergraduates, 68 postgraduates and two holding other degrees. With respect to length of work experience in the construction industry, 39 had between 1 - 5 years, 31 between 6 -10, 29 between 11 – 15 years, and 66 with more than 15 years of experience. With respect to the number of green building projects that these practitioners were involved in, 12 had zero experience with green building projects, 73 with between 1 – 4 projects, 30 with between 5 – 10 projects, and 50 with more than 10 green building projects.

Data Reliability. A reliability test called Cronbach's Alpha was carried on the data collected from the online questionnaire. It is considered as the most accepted method for examining reliability. The following cut-off points can be used as a guide to interpret the test results [17]: 1) equal or above 0.90 illustrates excellent reliability, 2) 0.70 to 0.90 indicating high reliability, 3) 0.50 to 0.70 indicating moderate reliability, 4) below or equal to 0.50 indicating low reliability.

The results of the reliability test are shown in Table 3. It includes the collected data for the risk evaluation of all risks for each of the nine technologies.

Table 3 Data reliability

Data source	Cronbach's Alpha
Chilled beams	0.902
Radiant system	0.908
Underfloor air distribution	0.928
Night ventilation	0.925
Energy efficient light bulbs	0.917
Motion sensors	0.937
Photovoltaic panels	0.937
Solar thermal heating	0.949
Wind turbines	0.929
Stakeholder/s	0.969
Technology or building lifecycle stage/s	0.970

The Cronbach's Alpha values for all of the collected data were above 0.90 which indicates an excellent reliability outcome for all of the data used in this study.

Part One: Identification of Critical Risks. The questionnaire participants were asked to evaluate the risks for each one of these technologies based on the likelihood of occurrence and the impact on stakeholders. Six options were defined to measure the likelihood of occurrence, i.e., rare, unlikely, possible, likely, almost certain, and not applicable. Similarly, six options were defined to measure the impact on stakeholders, i.e., negligible, minor, moderate, major, severe, and not applicable. A total numbers of 30 risks were evaluated (Refer to the risks listed in Table 2.

Critical risks were identified through a semi-quantitative approach, where the level of risk impact was calculated by using Equation 1 [7].

$$\text{Risk impact} = \text{Consequence} \times \text{Likelihood} \quad (1)$$

In order to measure the level of risks for each technology and to know whether they were critical or not, a risk matrix was developed with reference to two established risk matrixes. This is because the relationship between the consequence and likelihood in a certain risk matrix may defer from one application to another [7]. The first risk matrix was obtained from the Australian New Zealand standard 2004. The second risk matrix was obtained from a study undertaken by John Mankins, where he described a new concept for the integration of the technology readiness levels and the concept of risk matrix for new technologies [18].

The new matrix created for this study (see Table 4) has combined features from both of the aforementioned risk matrixes as well as made specific modifications that convoy with the data analysis outcome.

Table 4 Risk evaluation matrix

Likelihood	Consequence				
	Negligible (1)	Minor (2)	Moderate (3)	Major (4)	Severe (5)
Almost certain (5)	Medium	Medium	High	High	High
Likely (4)	Low	Medium	High	High	High
Possible (3)	Low	Medium	Medium	High	High
Unlikely (2)	Low	Low	Medium	Medium	Medium
Rare (1)	Low	Low	Low	Low	Medium

According to the risk matrix, if the level of risk impact for a particular risk is less than or equal to four, it will be considered of a low level risk. If the level of risk impact is greater than four and less or equal to 10, then it will be considered of a medium level. Finally, if the level of risk impact is greater than 10, then it will be considered of a high level and therefore critical.

The final level of risk impact was calculated for each risk for each one of the nine technologies by taking the average risk score from all participants. After analysis was conducted, it was found that six of the nine are subject to critical risks. Table 5 illustrates the critical risks and the associated technologies.

Table 5 Critical risks of EERTs with its mean risk impact values

Risk	HVAC			Solar		Wind
	CB	RS	UFAD	ST	PV	WT
Emerge of new, superior technology				11	11.73	10.24
Future change in regional climate and weather fluctuation					10.19	10.42
Hidden costs		10.18				11.11
Lack of access to funds	11.57	12.20	10.59	12.75	13.31	12.87
Lack of availability of skilled personnel		10.17				10.05
Low consumer demand and acceptance		10.53				
Misplaced incentives				11.58	10.56	10.09
Noise and building vibration						10.87
Presence of system constraints	10.78	10.83	10.24	10.53	10.58	11.25
Slow response rate to temperature changes		10.19				
Surface condensation and mold growth	10.14					
Uncertain availability of incentives				14.08	13.85	11.89
Uncertain governmental policies				14.35	13.85	12.13
Uncertain payback period		10.77		11.58	12.82	13.09

Part Two: Comparison of Practitioners Opinion on Risks. A statistical tool was used in this study to compare the different views between the four main stakeholder groups that participated in this survey. ANOVA test was used in SPSS to identify those risks with significance difference in the experts' opinion. Furthermore, Post Hoc test was used to compare the different opinions and look into more details in the differences. The analysis gave the chance to find those risks with significance differences in the opinions of the stakeholders group with regards to its level of risk impact. Only risks where stakeholders had significance difference in opinion at $p<0.05$ will be illustrated. Table 6 summarizes the outcome of the analysis.

Table 6 Comparison of stakeholders risk perception

Technology	Risk	Stakeholder with higher risk perception (A)	Stakeholder with lower risk perception (B)	Mean Difference (A - B)	Significance
CB	Emerge of new, superior technology	Architect	Engineer	5.686	0.002
NV	Uncertain payback period	Engineer	Architect	4.442	0.028
	Low consumer demand and acceptance	Project Manager	Architect	7.642	0.012
PV	Uncertain payback period	Contractor	Project Manager	8.306	0.006
	Hidden costs	Contractor	Project Manager	6.014	0.038
	Lack of access to information about technology	Contractor	Engineer	6.567	0.003
	Lack of availability of skilled personnel	Project Manager	Engineer	2.964	0.042
	Lack of access to the technology itself	Contractor	Architect	5.611	0.018
		Contractor	Engineer	5.290	0.017
	Emerge of new, superior technology	Project Manager	Engineer	5.268	0.018
	Physical degradation	Contractor	Architect	5.222	0.039
		Contractor	Project Manager	5.375	0.037
RS	Misplaced incentives	Contractor	Architect	9.524	0.036
		Contractor	Engineer	10.137	0.011
ST	Emerge of new, superior technology	Contractor	Engineer	8.461	0.006
UFAD	Lack of access to necessary spare parts	Engineer	Contractor	2.985	0.012
		Project Manager	Contractor	6.436	0.017
	Emerge of new, superior technology	Architect	Engineer	4.722	0.035
WT	Lack of availability of skilled personnel	Contractor	Engineer	7.357	0.039
		Contractor	Architect	7.850	0.036

Part Three: Most Affected Stakeholder/s by Risks. In this part, for all 30 risks, an assessment was made to examine which stakeholder/s was/were the most affected by each risk. Participants

were asked to select the most affected stakeholder/s for each risk. The stakeholders included architects, engineers, project managers, suppliers, occupier and owners. The Chi-Square test was selected to carry out the analysis.

After running the test on the 30 risks, the selection of the most affected stakeholder/s was/were made based on the standardized adjusted residual (SAR) value. Whenever the value of SAR lies outside ±1.96 then it is considered significant at $p<0.05$ [19]. For each risk the participants were asked to place a tick for every stakeholder they think is going to be mostly affected by the risk. In the Chi-Square analysis the comparison was done between Yes for affected by the risk and No for not affected by the risk. Yes selection is indicated by positive digits of SAR value, while No selection is indicated by negative digits of SAR values. The cells in bold represent those stakeholders that are the most affected by the risk. Table 7 illustrates the SAR values for yes answers, which represents the affected stakeholders.

Table 7 Most affected stakeholders by EERTs risks

Risk	SAR value						
	Architect	Engineer	Project Manager	Supplier	Contractor	Occupier	Owner
Aesthetically unpleasing	**9.8**	-5.7	-5.5	-6.1	-6.6	**6.5**	**7.6**
Birds collision	-1.4	-1.6	-2.9	-4.7	-3.9	**6.8**	**7.8**
CO2 suffocation	-3.6	1.5	-4.3	-4	-3.2	**8.7**	**4.9**
Dangerous emissions from unit production	-3.6	-0.3	-3.9	0.2	-3.6	**6.6**	**4.7**
Draught & thermal discomfort	-3.5	0.7	-4.4	-4.4	-3	**10.9**	**3.8**
Emerge of new, superior technology	-1.1	**3.1**	-4.1	0.5	-3	-2.6	**7.2**
Fire risk	-4	-0.5	-4.2	-3.8	-2	**6.7**	**7.8**
Future change in regional climate and weather fluctuation	-3.3	**3.6**	-3.8	-2.6	-4.9	**4.7**	**6.3**
Glare risk from collector sunlight reflection	0.5	0.8	-4.8	-5.3	-5.5	**8.7**	**5.7**
Headaches, skin rash and depression	-3.4	-1.1	-4.8	-4.1	-4.3	**12.5**	**5.1**
Hidden costs	-5.1	-3.2	0.5	-5.1	-0.8	0.3	**13.5**
Lack of access to funds	-2.9	-2.4	-0.2	-2.4	-4	-3.1	**15.1**
Lack of access to information about technology	**4.3**	**8.8**	-2.6	-5.1	-1.4	-5.1	1.1
Lack of access to necessary spare parts	-6.6	-3.8	-4.4	1.3	**6.1**	0.4	**7**
Lack of access to the technology itself	-0.2	**4.3**	-1.6	0	**3**	-5.2	-0.2
Lack of availability of skilled personnel	-4.1	-1.6	**2.4**	-2.2	**9.8**	-5.2	0.9
Leakage of hazardous material	-4.4	-1.2	-4.6	-2.5	-0.3	**7.1**	**6**
Low consumer demand and acceptance	0.6	-1	-3.3	**2.4**	-3.3	-0.5	**5.1**
Low product and performance reliability	-4.7	0.4	-5.1	-1.7	-1.5	**4.5**	**8.1**
Misplaced incentives	-2.7	-2.9	-2.4	-1.7	-3.4	0.4	**12.7**
Noise & building vibration	-3.6	1.8	-3.9	-5.2	-3.9	**8.8**	**6**
Operation failure	-6.9	-2.8	-4.9	-2.2	**2.8**	**6.1**	**7.8**
Physical degradation	-3.1	-0.6	-5	-1.7	-2.4	**3.1**	**9.8**
Presence of system constraints	0.4	**7.1**	-1.5	-4.6	-0.2	-2.3	1
Slow response to temperature changes	-3.9	1.1	-4.8	-3.7	-3.7	**10.2**	**4.7**
Surface condensation and mold growth	-4.1	1.2	-5.4	-4.7	-1.7	**7.5**	**7.3**
Unauthorized building entrance	-1.5	-3.2	-3.2	-4.5	-3.5	**9.1**	**6.9**
Uncertain availability of incentives	-3.4	-3.2	-3	-1.8	-3.9	0.1	**15.2**
Uncertain governmental policies	-2.6	-1.2	-3.1	-1.9	-3.3	1.1	**11.2**
Uncertain payback period	-3.2	-1.6	-0.9	-4.9	-5.8	0.4	**16**

Part Four: Lifecycle Stage of Technology or the Green Office Building That the Risk is Most Likely to Occur. Part four investigates the lifecycle stages of the technology or the green office building where the 30 risks might occur at. For this part the method used for data analysis was similar to the one used in part three. The only difference is that the practitioners were asked to select the lifecycle stage at which they suspect the risk will most likely occur. The lifecycle stages included the following six stages, i.e., technology manufacturing, building concept, building design, building construction and technology installation, operation and maintenance, and demolition and recycle. A total of 29 risks were evaluated in this part, as the risk of dangerous emissions from unit production was not considered as the stage at which this risk might occur was clear in the risk name.

For more details on the analysis please refer to part three. Table 8 illustrates the SAR values, Yes for risk occurring in this/these lifecycle stage/s (positive digits) and No for risk not occurring in this/these lifecycle stage/s (Negative digits), which represents the lifecycle stage at which the risks might occur.

Table 8 Technology or Building lifecycle stage at which EERTs risks might occur

Risk	SAR value					
	Manufacturing	Concept	Design	Constriction	Operation	Demolition
Aesthetically unpleasing	-3.9	**5.6**	**7.5**	-2	-1.3	-6
Birds collision	-3.5	-1.8	-1.2	-2.6	**12.6**	-3.5
CO2 suffocation	-2.9	-3.7	-0.3	-1.9	**12.6**	-3.7
Draught & thermal discomfort	-3.4	-2	0.4	-2.6	**12.1**	-4.4
Emerge of new, superior technology	1.4	1.6	1.6	-2.3	1.1	-3.4
Fire risk	-2.1	-3.3	0.1	-2.3	**11**	-3.3
Future change in regional climate and whether fluctuation	-1.1	-0.8	1.2	-2.6	**7.4**	-4.1
Glare risk from collector sunlight reflection	-3.5	-0.3	1	-2.4	**9.4**	-4.2
Headaches, skin rash and depression	-2.5	-3	-0.8	-3.6	**12.9**	-3
Hidden costs	-4.6	-3.2	-0.6	**5.7**	**6.6**	-3.9
Lack of access to funds	-1.9	**7.5**	**3.5**	0.7	-3.6	-6.2
Lack of access to information about technology	-0.7	**3.5**	**7.6**	-0.5	-3.4	-6.5
Lack of access to necessary spare parts	-0.8	-3.8	-3.6	-0.3	**13.4**	-4.8
Lack of access to the technology itself	**2.6**	**2.2**	**3.3**	1.5	-3	-6.6
Lack of availability of skilled personnel	-3	-4.3	-1.3	**8.5**	**5**	-5
Leakage of hazardous material	-2.2	-3.4	-3.2	-1.7	**9.8**	0.7
Low consumer demand and acceptance	1	**5.5**	**2.3**	-3.9	0.3	-5.2
Low product and performance reliability	-1.6	-4.2	-2.6	0.6	**13.2**	-5.4
Misplaced incentives	-0.6	**3.6**	1.6	0.2	0.4	-5.2
Noise & building vibration	-2.6	-2.6	-0.3	-0.8	**10.8**	-4.5
Operation failure	-3.6	-4.6	-4.6	-1.2	**16.8**	-2.8
Physical degradation	-2.1	-3.9	-2.3	-3.1	**13.1**	-1.5
Presence of system constraints	-3.3	**2.8**	**8.2**	0.1	-1.1	-6.7
Slow response rate to temperature changes	-2	-2.3	1.3	-2.8	**10.7**	-4.9
Surface condensation and mold growth	-3.2	-3.7	-1.1	-1.6	**12.3**	-2.7
Unauthorized building entrance	-4.1	-3.2	-1.4	-0.5	**12.8**	-3.5
Uncertain availability of incentives	-0.2	**2.7**	0.5	-1.2	**2.2**	-4.1
Uncertain governmental policies	0.4	**2.8**	1.6	-2.3	1.9	-4.5
Uncertain payback period	-2.2	**4.5**	**3.1**	-3.4	**3.4**	-5.4

Discussion of Results

Part One: Critical Risks Associated with the Implementation of EERTs. From Table 5 we can see that critical risks were found in six out of the nine technologies and these technologies were categorised under three out of the four main categories including HVAC, solar, and wind. None of the lighting technologies were found to be critically influenced by any critical risk. This might indicate either the maturity of these technologies or their medium to minor impact on its stakeholders. Similarly with NV in the HVAC category, no critical risks were identified for this technology.

In general, the majority of the critical risks were identified for renewable energy technologies with wind turbines subjected to most of these critical risks. On the contrary, UFAD systems had the least identified critical risks out of the six different technologies. This indicates that industry practitioners see renewable energy technologies as a risky investment compared to energy efficient technologies. Unlike efficient energy technologies, renewable energy technologies share a number of critical risks between them, giving a feeling that these technologies might not be ready to be implemented in the Australian market and that more in depth investigation should be carried out to find methods to manage these critical risks.

Two critical risks were shared among the energy efficient technologies, these are *lack of access to funds* and *presence of technical constraints*. This shows that energy efficient technologies can be mainly subjected to financial and technical issues. Renewable energy technologies on the other hand share seven critical risks among them, e*merge of new, superior technology, lack of access to funds, misplaced incentives, presence of system constraints, uncertain availability of incentives, uncertain governmental policies,* and *uncertain payback period* .This indicates that renewable energy technologies can be mainly subjected to financial, market, political and technical issues.

The critical risk of *future change in regional climate and weather fluctuation* was found to be critical for two technologies, PV and WT, which are renewable energy technologies. But the same risk was not identified as critical for ST although it is a renewable energy technology. Possibly this is due to the fact that both PV and WT produce electricity, whereas ST produces heat and that the impact of loss or shortage of electricity is greater than that of loss or shortage of heat as a result of climate change or whether fluctuation.

Two critical risks, *lack of access to funds* and *presence of system constraints* were identified as critical for all of the six technologies. Despite the Australian government measures to resolve the issue of funding for green buildings, for example by offering a green building fund, industry practitioners are still considering it as a critical risk for green technologies. The *presence of system constraints* usually reflects the limitations in the use of a certain technology, this emphasise that these technologies haven't yet reached a mature level of operation. Thus, more in depth approaches to manage these critical risks should be discussed.

The critical risk with the highest mean risk impact value was *uncertain governmental policies.* This might denote that the majority of green industry practitioners are not confident with government policies or the way these policies are structured. Simultaneously, they are worried about the consequence of these uncertainties. This could also explain the high mean risk impact value for *uncertain availability of incentives* which represent a significant part of government policies.

Part Two: Comparison of Different Stakeholders Opinion on Risks of EERTs. Different industry practitioners' perception was found regarding different risks occurring in different technologies. Table 6 presents the only technologies and risks with significant perception difference among the industry practitioners.

All EERTs where illustrated in Table 6 except to the lighting technologies, where none of the industry practitioners showed any differences in risk perception, indicating an agreed position on lighting technologies.

The risk of *emerge of new superior technology* had significant differences in risk perception among industry partitioners in four technologies, CB, PV, ST, and UFAD. Architects, project managers, and contractors were found to be more concerned about this risk than engineers. This

could be due to the fact that engineers most often have the opportunity to select the EERTs to be implemented in green buildings and therefore they are confident of their selection to the technology and less worried about new superior technologies emerging as much as the other industry practitioners who have to deal with design alterations and site preparation if such a risk occur.

Generally, contractors showed higher risk perception over the other industry practitioners in all renewable energy technologies, especially with PV technology where contractors demonstrated higher risk perception in seven risks. This might be due to the fact that contractors are the most subjected to risks of EERTs as they are responsible for transferring the ideas and design from paper into reality and dealing with these risks on daily bases.

Part Three: Most Affected Stakeholder/s by Risks. It's very clear from Table 7 that the most affected stakeholder by these risks is the owner followed by the occupier and that the least affected stakeholders are the project manager and technology supplier and thus, the project managers and the technology suppliers can be the best to promote for EERTs. This shows that the owner will always be affected by all sorts of financial, political, market, technical, and environmental risks. The occupier on the other hand is affected by risks that will impact him during his occupancy period in the building with the majority of these risks occurring during the operation of these EERTs.

It seems that *lack of access to information* and the *presence of system constraints* in EERTs are the two risks that engineers are majorly affected by. True, because engineers must have a solid knowledge in order to select the most appropriate technology for a green building and the presence of system constraints can have a major consequence on the application of certain technology. Other risks that have an effect on engineers include *lack of access to the technology itself*, *emerge of new superior technology*, *future change in regional climate and weather fluctuation*. Because engineers have a significant role in selecting the EERTs for buildings which ask them to take the responsibilities and hence make them more venerable to these risks. The difficulty in getting access to EERTs can cause an issue and might increase costs or delay project schedules even though the suitable technology was selected. Simultaneously, a sudden emerge of a superior technology with enhanced performance might be frustrating to the owners who might have lost the chance for acquiring a better option due to the lack of market awareness by the engineer. Climate change and weather fluctuation can also affect the engineer, that is when technology selection is not considered carefully as technologies might become obsolete if weather patterns change to what the technology was designed for.

Contractors are mostly affected by the following risks, *lack of availability of skilled personnel*, *lack of access to the technology itself*, *lack of access to necessary spare parts*, *operation failure*. It's clearly that all of these risks are part of the daily struggle that contractors may face in their work and that they significantly affect the contractors if not managed appropriately. For instance, a lack in skilled personnel will definitely cause job complications, especially with EERTs which require particular skills for installation and commissioning.

Like engineers, architects are also affected by the risk of *lack in access to information* about EERTs as it is vital for them to have a sufficient amount of information on the technology. Architects are affected the most by the occurrence of the risk *aesthetically unpleasing* outlook, as this plays a big role in their job.

Like contractors, project managers are also affected by the risk *lack of availability of skilled personnel*. This is because not having the knowledgeable and skilled personnel in the area of green buildings on the team might lead to an increase in the number of risks, which in turn can affect the project progress significantly.

Finally, suppliers are affected by the risk of *low consumer demand and acceptance*, simply because if the demand on EERTs reduces then their businesses will be considerably affected.

Part Four: Lifecycle Stage of Technology or the Green Office Building That the Risk is Most Likely to Occur. Table 8 captures the relationships between the risks associated with EERTs and the lifecycle stage of the technology or the building when these risks will most likely occur. The operation stage of the building and the technology seems to be the most critical stage for

EERTs, as the majority of risks occurs at this stage, including financial, technical, environmental, and market risks. This is due to the fact that EERTs where built to work at this stage and is the longest in their lifecycle.

The second stage at which most of the EERTs risks are likely to occur is the concept stage. This is due to the fact that during this stage everything is still on paper and any unclear or ignored issues will become a future risk if not resolved timely.

Similarly with design stage, which comes in third position with the number of risks occurring in it, if issues were not resolved then complications will definitely appear during the later stages of technology or building lifecycle.

Hidden costs and *lack of availability of skilled personnel* are the two risks associated with EERTs that will mostly occur during the construction and technology installation stage. The risk of *lack of access to the technology itself* was selected to occur during the technology manufacturing stage. This could refer to the difficulty in accessing EERTs from the manufacturer due to many reasons, such as high shipping cost from the country of manufacturing to Australia, especially if these EERTs were not manufactured locally.

The only lifecycle stage where no risks were selected to occur in it was the building demolition and technology recycles stage, probably because the number of risks that could occur in that stage were insufficient and that more research should be done in that area.

One of the risks, *emerge of new superior technology* was not identified to occur during any stages. This is because new superior technologies might be introduced at any stage or either the technology or building lifecycle.

General Observations

It was observed from Tables 5, 6 and 7 that the *emerge of new superior technology* is a critical risk for more than one technology. Engineers' perception to this critical risk was observed to be less significant than for other industry practitioner groups, although when it comes to the most affected stakeholder by this critical risk, engineers were one of the most affected by it. Therefore, with respect to EERTs engineers should give more attention to this critical risk to avoid or at least reduce the level of risk impact on them.

Furthermore, from Tables 5, 6, and 7 the *lack of availability of skilled personnel* was identified as a critical for more than one technology. Project managers and contractors have perceived this critical risk higher than engineers and they both were identified to be the most affected by this critical risk. Hence, more attention should be given to these two groups of EERTs stakeholders in order to manage this critical risk successfully.

Conclusions

EERTs are generally wanted but the uncertainty and risks associated with these technologies are driving them away from implementation. Strong measures should be done to promote for their usage. Research and development can assist in eliminating or reducing these implementation barriers and therefore increase EERTs chances for adaptation by the public or private sector. This paper has evaluated a number of EERTs risks and identified stakeholders most affected by the risks, in addition to the technology or building lifecycle stages at which these risks might occur, in a step to increase awareness and facilitate future research to improve and increase the interest in EERTs.

References

[1] P. Lam, E. Chan, C. Poon, C. Chau, K. Chun,, Factors affecting the implementation of green specifications in construction, Journal of Environmental Management, 3 (2010) 654-661.
[2] GBCA, The dollars and sense of green buildings, Green Building Council Australia, Sydney, 2008.
[3] I. Mosly, G. Zhang, Review of risks for the implementation of energy efficient and renewable technologies in green office buildings, in: Proceedings of the Sustainable Building Conference, Wellington, New Zealand, May 26 – 28, 2010.
[4] L. Lombard, J. Ortiz, C. Pout, A review on buildings energy consumption information, Energy and Buildings, 3 (2008) 394-398.
[5] P. Torcellini, S. Pless, M. Deru, Zero energy buildings: A critical look at the definition, ACEEE Sumer Study, Pacific Grove, California, 2006.
[6] M. Modarres, Risk Analysis in Engineering: Techniques, Tools and Trends, Florida CRC Press, Taylor and Francis Group, 2006.
[7] AS/NZS, Risk management guidelines companion to AS/NZS 4360:2004, Australia/New Zealand Standards, Wellington, 2004.
[8] I. Mosly, G. Zhang, Study on risk management for the implementation of energy efficient and renewable technologies in green office buildings, in: Proceedings of the Transition to Sustainability Conference, Auckland, New Zealand, November/December 30 – 03, 2010.
[9] B. Sovacool, The importance of comprehensiveness in renewable electricity and energy efficiency policy, Energy Policy, 4 (2009) 1529 – 1541.
[10] A. Singh, S. Srivastava, R. Shrestha, Barriers to adoption of clean and efficient technologies in the Indian power sector: an analysis using AHP, in: BAQ Conference, Yogyakatra, Indonesia, December 13 – 15, 2006.
[11] J. Pinkse, M. Dommisse, Overcoming barriers to sustainability: an explanation of residential builders reluctance to adopt clean technologies, Business Strategy and the Environment, 8 (2009) 515 – 527.
[12] B. Reddy, R. Shrestha, Barriers to the adoption of efficient electricity technologies: a case study of India, International Journal of Energy Research, 3 (1998) 257 – 270.
[13] J. Painuly, Barriers to renewable energy penetration; a framework for analysis, Renewable Energy, 1 (2001) 73 – 89.
[14] H. Feustel, C. Stetiu, Hydronic radiant cooling– preliminary assessment, Energy and Buildings, 3 (1995) 193 – 205.
[15] M. Henderson, Application of chilled technology in modern office buildings, in: Natura Hybrid or Air-conditioning Conference, Melbourne, Australia, September 17, 2003.
[16] G. Zhang, J. Yang, Factors influencing the implementation of the raised floor system in Australian office buildings, Construction Management and Economics, 5 (2006) 529 – 543.
[17] P. Hinton, C. Brownlow, I. McMurray, B. Cozens, SPSS explained, Routledge, Hove, United Kingdom, 2004.
[18] J. Mankins, Technology readiness and risk assessment: A new approach, Acta Astronautica, 9-10 (2009) 1208-1215.
[19] A. Field, Discovering Statistics using SPSS, 3rd edt, SAGE publications Ltd, London, United Kingdom, 2009.

© (2012) Trans Tech Publications, Switzerland
doi:10.4028/www.scientific.net/AMM.238.525

Thinking on Architectural Design of Rural Supermarket

Lijun Hao

North China University of Water Resources and Electric Power, Zhengzhou 450011, China

hao_323@126.com

Keywords: rural supermarket; architectural design; optimal design.

Abstract. As a new business model, rural supermarket has gone into the lives of rural residents. Going to the supermarket shopping has become a choice of more and more rural residents. It is worth noticing that rural supermarket is not a simple copy and repeat of the urban supermarket. The paper analyzes rural supermarket's characteristics and inadequacies in current situation, and presents optimal design ideas of rural supermarket considering plane layout, facade selection and external environment design. It is hoped to inspire development of rural supermarket.

Introduction

As a new business model, rural supermarket has gone into the lives of rural residents. With the further development of new rural construction, the living level of rural economy and rural residents has improved significantly. Therefore, the farmer's consumption concept gradually mature and the rapid development of rural supermarket gradually replace some traditional vendors and fair trade mart. Go to the supermarket shopping which has become a choice of more and more rural residents. It is worth noting that the rural supermarket is not a simple copy and repeat of the urban supermarket. Rural life, production, consumption and entertainment also put forward new requirements for architectural design of rural supermarket.

Rural Supermarket and Its Characteristics

Rural Supermarket. Since Michael Cullen founded the customer self-service checkout and one-time checkout in 1930s, the supermarkets are recognized by consumers worldwide. In China, with the reform and opening up, the supermarket is also experienced from none to exist, from less to more, from small to large, from single function to multi-element composite. At present, city residents go to the supermarket shopping has formed a habit of life, and In the beginning, the supermarket is mainly engaged in food, but now it has gradually developed to the family daily sundry goods, clothing and footwear, household appliances, toys, furniture and medical supplies, etc. Philip Kotler defined the supermarket as a self-help industry form that large-scale, low cost, low profits and rely on the sales-winning. This feature is also destined to the supermarket is unique in its architectural design. In china rural economy is vigorously developed which is leading to the new consumption habits of rural residents being into the life of farmers, and the rural supermarket will soon be prevalent in rural.

The rural supermarket is located in the town center area and big central country. As the large-scale comprehensive supermarket, rural supermarkets mainly sold daily necessities, combined with home appliances, digital products, agricultural sales, and agricultural food acquisition. Apart from the shopping area, storage area and office area in the functional partition, rural supermarkets added the functional areas with the characteristic of rural area for grain purchase and agricultural sales. So it achieved one-stop service for sells food, shopping, dining, entertainment, and so on. This is also must to be polymerized and sublimated in the process of the rural supermarket localization development.

The Characteristics of Rural Supermarkets. As a new rural business format, the rural supermarket shows a strong momentum of development. Supermarket has its own independent and iconic architectural form in architectural features .In site design, because the supermarket itself bears a part function of city design so there will be some pleasant space. More importantly, the supermarket stores have all kinds of goods, daily necessities, clothing and footwear, household appliances, toys, furniture and medical supplies goods are available in all varieties. It meets the one-stop shopping

demand of the modern rural residents, especially in the people who born in 1980s and 1990s. According to the research group's thousands of sample survey it shows that modern rural residents pay more attention to the quality of consumer goods and brand, 85% of young people significantly improve requirements of consumer convenience and comfort level. They enhance the comfortable requirements and pay more attention to consumer demand for leisure and culture.

The Status of Rural Supermarkets and Its Optimization Design

The Status of Rural Supermarkets. The causes of rural supermarkets development are market economy, but also it is affected by the rural areas of existing ideas and the social environment. Most of rural supermarkets have its name but not the kind. Their building layout and appearance are not divorced from the original small shop and market. So they can not meet the urgent requirement of the rapid development of rural economy and rural residents' life tastes constantly improving. The trail of rural supermarket building mainly shows in the following areas: ①Function of general layout is simple, just set the shopping space. It can not meet agricultural materials, parking and other diversified functions. ②As derived from the rural society environment and the rural residents' traditional ideas of generally underestimating the effect of the building facade, so it makes the rural supermarket building facade is grossly similar, lacking of fine facade design, no making and lacking of business climate. ③The interior design is only to meet a simple sales, and the supermarket due lighting, fire protection design, heating design are considered less, that it is difficult to comparable to city supermarket shopping environment.

Optimal Design of Rural Supermarket. Rural residents need rural supermarket function is compound, they expect to have a multi-functional spaces that consist of agricultural market, grain purchasing and boutiques. It is must able to fully reflect the needs of modern rural life and this is also the optimal choice of one-stop shopping.

The Principle of Rural Supermarket Layout

The Basic Components of Internal Functions. Rural supermarkets as a supermarket commercial buildings, its function constitute is unique because its location. In order to improve their own competitiveness and to meet the needs of the market, in rural supermarket business process, there is a new integrated commercial industry gradually formed .This industry as supermarkets as the main body and have a larger, more complete, more flexible mode of operation. Rural supermarket is introduced in the other mode of operation, can reduce management risk at the same time rich commercial space, and avoid simplification. Consideration to business lines to increasing, rural supermarket increase agricultural trade, food acquisition and small durable consumer goods even home appliance, furniture, and so on. This makes rural supermarket to make full use of location advantage, and base on the rural consumer goods and agricultural production information, and business services include daily, agricultural, grain purchasing, digital products. At the same time, it should develop telecommunications, postal, chess entertainment and agricultural advisory services. Rural supermarket should combine surrounding public service facilities to extend the service scope, and become shopping and leisure centre as regional and cultural activities center, senior center, and so on(Table 1).

Generally speaking, the supermarket is composed of three parts: The shopping area, storage area and office area. The rural supermarket shopping district is large division that is directly effect to shunt people flow. In developing the design, it is pay particular attention to the layout of boutique, agricultural market and food acquisition (Fig 1).

①The boutique setup: From the research group studied, at present, on the purchase of shoes and clothing, small appliances, including digital toys, leisure goods, 70% of the rural residents tend to brand. Especially in the young people's consumption concept, stores and chain stores is recognized. These small shops are often nested in large supermarket, as a useful supplement to commercial form. In space, boutiques are generally located in the supermarket near the entrance to both sides, and adjacent street in the first floor. Supermarkets and shops promote each other's products. In the first

floor, surrounding of the street, some catering, leisure, fashion and other scattered shops can be arranged. These can be achieved by a variety of products to attract people flow, and this is a win-win situation of mutual benefit.

Table 2 The rural supermarket function table

Commercial space	Commercial Section	Storage	The goods stored in a business hall（Can be equipped with small auxiliary storage space）	
		Sale	Supermarket	Fresh, daily necessities, clothing and footwear, medical supplies
			Other products	Farmer's market, grain purchasing, digital small appliances
			Extension	Telecommunications, postal, advisory services, science and technology culture, elderly activity center
		Service	Inquiries, bathrooms, storage and other services	
	Auxiliary parts	Management	Office, accounting, guards, etc.	
		Processing	Raw and cooked food, commodity processing, transportation, loading and unloading（flow station for commodity from rural to city）	
		Equipment room	Power distribution, electricity, air conditioning, central control room, ect.	

②Setup of agricultural markets: With the regional characteristics, rural supermarket is different from city supermarket. The demand for pesticides, fertilizers, seeds, plastic sheeting, farm machinery, equipments and other agricultural products are very common in rural areas. Because traditional agricultural sales have so many channel levels, so its supervision is relatively difficult. For along time, agricultural markets have a serious problem of credit lack in our country. The agricultural market provides a wealth of brand name products to buyers, and guides users to use it scientifically. In the agricultural market, the users can enjoy uniform price, quality assurance and fast search just like optional purchase in daily necessities supermarket. The new agricultural markets will become the future development trends. Agricultural markets should stay away from the boutiques, restaurants, entertainment and other shops in the partition, but it must be separated but no separation from the supermarket in the planning, and it should has its own separate partition, so as to realize one-stop shopping for rural residents.

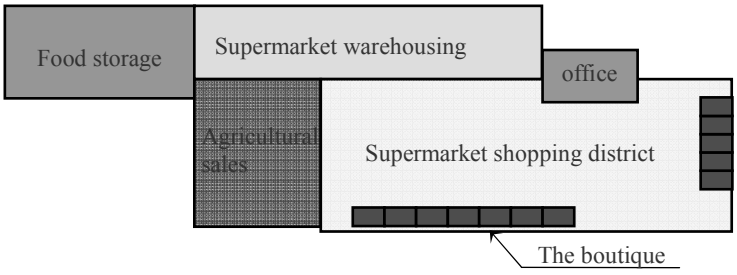


Fig. 1 Plane function analysis diagram

③Grain purchasing: Grain purchasing as a market behavior is universal in the rural areas. It is not only to buy food, but also there are various types of seasonal agricultural products, it must have storage function, so it takes up a larger site. It is better to be arranged in one location with the supermarket warehouse in the design, forming the same goods flow.

Streamline Design. The changes of rural supermarket's functions lead to it are changed in layout and streamline design. At present, land price in the rural area is relatively low, and most of the buildings tends to 1~2 layers (no more than 4 layers), so its plane shape is rectangular in shape for optimal. In addition, supermarket itself has its own operating characteristics, and that is often in order to gain the most effective business area as a graphic selection based. For example, there is a rural supermarket in the crossroads. About its streamline design, it would be same streamline design with city supermarket business hall, and the difference is the collection and transfer of some of the

functional partitioning. In the design, it would be best to through but no smooth, separated but no isolation. That makes several shopping behavior can be one-time to meet, and not to make the flow more complex, avoids the cross interference.

The Façades of Rural Supermarket. Rural supermarket service rural areas, thus, in the facade design, it should also has regional characteristics. Rural supermarket is located in the vast rural areas, and it should reflect the new rural life, and it is an integrated business forms which guides rural life's style. In the image of the construction, it should be marked to fit the aesthetic of masses of rural population. It can use the proper title to attract people, such as "maiduo supermarket" naming, which fully reflect the hope and confidence of the farmer.

The Design of the External Environment of the Rural Supermarket

Entrances and Exits. Entrances and exits are the transition space that connects internal and external of supermarket. Its function is to solve the problem of people flow. It is free in the use of modeling, materials and color, and it should be designed grand and iconic, and should be the spot of the architectural modeling. In this respect, city supermarket is a good example, For example, Wal-Mart, Carrefour and other international supermarket have strengthened their entrance. Combined with the current rural transport coexist and other factors, entrance should be set to a certain area of the entrance square to meet parking, walk, bicycle, electric vehicles and other shopping crowd can smoothly enter and flow.

Parking. Urban supermarket's business scope is big, so its parking needs to meet the requirements, especially being large supermarkets. Although rural supermarket's parking is not as good as the city, but also should be divided into motor and non-motor vehicles (bicycles, electric vehicle). At present, most of rural supermarket parking is ground parking. Motor vehicle parking should break up the whole into parts. We should organize reasonable and orderly traffic flow, and attention in the choice of water permeable paving the ground and ecological tile material, chose suitable shade trees to increase the parking "microclimate", in order to optimize the environment for shoppers, create a good shopping environment. Non-motor vehicle parking should avoid supermarkets' main people flow direction at the same time as close as possible to the supermarket entrance, short the distance, and we should be combined with landscape overall consideration, and in order to integrate into the surrounding environment.

For motor vehicle or non-motor vehicle parking, village supermarket should strengthen the logo design, to guide the traffic line, so that the parking becomes an integral part of the village supermarket external environment optimization.

Conclusions

Rural supermarket development is the main business mode of the new rural supermarket development in the future. It combines the local production, life habit, so in the design that should be paid close attention to and research. Rural supermarket should not only through rural life characteristics, but also satisfy the supermarket commercial building design and use requirements. This requires the joint efforts of all sectors of the community. The paper hopes that the understanding of rural supermarket is deepen. Rural supermarket can also guide the farmers to form a new habit just as in the city the supermarket has been the majority of city residents' habits and dependence.

References

[1] Z. Liu, L. Diao, How to develop rural supermarket, Country Agriculture Farmer Journal, 3 (2006) 17.

[2] X. Wang, C. Yan, Modern Commercial Architectural Design, China Architecture & Building Press, Beijing, 2005.

[3] G. Wang, Study on development strategy of rural supermarket taking Nanyang city in Henan province as a example, China Business & Trade Journal, 2 (2012) 20.

© (2012) Trans Tech Publications, Switzerland
doi:10.4028/www.scientific.net/AMM.238.529

Economic Thinking of Landscape Design in Residential District

Ning Wang [1,a] and Wei Sun [2,b]

[1]Zhengzhou University, School of Architecture , Zhengzhou, Henan Province, P. R. China

[2] Beijing Capital Land Ltd, Beijing, P. R. China

[a]ppmwnn@126.com, [b]sunwei4161@163.com

Keywords: landscape design; quality; cost; economic.

Abstract. The landscape design has the characters of artistry, scientific nature and the efficiency. This article researched the cost factors of landscape design, and the study has important practical significance in enhancing the benefit of the residential district landscape investment.

Introduction

With the development of China's economic, cultural and social, the concept of green, ecology, sustainable development and conservation-oriented society has gradually become the consensus of the community. People put forward higher requirements for their own living environment, and the landscape effects become one of the most important criterions to measure the overall quality of residential districts. The designer should not only provide residents with a harmonious and comfortable, livable living environment, but also take into account the cost factors in landscape investment. However, in design practice, the landscape design of some projects have ignored the economic principles in the design, resulting in a substantial increase in development costs .This paper focuses on "cost optimization instead of cost minimization", tries to discuss the design-optimization of residential district landscape elements, and made a preliminary economical thinking and analysis of landscape design.

The Spatial Layout and Vertical Plan of the Residential Landscape

To determine the spatial layout of the residential district landscape, firstly, we should make space value analysis in accordance with the general layout plan, and identify reasonable important landscape areas, the general landscape areas and secondary landscape areas according to the residential market positioning, because the landscape investment is often different in the different region. Generally speaking, the landscape space value analysis must coordinate with the daily habits of people, such as the main entrance of the residential district, the both sides of the main sidewalk, the entrance of residential units and so on, is a public place that the people use and stay frequently, therefore we should focus on the design of these parts.

The vertical planning of district landscape also should be combined with the district's overall vertical design. When necessary, we should make the entire site and the key areas vertical section design, and reasonably determine relative relationship both the square, roads, retaining wall, steps, the other landscape elements and building, we should pay attention to the important and larger area of the landscape through the terrain height difference processing, Combined with high and low terrain, the designers adjust the plants' location, height and size to form the changes of the line of sight ,and enhance the ornamental and as far as possible to ensure to eliminate the slope in the shortest distance in the treatment of terrain, and set aside a maximum landscape viewing area. At the same time, the slope gradually flat close to the residential portion, which is to avoid occluding and save earth volume.

The Configuration of the Community Planting Landscape

Green plants are the focus of the residential landscape design, compared with the hard material, the plants have the features such as growth, value-added etc. Landscape plant species are rich, and the price elasticity is large, so value analysis of residential landscape should be based on the stage of

landscape design, the designer should reasonable arrange the variety, quantity and specifications of the plants, and different regions use the corresponding program of the plants. For example, in order to create high-quality landscape effect, we may transplant a lot of large trees in the entrance landscape area and the core area of the district, and make people to obtain high quality enjoyment of the landscape in a limited space through multilevel collocation with the trees, shrubs and flowers, ground cover plants. The principle that the basic landscaping and plants infrequent should be ensured in other secondary areas of the landscape design .Combined with the landscape level, by appropriately increasing the proportion of the lawn, configuring proper shrub area, applying node trees and other design techniques to create a beautiful landscape. Its relatively low cost can greatly enhance the landscape effects, so landscape design should make full use of them.

The Construction of Residential Area Waterscape

Water is the soul of garden design, and waterscape is usually the center in the landscape design, but the water landscape has the higher construction costs, and will give property management a lot of problems. Therefore, the waterscape design should be paid attention to key areas such as the district's center, other regions should strictly control the size of the water features, in order to improve the utilization of the water landscape. Taking into account the climatic, ecological factors, water shortage region in northern china should minimize the large area of landscape water surface, by fountain, waterfalls and other features as the visual focus in the entrance and the core area, can foil more exquisite and interesting. "Dry landscape" approach can also be used to achieve good visual effects.

The Optimization of the Rigid Pavement

Taking Beijing as an example, $1m^2$ landscape land, to do the lawn the cost is about 25 ¥, to use ordinary water permeable brick paving need to be 70 to 90 ¥, to use the ordinary stone need to be 120 to 130 ¥, as for cost of granite will significantly improve, the rigid pavement to the influence of landscape construction cost is remarkable, so its cost can be optimized through the following four ways:

1) Trying to reduce the pavement area, it is a green environmental protection and cost reduction.

2) Pavement design should follow the principle of value analysis, the center landscape, key regional with stone, the general area used mainly with the water-permeable bricks, by increasing the sense of design in the way of permeable brick paving, and attention to detail designed to enhance the quality of the pavement.

3) According to the actual needs to reasonably determine the wide size of residential footpath, because permeable brick costs are much lower than that the road teeth. The road sub-teeth can be used permeable brick to replace, which is beautiful, environmentally friendly and cost savings.

4) Compared with the landscape material, building exterior wall decorative material is relatively cheap. If exterior wall tile, paint etc are used properly on the landscape hard paving, not only can achieve good results, you can also echoes with the construction, and enhance the integrity and coordination of the whole community environment.

The Economic Analysis of Landscape Material

Green Plant Material. Adhere to the "native" route, native tree species are easy to cultivate and lower-cost, it should be used as much as possible in design. We should reduce the number of valuable tree species and specifications (except key areas), and appropriately increase the specifications and quantity of native ones.

About flowers, the designer should choose mainly long flowering perennial flowers, because perennial flowers need lower maintenance costs than herbaceous flowers.

Landscaping Material. The choice of landscape stone should adhere to the principle of local materials, for example, local stone, though not expensive but as long as properly designed and combined with the green plants terrain to play a beautiful effect.

Gallery frame, bridges, landscape structures in the residential area should be made of wood and iron, and stone, stainless steel, copper, other metal materials should be avoid. Retaining wall decoration materials and building materials should be echoes. District civil air ventilation, gas pressure regulating station can be shielded by the bamboo, cypress or evergreen shrubs.

Designers are advised to reduce the number of landscape structures, to do so will not only help enhance the natural effect of the landscape also helps to reduce the landscape investment.

Garden Facilities. When the landscape lighting should be selected, according to different type of lighting, reasonably decide the lamp's illumination, height, material and production technology. Garden lamp and lawn lamp are important landscape components, their shape and color should be considered in designing. And buried lights, underwater lights, mainly in order to create a beautiful environment of light, the outward appearance is not necessary to consider, of course lighting quality is also very important.

Landscape seats are important landscape elements too, and the purchase of finished product seat spent a lot of money but the results often are disappointed. While on-site production of wood, stone seat is simple and generous, and the price is relatively cheap.

Covers are problems that landscape designers often have to face, covers in lawn can be use a special planting covers to enhance the visual effects. Covers at the plaza of the landscape we can use a special kind of covers, whose upper part can be lay by the same materials used with surrounding ground, the price of these special covers is high, but it can achieve good landscape effect.

Children activity facilities should be considered for routine maintenance and repair convenient, the price of rocker, slide, bunkers etc is not high but is very favored by children.

Conclusions

Pursuit of the economy does not simply reduce the cost of the landscape design but to create the best landscape effect with the effective cost control. Residential landscape design, it is necessary to avoid the trend which excessively pursue the cost effect and ignore the cost, but also to avoid too much emphasis on cost to the neglect of the product quality. The cost-effectiveness should be used as the starting and ending points of the design, and constantly improve the landscape design of economic rationality.

References

[1] X. Su, Residential Landscape Design, first edition, China Building Industry Press, Beijing, 2010.

© (2012) Trans Tech Publications, Switzerland
doi:10.4028/www.scientific.net/AMM.238.532

Some Points about the Local Living Environment Research

Hongguang Li [a], Yuqing Liu [b] and Yi Ding [c]

North China University of Water Resources and Hydroelectric Power, Zhengzhou 450011 China

[a] lhg123ok@yahoo.com.cn,[b] lyq123ok@yahoo.com.cn, [c] dingyiarch@qq.com

Keywords: inhabited region; local architecture; spirit of place; stamped; environment; educational scenes.

Abstract. By the analysis of the direction and situation of traditional inhabited region and the local living environment research, this paper points out that the weakness and shortage of extent and effects had been quite serious. Some advices are given out to rediscover researching ranges, targets and methods, and make alive develop traditional culture of architecture.

Introduction

In China, the research in traditional architectural remains started since 1920s, while the western building technique and urban architecture had landed this old country for over half century. Elites, like Sicheng Liang, Dunzhen Liu and *et al.*, constructed solid foundation of research to Chinese architectural heritages in the next several decades, through their efforts risking of war and poverty. Perhaps being the outstanding results or the limits of recognizing, architecture as cities, palaces, temples, tombs have been thoroughly researched.

And what is more, people all think Chinese traditional architecture useful, but highly store it in bookcases. They treat it as 'History'. 'History' means things in the past and has not exact use to modern design and construction [1].

We think it is still having a long way to reach the core of traditional architecture. We could not get something new through the way of traditional research. More and more new theories, method, testing skills, angle of observation are needed to put into studying course in order to make the results practical. The fast developments of architecture push us to recreate the living environment with Chinese cultural character and interests. We point out one new mode like this: Complicated Public Places + Neighborly Residence [2].

Problems about Situation and Direction of Architecture Research Now

Almost main types of traditional inhabited region and local residence have been researched, but seldom sub-types have been done. It is more uncommon to compare relationship between sub-types.

The use and research about traditional architecture could not pace up to modern society needs. It remains the state in the tower of ivory splitting from society. We will lose many objects disappearing by nature or artificially created factors. Photo 1 was taken on October, 2003, but this scene would not be seen for over 1 year later. Photo 2 was taken on July, 2004, showing the situation that traditional houses was surrounding by giant western style building. Someone said: The most terrible enemy to traditional factors is developing! For keeping and continuing the objects we will study, we have to race with time going and economic developing.

The research thinking and method in the past has fallen behind time. On the one hand, talking about protecting and research, people firstly thought it as certain to classify it to some protecting grade and keep it in museum or institute. In fact, to numerous local residences, they could not be protected as exhibits because they are "living" for usual life. If being separated from daily use, they would be nothing [3].

On the other hand, the research before have made efforts to single building or simply groups, while not noticing the complex of many buildings and surroundings. In fact, the complex of many buildings and surroundings mean much more than single building or simply groups. It means that 1+1>2.



Photo 1



Photo 2

Our Points

Pan-architecture should be put into use. We suggest adopt more new theories such as systems theory, wide vision, pan-relation theory and etc to examine the relationship of whole system, different parts and any part to the whole system.

The forms of buildings are concise, abstract and imply with rich culture and philosophical wisdoms. From angle of technique and material, local residences have not enough spaces to study because of simply rules, components and modes. However, do we really know everything of traditional architecture? How can we explain that the simply and popular buildings system feed out so many artists, writers and heroes?

The orient society is good at producing mixed meanings with simply form. Does it exit some imply and deep meaning behind simply form? We thought it a overstep with senior level of simply, abstract, imply and nature things according to Chan theory above junior level of concrete, straight-forward, repeatedly illustration. We named that “Educational Environment” where people realized more, stirring and far back from uncomplicated and unadorned surroundings than the professing in petty, straight-forward and tedious ways. In the same way, people in the past paid more emphasis and priority on emotion and spirits than on materials. That is just the Orientation (Dao) and Rite (Li) widely spoken in the past. It mentions us: we should research how it does get power of spirits, cultural nurturing and moral incentive mechanism through the surface of matter.

In the traditional living building system, solid things and empty spaces, solid matters and non-solid things, architectural method and non- architectural ways were widely used. With complexes and smart way, effects were implied and efficiency, practicing and interesting without crowded viewing and liberal feeling [4].

Photo 3 is a clear example. The old building which could not be changed in many years used to be posted new antithetical couplets in beginning of each New Year. None could not be excited by the happy and rich meaning scene at every season and every new years.



Photo 3

As a fact, we must not ignore it, which the building were never changed a little while the antithetical couplets changed every times. Without rich resources of culture and spirit to the soft and material systems, how can we get such high efficiency skills of packing matter and educational method?

More magic skills will be digger out in the traditional living building systems, which show intelligence to pit the weakness against the strong, like that four taels could turn around over 1000 Jins in Orient thoughts. It would tell us the researching targets must include not only material skills but also virtual technique and mixture of them.

In ancient China, without helps of urban plan, villages and towns are filled with systemic, essential, cultural and thick nature with superiority in time of handwork and partiality for literature and education. Well social surrounding had been constructed easily in the past, with ways of close to people, polite treatment, kindness, popularity, neighborliness, unity and mutual help. We could read it from Photo 4. There were no nonchalant and exact boundary between families and peoples, while the fuzzy and public places existing. It was more important to consider about Public Places and neighbor than economic and ethylic relationships.

China owns strong united thoughts such as “Confucianism (RU thought)” and cohesive force. However, we have to admit the differences between local cultures. It is said different areas nurture different natural peoples. What is relationship between the local area and different natural peoples? How do the soft and material systems get function? That is what we want to reveal.



Photo 4



Photo 5

Chinese old words said: ‘A distant relative is not as helpful as a neighbor!’ It shows the consensus had been founded that people should pay more attention to construct good public relations. Traditional environment system provided it with material and technique ways. It promoted function that many kinds of public places, contacting areas, facilities arranged everywhere and every time, intensifying invisible belts between neighbors and others.

Photo 5 showed a narrow street be rebuilt carelessly with poor buildings. But, the impression of public contacting places function now. A natural turning with wider street under an old tree provides natural contacting, relaxing and entertainment place between neighbors. They have their place and times not separated from public. Concepts of long-time neighbor, fellow villager and compatriot could not be separated with well known scenes bellow: old houses, small streets, ancestral hall, family school, tiny temple housing the village God, GuanDi temple, stage, courtyards, lanes and alleys, place for harvest, wells, high old tree, field for Dinner, gate building, village entrance, dock, mountains, famous people, point of tourist interesting, ruins and etc. All that called “Stamped environment” by us. Our contemporary architecture and cities are imported from western world. But, it does have many problems as overlooking the difference of local culture and moral needs to personality, solving question with technique and material ways only. Therefore, our society occur many illness of city and civilization which separate people and treat others nonchalantly. None could expert being trust and depended on. Modernizations mean people not only modern material but also the substantial and satisfied feeling in spirit. The contemporary mode could not provide all these for our society. We could not transplant the mode of western city and public places simply and directly [5].

Paying attentions to the function of the soft environment in Chinese traditional society, researching the mechanism and conditions while the soft environment build the social atmospheres with solid building and other matters complementing each other.

We think that the researches to traditional buildings should be related with the surroundings when civil culture, materials, weather, economy, environment, selected mode, lifestyle, public feelings, folkways, local interesting, folk music and other conditions get function. Researches to static building matter must be related with soft and material systems nurtured the civil spirit, local culture and personal nature.

Examining results pressed before, we could not deny the depth to the single material parts of residences in the past researches, but we could not equal gathering buildings pluses one by one to the whole living environment. It was common knowledge for us, empty spaces and solid drawing matters are all carefully creation maybe meaning more in Chinese traditional paintings. It would tell us the simply form of traditional buildings could not function as equal level as what the whole empty matter system and solid matter system commonly did.

And more, developing some new field about living environment systems in villages and towns exited for a long time in China could be taken.

Conclusions

We suggest researching every states and types of middle and small scaled public space, neighbor boundary, common areas and etc in Chinese traditional living environment, and distinguishing what value in modern society. We should introduce new researches and results which could overtake mistakes in our city and village, and construct new public places with Orient nature.

Basing on rich and successful social resources and cultural accumulating in Chinese tradition, we look forward to work out new kind, factor-complicated public places, action systems, relations and contacting areas in village and town, in order to build active system for being extremely considered in culture, emotion and mind to human being in resident, while pushing cities and towns to modernization and humanity.

We try to transplant advantages of other subjects into architectural research, such as architectural economics, technique transmitting, exact model of evaluating, function of media and public opinions, education system, relation between literature and technique. These would help to develop new theory, method and skills.

References

[1] Z. Guan, Suggestion to contemporary architecture, Architecture Journal, 3 (2003) 11-12.

[2] Z. Chen, Architecture in NANXI river area, Tri-Jointed Press, 2002.

[3] H. Li, Y. Liu, Architecture sense and scenes, Gansu Science & Technology, 9 (2006)161-165.

[4] H. Li, Z. Li, The collection of theses in 16th Conference of international anthropology and Ethnology, Yunnan University Press, 2009.

[5] H. Li, C. Gao, The collection of theses in 7th Conference of China urban housing, China Architecture &Building Press, 2008.

© (2012) Trans Tech Publications, Switzerland
doi:10.4028/www.scientific.net/AMM.238.536

Planning and Design of Urban Barrier Free Building Environment with Aging of Population

Ling Song[1, a], Shaowei Zhang[1, b] and Zhimin Li[2, c]

[1]School of Architecture, North China Institute of Water Resources and Electric Power, Zhengzhou, Henan 450011,China

[2]School of Architecture, Xi'an University of Architecture and Technology, Xi'an, Shaanxi 710055,China

[a]songling@ncwu.edu.cn, [b]zhangshaowei@ncwu.edu.cn, [c]lizhimin710055@yahoo.com.cn

Key words: aging; barrier free environment; application groups; planning and design.

Abstract. With the development of the times, the quality of human life and environment gets ameliorative ceaselessly. It is the main goal for ensuring every public safety, health, comfort and convenience of modern society civilization and city construction, and "concern for people" is the most basic principles. On the basis of helping the different application groups, such as different age, different view of life and physical condition to set up independent life, this paper proposes the ideas and methods for planning and design humane architecture and city environment with complete and perfect building facilities.

Basic Principle of Planning and Design

There are many essential activities in daily life, such as travel, work, study, play, rest, diet and health and so on, the corresponding space should be provided to meet these activities. The primary task of architectural environment planning and design is to ensure that the pedestrian can go to anywhere according to their own will without barriers in access. People cannot be deprived of participation and the use of building environment rights because of some form or degree of movement disorders, or participate social activities unequally with others. Therefore, the design should follow a few basic principles.

Accessibility. The emphasis of barrier-free environment design is environment accessibility in order to encourage a variety of physical status of people blending in social. Accessibility is a kind of convenience for people to feel, arrive, access to and be use of environmental facilities, through imposing effect and influence on the environment to complete their actions and purposes. It contains three meanings: perceptibility, reachability and maneuverability.

Accessibility is the most basic principle of building environment design. So it should be meet in designing that all people especially for disabled and elderly people can reach places and buildings as many as possible, and they can access to, through and enter unimpeded without assistant, successfully use the facilities. In addition, the behavior characteristics and human scale of applicable groups must also be met, avoiding to complete the operation with two hands at the same time, so that the difficulty of the operation become the most simple, convenient as far as possible.

Safety. Safety is the functional elements of design which can not be ignored for architect. The main service object of barrier free environment is disabled. The elderly and other inconveniences, due to their physiological, age, disease, special status, perception to environment is poor. Response to stimulus sensitivity is low, it is sometimes difficult to overcome some obstacles, and the danger is easy to happen. Therefore it must be give up from design of environmental in order to use safely.

Systematicness. Design of barrier-free environment is a comprehensive and systematic project, involve wide. Not only confined to local such as entrances, ramps, elevators, and bathrooms of certain building, systematization is the key which create a barrier-free environment completely. In addition to building space, city road, traffic facilities and outdoor public space must also achieve accessibility. How to build the barrier-free building environment and facilities meeting the needs of different age levels and the multiple needs, at the same time, these facilities can support each other

in the overall planning, Which requires the architect designing barrier-free environment with a systematic view. The barrier-free facilities should be constantly adjusted along with the social development and people's demand, create dynamic space network timely which is made of point, line, surface and body, so that the disabled such as the disabled and the elderly can be sharing the social civilization and material environment synchronously and equality.

Research Object on Planning and Design

How to set up the specific object of study on when design barrier-free environment taking people as the starting point? Generally, according to the different buildings, those with inconvenient action or life limited can be considered as a design object.

The design to Barrier free building environment is intended for everyone to use and enjoy, which is the important principle to improve artificial environment facing the public. These non-barrier facilities facilitate the use of the disabled, and help the elderly, children, pregnant women, carrying heavy loads and other disabled people at the same time, must be considered to be used by prefect people. On a certain kind of facility space, enhancing its adaptability can promote the use of facility space.

Basic Ways of Planning and Design

Meet Physiological Needs of Applicable Groups. Fit the physiological needs of applicable groups is the basic requirement and foundation of barrier-free design. According to Maslow's theory of hierarchy of needs, basic physiological and safety needs are basis of all spiritual pursuit. It is primary to meet the requirements of accessibility and safety of application groups by barrier free design.

Different types of behavioral disorders, their specific physiological requirements vary; the obstacles are also different types, so the barrier-free design approach needs to be treated differently. Improving the information obstacles, movement disorders and fine operation disorder, is to meet the most basic requirement of physiological groups.

Meet Psychological Needs of Applicable Groups. Based on meeting the basic physiological demand, the psychological need occupy a very important position. A barrier-free design results will be low level, cold, formalism and impersonal if only to meet basic living requirements of disabled person.

The demands to social contact, esteem and self-actualization of behavioral disorder are achieved with design principle of applicability and open.

Meet Requirements of Economic and Sharing. The main service object of Barrier-free design is disabled, but it is not the only. It can be seen clearly on the analysis by principles of sharing, the results of barrier-free design are provided for all applicable crowds, including people with disabilities. If barrier-free facilities are arranged only or deliberately for disabled, it is not economical and science obviously. Because of the limited investment, we can maximize to expand the number of users of barrier-free environment and facilities, which is the appropriate act along to the direction of the barrier-free design. Some investors and designers often concerns the barrier-free design or facilities will cost a lot of money, take up a lot of valuable time and area, in fact it is a kind of wrong understanding. The construction of barrier-free environment does not need too much investment, in the new construction project, the cost of barrier-free design and construction of engineering is not too big effect.

According to the United States Department of housing and urban development survey, general construction of barrier-free facilities accounted for only 1% of the total investment; wherein, many facilities do not need to increase another space, such as the width and the opening direction of the door, the suitable height of wash table in bathroom, installation of handrails of sanitary ware, canceling the ground around the threshold. There is a special investigation on Enjili district, situation is also so. It can realize economic and reasonable layout as long as the elaborate design, proper arrangement. Conversely, if not to be considered in the design stage, after the completion of the project and then the non-barrier transformation spend much.

Main Factors of Planning and Design for Elderly

In order to create the barrier-free building environment for the elderly conducive to life and health, in addition to meet the general requirements of the design, it is more important to emphasize the remedy, prevention and development possibilities. Creating the environment is favorable to them but not overly protective, so that the elderly can be convenient, safe, and maximize its role. The selection of the space scale of building should be appropriate, providing some of the smaller scale of the environment, creating a close contact, it should be avoided to create misunderstandings for the elderly due to telling various sound difficultly, which leads to the misconduct, or endanger the safety and health behavior. When designing space form, the figure, symbol and identification should be familiar and evoking memories, so that the elderly can generate echoes relying on the information stored in the brain past, which would compensate for the reactive and functional deficiencies. A more stable living environment helps them formed in the brain on the environment around a familiar "cognitive map", produced by the sense of security and a sense of belonging for older people to create a relaxed, pleasant atmosphere for communication, older adults in good physical and mental health has provided a guarantee. Design elements include the following aspects:

Safe Pedestrian Environment. 1) No difference between the walking surface, avoid fall in walking or trip by obstacles. 2) Pave non-skid material. 3) Consider particularly to the outer channel and the parts easy wet. 4) When the elderly use of auxiliary equipment or a shopping cart, the width of pedestrian road should be considered. 5) Avoid walking space is provided with the bulge.6) Set the appropriate places to rest.

Signal and Information Environment of System. 1) Signal designing should consider the size of text, color recognition and comparison. With reducing of the sense of direction and dropping of the memory and judgment, it will appear that the elderly cannot read complex text, line, so the identification which is uniform and easy to identify need to set inside and outside the building, helping them overcome obstacles. 2) Setting of visual information and audio information. Stereo orientation and the volume of the alert sound is important, but it should also be noted that the surrounding noise sound background. 3) The signal should be used to understand, bright lighting facilities.

Comfortable Operating Environment for Apparatus. 1) Choose the easy to grip, to facilitate the operation of the door handle and faucet. 2) Development barrier apparatus and equipment automation using.

So that, formulating corresponding design principle for special needs of various groups is the fundamental content by a barrier-free environment planning and design. Analyzing and understanding deeply the reason which makes the elderly obstacles, mastering their special requirements, that is important factor of creating barrier-free building environment.

References

[1] B. Chen, Problems and trend of Chinese city planning, Urban-rural Construction, 12 (2001) 23-27.

[2] Z. Liu, Explore on urbanization to citizens' health and landscape planning strategies, Sichuan Building Science and Research, 3 (2008) 207-209.

[3] J. Wang, Analysis on the influence of fast growth urbanization to China's city planning, Journal of Jinan University (Science and Social), 2 (2006) 34-37.

[4] Y. Zhang, X. Liu, Problems in Chinese urbanization, Agriculture and Science in Anhui, 23 (2009) 233-236.

© (2012) Trans Tech Publications, Switzerland
doi:10.4028/www.scientific.net/AMM.238.539

On the Elements of Contemporary Architectural Styling

Conghuai Xu [1, a], Ying Song[1, b], Shuchen Xu [2, c], Qing Feng [1, d] and Hao Wu [1, e]

[1]School of Architecture and Engineering, Nanchang University, Nanchang, China

[2] College of Architecture and Urban Planning, TongJi University, Shanghai, China

[a] xch108@126.com, [b] carriesong@qq.com, [c] xushuchen@gmail.com

[d] fengqing966@163.com,[e] wuhaonicol434711417@yahoo.com

Keywords: integrity, stretching, transparency, exquisiteness.

Abstract. This article written with a guide of a basic theory of modern architectural aesthetics, aesthetic psychology, constitutes the basic principles of practice of science and art to use as the core to form. Combined with the author' feelings and experiences and a large number of examples from architectural education, design practice and research in the professional career, we grouped the creation of contemporary architecture modeling skills into four elements, in order to meet the desire for the students and architects to increase their own artistic creativity and build up innovation capability, and a way to follow a truly theory and practice.

Introduction

Contemporary architectural design is not only to meet the requirements of the building function, but also to create the ordinary people's inner needs and who can not or difficult to use language to express - architectural modeling; All this stems from the in-depth analysis of the architectural elements and precision grasp. Contemporary architectural design can achieve this through the use of certain building elements.

Integrity

In order to adapt to the flexibility in the use and variable function, Contemporary buildings partitions separated by increasingly free interior space without restrictions. Due to the weakening of space defined space interface with a variety of interface to the tendency of performance ambiguity. With the development of modern architecture, the late modernism is in pursuit of space of uncertainty and ambiguity, such as the pursuit of a fuzzy feeling of space; or internalization of the outside the interior space and exterior spaces; or the neutralizations of a between indoor and outdoor areas. Some components are needed to integrate scattered building monomers to form a highly magnificent integrity, the integrity of the inside and outside space shaped the visual effect of the momentum of the building and give the street sight a great impact.



Fig. 1-A



Fig. 1-B



Fig. 2



Fig. 3-A

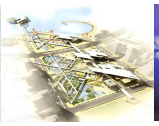


Fig.3-B

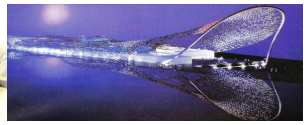


Fig. 4

Fig. 1A-B: The science buildings of Nanchang University: Facing south, three science laboratory buildings paralleled arranged in the center of the base. In addition, under the framework the outdoor space changed into a transitional space in half-indoor and outdoor, combined with the monotonous and the reality of the facade fenestration contrast rigid frontages become colorful.

Fig. 2: The office buildings of China Nerin Engineering Co., Ltd. With office, conference, leisure, accommodation, dining in one, using piece wall, cylinder and other frameworks connected to the four functional buildings, and the indoor atrium, outdoor courtyard and the closed corridor in use of the space of fuzzy boundaries, while the formation of bridges between the various functional elements of the transport connection. The formation of various surfaces mutually coherent grand, atmospheric visual effects, and yet the considerations in the handling of the details of the facade, and the architectural use of color complemented the surrounding environment.

Fig. 3-A.B: Commercial center design, the three buildings lingering mutual contact, and its shape around the parallelogram elements cutting reorganization can be found in each building each other's shadow, but not identical. Icing on the cake, overhead bridges, roads and green external space around the plane geometry of this element, and thus the design work is complete and compact.

Fig. 4: Expo architectural design, the original scattered individuals within, and added externally with a LED and other beautiful form, the Light and the shell, so the design work's exterior styling is becoming unified, complete, and momentum.

Stretching

The purpose of the building is not only the building itself, but the space formed by the building and it create the environment to show a spiritual connotation. Architects use various means to create a variety of pleasant space, besides, tension and stretch the shape shown give the viewer a great psychological feelings. Coherent architectural form often designer apartment as a "stretch" the "boom" good intentions, coupled with the integration with the surrounding environment, making the overall building form a "by people for like days to open the grand momentum. Therefore, in the shape of the iconic and recognizable to other small-volume construction can not be compared. Today, with the rapid development of construction materials, coupled with the improvement of computer-aided design level, building the whole body of free curve through parametric design optimization, making the form stretching buildings to come into the front of the world.

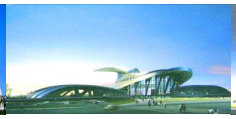
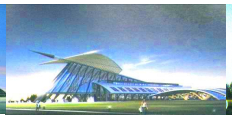
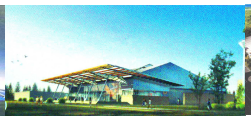








Fig. 5 Fig. 6-A Fig. 6-B Fig. 7 Fig. 8 Fig. 9-A Fig. 9-B

Fig. 5: Different from the general high-rise buildings in the square box shape. The building on both sides of the interior space of external curve of a thin layer of wallboard, and the front glass constitute. Like the outline of the image of the whole building from the land to grow thick at the bottom of the more upwardly mobile, the thinner cross-section of the building.

Fig. 6-A, B: The shape of the building, stretching off like wings of birds

Fig.7: The construction is based on box-body, canopy span cantilever shape is simple and capable.

Fig. 8: The building complex is a school, the layout as a whole, unified modeling stretch, lively, transparent.

Fig. 9: This is the teaching building of the Art Institute of Nanyang University of Technology, Singapore. The Stretching shape integrated the intertwined two parts of the building, large areas of green roofs and landscape design not only makes the block layout intimate, but also unified the building and the environment to achieve the effect of integration and the pursuit of Man and Nature as one.

Transparency

In general, the permeability of the charm of the architectural form, mainly in its open space, transparent use of the shape become more common in the modern architectural space design techniques - careful handling two or more of the relationship between the spatial level practices in order new transparent material with a new structure to design changes in the infinite space in the form permeability changes in the spatial form processing, so light, sight, air unimpeded freedom of fusion.

Crazy building is well known, it seems people are tired of the architects have brought all kinds of “confrontation with space”, as proposed by the Japanese architect Kengo Wusuo negative construction – “building should disappear in the environment”, and thus, modern architecture is blurring the boundaries of space qualified design.

Transparent shape is the modern methods of design, but also the pursuit of the natural view of the building, the use of modern materials and construction techniques to improve the shape and space. Transparent space, including the permeability of space, visual permeability, air permeability, etc., can improve the efficacy of spatial form and visual psychological feelings. Reasonable use of the transparent approach, can not only improve the function, can also create new and unique architectural style.

Permeability is a dynamic design elements of the human pursuit of free space and one of the important manifestations of contemporary architecture. Compared with enclosed, transparent is more flexible. Through transparent shapes, you can see the scene inside the multi-space, thus resulting in an infinite far-reaching sense of.



Fig. 10-A Fig. 10-B Fig. 11-A Fig. 11-B Fig. 11-C Fig. 11-D

The glass of the building with new materials combine to make the building has been somewhat "transparent" texture. Look from the outside of the building, under the effect of light and shadow perspective, where the scenery seems to burst out of the light.



Fig. 12-A Fig. 13-B Fig. 12-C Fig. 12-D Fig. 12-E

Fig. 12-A ~ E: The building is a university in India, its architectural form is taken from Wu Bisi ring, it is mutual penetrating inside and outside the space, with no obstacle in the passage, while its walls with large areas of glass curtain wall. Although the huge building capacity, its design is the overall light permeability and gives you a good feeling.



Fig. 13-A Fig. 13-B Fig. 13-C Fig. 13-D

Fig. 13-A～D: House N designed by Takeshkai Fujimoto is located in a traditional residential area of Japan's Oita City. The buildings in the neighborhood are mostly dark in their quiet appearance. The White House N’s large area transparent wall opening is like new shoots in spring, which broke the silence. So not only external, and even inside the building’s separation is also ambiguous. The designer has ensured residential privacy and at the same time created the outside feelings inside, in which the fuzzy boundaries of the space is used just right.

Exquisiteness

Good architectural design should not only consider whether the design of a complete and unified, building transparent whether the shape of its building is beautiful stretch, etc., should also pay attention to design detail components, and improve its work, making it the amount of sublimation, a qualitative leap. As the saying goes, an outstanding architectural works not only for the distance, to be more resistant to close.

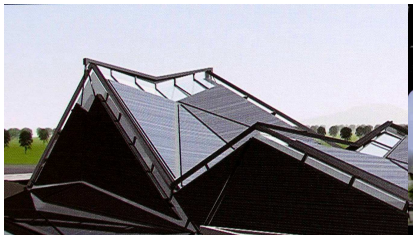


Fig. 14-A

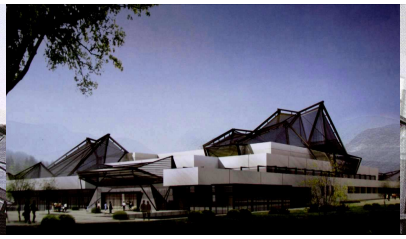


Fig. 14-B

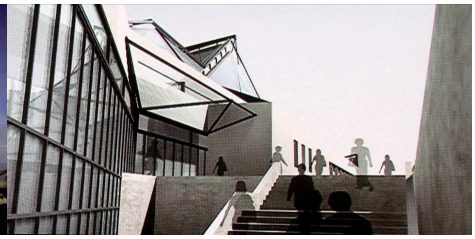


Fig. 14-C

Grasp of detail is an architect sign of maturity. Today's architectural design will not only focus on solving specific functional requirements, such as the waterproof thermal insulation firmly and other basic functions, more and more attention to the design of the node structure, so the architects began to pursue to obtain a change in the ordinary.

Fig. 14-A.B.C: The building is the Zhejiang Museum of Art, by Cheng Taining, soft with Oriental elements, mainly in the roof of the addition, The building is neat endowed with variability



Fig. 15

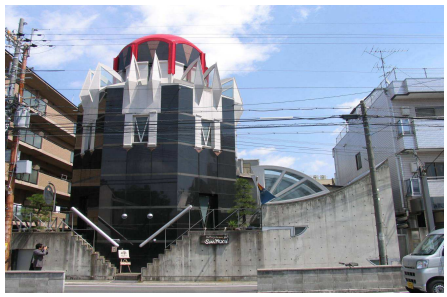


Fig. 16

Fig. 15: The building is an office located in Tokyo, which has a strong sculptural stainless steel exterior, in the reflection of the surrounding buildings, colorful.

Fig. 16: The building is located in Kyoto, the works of Taka Matsushin, its appearance has a strong mechanical camp style, and the wall decoration is very delicate.

Conclusions

The architectural design involves not only the function of the buildings, but also to take into account their shape. The Function of the building features a objective standard to measure; but opinions on modeling problems showed some confusion in the construction practice. To reflect the contemporary architectural styling characteristics of the four elements: c–Integrity, stretching, transparency and exquisiteness on the basis of a large number of instances. After consultation with the different occupations, different genders, different ages among all walks of people, we got the majority of people's identity. The feeling is that what each person is born with. Also, everyone can feel the mental activity. The above four elements used in architectural design, is the appropriate language to create a contemporary architectural style, which meets the aesthetic needs of contemporary architecture on thinking and emotional level.

© (2012) Trans Tech Publications, Switzerland
doi:10.4028/www.scientific.net/AMM.238.543

A Study on Architectural Style of Buildings along the Northern Foot of Qinling Mountains Taking Xi'an Garden as Example

Zhetao Xiao

Xi'an University of Architecture and Technology, Xi'an 710055, China

North China University of Water Resources and Electric Power, Zhengzhou 450011, China

haoxiao521@126.com

Keywords: northern foot of Qinling Mountains; architectural style; Xi'an Garden.

Abstract. The paper researches the location along the northern foot of Qinling Mountains and its architectural style. The particularity of the location and the relationship between natural environment and architectural style are analyzed. From the points of climatic characteristics, landform, water system and culture, the impaction of natural environment on architectural style of Qinling Mountains is studied. Taking Xi'an Garden as an example, the reason is explained. With studying architectural style in the particular location which is the northern foot of Qinling Mountains, it is hope to protect Qinling ecological environment though architectural style in harmony with natural environment.

The Particular Location along the Northern Foot of Qinling Mountains

The Qinling Mountains are a major mountain range, west to Gansu province, and east to the west of Henan Province. Most of them are in the Eastern province of Shanxi, in China. The mountains provide a natural boundary between the north and south of the country. They are the boundary of north-south climate and natural ecology, important biological functional areas, and important water conservation district. Qinling Mountains have not only beautiful landscapes, dense forests, a variety of biological populations, but also plenty cultural relics, historical and cultural heritages, and gave birth to the Qin culture, the Guanzhong culture. They have an irreplaceable position in the development of Chinese civilization. Qinling Mountains, as the natural ecological barrier of Guanzhong city and especially Xi'an, are not just mountains, but the source of our blood to develop and prosper.

With the construction and development of city, the ecological environment of Qinling Mountains has suffered enormous damage, such as environmental pollution, soil and water loss, and water protective function decline and so on, and these have aroused the attention of various circles at home and abroad. Shanxi provincial government and Xi'an municipal government increase efforts to protect and develop ecological environment of Qinling Mountains, especially Xi'an section along the northern foot of Qinling Mountains, a series of protective measures were drew up. The region along the northern foot of Qinling Mountains is the ecological coordination region of Qinling. Due to relatively close regional relationship with the Qinling Mountains, the construction project along the northern foot of Qinling Mountains must be constructed under the ecological protection's framework of Qinling Mountains. All construction projects can only be a useful component of Qinling ecological environment, rather than spoilers. Special region give special requirements for construction projects along the northern foot of Qinling. Architectural style is just an embodiment of such special requirements, and this is also the significance of the paper.

The Relationship of Natural Environment and Architectural Style along Qinling

The Relationship of Natural Environment and Architectural style. The architectural style is defined as "big style" and "small style". "Big style" is the universality and commonality of architectural style, and refers to the generalization of the typical features of the building under certain historical conditions, ideological and artistic image. It reflects the prevailing social system, the mental outlook, the social needs and awareness, national traditions, national characteristics, and the

development of scientific and cultural level. “Small style” refers to the special architectural style, and mainly the regional characteristics (such as natural conditions, local materials, local life, customs and local traditions, etc.) of the local architectural style, or reflect the worldview of the creators, creative, creative skills for specific building or buildings though the ideas expressed in the form of the obvious features and content.

The architectural style discussed in the paper refers to the unique and representative appearance which is present by construction combined with the natural environment. It is a typical performance of national character, local and traditional characteristics. Different natural environment has given birth to different buildings with different architectural styles. North cave and southern bamboo house is the product of natural environment, and they are not interchangeable to build. They reflected regional architectural style of north and south in different natural environment.

Architectural style in the city being rapidly developed today are diversified, but no matter how architectural style changed, natural environment is still relatively constant, reflection and integration is the developed way of architectural style. These should be reflected in four aspects: ① to reflect the topography, and climatic conditions of the location where buildings were built; ② the use of local materials, energy and construction techniques; ③ to absorb the local culture of achievement; ④ there is specificity other regions do not have. A variety of architectural styles, in order to meet certain requirements, are approved by the local culture and values, and are suitable for the local economic level and in accordance with local traditions, customs, and the way of life.

Natural environment include climate characteristics, landform and water system, geology and vegetation, and based on them to form religious beliefs, customs, and cultural life, and economy and technology, etc. They limit the generation of architectural style. The elements which are group layout, monomer space structure, overall shape and appearance feature, and component, compose architectural style, at the same time, always reflect natural environment (Fig. 1). People settling in one place for long, they need to produce the corresponding construction activities. Construction materials, of course, firstly being choice, are local wood, clay or stone. Because of different materials, different natural environment needed to be adapted, thus, architectural style will be different. Architectural style cannot be made in short-term. Experiencing so many years, it constantly adapts to the local natural environment, reflects local life and culture, and gradually forms by constant interaction. Architectural style must be the product of harmonious coexistence by local architecture and natural environment, and local life and culture.

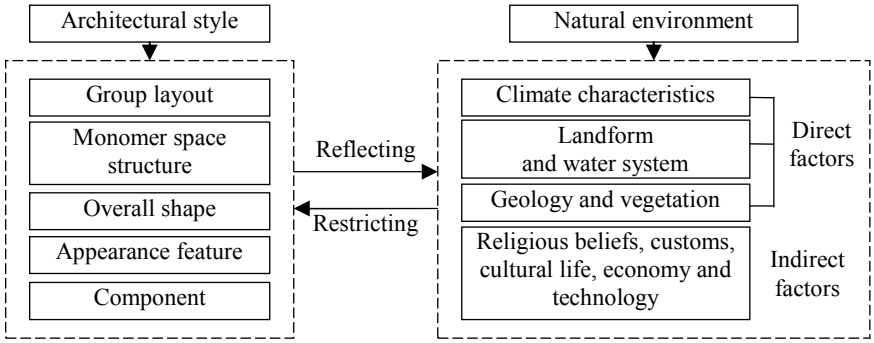


Fig. 1 The relationship of natural environment and architectural style

Natural Environment Impact the Style of Buildings along the Northern Foot of Qinling Mountains

The Effect of Climate Characteristics. Natural environment of Qinling gave birth to the Guanzhong Plain, and also the unique architectural style of houses in Guanzhong. “Shaanxi Vernacular Dwelling” written by Zhang Bitian and Liu Zhenya summarized climate characteristics in Guanzhong: it is warm zone, with four distinct seasons, winter and summer long, spring and autumn temperatures abruptly changing. Summer have summer drought, and autumn have more than even the rain. Therefore, most of vernacular dwelling in Guanzhong were flush gable roof, adopted

north-south narrow court on plane layout, made inner courtyard in the shadow region in order to relatively cool in summer. So pitched roof and inner courtyard which is the elements to reflect architectural style, inherited from generation to generation, and carried forward.

The Effect of Landform and Water System. Relative to Xi'an city, landform of Qinling is high in the south and low in the north. All of the areas which can be built along Qinling are in such a gentle slope zone. Southern Qinling Mountains are the natural background outline of the buildings along them. Winding and undulating mountains, green and lush vegetation, all give a unique natural environment for architectural design along the northern foot of Qinling. Construction was built with backdrop of mountains, its style can only be reasonable embellishment of Qinling, not towering construction, and its style can only take a symbiotic and harmonic way with the Qinling Mountains' natural environment.

Qinling Mountains is an important water conservation district. In Xi'an territory, 51 of the 54 rivers were originated from Qinling. Abundant water resources and the majestic mountains make the building along Qinling, building close to the mountains, borrowing water to create landscape, that have an unique landscape architectural style.

The Effect of Culture. The culture originated from Qinling can be traced back to Lantian culture, Yangshao culture, Banpo culture which was pregnant with Chinese nation. Qinling is aggregated point and intersection of Chinese culture that is northern and southern, eastern and western culture. Qinling Mountains sets Confucianism, Buddhism and Taoism together. They are a melting pot of Chinese traditional cultural. They created the brilliant civilization of the Zhou Dynasty, Qin Dynasty, Han Dynasty, Tang Dynasty, and breed Qin, Han and Tang culture. Xi'an as historical city, from ancient times to the present, its change is closely related with Qinling. The culture was accretion though thousands of years. From the style of Guanzhong vernacular dwelling to Han-tang style being presented by modern building in Xi'an, all are the continuation and development of Qinling culture. The architectural style of construction along the northern foot of Qinling Mountains reflects Guanzhong vernacular dwelling's style, embodies the style of Han and Tang Dynasties, this is the best interpretation of Qinling culture.

Analysis of Architectural Style of Xi'an Garden Project

Xi'an Garden is a real estate development project along the northern foot of Qinling Mountains. The mainly form of the project buildings are residential buildings. It is located Taipingyu area where is the combined area of Qinhua mountain and Guifeng Mountain in Caotang Town, Hu county, east to Zigeyu, west to Taiping River, south to Qinling, and north to Yufeng Road. Since geographical location is particular, Xi'an Garden, its architectural style must take into account the response of Qinling ecological, historical and cultural protection.

Reflect Landscape Feelings. Qinling is most valuable asset to Xi'an Garden. The architectural style of Xi'an Garden is first reflected landscape feelings that is Tian Ren He Yi (theory that man is an integral part of nature). It fuses Qinling landscape and history and culture of Changan so that forest, landscape, historical and cultural landscape can reflect each other. In the specific design, it makes Qinling Mountains as a background, relies on Guifeng Mountain and Taipingyu, and builds around the mountains. In original ecological landscape and environment of Qinling, it cleverly set courtyard, then evolved and combined architectural symbol by brick and gray tiles, pitched roof, carved brick, etc. It abandoned the unexpected European construction, and formed courtyard and building group which are a part of nature, and represented people, buildings, landscape being harmonious. Really mountain and water of Qinling have made Xi'an Garden return to the embrace of natural landscape, achieve harmony of people and courtyard, courtyard and landscape, people and ecological environment (Fig. 2).

Response of Regional Culture. Qinling Mountains created the Qin culture, but also created a culture of Han and Tang dynasties. Xi'an Garden derives the design ideas of courtyard from Guanzhong vernacular dwelling reflecting cultural heritage, at same time, it uses Han culture to represent regional cultural characteristics. Its design integrates Han culture, Han landscape and Han architectural elements, is based on nature and Guanzhong region, combines modern design concepts

together, in order to seek the ultimate goal that is the integration of courtyard and nature landscape, and Guanzhong regional culture. The Component reflecting Han architectural style, such as blue bricks and grey tiles, cornices and brackets, brick and stone carving, reveals the characteristics of regional culture (Fig. 3).



Fig. 2 The style of Xi'an Garden



Fig. 3 The wall carving to reflect architectural style

The Integration of Ecological Environment. Landscape design of the courtyard is an important element to represent architectural style. Xi'an Garden emphasizes courtyard design, in the design, cleverly uses water and plant to achieve the effect integrating Qinling ecological environment. It takes Taiping River and mountain spring water to inner courtyard, makes flowing water design, and connects water of every inner courtyard to make up water network in order to create the charm of nature water landscape. After the water becomes the landscape of ornamental value, the water is drew into advanced circulating water treatment system to recycling for watering flowers, trees etc. Besides water landscape design, hundreds of plants is planted in the courtyard, they are high and low, evergreen, form a unique ecological environment of courtyard in Xi'an Garden. The internal ecological balance and external harmonious symbiosis with Qinling ecological environment make Xi'an Garden to become a useful component of Qinling ecological protection, rather than a destroyer.

Conclusions

Rapid development of urban construction and the natural resource of Qinling Mountains being abused give the natural environment of Qinling Mountains a painful scar. It is the consensus to protect the natural environment of Qinling Mountains and remodel ecological balance. To protect Qinling Mountains that can't deny the development activity along mountain. How to make the various constructions to promote Qinling Mountains' ecological protection and harmonious development with natural environment that is a very important. Architectural style with the Qinling natural environment is the inevitable response to the ecological protection of Qinling. Architectural style is a diversified proposition. With the depth of Qinling ecological protection, the style should take a more harmonious way with Qinling natural environment that is more ecological and human culture.

References

[1] H. Zhang, Cultural gene of Qinling Mountains, Journal of National Culture. 60 (2011): 6-23.
[2] H. He, Xi'an & I (2): Planning Course, Tianjin University Press, Tianjin, 2011.
[3] H. He, Xi'an & I (3): Architectural Creation, Tianjin University Press, Tianjin, 2011.
[4] L. Hao, Xi'an Residential Architecture Regional Style and Natural Characteristic Relation to Primeval Study, Ph.D. Thesis, Xi'an University of Architecture and Technology, Xi'an, 2006.
[5] Information on http://www.xaqlb.gov.cn.
[6] Information on http://www.xianyuanzi.com

© (2012) Trans Tech Publications, Switzerland
doi:10.4028/www.scientific.net/AMM.238.547

Preservation and Renewal of Huaiyu Street Historical Blocks in Xunxian County

Changzheng Gao [a] and Yating Song [b]

Department of Architecture, North China University of Water Resources and Electric Power, Zhengzhou 450011, China

[a]380636290@qq.com, [b]yating_sou@163.com

Keywords: the Historical Block; protection and renewal; value remodeling.

Abstract. According to a large number of interviews and investigation in Xunxian County, which is the Historical and cultural city of the whole country, we carried out a close analysis about the formation of the Historical Blocks of Huaiyu Street, and explored the street style and spatial pattern. Thus we put forward some specific measures to the renovation of street blocks, combined with the influential factors the Historical Blocks of other cities' protection methods. And we expect to provide a reflect way for the renewal of street blocks.

Introduction

China is at the stage of rapid urbanization. Does urbanization mean dismantling the old city and building a new one? It is the responsibility of every architect to discover valuable buildings in the process of urbanization and protect them in right ways. What should we do to find ideological roots and human wisdom expressed in architecture from the traditional architectural culture, and thus giving it a modern interpretation? And how should we retain and develop the regional characteristics of architecture, while blending them with the modern architecture? Based on the research topic, a field investigation and mapping at the Historical Blocks of Huaiyu Street in Xunxian County, Henan province, has been carried out, in an attempt to give a summary of the renewal Huaiyu Street Historical Blocks and retain the regional characteristics of it.

Xunxian County, located in the north of Henan Province, used to be named Liyang. With a long history, it was designated the state-level historical and cultural city by the State Council in 1994. The county is made up of three parts: the Old District, the New District and the Weixi District. As it is recorded in Discussion on the Tribute of Yu, Yu dredged the Yellow River, eastwards passing the junction of Luoshui River and Yellow River,up to Dapi Mountain. In order to commemorate the deeds of Dayu, later generations named this street Huaiyu Street, which means to cherish the memory of Yu. Huaiyu Street is about a kilometer long,30 meters wide, both of which are lined with street hotels and commercial shops. The Historical Blocks of Huaiyu Street is located in the old town, connecting the Dapi Mountain with Fuqiu Mountain. In the long process of history, the unique historical patterns of "two mountains, a street" has been formed in Huaiyu Street. Dapi Mountain and Fuqiu Mountain make up the Dapi Mountain scenic spot together. In the scenic spot, there stand nine Buddhist and Tao architectures. Pavilions, terraces, open halls, as well as temples can be found all over the mountains. Tianning Temple, constructed in Northern Wei Dynasty(A.D.386-A.D.534), is famous for its eighty-foot stone Buddha and seventy-foot tower; Thousand-Buddha Cave carved in the Tang Dynasty is the classical rock art of Central Plains. Bixia Temple, the Taoist Holy Place, which was primarily built in Ming Dynasty, remains unexceptionally large in scale and delicate in structure. The most characteristic of Xunxian County is its Ancient Temple Fair in large quantity and scale What is more, the annual Lunar January Assembly of Fuqiu Mountain has long been known as the number one temple fair of North China.

Landscape Characteristics and Spatial Pattern of the Historical Blocks of Huaiyu Street

The most important value of landscape and spatial pattern of the Historical Blocks of cities is the sentimental value, which includes continuation of the historic pattern, cultural identity, spirit symbols and so on. With the development of economy, people tend to focus more on cultural and

psychological needs, but not just general material requirements. Most of residents in the Historical Blocks of Huaiyu Street are the original inhabitants. And they still carry on the traditional lifestyle and preserve non-material heritages such as folklore activities, performing arts, festivals, traditional crafts and so on which is the soul of the protection of the Historical Blocks. During the protection of the Historical Blocks, reconstruction and integration can be reached through full use of the method of traditional space assembling and architectural context. To further protect and develop the Historical Blocks, it is the best to keep the original artistic conception and pattern and inherit historical context. The Huaiyu Street blocks are composed of one horizontal street, two vertical streets and several cross-lanes. To be precise, the horizontal street refers to Huaiyu street from east to west; two vertical streets stand for the east of Pifu street, and the outside of Nanguan street, both spreading from south to north. A large quantity of crooked lanes, varied in length and width, stand along both sides of the main road, decorated by high walls and deep lanes, which gather together to show a typical picture. The basic unit of the blocks is courtyard, following the courtyard pattern of the Central Plains and forming the traditional plane pattern.

Factors Affecting the Protection of the Historical Blocks of Small and Medium-Sized Cities

Botengxiao said, "City planning is indeed necessary, because it not only facilitates urban development and meet the challenges of the future, but also fits today's situation without breaking the relevance with the past." With guidance of this principle, encouraged residents to participate in planning and protection and turned focus from material form to the remodeling of the intangible cultural heritage when we studied the Historical Blocks of Xunxian county.

Factors of Remodeling of Value. As the subject of blocks development, residents should not only participate in the compilation of the planning, but also carry it out. They are the ultimate beneficiaries of the planning. Social development shall follow human’s will, so residents, as an indispensable factor in the Historical Blocks, shall take an active part in it. The degree of their participation in the preservation and renewal of the blocks concerns directly the success of the protection and renewal of the Historical Blocks.

It requires certain carriers to keep cultural heritage in the Historical Blocks. Heritage, monuments and historical buildings in the blocks are static and silent, while residents in the blocks are dynamic and audible. Indigenous peoples should be retained and their original lifestyles and the joy of life should be kept in the protection of the Historical Blocks-this is the real protection. As Huaiyu Street Historical Area is residential blocks, we shall focus on the residents' participation in planning and the issue of "go" or "stay" of the resident. What’s more, we shall focus on the residents’ value of emotional belonging, and turn our attention from tangible material forms to the remodeling of Value of intangible emotional culture and the intangible cultural heritage.

Factors of Protection Mode. Historical blocks, which embodies the value of traditional culture, are memories of the urban development , areas where the most complete and richest memories of cities are kept, and an important part of the background of today’s life. This requires us to realize the significance of the protection: Protection is to keep the historical heritage our ancestors left to us so that it can present the current characteristics of history; while renewal is to change the old and outdated infrastructure in the blocks and to provide the non-coordination parts with modern life such as construction quality, so as to adapt to society's development and achieve the sustainable development in the Historical Blocks.

So on the historical blocks of HuaiYu Road neighborhood protection and renewal strategy can be drawn lessons from southern Wuzhen, Beijing Nanchizi the protection update mode, adhere to the government as the leadership, the small scale gradual protection and renovation methods, adhere to local residents and other social groups to participate in a wide range, so that it can help with Yu Road neighborhood characteristics and healthy development. Especially for the small and medium-sized city in the Midwest of Xunxian County, take the small progressive pattern of protection and renewal, let residents and social groups are widely involved, fairly practical.

Protection and Renewal Strategies of the Historical Blocks of Huaiyu Street

Protection and Renewal of Spatial Forms of the Historical Blocks. On the basis of evaluation and analysis of present land function, construction quality, and architectural and heritage value, we delimit land function and determine the scope and countermeasures of the protection and renewal of the Historical Blocks. Planning can be summarized as 4 districts and 5 joints. The four regions include a square landscape area, retaining the remediation area, transform promotion area, public recreation area.

The first is square landscape area. Cultural square shall be provided at the entrance of Fuqiu Hill at the west end of Huaiyu Street, thus highlights the atmosphere of street culture. As the key landscape district, the shaping planning shall focus on highlighting the historical and cultural connotation of Fuqiu Hill. Square not only allow tourists to enjoy a spacious view, but also a place for the Fuqiu Hill Temple Fair and Shehuo, where there are Wishing Trees, Diagrams of Totem, Scenery Walls, Sensors and Columniations landscape element, for the entire neighborhood characteristics to create a good cultural atmosphere of entrance.

The second is retaining the remediation area. From the west end of Huaiyu Street to Nanguanwai Street, most housing are temporary and the whole street interface is confusing, renewal is preferable; in the north-east intersection of Huaiyu Street and Huanghe Street, there is no spatial connection with Huanghe Street, most buildings are temporary, it is preferable to dismantle them, take the coordination of the whole style into consideration during reconstruction and extend it up to Huanghe Street by Transfer Tower; in the front of Pishan Hotel, in the east section of Huaiyu Street, no wide open space is available, and the hotel is not in harmony with Pishan Street, so it is favorable to construct a public green land, for more public space as well as harmony; the height of new buildings in the north section shall be limited so that Pishan Hotel is outstanding.

The third is transform promotion area. From Nanguanwai Street to Huanghe Street, there are primary schools and hospitals, and the building is structured, so renovation is preferable here. Considering the tourism advantages in Xunxian County, it is recommended to establish a comprehensive center, serving Pishan Mountain scenic spot, containing folk activities, leisure, dining, and tourist shopping, and being a commercial and cultural block of characteristics, as "Colorful Yunnan", a comprehensive district in Kunming City, which includes tourism and shopping and entertainment.

The forth is public recreation area. From Huanghe Street to Dapishan Hotel, a plot in the west of Dapi Mountain is set to be a public place with street parks. It can provide not only service to the local people but also great visual and mental enjoyment to the tourists to Dapishan Hotel.

The 5 joints are: Cultural Square at the entrance of Fuqiu Mountain, Transfer Tower in the intersection of Nanguanwai Street and Huaiyu Street, skyline control joint of streets between the County Hospital's street buildings, Dismanting for green in the County hospital, Small Park in front of Dapi Mountain. With the 5 joints, space in Huaiyu Street is controlled flexibly, and blocks are in good up-and-down order.

Fusion of Traditional and Modern Business Atmosphere in the Historical Blocks of Huaiyu Street. "Two mountains, one street", the historical pattern in the Historical Blocks of Huaiyu Street, gives the Huaiyu Street a special value system of living, commerce and culture all in one. And Dapi Mountain and Fuqiu Mountain brings the Historical Blocks of Huaiyu Street a higher commercial value. In order to upgrade the quality of tourism services and promote the economic development, a comprehensive block, which is in harmony with tradition, is established on the basis of traditional small private workshops. It is a block containing folk activities, leisure, dining, and tourist shopping, serving Pishan Mountain scenic spot. And it will be a block with commercial and cultural characteristics. At present, only Dapishan Hotel has larger scale. Considering the present commercial situation, it is favorable to protect family hotels and allow their operation in the mode of family hotel or travel agency. To make the blocks more energetic, the design of "shop in front of residence" and "shop below residence" is applicable, in which keeps the appearance style and renovates inside plant so as to combine the representation of the historical appearance with the improving of residents' living conditions. There is a great adjustment of commercial facilities after

the renewal (Table-2 and Table-3). After the renewal, it not only focuses on serving the local people, but also taking into account the historical value of Huaiyu Street, taking it a cultural exhibition of Xunxian County.

Conclusions

Containing a wealth of historic information and cultural connotation, the Historical Blocks of Huaiyu Street are important components of city connotations, an important aspect supporting residents' spiritual life and the source of forming the uniqueness and diversity of city culture. In view of the characteristics of the Historical Blocks of Huaiyu Street in Xunxian county and the present situation, the renewal measures include reasonable zoning, the remodeling residents' value, the selecting of protection mode and so on should be taken. Restoring and renewal of the Historical Blocks of Huaiyu Street has 3 main aspects: protecting and keeping the traditional pattern, inheriting and carrying forward the traditional city culture, and developing tourism reasonably. Only by doing these can we protect all kinds of tangible and intangible heritages and activate the Historical Blocks of Huaiyu Street finally.

References

[1] Steven·Tiesdell, Tim·Heath, Taner·Oc, Revitalizing Historic Urban Quarters — City Planning & Design Theory, China Architecture & Building Press, Beijing, 2006, 13-15.

[2] Y. Ruan, X. Gu, Analysis of the protection model of the historical blocks in our country, Journal of Tongji University (Social Sciences) , 5 (2004) 1-6.

[3] L. Wu, X. Wang, Ways of protection and renewal of the historical blocks, Journal of Architecture Science and Engineering, 1 (2007) 84-87.

[4] Z. Zhao, C. Qiu, Y. Xie, B. Wang, Study of the planning of protection and renewal of the historical blocks of Xiangtanyao sinus, Chinese and Overseas Architecture, 5 (2009) 142-143.

© (2012) Trans Tech Publications, Switzerland
doi:10.4028/www.scientific.net/AMM.238.551

A Tentative Research on Site Selection of Shanxi Buddhism Temple Architecture

Yuanxin Li [a], Xiangdong Zhu [b] and Chongen Wang [c]

The Architecture Department, Taiyuan University of Technology, Shanxi Province, China

[a]li_yuan_xin_happy@163.com, [b]zxd0110@sohu.com, [c]wangchongen@tyut.edu.cn

Keywords: Shanxi; Buddhist temple; site selection; Chinese traditional culture.

Abstract. Buddhist architecture which was introduced to China from India had become an important component of traditional Chinese architecture, and the characteristics of different regions had formed after the long-term development. This article starts from Shanxi's location environment, analyzes the considerations of geographical environment of Shanxi temple construction's site selection and the historical regularity of their distribution combining with the site selection factors of traditional Chinese architecture. Thus, the general rules of site selection of Shanxi temples and its particularity of distribution are revealed preliminarily from the viewpoint of space and time.

Introduction

Shanxi Province, known as the ancient Chinese cultural museum, has the largest national ground relics and more than 70% of well-preserved ancient buildings. These ancient buildings are of great number, high value. Among them the Buddhist temples are the most abundant, and all of them are the valuable material heritages of our country.

In history, Shanxi was located in the confrontation zone between nomadic culture beyond the Great Wall and the culture of Han nationality in central plain, so it had played an important geopolitical role in the integration and development of the nation. Therefore, on this basis, studying the problem of the site selection of Shanxi temple can help us seek out its characteristics and regular pattern. We can also understand the development of social ideology at that time, as well as the fusion course of Buddhism and the Chinese traditional culture.

Factor Analysis of Buddhist Temple Site Selection

Buddhism was introduced into China long ago. During the communication process, it had been absorbing the essence of Chinese native culture, and gradually formed a religion that filled with Chinese characteristics. The Buddhist architecture was also influenced by the traditional Chinese architectural culture and this characteristic is particularly evident in the site selection of the temple building. Usually, the main factors are as follows:

Pay Attention to Geomancy. The Chinese geomantic art with a long history and profound connotation is an important application of the traditional Chinese culture in architecture. Although it has superstitious color, it essentially contains the scientific nature of environmental design. Literally, "Feng shui" means "hide wind" and "close to water". There is no better location than that of fronting water and with hills on the back, bearing shade and facing the sunshine, forming the geomancy pattern of that the blue dragon on the left, white tiger on the right, rose finch on the South, and black tortoise on the North. This kind of temple sit selection is common in Shanxi. For example, the Longquan Temple, it is located in the southeast of Taiyuan City, faces south, with Tai Mountain behind the back and Fengyu River in the front. It conformed to the traditional geomancy theory strictly and well meets the quiet and leisure psychological factors of environment which Buddhist pursued.

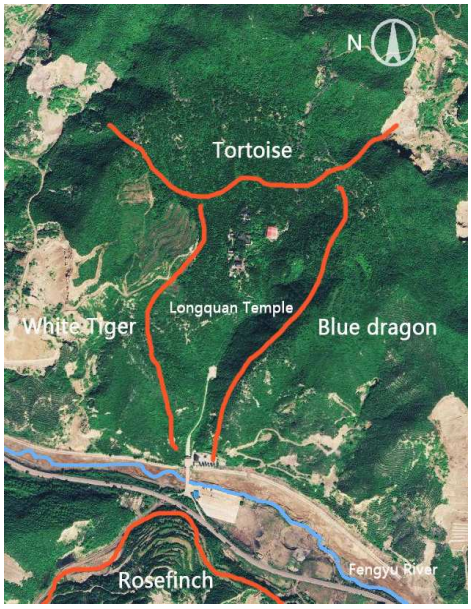


Fig. 1 Longquan Temple location analysis

Harmony between Man and Nature. Early in The Spring and Autumn Period, Lao Tzu had put forward the viewpoint that "Man takes his law from the Earth; the Earth takes its law from Heaven; Heaven takes its law from the Tao. The law of the Tao is its being what it is", which pointed out the relationship between man and nature clearly. Nowadays, this view has integrated the astronomy, physiography and humanity as a whole, and has been condensed into one unity cosmological outlook and risen to the core value of the ancient Chinese traditional culture. This traditional philosophy of imitating the nature coincides with the "nirvana" state. Therefore, Buddhist temple site selection also adheres to this idea, adjusting measures to local conditions and locating in scenic mountain forests. However, this concept not only applies to the inherently good natural environment, but also fits well in the odd-shaped environment. The Buddhist architecture resorts to some environmental means to heighten the mystery of religion. Such as the Xuankong Temple which was built by ingenious using the shape of the mountain is one of the classical works of Shanxi temple. It was beside the mountain and deep valley and hanged in the Cui Ping peak of Mount Heng which is more than 60 meters high. It was built splendidly in the form of hanging house which was only supported by wood frame.

The Geographical Distribution Rule of the Site Selection of Shanxi's Temple Construction

The spatial distribution of the temple in Shanxi is very extensive. Concretely Speaking, the distribution in the regions of northern Shanxi and central Shanxi are concentrated relatively, mainly located in mountainous area, especially dense in Wutai County and Fanshi County while the temples in southern of Shanxi are chiefly located in Fenhe Basin and the Yuncheng Basin which elevation is lower. According to statistical survey, we found that it has the following characteristics:

Adapt to the Terrain, and Be More Concentrated in Places with Dense Population and Prosperous Politics and Economy. The landform of Shanxi is undulate and variable. Datong, Xinzhou, Taiyuan, Linfen and Yuncheng basins are scattered distributed along the Fen river Basin from north to south. These basins are flat, open, and soil fertile, or due to military defense or depend on its natural external transportation advantages, forms a populated area of Shanxi. Consequently most of the Shanxi temple distribution complies with the terrain trend, mainly concentrated in such areas. To probe its reasons, on the one hand, it was conformed to the urban historical development. On the other hand, from the view of monks' daily activities, it was closely linked the material living conditions which could provide great convenience to the monks' life. The national historical and cultural cities which are announced by the State Council are the representative cities of great historical and commemorative significance in China. Now we take the six famous Shanxi historical and cultural cities (Datong, Pingyao, Xinjiang, Qi County, Dai County and Taiyuan) as examples, the total area of them accounts for only 3.3% of Shanxi Province. However, through the statistics of temples which were recorded in "A complete collection of Shanxi temple", the temples built in those cities were up to more than two hundred, accounted for nearly 12% of the total number of the province. The temple's construction density is higher than other regions.

Often Distributed in the Mountains. The Buddhist practices pay attention to the sincere and pure spirit which is not subjected to outside interference. So the verdant and quiet mountain environment meets the external conditions of Zazen compatibly. Building temples in the mountains is not only in line with the characteristics of the Buddhist architecture that respect for the nature, but is also the perfect combination of Buddhist aesthetic and site selection of religious building. Shanxi has many mountains that provide many natural places for the site selection of temple. Only in the vicinity of Wutai Mountain, the number of the existing temples is over 180, however, in the period of history that the Buddhist activities were the most prosperous, the temples had been up to nearly 360, which can be described as "the monks have occupied most of the world famous mountains".

Distributed Densely in the Regions Prevailing Buddhism. The predominantly Buddhist areas of Shanxi are mainly concentrated in the north. During the Liao Dynasty, the ethnic boundaries were broken and the political situation that the backward minority ruled the advanced Han nationality had formed in Northern of Shanxi. Due to the social unrest, people found spiritual sustenance from the Buddhist faith gradually. However, the rulers had to use the power of religion for their interests of the political group. They had adopted many measures to support the construction of temples. Therefore, there are a large number of temple architectures in the local authority territories which had been preserved until today, such as Huayan Temple and Shanhua Temple. These temples were located in the prominent position of the city. Firstly, it was convenient for the people to pray. Secondly, it was benefit for the management of rulers and could facilitate the monks to exchange Buddhism with the outside world. Through statistics of temples which were recorded in "A complete collection of Shanxi temple ", up to 487 temples were built in northern of Shanxi where the Buddhism is prevailing, accounting for 29.48% of the total number.

The Historical Changes of Site Selection of Shanxi Temple

Architecture is the reflection of a country's national culture, during the long development, the Buddhist temple architecture was deeply influenced by the Chinese particular social system, national customs and ideology. The site selection of the Shanxi temple also shows the rules of different historical changes of the temple construction from mountains to cities. Now, we divide the time by the development of Buddhism in China as time slot, the rules of its historical changes are showed below: the introduction period of Buddhism (Han Dynasty): the temples which were built in the mountains accounted for 26.67% of the total number of the temples; the development period of Buddhism (Jin Dynasty- Northern and Southern Dynasty): the proportion of the mountain forest temple was up to 35.34%; the heyday of Buddhism (Sui Dynasty – the Five Dynasties): the proportion of the mountain forest temple was 21.26%; the mature period of Buddhism (after the Song Dynasty): the proportion of the mountain forest temple had fallen to 12.82%. The emergence of such rules is not accidental, which are all closely linked with the political, social, cultural and economic conditions of that time.

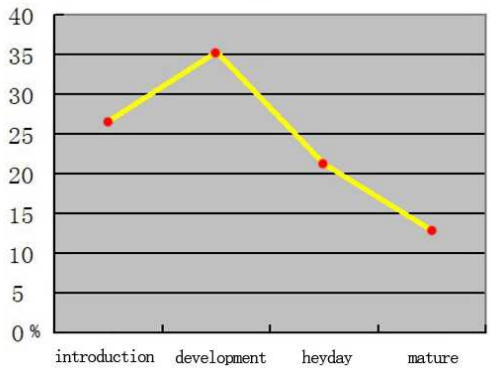


Fig. 2 The proportion of mountain temple in different development stage of Buddhist

During the introduction period of Buddhism, the temple construction was in the rise stage. To provide a quiet place for monks' concentrated study of Buddhism, the early site selection of temple was similar to the Taoist architecture which often site among the scenic and tranquil mountains.

During the development period of Buddhism, the politics was turbulent, people's painful became more increasingly. The idea of Buddhism that advocates to enjoy happiness by doing a good deed was widely accepted by the needy people. Temples began to move toward the city from the mountain, many princely nobles even "turn their residences into temples". So a great deal of Buddhist architectures appeared in the villages, towns and other populated areas which provided convenience for the spread of Buddhism. Into its heyday, though the Buddhism was prohibited by Emperor Wuzong for a short time in, but because of the good social environment, many Buddhism sects were increasingly prosperous later. Till the early Song Dynasty, the influence of Zen Sect had been prominent. Owing to the Zen advocated tranquil and ultramundane, the location of Buddhist temples had transferred from the cities to the mountains once again. After the Song Dynasties, the rulers provided protection and support for Buddhism, the temple constructions became prevalent throughout the country. The site selection of the temple was influenced by the traditional Chinese culture, paying attention to the pattern of geomancy, while most of the temples tended to "go into the society", the number of temples which were built in the village or town had increased significantly.

Conclusions

According to the whole paper, we can figure out the characteristics as follows: First of all, the distribution of Shanxi temple is widespread, but is concentrated relatively in each basin range. Secondly, the characteristics of different regions are not the same. Finally, it is greatly influenced by the social and historical environment and the feudal autocratic ideology. The site selection of Buddhist temple which takes “harmony between man and nature” as emotional basis not only meets its physical function, but also meets the mental function. In brief, Shanxi temple architecture which owns a considerable proportion in the ancient Chinese architecture has strong representative significance, and the studying on the site selection of temple has well reflected the development path of Buddhist architecture in Shanxi Province, and provides foundation for the better study of the ancient architecture, Buddhism and social development.

Acknowledgements

This study is supported by the National Natural Science Foundation of China (51078251) and the Shanxi Provincial Development Planning Project (982181).

References

[1] Q. Wang, H. Zhang, The geographical distribution in the site selection phase of the Chinese Buddhist temple, Journal of Hebei Normal University, 3 (1993) 34-38.

[2] Q. Bai, A Complete Collection of Shanxi Temple, Shanxi Economic Press, Taiyuan, 1995.

[3] Y. Zhang, The Lecture of Chinese Buddhist Temple Architecture, Contemporary China Publishing House, Beijing, 2008.

© (2012) Trans Tech Publications, Switzerland
doi:10.4028/www.scientific.net/AMM.238.555

Application of Display List Group Technology in Forming of Complex Building Model

Lihua Li

School of Civil Engineering and Communication, North China University of Water Resources and Electric Power, Zhengzhou 450011, China

lilihua1965@163.com

Keywords: OpenGL display lists; complicated building; forming model; CAD.

Abstract. The display lists function for OpenGL technique is applied in the process of forming complicated building model in this paper. It is used to increase the speed of forming model and editing while the demonstrating table is reasonably organized by dividing group technique.

Introduction

As is known to all, in the field of CAD application of three-dimensional graphics libraries to OpenGL technology is most extensive [1]. It is one of the most suitable tools for 3d model to create and edit. OpenGL provides display list function so as to speed up the building graphics and displaying speed. In general smaller CAD system, because it involves basic graphic (such as triangle, etc) small number, in the display and editing process, system response speed is generally can be acceptable. But for complex buildings, such basic graphics may have a million or even more. And, in the course of forming model, it is necessary to restructure the display data at any time, such as the situation that if a component is selected, the corresponding display data will be modified and the display list updated. If the general method is used to employ a display list for processing simply, the response speed of system would be greatly reduced, and make the person not accept it [2]. Such tough problems as these are met in the development of a high-rise building CAD system. How can rationalize display tabular data management, so that every time you need to change the total number of display list at least, so as to improve the system response speed, all of these problems will be discussed in this paper.

Display List Group

In the forming mode of complex building, grouping to display list is a feasible method, but how to divide it and make it more reasonable is a critical issue. In CAD system for high-rise buildings, it is divided according to the hierarchical structure of the actual building, namely every natural layer is set two display lists. One for the not selected components, the other for the selected component. When a component is selected or cancelled selected, the graphics data transfer in two display list. So every time only display tabular data is updated for the layer of the components. Experiments show that the method is effective. But when single component up to ten thousand, including figure data generated between connection nodes of the components, then the basic graphic data (triangle) scale can reach nearly a million, at this moment the system response speed still cannot meet the requirements. Then, the component of each layer is more detailed divided, namely group method to component of the layer [3]. It means that the component of each layer is divided into more display list. Each display list includes only a certain number of components. The results show that the response speed of the whole system can be improved extremely through the reasonable design data structure, the result is satisfactory. Display list group data structure is as shown in Fig. 1.

The Implementation Method of the Display List Group

VC++ class structure is used to achieve the idea. The main class has three: CAllDisplayList, the class of management to the entire building display list; CFLDisplayList, the class of Managing a single layer of the display list; CObjectsDisplayList, the class of with a certain number of components in the management.

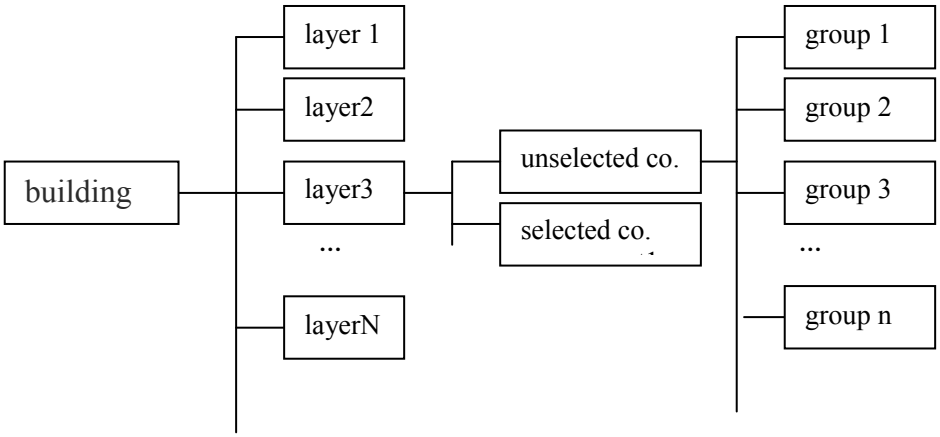


Fig. 1 Display list group data structure

The main properties and methods are listed below:

```
class CAObject;//component class
class CAllDisplayList
{
public:
    CObList mFLDisplayList;// display list corresponding to each layer
    void Display();
    CFLDisplayList* GetAObjectFL(CAObject*);
};
class CFLDisplayList:public Cobject//display list corresponding to the layer
{
public:
    CObList mObjectsDisplayList;
    void Display();
    CObjectsDisplayList* GetObjectsDisplayList(CAObject*);
    void AddObject(CAObject*);
    void DeleteAObject(CAObject*);
    void SetSelect(CAObject* pAObject,BOOL bSelected);
};
class CObjectsDisplayList:public Cobject//display tabular data of division
{
    public:
    int mDisplayListNormal; //OpenGL display list value of generation
    int mDisplayListSelect;    //OpenGL display list value of generation
    int Sum;    //the total component number of partition
    float *parrayNormal; // graphics vertices array of unselected component
    float *parraySelect;
        //graphics vertices array of selected component, display in the red
    void Display();
    void AddObject(CAObject*);
    void DeleteAObject(CAObject*);
    void SetSelect(CAObject* pAObject,BOOL bSelected);
};
```

Three kinds of the above, the most important is CObjectsDisplayList class. In the whole model and editing process, its efficiency played a decisive role. When adding a component, the system automatically find division display tabular data instance, that is not up to the total number of designated components for this layer, or create a new examples, and then add it to, and at the same time make a position record in the component class; When a component is selected , the system

should be able to quickly locate display tabular data examples in its place partition, and move the vertex data in two list; When a component is deleted, the system should be able to delete corresponding vertex data, and reduce the Sum, when the Sum is 0, the display tabular data examples should be deleted.

In CAD system of high-rise buildings, after testing (as shown in Fig. 2), the maximum Sum inside the system will be set for 200 (which is relevant to the complexity of the component). This data is justified, because OpenGL itself is limited to the total number of display list. But generally, it is not more than the limits for the real project. With the maximum Sum set for 200, system response speed is the most ideal for many different types of computer and operating system.

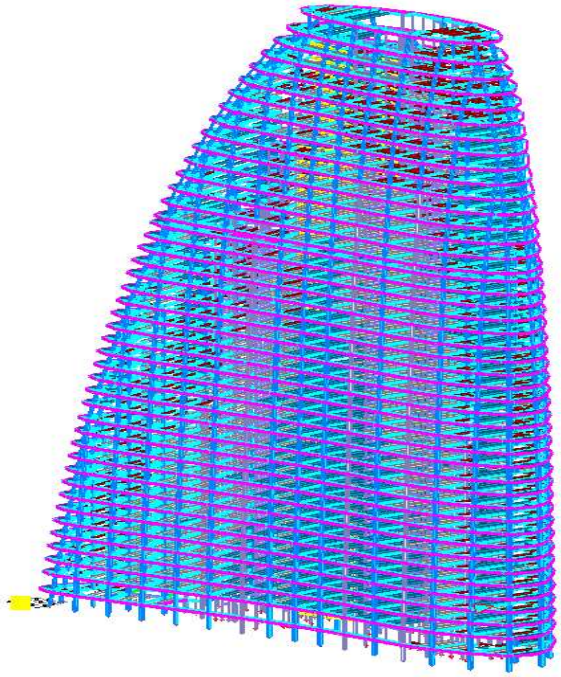


Fig. 2 A high-rise steel structure

Conclusions

For using OpenGL display list function and forming 3D model of complex structure, there have been a lot of research achievements, but the developers have been puzzled by response speed problems. Forming model problem for high-rise buildings CAD system is solved by using the method of display list set up with layer group. At the same time it is also convinced that, with the development of computer hardware and software and efforts of industry peers, a more effective solution method will be found in the future.

References

[1] Y. Shang, Y. Chen, OpenGL Graphics Programming Guide, China Waterpower Press, Beijing, 2001.

[2] J. Shi, W. Cai, Scientific computing visualization algorithm and the system, Science Press, Beijing, 1999.

[3] S. Xu, Computer Algorithms, Tsinghua University Press, Beijing, 1995.

© (2012) Trans Tech Publications, Switzerland
doi:10.4028/www.scientific.net/AMM.238.558

Study of Natural Disasters Contract Conditions Based on the FIDIC Criteria

Zhanglin Guo[1,a] and Hua Zhang[2,b]

[1]Department of civil engineering, North China Institute of Science and Technology, Beijing 101601, China

[2]Hebei University of Engineering, Handan 056038, China

[a]gg_zz_ll@163.com, [b]316080624@qq.com

Keywords: construction; FIDIC; natural disaster; contract condition; risk responsibility.

Abstract. In the trend of global warming, storms, hurricanes, high temperature and other extreme weather phenomena occur frequently. In the field of project construction, the assets value of the building is exposed, so the construction projects are very vulnerable to natural disasters causing huge losses. Who bears in the both sides of engineering contract, the reasons and consequences of the loss and the specific responsibilities are ambiguous without clearly defined. This paper states the importance to grasp the principle of appropriate risk sharing and explain both responsibilities clearly in natural disasters, how to choose appropriate method to evaluate the natural disaster risk and select suitable building construction contract.

Introduction

In recent years, with the speeding ahead of the urbanization process, the rapid economic growth and the rapid expansion of the size of the cities in China, the infrastructure construction programs in our country are increasing the investment of infrastructural project. Because of the objective conditions of economic growth and human life, it is necessary to build construction projects in those areas with larger risks of natural disasters. Though the occurrence of natural disasters is very rare event, the constructions have not reached disaster-resistant requirement during the course of constructing and it is easy to be damaged by the attack of natural disasters. So far, there are a lot of international project-builders who transfer the risks of natural disasters in construction period by insuring Construction All Risks Insurance. Yet, the construction insurance in China is still in the developing period and the rate of the ones with Construction All Risks Insurance is very low. As a result, it is essential for the participants of construction projects to strengthen the ability of disaster prevention and reduction. Correct analysis and evaluation of natural disaster risks are beneficial for both contractor and outsourcer to choose proper construction contract conditions. The fairness and justice of the construction project contracts' performing can be guaranteed after their holding the proper principle of risk sharing and knowing the responsibility of both sides when natural disaster happens.

Natural Disasters and the Relevant Terms of Natural Disasters

The Relevant Attributes of Natural Disasters. Natural disaster is a kind of risk that causes property loss and casualties because of natural substantive risk factors. Their happening is usually caused by bad natural surroundings such as earthquake, tsunami, wind, rain, snow, flood, fire and thunder etc.

The influential factors of natural disasters on construction projects are as follows: the effect of engineering geology and humanistic geology; the effect of bad climate such as high temperature, bitter cold, rain and snow, wind and thunder etc; the effect of earthquake, tsunami, typhoon and other natural disasters. So far, the standard of technology is not able enough to deal with natural disasters by using manpower. It can only lessen loss by taking appropriate measures in limits. But the effect of bad weather on engineering geology and humanistic geology can be prevented or avoided to some extent. Yet, the damage degree and damage content of natural disasters' happening is uncertain, so is the definition.

The Terms of Natural Disasters. Natural disasters belong to force majeure in Chinese law and relevant construction contract conditions. Force majeure is an exception clause in Contract law and FIDIC civil engineering construction contract conditions. Exception clause is described from item 19.1 to item 19.7 in FIDIC civil engineering construction contract conditions. In item 19.1, the definition of exception clause means the special incidents or conditions as follows: in this clause, "force majeure" means an event beyond the control of the employer and the contractor; which makes it impossible or illegal for a party to perform, including but limited to:

(a) act of god.

(b) neither the employer nor the contractor shall be considered in default.

(c) in contractual breach to the extent that performance of obligations is prevented by a force majeure event, which arises after the effective date.

However, it is difficult to identify so-called special incidents and conditions. Since in most conditions, people like to judge things with their experience and perceptual knowledge, the boundaries are difficult to be lined clearly. For instance, an item of construction contracts says that "an experienced contractor cannot properly foresee and prevent any effect of natural force", in which how the effect of natural force that cannot be properly foreseen and prevented should be defined? The description of force majeure of natural disasters is obscure. Besides, as the effect of damage is caused by natural climate, which level can the damage be called natural disaster? Not all the natural phenomenon such as bad weather or climate change will have a disastrous influence on construction projects. There exist some disagreements in all aspects of construction on the definition of natural disasters. As a result, it is necessary to exactly formulate the quality and quantity of natural disasters so that the responsibility and obligation can be expressed and the conflicts and disputes can be avoided.

Relevant Division of Responsibility on Natural Risk. Since the period of construction project is long and the scale is big, and the construction project and value is often in open-air where the surrounding is complicated, during the time there always occur some unavoidable and insuperable natural environmental risks such as exceeding earthquake, fire, flood, storm, downpour, mud-rock flow, landslide, landfall, rock burst and other insuperable natural force, which are also called natural disasters that are recognized as the most classic force majeure in Chinese legislative and academic area, during the construction period. One thing should be noted is that not all the natural disasters can be the exempting reason of force majeure. Those natural disasters that are light and have not caused parties serious influences cannot become force majeure.

Thus, the constructor should consider these factors and require the bidder to definite the degrees of force majeure in contract terms and consider the effect of natural environmental risks on engineering construction in bid documents when he bids. The definition of force majeure concerns a vital problem about allocation of risks during construction period, because the risks caused by force majeure mainly include the natural conditions which exceed the levels contract stipulates and which are special and not forecasted. According to usual contract conditions, this kind of risks ought to be undertaken together by contractual subjects and generally, the contractor can only get compensation of project delay.

In construction contract model test, there is a clear formulation about the aftermath of natural disaster. Since the project delay caused by natural disaster will be undertaken by the owner, the contractor can claim indemnity from the outsourcer based on relevant documents. On the one side, the damage of constructor's construction equipment and tools, as well as the casualties of the site operators and the loss of sabotaging will be undertaken by the constructor himself. On the other side, the damage of construction itself and the cost of descaling machine recovering are on the owner. It can be seen that the risk effect of the construction contrast is based on the principle of sharing the risks, which means every member undertakes fixed risk.

It makes the risk of natural disasters of force majeure vested in the owners. In accordance with Clause 20.1 [Contractor's Claims] to obtain an extension of the duration and increase the costs associated with the occurrence of the risk caused by the contractor fails to fulfill its contractual obligations and its duration suffered delays and cost increases in general condition of contract.

Criteria for Defining the Occurrence of a Natural Disasters. In the process of the project, Occurrence of natural disasters are often closely related to the project in which the natural environment, on-site geological and construction situation. The core content of the natural disasters was the relations of probability and intensity of the natural risks which is the focus of the engineering designer and project insurance company attention.

Based on the related analysis of natural disasters, the return period or annual probability of exceedance of the intensity of natural hazards may be gotten by accessing into the historical statistics of local natural risks. And by calculated it would be transformed the probability for a construction period of the disaster event. Assumed that the natural disaster risk probability is uniformly distributed during the construction period, the return period for the probability of the N years of natural disasters in any time period Δt can be expressed with the following formula:

$$p = 1-(1-1/N)^{\Delta t} \tag{1}$$

Where R is the probability of disasters in a return period Δt. N is the return period, Years (ten, twenty five or fifty years).

Fig. 1 was analysis results of hazard risk in the time of Δt. Because of the different indicators and units of various types of disasters strength and intensity of the horizontal axis disaster only to reproduce the period that, when applied to various natural disasters, should be replaced for the return period corresponding to the disaster strength. When the probability of exceedance of 0.1 is equivalent to once in ten years, when the probability of exceedance of 0.01 is equivalent to once-in-a-century, when the probability of exceedance of 0.001 is equivalent to the Millennium once.

The losses of construction caused by natural disasters were different at different times of the engineering construction. If only to consider the project construction value of the assets for a period of time, shown in Fig. 2, the construction period T is divided into N time segments, and calculation by application of calculus can get the total expected loss values E of the project in a natural disaster occurs, in T_{i-1} to T_i period of the construction project to build the value of $(V_{i-1}+V_i)/2$, expected loss can be expressed as the following formula:

$$E = \int_0^{T_N} (V_{i-1} + V_i)/2 dt \tag{2}$$

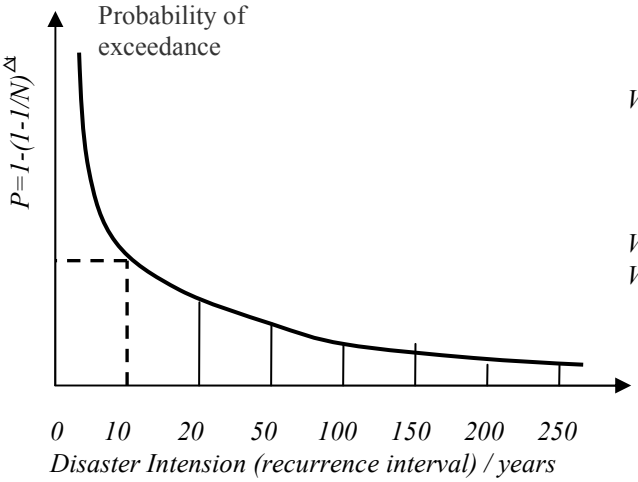


Fig. 1 Construction projects of natural disasters strength - the probability of relationship

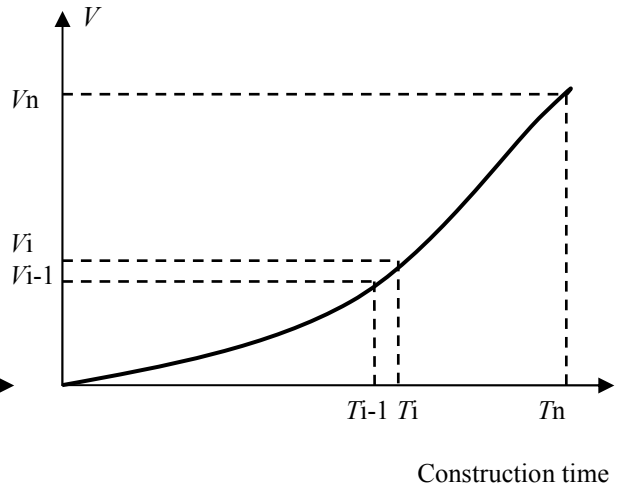


Fig. 2 Construction in progress have completed the changes in the value of curve

Based on the risk of calculation expression:

$$R = F(O, P, L)$$

Where R is a risk factors affect the extent of the management objectives of the project; O is the results of all the risks of the risk factors set; P is the probability value set corresponding to the results of all the risks; L is the said the public's attitude.

O={ Slight, ordinary, critical}
P={ Small, medium, large}
Combined with the above formula (1) and (2) Value at risk of natural disasters:
$R = F(E, P, L)$.

Intuitively, against the larger natural disasters, low probability, while the probability of less harmful natural disasters are more frequent. For its distribution trends from the phenomena to match a certain distribution, but from the mathematical theory, it was difficult to get proved.

Conclusions

This paper analyses the natural disaster risks in construction projects, and expect to distinguish the risk factors based on various types of natural disasters by Selection of appropriate methods of analysis that obtain the boundary value of natural risks to define the risk of natural whether or not to constitute a force majeure elements. For the Employer and Contractor, it can be defined clearly the responsibilities and obligations of both parties in a signed construction contract upon the natural results of the analysis. This can reduce unnecessary conflicts and disputes, and benefit to the construction of the project smoothly.

References

[1] B. Liu, M. Tang, Research and development of catastrophe risk assessment models, China Journal of Natural Disasters, 6 (2011) 47-52.

[2] Z. Guo, Y. Sun, Study of natural disasters conditions of contract based on Fidic guidelines, China Construction Economy, 2 (2009) 23-25.

[3] Rudolf Enz, Sigma Catastrophe report (2011), Switzerland: Swiss Reinsurance Ltd Economic Research & Consulting, (2011): 7-19. http://www.swissre.com.

[4] Stuart CURTIS, RTR Bridge Construction Services, Australia, How an Owner can Prevent Falsework Collapses and other Construction Disasters on its Projects by Effective Application of the Project Specification. 3rd Int. Conference on the Concrete Future: 17-19 October (2008). Yantai, China.

[5] S. Dai, Engineering Risk Analysis Techniques, Chemical Industry Press, Beijing, 2007.

[6] Z. Tian, Project Risk Prevention Manual, China Architecture & Building Press, Beijing, 2009.

© (2012) Trans Tech Publications, Switzerland
doi:10.4028/www.scientific.net/AMM.238.562

Discussion on Construction Contract Management

Baoxia Cui

Architectural and Civil Engineering Institute, Inner Mongolia Scientific and Technical University, Baotou Inner Mongolia 014010, China

cuibaoxiapt@yahoo.com.cn

Key Words: construction project, construction, contract management.

Abstract. Construction contract is a code conduct for both the contractor and the outsourcer to abide in the Market Economy environment, as a result, the enforcement and improvement of contracts management becomes essential. By analyzing the issues laying in the construction contracts management and their causes, this paper puts several proposals for enhancing the construction contracts management.

Introduction

Construction contract in the construction project is a natural result of the constant development of market economy. As a legal documents signed by the owner and the contractor, it aims to complete the construction and installation project, to specify mutual rights and obligations and to bind each other's behavior, furthermore, it is also the highest standard code of conduct for the contractor and the outsourcer, where the contractor should accomplish the installation construction project assigned by the owner, while the owner should provide necessary construction conditions according to the contract terms and pay the project money. The enhancement of construction contracts management on one hand is essential for making prediction to the project contracting activity from the perspective of laws, making proposals for avoiding legal risks and improving the company's ability for changes, development and competition, on the other hand, the enhancing of the contract management and increasing of the awareness of self-disciplined contract performance can keep a good order within the construction market. Meanwhile, it poses advantages on several aspects as forming an open, fair and equal competition mechanism, improving the project quality, lowering the project cost and shortening the project period, etc. While under the current situation with an unperfect construction market, still many problems exist in normal implementation and management of the constructing project, the enhancement of construction contract becomes absolutely necessary.

Common Issues in Construction Contract Management and Causes Analysis

In the construction market with an increasingly fierce competition, the contractors are laying too much focus on the contracting business, with a weak contract sense and with a short knowledge of terms and clauses in these construction contracts, which are hidden dangers for the post-project management and claims. Some constructing enterprises have been taught with a good lesson of this fact in the international projects. The major reason can be traced as: the transfer from planned economy to market economy and the un-establishment of market concept fail in providing necessary experience and means for the functioning projects contracting.

The model text for construction contract is not popular among some small and medium projects. Ministry of Construction and the State Administration for Industry and Commerce jointly developed a "model text of Construction Contract" in the year 19911, later in 1999, they revised and improved the model text, aiming to standardize conducts for the contract parties, and maintain the normal economic order within the construction industry. Relying on a good relation with the owners, some contractors are not always in strict accordance with the procedures for specifying the rights and obligations of both parties and neglecting the contents and terms on paper, which causes high hidden contractual risks. The major reason is a short-term view and a severe knowledge lacking in the seriousness of the State Model Text of Construction Contract.

The failed prohibition of "Oral Agreement". A common phenomenon exists in the implementation process of construction project is the "Oral Agreement " for the contractor to meet the requirements from owners' representatives or project supervisors. Agreements accompany contracts in the same constructing project. The formal contact employs Model Text of Construction Contract, while it always a protection against inspection from various management departments instead of the actual conducts basis for both parties. The Supplementary Provisions of the contract or even the Oral Agreement is what they follow. This kind of agreement, which is also known as private contract, would undermine the seriousness of the contract, disturb the normal order for constructing market and would lay hidden dangers for the contract performance. As a result of that, the legal rights of the constructing party would meet obstacles to be guaranteed once the problems occur. The cause of this issue is also the knowledge lack in seriousness of the contract.

A weak attention of the contract management department on the contract signing, resulting in a mere formality of the contract, failing the contract in valid accreditation and anticipatory management and would seldom guide and coordinate the performance of the contract process. The old-fashioned idea deprives them of the anti-risk awareness for the contract.

The construction contract is deviated from the tender documents. Tender documents are basis for signing the construction contract. But in actuality, relying on such an advantage as the buyer's market, some owners would demand some additional terms or make the constructing enterprises for advanced profit concession while excluding the risk lump sum fee, which cause a big deviation of the construction contracts from the tender documents. These issues pose great obstacles to the performance of the construction contracts, such as forcing the construction companies to construct with advanced money, condensing the project duration randomly, compressing the cost while improving the constructing quality,etc. The major reason is the construction teams are in comparative excess, in contrast to the comparatively smaller size and less number of the construction projects, the fierce competition put the contractors in the current inferior position.

Proposals for Improving and Enhancing the Construction Contracts Management

The realization of cost reform, the volume and cost separation and the market pricing are priority for straightening out the correlation between tender management and construction contract management. The project cost of "Economic Standard" is comprehensively complied according to social average production capacity and the market average price of workforce, materials and machines. Different from quota construction and the average price of workforce, materials and machines, this kind of system can maintain for years. Therefore, in the actual construction, a new construction budget will be needed for the medium and small enterprises to compile and to modify the construction design. After achieving the separation of volume and price in the project cost, the only responsibility left for the construction unit in the bidding is to audit project amount calculated directly in accordance with design drawings by the designing unit that agented by investors or owners, and to offer the individual project quotation on the basis of specific conditions of the company, hence realizing the inherent relation between tender management and constructing project management, the consistency between implementation and management is also guaranteed.

Guarantee the Managing Work before Construction Contract Signing. The first thing for a mature construction contract is the careful assessment from the contractor and select those with a comparative high value, with a high bid winning possibility and avoid the target-less bidding in order to improve the bid winning rate and lower the cost. Secondly, the contract assessment will be necessary, to carry out a careful study of the meaning and requirements for each term and work out correct quotation proposals and complete tenders. To those non-standard contracts, to assess the conformity with laws, perfectness, concreteness and operating capacity, with a clear rewarding and punishment standard or not, whether there are solutions for contracts disputes, omissions in terms, with a clear intention of tender documents and with a standardized text format or not.

Popularize the demonstration text for construction contract and tendering documents, with which to standardize the contracts' form of presentation. The construction contract demonstration text is perfecting with the constant standardization of construction market in our country. Owners and

construction enterprises should get more knowledge of contract text, popularize the model text for construction contracts and standardize the demonstration form of contracts, It is bound to change the status of contract management fundamentally, reduce various risks in the contract, improve contract compliance rate, thereby increasing the level of construction site management.

Strengthen the management throughout the contract compliance process, the contractor shall strengthen the dynamic management throughout the mortgage contract performance period to prevent the occurrence of an event. Professional managing people should be set to carry out the contracts managing work, collecting information about the contracts performing situation, searching deviation reasons from the plan and correct timely and switching the risk loss to the minimum size. In addition, project files should be established and important data should be filed in time, providing technical support for claiming and counterclaiming.

Strengthen the contractors and outsourcers for the legal understanding of the contracts, with continuous propaganda, learning and training, making them realize that laws are essential approach for the smooth implementation of construction and protecting each others' rights and interests. They are bridge to reach the scientific management goal in economy market. The legal employment of management means as construction contract supervision and evaluation can decrease or avoid the issues or deviation occurred in construction progress, quality and cost, would avoid the possible contracts disputes, hence the loss resulted from it will be lowered, too.

Importance for Strengthening the Construction Contract Management

Increasingly close relations are bonding between the construction contracts and owners as well as the contractors with the deepening of market economy, which bonds their interests together. The construction contract management will be a core content of project management and the managing conscious as contract performing will be a common standard for restraining the market behavior in construction. To put the contract management into reality, both the contractor and the outsourcer should be equipped with strengthened conscious, the pre-event, in-event and post-event management in the construction contract will be necessary, constant innovation will also be needed for management. The support from law is essential for the law and regulation system that the Socialism Market Economy needs. Strengthen administrative supervising over the contract performing and the legal punishment strength to show deterrent force of the law. Only by this means will the construction contract become an effective approach for project management, hence the quality leap for the construction management can be realized.

References

[1] X. Qu, et.al, Legal System of Construction Contract, China Planning Press, Beijing, 2002.

[2] C. Hu, Management and Claims for Construction Contracts, Southeast University Press, Nanjing, 2001.

[3] C. Hu, Project Contract Management, Architecture & Building Press, Beijing, 2005.

[4] Q. Li, Civil Engineering Contract Management, Southeast University Press, Nanjing, 2003.

[5] Y. Liu, Construction project Tendering and Contract Management, Northern Transportation University Press, Beijing, 2002.

© (2012) Trans Tech Publications, Switzerland
doi:10.4028/www.scientific.net/AMM.238.565

Partner Selection for Partnering Mode Based on Vertical Projection Method

Xiangtian Nie [a] and Jinghai Lan [b]

North China University of Water Resources and Electric Power, Zhengzhou 450011, China

[a] xtnie@126.com, [b] lanjinghai1@163.com

Keywords: partnering mode; partner selection; entropy and vertical projection method.

Abstract. Selecting excellent partnering partners is crucial for project implementation. In view of the drawbacks of traditional methods which only consider the rigid index such as business index, technical data and management data, this paper establishes an evaluation system which considers soft level index and is appropriate for the project of partnering mode. From this system, this paper sets up a comprehensive evaluation mode for partners' selection based on the entropy and vertical projection method. This mode provides a simple and scientific new way for selecting excellent partnering partners.

Introduction

Although the partnering mode is a new project management mode that springs up in the internationality in recent years, it had achieved very great economic and social benefits in engineering practice in Europe and America, Australia, China and other countries. At present, our academic circles give it high hopes, engineering practice fields also have urgent needs to introduce this model. Partnering mode also says partner mode, and is a "Benefit sharing, Risk sharing" cooperation relationship built up on the basis of trust by project participants in order to achieve a common goal. As the cooperation state directly related to the performance of the project operation and its success or failure, how to choose the right partner become a pressing problem to resolve. Two critical questions in partner selection: one is the criterion to evaluate choices, namely how to establish the evaluation index system; another is the research and application of this method.

In recent years, partner selection is a hot research area. For example, Mao gave out the comprehensive evaluation index system of project partner selection, and designed the three-stage model of partner selection [1]; Sun studied the project partner relationship based on virtual organization, put forward the comprehensive evaluation index system of partner selection under partnership cooperation situation [2]; Sun gave out partner selection principles according to the characteristics of engineering project, used AHP to analysis optimization technique, and put forward the partner selection index system exclusive to project management [3]; Tang put forward the evaluation index system and relevancy evaluation method based on the grey relevancy evaluation [4]; Tian and Zhu constructed AHP partner selection model based on entropy weight [5]; Wang and Feng used SPA theory to establish Partnering comprehensive evaluation model, and gave out a specific case to prove [6]; On the basis of the game between the owner and the contractor analysis, according to partnering management mode of partner selection method and combined with our country's actual situation, Ni put forward a new screening mechanism [7].

This paper argues that it is difficult to guarantee the partnering mode project successfully complement that partner selection only based on the bid assessment index and method, so innovation research to current selection index system and method is quite necessary. In the existed research about partnering mode project of partner selection, the construction thought and method is not clear, and the study is not enough, especially on deciding the weight coefficient of each index, a good solution is not given.

Establishment of Partner Selection Index System

Establishment of index system is the basis and foundation towards partner selection. At present, there are kinds of researches about partner selection index system. They are different emphasis, but also have many commons. In view of the drawbacks of traditional methods which only consider the rigid index such as business index, technical data and management data. The paper also considers soft level index-CSF (Critical Success Factors) [8]. In addition, the paper also lessons the construction of the train of thought from the supply chain partners selecting and virtual enterprise partner selection about evaluation index system [9, 10].

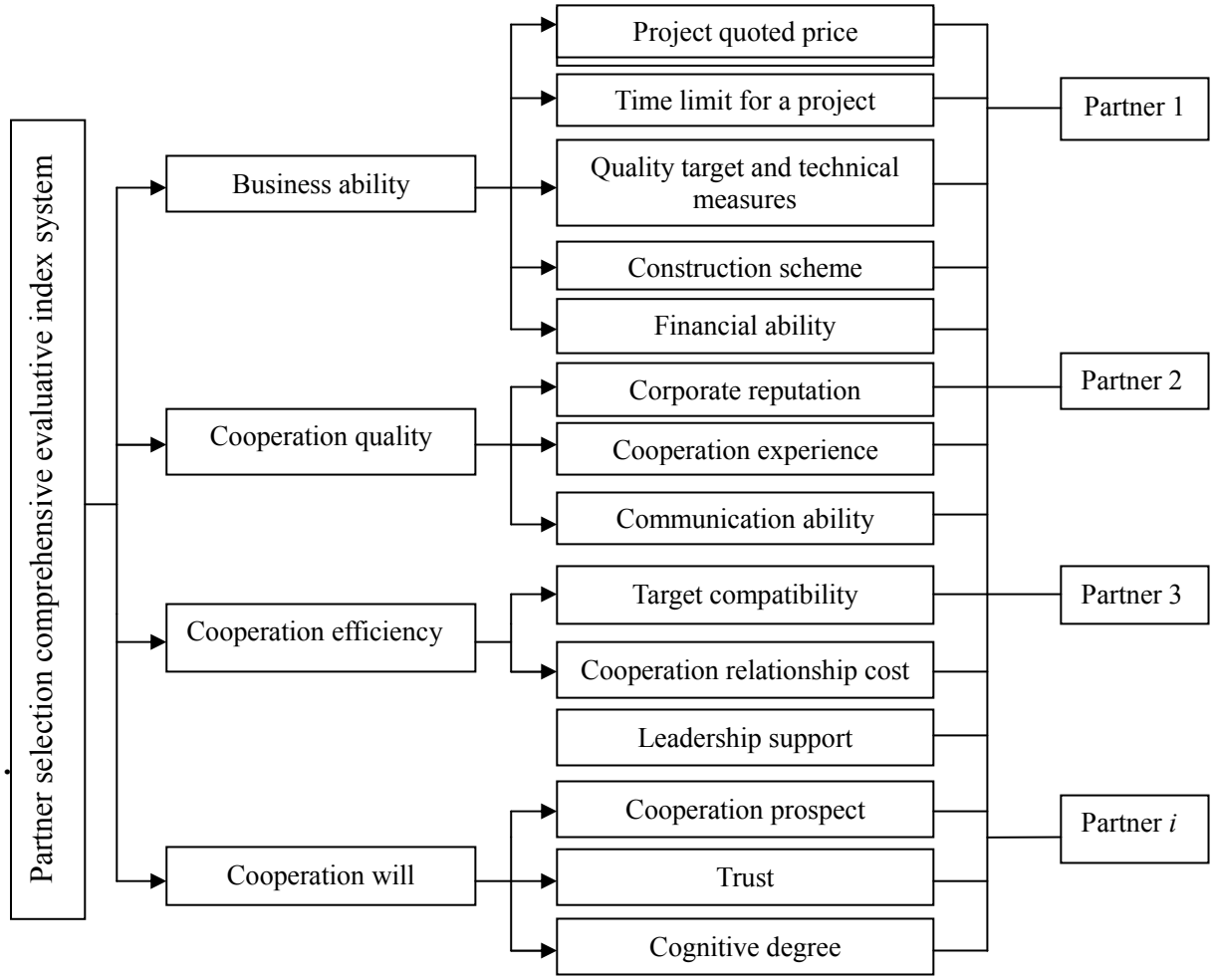


Fig. 1 Partner selection of comprehensive evaluation index system

Weight Design of Partner Selection in Partnering Mode

The process of partner selection may be divided into two stages: partners qualitative coarse screening, quantitative fine screening and confirm.

On the first stage, it requires the run units to provide some basic cooperation information, which including willing of cooperation, top management support, cooperation goal, willing to long-term cooperation, resources, enterprise culture, understanding degree of regulators to partnering project management pattern (understanding or attitude), cooperation experience and so on. This information is the basis and premise of cooperation. The experts make eligible as a candidate entering the second stage.

On the second stage, the candidate units are required to provide construction period, quality, quotation, historical performance, enterprise credit records and other detailed information. As the partner selection choosing relatively the best one of the enterprises from the determining candidate, the boundaries among these optional partners are not absolutely clear but fuzzy.

This article utilizes the Fuzzy Mathematics and Vertical Projection Method based on Entropy in the process of partner selection.

Definition: O is object set with m candidate partners, and then object set is expressed as:

$$O = \{o_1, o_2, o_3, ...o_m\}$$

Where o_i is the i^{th} partner, i=1, 2, …, m.

Each candidate is identified by m index, and the index set can be expressed as:

$U = \{u_1, u_2, u_3, ...u_n\}$

Where u_j is the j^{th} index, j=1, 2, …, n.

Definition: The evaluation matrix is:

$$A = (x_{ij})_{m\times n} = \begin{bmatrix} x_{11} & x_{12} & x_{13} & \cdots & x_{1n} \\ x_{21} & x_{22} & x_{23} & \cdots & x_{2n} \\ x_{31} & x_{32} & x_{33} & \cdots & x_{3n} \\ \cdots & \cdots & \cdots & \cdots & \cdots \\ x_{m1} & x_{m2} & x_{m3} & \cdots & x_{mn} \end{bmatrix}$$

Where x_{ij} is the j^{th} evaluation index of the i^{th} partner; i=1, 2, …, m.j=1, 2, …, n.

Quantitative indexes use the actual physical quantities to measure, these indexes include project quoted price, financial ability and so on. Qualitative indexes are usually decided by expert surveys and set-valued statistics. Set-valued statistics is a promotion of classical statistics and fuzzy statistic. It only requires experts to give these indexes an interval but not a specific value. Firstly, each expert needs to give x_{ij} (Qualitative index) a proper interval.

Definition: $x_{ij}^{l} \in [x_{1ij}^{l}, x_{2ij}^{l}]$ (l=1，2，3… L)

Where x_{ij}^{l} is l^{th} expert's answer interval, x_{1ij}^{l} is the lower limit and x_{2ij}^{l} is the upper limit.

So the fuzzy interval of the qualitative index can be calculated by the following formulas:

$$x_{ij} = \frac{\sum_{l=1}^{L}\left[(x_{2ij}^{l})^2 - (x_{1ij}^{l})^2\right]}{2\sum_{l=1}^{L}\left[x_{2ij}^{l} - x_{1ij}^{l}\right]} \tag{1}$$

At present, there are dozens of methods which have different features to indentify weight. Generally speaking they can be divided into two categories: one is subjective empowerment and the other is objective empowerment.

Because there are dependent relationship between the internal elements from the partner selection index system, and the lower also have a feedback control the upper, the papers decide to use Entropy to sure indexes' weight.

Entropy produced in thermodynamics, and later in information theory it used Entropy to describe the appearance of uncertainties. The Entropy weight calculated from evaluation matrix signifies the relative intensity coefficients of each index in the competition [11].

The weight function of Evaluation index x_{ij} between j^{th} index can be calculated by formulas:

$$p(x_{ij}) = x_{ij} \Big/ \sum_{i=1}^{m} x_{ij} \tag{2}$$

for the Entropy of j^{th} index:

$$e_j = -k\sum_{i=1}^{m} p(x_{ij}) \ln p(x_{ij}) \tag{3}$$

Where $k>0$, $e_j \geq 0$, if each x_{ij} is equal towards the given j, so $p(x_{ij}) = x_{ij} \Big/ \sum_{i=1}^{m} x_{ij} = 1/m$ and e_j reaches a maximum value $e_j = -k\sum_{i=1}^{m} p(x_{ij}) \ln p(x_{ij}) = k \ln m$; if $k = 1/\ln m$, so $0 \leq e_j \leq 1$.

Definition: Difference factor vector $G = (g_1, g_2 ... g_n)$,

$$g_j = 1 - e_j \tag{4}$$

Where g_j reflects a significant degree, the bigger it is the more significant.

Definition: $a_j = b_j \times g_j, j = 1,2,3....n$ (5)

Where a_j means the adjustment weight, b_j means preliminary given weight in advance.

Normalized a_j, $w_j = a_j / \sum_{j=1}^{n} a_j, j = 1,2,3...n$ (6)

Partner Selection Based on Vertical Projection Method

Vertical Projection Method is an improved TOPSIS method, solving the limited programs of multiple objective decision making problems. The basic change is using vertical surface distance instead of Euclidean distance, so as to solve the problems of the traditional TOPSIS method application.

Principle of Vertical Projection Method. As shown in Fig. 2, asumed that A and B are respectively the gotten positive ideal solution and negative ideal solution. The vertical surface distance between point X and point Y refers to the Euclidean distance between two surface (one is through point X ,the other through Y) , and AB is the normal vector of them. Assumed that the points A, B, X and Y correspond to the vectors *a*, *b*, *x* and *y*, the distance between the points of the orthogonal projection of the points X and Y on the straight line *AB* is the seeking the vertical surface distance, which can be calculated by the following formulas:

$$d = \frac{|(a-b)\cdot(x-y)|}{\|a-b\|} \tag{7}$$

Where "·" is Dot product between the vector, "$\| \ \|$" is the bound norm.

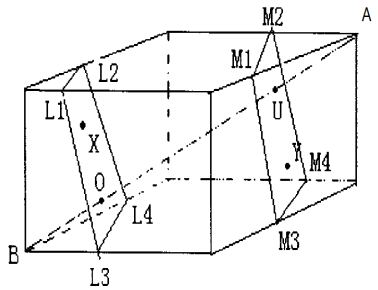


Fig. 2 Principle of Vertical Projection Method

Nature 1: The nearer it is closes to the Positive Ideal Solution, the farther it will be Negative Ideal Solution;

Nature 2: Vertical distance reflects the relative degree of no satisfaction towards the i^{th} partner.

Process of Vertical Projection Method. To eliminate the influence due to difference dimension, it should normalize the evaluation matrix.

Definition: standardization evaluation matrix $V = (v_{ij})$.

$$v_{ij} = x_{ij} \Big/ \sqrt{\sum_{i=1}^{m} x_{ij}^2} \tag{8}$$

Weighted evaluation matrix $R = (r_{ij})_{m\times n}$

Where r_{ij} can be calculated by the following formulas:

$$r_{ij} = v_{ij} \times w_j . \tag{9}$$

Positive Ideal Solution:

$$S^+ = \left\{ S_J^+ \middle| S_J^+ = \max_{1\le i\le m} (r_{ij}) j = 1,2,..., n \right\} \tag{10}$$

Negative Ideal Solution:

$$S^- = \left\{ S_J^- \middle| S_J^- = \min_{1\le i\le m} (r_{ij}) j = 1,2,..., n \right\} \tag{11}$$

In order to simplify the calculation, the paper translates the zero to the point of Positive Ideal Solution,

Namely: $t_{ij} = r_{ij} - s_j^+ .$ (12)

After the translation of the coordinates, the Negative Ideal Solution will be:

$H^- = \{H_J^- | j = 1,2,...n\}$, $H_J^- = t_{kj}$.

Where $|t_{kj}| . \ge |t_{ij}|$, $1 \le k \le m.\ i = 1,2,...m;\ j = 1,2,...n.$

Because the distance between the Positive Ideal Solution and Negative Ideal Solution is constant, it just needs to calculate $|(a-b)\cdot(x-y)|$.So the vertical distance can be simply expressed by the following formulas:

$$P_t = |(a-b)\cdot(a-T_i)| \tag{13}$$

Where a is Zero vector, b is the Negative Ideal Solution H^- after the translation, T_i is i^{th} Row vector of T vector. So the formulas (13) can be further simplified as formulas (14):

$$P_t = |H^- \cdot T_i| = \sum_{j=1}^{n} H_j^- \cdot t_{ij} \tag{14}$$

P_t is the better while it is the smaller.

Example Analysis

Assumed the previous data given by experts about the evaluation index is the following:

Table 1 Evaluation index data tables

b_j={0.097, 0.0979, 0.043, 0.071, 0.077, 0.067, 0.036.0.073, 0.172, 0.056, 0.069, 0.06, 0.072,0.048}

i / j	G_1	G_2	G_3	G_4	G_5
Leadership support	80	60	85	85	60
Cooperation prospect	70	80	80	90	60
Trust	73	64	86	84	74
Cognitive degree	80	90	80	60	60
Corporate reputation	85	80	70	85	85
Cooperation experience	40	60	80	60	30
Communication ability	80	80	75	80	90
Construction scheme	80	80	80	90	70
Project quoted price	2.46	2.30	2.26	2.35	2.45
Quality target and technical measures	80	60	60	80	60
Time limit for a project	520	500	510	510	525
Financial ability	60	70	60	70	40
Target compatibility	60	70	65	65	75
Cooperation relationship cost	80	60	20	60	80

Label □ means qualitative index, calculated by formulas(1).

Positive Ideal Solution:

S^+=[0.047,0.023,0.009,0.038,0.008,0.17,0.004,0.009,0.009,0.021,0.003,0.041,0.008,0.168]

Negative Ideal Solution:

S^-= [-0.014,-0.008,-0.002,-0.013,-0.015,-0.106,-0.001,-0.002, 0,-0.005,0,-0.013,-0.002,-0.126]

According to formulas (1)-(14):

P_1= 0.009267; P_2 =0.010078; P_3 = 0.016296; P_4=0.009996; P_5=0.01198;

Based on the evaluation criteria, we know $P_1<P_4<P_2<P_5<P_3$, so partner 1 is the best.

Conclusions

Choosing the right partner is the key to the success of project. The paper mainly does the following innovations on the process of partner selection.

In view of the drawbacks of traditional methods which only consider Rigid Index such as Business index, Technical data, Management data. The paper also considers soft level index--KSF (Critical Success Factors). In addition, the paper also lessons the construction of the train of thought from the supply chain partners selecting and virtual enterprise partner selection about evaluation index system.

Partner selection process is designed into two stages: partner qualitative preliminary sizing and quantitative fine screening; at the same time in the evaluation matrix, using the quantitative and qualitative analysis.

Using the method of entropy weight for partner selection avoids the usual AHP, but uses TOPSIS Based on the modified-Vertical Projection Method.

The writer believes that this method can provide a simple and scientific new way for selecting excellent partnering partners.

Attached Tables

Table 2 $P(x_{ij})$

i \ j	1	2	3	4	5	6	7	8	9	10	11	12	13	14
G_1	-1.531	-1.692	-1.652	-1.531	-1.561	-1.910	-1.622	-1.609	-1.570	-1.447	-1.598	-1.609	-1.720	-1.322
G_2	-1.819	-1.558	-1.784	-1.411	-1.625	-1.504	-1.622	-1.609	-1.637	-1.735	-1.635	-1.455	-1.566	-1.609
G_3	-1.471	-1.558	-1.488	-1.531	-1.755	-1.216	-1.686	-1.609	-1.655	-1.732	-1.615	-1.609	-1.640	-2.718
G_4	-1.471	-1.444	-1.512	-1.819	-1.561	-1.504	-1.622	-1.492	-1.610	-1.447	-1.615	-1.455	-1.640	-1.609
G_5	-1.819	-1.846	-1.639	-1.819	-1.561	-2.189	-1.510	-1.743	-1.574	-1.732	-1.586	-2.010	-1.497	-1.322

Table 3 $\ln P(x_{ij})$

i \ j	1	2	3	4	5	6	7	8	9	10	11	12	13	14
G_1	0.216	0.184	0.192	0.216	0.210	0.148	0.198	0.200	0.208	0.235	0.202	0.200	0.179	0.267
G_2	0.162	0.211	0.168	0.244	0.197	0.222	0.198	0.200	0.195	0.176	0.195	0.233	0.209	0.200
G_3	0.230	0.211	0.226	0.216	0.173	0.296	0.185	0.200	0.191	0.177	0.199	0.200	0.194	0.066
G_4	0.230	0.236	0.220	0.162	0.210	0.222	0.198	0.225	0.199	0.235	0.199	0.233	0.194	0.200
G_5	0.162	0.158	0.194	0.162	0.210	0.112	0.221	0.175	0.207	0.177	0.205	0.134	0.224	0.267

Table 4 $P(x_{ij}) \ln P(x_{ij})$

i \ j	1	2	3	4	5	6	7	8	9	10	11	12	13	14
G_1	-0.331	-0.312	-0.317	-0.331	-0.328	-0.283	-0.320	-0.322	-0.327	-0.340	-0.323	-0.322	-0.308	-0.352
G_2	-0.295	-0.328	-0.300	-0.344	-0.320	-0.334	-0.320	-0.322	-0.319	-0.306	-0.319	-0.340	-0.327	-0.322
G_3	-0.338	-0.328	-0.336	-0.331	-0.303	-0.360	-0.312	-0.322	-0.316	-0.306	-0.321	-0.322	-0.318	-0.179
G_4	-0.338	-0.341	-0.333	-0.295	-0.328	-0.334	-0.320	-0.336	-0.320	-0.340	-0.321	-0.340	-0.318	-0.322
G_5	-0.295	-0.291	-0.318	-0.295	-0.328	-0.245	-0.334	-0.305	-0.326	-0.306	-0.325	-0.269	-0.335	-0.352
∑	-1.597	-1.600	-1.604	-1.596	-1.606	-1.557	-1.607	-1.606	-1.608	-1.600	-1.609	-1.592	-1.607	-1.528

Table 5 e_f, g_f, a_j, w_j

J \ index	0.097	0.059	0.043	0.071	0.077	0.067	0.036	0.073	0.172	0.056	0.069	0.06	0.072	0.048
	1	2	3	4	5	6	7	8	9	10	11	12	13	14
e_f	0.992	0.994	0.997	0.992	0.998	0.967	0.998	0.998	0.999	0.994	0.999	0.989	0.998	0.949
g_f	0.008	0.006	0.003	0.008	0.002	0.033	0.002	0.002	0.001	0.006	0.001	0.011	0.002	0.051
a_j	0.0008	0.0003	0.0001	0.0006	0.0001	0.0022	0.0001	0.0001	0.0002	0.0003	0.0000	0.0006	0.0001	0.0024
w_j	0.093	0.043	0.018	0.071	0.018	0.270	0.008	0.018	0.020	0.041	0.006	0.079	0.016	0.299

Table 6 The normalized processing results

Normalized	1	2	3	4	5	6	7	8	9	10	11	12	13	14
G_1	0.478	0.408	0.426	0.477	0.468	0.315	0.441	0.446	0.465	0.521	0.453	0.440	0.399	0.560
G_2	0.358	0.467	0.374	0.537	0.441	0.473	0.441	0.446	0.435	0.391	0.436	0.513	0.466	0.420
G_3	0.508	0.467	0.502	0.477	0.385	0.630	0.413	0.446	0.427	0.391	0.445	0.440	0.433	0.140
G_4	0.508	0.525	0.490	0.358	0.468	0.473	0.441	0.502	0.444	0.521	0.445	0.513	0.433	0.420
G_5	0.358	0.350	0.432	0.358	0.468	0.236	0.496	0.390	0.463	0.391	0.458	0.293	0.499	0.560

Table 7 Weighted evaluation matrix data tables

Weight	1	2	3	4	5	6	7	8	9	10	11	12	13	14
G_1	0.044	0.018	0.008	0.034	0.008	0.085	0.004	0.008	0.009	0.021	0.003	0.035	0.006	0.168
G_2	0.033	0.020	0.007	0.038	0.008	0.127	0.004	0.008	0.009	0.016	0.003	0.041	0.007	0.126
G_3	0.047	0.020	0.009	0.034	0.007	0.170	0.003	0.008	0.009	0.016	0.003	0.035	0.007	0.042
G_4	0.047	0.023	0.009	0.025	0.008	0.127	0.004	0.009	0.009	0.021	0.003	0.041	0.007	0.126
G_5	0.033	0.015	0.008	0.025	0.008	0.064	0.004	0.007	0.009	0.016	0.003	0.023	0.008	0.168

Table 8 Translation matrix T

T_{ij}	1	2	3	4	5	6	7	8	9	10	11	12	13	14
G_1	-0.003	-0.005	-0.001	-0.004	0.000	-0.085	0.000	-0.001	0.000	0.000	0.000	-0.006	-0.002	0.000
G_2	-0.014	-0.003	-0.002	0.000	0.000	-0.043	0.000	-0.001	0.000	-0.005	0.000	0.000	-0.001	-0.042
G_3	0.000	-0.003	0.000	-0.004	-0.015	0.000	-0.001	-0.001	0.000	-0.005	0.000	-0.006	-0.001	-0.126
G_4	0.000	0.000	0.000	-0.013	0.000	-0.043	0.000	0.000	0.000	0.000	0.000	0.000	-0.001	-0.042
G_5	-0.014	-0.008	-0.001	-0.013	0.000	-0.106	0.000	-0.002	0.000	-0.005	0.000	-0.018	0.000	0.000

Table 9 Vertical distance P_t

P_t	1	2	3	4	5	6	7	8	9	10	11	12	13	14	∑
G_1	3.53E-5	4.3E-5	2.3E-6	5.5E-5	0	0.00901	4.7E-7	2.4E-6	0	-6E-7	0	8E-5	3.3E-6	3.4E-5	0.009267
G_2	1.91E-4	2.28E-5	4.3E-6	-7E-8	0	0.00451	4.7E-7	2.4E-6	0	2.6E-5	0	4.8E-6	1.2E-6	0.00532	0.010078
G_3	-3.6E-6	2.28E-5	-5E-7	5.5E-5	2.2E-4	3.9E-6	6.9E-7	2.4E-6	0	2.6E-5	0	8E-5	2.2E-6	0.01588	0.016296
G_4	-3.6E-6	2.69E-6	-4E-8	1.6E-4	0	0.00451	4.7E-7	4E-7	0	-6E-7	0	4.8E-6	2.2E-6	0.00532	0.009996
G_5	1.91E-4	6.31E-5	2.1E-6	1.6E-4	0	0.01126	3.2E-8	4.3E-6	0	2.6E-5	0	2.3E-4	1.1E-7	3.4E-5	0.01198

References

[1] Y. Mao. The Research of Partnering Mode, Southwest Jiao tong University, 2004.

[2] H. Sun, Virtual Organization Based Partnering of Construction Projects, Tianjin University, 2006.

[3] L. Sun, Research on partner selection based on partnering mode, Nonferrous Metal Design, 2 (2007) 63-70.

[4] Q. Tang, Based on the relevance of grey partnering partnership choice, Chinese and Overseas Architecture, 7 (2008) 135-137.

[5] H. Tian, Z. Zhu, Partner selection based on partnering mode. Project Management Technology, 4 (2010) 18-23.

[6] L. Wang, D. Feng, Partner selection for partnering mode based on Set Pair analysis, Journal of Engineering Management, 4 (2010) 424-427.

[7] X. Ni, Partnering partner selection mechanism based on partnering mode. Shanxi Architecture, 31 (2010) 21-23.

[8] L. Zhang, Engineering project management key success factors analysis of partnering mode, Market Modernization, 2010.

[9] M. Nie, Hierarchy variable weight decision-making in the selection of supply chains cooperators, Systems Engineering–Theory and Practice, 3 (2006) 38-41.

[10] J. Chen, Y. Wang, Study on processes and methods of partner selection in virtual organization, Systems Engineering–Theory and Practice, 7 (2001) 48-53.

[11] B. Wang, Entropy and Information, Northwestern University Press, Xi'an, 1994.

[12] X. Hua, J. Tan, Revised TOPSIS method based on Vertical Projection Distance-Vertical Projection Method, Systems Engineering–Theory and Practice, 1 (2004) 114-119.

© (2012) Trans Tech Publications, Switzerland
doi:10.4028/www.scientific.net/AMM.238.572

Design and Analysis of a Light-weight Steel Gabled Frames Structure

Wenfeng Du [a], Zhifei Sun [b], Hui Zhang [c] and Fudong Yu [d]

College of Civil Engineering and Architecture, Henan University, Kaifeng 475004, China

[a]dwf@henu.edu.cn, [b] sunzhifei88@126.com, [c] hedazhanghui@163.com, [d] vipyfd@163.com

Keywords: gabled frame, suspended loads, optimization of column spacing.

Abstract. This paper, based on the practical engineering of the steel structure of Henan Shangpin food Co. LTD, introduces the design of a light-weight steel structure with three-span gabled frames, and discusses the solution of the large suspended loads. By taking the steel quantity as the target, the depth calculations and statistical analysis of the reasonable value of the column spacing were carried out. The results show that the large suspended loads should be imposed in the form of live load. When the column spacing is about 8m, the steel quantity is the lowest.

Introduction

The length of the steel structure belonging to Henan Shangpin food Co. LTD is 168m and its total width is 72m. The major structure adopts the light-weight steel structure with three-span gabled frames along the direction of the width. The span is 24m and the frame spacing is 6m. There are 29 frames in total. The top of a pillar is 8m high and the slope of the roof is 1:10. The architectural appearance is shown in Fig.1. The materials are steel Q345B.

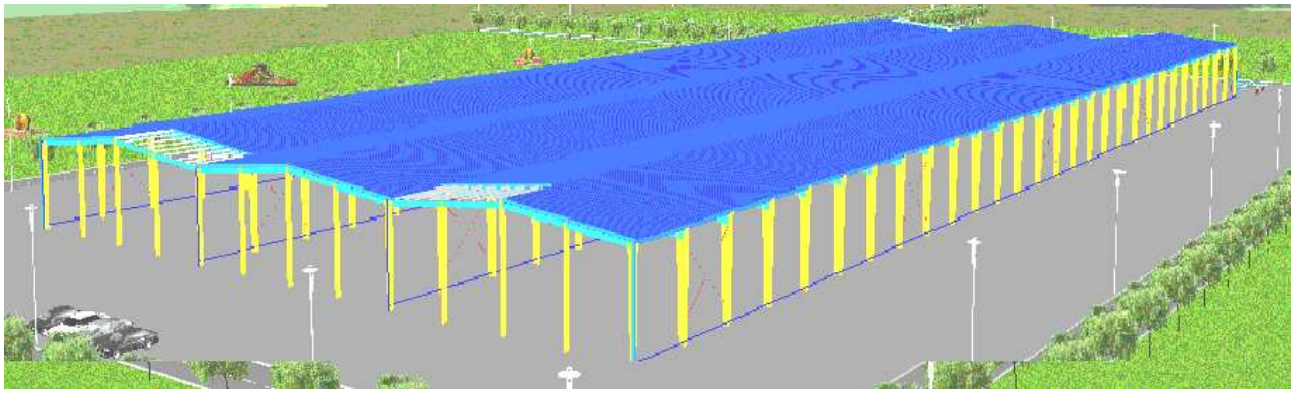


Fig. 1 Picture of architectural appearance

Layout of the Structure

Under the condition of satisfying the functional requirements, the gabled frames have better economic benefits than other structures, such as trusses, arches, and concrete frames. So it is decided to adopt the gabled frames. The frames at the edge with wind resistant pillars are defined as Frame1 and the internal frames are defined as Frame2. The exterior walls of the plant are brick masonry with thickness 240mm and the roof is colored rock wool plate. The spacing of continuous purlin is 1.5m and each purlin is designed as single span members with the section C180 x 70 × 20 x 2.0mm. In the middle of each purlin there is a strutting piece and the strutting piece is round steel bars with the diameter of 10mm. Moreover, the angle L56×4, called knee-bracing is set at the connection of every purlin and the beam of corresponding gabled frame. To make the strutting piece form an integrated fixed system, the batter braces and rigid poles are set at the fastigium and cornice [1-5].

To ensure the stability of the whole structure, the level supports are set in the roof. The level supports are cross round steel bars with the diameter 20mm, hinged to the gabled frames. At the location that sets level supports, vertical supports are set at the same time. The vertical supports are also cross round steel bars with the diameter of 20mm [6, 7].

Analysis of Loads

Use the software STS to carry on the calculation of the gabled frames. Beside of the self-weight of the structure, following loads are included [8-10]:

The dead load: 0.42kN/m²;
The live load: 0.3 kN/m²;
The reference wind pressure: 0.4 kN/m²;
The reference snow pressure: 0.45 kN/m²;
The temperature difference is ±30°C;

According to the Code for Seismic Design of Buildings, the earthquake effect is needn't to be calculated. There is no crane in the plant, but other equipment need to be fixed on the gabled frames, which causes a load of 1.57 kN/m^2.

Design of the Structure

The sections of the columns and beams are H section. The height of the sections is variable, as shown in Fig. 2 and Fig. 3. The changes of the sections are fit to the changes of the bending moment. Thus it can save steel and be easy to transport.

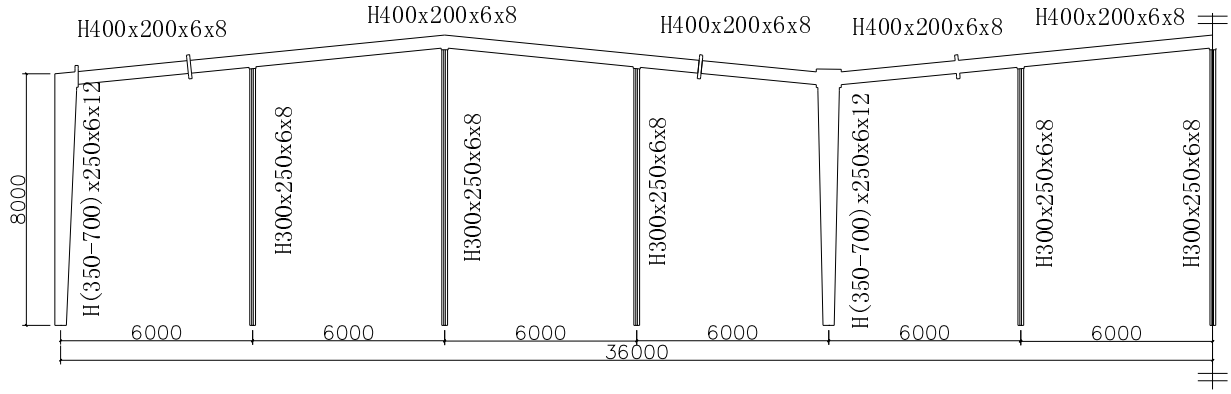


Fig. 2 The elevation of the frame1

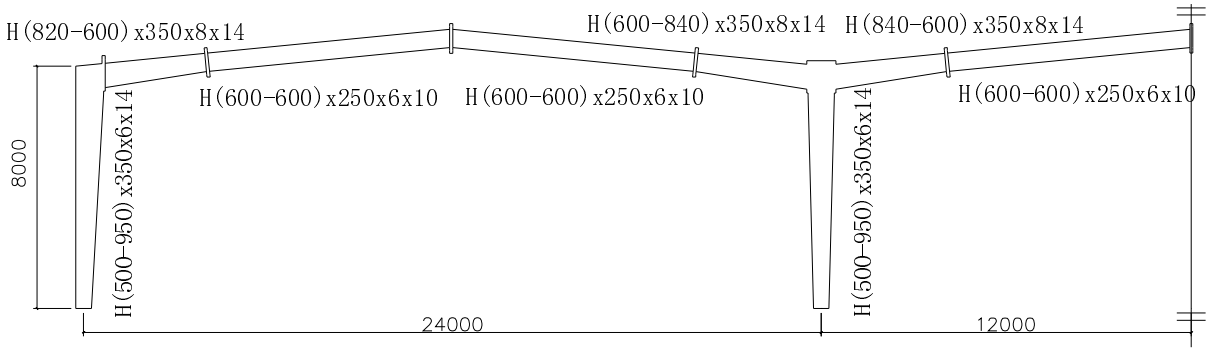


Fig. 3 The elevation of the frame2

The columns are hinged on the foundations. If they are fixed on the foundations, the steel quantity of the beams and columns will be reduced. But the columns will transmit large moment (shown in Table 1) to the foundations, thus the independent foundations will be very large. If the connections are hinged, the columns only transmit axial force and shear to the foundations, thus the independent foundation will be small.

Analysis of the Suspended Load

The total steel quantity is about 29kg/m² after calculation, which is larger than similar projects. It is due to the large suspended load applied on the structure. If there is no suspended load, the total steel quantity is 19Kg/m², which is almost the same as similar projects. It shows that the suspended load has a great impact on the steel quantity.

At present there are two kinds of methods to apply the suspended load. The first one is applying the suspended load as a kind of live load and the second one is applying the suspended load as a kind of dead load. In this project, two kinds of methods are used separately. When the suspended load is applied as live load, the section size of the columns and beams is larger, thus the structure tends to be safe. This is because that the subentry coefficient of the live load is larger than the dead load. In this project there are some equipments, such as the mobile shelves, their locations are not fixed. It is better to apply the suspended load as live load.

Table 1 Reactions when the columns are fixed or hinged on the foundations

fixed on the foundations			hinged on the foundations		
Moment(kNm)	Axial force(kN)	Shear(kN)	Moment(kNm)	Axial force(kN)	Shear(kN)
3.17 (max)	32.13	0.62	0(max)	46.23	-12.34
- 432.78(min)	201.95	-150.02	0(min)	46.23	-12.34
- 432.78	201.95(max)	-150.02	0	201.73(max)	-98.77
3.17	32.13(min)	0.62	0	29.04(min)	4.43
- 432.78	201.95	-150(max)	0	29.04	4.43(max)
3.17	32.13	0.62(min)	0	195.77	-99.0(min)

Optimization of the Column Spaces

When the spaces of gabled frames increase, the numbers of gabled frames decrease, but the steel quantity of other members, such as the purlins, increase. When the space of the gabled frames decrease, the number of gabled frames increases, while the steel quantity of other members, such as the purlins, decrease. So that there is an optimal spacing of the gabled frames to make the total steel quantity achieve the minimum value. In this paper, the optimization design of the structure is carried out to get the reasonable space of gabled frames. Fig.5 shows the relationship between the steel quantity and the spaces.

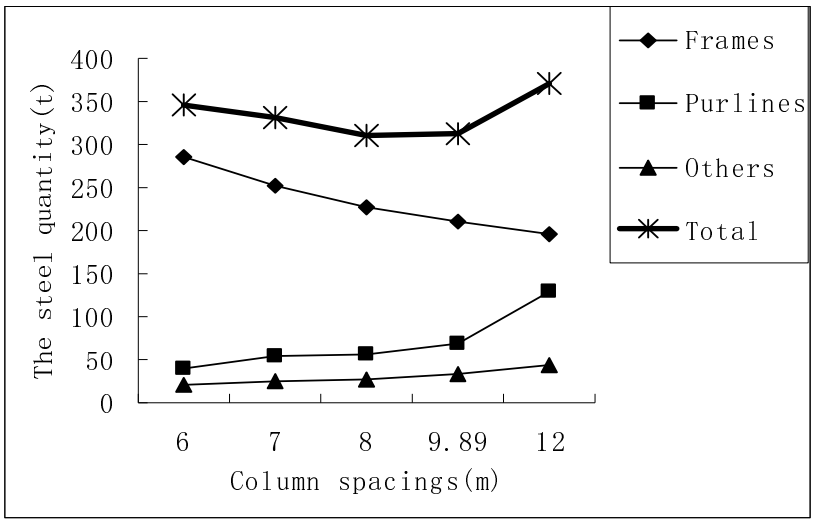


Fig.5 Relationship between the steel quantity and the spaces

From the Fig.5, it can be concluded that when the space of gabled frames is between 8 and 9.89m, the steel quantity is minimum. It is in accordance with the conclusions from documents. Fig.5 shows that as the space increases, the amount of steel of the main frames is gradually decreased, but when the space increases to a certain value, the decrease of the amount of steel is flattened.

The amount of steel of the purlins increases due to the increase of the purlin span, resulting in the cross-sections of the purlins to be larger. The amount of steel of other components increases. But it has little impact on the total amount of steel of the structure. For the total amount of steel, with the spacing increasing, it is first decreased and then increased.

The reasonable value of space only applies to this type of portal frame structure, for other types of structure, further calculation is needed.

Conclusions

This paper introduces the design of a light-weight steel structure with three-span gabled frames, and discusses the solution of the large suspended loads. Following conclusions can be obtained.

(1) For the large-span gabled frames, it should adopt the variable sections according to the changes of moment. Thus it can reduce the weight of the frames and be easy to transport.

(2) For this kind of gabled frames, the connections between columns and foundations are fit to be hinged, because it can reduce the foundations effectively.

(3) When the space is between 8 and 9.89m, it can gain good economic benefits.

References

[1] S. Dong, Y. Zhao, The future and prospect of latticed shell structures, Spatial Structures, 1 (2004) 3-10.

[2] S. Dong, Development and prospect of long-span space structures, Spatial Structures, 6 (2000) 3-13.

[3] Chinese Code JGJ 7-91, Design and Construction of Shell Structures Code, China Building Industry Press, Beijing, 1991.

[4] S. Dong, H. Deng, A simple computation method of prestressed space truss and its global process pretensioning analysis, Journal of Building Structures, 22 (2001) 18-22.

[5] S. Dong, X. Zhuo, Y. Zhou, One-time pretensioning analysis method for prestressed space truss, Journal of Zhejiang University (Engineering Science), 37 (2003) 629-633.

[6] W. Du, L. Zhu, H. Zhang, Study on static stability and the limited load carrying capacity of Vierendeel latticed shells, Journal of Zhengzhou University (Engineering Science), 29 (2008) 99-102.

[7] F. Guan, B. Gao, L. Li, Stability analysis of single-layer latticed shell, Engineering Mechanics, 13 (1996) 93-104.

[8] Chinese Code GB50009-2002, Load Code for Design of Building Structures, China Building Industry Press, Beijing, 2002.

[9] Chinese Code CECS102:2002, Technical Specification for Steel Structure of Light-weight Buildings with Gabled Frames, China Plan Press, Beijing, 2002.

[10] Chinese Code GB50011-2010, Code for Seismic Design of Buildings, China Building Industry Press, Beijing, 2010.

© (2012) Trans Tech Publications, Switzerland
doi:10.4028/www.scientific.net/AMM.238.576

Research on Secondary Stress for Steel-pipe Truss under the Influence of Geometric Parameters

Hui Wang

North China University of Water Resources and Electric Power, Zhengzhou 450011, China

897672585@qq.com

Key words: steel-pipe truss; secondary stress; geometric parameter; chord member; web member.

Abstract. Based on FEA software ANSYS, 26 steel-pipe truss models with hinge joints or rigid joints are presented, the distributions of total structure secondary stress are analysed under the influences of the mechenical behavior of total structure. The results indicate that the secondary stresses on several links have reached the certain value, and changed regularly following the change of geometric parameters. These changes should be considered in engineering design.

Introduction

Due to the concise configuration and wide application fields, the tube truss structure frequently appeares in trestle, industrial workshop, stadium, TV tower and so on. Truss systems are under complex stresses. To simplify the calculation, the truss nodes are usually asuumed hinged, and only the axial forces of members are considered [1-2]. But the ideal hinge hypothesis is different from the true truss node stress. Under the influences of welding, node board and other factors, both the axial force and the bending moment exist in the truss poles. The moment is scondary internal force. Reference [3] regulation: when the ratio of section height to internode length is more than 1/12 for main pipe, or 1/24 for branch pipe, the secondary stress should be calculated.

With large finite element software ANSYS and 26 simply-supported steel-pipe truss models [4], the impacts on scondary stress such as the secondary stress distribution, the ratio of scondary stress to normal stress and the geometrical parameters are discussed [5-6].

The Finite Element Model

The transverse concentrated forces are imposed on the upper chord joints, the two ending points are $p/2$=60kN and the middle joints are p=60kN. The calculation model and related geometric dimensions are shown in table 1 and Fig. 1.

Researches are focused on the relationship between the following five dimensional parameters and the truss stress: (1) the ratio of truss height and span; (2) the ratio of web member width and chord member width; (3) the ratio of web member wall thickness and chord wall thickness; (4) the ratio of chord rod wide and wall thickness; (5) the ratio of web member wide and wall thickness. Geometrical parameter groups can be seen from Table 2.

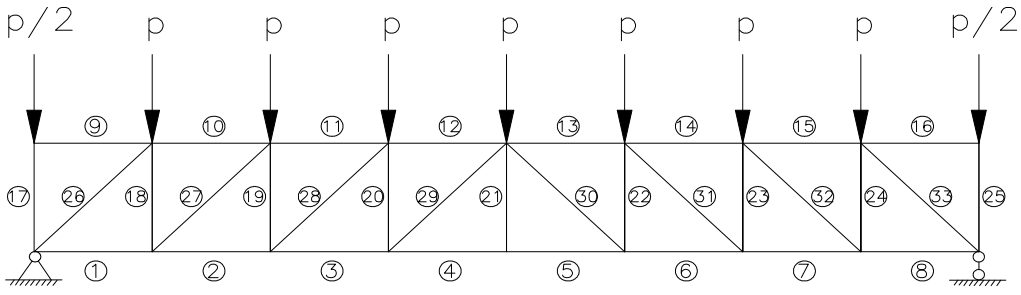


Fig. 1 Simple truss calculation model

2-D and 3-D models are respectively established with *link*1 element and *shell*188 element, which can monitor the hinge joints and the joints with certain stiffness.

Table 1 Truss geometrical dimension

No. of model	Truss geometrical dimension [m]	Specification of chord and support vertical member [mm]	Specification of web member [mm]	No. of model	Truss geometrical dimension [m]	Specification of chord and support vertical member [mm]	Specification of web member [mm]
1	3×8×1.8	200×200×8	150×150×6	8	3×8×2.4	240×240×8	150×150×6
2	3×8×2.4	200×200×8	150×150×6	9	3×8×2.4	200×200×8	150×150×5
3	3×8×3.0	200×200×8	150×150×6	10	3×8×2.4	200×200×8	150×150×8
4	3×8×3.6	200×200×8	150×150×6	11	3×8×2.4	200×200×6	150×150×6
5	3×8×2.4	200×200×8	60×60×6	12	3×8×2.4	200×200×10	150×150×6
6	3×8×2.4	200×200×8	100×100×6	13	3×8×2.4	200×200×12	150×150×6
7	3×8×2.4	180×180×8	150×150×6				

Note: Truss geometrical dimension=internode length×node numbers×truss height

Table 2 Truss geometrical parameter

No. parameter group	No. model	Geometrical parameter	No. parameter group	No. model	Geometrical parameter
1.1	1	$\lambda=1/13.3$	3.6	12	$\beta_{2-2}=0.6$
1.2	2	$\lambda=1/10$	3.7	13	$\beta_{2-2}=0.5$
1.3	3	$\lambda=1/8$	4.1	11	$\gamma_{1-1}=33.3$
1.4	4	$\lambda=1/6.7$	4.2	2	$\gamma_{1-1}=25$
2.1	5	$\beta_{1-1}=0.3$	4.3	12	$\gamma_{1-1}=20$
2.2	6	$\beta_{1-1}=0.5$	4.4	13	$\gamma_{1-1}=16.7$
2.3	2	$\beta_{1-1}=0.75$	4.5	7	$\gamma_{1-2}=22.5$
2.4	7	$\beta_{1-2}=0.83$	4.6	2	$\gamma_{1-2}=25$
2.5	2	$\beta_{1-2}=0.75$	4.7	8	$\gamma_{1-2}=30$
2.6	8	$\beta_{1-2}=0.625$	5.1	5	$\gamma_{2-1}=10$
3.1	9	$\beta_{2-1}=0.625$	5.2	6	$\gamma_{2-1}=16.7$
3.2	2	$\beta_{2-1}=0.75$	5.3	2	$\gamma_{2-1}=25$
3.3	10	$\beta_{2-1}=1$	5.4	9	$\gamma_{2-2}=30$
3.4	11	$\beta_{2-2}=1$	5.5	2	$\gamma_{2-2}=25$
3.5	2	$\beta_{2-2}=0.75$	5.6	10	$\gamma_{2-2}=18.75$

Calculation Results and Analysis

The Secondary Stress Distribution. The geometrical parameters of No.2 model are adopted, that is: span of 24m, 2.4m high, internode length of 3m, 200×200×8 for chord and support vertical member, 150×150×6 for web member, and Q235 steel. The models are seperately set with two types of units, and the axial force and stress values are compared in Table 3.

N_2/N_1: From Table 3, in addition to individual menbers, the value of N_2/N_1 are nearly between 85% and 100% .The axial force values of actual truss are slightly less than those of ideal truss and the difference is small.

σ_c/σ_z: From the second internode near the truss support to midspan, σ_c/σ_z has a descending trend. The bottom chord values are lower than 20%,but the top chord and inclined web member values are close to 50%, meanwhile,straight web member values have volatility and are more than 100%.

So one can see, the secondary stress influence degree is big in some ideal truss members where the axial forces are small; conversely, the secondary stresses are relatively small at about 10% in those members who have larger axial force. The above trend complies with the structural

arrangement form: The shorter the distance between member and support, the larger the secondary stress is because the pole deformation is prone to be contained by support constraints; And in mid-span truss, the bearing constraint influence is the least, so corresponding secondary stress is lesser also.

Table 3 Comparison of member axial force and stress

No. of member	N_2/N_1	σ_c/σ_z	No. of member	N_2/N_1	σ_c/σ_z	No. of member	N_2/N_1	σ_c/σ_z
1	87.06%	101.10%	11	87.06%	21.71%	26	90.34%	14.99%
2	93.46%	18.02%	12	95.12%	9.49%	27	97.75%	44.99%
3	94.76%	15.40%	18	85.31%	116.95%	28	95.65%	30.66%
4	95.35%	10.32%	19	96.28%	108.98%	29	98.40%	33.25%
9	4.90E+13	5.01E+14	20	92.34%	172.80%			
10	89.79%	50.42%	21	0	0			

Note: N_1 and N_2 are member axial forces for models with *link*1 unit and *shell* 181 unit. σ_c and σ_z are member axial stress and bending stress (i.e. secondary stress) for the two former.

Geometric Parameter Effect Analysis. With reference to the above method and based on the geometric parameters in Table 2, 13 trusses with *link*1 unit and the other 13 trusses with *shell*181 unit are established. Then the σ_c/σ_z of each member is expressed with bar charts, so as to analyze the geometric parameter effection effection on menber secondary stress.

Ratio of Truss Height and Span λ. In Fig. 3, from model 1 to 4, λ increases gradually, but the σ_c/σ_z decline basically, but the values of the chords and inclined menbers at the end of the truss have certain fluctuations. The lower is the truss height is, the bigger is the member bending moment and the secondary stress.

As the rise of the structure height increases, its whole stiffness increases too. Under the similar load, vertical and horizontal displacements of the truss wouldreduce, chord bending moment and secondary stress would decrase significantly. Because the web members play more important role in the whole structure, the secondary stress in some internodes will increase with λ increasing, but basically within 30%.

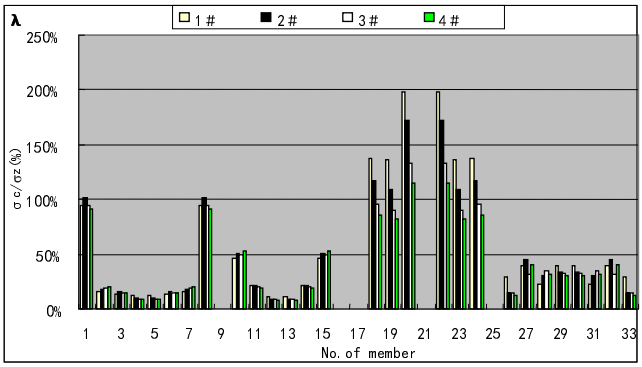


Fig.3 The effect of λ on σ_c/σ_z

Ratio of Web Member Width and Chord Member Width β_1. (1) Change the web member width: model 5, 6 and 2 (Fig. 4), parameter $\beta_{1\text{-}1}$;

(2) Change the chord member width: model 8, 2 and 7 (Fig. 5), parameter $\beta_{1\text{-}2}$.

Along with the increase of β_1, σ_c/σ_z decreases gradually.The values of most lnclined web members are more than 60%, which explains that when β_1 is too small,the web member would be influenced sigmificantly. When the Chord rod width is up to 240mm, σ_c/σ_z in most inclined web members will be higher than 60% and then this truss will be seriously affected by secondary stress.

In conclusion, when there is large stiffness difference between chord and web member, such as the former for 240mm wide or the latter for 60mm wide, the structure stress would be seriously influenced. Because right now the stiffness distribution of each pole is ununiform, the flexibility of large cross-section component is small and those poles are prone to bend. So the too small β_1 should be avoided to reduce section differences, the values above 0.75 are appropriate.

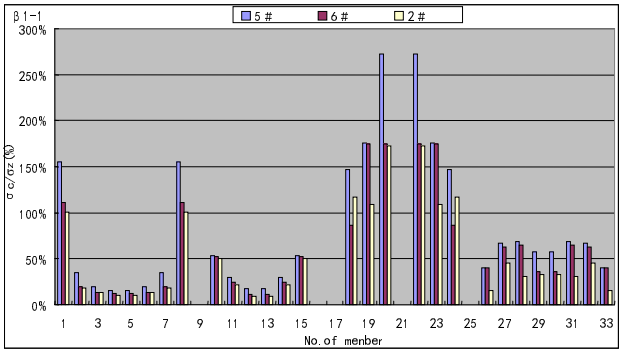


Fig.4 The effect of $\beta_{1\text{-}1}$ on σ_c/σ_z

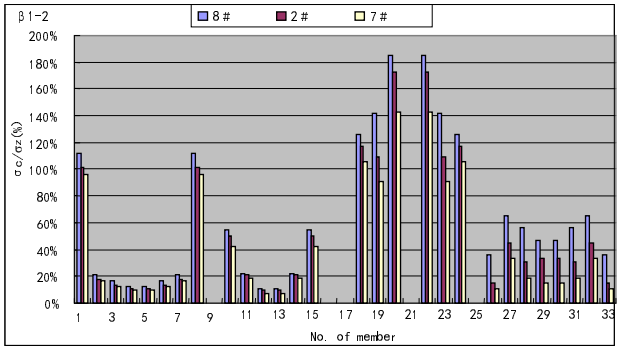


Fig. 5 The effect of $\beta_{1\text{-}2}$ on σ_c/σ_z

Ratio of Web Member Wall Thickness and Chord Wall Thickness β_2. (1) Change the web member wall thickness :model 9,2 and 10(Fig.6), parameter $\beta_{2\text{-}1}$;

(2) Change the chord member wall thickness: model 13, 12, 2 and 11 (Fig. 7), parameter $\beta_{2\text{-}1}$.

With the increase of β_2, σ_c/σ_z in the chords and straight web members decline. There is certan fluctuation in inclined web members and even some poles present rising. The reason lies in the increasing member section area and stiffness. The inclined web member gradually takes more moment. The sections of chord and web member are gradually close through improving the β_2 value, meanwhile the section stiffness differences are reduced and secondary moment value falls, which is beneficial to the whole structure.

By comparing the analysis results of 2.2.2 and 2.2.3, along with the change of the member width, σ_c/σ_z almost rise and fall between 20% and 65%.While the thickness changes, the value nearly concentrates in the range of 20% to 40% except model 8 (up to 80%). It shows that the change of the member width is more important than that of wall thickness.

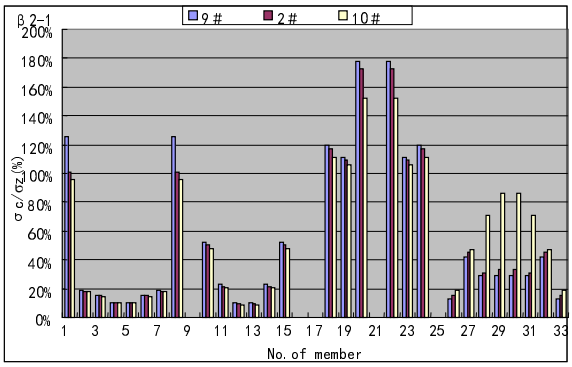


Fig. 6 The effect of $\beta_{2\text{-}1}$ on σ_c/σ_z

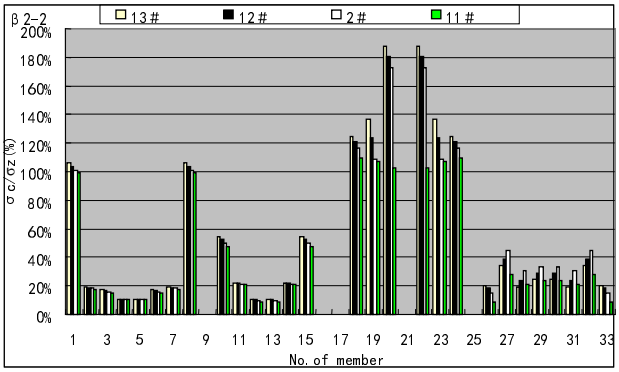


Fig. 7 The effect of $\beta_{2\text{-}2}$ on σ_c/σ_z

Ratio of Chord Member Width and Wall Thickness γ_1. (1) Change the chord member wall thickness: model 13, 12, 2 and 11 (Fig. 7), parameter $\gamma_{1\text{-}1}$.

With the rise of γ_1, σ_c/σ_z overall drops, when the chord and web member wall are both 6mm thick, the secondary stress is the smallest.

(2) Change the chord member width: model 8, 2 and 7 (Fig. 5), parameter $\gamma_{1\text{-}2}$.

With the decrease of the member width, besides the fluctuation in the inclined web members σ_c/σ_z of most member reduces basically. When the chord and web member wall are both 8mm thick, the secondary stress is the smallest.

Ratio of Web Member Width and Wall Thickness γ_2. (1) Change the web member width: model 5, 6 and 2 (Fig. 4), parameter $\gamma_{2\text{-}1}$;

With the rise of γ_2, σ_c/σ_z overall drops. When the chord member wdith reaches 150mm, the secondary stress is the smallest.

(2) Change the web member wall thickness: model 9, 2 and 10 (Fig. 6), parameter $\gamma_{2\text{-}2}$;

With the decrease of γ_2, σ_c/σ_z basically drops too, besides the fluctuation in the inclined web memebers σ_c/σ_z of most members reduces basically except the rise of all inclined web members. When the chord and web member wall are both 8mm thick, the secondary stress is the smallest.

Comprehensively, only when the width or the wall thickness of chord and web member are similar, the component stiffness spreads evenly, and the secondary stress has little influnce on the members.

Conclusions

The member axial force with shell element is slightly below those with link element, the difference is less than 15%.

The σ_c/σ_z is large in those poles with small axial stress; instead, the value is relatively small in those large axial stress poles. Therefore, the support poles need to be strengthened support in design.

The width or wall thickness between chord and web members should be close so as to increase the stiffness distribution uniformity and improve the bearing capacity of components.

Pole width changes have large effect on the structure stress and is the main factor affecting secondary stress factors. When selecting components section, the ratio of web member width and chord width should be controlled more than 75% as far as possible.

References

[1] J. A. Packer, J. E. Henderson, J. J. Cao, Design Guidelines for Hollow Tube Structure Connection, Science Press, Beijing, 1997.

[2] F. Zhang, X. Liu, Structural design of welded square steel pipe trusses, Steel Structure, 16 (2001): 41-45.

[3] GB50017-2003, Code for design of steel structure, China Planning Press, Beijing, 2002.

[4] H. Wang, Finite element analysis on secondary stress for square steel-pipe truss, Wuhan University, Wuhan, 2005.

[5] Y. Li, D. Yang, Joint rigidity and secondary stress analyses on H-section steel truss, China Water Transport, 9 (2009) 248-251.

[6] Y. Bao, P. Lu, Analysis of the secondary stress of welded parallel-chord steel trusses, Journal of Wuhan Institute of Chemical Technology, 25 (2003) 22-24.

© (2012) Trans Tech Publications, Switzerland
doi:10.4028/www.scientific.net/AMM.238.581

Comparative Study on the Design Schemes of Residential Steel Structure

Yongchun Xu[a] and Zhongping Tang[b]

Zhejiang Business Technology Institute, Department of Building and Art, Ningbo 315012, China

[a]xuyongchun@zjbti.net.cn, [b]tzp@zjbti.net.cn(corresponding author)

Keywords: square steel tube, H sections, residential steel structure, model analysis, economic and technology analysis, anti-seismic.

Abstract. This paper choses a duplex apartment which is six floors steel structure as the research object, on the ground of the same building size, with the same beam & tie rod, and the same material for the floor ground & wall plate, two structure system schemes are designed respectively using the H sections and square steel tube as the form of pillar section. The calculate model are made respectively applying the FEA software. From the model graph, natural frequency, economic and technology and other index, the following conclusions are given out comparing the two schemes: the multi floor residential building of light steel structure with square steel tube and H sections is feasible in seismic performance, the steel consumption of the square steel tube system is lower than the H sections system. The square steel tube system is superior to the H sections system in interior decoration and utilizing construction area.

Introduction

The steel structure residential compared with the traditional reinforced concrete and brick structure building, it have more merits, such as: high strength, light quality, good performance on wind resistance & anti seismic, simply in processing, short working period, and can protcet environmental protection. So people pay more and more attentions to this structure. Now, the normal residential system with steel structure mainly have H sections support with light steel enclosure skeleton system(H+H skeleton system), square steel tube column and H section beam skeleton system(E+H skeleton system), square column and U steel beam skeleton system(E+U skeleton system), C steel column support with light steel enclosure skeleton system(C+C skeleton system), whole light steel keel skeleton system and so on[1].This paper chose a six floors duplex apartment as the research object, design the H+H skeleton system and E+H skeleton system respectively, then compared them.

Project Overview

There is a six floors duplex apartment with steel structure system, the storey height is 5.4m, the total height for the building is 32. 4m.The first floor is 5 hinged steel frame, the bay is 6m, the depth is 9m, the whole plane size is 24m×9m; the second-sixth floor are three hinged frame, the whole plane size is 12m×9m, and the 3D steel frame model as Fig. 1 shown. To reach a better technology and economic benefit, after learned from the node research results of literature [1,2], the writer get this steel frame structures' design schemes as table1 shown. The floorboard used the OSB board with 18mm thick, and pouring 50mm fine stone concrete on it; the wall plate used 12mm OSB composite wall in both side.

Table.1 The design data for a steel structure apartment

	frame column	beam	pull rod	steel grade
Scheme 1	H200×200×8×12	H200×150×7×10	φ60	Q235
Scheme 2	□250×250×6	H200×150×7×10	φ60	Q235

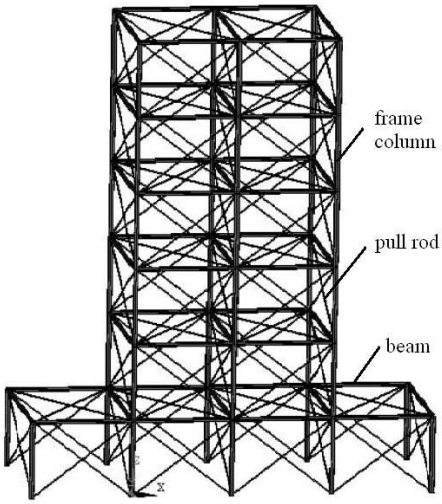


Fig. 1 The 3D shown of a steel structure apartment

Modal Analysis Comparison

The so-called modal, is a math expressing way for the natural vibration characteristic of the building steel frame structure, including natural frequency and model of vibration. Based on the premise of linear system, transform the physical system into modal space according to the principle of linear superposition, make the complicated vibration system decoupling, arrange them again according to the discretion of the vibration frequency, then express the vibration problem with a set of mutual independence modal, and each stage modal have its' special natural frequency and modal vibration model [3]. The aim of the modal analysis is to identify the system's modal parameter, and provide reference to the structures' dynamic characteristic research and to avoid structure resonance.

ANSYS Software is a good large general finite element software in effectively analysis of structure modal. This paper applies ANSYS 12.0 to comparison analysis the scheme 1 and scheme 2.

Set Model and Solving. (1) Material characteristic: E_X=2.05×10^{5}N/mm^2, poisson ratio υ=0.3; convert the quality of ground floor and wall plate to the quality of main frame, the density for the scheme 1: ρ_1=24.18×10^{-9}t/mm^3, the density for the scheme 2: ρ_2=24.54×10^{-9}t/mm^3.

(2) Element characteristic: The main frame and the beam use the "Beam 188" unit, the tie rod use the "Link8" unit.

(3) Model input: Through APDL command stream, set a bar model, input the corresponding parameter of section property through "Preprocessor"-"Sections"-"Beam".

(4) Constraints: Put constraints on the ten column bottom of the frame (ALL DOF); the modal calculate needn't impose loads, the structure's quality is calculated automatically by the ANSYS according to the density which had input.

(5) Solving: Enter into ANSYS solver, chose the analysis type "Modal", then chose the solving way "Full"; chose the "Analysis Options"-"Analysis Options" under the "Analysis Type", and set the modal number and the extension modal number as 14; click the "Solve-Current LS" to solve.

Modal Figure Comparison. From the calculate result of the ANSYS FEA, we can get that:

The Scheme 1（H type steel）and the Scheme 2（square tube steel）almost have the same modal figure and the direction of the displacement deformation.

In the first four modal figure, the first deformation from the *x-z* planar to the – *x* direction, the second deformation from the *x-z* planar to the + *x* direction, the third deformation from the *y-z* planar to the - *y* direction, the third deformation from the *y-z* planar to the + *y* direction, the after modal figures' are all rotation or compound deformation.. Then we take the scheme 2's first four modal figures as example to explain.

Nature Frequency Comparison Analysis. The scheme1 (H type steel) and the scheme 2 (square tube steel) almost have the same nature frequency with the first fourteen orders, very few in numerical, as shown in Fig. 6.

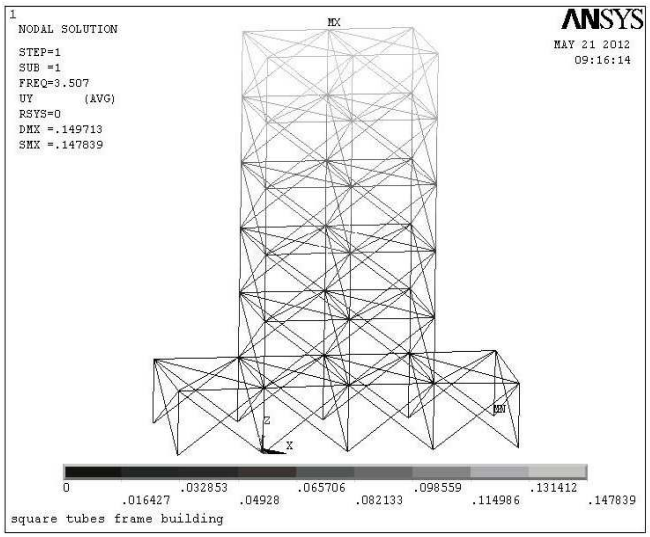


Fig. 2 The first modal of scheme 2

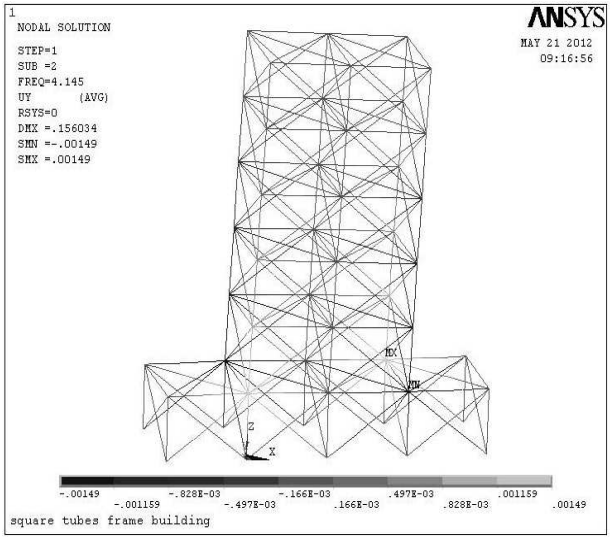


Fig. 3 The second modal of scheme 2

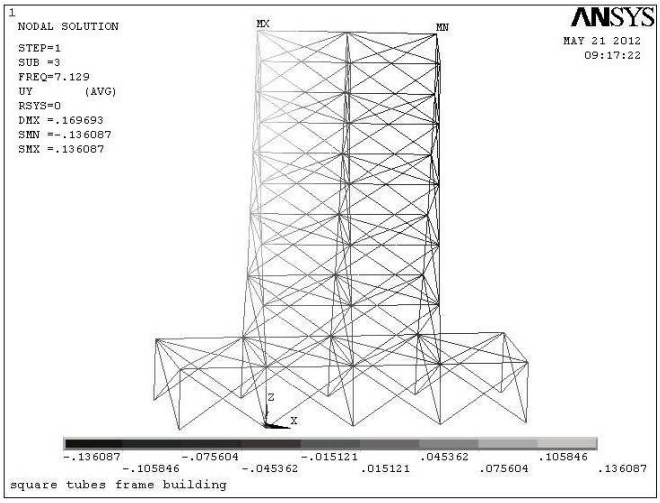


Fig. 4 The third modal of scheme 2

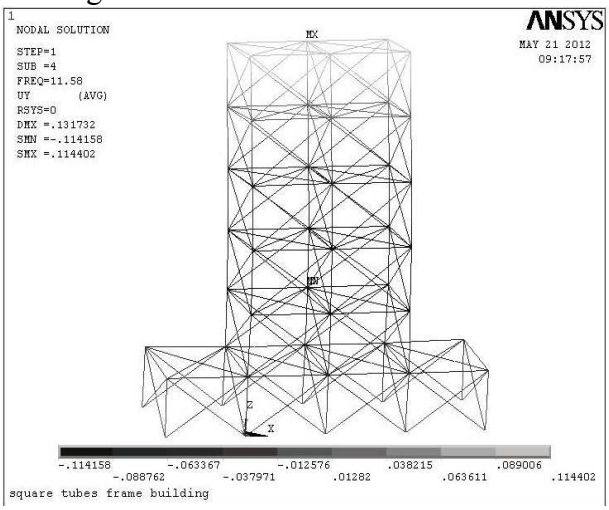


Fig. 5 The fourth modal of scheme 2

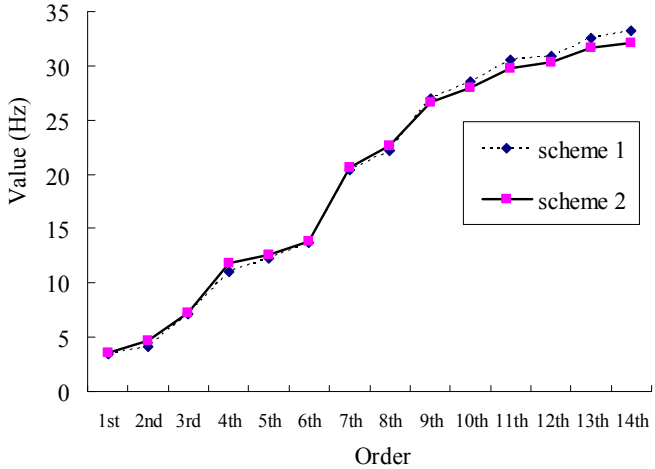


Fig. 6 Natural frequency comparison for the scheme 1 and scheme 2

Seem from the whole, for the first eight natural frequency, the scheme 2（square tube steel）is just above the scheme 1,but for the after six natural frequency, the scheme 1 is higher than the scheme 2.

From the first two order main frequency which largely influence the structure's vibration, the first order natural frequency of the scheme 1（H type steel）is 3.5836Hz，the second order natural frequency is 4.7011 Hz；the first order natural frequency of the Scheme 2 （square tube steel）is 3.5072Hz，the second order natural frequency is 4.145Hz，the frequency of these two scheme is almost the same, and will not easy to occur resonate under the effects of normal dynamic load.

Economic and Technology Comparison

Economic Comparison. As the above two scheme apply the same building size, same steel grade, and the same section of the beam and pull rod, just the section of the frame column is differ, so the economic index analysis mainly analysis the economic index of the frame column.

Through the calculate, we can get the steel consumption ,the scheme 1 is 10.526t, and the scheme 2 is 9.930t, the scheme 2 can save steel around 5.7%. And as checked the price information from main steel market in china in May 2012, we can know the price is almost same for these two type steel. So we can get the project price of the frame column will save 5%~8% for the scheme 2.

Technology Comparison. Seem from the section characteristic, with the same axis inertia , the section characteristic and the carrying capacity is close to for the two axis of square tube steel, and the shape is regular, Compared to the H-type steel, this steel is more convenient in the interior and exterior decoration construction.

Seem from the processing, compared to the square steel, for the H-type steel, the blanking need more accurate, the require of the flatness for the boards of the girder ends is more higher, and is more hard to lifting.

Conclusions

As the multi floor residential steel structure, the light steel structure which using the square steel tube and the H sections as the column, is feasible in seismic performance, will not easy to occur resonate.

Compared to the scheme 2, for the square steel tube structure, the steel consumption is lower than the H-type steel structure, and it is superior in the interior decoration and the usage of the construction area.

Acknowledgements

The research is partially supported by Education Bureau Scientific Research Project of Zhejiang Province in China (Y201119998).

References

[1] Y. Shi, Study on the Seismic Performance of the Cold Bending Thin-walled Steel Residence under the Horizontal Earthquake, Ph. D Thesis of Chang-an University, 2000.

[2] L.g Zhou, Y. Xu, Z. Cai, Experimental study on the behavior of rigid joint for multi floor steel frame beam and concrete filled steel tubular framed structures, China Water Transport, 8 (2008) 51-59.

[3] S. Liang, C. Chen, H. Yin. Electric Spindle Modal Analysis Based on the Finite Element Method, 34 (2012) 57-60.

[4] L. Wei, ANSYS application example in civil engineering, China Water Conservancy and Electricity Press, Beijing, 2007.

© (2012) Trans Tech Publications, Switzerland
doi:10.4028/www.scientific.net/AMM.238.585

Wind-induced Response Analysis of Steel Tower Structure

Chunfeng Wan[1,a], Jiang Wang[2,b], Hong Zhu[1,c], Lei Huang[1,d],
Hao Wang[1,e] and Zhaodong Xu[1,f]

[1] International Institute for Urban systems Engineering & School of Civil Engineering, Southeast University, Nanjing 210096, China

[2] Anhui Electric Power Research Institute, Hefei 230601, China

[a]chunfengwan@gmail.com, [b]jiangw75@163.com, [c]seuzhuhong@gmail.com,

[d]huang1210lei@126.com, [e]whzjn@sina.com, [f]zhdxu@163.com

Keywords: wind load; AR model; wind-induced response; time series analysis; tower structure.

Abstract. In this paper, autoregressive (AR) method is firstly introduced to simulate wind speed time series. The agreement of the simulated wind speed spectrum to the target spectrum is verified. A 42m-high steel tower subjected to wind load is analyzed using ANSYS. Through modal analysis, it can be found that the first several modes of the structure are all translational vibration modes. Torsional vibration modes and local vibration modes appear from the 3th order mode. Meanwhile, time history analysis is applied to analyze the structural response. Results show that, under wind loads, the steel tower has large stresses in the chords which have abrupt section area change.

Introduction

Steel tower structures become common nowadays, and are applied widely in many areas, such as communication, electricity transmission, etc. Among which, wireless communication tower is a typical example due to the fact that wireless industry infrastructures are intensively constructed. Even though most of them are fairly small and usually are put on the top of the buildings, some of them, however, are fairly big and very tall. Considering the safety of the structures, dynamic response analysis is necessary.

These kinds of structures belong to the high-rise structures since their longitudinal sizes are usually much larger than the vertical ones. Wind load is the main reason for structural vibration and lateral displacement. The wind load includes mean wind load and fluctuating wind load along the wind direction, and the wind whirlpool interference at the vertical direction of the wind. The mean wind load can be regarded as the static load. However, since the natural period of the fluctuating wind is close to the natural period of such structure, it usually results in large vibration along the wind direction. In order to well study the dynamic characteristics under wind loads, wind-induced response analysis is required. In this paper, dynamic characteristics of a steel communication tower subjected to wind loads will be studied in detail.

Fluctuating Wind Speed Simulation

For wind-induced response analysis in time domain, time series signals of the fluctuating wind speeds at all key nodes should be obtained at first. At present, two methods are often used, that is, harmony superposition method and linear filtering method. Harmony superposition method is simple but accurate, and could be used for any stable Gaussian stochastic process. But it is limited to only one dimension [1]. Linear filtering method is also called White Noise Filtration Method. In which Auto-Regressive (AR) method is a popular one, with its advantage of the simplicity and fast calculation speed, and therefore widely used [2]. In this paper, AR method is used to simulate time series of fluctuating wind speeds at nodes of the steel tower structure.

The AR model of M special coherent fluctuating wind speeds $V(X, Y, Z, t)$ can be described as

$$V(X,Y,Z,t) = -\sum_{k=1}^{p} \Psi_k V(X,Y,Z,t-k\Delta t) + N(t) \tag{1}$$

Where $X=\{x_1,\cdots,x_M\}$, $Y=\{y_1,\cdots,y_M\}$, $Z=\{z_1,\cdots,z_M\}$, in which $\{x_i,y_i,z_i\}^T$ is the coordinate of the ith node (i=1,$\cdots$,M); p is the model order, Δt is the time step, Ψ_k is the autoregressive coefficient matrix; N(t) is M dimensional Gaussian distributed stochastic process vector whose mean is zero and covariance matrix is R_N. For convenience, $V(X, Y, Z, t)$ is simplified to be written as $V(t)$.

Multiplying Eq. 1 by $V^T(t)$ and then taking the expectations yields

$$V(t+j\Delta t)V^T(t) = -\sum_{k=1}^{p} \Psi_k V(t+j\Delta t-k\Delta t)V^T(t) + N(t)V^T(t) \tag{2}$$

From which we can get the expectations as

$$R_V(j\Delta t) = -\sum_{k=1}^{p} \Psi_k R_V[(j-k)\Delta t] \quad j=1,\cdots,p \tag{3}$$

$$R_V(0) = -\sum_{k=1}^{p} \Psi_k R_V(k\Delta t) + R_N \tag{4}$$

Eq. 3 and Eq. 4 can be written as：

$$R \cdot \Psi = \begin{bmatrix} R_N \\ O_p \end{bmatrix} \tag{5}$$

Where elements of R can be obtained by

$$R_V^{ij}(m\Delta t) = \int_0^{\infty} S_{ij}(n)\cos(2\pi n \cdot m\Delta t)dn \quad i,j=1,\cdots M; m=1,\cdots p \tag{6}$$

Where $S_{ij}(n)$ is the power spectrum density of the wind. Here, Davenport spectrum is applied.

From Eq. 5, Ψ and R_N can be obtained. Cholesky decomposition of R_N yields:

$$R_N = L \times L^T \tag{7}$$

Then $N(t)$ can be calculated as

$$N(t) = L \cdot n(t) \tag{8}$$

Where $n(t)=\{n_1(t), n_2(t), \ldots, n_M(t)\}$, here $n_i(t)$ is a Gaussian distributed stochastic process

Substitute of Ψ and N(t) into Eq. 1 and regard initial wind speed as 0 yields the wind speeds

$$V_i(j\Delta t) = \sum_{k=1}^{p} \psi_{ik} V_1[(j-k)\Delta t] + N_i(j\Delta t) \quad (i=1,2\cdots,M) \tag{9}$$

Wind-load Calculation

The wind pressure at the ith node is

$$w_i(t) = \frac{1}{2}\rho v_i(t)^2 \tag{10}$$

Where v_i(t) is the wind speed and is composed by average speed $\overline{v_i}$ and fluctuating speed $\tilde{v}_i(t)$. Considering that average wind speed is always much larger than fluctuating speed, Eq. 10 can be

$$w_i(t) = \frac{1}{2}\rho[\overline{v_i} + \tilde{v}_i(t)]^2 \approx \frac{1}{2}\rho\overline{v_i}^2 + \rho\overline{v_i}\tilde{v}_i(t) \tag{11}$$

According to the Chinese load code [3], the load on the node can be calculated as

$$\overline{F_i} = \mu_{si}\mu_{zi}A_i w_0 \tag{12}$$

$$\tilde{F}_i(t) = 2\overline{F_i}\frac{\tilde{v}_i(t)}{\overline{v}_i} \tag{13}$$

Where $\overline{F_i}$ is the mean wind load and $\tilde{F}_i(t)$ is the fluctuating wind load, μ_{si} is the shape coefficient, μ_{zi} is altitude variation coefficient, A_i is the area of the node and $w_0$is the basic wind pressure.

Simulations

In this paper, a steel communication tower in Jiangsu Province of China was used for the prototype. The tower is totally 42 meters high with 7 sections and made of Q235 steel. Its principal members are simulated using beam element while web members are simulated using link element. The tower is fixed at the base platform. ANSYS is used to model the structure and make the time series analysis. Fig.1 shows the three dimensional model. To simplify the problem, the top maintaining platforms are simulated as the equivalent loads on the structure. Fig.2 shows the computational model. Wind load shown in Fig.2 contains the fluctuating load and the mean wind load as well. Fluctuating wind speeds are simulated using MATLAB. Fig.3 shows the time history of the simulated fluctuating wind speed at the top node. The spectrum is found to agree with the target spectrum. In this paper, considering the fact that the tower is not very high, the Davenport spectrum is applied for the target spectrum.

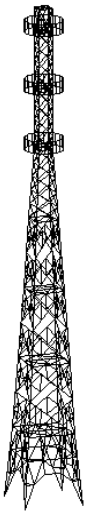


Fig. 1 Tower model

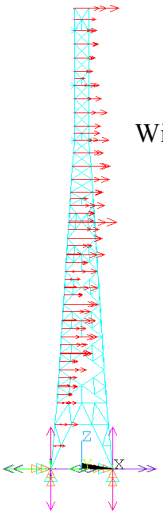


Fig. 2 Computational model

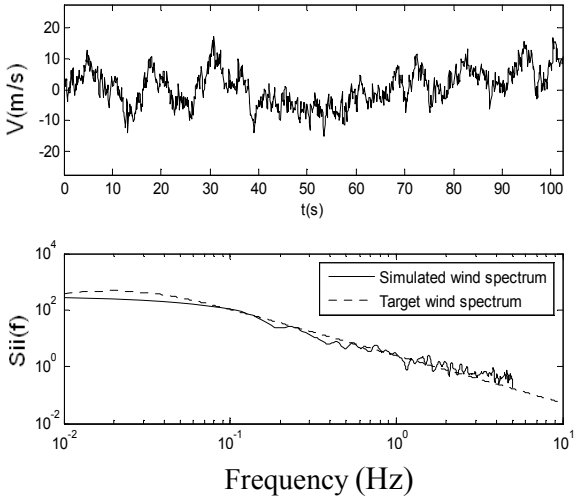


Fig. 3 Simulated fluctuating wind speed time series

At first the natural frequencies and modes are calculated by ANSYS. The natural frequencies and modes for first 4 orders are listed in Table 1. It is shown that for modes of first two orders, they have both x and y direction modes, and the frequencies at the two direction for each order is very close, because of the structural symmetry at these two directions. From the 3rd order, torsion modes and local vibration modes appear. The first two *x* direction modes can be seen in Fig.4.

Table1 Natural frequencies and mode types

Order	Frequency (Hz)	Mode type
1st	2.6576	Translational mode (*x*)
	2.6582	Translational mode (*y*)
2nd	7.5206	Translational mode (*x*)
	7.5523	Translational mode (*y*)
3rd	12.085	Torsional & translational mode
4th	12.405	Local vibration mode

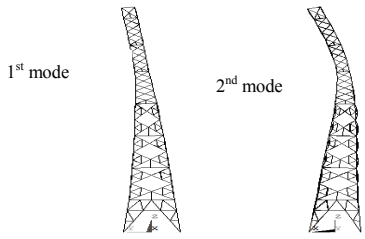


Fig. 4 The first two modes (*x*)

Fig. 5 shows the element force cloud figure, where force of each element is indicated. Meanwhile Fig.6 shows the stress of each element. Both the force and stress have the effects of both fluctuating wind and mean wind. It can be found that for the element forces, the maximum force is at the downside chord. However, due to the change of the section area of the structure and also the element, the maximum stress is at the chord (No.24 as shown in Fig. 6) where the section area changes.

Fig. 7 and Fig. 8 shows the time series of the vertical displacement and acceleration respectively at the top node. It is found that the max vertical displacement reaches about 200mm, about 0.5% of the tower height. It is also found that the time series of acceleration value are roughly symmetrical to zero, while for displacement, there is no such phenomenon. It shows average wind has little effect on the acceleration, but will have large effect on displacement.

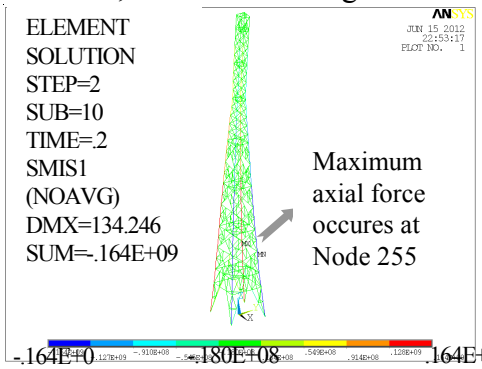


Fig. 5 Element force cloud figure.

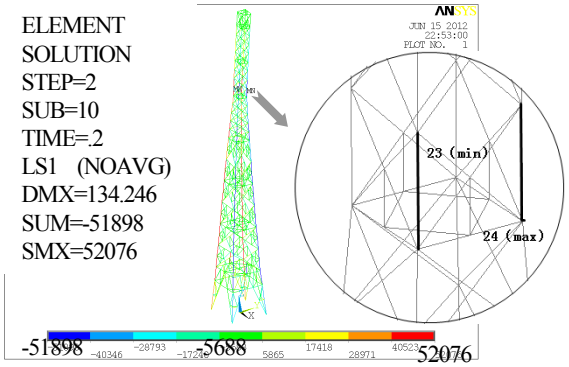


Fig. 6 Stress cloud figure.

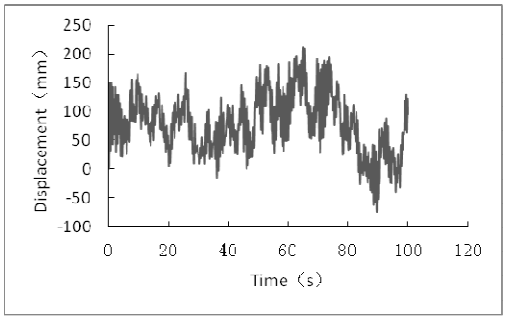


Fig. 7 Displacement at the top node

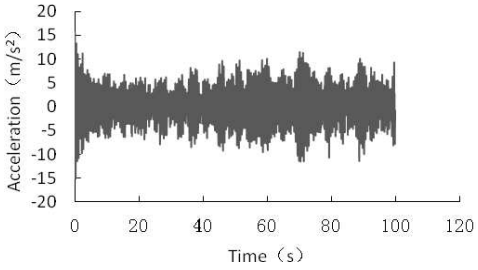


Fig. 8 Acceleration at the top node

Conclusions

Wind-induced vibration analysis is very important for steel tower structures. In this paper the time series of fluctuating wind loads are simulated according to the Davenport wind speed spectrum. ANSYS is used to make the modal and time series analysis. Result shows the basic modes are traslational modes, while torsional and local vibration modes also exsit. In the structure, elements have maximum axial forces at the downside chords. However, due to the change of the Cross-section area of the chords, maximum stress actually happens at the places where maintaining platform locates.

Acknowledgements

This work is supported by the National Key Technology Research and Development Program of the Ministry of Science and Technology of China (2011BAK02B03), the Project Funded by the Priority Academic Program Development of Jiangsu Higher Education Institutions (PAPD), the National Natural Science Foundation of China (50908045 & 50908046) and Doctoral Fund of Ministry of Education of China (6205000009).

References

[1] M. Shinozuka, Simulation of multivariate and multidimensional random process, Journal of the Acoustical Society of America, 49 (1971) 357-368.
[2] Y. Iwatani, Simulation of multidimensional wind fluctuations having any arbitrary power spectra and cross spectra, Wind Engineering, 11 (1982) 5-18.
[3] GB 50009-2001, Load Code for the Design of Building Structures, Beijing, 2006.
[4] GBJ 135-90, Code for Design of Highrise Structure, Beijing, 1991.
[5] B. Huang, Structure Wind Resisting Principal and Application, Tongji University Press, Shanghai, 2001.

© (2012) Trans Tech Publications, Switzerland
doi:10.4028/www.scientific.net/AMM.238.589

Research on Ultimate Bearing Capacity of Single-layer Cylinder Latticed Shells Considering the Influence of *P-δ* Effect

Wenfeng Du [a], Zhiyong Zhou [b] and Pei Zhu [c]

College of Civil Engineering and Architecture, Henan University, Kaifeng 475004, China

[a]dwf@henu.edu.cn, [b] zzy569@163.com, [c] 365662511@qq.com,

Keywords: single-layer cylinder latticed shell; ultimate bearing capacity; *P-δ* effect; multi-element simulation method.

Abstract. The ultimate bearing capacity of the single-layer cylinder latticed shell structure, calculated without considering the single-member instability(P-δ effect), was not consistent to the actual value of ultimate bearing capacity in practice. The ultimate bearing capacity of the single-layer cylinder latticed shell structure was studied in detail by proposing a method of multi-element simulation, considering the member instability. The value of the ultimate bearing capacity decreased by 1.2% after considering the member instability taking a single-layer latticed shell structure with a 40m span as example. The analysis results show that the value of ultimate bearing capacity is tiny affected for the single-layer cylinder latticed shell structure with a small span and high rise-span ratio.

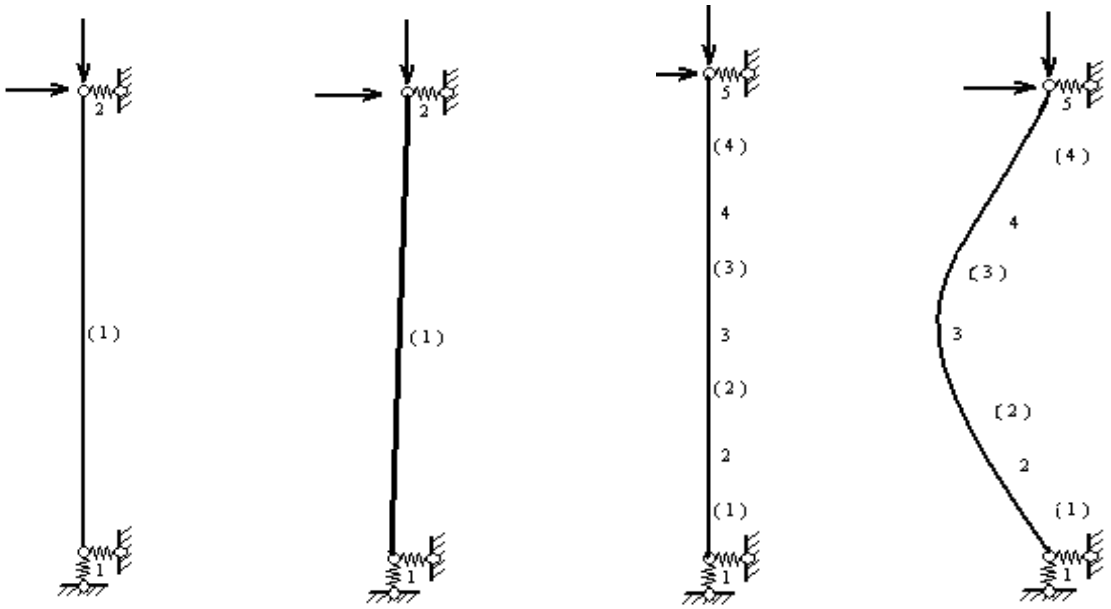
Introduction

Reticulated shell has been used widely in engineering, which has comprehensive advantages such as reasonable stress and easy construction. Reticulated shell has a main characteristic of membrane stress with a small vertical rigidity, so that instability occurred easily. Therefore, one of the key problems of cylinder latticed shell is how to define the ultimate bearing capacity of reticulated shells precisely. In view of the problems of stability and ultimate bearing capacity of the vierendeel latticed shell structure, study is carried out based on nonlinear finite element method [1]. The buckling modal and the whole course of instability are shown. The sensitivity of member failure was analyzed [2].

The ultimate bearing capacity of the single-layer latticed shell structure is obtained by the whole stability analysis [3]. However, the influence of geometrical nonlinear (*P-Δ* effect) is considered, but the influence of single-member instability (*P-δ* effect) is not considered in the analysis of the whole stability of reticulated shell. From engineering practice we can find that some members buckle before reticulated shells reach the ultimate bearing capacity. If the influence of the single-member instability is not considered, the ultimate bearing capacity and the failure mode are not perfect. This paper put forward a multi-element simulation technique which can calculate the influence of the single-member instability.

Analytical Theory and Method

At present, the ultimate bearing capacity is calculated according to the finite element method. The grid structure is formed by members and each member is divided as an element. The calculated model is shown in Fig. 1 (a). The number in Fig. 1 denotes the node, and the number in bracket denotes the element. The deformation of the member is shown in Fig. 1 (b). The shape of the member after deformation is line, which shows that the instability of single member is not considered. From many engineering practices we can find that the shape of member after buckle is curved. So the ultimate bearing capacity of structure is not perfect if the single member instability is not considered. In fact the displacement of node increases with the instability of single member, which makes the ultimate bearing capacity reduce. If a member is divided into multi element, as shown in Fig. 1 (c), the shape after buckle is shown in Fig. 1 (d). It fits with the fact. This method is called multi-element simulation technique.



(a) (b) (c) (d)

(a) one element (b) deformation of one element (c) multi elements (d) deformation of multi elements

Fig. 1 Analysis model of a member:

Analysis of an Example

Structural Model. The single-layer cylinder latticed shell is taken as the structural model, which is shown in Fig. 2. The span, length, rise, number of length grid, number of radial grid is 40m, 60m, 8m, 30 and 30 respectively. The material is Q235 steel with yield strength of 235MPa, density of 7800 kg/m^3, Young's modulus of 2.06×10^{11}N/mm^2 and Poisson's ratio of 0.3. The design dead load is 1kN/m^2. The structure is supported by simply opposite side supports. The cross section is determined by method of full stress design. The ultimate bearing capacity and the course of instability are analyzed by ANSYS. The member is simulated by beam 4. The nodes of structure are rigid connection.

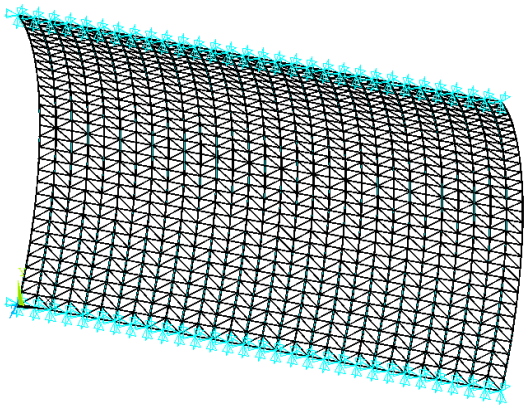


Fig. 2 Structural model for analysis

Result Analysis. Two models are used for comparison in this example. Model 1 adopted ideal elastic-plastic constitutional relationship without consideration *P-δ* effect. Model 2 adopted ideal elastic-plastic constitutional relationship. Every member is divided into 6 elements, which consider the influence of instability of single member. Instability modal of single layer latticed shell without considering the *P-δ* effect is shown in Fig. 3. Instability modal of single layer latticed shell after considering the *P-δ* effect is shown in Fig. 4. Fig. 3 shows that the shape of member is still linear after instability of the structure without considering *P-δ* effect. Fig. 4 shows that the shape of member doesn't have obvious bend after instability of the structure considering *P-δ* effect.

Fig. 5 shows the load-displacement curve of the example of single-layer cylinder latticed shell, from which we can find that the ultimate bearing capacity of model 1 is 3.47*P* and the ultimate bearing capacity of model 2 is 3.43*P*. The ultimate bearing capacity with considering the single-member instability is 1.2% lower than that without considering the single-member instability. So the influence of instability of single member doesn't play an important role in the ultimate bearing capacity of structure.

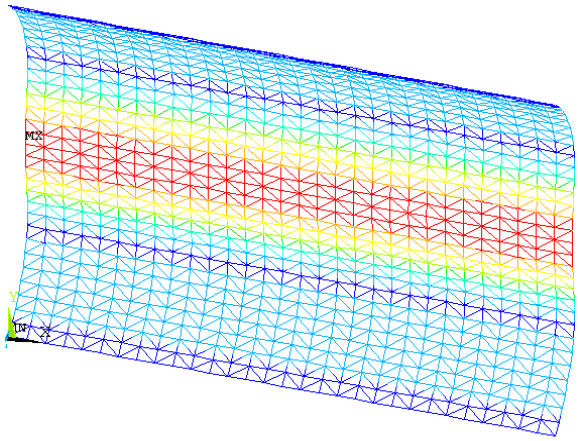


Fig.3 Instability modal of single layer latticed shell without considering the *P-δ* effect

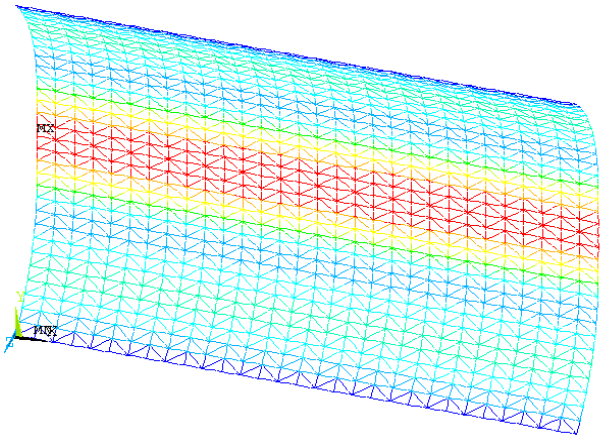


Fig.4 Instability modal of single layer latticed shell considering the *P-δ* effect

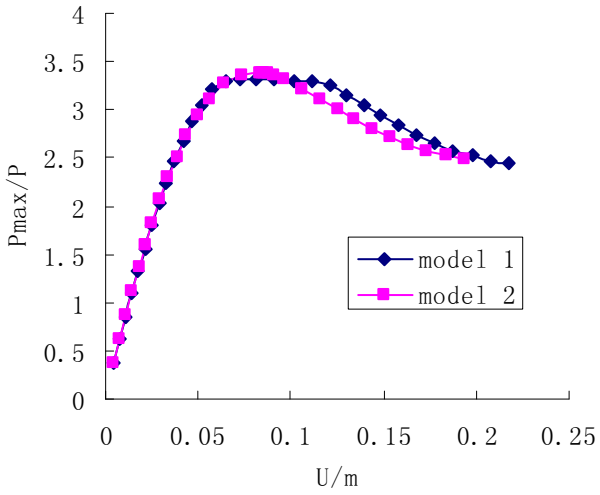


Fig. 5 Load-displacement curve of the example of single-layer cylinder latticed shell

Single-layer cylinder latticed shell is in state of membrane stress before instability. The membrane stress change into bending stress as result from a great geometrical displacement after instability. It can accelerate the course of membrane stress change into bending stress considering the singe-member instability, which can decrease the ultimate bearing capacity. Single-layer cylinder latticed shell is in state of membrane stress before instability. The membrane stress change into bending stress as result from a great geometrical displacement after instability. It can accelerate the course of membrane stress change into bending stress considering the singe-member instability, which can decrease the ultimate bearing capacity. So the two results are different.

In order to ensure the accuracy of the simulative instability of single member, we compare differences of dividing the member into 4, 6, or 8 elements. The result of dividing one member into 6 elements is more accurate than that dividing one member into 4 elements. The result of dividing one member into 8 elements is nearly equal with that dividing one member into 6 elements.

In order to comprehend the influence of P-δ effect, we carry out an analysis with different spans and different rise-span ratios. Table.1 shows the analysis results of cylinder single layer latticed shells. From Table.1 it can be found that the max value of decrease in the ultimate bearing capacity is 1.46%, so the influence of instability of single member can be neglected.

Table 1 Analysis results of cylinder single layer latticed shell

Structural span (m)	Rise-span ratio	Value of decrease
20	1/3	1.46%
	1/5	1.45%
	1/7	1.35%
40	1/3	0.81%
	1/5	0.75%
	1/7	0.74%
60	1/3	1.15%
	1/5	1.07%
	1/7	1.03
80	1/3	1.23%
	1/5	1.18%
	1/7	0.79%

Conclusions

At present, the ultimate bearing capacity is calculated without considering the influence of the single member instability (P-δ effect). P-δ effect can make the ultimate bearing capacity of single-layer cylinder latticed shell decrease, as the single member instability can aggravate the second order effect. The influence of the single-member instability should be considered.

From the example of single-layer cylinder latticed shell with the span 40m and rise-span ratio 1/5, it can be found that the ultimate bearing capacity decreases by 1.2%.

As for cylinder single layer latticed shells supported by opposite side, they have a smaller restraint than cylinder single layer latticed shell. It always happens that the overall whole instability destroys with small vertical rigidity. So it has a tiny influence in instability when the instability of single member is considered.

References

[1] W. Du, L. Zhu, H. Zhang: Study on static stability and the limited load carrying capacity of vierendeel latticed shells. Journal of Zhengzhou University (Engineering Science), 3 (2008) 99-102.

[2] Y. Wang, H. Wu: Optimized design method of space grid structures based on the ultimate bearing capacity. Spatial Structures, 3 (2010) 34-40.

[3] F. Guan, B. Gao, L. Li: Stability analysis of single-layer latticed shell. Engineering Mechanics, 3 (1996) 93-104.

© (2012) Trans Tech Publications, Switzerland
doi:10.4028/www.scientific.net/AMM.238.593

Monitoring and Test on Load Bearing Transform of Large Span Steel Truss of Archaized Tower

Xiaoke Li [b], Pengfei Han [a], Zhihao Wang [c] and Jian Liu [d]

North China University of Water Resources and Electric Power, Zhengzhou 450011, China

[a]lixk@ncwu.edu.cn, [b]531834812@qq.com, [c]wangzhihao916@126.com, [d]59993455@163.com

Keywords: load bearing transform; truss; monitoring test; finite element analysis (FEA); unload.

Abstract. Combined with construction of large span steel truss in the bottom of an Archaized tower, stresses in key members, displacements in control nodes and temperature variation were monitored and measured before and after moving construction temporary constraints. The unloading process based on the rule which constraints were unloaded gradually from outer to inner and four steps were carried out in the field. Compared with measured and theoretical results, they can meet with each other perfectly. The mechanical sensibility of steel stresses with temperature changing were also revealed. Then the reasonable conditions of unloading for the steel truss were advised. The process and method given in this paper provides the basis for safely construction of the Archaized tower, which would be reference for similar load bearing transform of steel structrues.

Introduction

In recent years, more and more steel structures were applied in China and more studies were given on their mechanical behaviours. Especially with increasing of span or height of steel structures, more complicated and miraculous drafts are made into the buildings. How to erect them sucessfully would be a key problem. Many researchers and engineers have given their great efforts and try to solve all these blocks as perfectly as possible. Zeng and Zhang [1] carried out tracking and monitoring on the National Stadium (Bird's Nest) during whole unloading process in 2008. The developing of strcutural mechanical behaviours was revealed when load bearing system of steel structure was transformed. Lu and Zhi [2] took construction monitoring on steel structure of Shenzhen Kingkey Financial Center in 2010 in the filed. The construction deviations were adjusted based on monitored results and then the specification requirements could be guaranteed effectively. Hao and Zhang [3] proved it was a reasonable process by monitoring on the steel structrue construction for Changchun Vehicle Museum. During the erection of buildings, temporary constraints are needed to keep safety of steel structures in most projects. Before and after moving them, there will be great changes to force and deformation of the structure. Monitoring and adjusting the structure in time is very important. It is the key construction stage to control project quality. In this paper, the load bearing transform of steel trusses in an Archaized tower will be introduced and the results by monitoring and testing are dicussed with numerical analysis.

Engineering Situation

Tiantang steel structural Archaized high tower is a Site Protection Exhibition Project in Luoyang, China. To aviod new building destory the ruins, an annular pre-stressed concrete foundation beam is designed around it [4]. The loads from the superstructure, a steel tower with 69.4m high, could be transmitted to the annular foundation beam by a set of trusses with 54.0m span at the bottom, as shown in Figure1. That is, 12 large span steel trusses are needed to pass over the ruins. The load bearing transform system in bottom of tower is shown in Fig. 2.

At the beginning of erection, steel structure of the tower need some constraints to keep structure steady. With constrution process moving on continiously, the temporary restraints will quit gradully. Then the external forces would be beared totally by steel structure itself. The internal forces of structure will be re-distributed. To confirm tower safety of the following, monitoring on bearing transform process to meet the design is the effective way [5].

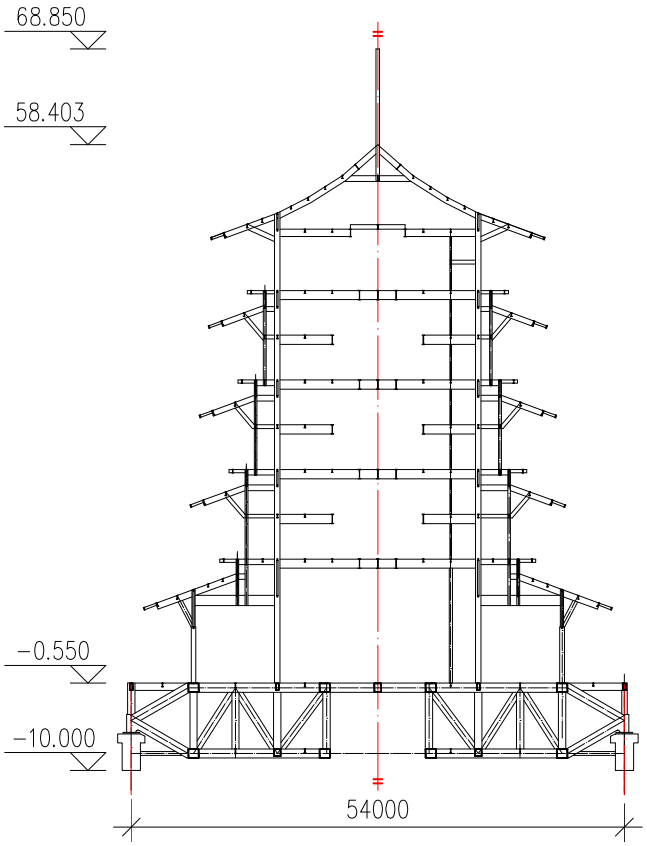
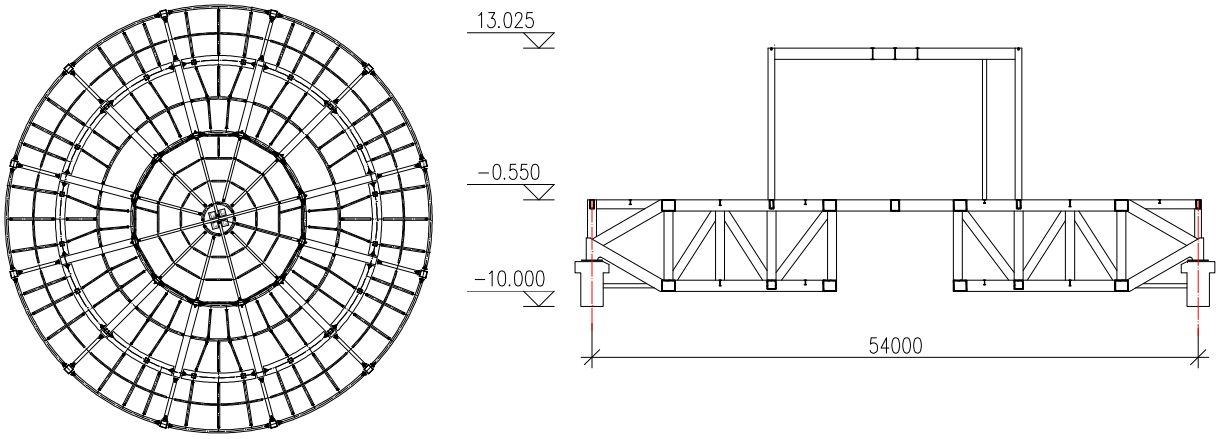


Fig. 1 Overall profile of Archaized tower



a) Top view b) Profile along symmetry vertical axis

Fig. 2 Load bearing transform system in bottom of tower

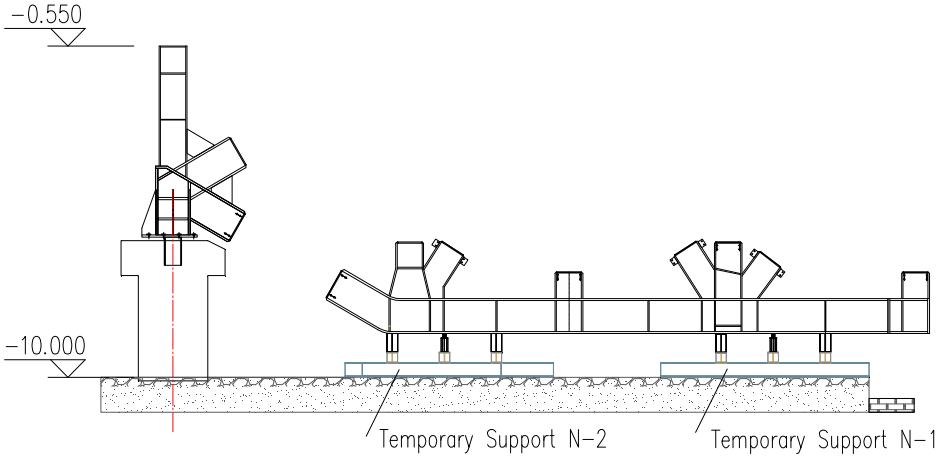


Fig. 3 Sketch of temporary support

There are 24 temporary supports in the bearing transform system. One truss is restrained by two temporary supports and one temporary support includes 2 screw jacks and 4 supporting blocks to hold, as shown in Figure3. All these supports would be removed synchronously from the outer steel annular beam to the inner. Before unloading, the 2 screw jacks would be pushed tightly under the bottom chord of the struss. When the supports at top of prestressed concrete annular foundation beam will be loosed, that is, all structural loads are transfered to the jacks, the supporting blocks for adjusting elevation can be cutted off. The unloading can be controlled by rotation angle value with jack handle. Then the whole unloading process can be sheduled four steps as the following. The first step is to shrink N-2 jacks 2.0mm; The second step is to shrink N-1 jacks 4.0mm; The third step is to shrink N-2 jacks 2.0mm and the last step is to shrink N-1 4.0mm. Where N-1 jack is the jack below the inner steel annular beam, N-2 jack is the jack below the outer steel annular beam and N is the number of the truss.

Monitoring and Testing

Three items such as axial stress in key member, displacement in control node and structure temperature will be given to monitor and test [6].

The vibrational chord strain gauge is adopted to measure the axial strain at the given place in key member. A typical truss in load bearing transform system is selected to install the gauges, as shown in Fig. 4. According the measured strains, the stresses can be obtained easily by multiplying the steel elastic modulus. Body temperature can be measured with same gauges.

A total station is appiled to monitor the settlements of control nodes in the structure. Along axis B and C of steel annular beam, 24 control nodes are arranged uniformly. 4 displacement meters are installed below the steel annular beam D to confirm the vertical displacements of the system, as shown in Fig. 5.

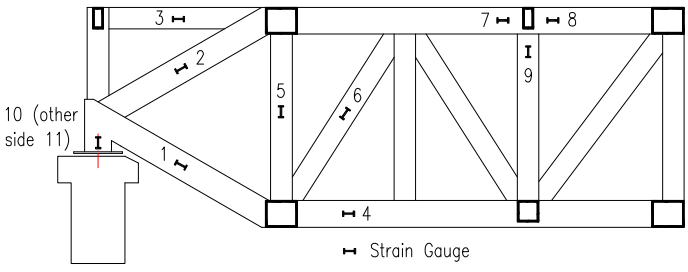


Fig. 4 Diagram of Stain Gauge in Struss

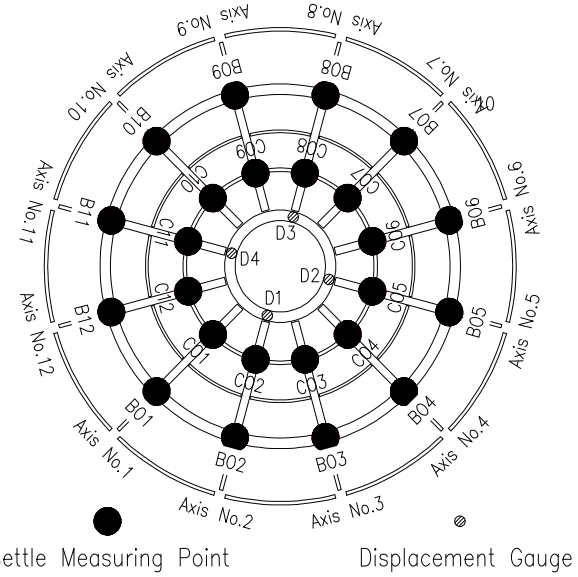


Fig. 5 Arrangement of Displacement Measuring

Numerical Model

In order to compare with measured results, a numerical analysis is carried out used by Ansys FEA software. The connections between components in load bearing transform system are simulated as rigid coupling. Then the element type, beam188 is adopted. Totally there are 9528 nodes and 4815 elements in the numeircal simulation model, as shown in Fig. 6. The "birth and death" element method is applied to simulate the gradual unloading process.

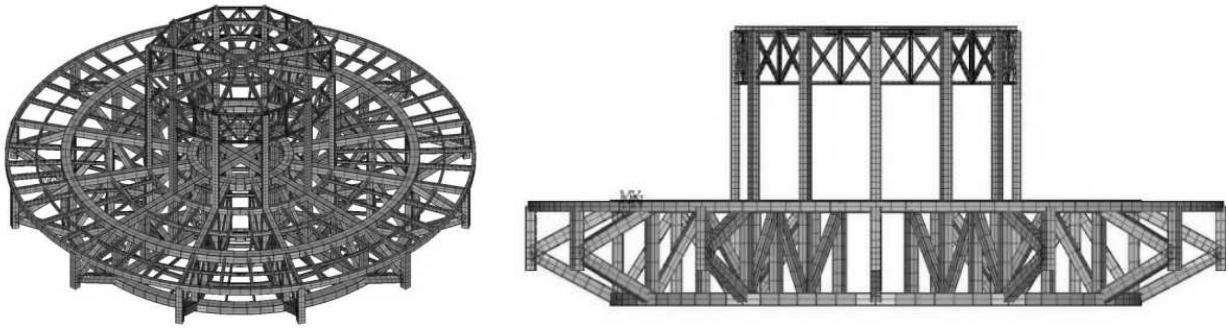


Fig. 6 Finite element model

Result Analysis

Stress of Truss. The measured and FEA axial stresses of key members in steel truss No.5 and No.11 after unloading are shown in Fig. 7 and Fig. 8. The steel truss No.5 is symmetrical with steel truss No.11. Bcause of variational temperature of steel truss during construction period, the temperature in a member bar is different with another. The axial stresses of same number bars in steel truss No.5 are not same as steel truss No.11. For examples, the FEA axial stress of 6^{th} bar in steel truss No.5 and No.11 are -9.50MPa and -9.9MPa respectively. And the measured values are -8.80MPa and -3.74MPa respectively. It's ture that the measured axial stresses in some bars have deviations with the FEA values. At the same time, the size effect would give the effort for these deviations because of large cross sections and small strain gauges. The partial stress concentration would also enlarge the variations. But the whole trends of axial stresses in steel truss No.5 and No.11 are same , compared measured and FEA results. Anyway, they are all smaller compared with design tensile or compressive strength of steel. All steel trusses during unloading periods could be kept good conditions to carry out the following construction.

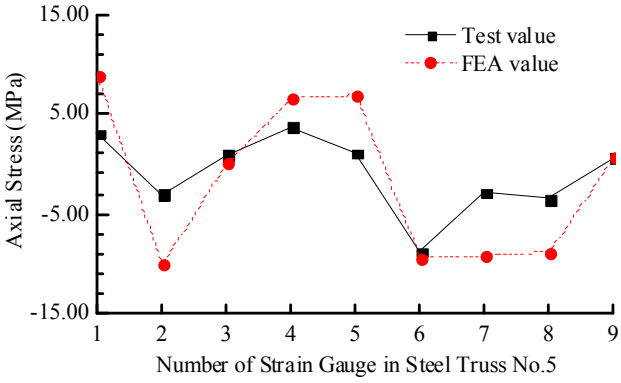


Fig. 7 Axis Stress in Steel Truss No.5

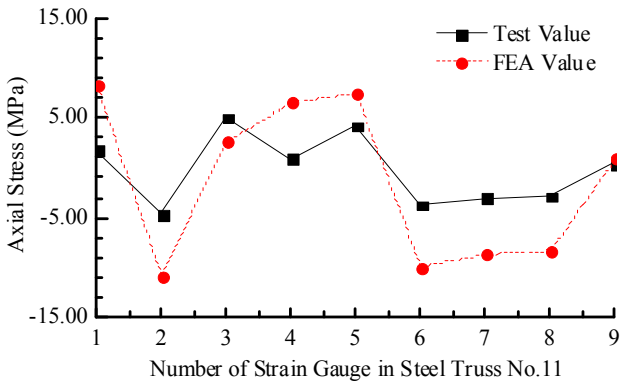


Fig. 8 Axis Stress in Steel Truss No.11

Displacement. To monitor the settlement uniformity and adjust the unloading process in real time, the vertical displalacements below the steel annular beam D for all unloading steps are shown in Fig. 9. With unloading steps, the displacement of each point increases. Because all jacks couldn't be shrinked synchronously same as the theory, the difference always exists. It leads to the result which the values at point D2 are all less than the other points. The measured vertical displacemnts at points D1, D2, D3 and D4 are 3.60mm, 2.41mm, 3.61mm and 3.80mm respectively after unloading. But they are all within 4mm. It reveals that it is normal during unlaoding process and welding quality can be guaranteed.

The vertical settlements along circle B and C are shown in Fig. 10. Almost all displaments of the measured points are less than the FEA except D2 point. But this difference between measured and FEA values is small. That is, the measured displacements could keep in accordance with the FEA results. It also showed that the unloading process was controlled seccessfully although slight nonuniformity of vertical settlements in circle C could be found.

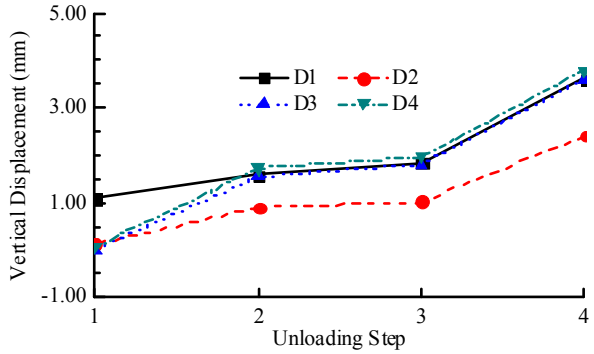
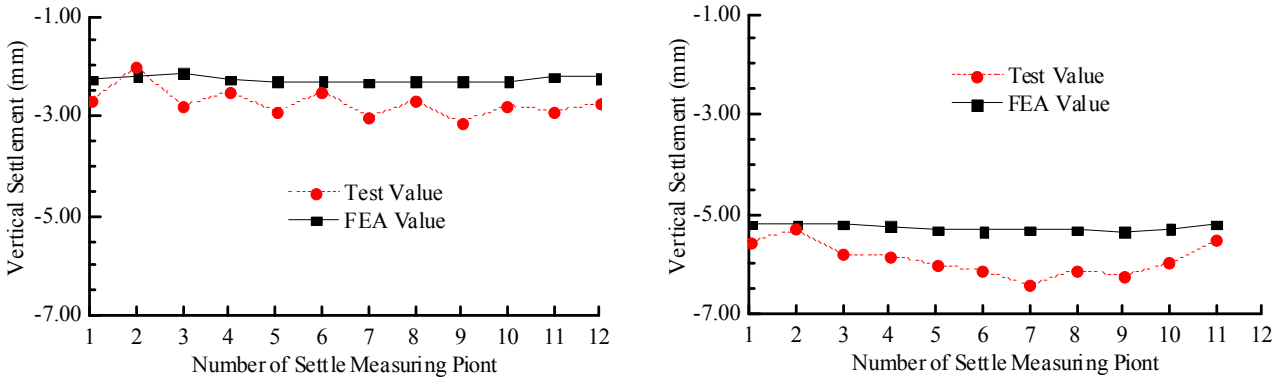


Fig. 9 Vertical Displacement Along Circle D



a)Along Circle B b) Along Circle C

Fig. 10 Vertical settlement

Temperature. The temperature of whole structrue must be different in day or night, sunshine in the morning or afternoon, exposed to the sun or in the shadow. The temperatures of given points in steel truss during unloading periods are listed in Table1. The highest tempertures in given points before unloading are 17.7°C and 18.6°C in steel truss No.5 and No.11 respectively. The lowerest values are 8.1°C and 6.4°C respectively. Then After unloading, the highest tempertures in given points are changed to 15.1°C and 18.9°C in steel truss No.5 and No.11 respectively. The lowerest values are 9.4°C and 12.0°C respectively.

As unloading process was done in winter, overall temperature rise or drop is not intense. However the temperature nonuniformity caused by sunshine could affect the internal forces of steel structure. The measured values at 3th point in steel truss No.5 and No.11 are greater than others. The result would lead to greater stress variation in strusses. Therefore, temperature effect should be empasized during design and construction periods.

Table1 Temperature in steel truss during unloading periods (°C)

Unloading Step	Number of Strain Gauge in Steel Truss No.5								
	1	2	3	4	5	6	7	8	9
Ready Unloading	9	9.4	17.7	10.1	9.2	10.5	13.2	8.8	8.1
Step1	9.5	9.8	17.4	9.4	9.6	11	13	9.2	8.5
Step2	9.8	10.1	17.8	9.9	10	11.9	12.9	9.5	8.9
Step3	9.9	10.2	17.1	10.3	10.9	11.4	12.5	9.9	9.2
After Unloading	9.4	10.8	15.1	10.6	11	11.3	12.2	10.3	9.6
Unloading Step	Number of Strain Gauge in Steel Truss No.11								
	1	2	3	4	5	6	7	8	9
Ready Unloading	10.9	6.4	18.6	8.8	11	9.7	11.5	11.4	9.4
Step1	12	10.1	18.6	9.7	11	9.9	11.6	11.6	10.3
Step2	13.4	10.9	18.6	10	11.6	10.5	11.9	11.8	10.8
Step3	14	11.7	19.5	12.1	11.7	11.6	12.1	11.9	11.6
After Unloading	13.9	12	18.9	12.8	13.1	12.7	12.3	12.1	11.7

Conclusions

It is very important for complex steel structure to remove temporary restraints during construction periods. The results from test show that it is reasonable to apply 4 unloading steps. The temporary restraints in the bearing transform system could quit gradully and successfully. Compared with measured and theoretical results, they can keep accordance with each other. It reveals that it is normal during unloading process and welding quality was guaranteed perfectly. The changes of overall temperature and surface temperature show it is important to emphasize seriously during design and construction periods. The results obtained from the paper could provide some valuable reference for the construction of similar steel structure.

References

[1] Z. Zeng, Y. Zhang, Stress monitoring of the large-span steel structure of the National Stadium during unloading, China Civil Engineering Journey, 3 (2008) 1-6.

[2] J. Lu, X. Zhi, H. Xu, Moultoring in technology of steel strueture construetion Shenzhen King Key Financial Center, Construction Technology, 8 (2010) 136-140.

[3] Y. Hao, Y. Zhang, Z. Zhang, Construction monitoring of steel structure in Changchun Automotive Museum, Construction Technology, 350 (2011) 33-35, 81.

[4] C. Wang, K. Xu, L. Tian, Structure design of Tiantang for the protection of the ruins of Ancient Buildings which built in Sui &Tang Dynasty in Luoyang city, Steel Structure, 26 (2011) 32-36, 79.

[5] GB50017-2003, Code for Design of Steel Structure, China Architecture & Building Press, Beijing, 2003.

[6] JGJ8-2007, Code for Deformation Measurement of Building and Structure, China Architecture & Building Press, Beijing, 2007.

© (2012) Trans Tech Publications, Switzerland
doi:10.4028/www.scientific.net/AMM.238.599

Design and Analysis of a Suspended Lattice Shell

Wenfeng Du[1, 2, a], Fudong Yu[1, b], Zhiyong Zhou[1,c] and Liming Zhu[1,d]

[1] College of Civil Engineering and Architecture, Henan University, Kaifeng 475004, China

[2] Zhejiang Bada Construction Group CO. LTD, Hangzhou 311800, China

[a]dwf@henu.edu.cn, [b] vipyfd@163.com; [c] zzy569@163.com; [d] zlm811224@163.com

Keywords: suspended lattice shell, tensile cable, construction, tension slacken analysis method.

Abstract. The design and analysis of the suspended lattice shell located in Zhejiang province of China is introduced, and some key problems are discussed in this paper. Especially, tensile cable is a key element in large span suspended structures. And the construction of tensile cable is the key technology problem as the tensile force of tensile cable is very sensitive to the construction precision. The tension slacken analysis method is used to obtain the control stress and complete the work with only one time tensile construction. Results of the engineering show that the construction process is simple and the construction scheme is economic.

Introduction

With the development of our society, more and more innovative and complex large-span space structures have been put forward in the past few decades [1, 2]. The suspended lattice shell project located at the city of Zhuji, Zhejiang province of China is one of those representative buildings. The requirements on the functions and the esthetics make it distinguished from a traditional building. The structure of the suspended lattice shell is shown in Fig.1.The thickness of the structure is changed along two directions. The maximum thickness in the middle of the structure is 2.5m. The span of the structure is 84m. One end of the tensile cable is joined with the shell structure. The other end is joined with the tower column. The horizontal spacing between two tower columns is 54m. The external tensile cables connect the tower columns and ground. The sum of tensile cables is 8. The serial numbers are shown in Fig. 2.

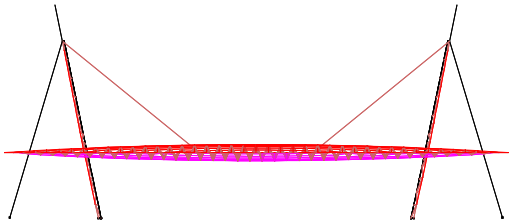


Fig. 1 Model of the suspended lattice shell

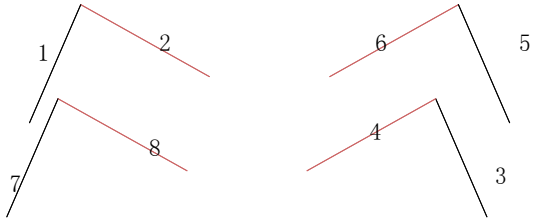


Fig. 2 Numbers of tensile cables

Loads and Load Combinations

Besides the self-weight of the structure, following loads are included:

(1) Dead loads (*D*):

Uniformly distributed loads of the upper chord 0.3 kN/m^2

Uniformly distributed loads of the nether chord 0.4 kN/m^2

(2) Live loads (*L*):

The live load located at the whole roof 0.5 kN/m^2

(3) The wind loads (*W*)

The wind load located at the upper chord -1.21 kN/m^2

(4) The temperature (*T*)

The temperature changes between -30°C and 30°C, which are determined according to the environmental data.

According to the Chinese code, 8 kinds of load combinations of dead loads, live loads, wind loads and temperature are considered in the calculation as list in Table 1.

Results of Static Analysis

The analysis of this structure is carried out by the analysis and design software MSTCAD, then software ANSYS and MIDAS are used to do the further analysis. All the members are taken as link elements. The structural parameters of analysis are as the followings:

(a) Material: all the members and connections are Q235B steel.

(b) Design stress (control strength) of Q235B steel is 215 N/mm^2. The permitted slenderness ratio for pressed members is [λ] = 180 and for pulled members is [λ] = 300.

(c) Control deflection: according to Chinese Code for shell structures, the control deflection of reticulated shell structure is L / 250=336mm, here L is the structural span.

The static responses of the structure under the eight load combinations are shown in Table 1. Fig. 3 shows the nodal displacement along direction Z under the 1st load combination.

Table 1 Results of static analysis

Load combinations	displacement X	displacement Y	displacement Z	Maximum stress	Minimal stress
(1) 1.35D	-39.3	-12.4	191.0	136.7	-135.6
(2) 1.2D+1.4L1	-143.0	-308.5	316.4	181.2	-182.1
(3) 0.9D+1.4W1	-39.7	106.2	-94.8	63.4	-119.6
(4) 1.2D+1.4L1+0.8W1	-79.9	-228.8	171.8	99.4	-98.2
(5) 1.2D+1.0T (+30)	89.7	-270.7	212.9	123.4	-122.7
(6) 1.2D+1.4L1+1.0T (+30)	-130.0	-301.5	318.3	182.6	-182.3
(7) 1.2D+1.0T (-30)	-110.2	-284.7	209.0	119.6	-118.3
(8) 1.2D+1.4L1+1.0T (-30)	-156.0	-315.5	314.4	180.0	-181.9

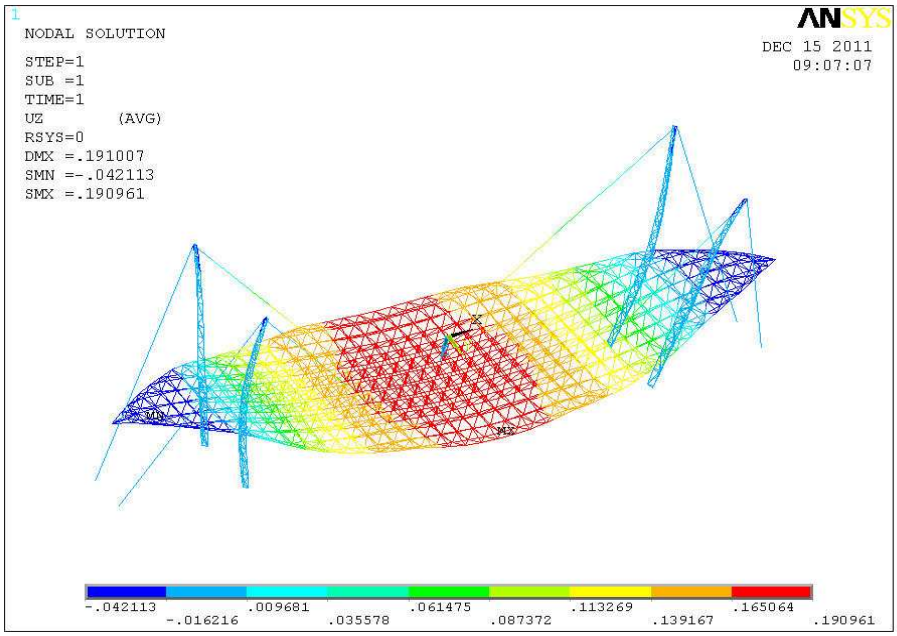


Fig. 3 Nodal displacement along direction Z under the 1st load combination

From the calculation results in Table 1, it is known that the internal force and deformation in various load combinations can satisfy the requirements of the design code. Among them, the structure has a big upward displacement in the wind load, which shows that the wind load has a great impact on the structure. This is because of the structural large span and its coastal environment.

Calculation of Construction Control Stress of Tensile Cables

It is important to assure the construction accuracy for the tensile cables. Because the construction accuracy of tensile cables in suspended lattice shell is sensitive to internal force of tensile cables [3, 4]. Especially, when the latter tensile cable is tensioned, the internal force of the former tensile cable which has been tensioned to reach full stress will change. That brings the difficult for the construction of tensile cables. Aiming at the above-mentioned problem, the control stress is obtained by tension slacken analysis method in this paper. Then each tensile cable should be tensioned to construction control stress in order. In this way, just once, the construction of tensile cables can be completed.

Following is computational method of tension slacken analysis method [5, 6].

(1) All cables should be applied initial prestressing force.

(2) According to release the initial prestressing force of last tensile cable, the control stresses of the next to last tensile cable can be obtained.

(3) Then releasing the initial prestressing of the next to last tensile cable, the control stresses of the third to last tensile cable can be obtained.

(4) Deducing by analogy.

(5) Releasing the initial prestressing of the second tensile cable, the control stresses of the first tensile cable can be obtained.

There are 8 tensile cables in this project. The construction control stresses can be obtained by above method, shown in Table 2.

Table 2 Construction control stresses (MPa)

	1	2	3	4	5	6	7	8
Designed value (Tensile 8th)	131	113	131	113	131	113	131	**113**
Releasing 8th (Tensile 7th)	124	102	163	144	84	79	**1**	
Releasing 7th (Tensile 6th)	124	102	163	144	84	**79**		
Releasing 6th (Tensile 5th)	150	129	149	128	**1**			
Releasing 5th (Tensile 4th)	150	129	149	**128**				
Releasing 4th (Tensile 3rd)	74	69	**1**					
Releasing 3rd (Tensile 2ed)	74	**69**						
Releasing 2ed (Tensile 1st)	**1**							

When calculating, the order is contrary to construction. Cables must be dislodged by cable number (8, 7, 6, 5, 4, 3, 2, 1). The value in diagonal line with black italic type (1MPa, 69MPa, 1MPa, 128MPa, 1MPa, 79MPa, 1MPa, 113MPa) can be obtained. Then tensing the cables (1, 2, 3, 4, 5, 6, 7, 8) in former order. The cables with value 1MPa are connected with ground. That is to say the cable can be just tensioning. So the value is 1 MPa. The values of first line are actual values after tension, which is equal to designed value. The cable can just be tensed once to calculated value by this method.

Tensioning Monitoring of Tensile Cable

In order to check the actual value of tensile cable, the tensions of 8 cables are monitored. Table.3 shows the compares between actual values and theoretical values. The actual stresses are obtained by test tension dividing cross section.

The actual values show that the actual values are within 5% of errors comparing with the theoretical value by this method, which can satisfy the project precision.

Table 3 The compares between actual values and theoretical values

Cable number	1	2	3	4	5	6	7	8
Actual value (MPa)	124.2	108.7	124.8	109.0	125.4	109.3	125.5	109.7
Theoretical value (MPa)	131	113	131	113	131	113	131	113
Error (%)	5.2	3.8	4.7	3.5	4.3	3.3	4.2	2.9

Conclusions

The internal force and deformation of structure in various load combinations can satisfy the requirements of the design code.

The control stress of each cable can be calculated by tensile force slacken analysis method with considering the influence of each cable. The tensile force of each cable just equals to the design value, when the construction is done.

The monitoring of tensile cable shows that the actual values are almost equal to the designed values, which reaches the expected requirements.

The tensile force slacken analysis method in this paper not only satisfies the construction precision, but simplifies the construction process and reduces the cost greatly. This method is worth to be used widely in similar projects.

References

[1] A. El-Sheik: Development of a new space truss system. Journal of Constructional Steel Research. 37 (1996) 205-27.

[2] S. Dong and Y. Zhao: The future and prospect of latticed shell structures. Spatial structures. 1 (2004) 3-10.

[3] S. Dong: Development and prospect of long-span space structures. Spatial Structures, 6 (2000) 3-13.

[4] China Code JGJ 7-91: Design and Construction of Shell Structures Code. Beijing: China Building Industry Press, 1991.

[5] S. Dong and H. Deng. A simple computation method of prestressed space truss and its global process pretensioning analysis. Journal of Building Structures. 22 (2001) 18-22.

[6] S. Dong, X. Zhuo and Y. Zhou: One-time pretensioning analysis method for prestressed space truss. Journal of Zhejiang University (Engineering Science). 37 (2003) 629-633.

© (2012) Trans Tech Publications, Switzerland
doi:10.4028/www.scientific.net/AMM.238.603

Development and Application of the Virtual Simulation Teaching System of Steel Structure Construction

Zhongping Tang [a] and Yongchun Xu [b]

Zhejiang Business Technology Institute, Department of Building and Art, Ningbo 315012, China

[a]tzp@zjbti.net.cn, [b]xuyongchun@zjbti.net.cn

Keywords: virtual simulation; steel structure construction; develop; working process; teaching model; studying style.

Abstract. This paper introduces the concept and application of virtual simulation technique, faced to the problems in teaching steel structure construction, develops the virtual simulation teaching system of steel structure construction with virtual simulation technique and 3D production technique. After that, it introduces the software's system structure, content structure, interface design and application in teaching. The development of this system, not only change the traditional teaching model and studying style, but also promote the teaching efficient, save the teaching time and costs.

Introduction

Steel structure construction is an important course of the civil engineering major, how to improve the students' skill of steel structure construction in school is an important work which we had discussed always. In the past, as the limits of the teaching conditions, this course applied the traditional teaching way "mainly teach with theory, accompany with cognition practice", and the effect was not so good, mainly showed the following points: Firstly, there are so many knowledge points, and are all scattered, the lecture often seems boring, the students are always without interest to listening. Secondly, the lecture can't give students deep impression in brains, so they still don't know the whole process and key points of the construction after the class. Thirdly, there is high risk to take the students to practice in construction site, and the students can't see the whole process of the steel construction as the short practice time. Finally, regardless of the lecture in class or practice in construction site, the students have no chance to shoulder the specific jobs as a worker, their professional skill can not come up to the requirements.

Brief Introduction of Virtual Simulation Technique

Virtual simulation technique is the combination of the virtual reality technique and the system simulation technique, is an advantage technique which can realize the human-computer interaction. Its essence is, establishing a 3D virtual reality scenery and perceive objects by virtual reality technique, and establishing mathematic models by system simulation technique. When people operate the virtual objects and scenery with mice, keyboards and other special controllers, the computer will make corresponding dynamic responses in accordance with the established algorithm, and show the results fit for rules.

Now, the virtual simulation technique is widely used in the area of military, industrial and medical, some universities try to use it in the simulation of the complex and expensive material-cost experiments, to improve experiments' efficiency, effectiveness and safety.

Development of Steel Structure Virtual Simulation Teaching System

Faced to the above problems in teaching steel structure construction, with the background of a certain steel structure factory's installation, Zhejiang Business and Technology Institute developed the virtual simulation teaching system of steel structure construction by 3D production technique and virtual simulation technique.

This system simulates the working scenery, equipments and working environment vividly, simulates the steel factory's installation process and some equipments' operation process in detail, and simulates some dangerous operations such as high altitude operation, power operation and deep foundation pit operation etc. During the teaching of this course, students can shoulder some virtual jobs of the steel factory's installation such as cutting, Hoisting, welding etc. And the system can explain the corresponding rules of steel structure construction code along with the operating in time, record the students' operation process, and judge their results.

Structure of Virtual Simulation Teaching System. The teaching system mainly virtues the working scenery and simulates the construction operation, changes the teaching method of steel structure construction from "taking teacher as main part, give priority to knowledge inculcation" to "taking student as main part, give priority to learning by simulation operating". The whole structure of this system is shown in Fig. 1.

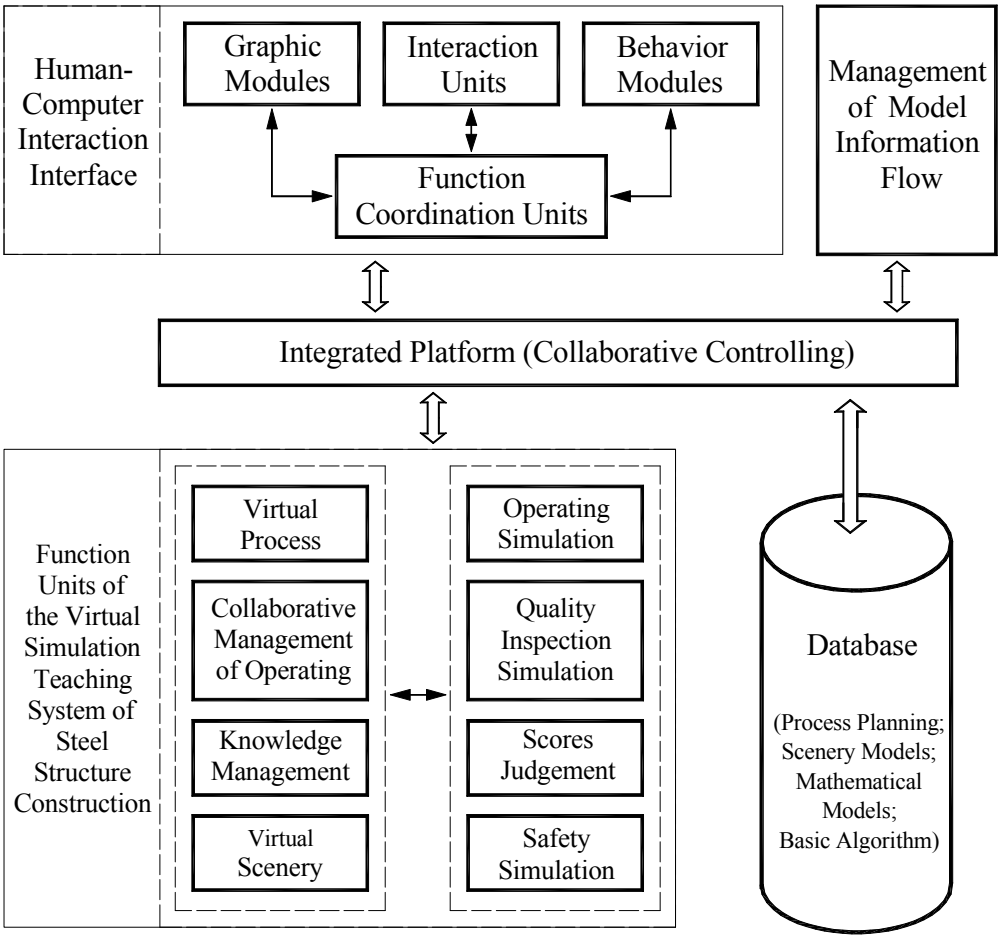


Fig. 1 Structure of the virtual simulation teaching system of steel structure construction

In this system, the merits degree of working scenery and entity models will influence the sense of reality and interactivity of virtual construction directly; the precision degree of mathematic models and algorithm will influence the effects of simulation operating. So, we use 3DsMax to set the models of working scenery and objects, and render them; use the mature algorithm and calculate theory to confirm the corresponding relationship for the models and operating [2].

Content Structure of the Virtual Simulation Teaching System. Based on the idea of learning by simulation operating, the virtual simulation teaching system of steel structure construction, with the background of a certain typical steel structure factory's installation, includes 9 simulation tasks (Checking bolts of foundation, steel columns installation, tied and scissors installation between columns, purlins installation etc.) which were designed according to the working process and 9 function modules (engineering drawings, construction codes, construction technical clarification, construction safety clarification etc.) which were used for each task, and includes rules' explanation of steel structure construction code, judgment systems of students' operations (Fig. 2).

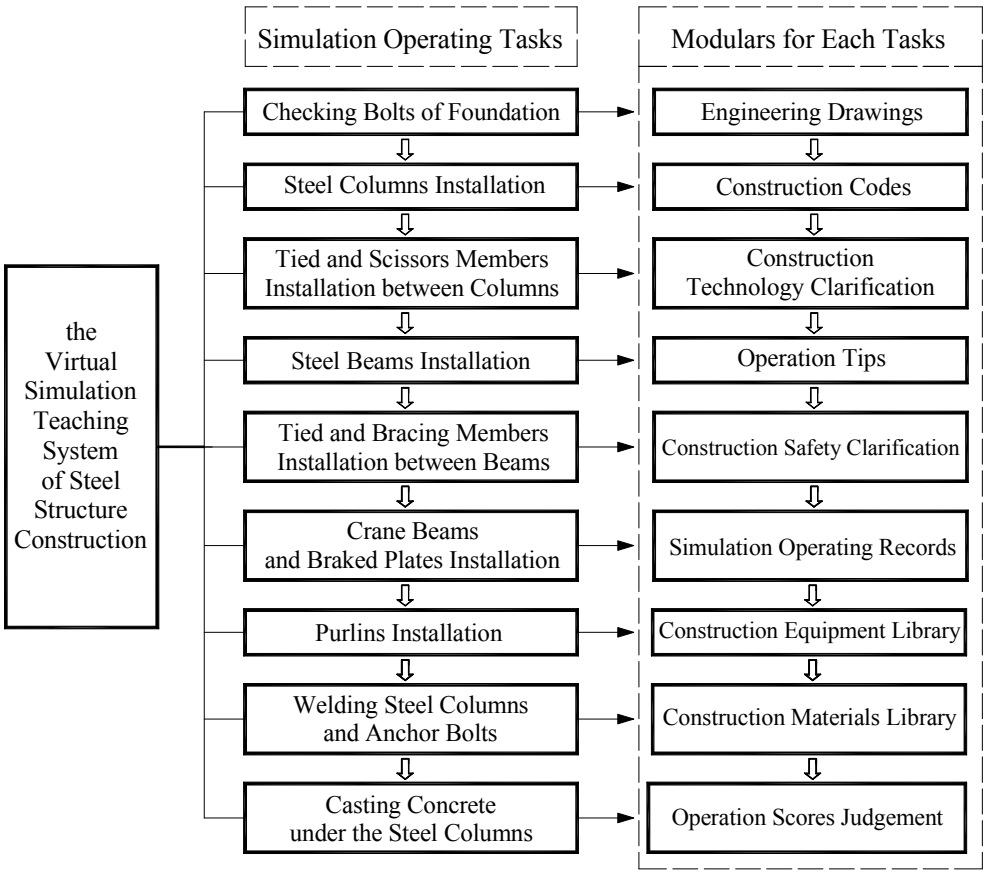


Fig. 2 Content structure of the virtual simulation teaching system of steel structure construction

Interface Design of 3D Human-computer Interaction. In one way, the human-computer interaction performance is the key to success of the virtual simulation teaching system [3], so designer should design the interaction interface well.

And the young students who were born in 1990s are the main users for this system, they are interested in new software, with strong curious, master network technology, frankly and directly, so the interface design of this system should follow the principles: intuitive and obvious, easy to learn, rich in interest, highly in reliable[4-6].

In this system, the designers simplified the menus bar and tool strips, used the stereo arrow with bubble function to indicate the operate position dynamically, used the 3DsMax technique to render the working scenery to enhanced the sense of 3D and realism, at the same time, fused multimedia sound in the page to add some funny.

The interface and simulation effect of this system is shown in Fig. 3- Fig. 6.



Fig. 3 Interface of the teaching system



Fig. 4 Prompting the key point of steel beam installation



Fig. 5 Hoisting simulation of the steel beam

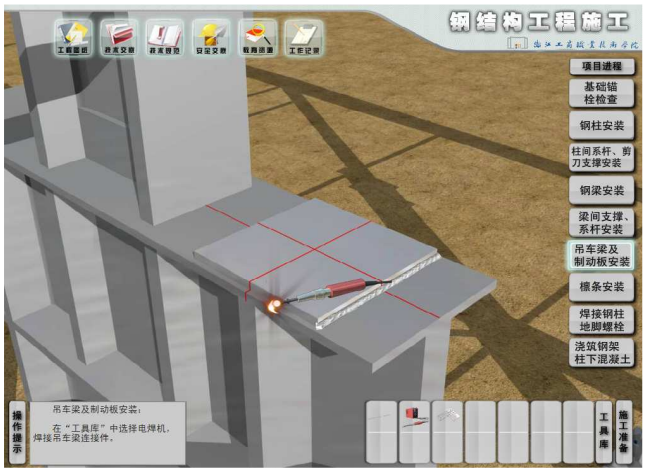


Fig. 6 Welding simulation of brake plate (magnified display)

Application of the Virtual Simulation Teaching System

The development and application of the virtual simulation teaching system of steel structure construction, bring some impact to the traditional teaching method, and deeply changed the student's learning way and the course judgment form.

Looking from the teaching place, the traditional class had been changed to an operate factory; looking from the teaching content, teachers spoke less, and students done more; looking from the participant roles, the students had been changed from a listener to an operator, the teacher had been changed from a speaker to a tutor; looking from learning way, in the past, the students used to accept knowledge passively in the class, and now, they begin to experience and comprehensive during operating; looking from judgment form, the paper exam had been changed into simulation operating judgment.

Conclusions

The virtual simulation teaching system of steel structure construction has the characteristic of virtual simulation and interactive operation. Its application in the course of *steel structure construction* overcomes the shortage of practice in construction sites, avoids the un-safety risk effectively, saves the teaching costs, reduces the dependence on Construction Company which applied practice opportunity to students, improves the teaching efficiency and effect, and strengths the idea of learn to meet practical needs.

If the virtual simulation teaching system combined with the network technology, it will make the teaching & studying were unlimited by the times, spaces and locations, has wide application prospect. We should develop more virtual simulation teaching system to promote the level of education information, and promote the education reform go forwards.

Acknowledgements

The research is supported by Education Technology Center of Zhejiang Province in China (Grant No. JB113) and Adult & Occupation Education Association of Zhejiang Province in China (Grant No.Y12-51).

References

[1] G. Chang, G. Quan. The design of PID control system for interactive virtual simulation software, Jouranal of Laboratory Science. 14 (2011) 69-72.

[2] X. Yan, Y. Guo. The system structure design of optical simulation software, Journal of Computer Simulation, 26 (2009) 264-268.

[3] Y. Dong. The design and realization of HF ground wave radar system performance simulation system, Journal of Modern Radar, 31 (2009) 30-34.

[4] H. Sun. The design of 3D virtual distribution simulation training, Journal of Anhui Electrical Engineering Professional Technique Institute, 16 (2011) 111-112.

[5] K. Teng. The design of NC simulation software which has function of multimedia and network teaching, Journal of Machine Tool & Hydraulics, 40 (2012) 107-111.

[6] Y. Ren, W. Wu. Dicusstion of CNC system human-computer interface design, Journal of Guangxi Light Industry, 146 (2011) 41-42.

© (2012) Trans Tech Publications, Switzerland
doi:10.4028/www.scientific.net/AMM.238.608

Research Status and Development Application of Ceramsite Concrete Short Pier Shear Wall

Bin Hu [a], Rongyue Zheng [b] and Bifei Zhou [c]

Department of Civil Engineering, Ningbo University, Ningbo, 315211, China

[a]tomey123@sina.com,[b]rongyue@nbu.edu.cn, [c]bfzhou@126.com

Keywords: ceramsite concrete short pier shear wall; research status; development application.

Abstract. Currently our country high-rise construction technology develops forward an important content to reduce the structure dead weight. The ceramsite concrete which makes full use of industry waste material obtains the good social efficiency and helps to reduce the structure dead weight effectively. At the same time, it has the good heat preservation performance as well as the fire protection performance. The short pier shear wall comes by the general shear wall development. It has absorbed irregular cross-section column structure's merits. It is also easy to satisfy each kind of building plane request. Moreover, it has the lighter weight, saves the material and decreases earthquake function contrast to the general shear wall.

Introduction

The ceramsite concrete refers to the lightweight concrete which takes the ceramsite as the thick aggregate. The short pier shear wall is defined as the shear wall with a ratio of section depth to width being 5~8. The ceramsite concrete short pier shear wall which unifies the merits of the ceramsite concrete as light quality, heat preservation, energy conservation and the short pier shear wall structure as beautiful, suitable, earthquake resistance, has the broad prospects for development.

Ceramsite Concrete

Characteristics of Ceramsite Concrete. The characteristics of the ceramsite are the surface roughness and the interior porous. The ceramsite is hygroscopic. When the full-water ceramsite is put into the concrete, it will have the maintenance function from the interior concrete which is called as "interior maintain". This can help to prevent the concrete to crack [1].

Research Status and Development Application in China. China started to develop the man-made ceramsite in the 1960's. The ceramsite products were mainly the shale ceramsite, the pulverized coal ash ceramsite and the clay ceramsite. However, their quality is bad. Generally, the apparent density of the ceramsite concrete is 1800~1950kg/m^3, the compressive strength is 5.0~25MPa. It means that the density is big while the intensity is somewhat low, which limits its application and development [2]. Meanwhile, as the construction cost, the economic efficiency which manifests unremarkable in the non-structural engineering. At present, the ceramsite concrete application is mainly used in the non-load-bearing member. China's application in the high-rise construction and in the great span bridge is fewer compare with overseas.

Overseas Research Status and Development Application. In overseas, the application of the ceramsite concrete is widespread. In 1965, US substituted the ceramsite concrete for plain concrete. 218 meters high Houston shell square building was constructed, which obtained the remarkable technical economic efficiency. In 2001, US completed the Benicia-Martinez Bridge in California with the ceramsite concrete. The total length of this bridge was 2716 meters [3].

Ceramsite Concrete Short Pier Shear Wall

Characteristics of Ceramsite Concrete Short Pier Shear Wall. The ceramsite concrete short pier shear wall is on the rise. It synthesizes characteristics of the ceramsite concrete as well as the short pier shear wall. It has displayed both superiorities for it has made up shortcomings of the tradition

concrete building structure. The ceramsite concrete short pier shear wall not only is advantageous to heat insulation, but also is advantageous to reducing the house weight and the foundation construction cost. The elasticity coefficient of the ceramsite concrete is lower than that of the plain concrete. Simultaneously it can absorb much vibrational energy, therefore the ceramsite concrete pier shear wall has bigger distortion ability, stronger earthquake resistance ability.

(1) The deadweight is light. The ordinary concrete bulk density is generally 2400kg/m^3, but the ceramsite concrete bulk density is generally 1600-1950kg/m^3.The apparent density of the ceramsite concrete may reduce 1/4 to 3/4 compare with that of the ordinary concrete. As a result, the dead weight can be reduced obviously as well as the expense of the foundation treatment. Besides, it can reduce the sectional dimensions of the pillars to speed up the construction progress.

(2) Heat preservation property is good. The coefficient of heat conductivity of the ordinary concrete in dry situation is 1.22-1.45w/(mk), but reaches 1.62-1.74W/(mk) in the moist situation. The coefficient of heat conductivity of the ceramsite concrete is 1/3-1/2 lower than that of the ordinary concrete. Therefore the ceramsite concrete short pier shear wall usually has the good heat preservation property to reduce the energy consumption of buildings.

(3) Fireproof performance is good. The ceramsite concrete short pier shear wall has the good heat preservation performance. The coefficient of heat expansion is small. It is suitable for the high high-rise constructions and the industrial architectures which have high fireproof rank requests.

(4) Mechanics performance is good. The elasticity coefficient of the ceramsite concrete short pier shear wall is small. The wall may absorb the earthquake energy effectively to enhance the building earthquake resistance ability. Therefore it is suitable for the constructions which have high earthquake resistance request. According to presentations, the relative earthquake resistance coefficient of the ceramsite concrete is 109, while the ordinary concrete is 84, the brick masonry is 64.We can see from the result of the actual earthquake that several ceramsite concrete industries and civil constructions in Beijing and Tianjin area were in good condition after Tangshan strong earthquake in 1976. But most of the brick-concrete structures were destructed or collapsed [4].

(5) The sound-insulated performance is good. This is mainly because of the porosity of the ceramsite concrete, its sound-insulated effect surpasses the ordinary concrete.

Ceramsite Concrete Short Pier Shear Wall Research Status and Development Application. The research of the ceramsite concrete short shear wall is only restricted in China at present. Some universities and scientific research institution have conducted the research to the ceramsite concrete short pier shear force wall.

In 1994, Shi [5] and other colleagues studied the intensity and the distortion performance of the ceramsite concrete short pier shear wall compared with the ordinary concrete short pier shear wall through the experiment of seven ceramsite concrete short pier shear wall and a ordinary one under the concentrate cyclic lateral load. This experiment indicates that the stress performance and the destruction shape of the ceramsite concrete short pier shear wall is similar to the ordinary concrete short pier shear wall, and its energy dissipation ability and extensibility surpass the ordinary concrete short pier shear wall. On the basis of the experiment, the discriminant of the boundary to cut the cross ratio is established.

In 2007, Ren [6] applied two ceramsite concrete shear wall with different style reinforcements to study the earthquake resistance performance under low cycle reciprocate load. Through the test, their loading behavior, deforming behavior, ductility, energy dissipation capacity and destruction character have been compared. It indicates that the stress performance of ceramsite concrete short pier shear wall is similar to the ordinary concrete. The ceramsite concrete shear wall with the diagonal reinforcement improves earthquake resistance performance. Besides, it enhances the distortion performance, the ductility and so on. The limit supporting capacity is enhanced 8.5%, the biggest elastic-plastic displacement is enhanced 27%, the coefficient of ductility enhanced 30%, the ability to consume energy is enhanced 19.5%. It indicates that the ceramsite concrete shear wall with the diagonal reinforcement enhances both earthquake resistance and the economic efficiency.

In 2007, Zhu [7] conducted the experiment of 5 ceramsite concrete T-shaped section short pier shear wall. Based on the experimental study ,this thesis reveals the failure pattern of ceramsite concrete T-shaped section short pier shear wall under biaxel eccentric compression, reaches on the behavior of ultimate strength of T-shaped members ,examines the hypothesis of plane cross-section of average strain, and summarizes the general regularity of ultimate strength of ceramsite concrete T-shaped section short pier shear wall.

The ceramsite concrete short pier shear wall has a lot of merits. Both the 22 commercial building in Fuxin and the 20 commercial building in Benxi apply ceramsite concrete short pier shear wall [8].At present, our country takes the technical measures to conserve energy mainly through the traditional wall materials which brings a series of difficult questions. The wall reform is imperative. The characteristics of the ceramsite concrete short pier shear wall are the heat preservation, the heat insulation and so on. It has the broad prospects for the development of the construction energy conservation. However, the development of ceramsite concrete short pier shear wall is relatively slow at present. Following questions remain to be solved:

(1) The scale of ceramsite manufacturer is small, and the equipment is relatively obsolete and backward. The ceramsite product of high quality is scarce, and the cost is high. It has seriously hindered the ceramsite concrete short pier shear wall widespread application.

(2) There are a lot of research and application achievements of ceramsite concrete product. But the research of ceramsite concrete short pier shear wall is relatively few. The mature construction craft and construction method lack. Pumping construction of ceramsite concrete in high-rise construction remains to be improved.

(3) The research on how to enhance the ceramsite concrete structure mechanics performance is relatively few .So is its heat preservation.

If above questions can be solved, it must promote the ceramsite concrete short pier shear wall greatly in engineering and enrich the technical method of construction energy conservation.

Conclusions

The ceramsite concrete short pier shear wall has many merits which enable it to have a broad prospect in the future high-rise construction. It is inevitable that architecture move towards the sustainable development alone with the improvement of recognize in development, energy consumption and environment. The superiority of the ceramsite concrete short pier shear wall is extremely obvious.

References

[1] J. Guo, Green-high-strength ceramsite development, Concrete and Cement Product, 5 (2005) 44-45.

[2] Q. Li, Brief analysis of lightweight aggregate concrete development, Construction Structure Journal, 4 (2009) 23-25.

[3] D. Fu, The lightweight aggregate concrete research status, Materials Science and Technology of China's Building, 1 (2009) 47-51.

[4] Q. Yang, K. Ma, The lightweight aggregate concrete research status, Railroad Construction, 6 (2006) 104-106.

[5] X. Shi, Q. Yu, H. Tao, Lightweight aggregate concrete shear wall experimental study, Hebei Engineering Institute Journal, 3 (1993) 33-47.

[6] H. Ren, Y. Zu, Z. Ren, P. Liu, Experimental study on lightweight aggregate concrete shear wall of earthquake resistance performance, Hebei Industrial University Journal, 6 (2007) 94-98.

[7] S. Zhu, Ceramsite concrete T-shaped section short pier shear wall research, Thesis for Master Degree, Guangxi University, 2007.

[8] B. Liu, J. Tan, Z. Fu, Research on self heat-insulation system of High-rise construction, Wall Material and Energy Conservation, 6 (2006) 387-390.

© (2012) Trans Tech Publications, Switzerland
doi:10.4028/www.scientific.net/AMM.238.611

Application of Improved Response Surface Method Based on Kriging Model to Structural Reliability Analysis

Buyu Jia [a], Quansheng Yan [b] and Xiaolin Yu [c]

School of Civil Engineering and Transportation, South China University of Technology, Guangzhou 510641, China

[a]jbyretop@126.com, [b] yancy95@gmail.com, [c] XLYU1@scut.edu.cn (corresponding author)

Keywords: Kriging model; Monte Carlo; improved response surface method; first excursion dynamic reliability; randomness of structural parameters.

Abstract. The paper aims to do the reliability analysis by the Kriging model. Its excellent approximating capability is taken into consideration, which is superior to traditional response surface method. An improved response surface method has been proposed based on the Kriging model. The seismic response of structure is characterized by nonlinear and complexity, more difficulties in the reliability analysis have been found as well. Compared to other methods of reliability analysis, the response surface method is regarded as an effective way to solve such problems. Thus the improved response surface method based on the Kriging is utilized to analyze the structural first excursion dynamic reliability problem under random seismic excitation. Meanwhile, the influence on the reliability due to the randomness of structural parameters is analyzed.

Introduction

The traditional quadratic polynomial response surface is difficult to truly approximate a real limit state function with a high degree of nonlinear. The Kriging-based response surface method could be used to solve the problem. The Kriging method was first proposed by South African geologist Krige in 1951, although the Kriging method was used for some applications for deterministic engineering problems, its application to structural reliability problems had not been realized by Romero et al. until 2004 [1], in which the Kriging method based on Latin sampling was compared to other methods with interpolation techniques. Kaymaz [2] proposed a Kriging-based response surface method, which was combined with FORM method for reliability analysis. The author pointed out that the selection of parameter θ in the correlation function $R(\theta, w, x)$ of Kriging model will directly affect on the accuracy of reliability index, unfortunately, so far no solution is given.

Kriging Model

The Modeling and Prediction of Kriging. The section headings are in boldface capital and lowercase letters. Second level headings are typed as part of the succeeding paragraph (like the subsection heading of this paragraph). Kriging model consists of two parts of the polynomials and the random distribution [3]

$$\hat{y}(\mathbf{x}) = \left[f_1(\mathbf{x}) \cdots f_p(\mathbf{x}) \right] \boldsymbol{\beta} + z(\mathbf{x}) = f(\mathbf{x})^T \boldsymbol{\beta} + z(\mathbf{x}) \tag{1}$$

Where $\boldsymbol{\beta}$ is the regression coefficient vector, $f_i(\mathbf{x})$ denotes a known function of $\mathbf{x}$, p denotes the number of the basis function in regression model. The $z(\mathbf{x})$ is assumed to be a Gaussian stationary process with zero mean and covariance

$$E\left[z(\mathbf{w}) z(\mathbf{x}) \right] = \sigma^2 \mathrm{R}\left(\theta, \mathbf{w}, \mathbf{x}\right) \tag{2}$$

Where σ^2 is the process variance, $\mathrm{R}\left(\theta, \mathbf{w}, \mathbf{x}\right)$ is the correlation model with parameters θ between $\mathbf{w}$ and $\mathbf{x}$. For the set D ($D = [\boldsymbol{d}_1, \cdots \boldsymbol{d}_m]^T$) of training points, we have the expanded $m \times p$ design matrix $\mathbf{F}$

$$\mathbf{F} = \left[f(\boldsymbol{d}_1), \cdots f(\boldsymbol{d}_m) \right]^T, \mathbf{F}_{ij} = f_j(\boldsymbol{d}_i) \tag{3}$$

The stochastic process correlation between training points $\left(\boldsymbol{d}_i, \boldsymbol{d}_j\right)$ is written as

$$R_{ij} = \mathrm{R}\left(\theta, \boldsymbol{d}_i, \boldsymbol{d}_j\right), \quad i, j = 1, \cdots, m \tag{4}$$

Where R_{ij} is the element of correlation matrix $\boldsymbol{R}$, while the vector of correlations between $\boldsymbol{d}$ and $\mathbf{x}$ is written as

$$\boldsymbol{r}(\mathbf{x}) = \left[\mathrm{R}\left(\theta, \boldsymbol{d}_1, \mathbf{x}\right), \cdots, \mathrm{R}\left(\theta, \boldsymbol{d}_m, \mathbf{x}\right)\right]^T \tag{5}$$

The linear predictor ($\mathbf{Y} = \left[y_1, \cdots, y_m\right]$) is given as

$$\hat{y}(\mathbf{x}) = \boldsymbol{c}^T \mathbf{Y} = \boldsymbol{c}^T (\mathbf{F}\boldsymbol{\beta} + Z) \tag{6}$$

Where $\boldsymbol{c} = \boldsymbol{c}(\mathbf{x}) \in R^m$. From these outputs the unknown parameters $\boldsymbol{\beta}$ and σ^2 can be estimated as

$$\begin{cases} \hat{\boldsymbol{\beta}} = \left(\mathbf{F}^T \boldsymbol{R}^{-1} \mathbf{F}\right)^{-1} \mathbf{F}^T \boldsymbol{R}^{-1} \mathbf{Y} \\ \hat{\sigma}^2 = \dfrac{1}{m}\left(\mathbf{Y} - \mathbf{F}\hat{\boldsymbol{\beta}}\right)^T \boldsymbol{R}^{-1}\left(\mathbf{Y} - \mathbf{F}\hat{\boldsymbol{\beta}}\right) \end{cases} \tag{7}$$

So the predictor can be rewritten as

$$\hat{y}(\mathbf{x}) = f(\mathbf{x})^T \hat{\boldsymbol{\beta}} + \boldsymbol{r}(\mathbf{x})^T \hat{\gamma} \tag{8}$$

Where $\hat{\gamma} = \boldsymbol{R}^{-1}(\mathbf{Y} - \mathbf{F}\hat{\boldsymbol{\beta}})$ .As $\hat{\boldsymbol{\beta}}$ and $\hat{\sigma}^2$ depend on the correlation parameters θ, it is first required to obtain them using maximum likelihood estimation:

$$\min_{\theta > 0} \left\{ \left|\boldsymbol{R}\right|^{\frac{1}{m}} \hat{\sigma}^2 \right\} \tag{9}$$

By solving the minimum optimization problem of equation (9), the parameter can be obtained and the best prediction model of Kriging can be built. In this paper, the linear regression function and the Gauss correlation function are adopted, which are more suitable for the problems with a nonlinear limit state function.

The Optimization of Correlation Function Parameter. As $\hat{\boldsymbol{\beta}}$ and $\hat{\sigma}_z^2$ depend on the correlation parameter θ, the value of θ has very important influence on the entire model, which can be obtained by solving the optimization problem (9) with respect to θ. In order to get accurate reliability results, the approximate response surface is required to accurately fit the limit state function near the design point, therefore, the selection of θ will directly affect the accuracy of reliability index. The genetic algorithm is used to optimize the parameter θ in this paper.

The Improved Response Surface Method Based on Kriging Model

LHS method. Kriging is a learning and prediction theory based on limited number of samples, therefore, how to select typical samples is particularly important, in other word, the experiment design for the initial input training sample is needed. The LHS is considered as a more effective method of experimental design, and it is adopted in this paper.

The Improved Response Surface Method Based on Kriging Model for Reliability Problems. At present in the domain of Kriging-based reliability, generally, the Kriging model is only used to build an approximate model with the establishment of the mapping between input and output, and then the calculation of reliability is implemented by using the FORM method or MC simulation. Sometimes for the sake of the accuracy of reliability, the training samples have to be increased in order to enhance the generalization ability of Kriging. In such way, it can be acceptable for small-scale problems, however, in practical engineering, we are generally encountered in large-scale finite element solution, the finite element analysis of complicated structure is very time-consuming, the practical application of this approach will be hindered if the size of training samples is large.

In this paper, the selection of training points has been improved, so that the selected training points can be relatively concentrated in the vicinity of design point, and by means of increasing the fitting accuracy of the approximate response function in the vicinity of design point, the accuracy and efficiency of reliability analysis will be improved. Unlike the general MC-RSM method, the proposed improved response surface method just needs a small amount of training points to update the iterative process, which can take advantage of the Kriging and the MC method jointly, at last the accuracy and efficiency of reliability analysis will be considerably increased. Based on the inherent characteristics of Kriging model, a criterion to determine the new "important training points" is presented in this paper as follows:

Considering the approximate limit state function value $|g(x)|$ as well as the probability density of test point , obviously, the smaller the value $|g(x)|$ of test point, the higher its importance, meanwhile, the higher the probability density of test point, the higher its importance, so we a can construct such a thought :

First select a small number of training points used to construct the initial Kriging model, next, implement the Kriging prediction of test sample points, and then view those test points which have the "importance" as the important points, the criterion to determine the "importance" is described by the criterion function $C(x)=|g(\mathrm{x})/f(\mathrm{x})|$. The smaller the value of $C(x)$, the higher importance of x. Normally, we can pick one or a small amont of test points which have the minimal value of $C(x)$ as the new additional training points. The algorithm flow can be written as follows:

Setp1: Take advantage of the MC simulation to get the test sample points of random variables $\boldsymbol{v}_i = (v_{i1}, v_{i2}, \cdots v_{in})^T$, $(i = 1, 2, \cdots, n_{MC})$.

Setp2: Select part of test sample points as initial input training sample points, and the experiment design of initial training sample points is implemented by using LHS method.

Setp3: Based on the initial training sample points which have been passed through the experiment design, carry out the structural finite element analysis to obtain the structural response.

Setp4: Optimize the parameter θ using the genetic algorithm and construct the Kriging model.

Setp5: Implement the prediction by Kriging to get the approximate value of performance function $\hat{g}_X(\mathbf{v})$, then calculated the failure probability $\hat{p}_f$. If the difference between the new result and previous results satisfies a selected threshold $\left|\frac{Pf_{(k)} - Pf_{(k-1)}}{Pf_{(k-1)}}\right| \le \zeta$, then go to Setp7, otherwise, go to next step.

Setp6: Calculate the value of criterion function with the test points and the corresponding response values, then according to the results of calculation select those test points which have the minimal value of criterion function as new additional training points to update the Kriging model, and go back to Step3. We can take a strategy to reduce the number of additional training points to improve computational efficiency during the iterative process with gradual convergence. The strategy is: given a threshold ζ^* which is slightly larger than the ζ, it can be considered to be about to converge when $\left|\frac{Pf_{(k)} - Pf_{(k-1)}}{Pf_{(k-1)}}\right| \le \zeta^*$, and the number of new additional training points is reduced to one, that to say, only one new training point will be added to the previous training sample in the subsequent iterations.

Setp7: The end

The Application in Seismic Structural Reliability Analysis

The improved response surface method based on Kriging model as mentioned before is applied to solve seismic structural reliability problems, and its high efficiency is validated through numerical examples.

Discretization of Random Seismic Load. Generally, seismic load is a random procedure, which needs to be dispersed into random variables. There are several main discrete methods: Karhunen-Loève series expansion method [5], normal series expansion method [6], trigonometric series expansion method [7], and impulse response of filter Method [8]. The impulse response of filter Method is particularly well suited to modeling earthquake ground motions represents the process in terms of the response of a filter to a train of random pulses [8]. The pulses may represent intermittent ruptures at the fault, whereas the filter may represent the medium through which the waves travel. If the impulse is a Gauss procedure and the filter is linear, the random procedure $f(t)$ is a Gauss procedure. Natural vibration frequency ω_f and damping ratio ζ_f are related to the characteristics of cover soil. Usually, it can select different values based on the soil hardness. The impulse response of filter Method is adopted as the discrete method in this paper. For a Gaussian process $f(t)$ with a mean function $\mu(t)$, its discrete form can be written as

$$f(t) = \mu(t) + \mathbf{a}(t)^T \mathbf{u} = \mu(t) + \sum_{i=1}^{n} u_i a_i(t) \tag{10}$$

Where $\mathbf{a}(t) = [a_1(t), \cdots, a_n(t)]^T$ is the determinate primary function vector decided by related structures of the random procedure, $u=[u_1,\ldots u_n]^T$ is a vector of standard normal variables. Suppose that the process $f(t)$ is the response of a linear filter to a white noise excitation, according to the method described in Ref. [8], $a_i(t)$ can be explained as follows

$$\begin{cases} a_i(t) = \sigma h_f(t - t_i) \\ \sigma = \sqrt{2\pi S_0 \Delta t} \end{cases} \tag{11}$$

Where S_0 is the power spectral density of white noise, $h_f(t)$ is the impulse-respond function of the filter, given as:

$$h_f(t) = -\left[\frac{\omega_f}{\sqrt{1-\zeta_f^2}} \sin\left(\omega_f t \sqrt{1-\zeta_f^2}\right) + 2\zeta_f \omega_f \cos\left(\omega_f t \sqrt{1-\zeta_f^2}\right) \right] e^{\left(-\zeta_f \omega_f t\right)} \tag{12}$$

Where ω_f and ζ_f represent the natural frequency and the damping ratio of the filter, respectively.

The above characterization defines a stationary process. However, seismic load is usually a non-stationary random procedure in time domain and frequency domain. In order to represent the non-stationary in time domain, the random impulse can be multiplied by a certain modulation function q_t. The random procedure $f(t)$ can be rewritten as:

$$f(t) = \sum_k g_k(t) \left[\mu(t) + \sum_{i=1}^{n} u_i a_{ik}(t) \right] \tag{13}$$

Where $g_k(t)$ denotes the modulation function for the k-th filter and $a_{ik}(t)$ denotes thebasis function obtained from (11) for the k-th filter. There are various forms of modulation functions, in this paper the form of modulation function is as follows:

$$g(t) = a_1 t^{a_2} e^{-a_3 t} \tag{14}$$

The Limit State Function of Seismic Structural Reliability. First excursion failure and fatigue failure are two essential models in dynamic reliability analysis. Owing to the simplified and idealized performance, first excursion failure model is adopted in this paper. The criteria of failure based on the first excursion failure can be defined that structural response $x(t)$ (such as displacement, internal force) exceeds a selected threshold b at arbitrary time during an interval (0, T). The failure probability of the structure in given time T can be expressed as:

$$P_f = P\left\{ \min_{0 \le t \le T} G(\mathbf{x}) < 0 \right\} \tag{15}$$

The corresponding limit state function can be written as

$$G(\mathbf{x}) = b - \left| z(\mathbf{x})_t \right|_{\max}, 0 < t \le T \tag{16}$$

Where **x** are the random variables, which denote the discrete random seismic load or random parameters of structure (such as geometry and physical properties). b is the selected threshold , $|Z_t(x)|$ denotes the absolute value of structural response at time t during an interval $(0, T)$.

Numerical Example of Seismic Reliability. As seen from Fig. 1, a three bay three storey rigid frame structure under horizontal seismic excitations, consist of beams and columns, is selected as the structure background. All beams have the same characteristics, all columns have the same characteristics too. The characteristics of beam in this example are summarized as follows: elastic moduli 2×10^{11}Pa, area 0.01787m^2, cross sectional moment of inertia 0.001124m^4, weight 1371.7 N/m. And the characteristics of column are: elastic moduli 2×10^{11}Pa, area 0.02161m^2, cross sectional moment of inertia 0.001702m^4, weight 1663.6N/m. The uniformly distributed load of floor is 26267.7N/m. The weights of floor, beams and columns are transformed into equivalent nodes qualities. Rayleigh damping method is used to determine the system damping. The seismic load is simulated by using white noise procedure filter. The power spectral density is S_0=0.00016 m^2/s^3. Two linear filters are adopted, of which the natural frequency are ω_{f1}=62.83 and ω_{f2}=20.94 respectively, and both damping ratios are ζ_f=0.05. Modulation functions are defined as follows

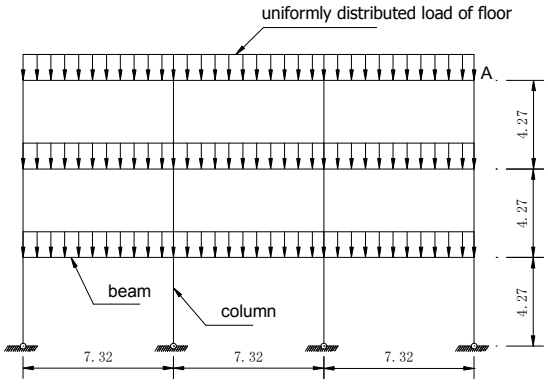
$$g_1(t)=0.0035t^{10}e^{-2.5t},\ g_2(t)=0.14t^5e^{-1.9t}$$

The duration of seismic excitations is assumed to be $T\in[0,10s]$, and the interval of random impulse is Δt=0.1s. A typical sample after discretization is presented in Fig. 2. The limit state function of the structure is defined as:

$$G(\mathbf{x})=b-\left|u_A(\mathbf{x})_t\right|_{\max}\quad 0<t\le T$$

where b=0.004, u_A(x) is the displacement response at location A as shown in Fig. 1.

The analysis of the example is implemented by the proposed method. The number of initial training sample points of each random variable is 100, and the number of test sample points created by MC simulation is 2×10^4. The calculation of reliability achieves convergence after 11 iterations (see Fig.7(a)) with 110 calls of structural dynamic analysis. Finally, the failure probability is $P_f=1.00\times10^{-3}$, and the corresponding reliability index is β=3.7190.



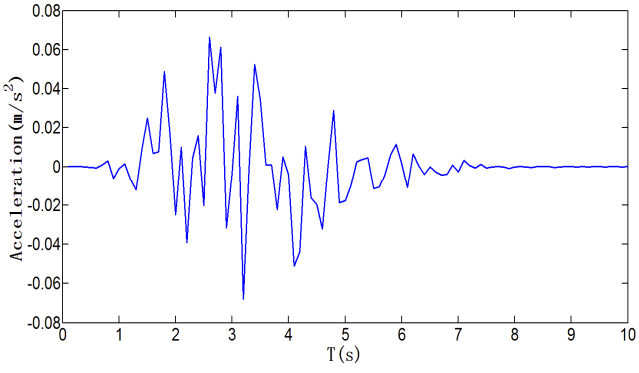


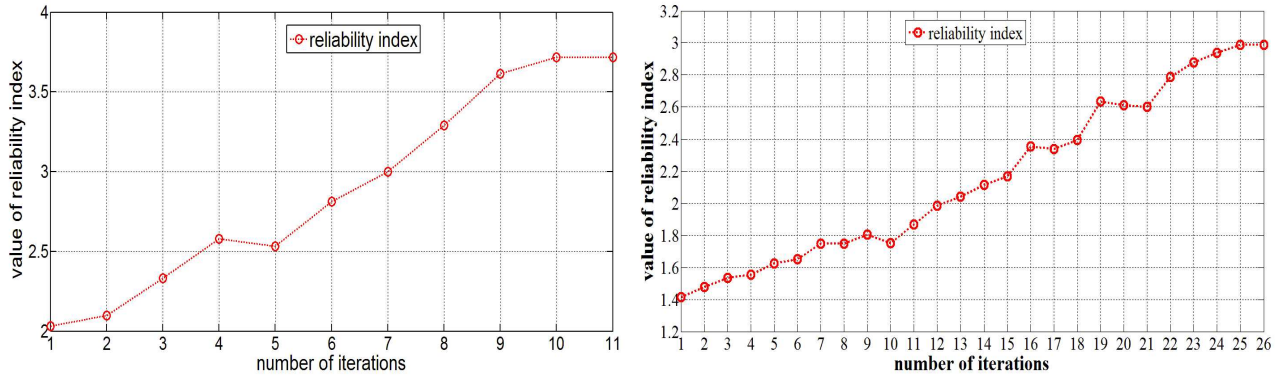
Fig.1 3-bay, 3-story frame(m) Fig.2 Discrete sample of non-stationary seismic random procedure

As well as the randomness of seismic load, the randomness of structure parameters also has a great influence on the structure reliability. Therefore, this paper takes the randomness of structure parameter into consideration, and consider the elastic moduli, area and cross sectional moment of inertia of beams and columns as random variables as shown in Table 1.

Table 1 Characteristics of random variables of structural parameters

Random variable		Distribution type	Mean	COV
Area of column	A1[m^2]	lognormal	0.02161	0.1
Area of beam	A2[m^2]	lognormal	0.01787	0.1
inertia moment of column	I1[m^4]	normal	0.001702	0.1
inertia moment of beam	I2[m^4]	normal	0.001124	0.1
elastic moduli (beam and column)	E[N/m^2]	normal	2.00E+11	0.1

There are 26 iterations in the calculation process as shown in Fig. 3(b). The failure probability is P_f=1.40×10^{-3}, and the corresponding reliability index is β=2.9889. Compared to Fig. 3(a), it can be found that the randomness of structural parameters has an important influence on the seismic reliability result, since it will significantly decrease the value of seismic reliability.



(a) Only the randomness of seismic load (b) Add the randomness of structure parameters

Fig. 3 Iterative processes with different random variables

Conclusions

Kriging Model is treated as a response surface function, so its excellent approximation capability could be fully used to approximate the real limit state function. The LHS sample method is used as a tool to implement the experimental design for initial training sample, as it can improve the representativeness of initial sample obviously. Meanwhile, genetic algorithm is utilized to optimize the parameter, because it will apparently reduce the mistakes which result from unreasonable model parameter. A criterion to determine the new "important training points" is developed to improve the selection of new training points, by which the new training points will be relatively focused on the vicinity of design point, and the accuracy and efficiency of reliability analysis will be improved rapidly. The proposed method is applied to solve seismic structural reliability problems, and its high efficiency is validated through numerical example. Meanwhile, the reliability calculation result which is achieved by considering the structure parameter randomness shows that the randomness of structure parameter will significantly decrease the value of seismic reliability.

References

[1] V. J. Romero, L. P. Swiler, A. A. Giunta, Structural Safety, 2 (2004) 201-219.

[2] I. Kaymaz, Application of kriging method to structural reliability problems, 2 (2005) 133-151.

[3] S. N. Lophaven, H. B. Nielsen, Sondergaard J. Dace, A MATLAB Kriging Toolbox, 2003.

[4] Z. Zhang, S. Li, L. Shi, et al, Engineering Mechanics, 8 (2007) 111-115.

[5] R. G. Ghanem, P. D. Spanos, Journal of Engineering Mechanics, 10 (1991) 2351-2372.

[6] J. Zhang, B. Ellingwood, Journal of Structural Engineering, New York, N.Y. 6 (1996) 701-704.

[7] M. Grigoriu, Journal of Engineering Mechanics, 2 (1993) 328-343.

[8] A. Der Kiureghian, Probabilistic Engineering Mechanics, 1 (2000) 81-90.

© (2012) Trans Tech Publications, Switzerland
doi:10.4028/www.scientific.net/AMM.238.617

A New Bending Stiffness Measurement Technique Based on Distributed FBG Sensing Technology

Yunlong Wang[1, 2, a], Xiaoming Yuan[1,b], Xiaoguang Cai[3,c] and Yongzhi Wang[1,d]

[1]Institute of Engineering Mechanics, China Earthquake Administration, Harbin 150080, China

[2]Key Laboratory of Earthquake Engineering and Engineering Vibration, Institute of Engineering Mechanics, CEA, Harbin 150080, China

[3]Institute of Disaster Prevention, Beijing 101601, China

[a]wyl_iem@hotmail.com, [b]yxmiem@163.com,

[c]caixiaoguang123@163.com, [d]yong5893741@163.com

Keywords: bending stiffness EI; laboratory tests; distributed FBG; sensing technology.

Abstract. Distributed fiber Bragg grating (FBG) sensing technology is used to measure the bending stiffness of a thin-walled aluminum tubes beam. In this work, the FBG sensing method is introduced, and the test result is compared with the nominal value based on the traditional mechanics of material computation.

Introduction

EI is defined as the bending stiffness of flexural members. It is an important parameter in the static analysis and dynamic analysis of structures. Generally, modulus of elasticity E was obtained by mechanical testing of materials or code table look-up, then moment of inertia I can be got by Geometric measurement and mathematical computation [1]. However, when the corrosion materials were unwittingly used to make the specimen or the local mini damage was happened on the member, which usually appears on the thin-walled structural element, there would be an error between the calculated nominal value and the real, leading to considerable errors of the experimental results.

A fungible measurement technique, which based on distributed FBG strain sensing technology, was proposed whereby the bending stiffness of actual components was obtained when only small deformation was appeared. This measurement technique can bring advantages such as electromagnetic immunity (EMI), high resolution, non-destructive testing, and real-time sensing capability to experimental results. In this paper, the new method is introduced and a real measurement is carried out with a structure shaking table tests to measure the bending stiffness of a thin-walled aluminum tubes beam. The test result was compared with the traditional mechanics of materials computation.

FBG Sensing-Deflection Method

Optical fiber sensor systems have been confirmed to be particularly effective for obtaining distributed strain measurements, which can then be converted to desired displacements within the constraints of an appropriate model [2, 3]. For this method, measurements were obtained using a fiber Bragg grating-based strain sensor system [4]. The wavelength shifts $\Delta\lambda$ encountered at each grating then known to be proportional to strain ε via the strain-optic relationship

$$\Delta\lambda = \xi\lambda_0\varepsilon \tag{1}$$

Where $\xi = 0.78$ for light centered near 1550 nm (infrared). A schematic diagram of the FBG sensing beam can be seen in Fig. 1.

Based on the strain equation measured by the FBG sensors, the deformation and rotation angle can be calculated through the equation (2) [4].

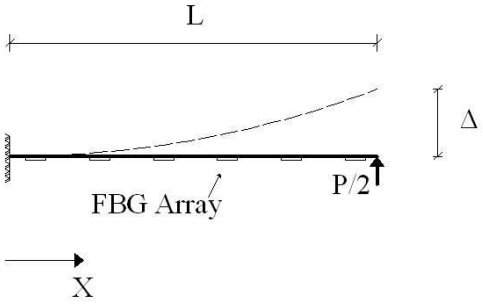


Fig. 1 Schematic diagram of a FBG sensing beam.

$$\Delta_k(x) = \frac{1}{z}\iint \varepsilon_k(x)dzdz = \frac{1}{z}\iint (a_k + b_k x)dxdx \tag{2}$$

Where strain is linear, and a_k and b_k are unknown constants which can be obtained by fitting method based on the strains measured by FBG sensors at a certain time k, $\Delta_k(x)$ is the lateral displacement along the sensing beam at a certain time k. Corresponding calculated sketch is presented in Fig. 2.

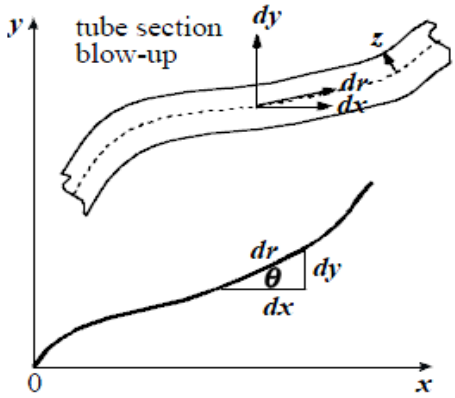


Fig. 2 Computing model of a FBG sensing beam.

The deflection of the cantilever end Δ can be calculated through the equation (3) [5].

$$\Delta = \frac{1}{6}PL^3 \cdot (EI)^{-1}. \tag{3}$$

Where P is twise the load on the cantilever end, and L is the effective beam length. Corresponding calculated sketch is presented in Fig. 1.

In the test, P, L are known conditions, and Δ can be calculated through FBG method. Then, bending stiffness EI can be obtained through the equation (3).

The Test and Results

The bending stiffness EI of a thin-walled rolled aluminum tubes beam was measured with the FBG sensing technology in the test. The parameter of the girder was presented in Table 1.

Table 1 Parameters of the thin-walled aluminum tubes beam

Effective length $2L$ (m)	Outer Diameter D (mm)	Internal Diameter d (mm)	Nominal Modulus of Elasticity E(Gpa)
0.5	12.1	10.1	69

Load is applied to the midpoint of the simply supported beam. There are both loading process and unloading process. For each loading step, the load P is recorded and the deflection Δ is calculated the arrangement diagram is shown in Fig. 3.

According to the symmetry of the structure, half of the beam is regarded as the computational model, which was described in Fig. 1. The relationship between load P and deflection Δ was shown in Fig. 4, a strong linear relationship can be observed.

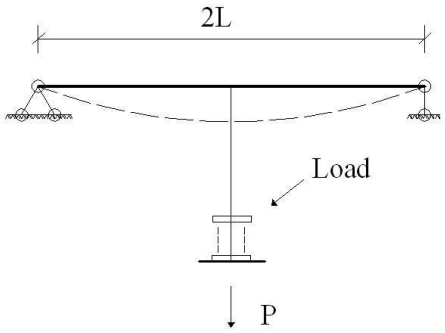


Fig. 3 The arrangement of instrument in the test

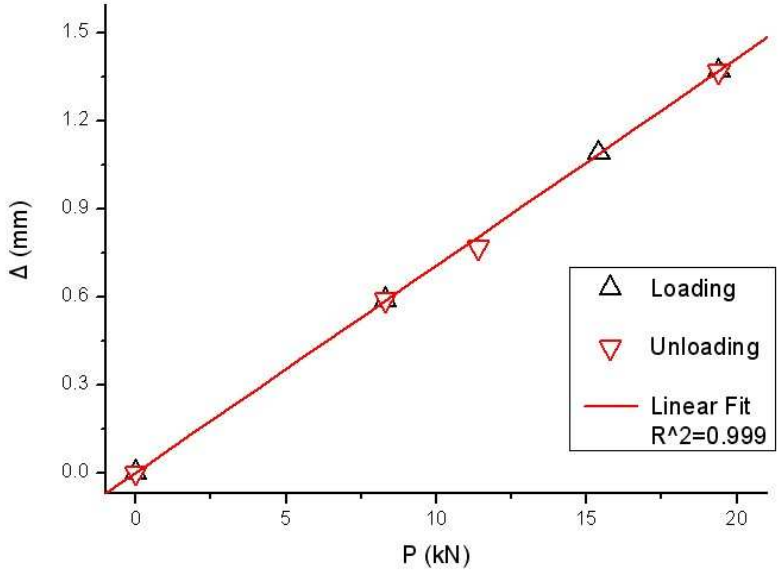


Fig. 4 Relationship between cycle number and ratio of liquefaction shear stress.

The test result of the bending stiffness of the aluminum piles and the nominal value was recorded in Table 2. The nominal value can be calculated through the equation (4). The meanings of the symbols are explained in Table 1.

$$EI = \frac{1}{64} E \cdot \pi \cdot (D^4 - d^4) \,. \tag{4}$$

Table 2 *EI* of the thin-walled aluminum tubes beam

Test Result ($Pa \cdot m^4$)	Nominal value ($Pa \cdot m^4$)	Absolute Error ($Pa \cdot m^4$)	Relative Error (%)
37.30	37.36	-0.06	0.17

Conclusions

A real measurement is carried out to measure the bending stiffness of a thin-walled aluminum tubes beam. The test results were compared with the mechanics of material computation. Following conclusions can be obtained.

The FBG based methods are effective on measuring the bending stiffness *EI* of a beam, in which the error is less than 2‰.

The FBG sensor can be used to monitor the beam deformation in structural mechanics experiments after measuring *EI*. There is no additional workload in the methods.

The nominal value based on the traditional mechanics of materials computation, which is more than the real value, makes test result of the structural mechanics experiments incline to be dangerous. It is necessary to measure *EI* before the test with non-destructive testing methods, and the method proposed in this paper is an acceptable choice.

Acknowledgements

This work was financially supported by Specific Item of Fundamental Scientific Research in Institute of Engineering Mechanics (2011B07) and Earthquake Engineering and Engineering Vibration Laboratory Fund, Institute of Engineering Mechanics (2009A04).

References

[1] H. Liu, Mechanics of Materials, Higher Education Press, Beijing, 1992. (in Chinese)

[2] L. A. Overbey, M. D. Todd, M. Seaver, L. He, A. Elgamal, in: Proc. 23rd International Modal Analysis Conference (2005 IMAC-XXIII): Conference & Exposition on Structural Dynamics, Society for Experimental Mechanics, Inc., Orlando, Florida, USA, 2005.

[3] M. D. Todd, G. A. Johnson, C. C. Chang, Real-Time Girder Deflection Reconstruction Using a Fiber Bragg Grating System, in: Proc. 18th International Modal Analysis Conference., San Antonio, TX, February 7-10, 2000.

[4] A. D. Kersey, M. A. Davis, H. J. Patrick, M. LeBlanc, K. P. Koo, C.G. Askins, M. A. Putnam, E. J. Friebele, Fiber Grating Sensors, J. Lightwave Technol., 15 (1997) 1442-1463.

[5] Y. Long, Structures Mechanics (I), Higher Education Press, Beijing, 2000. (in Chinese)

© (2012) Trans Tech Publications, Switzerland
doi:10.4028/www.scientific.net/AMM.238.621

Fire and Post-fire Performance of Space Grid Structures

Guangyong Wang[1,a], Xingqiang Wang[2,b] and Guangwei Liu[3,c],

[1] Institute of Building Fire Research, China Academy of Building Research, Beijing 100013, China

[2] Shandong Polytechnic, Jinan 250013, China

[3] Water Affairs Bureau of Pinyin County, Jinan 250400, China

[a]wanggy0609@163.com, [b]wxqyy03@163.com, [c]pingyinshuiwuju@163.com,

Key words: fire performance; after fire; grid structures; tensile membrane action.

Abstract. A fire performance finite element (FE) model of space grid structures in fire and after fire is proposed, and deformation, stress redistribution, failure modes of grid structures are also studied. The result shows that tensile membrane action arises when the grid is loaded after fire, and the load bearing capacity after fire is reduced by fire damage.

Introduction

The potential fire hazards make it very important to study the fire performance of grid structures. At present, the research is primarily focused on the fire performance in fire. For example, Li G Q [1] proposed a temperature field calculation method for large space buildings; Xue S D [2] studied the effect of smoke emission on fire temperature field of large space structures. Few literatures focus on the fire performance during fire and after fire. This paper proposes a method for the fire and post fire performance of grid structures.

A FE Model for Fire and Post Fire Performance of Space Grid Structures

Grid Structure Model. A large mall with a length of 45m, width of 45m, was chosen as the typical model. The grid is composed of orthogonal pyramids, and every pyramid has a plane dimension of 3m×3m and a depth of 2.4m. Steel tubes are used as truss bars; the diameter and wall thickness of the chord bars are 80mm and 4mm, respectively, and they are 45mm and 3.5mm respectively for web bars.

ABAQUS was used to construct the FE model for the grid structures, the model is shown in Fig.1.

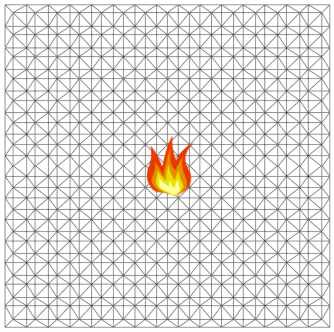


Fig.1. Grid structure model

Fire Model. A typical fire process can be divided into the heating stage and the cooling stage.

Heating Stage. Because the building area of a grid structure is usually large compared with an apartment, the fire occurs in a grid structure building is a large space fire. Literature [3] proposed a large space fire model

$$T(x,z,t) - T_{\mathrm{g}}(0) = T_{\mathrm{z}}[1\text{-}0.8\exp(\text{-}\beta t) - 0.2\exp(-0.1\beta t)] \times [\eta + (1-\eta)\exp(\frac{-(x-b)}{\mu})] \quad t \leqslant t_{\mathrm{h}} \quad (1)$$

Where $T(x,y,t)$ is the temperature (℃) of a space point with a distance x from the fire center and a vertical distance z from the ground at time of t; T_{z} is the maximum temperature increment (℃) of the

fire center with a vertical distance z(m) from ground; t is time (S); t_h is the critical time between the heating stage and the cooling stage; b is the radius of the fire which is postulated as a circle fire mode; $T_g(0)$ is room temperature; β, η, μ can be referred to literature [3].

The height of the grid is 6m. The fire is assumed to be a high power fire, and the heat release rate is assumed as 25MW. According to literature [3], the parameters can be determined as follows: T_z=672 ℃, b=5.64m, β=0.0008, η=0.44, μ=6.6.

Cooling Stage. At present, there is no sufficient information about the cooling stage of a large space fire, so it is assumed that all the temperature decreases linearly to room temperature in the same time period. The environmental temperature-time curve in the centre of the grid is shown in Fig.2.

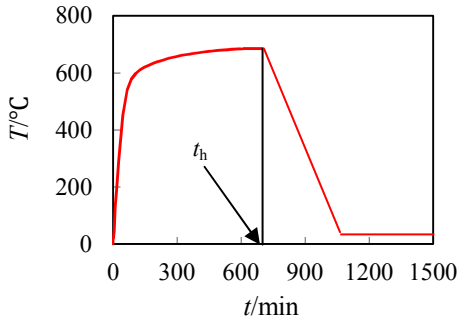


Fig. 2 Environmental temperature-time curve in the centre of the grid

Post Fire Stage. After fire, the grid structure is at room temperature, and it still has residual load bearing capacity, but the structure is suffered from fire damage.

Fire Scenarios. The fire center is assumed to be located at the center the grid as shown in Fig. 1.

Steel Mechanical Properties. Elasto-plastic isotropic hardening model was used. The axial stress-strain relation and modulus of elasticity of steel at high temperatures recommended by EC3 [4] was adopted. Literature [5] shows the modulus of elasticity after fire is the same as room temperature. The residual strength of steel after fire depends on the maximum temperature in fire, and the model recommended by literature [5] is used, which is shown bellow

$$\begin{aligned} f_{yTm}/f_y &= 1.0 && T_m \le 400^oC \\ f_{yTm}/f_y &= 1+2.23\times10^{-4}(T_m-20)-5.88\times10^{-7}(T_m-20)^2 && 400^oC<T_m\le 800^oC \end{aligned} \tag{2}$$

Where f_{yTm} is yield strength when the maximum temperature is T_m; f_y is yield strength at room temperature.

Thermal-mechanical Coupling Method. A thermal-mechanical coupling model is proposed based on the sequential coupling calculation of ABAQUS.

Literature [3] defined the section shape coefficient, which can be expressed as F/V for circular section, where F is the surface area per unit length of a steel bar, and V is the volume per unit length of the steel bar. Literature [3] gave a conclusion that the section temperature of the steel member can be considered as uniform when F/V is greater than 10. In this paper, one dimensional heat conduction element DC1D2 was used in the heat transfer model, and a user defined subroutine for temperature field analysis was programmed. Truss element T3D2 were used for mechanical analysis.

Implementation Method. In fire the steel mechanical property is related to the temperature, and the steel mechanical properties after fire depend on the maximum history temperature even though the current temperature is at room temperature.To define a material model for both fire and post fire stage, a field variable was used to represent the maximum temperature. So the steel material model can be defined to be a function of temperature and the field variable.

The mechanical analysis procedure is divided into 3 load steps. In the first step, the loads increase linearly with time while the temperature remains constant. In the second step, the temperature increases firstly and then decreases to room temperature In the third step, the loads increase while the temperature is at room temperature. In this analysis, it was assumed that the air temperature increases first during 60min, and then decreases to room temperature during 20min. The step time period is 300

min considering the lag of structure temperature change compared to the air temperature, and the time is the true time. The period of step 3 is 100 min during which the top chord joint loads increases linearly from 10KN to 100KN. The 100 min time period denotes only the loading sequence, and it isn't the true time.

Mechanical Behavior in and after Fire

Deformations. The vertical displacement-time relationship of the central joint of the grid during and after fire is shown in Fig.3., in which U3 is the vertical displacement in meters and *t* is time in minutes. Point A shows the maximum vertical displacement, and AB stage shows the displacement recovers during cooling stage. Point C shows the beginning of post fire loading. It can be seen that the vertical displacement increases accompanied with the rise of the temperature. In the cooling stage, the displacement decreases, and it indicates that the deformation recovers to some extent. The maximum displacement is 0.62m, and changes to 0.50m after cooling stage with the recovery of 0.12m.Therefore the displacement of the grid recovers after fire to some extent, but because the maximum air temperature is high, the recovery is small. After point C, the displacement increases with the increment of the loads until the grid structure fails.

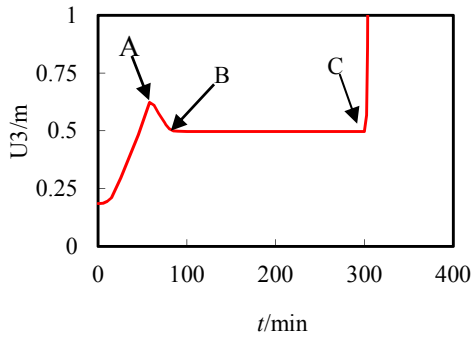


Fig. 3 Node vertical displacement-time relation

The grid centre deflection (*f*)-time (*t*) relation curve in post fire stage is shown in Fig. 4. The value of the time (*t*) in this figure can be regarded as the load magnitude. It shows that the deflection increases dramatically at point A until point B, after which the deflection increment velocity gets smaller. After point C it increases dramatically again, and point C can be defined as the ultimate state.

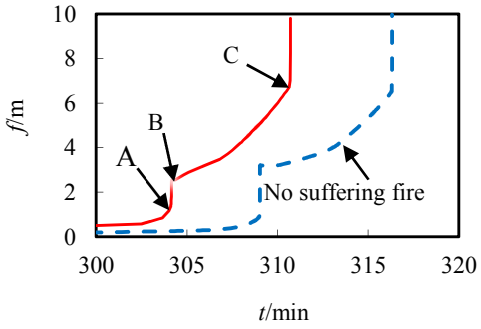
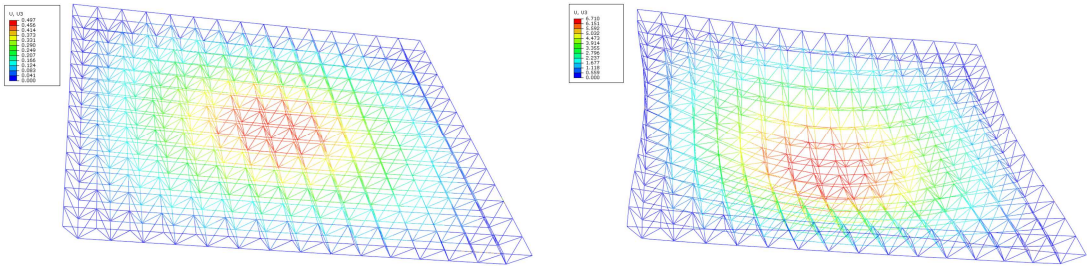


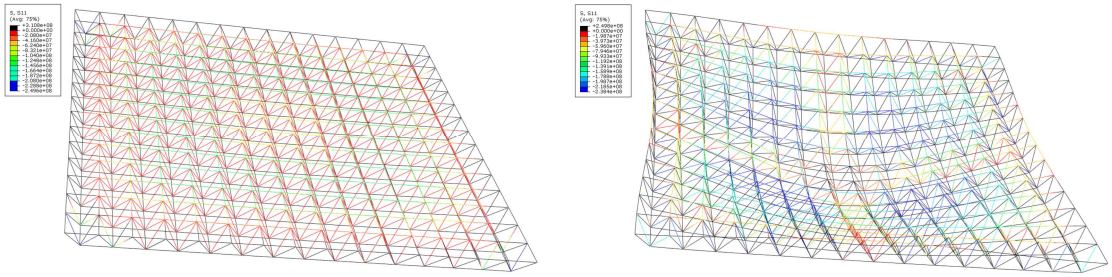
Fig. 4 Load-deflection curve

The vertical displacement (U3 in m) and stress (S11 in MPa) at some time points are shown in Fig. 5. and Fig. 6. respectively. It can be seem that when time is 300min, the displacement is small, and compressive stress appears in top chord bars and tensile stress appears in bottom chord bars. When time is 311min, the grid deflection gets larger, and the stress of the top chord bars in the central region becomes tensile stress while the stress of bottom chord bars remains tensile. So, tensile membrane action occurs in the grid structure.



(a) t=300min (b) t=311min

Fig. 5 Deformation of the grid structure



(a) t=300min (b) t=311min

Fig. 6 Stress of the grid structure

Post-fire Load Bearing Capacity. The load bearing capacity of a grid which doesn't suffer fire damage was also shown in Fig. 4. The load bearing capacity of the grid structure subjected to fire is 19.5kN, while the grid of no fire damage is 24.4kN. From the data above, it can be seen that the load bearing capacity decreases about 20% after fire.

Conclusions

A finite element model is proposed to analyze the mechanical properties of space grid structures considering heating, cooling and post fire stages, and some conclusions can be drawn:

Tensile membrane action arises in the post fire stage.

In cooling stage, the displacement recovers to some extent, but the residual displacement is large.

The load bearing capacity of the grid structure reduces after fire.

Acknowledgements

This work was financially supported by China Academy of Building Research Fund (20110111330730002, 20110106330730001).

References

[1] G. Li, Y. Du: Utility Temperature elevation empirical formula in large space fire, Fire Science and Technology. 24 (2005) 283-287.

[2] S. Xue, J. Liang, X. Li: Effect of smoke emission system on fire temperature rise in large space structures, Journal of Disaster Prevention and Mitigation Engineering, 30 (2010), 528-542.

[3] CECS 200-2006, Technical Code for Fire safety of Steel Structure in Buildings, Beijing, 2006.

[4] BS EN1993-1-2: 2005, Design of steel structures-Part 1-2: General rules-Structural fire design, Brussels, 2005.

[5] W. Cao: Analysis of fire behavior of steel frames considering the damage accumulation, Tongji University, Shanghai, China, 1998 .

© (2012) Trans Tech Publications, Switzerland
doi:10.4028/www.scientific.net/AMM.238.625

Study of Building Design and Reinforcement Technology under the Mining Damage

Qinshan Li[1,2,3,a] and Tiecheng Wang[1,2,b]

[1]School of Civil Engineering, Tianjin University, Tianjin 300072, China

[2]Key Laboratory of Coast Civil Structure Safety (Tianjin University), Ministry of Education, Tianjin 300072, China

[3]Pingmei Shenma Construction Engineering Group Co., Ltd. Pingdingshan 467000, China

[a]pmjglqs@126.com, [b]wangtiecheng@eyou.com

Keywords: mining; design theory; new technology of reinforcement; the overall firmness; whole prestressing reinforcement technology.

Abstract. With the development of society, the demand for mining resources is increasing. Associated with underground mining of mining resources, inhomogeneous deformation such as lever tension, compression, tilt, curvature of the surface has been aroused, which generate additional forces to the building foundations, causing damage and destruction to the surface housing. This paper describes the impact on surface buildings by the surface movement and deformation due to underground mining, explores the anti-mining structural system of the surface housing, the structural design theory and the anti-mining reinforcement of new technologies. The aim is to make the building more effectively absorb and resist surface movement and deformation. The measures and recommendations of mine surface housing design and reinforcement are proposed.

Introduction

As the national economy develops, coal demand increases sharply, the amount of coal mining also become larger, the range of coal mining is becoming wider and wider, resulting in a large number of buildings and structures above the mine goaf, making the amount of coal under the ground buildings and structures is increasing in each mining area. According to concerning data reported [1, 2], the total quantity of coal is about 13.79 billion tons under state-owned coal mines (under buildings, under water, under railway), the amount of coal under buildings is up to 87.6 billion tons (about 63.5%), while the amount of coal under villages accounts for 60% of the amount of coal under buildings, about 600,000 residents' live and work are affected. After underground minerals are mined, the surface above the goaf area will produce movement and deformation, movement and deformation of the surface will spread to the building foundations, making buildings affected by varying degrees of influence, threaten the safety of the buildings. So how to take effective measures of protection, protect the buildings of mine subsidence area from the mining damage, as well as how to design more reasonable anti-mining buildings, which is one of the technical problems of coal mining under villages particularly fully mechanized top coal caving mining has not thoroughly solved.

Surface Movement and Deformation due to Mining and its Effects on Buildings

The Impact of Mining on the Surface. Definition of mining damage can be divided into two types: narrowly speaking, due to underground mining of minerals, the effects of ground and underground buildings, structures and natural objects are collectively known as the mining damage, which correspond to mine rock engineering mechanics; broader mining damage mainly refers to the rock formations and surface are affected by mining with the occurrence of a large number of mobile deformation, resulting in all the harmful consequences. There are many manifestations of mining damage, ground subsidence damage, ground tilt damage (that is non-uniform subsidence caused by mining has changed the original slope of the earth's surface, causing ground tilt), bent surface damage, level ground deformation damage etc. is its main forms.

The form of surface movement and destruction, are summed up as follows: ① The emergence of the surface movement basin. After the impact of the mining spread to the surface, the surface affected by mining down from the original surface elevation, thus a larger settlement area than the goaf area formed above the surface of the goaf, the surface subsidence in the area is known as the basin of surface movement. ② The emergence of cracks and steps. On the extranodal marginal zone of the surface movement basin, the surface may crack. ③ The emergence and formation of collapse pit [3, 4].

Mining caused surface subsidence, making the surface appear to sink, tilt, curvature, horizontal movement and level deformation etc, which led to the damage to the construction(such as natural village, railway, highway, industrial square, pipeline facilities etc) within the affected scope of mining, severe cases construction will lose their original use value. The mining subsidence on residential damage is not common, as shown in Fig. 1.



Fig. 1 Wall crack and the housing collapse

The Impact of Mining on Buildings. In mining subsidence area, the surface above the mine goaf and the surrounding surface produce movement and deformation to the foundation of the building, leading to the additional stress interaction to the building, which contribute to the deformation and the destruction of buildings (structures). The influence of mining subsidence on buildings is related to the size and the nature of surface deformation, the structural characteristics of the building itself, its impact forms are as follows:

The Destruction of the Buildings due to the Horizontal Deformation. Horizontal deformations of the surface include tensile deformation and compressive deformation. Among the surface horizontal deformation, tensile deformation is particularly of great damage to the buildings. Because buildings' capacity to resist tensile deformation is far less than the ability to resist compression deformation, therefore, smaller tensile deformation can make the building cracks. In general, the crack is most likely to produce in the weakest part of the door and window openings. Combination of brick joints can also be easily be opened.

The Subsidence Effects on Buildings. In the conditions of surface sufficient mining, flat-bottom appears in the mobile basin. Because the surface evenly sinks, when the buildings are located in the flat-bottom position, the building only has the overall displacement, in general, that's harmless. But, if there is a large amount of subsidence of the flat-bottom position and underground latent water level is shallow, these bring about long-term accumulation of stagnant water around the building or foundation excessive wet, it will affect the normal use of the buildings, seriously may result in buildings destroyed or abandoned.

Under normal circumstances, in the mining process, the buildings of the uniform subsidence area after the surface movement, will also be affected by surface "dynamic" effects of deformation, that is buildings affected by surface tension (positive curvature) deformation effects (I position in Fig. 2), with the face forward, buildings affected by surface compression (negative curvature) deformation (II position in Fig. 2). When the distance of face is greater than the 0.6H away from buildings (H is the mining depth), the buildings restore the status quo ante (III position in Fig. 2), only to have an overall vertical displacement. Therefore, one could argue that as long as the surface buildings can withstand the mining process dynamic deformation, the uniform subsidence of the surface does not cause harm to the buildings.

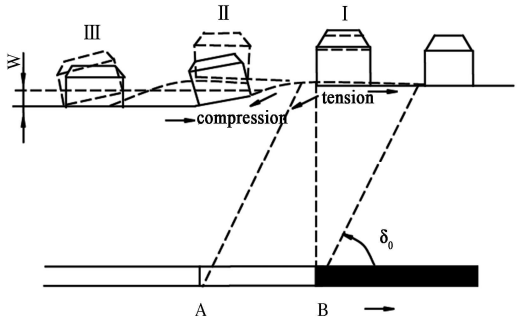


Fig. 2 Ground movement and building deformation process when underground mining

The Destruction of the Buildings due to the Tilt. After surface tilt, the buildings also will tilt. The surface tilt tends to occur in the edge of mobile basin area, the surface tilt maximum at the inflection point. The inflection point is located above the coal wall.

The surface tilt mainly has a great impact on the buildings with small basal area and large height (such as chimneys, cooling towers, etc). When they skew with the surface tilt, their weight to the formation of eccentric loading generate additional overturning moment, the interior of load-bearing structure will produce additional stress, the capacity of bearing of the substrate will be redistributed.

The Destruction of Buildings due to Curvature. Curvature represents for the difference in tilt of the surface per unit length, also represents the extent of the tilt changes on the unit length, the surface curvature has positive and negative curvature. When the buildings are affected by the positive or negative curvature, the damage characteristics is different, as shown in Fig. 3. Under the influence of negative curvature deformation on the surface, the foundations of the buildings are as if beams, which supported at both ends., the middle part left vacant, resulting in the wall to produce the "eight" shaped cracks (Fig. 3a); Being under the influence of curvature deformation on the surface, both ends of the building foundation vacant, resulting in the wall to produce the inverted "eight" shape cracks (Fig. 3b).

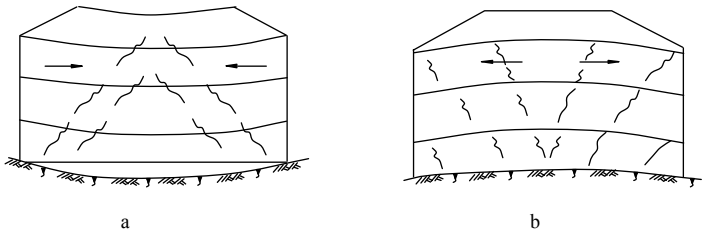


Fig. 3 The affection of ground deformation to buildings

The Theory of Mine Surface Buildings Design and Construction Details

New Housing Structure System and Theory of Design Elements. Generally speaking, in accordance with the materials, building structure systems can be divided into the masonry structure with the bulk (standard clay brick) as the main material and the structural system with concrete or steel as the main material. The latter also includes a frame structure, shear wall structure and frame-shear wall structure.

According to the actual characteristics of the surface buildings in subsidence area, we take into account two kinds of structural systems thinking—"resistance" and "drop". "Resistance" is to adopt a rigid structural system, increase the capacity of structures resisting mining deformation. "Drop" is to adopt a flexible structure system, make the buildings adapt to the surface deformation, such as the structures and measures mentioned in reference [5, 6]. Housing design theory in subsidence area including: the design theory of strip foundation and the design theory of rise-fall dot foundation.

Anti-mining Methods and Recommendations. The anti-mining protection measures to existing buildings are mainly two kinds of flexible and rigid. The flexible protective measures are to set the sliding layer and the buffer groove. The rigid protection measures are to set structural columns and ring beams, set reinforcing band under the window. The flexible protective measures are based on self organization theory under the guidance of the protection measures.

Set the Ring Beams. Reinforced concrete ring beam can enhance the integrity and stiffness of the buildings and improve bending, tensile and shear strength of the masonry structure, which is the main technical measure to improve buildings' resistance to deformation. Set reasonable ring beams can prevent or reduce the occurrence of destruction phenomenon such as the wall cracks, so as to reduce the damage to the buildings. Under the influence of horizontal deformation and curvature deformation, stress concentration will occur in the connection of vertical and horizontal walls of the buildings, reinforcing bars can be set in these places, to enhance the resistance to deformation of the walls.

When the above ring beams still can not resist the additional stress which due to the expected deformation, composite ring beams can be used. In the case of ring beams section unchanged, composite ring beams can enhance flexural capacity of the foundations.

Set the sliding layer between the ring beams and the foundations. When the surface has the horizontal displacement, the following sections of the sliding layer move with the surface, while the above portion of the sliding layer is relatively static because of their gravity. This reduces the influence of the surface movement to the superstructure and enhances the overall stiffness and strength of the buildings.

Setting the ring beams of sliding foundations is the flexible anti-distortion measure and widely used in anti-mining variant design. These ring beams can effectively absorb horizontal movement come from foundation, making the main structure of the buildings produce smaller horizontal deformation, thus they play the role of protecting the buildings.

Set Rachel Reinforcing Bars and Constructional Columns in the Walls. For general buildings, when the movement and deformation of the surface passed to the buildings, the most obvious destruction is the wall cracks, especially in the weaknesses such as the corners of the doors and windows, the "eight" shaped cracks easily generate. Vertical fractures are easy to produce in the connection of vertical and horizontal walls. Usually, in the design of the buildings resist deformation, the following kinds of anti-deformation technical measures are adopted.

① Set rachel reinforcing bars. When the surface subjects to tensile deformation, vertical fractures are easy to produce in the connections of vertical and horizontal walls, making the vertical and horizontal walls separated. Therefore, rachel reinforcing bars can be set in the connections.

② Set constructional columns. When the projected value of surface movement and deformation is large, especially when the buildings are required to withstand multiple mining influence, the constructional columns are set in the appropriate location of the wall ring beams and foundation ring beams, making them form a rectangle as a whole, this moment buildings have strong ability to resist tension and compression deformation.

③ Improve the strength of the walls. In most wall cracks, all of them develop along the brick joints. So in order to enhance the integrity of the walls, masonry and mortar strength grade should be appropriately improved.

The Use of Reinforced Concrete Strip Foundation. Reinforced concrete strip foundations have the characteristic of good integrity and the ability to resist vertical deformation. Based on this characteristic, the longitudinal foundation beams along foundations longitudinal direction of foundations should be set. Section size and reinforcement of the foundation beams are determined by calculating. Section size is designed according to the needs of longitudinal reinforcing bars and concrete structures construction standards. When design the amount of longitudinal reinforcing bars, foundation beams are regarded as longitudinal tension components, longitudinal reinforcement is designed according to the concrete tensile components. The ground cracks appear in the central beam causing slippage between the foundation and the foundation soil within the range of a half full-length, the friction generated. The design tensile stress of the beams is designed according to the friction standard values, making the cracks appear in the structure units without causing destruction to the foundations.

New Reinforcement Technology to the Existing Buildings on the Goaf Surface

Reinforcement Technology and Methods to the Existing Buildings. The commonly strengthening methods to the engineering structures are enlarging section method, paste composite material, prestressing method, sticking steel, outsourcing steel method and so on. Normally, the concrete components with cracks should firstly be repaired and reinforced by using the chemical grouting. Whether the additional reinforcement needed should be defined according to the bearing capacity of components. Reinforcement design is different from new design greatest lies in the constraints of original component. In addition to security and economic factors are taken into account in the choice of strengthening scheme, the actual force situation of the components, the surrounding environment, the possibility of construction and so on should be also considered. A method may be applicable to certain structural forms in particular, while it may not be applicable to the other structure. Or it is applicable for this project, but not very effective to the other. For reinforcement technology and methods to the existing buildings, this article only addresses the reinforcement technology and methods of concrete structure buildings and masonry structure buildings. ① Common reinforcement technology and methods of concrete structure. Commonly used methods: Enlarging section method—pour new reinforced concrete outside of the original concrete structure, increasing the cross-sectional area and reinforcement of the components, to reach the purpose of improving the components' bearing capacity and stiffness. Outsourcing steel method —a reinforcement method of outsourcing section steel to the original concrete structures, thus drastically improving the bearing capacity of components. This method is usually applied in the reinforcement of columns, but also for the girders. There are many reinforcement means of changing force transmission way. The purpose of these means is to reduce internal force peak of the components and adjust internal force distribution of all cross sections of the components, thus improving the bearing capacity of structure. The reinforcement methods of changing force transmission way mentioned here, can mainly be divided into two methods. a) Add pivot points: The method is to reduce calculation span and deformation of the structure, to improve structure' bearing capacity. b) Support beams and remove columns: in the case of not demolish or less demolish the superstructure, demolition replacement, take a long column. ② The stiffening and reinforcement of masonry structure, mainly including the reinforcement method of brick walls and brick columns. The reinforcement method of brick walls include counterfort columns method and mesh reinforcement cement mortar method. The main reinforcement method of brick columns are mainly with additional reinforced concrete, including the two reinforcement types of lateral external reinforced concrete (referred to the lateral reinforcement) and the outsourcing reinforced concrete.

New Ideas and New Technologies of Reinforcement to the Existing Buildings. For the reinforcement of the buildings in mining subsidence area, apart from the general reinforcement technology, new reinforcement technology and methods should be also considered. The new technologies of structural reinforcement that developed in recent years, include the high-strength carbon fiber reinforcement technology, the prestressing reinforcement technology and the bonding steel reinforcement method. In addition, there is a whole prestressing reinforcement technology based on the guidance of overall firmness of reinforcement ideas.

External prestressed steel tie rods or struts are applied to reinforce structure in the prestressed reinforcement method. This method not only improve the bearing capacity of the components, reduce the deflection and enhance crack resistance of the components, but also eliminate and slow stress hysteresis of added members, making the added parts to participate effectively in the work. Sticking steel reinforcement is a method of pasting steel plate outside of the components with cementing agent. The construction period of this method is short, stick steel occupies little space, almost without changing the components shape. Yet it can greatly improve the bearing capacity and performance of normal use stage of the components.

The whole prestressing reinforcement is the reinforcement technology and method that based on the guidance of overall firmness of reinforcement ideas. It is a reinforcement method, that the object being reinforced are regarded as a whole and prestress (through steel tie rods or steel stranded wire, etc) the reinforcement object (structural integrity).Through overall prestressing reinforcement,

making the added parts (such as steel tie rods or steel stranded wire, etc) force the original structure to generate the redistribution of internal forces, reducing stress level of the original structure, so that the unique stress-strain hysteresis phenomenon of the general reinforcement structure can be eliminated. So, added parts and the original structure can work preferably together. The overall carrying capacity of the structure can be significantly improved. The whole prestressing reinforcement method has the triple-effect with unloading, reinforcement, changing the internal force distribution of structure, which is suitable for large-span structure reinforcement. And it is suitable for using the general method can not be reinforced or reinforcement effect is far from ideal in the large-scale structural reinforcement in higher stress-strain state.

Conclusions

Scientific research methods tend to obtain a multiplier effect. The whole firmness of reinforcement allows structural engineers to broaden their thinking, get onto the right path and improve efficiency. It can help structural engineers to grasp the overall situation, correctly handle the practical engineering problems. Engineering reinforcement problems can not totally dependent on “the design calculations” and computers. Engineers regard computers as source to solve engineering problems, they should get a foothold in basic concepts and basic theories of engineering structure reinforcement, summary of long-term project structure reinforcement experience. Engineers grasp the scientific reinforcement method, which make structural engineers do not adhere to the existing structural system and mode. It makes engineering structural reinforcement work to meet the demands of the times, and let the work becoming creative and innovative.

Acknowledgements

The research was strongly supported by natural science foundation of China (NSFC), scientific and technological project of Henan province, natural science foundation of Henan Province.

References

[1] S. Si, Y. Zhang, J. Ma, L. He, S. Qin, The discussion of ecology geological environment restoration and sustainable development of coal mining subsidence area, Geological Hazards and Environmental Protection, 3 (2004) 11-16.

[2] Y. Zou, K. Deng, W. Ma, Mining Subsidence Engineering, China University of Mining Press, Beijing, 2003.

[3] H. He, Y. Wang, X. Chen, A. Zheng, The law of weibei mining subsidence area surface cracks in and rural resistance to deformation houses design and analysis, Journal of Xi'an Institute of Technology, 4 (2002) 249-255.

[4] Z. Meng, Method of deformation-resistant mining design under buildings, Surveying and Mapping in Sichuan, 4 (2002) 38-40

[5] Z. Chen, The Safety and Durability of Civil Structural Engineering, China Architecture and Building Press, Beijing, 2003.

[6] E. Duan, S. Li, G. Zhao, The Engineering Safety Appraisal and Reinforcement Technology, People's Traffic Press, Beijing, 2004.

© (2012) Trans Tech Publications, Switzerland
doi:10.4028/www.scientific.net/AMM.238.631

Study on the Ductility of T-Shaped Short-Limb Shear Walls(I)

Di Guo[1 a], Hua Feng[1,b], Zhipeng Li [2 c] and Jieyu Liu [3 d]

[1]Xi'an University of Architecture and Technology, Xi'an, Shaanxi 710055, China

[2] XuHui Architecture Design institute, Henan 450008, China

[3]Hehan City Urban Planning Design institute, Henan 450000, China

[a]guodjl@xauat.edu.cn, [b]fenghuafly@163.com, [c]200502612@163.com, [d]liujieyu1987@126.com

Keywords: T-shaped short-limb shear walls; ABAQUS; ductility; elastic and plastic analysis.

Abstract. In this paper, the author takes on the experiment of low cyclic load and analyzes the tenacity and ductility characteristic of the specimen, and simulates the elastic-plastic failure modes of T-shaped short-limb shear walls by using the finite element software ABAQUS and applying the damage plasticity model to select the proper unit type. Results indicate that the mechanical behavior of T-shaped short-limb shear walls under the condition of horizontal load force may be accurately simulated by the method proposed in this paper.

Introduction

Short-shear walls have been widely used in high-rise residential buildings. T-shaped short-limb shear walls are one representative form. In this paper, the author takes on the experiment of low cyclic load and analyzes the tenacity and ductility characteristic of the Specimen, as well as simulates the elastic-plastic failure modes of T shape short-swear walls by using finite element software ABAQUS .

Experimental

The low cyclic loading test of four 1/2 reduced scale specimens of T-shaped short-limb shear walls has been taken, the parameters, reinforcement and the cracks which eventually are destroyed of the specimens are shown in the essay [1].

Synthesizing the failure modes of the four specimens, we can see the webs of specimens are pulled open by the shearing force first then appeared curved scissors and the shear skew cracks. The edges of specimens are pulled but there are no obvious cracks. When the webs are pulled, there is no significant change except the cracks became wider, which shows the big eccentric failure feature; when the webs are compressed, the higher part of concrete suddenly closes to the cracks vertically so that the cracks are crushed, which shows the weak eccentric failure feature.

The test value of the four specimens, bearing capacity and the coefficient of displacement ductility are shown in Table 1.

Table 1 The test value of compressive load, limit load and displacement ductility coefficient

Patterns	n	$\frac{h}{B}$	Tensile flange					Compressive flange				
			p_y	p_u	Δy	Δu	μ_Δ	p_y	p_u	Δy	Δu	μ_Δ
ZT5-5	0.324	5	15	130	9.46	22.3	2.36	6	7	15.1	84.9	5.6
ZT7-7	0.459	5	18	142	16.5	28.5	1.76	24	11	13.5	59.8	4.4
ZT9-9	0.302	6	21	231	8.55	14.1	1.70	29	26	15.4	59.5	3.8
ZT11-1	0.488	6	25	219	8.36	13.5	1.62	23	2	10.4	43.5	4.2

From Table 1, T-shaped short-limb shear walls are under the condition of flange compression and tensile force, the specimens' strength, stiffness and ductility have bigger difference. When the webs are compressed, the deformability of the specimen is weak, its ductility is poor. When the webs are pulled, the deformability of the specimens is strong, its ductility is well.

Elastic-Plastic Finite Element Analysis

The Construction of the Finite Element Model. The finite element model material parameters take in the form of experimental values. The steel bars apply double linear model to consider the influence of strain hardening [2]. Modulus of elasticity in the hardening segment E_s' is taken one percent of initial modulus of elasticity E_s [3].

Concrete took the damage plasticity model. Compressive Stress-Strain Curve took the Saenz model:

$$\sigma = \frac{E_0 \varepsilon}{1+\left(R+R_E-2\right)\frac{\varepsilon}{\varepsilon_0}-\left(2R-1\right)\left(\frac{\varepsilon}{\varepsilon_0}\right)^2+R\left(\frac{\varepsilon}{\varepsilon_0}\right)^3} \tag{1}$$

In this expression: $R=\frac{R_E\left(R_\sigma-1\right)}{\left(R_\varepsilon-1\right)^2}-\frac{1}{R_\varepsilon}$; $R_E=\frac{E_0}{E_S}$; $R_0=\frac{\sigma_0}{\sigma_u}$; $R_\varepsilon=\frac{\varepsilon_u}{\varepsilon_0}$。

Here, $\boldsymbol{E_0}$ is the modulus of original point; $\boldsymbol{E_s}$ is Vertex cuts modulus and tangent modulus.

The rise segment of Tensile Stress-Strain Curve is supposed as straight line, for the declined curve takes in the form of Tensile curves of concrete according to Code for Concrete Structure Design [4] its expression is:

$$\sigma = E_s\varepsilon \qquad \varepsilon \le \varepsilon_0 \tag{2}$$

$$\sigma = \sigma_0 \frac{\varepsilon/\varepsilon_0}{\alpha_t\left(\varepsilon/\varepsilon_0-1\right)^{1.7}+\varepsilon/\varepsilon_0} \qquad \varepsilon > \varepsilon_0 \tag{3}$$

In this expression, $\boldsymbol{E_s}$ is Vertex cuts modulus; σ_0 is concrete uniaxial tensile strength; ε_0 is the corresponding concrete peak tensile strain; $\varepsilon_0=\sigma_0^{0.54}\times65\times10^{-6}$; α_t is the parameter in the declined segment of Tensile Stress-Strain Curve, $\alpha_t=0.312\sigma_0^2$.

The damage factor is based on the principle of the energy equivalent of damage evolution equation stated in [5]. The damage evolution equation of concrete under the compression and tensile is shown in the following expression:

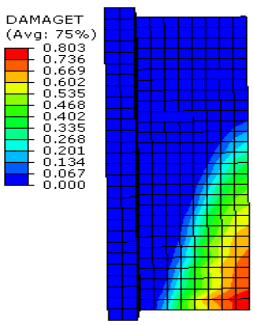
$$d_c=1-\frac{1}{\sqrt{A+B\left(\frac{\varepsilon}{\varepsilon_0}\right)+C\left(\frac{\varepsilon}{\varepsilon_0}\right)^2+D\left(\frac{\varepsilon}{\varepsilon_0}\right)^3}}; \quad d_t=1-\frac{1}{\sqrt{\alpha_t\left(\frac{\varepsilon}{\varepsilon_0-1}\right)^{1.7}+\frac{\varepsilon}{\varepsilon_0}}}.$$

The concrete used C3D8R and the steel bar used T3D2 to simulate. To embed the steel bars into the concrete by using EMBED order and to consider approximately the interfacial effect of the concrete and the steel bars by introducing the method of "Tension stiffness" in the ABAQUS damage plasticity model [6].

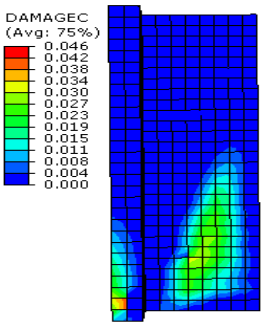
Destructive Process Simulation of Specimens. Considering the failure modes difference occurred when the T-shaped short-limb shear walls were in the bidirectional stress, in order to analyze in two directions of webs' Compression and Tensile force, the author only adopted the destructive process of ZT5-5 simply in this paper.

When webs are in the direction of tensile force (Fig. 1), the concrete of webs is pulled open first, then the specimens are yielded, at last the damage is serious when the concrete is destroyed and the damage root of the flange is also serious. In this condition, the specimens experience strong deformation and are characteristic with the blending failure. The ductility is well.

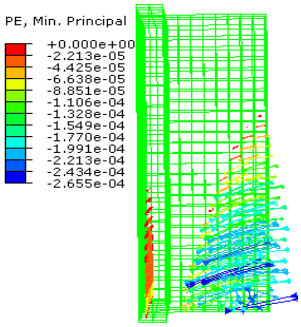
When webs are in the direction of compressive force (Fig. 2), the root of webs is destroyed, and the damage is closed to the junction between the flange and the root. The specimens experience weak deformation first, then are destroyed. In the junction between the webs and the flange, the serious damage appears on the flange and the concrete of root of webs was crashed seriously. On this occasion, the plastic strain of the specimens is small, so the deformability is weak correspondingly.



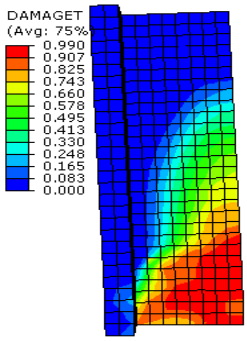
(a) Tensile damage of concrete which is yielded



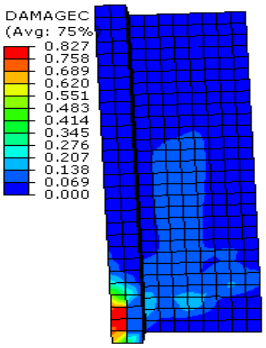
(b) Compressive damage of concrete which is yielded



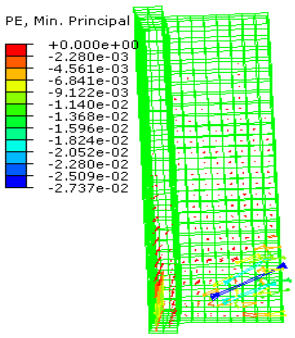
(c) Principal tensile plastic strain of concrete which is yielded



(d) Tensile damage of concrete which is destroied

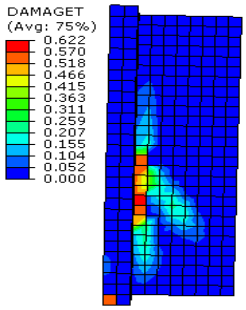


(e) Compressive damage of concrete which is destroied

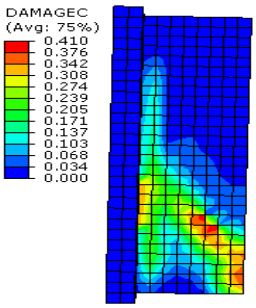


(f) Principal tensile plastic strain of concrete which is destroied

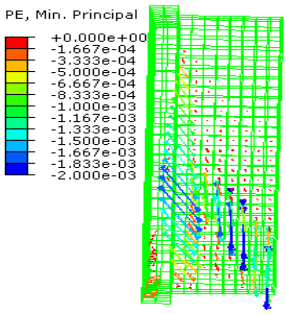
Fig. 1 Simulation for failure process of specimens with webs tensioned in failure direction



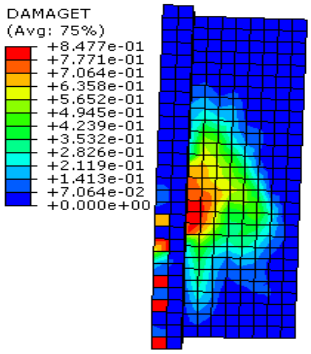
(a) Tensile damage of concrete which is yielded



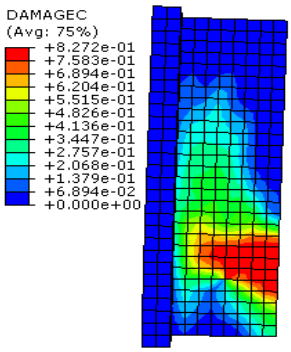
(b) Compressive damage of concrete which is yielded



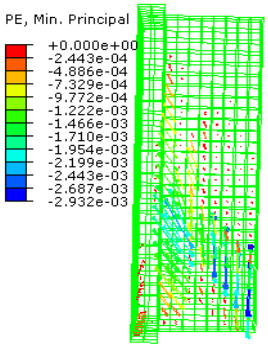
(c) Principal tensile plastic strain of concrete which is yielded



(d) Tensile damage of concrete which is destroied



(e) Compressive damage of concrete which is destroied



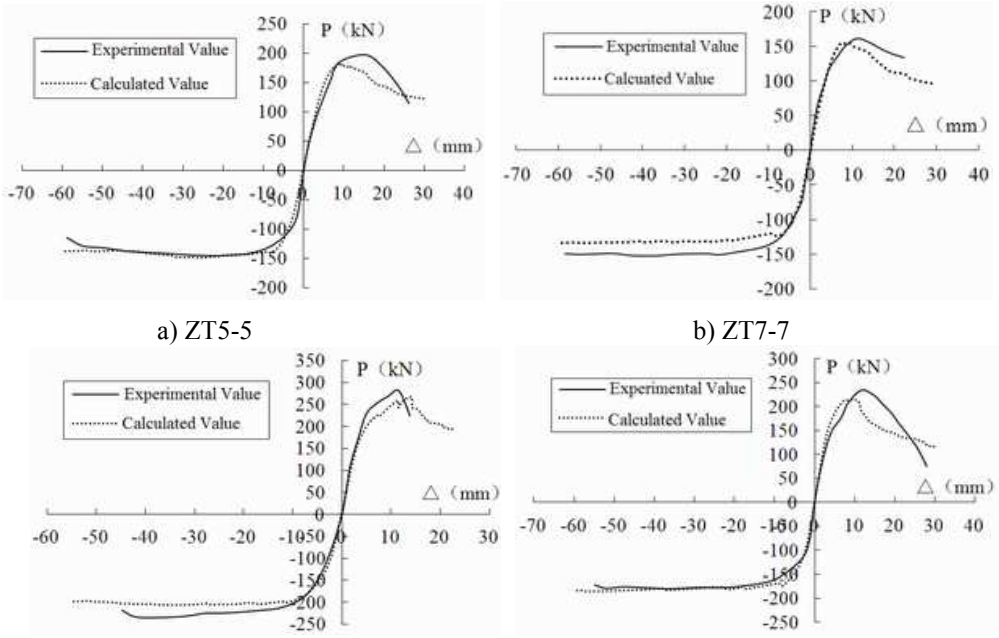
(f) Principal tensile plastic strain of concrete which is destroied

Fig. 2 Simulation for failure process of specimens with webs compressed in the failure direction

The Load-displacement Curves of the Specimen. The load-displacement curves of the four specimens whose stirrups have been adjusted are calculated by finite element under the monotonic loading condition, which is shown in Fig. 3.

As shown in the Fig. 3, the curve of load-displacement of finite element calculation is closed to the skeleton curve, which indicates the reasonability and applicability of the construction of the finite element modes. As is shown from the skeleton curve and the load-displacement curve, we can

one curve is coincide with the other well. The peak load of two curves is approximately and the peak ground displacement which calculated is lower to the experimental values.



a) ZT5-5 b) ZT7-7

c) ZT9-9 d) ZT11-11

Fig. 3 Finite element calculation load-displacement curve and skeleton cure of test

Conclusions

The low cyclic load experiment of T-shaped short-limb shear walls shows that the tenacity and ductility of the specimens have a significant difference under two different conditions compression: and tensile force. If the webs are in compressed, the ductility of specimens is poor; when the webs are in the tensile force, it is easy to be damage in the big eccentric failure, so the ductility is well.

It is better to simulate the force characteristic of T-shaped short-limb shear walls by using the finite element software ABAQUS and applying the plastic failure modes. Using the finite element software and the damage plasticity model and embedding the steel into the concrete by carrying out the embed order, which is a reasonable method to analyze the load property and failure characteristic of T shape short-limb walls.

References

[1] D. Guo, Experimental study on seismic behavior for broad limb specially shape column, Xi′an University of Architecture and Technology, Xi′an, 2001.

[2] F. C. Filippou, E. P. Popov, V.V. Bertero, Effects of bond deterioration on hysteretic behavior of reinforced concrete joints, EERC Report 83/19, Berkeley, 1983.

[3] X. Lv，G. Jin，X. Wu, The nonlinear finite element theory and application of the reinforced concrete structure, Tongji University Press, Shanghai, GB50010-2010, (1997).

[4] GB50010-2010, Code for Concrete Structure Design, China Architecture & Building Press, Beijing, 2010.

[5] X.W. Liang, L. Qian, L.N. Tan, Study on the concrete damaged plasticity Constitutive Relationbased on ABAQUS, Journal of Civil, Arehiteetural & Environmental Engineering, 32 (2010) 646-648.

[6] X. Lu, L. Ye, Z. Miu, Seimic Elasto-plastic Analyses on Building Structure, China Architecture & Building Press, Beijing, 2009.

© (2012) Trans Tech Publications, Switzerland
doi:10.4028/www.scientific.net/AMM.238.635

Study on the Property of Ductility of T-Shaped Short-Shear Walls(Ⅱ)

Zhipeng Li [1, a], Di Guo [2,b], Hua Feng[2, c] and Jieyu Liu [3,d]

[1] XuHui Architecture Design institute, Henan 450008, China

[2] Xi'an University of Architecture and Technology, Xi'an 710055, China

[3]Hehan City Urban Planning Design institute, Zhengzhou 450000, China

[a]200502612@163.com, [b]guodjl@xauat.edu.cn, [c]fenghuafly@163.com, [d]liujieyu1987@126.com

Keywords: T-shaped short-shear walls; ductility; elastoplastic analysis; reinforcement form.

Abstract. Based on the experimental study, this paper analyzes the strength and ductility of T-shaped short-shear walls and studies the measures to improve the ductility of specimens by adjusting its sectional reinforcement form. Using finite element software ABAQUS to simulate the elastic and plastic damage process of T-shaped short-shear walls after adjusting the sectional reinforcement, and then to analyze the force characteristic and ductility of the structural elements. The results indicate that under the premise of keeping the total quantities of sectional reinforcement basically constant, the proposed method can effectively improve the ductility of T-shaped short-shear walls while the webs are compressed and the reinforcement form is reasonable.

Introduction

Short-shear walls have been widely used in high-rise residential buildings. T shape short-shear walls are one representative form of which and are always used in the outside edge of buildings. Now, some researches on the mechanical behavior of T shape short-shear walls have not been fully known, especially its ductility property. This essay which was based on the experimental study uses finite element software ABAQUS to analyze the ductility of T shape short-shear walls so as to discuss the reasonable reinforcement forms.

Experimental

The low cyclic loading test of four 1/2 reduced scale structural elements of T shape short-shear walls has been taken on and parameters of the specimens are listed in the Table 1, the reinforcement of the structural element are shown in the Fig.1.

The parameters of specimens and cracks which eventually are destroyed are stated in the reference [1].Synthesizing failure modes of the four specimens, webs of specimens are pulled open by the shearing force first then appeared curved scissors and the shear skew cracks. The edges of specimens are pulled but there are no obvious cracks. When the webs are pulled, there is no significant change except the cracks will become wider and wider, which shows the big eccentric failure feature; when the webs are compressed, the higher part of concrete suddenly closes to the cracks vertically so that the cracks are crushed, which shows the weak eccentric failure feature.

The skeleton curves of the four specimens are shown in Fig. 1.

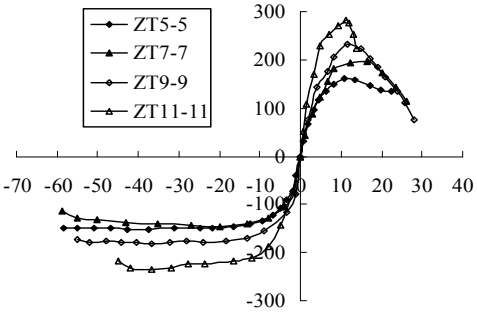
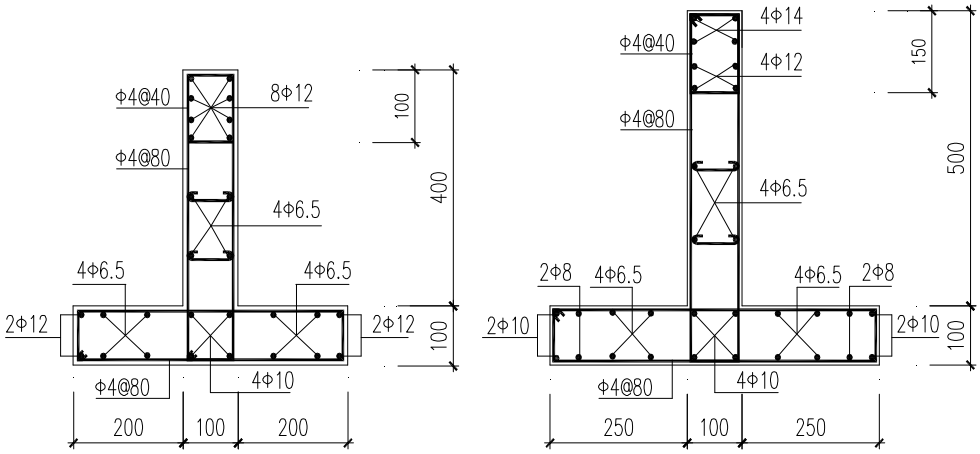


Fig. 1 Skeleton Curves of the Specimens

From Fig. 1, we can see that T shape short-shear walls are under the condition of flange compression and tensile force, the specimens' strength, stiffness and ductility have bigger difference. When the webs are compressed, the deformability of the specimen is weak, so its ductility is poor. When the webs are pulled, the deformability of the specimens is strong, so its ductility is well.

Elastic-Plastic Finite Element Analysis

Theoretical analysis shows that when the T shape short-shear walls are under bidirectional load, difference of the ductility property is mainly due to the serious asymmetry of specimens' section form. In order to reduce the difference, in this paper, under the condition of keeping the total quantities of Section Reinforcement basically unchanged, an adjustment of the distribution of Longitudinal Reinforcement of specimen which reduces flange reinforcement, increases the webs reinforcement and the redesign of the stirrup configuration, is adopted. Using finite element software ABAQUS to simulate the elastic and plastic destructive process of T shape short-shear walls of which the Section Reinforcement have been adjusted and analyze the force characteristic and ductility of the structural elements. The reinforcement of structural elements and the ratio reinforcement of section after adjustment are shown in the Fig. 2.and Chart 1, respectively.



(a) ZT5-5, ZT7-7 (b) ZT9-9, ZT11-11

Fig. 2 The reinforcement of structural elements after adjustment

Table 1 The ratio reinforcement of section through adjustment

Specimens	ZT5-5(7-7)		ZT9-9(11-11)	
	Before Adjustment	After Adjustment	Before Adjustment	After Adjustment
Flange Reinforcement (%)	1.43	1.14	1.29	0.99
Webs Reinforcement (%)	0.82	1.15	0.88	1.09

Note: The ratio of reinforcement showed in the table is that of the whole section.

The Construction of the Finite Element Model. The finite element model material parameters take in the form of experimental values. The steel bars apply double linear model to consider the influence of strain hardening [2]. Modulus of elasticity in the hardening segment E' is taken one percent of initial modulus of elasticity *E*. [3].

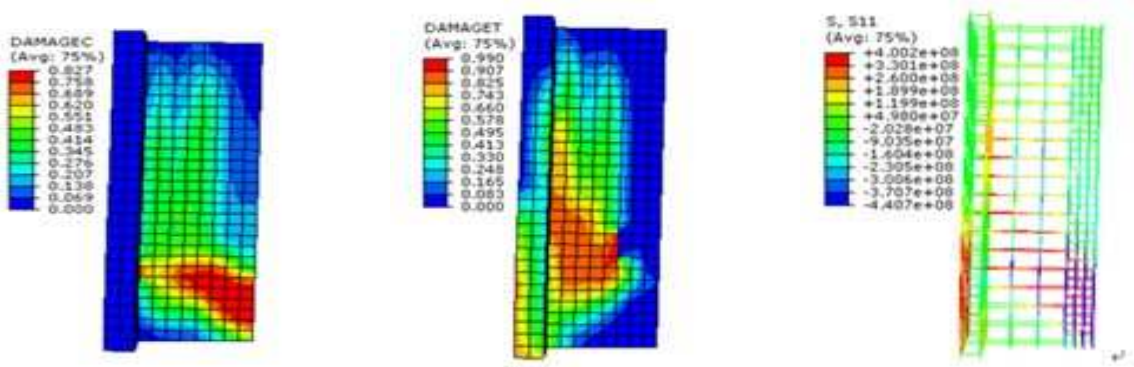
The rise segment of Tensile Stress--Stress Strain Curve is supposed as straight line, for the declined curve takes in the form of tensile curves of concrete according to Code for Concrete Structure Design [4].

The damage factor is based on the principle of the energy equivalent of damage evolution equation which stated in [5].

The concrete used C3D8R and the steel bar used T3D2 to simulate. To embed the steel bars into the concrete by using EMBED order and to consider approximately the interfacial effect of the concrete and the steel bars by introducing the method of "Tensile Sclerosis" in the ABAQUS damage elastic-plastic model [6].

The Destructive Process Simulation of Specimens. Considering the destructive difference occurred when the T shape short-shear walls were in the bidirectional stress, the analysis is carried out in two directions of webs' Compression and Tensile force. In this paper, it only gave a simple description on the destructive process of ZT5-5 and ZT9-9.

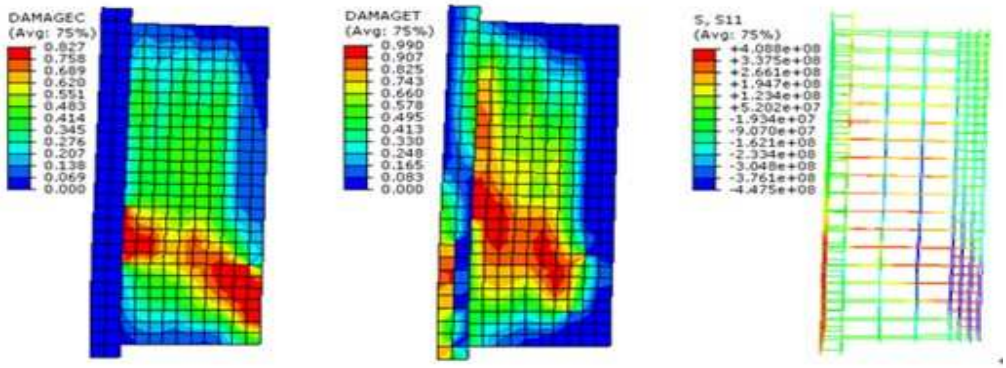
The Destructive Process Simulation of ZT5-5. When the flange of the specimen was in the tensile force (Fig.3), the concrete of webs appeared the Tension and Compression damage and the damage rose to the top gradually along about 45°slash direction. Then, there is serious tensile damage in the junction of the flange and the webs. However, the destructive power of embedded column is smaller above the section height. From the corner of webs inclined upward to flange, stirrup was forced by the large Tensile force and already came to the yield hardening segment, which indicates the concrete extended seriously in the inclined direction.



(a) destruction compression artifacts (b) destruction tensile damage (c) reinforced axial stress

Fig. 3 The finite element calculation of specimen ZT5-5 with webs compressed in the failure direction

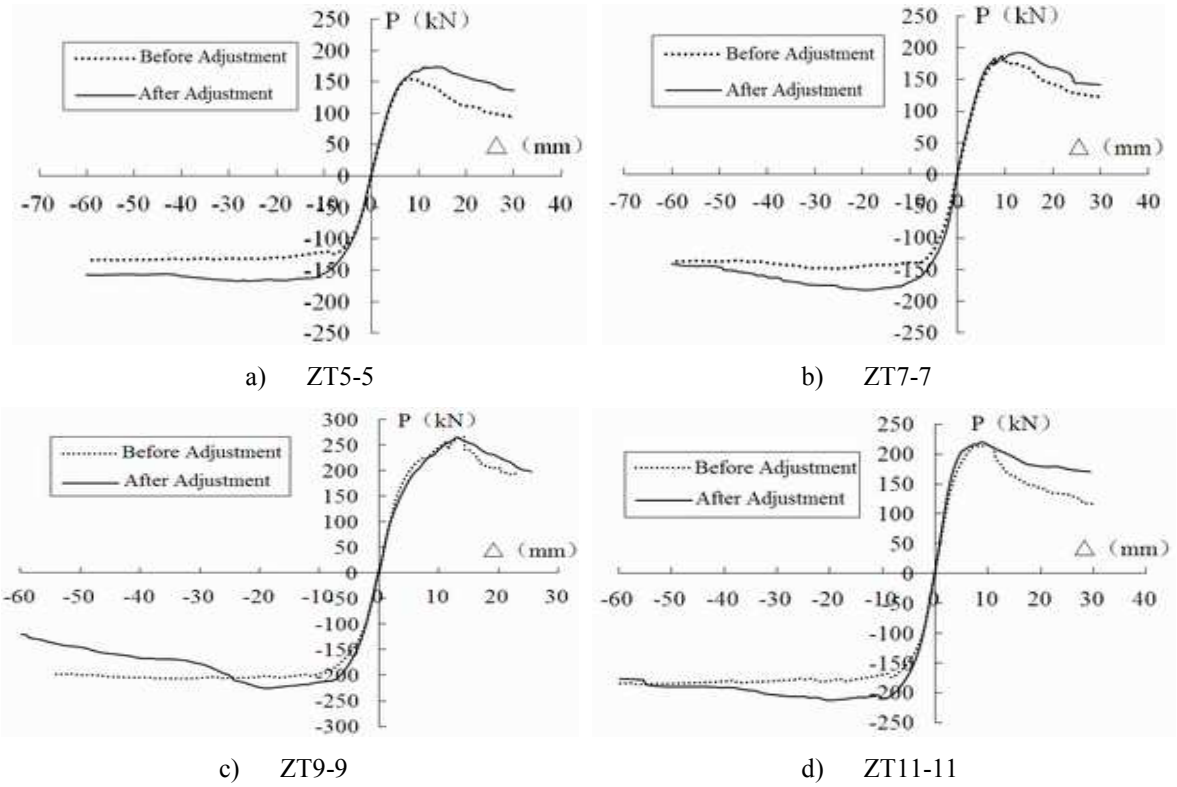
The Destructive Process Simulation of ZT9-9. When the flange was in the tensile force (Fig. 4), the concrete in the junction of the flange and the central inclined upward webs was damaged badly, and has a rising trend. The longitudinal bar on the top of the webs was bowed while lots of stirrups which in the centre reached the yield point, at this time, the specimen was influenced by the shear force obviously. And the destructive process is: first, the concrete was crushed and in the compressive area the longitudinal bar was bowed, then in the tensile force area the longitudinal bar was bowed, finally, the horizontal bar was bowed. The damage of the specimen had the characteristic of both bending destruction and shear destruction. And the shear destruction played an obvious role in the later stage, but the destructive process was relatively slow, which is a special kind of shear destruction feature.



(a) destruction compression artifacts (b) destruction tensile damage (c) reinforced axial stress

Fig. 4 The finite element calculation of specimen ZT9-9 with webs compressed in the failure direction

The Load-displacement Curves of the Specimen. The load-displacement curves of the four specimens whose stirrups have been adjusted are calculated by finite element under the monotonic loading condition, which is shown in Fig. 5.



a) ZT5-5 b) ZT7-7

c) ZT9-9 d) ZT11-11

Fig. 5 The component of load-displacement curve before and after adjustment

As Fig. 10 shown, after adjusting the reinforcement, when the webs of the specimens are compressed, the load-displacement curves drop quietly and the ultimate displacement increased significantly. The ductility of the specimens improved correspondingly. The asymmetry of curves which is to the tensile and compressive direction has improved considerably.

The Coefficient of Displacement Ductility. The coefficient of displacement ductility of the specimens after adjusting is shown in Fig. 5. In Fig. 5, the forward direction means the direction of compressive forces, the reverse direction means the direction of the tensile force.

Table 2 The coefficient of displacement ductility of the specimens after adjusting

Specimens	ZT5-5		ZT7-7		ZT9-9		ZT11-11	
	positive	reverse	positive	reverse	positive	reverse	positive	reverse
Before Adjustment	2.97	27.51	2.81	21.35	2.58	27.91	2.31	22.48
After Adjustment	4.52	13.3	3.96	9.72	3.92	12.22	3.24	4.56

As shown in Fig. 5, after adjusting the reinforcement, in the direction of compressive force the coefficient of displacement ductility have been enhanced significantly and the ductility of the specimens also have been improved. But in the direction of tensile force, the coefficient of displacement ductility of the specimens has a downward trend with the increase of the reinforcement of the webs. ZT11-11 was outstanding example. Therefore, we should not just improve the reinforcement of the webs lest the longitudinal reinforcement should not yield under the tensile force condition, the concrete should crash prematurely, and the small eccentrically brittle damage should occur.

The Analysis of the Destructive Form of the Specimens. From the results of finite element simulation, we can see that the specimens with different section width-depth ratio have different constructive characteristics. When the specimen whose width-depth ratio is 5 was loaded

horizontally toward the direction of compressive force, its weak eccentric destruction has been changed to the strong eccentric construction. At this time, its ductility could be improved significantly. If it is loaded in the direction of tensile force, the specimen is characterized with bending damage controlled by bending movement. The final type of damage of the specimen whose width-depth ratio is 6 is the shear damage, but this type of damage is caused by compressing the longitudinal reinforcement and the stirrup to yield, which is a special and slow type of shear damage.

Lots of longitudinal reinforcement and dense stirrup were set on the high part of the webs, which provided the strong constrain power for the core concrete to improve the deformation capacity of the concrete. When the specimen was destroyed finally the concrete of the lower part of the webs was destroyed seriously, at this time, the horizontal stirrup was bowed by the tensile force to impose a strong constraint power to the longitudinal reinforcement. There is connection between strain value of longitudinal reinforcement instability and unsupported length of longitudinal reinforcement(s), the diameter(d) and the pattern of loading.[7]The horizontal stirrup has reached the yield point when the specimen was destroyed, which indicated that the dense stirrup can effectively relieve instability of the longitudinal reinforcement when it was compressed and add the strain value , which relieve the damage of the specimen to improve the bearing capacity and deformability in the plastic hinge area.

Conclusions

The analysis indicates that under the premise of keeping the total quantities of Section Reinforcement basically unchanged, adjusting the form of Section Reinforcement, increasing the ratio of reinforcement, as well as improving the congregation of stirrup, applying this method can strengthen the poor part of the webs to improve effectively the ductility of T shape short-shear walls under the compressive condition. This is a reasonable method to reinforcement.

Comprehending above conclusion, in this paper, the author argues that we can use this method in the engineering practice to redesign the section for T shape short-shear walls. The length of embedded column of the higher part of the webs may take for 1.0-2.0. however, we should not only increase the ratio of reinforcement at lest cause the weak eccentric damage when the webs are compressed.

References

[1] D. Guo, Experimental study on seismic behavior for broad limb specially shape column, Xi′an University of Architecture and Technology, Xi′an, 2001.

[2] F. C. Filippou, E.P. Popov, V. V. Bertero, Effects of bond deterioration on hysteretic behavior of reinforced concrete joints, EERC Report 83/19, Berkeley, 1983.

[3] X. Lv，G. Jin，X. Wu, The nonlinear finite element theory and application of the reinforced concrete structure, Tongji University Press, Shanghai, 1997.

[4] GB50010-2010, Code for Concrete Structure Design, China Architecture & Building Press, Beijing, 2010.

[5] X. Liang, L. Qian, L. Tan, Study on the concrete damaged plasticity Constitutive Relationbased on ABAQUS, Journal of Civil, Architectural & Environmental Engineering, 32 (2010) 646-648.

[6] X. Lu, L. Ye, Z. Miu, Seimic Elasto-plastic Analyses on Building Structure, China Architecture & Building Press, Beijing, 2009.

[7] Z. Cao, Y. Chen, L. Yong, et al, Study on strength, ductility and hysteretic behavior of reinforced ceramsite concrete members subjected to axial load and flexure, Building Structure, 6 (1988), 2-16.

© (2012) Trans Tech Publications, Switzerland
doi:10.4028/www.scientific.net/AMM.238.640

Seismic Research and Development of Steel Plate Concrete Composite Shear Wall

Yabin Yang

North China University of Water Resources and Electric Power, Zhengzhou 450011, China

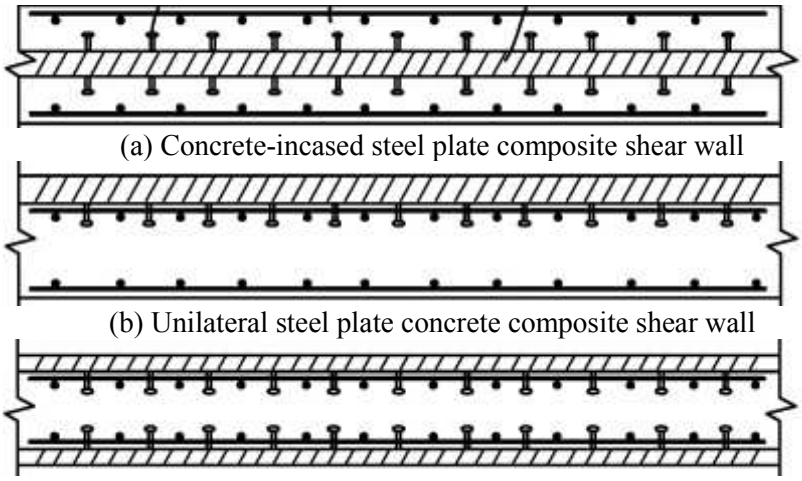
Yabinyang@126.com

Keywords: steel plate; composite shear wall; seismic research; engineering application.

Abstract. Shear wall is the main component that resists the lateral force for high-rise buildings. With the rapid development of high-rise buildings, especially the super high-rise buildings, requirements for seismic performance of shear walls have become more sophisticated. The steel plate concrete composite shear wall shows good seismic performance. It has made rapid development through the research of seismic performance in the way of seismic design to the practical engineering application of steel plate concrete composite shear wall. Recent research situation and prospect of composite shear wall around the world have been introduced in this paper.

Introduction

Steel plate shear wall structure is a new type of lateral force resisting system, which was developed in the 1970s. Through experimental studies by home and abroad scholars, Steel plate shear wall has large initial stiffness, large deformation and good plasticity performance advantages, but it is seldom used, mainly because it is buckling easily, poor stability and fire resistance, so the steel plate concrete composite shear wall came into being. After the combination, the concrete outside played constraint, anti-fire and anti-corrosion effect, enhance the shear wall seismic performance. Steel plate concrete composite shear wall can be divided into concrete-incased steel plate composite shear wall, unilateral steel plate concrete composite shear wall and composite shear wall with double steel plates and filled concrete according to the position between the plate and the concrete (Fig. 1).



(a) Concrete-incased steel plate composite shear wall

(b) Unilateral steel plate concrete composite shear wall

(c) Composite shear wall with double steel plates and filled concrete

Fig. 1 Steel plate concrete composite shear wall

Current Research

Concrete-Incased Steel Plate Composite Shear Wall. Concrete-incased steel plate composite shear wall make the steel plate as the basic support unit, the steel plate connected to the steel beam in the framework, concrete provide lateral restraint to prevent the steel plate to premature buckling. 3 Concrete-incased steel plate composite shear walls repeated loading test were accomplished by Tongji university Li Guoqiang [1], meanwhile, a pure steel plate shear wall repeated loading test was

accomplished for comparison. The results show that: steel plate and concrete work together before the concrete cracking, the wall represent large lateral stiffness, in favor of improving the lateral bearing capacity under non-seismic conditions or small seismic conditions of the structural integrity. In addition, the ductility of the Concrete-incased steel plate composite shear wall was fine, which can reach about 10. Thus, the shear wall panel can consume a lot of energy under large earthquake to ensure the whole structure does not collapse, has a good seismic performance. Seen from the test phenomenon, the maximum force position of Concrete-incased steel plate composite shear wall was the corner, so in order to improve its ultimate strength and deformation capacity, the four corners of the shear wall should be properly configuring the stiffener.

Unilateral Steel Plate Concrete Composite Shear Wall. Unilateral steel plate concrete composite shear wall is weld the steel plate to beam framework, and then anchoring steel plate and concrete panel through stud. This shear wall has been used in seismic regions. The University of California Astaneh-Asl and Zhao carried on research of unilateral steel plate concrete composite shear wall [2-3], The results showed that: under cyclic loading, the concrete wall panel appeared cracks in the four sides and border junction first; then steel plate buckling partly; concrete wall panels appeared main diagonal crack, borders emerged plastic hinge; concrete wall panels fragmentation damage at last. Stud in the process of force not only withstand shear, but also withstand the pulling force because of the buckling of the steel plate, and damage in the complex under stress finally. This composite shear wall has large post-bearing capacity, deformation capacity, fine ductility and energy dissipation capacity.

Composite Shear Wall with Double Steel Plates and Filled Concrete. Composite shear wall with double steel plates and filled concrete provide high bearing capacity and good ductility, but the cost is high and the construction is more complicated, and therefore rarely used in the project. Research on seismic behavior and the mechanical characteristics of composite shear walls with double steel plates and filled concrete was studied by home and abroad scholars [4-9]. Emori discovered the composite shear wall has high bearing capacity and good ductility, but because of the high cost, it is only used in the nuclear power plants, offshore platforms and other harsh environments. Tsinghua University Nie jianguo accomplished low cyclic loading tests of two groups of composite shear wall with double steel plates and filled concrete. The structural mechanism and the typical failure modes were investigated. In the tests，all the specimens illustrated good ductility and energy dissipation ability with stable and full hysteretic curves. The ultimate drifts of all the specimens exceeded the limit value recommended by the current design code， and were also larger than the similar test results provided by other researchers. Batten plates tied the double steel plates can effectively prevent the steel plates from local buckling and enhanced the confining effect on the infill concrete. As a result, the high-strength concrete can be used in seismic shear wall structures and the design requirements of ‘high compression， high ductility and small thickness’ for shear walls in super high-rise buildings can be fully satisfied.

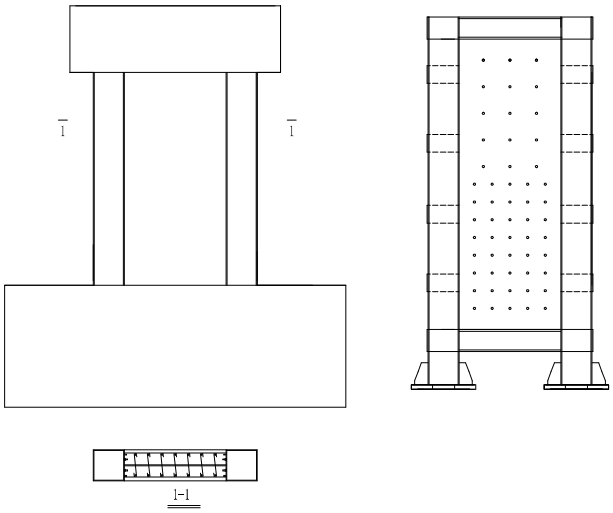


Fig. 2 Steel plate concrete shear wall with concrete filled steel tube columns

Steel Plate Concrete Shear Wall with Concrete Filled Steel Tube Columns. Beijing University of Technology Cao wanlin proposed Steel Plate Concrete Shear Wall with Concrete Filled Steel Tube Columns [10]. The tests of 7 specimens under cyclic loading have been accomplished (Fig. 2). The performances of specimens such as load-bearing capacity，energy dissipation，ductility and hysteretic behavior have been investigated．It is shown that the steel plate concrete shear wall with concrete filled steel tube columns has excellent seismic features of higher capacity，better ductility，larger energy dissipation and more stable hysteretic behavior．This new kind of composite shear wall has been applied to projects.

Conclusions

Steel plate concrete composite shear wall is a kind of multiple composite shear wall. It combined two materials which are steel and concrete, and reflects the advantages of different lateral force resisting systems and different materials. Meanwhile, the combination of steel and concrete make the mechanical properties of the wall complex. With the research on the steel plate concrete composite shear wall deeply, the test research, theoretical research and engineering applications will become increasingly widespread.

References

[1] G. Li, X. Zhang and Z. Shen, Experimental study on hysteretic behavior of concrete-incased steel plate shear walls, Industrial Construction, 25 (1995) 32-35.

[2] A. Astanehasl, Q. Zhao, Seismic studies of an innovative and traditional composite shearwalls, Composite and Hybrid Structures. LosAngeles, California: Association for International Cooperation and Research in Steel 2 Concrete Composite Structures, 2000, pp. 1009-1024.

[3] Q. Zhao, A. Astanehasl, Cyclic behavior of traditional and innovative composite shearwalls, Journal of Structural Engineering, 130 (2004) 271-284.

[4] H. D. Wright, The behavior of composite walling under construction and service loading, Construct Steel Research, 35 (1995) 257-273.

[5] K. M. A. Hossain, H. D. Wright, Experimental and theoretical behavior of composite walling under in plane shear, Journal of Constructional Steel Research, 60 (2004) 59-83.

[6] K. M. A. Hossain, Design aspects of double skin p rofiled composite framed shear walls in construction and service stages, ACI Structural Journal, 101 (2004) 94-102.

[7] K. M. A. Hossain, H. D. Wright, Performance of double skin profiled composite shear walls experiments and design equations, Canadian Journal of Civil Engineering, 31 (2004) 204-217.

[8] R. A. Link, A. E. Elwi, Composite concrete steel plate walls: analysis and behavior, Journal of Structural Engineering, 121 (1995) 60-71.

[9] K. Emori, Compressive and shear strength of concrete filled steel box wall, Steel Structures, 26 (2002) 29-40.

[10]W. Cao, W. Zhang, J. Zhang, Seismic research and application on embedded steel plate concrete shear wall with concrete filled steel tube columns, Journal of Civil Engineering and Management, 28 (2011) 219-225.

© (2012) Trans Tech Publications, Switzerland
doi:10.4028/www.scientific.net/AMM.238.643

Testing and Control for Strands Embedded in Annular Concrete Foundation Beam of Steel Archaize Tower

Xiaoke Li [a], Jian Liu [b], Zhihao Wang [c] and Pengfei Han [d]

North China University of Water Resources and Electric Power, Zhengzhou 450011, China

[a]lixk@ncwu.edu.cn, [b]59993455@163.com, [c]wangzhihao916@126.com, [d]531834812@qq.com

Keywords: pre-stressed concrete; annular anchor; friction coefficient; circumferential stress; field test.

Abstract. Combined with the design and construction of annular pre-stressed concrete foundation beam of Tiantang Site Protection Exhibition Project in Luoyang, China, this paper introduces the test process of frictional lose for annular strands. The calculation method is given to deal with the original data to get the friction coefficient of the strands. The controlling parameters such as control tensioning stress and theoretical elongations of strands are advised. The rational pre-stressing process and key indexes are confirmed by the comparison of test and theoretical circumferential stresses of the foundation beam. It is reasonable to fulfill the design requirements by strict controlling in the fields. It is believed that the process and method in this paper would give some reference for the construction of similar annular pre-stressed concrete structures.

Introduction

Annular anchor is a special anchor system for prestressed concrete structures used in water conservancy project, municipal engineering, silo, gas and oil storage tanks, reactor containment, and so on. In this system, stretching end and dead end are anchored in the same anchor block, without bearing steel plate, without concrete partial stress concentration near dead end. The anchor block can be slipped in the anchor slot. It is equivalent to jack the strands at both ends and the prestressed friction loss is relatively small. Usually strands use 90^o, 180^o, 270^o, 360^o or 720^o wrap angle to place and make an integrated circle by annular anchor. No vacant and overlap areas are left. It is very effective to build the pre-compressive circumferential stress to bearing external loads [1].

As is well-known, prestressing loss of strand is directly related to the effective stress under service loads, where frictional loss is the dominating part of prestressing loss. To predict it as real is one of key problems to guarantee the structure safe. Two parameters would be needed to deal with frictional loss. One is the friction coefficient between the pre-stressing steel reinforcement and the duct. The other is the wobble friction coefficient [2]. The losses due to friction and wobble are grouped together under friction. Usually the values advised by the code are applied to design directly. However the real coefficients would be changed because of the complex uncertain factors such as materials origin, construction level and construction craft etc. The key parameter values should be obtained according to the actual engineering, especially to the important and large scale project. The test in the field must be considered seriously. All controlling parameter values deduced from the test are the guide to construct and the base to revise the design. More than that, the actual effects of prestressing steel reinforcement could be tested by embedded professional sensors in the structure. Compared with tested and theoretical controlling stress and deformation of the structure, the prestressing process and key indexes could be finally confirmed. All these works are the important safeguards to design and construct structure, especially to deal with the complex annular prestressing technology.

Engineering Background

Tiantang steel structural archaize high tower is a Site Protection Exhibition Project in Luoyang. Because the origin area covered by the ancient tower doesn't be permitted to change anything [3], an annular pre-stressed concrete foundation beam with 2.0m thick, 4.0m high and 51.0m inner

diameter is designed around the ruin, as shown in Fig. 1. The loads from the superstructure, a steel tower with 55.0m high, could be transmitted to the annular foundation beam by a set of trusses with large span at the bottom of the superstructure. Then the loads could be transmitted to the piles below the annular foundation beam.

To enhance stiffness, resist temperature stress and control deformation of annular foundation beam, the post-tensioned unbonded prestressed technique is applied. From top to bottom along the height of foundation beam, there are 13 prestressing tendons which are numbered from 1st to 13th, as shown in Fig. 2. The radiuses of tendons from 1st to 4th are 28.18m and from 5th to 13th are 27.80m. The pre-stressed reinforcement is the low relaxation unbonded PC strand with 1860MPa ultimate tensile strength and 15.2mm nominal diameter. And each tendon includes $6\times\phi^s15.2$ strands. In the same horizontal plane, three segments of strands with 120° wrap angle connected a whole circle by 3 annular anchors. The annular anchors of the adjacent tendon along height are arranged by offsetting 30° and the pre-compressive circumferential stresses in the beam would be more uniform. The tension control stress $\sigma_{con}=0.70f_{ptk}=1302$MPa. The anchor is QMZ15-6 and the anchorage slot is 1.0m width and 0.345m depth. The strength grade of concrete is C40.

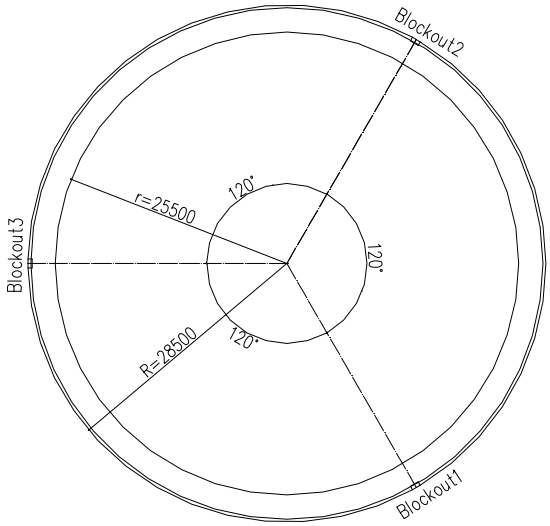


Fig. 1 Survey of Annular Foundation Beam [mm]

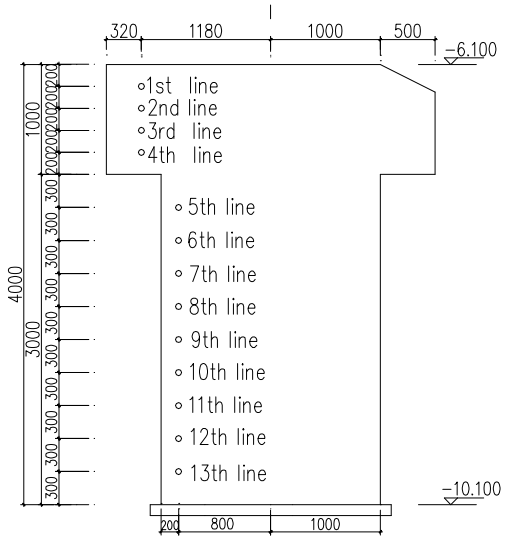


Fig. 2 Tendon Arrangement [mm]

Testing and Evaluation of Friction Coefficient

Test Process. Given consideration to typicality of test results and convenience of field test, three tendons including 5th, 9th and 13th are selected and one segment of the strands with same tendon is selected randomly to carry out the test. As a matter of convenience, three selected segments are named as 5#, 9# and 13# strands according to the number of tendon from top to bottom. The actual tension force in each end of strand can be measured with building anchor tester and load cell. The tension is applied by electric pump and supporting jack.

The test process of friction coefficient for each segment is listed as follow.

1) Test and calibrate each component of the testing system and make sure them work well.

2) Install tensioning equipment, load cell and steel plate with a round hole on one end of the segment as shown in Fig. 3. Then install load cell and steel plate on the other end as shown in Fig. 4. It means one end of segment is tensioned and the other end is fixed.

3) Debug whole testing system work well. Tension the strand from 0 to 20MPa and keep loads 1-2min, that is to say, firstly carry out pre-tension. Then tension the strand from 20MPa to σ_{con}. Read and record testing values from building anchor tester in each stage.

4) Release tensioning loads to 0.

5) Repeat step 3)-4) three times.

6) Exchange the tensioning and dead end. Repeat steps 3)-5).

All three segments of strands take the tests according to the former process. To guarantee the safe of structure, the maximum tensioning load of the strand was reduced appropriately.

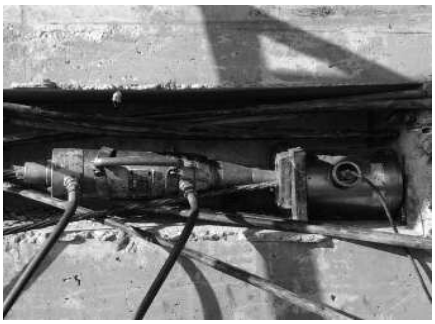


Fig. 3 Jacking End of Segment



Fig. 4 Dead end of Segment

Analysis and Evaluation. Friction coefficient μ and wobble factor κ are two key parameters to determine the frictional loss. Wobble factor κ depends on the quality of workmanship and on the distance between supports of the tendon. It is not control factor for the friction loss and the effect is slight. As complexity of calculation, compared with other similar engineering, wobble factor κ is given with China code. That is, $\kappa=\kappa_{code}=0.004$. Then according to the measured values at two ends of strand, friction coefficient μ of each segment can be obtained and $\mu_{average}$ is 0.107 [4]. All μ of three segments in the selected tendons are shown in Table 1.

Compared with $\mu_{code}=0.09$, the friction loss of the strands is more than the design value. μ should equal with $\mu_{average}$, that is $\mu=\mu_{average}=0.107$.

Table 1 Measured Results of Friction Loss Field Test for Annular Foundation Beam

Segment No.	Force In Jacking End [kN]	Force In Dead end [kN]	k	μ_{cal}	$\mu_{average}$
$5^{\#}$	101	66.9	0.004	0.089	0.107
	91.2	56.4		0.122	
	96	61.7		0.103	
$5^{\#}$ Swap Ends	66.7	40.9		0.126	
	68.3	42.3		0.121	
	69.6	43.2		0.120	
$9^{\#}$	69.6	46.9		0.081	
	70.9	48.3		0.075	
	70.9	49.6		0.063	
$9^{\#}$ Swap Ends	64.1	38		0.142	
	65.7	39.2		0.139	
	67	39.4		0.146	
$13^{\#}$	56.9	35		0.124	
	57.7	37.2		0.102	
	59.1	38.4		0.098	
$13^{\#}$ Swap Ends	59	40		0.078	
	57.6	36.7		0.107	
	63.1	41.6		0.091	

Key Indexes and Process for Tension

There are two key indexes to control the tensioning process. One is tension force P_{con} and the other is elongation of strand Δ_l^p.

It is easy to calculate P_{con} based on σ_{con} and area of stands. By interpolating the calibration curve of tension system, the value of oil pressure gauge can be obtained. Then it is the actual control value for worker to tension strands. The elongation of strand Δ_l^p can be calculated as Eq. 1 [5].

$$\Delta_l^p = \frac{F_p l_{pq}}{A_p E_p}\left[\frac{1-e^{-(\mu+\kappa r_c)\phi_1}}{(\mu+\kappa r_c)\phi_1}\right] \tag{1}$$

Where F_p is tension force of strand at stressing end, ϕ_1 is rotation angle of strand with annular arc curve (rad), l_{pq} is length of strand, A_p is cross-sectional area of strand, E_p is elastic modulus of strands and r_c is curvature radius of strand.

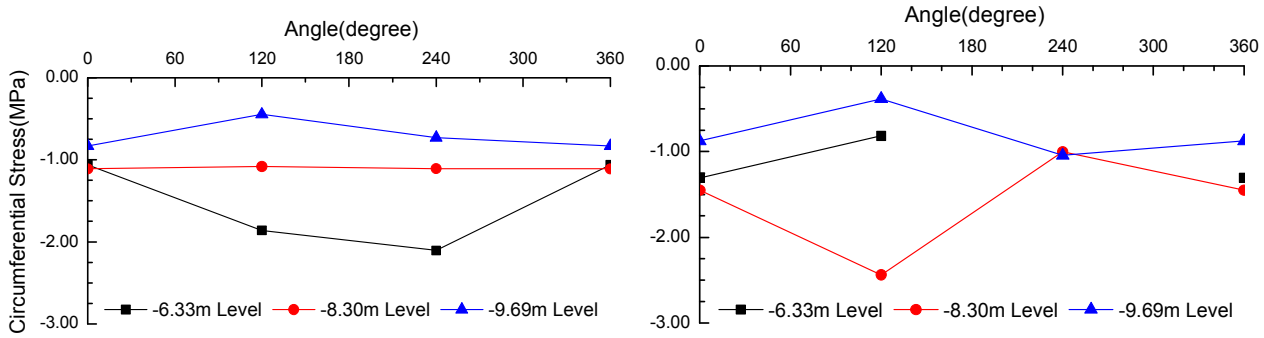
Radius of strands in tendons No.1-No.4 is 28.18m and radius of strands in the left tendons is 27.80m. Then the theoretical elongations of strands Δ_l^p are 316mm and 312mm respectively. The tested values should be less than $1.10\Delta_l^p$ and more than $0.95\Delta_l^p$ [6]. Otherwise strand tension should be interrupted to check what would cause it. Only if the problems would be solved, tension work of annular foundation beam could be continued.

To make sure safety of annular foundation beam during tension stage, it is important to apply reasonable tension process, which follows requirements such as symmetric tension, facilitating construction, keeping safe operation and mechanical characteristics of annular beam etc. Then the strands were tensioned from tendon No.13 to No.1. Each circle of strands including three segments is tensioned with double direction synchronous construction technique. That is to say, three set of tensioning equipment are needed at same time. Then tension stress of strands will be graded as $0.2\sigma_{con} \rightarrow 0.5\sigma_{con} \rightarrow 0.8\sigma_{con} \rightarrow 1.03\sigma_{con}$. When prestressing force of strands reaches the given value, the loads should be kept more than 2min in each tension level. Then the elongation is measured. According to the key indexes for tension, the testes values and theoretical values of elongation should be compared and the conclusion would be obtained based on the former requirements.

Check of Theoretical and Measured Results

Based on the theory of multiplayer axisymmetric plane strain model, the concrete circumferential stresses of annular foundation beam can be obtained after all strands are tensioned [7]. Corresponding to inner and outer reinforcement location, the stress values of annular foundation beam are -1.49MPa and -1.31MPa respectively between level -6.1m to -7.1m, -1.46MPa and -1.34MPa respectively between level -7.1m to -10.1m.

All 18 reinforcement strain gauges are installed in the inner and outer reinforcements with 120° interval along the circle, which locates at level -6.33m, -8.30m and -9.69m. For analysis convenience, the circumferential reinforcement stresses were transferred to concrete stresses by divide elastic modulus ratio of reinforcement and concrete. The distributions of circumferential stresses in inner and outer reinforcement of foundation are shown in Fig. 5.



a) Inner Layer of Reinforcement b) Outer Layer of Reinforcement

Fig. 5 Distribution of circumferential concrete stress of reinforcement after tensioned

The average measured values of circumferential stresses in inner layer of reinforcement are -1.52MPa, -1.10MPa and -0.71MPa corresponding to level -6.33m, -8.30m and -9.69m respectively. The circumferential stresses are distributed almost evenly at each level and the higher level is more than the lower level, which is consistent with the theoretical values basically. The average measured values of circumferential stresses in outer layer of reinforcement are -1.06MPa, -1.23MPa and -0.77MPa corresponding to level -6.33m, -8.30m and -9.69m respectively. It is opposite to the rules of circumferential stresses in inner layer. Due to temperature variation in concrete before and after tensioned by changed environment temperature and the non-uniformity of temperature variation, the outer values are uneven more than the inner. Because the bottom of beam is restrained

by piles and the horizontal cross section of the top of beam is free, the measured value of hoop compressive stress of inner and outer layer of reinforcement at level -9.69m is less than the theoretical values and also less than the measured values at high level.
Generally, the measured stresses could be consistent with the theoretical values. That is, the results would fulfill the design and it is reasonable for the adopted process for tension.

Conclusions

The annular foundation beam is an important part of Tiantang steel structural archaize high tower. The friction coefficient and wobble factor are the key parameters for the design and construction of pre-stressed concrete structure. In this paper, the procedure in field test is given to obtain the frictional lose for annular concrete foundation beam. Based on μ=0.107 and κ=0.004 which are deduced from tests. The key indexes, control stress for tension and theoretical elongations of strands are advised when tensioned. The process of tension is established to keep safety of beam. Compared with tested and theoretical circumferential stresses of foundation beam, it proved that the advised process for tension and the decided key indexes were effective and reasonable. The ways and methods would serve as a reference for similar engineering structures.

References

[1] X. Li, Investigation of Performance under Loads and Calculating Methods of Prestressed Concrete Penstock, Thesis for Ph.D Degree, Dalian University of Technology, 2003.

[2] GB50010-2010, Code for Design of Concrete, China Architecture & Building Press, Beijing, 2010.

[3] C. Wang, K. Xu, L. Tian, Structure design of Tiantang for ruin protection of ancient buildings in Sui and Tang Dynasty in Luoyang city, Steel Structure, 8 (2011) 26-31.

[4] G. Hu, D. Chun, Y. Zhao, Test study on prestress loss due To friction for space-curved tendons and inversion analysis on friction coefficient, Building Science, 5 (2004) 26-29.

[5] S. Zhao, X. Li, Z. Yan, X. Liu, Techniques and Engineering Applications of Annular High-Performance Prestressed Concrete, Science Press, Beijing, 2008.

[6] JGJ 92-2004, Technical Specification for Concrete Structures Prestressed with Unbonded Tendons, China Architecture & Building Press, Beijing, 2004.

[7] X. Li, S. Zhao, G. Zhao, Method of designing steel-lined prestressed concrete penstock, Water Resources and Hydropower Engineering, 4 (2004) 25-29.

© (2012) Trans Tech Publications, Switzerland
doi:10.4028/www.scientific.net/AMM.238.648

Free Vibration Analysis of Frame-Core Tube Structures Attached with Damped Outriggers

Zhihao Wang

North China University of Water Resources and Electric Power, Zhengzhou 450011, China

wangzhihao916@126.com

Keywords: frame-core tube structures; outrigger; viscous damper; free vibration analysis.

Abstract. The classical outrigger in frame-core tube structure cantilevering from the core tube or shear wall connected to the perimeter columns directly, which can effectively improve the lateral stiffness of the structure. A new energy-dissipation system for such structural system is studied, where the outrigger and perimeter columns are separate and vertical viscous dampers are equipped between the outrigger and perimeter columns to make full use of the relative big displacement of two components. The effectiveness of proposed system is evaluated by means of the modal damping ratio based on the proposed simplified model. The mathematic models of the structural system are obtained with both the assumed mode shape method and finite element method according to the simplified calculation diagram. Based on the modal damping ratio, the optimal damping coefficients of linear viscous dampers are determined, and effectiveness of proposed system is confirmed.

Introduction

The buildings have continued to soar skyward with the development of material and construction technology. However, flexible structures may fall victim to excessive levels of vibration under the action of wind, adversely affecting serviceability and occupant comfort. To ensure the functional performance of flexible structures, various design modifications are possible, ranging from alternative structural systems and aerodynamic modifications to the utilization of passive and active control devices [1]. One of such structural system is frame-core tube structure with outriggers, which has become a popular approach to improve the efficiency of the core system by simply engaging the exterior columns to aid in resisting part of the overturning moment resulting from lateral loads [2]. It is obvious that the outriggers mainly focus on the static design of wind. To further improve the dynamic response of structure, a new damping system that adding viscous dampers between outriggers and perimeter column is first presented [3]. Smith and Willford has developed a similar system [4], and successfully applied the outrigger damping system to a high rise building in Philippine [5].

A simplified model with one outrigger in a frame-core tube structure is adapted to evaluate the effectiveness of this energy dissipation system, and the outrigger location and damping constant of linear viscous damper are analyzed based on parametric analysis, which can be a good reference for the preliminary design of such kind of structure.

Simplified Analysis Model

It is well known that the deformation of the core due to external horizontal load shows similar characteristics with the cantilever beam. As a result, a simplified model of the core-to-perimeter-column outrigger system is proposed, in which the building core is modeled as a uniform cantilever beam, and the outrigger, located at αh, is assumed to be mass-less and infinitely rigid. The intrinsic damping of the structure is zero. The only damping source for the structural system is from the two dampers with damping constant c_d equipped between the outrigger and the perimeter columns. The calculation diagram is shown in Fig. 1.

SDOF Model. To get the single degree of freedom (SDOF) model, only one assumed mode is defined. $w(x,t)=\phi(x)q(t)$, and it satisfies the boundary condition $\phi(0)=0$, $\phi'(0)=0$. For any random virtual displacement $\delta w(x,t)$ of structure, the following equation is established:

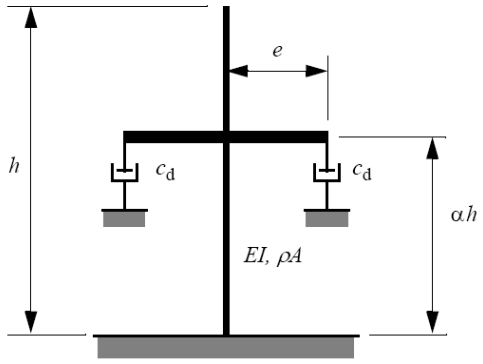


Fig. 1: The calculation diagram of passive energy dissipation system

$$\delta W_1+\delta W_2=0 \tag{1}$$

Where δW_1 and δW_2 represent the virtual work of practical and inertia force respectively. Then, the equation can be calculated as follows:

$$\delta W_1 = -\int_0^h M\delta w''(x,t)dx - M_d\delta w'(\alpha h,t) \tag{2}$$

$$\int_0^h M\delta w''(x,t)dx = \int_0^h EI\phi''(x)q(t)\phi''(x)\delta q(t)dx = EIq(t)\delta q(t)\int_0^h(\phi''(x))^2dx \tag{3}$$

$$\begin{aligned} M_d\delta w'(\alpha h,t) &= 2ec_de\frac{d\sin(w'(\alpha h,t))}{dt}\phi'(\alpha h)\delta q(t) \\ &\approx 2e^2c_d\phi'(\alpha h)\dot{q}(t)\phi'(\alpha h)\delta q(t) = 2e^2c_d(\phi'(\alpha h))^2\dot{q}(t)\delta q(t) \end{aligned} \tag{4}$$

$$\delta W_2 = -\int_0^h \rho A\ddot{w}(x,t)\delta w(x,t)dx = -\rho A\int_0^h \phi(x)\ddot{q}(t)\phi(x)\delta q(t)dx = -\rho A\ddot{q}(t)\delta q(t)\int_0^h\phi^2(x)dx \tag{5}$$

Defining $\bar{M} = \rho A\int_0^h\phi^2(x)dx, \bar{C} = 2e^2c_d(\phi'(\alpha h))^2, \bar{K} = EI\int_0^h(\phi''(x))^2dx$ as the modal mass, damping and stiffness, respectively, the following equation that represents the SDOF model can de derived as:

$$\bar{M}\ddot{q}(t)+\bar{C}\dot{q}(t)+\bar{K}q(t)=0 \tag{6}$$

From the Eq. (6) and the definition of modal damping, some conclusions can be drawn: the equivalent damping of structure has been amplified as a result of term "e^2"; the rotational angle of core at the outrigger location also has a great effect. It seems that the bigger damping constant is, the bigger modal damping is. However, when the damping is large enough, it acts as a rigid link, and it won't dissipate energy at all. Therefore, SDOF model can only be used as qualitative analysis, and the precise MDOF model is needed to carry out quantitative analysis.

MDOF Model. To accelerate the convergence rate of assumed shape method, the static deformation due to external damping force is chosen to be the first mode shape [6], so the static deformation of core due to a moment at the outrigger location is adopted as the first mode shape. The non-dimension form of all the mode shapes is assumed as:

$$\phi_1(x) = \begin{cases} \frac{1}{2}\left(\frac{x}{h}\right)^2 & 0\le x\le ah \\ a\frac{x}{h}-\frac{a^2}{2} & ah\le x\le h \end{cases} \qquad \phi_i(x) = \left(\frac{x}{h}\right)^i \quad i=2,3,...,n \tag{7}$$

The free vibration equation of the system can be written as:

$$\mathbf{M}\ddot{\mathbf{q}}+\mathbf{C}\dot{\mathbf{q}}+\mathbf{K}\mathbf{q}=\mathbf{0} \tag{8}$$

Where the mass M, damping C and stiffness matrix K is calculated as follows:

$$\begin{cases} M_{ij} = \int_0^h \rho A \phi_i(x)\phi_j(x)dx \\ C_{ij} = 2c_d e^2 \phi_i'(\alpha h)\phi_j'(\alpha h) \quad i=1:n, j=1:n \\ K_{ij} = \int_0^h EI\phi_i''(x)\phi_j''(x)dx \end{cases} \tag{9}$$

FE Model. To validate the result of MDOF model, a finite-element approach has been adopted which states the governing equation of the system in the following form:

$$\mathbf{M}_f\{\ddot{U}\} + \mathbf{C}_f\{\dot{U}\} + \mathbf{K}_f\{U\} = \mathbf{0} \tag{10}$$

A standard two-node beam element with two degrees of freedom for each node is considered in this study. The global stiffness matrix and mass matrix are omitted here; the damping matrix is given as follows:

$$C_{ij} = \begin{cases} 2c_d e^2 & i=j=2(m-1) \\ 0 & \text{else} \end{cases} \tag{11}$$

Where m represents the node number where the dampers are attached. It is noticed that in C_f matrix, only one position has real value, and all the left is equal to zero.

Parametric Analysis. To get the modal information, the complex-modal analysis for both MDOF model and FE model is needed. The state matrix of system derived from assumed mode shape method and FE method can be expressed respectively as:

$$\mathbf{A}_m = \begin{bmatrix} \mathbf{0} & \mathbf{I} \\ -\mathbf{M}^{-1}\mathbf{K} & -\mathbf{M}^{-1}\mathbf{C} \end{bmatrix}; \mathbf{A}_f = \begin{bmatrix} \mathbf{0} & \mathbf{I} \\ -\mathbf{M}_f^{-1}\mathbf{K}_f & -\mathbf{M}_f^{-1}\mathbf{C}_f \end{bmatrix} \tag{12}$$

According the previous research [2, 4] and the rotational angel mode shape of classical cantilever beam, the outrigger location α is optimized as 0.6. The building model parameters are set as: ρA=85000kg/m, EI =4E^{12}(Nm^2), h=140m, e=15m parisons between the MDOF model and FE model, it is found that when the number of assumed mode shapes n equals to 8, it is enough to reach the same accuracy as the FE model with 50 degrees-of-freedom for the first forth modes.

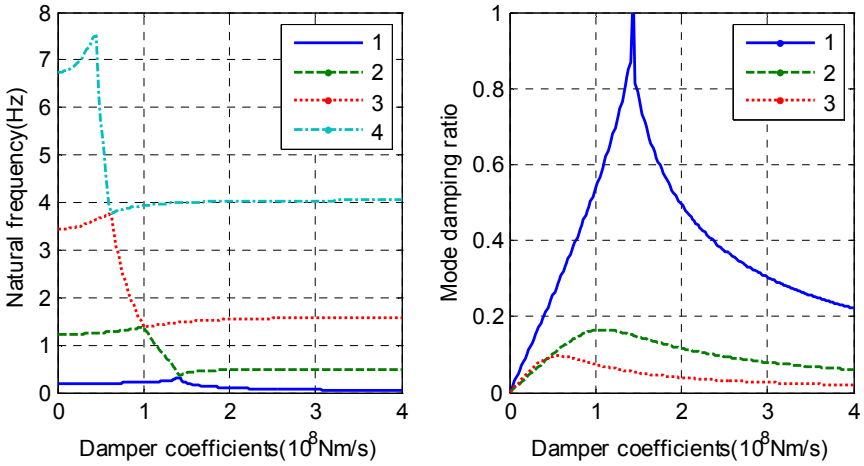


Fig. 4 The natunal frequency and modal damping with different damper coefficients

Fig. 4 has shown the calculation result of structural natural frequency and modal damping with the changing damping constant of linear viscous damper, in which '1', '2', '3', '4' represent the corresponding mode number. From the figure, one interesting phenomenon can be seen that the structure shows modes shift with the increasing of damping constant, and the higher modes gradually move to its nearest lower modes. As pointed out in the previous research [7], when the natural

frequencies of a structure with zero damping constant and infinity damping constant of damper are quite close to each other, a modest modal damping is achieved, or the critical modal damping will be expected and the modes shift accordingly. Therefore, the structural system described in this paper is quite different from the cable damping system [6], in which the damper is always set on the position close to the support, the frequency shift is quite small for two limiting conditions that one is without damper, and the other is when damper works as the rigid link.

Conclusions

A novel energy dissipation system for tall buildings that vertical viscous dampers are equipped between the outrigger and perimeter columns is studied, which can achieve the amplified damping ratio. It is proposed to effectively improve the dynamic performance of structure at the expense of static stiffness and strength. The modal characteristics of the structural system are theoretically analyzed based on the simplified model by parametric analysis, which can provide useful references for the preliminary damping design of frame-core tube structures. However, the nonlinear time histories analysis still need to validate the final design in the engineering practice. To further evaluate the effectiveness of the system, the control performance of building with the proposed outrigger damping system subjected to strong winds or earthquakes should be investigated.

References

[1] Kareem, T. Kijewski, Y. Tamura, Mitigation of motion of tall buildings with recent applications, Wind and Structures, 2 (1999) 201-251.

[2] B. S. Smith, I. Salim, Parameter study of outrigger-braced tall building structures, Journal of Structural Division 6 (1981) 2001-2014.

[3] C. Jeremlah, Application of damping in high-rise building, Massachusetts Institute of Technology, 2006

[4] R. J. Smith, M. R. Willford, The damped outrigger concept for tall buildings, The Structural Design of Tall and Special Buildings, 16 (2007) 501-517.

[5] M. Willford , R. Smith, D. Scott, et al. Viscous dampers come of age, Structure Magazine, 6 (2008) 15-18.

[6] E. A. Johnson, R. E. Christenson, B.F. Spencer, Semi-active damping of cables with sag, Computer-aided Civil and Infrastructure Engineering, 18 (2003) 132-146.

[7] K. Engelen, H. Ramon, W. Saeys, et al, Positioning and tuning of viscous damper on flexible structure, Journal of Sound and Vibration, 304 (2007) 845-862.

© (2012) Trans Tech Publications, Switzerland
doi:10.4028/www.scientific.net/AMM.238.652

Three-spring Model for Spatial Walls

Linjun Si[1,a], Gonglian Chen[1,b] and Huali Wang[2,c]

[1]North China University of Water Resources and Electric Power, Zhengzhou 450011, China

[2]Henan Sunrise Architectural Design Institute, Zhengzhou 450008, China

[a]silinjun1980@163.com, [b]chengonglian@ncwu.edu.cn, [c]hlw2003@126.com

Keywords: three-spring model; spatial wall; elastic-plastic analysis; axial deformation.

Abstract. Shear wall structures, frame-shear wall structures and frame-tube wall structures are usually used in tall buildings, especially in China seismic regions. How to simulate the mechanical behaviors of these walls is the key to elastic-plastic analysis for tall buildings. Based on two-spring model, a nonlinear model for spatial walls is proposed. In this model, the axial, shear and flexural elastic-plastic deformation of the walls can be considered, the deformation compatibility between the wall and beam elements is also considered. The model was used to analysis the elastic-plastic behavior of spatial walls. Calculation example for verifying the model indicates that the result obtained by this method has the characteristics of fewer degrees of freedom and high accuracy. Therefore the nonlinear model for spatial walls provides a practical and efficient analysis method for tall buildings with complex type.

Introduction

In many tall buildings, shear walls provide the required stiffness and strength to resist lateral loads. These shear walls are commonly used in the structural systems such as shear walls or frame-shear wall structures. Therefore much research on efficient analysis of such structures has been undertaken by Kim [1]. Under the rare earthquakes, in order to prevent the collapse of these structures, the elastic-plastic deformation must be calculated. Many analytical models have been proposed to predict the nonlinear response of reinforced concrete (RC) structural walls. However, they can be classified into two broad groups: (1) detailed models derived using mechanics of solids and shells(microscopic approach); (2) simplified models to predict a specific overall behavior.

Models derived from a microscopic approach are based on a detailed interpretation of the local behavior. Even though the microscopic approach is desirable, its implementation involves many difficulties due both to the lack of completely reliable basic models and complexities involved in a detailed solution. Although, the Finite Element Method offers a powerful analytical tool to perform the numerical analysis, the computation is generally very time-consuming and requires a large storage [3].

On the other hand, models based on a macroscopic approach attempts to describe the overall behavior by means of a simplified idealization. The main advantages of these models consist in the relatively limited storage and, above all, in the significantly less computational effort than that required by detailed analytical models [4].

The model shown in Fig. 1 was formulated by Vulcano to idealize a generic wall element as horizontal and rotational springs with infinitely rigid beams at the top and bottom floor levels [5]. This wall model incorporates the main features of the experimentally observed behavior.

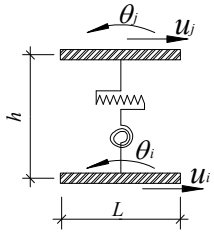


Fig. 1 Two-spring model

In this paper, a nonlinear three-spring model for spatial walls is proposed base on two-spring model. In which, the inelastic axial deformation of wall element is considered, and reasonable connection systems between wall elements and frame-wall elements are considered to obtain reliable analytical results.

Formulation of Three-spring Wall Element

Basic Formulation of Two-spring Wall Element. In Fig. 1, the shear resistance of the wall was provided by the horizontal spring in the central element and the flexural prosperities were provided by the rotational spring. The hysteresis models and the stiffness of the springs were defined in [6].

Stiffness Matrix Formulation of Three-spring Wall Element. In the shear wall local coordinate system (Fig. 2), the three-spring wall model is chosen here. This model is composed of axial spring, shear spring and flexural spring.

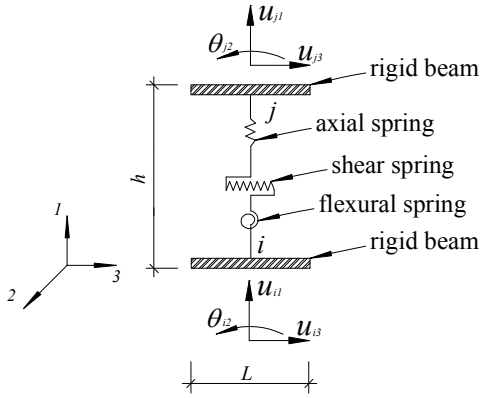


Fig. 2 Three-spring wall element

Considering the inelastic axial, shear and flexural deformation, the equation for wall element has the form:

$$\begin{Bmatrix} F_{i1} \\ F_{i3} \\ M_{i2} \\ F_{j1} \\ F_{j3} \\ M_{j2} \end{Bmatrix} = \begin{bmatrix} K_a & 0 & 0 & -K_a & 0 & 0 \\ 0 & K_s & -K_s ch & 0 & -K_s & -K_s(1-c)h \\ 0 & -K_s ch & K_\phi + K_s c^2 h^2 & 0 & K_s ch & -K_\phi + K_s(1-c)^2 h^2 \\ -K_a & 0 & 0 & K_a & 0 & 0 \\ 0 & -K_s & K_s ch & 0 & K_s & K_s(1-c)h \\ 0 & -K_s(1-c)h & -K_\phi + K_s(1-c)^2 h^2 & 0 & K_s(1-c)h & K_\phi + K_s(1-c)^2 h^2 \end{bmatrix} \cdot \begin{Bmatrix} u_{i1} \\ u_{i3} \\ \theta_{i2} \\ u_{j1} \\ u_{j3} \\ \theta_{j2} \end{Bmatrix}$$

The above equation can be written as:

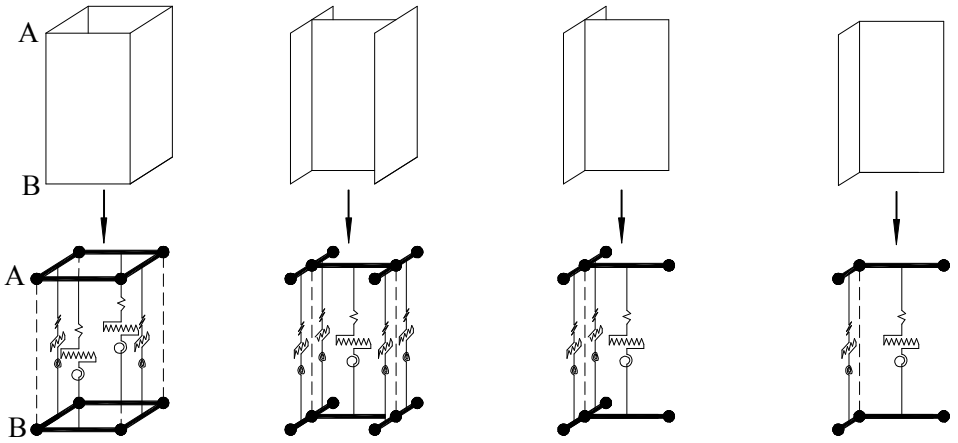
$$\{F_e\} = [K_e]\{\delta_e\} \tag{1}$$

Where K_a, K_s and K_ϕ denote the stiffness of axial spring, shear spring and flexural spring respectively with the calculation methods were defined in [6]; h is inter-story height; c is the coefficient of relative rotation center, and it is equal to 0.5; $[K_e]$ is the stiffness matrix for three-spring wall element.

If a different coordinate system is used, the expressions above may be different.

Computational Model for Spatial Walls

Compartmentalization of Spatial Walls. Wall elements (Fig. 3) treated as vertical strips, are described by three-spring model taking into account the axial, shear and flexural deformation. As shown in Fig. 3(a), considering the compatibility of connections such as node A and B, connections of the tube wall at the top and bottom floor levels, four three-spring models was used to simulate the tube wall. Using the same method, the H-type, T-type and L-type spatial walls can be analyzed. The spatial walls have two translational degrees and one rotational degree of freedom at the top and bottom floor levels, whereas the connections have one vertical translational degree of freedom.



(a)Tube wall (4 three-spring elements) (a)H-type wall (5 three-spring elements) (a)T-type wall (3 three-spring elements) (a)L-type wall (2 three-spring elements)

Fig. 3 Compartmentalization of spatial walls

Calculation Model for Spatial Walls Connected to Frame Elements. Frame structures with shear wall cores are frequently adopted as the structural system for high-rise structures. In these structures, there will be frame element connected with walls. Therefore, reasonable connection systems between beam and wall element are required. So we select the following model (Fig. 4) to obtain the compatibility between frame element and wall element, in which, the bend and shear stiffness of the elastic beam in the wall plane is 100 times of the spatial beam element. And the correctness of this method has been estimated and implemented by Wilson [7].

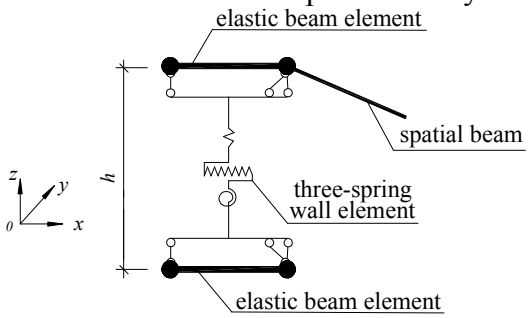


Fig. 4 Calculation model for spatial walls which connected to the beam

A typical coupled shear wall structure with symmetrical walls and a single band of openings is shown in Fig. 5. The wall piers were modeled by the element (Fig. 4) that incorporates axial, flexural, and shear deformations in the elastic and inelastic range. And the multi-spring model which for beam element was adopted to simulate the elastic and inelastic behavior of coupling beam. This multi-spring model considering elastic-plastic shear deformation affects and its details are described by Si [8].

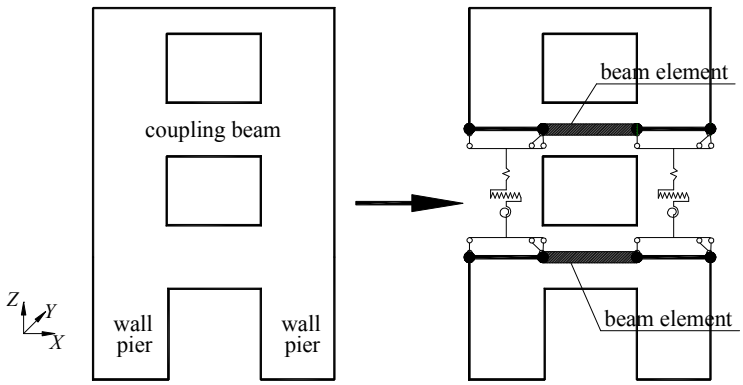


Fig. 5 Analytical modeling for coupled shear walls

Conversion of Master-slave Degrees for Spatial Wall Element. The conversion of master-slave degrees under the local coordinate system is shown in Fig. 6. Through this conversion, the wall piers can be easily combined and the deformation of connections can keep compatibility.

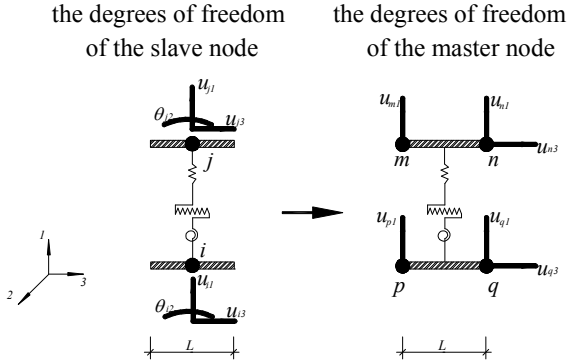


Fig. 6 Conversion of master-slave degrees under the local coordinate system

Considering the master-slave constraint conditions based on Fig. 6, the degrees of freedom of the slave node can be replaced by the degrees of freedom of the master node.

①According to node i and j, when changing the deformation from master degree to slave degree, the transformation matrix is shown in the following equation:

$$\begin{Bmatrix} u_{i1} \\ u_{i3} \\ \theta_{i2} \\ u_{j1} \\ u_{j3} \\ \theta_{j2} \end{Bmatrix} = \begin{bmatrix} \frac{1}{2} & \frac{1}{2} & 0 & 0 & 0 & 0 \\ 0 & 0 & 1 & 0 & 0 & 0 \\ -\frac{1}{L} & \frac{1}{L} & 0 & 0 & 0 & 0 \\ 0 & 0 & 0 & \frac{1}{2} & \frac{1}{2} & 0 \\ 0 & 0 & 0 & 0 & 0 & 1 \\ 0 & 0 & 0 & -\frac{1}{L} & \frac{1}{L} & 0 \end{bmatrix} \cdot \begin{Bmatrix} u_{p1} \\ u_{q1} \\ u_{q3} \\ u_{m1} \\ u_{n1} \\ u_{n3} \end{Bmatrix}$$

Where L is the length of the wall (Fig. 6).

The above equation can be simplified written as:

$$\{\delta_e\} = [D'_\delta]\{\delta^*\} \tag{2}$$

As the same, according to node i and j, when changing the force from slave degree to master degree, the transformation matrix is shown in the following equation:

$$\{F^*\} = [D'_f]\{F_e\} \tag{3}$$

in which:

$$[D'_f] = [D'_\delta]^{\mathrm{T}} \tag{4}$$

Since Eq.(1) can be described as $\{F_e\} = [K_e]\{\delta_e\}$, we obtain Eq.(5) from Eqs.(2) and (3):

$$\{F^*\} = [D'_f][K_e][D'_\delta]\{\delta^*\} = [K^*]\{\delta^*\} \tag{5}$$

Transformation of Coordinate System from Local to Globa. In the analysis of spatial walls, the stiffness matrix in the local coordinate system (1-2-3) should be changed to global coordinate system (*X*-*Y*-*Z*), as shown in Fig. 7. The axis 1 of the local coordinate system is parallel with the axis *Z* of the global coordinate system, and the angel between axis 3 and axis *X* is γ. According to the nodes in Fig. 7, when changing their deformation from global coordinate system to local coordinate system, the transformation matrix is shown in the following equation:

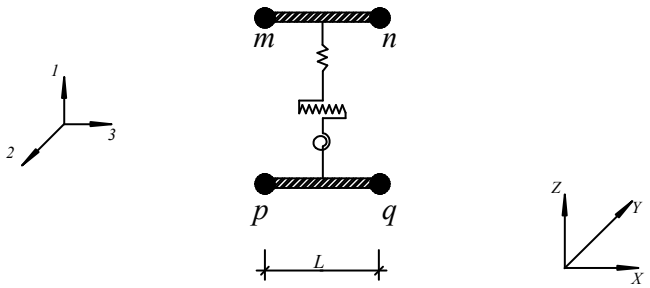


Fig. 7 Coordinate transformation for wall element

$$\begin{Bmatrix} u_{p1} \\ u_{q1} \\ u_{q3} \\ u_{m1} \\ u_{n1} \\ u_{n3} \end{Bmatrix} = \begin{bmatrix} 1 & 0 & 0 & 0 & 0 & 0 & 0 & 0 \\ 0 & 0 & 0 & 1 & 0 & 0 & 0 & 0 \\ 0 & \cos\gamma & \sin\gamma & 0 & 0 & 0 & 0 & 0 \\ 0 & 0 & 0 & 0 & 1 & 0 & 0 & 0 \\ 0 & 0 & 0 & 0 & 0 & 0 & 0 & 1 \\ 0 & 0 & 0 & 0 & 0 & \cos\gamma & \sin\gamma & 0 \end{bmatrix} \cdot \begin{Bmatrix} u_{pz} \\ u_{qx} \\ u_{qy} \\ u_{qz} \\ u_{mz} \\ u_{nx} \\ u_{ny} \\ u_{nz} \end{Bmatrix} \tag{6}$$

The Eq.(6) can be simplified written as:

$$\{\delta^*\} = [D_\delta]\{\bar{\delta}\} \tag{7}$$

The following Eq.(8) shows the relationship of the nodes' force between local coordinate system and global coordinate system.

$$\{\bar{F}\} = [D_f]\{F^*\} \tag{8}$$

$$[D_f] = [D_\delta]^{\mathrm{T}} \tag{9}$$

Since Eq.(5) can be described as $\{F^*\} = [K^*]\{\delta^*\}$, we obtain Eq.(10) from Eqs.(7) and(8):

$$\{\bar{F}\} = [D_f][K^*][D_\delta]\{\bar{\delta}\} = [\bar{K}]\{\bar{\delta}\} \tag{10}$$

Consideration of Rigid Floor. In the analysis of spatial walls, in order to realizing the torsion resistance of the walls, the assumption of rigid floor is also taking into account. The calculation method of the rigid floor is described in detail in paper [9] by Fang. The information relevant to the conversion of master-slave degrees is not repeated herein.

Verification with Experimental Results

The numerical analysis presents the verification of the correctness, accuracy and efficiency of the proposed computational model by comparison with the results obtained by experimental tests.

Introduction of H-type Spatial Wall Experiment. The experiment used for validation was performed at Chongqing University by Fu 0, China. The specimen dimensions were shown in Fig. 8. The top of the wall was horizontally displaced back and forth in a plane perpendicular to the wall by a hydraulic actuator located at 1.6m above the wall footing. Referring to Fig. 9, the reinforcement details is given. The concrete strength f_{cu} is based on average of 18.8MPa. The yield strength is 341.0MPa for reinforcement with ϕ4mm and 271.0MPa for ϕ6.5mm.

Comparison with Experimental Results. As shown in Fig. 3(b), considering the compatibility of connections and the assumption of rigid floor, five three-spring elements was used to simulate the H-type wall. Axial load was applied from the top. For the flange and wed, the vertical load was about 68.64kN and 224.22kN, respectively. The axial load ratio was approximately 0.2.

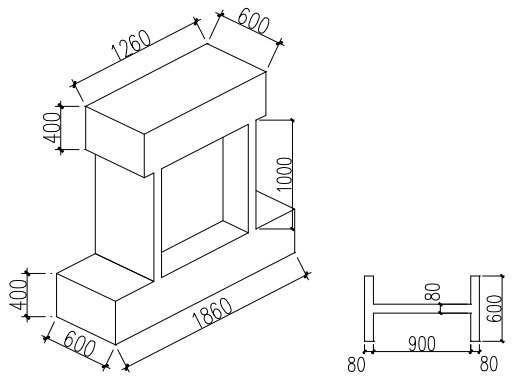


Fig. 8 Dimension of specimen W-1 (unit: mm)

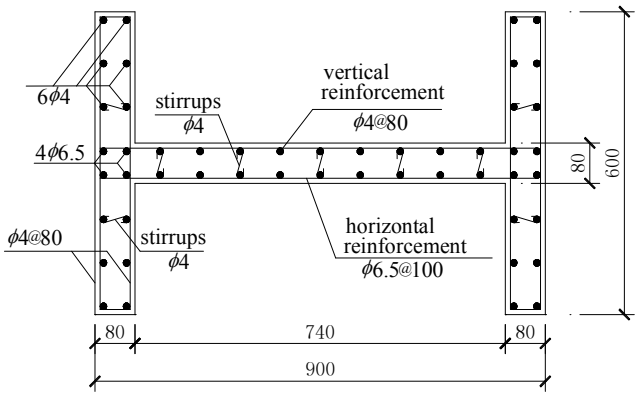


Fig. 9 Reinforcement details of specimen W-1

As shown in Fig. 10, deformation controlled loading history was applied on W-1 to simulate its seismic actions.

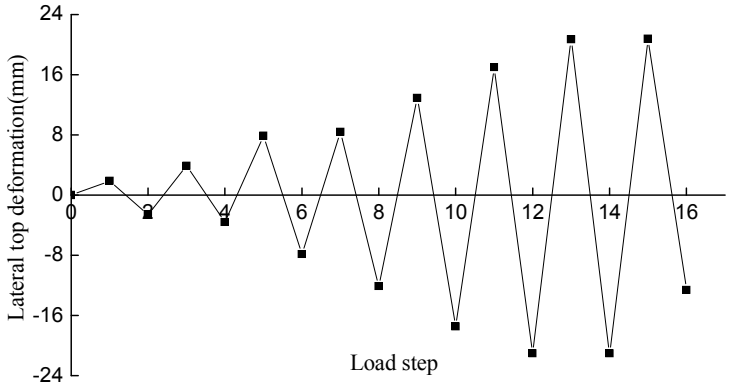
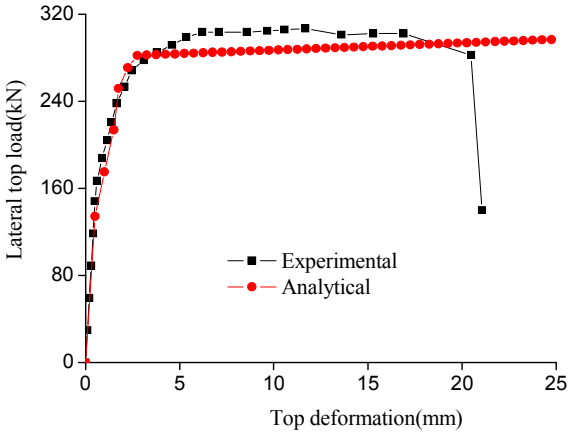
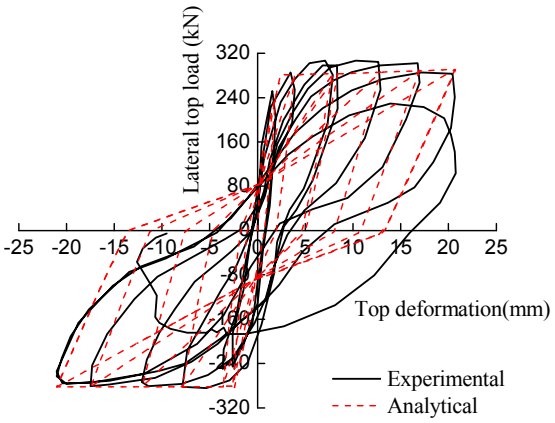


Fig. 10 Loading history of specimen W-1

Fig. 11 presents the response in the form of load-deformation of specimen's top. The results shows that proposed model can well describe response of the walls and can provide accurate results with significantly reduced computational time. Close agreement in Fig. 11 does give sound proof that the model proposed in this paper is an efficient one.



(a) Load versus deformation skeleton curve of W-1



(b) Load versus deformation hysteresis curve of W-1

Fig. 11 Results Comparison of specimen W-1

Conclusions

The paper presents an efficient three-dimensional computational model based on subdivision of the structure into building elements such as three-spring wall elements and multi-spring frame elements, that could provides accurate results with significantly reduced computational time. The major observations and findings are summarized as follows:

The axial load-deformation relationship has been added to the classical two-spring element. And the description allows obtaining reasonable internal forces for every wall that can be very useful in the engineering practice.

The description of stiffness changes, which is determined at the level of the individual cross-sectional areas of the wall elements, does not increase the number of unknowns. Such a modeling and description of stiffness changes allow creating a computational model with a comparatively small number of unknowns.

Proposed model can be useful for the analysis of three-dimensional structures subjected to dynamic and static loads but especially for the analysis of building structures, where mainly walls are responsible for the stiffness of the building. The presented method opens possibilities for the modeling of complex three-dimensional building structures.

Acknowledgements

The reported work is financially supported by the State Key Laboratory of Science and Technology Fund, Science and Technology of China (SLDRCE08-A-06) and the High Level Talent Startup Funding Project of North China University of Water Resources and Electric Power (001379).

References

[1]. H. S. Kim, S. M. Hong, Formulation of transition elements for the analysis of coupled wall structures, Computers and Structures, 2 (1995) 333-344.

[2]. H. S. Kim, D. G. Lee, Analysis of shear wall with openings using super elements. Engineering Structures, 8 (2003) 981-991.

[3]. J. Jang, X. Lu, L. Ye, Finite Element Analysis of Concrete Structures, Tsinghua University Press, Beijing, 2005. (in Chinese)

[4]. X. Zhuo, Y. Cai, Analysis of frame structures with shear walls using wall panel elements, Journal of Building Structures, 3 (1992) 29-41. (in Chinese)

[5]. A. Vulcano, V. V. Bertero, V. Colotto, Analytical model for predicating the lateral response of RC shear walls: Evaluation of their reliability. Report No. EERC-87/19, Earthquake Engineering Research Center, University of California, Berkeley, 1987.

[6]. L. Si, G. Li, F. Sun, Study on validity of two spring model for reinforced concrete shear walls. Structural engineers, 4 (2008) 19-24. (in Chinese)

[7]. E. L. Wilson, Static and Dynamic Analysis of Structures, Translated by Beijing Civil King Software Technology Co., Ltd., China Architecture Industry Press, Beijing, 2006. (in Chinese)

[8]. L. Si, Study on Practical Plastic Dynamic Analysis Method of Spatial Steel Frame-Reinforced Concrete Shear Wall Structures. Tongji University, Shanghai, 2010. (in Chinese)

[9]. M. Fang, Study on practical 3-d plastic dynamic analysis method of braced steel frames. Tongji University, Shanghai, 2005. (in Chinese)

[10] J. Fu, Y. Wu, T. Pi, Experimental research on seismic shear capacity of I-shape ductile reinforced concrete structural walls, Journal of Chongqing University (Natural science Edition), 12 (2004) 52-55. (in Chinese)

© (2012) Trans Tech Publications, Switzerland
doi:10.4028/www.scientific.net/AMM.238.659

Discussion on Masonry Structure Model Mechanical Property Test

Gonglian Chen [a] and Linjun Si [b]

[1]School of Civil Engineering and Communication, North China University of Water Resources and Electric Power, Zhengzhou 450011, China

[a]chengonglian@gmail.com, [b]silinjun1980@163.com

Keywords: masonry; mechanical property; test.

Abstract. The problems in the mechanical test of masonry structure model were discussed in this paper, including the masonry material, similar relationship, shaking table test device, judgment of wall cracking and number of cycles in pseudo-static loading test. The conclusions are: (1) for the masonry material mechanical test, usually the size decreased the strength increased, but if the laying method and appropriate adjustments in the process of the test mixture ratio, the size effect can be greatly reduced; (2) In the dynamic test of the masonry structure, for the gravity distortion model, the common way is the external prestressing method, but in this method the tension force is not constant, which is differ from the actual situation; (3) The wall cracking can be judged when the main tension crack of the wall appeared; (4) The loading cycle in the pseudo-static test of masonry wall would be twice.

Introduction

In structure mechanical property test, because of the prototype structure test has many shortcomings, such as large investment, long period, strict laboratory equipment, measurement accuracy is affected by the environmental, and so on, the structure model test played an important role in the research of structure engineering. In structure engineering, model is defined as the structure elements or the assembly, which is constructed by the reduced scale, the model is use in the test, and similarity rule must be used in the analysis of the result [1].

In this paper, the problems in the mechanical test of masonry structure model were discussed, which can provide a more accurate method in the masonry structure model test.

Masonry Material

The masonry structure is a composite material of bulk materials (brick, block) and the mortar, from the material sense, the mechanical properties of the masonry structure to simulate is too complex, the reason is that: masonry is a composite material, all part of the component must be simulated, such as brick and block, mortar and steel. Meanwhile, because of the small dimension of the brick or block, it is difficult to produce [1]. As the stress-strain relationship of the model and the prototype is often the same as each other, in fact the same material as the prototype structure is used [2].

Because of the dimension of the brick or block is restricted in the production, the reduced scale ratio is often adopted as 1/2, 1/3 or 1/4 [3] 4]. Along with the development of manufacturing, for small concrete hollow block, the 1/4 ratio model block has produced [1] (Fig. 1); and for concrete perforated brick, which is a special type in China, because of the multi-holes and the thin walls, the production is difficult, and the 1/3 ratio model brick has produced [6] (Fig. 1). For the mortar, the main problem is the particle size, which needs to sift.

For mechanical performance of the material, in the elastic range, structure model material was usually selected with the same stress strain relationship with the prototype. For masonry structure, before the model test, the basic mechanical performance must be tested. Because of the difference of the size between the model specimen and prototype specimen, its mechanical properties are also different to each other. The reason is mainly on the masonry construction quality, loading rate and loading method, cement solidification rate and degree of drying, and so on.

Because of the size effect, usually the size decreased the strength increased. But some test results indicate that with the same laying method and appropriate adjustments in the process of the test mixture ratio, the size effect can be greatly reduced, including compressive strength, elastic modulus, shear strength, bending strength and so on[1].



(a) small concrete hollow block [5]



(b)concrete perforated brick [6]

Fig. 1 The model and prototype of the block and brick

Similar Relationship

Static Similarity Relationship. The static similarity relationship is simple, commonly used similar constants are shown in Table 1.

Table 1 Static similarity relationship of masonry structure

Type	Physical quantity	Physical quantity	Relationship	Utility model
Material peroformance	Strain ε	--	1	1
	Stress σ	FL^{-2}	$S_\sigma=S_E$	1
	Elastic modulus E	FL^{-2}	$S_E = S_\sigma$	1
	Possion's ratio υ	--	1	1
	Mass density ρ	$FL^{-4}T^2$	$S_\rho= S_E/S_l$	$1/S_l$
Geometric characteristics	Length l	L	S_l	S_l
	Linear displacement x	L	$S_x= S_l$	S_l
	Angular displacement β	--	1	1
	Area A	L^2	$S_A= S_l^2$	S_l^2
Load	Concentrated force, shear force P	F	$S_P= S_E S_l^2$	S_l^2
	Linear load W	FL^{-1}	$S_W= S_\sigma S_l$	S_l
	Surface load q	FL^{-2}	$S_q= S_\sigma$	1
	Torque M	FL	$S_M= S_\sigma S_l^3$	S_l^3

Dynamic Similarity Relationship. The dynamic similarity relationship of the masonry structure is shown in Table 2. Usually with the same material for model and prototype, the reduced scale ratio S_l can be obtained by the ratio of brick/block. In the dynamic test, inertia force is the main force implied on the structure, but the model structure and the prototype should be in the same gravity acceleration, so in general the sense S_g=1 and S_a=1, but from Table 2, the density ρ>1, it is difficult to find the similar materials, therefore, the usual approach is to attach the appropriate distribution of weight on the model. However, due to the carrying capacity of the shaking table, additional weight can not be added unlimited, when the artificial weight is not added enough, in order to meet the dynamic equilibrium in the horizontal direction, the relationship S_a must be increased (Table 2), this is the common way to solve this issue, but will cause distortion in the vertical gravity, vertical compressive stress of the wall becomes small, led wall cracking ahead of time and collapsing delayed.

Shaking Table Test Device

For the gravitational distortion model, the approach is divided into two cases, for the confirmatory test, the results are used to verify the correctness of the calculation method, the results need not to be treated; but for the mechanistic test, which is used to make a clear understanding of the masonry mechanism, generally, the solution is the external prestressing method (Fig. 2). In this method, the vertical compressive stress of the model is the same as that of the prototype, and without increasing the additional weight, but when the wall deformed, the pulling force of the cable is uncertain, which is differ from the actual situation. If the cable elongation and tension force are not related, that is when the cable elonged or shortened, the tension force is constant, this method may be a better solution to the gravitational distortion of the test methods.

Judgment of Wall Cracking

In masonry mechanical test, especially the pseudo-static test, there are two ways in the judgement of wall cracking, the first is the time when the first crack appeared on the wall, the second is the time the main tension crack appeared. The former approach in determining has a great chance and human factors, and the latter approach is more direct and objective. According to the test [6], for the wall without structural column, in Fig. 3, minor cracks appeared in the corners of the wall when the horizontal load is 60kN, but the skeleton curve is almost a line, and stiffness is basically no degradation, until the main crack occurs, the significant degradation of stiffness was occurred, so if the cracking is judged in this time, the mechanical properties are relatively clear.

Table 2 Dynamic similarity relationship of masonry structure

Type		Physical quantity	Relationship	Utility model
Geometric characteristics	Length l	L	S_l	S_l
	Linear displacement x	L	$S_x=S_l$	S_l
	Area A	L^2	$S_A=S_l^2$	S_l^2
Material peroformance	Stress σ	FL^{-2}	$S_\sigma=S_E$	1
	Strain ε	/	$S_\varepsilon= S_\sigma/S_E$	1
	Elastic modulus E	FL^{-2}	S_E	1
	Possion's ratio v	/	S_E =1	1
	Bulk density γ	FL^{-3}	$S_\gamma=S_\sigma/ S_l$	$1/S_l$
	Density ρ	FT^2L^{-4}	$S_\rho=S_E/(S_lS_a)$	$1/(S_lS_a)$ (artifical weight)
Load	Surface load q	FL^{-2}	$S_q= S_E$	1
Dynamic characteristics	Weight m	FT^2L^{-1}	$S_m= S_\rho S_l^3$	$S_\rho S_l^3$
	Stiffness K	FL^{-1}	$S_K= S_E S_l$	S_l
	Damp C	FTL^{-2}	$S_C= (S_E/S_\rho)^{0.5}S_l^2$	$(1/S_\rho)^{0.5}S_l^2$
	Frequency ω	T^{-1}	$S_\omega= S_l^{-1}(S_E/S_\rho)^{0.5}$	$S_l^{-1}(1/S_\rho)^{0.5}$
	Acceleration a	LT^{-2}	$S_a=S_E/(S_lS_\rho)$	S_a=3/2
	Time t	T	$S_t= S_l(S_E/S_\rho)^{-0.5}$	$S_l(1/S_\rho)^{-0.5}$
	Velocity v	LT^{-1}	$S_v= (S_E/S_\rho)^{0.5}$	$(1/S_\rho)^{0.5}$

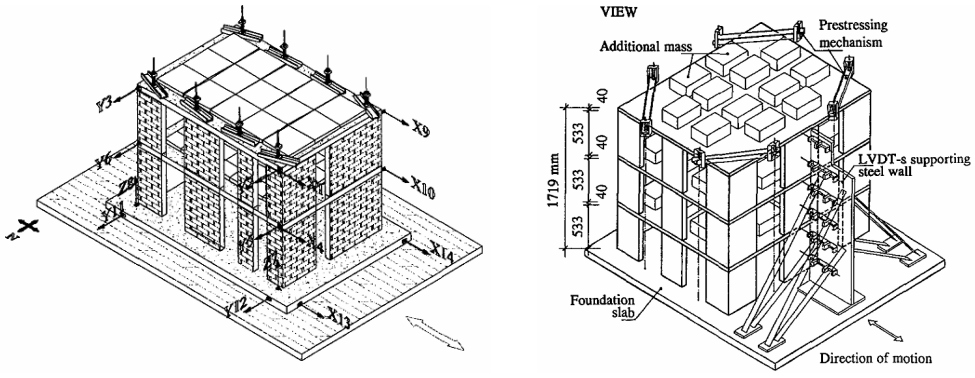


Fig. 2 Prestress on the structure [3]

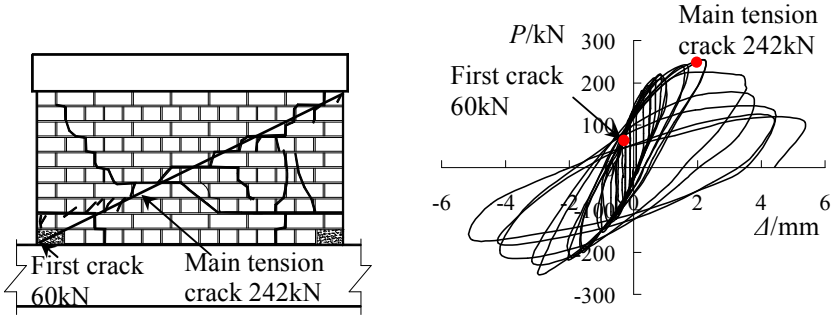


Fig. 3 Judgement of crack and failure for masonry wall

Number of Cycles in Pseudo-static Loading Test

In pseudo-static test, every stage of loading cycles depending on whether the deformation of the specimen may be stabilized, usually each stage of loading repeated once. After cracking the wall produced certain plastic deformation and friction deformation, under normal circumstances, repeated 2 or 3 times the wall is basically stabilized. Other scholars consider that masonry is brittle material, so one cycle loading can reflect the deformation performance of the member. According to the test result as shown in Fig. 4 and Fig. 5 [6], when the wall cracked, the stiffness degenerate is bigger in the second load cycle, but the third cycle is almost the same as the second cycle. Therefore, when the wall cracked, the number of the loading cycle would be twice.

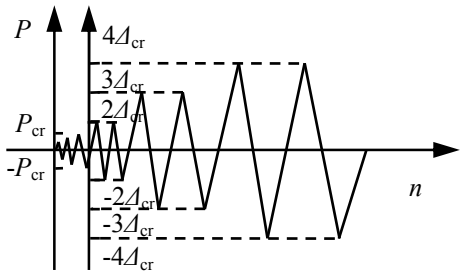


Fig. 4 Wall pseudo-static test load

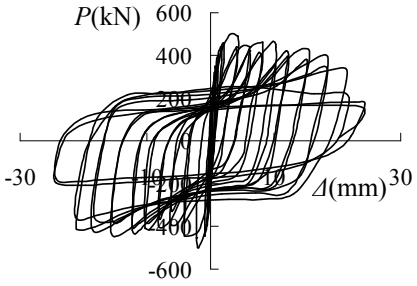


Fig. 5 Hysteresis loops of walls

Conclusions

The masonry material mechanics relies on the size of specimen. If the laying method and appropriate adjustments are made in the process of the test mixture ratio, the size effect can be greatly reduced.

In the dynamic test of the masonry structure, due to the carrying capacity of the shaking table, additional quality can not be added unlimited, the relationship S_a must be increased, but will cause distortion in the vertical gravity, vertical compressive stress of the wall becomes small, led wall cracking ahead of time and collapsing delayed. The common way is the external prestressing method, but in this method the tension force is not constant, which is differ from the actual situation.

The wall cracking can be judged when the main tension crack of the wall appeared. The loading cycle in the pseudo-static test of masonry wall would be twice.

Acknowledgments

This work was financially supported by High-level personnel research start-up projects of North China Institute of water conservancy and hydroelectric power (201159).

References

[1] G. M. Sabnis, H. G. Harris, R.N. White, et al: Structural Modeling and Experimental Techniques, China Railway Press, Beijing ,1989.

[2] Z. Yao, Z. Liu: Building Structure Test, Tongji University Press, Shanghai, 1996.

[3] Z. Zonta, G. Zanardo, C. Modena: Materials and Structures, 12 (2001) 637-644.

[4] X. Lv, B. Zhu: Journal of Tongji University, 14 (1986) 13-26.

[5] L. Huang. MDOF Substructure Pseudo-dynamic Testing and Nonlinear Seismic Response Analysis of Frame-supported Reinforced Masonry Shear Wall. Hunan university, 2005.

[6] G. Chen. Study on static and dynamic mechanical behavior of concrete perforated brick masonry structures. Tongji University, Shanghai, 2010.

[7] M. T. G. Hughe: Prototype and model masonry behavior under different loading conditions. 44 (2011) 53-65

[8] M. Tomazevic, P. Weiss: Journal of Structural Engineering, 20 (1994) 323-338.

© (2012) Trans Tech Publications, Switzerland
doi:10.4028/www.scientific.net/AMM.238.663

Manufacturing Technology of High-Strength Continuous Compound Spiral Hoop

Junfeng Guan[1, a] and Qian Zhang[2, b]

[1]North China Institute of Water Conservancy and Hydroelectric Power, Zhengzhou 450011, China

[2]Faculty of Infrastructure Engineering, Dalian University of Technology, Dalian 116023, China

[a]shuaipipi88@126.com, [b]phoenix1012@126.com

Keywords: high-strength; continuous compound spiral hoop; construction.

Abstract. This paper proposes the use of high-strength continuous compound spiral hoop in avoiding various weaknesses, such as steel wastes from conventional hooped reinforcement, overcrowding of hoop at reinforcement areas, and difficulties in concrete vibration and construction. It also analyzes the advantages of high-strength continuous compound spiral hoop in construction processes, operational key points, and quality control. It shows that the high-strength continuous compound spiral hoop can prevent various weaknesses in conventional hooped reinforcement, minimize the consumption of steel and improve work efficiency.

Introduction

High-strength continuous compound hoop is a continuous hooped reinforcement made with high-strength heat-treated rebars ($f_{yk} \geq 1100$ MPa). High-strength heat-treated rebar is manufactured from low-carbon steel alloy using special technology. Compared with pc steel bars, high-strength heat-treated rebar has low cost, good weldability, and high plasticity. Conventional compound hoop cannot completely bind with concrete under pressure and has low hoop strength. In addition, the hoop can easily yield and lose its binding force to the concrete when the concrete under pressure expands or shear slips. Meanwhile, high-strength continuous compound spiral hoop can effectively bind the concrete, resulting in an increased bearing capacity of the components and resistance to deformation. Continuous compound spiral hoop cancels the 135°C hook at the end of a single hoop, thus, preventing the problem of hoop ineffectiveness during earthquake. It effectively solves the problem of loose hooking for conventional hoop due to repeated actions of earthquake force. The effect of concrete binding is close to round hoop, which is better than square steel pipe in increasing and improving the earthquake resistance of concrete columns [1-5].

Advantages of High-Strength Continuous Compound Spiral Hoop

High-strength continuous compound spiral hoop cancels the two hook lengths at the end of the hoop bars, saving the consumption of rebar for approximately 24d per bar (where d refers to rebar diameter) considering earthquake conditions, thus, resulting to lowered cost and reduced consumption of resources. Continuous compound spiral hoop is manufactured by machines in large quantities and has high accurate dimensions. Rebar binding in construction sites are simple with less binding points, thus, saving time and manpower, and effectively increases construction progress and work efficiency. Continuous compound spiral hoop also prevents the rebar hook from attaching to the immersion vibrator that can reduce the vibrating speed and increase vibrating difficulty, thus, increasing concrete vibrating density, ensuring structural quality and safety, greatly increasing concrete placement quality and visual appearance, and reducing the processes of grinding and repair. The continuous compound spiral hoop forms the space structure with longitudinally-bound rebar, which will not deform or change due to treading, and ensures the correct position of the rebar in concrete, maintaining the strength and quality of concrete parts. Moreover, continuous compound spiral hoop increases the overall construction quality and life of the building and provides benefits in structural safety.

Manufacturing Processes of High-strength Continuous Compound Spiral Hoop

Binding of Spiral Hoop Bars. A bundle of spiral hoop bars is placed into the main reinforcement → The bars are then connected to the long main reinforcement → Bound bars are loosened → The end of the spiral hoop bars are pulled to the top of column (or bottom of beam) → Hoop bars and lengthwise bars are bound at the four corners of the column → Finally, quality inspection and acceptance.

Processes of Binding Spiral Hoop Reinforcement Bars with Beam and Column Joints. A bundle of spiral hoop reinforcement bars is placed at the middle of the beam span and, at the same time, the joints of beam, column, and spiral hoop are temporarily fixed to the main reinforcement of the column → The bars are placed into the longitudinal reinforcement of the upper and lower beams → Longitudinal reinforcement of the upper and lower beams are underlain → The binding of the upper hooped reinforcement is loosened and both ends are pulled to the side of column → Bound → The spiral hoop of the beam and column joints are loosened and fixed to the rebar under the beam; the hooped reinforcement of the beam and column joints are bound → Hooped reinforcement of beam and column joints are bound → Finally, the quality acceptance.

Operational Points of Spiral Hoop

The beam internal spiral hoop must be set at the column side. The end of column internal spiral hoop must be set at the beam side. The end of the joint internal spiral hoop must be set beneath the bottom layer of the rebar on top of the beam and on top of the rebar beneath the beam. During the sectional setting of spiral hoops for the beam and column, the sectional joint at the end of the spiral hoop must satisfy the lap length larger than one round.

The lap section of the spiral hoop must be at the external side of plastic hinging area.

The spiral hoops of the beam and column ends must have one overlapping round and the 135°C hook at the end must be fixed to the concrete by turning the longitudinal rebar round.

The spiral hooped reinforcement must be bound, tagged, and kept in a dry area after being manufactured to avoid transportation and usage difficulties. In addition, hooped reinforcements are difficult to separate when they are attached to each other.

The spiral hooped reinforcement bars must be extended larger than the set space during binding to eliminate the stress for easier binding.

Quality Control Spiral Hoop

High-strength steel wires are cut using a machine instead of a torch or welder.

Anti-rust measures must be applied during transportation and storage.

The spiral hoop must be formed using automatic machines and ensure that the accuracy of the side length is not larger than ± 1 mm and the bending accuracy is ± 0.5. Sampling inspection must not exceed 10% and must not be less than three pieces during batch manufacture of spiral hoops.

The spiral hoop must be correctly positioned in compliance with the dimensions specified in the drawing and the error should be no larger than ± 3mm.

Tensile test of spiral hoop welding: The tensile strength of three testing samples must not be lower than the tensile strength value of the rebar of the same standard. In addition, at least two testing samples should be broken outside the welding seams and have ductile fracture. Testing must be repeated in case the tensile strength of a single testing piece is smaller than the specified value, or two testing pieces showed brittle fracture at the welding area or heating areas, and that the tensile strength is 1.10 times less than the specified strength for the rebar. Six testing samples must be used during testing repetition. A batch of joints must be regarded as unqualified when the repeated testing showed that the tensile strength of a testing piece is smaller than the specified value, or three testing pieces have ruptured at the welding seams or heating area, and have brittle fracture, and that the tensile strength is 1.10 times less than the specified strength for the rebar. Using poor quality hooped reinforcement on beam and column is strictly prohibited.

Analysis of Economic and Social Benefits

High-strength continuous compound spiral hoop can save large amounts of steel and mineral resources and is useful for preserving iron ores and coal. In addition, it can lessen consumption and preserve resources and energy. High-strength continuous compound spiral hoops are manufactured by CNC hoop bending machine and are distributed and transported systematically, which proved beneficial to employment and optimized resource configuration.

Conclusions

In this paper, the advantages of high-strength continuous compound spiral hoop, construction processes, operational key points, and quality control was analyzed.

Construction processes has proven that high-strength continuous compound spiral hoop can prevent various weaknesses in conventional hooped reinforcement, minimize the consumption of steel, and improve work efficiency, providing favorable social and economic benefits.

Acknowledgements

This study was financially supported by the High-level Personnel Research Project of North China Institute of Water Conservancy and Hydroelectric Power (201064) and Research Center on Levee Safety and Disaster Prevention of Ministry of Water Resources (201202).

References

[1] A. Azizinamini, S.S.B. Kuska and P. Brungardt, ACI Structural Journal, 91 (1994) 336-345.

[2] S.R. Razvi, M. Saatcioglu, ACI Structural Journal, 91 (1994) 1-10.

[3] O. Bayrak, S.A. Sheikh, Journal of Structural Engineering, ASCE, 124 (1998) 999-1010.

[4] O. Bayrak, S.A. Sheikh, ACI Structural Journal, 94 (1997) 708-722.

[5] S.K. Hwang, H.D. Yun, Engineering Structures, 26 (2004) 1-12.

© (2012) Trans Tech Publications, Switzerland
doi:10.4028/www.scientific.net/AMM.238.666

Optimal Calculation Method of Eccentric Bearing Capacity of Concrete-filled Steel Tube Short Columns

Jianwei Zhang[1, a], Xingjie Kuang[2, b], Weifeng Bai[1, c] and Juan Wang[3, d]

[1] North China University of Water Resources and Electric Power, Zhengzhou 450011, China

[2] Beijing Corona Science & Technology Co.,Ltd, Beijing, China

[3] College of Water Conservancy and Environment Engineering, Zhengzhou University, Zhengzhou, 450001, China

[a] zhangjianwei@ncwu.edu.cn, [b]13683500326@163.com, [c]yf9906@163.com, [d]wangjuan@zzu.edu.cn

Keywords: concrete-filled steel tube; short column; eccentric capacity; bearing capacity; mechanical derivation.

Abstract. The currently formulae with many coefficients are too complicated to calculate the bearing capacity of concrete-filled steel tube (CFST) short columns. In this paper, an optimal calculation method was proposed for calculating the eccentric bearing capacity of CFST short columns by means of mechanical derivation. Additionally, the calculating results are compared with experimental data. It is shown that the optimal calculating formulae are highly accurate and easily applicable in engineering design.

Introduction

Concrete-filled steel tube (CFST), in which a steel tube is fully filled with concrete, takes advantage of the force interaction process of steel and concrete to form its bearing capacity. The advantages of steel's strong tensile ability and concrete's high compression capability are combined well in CFST structures, which endow CFST structures with high bearing capacity and deformation capacity, so the CFST is quite widely applicable for some structures like the high-rise buildings, super high-rise buildings and bridges, and so on. Due to the complexity of the interaction between steel and concrete, there are many different ways to study of the CFST structures, which lead to many different methods to calculate the eccentric bearing capacity of CFST short columns.

Current Formulae for Eccentric Bearing Capacity of CFST Short Columns

The formulae for eccentric bearing capacity of concrete-filled circular steel tube short columns (N) are mainly included as follows[1]:

$$N \le \varphi_1 \varphi_c N_0 \tag{1}$$

Where, φ_1 is the reduction factor of bearing capacity considering the influence of slenderness ratio; φ_c is the reduction factor of bearing capacity considering the eccentricity effects; N_0 is the design value of bearing capacity of CFST short column, $N_0=f_c A_c(1+\sqrt{\theta}+\theta)$, f_c is the design value of axial compressive strength of concrete, A_c is the cross-sectional area of concrete inside the steel pipe, θ is the steel tube confinement index, $\theta=f_s A_s/(f_c A_c)$, f_s is the design value of axial compressive strength or tensile strength of steel pipe, A_s is the cross-sectional area of steel pipe.

In Eq. (1), the reduction factors of bearing capacity considering the influence of slenderness ratio and eccentricity were proposed by regression analysis based on lots of experimental data according to the selected parameters. Although this method has considered the slenderness ratio and the eccentricity simultaneously, the relationship between the two was clearly ignored. So it would cause certain error.

$$N \le \gamma\, \varphi_c (A_s f_s + K_1\, A_c f_c) \tag{2}$$

Where, φ_c is the reduction factor of bearing capacity of eccentric bearing capacity of CFST; γ is the correction value of φ_c, γ=1.124-2t/D-0.0003f_s; K_1 is the added coefficient of strength of core concrete;

The eccentricity amplifier method has been adopted in equation (2). The mechanics concept of this method is clear. But there are more coefficients in equations (2), which need to be calculated by table look-up. It is not suitable for structural design applications.

When $N/A_{sc} \geq 0.2\varphi f_{sc}$,

$$\frac{N}{\varphi A_{sc} f_{sc}} + \frac{\beta_m M}{1.071\gamma_m W_{scm} f_{sc}(1-0.4N/N_E)} \leq 1 \tag{3a}$$

When $N/A_{sc} < 0.2\varphi f_{sc}$,

$$\frac{N}{1.4\varphi A_{sc} f_{sc}} + \frac{\beta_m M}{\gamma_m W_{scm} f_{sc}(1-0.4N/N_E)} \leq 1 \tag{3b}$$

Where, φ is the stability coefficient of axial compression; A_{sc} is the cross-sectional area of member; f_{sc} is the design value of combination strength of CFST; β_m is the equivalent bending moment coefficient; γ_m is the plasticity coefficient of member; W_{scm} is the sectional resistance moment of member; N_E is the Euler critical stress, $N_E=\pi^2 E_{scm} A_{sc}/\lambda^2$, E_{scm} is the combination of flexural modulus of elasticity of CFST.

The above formulae are complex, within many coefficients, so inconvenient in the engineering design.

Optimal Formulae for Eccentric Bearing Capacity of CFST Short Columns

Optimal Formulae for Eccentric Bearing Capacity of CFST Short Columns in the Elastic State. According to the mechanics of materials in the elastic state, the formula can be expressed as follows:

$$\sigma_{max} = \frac{F}{A} + \frac{M_{max}}{W_Z} \tag{4}$$

The sectional resistance moment of circular steel can be expressed as follows:

$$W_Z = \frac{\pi D^3}{32} \tag{5}$$

Substituting Eq. (5) into Eq. (4), obtaining

$$F = \frac{F_0}{1+8e/D} \tag{6}$$

Where, F_0 is the axial load bearing capacity; F is the eccentric load bearing capacity; e is the eccentricity and D is the diameter of steel pipe.

Optimal Formulae for Eccentric Bearing Capacity of CFST Short Columns in the Plastic State. When CFST short column is in the plastic state, the sectional resistance moment of circular steel can be expressed as follows:

$$W_Z = \frac{\pi D^4}{64} + \frac{D^4}{9\pi} \tag{7}$$

Substituting formula (7) into formula (4), it can be obtained that

$$F = \frac{F_0}{1+e/0.107D^2} \tag{8}$$

Accuracy Verification for Optimal Formulae. The test members in Table 1 are given by the scholars [1-4]. The measured value of CFST was marked N^t and the calculated value by formula (8) was marked N^c. The mean and coefficient of variation of N^t/N^c are listed in Table 1. The comparison results show that the precision of formula (8) is better, and can be used for engineering design.

Table 1 Comparison of experimental values with calculated values

Size of steel tube (mm×mm×mm)	Slenderness ratio λ	Eccentricity ratio	Compressive strength of concrete f_{cu} (MPa)	Steel yield strength f_s (MPa)	Test value N^t (kN)	Test value N^c (kN)	Test/ calculated value N^t/N^c
166×5×710	4.28	0.128	47.7	277.3	1642	1549	1.060
		0.128	47.7	277.3	1568	1549	1.012
		0.256	47.7	329.3	1568	1528	1.026
		0.256	51.2	294	1600	1550	1.032
		0.385	51.2	286	1201	1223	0.982
		0.385	51.2	248.9	1127	1050	1.073
		0.513	47.3	313.6	1039	1030	1.009
		0.513	47.3	279.3	990	970	1.020
		0.769	47.7	279.3	735	850	0.865
		0.769	47.7	296	843	870	0.969
		1.282	51.2	296	564	580	0.972
		1.282	51.2	296	510	580	0.879
Mean of N^t/N^c							0.992
Coefficient of variation of N^t/N^c							0.004
166×5×870	5.24	0.256	51.2	289.1	1431	1412	1.001
		0.256	51.2	296	1524	1499	1.017
		0.513	51.2	298	1019	1107	0.921
		0.513	51.2	279.3	1039	1056	0.984
		0.769	51.2	296	815	868	0.939
		0.769	51.2	296	799	868	0.921
		1.282	51.2	313.6	510	598	0.853
		1.282	51.2	303.8	490	570	0.856
Mean of N^t/N^c							0.937
Coefficient of variation of N^t/N^c							0.110

Conclusions

In this paper, an optimal calculation method of eccentric bearing capacity of CFST short columns has been proposed. The comparison with experimental data showed that the optimal calculating formulae performed high accuracy and can be easily used for engineering design.

Acknowledgements

This study was financially supported by the High-level Personnel Research Project of North China Institute of Water Conservancy and Hydroelectric Power (201064) and Research Center on Levee Safety and Disaster Prevention of Ministry of Water Resources (201202) and the National Natural Science Foundation of China for Youth ((51009020).

References

[1] L. Han, Y. Yang, Advanced Concrete Filled Steel Tubular Structure Technology, China Architecture & Building Press, Beijing, 2007. (in Chinese)

[2] Z. Tao, Q. Yu, New Types of Composite Columns-experiments, Theory and Methodology Science Press, Beijing, 2006. (in Chinese)

[3] S. Zhong, The Concrete-Filled Steel Tubular Structures, Tsinghua University Press, Beijing, 2003. (in Chinese)

[4] S. Cai, Journal of Building Structures, 4 (1985) 32-42. (in Chinese)

© (2012) Trans Tech Publications, Switzerland
doi:10.4028/www.scientific.net/AMM.238.669

Experimental Studies on High Strength Concrete Beams Reinforced with Steel and GFRP Rebars

Yinghao Liu[1, a] and Yong Yuan[2,b]

[1]Department of Underground Engineering, Tongji University, Shanghai 200092，China

[2] Key Laboratory of Geotechnical and Underground Engineering of Ministry of Education，Tongji University，Shanghai 200092，China

[a]smouse@qq.com, [b]yuany@tongji.edu.cn

Keywords: HSC; flexural strength; deflection; GFRP; hybrid reinforcements.

Abstract. The paper analyzes the structural behavior of high strength concrete (HSC) beams reinforced with hybrid glass fiber reinforced polymer (GFRP) and steel reinforcements. The analysis refers to HSC beams reinforced with GFRP rebars and steel rebars placed in different layers. Results of the experimental and theoretical investigation are represented and discussed. Significant features of the structural behavior regarding flexural strength, deflection, are pointed out.

Introduction

Fiber reinforced polymer (FRP) materials have advantage of high strength, light weight and excellent corrosion resistance. However, FRP rebars are linear elastic material, and FRP reinforced structure will lead to brittle failure. In addition, FRP rebars usually have low elastic modulus, which result in larger components deflection and crack issues.

To use FRP rebars hybrid with steel rebars in concrete components is considered to be an effective way to resolve these problems. Tan tested concrete beams reinforced with hybrid of aramid fiber-reinforced polymer (AFRP) and steel rebars [1]. Nanni and De Lorenzis found that placing the FRP rebars near the outer surface of the tensile zone with small cover thickness values and steel rebars at the inner level of the tensile zone is an optimal solution [2]. Aiello and Ombres analyzed the serviceability and flexural capacity of a set of hybrid AFRP-steel reinforced concrete beams [3]. Leung and Balendran tested concrete beams reinforced with a combination of glass fiber-reinforced polymer (GFRP) and steel rebars, which places GFRP rebars near the surface and steel rebars in the upper level [4].

In the represent paper, the behavior of flexural high strength concrete beams reinforced with a combination of GFRP and steel rebars is described. The aim of this paper is to study the flexural behavior of high strength concrete beams reinforced with GFRP and steel rebars. And the measured deflections at midspan for these beams are compared with predicted values using the ACI-440 model [5] and Bischoff model [6].

Experimental Program

The experimental investigation has been carried out on four concrete beams—one reinforced with only GFRP rebars, and three reinforced with a combination of GFRP and steel rebars.

Materials. The average compressive concrete strength f_c was 80.1 MPa as evaluated by tests on six cubic specimens 150 mm high. The yield strength of the steel rebars used as tensile has been determined by standard tensile tests, the average yield strength f_y was 374.5 MPa; and the tensile elastic modulus E_s was 197.57GPa. Tensile tests have been carried out to evaluate the properties of the GFRP rebars, the tensile strength f_{fu} and tensile elastic modulus E_f was 1301MPa and 75.98 GPa respectively.

Test Specimens. Four simply-supported HSC beams was tested as shown in Table 1. The beams made of 2,000 mm length, and with a rectangular cross section of 150mm wide and 250mm high, as shown in Fig. 1. Specimen S1 is only reinforced with GFRP rebars. And S2, S3, S4 refers to beams

reinforced with GFRP and steel rebars. For the beams s2 and S3, the steel rebars and the GFRP rebars are placed in two separate layers. Two steel rebars of 8 mm diameter have been used as reinforcement at the compression side of the beams; steel stirrups of 8 mm diameter and 100 mm spacing have been used as shear reinforcement.

Table 1 Details of Tested Beams

Beam	Number of steel rebars	Number of GFRP rebars	[7] $\rho_{eff,b}$ (%)	ρ_{eff} (%)	Beam classification
S1	0	4	0.7	1.2	Over-reinforced
S2	2	2	8.56	2.64	Under-reinforced
S3	2	2	8.56	2.64	Under-reinforced
S4	2	2	8.56	2.64	Under-reinforced

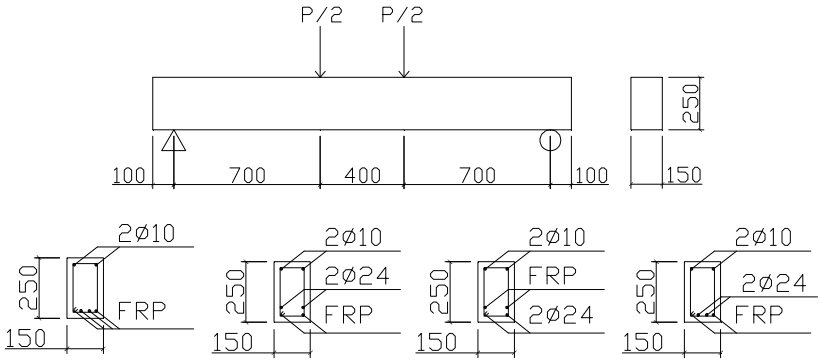


Fig. 1 Test specimens(mm)

Test Results and Discussions

General Situation. The failure of S1 represents more deflection more crack than other beams. When the load of specimens reached their ultimate load, the load capacity of S1 declined quickly compared with that of S2, S3 and S4. And the cracks of S1 illustrated widely than that of other specimens. There were no obvious difference between the S2, S3 and S4 except the ultimate load and the deflection.

Neutral Axis. Fig. 2 shows the strain distribution of the beam cross section at various load levels. The strain distribution was nearly proportional to the distance from the neutral axis, indicating that the assumption of plane cross section was valid for the hybrid GFRP/steel reinforced concrete beams. It should be noticed that the neutral axis didn't change obviously with loading in these beams.

Flexural Capacity. Table 3 summarizes the maximum loads and failure modes for all tested specimens. Experimental results indicate that the introduction of steel bars alter significantly the beam's maximum load and the mode of failure. Using only GFRP rods in concrete beams (S1) gave a slightly lower maximum load carrying capacity than the beam hybrid with steel rebars and GFRP rebars (S4). A hybrid use of steel rebars and GFRP rods provided an enhanced load capacity. And the influence of different level of reinforcement on flexural strength is also obvious. The flexural strength increased with the decline of the site of steel bars. The observed failure modes of the tested beams are also represented in Table 2.

Table 2 Flexural capacity

Specimens	Theoretical ultimate moment $M_{u,th}$(kNm)	Actual ultimate moment $M_{u,exp}$(kNm)	$M_{u,th}/M_{u,exp}$	Failure mode
S1	81.3	72.5	1.12	Concrete crush
S2	80.3	69.9	1.14	Steel yield, concrete crush
S3	80.3	74.8	1.07	Steel yield, concrete crush
S4	80.3	82.0	0.97	Steel yield, concrete crush

For hybrid reinforced beam, in the case of steel yield, the stress in tensile GFRP bars, and the nominal moment capacity in the ultimate limit state can be calculated by following equations.

$$f_f = \left(\sqrt{\frac{1}{4}\left(\frac{A_s f_y}{A_f} + E_f \varepsilon_{cu} \right)^2 + \left(0.85 \frac{\beta_1 f_c^{'}}{\rho_f} - \frac{A_s f_y}{A_f} \right) E_f \varepsilon_{cu}} - 0.5 \left(\frac{A_s f_y}{A_f} + E_f \varepsilon_{cu} \right) \right) \le f_{fu} \tag{1}$$

$$M_n = \left(\rho_f f_f + \rho_s f_y \right) \left(1 - 0.59 \frac{\rho_f f_f + \rho_s f_y}{f_c^{'}} \right) bd^2 \tag{2}$$

The theoretical ultimate moment of beams ($M_{u,th}$) are also represented in Table 2. The theoretical value calculated by Eq. 1 and Eq. 2 fit the actual value well, but these equations did not consider the impact of different reinforcement locations.

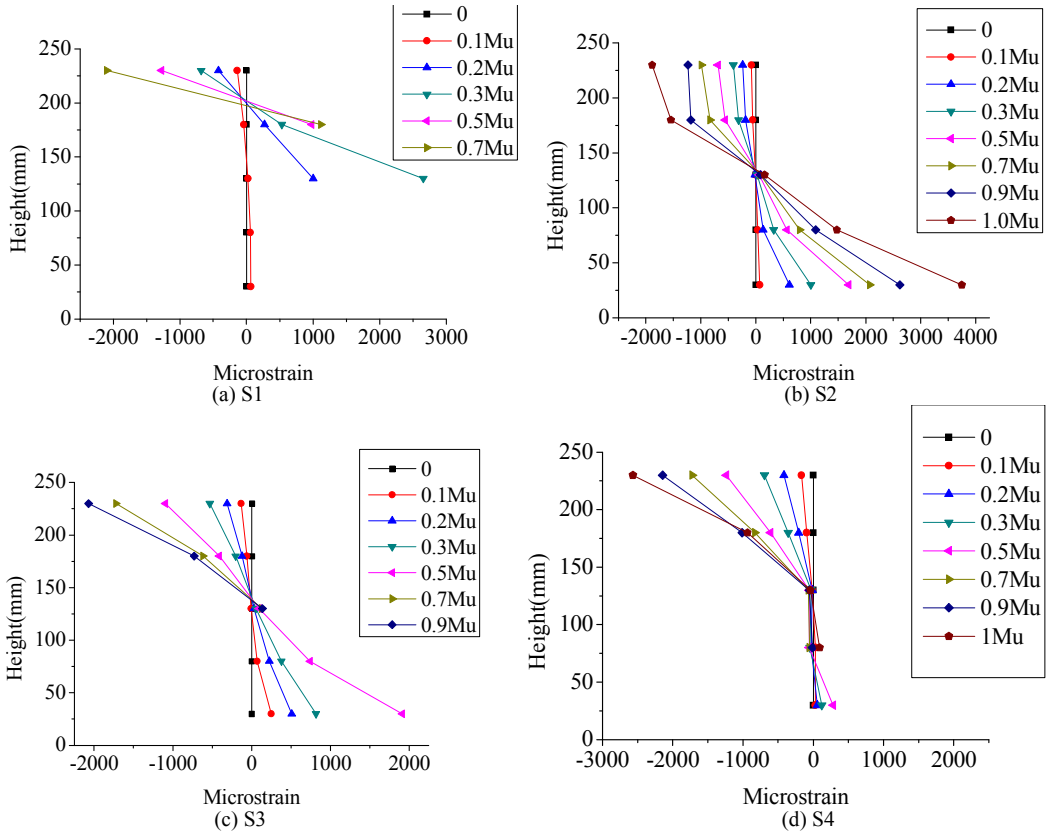


Fig. 2 Midspan strain of beams

Deflection. The recorded deflection behavior of all the tested beams is illustrated in Fig. 3. The deflection of S1at the peak load is about 4~5 times to that of hybrid reinforced beams. This behavior represents that the hybrid system enhanced the serviceability of the component. For hybrid system, the initial linear part of the curves was similar for all beams. At the end of the linear phase, the beams crack. The second segment had a smaller slope than the initial linear part. This indicated that the stiffness of the beams decreased after cracking although the reduction in stiffness varied between beams. The largest stiffness reductions were in S2, while S3 and S4 had similar slope before steel yield, and followed with gentler slopes in the curves until concrete crush. This indicated that the steel bars are the control factor to deflection in the hybrid system.

In the analysis, the Bischoff model [6] also was used to predict the deflection. The model refers to simply supported FRP reinforced beams, subjected to four-point loading; it introduces a modified moment of inertia I_e to calculate deflections. This model represents a rational development of appropriate modification factors needed to reduce the tension stiffening component in Branson's original expression to realistic levels. Bischoff's expression for the effective moment of inertia I_e that showed a good agreement with test results for both steel and FRP reinforced concrete beams [7]

$$I_e = \frac{I_{cr}}{1 - \eta (M_{cr} / M_a)^2} \le I_g \tag{3}$$

$$\eta = 1 - \frac{I_{cr}}{I_g} \tag{4}$$

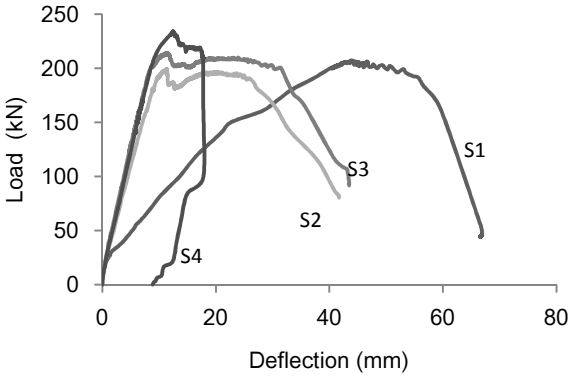


Fig. 3 Load-deflection curve

The comparisons between the experimental load-deflection curves and the theoretical curves are showed in Fig. 4. In the initial linear stage, all theoretical results fit the experimental ones well. At this moment, the beams were not crack yet, and the deflection is calculated by the moment of inertia of gross concrete section about centroidal axis, neglecting reinforcement (I_g). The experimental results show that I_g is applicable for both GFRP and hybrid reinforced beams. When the concrete was cracking, the deflection is calculated by the effective moment of inertia (I_e). In the deflection prediction of GFRP reinforced beam (S1), I change from I_g to I_e ($=\beta_d I_g$), which leads the immediately increase of the deflection. But in the experiment, no such phenomenon happened, so the ACI-440-06 model should be improved in the latter work. After the concrete cracked, the prediction for FRP bars reinforce beams works well. Meanwhile, the model used to compute the deflection of hybrid beams had huge deviation. In hybrid beams, the computation I_{cr} seems to be little bigger than actual value, which lead more deflection in calculation.

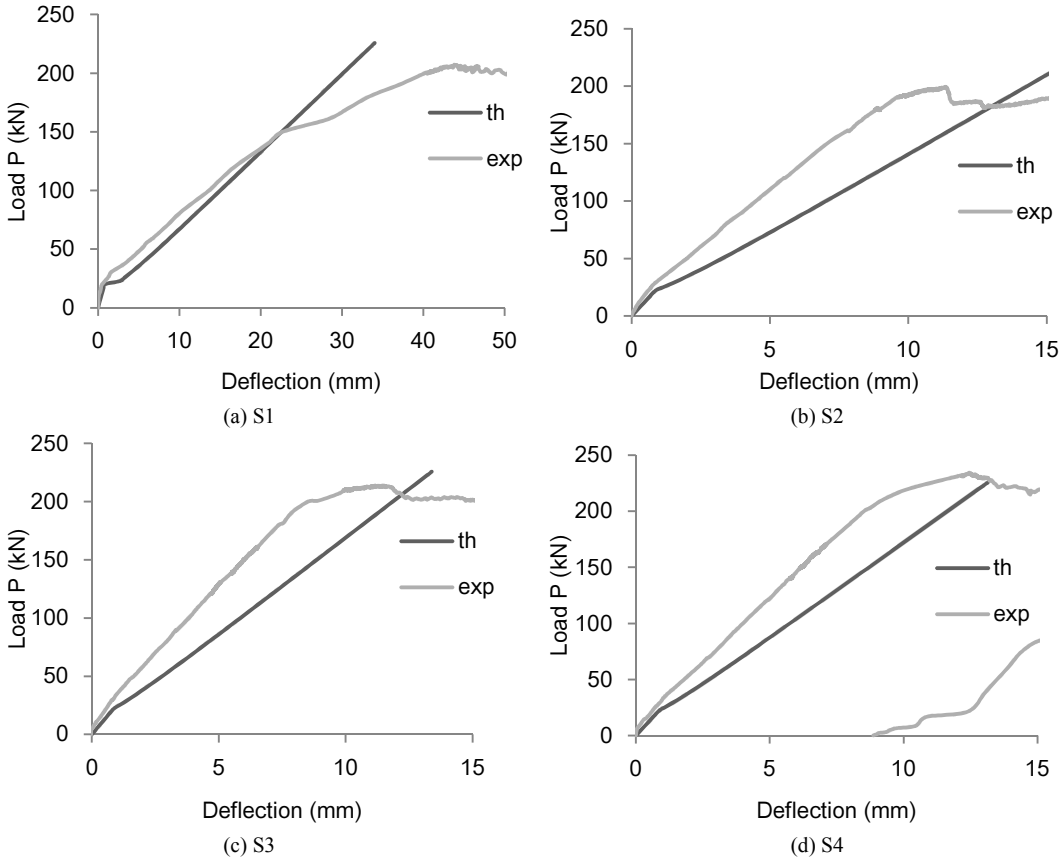


Fig. 4 Comparison of theory and experiment curves

Conclusions

The tests on beams carried out in this study describe the possibility of using GFRP bars hybrid with steel bars in high strength concrete structures. The ultimate load carrying capacity, deflection, were predicted theoretically and measured experimentally. From the results we draw the following conclusions.

The use of steel reinforcement in combination with GFRP reinforcement enhances the flexural behavior of GFRP reinforced concrete beams. It's control the deflection of beam well. And use GFRP bars partially instead of steel bars can decrease the reinforcement ratio and the weight of structures.

The strain distribution measured in this study indicator that the hybrid reinforced high strength concrete beam have a steady neutral axis, which is not impact by the load obviously.

The flexural strength of the beams elucidate that the strength is associated to the level of the beams. The proposed model for flexural capacity is valid for hybrid reinforced concrete beams. But it nether consider the level of the bars.

The deflection of the beams implies that the deflection of hybrid beams is mainly impact by the steel bars and their position. The ACI-440.06 model can evaluate the GFRP reinforce beams well, except the cracking moment. And deflection predict by the modified ACI-318.05 model in hybrid reinforce beams shows a little deviation from the experimental results. The I_e is under estimated in this model.

References

[1] K. Tan, Behaviour of hybrid FRP-steel reinforced concrete beams, in: Proc, 3rd Int Symp on Non-Metallic (FRP) Reinforcement for Concrete Structures (FRPRCS-3). Sapporo. 1997: 487-94.

[2] A. Nanni, De Lorenzis L, Shear strengthening of RC beams with near surface mounted FRP rods, ACI structural journal, 1 (2000) 60-8.

[3] M. A. Aiello, L. Ombres, Structural performances of concrete beams with hybrid (fiber-reinforced polymer-steel) reinforcements, Journal of Composites for Construction, 2 (2002) 133-40.

[4] H. Y. Leung, R. V. Balendran, Flexural behaviour of concrete beams internally reinforced with GFRP rods and steel rebars, Structural Survey, 4 (2003) 146-57.

[5] American Concrete Institute (ACI), Guide for the design and construction of structural concrete reinforced with FRP bars, ACI 4401R-06, Detroit, 2006.

[6] P. H. Bischoff, Deflection calculation of FRP reinforced concrete beams based on modifications to the existing Branson equation, Journal of Composites for Construction, 1 (2007) 4-14.

[7] W. Qu, X. Zhang, H. Hai, Flexural behavior of concrete beams reinforced with hybrid GFRP and steel bars, Journal of Composites for construction, 5 (2009) 350-90.

CHAPTER 4:

Innovation in Bridge and Underground Engineering

© (2012) Trans Tech Publications, Switzerland
doi:10.4028/www.scientific.net/AMM.238.677

Key Design and Construction Techniques for Collisionproof Steel Cofferdam for Large Span Cable-stayed Bridge

Weizhou Li[1,a], Zhongju Feng[1,b], Zhongchao Hu[2,c], Dongliang Xun[3,d], Jian Zeng[4,e] and Qiang Peng[3,f]

[1]The Highway school of Chang'an University , Xi an 710064, China

[2]CCCC-2nd Navigational Engineering Co., Ltd., Wuhan 430040, China

[3]Key Lab for Large-Span Bridge Construction Technology, Wuhan 430040, China

4CCCC-Wuhan Harbour Engineering Design & Research Institute, Wuhan 430040, China

[a]248806276@qq.com, [b] ysf@gl.chd.edu.cn, [c] techcenter@163.com, [d] bridgexun168@163.com

[e]277507986@QQ.comemail: [f]63443097@QQ.com

Key words: long span cable-stayed bridge; anti-ship collision; suspended steel cofferdam; design; construction.

Abstract. As an example, the design and construction technology of the anti-ship collision suspended steel cofferdam in Shanghai Changjiang River Bridge has been discussed. Design analysis shows that: by using the anti-ship collision suspended steel cofferdam the bridge pier can be protected and adopted lots of collision energy. At the same time, the collision injury degree of the vessel could be reduced. By using the finite element method, the deformation and strain state under the stage of construction and floating-transportation had been analyzed. Considering both the anti-ship collision and the construction, the anti-ship collision suspended steel cofferdam has been designed. In construction stage, the following methods had been developed: the integrally manufacturing method in factory, launching method to river in slideway, fioating-transportion method to the pier position in long distance and set-to-place method by synchronous lifting of two floating cranes. These results listed in this paper are beneficial to the design and construction of the anti-ship collision suspended steel cofferdam.

Introduction

Overview of the Main Bridge of Shanghai Yangtze River Bridge. The Shanghai Yangtze River Tunnel & Bridge project is an important part of Shanghai-Xi'an highway listed in key highway planning of the State as determined by the Ministry of Communications. With a total length of 25.5 km, it is the largest tunnel & bridge combination project in the world so far. The main navigation span bridge is a full-floating large span cable-stayed bridge with two pylons and double cable planes. The span of the main bridge is arranged as: 92m+258m+730m+258m+92m=1430m. The main pylon is in herringbone shape and the master beam is split-type steel box girder with a width of 51.5 m; its superstructure is a shared plane for highway (six-lane two-way) and railway (light rail at two sides of the highway); the stayed cables are sector shaped with double cable planes (as shown in Fig.1).

Piers of Main Bridge. Foundations of the two main piers are composed of 60 non-uniform bored piles with the diameters from 3.0m to 2.5m; the pile bottom elevation is -109.85m (south main pier) and -106.85m (north main pier), and the pile top elevation is -2.0m; the size of the pile cap is 72.2m×37.2m×6.0m (length×width×height); the top elevation of the pile cap is +4.0m, bottom elevation is -2.0m; the thickness of the pile cap is 6m, with a pointed round shape from upstream to downstream.

Overview of Anti-collision Research for Bridge Piers. The research on the vessel-bridge collision started at the end of 1960s, but in the first decade, the research didn't make big progress. Until 1983 the IABSE (International Association for Bridge and Structural Engineering) held an international seminar with the theme of "reasonable design and analysis on vessel-bridge collision",

which was the first one with this theme in the world. After the seminar, the research on vessel-bridge collision [1] started to develop in a faster way. In China, the research on vessel-bridge collision started in 1990s.

Generally speaking, the research on anti-collision of bridge involves two points: the research on vessel collision force standard and anti-collision design [2]. There are normally two methods for anti-collision of bridge: active anti-collision and passive anti-collision [3]. Active anti-collision means to prevent collision from happening through controlling and interfering with the navigation of the vessels.

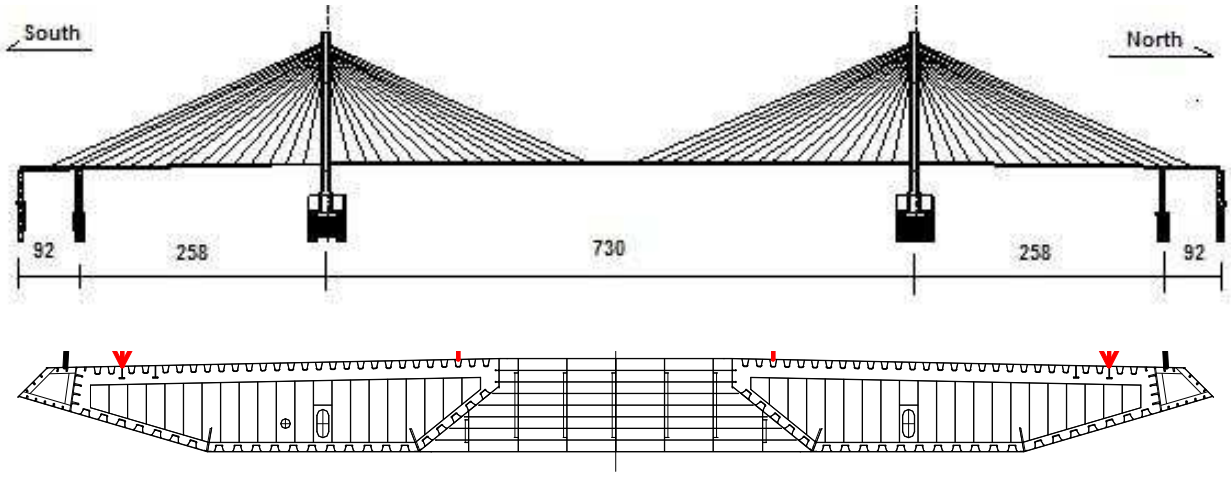


Fig. 1 Main bridge of the Shanghai Yangtze River tunnel & bridge project

Design and Analysis of Collisionproof Steel Cofferdam

Design Idea and Collision Analysis of Steel Cofferdam. In order to save material and simplify construction procedures, the general idea is to design a structure incorporating both collisionproof function for the main piers and the cofferdam required for construction. This structure shall not only satisfy anti-collision requirements, but also act as a water retaining structure during construction of pile cap to meet different load requirements. The collisionproof steel cofferdam is a large steel structure integrating the functions of buffering, energy dissipation and cofferdam for pile cap. The four walls of the structure have the function of protecting the piers from collision through energy dissipation. In case of damage of the walls due to vessel collision, the damaged parts can be cut off and replaced. Under normal designed conditions of use, the service life of the structure is 30 years.

The main navigation span of Shanghai Yangtze River Bridge is large, and the main piers are designed with firm structure, so in the near future, the anti-collision method mainly adopts self anti-collision, supported with cofferdams installing around the piers [4]. In case of collision, the cofferdams will dissipate the energy through distortion and thus to reduce the force of collision; also to protect the foundation structure of the piers and reduce the damages to the pier due to collision [5]. The cofferdams of the main piers of Shanghai Yangtze River Bridge adopt passive anti-collision design, i.e. to protect the bridge from vessel collision through reinforcement of the piers or installing additional protections devices. The cofferdams are carefully calculated and analyzed [6] by the designing unit. The finite element simulation analysis shows that, in case of the collision of a 50,000 kN vessel, 21MJ energy will be dissipated through distortion of the vessel in 1.5s, and meanwhile 27MJ will be dissipated through distortion of the cofferdam, as shown in Fig. 2 and Fig. 3. The collision proof cofferdams are installed not only to protect the bridge by reducing the force of collision to a large extent, but also to effectively protect the vessel and reduce damage to it.

Design Conditions of Construction. (1) Wave: according to water condition at the site, the max. wave height is considered as H_{max}=2.0m (ENE, E) after installation of cofferdam and before construction of pile cap

(2) Flow rate: the max. flow rate V=1.86m/s (flow rate is vertical to bridge axis) during the construction..

(3) Wind speed: V=25.0m/s.

(4) Design tide level: 0.8-4.5m.
(5) Elevation of mud surface: the elevation of mud surface is about -12m to -16m.
(6) Casing size: φ3186×18mm; casing top elevation: +6.2m.
(7) Bottom sealing thickness: 2.0m; one-time bottom sealing considered.
(8) Transportation method: float transportation.
(9) Hoisting method: by two floating cranes.
(10) Hoisting dynamic coefficient: 1.25.
(11) Bond stress between bottom concrete and steel casing: 150kN/m^2.

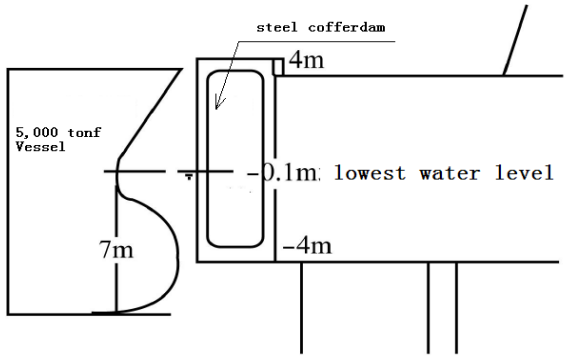


Fig. 2 Collision between vessel and steel cofferdam

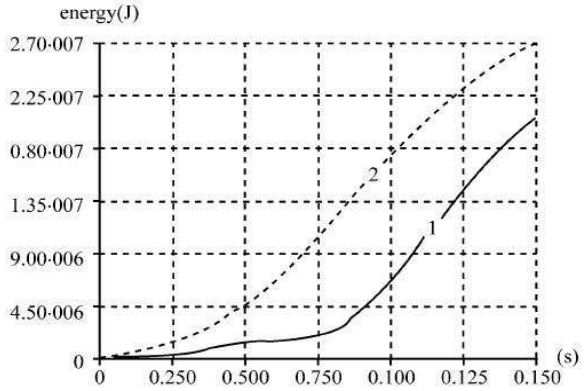


Fig. 3 Graph of energy dissipation by cofferdam (1-vessel; 2-collisionproof)

Structure Design of Steel Cofferdam. The steel cofferdam is rectangle shaped with a total size of 76.4m (length)×41.4m (width)×10m (height). It is a two-layer grillage structure and the space between the two layers is 2m. The vertical bulkhead plate and horizontal annular plate are installed between the layers; vertical angle steel is installed on outer wall of the cofferdam, and inner and outer walls are connected by the bulkhead plate to form a whole; the inner wall is sealed, and the outer wall is pored and connected with sea water.

The master beam of the steel cofferdam adopts H400 steel, slave beam adopts H175 steel, and bottom plate adopts 6mm steel plate. In order to increase rigidity of bottom plate, two girders are placed parallel to the long edge of steel cofferdam and one girder is placed parallel to the short edge. Meanwhile, in order to resist the horizontal force generated during hoisting and water pumping, horizontal braces (adopts Φ1000×10 steel pipes) are placed at the longitudinal and transverse directions of the top opening of steel cofferdam. In order to satisfy float transportation requirements, all the wave elimination holes within 4 meters area above the bottom opening of the steel cofferdam are sealed to form a close structure.

During the construction, it is finally determined to seal all the wave elimination holes within the 4 meters area below the collisionproof structure, meanwhile, the wall is divided into 8 pressurized cabins, so that even in the case of leakage of two of them, the cofferdam will still float on the water. See Fig. 4 for basic structure of the collisionproof structure.

Parameters of Loads. Refer to relevant standards for water flow force, wind load and wave force of collisionproof steel cofferdam, and the wave force and water flow force of the piles.

Calculation of Structure Design of Steel Cofferdam. The structure design and calculation of the collisionproof steel cofferdam adopt finite element program ANSYS to simulate any adverse load conditions of the cofferdam in different stages of the construction. The calculation of the cofferdam can be divided into 6 working conditions.

Working Condition 1 – Calculation of Load on Cofferdam during Launching into Water. According to the calculation of partial structure strength during launching of the cofferdam, the reaction forces at four outer supports are all 3200kN, while the reaction forces at four inner supports are all 520kN.

Working Condition 2 – Calculation of Load on Cofferdam during Float Transportation. After launching and floating up, tow the cofferdam with a tug to the construction site. According to Archimedes law, the buoyancy F=17334kN; during towing, the short edge of the cofferdam is facing

the water, and in case of collision, the two cabins there are easy to suffer water intrusion; the buoyancy of the two cabins is F=2370kN; the remaining buoyancy F_r=1733.4-237=1496.4kN > 1430kN. Therefore, even if the two cabins at the short edge of the cofferdam are suffered from water intrusion, the cofferdam will still float on water.

Main Calculation Results of Working Conditions 3 – 6. Working conditions from 3 to 6 are as described as follows: 3 – calculation of load on cofferdam during hoisting (see Fig. 5), 4 – structural strength of cofferdam when only two rows of rods are installed around and at center, 5 – structural strength of cofferdam when all rods are installed in place and the walls are fastened, 6 – structural strength of cofferdam when 2m thick concrete is casted on bottom plate for sealing purpose. They are the main construction phases. The calculation model is shown in the following figure and the main calculating results are shown in the below Table 1, it can be seen that the max. stress of the cofferdam is 258MPa, which is within the safety range; the max. vertical distortion of the cofferdam is 93mm, and the max. vertical distortion of the steel casing is 101mm. Stresses of other supporting structures such as the lifting lug all satisfy the requirements.

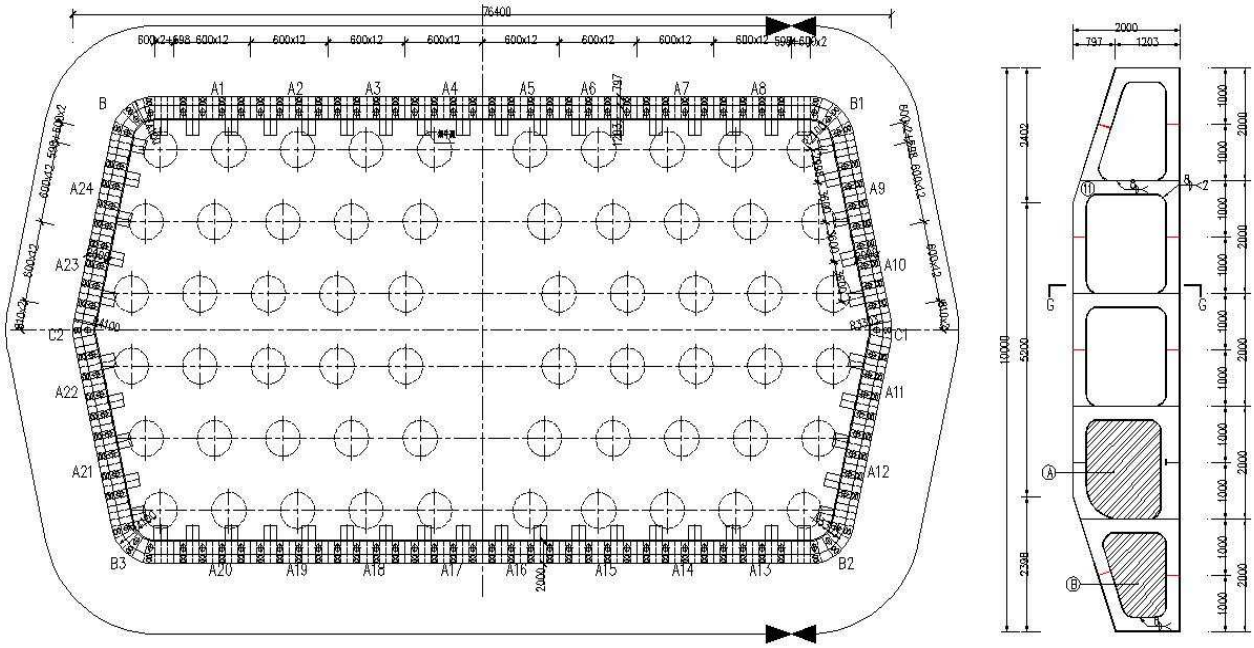


Fig. 4 Basic structure of the collisionproof structure

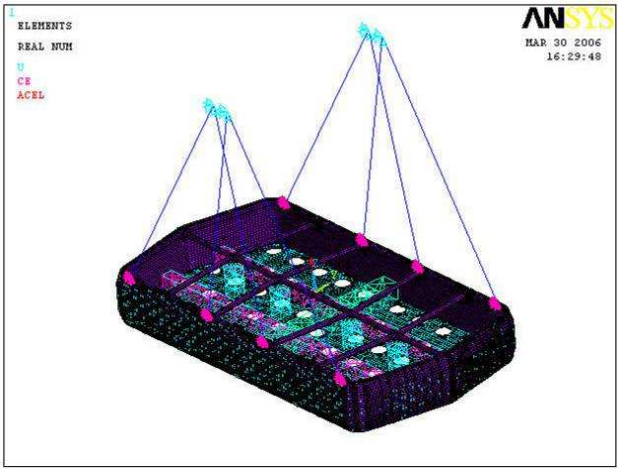


Fig. 5 Calculation model

Key Techniques for Construction of Collisionproof Steel Cofferdam

Overall Construction Technique. At present, the common construction method for ultra-large steel cofferdams is: after completion of the boring and pile testing project, build the assembling platform on the boring platform, then assemble the cofferdam on the platform, and finally install the

cofferdam in place with the floating crane or lifting jack after assembling; or alternatively, in order to reduce the construction time, assemble the cofferdam on a large barge at the site, then install the cofferdam in place with the large floating crane after assembling. The collision proof steel cofferdams for the main piers of Shanghai Yangtze River Bridge are manufactured and launched in the factory and towed to the construction site with a tug, and then installed in pace with the floating crane at the site.

Manufacturing of Cofferdam. Manufacturing of the cofferdam includes manufacturing of collision proof walls, bottom plate, girders, cross arms and rods. The collision proof walls are divided into 30 sections (including 24 standard sections, 4 corner arc sections and 2 pointed circular arc sections). The process of manufacturing sections is: support building –material preparation –unit plate welding –section assembling – welding – sand blasting and rust removing – coating.

Table 1 Calculation results of cofferdam under working condition 3 to 6

S/N	Type	Location	Working condition 3	Working condition 4	Working condition 5	Working condition 6
			Cofferdam hoisting and installing process	Only two rows of rods are installed around and at center	All rods are installed in pace	2m thick concrete is casted on bottom plate
1	Stress [MPa]	Bottom plate panel	62.9	101	189	-211
2	Stress [MPa]	Bottom plate master beam	67.8	-185	-239	-184
3	Stress [MPa]	Bottom plate slave beam	-45.9	-173	-148	-191
4	Stress [MPa]	Master girder	-83.4	23.8	-179	-33.6
5	Stress [MPa]	Slave girder	-135	-88.1	-160	-49
6	Stress [MPa]	Girder pole	18	-96.2	-107	-70
7	Stress [MPa]	Steel pipe support	102	56.5	165	55.3
8	Max. vertical distortion of cofferdam [mm]	\	81.2	90.9	93.3	16
9	Max. vertical distortion of casing [mm]	\	\	101	12.3	11.4

Launch of Cofferdam. Upon completion of manufacturing of the cofferdam on the platform, apply paraffin on the slide track before launching, and hold the cofferdam with two hoists at both sides of the platform, then remove the support under the bottom plate and wall of the cofferdam and drill quick piles, so that all the loads of the cofferdam will be on the slide track; finally cut the steel wire rope at the rear end of the cofferdam to allow it to slide into the water because of gravity.

The slide force of the cofferdam is 830kN, the distance between the head and the center of the cofferdam is 1600mm, and two 600kN lifting lugs are welded on the bottom plate, which are connected to the platform via a Φ43 steel cable. 2 pieces of 500kN lubricated lifting jacks are adopted on the slide track.

Transportation of Cofferdam. The cofferdam is transported from the factory to the construction site of Shanghai Yangtze River Bridge between Chongming and Changxing Island, with a geographic distance of about 200km and a shipping distance of more than 240km.

According to the calculation, under working condition 1 (calculation of the effective power of the towing under normal wind speed and flow rate), the towing force of the tug should be no smaller than 16.823/0.36=467.3kN; under working condition 2 (calculation of the effective power of the towing in case of large tide and adverse current), the towing force should be no smaller than 36.64/0.36=1018kN. Through comparison, to tow by three tugs, the rated total towing force is 1335kN ton. In addition, the measures for anti-flood, anti-wind and anti-frog during the transportation are made according to actual conditions.

Installation of Cofferdam. The construction of the pile cap of the two main piers PM61# and PM62# adopts the cofferdam as the structure to keep water out. In order to reduce construction cost, the cofferdam and collisionproof structure designed and manufactured as a combination, namely the collisionproof structure is used as the wall plate of the cofferdam. The plane size of the steel cofferdam is 76.4m (length)×41.4m (width), and the weight is about 14800kN.

Construction Techniques of Bottom Sealing. One-time bottom sealing means to complete the bottom sealing of the cofferdam in one time. This method is usually adopted for small cofferdams. The advantage of one-time bottom sealing is that it allows the bottom plate of the cofferdam to coordinate the distortion and that the number of seam required for the construction is relative less. In addition, it can help reduce use of material, work load and hoisting load.

Flow Chart of construction techniques of cofferdam.

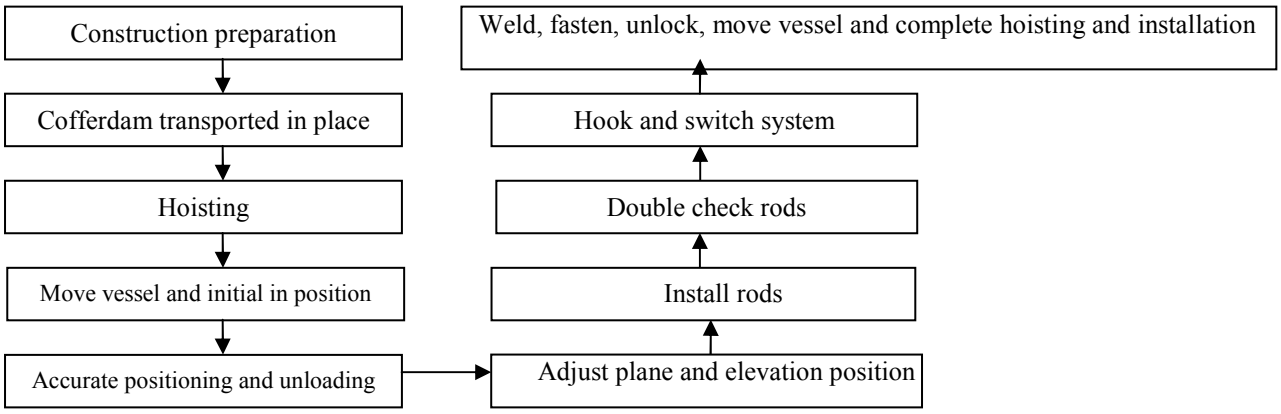


Fig. 6 Flow of Construction Techniques of Cofferdam

Conclusions

The cofferdams of the two main piers of Shanghai Yangtze River Bridge were successfully installed in place on 2nd July and August 3rd 2006. The overall project of the tunnel and bridge was completed and started operation on October 31th 2009, and is in normal operation without suffering any vessel collision. There are several points of innovation in the design and construction of the installation of large steel cofferdam under the complicated working environment of the bridge:

Relevant researches have been made to establish a set of design and construction technique combining the collisionproof structure and the cofferdam, which sets an example for similar projects;

A series of researches have been made in slide track, tail float, instant reaction force, sloping length, etc. of the ultra-large steel cofferdam (76.4m×41.4m×10m and weight 14,800 kN) to form a key construction technique for lunching through slop track of ultra-large steel cofferdam;

The wall of the cofferdam is evenly divided into 8 pressurized cabins and the barge with a size of 76.4m×41.4m×10m and a weight of 1480 ton (equivalent to more than 300,000 kN) is safely and successfully towed to a distance over 200km, which is the first time in China;

The paper provides a good reference for the design and construction of collisionproof cofferdams to avoid bridge-ship collision.

Acknowledgements

The work was supported by the Eleventh Five-Year National Key Technology R&D Program (2012BAG07B03) and Scientific Research of National West Communications Construction (200931800003).

References

[1] O. D. Larsen, Ship Collision with Bridges, Denmark: IABSE, 1993.

[2] Y. Xu, Research on simulation-based pre-control of ship navigation safety in bridge area, Degree for Ph. D, Shanghai Jiaotong University, 2010.

[3] J. Wang, B. Geng, Measurements and Risk Assessment of Probability in Ship-bridge Collision, China Communication Press, Beijing, 2010.

[4] Z. Li, Z. Yang, L. Tang, Construction techniques for steel box cofferdam of main pier of Shanghai Changjiang River bridge, Bridge Construction, 5 (2007) 59-61.

[5] M. Liu, W. Ai, Z. Cheng, Research of navigating capacity in the area nearby Sutong bridge, Journal of Vessels and Ocean Engineering, 4 (2006) 80-82.

[6] J. Jiang, Y. Jin, L. Pan, Techniques and methods in ship-bridge collision avoidance research, Journal of SSSRI, 6 (2008) 23-27.

© (2012) Trans Tech Publications, Switzerland
doi:10.4028/www.scientific.net/AMM.238.684

Study on Thermal and Structural Behavior of a Cable-Stayed Bridge under Potential Tanker Truck Fires

Yongjun Liu[a], Bo Ning[b] and Yu Wang[c]

School of Civil Engineering, Shenyang Jianzhu University, Shenyang 110168, China

[a]liuyongjun66@hotmail.com, [b]lnjznn@126.com, [c]ceywang@sjzu.edu.cn

Keywords: cable-stayed bridge; tanker truck fire; fire resistant time; numerical simulation.

Abstract. Bridges are important parts of traffic systems and need to provide the necessary safety for the traveling public. Fire is one of the most severe hazards that bridges may subject to during their lifetime. In recent years, due to rapid development of transportation systems, as well as increasing transport of hazardous materials, bridge fires have become a concern. Bridge fires caused by crashing of vehicles and burning of gasoline are much more severe than building fires and are characterized by a fast heating rate and a higher peak temperature which could lead to bridge collapse. Bridge failures during a fire can result in the disruption of commerce and services, and most importantly the loss of human life. It has become necessary to consider the potential exposure of bridges to flames from oil or liquefied petroleum gas fires. In this paper, potential fire scenarios relevant for a cable-stayed bridge crossing the Yangtze River are analyzed firstly, then the temperature distribution in key elements and the global structural behavior of the bridge under tanker truck fires is calculated by using general purpose finite element analysis software ANSYS. Numerical simulation results demonstrate that cable-stayed bridge may collapse under some specific fire scenarios and it is necessary to consider fire safety in bridge design.

Introduction

Bridge fires are typically petrol fires generally caused by crashing of vehicles and burning of gasoline, also referred to as hydrocarbon fires or liquid pool fires, which are characterized by fast heating rates and can reach very high temperatures within the first few minutes of fire exposure [1]. In recent years, due to rapid development of transportation systems, as well as increasing transport of hazardous materials, bridge fires may lead to significant economic and public losses. Reference [1] summarizes some of the major bridge fire incidents in the past 15 years. In some cases, bridge fires can damage structural members and even lead to bridge collapse.

On the morning of April 29th 2007, a tanker truck carrying 32.6m^3 of gasoline overturned and burst into flames (see Fig. 1) on the I-80/880 interchange in Oakland, California, while passing under I-580. The high intensity fire resulted in the collapse of two I-580 spans about 22min after the fire started (see Fig. 2). The federal government spent more than $9 million to repair the damage [2].



Fig. 1 Oakland highway bridge fire



Fig. 2 Collapsed highway bridge

On the morning 4:35 of June 26th 2010, a tanker truck carrying 21.0 tons of gasoline overturned and burst into flames (see Fig. 3) on the G15/G324 interchange in Guokeng town, Fujian Province,

China. The tanker truck fire damaged the bridge serverly because the concrete cover of some main giders spalled (see Fig. 4) and steel reinforcements exposed to fire directly and some falled down to ground, as a result, the bridge was demolished.



Fig. 3 Guokeng highway bridge fire



Fig. 4 Damaged Guokeng highway bridge

On the Mezcala cable-stayed bridge in Mexico, a traffic incident on March 17th, 2007, involving two school busses and a truck transporting coconuts overturned (see Fig. 5) and produced a fire at deck level resulting in the failure of one stay cable and limited damage to an adjacent cable. The bridge was immediately closed to traffic and reopened to limited traffic prior to cable replacement. Xupu Bridge is a cable-stayed brige span Huangpu River in Shanghai, China. Since its closing, Xupu Bridge has seen occasional fires in 2008 and 2011. On May 3, 2011, the bridge caught fire due to a chemical tank truck carrying xylene burst into flames (see Fig. 6). Similarly, the bridge was immediately closed to traffic. Would these two cable-stayed bridges have survived the loss of two or three adjacent cables? Would a fire that caused the failure of three adjacent stays result in a progressive collapse event? In this paper, a cable-stayed bridge crossing the Yangtze River is analyzed.



Fig. 5 Truck overturned on Mezcala Bridge



Fig. 6 Closeup of Xupu bridge fire, May 3, 2011

Analyzed Cable-Stayed Bridge

A cable-stayed bridge is a bridge that consists of one or more towers with cables supporting the bridge deck. Compared to other bridge types, the cable-stayed is optimal for spans longer than typically seen in cantilever bridges, and shorter than those typically requiring a suspension bridge. Unlike a normal short-span bridge where the potential impact of fire is rarely considered, it may be necessary to consider the impact of fire on a major cable-stayed bridge for the following reasons: (1) Loss or closure of the bridge for a significant time may lead to unacceptable commercial consequences. (2) It may be impossible to undertake repairs if significant damage occurs.

The cable-stayed bridge considered for the present study spans the Yangtze River (see Fig. 7). The length of the bridge is longer than 1000m with a main span of 360m, and the width of the main span is 30.6m. This paper considers fire safety aspects of the structure such as fire scenarios, temperature distributions in key elements, and global structural behaviors.



Fig. 7 The analyzed cable-stayed bridge

Fire Scenarios

Potential fire scenarios (see Fig. 8) that would have the most adverse effect on structural elements are: (1) A heavy tanker truck catches fire at middle of the main span above bridge deck. (2) A heavy tanker truck catches fire at one end of the bridge above bridge deck. (3)A large oil tanker ship catches fire below bridge deck following a collision. In this paper, first fire scenario is employed.



Fig. 8 Cable-stayed bridge with fires above and below bridge deck

The range of fire severities associated with recorded truck fires is difficult to obtain from statistical records. The actual duration will be dictated by the quantity of fuel and the rate at which it is being consumed. Reference [3] presents a temperature-time curve from FDS numerical simulation of tanker truck fire, in which the tanker size is 24m×1.9m×2.7m. In this paper, it is assumed that a tanker truck fire according to RABT curves (see Fig. 9) occurs above the middle of the cable-stayed bridge, which results in the temperature increase in 6 steel cables and two reinforced concrete main beams.

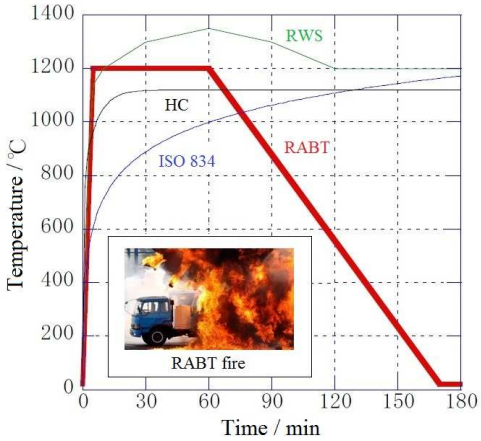


Fig. 9 Tapical temperature-time curves of fires

Thermal Analysis of Key Bridge Elements

The key elements of the cable-stayed bridge structure that could be adversely affected by a fire are the cables, beams, and towers. As steel is extremely strong but very flexible, steel cables are widely used in cable-stayed bridge. Here, we just study temperature distribution in cables and in beams.

Temperature Evolves in Steel Cables. Three crucial thermal material parameters that influence temperature evolution in steel cables are density, specific heat capacity, and heat conductivity respectively. The thermal characteristics adopted for steel cables are those proposed by Lie [4]. All round of the cables are exposed to the tanker truck fire. It is Assumed that heat flow across the fire-exposed surface is caused by both convection and radiation. Convection coefficient is taken as 25(W/(m^2.K)), and resultant emissivity is taken as 0.7. Fig. 10 illustrates the finite element mesh of the cables, and Fig. 11 shows the temperature distribution at specil time calculated by ANSYS.

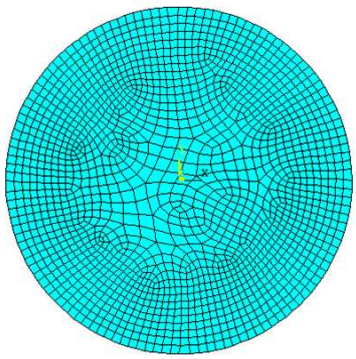
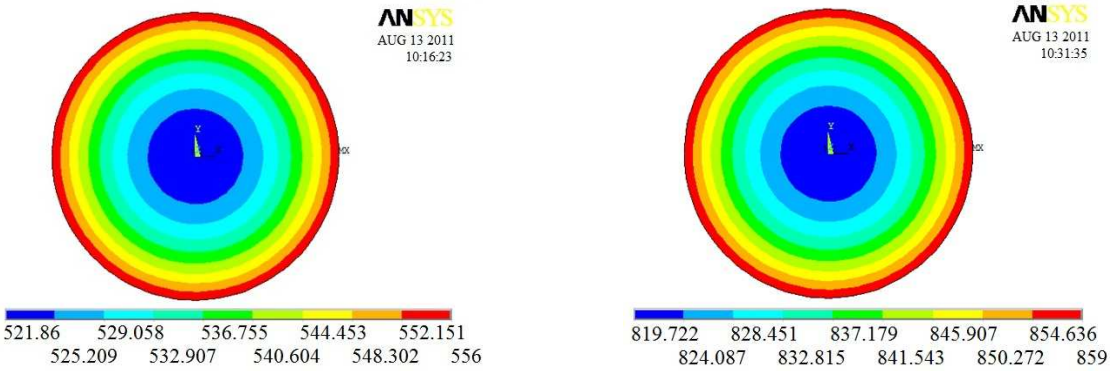


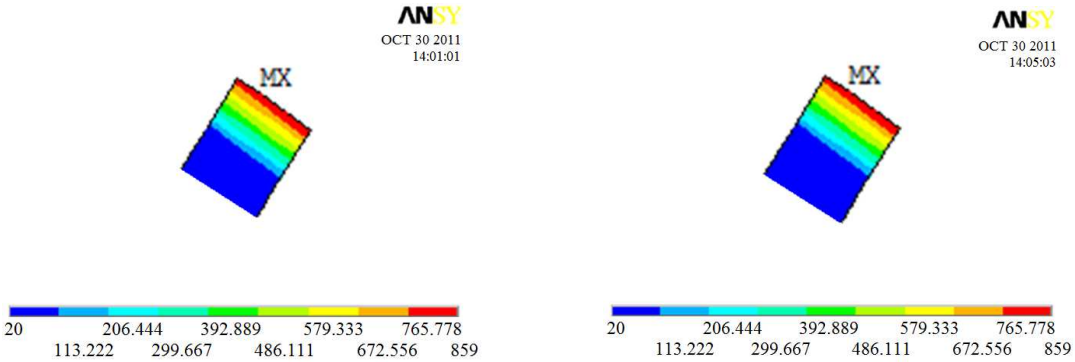
Fig. 10 Finite element mesh of steel cables



(a) Time=150s (b) Time=210s

Fig. 11 Temperature distribution in cross section of steel cables

Temperature Distribution in Main Beams. Like steel cables, the thermal characteristics adopted for reinforced concrete main beams are those proposed by Lie [4]. Convection coefficient is taken as 25(W/(m^2.K)), and resultant emissivity is taken as 0.7. Fig. 12 shows the temperature distribution in part of main beams at specil time calculated by ANSYS.



(a) Time=3000s (b) Time=4500s

Fig. 12 Temperature distribution in hot part of cross section of main beams

Strength Analysis of the Global Bridge

Beam 189 element and Link 10 element in ANSYS are used to model main beams, secondary beams, towers, and cables. The finite element model consisted of approxomatelu 300,000 elements and

approxomately 60,000 nodes (see Fig. 13) . The stress-stain relationships of concrete and steel under high temperature suggested by Lie [4] is adoped in the simulation. The displacements of the cable-stayed bridge under tankertruck fire are given in Fig. 14, Fig. 15 and Fig. 16.

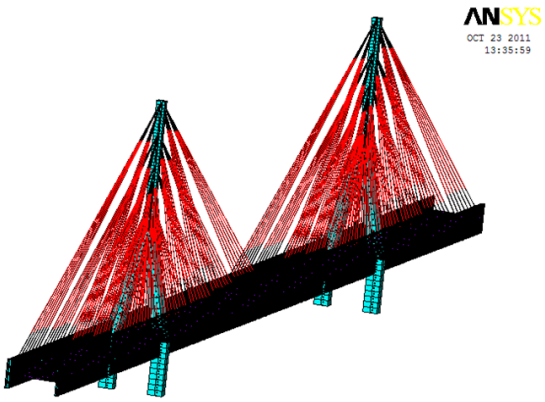


Fig. 13 FEM model of the bridge

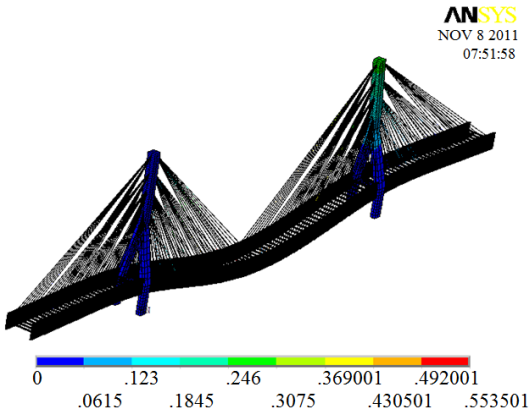


Fig. 14 Vertical displacement at 300s

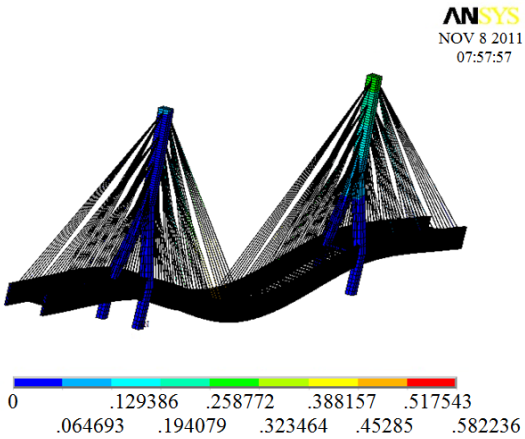


Fig. 15 Vertical displacement at 450s

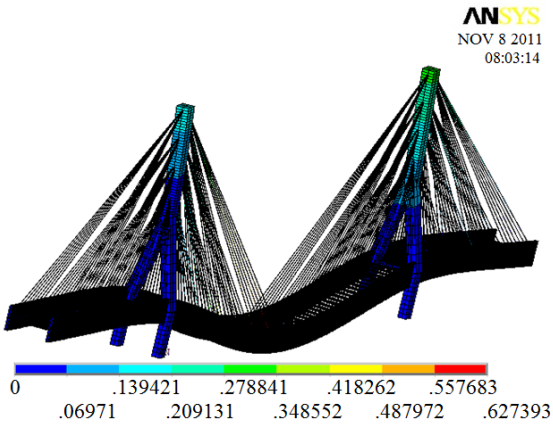


Fig. 16 Vertical displacement at 600s

Conclusions

Tanker truck fires have potential threatern to cable-stayed bridges. Although fire resistant design is not considered in Chinese code, it is necessary to conduct sophisticated fire behavior anlysis for some critical cable-stayed bridges.

Determining bridge fire scenerios is an important step in bridge fire safety design. More experimental and numerical studies are urgently needed to understand the development and spread of tanker truck fire above bridge desk and tanker ship fire under bridge desk.

Acknowledgments

This work is supported by National Key Technology R&D Program in the 12th Five Year Plan of P.R.China under grant 2012BAJ11B02.

References

[1] M. Garlock, I. Paya-Zaforteza, V. Kodur, L. Gu, Engineering Structures, 35 (2012) 89-98.

[2] J. Choi, Ph.D. Dissertation, Georgia Institute of Technology, Atlanta, 2008.

[3] Y. Jia, Thesis for Mater Degree, North University of China, Taiyuan, 2010.

[4] T.T. Lie, B. Celikkol, ACI Material Journal, 88 (1991) 84-91.

© (2012) Trans Tech Publications, Switzerland
doi:10.4028/www.scientific.net/AMM.238.689

Rhombus Cradle System Checking Computation of Jinqinggang Bridge

Shiming Liu [1,a], Zulin Yang[2,b] and Hui Zhao[2,c]

[1]North China University of Water Resources and Electric Power, Zhengzhou 450011, China

[2]Second Design and Research Institute of Water Conservancy and Hydroelectric Power of Hebei Province, Shijiazhuang, China

[a]sokd_0@163.com, [b]yangzhulin@126.com, [c]418058127@qq.com

Keywords: bridge engineering; prestressed concrete box girder; rhombus cradle system; checking computation; probabilistic limit state.

Abstract. In order to be sure the safety of rhombus cradle system during the concretes cantilever cast-in-place construction, the paper makes use of probabilistic limit state method, and carries out the checking computation. According to the rhombus cradle design drawings of the Jinqinggang bridge and the actual load case, the analytical model is founded through the finite element analysis software MIDAS/CIVIL. The results show that stress of all parts of the rhombus cradle system and the concrete local pressure stress is less than the corresponding material design value, and the safety factor of anchor rod tensile stress is less than 2.0 which should be strengthened, and the deformation of the steel moulding plate is less than 20mm.

Introduction

During the cantilever cast-in-place method construction of the bridge, in addition to the No.0 and No.1 piece concretes, concretes are cast on cradle system, rhombus cradle system is a wide-used types of cradle system. The rhombus cradle system is important for the safety of the construction process, and domestic scholars have many papers on it. Ying Xu [1] combines with the rhombus cradle system design and construction of the real project, and uses manual calculation and allowable stress method, and the stress, deformation and construction are discussed. Zhiqiang Wu [2] combines with the actual condition, and uses finite element software and allowable stress method, and carries out the design and calculation of the triangle cradle system, strength and stability are viewed. Y Ji [3] uses finite element analysis software SAP2000, and points out design features, calculation method and structural analysis. However, according to the current bridge construction standard [4] requirements, the current steel structure design code [5] and probabilistic limit state should be used during the calculation of rhombus cradle system.

Combined with the construction monitoring work of Jinqinggang bridge, used probabilistic limit state method and the finite element analysis software MIDAS/CIVIL, the paper checks stress of all parts of the bracket structure, concrete local pressure stress of embedded part,safety factor of anchor rod tensile stress, deformation of the steel moulding plate and overall resistive overturning stability coefficient. It can be as a reference for the similar construction works.

Overview of Project

Jinqinggang bridge is located at No.75 provincial road, and is a prestressed concrete continuous box girder variable cross-section. The total length is 220m with span arrangement 60m+100m+60m and double width, the single width of the bridge is 16.25m. The box girder beam depth of root is 5.8m, and the depth of mid-span and beam end is 2.5m. From No.2 to No.14 piece with the total length 48m concretes are cast on the rhombus cradle system,the maximum concrete volume of one piece is 55.48m^3.

According to the drawings of rhombus cradle system, all materials are used Q235 steel. The rhombus cradle composes of lower horizonal rod, upright rod, backstay rod, upper horizonal rod, front sloping rod, back anchor beam,back anchor bracing, xbracing rod, flat league truss, 6m orbit,outside guide beam, outside sliding beam and inside sliding beam, the materials of the parts are channel steels or joist steels. Longitudinal, transverse and plan view of the bracket structure can be seen from Fig.1 to Fig. 3.

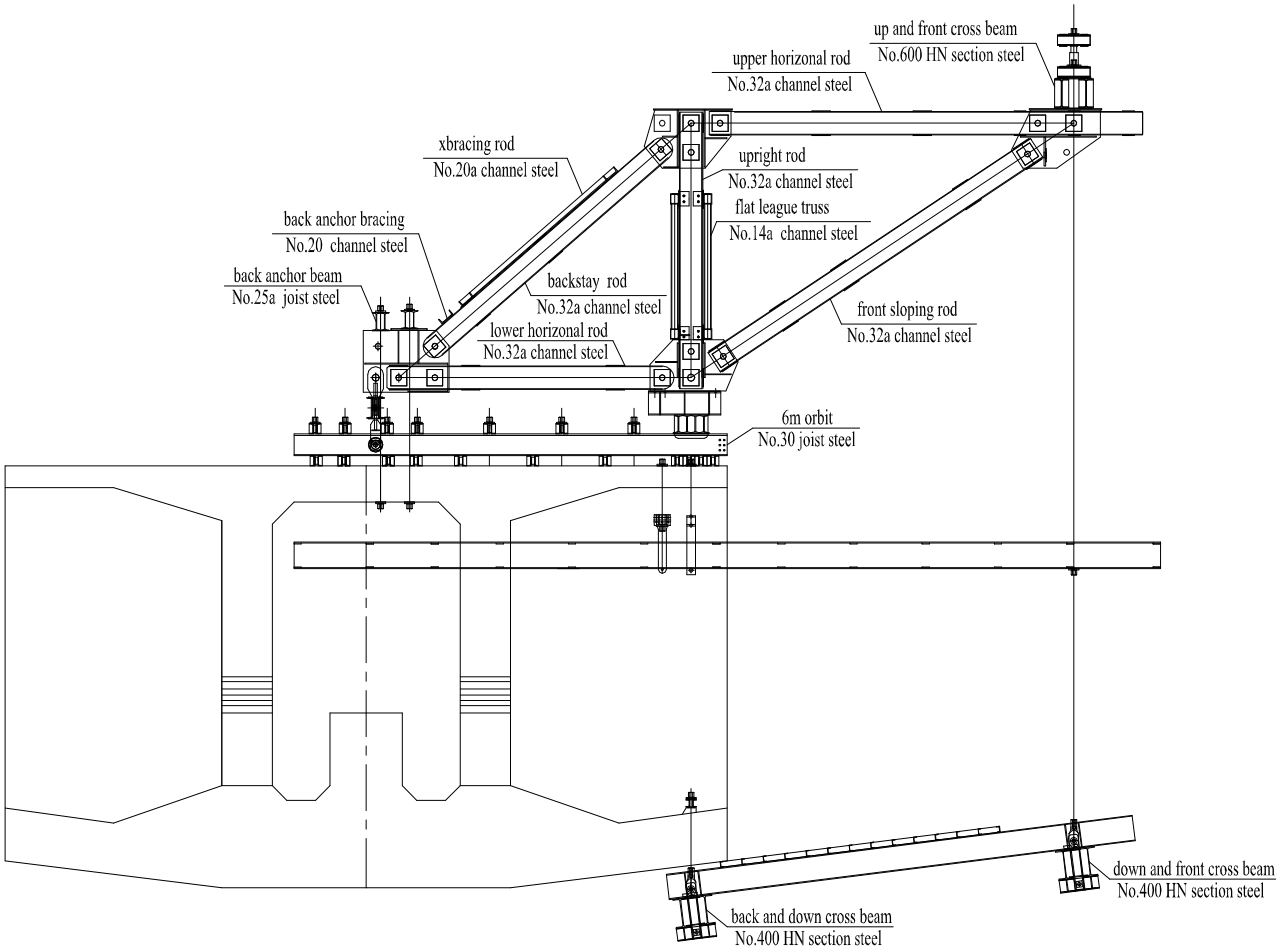


Fig. 1 Longitudinal view of the rhombus cradle

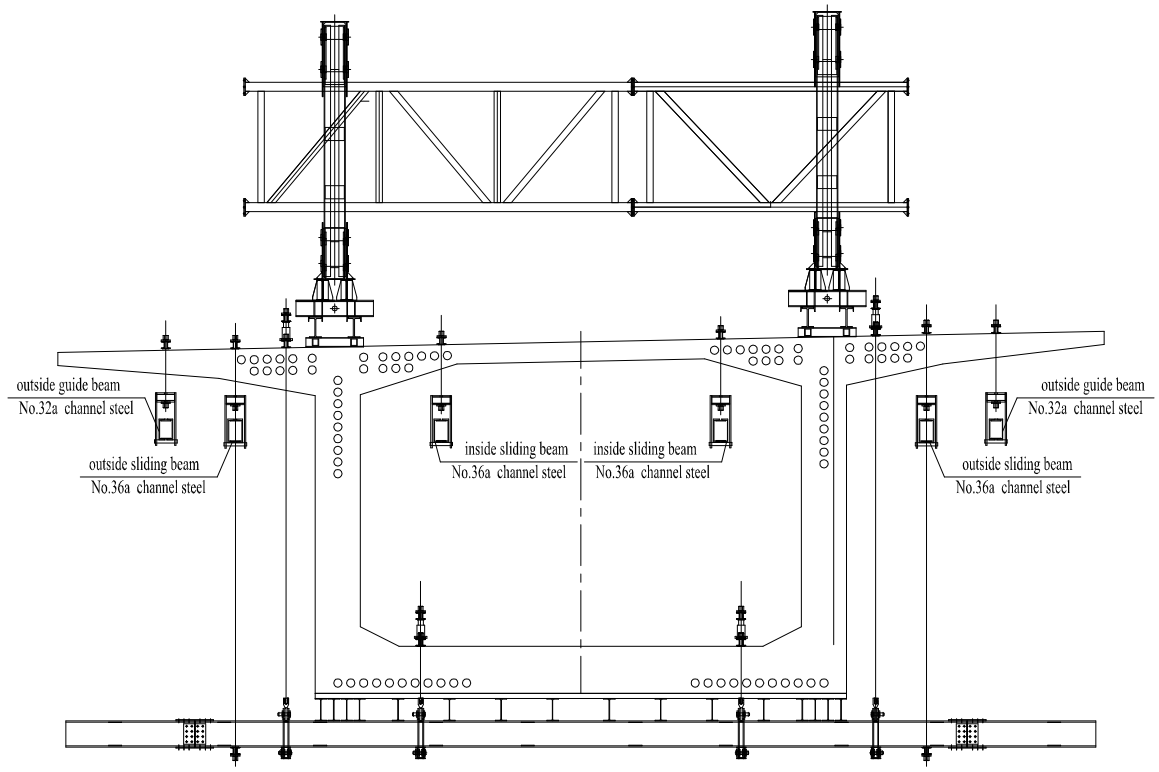


Fig. 2 Transverse view of the rhombus cradle

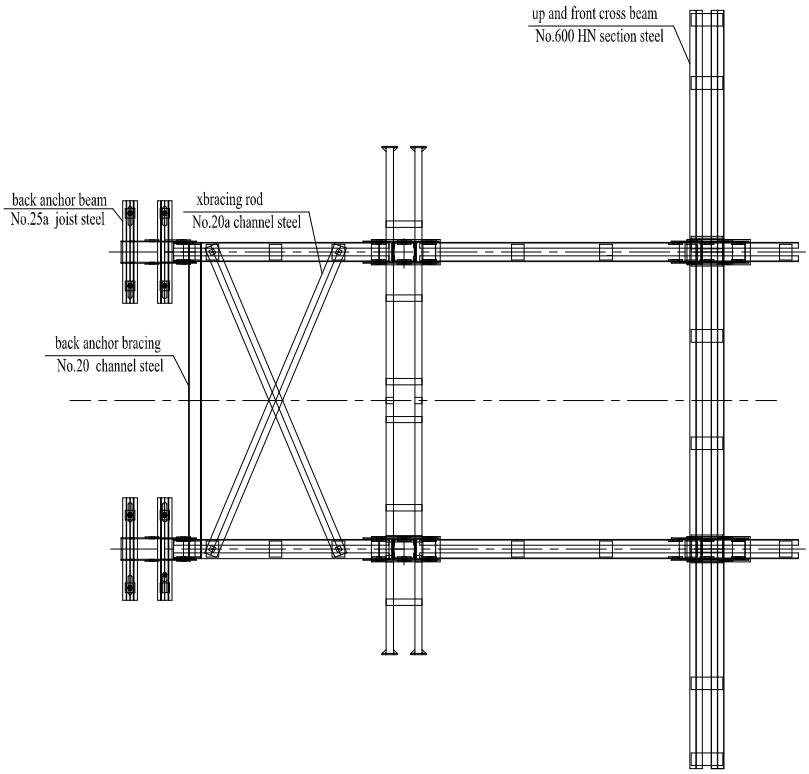


Fig. 3 Plan view of the rhombus cradle

Establishment of Computation Model

According to the structure materials, sizes, loads and boundary conditions, the paper makes use of the software MIDAS/CIVIL, and establishes the three-dimensional finite element model which has a total of 754 nodes, 967 elements. The actual connection and loading case of the various components are respectively modeled by plate and beam element. Computation model of the rhombus cradle system can be seen Fig. 4.

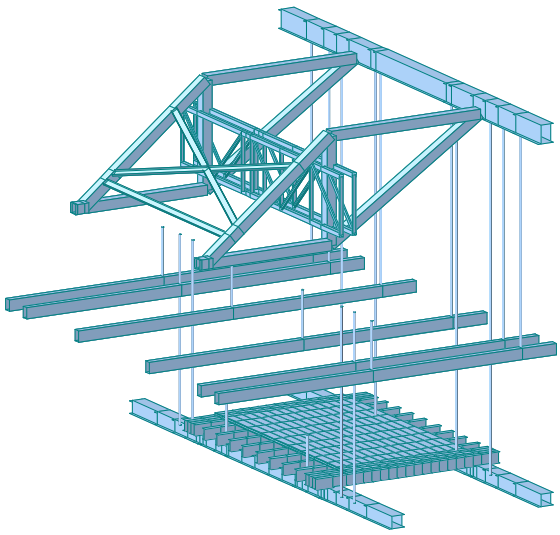


Fig. 4 Computation model of the rhombus cradle

Loads and its Combination

Loads consist of two types which are dead loads and live loads, dead loads refer to the structure body weight, the dead loads are broken into four groups which are flange part, girder web part, top plate part and bottom plate part, live loads refer to the personnel and mechanical weight, the force of concrete vibration.

When calculating the strength, dead loads combination coefficients are 1.2, and live loads combination coefficient are 1.4. When stiffness checking computation, just consider dead loads and its combination coefficients are 1.0.

Stress and Deformation Results

Bending moment and axial force causes extreme stress can be seen Fig. 5. The maximum tensile-stress is 130.68MPa, and the maximum compressive stress is 102.76MPa, which is less than the design value of material strength 215MPa.

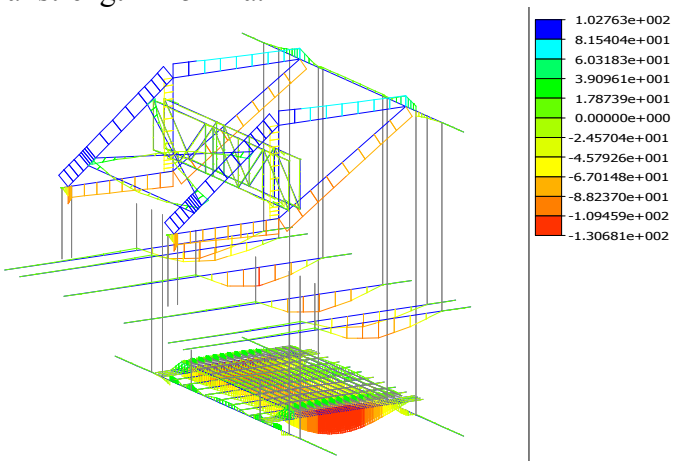


Fig. 5 Extreme stress caused by bending moment and axial force (MPa)

Shearing stress can be seen fig.6. The maximum shearing stress is 82.53MPa, which is less than the design value of material strength 125MPa.

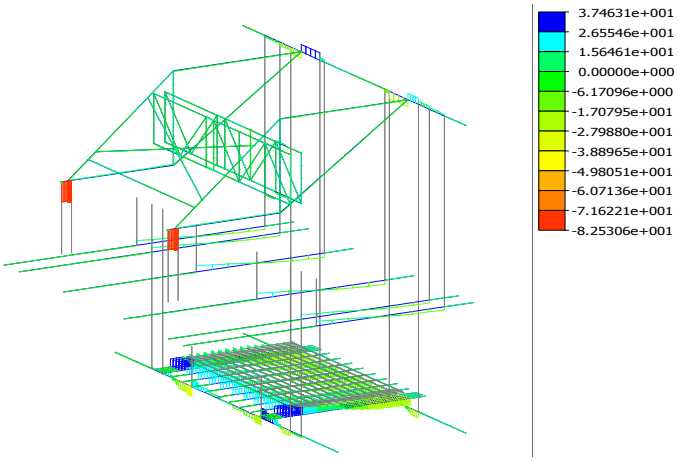


Fig. 6 Shearing stress of bracket structure (MPa)

Deformation of steel moulding plate can be seen fig.7.The maximum deformation is 18.06mm, which is larger than standard allowance value 20mm.

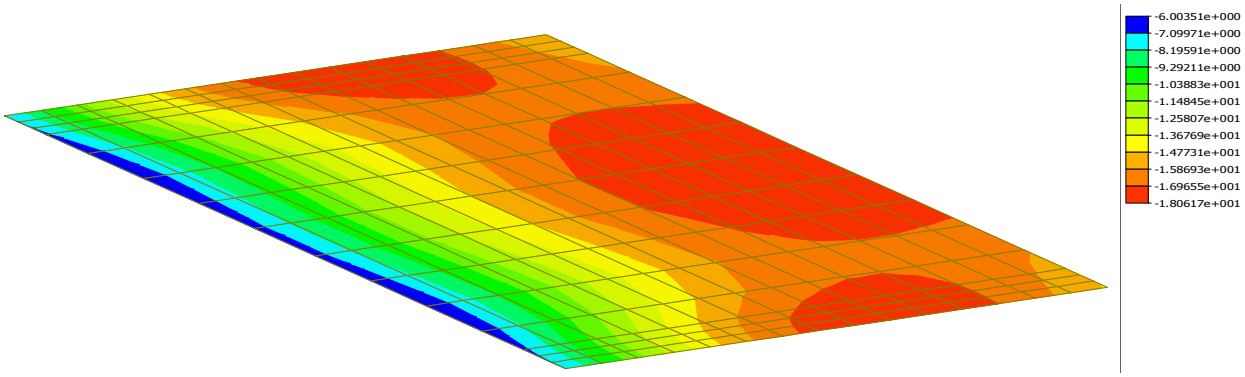


Fig. 7 Deformation of steel moulding plate (mm)

Concrete Local Pressure Stress

The local pressure stress of main beam concrete under buried steel plate should be checked, according the support pressure of the computation model which is 382798.9N and the area of plate which is 140mm by 140mm, the maximum tensile stress is 19.53MPa, which is less than the corresponding concrete standard allowance value 24.40MPa.

Safety Factor of Anchor Rod Tensile Stress

The maximum tensile stress of anchor rod is 476MPa, and the corresponding steel bar tensile stress standard design value is 650MPa, and the safety factor of anchor rod tensile stress is 1.37 which is less than the standard allowance value 2.0.

Conclusions

According to the probabilistic limit state method and the finite element analysis software MIDAS/CIVIL, the model of the bracket structure is founded. The results show that the maximum tensile, pressure and shearing stress of all parts of the rhombus cradle system are less than the corresponding material design value. The concrete local pressure stress is 19.53MPa which is less than the corresponding concrete standard allowance value 22.40MPa. The safety factor of anchor rod tensile stress is 1.37 which is less than 2.0 which should be strengthened. The maximum deformation of steel moulding plate is 18.06mm which is less than the standard allowance value 20mm. The result can be as a reference for the similar construction works.

References

[1] Y. Xu, Y. Guo and F.Song: East China Highway,No.6 (2010), p.10-14.

[2] Z. Wu: Guangdong Building Materials, No.11 (2010), p.63-64.

[3] Y. Ji: The Bridge Construction, No.4 (2007), p.46-48.

[4] JTG/T F50-2011: Technical Specification for Construction of Highway Bridge and Culvert (China Communications Press, Beijing, 2011).

[5] GB 50017-2003: Code for Design of Steel Structures (China Building Industry Press, Beijing, 2003).

© (2012) Trans Tech Publications, Switzerland
doi:10.4028/www.scientific.net/AMM.238.694

Bridge Structure Performance Evaluation Based on Dynamic Load Test

Yan Zeng

North China University of Water Resources and Electric Power, Zhengzhou 450011，China

zy800426@sina.com

Keywords: continuous beam bridge; dynamic load test; detection of bridge; natural vibration frequency; vibration mode.

Abstract. Static load test was carried out on Hengshui interchange ramp bridge of Lin-Chang expressway. The superstructure of the bridge is cast-in-place prestressed concrete continuous box-girder. The actual service state of the bridge is analyzed by the comparison of experimental and calculation results. The study provides the initial technical files and the basis of acceptance, operation, maintenance and management for the bridge.

Introduction

In order to ensure the bridge engineering quality, safety and durability of bridge, bridge detection is the most direct and effective method for completed bridges. The bridge loading test is the most important means of bridge detection. The bridge structure free vibration characteristics and dynamic loads of vehicle and bridge structure with vibration were studied by bridge structure dynamic test study. The testing data is the identification of bridge structure operation condition and bearing the important characteristics. Moving load on road and bridge design is very important; because it is one of the main factors impacting there service life. Dynamic load on deck to produce additional hydrodynamic pressure and dynamic strain, although its mechanism of action is still not clear, but it may accelerate the bridge damage, so the study of the dynamic loads on the bridge design and maintenance are very important.

Project Overview

Lin Chang high speed horizontal water interchange ramp A bridge is total length of 71m, Single radial separation, single bridge width 12.75m. Designed load is road - I. Span arrangement is the 20m+25m+20m. Prestressed concrete single box double chamber of vertical web of continuous box girder is used as the superstructure and Box beam height is 1.5m. The main box beam in the pier top is provided with a thickness of 1.5m Diaphragm beam in side span and 1.0m thickness in end cross beam. For the Stress improvement of box girder, base plate of local was thickened in the pivot near1m section. 5% one-way bridge cross slope was set.

Dynamic Load Test

Bridge dynamic loading test includes two aspects: one is the determination of the bridge structure forced vibration characteristics in the vehicle loads under, such as the impact coefficient, forced vibration, dynamic displacement and dynamic stress; second is the determination of the bridge structure vibration characteristics, such as frequency, mode and damping characteristics. There are two kinds of method which can simulate the structure dynamic excitation from outside, including steady state vibration and pulsation induced vibration. Generally one or a number of parallel loaded train at different speeds in the bridge Current in order to Formation Steady state excitation. On the other hand Pulsation induced vibration is directly outside random vibration excitation.

The bridge inspection mainly includes two aspects: one is the modal test which the vehicle and periodic interference force from other larger (or artificial) aren't Existence and there aren't irregular source cases near bridge site, micro amplitude vibration response caused by such as the wind load, ground pulsation, waters and other random load vibration at the bridge site is Measurement by the

high sensitivity of the vibration pickup. Therefore, we can use the natural pulsation excitation bridge and through the pulse measurement bridge response for anglicizing bridges' inherent modal characteristics and determining the natural frequency of the structure. The other is running test. In the experiment the bridge structure vibration response and vibration attenuation were tested after the Vehicles were through the bridge. In the course of test, load vehicle speed is 5 ~ 25km / h, every Increasing 5km / h as a condition and there are a total of five conditions through bridge structure. According to the dynamic test system for the determination of test section of dynamic deflection and dynamic strain time history curve, we can measure the amplitude response of dynamic strain in driving conditions.

Dynamic Load Test Results of Measurement and Analysis

Basis of Dynamic Performance Evaluation. Structural self-vibration frequency should be greater than the minimum standard limit and maximum amplitude should be less than the corresponding standard limit. Structural damping coefficient damping ratio D_n is expressed as: $D_n=\ln(A_n/A_{n+1})/2\pi$ (of which: A_n Means vibration amplitude of the n second). Half power spectrum bandwidth from the experimental spectrum was calculated the damping ratio of D_n: $D_n=\ln(f_n/f_{n+1})/\Delta f$. f_n Means the n order frequency and Δf was thinking the n order half power bandwidth frequency. The damping ratio is larger which explains the structure of dissipative external energy input of ability is more strong and the faster the vibration attenuation.

The deflection about dynamic increasing factor should be calculated by using the dynamic strain time curve. Dynamic magnification factor expressed as $1+\mu=1+f_d/f_j$. Under different speed, we can obtain the Maximum value of the dynamic magnification coefficient, so we can evaluate bridge dynamic performance.

Modal Test Results. We can measure relevant in response to data through the natural excitation. After the modal identification and theoretical calculation, modal frequencies are shown in Table 1.

Table 1 The frequency of test results

Project	Frequency(Hz)	Ratio
a frequency measurement	7.531	1.18
the first-order frequency theory	6.392	

Vehicle Field Tests. The experiments obtained the dynamic deflection and moving velocity of vertical vibration response of bridge structure cross under five working conditions. To save space, only fifth condition of the test results listed as follows.

Analysis of the Dynamic Load Test Results. From Fig. 1, the measured frequency of the bridge is 7.531, which is bigger than the structure' the first order frequency calculation 6.392. It shows that the stiffness of the structure is Inadequate.

The maximum dynamic magnification coefficient of 1.039 is less than the calculated value basis on general code for design of highway (JTG D60-2004). Dynamic impact coefficient measured value is moderate which show that driving is comparatively smooth and bridge deck smoothness is good.

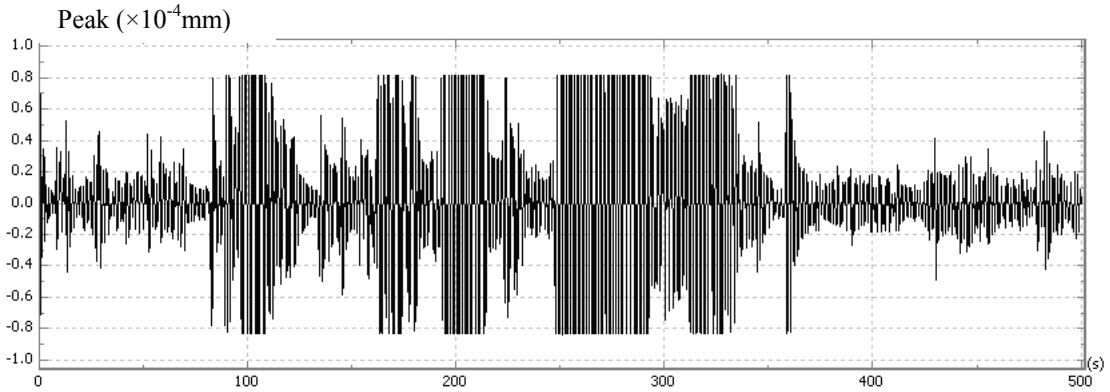


Fig. 1 Whole wave pattern of the bridge

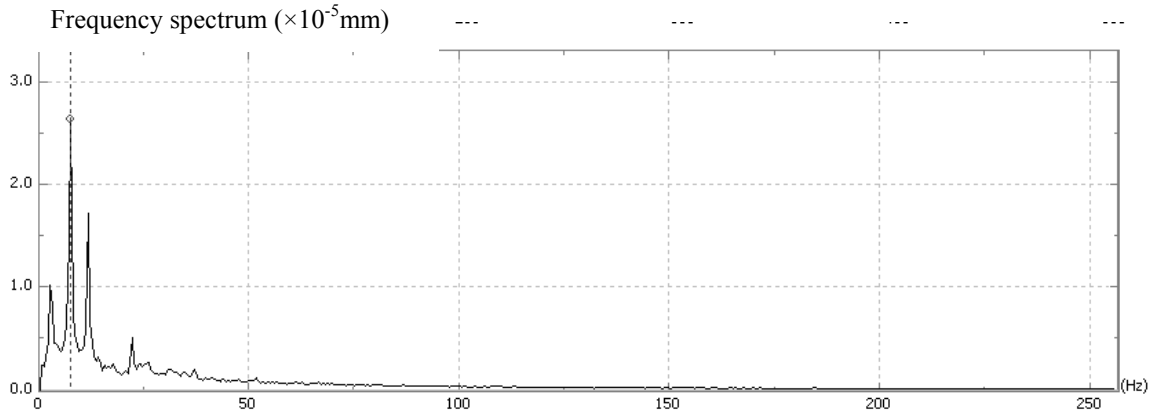


Fig. 2 Frequency spectrum of the bridge

Conclusions

Through the dynamic load test and theoretical analysis, to determine the bearing capacity of the bridge structure to meet the requirements, operating in good condition. Combining the engineering practice, discusses the monitoring of bridge dynamic test content and method, hope for the future to provide some experience for bridge detection.

References

[1] JTGFS0/1-2004, Standard for Quality Inspection and Assessment of Highway Engineering, China Communications Press, Beijing, 2004.

[2] J. Wu, X. Zheng, T. Zhang, Experimental study about dynamic loading of road and bridge engineering, Railway Construction, 3 (2011) 26-28.

[3] B. Fan, Long span prestressed concrete continuous beam bridge detection and evaluation, Gansu Science and Technology, 27 (2011) 116-118.

© (2012) Trans Tech Publications, Switzerland
doi:10.4028/www.scientific.net/AMM.238.697

Construction Technology of Transverse Bonded Structural Steel for Strengthening PPC Hollow Slab Bridge

Jihao Chen[1, a], Lihong Bai [2, b], Shunbo Zhao[1, c],
Xionghuai Yu[1, d] and Cheng Chen[1, e]

[1] North China Institute of Water Recourses and Electric Power, Zhengzhou 450011, China

[2] Henan School of Architectural Engineering, Zhengzhou 450007, China

[a] cjh@ncwu.edu.cn, [b] zz3961@163.com, [c] sbzhao@ncwu.edu.cn,

[d] xionghuai-yu@163.com, [e] 271075314@qq.com

Keywords: PPC hollow slab bridge; construction technology; transverse bonded structural steel; bolt connection.

Abstract. Combined with the actual engineering, this paper presents the construction technology for the transverse bonded structural steel for PPC hollow slab bridge. The steel plate and channel steel were first respectively bonded on the top and bottom of the PPC hollow slab by structural adhesive, and then they were connected by bolt. The transverse connection is formed between hollow slabs to enhance the structural integrity of the bridge. The bolt connection may subject to the structural adhesive fatigue failure due to vehicle loads. Compared with other strengthening method, this method has the advantage of saving investment and construction time.

Introduction

The phenomenon of single beam bearing is one of the most familiar diseases of the PPC hollow slab bridge [1]. The replacements of mesh reinforcement and concrete were always adopted for the deck pavement, the transverse post-tensioning in the bottom of the PPC hollow slab was used to enhance the entirety of bridge [2]. The transverse bonded structural steel is one of the effective ways to strengthening the bridge, but the construction technology of transverse bonded structural steel was scarcely reported. The strength and fatigue resistance of structural adhesive should be ensured in the method, the method should be studied to ensure the strength effect.

The Beijing-Zhuhai freeway located in area under jurisdiction of Xinxiang City is designed as bidirectional four traffic-lanes, and it will be widened to bidirectional eight traffic-lanes after the renovation project to take the increased traffic. Connecting the superstructure of the old and new bridges, and disconnecting the substructure of the old and new bridges is the main connection form of the new-old bridge. But the phenomenon of "single beam bearing" appears in the area of old-new connection after it has been put into service not very long.

With the examined result by the test section, the technical of lateral steel-bonded reinforcement was systematically studied in the paper. And a construction technology for the lateral steel-bonded reinforcement for PPC hollow slab bridge is introduced.

Construction Process

Construction preparation →determine the zone bonding of external steel thin plate onto the bottom surface of the cast-in-plate reinforced concrete slabs →identification of the construction area on the bridge surface →remove the pavement in the construction area and cutting the bars→identification of the reinforcement position on the surface of the slab →drilling →construction lofting of bolt-holes in the channel and steel plate →leveling of slabs on the top and bottom of slab →bonding channel steel and steel plate and installing bolt →connect the bars in the pavement →pouring concrete pavement and casting asphalt concrete pavement →anticorrosion treatment of the channel steel.

Operation Points

Determine the Zone Bonding of External Steel and Lofting. The number and location of the hollow slabs which will be connected in the transverse direction were determined and the zones of bonding the external steel plate onto the bottom surface of the slabs were also determined. And then the distance between the edge of the bonding zone and the ends of the side slab was measured, which is the main control measures for setting out of the bonding steel plate zone on the top of the slab. Considering the convenient for construction, the lengths should be increase by 10cm.

Cut the Deck Paving. Remove the hinge joint concrete while cut the deck paving. It should take care not to damage the slab and hinge joint.

Drilling. After removing the deck paving, determine the position of the bolt holes which should be in the middle of the hinge joint. And then drill the hole with water drilling. The verticality of the hole is very important for the bolt installation and preventing the bars in the slab damage. So perambulation and inspect the verticality and remind the operator to adjust the water drilling in time is very important for the quality control in the reinforcement of bonding steel.



Fig. 1 Drilling

After drilling, recheck the holes location and modify the design bolt holes pitch to ensure the holes in the steel plan are corresponding to the holes in the channel steel. Finally, drill the bolt hole in the steel plan and channel steel with bench drill.

Leveling of Slabs on the Top and Bottom of Slab. After drilling, leveling of the slabs on the top of slab with epoxy mortar, and whose compressive strength is no lower than that of the hollow slab. It is difficult to make level with epoxy mortar on the bottom of the slab, so it can be leveling by the backing plate.

Bonding Channel Steel and Steel Plate.

(1) Surface treatment. The concrete surfaces were removed a 1-2mm layer with angle grinders, and the top of the slabs were leveled by epoxy mortar. PVC duct were used to protect bolt holes. The epoxy mortar surface was covered with films to prevent dust pollution. The steel plate surfaces were polished with angle grinders in order to keep a uniform metal substrate. The prospective bonding faces were washed with acetone and then rinsed with ethanol prior to bonding process. The adhesive materials were poured on the treated surfaces.

(2) Fixed and unloading system. Traffic was diverted around the scene of the reinforcing area. The temporary construction loads should be as small as possible.

The plates were fixed with the load which was stacked along the plate. And it can also be fixed by expansion bolt. The bolts should be tightened before the structural adhesive solidification.

(3) Adhesive preparation. Building structural adhesives are always two-component component. The components A and B were mixed by a mix ratio with purity container and weighing device, and then stir 5-10 minutes until color and luster even.

(4) Gumming and bonding. The adhesive was brushed on the steel plate surface and concrete surface with spatula after adhesive formulated. The adhesive section should form a triangle, in the middle about 3 mm thick, the edge about 1 mm thick. And then bond the steel plate on the concrete surface, fix the plate and press with the pressurized system until the adhesive was extruded form the edge of the steel plate.

(5) Curing. The term open working time is the approximate time after mixing components A and B, depending on the bonding conditions that the adhesive remains fluid and bondable. Fixture time is the approximate time after mixing components A and B required for the adhesive to develop sufficient strength to allow careful movement, unclamping or de-molding of assembled parts.

(6) Test. JGN-G building structural adhesive has good working performance, the plumpness of adhesive can reach 100% under normal operating. The bond performances can be judged by the sound of the steel plates which is tapped by the small hammer. And the bond performances can be test by the phosphor. The load test can be used for the bond performances test of the important structure. If the effective bond area less than 90% in the anchorage zone or 70% in the unanchored zone, remove the steel plate and bond again.

Hoisting of Channel Steel. The channel steels were hoisted in position by hand chain hoist and wire rope as shown in Fig. 2. The numbers and positions of hand chain hoists should be geared to actual conditions and hold people accountable for every hand chain hoists generally and equally rise. The hoisting of the channel steel should be done before the adhesive curing.



Fig. 2 Hoisting and installation of channel steel

Assembling Bolt. Corrosion control of screw should be achieved before assembling by paint epoxy resin.

Pour the Pouring Sealant into the Gap. The gap between the slabs and the gap between the bottom of the slab and the steel plate can be filled by pouring sealant. If the distance between the bottom of the slab and the bonding surface of the channel steel greater than 4mm, the steel plate should be processed as the plate to fill in them.

Labor and Machinery

The labor organization is shown in Table 1. The main machinery and equipment are shown in Table 2.

Table 1 Labor organization

Serial number	Single project	The number of required persons
1	manager	1
2	technician	2
3	welder	1
4	gas cutting worker	1
5	odd-job worker	4

Table 2 Machines equipment

Serial number	Equipment name	Quantity	Application
1	water drilling	2	drill hole in the slab
2	hand chain hoist	4	hoist the channel steel
3	electric welding machine	1	reinforcing bar processing
4	steel bar cutting machine	1	reinforcing bar processing
5	angle grinder	1	polish the steel plate surface

Quality Control

The edge distance or span of the bolts should meet Design Code for the Steel Structures (GB50017-2003) [3], and the design and construction should meet the Specifications for Strengthening Design of Highway Bridges (JTG/T J22-2008) [4].

If no special instructions, the materials which were used in the construction technology should meet the relevant standards and requirements. Several Cautions should be taken into consideration:

(1) The bond performances should be judged by the small hammer tapping or by the phosphor.

(2) The bit should match with the screw, and damage the steel bar during drilling is not allowanced.

(3) Clean up the hole before assembling bolt, and avoid the water accumulate in the hold.

(4) The steel plate should be processed as caul plate when the distance between the bottom of the slab and the bonding surface of the channel steel is great.

Security and Environmental Protection and Measures

The road unblocked and the safety and health of workers should be ensured in expressway construction. The workers should wear a reflective vest or a safety triangle. And the construction safety zone should be formed by the cones and water horse which were placed on the road. The oxygen cylinder was stored separately from the acetylene cylinder. The chemical and building structural adhesives must be stored in an area specially and be charged by special men. The rest of chemical and building structural adhesives should be carried out innocent treatment.

Conclusions

Bending steel strengthen technique was used to solve the single plank of PPC hollow slab bridge. The hole was drilled in the middle of the hinge joint, which can be used for fixing the bolt. The steel plate and channel steel were bonded to top and bottom of PPC hollow slab bridge by structural adhesive respectively, which were connected by bolt. The bolt connection can well solve the structural adhesive fatigue failure and can subject to vehicle loads. Compared with other strengthening method, this method has the advantage of saving investment, simple construction and timesaving.

References

[1] H. Chen, Y. Zhan, Research on strengthening fabricated hollow slab bridge by applying transverse prestress, Journal of Highway and Transportation Research and Development, 10 (2008) 58-62.

[2] L. Jian, J. Li, The Application of Sticking Steel Slab Technology in Bridge Transverse Connection Strengthening Construction, Transportation Science& Technology, 5 (2006) 27-28.

[3] National Standard of the People's Republic of China GB50017-2003, Code for Design of Steel Structures, China Planning Press, Beijing, 2003.

[4] National Standard of the People's Republic of China JTG/T J22-2008, Specifications for Strengthening Design of Highway Bridges, China Communications Press, Beijing, 2008.

© (2012) Trans Tech Publications, Switzerland
doi:10.4028/www.scientific.net/AMM.238.701

Checking Computation for Bracket Structure of Jinqinggang Bridge

Shiming Liu[1 a], Hui Zhao[2 b] and Zulin Yang[2 c]

[1] North China Institute of Water Conservancy and Hydroelectric Power, Zhengzhou, China

[2] The Second Design and Research Institute of Water Conservancy and Hydroelectric Power of Hebei Province, Shijiazhuang, China

[a]sokd_0@163.com, [b]418058127@qq.com, [c]yangzhulin@126.com

Keywords: bridge engineering; prestressed concrete box girder; bracket structure; checking computation; probabilistic limit state.

Abstract. In order to ensure the safety of bracket structure during the cast-in-place construction of No.0 and No.1 piece concretes, this paper makes use of probabilistic limit state method to do the checking computation. According to the design drawings of bracket structure of the Jinqinggang bridge and the actual load case, the analytical model is founded by the finite element analysis software MIDAS/CIVIL. The results show that the stresses of all parts of the bracket structure including the concrete local compressive stress and the tensile stress of embedded steel bar are less than the allowed value of corresponding materials, but the deformation of the steel moulding plate is larger than standard allowance value. The weld joint between upper chord and slanting pole with embedded steel plate satisfies the design requirement.

Introduction

During the cantilever cast-in-place construction of the bridge, the No. 0 and No. 1 piece concretes are always cast on the temporary bracket structure. The bracket structure is important for the safety of the construction process, and domestic scholars have many papers on it. Lin [1] combines with the bracket structure design of the real project, and uses manual calculation and allowable stress method, and the stress and deformation are discussed. Zhang [2] combines with the actual condition, and carries out the design and construction of the bracket structure, and points out the advantages of the structure. Wang et al [3] use the software MIDAS/CIVIL, and study the stress and deformation of the bracket in the standard load, and point out the precautions during the construction. However, according to the requirements of the current bridge construction standard [4] and the current steel structure design code [5], the probabilistic limit state should be used during the calculation of bracket.

Combined with the construction monitoring work of Jinqinggang bridge, using probabilistic limit state method and the finite element analysis software MIDAS/CIVIL, this paper checks the stress of all parts of the bracket structure such as the concrete local compressive stress and the tensile stress of embedded steel bar, and the deformation of the steel moulding plate. It can be as a reference for the similar construction works.

Numerical Model and Load Conditions

Overview of Project. Jinqinggang bridge is located at No.75 provincial road, and is a prestressed concrete continuous box girder variable cross-section. The total length is 220m with span arrangement 60m+100m+60m and double width, the single width of the bridge is 16.25m. The box girder beam depth of root is 5.8m, and the depth of mid-span and beam end is 2.5m. The No.0 and No.1 piece with the total length 10m concretes are cast on the temporary bracket structure, the length of No.0 piece is 4m, and No.1 piece is 3m.

According to the drawings of bracket structure, the type of the bracket structure is triangle, and there are master bracket and times bracket, and all materials are used Q235 steel.The paper only study the master bracket which have five triangle supports along the lateral, and welds with the plate embedded in the pier. The master bracket structure composes of upper chord, slanting pole, vertical bar, big beam transverse distribution, vertical bar, longitudinal beam distribution, small beam transverse distribution and steel moulding plate, the materials of the parts are channel steels or joist steels. Longitudinal and transverse view of the bracket structure can be seen Fig. 1 and Fig. 2.

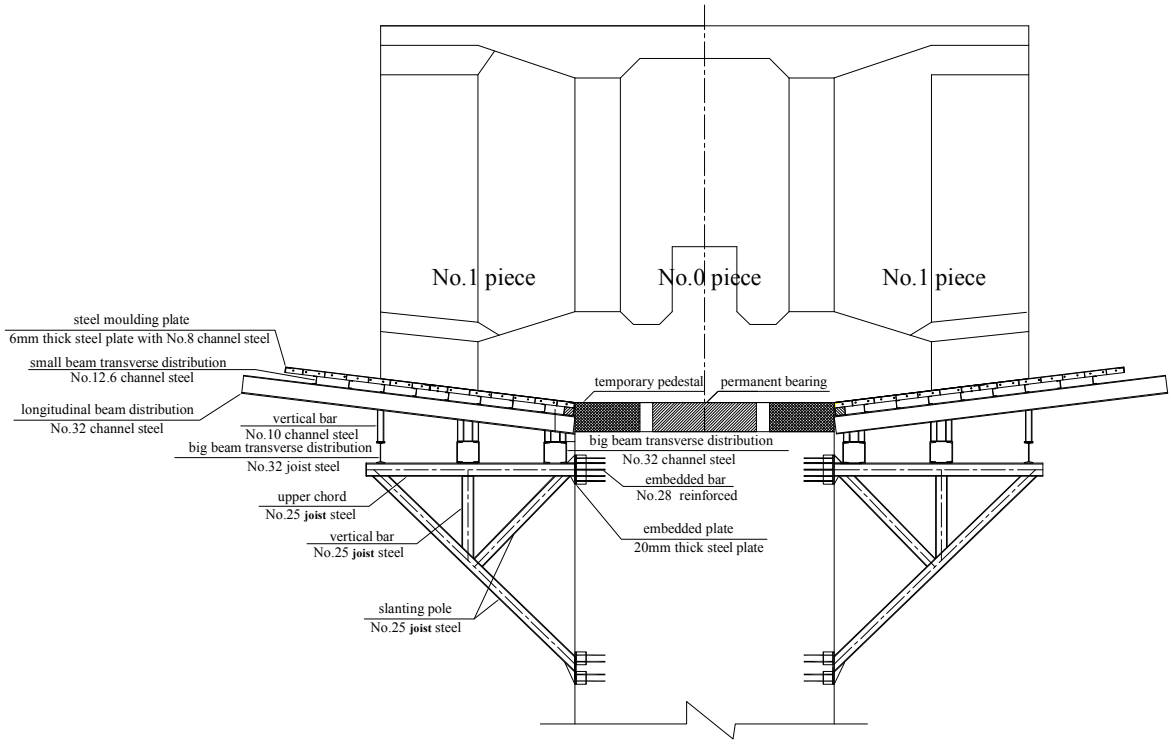


Fig. 1 Longitudinal view of the bracket structure

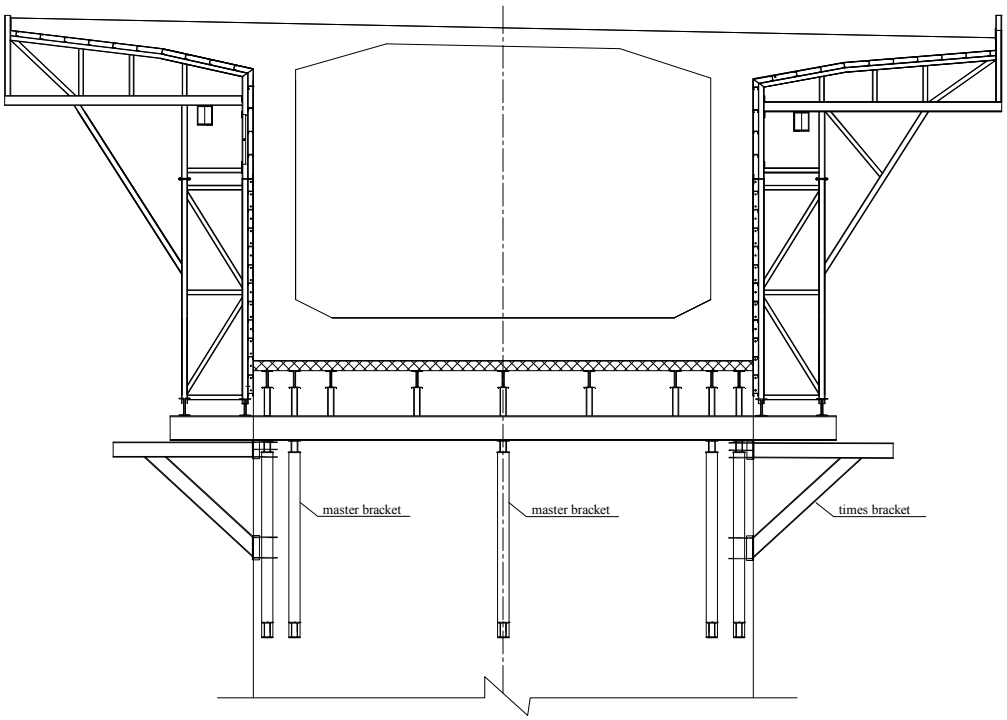


Fig. 2 Transverse view of the bracket structure

Establishment of Computation Model. According to the structure materials, sizes, loads and boundary conditions, the paper makes use of the software MIDAS/CIVIL, and establishes the three-dimensional finite element model which has a total of 1280 nodes, 2195 elements. The actual connection and loading case of the various components are respectively modeled by plate and beam element. Computation model of the bracket structure can be seen Fig. 3.

Loads and its Combination. Loads consist of two types which are dead loads and live loads, dead loads refer to the structure body weight, the dead loads are broken into three groups which are flange part, girder web part and chamber part, live loads refer to the personnel and mechanical weight, the force of concrete vibration.

When calculating the strength, dead loads combination coefficients are 1.2, and live loads combination coefficient are 1.4. When stiffness checking computation, just consider dead loads and its combination coefficients are 1.0.

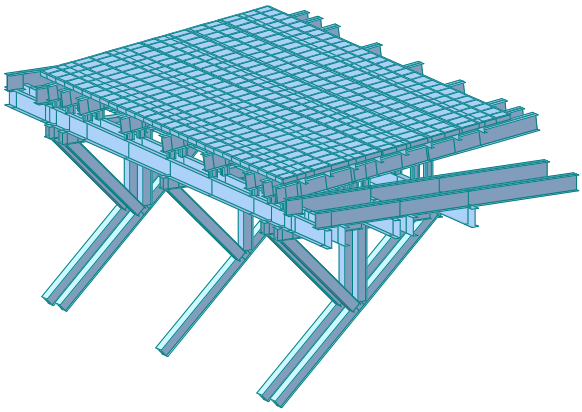


Fig. 3 Computation Model of the bracket structure

Results and Analysis

Stress and Deformation Results. Bending moment and axial force causes extreme stress can be seen Fig. 4. The maximum tensile-stress is 180.41MPa, and the maximum compressive stress is 192.88MPa, which is less than the design value of material strength 215MPa.

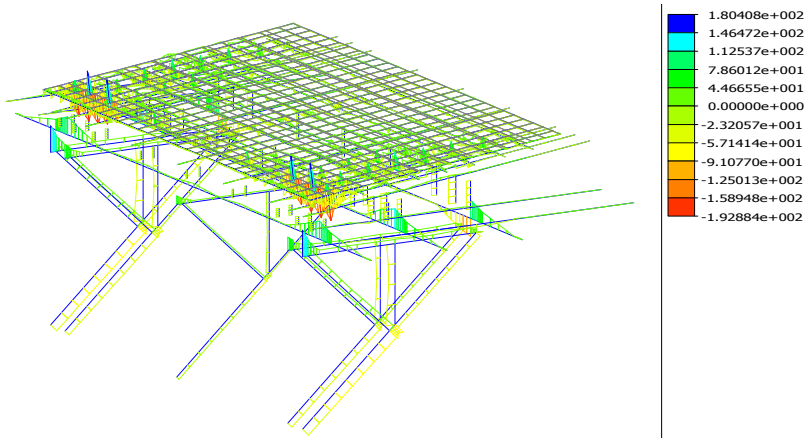


Fig. 4 Extreme Stress Caused by Bending Moment and Axial Force (MPa)

Shearing stress can be seen Fig. 5. The maximum shearing stress is 117.14MPa, which is less than the design value of material strength 125MPa.

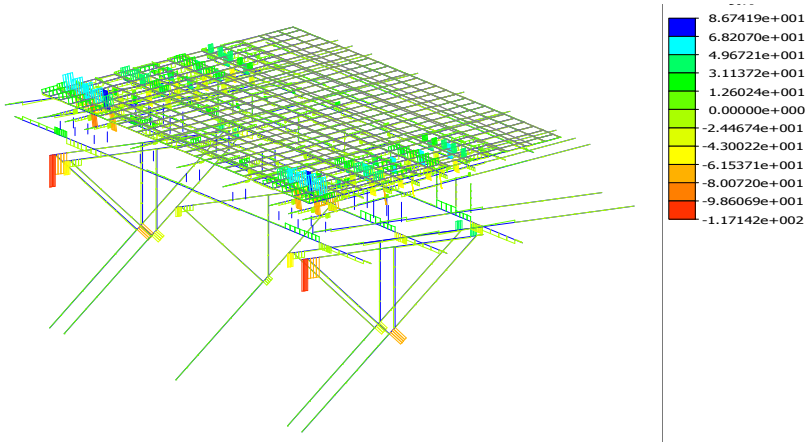


Fig. 5 Shearing Stress of bracket structure (MPa)

Deformation of steel moulding plate can be seen Fig. 6. The maximum deformation is 1.85mm, which is larger than standard allowance value 1.5mm.

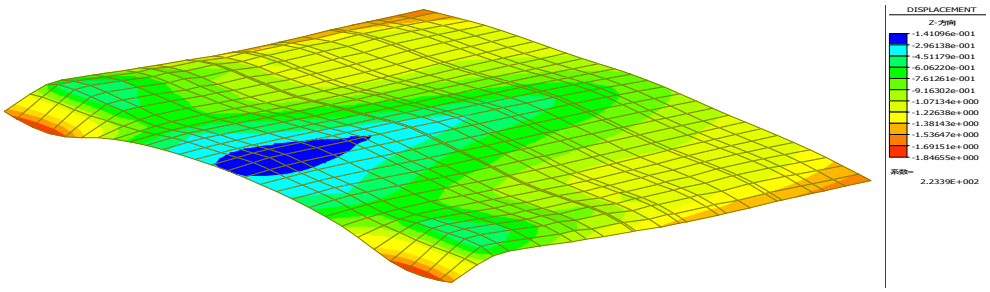


Fig. 6 Deformation of steel moulding plate (mm)

Concrete Local Compressive Stress and Steel Bar Tensile Stress. The upper embedded steel plate is in tension, the tensile stress of bar welded with the plate should be checked, according the support pressure of the computation model and the area of bar, the maximum tensile stress is 44.47MPa, which is less than the corresponding bar standard allowance value 280MPa. The lower buried steel plate in pressure, the local pressure stress of pier body concrete under the plate should be checked, according the support pressure of the computation model and the area of plate, the maximum tensile stress is 2.28MPa, which is less than the corresponding concrete standard allowance value 18.4MPa.

Weld Joint Checking Computation. The upper chord and the sloping pole are connected with buried plate by weld joint, and the upper weld joint is in the worst condition. The checking result can be seen in Table 1, stress vector sum is 143.39MPa, which is less than the standard allowance value 160MPa.

Table 1 Checking computation of weld joint between upper chord and buried plate

Axial force(N)	410738	Weld tensile strength design value(MPa)	160
Shearing force(N)	502978.6	Angle the weld design value increase coefficient values	1.22
Bending moment(N.mm)	101357155	Angle weld section modulus(mm^3)	875927.2
Size of a fillet weld(mm)	12	Total length of weld angle(mm)	1075
Stress caused by bending moment and axial Force(MPa)	132.13	Calculation thickness of angle(mm)	8.4
Shearing stress(MPa)	55.70	Stress vector sum(MPa)	143.39

Conclusions

According to the probabilistic limit state method and the finite element analysis software MIDAS/CIVIL, the model of the bracket structure is founded. The results show that the maximum tensile, pressure and shearing stress of all parts of the bracket structure are less than the corresponding material design value. The concrete local pressure stress is 2.28 which is less than the corresponding material design value 18.4MPa. The steel bar tensile stress of embedded part is 44.47MPa which is less than the corresponding material design value 228MPa. The maximum deformation of steel moulding plate is 1.85mm which is larger than the standard allowance value 1.5mm and should be strengthened. The weld joint stress is 143.39MPa which is less than the standard allowance value 160MPa. The result can be as a reference for the similar construction works.

References

[1] Z. Lin, Urban Roads Bridges & Flood Control, 8 (2010) 62-66.

[2] W. Zhang, Railway Engineering, 3 (2007) 25-26.

[3] J. Wang, Y. Li, X. Tong, Qinghai Transportation Science and Technology, Supp. (2010) 55-57.

[4] JTG/T F50-2011, Technical Specification for Construction of Highway Bridge and Culvert, China Communications Press, Beijing, 2011.

[5] GB 50017-2003, Code for Design of Steel Structures, China Building Industry Press, Beijing, 2003.

© (2012) Trans Tech Publications, Switzerland
doi:10.4028/www.scientific.net/AMM.238.705

Anti-overturning Stability Numerical Analysis of Single Column Bridge

Xianmin Zhang [a] and Bin Dong [b]

Airport College, Civil Aviation University of China, Tianjin, China

[a]cauczxm@126.com, [b]db_200571@126.com

Keywords: single column bridge; overturning; the bearing disengaging; stability.

Abstract. Anti-overturning stability numerical analysis of a concrete single column bridge is introduced in this paper. The bearing capacity of the bridge is calculated under the condition of the bearings disengaging. The major factors making the bridge overturn are analyzed, and the preventive measures are given out. The results provide reference for the design of similar projects and driving demand.

Introduction

Single column bridges are widely used in city ramp bridges and interchange with their advantages, for example the good permeability under the bridge, good appearance, small land occupation and so on. However, with the increase of traffic demand, overload and partial load affect the stability of single column bridge seriously. Bearing disengaging and the whole bridge overturn occurred constantly. A single column pier ramp bridge on the Jin-Jin highway overturned and collapsed in July 2009, which resulted in serious economic losses and social influence. The main reason was 3 overloaded vehicles parked intensively and deviated from the carriageway. Therefore, the calculation of the bearing capacity about single column bridge is very important in order to ensure the bearings safe.

Project Summary and Field Testing

Bridge Layout and Bridge Structure. The interchange ramp bridge is separated to the left and right sides. There are 2 cm settlement joints between two sides. The angle between the ramp center line and the main center line is 75°. Each bridge deck is 0.5+6.75+0.5 meters wide. The upper structure is common reinforced concrete box girder of 17.95+23+23+17.95 meters long. The bottom structure is bored pile foundation. The bridge piers are single column piers and are consolidated with the upper structure. Design load is car over 20 hanging 120. The concrete compressive strength of the box girder is 40 MPa and the piers' compressive strength is 30 MPa.

Measuring-point Arrangement. Four strain sensors are arranged on the east of the pier column 2 (Fig. 1). Two leash sensors are arranged on both sides of the box girder that is located in the upper side of the pier column 2 (Fig. 2).



Fig. 1 Arrangement of strain sensors

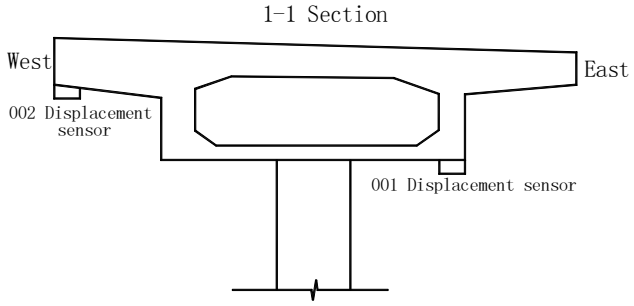


Fig. 2 Arrangement of displacement sensors

Loading and Testing Results Three standard cars of 30 tons are used for loading respectively. The weight of front axle of each car is 7 tons and the rear axle is 23 tons (Fig. 3 and Fig. 4). When increasing a car one time, a series of sensor's readings are recorded. The readings can provide foundation for the computer simulation.



Fig. 3 Actual loading

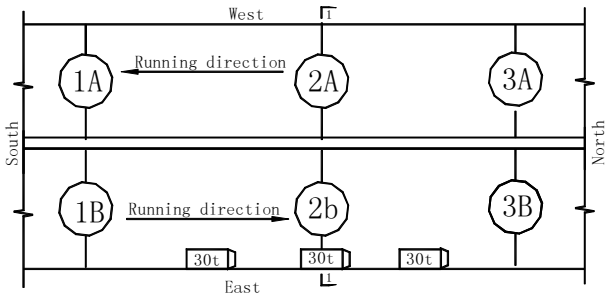


Fig. 4 Location of loading

Comparison between Computer Simulation and Measured Results

A finite element model is created according to the design drawings of the bridge (Fig. 5 and Fig. 6), which is used to simulate the working state of the bridge. The accuracy of the finite element model is judged by the comparative results (Fig. 7 and Fig. 8).

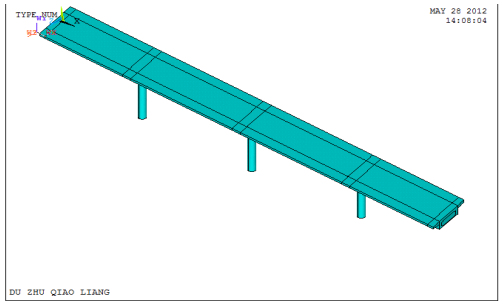


Fig. 5 Finite element model

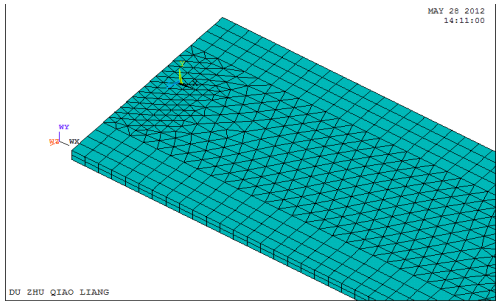


Fig. 6 Finite element model grid

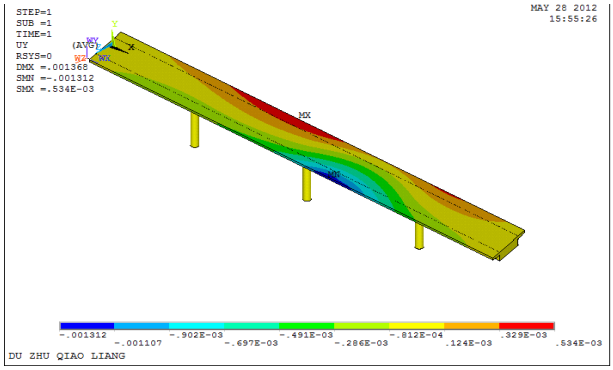


Fig. 7 One 30t car contours of deflection

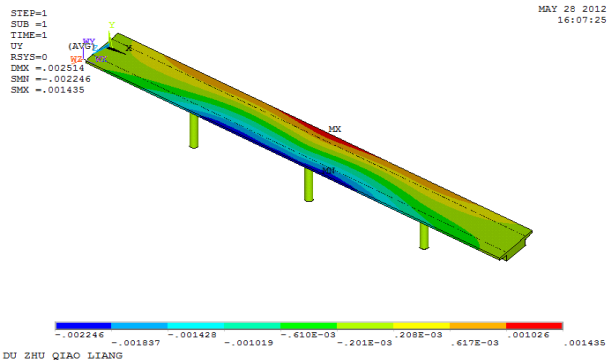


Fig. 8 Three 30t cars contours of deflection

The Displacement Results Comparison. It shows in the Table. 1 that the bridge deck is pressed on the loading side, whose displacement is down, but the displacement of the bridge deck is up on the no-loading side. The displacement increases with the increase of the loading. There are smaller errors between the computer simulation results and the measured results (Table 1 and Table 2). The results above can provide reference for inverting the actual mechanics model of the bridge.

Table 1 Leash sensor measured data (mm)

Numbers	Initial reading	One car	Two cars	Three cars	Total changes	Remarks
One	42.4	41.9	41.4	41	-1.4	Loading side
Two	17.1	17.5	18.0	18.5	1.4	

Table 2 ANSYS numerical simulation data (mm)

Sensor position	One car displacement on Y	Two cars displacement on Y	Three cars displacement on Y
One	-0.4	-0.9	-1.2
Two	0.5	1.0	1.4

The Shape of Analysis Results Compared with the Calculative Results. The shape of analysis results is similar to the calculative results (Fig. 9 and Fig. 10). It shows that the ANSYS finite element model can reflect the real working state of the bridge by the comparative results above (Table 3). The computer model can be used to calculate the bearing capacity of the single column bridge under the condition of its bearings disengaging.

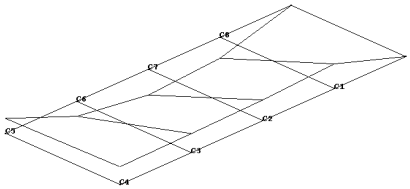


Fig. 9 Analysis results of the first shape

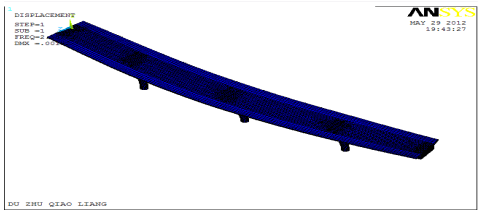


Fig. 10 Calculative results of the first shape

Table 3 The comparison of modes

Orders / Methods	First Mode	Second Mode
Test analysis results	2.73Hz	7.46Hz
Computer calculative result	2.83Hz	7.66Hz

The Bearing Capacity of the Bridge

In order to calculate the bearing capacity of the bridge, we can use the finite element model to load. Different loading methods are applied to the finite element mode. According to the counterforce of the bearing, we can judge whether the bearing is disengaging.

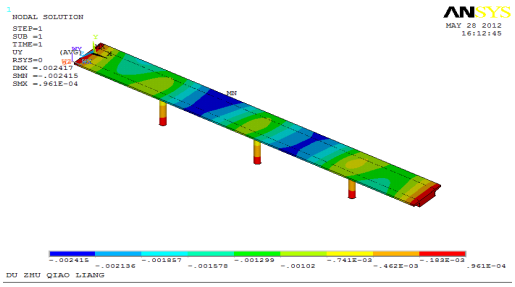


Fig. 11 Gravity contours of deflection

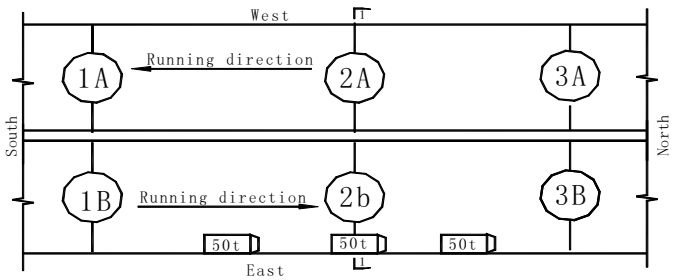


Fig. 12 50t+50t+50t plane loading

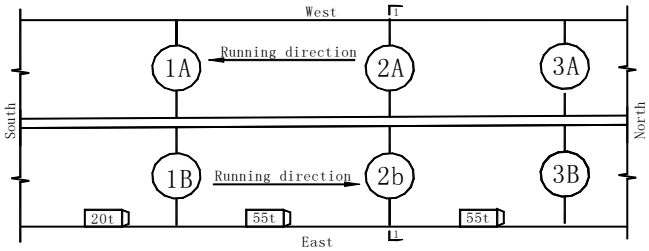


Fig. 13 20t+55t+55t plane loading

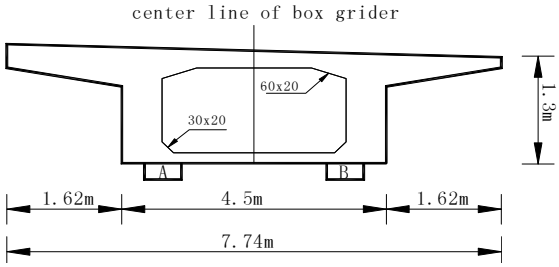


Fig. 14 Bridge bearings

Table 4 Loading and the bearing counterforce

Loading / Counterforce	gravity	90t+gravity	150t+gravity	110t+gravity	130t+gravity
A (kN)	477.5	763.6	932.7	830.0	1045.7
B (kN)	436.5	161.6	-18.4	94.1	-25.7

The Table 4 shows that under the action of gravity, the counterforce of the A bearing and the B bearing are without big differences. The counterforce of the A bearing is bigger than that of the B bearing. That is because the structure of the bridge is inclined plane and the side of A is higher than the side of B. Under the action of 30t+30t+30t and gravity, the counterforce of the A bearing and the B bearing are both changed. When the loads increase to 50t+50t+50t and gravity (refer with Fig. 12), the counter-force of the A bearing is -18.4kN. It shows that the A bearing is disengaging.

The load of 20t+55t+55t and gravity are located in the middle of the bridge span (refer with Fig. 13). The counterforce of the A bearing is -25.7kN. It shows that the A bearing is also disengaging. When the load of 55t+55t and gravity are applied to the bridge, the counterforce of the A bearing is 94.1kN. The bearing A is not disengaging, but its counterforce is small. If accidental load and 55t+55t heavy vehicle run on the bridge at the same time, the bridge is dangerous.

Conclusions

The results of calculation and analysis above indicate that the stability of the bridge is not only related to the load size, but also to the load location. In order to insure the traffic security, the overload should be limited and two 55t heavy vehicles should also be forbidden.

References

[1] Y. Wu, R. Cai, Y. Yang, Analysis of influence factors of structure stability for single-column pier continuous girder bridge, Highway Engineering, 6 (2011) 110-114.

[2] W. Chang, Force analysis of urban bridges with single-column pier, Thesis for Master Degree, Dalian University of Technology, 2009.

[3] X. Lu, J. Jiang, Analysis for concrete structure under complex stress condition with Solid 65 FEA element of ANSYS, Building Structure, 6 (2003) 230-233.

[4] H. Ding, H. Liu, Overturning stability analysis of curved box girder bridge, Journal of Traffic and Transportation Engineering, 3 (2004) 78-81.

[5] B. He, ANSYS Civil Engineering Application Example, third ed., Water Conservancy and Electricity Press, Beijing, 2011.

[6] X. Shang, F. Qiu, H. Zhao, ANSYS Finite Element Analysis Method and Senior Samples Analysis, second ed., Water Conservancy and Electricity Press, Beijing, 2008.

© (2012) Trans Tech Publications, Switzerland
doi:10.4028/www.scientific.net/AMM.238.709

Study on Construction Process of Suspension Bridge Based on a Co-rotational Framework

Bingjian Wang [a], Jianyong Song [b] and Jianming Lu [c]

Research Institute of Highway Ministry of Communication, Beijing 100088, China

[a]bj.wang@rioh.cn, [b]jy.song@rioh.cn, [c]jm.lu@rioh.cn

Keywords: co-rational; corot-truss; cable; geometric nonlinear; suspension bridge.

Abstract. Based on a co-rational (CR) framework, a 2-noded element formulation of 3D truss was presented, which was used for accurately modeling of suspension bridges with large displacements and rotations. The CR framework could consider the out-plane stiffness by the geometric stiffness, which was applicable to the analysis of 3D cable bridges. Using the co-rational truss united with the energy convergence criteria and the Newton with Line Search Algorithm, the nonlinear behavior of 3D cable structural system was simulated conveniently and accurately. Therefore, the traditional truss elements based on elastic modulus modified method and complex catenary elements were avoided. In order to simulate the hanging of girder and the structural system changing during the construction, the elements' killing and activating methods were realized by the modulus modified methods.

Introduction

The structural nonlinear properties of cable supported structures were studied by many researchers. The analysis methods could be conclude as follows: First was the Ernst method [1],in which the geometric nonlinear properties were simulated by modulus modified methods. Then, F. Leonhardt [2] modified the method and improved its accuracy. However, the method could not account for the stiffening effect induced by large displacement. Therefore, the method was only fit for the structures with large stiffness and small displacement, not fit for the strong nonlinear geometric case with large displacement。The second, Jayaraman [3] developed the isoparameter cable element [4], which induced the curve freedom besides the regular displacement freedoms. However, the element stiffness matrix need be formed by numeric integration, which restrict its computational Efficiency。The third was the elastic catenary cable element, which first developed by Irvine HM [5]. Pan [6] and Luo [7] improve the element properties. It had a very complex expression in the shape function, so had difficulty in application, especially, in three dimension analysis. In the last method, the cable structure was meshed into several truss elements to simulate the geometric curve of the structure [8]. In the three dimension case, especially under the large displacement and large rotation, the method can't be used under the regular fixed coordinates, because the uniaxial stress could not be expressed by the displacements in tensors. So the equilibrium conditions for the mid-node was impossible to be satisfied, which would induce the difficulties in numerical solution。In order to overcome the difficulties above, the paper abandoned the regular truss element and took use the corot-Truss elements to simulate the cables. Each corot-Truss element has a corot-coordinate。A coordinate axis was in align with the axial of the bar, would clear the non-axial stress to reach the equilibrium of the space truss, and solve the problem of numerical convergence.

Belytschko and Glaum [9] first invented the concept of "corotational" in the field of finite element method. Horrigmoe and Bergan [10] developed the method of attaching each element with CR frame. Crisfield [11] developed the Formulation of "Consistent CR". He derived the stiffness matrix of CR element by internal forces variable methods. CR formulation had the same reference configuration with UL formulation [12]. The external node forces and the mass matrix were also computed under the total coordinates like the UL. They also had the same iteration. So the CR formulation was improved on the basis of UL formulation. But they were different in two points:

(1) Multiple frames: In UL formulations, the derivative was derived under the Eulerian coordinates. The weak forms were the integrations under the entire current configurations. In contrast, the weak forms of CR were the integrations under the deformed current configurations of each element;

(2) Geometric-Based RBM Separation. The rigid body motion is separated directly from the total element motion using elementary geometric methods. For example in a 2-node bar or beam one axis is defined by the displaced nodes, while for a 3-node triangle two axes are defined by the plane passing through the points.

Corotational Truss Element

In order to derive the formulation of the CR truss element [13], the relationship between the displacement vectors under the corotational coordinates and the global coordinates must be made clear. In order to understand more clearly and program more easily, the stiffness matrix of corotational truss were derived as follows:

The two nodal coordinates of the bar were (X_1, Y_1, Z_1) and (X_2, Y_2, Z_2). Its displacements were(u_1, v_2, w_3) and (u_2, v_2, w_2). The angles between the axial and the global coordinates were $\beta_1\beta_2\beta_3$,L_0 was the initial length. L was the deformed length.

$$L_0=\sqrt{(X_2-X_1)^2-(Y_2-Y_1)^2-(Z_2-Z_1)^2}\,,\ L=\sqrt{(L_1)^2+(L_2)^2+(L_3)^2}\,,$$

$$L_1=(X_2+u_2)-(X_1+u_1)\,,\ L_2=(Y_2+v_2)-(Y_1+v_1)\,,\ L_3=(Z_2+w_2)-(Z_1+w_1)\,,\ c_1=\cos\beta_1=L_1/L\,,\ c_2=\cos\beta_2=L_2/L\,,$$

$$c_3=\cos\beta_3=L_3/L \tag{1}$$

The axial displacements matrix was

$$\delta u_l=\begin{Bmatrix}\cos\beta_1\\ \cos\beta_2\\ \cos\beta_3\end{Bmatrix}^T\begin{Bmatrix}\delta u_2-\delta u_1\\ \delta v_2-\delta v_1\\ \delta w_2-\delta w_1\end{Bmatrix}=-c_1\delta u_1+c_1\delta u_2-c_2\delta v_1+c_2\delta v_2-c_3\delta w_1+c_3\delta w_2 \tag{2}$$

$r=(-c_1,-c_2,-c_3,c_1,c_2,c_3)^T$, $R=rr^T=r\otimes r$. The element of rr^T was $a_{ij}=r_ir_j$. $s\,\delta u=(\delta u_1,\delta v_1,\delta w_1,\delta u_2,\delta v_2,\delta w_2)=\delta L$. Then the internal forces could be the derivatives of potential energy under the global coordinates:

$$P=\frac{\partial U}{\partial u}=\frac{\partial U}{\partial e}\frac{\partial e}{\partial u}=L_0(N_0+EA_0e)\frac{\partial e}{\partial u}=L_0N\frac{\partial e}{\partial L}\frac{\partial L}{\partial u}=L_0N\frac{\partial e}{\partial L}r \tag{3}$$

The global stiffness matrix could be get by the twice derivatives of U：

$$K=\frac{\partial^2U}{\partial u\partial u}=\frac{\partial p}{\partial u}=L_0\frac{\partial N}{\partial u}\frac{\partial e}{\partial L}\frac{\partial L}{\partial u}+L_0N\frac{\partial^2e}{\partial L^2}\frac{\partial L}{\partial u}(\frac{\partial L}{\partial u})^T+L_0N\frac{\partial e}{\partial L}\frac{\partial^2L}{\partial u\partial u}=L_0EA_0\frac{\partial e}{\partial L}\frac{\partial e}{\partial L}\frac{\partial L}{\partial u}(\frac{\partial L}{\partial u})^T+L_0N[\frac{\partial^2e}{\partial L^2}\frac{\partial L}{\partial u}(\frac{\partial L}{\partial u})^T+\frac{\partial e}{\partial L}\frac{\partial^2L}{\partial u\partial u}]$$

$$=L_0EA_0(\frac{\partial e}{\partial L})^2rr^T+L_0N[\frac{\partial^2e}{\partial L^2}rr^T+\frac{\partial e}{\partial L}G]=K_{\mathrm{M}}+K_{\mathrm{G}} \tag{4}$$

In formulation (3), K_{M} was the material stiffness matrix, K_{G} was the geometric stiffness matrix. As to different strains, the stiffness matrix had different expression. In Green-Lagrange strains,

$$e=(L_2-L_0^2)/2L_0^2,p=NL/L_0r,\ K_{\mathrm{M}}=(EA_0L^2/L_0^3)rr^3. \tag{5}$$

The forces at the end were:

$$(f_{iI}^{\mathrm{int}})^T=\int_\Omega\partial N_I/\partial x_j\sigma_{ji}d\Omega\,,(f_{iI}^{\mathrm{int}})^T=\int_\Omega N_{I,X}^TR^TR\sigma R^Td\Omega\ \ \text{(Eq. 6).} \tag{6}$$

The Shape-Finding Algorithm

The shape-finding was the most important work before the structural analysis. The shape-finding algorithm and procedure using CR formulations were the same as others：

(a) First, compute the global stiffness matrix "K". Then update the variables (c, L, L_0, N) according to current values. And the displacements increments were solved under the global coordinate: $du=k^{-1}df$; (b) The nodal displacements were Updated: $u^{n+1}=u^n+du$; (c) The nodal forces were Updated: $F^{n+1}=F+df$; (d) Updating c and L; (e) The axial forces of trusses were updated: $N_i^{n+1}=(A_{ie}/L_{oi})u_{li;}$ (f)The energy error norms were computed: R; (g) If R was less than the tolerance, then the convergence was satisfied; Others, back to step (a).

In the simulation of the hanging erection process, the element birth and death method technologies was used as follows：

1) In the procedure of hanging the beam, all the beam nodal displacement degrees in longitude and transverse were constraint. They would be released after the completion of the construction;

2) The under hanged beams were given very small elastic modulus;

3) The dead load of each hanged beams were simulated by concentrated forces;

4) After the completion of the hanging procedures, all the beams were activated, which was simulated by given them their true elastic modulus.

The solution of the problem involved the strong geometric nonlinear. So the effective solving strategies must be chosen. The most frequently used method was the Newton-Raphson methods. As to the problems with large deformations and rotations, the Newton method with Search algorithm and the convergence criteria of energy error norm would be the most appropriate solution strategies.

Applications

The OpenSees software framework has been developed for simulating the seismic response of structural [14]. It had already imply the truss element based on CR. But the stress updating methods were lack in the program. And the coordinate transforms of the internal forces were also absence. The paper modified and added the above functions based on OpenSees. The three following examples confirmed its feasibilities.

Example 1. A cable with its two end points fixed in three dimensions. The length is 2m. The parameters could be referred as Table 1 and Fig. 1. The displacements under dead loads were computed by modified OpenSees and ANSYS. The results were compared in Table1 and Fig. 2.



Fig 1 Cable model

Table 1 Parameters of cable model

	OPENSEES	ANSYS
Element	coroTruss/Cable	Link10/Elastic
Model	32 elments,33 nodes	
Elastic modulus	212E9,initial strain :0.0025345	
Load	24.89Kg/each node	
Element length	0.0625m	
Element area	0.01232e-4m^2	
Max deformation	0.2230m	0.2211m

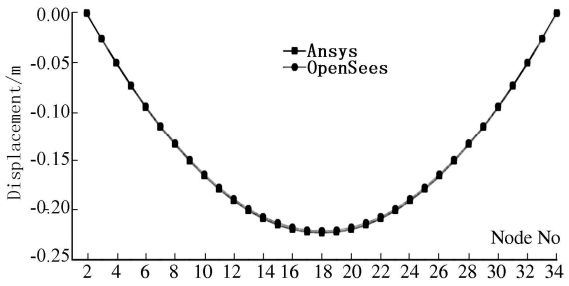


Fig. 2 Displacements comparison of cable model

When the nodal loads were changed to 0.02489kg and the initial strains changed to 0.0000025345 (0.54MPa), the max displacements in middle nodes were 0.0225m (ANSYS) and 0.0223m (OpenSees).

Example 2. A suspension bridge with three towers and two spans under construction was taken as the examples (Fig 3a, b). The two main span lengths were 1080m. The rise-span ratio was 1/9, the transverses width was 35.8m. The shape-finding problems were analyzed by the problems of Midas and OpenSees. The results were in Table 2.

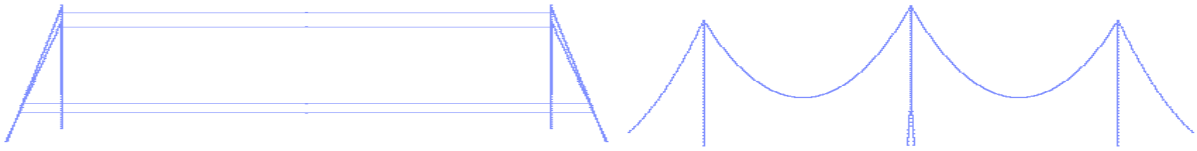


Fig. 3 (a) Side view of model (b) Front view of model

Table 2 Analysis Result of initial status of suspension bridge

	Midas	OpenSees
Longitude forces (N)	3.5928E+7	3.513E+7
Longitude displacement in top of side tower(m)	1.26	1.20
Vertical Coordinate in mid span (m)	80	79

Example 3. The main beam hanging process were simulated based on shape-find results of the main cables in example 2. The hanging procedures were as follows: The middle main beams were hang firstly, then the two side beams next to the middle. There were totally 17 hanging steps in the procedures, and four joint section constructions. The simulations results of constructions after hanging were shown in Fig. 4 to Fig. 6. After the completion of the System transformation, the accumulate displacement were shown in Fig. 7 and Fig. 8.

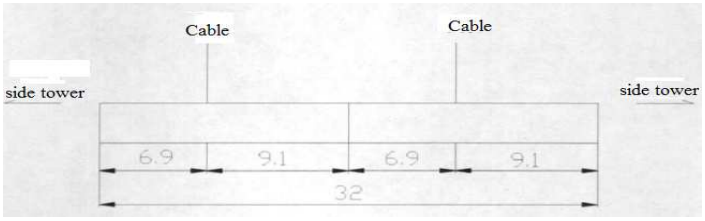


Fig. 4 Segmental model of the girder at the mid-span

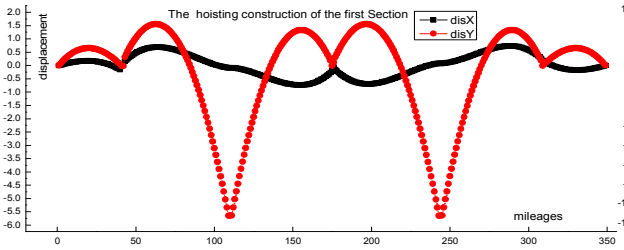


Fig. 5 Displacement of main cable under hanging

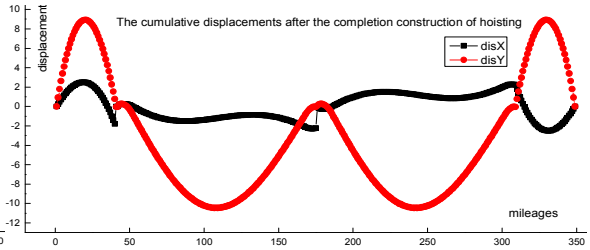


Fig. 6 Cumulative displacement after the completion of hanging

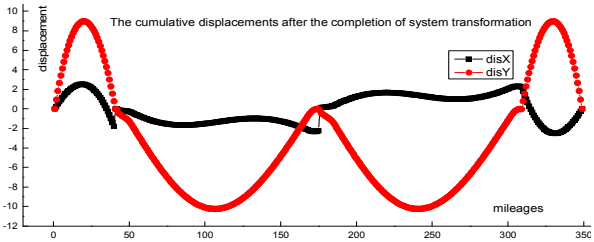


Fig. 7 Cumulative displacements of main cable

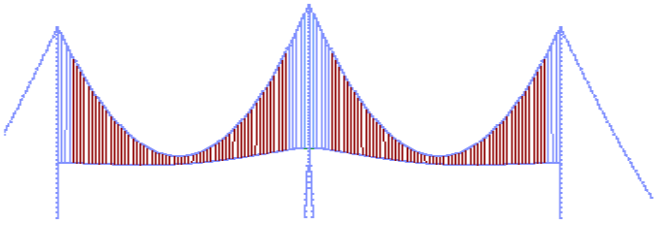


Fig. 8 Cumulative displacements of the bridges

Conclusions

The CR formulations and its application methods were introduced. The methods were most feasible for the simulation the structural behaviors of cable-support structures which with strong nonlinear.

A simulation method in three dimensions is suggested for long span suspension bridges under construction, which is easily implied by programming. When in simulating the erection process of suspension bridges, not only the empty shape could be found easily and accurately, but also the hanging step could be simulated accurately and stably.

Further research and application of CR could be focus on the simulation of the main beams and towers by corotational shell and plates besides the CR cables. And these would be expected to improve the accuracy of the analysis of the cable supported systems.

References

[1] W. C. Knudson, Static and dynamic analysis of cable netstructures, University of California, Berkely, California, 1971.

[2] F. Leonhardt, W. Zellner, Past, present and future of cable-stayed bridges, in: Proceedings of the Seminar of Cable-stayed Bridges, Recent Developments and Their Future, Yokohama, Japan: 1991, pp. 1-33.

[3] H. B. Jayaraman, W. C. Knudson, A curved element for the analysis of cable structures, Computer & Structures, 14 (1981) 325-244.

[4] H. J. Ernst, Der E-modul von seilenunter beruksichtigungdes durchhanges, Der Bauingenieur, 40 (1965) 52-55.

[5] H. M. Irvine, Cable Structures, The MIT Press, London, 1981.

[6] Y. Pan, G. Du, L. Fan, A fine calculation of the geometry and internal force of suspension-bridge under dead load, Journal of China Highway and Transport, 13 (2000) 10-15.

[7] X. Luo, R. Xiao, H. Xiang, Cable element based on exact analytical expressions, Journal of Tongji University, 33 (2005) 445-450.

[8] X. Yuan and S. Dong, A two-node curved cable element for nonlinear analysis, 16 (1999) 59-64.

[9] T. Belytschko, L.W. Glaum, Application of higher order corotational stretch theories to nonlinear finite element analysis, Computers and Structures, 10 (1979) 175-182.

[10]P. G. Bergan, G. Horrigmoe, B. Krakeland, T. H. Soreide, Solution techniques for nonlinear finite element problems, International Journal for Numerical Methods in Engineering, 12 (1978) 1677-1696.

[11]M. A. Crisfield, Nonlinear Finite Element Analysis of Solids and Structures, John Wiley & Sons, 1996.

[12]Z. Chen, Q. Zeng, Q. Yan, A UL formulation for internal force analysis of special frame structures with large displacement, Journal of China Civil Engineering, 25 (1992) 34-44.

[13]C. A. Felippa, The CR Formulation: Space Bar, Online Web Document, 2006.

[1 4]S. Mazzoni, Open System for Earthquake Engineering Simulation (OpenSees), User command-language manual, Pacific Earthquake Engineering Research, CA, 2006.

© (2012) Trans Tech Publications, Switzerland
doi:10.4028/www.scientific.net/AMM.238.714

Design of Mitigation Damper with Support Flexibility for Stay Cable under Bridge Deck Excitation

Shuai Luo[1, a], Quansheng Yan[1, b] and Hongjun Liu[2, c]

[1]School of Civil Engineering and Transportation, South China University of Technology, Guangzhou 510641, China

[2]Shenzhen Graduate School, Harbin Institute of Technology, Shenzhen 518055, China

[a]200677@gmail.com, [b]cvqshyan@scut.edu.cn, [c]liuhongjun@hit.edu.cn

Keywords: Stay cable; bridge deck vibration; damper; support flexibility; modal damping.

Abstract. This paper studies cable-damper mitigation model due to indirect excitation caused by bridge deck excitation. In the new mitigation model, as a rule of thumb, we considered an attached spring associated in tandem with a damper to simulate the supporter flexibility. The result shows that the interaction between the flexibility of the support in the viscous damper could deeply impact the damper effectiveness, and the external damping should be increased deeply to provide the same non-dimensional modal damping when the inclined angle of cable decreases. The optimum damping coefficient of the non-idealized damper increases when the flexibility of the supporter increases.

Introduction

As engineers around the world continue to extend the spans of cable-stayed bridges, the cable systems in these bridges become lighter, more flexible, and less damped. This extremely low damping inherent in such cables, typically on the order of a fraction of a percent is insufficient to eliminate the vibration caused by the motion of the bridge deck, causing reduced cable and connection life due to fatigue and breakdown of corrosion protection, as well as the risk of losing public confidence in such structures[1, 2]. To overcome cable vibration problems, a common practice is to install mechanical damper to connect the cable to the bridge deck, and a number of control methods have been proposed to mitigate cable vibrations. Li carried out a series of in situ tests to investigate the effectiveness of damper to reduce the vibration of stay cables [3]. Fujino and Hoang analyzed the effects of bending on the modal properties of a stay cable with a transverse damper [4]. The current widely used by researchers in the theoretical model assumed that the damper is fixed outside of the deck, and the non-idealized factors such as support flexibility are neglected in the idealized mitigation analysis model, is not reasonable to consider the bridge deck-cable-damper coupled vibration impact caused by the motion of the bridge deck and viscous damper non-idealized characteristics. In this paper, a new analytical model would be developed in order to investigate the coupling effects among deck-cable-damper and damper non-idealized characteristics, which have thus far been omitted from previous models of indirect excitation of inclined cables.

Equations of Motion

The cable and the concentrated viscous damper are shown in Fig. 1. The length of the cable is L, the damper is located at the distance from the left end. The cable force is T, and the mass per unit length is m. The coefficient of the concentrated damper is denoted c. In the following it is convenient to introduce the complementary length l_2=L-l_1 and the complementary coordinate x_2=L-x_1. Assuming that the tension in the cable is large compared to its weight, and deflections are small, the following partial differential equation is satisfied over each segment of the both cable mathematical models

$$m\frac{\partial^2 y}{\partial t^2} = T\frac{\partial^2 y}{\partial x^2} \tag{1}$$

where θ is the inclined cable angle measured from the horizontal axis; u_k is the cable dynamic displacement component in the y coordinate measured from the static equilibrium position of the cable, k =1,2 indicates the cable segment number shown in Fig. 1.

The partial differential Equation (1) is to be solved with the boundary conditions

$$u(0,t)=0, \quad u(L,t)=0 \tag{2}$$

The transverse displacement of free damped vibrations of the stay cable u_k can be expressed in the form:

$$u_k(x_k,t)=U_k(x_k)e^{i\omega t} \tag{3}$$

where ω is a complex natural eigenfrequency, and U_k is the corresponding complex mode shape. The complex mode shape U_k satisfies the ordinary differential equation

$$\frac{d^2U_k(x_k)}{dx_k^2}=\omega^2\frac{m}{T}U_k(x_k) \tag{4}$$

Continuity of the shape function at the damper installation place requires

$$u_1(l_1,t)=u_2(l_2,t)=\gamma \tag{5}$$

where the amplitude γ is undetermined in a free vibration. Complex wave number β has been introduced as $\beta=\omega\sqrt{m/T}$. Hereby the solution of Eq. (4) takes the form

$$U_k(x_k)=\gamma\frac{\sin(\beta x_k)}{\sin(\beta l_k)} \tag{6}$$

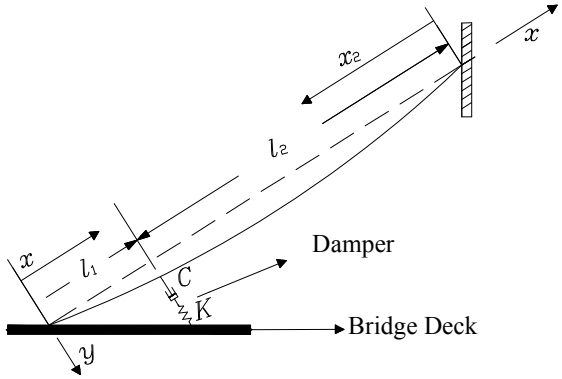


Fig. 1 Calculation model of stay cable with external damper

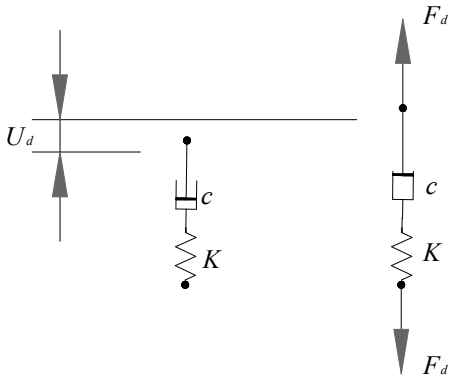


Fig. 2 Damping force vs. displacement of the damper

To investigate the effect of flexibility of damper, which is due to the flexibility of the anchor tube where the damper connected. The model idealized for such a situation is represented in Fig. 2, corresponding to a stay cable with an attached damper associated in tandem with a spring, whose constant k represents the stiffness of the anchor tube. This system is characterized by the dynamic equilibrium equation for which the damping force member is replaced by F_d, defined as following

$$\begin{cases} U_{\mathrm{d}}=\Delta_{\mathrm{D}}+\Delta_{\mathrm{S}} \\ \dfrac{\partial U_{\mathrm{d}}}{\partial t}=\dfrac{\partial \Delta_{\mathrm{D}}}{\partial t}+\dfrac{\partial \Delta_{\mathrm{S}}}{\partial t} \\ F_d=k\Delta_{\mathrm{S}}=c\dfrac{\partial \Delta_{\mathrm{D}}}{\partial t} \end{cases} \tag{7}$$

where U_{d} is the total displacement at the anchor point, Δ_{D} is the displacement of realistic damper, and Δ_{S} is the displacement of spring connected in series with the damper.

At the location of the damper there is a discontinuity in the inclination of the cable, which can be expressed for new boundary conditions as following:

$$T\left(\left.\frac{\partial u_{1v}}{\partial x_1}\right|_{l_1^+}-\left.\frac{\partial u_{2v}}{\partial x_2}\right|_{l_2^-}\right)=F_d \tag{8}$$

When deck movement occurs, the displacement in the direction of y projection is $f_y = Ve^{i\omega t}\cos\theta$, the relationship of the relative motion of Cable-Damper-Deck system under deck excitation should be included in the force balance equation for unrealistic damper assumption:

$$T\left(\left.\frac{\partial u_{1v}}{\partial x_1}\right|_{l_1^+} - \left.\frac{\partial u_{2v}}{\partial x_2}\right|_{l_2^-}\right) = k\Delta_s\left(1-\cos\theta\bullet\frac{l_2}{L}\right) \tag{9}$$

Substitute assumption solution (6) into the force balance relation Equation (7) and (8), and the boundary conditions are considered, yield the equations for determination of the complex eigenfrequencies:

$$\cot(\beta l_1)+\cot(\beta l_2)+\frac{(c\omega i)\left(1-\cos\theta\bullet\frac{l_2}{L}\right)}{\left[1+\frac{c\omega i}{k}\left(1-\cos\theta\bullet\frac{l_2}{L}\right)\right]T\beta}=0 \tag{10}$$

The solution of this frequency equation is treated in the following section.

Solution of the Cable-Damper System

The damping of the free vibrations is described by the imaginary part of the natural frequency ω n, represented in terms of the modal damping ratio

$$\lambda_n = \frac{|\omega_n|}{\omega_1}\left(\sqrt{1-\zeta_n^2}+i\zeta_n\right) \tag{11}$$

where ζ_n is the n-th $(n=1,2...)$ modal damping of the mitigation system. For convenience in subsequent manipulations, new symbols are introduced to denote the real and imaginary parts of the n-th eigenvalue

$$\sigma_n = \mathrm{Re}(\lambda_n),\quad \phi_n = \mathrm{Im}(\lambda_n) \tag{12}$$

It is noted that ϕ_n is the non-dimensional frequency of damped oscillation. The damping ratio ζ_n can then be computed from σ_n and ϕ_n

$$\zeta_n = \left(\frac{\phi_n^2}{\sigma_n^2}+1\right)^{-\frac{1}{2}} \tag{13}$$

In this Eq. (10) is expressed in terms of the trigonometric relation according to the complementary length $l_2 = L - l_1$

$$\cot\left(\omega\sqrt{\frac{m}{T}}l_2\right)=\cot\left(\omega\sqrt{\frac{m}{T}}L-\omega\sqrt{\frac{m}{T}}l_1\right) \tag{14}$$

Substitute Eq. (14) into Eq. (10) yields

$$\tan(\beta L)=\frac{\frac{c}{\sqrt{Tm}}i\sin^2(\beta l_1)\left(1-\cos\theta\bullet\frac{l_2}{L}\right)}{1+\frac{c}{\sqrt{Tm}}i\left(1+\frac{T}{kl_1}\right)\cos(\beta l_1)\sin(\beta l_1)\left(1-\cos\theta\bullet\frac{l_2}{L}\right)} \tag{15}$$

The asymptotic method was applied here to solve the Equation (15), hence in terms of the non-dimensional damping coefficient ζ_n, the relationship between modal damping ratio and damper parameters is:

$$\zeta_n = \frac{\mathrm{Im}(\beta_n L)}{|\beta_n L|}\approx\frac{\left(1-\cos\theta\frac{l_2}{L}\right)n\pi\frac{c}{\sqrt{Tm}}\left(\frac{l_1}{L}\right)^2}{1+\left[\left(1-\cos\theta\frac{l_2}{L}\right)\frac{c}{\sqrt{Tm}}n\pi\frac{l_1}{L}\left(1+\frac{T}{k_1 l_1}\right)\right]^2} \tag{16}$$

For convenience in subsequent manipulations, here κ is a non-dimensional parameter grouping defined as

$$\kappa = \frac{c}{\sqrt{Tm}} n\pi \frac{l_1}{L} \tag{17}$$

Then the system modal damping ratio of the expression Eq. (16) is:

$$\frac{\zeta_n}{\frac{l_1}{L}} = \frac{\left(1-\cos\theta\frac{l_2}{L}\right)\kappa}{1+\left[\left(1-\cos\theta\frac{l_2}{L}\right)\left(1+\frac{T}{k_1 l_1}\right)\kappa\right]^2} \tag{18}$$

From Eq. (18) we can see that the coupling motion of damper and the deck makes the system mode damping ratio affected by the stay angle θ and damper unrealistic distinctly.

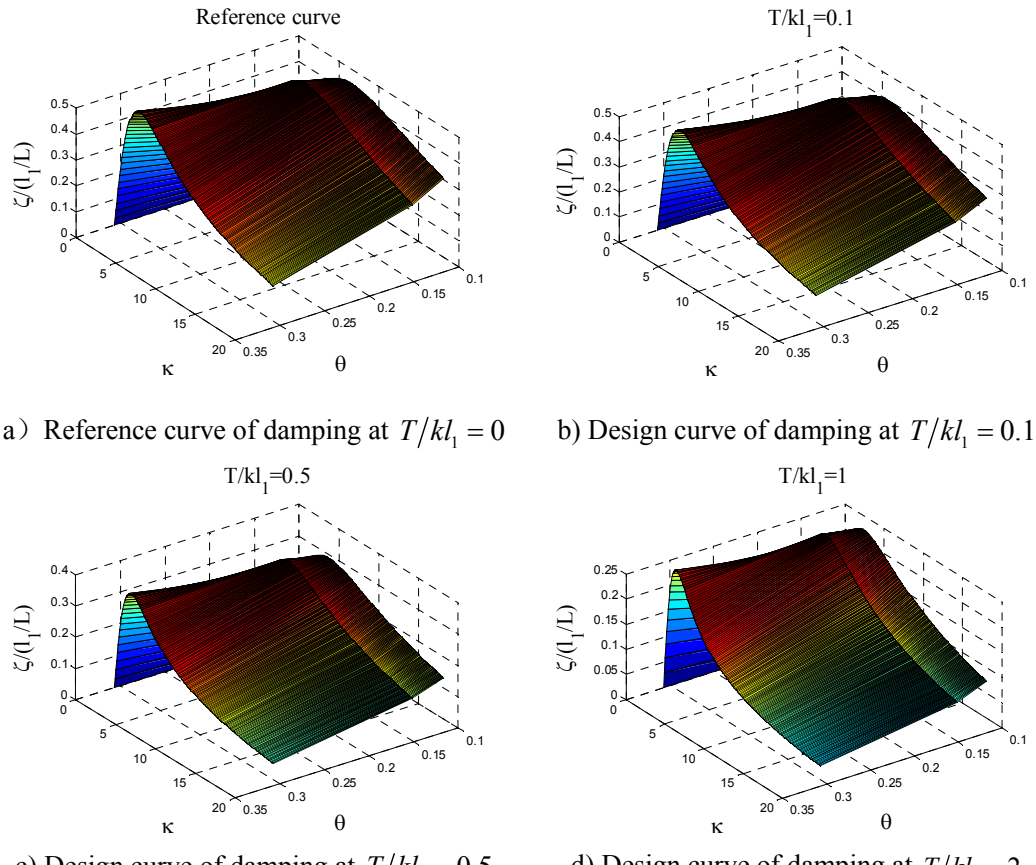
Parametric Analysis

Parameters such as the anchor location, inclined angle, damping, and stiffness of the damper will affect the mitigation system. The system modal damping is focused in this study, since it reflects directly the vibration control efficiency. Based on the basic parameter set, more parameter sets are chosen by varying one or more parameters around the basic one. The basic parameters and their variation ranges are listed in Table 1.

Table 1 Basic parameter set and the parameter variation range

	l_1/L	θ	κ	T/kl_1
Basic parameter	0.02	$\pi/7$, $\pi/6$, $\pi/4$	0-30	0,0.1,0.5,1
Parameters variation ranges	0.01-0.05	$0-\pi/4$	0-30	0-2

Fig. 3 shows the modal damping of the mitigation system according to the Eq. (18), and the other parameters are the basic values given in Table 1.



a）Reference curve of damping at $T/kl_1 = 0$ b) Design curve of damping at $T/kl_1 = 0.1$

c) Design curve of damping at $T/kl_1 = 0.5$ d) Design curve of damping at $T/kl_1 = 2$

Fig. 3 Mode damping rate design curve of cable vibration control system

Eq. (18) is equivalent to the "frequency equation" presented by Krenk [6], when ignoring the coupling effect of the cable-damper-deck and unrealistic of external damper. From Fig. 3, one can recognize that, with the flexibility of the supporter reduces, $T/(k_1 l_1)$ increases, the damper effectiveness. The optimum damping coefficient of the damper decreases when the flexibility of the supporter increases, the maximum modal damping ratio of cable-damper system decreases gradually, and the optimal value of damping coefficient of the external damper decreases accordingly.

The system modal damping affected by the cable-stayed inclination is another problem need to pay particular attention. Fig. 3 shows that under the considered amplitude of deck excitation, the system normalized damping ratio undergoes optimal external damping parameter peak in the estimation curves, and this 'universal curve' also had been determined from a numerical solution of the cable mitigation problem by Pacheco et al. However, their formulation for determining the optimal damper parameters installed and under real wind excitations, particularly under wind-rain excitation represents a difficult task for cables under deck excitation (as the reference curve shows). The trend in Fig. 3 shows that when the inclined cable angle decreases from $\pi/4$ to $\pi/7$ the external damping should be increase deeply to provide the same non-dimensional modal damping, and hence overestimating its value steadily in the old model, this matches well with the actual occurrence in bridge engineering. The newly designed analysis model shows a further investigation, it could describe the cable-damper system's modal damping changes under deck excitation more realistically.

Conclusions

From this study, the modal damping of cable-damper system under deck excitation has been analyzed in terms of complex-valued modes. Equations representing the dynamic characteristics of an inclined cable with a damper subject to different support assumption were reviewed. From the results of the above analysis, the dynamic characteristics of the mitigation system can be summarized as following: (1) Install the external damping device to improve the modal damping ratio of stay cable can effectively reduce the amplitude of the dynamic response subject to bridge deck excitation. (2) The new damper design method is similar to ignoring the coupling effect of the damper deck, also has the design optimization curve, this paper established a more reasonable analysis model taking into account the damper deck interaction and damper unrealistic for stay cable mitigation. (3) This study shows that the flexibility of the supporter in the viscous damper reduces the damper effectiveness. The optimum damping coefficient of the damper decreases when the flexibility of the supporter increases.

Acknowledgments

This research is supported by the NSFC program (51078119) and the Highway Administration Bureau of Guangdong Province research program (2011-15).

References

[1] S. C. Watson, D. G. Stafford, Cables in trouble. Civil Engineering, 58 (1988) 38-41.

[2] R. E. Christenson, B. F. Spencer, E. A. Johnson, Experimental verification of smart cable damping, Journal of Engineering Mechanics, 132 (2006) 268-278.

[3] H. Li, M. Liu, J. Li, X Guan, J. Ou, Vibration control of stay cables of the Shandong Binzhou Yellow River highway bridge using Magnetorheological Fluid Dampers, Journal of Bridge Engineering, 12 (2007) 401-409.

[4] Y. Fujino, N. Hoang, Design formulas for damping of a stay cable with a damper, Journal of Structural Engineering, 134 (2008) 269-278.

[5] S. Krenk, Vibrations of a taut cable with an external damper, Journal of Applied Mechanics, 67 (2000) 772-776.

© (2012) Trans Tech Publications, Switzerland
doi:10.4028/www.scientific.net/AMM.238.719

Dynamic Analysis of Bridge-approach Embankment Transition Segment

Zhenxia Li [a] and Yuanzhao Chen [b]

School of Civil Engineering and Communication, North China University of Water Resources and Electric Power, Zhengzhou 450011, China

[a] zhenxiali2009@ncwu.edu.cn, [b] cyz740513@ncwu.edu.cn

Keywords: bridge-approach embankment section; numerical model; track deflection angle; analysis.

Abstract. Dynamic responses of coupled system were analyzed when the speed of train was 350km/h and the transition was filled with graded broken stones mixed 5% cement. Results indicate that setting form of bridge-approach embankment section has little effect on dynamic responses, thus designers can choose it on account of practical circumstances. Based on the study from vehicle-track dynamics, we suggest that the coefficient of subgrade reaction (K30) should be greater than 190MPa within 0-5m zone behind abutment and be greater than 150MPa in other zones.

Introduction

In order to ascertain the dynamic responses of bridge-approach embankment section under train loads, a high-speed rail passenger dedicated line was selected as a prototype and a three-dimensional numerical model was developed by using the finite element method (FEM), where soil properties are known and the dynamic responses of bridge-approach embankment section were analyzed for a train with a speed of 350km/h. In the study, the effects of the transition configuration on settlement, track deflection angle and the length of "reasonable reinforced zone" were investigated. Finally, the allowable track deflection angle is proposed by considering different influence factors.

The Dynamic Response of the Bridge-approach Embankment Section

Longitudinal Distribution of Dynamic Response along the Roadway. In order to study the longitudinal distribution of dynamic responses of bridge-approach embankment sections under train loading, a number of monitoring points are set along centerline of the subgrade and located on the base bed surface. the results of these measuring points are shown as follows:

First, both the maximum settlement and the maximum track deflection angle of bridge-approach embankment sections occur at the bridge-subgrade joint, close to the abutment. One possible reason is that the large stiffness difference at the bridge-subgrade joint, which leads to a downward additional impact caused by train wheels when the train leaves the bridge and thereby increases its vertical deformation. The other possible reason is that the abutment is made of masonry material.

Second, distribution of the dynamic stress in the base bed surface of bridge-approach embankment sections subjects to the following rules: the values near the abutment are small and the values far away from the abutment are large; it has a double peak phenomenon, which is mainly related to the large stiffness of abutment and the stress redistribution action.

Third, accelerations of base bed surface in bridge-approach embankment sections change significantly along the longitudinal direction, the values near the abutment are large and the values far away from the abutment are small essentially.

The above-mentioned three conclusions are consistent with the measured data obtained on the Qinhuangdao-Shenyang Passenger Dedicated Line.

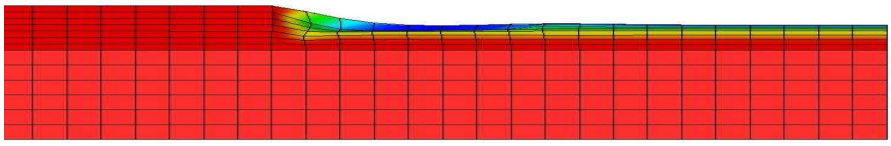


Fig. 1 Side view of dynamic deformation (part)

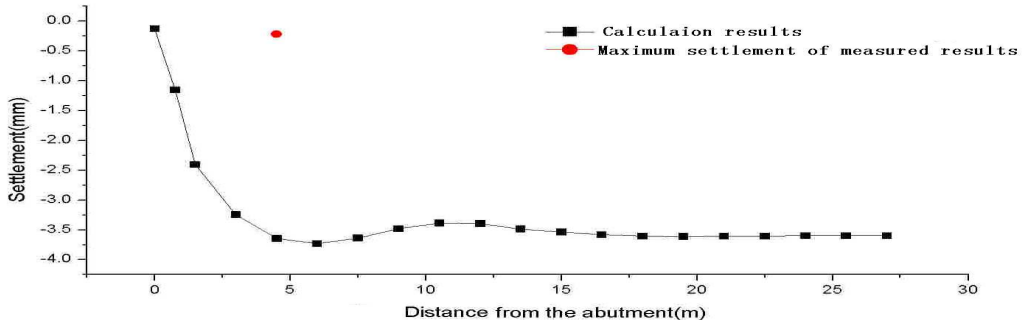


Fig. 2 Distribution curve of dynamic displacement of base bed surface along the longitudinal direction

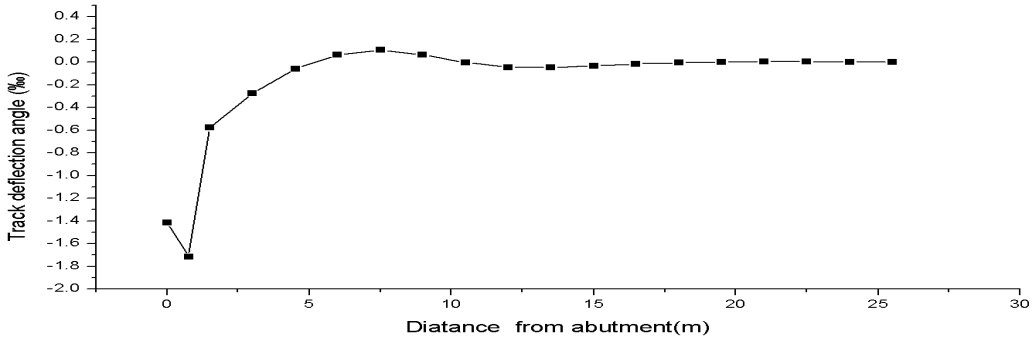


Fig. 3 Distribution curve of vertical angle of rail surface along the longitudinal direction

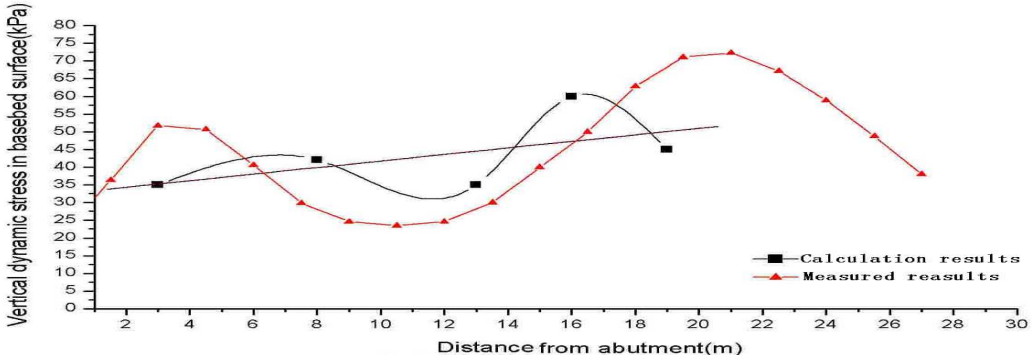


Fig.4 Distribution curve of dynamic stress of base bed surface along the longitudinal direction

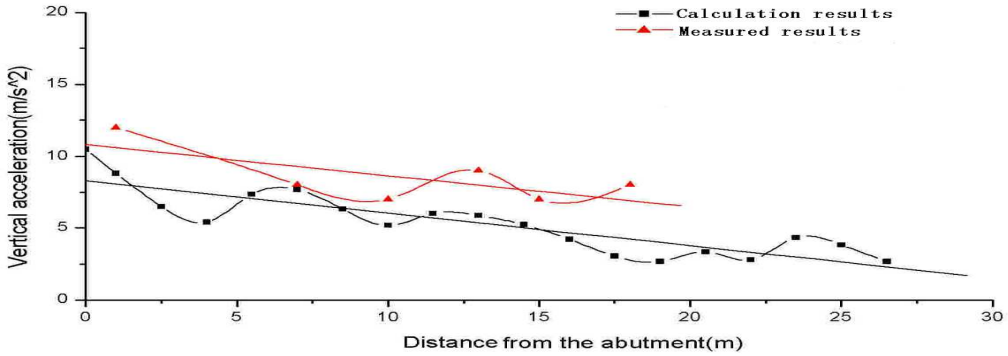


Fig. 5 Distribution curve of acceleration of base bed surface along the longitudinal

Lateral Distribution of Dynamic Response along the Roadway. In order to study the distribution of dynamic stress along the direction perpendicular to the route in bridge-approach embankment section under train load, the cross-section at a distance of 10.5m behind the abutment and selected four monitoring points spacing 0.75 m arranged on both sides of the center line in each structural layer were chose. As shown in Figure 15, the main conclusions are presented as follows:

First, distribution of the dynamic stress along the direction perpendicular to the route of the track slabs, the base bed surface, the base bed bottom, subgrade and the foundation are basically consistent with each other. All show "saddle" type distribution and the maximum values occur at the contact points between the rail and the track slab, the minimum values occur at the centerline location. The trends are consistent with the measured results of Qinhuangdao-Shenyang Passenger Dedicated Line.

Second, the fluctuation range of dynamic stress of the track slab is great along the direction perpendicular to the route and its distribution is very uneven. Uneven distribution of the dynamic stress will cause the uneven deformation of track structures, even cracking, which will affect the normal operation of the railway traffic. Therefore, we should consider optimizing the type of the track structure in order to improve the uneven distribution of the dynamic stress when designing the railway approach embankment.

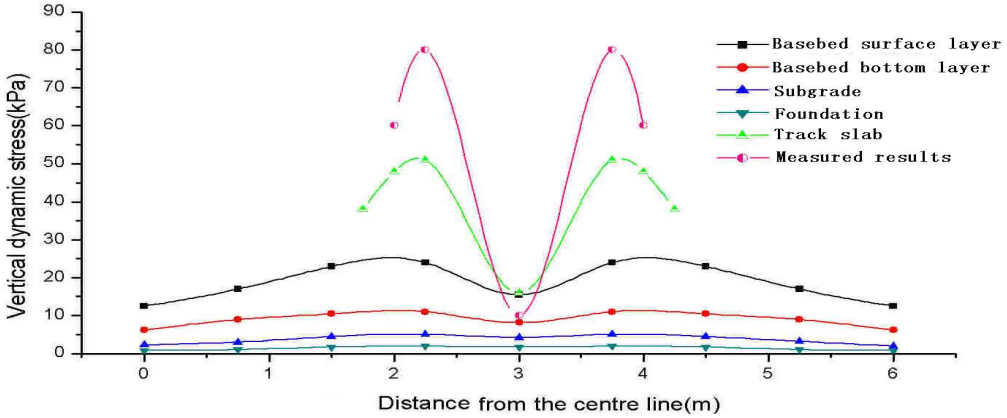


Fig. 6 Distribution curves of dynamic stress of each structure layer along the lateral direction.

The Effect of the Configuration of Transition Sections on the Settlement. The previous Chinese railway design specification requires that bridge-approach embankment sections should be designed in configuration of a trapezoid; however, bridge-approach embankment sections are in the form of an inverted trapezoid specified in the interim design provisions of Beijing-Shanghai High-speed Railway. Therefore, the above-mentioned setting forms of bridge-approach embankment sections are considered in numerical calculation to analyze the effect of the configuration of transition sections on the settlement. Under the conditions that material characteristic parameters and boundary conditions are constant. Distribution of the monitoring points is shown as follows: the first point is located at the end of the abutment; there are three points away from the abutment 9m, 13.5m, 19m, which are located in the base bed surface and rails, respectively. The points in rails are used to monitor the settlement. Calculation results are plotted in Fig. 7.

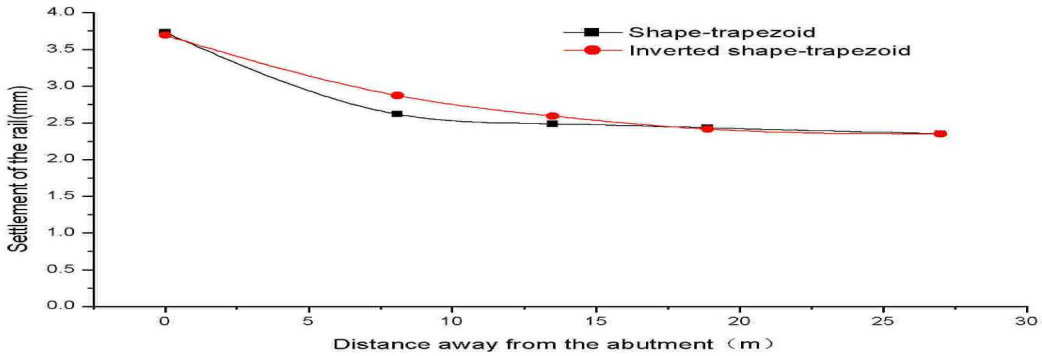


Fig. 7 Curves of dynamic displacement of base bed surface

The following conclusions can be obtained from Fig. 7. First, the settlement curves of the two setting forms of the transition section are generally similar. Second, the deformation slope of the trapezoidal transition is gentler than that of the inverted trapezoid. Third, the settlement of the inverted trapezoid transition is smaller than that of the trapezoid transition; however, the difference is insignificant. Hence, this paper argues that if material parameters and other conditions are the same, the setting forms of bridge-approach embankment section have little effect on the settlement. Therefore, designers can choose the setting form according to the practical circumstances.

Research on Reinforcement Measures and Reinforcement Effect

The above-mentioned analytical results demonstrate that the zone in the range of 0-5m behind the abutment is the weak link of the bridge-approach embankment sections. During the design, if K30 of the graded broken stone mixed with 5% of cement in transition sections adopts the minimum critical

value of "Beijing-Shanghai High-speed Rail Design Requirements," it will appear that the subgrade settlement, track deflection angle and the dynamic indicators of vehicle do not satisfy the specification, which will result in a serious impact on the safety of train operation.

In order to solve the above-mentioned issues, we increased K30 in the zone that is within 0-5m away from the abutment and investigated the impact on the settlement and the track irregularity to determine the critical value of K30. We performed calculations for three values of K30 in the zone that is within 0-5m away from the abutment (170MPa, 190MPa, and 210MPa) and a value of K30 in the other zones (150MPa). From the calculations, we get the settlement of bridge-approach embankment section and the distribution of the track deflection angle along the direction of route, which is shown in Fig. 8. Specific results are presented as follows:

First, Fig. 1-8 shows that both the track deflection angle and the settlement of the base bed surface decrease with the increase of K30.

Second, we suggest that design and construction of the reasonable reinforced zone should be different from the other zones and performed specially.

Third, based on related codes and the overall consideration of six dynamic indicators, we suggest that the designed limitations of K30 are as follows:

For the zone within 0-5m behind the abutment, K30≥190MPa;

For the zone beyond 5m behind the abutment，K30≥150MPa.

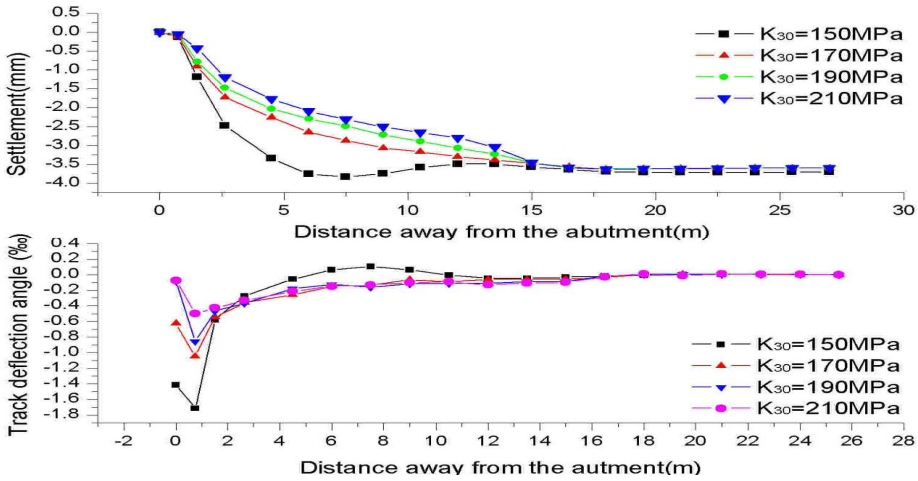


Fig. 8 Distribution curves of track deflection angle and vertical settlement of base bed surface along the longitudinal direction.

Conclusions

First, the setting forms of bridge-approach embankment section have insignificant effect on the dynamic responses; thus designers can choose it based on the practical circumstances.

Second, based on related codes and the overall consideration of six dynamic indicators, we suggest that the designed limitations of K30 are as follows:

For the zone within 0-5m behind the abutment, K30 ≥190MPa;

For the zone beyond 5m behind the abutment, K30 ≥150MPa.

References

[1] Z. Wanming, The vertical model of vehicle-track system and its coupling dynamics, Journal of Railway Engineering Society, 14 (1992) 10-21.

[2] W. Yu, Z. Wanming et al, A New Method to Determine the Length of Track Transition Section, Journal of Railway Engineering Society, 1999, pp. 25-28.

[3] W. Qichang, C. Chengbiao, Allowable value of track deflection angles on high-speed railway bridge-subgrade transition sections, Journal of Railway Engineering Society, 20 (1999) 109-113.

© (2012) Trans Tech Publications, Switzerland
doi:10.4028/www.scientific.net/AMM.238.723

Simulation of Composite Strengthening Technique in Prestressed Concrete Continuous Box Beam Bridges

Hongbo Jiao[1,2a] and Shuanghua He[3, b]

[1]School of Environment and Water Conservancy Engineering, Zhengzhou University, Zhengzhou, China

[2]School of International Education, North China University of Water Resources and Electric Power, Zhengzhou, China

[3]School of Civil Engineering and Communications, North China University of Water Resources and Electric Power, Zhengzhou, China

[a]jiaohongbo@ncwu.edu.cn, [b]heshuanghua222@126.com

Keywords: prestressed concrete continuous box beam bridges; composite strengthening technique; strengthening effectiveness; finite element.

Abstract. The damage features of concrete continuous box beam bridges are summarized combined with three prestressed concrete continuous box beam bridges on ZhengLuo highway. There are four common strengthening methods in bridge engineering practice, i.e. bonded steel plates, strengthening with R.C, carbon fiber reinforced polymer (CFRP) and external prestressed strands. By numerical analysis technique of three dimension finite element (3D FE), the stresses of the damaged bridge are compared with the results of the strengthened one which is strengthened by one of the former methods. The strengthening effectiveness of those methods is ascertained. Therefore, the composite strengthening technique (CST) is established, which is effective to improve the bearing capacity and crack resistance of the strengthened bridge. An optimal strengthening process is put forward in the paper. So the CST is reasonable and effective to strengthen a damaged prestressed concrete continuous box beam bridge, which provides a significant reference for other similar strengthening projects.

Introduction

The prestressed concrete continuous box beam bridges are widely used in practice. At present, a significant proportion of road bridges need to be strengthened because of the following main causes.

(1)The lower design loads cause the bridges insufficient bearing capacity today.

(2)There exist deficiencies in the design or the construction.

(3)The methods of maintenance and strengthening are improper.

The concrete cracks can be classified into 8 types according to the causes, i.e. shrinkage crack, creep crack, temperature crack, bend crack, shear crack, bend and shear crack, distortion crack and local stress crack. The cracks may appear in the web, on the top plate or under the bottom plate of the bridges. The cracks may weaken the bearing capacity and durability and affect the beauty of the bridges. So it is very important to do some research on the methods of bridge strengthening.

There are four common strengthening methods, i.e. strengthening with external prestressed strands, strengthening with bonded steel plate, strengthening with R.C and strengthening with CFRP. But their strengthening effectiveness is different in different kinds of bridges. So the strengthening effectiveness must be ascertained in the prestressed concrete continuous box beam bridges firstly. According to the strengthening effectiveness of different methods, the reasonable strengthening methods can be chosen and the damaged bridges can be strengthened in a proper construction process [1].

Single strengthening method hasdeficiency.in itself It is a good trial to combine several single strengthening methods to strengthen the damaged continuous box beam. This method is called composite strengthening technique (CST), which can make up for each other's deficiencies of different methods to make good work. It provides an important technical reference to the similar strengthening engineering.

Engineering Survey

Liaoyugou bridge, Yingyugou bridge and Rencungou bridge are three viaducts on the Zhengluo highway. They are all prestressed concrete continuous box beam bridges with multi-span of 5×45m and constant depth of 3m, which were constructed in incremental launching method in 1995. The bridges are separated single-box beam and bidirectional with four lanes. A single-box beam is 12m wide. The designed load is equal to that of highway. The designed vehicle speed is 100km/h. The substructure is concrete thin-wall piers and cast-in-situ pile groups.

The bridges have been working for more than 15 years. There are cracking phenomena to some extent on the beam webs of the three viaducts. The main cracks are diagonal cracks near the piers and the abutments. There are some cracks under the bottom plates. And there are some concrete peeled and some reinforcements and steel strands exposed in some parts of the bridges. The above damages weaken the bridges` bearing capacity, which had great effects on their normal and safe working. So some methods must be adopted to strengthen them.

Firstly, the above four common strengthening methods are adopt to analyze their effectiveness respectively. Then the four methods are combined in a rational way. The CST can develop each method's strong points and avoid its weak points, which is a valuable strengthening method to strengthen the continuous box beam bridges.

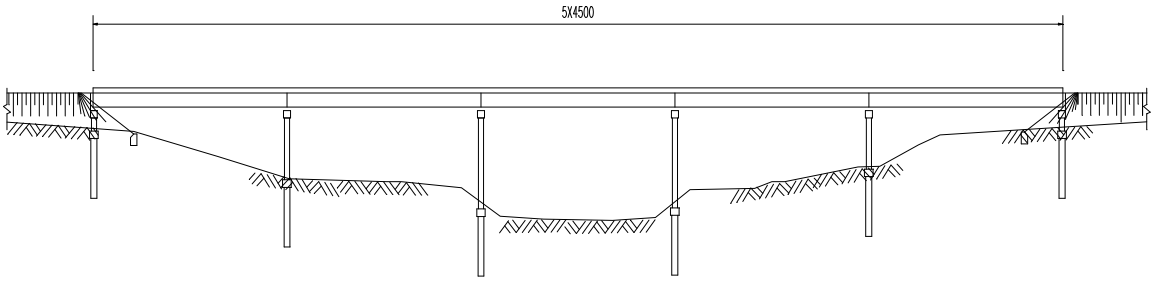


Fig. 1 Layout of the prestressed concrete continuous box beam bridge (cm)

3D FE Models

The 3D FE models are built to analyze the strengthening effectiveness. Seven bridge models need to be built including undamaged and damaged models, the four strengthening models and composite strengthening model. In these models, the 8-node solid elements are adopted to simulate the concrete. Prestressed strands are simulated by link elements. Beam elements are used to simulate the concrete thin-wall piers. The 8-node Shell elements are used to simulate the new concrete besides the webs and the bottom plate of the beam. There are some key techniques in the models as follows.

(1) When the elements are meshed, try to make the nodes of the internal prestressed strands in the same position with the concrete elements`. The two nodes are coupled in the same position.

(2) The concrete corrected elastic modulus is used because of the regular reinforcement.

(3) The prestress of the prestressed strands is dealt with initial strain method.

(4) The undamaged model is the basis of all the other models. The damaged elements and all the strengthened elements are calculated by using the element birth and death technology in the software of ANSYS.

(5) The substructure is considered into the models because the beam weight will increase after the strengthening. The top nodes of the beam elements will be coupled with that of the bottom concrete elements.

(6) The loads are combined with the worst combination principle, which makes the mid-span bending moment or the bearing shear force maximum [2-5].

The seven models are shown as Fig. 2~Fig. 6, which the four strengthening models are shown partly. The damaged model is as same as the undamaged one. But the elastic modulus of the damaged elements in the damaged model is lower than that of the undamaged elements in the

undamaged model. The damaged elements in the other five models are same with each other. The static structural analysis is done using these FE models, the results of which can ascertain the effectiveness of the strengthening methods.

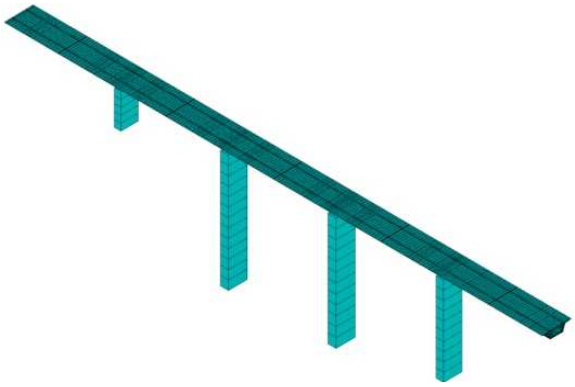


Fig. 2 FE model of Liaoyugou bridge



Fig. 3 Strengthening with R.C.

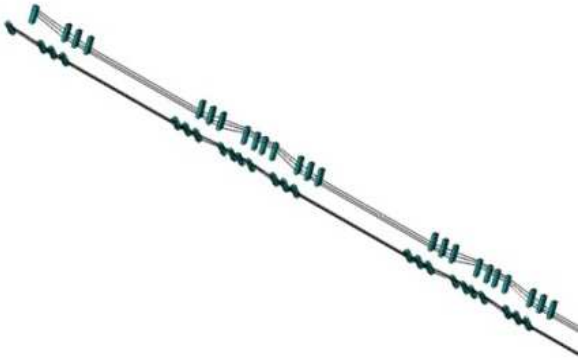


Fig. 4 Strengthening with external prestressed strands

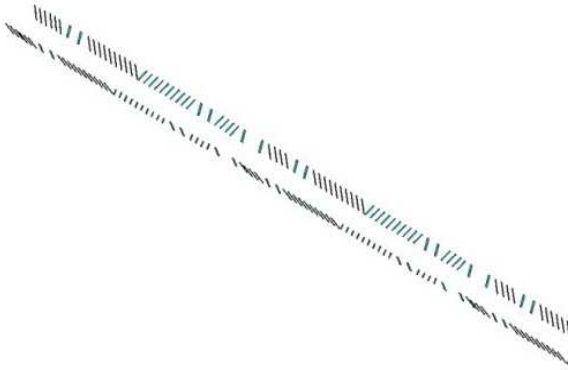


Fig. 5 Strengthening with bonded steel plates on the webs

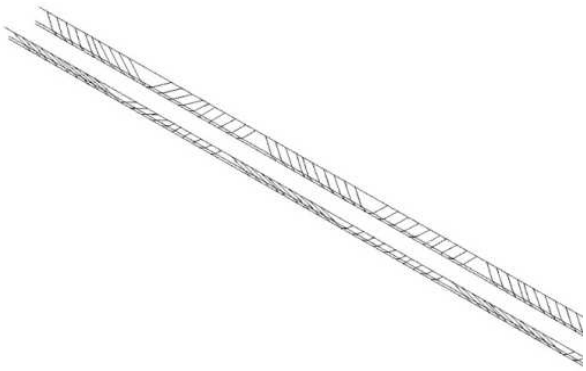


Fig. 6 Strengthening with CFRP

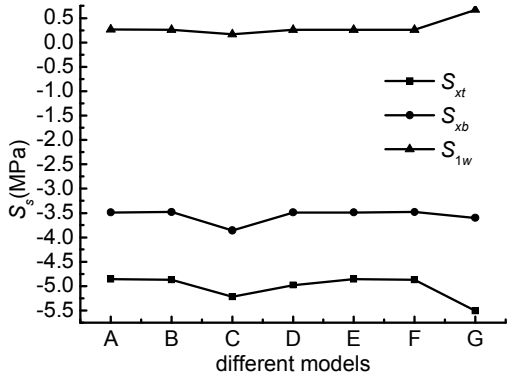


Fig. 7 Stresses in short term combination of the first mid-span

Strengthening Effectiveness Analysis

Under all kinds of combinations, the stresses and displacements meet the standards in the undamaged models. But in the damaged model, some stresses of the beam have exceeded the standards in short term or long term combination because of the cracks. For example, the principal tensile stress of the webs in short term combination is up to 1.50MPa, which exceeds the limit equal to 1.33MPa. So the concrete cracks in the webs and under the bottom plates. These cracks influence the bearing capacity and durability of the bridge, which may be potential safety hazards during the normal running. Therefore, the bridge must be strengthened to ensure the bridge safe running.

A~G means the seven models, i.e. undamaged model, damaged model, models of strengthening with R.C., external prestressed strands, bonded steel plates, CFRP and composite technique. Under the worst combination, the bending moments of the first three mid-span sections are up to the

maximum as well as the shear forces of the first three bearing sections according to the symmetry. The first span is chosen to analyze the strengthening effectiveness of all the above methods. The short-term and the long-term action effects are considered based on Chinese bridge standard [1]. The stresses of the three points in short term combination are showed in Fig.7 and Table.1.

S_{xt} and S_{xb} are the normal stresses of the top plate and the bottom plate.

S_s is the stresses in short-term combination.

S_{1w} is the principal tensile stresses of the webs.

S_{1wmax} is the maximum principal tensile stresses of the webs.

The negative stresses are pressure stresses. On the contrary, the positive values mean the tensile stresses.

From the calculated results of a single strengthening model, all the pressures satisfy the standards, but some tensile stresses exceed the limit. The maximum principal tensile stresses of the above seven models (A~G)of the first span are 1.09MPa, 1.50MPa, 1.45MPa, 1.61MPa, 1.27MPa, 1.20MPa and 1.12MPa. Obviously, strengthening with R.C. and external prestressed strands can improve the bearing capacity of the bridge, but they are not effective to inhibit the concrete cracks. The other two strengthening methods can decrease the principal tensile stresses effectively, but there exists stress lag-effect. The CST can make the best use of their good points to enhance the bearing capacity and control the cracks developing. The maximum principal tensile stress is 1.12MPa close to the design value in composite model.

The stresses of other parts of the bridge and other combinations have the same regularity. So the CST is an effective strengthening method.

Table 1 The stresses of the first span in short-term state (MPa)

section position	stresses	A	B	C	D	E	F	G
the left bearings	S_{xt}	0.99	0.99	1.02	0.92	1.00	0.99	0.97
	S_{xb}	-2.25	-2.27	-2.32	-2.29	-2.27	-2.27	-2.38
	S_{1w}	1.16	1.50	1.57	1.30	1.51	1.50	1.22
the midspan	S_{xt}	-4.86	-4.87	-5.22	-4.98	-4.86	-4.87	-5.51
	S_{xb}	-3.49	-3.48	-3.86	-3.49	-3.49	-3.48	-3.60
	S_{1w}	0.27	0.26	0.17	0.26	0.26	0.26	0.67
the first span	S_{1wmax}	1.09	1.50	1.45	1.61	1.27	1.20	1.12

According to the results of 3D FE numerical analysis to the above four strengthening methods, some valuable conclusions are obtained as follows.

(1) Strengthening with R.C can cover the cracked surface of the bottom plate and the webs of the box beam. The new and the old concrete can deform in step and bear the loads together. But the beam weight increases a lot, which makes the inner forces of the beam increase greatly.

(2) The external prestressed strands act on the bridges through the anchoring plates and the deflecting plates and exert pressure to the concrete. They can decrease the stresses of the damaged bridge. In addition, this method has little effect on the appearance of the bridge, because the strands are installed in the box.

(3) The steel plates can inhibit the developing speed of the crack and improve the bridge durability. But it is difficult to take full advantage of the steel plates because of the stress lag-effect.

(4) CFRP can improve the bearing capacity and ductility of the concrete without weight increasing. But the damaged bridges had cracked and there is a certain lag to develop CFRP`s full play.

(5) The CST is an effective strengthening method that can reduce the influence of the increasing weight and have a good control to the crack developing. So the bearing capacity and crack resistance of the damaged bridge is better than the old one.

Construction Process of the CST

According to the results of the strengthening effectiveness, the construction process (shown in Fig.8) is as follows.

(1) Clear the surface of the bottom plate and the webs of the box beam and grout the cracks.

(2) Cast the anchoring plates and the deflecting plates with steelfabric to install the external prestessed strands.

(3) Strengthen with R.C. The steelfabric must be embedded in the old concrete on the webs and under the bottom plates outside. Then the new concrete (10cm-thick) is cast into the templates shown in Fig. 3.

(4) Strengthen with external prestressed strands. The external pretressed strands pass through the deflecting plates and are anchored in the anchoring plates shown in Fig. 4.

(5) Strengthen with bonded steel plates. According to the crack direction and degree, the steel plates are bonded normally to the cracks on the webs outside. Here the angles are 30° shown in Fig.5.

(6) Strengthen with CFRP. On the outward side of the webs, the CFRP are pasted at the same direction of the steel plates. But there are two pieces of continuous lognitudinal CFRP on the top and bottom of the each side web shown in Fig. 6. It is noteworthy that the CFRP surface must dealt with some protective materials.

After the strengthening, the bridge must be checked by static loading test or dynamic loading test to ensure the strengthening effectiveness and safe working of the bridge.

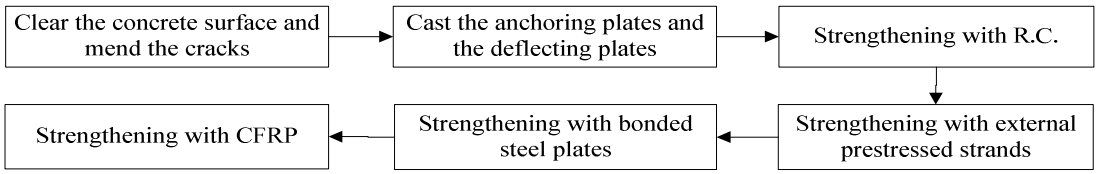


Fig. 8 Construction process of the CST

Conclusions

According to the results of 3D FE analysis, the effectiveness of single strengthening method is one-sided because of its deficiency. Strengthening with R.C. and external prestressed strands can improve the bearing capacity of the bridge greatly. Strengthening with bonded steel plates and CFRP can enhance the structure crack resistance and safety reservation. The CST is a rational combination of the above strengthening methods and can make up for each method's deficiencies. The technique is very economical and easy to construct, which is a valuable strengthening method and has a wide prospect in bridge strengthening.

References

[1] People's Republic of China Profession Standard (JTG/T522-2008), Specifications for strengthening design of highway bridges, China Communications Press, Beijing, China, 2008.

[2] X Gu, F Lv, Y Guan, Study of the design procedures for externally prestressed consolidation of beam bridge, Northern Communications, Liaoning, 4(2007) 97-98.

[3] J Li, Strengthening effectiveness analysis of continuous box beam bridge, Journal of China and Foreign Highway, Changsha, 4 (2007) 146-149.

[4] G Shu, Application of strengthening with CFRP in municipal engineering, China Municipal Engineering, Beijing, 2 (2009) 48-49.

[5] T Zhang, J Li, H Qiu, Application of sticking steel slab technology in bridge strengthening construction, Communications Standardization, Beijing, 7 (2007) 60-62.

© (2012) Trans Tech Publications, Switzerland
doi:10.4028/www.scientific.net/AMM.238.728

Full-scale Model Test for Anchorage Zone of Pylon of Cable-stayed Bridge

Xiaolin Yu [a], Buyu Jia [b], Weifeng Wang [c] and Quansheng Yan [d]

School of Civil Engineering and Transportation, South China University of Technology, Guangzhou 510640, China

[a]xlyu1@scut.edu.cn, [b]jbyretop@126.com (corresponding author), [c]ctwfwang@ scut.edu.cn
[d]cvqshyan@ scut.edu.cn

Keywords: cable-stayed bridge; full-scale model test; anchorage zone of pylon; numerical simulation.

Abstract. In this paper, the construction technology for main pylon of cable-stayed bridge is researched through test of full-scale model of anchorage zone of pylon of Guangzhou Bridge. Stress distribution and deformation condition of model under prestressed tendons and cable force are analyzed. Numerical simulation on this anchorage zone model is carried out. By comparing FEM results to the test results, some important conclusions are drawn out and give some advices to the optimum design of the bridge pylon. Parts of the achievements have been applied to actual bridge work and obtained successful engineering experience.

Introduction

The anchorage zone of the cable-stayed main pylon is an important structure to pass the weight of the upper structure and all external loads to the pylon. Strong cable force withstands by cable pylon itself. It is very important to ensure the safety of the anchorage zone of the cable-stayed main pylon. This is also a key factor to construct cable-stayed bridge successfully. Therefore, it is necessary to study the local stress state of the cable anchorage zone such as the size of stress, the distribution of stress, the direction of stress flow and crack resistance. It has great practical value on understanding the mechanical properties and guiding the design of the anchorage zone.

Regard to the plastic and non-uniformity of concrete and error of the construction technology, simple analysis by finite element model is difficult to reflect the actual working condition and the local stress distribution of the structure. Therefore, it needs to take advantage of model test to analysis the size and distribution of the local stress of the anchor cable pylon of cable-stayed bridge and ensure rationality and safety of the structure stress. Full-scale section model tests aiming at the cable force of pylon anchor were preceded by many cable-stayed bridges, such as Poyanghukou Bridg [1], Runyang Bridge [2], Songhuajiang River Bridge [3], Pengxi River Bridge [4] and Malinghe Super-bridge [5].

The upper structure of Guangzhou Bridge crossing MeiJiang River is a concrete cable-stayed bridge with single-pylon and single cable plane. Its main span is 139+106m. A 1:1 model test of the anchorage zone of cable pylon of section 21 was preceded.

Contents of the Model Test

The main research contents of the model test are as follows:

1) Choose the most representative segment, design the loading project and complete the production of model;

2) Product concrete test pieces of test model and test their mechanical properties;

3) Test prestressed friction loss and construction technology through the embedded sensors,;

4) Establish 3-d finite element model for section model of cable pylon by ANSYS and carry out simulation calculation;

5) Study working conditions of test model in different load levels by using string vibration sensor, the strain gauge, centigrade meter etc., and test stress distribution and deformation inside and outside of concrete;

6) Study crack situation of concrete and record the crack load, position, width and the development of cracks;

7) Compare the measured data of the test with the calculated data of numerical calculation, analysis the law of both and provide the reference for bridge maintenance and management in future.

Model Test

Model Making. The anchorage zone of stay cables in this bridge applies approximate rectangular hollow section. Stay cables through the anchorage block in anchorage pillar on the wall.

By analysis, the pylon section corresponding to cable S21 and cable C21 was selected as the object of this test. In order to ensure the prestressed anchorage thickness of the top and the bottom, the distances of the barycenter of the outermost prestressed to the concrete floor of the model were heightening to 20cm distance.

The height of the test section was selected 1.99 m finally. Appearance plane size was 6.5m×3.5m. The test model was shown in Fig. 1 to Fig. 5.

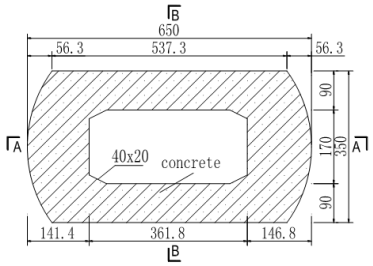


Fig. 1 Layout diagram of model(cm)

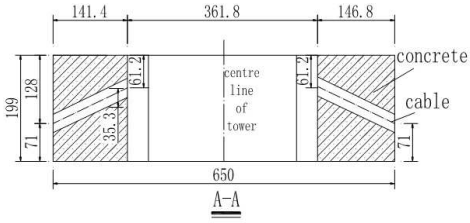


Fig. 2 Vertical plan of model(cm)



Fig. 3 Test Model



Fig. 4 Force transmission piece



Fig. 5 Pushing loading

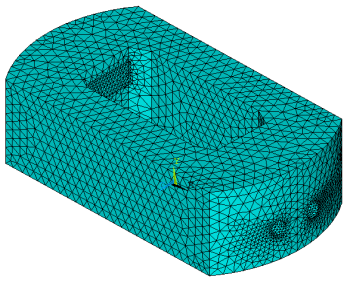


Fig. 6 Finite element model

While casting the model, make standard test pieces of the compressive strength and elastic modulus according to the requirement of concrete cube, place them around the model and maintain them in the same condition with the model, so that the specimen strength and elastic modulus can really reflect the actual situation of the model. After 7 days, standard cube compressive strength 54.2MPa and elastic modulus 33.6GPa were tested respectively.

The finite element model established by ANSYS was shown in Fig. 6.

Surface Stress Measuring Points Arrangement and Results. Considering mechanical characteristics of the anchorage zone of cable pylon and the need of test, surface stress sensors were arranged and the numbers were shown in Fig. 7 to Fig. 9.

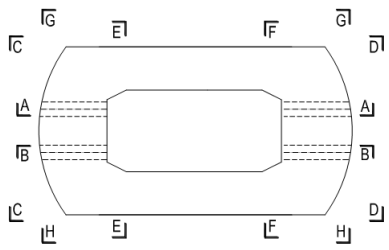


Fig. 7 Layout plan of measuring points

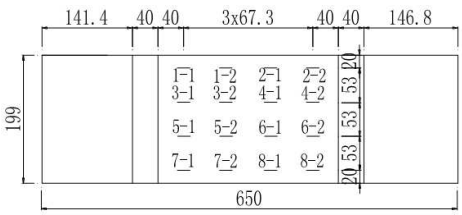


Fig. 8 Points of A-A section(cm)



Fig. 9 Surface sensors

After concrete pouring and curing of the full scale model, test the measuring points of concrete surface, the stress at that time were regard as zero.

There were 6 root U prestressed steel strand and 12 root linear prestressed steel strand in this model. Stress of surface points were tested after all steel strand tension completed and the results were shown in Table.1. "-" meant compressive stress and "+" meant tensile stress.

Table 1 Stress of surface points after all steel strand tension completed

Number of A-A	Measured Value (MPa)	Number of C-C	Measured Value (MPa)	Number of H-H	Measured Value (MPa)
1- 1	-6.11	39- 1	-13.12	25- 2	0.46
1- 2	-13.69	39- 2	-13.01	26- 2	-8.77
2- 1	-9.48	39- 3	-11.49	27- 1	1.06
2- 2	-6.35	40- 1	-9.12	27- 2	-3.01
3- 1	-7.75	40- 2	-8.16	28- 1	-7.18
3- 2	-6.08	40- 3	-12.64	28- 2	-6.70
4- 1	-7.96	41- 1	-8.64	29- 1	-8.40
4- 2	-14.52	41- 2	-3.58	29- 2	-3.04
5- 1	-4.47	41- 3	-2.64	30- 1	-6.37
5- 2	-4.08	42- 1	-3.55	30- 2	-4.95
6- 1	-5.51	42- 2	-3.15	31- 1	-5.77
6- 2	-8.35	42- 3	-5.21	31- 2	-7.57
7- 1	-7.98	43- 1	-10.68	31- 3	-2.85
7- 2	-5.46	43- 2	-7.16	32- 1	-2.66
8- 1	-6.82	43- 3	-4.32	32- 3	-3.62

It can be seen from the results that the stress of the surface points were basically compressive stress after all steel strand tension completed. Only several points were tensile stress. And they did not exceed the cracking strength of concrete.

The lateral component designed of stay cables was P_k =8866kN. Before formal loading, all jacks were preloaded to 2500 kN and then backed the oil to zero so as to eliminate elastic deformation etc during the process of pushing and to reduce the error. There were two recycles in this test. When formal loading was carrying out, each load recycle was divided into nine loading levels, that is, 1600 kN ($0.18P_k$), 3200kN ($0.36P_k$), 4800kN ($0.54P_k$), 6400kN ($0.72P_k$), 7200kN ($0.81P_k$), 7978 kN ($0.9P_k$), 8866 kN ($1.0P_k$), 9752 kN ($1.1P_k$) and 10640kN ($1.2P_k$).

Stresses of some surface points measured and calculated were shown in Fig. 10.

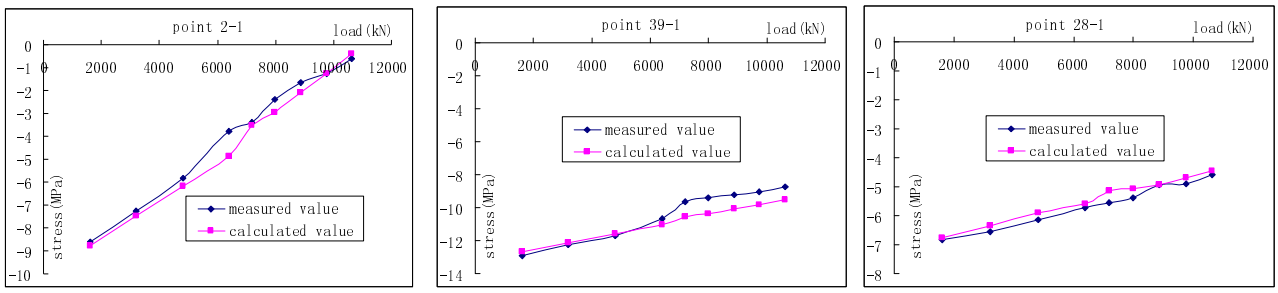


Fig.10 Stress of some surface points measured and calculated

It can be seen from the results that during the experimental process, compressive stress of most of measuring points was in the trend of decreasing on the whole. Compressive stress values of the outer surface of the model decreased smaller than that of the inner surface. Each point basically changed linearly in the same trend with the numerical simulation. When loaded to $1.2P_k$, structure was still in elastic stage.

Inner Stress Measuring Points Arrangement and Results. Inner stress sensors were arranged and numbered in Fig. 11. Prestressed tension can obviously improve the preloading stress of lateral wall of cable pylon. But it had less effect on the preloading stress of the anchor. Even there was some tensile stress in individual local. It may have some adverse effect on structure.

The above analysis showed that there were different degree of the compression stress produced in each part of the model after the prestressing and anchoring completed. The purpose of preloading stress to key parts of the model was obtained. The measuring and simulation of prestress values were basically matching, and the measured results and simulation results checked each other.

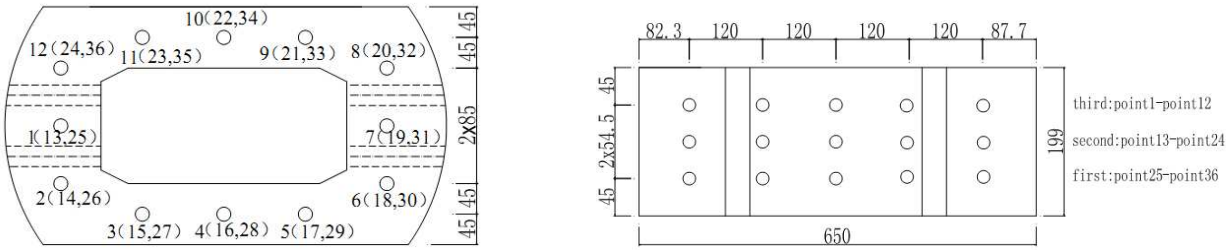


Fig. 11 Inner stress measuring points

Similar results were obtained by inner stress measured and surface stress measured. Stresses of some inner points measured and calculated were shown in Fig. 12. When loaded to 1.2P_k, structure was still in elastic stage.

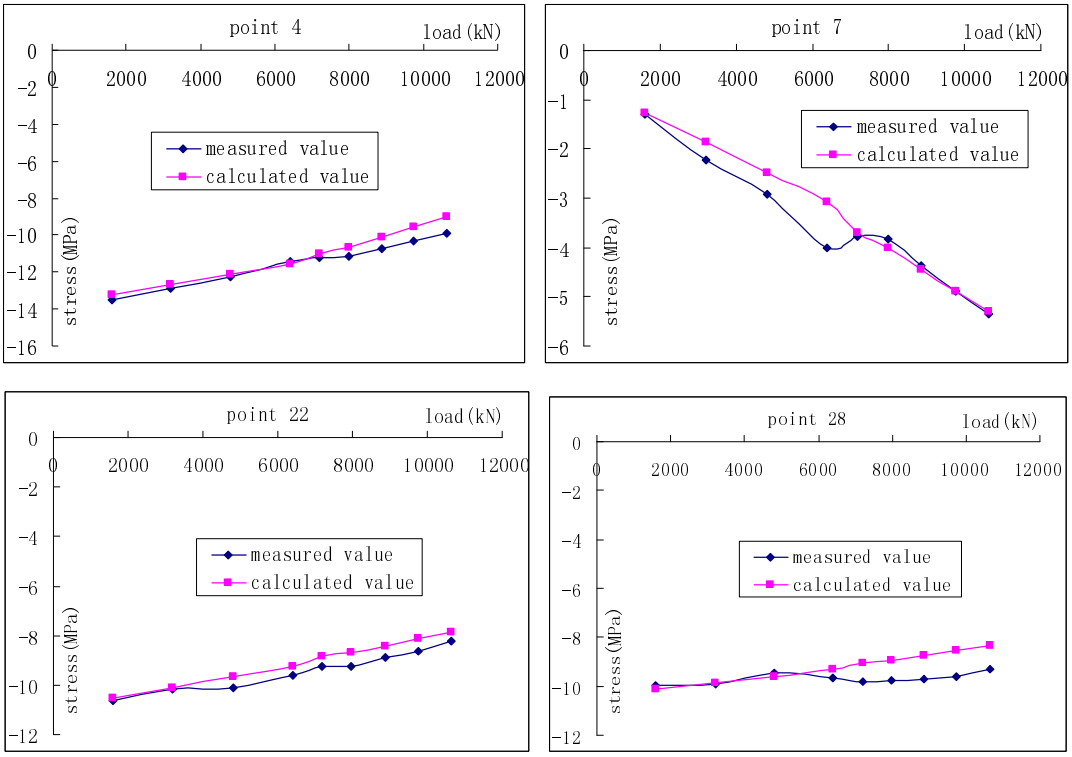


Fig. 12 Stress of some inner points measured and calculated

Surface Deformation Points Arrangement and Results. 12 Points monitoring the deformation of key parts of the model were arranged to test displacement of the model. The arrangement was shown in Fig. 13.

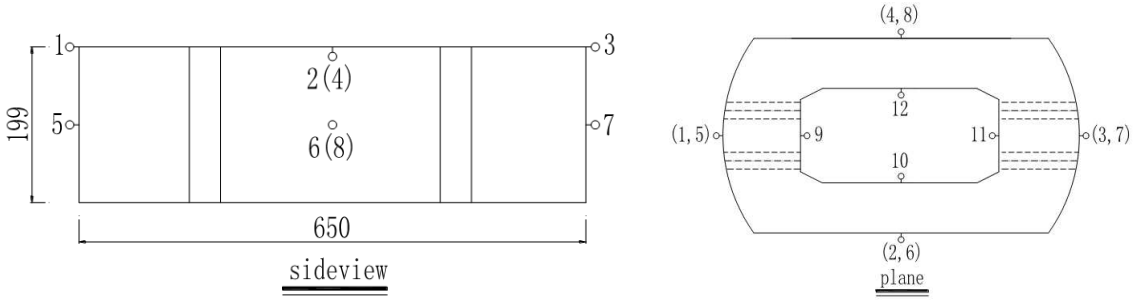


Fig. 13 Measuring points of deformation (cm)

Deformations measured and calculated were shown in Fig. 14. Longitudinal deformation was far away from the model center and horizontal deformation was toward the center of the model. With the increasing of loading, deformation of model linear was increasing too. The values calculated were bigger than measured. The main reason was that simulation analysis did not consider the role of the common reinforced. In the actual model, a large number of common reinforced frames can increase the stiffness of the concrete structure and make the measured value bigger than the calculated.

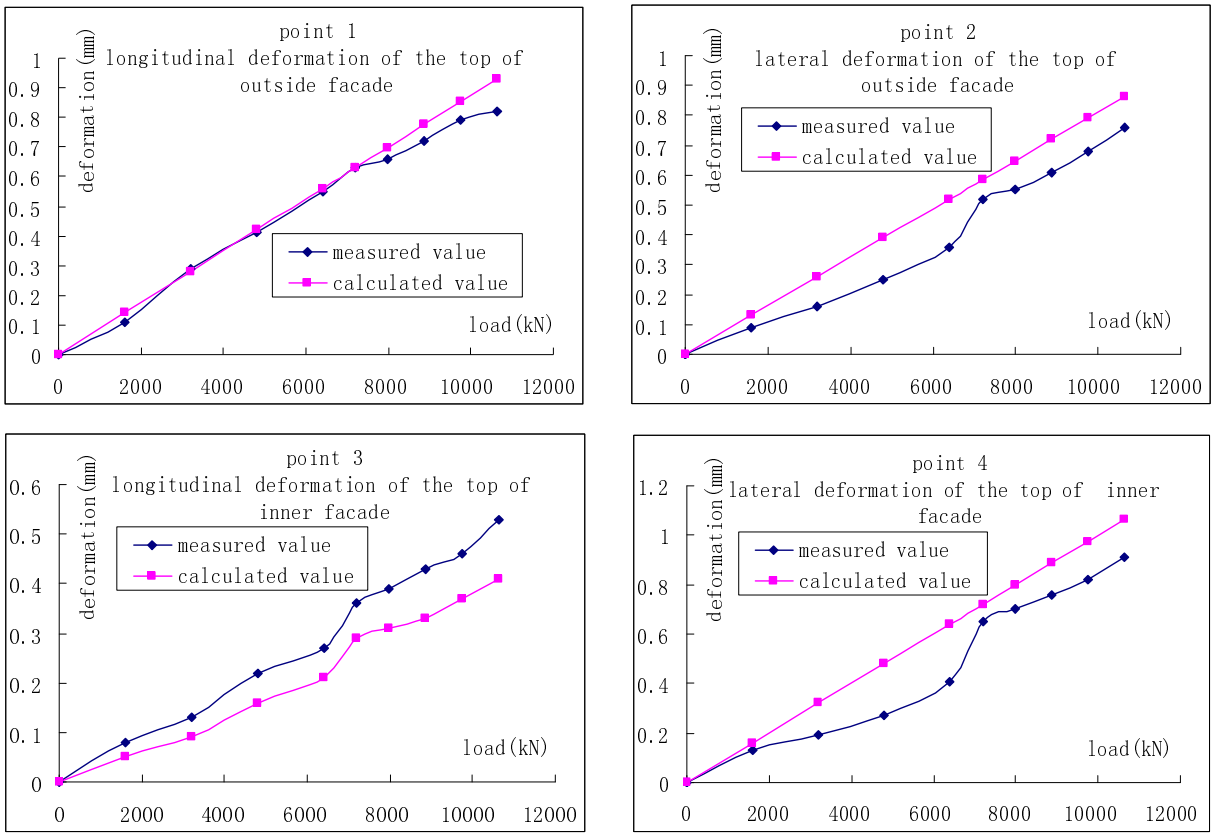


Fig. 14 Deformation measured and calculated

Conclusions

The stress results measured by the model experiment and calculated by finite element calculation procedure were basically the same. The deformation results measured and calculated were also in good agreement. It can be concluded that structure was still in elastic stage when it was loaded to $1.2P_k$. There weren't structural cracks.

References

[1] Y. Xiang, G. Chen, China Journal of Highway and Transport, 4 (2000) 74-78. (in Chinese)
[2]Z. Liu, S. Men, Z. Liu, China Civil Engineering Journal, 6 (2004) 35-40. (in Chinese)
[3]W. Shan, Y Li, L. Yu, Y. Nie, China Journal of Highway and Transport, 3 (2005) 68-72. (in Chinese)
[4]B. Wu, G. Chang, F. Zhang, Technology of Highway and Transport, 6 (2008) 61-65. (in Chinese)
[5] S. Mei, Y. Zhang, H. Zhu, F. Xiao, Journal Huazhong University of Science and Technology (Natural Science Edition), 12 (2009) 124-128. (in Chinese)

© (2012) Trans Tech Publications, Switzerland
doi:10.4028/www.scientific.net/AMM.238.733

Creep Effects on Simply Supported Prestressed Concrete Box Girder of High-speed Railway with Ballastless Tracks

Wang Fang [a], Bing Han [b] and Shaokun Yang [c]

School of Civil Engineering, Beijing Jiaotong University, Beijing 100044, China

[a]10121293@bjtu.edu.cn, [b]bhan@bjtu.edu.cn, [c]07231263@bjtu.edu.cn

Keywords: prestressed concrete box girder, creep, ballastless track.

Abstract. Creep will lead to increasing deflection of prestressed concrete girder, which may induce rails uneven, especially to ballastless tracks in high-speed railways. In this paper, two creep models, CEB-FIP90 and ACI209, were used in a finite element model to analyze influences of creep on simply supported prestressed concrete box girders which are used in high-speed railway in China. Sensitivity analysis was carried on towards curing age, secondary dead load, loading time and prestressing method on deformation of the girder. The results show creep should be controlled in engineering to ensure driving security.

Introduction

Nowadays, ballastless tracks have been applied widely in high speed railway [1, 2]. Because there are no ballasts to be used to adjust the height of ballastless track, the deformation of track is influenced directly by the deformation of the bridge [3, 4]. Therefore, the deformation of the bridge should be controlled to ensure driving safety.

Simply supported prestressed concrete box beams are applied widely in high speed railway. This new type beam has large self-weight and needs more prestress, the creep of the concrete beam becomes lager accordingly. Creep is generally 2 to 3 times of elastic deformation of concrete, so this issue has become a topic needed to be paid more attentions. M.G. Xu and F.G. Wang studied the deflection of simply supported prestressed concrete box beam used in railway bridge based on statistical analysis to find the main influence factor and put forward an effective measure to reduce the deflection caused by creep [5]. Y. B. He discussed the post creep deformation of long-span continuous concrete bridge with ballastless tracks and compared creep coefficient with text values [6]. The results show the creep deformation is sensitive to paving time of the track.

In this paper, two different creep models, CEB-FIP 90 [7] and ACI 209 [8], are used to analyze creep of simply supported box girder.

Finite Element Model of Simply Supported Prestressed Concrete Box Beam

Introduction of the Sample Girder. The sample is simply supported post-tensioned concrete box beam for double-line ballastless track. The span is 31.5m. The maximum design operating speed is 350km/s. Environment category is carbonization environment and effect grade is T_1, T_2. It is appropriate for area that seismic intensity is 8 or below (seismic peak ground acceleration $A_g \leq 0.3g$).

Structure Configuration. The section type is equal height with single box for single room. The top plate, base plate and web of the beam should be thickened inner side. Bridge deck width includes three parts. The clear width of inner side of protecting wall is 8.8m, the clear width of inner side of pavement steel railing is 11.9m. The width of bridge is 12.0m. The total width is 12.28m. The calculate span is 31.5m. The distance between two bearing centers along direction across bridge is 4.5m.The height of beam in the centre of bridge is 3.084m.

Load.

①Dead load:

Self weight: according to Basic Standard of Railway Bridge Design (TB10002.1-2005).

Secondary dead load: The secondary dead load includes the weight of steel rail, rail fasteners, track plate, mortar bed and other railway equipment. It also contains the weight of ancillary facilities such as waterproof layer, protective cover, protecting wall, pedestrian guardrail etc. It is 160kN/m.

Prestressing force: Control stress for prestressing is 930MPa or 1340MPa.

②Live load: Train vertical live load uses ZK standard live load.

Material Characteristics. Strength grade of concrete is C50. Prestressed steel strand is 1x7-15.2-1860-GB/T5224-2003.

Arrangement of Prestressed Steel Strands. There are 27 steel strands in the section. The tensioning process is divided into two stages, initial tension and final tension.

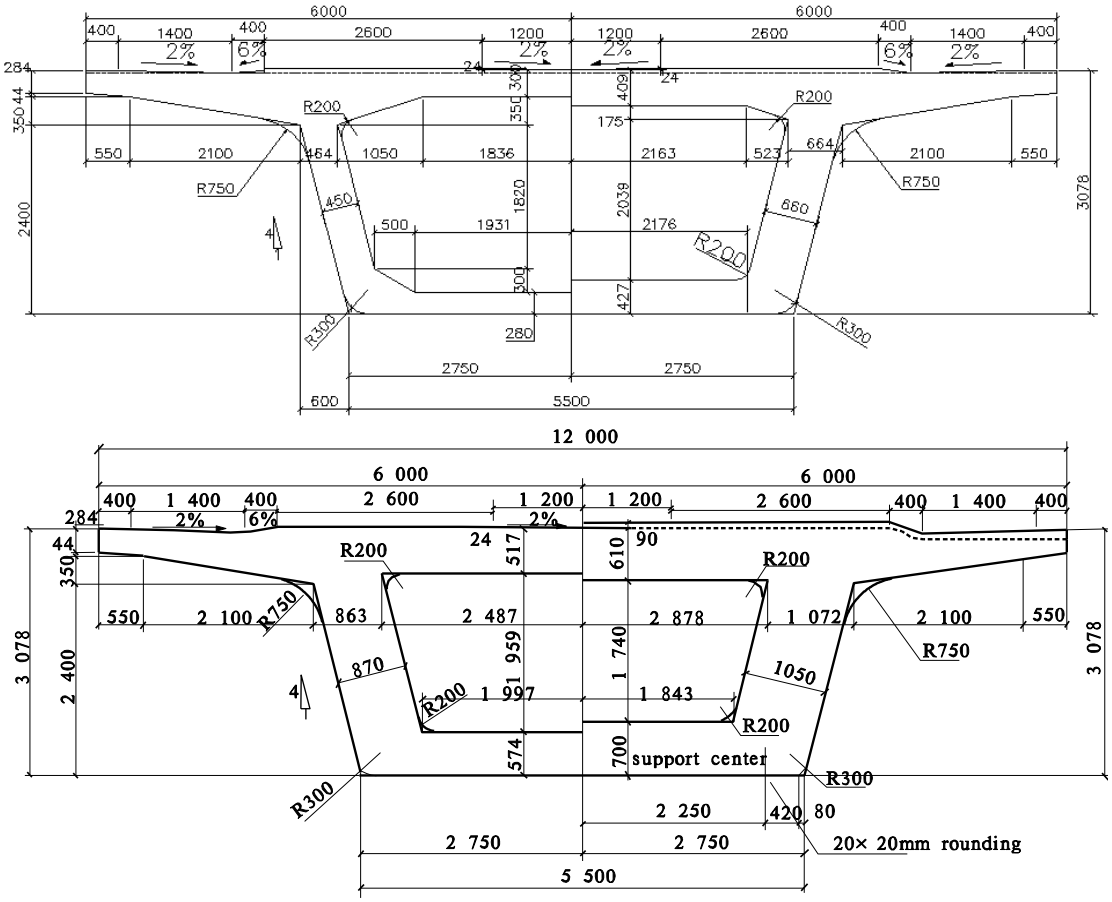


Fig. 1 Section dimension

Finite Element Model (FEM). Set a finite element model. Set a node in every 1m length to build an elementary unit. There are 32 units and 33 nodes. Set four kinds of sections include two PSC sections (in midspan and supports) and two variable sections.

Table 1 Boundary condition definition

Node number	D_x	D_y	D_z	R_x	R_y	R_z	Comment
1	1	1	1	1	0	0	Fixed hinge support
33	0	1	1	1	0	0	Sliding hinge support

Where D_x, D_y, D_z means translational degree of freedom respectively. R_x, R_y, R_z means rotational degree of freedom respectively. ‘1’ means the degree of freedom has been restrained, ‘0’ means this DOF without restrain.

Add the moving load into this model: adopt ZK moving load (include ZK standard load and ZK special load). Because this bridge is long-span continuous girder bridge, ZK standard load more adverse effect. ZK live load is shown as Fig. 2.

Creep calculation. There are various kinds of factors effect concrete creep. In order to discuss effect of the creep parameters on creep deformation and control these factors, we set this model for parameters sensitivity analysis. With the purpose of contrasting the rules of development of the creep between CEB-FIP90 and ACI209, the creep development curve of midspan is shown in Fig. 3.

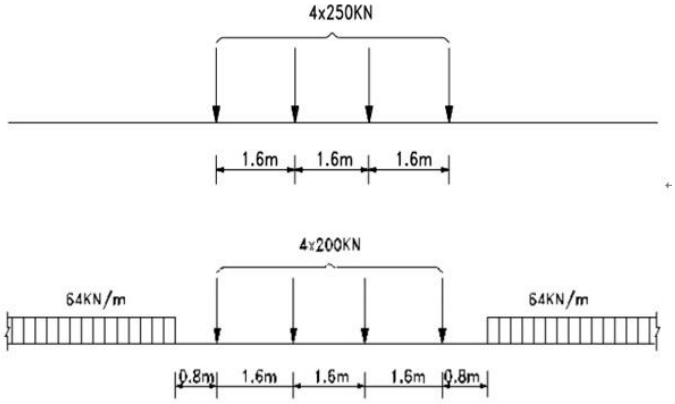


Fig. 2 ZK standard load and ZK special load

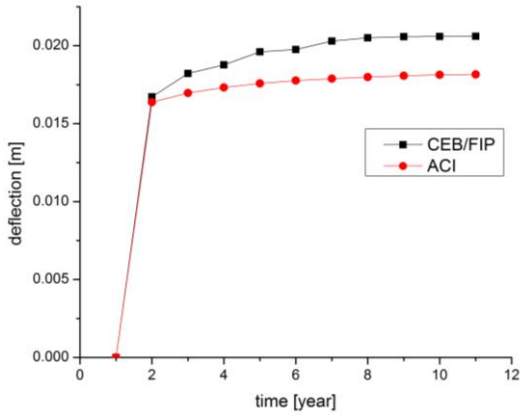


Fig. 3 Creep development curve of midspan

Discuss a Practical Engineering Project to Verify FEM

In order to verify the FEM model, the creep of simply supported box girder of Wuhan-Guangzhou high-speed railway is introduced, which is measured by X.C. Xu et al [9]. The structure is a double-line ballastless track simply supported post-tensioned concrete box gird, and 14 girders were measured. The measured values of mid-span deflection after 60 days of the girders tensioned range from 17.00mm to 20.00mm. Comparison is made with the results of FEM model in Table 2. It can be seen that the value of measurement is a bit larger compared with the value of FEM,

Table 2 Comparison of measurement results and MIDAS model results

Model	Measurement	CEB-FIP	ACI
Values of deflection 60 days after the girders were tensioned [mm]	17.00-20.00	16.03	15.87

Parametric Analysis

The creep coefficient expression and the influence factor considering the creep of two modes are different. Accordance to CEB -FIP model and ACI model, the creep deformations are also quite different. The comparison and analysis of the calculated results based on two standards are as follows. The deflection curve of box girder is shown in Fig. 4.

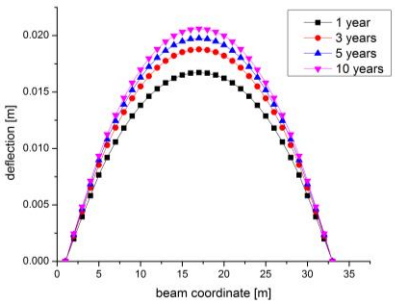


Fig. 4(a) CEB-FIP Model

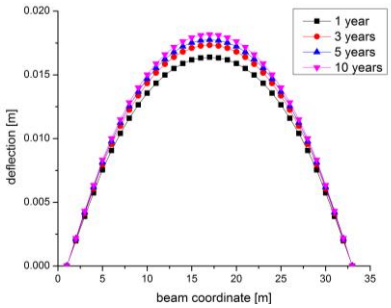


Fig. 4(b) ACI Model

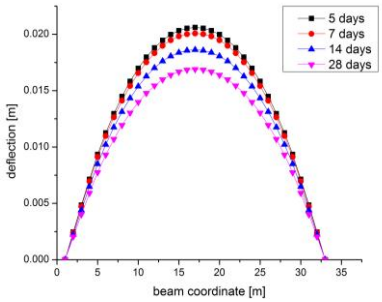


Fig. 5(a) CEB-FIP Model

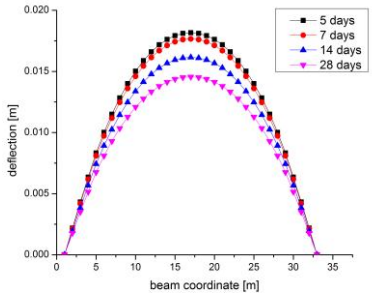


Fig. 5(b) ACI Model

As seen from the Fig. 4, the change laws of the beam deflection of the two models are consistent. As time grows, the concrete creep causes the increase of beam upwarp. The largest upwarp appears in the mid-span, and after the bridge was built, the creep in the previous three years has large influence on the later upwarp of beam [10]. The primary beam deflection caused by the creep in the previous three years accounts for 90% primary beam deflection caused by the creep in the previous ten years.

Loadingage. Comparing different loading ages, the deflection values are calculated after the bridge was built ten years. It is shown in Fig. 5.

It is known that the loading age has a greatly effect on the beam upwarp. Along with the increase of curing age, the whole upwarp is reducing gradually after the bridge was built ten years. When the loading age increases from 5 days to 28 days, the total upwarp is reduced by 16% after the bridge was built ten years. The appropriate growth of curing period can reduce the total upwarp. But the longer loading age can cause the insufficient development of pervious creep, and make the later creep upwarp larger.

According to the computational analysis of the ultimate creep with different loading ages, it can be concluded that with the growth of the concrete loading age, the ultimate creep decreases. Therefore, extending loading period appropriately, on the one hand, can make the ultimate creep decrease, and on the other hand can make the elastic modulus enhance and the elastic deformation value reduce.

Age of Secondary Dead Load. The bridge's later deformation is largely affected by the loading time of the secondary dead load. The secondary dead load was applied at different ages after initial tension. The calculation results of the deflection values after the bridge was built ten years are shown in Fig. 6. It can be seen that the later creep upwarp is largely affected by the loading time of the secondary dead load which is a sensitive control factor. With the time of applying the secondary dead load going backwards, the upwarp of beam increases. But the secondary dead load can reduce stress differences between upper and lower margin, thus it can increase the influence of the creep upon deflection.

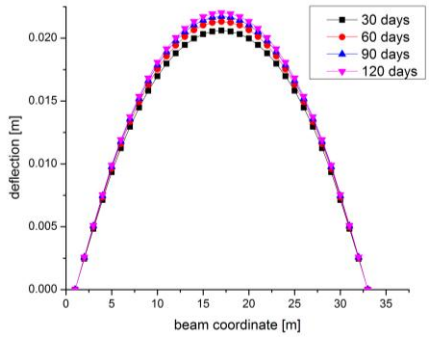


Fig.6(a) CEB-FIP Model

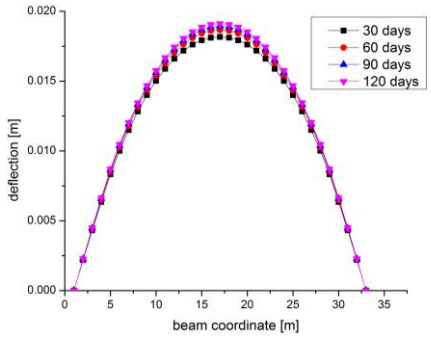


Fig.6(b) ACI Model

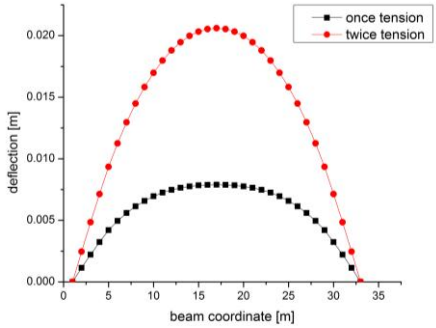


Fig.7(a) CEB-FIP Modle

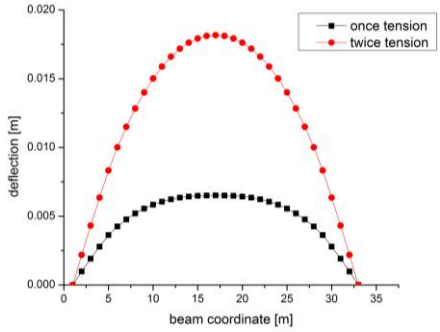


Fig.7(b) ACI Model

Tension Procedure of Presstressed Reinforcing Steel. In order to consider the impact of prestressing upon creep, the simply supported beam is prestressed both with stage tensions (includes initial tension and final tension) and once (once tension will merger initial and final tension). The creeps at later time of the two processing methods are compared. The calculation results after the bridge was built ten years are compared in Fig. 7. It can be known that one-time tension means can reduce later creep deformation. Because of two steps tension, loading age is advanced than one-step tension and concrete creep deformation increases. For simply supported beam by one-step tension, creep deformation in mid-span is reduced by 60% after the bridge was built ten years compared with that of two-steps tension.

Conclusions

In this paper the creep effect of typical 32m simply supported box beam was analyzed by finite element software. The following conclusions can be drawn. As the time grow, the deflection of the girder due to creep increases continuously. The maximum deflection appears at midspan. It about 90% of deflections caused by creep during the first decade, then the increase of deflection of beam slows down. As the increase of curing age, the deflection decreases gradually. If the loading age increases from 5 days up to 28 days, the deflection reduced 16% at the midspan. The loading time of secondary dead load is a sensitive factor which has large impact on the later deflection due to creep. With the time of applying the secondary dead load going backwards, the upwarp of beam increases. By one-time tension, creep deformation is reduced by 60% after the bridge was built ten years compared with that of two-time tension.

A practical engineering project was introduced to compare the actual creep deformation with the theoretical calculation once. The differences are too small that can be ignored. The theoretical calculation values are reliable.

References

[1] G. Zhao, The Structure of High-speed Railway with Ballastless Tracks, China Railway Press, Beijing, 2006.

[2] F. Guo, The structure of passenger dedicated line with ballastless tracks, Railway Standard Design, 2006.

[3] Z. Zeng, The technology of passenger dedicated line with ballastless tracks I, Railway Construction Technology, 2005.

[4] Z. Zeng, The technology of passenger dedicated line with ballastless tracks II, Railway Construction Technology, 2005.

[5] M. Xu, F. Wang, The study of the deflection of simply supported prestressed concrete box beam used in railway bridge based on statistical analysis, China Railway, 11 (1999).

[6] Y. He, The study of post creep deformation of long-span continuous concrete bridge with ballastless tracks, Journal of China Railway Society, 30 (2008) 120-124.

[7] Comité euro-international du béton, CEB-FIP Model Code for Concrete Structures, CEB, 1978.

[8] J.A. Rhodes, D.J. Carreira, Prediction of Creep, Shrinkage and Temperature Effects in Concrete Structures, American Concrete Institute, 1992

[9] X. Xu, W. Zhou, S. Chen, Analysis of the creep of simply supported box girder of Wuhan-Guangzhou high-speed railway, Railway Standard Design, 2 (2010) 78-80.

[10] W.K. Hatt, Notes on the effect of time element in loading reinforced concrete beams, Proceedings of ASTM，(1991) 531-555

[11] Z.P. Bazant, F.H. Wittmann, Creep and Shrinkage in Concrete Structures, New York, 1982.

© (2012) Trans Tech Publications, Switzerland
doi:10.4028/www.scientific.net/AMM.238.738

Static Analysis of Reinforced Concrete Arch-deck Bridge with Archaized Connective Corridors

Xiaoke Li [a], Lixin Liu [b], Shiming Liu [c] and Shunbo Zhao [d]

North China University of Water Resources and Electric Power, Zhengzhou 450011, China

[a]lixk@ncwu.edu.cn, [b]shengxin320@163.com, [c]sokd_0@163.com, [d]sbzhao@ncwu.edu.cn

Keywords: arch-deck bridge, connective corridor, loading property, static analysis.

Abstract. As the requirements of traffic functions and urban landscape, a reinforced concrete arch-deck bridge is designed with archaized connective corridors. The main dimensions and drawings are introduced and the static analytical results of the bridge are discussed in this paper. The numerical model was built by the integrated solution system for bridge and civil engineering- MIDAS/Civil. The results show that the temperature of bridge and the horizontal shift at arch toes due to sedimentation play important roles sensitively influencing the bending moments and displacements of control sections. Compared numerical results of the bridge only with dead loads, the maximum bending moments and displacements would reach 3.81 times and 6.52 times respectively. The axial force of arch is mainly resulted from dead loads, which gradually increases from arch crown to arch toes. The design and numerical results would give some references to similar bridges.

Introduction

A bridge is a landscape, especially for the municipal bridges. The arch-deck bridge is typical in style of bridge with the deck completely above the arch, which is marked by lightness of structural components and architectural expressiveness. Although the other economical structures are used today, it is also applied widely due to the special beauty of deck-arch bridge [1].

The bridge discussed here is an open-spandrel arch-deck bridge with a porch on sidewalks, as shown in Fig. 1. It includes two parallel bridges with 1.0cm gap. Each bridge is partitioned as 0.5m railing+4.7m sidewalk+4.5m non-motor vehicle lane+1.8m green belt+15.75m motorway +0.5m guardrail. The whole bridge is 85.00m long and 55.51m wide. The bridge deck is located along vertical curve with radius of 3500m and the design elevation of top deck of 92.354m. The design water level is 84.594m and the check water level is 85.928m.

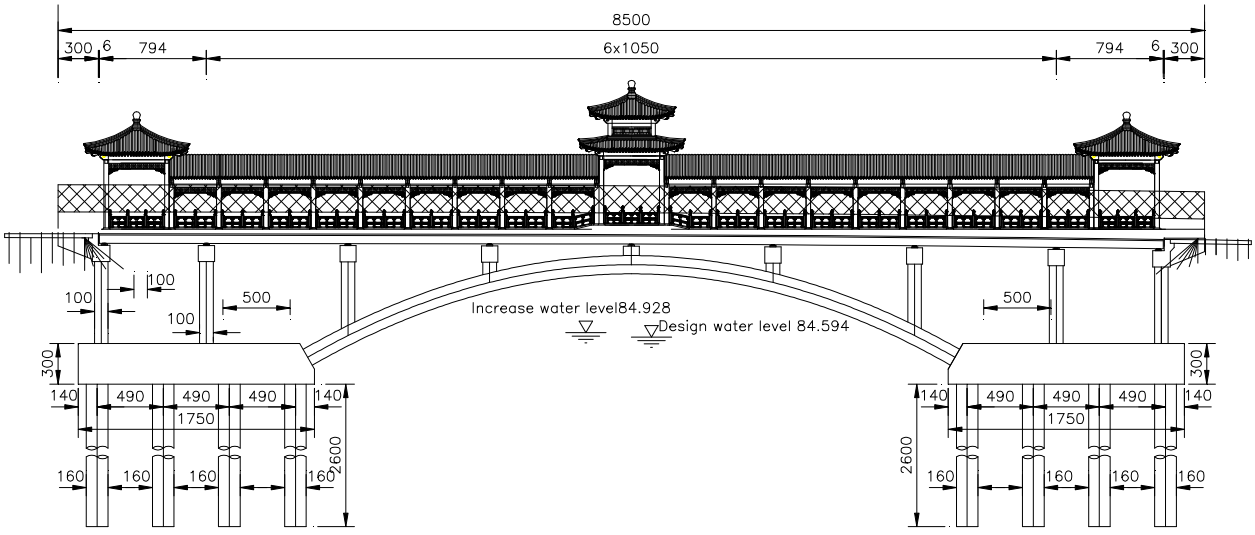


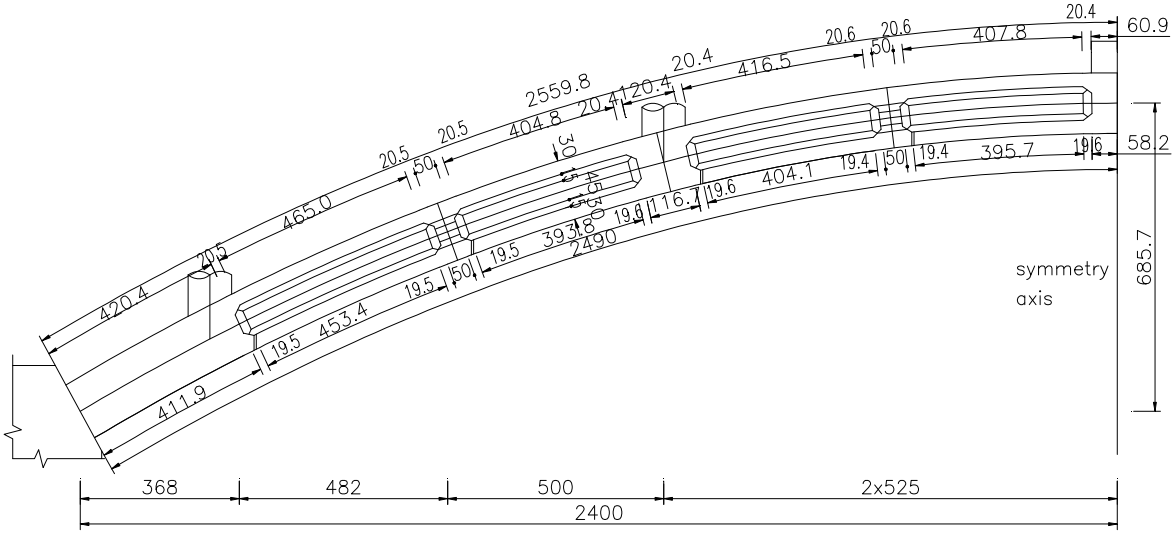
Fig. 1 Longitudinal view of concrete deck arch bridge

As main load bearing part of arch-deck bridge, a non-articulated arch is applied and links the piers with rigid connection. Computed span of arch *l* is 48.0m and computed rise of arch *f* is 6.857. The ratio of rise to span *f*/*l* is 1/7. The axial line of arch obeys a quadric parabola as shown in Fig. 2.

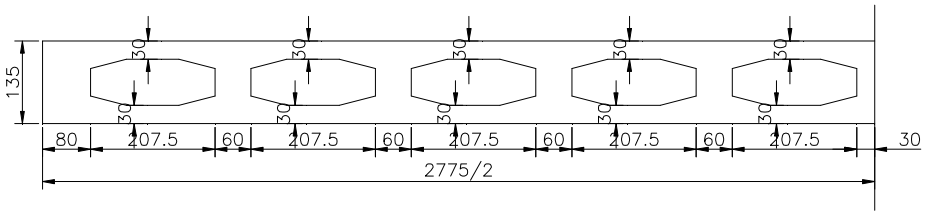
The cross section of arch is a single rectangular box of 27.75m wide divided into 10 rooms. The longitudinal section of arch is divided into 8 segments. That is, there are 80 rooms totally in each arch. Roof and floor thickness in each room are all 0.30m. Side web and middle web width are 0.80m and 0.60m respectively.

27 precast reinforced concrete hollow slabs in each span are put on the top of bridge piers. As the eqements of urban landscape, the archaized connective corridors are designed on sidewalks.

According to the difference of bearing capacity, concrete in strength grade C50 for arch and HRB335 steel bars as main reinforcement are used, more information about materials of the bridge are shown in Table 1.



a) Longitudinal section of arch



b) Cross section of arch

Fig. 2 Dimension of arch

Table 1 Applied materials in deck arch bridge

Component	Arch	Deck slab	Pile caps and piers	Piles
Concrete grade	C50	C40	C30	C25
Lengthways reinforcement	HRB335			
Stirrup	R235			

Numerical Model of Concrete Deck Arch Bridge

Build Numerical Model. Fig. 3 shows three dimensional numerical model of the arch-deck bridge built by MIDAS/Civil. There are 7608 elements and 6079 nodes totally. To confirm the calculating precise and fulfill requirement of engineering, the arch is meshed into 58 beam elements in length not longer than 1.0m. Sections of box girder and hollow slab can be drawn by AutoCAD and sectional characteristics can be obtained by MIDAS/SPC. The piles are simulated with beam elements by fixed all DOFs at bottom nodes. The rigid connections are between arch and pile caps, same as the relationship between arch and piers upper on the arch. The hollow slabs are placed on the top of capping beams or abutments with two-way spring joints. Transverse struts are used to simulate the connection between two contiguous reinforced concrete hollow slabs [2].

Loads and Loads Combination. (1) Dead loads include self-weight, overlaid pavement weight in 2nd phase, weight of archaized connective corridors and so on; (2) Vehicle loads of the arch bridge belong to Highway Class I and pedestrian load is 3.5kN/m^2; (3) The sedimentation of supports is taken as 10mm based on the geological condition in the field; (4) The shrinkage and creep of concrete within 10 years are calculated on the specification; (5) Combined with local atmosphere data, bridge temperature is selected between up 22^{o}C and down 22^{o}C compared with benchmark construction temperature; (6) the longitudinal shift at one arch toe due to sedimentation is ±10mm.

Four load/action combinations are considered as listed in Table 2 [3, 4], named as the comb. I, II, III and IV. Take comb I for example, comb. I=1.2(1) +1.4(2)+0.5(3)+1.0(4)+1.12(5)+0.5(6).

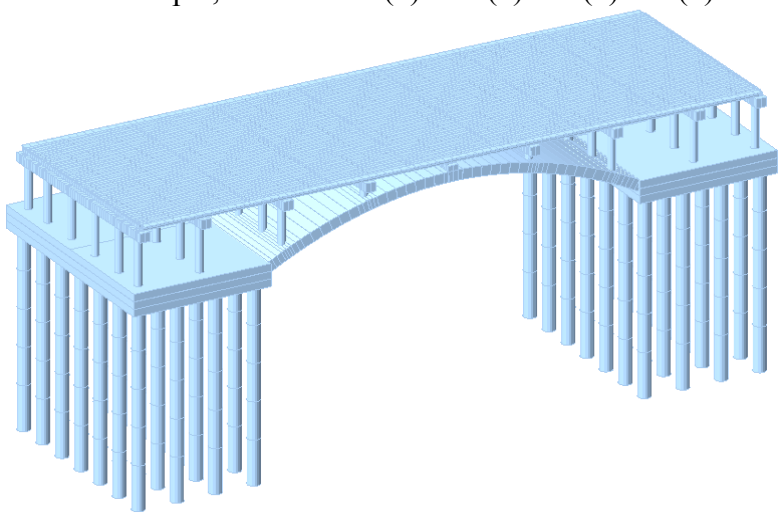


Fig. 3 Numerical model of deck arch bridge

Table 2 Load/action combinations

No. of Combination	Subentry coefficient of load/action							
	Dead load	Vehicle +pedestrian	Sedimentation of supports	Shrinkage /creep of concrete	Entire		Forced displacement	
					Warming	Cooling	+x	-x
	(1)	(2)	(3)	(4)	(5)		(6)	
I	1.2	1.4	0.5	1.0	1.12	-	0.5	-
II	1.2	1.4	0.5	1.0	1.12	-	-	0.5
III	1.2	1.4	0.5	1.0	-	1.12	0.5	-
IV	1.2	1.4	0.5	1.0	-	1.12	-	0.5

Static Analysis

The arch is the key component for keeping safety of whole bridge. Distributions of forces and displacements along arch axis are shown in Fig. 4 and some key values are listed in Table 3.

Bending Moment. Sharp points along bending moment curves can be found apparently at the intersection between arch and piers, as shown in Fig. 4a). The peak values can be obtained from dead loads and comb. I-IV, which are 15859.5kN.m, -26074.8kN.m, 24658.5kN.m, 32582.1kN.m, 75725.7kN.m at arch crown and -24006.5kN.m, -35827.1kN.m, -38894.3kN.m, -54683.1kN.m, -140271.8kN.m at arch springing respectively. Bending moments caused by dead loads is less than other load cases. Distribution curve of comb. I is totally opposite with dead loads and comb. II-IV. It shows that forced displacement of arch springing have remarkable effect on bending moment, compared curves from comb. I and comb. II. The same conclusion is also gotten by comparing curves from comb. III and comb. IV. When one arch springing is far away with anther, bending moments would increase rapidly. Forced displacement is one of key loads for safety of arch. Compared curves from comb. I and comb. III, comb. II and comb. IV, arch temperature is another key load. However, there are not apparent variance of bending moments compared curves from

dead loads, comb. II and comb. III, because of offsetting effect. That is to say, sedimentation displacement of arch toe and arch temperature need be considered seriously to ensure max and min of bending moments along the arch. The results show that bending moments of arch would reach 3.81 times maximally, compared numerical results of bridge only with dead loads.

Axial Force. Axial forces of arch increase gradually from arch springing to arch crown. The maximum axial force will be caught only with dead loads and the maximum pressure is -81914.5kN at arch springing. In other four load combinations, axial forces would be released, as shown in Fig. 4b). The axial force under dead loads is 1.26~7.12times at arch crown and 1.29~3.15times at arch springing than other 4 load combinations. The results show that forced placement and arch temperature are all also key loads for axial force of arch.

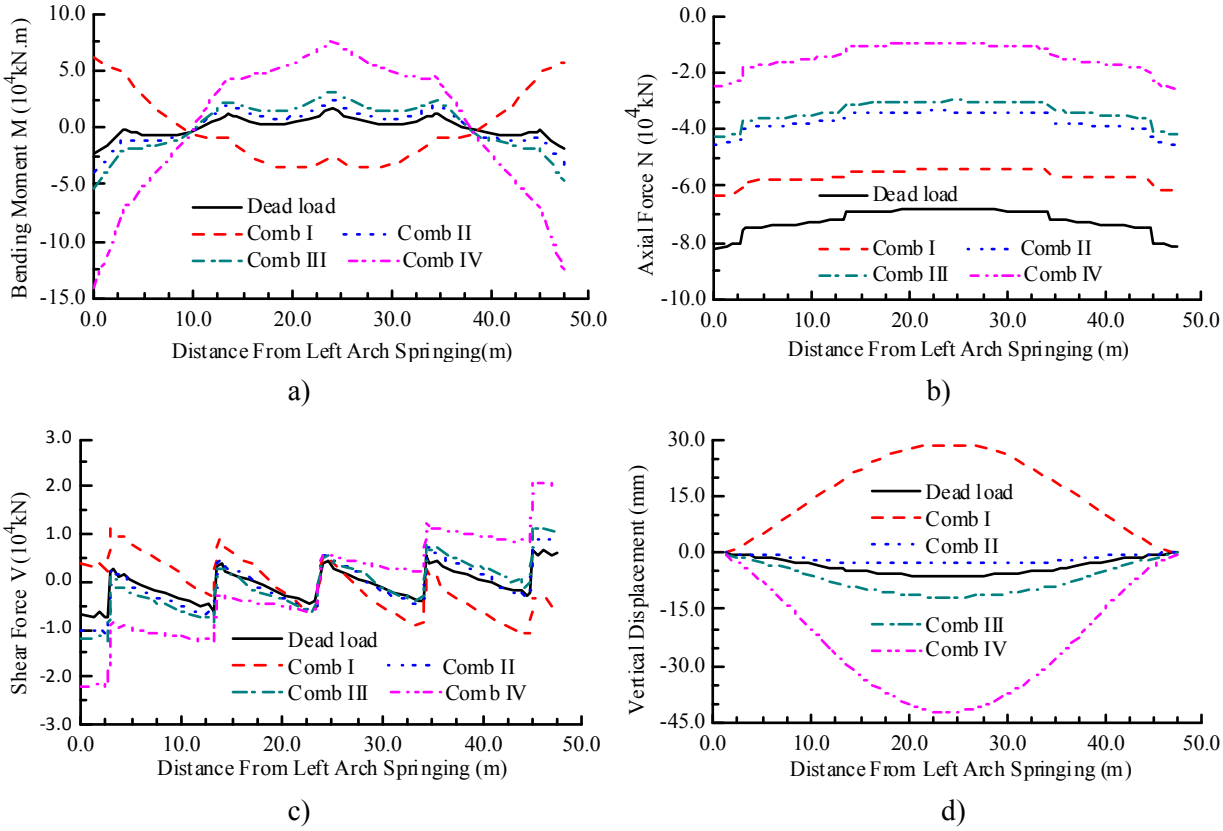


Fig. 4 Forces and displacements of arch during completed bridge phase

Table 3 Internal forces and displacements of arch

Item	Loads or Combinations		Dead load	Comb I	Comb II	Comb III	Comb IV
M (kN·m)	Max	Location	24	0/48	24	24	24
		Value	15859.5	61362.2	24658.5	32582.1	75725.7
	Min	Location	0	19.8	0	48	0
		Value	-24006.5	-35827.1	-38894.3	-54683.1	-140271.8
N (kN)	Max	Location	24	24	24	24	24
		Value	-67962.9	-53796.2	-33527.8	-29850	-9546.7
	Min.at arch springing		-81914.5	-63323.1	-46163.7	-43039	-25997.4
V (kN)	Max	Location	45.6 m	3.6 m	45.6	45.6 m	48 m
		Value	7626.5	11643.3	10710	12546.9	21752
	Min	Location	2.4 m	44.4 m	2.4 m	2.4 m	0 m
		Value	-7593.3	-11492.6	-10836.4	-12352.2	-21937
Arch max vertical displacement (mm)		Value	-6.48	28.52	-2.82	-11.81	-42.24

Shear Force. Sudden changes of shear force would happen at the intersection between arch and piers, as shown in Fig. 4c). The shear force caused by dead loads is smaller than comb. I-IV. Compared 5 curves of shear forces of the arch, the maximum shear force can be obtained at arch springing and the value is 21937.0kN.

Displacement. The peak displacement could be caught at arch crown. The vertical displacements are -6.48mm, 28.52mm, -2.82mm, -11.81mm and -42.24mm at this point under dead loads and comb. I-IV, as shown in Fig. 4d). Arch warming would lead to arch expansion. Closing one arch toe to another would lead to upwardly convex. On the contrary, arch cooling would lead to arch contraction and putting away one arch toe to another would lead to arch settlement. Then the maximum displacement happened under comb. I and the minimum happened under comb. IV. Compared numerical results of bridge only with dead loads, the displacements would reach 6.52 times maximally under comb. I-IV.

Conclusions

The numerical model of reinforced concrete arch-deck bridge was built in details by Midas/Civil. The piles, pile caps, piers, bent caps, deck slabs and connections between two contiguous reinforced concrete hollow slabs were all simulated. The forces and displacements of arch under the given loads and load combinations can be calculated close to the actual values.

The distributions of bending moment, axial force, shear force and vertical displacement along the arch axis prove that sedimentation displacement of arch toe and arch temperature are the key factors and need to be considered seriously during design process.

Load comb. IV is the control load combination for bending moment, the maximum bending moment can be decided at arch crown and arch toe. Dead loads are the control loads for axial force. Comb. IV is the control load combination for shear force at arch toe and for vertical displacement at arch crown.

References

[1] Information on http://en.wikipedia.org/wiki/Arch_bridge.

[2] S. Qiu, Midas for Bridge Design: Frequently asked questions, China Communications Press, Beijing, 2009.

[3] JTG D60-2004, General Code for Design of Highway Bridge and Culverts, China Communications Press, Beijing, 2004.

[4] JTG D62-2004, Code for Design of Highway Reinforced Concrete and Prestressed Concrete Bridge and Culverts, China Communications Press, Beijing, 2004.

© (2012) Trans Tech Publications, Switzerland
doi:10.4028/www.scientific.net/AMM.238.743

Effect of Pile-soil Action on Seismic Resistance of Prestressed Continuous Box-girder Bridge with Changed Sections

Fenglan Li[a], Shimin Zhang[b] and Shiming Liu[c]

School of Civil Engineering and Communication, North China University of Water Recourses and Electric Power, Zhengzhou 450011, China

[a] lifl64@ncwu.edu.cn, [b] alin2514@163.com, [c] sokd_0@163.com

Keywords: prestressed continuous box-girder bridge; seismic resistance; response spectrum; pile-soil action.

Abstract. Combined with the design of a bridge with prestressed concrete continuous box-girder, and in accordance with the Chinese guidelines of seismic design for highway bridge, the numerical models with and without considering the pile-soil action were built using Midas Civil software. The response spectrum method was used to analyze the seismic response of the bridge under E1 and E2 seismic actions. The vibration characteristics such as frequency, period and mode as well as the internal forces and displacements of piers are discussed in view of the effect of the pile-soil action.

Introduction

The south-to-north Water Transfer Project is one of the key engineering solving the long-term lack of water resources in the northern of China. As the engineering passes the seismic area, it is necessary to study the seismic resistance of the structures [1]. Aiming at providing design reference for these structures, this paper selected the typical structure, the bridge with prestressed concrete continuous box-girder, to do the seismic analyses.

The bridge was designed to be constructed on the main channel linking up the national-class highway across the channel in Xingtai city of Hebei province, China, which is 32.01m wide with 2× (15.5m vehicle lane+ 0.5m isolation belt) and a separation in 10mm wide at center in longitudinal direction [2]. As shown in Fig. 1, the structure of the bridge comprises the three span prestressed concrete continuous box-girder with changed section, the reinforced concrete piers with solid thin-thickness section, the reinforced concrete abutments and the reinforced concrete cast-in-place piles. Each vehicle lane was designed as the prestressed concrete continuous box-girder, the changed longitudinal section and the transversal section with three rooms are shown in Fig. 2 and Fig. 3. The arrangement of supports for single lane is shown in Fig. 4, 1# pier acts as brake marked by GD on top center, the symbol DX, SX mean the supports permitting displacement along single and double directions respectively [3, 4]. The strength grades of box-girder, abutments and piers are C50, C30 and C30. The foundation is the fractional pile with 1.6m diameter and C25 concrete.

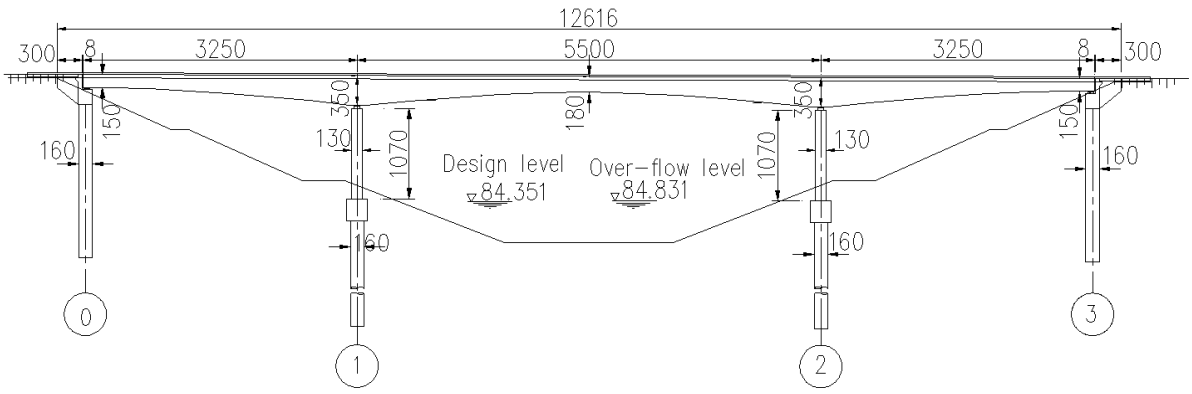


Fig. 1 Longitudinal side-view of the bridge (cm)

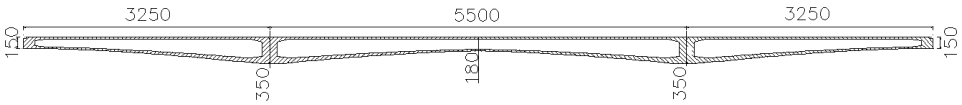


Fig. 2 Longitudinal section of the bridge (cm)

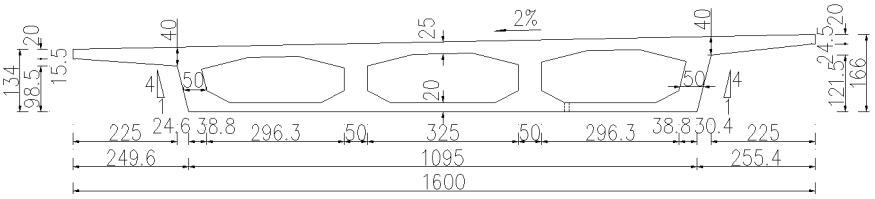


Fig. 3 Half mid-span transversal section of the bridge (cm)

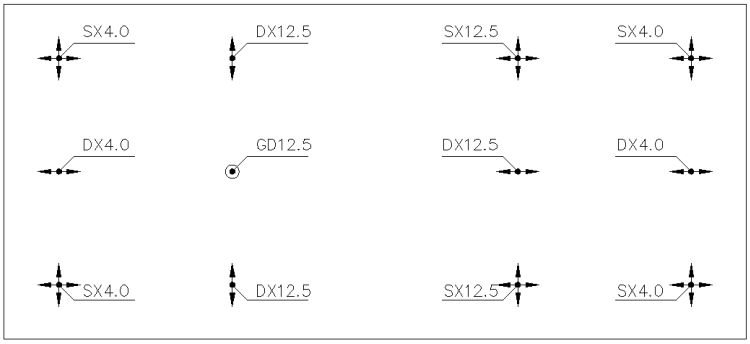


Fig. 4 Arrangement of supports of single lane

Numerical Models of the Bridge

The single vehicle lane of the bridge is selected to build the numerical model.

Model 1 Considering Pile-soil Action. As shown in Fig. 5, the box-beam, the piers and the piles were all simulated by the space beam-element, the whole bridge was simulated by 264 beam-elements and 126 spring elements. The sectional characteristics such as the rigidities of bending, torsion and shear, the centroid and the inertia moment were automatically computed by the software according to the drawings of the bridge [5]. The boundary conditions were simulated as follows: the nodes were made at the real place of supports at bottom of box-girder and recopied downward for the height of support to produce the bottom nodes of supports, the normal elastic linkages were made between the nodes at bottom of box-girder and those of support bottom, while the nodes at bottom of box-girder were rigidly linked on the beam, the nodes at bottom of supports were rigidly linked on the top of piers, and the nodes at bottom of supports on abutment were fixed. The interaction between pile and soil was simulated by the equivalent soil spring element with stiffness calculated by “m” method [6].

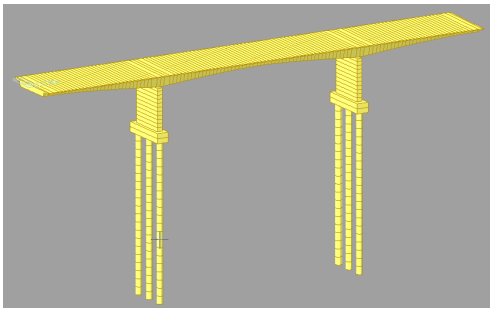


Fig. 5 FEM mode 1

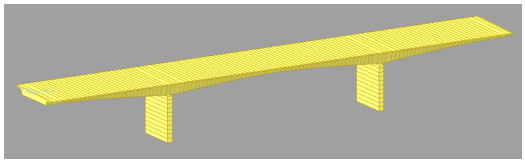


Fig. 6 FEM mode 2

Model 2 without Considering Pile-soil Action. This model did not consider the pile-soil action and neglected the effect of abutment, as shown in Fig. 6, 140 beam-elements were totally divided for the box-beam and piers. The boundary conditions were the same as the model 1 except that the nodes on bottom surface of piers were fixed.

Numerical Results and Analyses

Characteristic Values. The frequencies and periods of the first top 100 modal were obtained by the modal analysis using the multiple Ritz Vector Method. Theoretically, all modes should be included in the response calculation. However, in view of the seismic characteristics of bridge, the seismic action mainly arouses a few of modes with lower frequency, the modes with frequency larger than certain value could be neglected as their smaller contributions to the seismic response. In the accordance with Chinese code JTG/T B02-01-2008, when the calculation was made by multi-mode response spectrum, the number of mode considered in the calculation direction should reach the effective mass above 90%. Therefore, the first 15 modes of the two numerical models may represent the seismic response of the bridge, the results are listed in Table 1 and Table 2 respectively.

Table 1 The first top 15 modal vibration frequency and mode description of Model 1

Mode	Frequency (Hz)	Period (s)	Mode description
1	0.464	2.156	Longitudinal vibration of whole bridge with bend of 1# pier
2	2.019	0.495	Transversal vibration of whole bridge with synchronous bend of piers
3	2.230	0.448	Symmetrical vertical bend of box-beam, longitudinal bend of 1# pier
4	2.756	0.363	Transversal vibration of whole bridge with asynchronous bend of piers
5	3.089	0.324	Longitudinal bend of 2# pier
6	4.388	0.228	Symmetrical transversal bend of box-beam
7	4.457	0.224	Antisymmetrical vertical bend of box-beam, longitudinal bend of 1# pier
8	5.631	0.178	Symmetrical vertical bend of box-beam
9	8.213	0.122	Antisymmetrical vertical bend of box-beam, longitudinal bend of piers
10	8.646	0.116	Antisymmetrical transversal bend of box-beam with asynchronous bend of piers
11	9.897	0.101	Longitudinal bend of 1# pier
12	14.137	0.071	Symmetrical transversal bend of box-beam with synchronous bend of piers
13	15.708	0.064	Transversal and longitudinal bend of piers
14	15.783	0.063	Transversal and longitudinal bend of piers
15	16.004	0.062	Vertical bending of box-beam, longitudinal bend of piers

Table 2 The first 15 vibration frequency and mode description of Model 2

Mode	Frequency (Hz)	Period (s)	Mode description
1	0.738	1.356	Longitudinal vibration of whole bridge with bend of 1# pier
2	2.090	0.479	Transversal vibration of whole bridge with synchronous bend of piers
3	2.235	0.447	Symmetrical vertical bend of box-beam, longitudinal bend of 1# pier
4	2.795	0.358	Transversal vibration of whole bridge with asynchronous bend of piers
5	4.389	0.228	Symmetrical transversal bend of box-beam
6	4.462	0.224	Antisymmetrical vertical bend of box-beam, longitudinal bend of 1# pier
7	5.630	0.178	Symmetrical vertical bend of box-beam
8	6.217	0.161	Longitudinal bend of 2# pier
9	8.207	0.122	Antisymmetrical vertical bend of box-beam, longitudinal bend of piers
10	8.671	0.115	Antisymmetrical transversal bend of box-beam with asynchronous bend of piers
11	13.025	0.077	Symmetrical vertical bend of box-beam, longitudinal bend of 1# pier
12	14.139	0.071	Symmetrical vertical bend of box-beam, longitudinal bend of 1# pier
13	14.192	0.070	Symmetrical transversal bend of box-beam
14	16.635	0.060	longitudinal bend of 1# pier
15	26.597	0.038	Symmetrical transversal bend of box-beam

It can be seen that the first mode is the longitudinal vibration of whole bridge, the second mode is the transversal vibration of whole bridge. The behind vertical vibration explains that the vertical stiffness of the bridge is enough to resist the plain seismic actions. The vibration period of first mode of model 1 elongates obviously, while the first 4 modes of the two models have the same characteristics. From the 5th mode, the mode appeared in model 1 delay in model 2. The pile-soil action makes the bridge structure flexible with small entire stiffness, longer period and obvious changes of vibration characteristics.

Response Spectrum. The internal forces of these two models are listed in Table 3 and Table 4 considering the longitudinal and transversal seismic input under E1 and E2 seismic actions.

Table 3 Internal forces of piers under E1 seismic action

Pile No.	Place	Longitudinal seismic input				Transversal seismic input			
		Shear force (kN)		Moment (kN·m)		Shear force (kN)		Moment (kN·m)	
		Model 1	Model 2	Model 1	Model 2	Model 1	Model 2	Model 1	Model 2
1#	Top	1115.2	1504.7	0	0	1709.1	1533.4	20988.5	8229.4
	Bottom	1146.8	1535.8	12079.8	16324.7	1763.7	1550.0	2573.6	8265.2
2#	Top	24.0	18.5	0	0	1669.5	1498.0	20406.4	8040.0
	Bottom	358.7	213.8	2430.6	1605.8	1707.0	1514.9	2398.0	8076.5

Table 4 Internal forces of piers under E2 seismic action

Pile No.	Place	Longitudinal seismic input				Transversal seismic input			
		Shear force (kN)		Moment (kN·m)		Shear force (kN)		Moment (kN·m)	
		Model 1	Model 2	Model 1	Model 2	Model 1	Model 2	Model 1	Model 2
1#	Top	3791.6	5948.8	0	0	5810.8	6062.4	71361.1	32534.8
	Bottom	3899.2	6071.7	41071.2	64539.4	5996.5	6128.0	8750.2	32676.3
2#	Top	81.8	73.3	0	0	5676.4	5922.3	69381.6	31786.2
	Bottom	1219.5	845.1	8263.9	6348.6	5803.7	5989.1	8153.3	31930.5

It can be seen that almost all of the longitudinal inertial force of box-beam was undertaken by the brake pier (1# pier) while the small part was undertaken by 2# pier, the transversal inertial force was almost equally undertaken by 1# and 2# piers. Therefore, the longitudinal vibration was controlled by 1# pier, the transversal vibration was controlled by 1# and 2# piers. Under transversal seismic, the moment at bottom of pier in model 1 is smaller, the moments at bottom and top of pier in model 2 are basically equal, which means that pile-soil action makes the weak section move on the top of pier and reduce the possibility of the failure of bottom.

The displacements on top of piers under E1 and E2 seismic actions are listed in Table 5. It can be seen that the pile-soil action makes the longitudinal displacement on top of piers increase as it makes the pier flexibility.

Table 5 Displacements on top of piers under two seismic actions

Pile No.	E1 seismic action				E2 seismic action			
	In longitudinal direction (cm)		In transversal direction (cm)		In longitudinal direction (cm)		In transversal direction (cm)	
	Model 1	Model 2	Model 1	Model 2	Model 1	Model 2	Model 1	Model 2
1#	2.33	1.15	0.07	0.02	7.91	4.54	0.24	0.07
2#	0.49	0.10	0.07	0.02	1.66	0.38	0.23	0.07

Conclusions

From the numerical results of the prestressed concrete continuous box-girder bridge with changed sections, the effects of pile-soil on seismic resistance may be concluded as follows:

The first, second and third modes respectively correspond to the longitudinal, transversal and vertical vibration of whole bridge under longitudinal and transversal seismic actions, which reflects the structural characteristics of the bridge with prestressed concrete continuous box-beam.

The braking effect of 1# brake pier is obvious in longitudinal direction while the brake was taken place in transversal direction by 1# and 2# piers at the same time.

The pile-soil action makes the bridge structure flexibility with small entire stiffness, longer period and obvious change of vibration characteristics. It reduces the internal forces at bottom of piers and increases the displacements on top of piers.

References

[1] H. Wang, B. Zhang and J. Zhou: Study on safety of seismic resistance of South-to-north Water Transfer Engineering, South-to-north Water Transfer and Water Technology, 5 (2004) 1-3.

[2] F. Li, S. Zhang and S. Liu: Effect of side-web slope on loading properties of prestressed continuous box-girder bridge with changed sections, Advanced Materials Research, Vols. 446-449 (2012) 1333-1336.

[3] L. Fan: Seismic Resistance of Bridge, Tongji University Press, Shanghai, 1997.

[4] Chinese Code JTG/T B02-01-2008: Guidelines for Seismic Design of Highway Bridges. China Communication Press, Beijing, 2008.

[5] S. Qiu: Normal Question Explain for Bridge Software MIDAS/Civil, China Communication Press, Beijing, 2009.

[6] Chinese Code JTG D63-2007: Code for Design of Ground Base and Foundation of Highway Bridges and Culverts, China Communication Press, Beijing, 2007.

© (2012) Trans Tech Publications, Switzerland
doi:10.4028/www.scientific.net/AMM.238.748

The Research of Steel Bracket Jacking Experiment in Long Span Continuous Beam Bridge

Chen Zhou[1, a], Quansheng Yan [2,b], Hengbin Zheng [1,c] and Guo wei[1,d]

[1]School of Civil Engineering and Transportation, South China University of Technology, Guangzhou 510640, China

[2]School of Civil Engineering and Transportation, State Key Laboratory of Subtropical Building Science, South China University of Technology, Guangzhou 510640, China

[a]gscz19861985@126.com, [b] cvqshyan@scut.edu.cn, [c]hbzh1984@126.com
[d]guoweiscut@gmail.com

Keywords: bridge jacking; steel bracket; elasto-plastic; finite element; experiment.

Abstract. Bridge jacking technique in the old bridge reconstruction project have broad application prospect, this paper is aim to share the bridge jacking technique and design the steel bracket as the load carrying platform. The finite element calculation is conducted by ANSYS software considering the concrete material nonlinearity with reasonable stress-strain relationship of concrete and element type. Compared with the experimental data, the model reliabilities and the results of two test programs are evaluated. We can conclude that the second structure form of this paper is safer, which can provide the meaningful guidance for similar projects.

Introduction

With the development of economy, the traffic volume has been a great increase in the past decade, the density of vehicles and weights are bigger and bigger, the bridge under clearance is insufficient, bridge bearing and its function could not meet the requirement of traffic, adversely cause serious safety problems. If these bridges are demolished and rebuilt again, not only the cost is higher, but also that can cause great waste, and at the same time, accompanying by the negative social influence, because some bridges' bearing capacity can still meet the using requirement[1, 2]. Naturally, taking bridge jacking construction technique can solve these problems, but this technique is a higher difficult construction method with great risk factors. So we need theory calculation of construction schemes and experimental research, to ensure the safety reliable construction plan.

In jacking process, the strength and stability of jacking support platforms are very important, which have a significant impact to the construction safety. The steel bracket jacking for stress support platform was put forward [3]. Basing on the Beijiang river bridge jacking engineering of Fokai highway expansion, we design the steel bracket as the support platform in jacking process. Due to the union of steel and concrete, which are easy to cause concrete cracking, that means we may not consider these materials as elastic stuff but take into account of the material nonlinearity influence. Considering the above factors, we conduct theoretical calculations and experimental studies of two designing test schemes and analyze their structural safety and practicality.

Engineering Background

Beijiang river bridge of Fokai highway expansion, jacking ranges are: 1 # ~ 22 # (3 league 21 holes 420 m), 45 # ~ 58 # (2 league 13 holes 240 m), the original bridge structure form is: single deck wide12.098 m, bridge panel thick 0.2 m, 4 pieces of 20 m flange beam, the beam height 1.1 m, girder weight 19.8 tons, 6 holes, or 7 hole for a united league, the whole structure is a continuous beam bridge. The infrastructure is 1.4 m wide and 1.3 m high cover beam with diameter of 1.1 m pillar, pile foundation is diameter of 1.2 m reinforced concrete bored piles, jack height is 0.150 ~ 1.51 m. Directly jack up the cover beam to raise cushion stone in smaller jacking height. Construct through planting chemical anchor bolts at two sides of cover beam, weld the steel bracket to support jack to rise flanged beam, then use cushion stone to drive up the stone bridge.

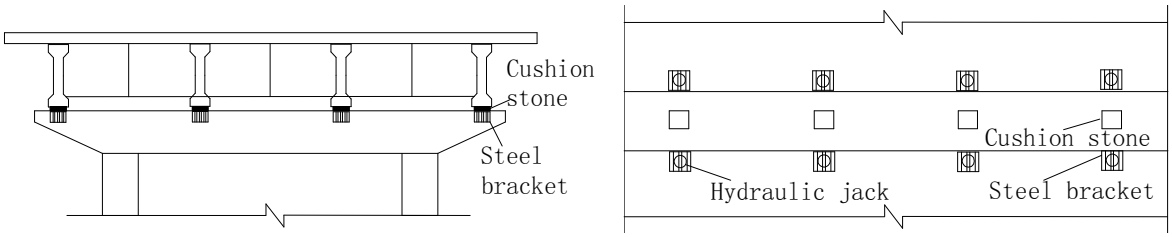


Fig. 1 Sketch map of jacked jack on the cover beam

Test Program

Because this technique is new both at home and abroad, having less reference of actual engineering, so we must conduct the finite element calculation and experimental research. In order to perform the comparison, we design two kinds of steel bracket scheme, which both use two root specifications of joist steels with I32×40cm dimensions, fixed thickness is 20 mm, each side of webs range set three pieces of ribs with 12 mm thick. Embedded 20 mm thick steel plate, the distance between the loading center and embedded steel plate is 15cm. Considering the column bearing upper constant load, adding the eccentric (caused by nonuniform jacking), construction temporary load, function of dynamic force and so on, the load factor will be multiplied by safety coefficient 1.2, calculation load and test load are both 570 kN, loading area is the radius of 11cm circle. scheme i: using planting glue to implant 16 root 6.8 magnitude rubber carbon steel rebar (Φ 16×250 mm); scheme ii: using planting glue to implant 16 root 6.8 magnitude rubber carbon steel rebar (Φ 20×300 mm).

In the process of test, based on 10%, 30%, 50%, 70%, 90%, 100% six levels of loading order and 90%, 50%, 0 three levels of unloading order, every time the loading or unloading stage was finished, waiting five minutes to collect data under stable stress numerical circumstance.

Concrete Elasto-plastic Analysis Theory and Model

Selection of Element Type. The difficult of reinforced concrete structure's finite element analysis is the accurate description of concrete material, concrete is regarded as a hybrid material, the constitutive relation is very complex, this paper use ANSYS finite element analysis software to analyze. ANSYS software has solid65 element type to specifically analyze reinforced concrete structure and relevant concrete material [4]. Solid65 is developed on the basis of solid45, which is dedicated to the concrete, rock with non-uniform material properties that compression strength far outweigh the tensile ability, meanwhile, this element type can reflect the crushing and cracking of the concrete, and compare the comprehensive definition of concrete strength criterion. Steel structure is calculated by solid45 element, through calculation of steel stress, we find its stress is still in the elastic range, so we only consider the linear elastic property of steel bracket.

Concrete Constitutive Model Selection. The multi-linear isotropic strengthen model (MISO) is adopted to simulate the constitutive relationship of concrete in this paper, this model use multi-linear isotropic strengthen features to express the stress-strain curve, which is suitable for the description according to the proportion loading and big strain analysis, along with the isotropic strengthen Mises yield criterion [5], and the ideal elasto-plastic model, the stress-strain relationship is shown as Fig. 2.

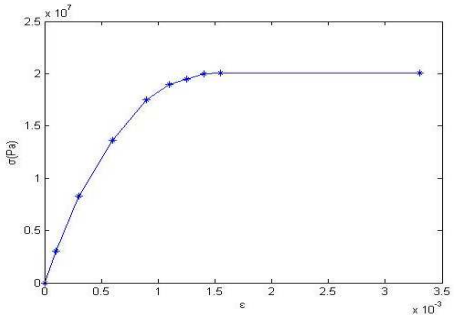


Fig. 2 Stress-strain Relationship Curve of Concrete

Model and Mesh. We use three dimensional entity elements to build model, suppose that the bonding of implanted steel rebar and concrete is good with no sliding. The common boundary conditions of concrete and steel reinforced is realized by segmentation. Due to the test is upon on the C30 cover beam with implanted steel rebar, cover beam is 1.4×1.3m. In order to save the computational time and space, and consider the stress of the concrete area, we select volume of 0.8×0.8×0.65m as concrete area, the calculation results show that, outside the scope, concrete structural boundary stress are tended to be uniform, which means that the selection of concrete volume is appropriate. Meanwhile this pattern constraint the all surface of implanted steel rebar.

In order to lower the difficulty of convergence, we close the concrete crush settings. Segmenting concrete around the anchor bars, so it is easy to grid division and beneficial to the convergence; Element number of scheme i is 102932, scheme ii is 103026, opening the large deformation effect, we adopt the displacement convergence criteria, the accuracy of convergence is 3% [6].

Theoretical Calculation and Test Results

Results of Two Groups of Scheme Theory Calculation Analysis. From calculation results by considering concrete material nonlinear features, we can get the maximum tensile stress, scheme i is 2.81MPa, scheme ii is 2.42MPa, which both exceed the ultimate tensile strength of C30 concrete, that means these structure will appear concrete cracks phenomenon under design load, but basically these cracks are appeared at surface concrete around the implanted steel rebar and a small part of the upper model. So in the test process, we need to watch the crack of surface concrete around the implanted steel rebar, when there have crack phenomenon, we need to control the loading series. Compared results from two schemes, in the same grade load, the stress of scheme i is larger than that of scheme ii, and scheme i has a larger crack area, meanwhile, the displacements of typical node in scheme i is also larger than that in scheme ii. From Fig. 5 and Fig. 6, we can find two structure forms are both having concrete crack phenomenon, but 570 KN load does not reach the limit load.

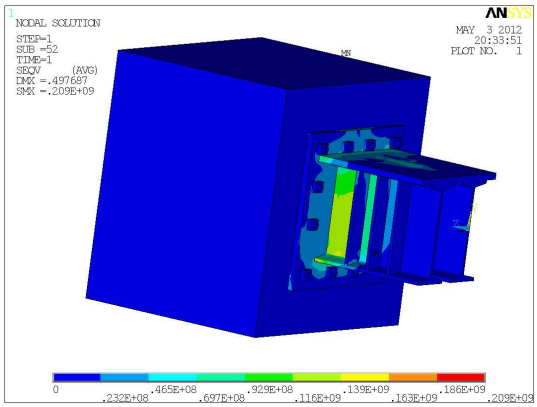


Fig. 3 Combination stress of scheme i

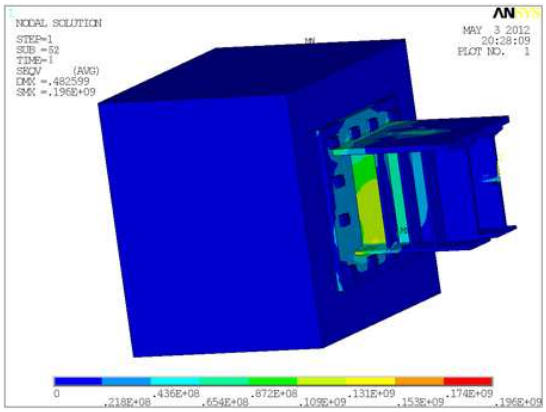


Fig. 4 Combination stress of scheme ii

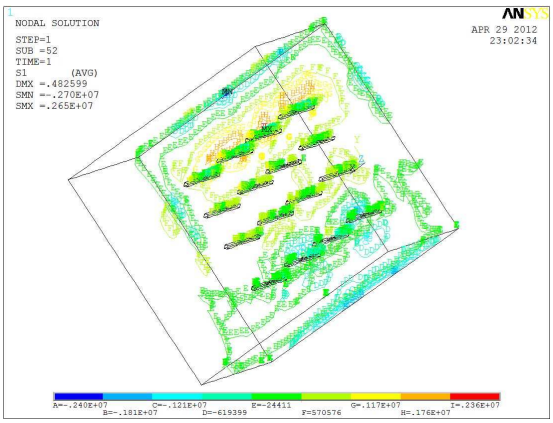


Fig. 5 The first concrete principal stress of scheme I

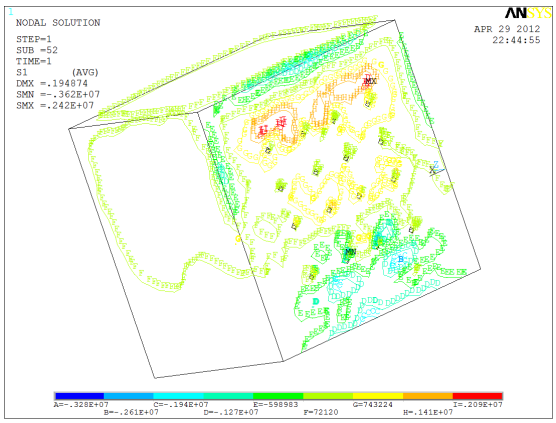


Fig. 6 The first concrete principal stress of scheme ii

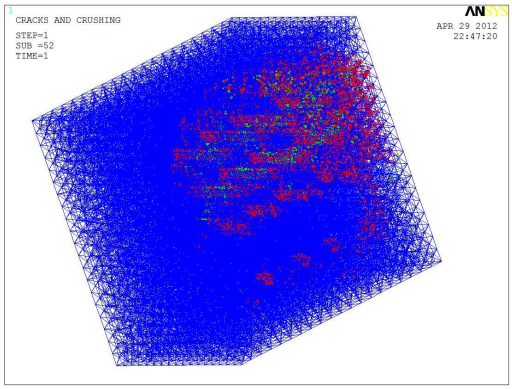


Fig. 7 Crack figure of scheme i

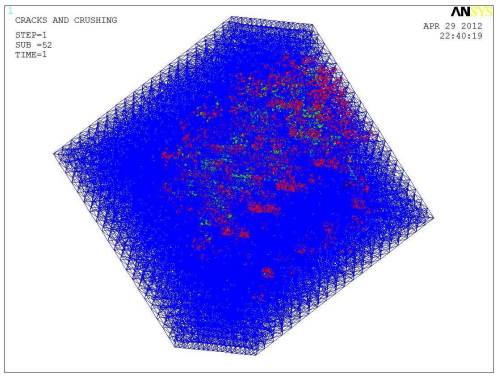


Fig. 8 Crack figure of scheme ii

（Note: Red means the first crack, green means the second crack）

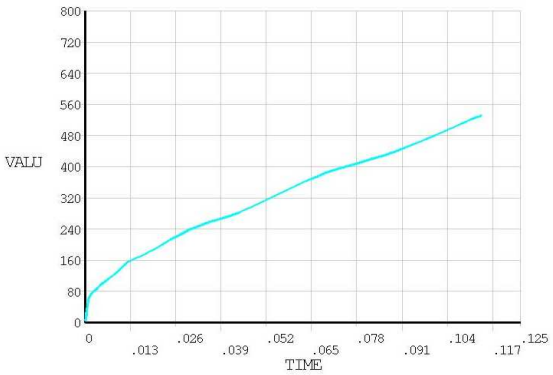


Fig. 9 Force-displacement curve of typical node of scheme i

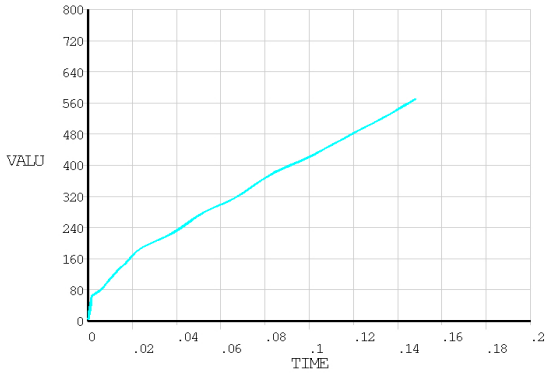


Fig. 10 Force-displacement curve of typical node of scheme ii

（Note: Typical node refers to the largest regional center point of stress）

The Contrast Test Results of Two Schemes. Although the concrete surface stress test is not convenient without knowing its stress value, we can observe through the concrete surface crack phenomenon after test, conclude that the finite element numerical calculation gets on well with the test result, surface concrete both had cracks around implanted steel rebar, concrete structure did not appear the large area destruction. At the same time, the crack phenomenon of scheme i is more obvious than that of scheme ii, the stress-loading level changing relationship curve of steel bracket ribs are shown in Fig. 13 and Fig. 14, we can notice that stress-loading level changing relationship curve of steel bracket ribs have a linear change, which means that steel bracket still work in elastic range, and the finite element calculation agree with experimental value well.

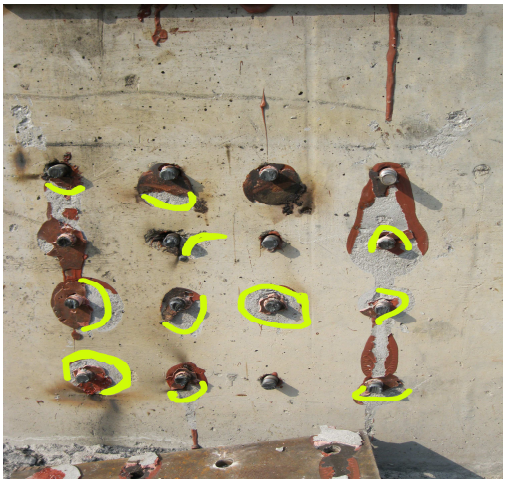


Fig. 11 Concrete surface crack figure of of scheme i After test



Fig. 12 Concrete surface crack figure of scheme ii after test

（note: yello marks refer to the concrete cracks）

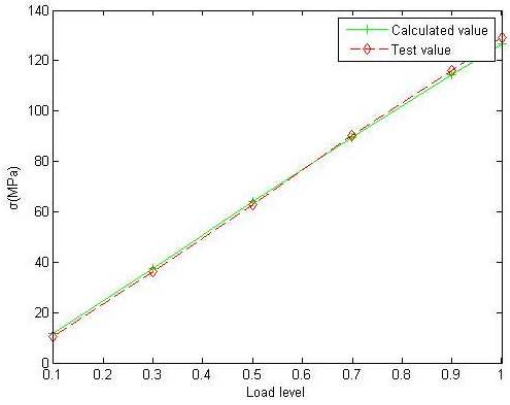


Fig. 13 Stress-loading level relationship of steel bracket ribs of scheme i

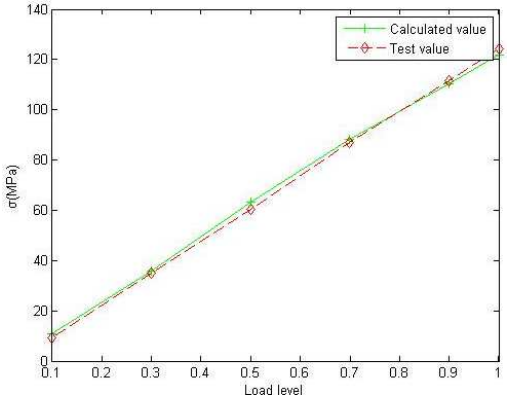


Fig. 14 Stress-loading level relationship of steel bracket ribs of scheme i

Conclusions

Steel bracket ribs are used as bridge jacking work platform, having less application both at home and abroad, and the study is also very few, the study of this paper mainly have following conclusions:

Through the finite element calculation and real test of the two schemes, the compared results illustrate that the solid65 element type of ANSYS software can analyze concrete elastic-plastic property with good results.

Although the concrete surface appeared crack, when loading to 570 KN, the structure did not lose bearing capacity, the maximum stress of steel bracket is less than that of Q235's design strength, and due to stress concentration, which then lead to bigger local stress. But these results indicate that the supported structure can achieve the strength and stability requirements of bridge jacking.

Comparing scheme i and scheme ii, shortening the length of implanted anchor steel and minimizing the diameter of anchor reinforcement, will make the concrete and steel bracket stress increase greatly with lager crack area. In order to guarantee the safety and reliability of the real project, we choose scheme ii structure as jack working platform.

From the finite element calculation and test, we can notice that the stress of anchor plate is not large, So we can reduce the thickness of anchor plate to save materials and reach the purpose of installation convenience.

The study for the bridge jacking offer the safe and reliable support platform, which can provide valuable experience and basis for similar projects.

References

[1] G. Li, Simulation analysis of continuous beam bridge jacking process, Xi'an: Chang'An University, 2009.

[2] Z. Han, Z. Zhang, Y. Zhang, The application of synchronous jacking technique in bridge reconstruction engineering, China Municipal Engineering, 1 (2007) 24 -25.

[3] H. Zhao, The monitoring and analysis of Nanpu Bridge jacking, Jinan: Shan Dong University, 2010.

[4] B. Si, Z. Sun, Q. Ai, The application of Solid65 element in the finite element analysis of concrete structure, Industrial Building, 1 (2007) 87-91.

[5] T. Yu, X. Cong, reinforced concrete beam elastic-plastic problems of computer simulation analysis, Journal of Northeast Forestry University, 4 (2004) 58.

[6] J. Ge, L. Wang, Based on ANSYS of Bridge Structure Analysis, Beijing, China Railway Press, Beijing, 2007.

© (2012) Trans Tech Publications, Switzerland
doi:10.4028/www.scientific.net/AMM.238.753

Research on Non-quantification Risk Factors Control and Management of Bridges during Construction

Qingfu Li[1, a], Hao Fu[2 b] and Weikang Gan[1 c]

[1] Zhengzhou University, Zhengzhou 450001, China

[2] Engineering Test and Design Centre of Zhengzhou Railway Administration, Zhengzhou 45000

[a]lqflch@zzu.edu.cn, [b]hellofuhao@yahoo.com.cn, [c]ganweikang006@163.com

Keywords: bridge engineering; construction stage; non-quantification factor; risk management.

Abstract. Proceed with manual work, materials and machinery, non-quantification risk factors control and management method of bridges during construction is studied. The results indicate that the key of controlling unquantifiable risk factors lies on supervision of careless mistake and accident, making clear responsibility, preparing measures of remediation for problems that may occur and minimizing negative influence of project risk by subjective factors which can be controlled. Research achievement can ensure bridge construction quality and safety, and then provide technical contribution.

Introduction

Non-quantification risk factors should be controlled at the construction site of the bridge, and the common non-quantification risk factors can be defined as the subjective controlled factors which can be influenced by human. In the construction, the factors generally include three parts, manual work, materials and machinery. And the construction departments will set up the corresponding project departments which can be responsible for the special involved contents. The subjectivity of these factors is strong, which have great influence on construction risks, and therefore, it should be controlled during construction.

Manual Work Control and Management in Construction

Manual work includes all the personnel participating in project construction. Bridge construction is a complex systematic engineering, and it is an essential process in which the design scheme of the structure can be realized, which containing complex physical labor and mental work. This process will be affected by many aspects of society and a large number of personnel, demanding high construction technology and management level. Manual work is an important aspect among the three projects and it determines the working conditions of the other two projects. As presented by the United States aviation engineer Edward A. Murphy in Murphy law, someone will do a job or task if it has more than one possible outcome, and one of them will lead to catastrophic or unexpected consequences. This law was developed into Finagle's Law of Dynamic Negatives later, which can be stated that any possible mistakes will appear in the worst way and at the worst time. This law is very appropriate to be used to discuss the risk of manual work during construction. In n times of Bernoulii tests, such results will be obtained when n tends to infinite: (1) It is an impossible event that any mistake does not occur; (2) It is a certain event that mistake occurs at least once.

It follows that the mistake caused by manual work during construction is inevitable, the reason of which is intricate. Existing research results show that the mistake is closely linked to people's cognitive process [1]. Therefore, it is very important to correctly understand the human error model during the bridge construction process and correctly analyze the reasons of the mistake caused by manual work, and which has great instruction to reveal the essence of the mistake caused by manual work and control the risk caused by manual work

Factors Affecting Reliability of Manual Work. A large number of engineering accidents investigation shows that only one third of the accidents are caused by external factors, and the rest are mostly related to the concealed danger of quality in structure design and construction. Most of the concealed danger of quality is mainly caused by manaul work. As a result, considering the influence on manaul work factor scientifically is the significant content for the construction risk control [2].

Human errors are influenced by many factors, including internal and external reasons [2-5]. The causes of the human error can be classified in Table 1.

Table 1 Factors affecting the reliability of the personnel

Human errors	Internal reason	Psychological factors	Subjective will	Degree of arbitrary work, whether intentionally jerry-build or information fraud
			Cognitive competence	Ability of handling difficulty and unexpected situation
		Physiological factors	Health degree	Having psychological and physiolgical disease or not
			Physiology rule	Fatigue work, excessive drinking or not, physiological reaction under special environment
			Skill level	Adequate training, being qualified to the work or not
	External reason	Organizing and management	Planning decision-making	Validity and rationality of planing decision-making
			Operating rules	Rule can be reasonably applied or not
		External environment	Natural environment	Weather, geography condition are suitable for manaul work, having protective measures or not
			Place layout	The layout of the site is safe and reasonable, easy for operating and having mutual interference or not
			Equipment	State of equipment and degree of hommization

Generally, the personnel are working as a team at the construction site, which can be served as the first level group of construction organization. The number of the staff in first level group is small and the members usually influence each other. The group has the same interests and their common target is to complete the same task. The members have direct, personal, face-to-face contact and relationship. In the cooperation work of the group, the individual will always show several properties including relative property, imitativeness, competitiveness and being complementary to each other. The properties can improve the reliability of the personal and the work efficiency when managers are good at management, but if not, it may cause serious negative effect and reduce the reliability [6].

Risk Control Measures for the people in Construction. Due to that the human error has great influence on the project risk, human reliability analysis (HRA) has been paid much attention in many engineering projects. The first study of the theory comes from ergonomics at the end of 1970s. After developed, it began to study the human dynamic cognitive process under the emergency situation. The hunman dynamic reliability analysis model can be defiened as puting people on the accident scene to explore human mistakes mechanism. In recent years, many cognitive models have been developed, however, it is difficult to be operated when combined with the engineering practice, and especially in the quantitative forecasting. Since human reliability model is hard to set up and the theory is immature, it may apply a new way instead which relys on strict organization management to improve the reliability of people during construction, that is, it can rely on the enterprise management of standardization, systematization to increase the reliability of the people, to avoid or reduce the risk of human error.

The ISO management certification system, which is presently used in international architecture industry, can greatly improve the reliability of people. This control system demands that every step and every node of the work should execute according to the strict procedures and have complete archive materials. Thus, it can greatly reduce the arbitrary work of construction process and improve the reliability of person, and then human error risk can be controled effectively. Table 2 and Table 3 are reference tables of quality-control points and annotation record made by most of highway engineering construction enterprises according to the ISO system.

Table 2 Reference table of quality-control points

Cotroll units	Control points		Executive	The main control contents	Manaul	Witness
Design clarification	1	Drawing technology	Chief engineer	Drawings are complete and meet the need of construction or not	Drawing technical documents	Self-examination record
	2	Design clarification	Chief engineer	Learning about design intention	Drawing technical documents	Meeting of esign clarification record
Formulating construction documents	3	Design of construction organization	Chief engineer	Formulating construction organization design, approval process	Drawing and technical standards of the state, acceptance specification	The approved construction organization design
	4	Construction scheme	Chief engineer	Formulating construction scheme	Enterprise resource	The approved construction scheme
Preparation of material and equipment	5	Formulating need plan	Chief engineer& manager	Formation, approval process	Blueprint, specification, quota	Demand planning of material and equipment
Construction tool comes into play	6	Construction equipment comes into play	Equipment technicist	Condition of equipment	Equipment/ plan	Construction equipment
Personnel qualification	7	Special operation staff	Technicist	Verifying qualification	Relevant stipulations	Qualification credentials
Construction starting report	8	Confirming construction conditions	Project Manager	Preparation of personnel, equipment, materials, facilities	Construction organization designing	The approved construction starting report
Technical annotation	9	Annotation	Technicist	Design intention, standard requirement, key technology	Blueprint and construction scheme	Technical annotation and meeting minutes
Construction progress	10	Ascertaining by major	Technicist	Formulating construction scheme and application manual, approval process, implementation	Blueprint, construction scheme, application manual	Construction records
Design change	11	Design change	Technicist	Confirm, ratification and implementation	Design change	Design change records
Annexe	12	Ascertaining by major	Technicist	Formulating construction scheme and application manual, approval process, implementation	Blueprint,specification construction scheme, application manual	Construction records
Acceptance of project	13	Subdivisional work	Technicist	Hidden content, quality standards	Blueprint, specification	Acceptance of project records
Final inspection test	14	Test items	Technicist	Making testing scheme, approval process, implementation	Standard, scheme	Testing records

Table 3 Record of technical annotation in construction

Project Name				Annotation date	
Object					
Compere		Annotation person		Recorder	
Content					

Materials Control and Management during Construction

The materials whose dosages are large during bridge construction include the cement, sand, stone, asphalt, various specifications of the steel, welding materials and so on. It is necessary to choose admixtures, additive, materials of sign and marking, tube cable, etc according to design and mix proportion. For management of construction materials, the construction materials which are in large amount use should purchased by competitive bidding, which can prevent purchasing inferior materials for saving cost. For those materials which can't be purchased by competitive bidding, the appointed enterprise should be recommend, and the supervisors should also control the source of the materials.

For those construction materials whose quality or sources may be unstable, different batches materials should be piled up separately and be tested by supervisor at any time. Once there are some quality problem, it should be reported to the construction department and the materials should be changed to qualified materials. The consumption of these materials is large and the price is low, as a result, it is easy to be ignored by the supervisor in the site. Therefore, it must be strengthened the management of this kind of materials. For the other materials, the quality should be monitorred through field tests. It must trace the cause once the concrete test pieces or steel welding specimens are discovered to be unqualified, such as the problem of additive, mix ratio, welding materials.

Materials supply and consumption should be coordinated with each other. Insufficient materials stock will severely affect the construction progress. On the contrary, surplus materials will occupy large amount of fund, and will influence the resource allocation, which needs greater preparation site and spends more for storage and turnover. Besides it may cause significant economic loss because of fluctuation of material supply market. Therefore, it should formulate a reliable inventory plan and ensure construction supply to reduce loss and waste of materials. Materials management should be emphasized on implementing control not only in supply plan but also in quality control. The treatment should be rectified once some problems are discovered to prevent the problems expanding.

Machine Control and Management during Construction

The kind of machines for bridge construction is various, and most of the machines need manual control and the maintenance is complex. There are three main factors affecting risk of construction machine, which in includes human, state of machine and economical efficiency use of machine.

Influence of Human Factor on Machinery Risk Machinery is the outspread of human, the operator and machine is an integral whole when a machine is in use. Some machines are belong to high technology equipments, such as welding machine, mobile crane, bridge girder erection machine, and their operation procedures are complex, difficult with high risk, which demands strict operation. Appropriate treatment measures should be taken immediately once there is an accident taking place, and it may cause serious accidents and loss if the problems can't be handled properly. Therefore, the machine should be preferably operated by a professional qualifications worker, and some important construction nodes should be operated by senior skilled workers, such as hoist and linking of beam, vertical and horizontal welding of beam section. If the skill level of the operators is too low and he has bad habits, it will raise the mechanical failure rate and increase the risk of machine use.

Influence of Machinery State and Performance on Machinery Risk. The equipments should be avoided working with problems, however if needed, the measures for the stoppage should be prepared. Special equipments, which are used in important construction nodes such as mixing machines used in concrete casting process, erection crane beam machines used in the process of lifting, can not work with problems, and emergency response for failure must be made in this case even that the machinery is in good condition.

Machinery in good state also should be avoided working in the mode of limit load as far as possible. For example, the hoisting equipment may be restricted that its homework load should not exceed 90% of its nominal operation capacity. Therefor, it should prefer using large power, high efficiency, multi-function, stable and reliable, high precision mechanical equipment when condition is allowed. Strengthening the daily maintenance for mechanical device is the key to improve the reliability of machine that. For different equipments, the relevant maintenance procedures should be made and the operators should be demanded to work according to the procedures.

Effect of Cost on Risk of Machinery. The using cost of some large machines are relatively high, and it is generally rented fee for short-term, which often cause the situation that equipments and construction process are not in coordination. In certain condition, lack of equipments also will lead to persons un-occupied, and it can affect the quality stability of the project. Therefore, the cost of equipment should be calculated according to the construction period, personnel, construction quality, resource consumption, etc. And allowance for equipment should be prepared in order to response to all sorts of change during construction and avoid rushing phenomenon.

Machinery Risk Control. The key point of machinery risk control lies in working on the base of manual, preparing backup machine, and developing reliable emergency measures for all kinds of conditions before construction.

Conclusions

The key of non-quantification risk factors control and management of bridges during construction lies in taking charge of leaks and mistakes, making responsibility clear. And remediation measures should be prepared for problems that may occur and minimize negative influence of project risk by subjective factors which can be controlled.

Acknowledgments

The authors would like to acknowledge the financial support received from the National Natural Science Foundation of China (Grant No. 50978234).

References

[1] J. Chen, Human Error Controlling and HRA Studying in the Course of Construction, Changsha University of Science & Technology, Changsha, 2004.

[2] A. C. Waller, Study and analysis of the first 120 failures cases, Syme. Struct., Failure in Bldgs., Inst. of Struct. Engrs., London UK, 1980.

[3] B. S. Dhillon, Human reliability (With human factor), Pergamon Books LTD Oxford England, 1986.

[4] E. W. Hagen, Human reliability analysis, Nuclear Safety, 1976.

[5] H. R. Beech, L. E. Burns, B. F. Sheffield, A behavioral approach to the management of stress, John Wiley and Sons, Chichester, 1982.

[6] H. H. Chen, M. J. Wang, Analysis of the design-construction union behavior based on game theory, Construction Management Modernization, 92 (2007) 16-19.

© (2012) Trans Tech Publications, Switzerland
doi:10.4028/www.scientific.net/AMM.238.758

Comparison Study on Crossbeam Web Cutout of Different Shapes for Orthotropic Steel Bridge Deck

Liqiang Gao[1,a], Qianhui Pu[1,b], Bing Han[1,c] and Zhenbiao Liu[2,d]

[1]School of Civil Engineering, Southwest Jiaotong University, Chengdu, China

[2]Design and Study Institute of Bridge, China Railway Siyuan Survey and Design Group Co., LTD. , Wuhan, China

[a]gaoliqiang1984@126.com, [b]qhpu@vip.163.com, [c]hanbing0218@gmail.com, [d]13545216930@139.com

Keywords: orthotropic steel bridge deck; crossbeam web cutout; fatigue; stress analysis.

Abstract. For orthotropic steel bridge deck (OSD), principle tensile stresses near the end of joint of crossbeam web and longitudinal rib and at the edge of crossbeam cutout are dependent on the shape of crossbeam cutout to a great extent. They are results of many factors, among which bending-shearing effect and in-plane supporting effect are in-plane factors, unsymmetrical loading effect and relative longitudinal deformation effect are out-of-plane factors. Comparison study on stresses at some fatigue sensitive regions of orthotropic steel deck with six types of crossbeam web cutout indicates that the top height of cutouts determines the distance between the end of joint and the neutral axis, which affects the bending effect seriously, and the area of cutouts determines the shearing effect. When OSD system is affected by bending-shearing effect, increasing the top height decreases the principle tensile stresses near the end of joint but increases the stresses at the edge of cutout, and increasing the area increases the principle tensile stresses both near the end and at the edge of cutout. When the top height of cutouts increases, the contact area between crossbeam web drops, then the principle tensile stresses near the joint produced by in-plane supporting effect increases. When the side width of cutouts increases, the constraint effect of the crossbeam web to longitudinal rib decreases, then the principle tensile stresses near the joint produced by out-of-plane effects decreases. Generally, OSD system with stiff cutouts behaves well when affected by in-plane effects, and OSD system with flexible cutouts behaves well when affected by out-of-plane effects.

Introduction

Due to many advantages [1], orthotropic steel bridge deck (OSD) is used in many long-span steel bridges. In the early stage, OSD is used in highway bridges in China, such as highway suspended bridge in Humen, Guangdong Province and highway suspended bridge across the Yangzi River in Jiangyin, Jiangsu Province. Recently, due to the advantages of good overall property, small impact effect and little noise, OSD system is used in the high-speed railway bridge instead of the traditional longitudinal-transverse beam system, such as Dashengguan Bridge across the Yangzi River in Nanjing in the high-speed railway from Beijing to Shanghai.

OSD system has complex structure and many weld joints, problem of fatigue crack of OSD system has been valued, and many crack examples about OSD were reported [2, 3]. Joint of crossbeam and longitudinal rib is fatigue sensitive forming many fatigue crack. In the early stage, longitudinal ribs are cut off when they encounter the crossbeam web, and joined to the crossbeam web with fillet weld. This structure had been proved with low fatigue performance which is not used now [4]. Now, continuous longitudinal ribs through crossbeam web are used, which also joined to the crossbeam web with fillet weld. In order to rectify the fabrication deviation more easily and decrease the residual stress, cutout is set up bellow the longitudinal rib on the crossbeam web.

There are two fatigue sensitive regions near the joint of the crossbeam web and the longitudinal rib. The stresses of the region near the end point of the weld joint is resulted from many factors such as bending-shearing effect, in-plane supporting effect, unsymmetrical loading effect and relative longitudinal deformation effect. The stress at edge of the cutout in the crossbeam web is resulted from

bending-shearing effect. The shapes of the cutouts affects much on these factors, and different shapes of cutouts are used in the world. In order to obtain more superior cutout shape, stresses of some fatigue sensitive regions under different effects are calculated with proper FE model for six represent cutout shapes used in the world.

Structure and Loading

Six Cutout Shapes and Investigated Points. Six typical crossbeam web cutout shapes are shown in Fig. 1, (a) cutout used in Eurocode 3 for steel railway bridge, (b) cutout used in AASHTO-LFRD, (c) cutout used in Williamsburg bridge in U.S., (d) cutout used in Bronx Whitestone bridge in U.S., (e) cutout used in steel bridge code of Japan, (f) cutout usually used in steel highway bridge in China. Main parameters of cutouts are the top height of the cutout C, the bottom height of the cutout C_b, the side width of the cutout D, radius of cutout R, angle from the tangent line of cutout at the end point of the joint to the rib web A, area of the cutout S (see Fig. 1, Fig. 2, Table 1). Cutout a, c and d are flexible cutouts with large area, meanwhile cutout b, e and f are stiff cutouts with small area.

As cutout c for the example, five investigated points are shown in Fig. 2. Point 1, Point 2 and Point 3 are points on the rib web near the end of joint of crossbeam web and rib, and 15mm away from the weld root. Point 4 is point on the crossbeam web near the end of joint of crossbeam web and rib, and 15mm away from the weld root, 6.4mm away from the edge of the cutout. Point 5 is point on the crossbeam web at the edge of cutouts. The site of Point 5 is not stable for different cutout, so definite site of Point 5 is not given in Fig. 2.

When bending-shearing effect is studied, the principal tensile stresses of Point 1, Point 2, Point 3, Point 4 and Point 5 are investigated. When in-plane supporting effect, unsymmetrical loading effect and relative longitudinal deformation effect are studied, the principal tensile stresses of Point 1, Point 2, Point 3 and Point 4 are investigated.

Table1 Parameters of six types of cutouts [mm]

Type	C	C_b	D	R_1	R_2	A	S
a	87.1	41.1	50	160	20	0	14478
b	90	20	20	20	20	90	7732
c	90	20	67.4	55	-	77	16013
d	90	20	67.4	55	25	23	17628
e	49.9	20	20	60	20	90	5442
f	46.7	20	29.2	35	-	100	6738

Note: The unit of A is degree, and the unit of S is square millimeter.

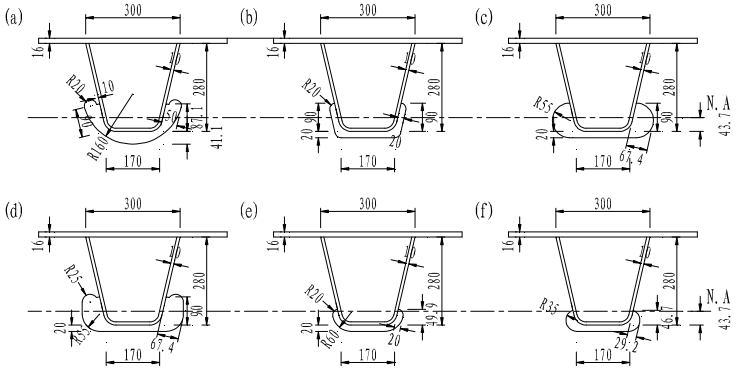


Fig. 1 Six typical cutout shapes used in the world

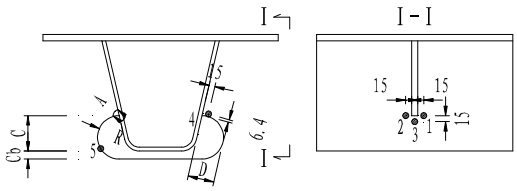


Fig. 2 Sites of investigated points

Model for Calculation and Loading Mode. The selected model for calculation and loading mode can reflect main effects investigated. When bending-shearing effect is studied, OSD structure with five longitudinal ribs is used. As cutout c for the example, model for calculation and the loading mode are shown in Fig.3. The ribs are 500mm long, and the crossbeam whose two ends are simple supported is 800mm high, 3000mm long. The longitudinal ribs made of 10mm thick steel plate used in the model are closed trapezoidal ribs. The top width of the ribs is 300mm, and the bottom width of

the ribs is 170mm. The steel plates of the crossbeam web and the deck are 16mm thick. Uniformly distributed load is applied on the deck over the middle rib, and the value of the load is 1200kN/mm^2. Four-node shell element of 10mm-long-side is used to imitate all the steel plates.

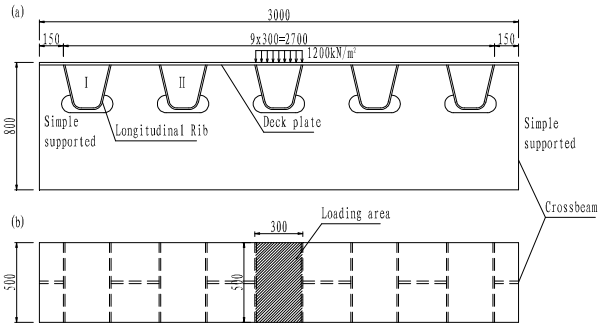


Fig. 3 Model for bending-shearing effect

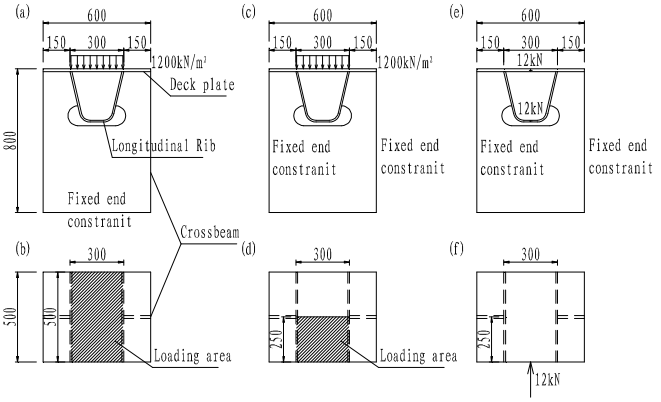
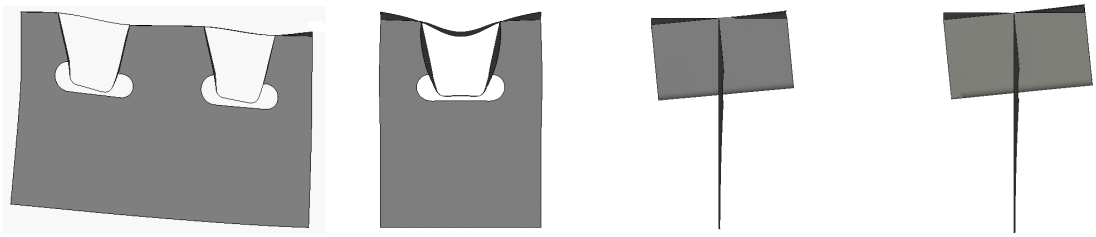


Fig. 4 Models for calculation.

The calculation models for studying in-plane supporting effect, unsymmetrical loading effect and relative longitudinal deformation effect are the same, only the boundary and loading mode are different. As cutout c for the example, models for calculation and the loading mode are shown in Fig. 4. The model is made up of one rib, crossbeam and deck. The rib is 500mm long, and the crossbeam is 800mm height, 600mm long. The other parameters of the model are the same as the model for bending-shearing effect. When supporting effect is studied, bottom side of crossbeam is fixed, uniformly distributed load is applied on the deck over the rib, and the value of the load is 1200kN/mm^2 (Fig. 4 a, b). When unsymmetrical loading effect is studied, two end sides of crossbeam are fixed, uniformly distributed load is applied on the deck at one side of the crossbeam over the rib, and the value of the load is 1200kN/mm^2 (Fig. 4 c, d). When relative longitudinal deformation effect is studied, two end sides of crossbeam are fixed, horizontal longitudinal concentrated load is applied on one side of rib and deck, and the value of the load is 12kN (Fig. 4 e, f). Four-node shell element of 10mm-long-side is used to imitate all the steel plates.

Comparison Study on Different Cutout Shapes

There are four factors which affect the principle tensile stresses at end of the joint of crossbeam web and lingintudinal rib, the deformation modes of structure under four effects are shown in Fig. 5, as cutout c for the example.



a) Bending-shearing b) In-plane supporting c) Unsymmetrical loading d) Relative longitudinal deformation

Fig. 5 Deformation modes of structure under different effects

Bending-shearing Effect. Crossbeam web appears discontinuous as the existence of longitudinal ribs when baring the bending-shearing effect, and stress concentration will happen at the end of joint of crossbeam web and rib and the edge of the cutout. The deformation mode is shown in Fig. 5(a).

More specifically, bending effect makes the crossbeam and longitudinal ribs compress each other, as the end of joint of crossbeam web and rib is over the neutral axis, such as the structure given in this paper, the neutral axis is 43.7mm over the bottom of the rib (Fig. 1). For cutout a, b, c and d, the joint of crossbeam web and rib is farther away from the neutral axis, so the compress effect of bending is stronger. For cutout e, f, the joint of crossbeam web and rib is closer to the neutral axis, so the

compress effect of bending is weaker. Rib closer to the middle line is compressive due to the larger bending moment of the crossbeam closer to the middle line. Compressing effect of Rib II is stronger than that of Rib I. Moreover, bending effect results tensile stress at the edge of cutout.

Shearing effect makes the rib rotate, the deformation results in compress effect at one side of the rib and tensile effect at the other, while it also results in compress stress at the edge of cutout of one side and tensile stress at the other with the direction opposite to the effect of the rib. Stress of the shearing effect is larger for the cutout at the end point of crossbeam due to accumulation of shearing deformation. For the structure in this paper, effect of shearing on Rib I is stronger than that of Rib II.

Principle tensile stresses of all investigated points are given in Table 2.

Table 2 Principle tensile stress of investigated points under bending-shearing effect (MPa)

Type	Rib I					Rib II				
	Point 1	Point 2	Point 3	Point 4	Point 5	Point 1	Point 2	Point 3	Point 4	Point 5
a	34.03	32.14	28.50	8.70	129.59	8.19	8.02	8.14	3.62	120.89
b	27.25	27.96	26.54	2.90	153.24	10.76	10.77	10.56	2.60	122.72
c	40.26	35.75	35.92	9.14	162.01	13.38	12.77	12.72	6.45	137.72
d	40.86	38.24	34.33	12.94	155.76	11.67	11.08	10.88	5.63	132.96
e	30.93	29.78	27.25	-0.62	130.24	13.59	13.44	14.60	2.59	115.95
f	30.48	29.94	28.74	7.26	148.11	13.86	13.62	15.73	3.32	127.60

For Rib Ⅰ, influence of bending effect is weaker, and influence of shearing effect is stronger. Parameter *C* of cutout a, b, c and d is similar, the influence of bending effect is similar for them. The stresses of cutout d at points (Points 1, 2 and 3) on rib web near the end of joint of crossbeam and rib are the largest among cutout a, b, c, and d, then cutout c, a and b. It's the reflection of shearing effect, increasing cutout area can enhance the shearing effect. Parameter *C* and *S* of cutout e and f are similar, so the stresses at points (Points 1, 2 and 3) on the rib web near the end of the joint of crossbeam and rib are similar for them. Parameter *S* of cutout e, f are smaller than that of cutout b, but the stresses at Points 1, 2 and 3 of them are bigger than that cutout b, it can be illustrated like this, shearing effect for cutout b is stronger than cutout e and f, but bending effect for cutout b is also stronger than cutout e and f. Sequence of stress at point 4 on crossbeam web near the end of joint of crossbeam and rib for cutout a, b, c and d is the same as that on the rib, stress for cutout d is the largest among them, then cutout c, a and b. Stress at Point 4 for cutout f is much larger than that of cutout e, thus parameter *D* is another factor affecting stress at Point 4 besides Parameter *C* and *S*. Factors affect stresses at point 5 on edge of cutout are bending effect, shearing effect and radius of cutout. Bending effect for cutout a, b, c and d are similar, shearing effect for cutout c and cutout d are stronger than the others. Although the radius of cutout c and d are larger than cutout b, the stress of cutout c and d of Point 5 is larger than that of cutout b, it is because shearing effect for cutout c and d is stronger than that of cutout b. Although shearing effect of cutout a are stronger than that of cutout b, the stress of cutout a of Point 5 is smaller than that of cutout b, it is because the radius of cutout a is much larger than that of cutout b. Bending-shearing effect for cutout e and cutout f are similar, but the radius of cutout e is larger than that of cutout f, so the stress of cutout e is smaller than that of cutout f.

Bending effect of Rib II is stronger than that of Rib I, and shearing effect of Rib II is weaker than that of Rib I, so stresses at Point 1, 2, 3 and 4 of Rib II are much smaller than that of Rib I, and stress at Point 5 of Rib II is a little smaller than that of Rib I. The sequence of stresses at Point 1, 2 and 3 of Rib II for cutout a, b, c and d is similar to that of Rib I, and the sequence of stresses at Point 1, 2 and 3 of Rib II for cutout e and f is also similar to that of Rib I. But stresses of Rib II for cutout e and f is a little larger than that for cutout a, b, c and d, because compress stresses produced by bending effect for cutout a, b, c and d are much larger than that for cutout e and f, it is different from Rib I. The sequence of stresses at Point 4 of Rib II for cutout a, b, c and d is similar to that of Rib I, and the sequence of stresses at Point 4 of Rib II for cutout e and f is also similar to that of Rib I. Because of larger bending effect, stress at Point 4 of Rib II for cutout a, b, c and d is a little larger than that for cutout e and f. The sequence of stresses at Point 5 of Rib II for all cutouts is similar to that of Rib I.

In-plane Supporting Effect. In-plane supporting effect means that the longitudinal rib is supported by the crossbeam web when wheel load is on the deck over the rib. As the existence of the cutout bellow the rib, compress and relative vertical deformation between crossbeam and rib produce stress concentration at the end of joint of crossbeam web and rib. The deformation mode is shown in Fig. 5(b). Stresses of investigated points under in-plane supporting effect are shown in Table 3.

Table 3 Principle tensile stress of investigated points under in-plane supporting effect (MPa)

Type	Point 1	Point 2	Point 3	Point 4
a	62.26	65.06	53.55	9.20
b	47.33	37.01	42.21	-8.76
c	50.87	45.92	46.11	12.51
d	59.63	61.45	53.86	14.89
e	29.31	33.21	27.07	-3.57
f	32.72	33.46	21.10	5.00

Stresses at points (Points 1, 2 and 3) on rib web near the end of the joint of crossbeam and rib under in-plane supporting effect are affected by three factors, they are parameter *C*, *D* and *A*. Stresses at Point 1, 2 and 3 for cutout a are the largest among cutout a, b, c and d, because parameter *A* of cutout a is 0^o, the smallest among them. Stresses at Point 1, 2 and 3 for cutout d are larger than that of cutout c, because parameter *A* of cutout d (23^o) is smaller than that of cutout c (77^o). Stresses at Point 1, 2 and 3 for cutout b are the smallest among cutout a, b, c and d, because parameter *D* of cutout b is 20mm, the smallest among them. Parameter *C*, *D* and *A* for cutout e and f are similar, so stresses at Point 1, 2 and 3 are also similar for them.

From the analysis above, Parameter *C* affects the stress at Points 1, 2 and 3 the most, because increasing Parameter *C* decreases contacting area between crossbeam web and longitudinal rib. Increasing Parameter *D* and decreasing Parameter *A* also decrease the stress at Points 1, 2 and 3, the reason may be that they weaken the compress effect and enhance relative vertical deformation effect between crossbeam and rib. But the influence on stresses at Points 1, 2 and 3 of Parameter *D* and parameter *A* is weaker than that of Parameter *C*.

The influence of Parameter *D* to the stress at point 4 on crossbeam web near the end of the joint of crossbeam and rib is the strongest, it is different from stresses on the rib.

Unsymmetrical Loading Effect. Unsymmetrical loading effect means that relative rotation between crossbeam web and rib will happen when load is on the deck of one side of the crossbeam. The deformation produces stress concentration at the end of the joint of crossbeam web and rib. The effect is a kind of out-of-plane effect to crossbeam web, which is different from the effects mentioned above. Out-of-plane deformation happens because of the effect, and the deformation mode of structure under unsymmetrical loading effect is shown in Fig. 5(c).

Table 4 Principle tensile stress of investigated points under unsymmetrical loading effect (MPa)

Type	Point 1	Point 2	Point 3	Point 4
a	64.84	70.82	34.19	146.99
b	84.86	99.40	52.14	174.97
c	76.05	84.94	39.50	158.41
d	66.82	70.71	42.00	145.70
e	89.38	105.45	60.09	179.17
f	83.88	107.33	53.17	146.54

Stresses of investigated points under unsymmetrical loading effect are shown in Table 4. Stresses at Point 1, 2, 3 and 4 are related to the parameter *S*. Parameter *S* of cutout b, e and f which are called stiff cutout is smaller, and the stresses of investigated points of stiff cutout are larger. Parameter *S* of cutout a, c and d which are called flexible cutout is larger, and the stresses of investigated points of stiff cutout are smaller. More specifically, the factor affecting the stresses under unsymmetrical loading effect the most is parameter *D*, then parameter *A* and *C*. Stresses of cutout b is larger than that of cutout c indicates that increasing parameter *D* decreases the stresses. Stresses of cutout a is smaller

than that of cutout c indicates that decreasing parameter *A* decreases the stresses. Stresses of cutout e is a little larger than that of cutout b indicates that decreasing parameter *C* increases the stresses, but the influence is weak.

Relative Longitudinal Deformation Effect. When OSD system is used in truss bridge, relative longitudinal deformation between crossbeam web and rib may happen because of action in a whole of deck and lower chord [2], it is also an out-of-plane effect. Relative rotation between crossbeam web and rib will happen because of the existence of cutout bellow the rib as is affected by unsymmetrical loading effect. The deformation also produces stress concentration at the end of the joint of crossbeam web and rib. Out-of-plane deformation happens because of the effect, and the deformation mode of structure under relative longitudinal deformation effect is shown in Fig. 5(d).

Table 5 Principle tensile stress of investigated points under relative longitudinal deformation effect (MPa)

Type	Point 1	Point 2	Point 3	Point 4
a	19.85	16.74	9.58	40.55
b	28.42	20.37	12.87	54.26
c	23.12	19.08	11.13	44.96
d	20.16	17.24	10.03	39.68
e	32.00	20.76	13.68	55.40
f	28.6	19.96	15.96	50.15

Stresses of investigated points under unsymmetrical loading effect are shown in Table 5. Influence law of different cutout shapes to stresses of investigated points under longitudinal deformation effect is the same as that under unsymmetrical loading effect, because they are both out-of -plane effects. The stresses of investigated points of stiff cutout are larger, and the stresses of investigated points of stiff cutout are smaller.

Conclusions

According to the comparison study on stresses at fatigue sensitive points of OSD system with six types of shapes of cutout, some conclusions are got as follows:

Principle tensile stresses at end of joint of crossbeam web and longitudinal rib on both crossbeam web and rib web are related to bending effect and shearing effect, enhancing the bending effect decreases the principle tensile stresses, and enhancing the shearing effect increases the principle tensile stresses. Principle tensile stresses at the edge of cutout of crossbeam are related to bending effect, shearing effect and radius of cutout, enhancing the bending effect and shearing effect increase the principle tensile stresses, increasing the radius of cutout decreases the principle tensile stresses.

Bending effect is related to vertical site of neutral axis and horizontal site of longitudinal rib, the farther the neutral axis is away from end and the closer the rib is away from middle line, the stronger is the bending effect. Shearing effect is related to the area of cutout, the lager the area of cutout is, the stronger the shearing effect is.

Principle tensile stresses at end of joint of crossbeam web and longitudinal rib on both crossbeam web and rib web are related to parameter *C*, *D* and *A*, and increasing parameter *C* and *D* or decreasing parameter *A* increases the principle tensile stresses. Parameter *C* affects the stresses on the rib a lot, and Parameter *C* and *D* affect the stresses on the crossbeam web a lot.

Unsymmetrical loading effect and relative longitudinal deformation effect are both out-of-plane effects. Principle tensile stresses at end of joint of crossbeam web and longitudinal rib on both crossbeam web and rib web are related to parameter *D*, *A* and *C*, and increasing parameter *D*, *C* or decreasing parameter *A* decreases the principle tensile stresses through weakening the constraint of the crossbeam web to longitudinal rib. Parameter *D* has the strongest influence on the stresses, and Parameter *C* has the weakest influence on the stresses.

Generally speaking, OSD system with stiff cutouts behaves well when affected by in-plane effects, and OSD system with flexible cutouts behaves well when affected by out-of-plane effects.

References

[1] L. Tong, Fatigue of Orthotropic Steel Bridge Decks, Ph.D dissertation, Tongji University, 1995.

[2] Y. Zhang, X. Xin, X. Liu, Analysis on fatigue design method of orthotropic floor details in steel bridge, Steel Construction, 120 (2009) 33-37.

[3] D. Qian, About the fatigue of orthotropic decks-simple introduction of the study when strengthening the severn bridge in britain, Bridge Construction, 2 (1996) 8-13.

[4] J. R. Cuninghame, Fatigue classification of welded joints in orthotropic steel bridge decks, TRRL Research Report 259, 1990.

[5] R. J. Connor, A comparison of the in-service response of an orthotropic steel deck with laboratory studies and design assumptions, Ph.D dissertation, Lehigh University, Bethlehem, Pa, 2002.

[6] L. Tong, Z. Shen, Static load experiment and finite element method analysis on the steel orthotropic decks, Journal of Tongji University, 6 (1997) 617-622.

[7] Z. Xiao, K. Yamada, S. Ya, Stress analysis and fatigue evaluation of rib-to-deck joints, International Journal of Fatigue, 8 (2008) 1387-1397.

[8] M. S. Pfeil, R. C. Battista, J. R. Mergulhãob, Stress concentration in steel bridge orthotropic decks, Journal of Construction Steel Research, 8 (2005) 1172-1184.

[9] J. H. Choi, D. H. Kim, Stress characteristics and fatigue crack behavior of the longitudinal rib-to-cross beam joints in an orthotropic steel deck, Advances in Structural Engineering, 2 (2008) 189-198.

© (2012) Trans Tech Publications, Switzerland
doi:10.4028/www.scientific.net/AMM.238.765

Plastic Hinge Analysis of Seismic Performance of High Bridge Pier

Ruihong Gao [a], Ruilin Chen [b], Sugong Cao [c], Zhang Tang [d], Xinqiang Xiao [e] and Hongbo Hu [f]

Department of Civil Engineering, Xiangtan University, China

[a] gaoruihong2003@163.com, [b] chenruilin8@hotmail.com (corresponding author), [c] csdxcsg@163.com, [d] tzhangxtu@163.com, [e] 522820199@163.com, [f] 470704103@qq.com

Keywords: high bridge pier; the second plastic hinge; ANSYS; seismic performance.

Abstract. To analyze the second plastic hinge of high bridge pier formed in the earthquake and study the pier seismic performance, this paper takes the Kunming Slope Railway Bridge as an example. The simulation model was built by the elastic-plastic finite element ANSYS software. The buckling load of piers was calculated by buckling analysis capabilities of ANSYS software, a small enough initial offset given to the model, then the buckling load of piers put into the model. The deformation of non-linear model under the loads was calculated, the process was recorded that the reinforced concrete bridge piers initially yielding on the cross-section, continuously rotating around the neutral axis, and finally forming the eventually plastic hinges in certain parts of pier. The location of the plastic hinges can be inferred by final data of analysis software. By analyzing the calculated results, the seismic performance of the second plastic hinge in high bridge is studied.

Introduction

For seismic safety bridge stability, seismic design of bridge pier is one of the key. Therefore, for the piers under seismic dynamic response characteristics, failure mechanism, the ability of research and knowledge components to become the focus of scholars' research projects. Hosner proposed a theory based on the seismic design response spectrum method [1]. Newmark made a non-linear response spectrum concept [2, 3]. Priestley and Park et al completed the first reinforced concrete bridge pier plastic hinge model more systematic research work [4], they adopted a large number of reinforced concrete piers cyclic loading test results, and then propose a simplified curvature of the plastic hinge region and a rectangular distribution pattern shows the equivalent plastic hinge length of experience in statistical formula. This is the current national standard used in the basic model. Berry and Eberhard based on PEER's seismic performance of reinforced concrete column test database (PEER Column Performance Data Base). The specimen parameters (axial compression ratio, shear span ratio, etc.) change the trend regression analysis to the top corner of the pier given concrete form protective layer off and buckling of longitudinal reinforcement statistical formulas [5].

At the same time with the development of society, the domestic in engineering technology has also made certain progress. Liu et al and other experts for the pier in the earthquake simulation of the stress state and failure characteristics of the less ductile reinforced concrete piers were studied, and obtained in the reinforced concrete piers under cyclic loading of some nonlinearity [6, 7]. In a typical pier for a detailed elastic-plastic earthquake response of numerical analysis based on the piers ductile seismic response of the main characteristics and influencing factors, Yan [8] proposed two particle ductility seismic simplified analytical model and the corresponding simplified analysis method. The first times give the decision to export a single row of pile piers yield the approximate location of cross-section formula. Zhang et al studied the Southern River Bridge line of water one hundred meters high pier in the box under operating loads and loads of construction under the most unfavorable stress state, deformation and ultimate bearing capacity and other aspects of the model tests also been made [9]. Sun et al made 24 large-scale static tests of the proposed pier column piers of the seismic performance of ductile [10]. Most previous studies were the object of study under the pier at the end of the level of load plastic hinge formation. However, in the high bridge pier as the role of seismic wave, the piers of the bridge trains and associated weight and dead load of the second plastic

hinge will form the study is not detailed. This article from start to consider the one hand, take Kunming Railway Bridge No. 8 slope high pier as example. It was carried out by ANSYS software simulation to study the buckling loads in the formation of plastic hinges occurrence and properties. Aim for high pier plastic hinge model provides the basis for a more complete, while promoting the development of seismic design of bridge piers.

Model

The formation of piers body cells using PLANE42 element, pier top unit formed using COMBIN14 bound spring unit. The research subjects were No.8 pier with 110m height, 10m wide and 10m thickness at the end section. Pier width of 2 meters vertical, horizontal thickness of 10 meters. Define the stiffness of the pier top spring 1×10^6 kN/m, to facilitate the piers of the overall force response analysis, will be reinforced piers homogenization, elastic modulus of concrete piers to take 25×10^6. Material Poisson's ratio is 0.17.

Model Analysis and Solution

Linear Model Analysis. As the pier is a high pier, according to the theoretical analysis, the main piers of the damage caused by unstable buckling failure. Therefore, the linear model analysis for pier gives the model 100 vertical unit load force.

Analysis of the model has the following diagram:

The results of the solution process, structural deformation as shown above, the maximum displacement of 0.834×10^{-3}.

The solution of the ANSYS program to change the options, set the buckling solution options, set the mode number, the selected subspace iteration method. And then solve it.

Analysis can be obtained as shown below:

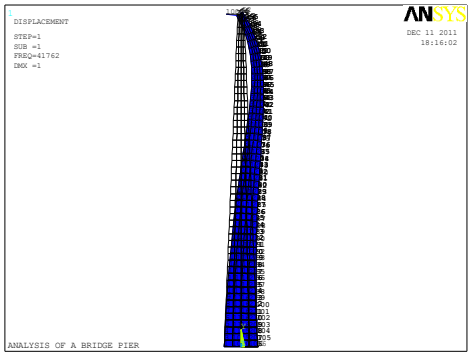


Fig.1 The displacement map of linear model buckling

The results of the solution process, structural deformation as shown above, calculate the result of 41762, so you can get the buckling loads of 4.1762×10N. And a map can be seen in the results of the linear state, the plastic hinge occurs at 92.4 m from the pier at the end, because here the maximum bending moment, the first plastic deformation.

Nonlinear Analysis Model. Based on the actual project situation, reinforced concrete stress-strain relationship is nonlinear, reinforced concrete piers under load elastic-plastic deformation will occur. It should be combined with concrete constitutive model for nonlinear analysis.

Concrete constitutive relations take the following form:

Ascent stage: when $\varepsilon_0\leq\varepsilon\leq\varepsilon_0$; Descending: when$\varepsilon_0\leq\varepsilon\leq\varepsilon_u$

$$\sigma=\sigma_0\left[2\left(\frac{\varepsilon}{\varepsilon_0}\right)-\left(\frac{\varepsilon}{\varepsilon_0}\right)^2\right]+250 \tag{1}$$

$$\sigma = \sigma_0 \left[1 - 0.15 \left(\frac{\varepsilon - \varepsilon_0}{\varepsilon_u - \varepsilon} \right) \right] + 250 \tag{2}$$

According to the model results to determine the linear analysis, the limits of the piers for the 4.1762×10^6 buckling load, load the model and solved by the iteration part of the final result is a unit beyond the pier deformation model was discontinued, and the results file for processing as follows:

In the first sub-step 462, the ultimate instability due to structural damage at this time, at a distance of approximately 103.1 m at the end of the pier, the formation of the maximum deformation DMX = 6.315, pier body fracture. As shown below:

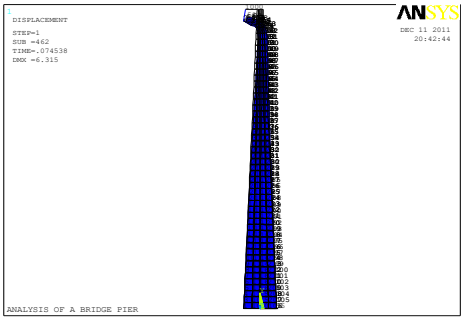


Fig.2 The deformation figure of 462 substep

In the first sub-step 462, the maximum compressive stress occurs away from the pier at the end of 103.4 ~ 105.6 m at the pier on the left, SMN =- 21112. Maximum tensile stress occurs away from the pier at the end of 96.8 - 107.8 m at Pier right, SMX = 20248.

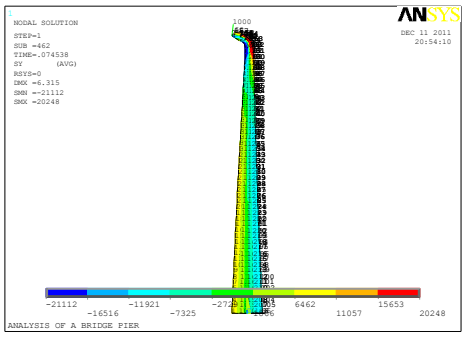


Fig.3 The cloud stress figure of 462 substep

Results. Model results show that 110-meter pier model in the limit load and buckling under the effect of the initial offset, when calculating sub-step operation to 181 sub-step, the deformation increases dramatically. End at a distance of approximately 103.1 m at the pier at the end of the formation of plastic hinges. the impact of plastic hinges in the 102.9 - 104.1 m range.

Conclusions

In this paper, taking the Kunming Slope Railway Bridge for instance, the actual of engineering integration parameters should be simplified and inputted to the ANSYS model. Focus on analysis and observation the deformation of high bridge pier under the P-wave seismic dead load and live load. The process of high bridge pier is very important. When the high bridge pier achieves the ultimate state, the pier unstable failure occurs, and then the second plastic hinge of bridge pier comes to appear.

Software analysis revealed that the bridge's 110-meter pier No. 8 which under the effect of the buckling loads forms the plastic hinge. The location of plastic hinge has distance for 103.1 meters above the bottom of bridge pier. The areas of plastic hinge affected within 102.9 - 104.1 meters. In the process of formation of plastic hinges, the locations of plastic hinges and both sides of the bottom

edge of the pier appear greater tensile and compressive stress. The result is in accordance with the performance characteristics of the roots in the pier line. From another point of view, the mode shape to a certain extent reflects the actual characteristics of the piers.

At the same time compared with the straight pier, the occurrence of plastic hinges in trapezoidal pier proved to be higher. This is also consistent with the Park and Priestley proposed the design principle based on ability. The principle emphasizes that not to make a great structural damage and loss of stability, control the formation of plastic hinge location, and enhance the seismic capacity. This raises the upper limit of the seismic forces that form plastic hinges, and enhance the structural safety. These trapezoidal piers have a significant contribution for enhancing the seismic performance of high pier. In this paper, finite element model of such an analysis for the calculation of high pier also proved this point.

Acknowledgements

The authors gratefully acknowledge that this research work has been supported by the Specialized Research Fund for the Doctoral Program of Higher Education of China(Grant No. 20104301120004), the Foundation for Key Program of Ministry of Education, China (Grant No. 211127), by the National Science Foundation for Post-doctoral Scientists of China (Grant No. 20110491260), the Natural Science Foundation of Hunan Province, China (Grant No. 10JJ6077), the Research Foundation of Education Bureau of Hunan Province, China (Grant No. 10B105) and the Hunan provincial Science and Technology Department, China(Grant No. 2010RS4020).

References

[1] L. Fan, Bridge Seismic, Tongji University Press, Shanghai, 1997.
[2] Nelson Lam, John Wilson, Graham Hutchinson, The ductility reduction factor in the seismic design of buildings, Earthquake Engng. Struct. Dyn., 27 (1998) 749-769.
[3] Tomaz Vidic, Peter Fajfar, Matej Fischinger, Consistent inelastic design spectra: strength and displace, Earthquake Engng. Struct. Dyn., 23 (1994) 507-521.
[4] M. J. N. Priestley, R. Park, Strength and ductility of concrete bridge columns under seismic loading, ACI Structural Journal, 8 (1987) 61-76.
[5] M. Berry, M. Eberhard, Performance models for flexural damage in reinforced concrete columns, University of California, Berkeley, PEER Report 2003/18.
[6] Q. Liu, L. Fan, Analysis of ductile reinforced concrete piers, Journal of Tongji University, 3 (1998) 245-249.
[7] Q. Liu, G. Yan, Y. Chen, Low seismic performance of reinforced concrete piers experimental study, Journal of Northern Jiaotong University, 5 (1996) 517-521.
[8] G. Yan, H. Xiang, Beam with a single-row pile pier seismic ductility practical method of checking, Journal of Civil Engineering, 2 (1993) 48-56.
[9] K. Zhang, T. Ma, B. Tong, One hundred meters high box-model test and analysis of pier, Bridge Construction, 2 (1997) 49-56.
[10] Z. Sun, J. Li, G. Yan, Reinforced concrete single column piers experimental study on seismic, Railway Engineering, 5 (2009) 36-39.

© (2012) Trans Tech Publications, Switzerland
doi:10.4028/www.scientific.net/AMM.238.769

Theoretical Calculation and Parametric Analysis of Tunnel Settlements Due to Neighboring Over-length Pile Groups

Kun Wang

Design & Consulting Co., Shanghai Geotechnical Investigations and Design Institute Co., Ltd, Shanghai, China

alex2005wang@hotmail.com

Keywords: over-length pile groups; load spreading property; tunnels; displacement field; plain strain.

Abstract. According to influence of pile groups of high-rise buildings on metro tunnels nearby, the research is made to analyze the stress of soil and the settlement of neighboring tunnels caused by pile groups. Based on the hypothesis of pile groups under flexible cushion cup, the plain strain of profile of tunnels is calculated by combining the load spreading property along over-length piles and Mindlin answer and the formula of displacement field of soil. In this way, MATLAB programs are made to get some useful conclusions by analyzing the influence factor of the settlements of tunnels such as the distance between them and the collocation of piles, the loading level and the scale of piles.

Introduction

With the rapid development of city construction in our country, a number of metro tunnels are being built in many cities to alleviate traffic pressure. Therefore, scholars pay more attention on the research of influence of pile groups of high-rise buildings on existing neighboring metro tunnels nowadays. In this article, assumed on over-length pile groups under flexible cushion cup, the plain strain of profile of tunnels in oval-shaped deformation pattern [1] is calculated by combining the load spreading property of over-length piles [2] and the amended answer of surface settlements due to tunnel deformation in an elastic half plane by estimating the undrained gap parameter [3]. The final formula is gotten in this way so that MATLAB problems could be made to get some useful conclusions by analyzing the influence factors.

Load Spreading Property of Over-length Piles

Load transfer curve takes an important role in the theory of settlement calculation of overlength piles, which shows the relationship between frictional resistance and settlement of the piles. Actually it's difficult to get the actual load transfer curve or express it by simple mathematical relational expression. It's still quite hard to get the answer of the function even if the actual load transfer function is obtained.

A large number of over-length pile tests shows that the change rule is fairly accord with the characteristics of the hyperbolic function when the frictional resistance of the pile is under its maximum value. Through the optimization analysis and statistical analysis of the piles and combining the functions given by Yang [2] and Xiao [4], the load transfer function may be expressed as follows to get the stress mechanism of the piles in this paper:

$$\tau(z) = 1/\{\frac{r_0}{G_s[1-0.75(\frac{z}{l})^{1.5}]\omega(z)}\ln\frac{2.5l(1-\upsilon)}{r_0}+\frac{1}{c+k_0\gamma z\tan\varphi}\} \tag{1}$$

Where $\tau(z)$ is the frictional resistance of a pile at the depth of z; and r_0 and l are the diameter and length of the pile; and k_0 is the coefficient of earth pressure at rest; and G_s and υ and γ and c and φ are the shear modulus and Poisson's ratio and unit weight and cohesion and angle of friction of the soil; and $\omega(z)$ is the pile settlements referring to Zhao [5] as follows:

$$\omega(z)=\frac{P}{\sqrt{\frac{2\pi G_s A_p E_p}{\ln\frac{2.5l(1-\upsilon)}{r_0}}}}\sinh[\sqrt{\frac{2\pi G_s}{A_p E_p \ln(\frac{2.5l(1-\upsilon)}{r_0})}}(l-z)]+\frac{0.85(1-\upsilon)P}{4r_0 G_s}\cosh[\sqrt{\frac{2\pi G_s}{A_p E_p \ln(\frac{2.5l(1-\upsilon)}{r_0})}}(l-z)] \quad (2)$$

Where P refers to load force on the top of the pile; and E_p and A_p are the elastic modulus and cross sectional area of the pile.

Tunnel Settlement Calculation

Taking the soil as semi-infinite elastic solid, the horizontal and vertical stress of each point along tunnel axes due to the loading of pile groups could be calculated by combining Mindlin answer (Minglin, 1936) [6] and Eqs. (1), which are named P_h and P_v. The problem is transformed into plane stress and strain analysis of the tunnel profile this way. Considering the tunnel loading level greater than soil specific gravity, the model is set to solve the tunnel settlement when the effect of shear stress is ignored as it shows in Fig. 1. A general solution has been proposed by Timoshenko (1970) [7] in the form of the Airy function. Taking the coordinates showed in Fig. 2, the function can be written as:

$$\phi=\frac{P_v+P_h}{4}r^2+\frac{P_v-P_h}{4}r^2\cos 2\theta \quad (3)$$

Then by applying the boundary conditions that $\sigma_r=\tau_{r\theta}=0$ when $r=a$, the stresses can be derived as σ_r, σ_θ, $\tau_{r\theta}$, u_r and u_θ [1] which are omitted in this paper.

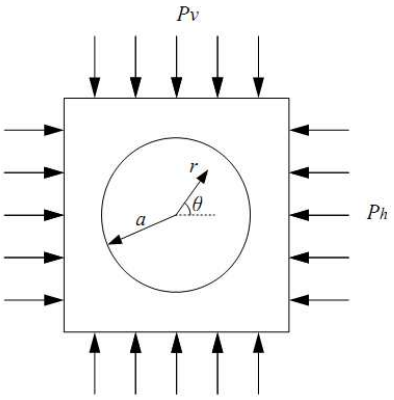


Fig. 1 Distribution of initial stress

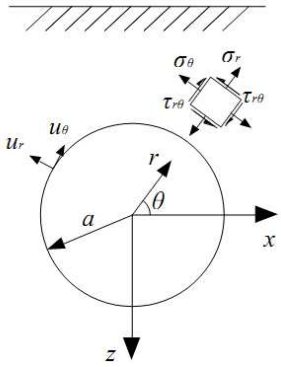


Fig. 2 Calculation diagram

Due to the lack of measured data of the oval-shaped deformation of the tunnel, the conception of ground loss ε and gap parameter g is taken in this paper given by Loganathan [3]. Supposing the soil volume remains the same in the process of deformation, the relationship between them can be written as:

$$\varepsilon=\frac{4gr+g^2}{4r^2}\exp[-\frac{1.38x_0^2}{(h+2r)^2}+\frac{0.69z_0^2}{(h+r)^2}] \quad (4)$$

Where h is the distance from the top of tunnel to the ground.

Through the distribution analysis of displacement and stress in homogeneous soil, Gonzalez [8] proposed an expression for the ground loss:

$$\varepsilon=\frac{P_v}{2G_s}[1+2(1-\upsilon)[2\frac{h+r}{r}(\frac{h+r}{r}-\sqrt{(\frac{h+r}{r})^2-1})-1]/[1-\frac{h+r}{r}(\frac{h+r}{r}-\sqrt{(\frac{h+r}{r})^2-1})]] \quad (5)$$

The gap parameter could be solved by combining Eqs. (4) and (5), which is expressed as:

$$g=\{4r^2+\frac{2P_v r^2\exp[\frac{1.38x_0^2}{(h+2r)^2}+\frac{0.69z_0^2}{(h+r)^2}]}{G_s}\cdot[1+2(1-\upsilon)\frac{2\frac{h+r}{r}(\frac{h+r}{r}-\sqrt{(\frac{h+r}{r})^2-1})-1}{1-\frac{h+r}{r}(\frac{h+r}{r}-\sqrt{(\frac{h+r}{r})^2-1})}]\}^{\frac{1}{2}}-2r \quad (6)$$

Assume on the form of tunnel deformation [9], modified boundary conditions of the prescribed displacement are considered around the tunnel:

$$u_r(r=a)=\frac{g}{8}(5+3\sin\theta-3\cos^2\theta) \tag{7}$$

According to the practical boundary condition that $u_r \to 0$ when $r \to \infty$, the simple correction is made by using $-u_\theta$ instead of u_θ in the estimation of the surface settlement. Therefore the settlements u_y can be estimated as:

$$\begin{aligned} u_y &= u_r\sin\theta-u_\theta\cos\theta=\frac{1}{2G_s}\{\frac{G_s g}{4}(5+3\sin\theta-3\cos^2\theta)ar^{-1}\sin\theta+ \\ &\frac{P_z-P_x}{2}[a^4r^{-3}-4(1-\upsilon)a^2r^{-1}]\sin\theta\cos 2\theta-\frac{P_z-P_x}{2}[a^4r^{-3}+2(1-2\upsilon)a^2r^{-1}]\sin 2\theta\cos\theta\} \end{aligned} \tag{8}$$

Thus the maximum displacement of the tunnel can be written as:

$$\delta_{\max}=u_y\Big|_{r=a,\theta=\frac{\pi}{2}}=g+\frac{4\upsilon-3}{4G_s}(P_z-P_x)a \tag{9}$$

Influencing Factor Analysis

To analyze the influencing factors, the model is simplified as a 4×4 pile foundation neighboring a tunnel with the relative position shown in Fig. 3. Soil and the other parameters are selected based on the Metropolis Project in Shanghai [10], which are listed as follows: pile diameter d = 1m; l = 50m; E_p = 3.25×10^{4}MPa; h_c = 2m; tunnel radius a = 4m; h = 4m; G_s = 82.4MPa; υ = 0.3; k_0 = 0.43; γ = 18.3kN/m^3; c = 10kPa; = 26.8; pile spacing S_1 = 3m; horizontal distance between the tunnel and the pile group S_2 = 3m; load on each pile top P_0 = 3000kN.

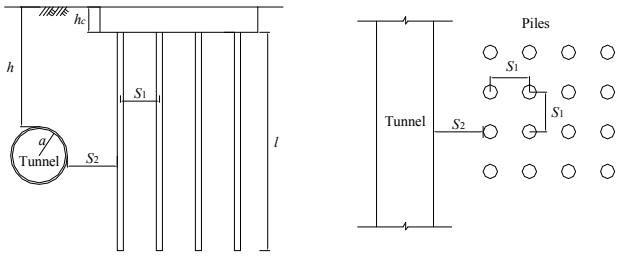


Fig. 3 Relative position of pile groups and tunnel diagram

MATLAB programs are made to analysis the influencing factors by the method mentioned above so that some conclusions can be got by changing certain variables.

Loading Location Factor. Fig. 4 shows that the tunnel settlement declines obviously with the increase of horizontal distance between the tunnel and the pile group with the trend of which more stable and the influenced range reduced. So the conclusion can be got that the location of pile groups brings a great influence.

Loading Level and Pile Collocation Factor. Increasing the number of piles perpendicular or parallel to the tunnel axis by two rows with each of the conditions containing two cases including the pile load remains constant (p') and the total pile load remains the same (P = 2P'/3), in this way the tunnel settlement curve is plotted as shown in Fig. 5 where 4×6 stands for 4 piles each row and 6 piles each column. From the figure it's known that the reduce ratio of tunnel settlement perpendicular to the tunnel axis is higher than the other with the total pile load remained the same; meanwhile, the tunnel settlement increases obviously in the case that each of the pile load stay the same, while the influenced range is not much affected at the same time.

Piling Scale Factor. Different type of pile foundation is designed from the scale of 4×4 to 6×6 with the relative position and pile spacing and pile load remained the same, and in this way Fig. 6 is got to describe the curve of the pile top and tunnel settlements. It shows that the pile top and tunnel

settlements increase with the development of the piling scope in this figure; and the curve of pile top settlements is nonlinear with the changing rate gradually coming to a standstill; and tunnel settlements curve is nearly linear with the influence factor of soil parameters and piling scope involved in where further study is needed.

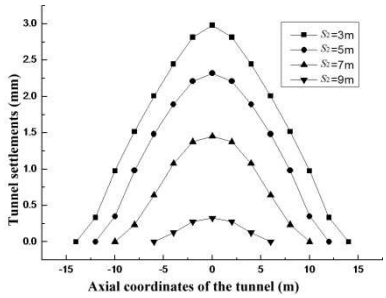


Fig. 4 Influence of loading location on tunnel settlements

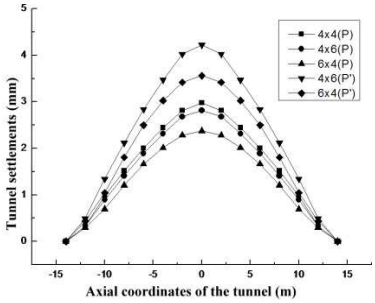


Fig. 5 Influence of loading level and piling mode on tunnel settlements

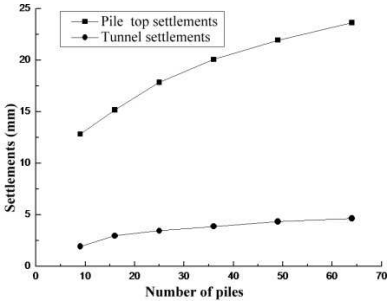


Fig. 6 Influence of piling scope on tunnel settlements

Conclusions

In this paper research is made to analysis the plain strain of profile of tunnels in given boundary conditions with the hypothesis of pile groups under flexible cushion cup by combining the load spreading property along over-length piles and Mindlin answer and the conception of gap parameter. In this method some useful conclusions is made as follows:

The relative position between them influences a lot in tunnel settlements so that pile groups should be arranged far away from neighboring tunnels in a project if possible; the increase of piles perpendicular to the tunnel axis makes it more efficient to reduce the tunnel settlements than that parallel to it, which means the distance from the center of gravity of pile groups to the tunnel should be increased according to the engineering site condition; the pile group and tunnel settlements increase with the development of the loading level and the scale of piles, and the minor increase of tunnel settlements is nearly linear and the change rule of which needs further study.

References

[1] K. H. Park, Elastic solution for tunneling-induced ground movements in clays, International Journal of Geomechanics, 4 (2004) 310-318.

[2] J. Yang, Research of Load Transfer Mechanism of Super-long Pile and Optimization Design of Pile Box (raft) Foundation, Ph.D. thesis, Tongji University, 1996.

[3] N. Loganathan, H.G. Poulos, Analytical prediction for tunneling-induced ground movements in clays, Journal of Geotechnical and Geoenvironmental Engineering, 124 (1998) 846-856.

[4] H. Xiap, H. Zhong and Y. Zhang, Numerical iteration method for determining load-settlement relationship of a single pile, Rock and Soil Mechanics, 23 (2002) 592-596.

[5] M. Zhao, L. Zhang and M. Yang, Settlement calculation of the long-short-pile composite foundation with shear displacement method, Chinese Journal and Geotechnical Engineering, 27 (2005) 994-998.

[6] R.D. Mindlin, Force at a point in the interior of a semi-infinite solid, Physics, 7 (1936) 195-202.

[7] P. Tinoshenko, J. N. Goodier, Theory of elasticity, New York: Mc Graw-Hill, 1970.

[8] C. Gonzalez, C. Sagazeta, Patterns of soil deformations around tunnels, Application to the Extension of Madrid Metro, Computers and Geotechnics, 28 (2001) 445-468.

[9] K. M. Lee, R. K. Rowe, K. Y. Lo, Subsidence owing to tunnelling. I: Estimating the gap parameter, Canadian Geotechnical Journal, 29 (1992) 929-940.

[10] F. Chu, Y. Li, F. Liang, Y. Li, Numerical analysis on deformation of deep excavation adjacent to metro considering small-strain stiffness of soil, Chinese Journal of Rock Mechanics and Engineering, 29 (2010) 3184-3192.

© (2012) Trans Tech Publications, Switzerland
doi:10.4028/www.scientific.net/AMM.238.773

Excavation Technology of Shield Tunneling in Mixed Ground

Shiliang Xu

Department of Geotechnical Engineering, Anhui Institute of Architecture & Industry, Heifei 230022, China

slxu@aiai.edu.cn

Keywords: Interval metro tunnel; Shield Tunneling Method, mixed ground, excavation technology.

Abstract. The excavation technology of shield tunneling in mixed ground is described in this paper. The interval metro tunnel is 2004 m long and 8.5 ~ 25 m deep below the ground surface. The 511 m long tunnel is located in the mixed ground. Especialy the upper of tunnel is soil and the lower of tunnel is rock. In order to improve the excavation advance and reduce the excavation cost by shield method, the tunneling mode, excavation parameters, cutter change, construction organization and management are adopted according to the ground properties. The excavation technology is successfully applied and provides a good reference for the similar ground conditions.

Introduction

With the rapid development of urban transportation, more and more city will choose metro tunnel as a solution to traffic congestion. The shield tunneling method has been widely applied in the underground tunnel excavation in the city [1-4], and tunnel shield is an advanced high-tech construction equipment for tunnel engineering. The basic advantages of shields are high safety and rapid excavation speed, with low over-break and low manpower. It has gained a great development since the nineteen sixties in China. The types of tunnel boring machines can be divided into open face shield, Slurry face Machine and Earth pressure balance (EPB) machine etc. The choice of shield machine and its facilities is a critical decision on tunnel engineering, and will be guided by thorough assessment of the encountered ground types and conditions and by numerous other aspects.

A interval metro tunnel in Shenzhen city is 2004 m long and the ground cover is 8.5 ~ 25 m. The geology condition is complex and the 511 m long of tunnel is located in the mixed ground. The mechanical properties, geological conditions and hydro-geological characteristics are different. In order to ensure the successful tunnel excavation, the shield tunneling method is adopted and the highly variable nature of surrounding rock poses significant challenges to tunnel excavation. Some change and modification of excavation mode and excavation parameters is very important according to the mixed ground situation. The boulders in soft soil is a perennial problem for shield tunnel construction. The condition that the upper part is in soil and the lower part of the working face is in rock will make displacement and ground settlement control more difficult, as well as the problem of cutter wear.

Geotechnical Conditions

According to the geological investigation report of interval metro tunnel, the ground formation is divided into 5 layers and 17 sub-layers, the main formations are quaternary artificial deposit, quaternary Holocene, quaternary alluvium and diluvium, and granite of Yanshan period. The soils can be classified into Quaternary artificial pile soil, miscellaneous fill, alluvial silt accumulation of argillaceous clay, clay, silt clay, silt, sand, gravel, colluvial clay, residual gravel clayey soil, sandy soil, soil including spherical boulders. Yanshan granite is medium to coarse grained with massive structure, and the main ingredient is quartz, feldspar, mica. The uniaxial compressive strength of granite is 60.6 ~ 167.0 MPa. The granite rock can be divided into full-weathered rock, highly weathered rock, moderately weathered rock, slightly weathered rock. According to the rock mass classification used in metro tunnel field in China, the rock masses in the tunnel area are generally categorized into grades III, IV, and V. Groundwater depth is 1.22 ~ 17.8 m and the water level amplitude is 0.5 ~ 2.0 m.

According to the tunnel line design, 511 m long of tunnel is located mainly in mixed ground. Especialy the upper of tunnel is soil and the lower of tunnel is rock. The ground distributions of DK22+060 ~ DK22+287 tunnel is shown in Fig. 1. The geological conditions are gravelly clay, clay, full-section granite rock mass, half section granite rock mass, clay including boulders, etc.

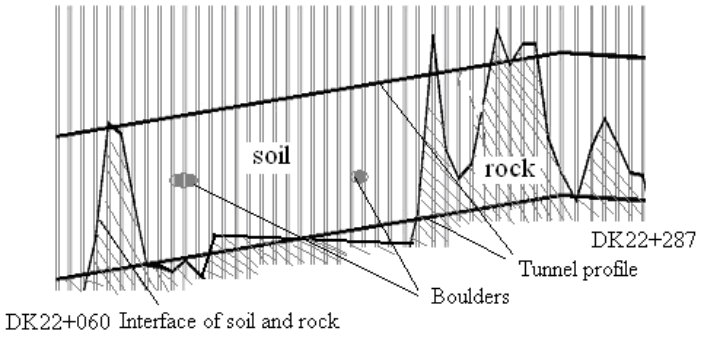


Fig. 1 Mixed face ground in DK22+060 ~ DK22+287

Principle of Composite Shield Machine

Shield tunneling in the mixed ground is a complex process, and the shield machine selection is very important for the tunnel excavation. Tunneling with a shield machine is characterized by a cyclic advance process. When a certain length is excavated, the erection of the segments begins. Shield machine consists of cutter wheel, machine chamber, screw conveyor, the segment erector, soil conditioning system, transportation system, synchronous grouting system, power supply system, water circulation system and ventilation system, etc.

Due to the high water level, the mixed ground conditions and the complexity of the tunnel surface environment, the composite shield machine is adopted in order to ensure the construction safety and reduce surface subsidence. In order to adapt to change of rock properties, The shield must be equipped with composite cutter for the rock breaking, and has the ability of cutting rock and deformation control. The foam injection system is used for maintenance of pressure, fluidizing the soil, creation of an homogeneous soil paste, permeability reduction, lowering of torque, reduction of soil stickiness and reduction of abrasion. The composite shield machine has been successfully applied in the metro tunnel of Guangzhou city. The flow chart of composite shield tunneling is shown in Fig. 2.

Technology of Shield Tunneling

Choice of Tunneling Mode. In order to adapt to the mixed ground condition, it is important to choose the tunneling mode. The composite shield tunneling method has with three modes including an open non-pressurized mode, a semi-open mode and a closed-face pressurized mode. When the shield is excavating through the stable stratum bearing little impact on the surrounding environment or less groundwater, an open non-pressurized mode is used. A semi-open mode is only needed with a small amount of residue in the soil bulkhead and compressed air or foam is aided in the excavation process. A closed-face pressurized mode can balance the excavation of surface soil pressure and groundwater pressure by the earth pressure in the machine chamber, and can maintain stability in the face to avoid the tunnel face collapse or ground subsidence.

According to the geological condition, an open non-pressurized mode is adopted in the full-face rock tunnel, and the foaming agents are used to improved muck. When tunneling through in full-face soft ground and upper soft lower hard ground, a closed-face pressurized mode is selected, and the muck is added with foam and an amount of bentnite. The earth pressure balance is a dynamic balance through the working of the screw conveyor. In the open mode the efficiency of cutting hard rock is heightened and the cutter wear is reduced effectively. When the encountered ground condition is changed, the composite shield machine may have to convert from a closed-face pressurized mode to an open non-pressurized mode when tunneling in harder ground types to avoid over stressing the

machine's mechanical functions. Such a change may require some modification of the machine and the reverse once again when the composite shield machine enters a soft, potentially unstable ground or upper soft lower hard ground.

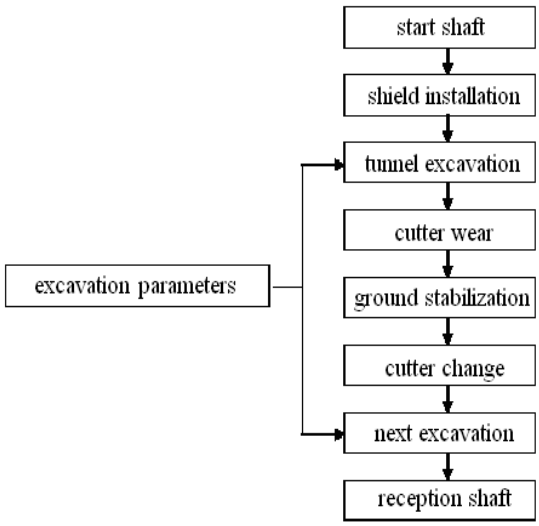


Fig.2. Flow chart of composite shield tunneling

Excavation Parameters. Shield tunneling through mixed ground will cause the cutter wear, frequent cutter change and high difficulty of construction. The excavation parameters are determined before the shield construction according to the different engineering geological characteristics and the embedment depth of the tunnel. These parameters are the advancing speed, the earth pressure, the rotation speed of cutter wheel, the cutter torque and the thrust force. In the shield tunneling process, jack thrust force is an important construction parameter [5]. It not only determines the advance speed, but also influences the cutting torque, the rotation speed of cutter wheel and other parameters. The excavation parameters of shield tunneling method are the key to overcome the difficulty and risk of excavation. The excavation parameters based on the trial error method and engineering experience in mixed ground condition are as follows:

During tunnel excavation with the full-face rock, the excavation parameters are: the total thrust force 900 ton, the advancing speed 10 mm/min, the earth pressure 0 bar, the rotation speed 1.8 rpm, the cutter torque 1.2 MN • m.

During tunnel excavation with the half-face rock, the excavation parameters are: the total thrust force 1100~200 ton, the advancing speed 15 mm/min, the earth pressure 1.2~2.6 bar, the cutter speed 1.3~1.6 rpm, the cutter torque 0.7~3.5 MN • m.

In boulder excavation process, the excavation parameters are: the total thrust force 1500 ton, the advancing speed 20 mm/min, the earth pressure 1.2 ~ 2.6 bar, the rotation speed 1.1 ~ 1.9 rpm, the cutter torque 0.7 ~ 4.0MN • m.

During excavation in the gravelly clay soil, the excavation parameters are: the total thrust force 1500 ~2000 ton, the advancing speed 35 ~ 60 mm/min, the earth pressure 1.3 ~ 2.4bar, the rotation speed 1.5 rpm, the cutter torque 1.6MN • m.

Cutter Changes. Shield tunneling in the mixed ground is likely to result in the overloading of local cutter and the cutters wear, and is very detrimental to the working status of shield machine. According to the hardness and abrasiveness of surrounding rock, the total thrust force is determined reasonably to prevent the cutter from overload and damage. In order to protect the shield machine during tunneling process, it is necessary to frequently check cutter status. The place of the cutter check and change should be in the stable ground. It is important to analyze ground stability before the cutter change in the mixed ground. The composite shield machine is equipped with pressure system in the bulkhead to ensure the tunnel face stability and security of cutter change. If the face stability can't be kept with pressure, the method of bored piles, jet grouting pile etc. are adopted to reinforce the ground.

Construction Organization and Management. The guiding principle of shield tunneling method in mixed ground is correct excavation mode, reasonable earth pressure, rapid excavation, timely grouting, frequent monitoring and rapid modification. In the shield tunneling process, it is important to carry out the detailed geological investigation using a variety of methods to reveal as far as possible to the geological conditions along the tunnel line. The careful analysis of different ground characteristic can provide the references for choice of excavation parameters. The cutter change must be conducted timely according to wearing degree of the cutter. Reasonable planning and layout of construction site and adequate equipment are also necessary. The coordination of transportation system, segment supply system, grouting system etc. must be strengthened Much attention shall be paid to the training of shield machine driver and the responsibility of other worker.

Conclusions

In this paper, the technology of the interval metro tunnel excavated by shield tunneling method in mixed ground is discussed. The following are the main conclusions:

The investigation of geological distribution must be carried out carefully during shield tunneling in mixed ground conditions. This will determine the tunnel layout and help minimize the risks of tunnel instability and the modification of the surrounding environment.

The tunneling mode, optimization of excavation parameters, and cutter change are determined based on the characteristics of rock or soil.

Strengthening the construction organization and management can ensure the safety of shield tunneling and successful excavation.

Acknowledgements

This paper is supported by Grant No. KJ2011B040, No. KJ2012A053 and No. KJ2012A061.

References

[1] Y. Ma, The shield mechanical driving adaptability analysis of composite formation in Guangzhou subway, Shanxi Architecture, 35 (2009) 322-323.

[2] Q. Xu, H. Zhu, S. Liao, Analysis of reasonable thrust force during tunnel excavation in homogeneous soft ground by use of earth pressure balance shield machine, Chinese Journal of Geotechnical Engineering, 30 (2008) 79-85.

[3] Z. Tan, K. Hong, J. Wan, Study on composite shield and construction technique in complex uneven strata, Chinese Journal of Rock Mechanics and Engineering, 25 (2006) 3945-3952.

[4] X. Liu, Causes for wearing of disc cutters of shield machines in mixed ground and counter measures, Tunnel Construction, 26 (2006) 77-80.

[5] M. Shao, X. Zhong, J. Yu, Research on thrust of shield in mixed face ground. Guangdong Architecture and Civil Engineering, 1 (2010) 36-39.

© (2012) Trans Tech Publications, Switzerland
doi:10.4028/www.scientific.net/AMM.238.777

Safety Analysis on the Structure of an Existing Metro Station Impacted by the Construction of an Adjacent Building

Liheng Ma [a], Qinghuai Liang [b], Liu Yifan [c] and He Mingran [d]

Beijing Jiaotong University, Beijing, China

[a]maliheng1984@gmail.com, [b]qhliang@center.njtu.edu.cn,

[c] liuyifan@gmail.com, [d]hemingran@sina.com

Keywords: metro station; adjacent construction; foundation excavation; safety assessment.

Abstract. Structural deformations of the existing metro station caused by adjacent building construction should be controlled strictly so as to keep the normal operation of the existing metro station and guarantee the safety of the station structure. Based on a foundation pit excavation and building project which is adjacent to an existing metro station in Beijing, a 3D finite element model of foundation pit, metro station and surrounding soil is established. Then, the structural deformations of the main body structure (rail area), the passageway and the fire fighting passageway in different construction stages are obtained. The control values of the station structure deformation during building construction process are proposed according to the calculation results.

Introduction

With the large-scale development and utilization of urban underground space and the rapid construction of urban rail transit facilities, more and more housing projects are constructed nearby the existing metro station. Foundation pit excavation and new housing load can affect the surrounding soils, causing stress redistribution, breaking the initial equilibrium state and leading to deformation of the station [1]. In order to ensure the safety of the existing station [2], it is necessary to assess the structural safety, and choose the deformation control values before the construction begins. What's more, the structural deformation of station must be controlled strictly during the whole process of construction. Many scholars had studied on this problem, and got some beneficial results [3-6].

Based on a foundation pit excavation and building construction project, which is adjacent to a existing metro station in Beijing, a 3-D finite element model is established in this paper. Through modeling the whole process of construction, the deformations of multi-parts of station structural at different construction stages are gotten, and the deformation control values are proposed, which is important to ensure the safety of the project.

Engineering Situation

JIAOMENXI underground station of Beijing metro line 4 is located at the crossroads of the MAJIAPUXI road and the SHILIUZHUANG road. The station runs north-south, and is double-layered and three-spanned. The longitudinal span of the station's main body is 193.4m, the altitude of the station's bottom plate is 23.5m which is about 6m below the ground. The material for primary station support is C20 early strength shotcrete; the secondary lining material is C35 waterproof concrete, of which the impermeability grade is S10; the material of columns and joint area is C50 concrete; the backfilling plain concrete of station bottom plate is C15.

The planning building is nearby the southeast passageway, three-layer frame structure, one underground layer and two above-ground layers. The planning foundation pit is 34.5m long, 17.5m wide, and 5m deep. Both retaining walls and cantilever piles for foundation pit supporting are needed in the excavation operation for the restriction of the surrounding roads, buildings and area. The cantilever piles, which are made of C25 concrete, and 0.6m in diameter, 8.0m in length, 5.0m in anchorage length, 1.0m in pile spacing, is bored pile. As shown in Fig. 1, there are 84 cantilever

piles in total, which are distributed around the foundation pit. The retaining walls are brick wall of 2.0m high and 240mm thick. The section size of constructional columns of retaining wall is 240mm × 240mm, and the column spacing is 3.0 m. The whole construction process can be divided into three main steps: foundation pit excavation→ retaining pile and retaining wall construction→ new building construction.

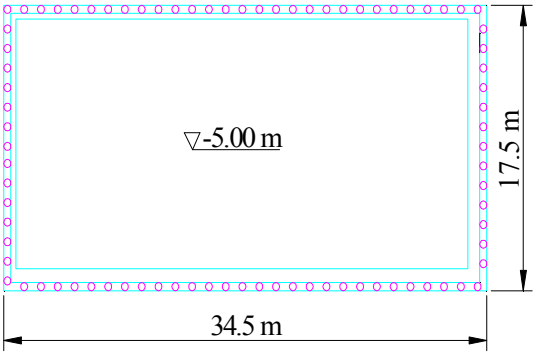


Fig. 1 Foundation pit in plan

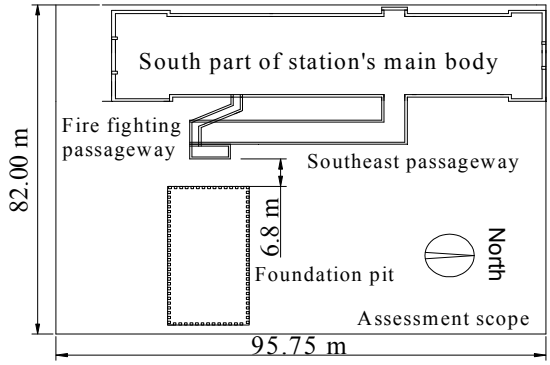


Fig. 2 Assessment scope and the location

As the horizontal distance from excavation foundation pit to southeast fire fighting passageway is only 6.8m, and the foundation pit locates in the protected area of the urban rail traffic according to relevant regulations, safety assessment of the construction project is needed. The specific location of the excavation pit is shown in Fig. 2.

Scope of Assessment

The "Urban Rail Transit Operation Management Method [7] mentioned "the following areas should be set as the urban rail transit protected areas: (a) within 50m away from underground stations and tunnels; (b) within 30m away from ground and elevated stations, as well as railway line; (c) within 10m away from passageways, ventilation shaft and other accessory structure of station." According to the above regulations, the assessment scope of this project includes excavation pit, the southeast passageway and fire fighting passageway of the metro station, and the south part of the station. The size of the assessment area is 82m × 95.75m, which is shown in Fig. 2. The north part of the station and the other accessory structures are far away from the excavation pit, and are separated by deformation joints between these structures which are relatively independent, hence, the assessment model does not contain these structures.

Model and Calculation Parameters

Hypothesis of Model. The following assumptions are demanded in finite element modeling calculation:

a. The surface and all the soil below are layers distributed, horizontal and homogeneous.

b. The soil gravity is reckoned in the calculation of initial ground stress; the tectonic stress of soil is ignored.

c. The constitutive model of site soil is Drucker-Prager model.

d. Soil parameters of the model use the measured values of geologic survey report.

e. The material strength of JIAOMENXI station reaches the designing strength, and the material strength doesn't reduce.

f. The material of station structure is elastic-plastic material. All the parts of station structure and the soil layers conform to the principle of deformation compatibility.

Calculation Parameters. According to the geological survey report, the terrain of construction site is flat. Ground surface is artificial accumulation layer of 2.20m to 2.80m in thickness, the main components of which is clayey silt and sandy silt. Recently deposited layer is below the artificial accumulation layer, which contains sandy silt, clayey silt, fine sand and gravel. Under the recently deposited layer is quaternary sediment layer of gravel. The measured soil parameters of the geological survey report are shown in Table 1.

Table 1 Soil parameters

Formation Lithology	Standard bearing capacity (kPa)	Compression modulus (MPa)	Internal friction angle (°)	Cohesion (kPa)
Clayey silt, Sandy silt, Plain fill	/	/	5	10
Sandy silt, Clayey silt	140	7.0	15	15
Silty clay	120	5.5	10	20
Fine sand	160	12.0	25	0
Gravel	250	35.0	/	/
Gravel	350	45.0	/	/

Groundwater wasn't found by the drilling depth of 20.0m according to the geological survey report. According to the hydrogeology data of Beijing, the buried depth of groundwater is about 25m below the ground in the recent 3~5 years. Because the buried depth of groundwater is deeper than the depth of excavation pit, so the influence of groundwater isn't considered in this construction project

Finite Element Model. ANSYS software and three-dimensional finite element method are used in numerical simulation and modeling. Boundary conditions of the structure model strictly accord with the requirements of the tunnel mechanics. The surrounding soil and structure can interact with each other. The SOLID45 element is used to simulate the structure of the main body, passageway, fire fighting passageway, surrounding soil, retaining pile and retaining wall; the ground surface of the whole model is free boundary, and the other five boundaries are normal constraint. The size of the whole model is 82m × 95.75m × 17 m, as shown in Fig. 3. Fig. 4 shows the model of excavation pit and the station structure, Fig. 5 shows the model of retaining pile and wall.

Calculation Results and Analysis

Calculation Results of Initial Self-weight Stress Field. In order to simulate the undisturbed soil of which settlement has been completed as the initial state of excavation simulation, initial self-weight stress field need to be constructed in finite element modeling calculation. The calculation results of initial self-weight stress field are shown in figure 6 and figure 7. The maximum settlement of the whole model is 7.29 mm, which includes the foundation pit, metro station and surrounding soil. The distribution of settlement is horizontal, along the direction of soil layer. The settlement decreases with the depth. The maximum settlement position is near ground.

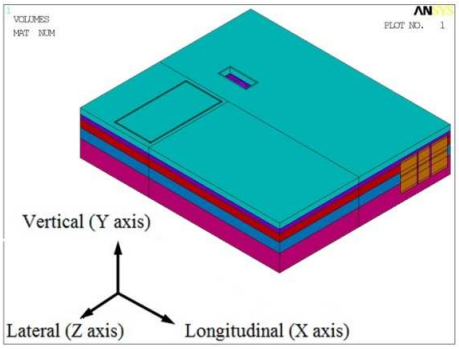


Fig. 3 Whole model

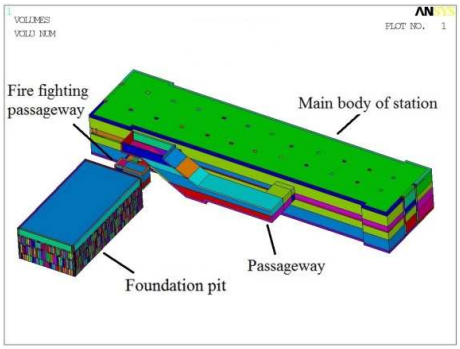


Fig. 4 Model of foundation pit and metro station

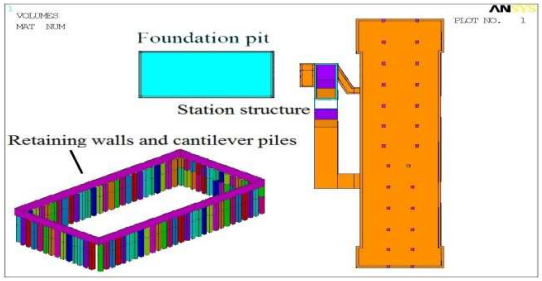


Fig. 5 Model of retaining pile and retaining wall

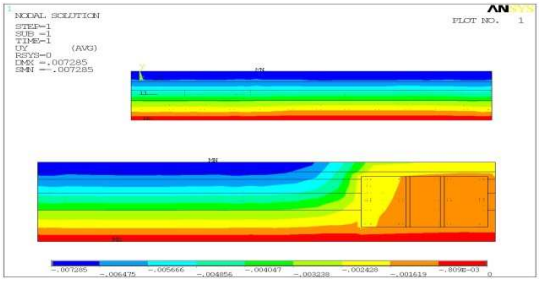


Fig. 6 Displacement contour under self-weight stress field (front elevation)

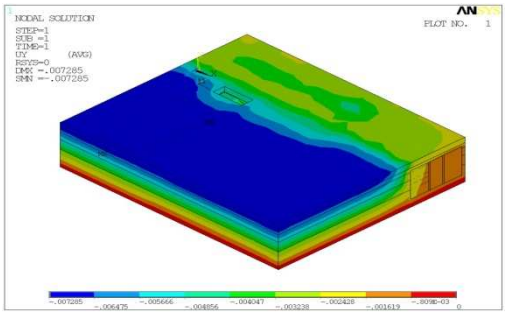


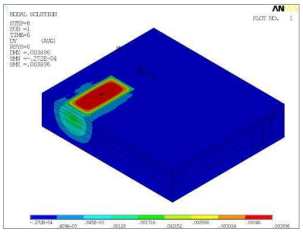
Fig. 7 Displacement contour under self-weight stress field (side elevation)

Influence of Foundation Pit Excavation. After the foundation pit excavation, the deformation amplitudes of each part of the model are shown in Table 2, and the displacement contour plots of the maximum deformation direction of each part are listed in Table 3.

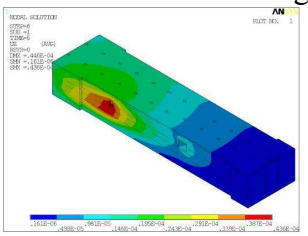
Table 2 Amplitude of structural deformation after excavation

Position	Longitudinal deformation/mm	Vertical deformation/mm	Lateral deformation/mm
Whole model	1.83	3.90	2.00
Main body (rail area)	0.01	0.01	0.04
Passageway	0.09	0.15	0.37
Fire fighting passageway	0.03	0.23	0.22

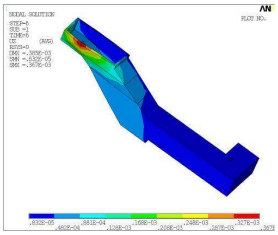
Table 3 Displacement contour of the largest deformation direction after excavation



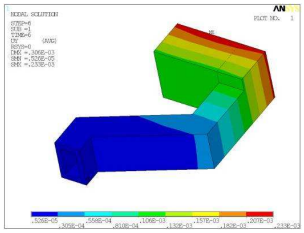
Whole model 3.90mm



Main body (rail area) 0.04mm



Passageway 0.37mm



Fire fighting passageway 0.23mm

Table 2 and Table 3 show that the maximum deformation of the whole model is vertical, which appears on the surrounding soil of foundation pit, and the amplitude is 3.9 mm. The maximum deformation of the main body of station (rail area) is lateral, which appears on the joint position that connected to fire fighting passageway, and the amplitude is 0.04 mm. The maximum deformation of the passageway is lateral, which appears on the position that close to the ground and on the side of foundation pit, the amplitude is 0.37 mm. The maximum deformation of the fire fighting passageway is vertical, which appears on the peripheral position and the position that near the foundation pit, the amplitude is 0.23 mm. Apparently, the influences of excavation to the passageway and fire fighting passageway is larger than to the main body, the influence to main body (rail area) is very small.

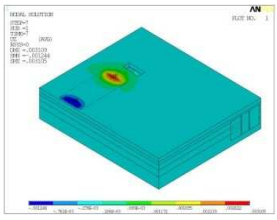
Influence of Retaining Pile and Retaining Wall. After the retaining pile and retaining wall construction complete, the deformation amplitude and the displacement contour plots of the maximum deformation direction of each model part are shown in Table 4 and Table 5. It is known that the maximum deformation of the whole model is lateral, which appears on the surrounding soil of retaining wall, and the amplitude is 3.11 mm. The maximum deformation of the main body of station (rail area) is lateral, which appears on the peripheral position and the joint position that connected to fire fighting passageway, the amplitude is 0.04 mm. The maximum deformation of the passageway is lateral, which appears on the position that close to the ground and on the side near the foundation pit, the amplitude is 0.62 mm. The maximum deformation of the fire fighting passageway is lateral, which appears on peripheral position that near the foundation pit, the

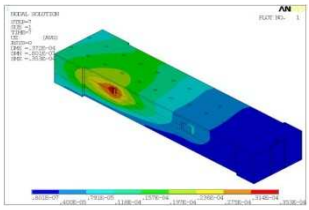
amplitude is 0.17 mm. When retaining pile and retaining wall construction complete, the deformation of the passageway and the fire fighting passageway is larger than the main body. The deformation of the main body (rail area) is very small, still remains at 0.04 mm.

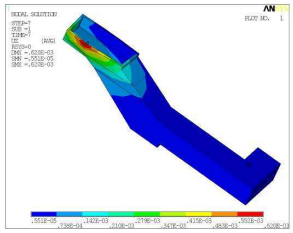
Table 4 Amplitude of structural deformation after foundation strengthening

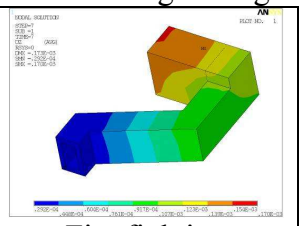
Position	Longitudinal deformation/mm	Vertical deformation/mm	Lateral deformation/mm
Whole model	2.83	2.14	3.11
Main body (rail area)	0.006	0.01	0.04
Passageway	0.15	0.07	0.62
Fire fighting passageway	0.02	0.04	0.17

Table 5 Displacement contour of the largest deformation direction after foundation strengthening


Whole model 3.11mm


Main body (rail area) 0.04mm


Passageway 0.62mm

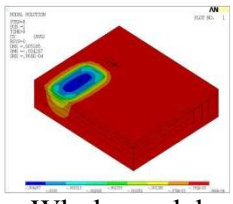

Fire fighting passageway 0.17mm

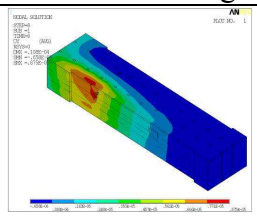
Influence of New Building Load. After building construction completed, the new building would give pressure to the surrounding soil. The deformation amplitude and the displacement contour plots of the maximum deformation direction of each model part under building load are shown in Table 6 and Table 7.

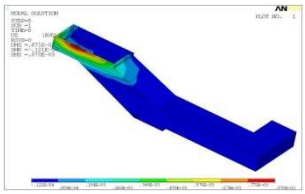
Table 6 Amplitude of structural deformation after building construction

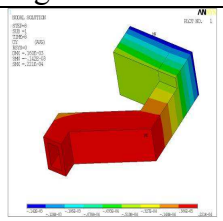
Position	Longitudinal deformation (mm)	Vertical deformation (mm)	Lateral deformation (mm)
Whole model	3.27	4.29	3.55
Main body (rail area)	0.001	0.009	0.008
Passageway	0.19	0.10	0.87
Fire fighting passageway	0.01	0.14	0.07

Table 7 Displacement contour of the largest deformation direction after building construction


Whole model 4.29mm


Main body (rail area) 0.009mm


Passageway 0.87mm


Fire fighting passageway 0.14mm

The Table 6 and Table 7 show that the maximum deformation of the whole model is vertical, which appears on the surrounding soil of the new building, and the amplitude is 4.29 mm.

The maximum deformation of the main body (rail area) is vertical, which appears on the peripheral position and the position that connected to fire fighting passageway, the amplitude is 0.009 mm. The maximum deformation of the passageway is lateral, which appears on the position that close to the ground and on the side near the new building, the amplitude is 0.87 mm. The maximum deformation of the fire fighting passageway is vertical, which appears on peripheral position and the position that near the new building, the amplitude is 0.14 mm.

Apparently, the influence of building load to the passageway and the fire fighting passageway is larger than to the main body. The deformation amplitude of main body (rail area) is very small with only 0.009 mm.

Suggestions on Deformation Control Values

The deformation control values of station is proposed based on the calculation results above, the engineering experience and field monitoring data of other similar projects, and the need of safety margin. The alarm values are 80% of control values, and the precaution values are 70% of control values, which are shown in Table 8.

Table 8 Deformation control values of station (mm)

Position	Precaution value	Alarm value	Control value
Main body (rail area)	0.03	0.04	0.05
Passageway	0.63	0.72	0.90
Fire fighting passageway	0.63	0.72	0.90

Conclusions

During the whole process of construction, the maximum deformation of station main body (rail area) is 0.04mm. The maximum deformation appears on the position that connected to fire fighting passageway, which has a certain distance away from the rail. At the same time, the deformation amplitude of the station main body (rail area) is very small and the safety margin is enough, so the third party monitoring for station main body is not necessary.

The maximum deformation of the passageway is 0.87mm, which is the maximum deformation of the whole station structure. The passageway is close to the foundation pit, so the third party monitoring for station main body is suggested if the conditions permit.

The maximum deformation of the fire fighting passageway is 0.23mm, which is the closest structure to the foundation pit, so the third party monitoring for station main body is suggested if the conditions permit.

The deformation control values of station are proposed as follows: 0.05mm for main body; 0.9mm for access channel; 0.9mm for firefighting passageway. The alarm values are 80% of control values, and the precaution values are 70% of control values.

When the deformation amplitude reaches the precaution values, warning should be issued and monitoring should be strengthened. When the deformation amplitude reaches the alarm values, the construction must be paused and effective measures should be taken to control the deformation. The construction could resume only when the deformation amplitude falls below the precaution values.

References

[1] V. A. Kontogianni, S. C. Stiros, Induced deformation during tunnel excavation: Evidence from geodetic monitoring, Engineering Geology, 79 (2005) 115-126.

[2] V. A. Kontogianni, A. Tzortzis, S. C. Stiros, Deformation and failure of the Tymfristos tunnel, Greece, Journal of Geotechnical Engineering, ASCE, 130 (2004) 1004-1013.

[3] Y. Jia, M. Wang, S. Ren, Mechanical and security evaluation of the existing metro station structure under construction of through tunnel of New Metro Line, Journal of China Railway Society, 29 (2007) 89-94.

[4] P. Gao, G. Gao, S. Feng, Control of deformation of operating metro induced by adjacent deep excavation, Chinese Journal of Geotechnical Engineering, 30 (2008) 818-823.

[5] X. Li, Safety analysis of running metro station structure adjacent to foundation excavation, Rock and Soil Mechanics, 12 (2009) 382-386.

[6] L. Tao, S. Tang, L. Jin, Deformation prediction and risk evaluation of the existing metro station structure with above-traversed tunnel, Chinese Journal of Underground Space and Engineering, 4 (2008) 442-447.

[7] The Decree No.140 of Ministry of housing and urban-rural development, Urban rail transit operation management method.

© (2012) Trans Tech Publications, Switzerland
doi:10.4028/www.scientific.net/AMM.238.783

Numerical Analysis of Effect of Blasting Vibration on Adjacent Roadway in 858 Mines

Guangyong Wang [1,2,a] and Junchao Liu [3,b]

[1]Opening Project of Key Laboratory of Deep Mine Construction, Henan Polytechnic University, Jiaozuo 454000，China

[2]School of Civil Engineering, Henan Polytechnic University, Jiaozuo 454000, China

[3] Department of politics and law management, Chizhou College, Chizhou 247100, China

[a]wanggy@hpu.edu.cn, [b]liujunchao333@163.com

Keywords: blasting vibration; the adjacent roadway; protect rock pillar; the maximum single-stage charge; numerical analysis.

Abstract. In order to avoid the effect of driving blasting on the adjacent roadway in 858 mines, numerical analysis of seismic intention was carried out. Based on monitoring data, the parameters suitable for local were obtained by Sadov's formula, by which the relationship between the maximum single-stage charge and the width of protect rock pillar were offered. According to design requirements, and considering the effect of driving blasting on the adjacent roadway, the maximum single-stage charge of driving blasting is 43.99kg.

Engineering Situation

858 mines has the area of 0.5437 square kilometers, its mining elevation is 1050~800m, and the mine type is molybdenum, its scale of production is 300 thousand tons/year, its design service life is 57.5 years. According to the primary design of the mine, “858” mines is ground collecting mine, mining method is the exploiting scheme of ramp vertical shaft combined with adit. Mining method is step room method and modernized mechanical mining, and it uses the method of automobile ramp transportation.

Calculation Model

Design of Numerical Model. In order to analyze effect of 858 mines blasting on adjacent tunnel, the size of the model is 446m×82.5 m×67.5m (final mining level), selecting 1/2 model, then chose 1.5 tunnels, in which a tunnel is partially excavated, that is 37.5 meters, the blast hole length is 2 meters, as shown in Fig. 1.

Rock mass medium is selected as SOIL-CONTRETE material, density is selected as 1.00 g/cm^3, explosive unit is selected as 1/4 of total quality, using JWL state equation:

$$p = A(1-\frac{\omega}{R_1V})e^{R_1V} + B(1-\frac{\omega}{R_2V})e^{R_2V} + \frac{\omega E}{V} \tag{1}$$

Where p, E, V respectively represent the pressure, the internal energy and the specific volume (unit volume) of detonation products (Table 1), A, B, R_1, R_2, ω are the necessary constant in JWL equation. ρ_1 is the explosive density, P_{CJ} is the detonation pressure, D_H is the detonation velocity, E_0 is the initial detonation energy.

Table 1 Material parameters of TNT, JWL

ρ_1 (g/cm^3)	P_{CJ} (GPa)	D_H (m/s^3)	A (GPa)	B (GPa)	R_1	R_2	ω	E_0 (GPa)
1.00	27	4500	169	3.67	5.69	1.19	0.3	4.26

Simulation Process and Boundary Conditions. In order to simulate propagation law of stress wave in semi-infinite body, the right and left boundary, the boundary in front and behind, the

boundary above and in bottom is set as transmitting boundary, the boundary in front is set as the boundary whose horizontal displacement is zero, then the above surface is set as free boundary, ignore the impact that rock mass make to stress wave propagation.

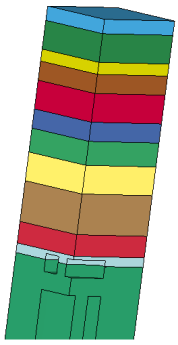


Fig. 1 Model of numerical analysis

Discussion of Numerical Analysis Results

Blasting Seismic Test Measuring Point Arrangement. In order to determine thickness of protecting rock pillar and the largest single explosive charge of 858 mines blasting, the influence of tunnel blasting on adjacent tunnel vibration is analyzed by the method of numerical simulation. Data is selected at the blasting side of the blasting point, as shown in Fig. 2.

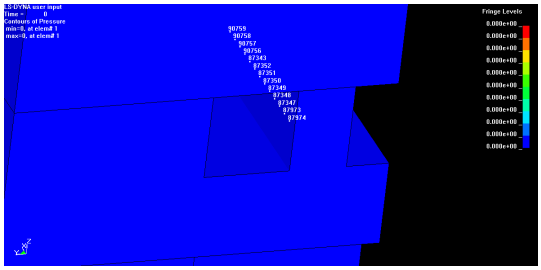


Fig. 2 Blasting measuring points arrangement in field

Numerical Simulation Results. Representative monitoring blasting results is selected at +1030 level in 858 mines. Largest single explosive charge is 160kg, 13 data is selected at +1030 level, the velocity curve is as shown in Fig. 3, the peak value of vibration velocity is shown in Table 2. Through the way of regressing data in the table by Sa Rodolfo J Ki formula, get K=746.17713，α=2.44048，r_2=0.93715.

$$V = K(\frac{\sqrt[3]{Q}}{R})^{a} \tag{2}$$

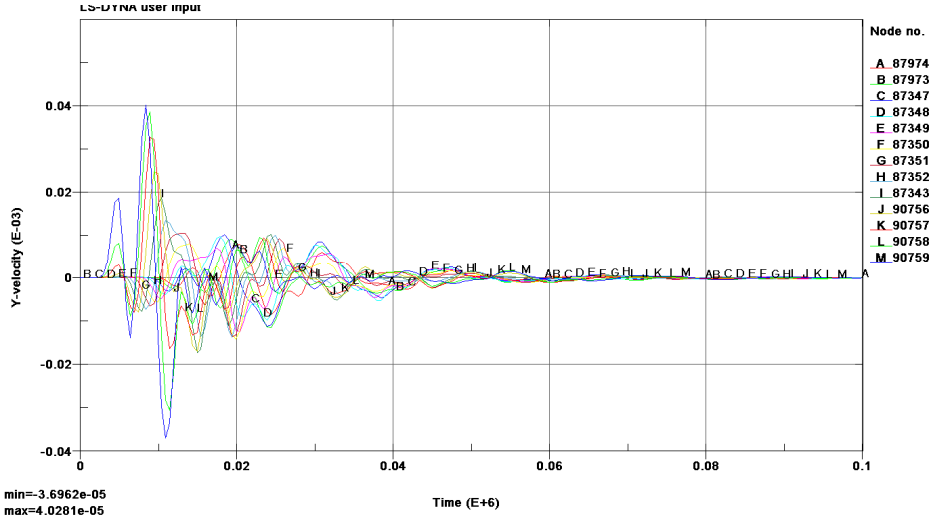


Fig. 3 Vibration oscillogram of some measuring points

Table 2 Blasting measuring results of 858 mines

Serial number	maximum single-stage charges Q (kg)	Distance of blasting R (m)	Proportional charge $\rho = Q^{\frac{1}{3}} / R$	Particle peak vibration velocity V (cm·s)
1	160	39.13	0.138734	8.5167
2	160	36.91	0.147075	11.409
3	160	34.73	0.15631	11.246
4	160	32.59	0.166549	9.8018
5	160	30.51	0.177899	12.359
6	160	28.50	0.190456	14.133
7	160	26.57	0.204281	13.703
8	160	24.74	0.219358	13.603
9	160	23.04	0.235536	18.806
10	160	21.50	0.252436	24.8
11	160	20.15	0.269346	32.673
12	160	19.03	0.285136	38.63
13	160	18.20	0.298283	40.281

In 858 mines stope, rock pillar expose area to limiting stope roof, maintenance of stope stability plays a dominant role, while pillar stability has a direct relationship with engineering blasting. According to the safe and permitted standard of blasting vibration in "blasting safety regulations" (GB6722-2003), in mine tunnel allowed working safety vibration velocity is less than 15~30cm/s, for safety reasons, lower limit value is selected for blasting vibration safety speed, namely the safe speed is selected as 15cm/s. By using of formula (2), the biggest single charge and width of protecting rock pillar is get, as shown in Table 3. We know that: with the largest single segment of dosage increasing, rock pillar width should also be increasing correspondingly.

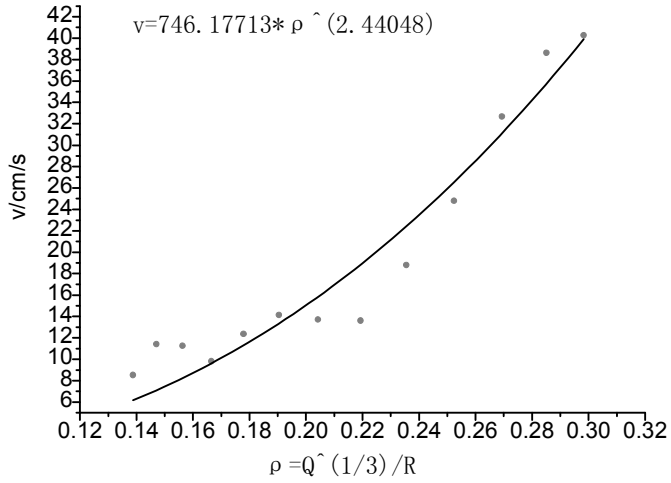


Fig. 4 The regression graph of blasting vibration

Table 3 The relationship between the different maximum single-stage charges and the width of protecting rock pillar

Parameter chosing principle	K	α	Safe velocity （cm/s）	maximum single-stage charges (kg)	Rock pillar width (m)	Remarks
Numerical simulation result of regression	746.17713	2.44048	15	10	10.68	
				20	13.46	
				50	18.26	
				100	23.01	
				200	28.99	
				500	39.35	

According to producing safety design requirements of 858 mines, in order to maintain the underground goaf stability and opening later stage production safety, length of protecting rock pillar in 858 mine stope must be greater than 15 m, if the influence of blasting on the adjacent roadway is considered, it can be obtained by the fitting formula that blasting maximum single charge is 43.99kg.

Conclusions

Through numerical analysis of the influence of the Luanchuan 858 mining tunnel blasting on adjacent tunnel, conclusions can be get as follows:

According to the numerical simulation selection of blasting vibration monitoring data in 858 mining tunnel, by the method of Sa Rodolfo J Ki formula regression, the value of K and α suitable for local is analyzed and calculated.

In order to avoid influence of engineering blasting on adjacent tunnel, the Sa Rodolfo J Ki formula obtained by regression is used to get the relationship between maximum single charge and protecting rock pillar width.

According to the 858 mining safety design requirements, 858 mine stope protecting rock pillar must be longer than 15 m, considering the influence of blasting on adjacent tunnel, the largest single explosive charge is 43.99kg.

References

[1] C. Yu, B. Liang, T. Ouyang, The vibration influence analysis of blasting excavation on existing tunnel in the situation of super large section tunnel, Tunnel construction, 2 (2010) 151-156.

[2] N. Li, Q. Gu, C. Zhang, The influence of adjacent adit blasting construction on existing adit, Chinese Journal of rock mechanics and engineering, 1 (2009) 30-38.

[3] D. Zhao, M. Wang, Blasting vibration response research in cross tunnels with small clearance, Chinese Journal of geotechnical engineering, 1 (2007) 116-119.

[4] C. Wu, G. Li, Y. Guo, Surrounding rock accumulated vibration effect research in the blasting excavation of Suspension bridge anchorage tunnel, Chinese Journal of rock mechanics and engineering, 7 (2009) 1499-1506.

[5] GB6722-2003, Rules of Explosion Safety, China Standard Press, Beijing, 2004.

© (2012) Trans Tech Publications, Switzerland
doi:10.4028/www.scientific.net/AMM.238.787

Analysis of Plastic-zone Radius Influenced by Mechanical Parameters in Tunnel Excavation and Support

Zhongming Su[1, a] and Rui Liu[2,b]

[1] Shanxi Provincial Research Institute of Communications, Key Laboratory of Highway Construction &Maintenance Technology in Loess Region, Ministry of Transport, China

[2] Supervision station of construction engineering quality, Jiangjin District of Chongqing, China

[a]375216207@qq.com, [b]80941291@qq.com

Keywords: elastic-plastic theory; plastic zone; axial force of anchor; resistance of support; dynamic support.

Abstract. According to the elastic-plastic theory, the analytical formula of plastic-zone radius is established for circular tunnel in its excavation and support, and the effect of anchor support is verified based on the radius of plastic zone from the perspective of measured axial force. The influences to plastic zone by the variations of mechanical parameters and resistance of support are quantitatively analyzed. The result is of great significance to the monitoring measurement and the dynamic design and construction of tunnel.

Introduction

Wholly grouted anchor is one of the most popular support means in the construction of highway tunnel, which can offer a kind of flexible support force, adjust the stress state of surrounding rock and ultimately make the good use of self-bearing capacity. Recently, axial force of anchor is merely measured and analyzed, but from which the study on the state of surrounding rock is not so much. The mechanism of wholly grouted anchor has often been studied by many scientific workers. Based on the measured axial force of anchor and the hypothesized uniform elastic-plastic rock mass, the analytical formula of plastic zone radius for circular tunnel is established, from which the support effect of anchor is analyzed, and the influence to scope of plastic zone is also quantitatively analyzed by the mechanical parameters and resistance of support.

Radius of Plastic Zone

The cross section of a circular tunnel is listed as in Fig. 1, hypothesized that the rock mass is uniform and elastic-plastic, and it is the axial symmetrical problem with plane strain.

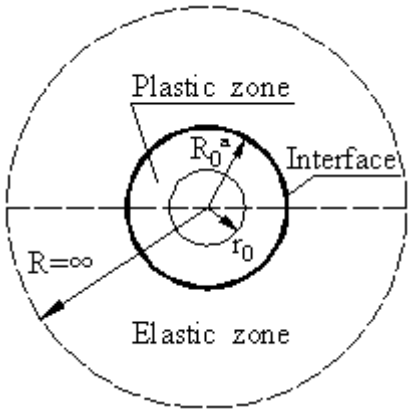


Fig. 1 The schematic diagram of plastic & elastic zone

The equilibrium equation in plastic zone is shown as in formula (1) and Morh-Coulomb plastic equation is shown as in formula (2).

$$\frac{\mathrm{d}\sigma_{\mathrm{r}}}{\mathrm{dr}}+\frac{\sigma_{\mathrm{r}}-\sigma_{\theta}}{\mathrm{r}}=0 \tag{1}$$

$$\frac{\sigma_r^p+C\cot\varphi}{\sigma_\theta^p+C\cot\varphi}=\frac{1-\sin\varphi}{1+\sin\varphi} \tag{2}$$

The stress in plastic zone can be listed as follows with the consideration of support resistance p_i and the boundary conditions of stress on the interface of support and surrounding rock.

$$\sigma_r^p=\left(p_i+C\cot\varphi\right)\left(\frac{r}{r_0}\right)^{\frac{2\sin\varphi}{1-\sin\varphi}}-C\cot\varphi \tag{3}$$

$$\sigma_\theta^p=\left(p_i+C\cot\varphi\right)\left(\frac{1+\sin\varphi}{1-\sin\varphi}\right)\left(\frac{r}{r_0}\right)^{\frac{2\sin\varphi}{1-\sin\varphi}}-C\cot\varphi \tag{4}$$

The stress difference $\sigma_\theta^p-\sigma_r^p$ on the interface of plastic and elastic can be shown as in formula (5).

$$M=\left(p_i+C\cot\varphi\right)\left(\frac{2\sin\varphi}{1-\sin\varphi}\right)\left(\frac{R_0^a}{r_0}\right)^{\frac{2\sin\varphi}{1-\sin\varphi}} \tag{5}$$

The maximum axial force of anchor can be expressed as in formula (6) on the hypothesis of common deformation between surrounding rock and anchor.

$$N_{\max}=\frac{k}{2}\left(\frac{M\left(R_0^a\right)^2}{4G}-r_0u_0^a\right)E_aA_s\left(\frac{1}{r_0^2}-\frac{1}{r_c^2}\right) \tag{6}$$

Then, the formula of plastic zone radius when supported can be listed as in formula (7), combined with formula (5) and formula (6).

$$R_0^a=\left[\frac{Ar_0^t}{t\left(p_i+C_1\cot\varphi\right)}\right]^{\frac{1}{t+2}} \tag{7}$$

$$A=4G\left[\frac{2N_{\max}}{kE_aA_s\left(\frac{1}{r_0^2}-\frac{1}{r_c^2}\right)}+r_0u_0^a\right];\quad t=\frac{2\sin\varphi}{1-\sin\varphi} \tag{8}$$

Where $G=\dfrac{E}{2(1+\mu)}$ is the shear elastic modulus of surrounding rock, $C_1=C+\dfrac{\tau_aA_s}{e\cdot i}$ is the cohesion of surrounding rock after support, e, i are the spacings of anchor, $N_{\max}$ is the measured maximum axial force of anchor, E_{a} is the elastic modulus of anchor, A_{s} is the cross section of anchor, r_{c} is the radius of internal end point of anchor, τ_{a} is the shear strength of anchor, u_0^a is the value of wall deformation before support.

Project Example

A circular tunnel is excavated with the radius of 5.8m, its mechanical parameters of surrounding rock are as follows: the deformation modulus E=1.62GPa, μ=0.32, c=0.18GPa, φ=30.6°. The primary support is adopted by anchor-shotcrete, and systematic anchor is the wholly grouted one with D=22mm, L=3m and the net spacing is 1m, of which the elastic modulus of is E_a=210GPa and the radius of internal end point is r_c=8.8m; the value of wall deformation before support is $u_0^a = 7.6mm$. The measured contact stress between shotcrete and surrounding rock is 252kPa and the measured maximum axial force of anchor at the neutral point ($r_m = \sqrt{\frac{2r_c^2 r_0^2}{r_c^2 + r_0^2}}$) is 10.2kN. According to formula (7), the calculated radius of plastic zone is 8.471m<5.8m+3m, which indicates that the adopted systematic anchor with the length of 3m is feasible.

Influence to Plastic Zone by Mechanical Parameters

In order to discuss the influence to plastic zone by mechanical parameters E, μ, c, φ, it is hypothesized that other mechanical parameters stay the same when discussed the variation of a certain parameter.

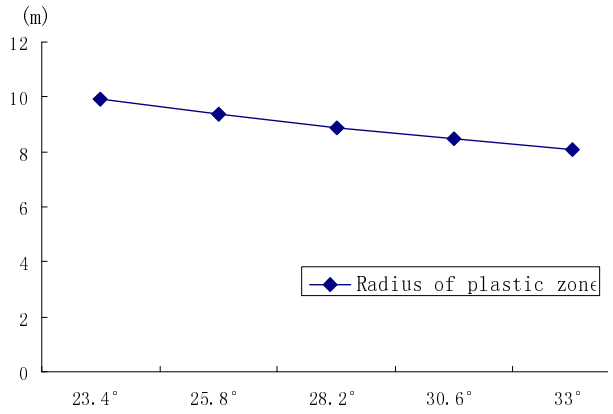


Fig.2 Influence by internal friction angle φ

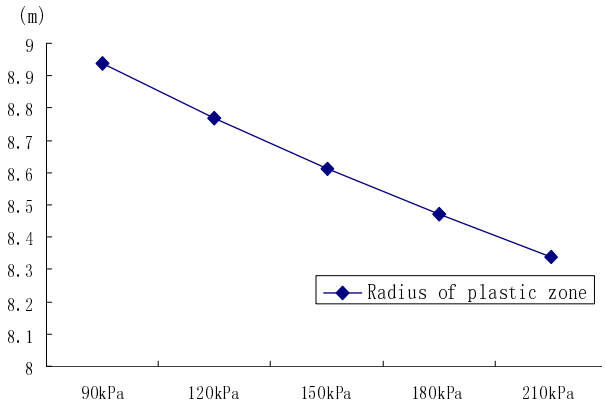


Fig.3 Influence by cohesion c

Fig.2 and Fig.3 indicate that with the increase of internal friction angle φ and cohesion c, the radius of plastic zone will decrease gradually, which shows that the surrounding rock with good structural strength itself will constrain the plastic zone. Different c and φ will lead to different scope of plastic zone, so correctly determining the value of c and φ will offer guidance to the optimum design of tunnel support.

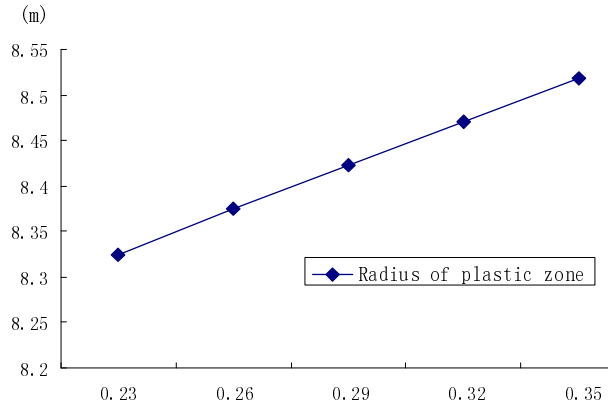


Fig. 4 Influence by passion's ratio μ

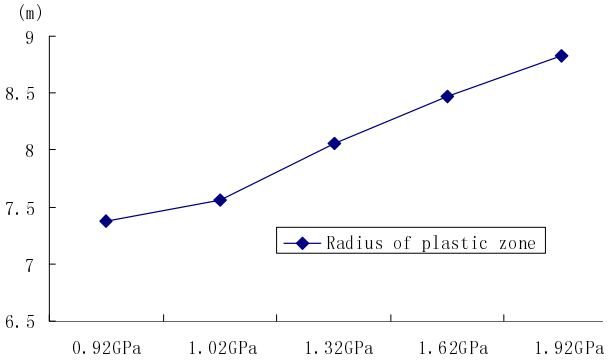


Fig.5 Influence by deformation modulus E

Fig. 4 and Fig. 5 indicate that with the increase of passion's ratio μ and deformation modulus E, the radius of plastic zone will also increase, which shows the influence to plastic zone radius by the variation of deformation modulus is bigger than that of passion's ratio.

Conclusions

Based on the hypothesized uniform and elastic-plastic rock mass, the radius of plastic zone in the tunnel excavation and support is expressed by the function of axial force of anchor; it is feasible and scientific to analyze the scope of plastic zone by the measured value of axial force of anchor.

The method discussed in the paper can judge the stability state of surrounding rock in the tunnel construction; Analysis of influence to plastic zone indicates that determining the mechanical parameters correctly is very important in the selection of primary support parameters.

References

[1] S. Yang, B. Zhang, Chinese Journal of Rock and Soil Mechanics, suppl. (2003) 279-282.
[2] C. Wang, Chinese Journal of Chongqing Jiaotong University, 2 (1990) 38-44.
[3] C. You, Chinese Journal of Rock Mechanics and Engineering, 3 (2000) 339-341.
[4] G. Xu, H. Bai, Y. Zheng, China WaterPower Press, Beijing, 2001.
[5] X. Yao, N. Li, Y. Chen, Chinese Journal of Rock Mechanics and Engineering, 13 (2005) 2272-2276.
[6] J. Wen, C. Wang, L. Liu, Chinese Journal of Underground Space and Engineering, 6 (2008) 1023-1026.

© (2012) Trans Tech Publications, Switzerland
doi:10.4028/www.scientific.net/AMM.238.791

Introduction of NO-NO_2-O_3 Recycle into Model for Air Pollutant Dispersion from Tunnel Portals

Shujiang Miao [a] and Dafang Fu [b]

Municipal Engineering Department, Civil Engineering College, Southeast University, Nanjing, China

[a]miaosj@seu.edu.cn, [b]fdf@seu.edu.cn

Keywords: air pollution; tunnel portal; NO-NO_2-O_3 recycle; GRAL-C module.

Abstract. NO-NO_2-O_3 recycle has been added into model dealing with air pollutant dispersion from tunnel portals-GRAL35TM to improve its performance. A mixed method GRAL-C has been discussed. It has been integrated into GRAL35TM to model dispersion in the street canyon where Tongjimen tunnel northern portal locates. It has been illustrated that GRAL35TM+C simulated NO_2 dispersion more precisely than the original GRAL35TM. It requires background O_3 concentrations.

Introduction

GRAL3.5TM[1-3] is the tunnel module (the update was in May 2003) of a Lagrangian model GRAL (Grazer Lagrange model, developed by Oettl et al.[1-3]). During the use of GRAL3.5TM to model air pollution dispersion from tunnel portals, the source strength is calculated through multiplying 80% and the NO_x emission factor in JTGB03-2006(Specifications for Environmental Impact Assessment of Highways, Ministry of Transportation of China) [4] to get the NO_2 emission factor. It is assumed that NO_2/NO_x is 80% when the chemical equilibrium is reached, and NO-NO_2 is assumed to be in steady state just after discharged from vehicles. This excluded chemical reactions of NO-NO_2, directly resulting in over-prediction. Therefore the chemical conversion for NO to NO_2 should be included here to obtain more approaching practical results.

Chemical Reactions

It is known that the ratio of NO_2-NO_x is approximately 10% in traffic emissions [5]. Most of NO released from traffic is oxidized to NO_2 within a time scale of a few minutes [6]. Far from the sources, an approximate photochemical equilibrium is reached, resulting in an NO_2/NO_x ratio of about 90% in typical ambient conditions.

The chemical reactions describing NO oxidized to NO_2 are listed below:

$$NO_2 + hv + O_2 \xrightarrow{j} NO + O_3 . \quad (1)$$

$$NO + O_3 \xrightarrow{k_1} NO_2 + O_2 . \quad (2)$$

The reaction rate constant of reaction (1) is

$$j = 8.9\times10^{-6} G(\mathrm{s}^{-1}) . \quad (3)$$

And for reaction (2) it is

$$k_1 = 5.86\times10^{-2} e^{-(1450/T)} (\mathrm{ppb}^{-1}\mathrm{s}^{-1}) . \quad (4)$$

Where j depends on the value of the global radiation G (Wm^{-2}) as in [7]. Reaction (1) is normally referred to as the photodissociation of NO_2, and the subsequent reaction of O and O_2 is already included. In conditions of chemical equilibrium the production and depletion of the three species is constant (so-called 'photostationary state').

When point releases consist of NO, a third reaction is generally added to reactions (1) and (2):

$$2NO + O_2 \xrightarrow{k_2} 2NO_2 . \quad (5)$$

Due to the low value of the reaction rate constant, the relevance of this reaction to the scheme depends on the value of NO concentration. Reaction (5) could therefore be important only in the vicinity of the release point because of high NO concentrations. Here the impact of background VOCs and other species are neglected, which should to be tackled in future.

Study of GRAL-C

One major challenge for modelling NO-NO_2-O_3 chemistry in a Lagrangian framework is, on the one hand, the treatment of chemical processes on the counting grid and particle redistribution, and on the other hand, the potential for interaction with "background" species such as O_3, VOCs etc.

A new hybrid Eulerian-Lagrangian approach capable of dealing with background O_3 levels is suggested here by Oettl et al [8], called as GRAL-C. The main idea of GRAL-C is that it treats NO and NO_2 with a lagrangian particle model, when treating O_3 with an Eulerian transport and diffusion model. In this model a main characteristic to the previous works lies in the use of a simple Eulerian model for the treatment of transport and diffusion of O_3. Generally the Eulerian approach is well known and follows standard principles. For instance, the increment of O_3 concentrations due to vertical turbulent diffusion is computed based on classical K-theory. The more details are in [8], here only some advantages of GRAL-C presented include:

In the case of small point sources K-theory mostly used in Eulerian models are no longer applicable close to the source. Lagrangian particle models do not have this limitation. In GRAL-C, K-theory is only used for O_3 when simulating turbulent vertical mixing.

The Lagrangian model GRAL, upon which the Lagrangian part of GRAL-C is based, has been well validated for treating dispersion in low wind speed conditions.

In general, a Lagrangian model is more flexible in simulating the geometry and location of sources exactly compared with an Eulerian model based on a fixed grid structure.

Application of GRAL-C to northern portal of Tongjimen Tunnel, Nanjing, China. GRAL-C has been combined with GRAL35TM, named as GRAL35TM+C.

The northern portal of Tongjimen tunnel locates in a street canyon with building heights of about 30 m in Longpan zhong Street. Street orientation is more or less South-North (9 degrees from north) and the section of the street canyon analyzed has a length of about 150 m. Receptor is Ruijin Road national air quality monitoring site.

Bias, correlation coefficient, and normalized mean square error (NMSE) are commonly used for model evaluation. According to model performance criteria established by Chang and Hanna [9]: bias $\leq \pm 30\%$; and NMSE<4 are acceptable model results. Bias is computed as:

$$bias = \frac{c_{sim} - c_{obs}}{c_{obs}} (\%) . \quad (6)$$

A linear regression plot for NO_2 is in Fig. 1, in which the dashed lines indicates a bias of a factor of two, the solid line indicates the linear regression trend. Almost all daily mean simulated NO_2 concentrations deviate less than a factor of two from observations. In addition, there is no bias towards under- or overestimation. The correlation coefficient is 0.83 and the bias is 15.9%. The reasonable results obtained for NO_2 indicate that the assumption of neutral stability throughout the year does not lead to significant errors.

GRAL-C has been employed to simulate NO_2 concentrations between Mar-Apr 2010 at other two monitoring sites Xuanwu Lake and Caochangmen, followed by the correlation coefficients (R) and normalized mean square errors (NMSE) to evaluate the modeling in Table 1. NMSE values range between 0.15 and 0.23 and meet the quality criteria for model performance as defined in [9]. It should be noted that actual hourly emission data for each source could not be provided, thus allowing for an additional source of uncertainty.

Application of GRAL35TM+C. GRAL35TM+C has been used to model NO_2 dispersion around northern portal of Tongjimen tunnel over 2009. The hourly data of first 5 day of January, April, July and October have been selected to use. The simualted and observed mean NO_2 concentrations over 2009 at Ruijin Road monitoring site in Nanjing are drawn in Fig.2.

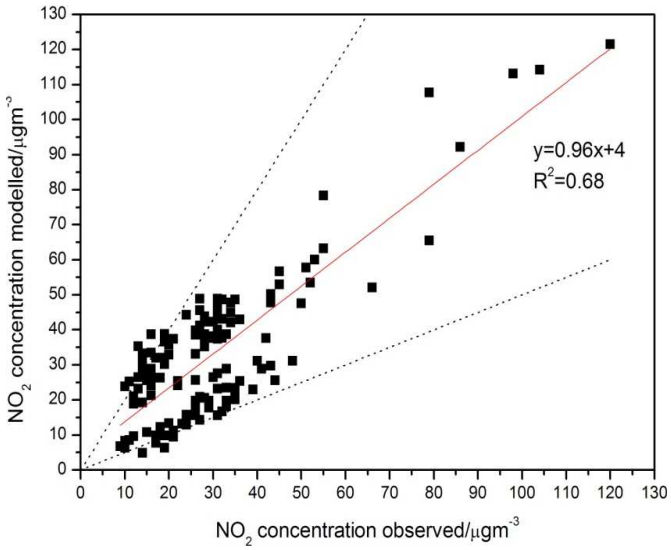


Fig. 1 Linear regression plot for daily mean observed vs. modelled NO_2 concentrations at Ruijin Road monitoring site in the city of Nanjing for the period of Mar-Apr 2010.

Table 1 Evaluation statistics for the national monitoring sites simulations for the time period between 4th Mar– 11th Apr. 2010.

Site	Ruijin Road	Xuanwu Lake	Caochangmen
R	0.59	0.68	0.61
NMSE	0.15	0.19	0.23

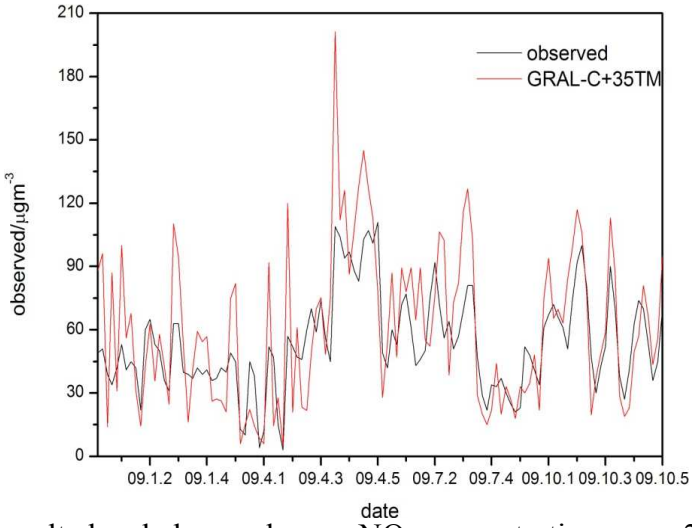


Fig.2 Simualted and observed mean NO_2 concentrations over 2009 at Ruijin Road monitoring site in the city of Nanjing.

It can also be seen from above figure that the modeled hourly concentration values vary more strongly than observed values. A possible explanation for this effect may be that the chosen particle density is still too low and should be increased to reduce the noise in the simulations.

Table 2 lists R and NMSE for the Ruijin Road monitoring site simulations with GRAL35TM+C. NMSE changes from 0.11 to 0.22, meeting the model evaluation standard.

Table.2 Evaluation statistics for the Ruijin Road monitoring site simulations with GRAL35TM+C over 2009.

Month	1	4	7	10
R	0.60	0.82	0.76	0.85
NMSE	0.11	0.18	0.19	0.22

Conclusions

We have analyzed the NO-NO_2-O_3 cycle mechanism. Results show that addition of NO_x-NO_2 conversion to GRAL35TM improves its performance. A hybrid Eulerian-Lagrangian approach capturing NO-NO_2-O_3 chemistry has been discussed and been chosen to combine with GRAL35TM to develop and evaluate the module dealing with dispersion of NO_x from tunnel portals. Results show that addition of NO_x-NO_2 conversion to GRAL35TM improves its performance.

Acknowledgements

Thanks to Dr. Dietmar Oettl and Prof. Peter Johann Sturm for their selfless help. The provision of the concentration data by Nanjing Environmental Monitoring station is greatly acknowledged. This project was funded by the National Natural Science Foundation of China (No. 80108012).

References

[1.] D. Oettl, P. J. Sturm, M. Bacher, G. Pretterhofer, R. A. Almbauer, A simple model for the dispersion of pollutants from a road tunnel portal, Atmospheric Environment, 36 (2002) 2943-2953.

[2.] D. Oettl, P. J. Sturm, R. A. Almbauer, S. Okamoto, K. Horiuchi, Dispersion from road tunnel portals: comparison of two different modeling approaches, Atmospheric Environment, 37 (2003) 5165-5175.

[3.] D. Oettl, P.J. Sturm, R.A. Almbauer, Evaluation of GRAL for the pollutant dispersion from a city street tunnel portal at depressed level, Environmental Modeling and Software, 20 (2005) 499-504.

[4.] Ministry of Transportation of China, JTGB03-2006, Specifications for Environmental Impact Assessment of Highways, Beijing, 2006.

[5.] A. Karppinen, J. Kukkonen, T. Elolähde, M. Konttinen, T. Koskentalo, E. Rantakrans, A modelling system for predicting urban air pollution: model description and applications in the Helsinki metropolitan area, Atmospheric Environment, 34 (2000) 3723-3733.

[6.] J. Härkönen, E. Valkonen, J. Kukkonen, E. Rantakrans, K. Lahtinen, A. Karppinen, L. Jalkanen, A model for the dispersion of pollution from a road network, Publications on Air Quality, 23 (1996) 34.

[7.] F.C. Bahe, U. Schurath, The frequency of NO_2 photolysis at ground level, as recorded by a continuous actinometer, Atmospheric Environment, 14 (1980) 711-718.

[8.] D. Oettl, U. Uhrner, Development and evaluation of GRAL-C dispersion model, a hybrid Eulerian-Lagrangian approach capturing NO-NO_2-O_3 chemistry, Atmospheric Environment, 45 (2011) 839-847.

[9.] J. C. Chang, S.R. Hanna, Air quality model performance evaluation, Meteorology and Atmospheric Physics, 87 (2004) 1-3.

© (2012) Trans Tech Publications, Switzerland
doi:10.4028/www.scientific.net/AMM.238.795

Underground Space Form Design of Large Centrifugal Shaker System and Analysis of Machine Foundation Vibration

Yongzhi Wang [a], Yunlong Wang [b], Zhuoshi Chen [c] and Xiaoming Yuan [d]

Key Laboratory of Earthquake and Engineering Vibration, Institute of Engineering Mechanics, China Earthquake Administration, Harbin 150080, China

[a]yong5893741@163.com, [b]wyl_iem@hotmail.com, [c]various@163.com, [d]yxmiem@163.com

Keywords: large centrifugal shaker; underground space form; mathematical model; machine foundation vibration.

Abstract. Centrifugal shakers are accounted the most effective and the most advanced test method of geotechnical earthquake engineering and soil dynamics, for a unique ability of exerting dynamic loads of sine waves and seismic waves on models while the same gravity stress as prototype is produced. Large centrifugal shakers are necessary to countries of frequent earthquake occurrences, but no one has been built in China. As state-of-the-art test equipments, its construction absolutely has many challenges. In the machine foundation design, its underground space employed a narrow rectangle as usual can't satisfy the required space of facilities, while the imbalance force of equipments against foundation stability is inherently high. For no relevant research findings can be available, the paper states the general layout of a large centrifugal shaker and the fiendish problems between two space forms. By theories of mass-spring-damper and elastic half-space, two foundation vibration mathematical models for large centrifugal shakers are proposed. The calculation results of both underground space forms show that a round space meeting the required space of facilities doesn't significantly increase foundation vibration, and is more ideal. Moreover the view of a narrow rectangular underground space more stable to large centrifugal shakers by experience is not true.

Introduction

Soil is a quite complex material with stress-strain behaviors affected by many and various factors, which show significant differences in mechanical characteristics under different loading paths and different gravity stress conditions. Via centrifugal shakers, the dynamic property and the failure mechanism of soil mass and geotechnical structures can be truly reproduced by exerting dynamic loads of sine waves and seismic waves on models while the same gravity stress as prototype is produced. In contrast with conventional research methods such as earthquake damage survey, physical tests and numerical simulations, this test method is more economical, reliable and catholicity. Therefore, it wins favour and attention of geotechnical engineering scholars and is considered as the most effective and the most advanced earthquake simulation method. Moreover, centrifugal shakers combined with numerical simulations to complement each other, can greatly increase the level of geotechnical engineering and seismic resistance research [1]. Large centrifugal shakers are necessary to countries of frequent earthquake occurrences, but no one has been built in China, which is inconsistent with the complicated engineering geotechnical conditions, the rapid engineering construction growth and the serious seismic risks in China [2].

Around the world, only two large centrifugal shakers exist in USA (in University of California, Davis) and Japan (in Public Works Research Institute) respectively, and their construction processes have showed many problems, many difficulties and long duration. Therefore, the large centrifugal shaker construction in China with limited international experiences to reference, definitely will encounters some unknown problems. For example, in the machine foundation design, underground space form employed a narrow rectangle as usual can't satisfy the space needs of facilities, meanwhile the imbalance force of equipments against foundation stability is inherently high, and no relevant research findings can be available. The paper states the general layout of a large centrifugal shaker and analyses the fiendish problems between two space forms of a round and a narrow rectangle. By theories of mass-spring-damper and elastic half-space, two foundation vibration mathematical models for large centrifugal shakers are proposed, and the foundation vibration of both space forms is calculated and analyzed.

Construction Layout

The general layout of the large centrifugal shaker system in UC Davis adopted two floor structures, while the one in PWRI adopted three floor structures. According to the functions and running characteristics of each facility constituting a large centrifugal shaker system, and referring to the experience from designers and users of both existing large centrifugal shakers, it is preferable to adopt three floor structures for a large centrifugal shaker system, as shown in Fig. 1.

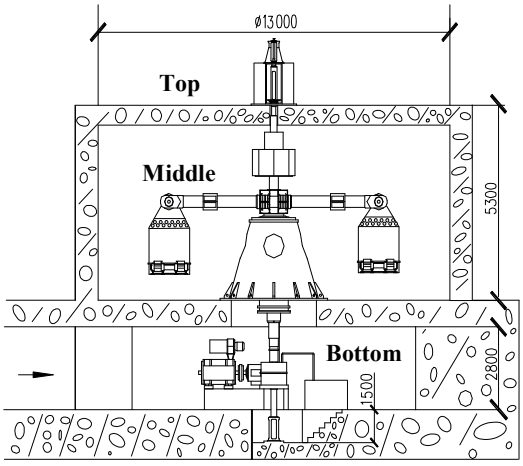


Fig. 1 Three floor structures of a large centrifugal shaker

Table 1. Foundamental components of a large scale centrifugal shaker

Subsystem	Foundamental Components
Shaker	Moving Platform, Exciting System, Power Source, etc.
Centrifuge	Bucket, Arm, Machine Base, Shaft, Reducer, Motor, etc.
Testing Auxiliary System	Data Acquisition System, Video Observation System, Container, Sampling Equipment, etc.
Supporting Facilities of Civil Engineering	Power Substation, Ventilation and Cooling System, Desiccation and Drainage System, etc.

The components of a large centrifugal shaker system can be divided into four subsystems, namely a shaker, a centrifuge, a testing auxiliary system and supporting facilities of civil engineering, as shown in Table 1. The shaker basically consists of a moving platform, an exciting system, power sources, etc. The centrifuge basically consists of a bucket, an arm, a machine base, shafts, a reducer, a motor, etc. The testing auxiliary system basically consists of a data acquisition system, a video observation, containers, sampling equipments, etc. The supporting facilities of civil engineering generally consist of a power substation, a cooling ventilation system, a desiccation and drainage system, etc.

As shown in Fig.1, the crane and upper instrument storage containing signal rings, optical fiber rings and power rings are installed on the top floor. As the operation hall, the main components of equipments are installed on the middle floor, including the arm, bucket, containers, machine base, arm support, drive bearings, lower instrument storage and observation equipment system etc. The bottom floor is installed with the driving motor, reducer, lubrication system, rotary joint, hydraulic source and cooling ventilation system etc., all of which have remarkable characteristics of large vibration, high noise and intense heat, so this floor is set up under the ground and generally adopts a narrow rectangle space form for within facilities. But for large centrifugal shakers, the facilities on the bottom floor are very large in size and great in quantity, if its space form adopts a narrow rectangle as usual used in medium and small centrifugal shakers, or large centrifuges without a shaker, the space needs of facilities can't be met [3]. Thus, some scholars propose that a round underground space form can be adopted instead of a narrow rectangle to obtain more space for facilities. However, other scholars feel anxious about the machine foundation stability for the imbalance force of equipments is extremely higher than the medium and small centrifugal shakers, and the view by experience is a narrow rectangle underground space is safer for the machine foundation stability than a round underground space [3]. Because foundation stability is one precondition of feasibility for the construction of a large centrifugal shaker, the key problem whether a round underground space satisfying the space needs of facilities is safe for machine foundation stability must be studied.

Mathematical Model

The imbalance force of a large centrifugal shaker is produced by three primary sources, what are the huge exciting force of shakers, centroid shifting in failure process of test models and remaining angle of swing buckets. The former two sources can generate a great instantaneous imbalance force, which is more dangerous for machine foundation stability. Due to all imbalance forces must pass through the arm and machine base to the machine foundation, the caused machine foundation vibration is a coupling movement of horizontal and rocking, in which the load can be substituted by a concentrated force *P*. If *P* is constant in the arm rotation, the horizontal vibration of machine foundation at each direction is sinusoidal periodic movements. Therefore, the foundation stability can be evaluated by the maximum horizontal amplitude in the coupling movement of horizontal and rocking.

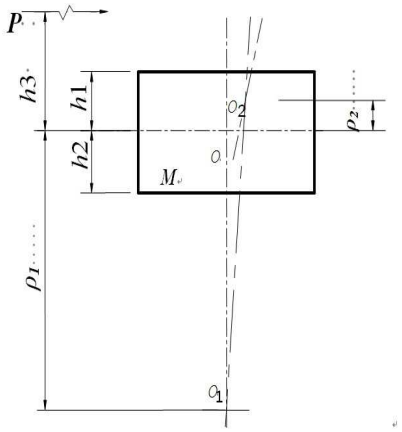


Fig. 2 Mathematical model based on mass-spring-damper theory

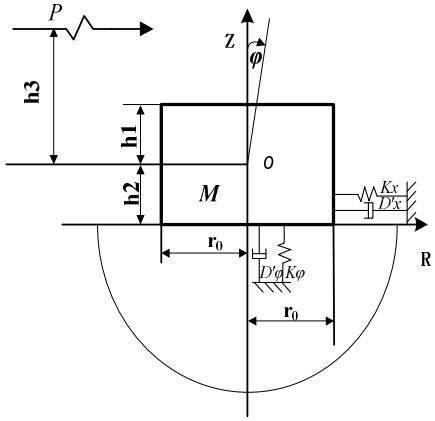


Fig. 3 Mathematical model based on elastic half-space theory

Presently, vibration analysis theories for dynamic machine foundation can be classified as the category of mass-spring-damper and the category of elastic half-space, the former is adopted in counties represented by China, India, and the current code for design of dynamic machine foundation (GB50040–96) in China also belongs to this category, while the latter is adopted in counties represented by America and Japan. Referring to both theories of mass-spring-damper and elastic half-space, two foundation vibration models for large centrifugal shakers are proposed, respectively shown in Fig. 2 and Fig. 3. Fig. 2 is the mathematical model based on the theory of mass-spring-damper, in which *P* is the concentrated force; *M* and *O* are the mass and the centroid of foundation; *h1* is the distance between the centroid and the top of foundation; *h2* is the distance between the centroid and the bottom of foundation; *ρ1*, *ρ2* are equivalent gyration radius corresponding to the first and the second natural frequencies respectively; and *O1*, *O2* are the centre of rotation. Fig. 3 is the mathematical model based on the theory of elastic half-space, in which *r0* is the equivalent radius; *Kx* is the equivalent stiffness of translation; *D'x* is the equivalent damping of translation; *Kφ* is the equivalent stiffness of shimmy; *D'φ* is the equivalent damping of shimmy; and other parameters are identical to Fig. 2. The computational formulas to the above mathematical models and further details can be found in the reference [4].

Result Analysis

In Fig.1, the whole lab including three floors are treated by integrated reinforced concrete together with the machine foundation, and built on the natural ground of soil bed. To the structures of lab with a density of 2500kg/m^3, when the underground space adopts a round form, its radius is 5.5m and height is 2.8m, in contrast, adopts a narrow rectangle, its length is 12m, width is 3.5m and height is 3.5m. Meanwhile, the parameters of the natural ground needed for calculation are the density of 1900kg/m^3, compression strength of 40000kN/m, Poisson ratio of 0.35 and shear modulus of 155Mpa. The maximum imbalance force of arm is 900kN, with a distance of 2m to the top of middle floor. Base on these parameters, the calculation results of foundation vibration are shown in Fig.4 and Fig.5, corresponding to the above mathematical models respectively.

The plots in Fig. 4 and Fig.5 represent the maximum horizontal amplitude versus frequency, which show two forms of the underground space are all safe under the safety index of 100gal in both methods, and the amplitude at resonant frequency in mass-spring-damper method is about twice larger than that in elastic half-space method. Simultaneously, they also indicate a round underground space meeting the space needs of facilities doesn't significantly increase foundation vibration, in comparison with a narrow rectangle underground space, in other words, the view of a narrow rectangle underground space more stable to large scale centrifugal shakers by experience is not true.

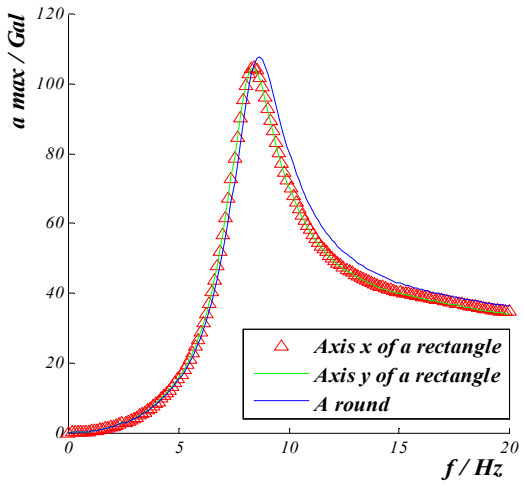


Fig. 4 Calculation results of mass-spring-damper method

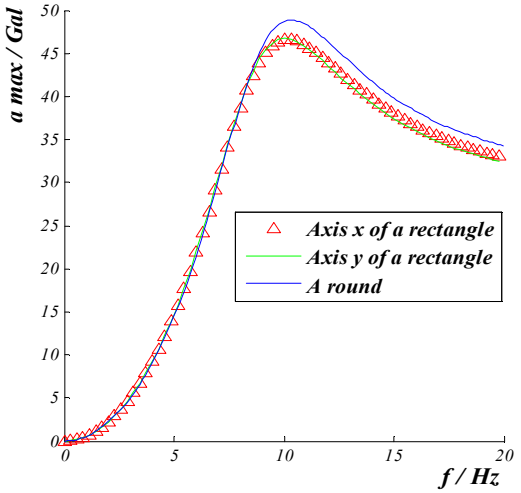


Fig.5 Calculation results of elastic half-space method method

Conclusions

The main conclusions herein can be got:

(1) The calculated results employed two mathematical methods of mass-spring-damper and elastic half-space show the underground space with two forms of a round and a narrow rectangle are all safe for the machine foundation stability. Moreover the amplitude at resonant frequency in the mass-spring-damper method is about twice larger than that in the elastic half-space method.

(2) The calculated results also indicate the round underground space doesn't significantly increase the foundation vibration in comparison with the narrow rectangle underground space. Therefore, the view of a narrow rectangle underground space more stable by experience is not true.

(3) The lab for a large centrifugal shaker system can adopts three floor structures, with a round underground space, which can meets the high space needs of facilities and is a more ideal form.

References

[1] X. Yuan, Z. Cao, R. Sun, et al, Preliminary research on liquefaction characteristics of Wenchuan 8.0 earthquake, Chinese Journal of Rock Mechanics and Engineering, 6 (2009) 1288–1296. (in Chinese)

[2] Y. Wang, X. Yuan, R. Sun, General layout and key construction technologies of large scale centrifugal shakers, Applied Mechanics and Materials, Vols. 90-93 (2011) 1627-1633.

[3] GB50040–96, Code for Design of Dynamic Machine Foundation, China Planning Press, Beijing, 2002. (in Chinese)

[4] Y. Wang, Y. Wang, H. Huang, et al, Influence on foundation vibration by underground space form of large scale centrifugal shaker, Rock and Soil Mechanics, accepted, (in Chinese)

© (2012) Trans Tech Publications, Switzerland
doi:10.4028/www.scientific.net/AMM.238.799

Research of Manually Excavated Pile Support for Large Foundation Pit

Zhiyong Deng

Zhejiang Business Technology Institute, Ningbo 315012, China

ddzzyy2005@sohu.com

Keywords: large foundation pit; supporting; manually excavated pile.

Abstract. For the large foundation pit, if the soil condition is good, the manually excavated pile support can be used. Based on the foundation pit from one office building project in Ningbo, this paper analyzes the details of the manually excavated pile support, and also analyzes the layout, structural measures and support construction method. This support method will be used more and more widely in the excavation of large foundation pit.

Introduction

The office building is located in the the new century modern business district, near to the Xueyuan road in east, close to the coastal southern line in south, approach to Taoyuan Road in west, and is adjacent to a neighborhood in north. The total project area is 13800 square meters, and the building area is 83690 square meters with one hundred meter of height. There are 23 layers are above the ground and two below.

Situation of the Foundation Pit

Section A: Foundation pit general situation. ±0.00 elevation for this project is yellow sea levation 23.900m, indoor and outdoor floor level height difference is 0.15 m, the basement floor surface elevation is -9.55 m, slab thickness is 20 cm, surrounding pile caps thickness is between 1.6 m and 2.4 m, under floor and pile caps is 100 mm thickness meal pad called C15. Foundation pit is rectangle, length from east to west is 108.5 m, length from south to north is 120 m, which belongs to large foundation pit.

Section B: Venue geological& hydrological conditions.

(1) The venue geological conditions: According to the Geotechnical engineering investigation report that's from Zhejiang engineering survey research institute in February 2010.The basic regional earthquake intensity is less than 6 degrees and construction site category is II. Stratum structure: filling soil, silty clay, round gravel which are for the soil from one to five layer respectively. According to the project building design load and the deformation, this building use the manually excavated pile, and have 4-2 Strong weathering silty sandstone as the bearing stratum in the pile end.

(2) Hydrological conditions: The highest water level for anti-floating design is 23.000 m.

(3) Foundation pit surroundings: There is one planning road in the north of this project area, and a under construction building is outside of the road. It's the same as north side in the east. Many sewage pipe lines, water pipelines and stormwater pipelines are arranged in the south side of foundation pit, and an outer ring road pass through outside. Finally, some wire lines cover the area of foundation pit west, and Taoyuan north road is near to it.

(4) Foundation pit construction features: According to the basic design and on-the-spot survey, meanwhile we considered the effect from surrounding building and road. The features of this foundation pit construction are as below:

①Deeper foundation pit digging: the actual depth is about 9.5 m. This scheme is needed to be demonstrated by expert ac the depth is more than 5 m.

②Better soil properties in the digging area: Clay and gravel soil are the main components, and the moisture content is small. This condition can help keep the whole stability and control deformation, so there is no need to make step-slope.

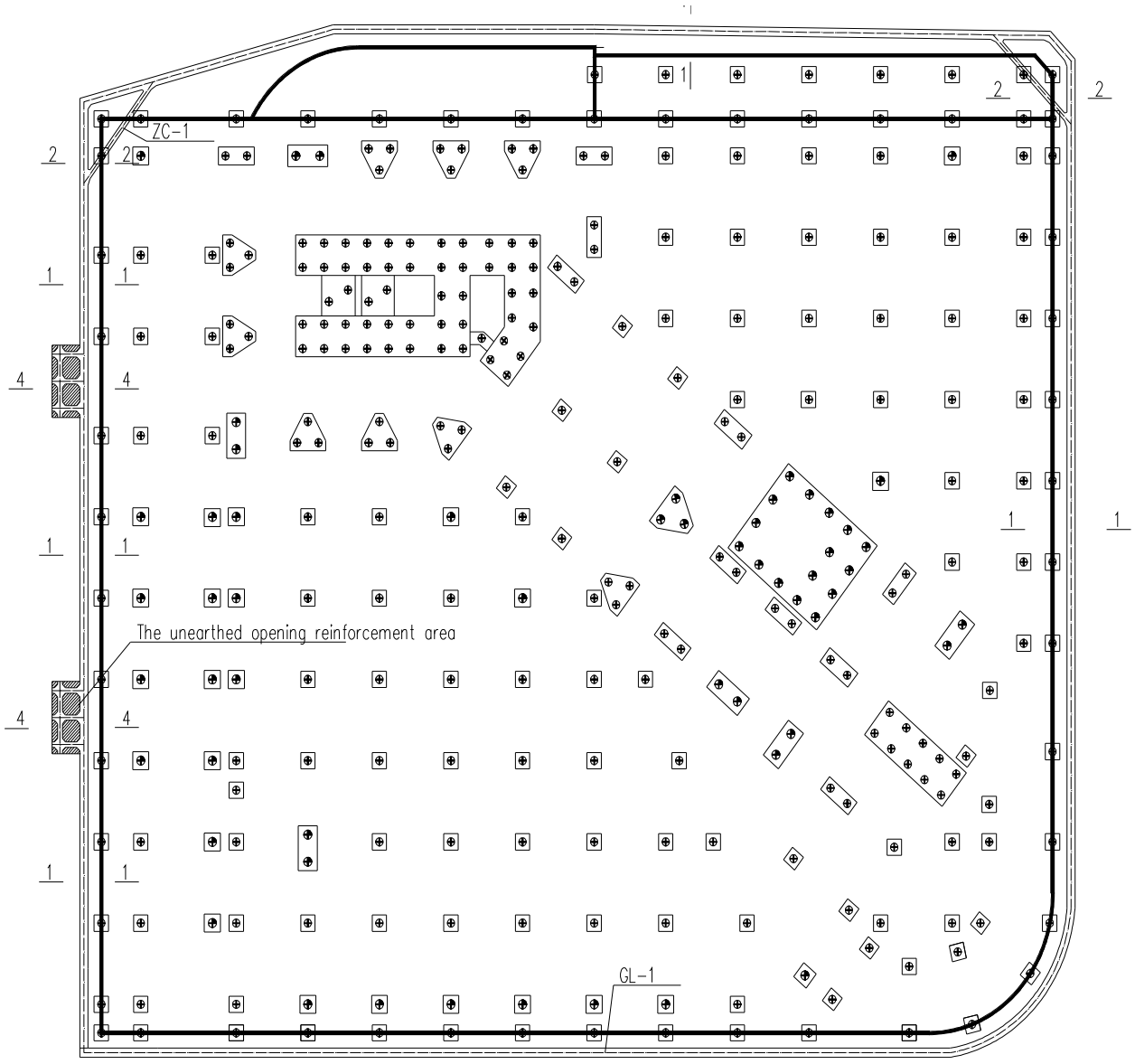
Foundation Pit Supporting Design Scheme

The engineering is situated in the city downtown, and there are existed under construction buildings, underground pipeline networks and roads around of the foundation pit. They can affect the horizontal displacement of foundation pit supporting structure sensitively, especially that there are underground pipeline in the south and west. So we need foundation pit support. In the spirit of safe, reliable and economic reasonable, we select the best scheme after careful calculation and alternative comparison. Firstly, use 9 m of distance for the manually excavated pile to keep soil around of the foundation pit, secondly, make soil anchor for support.

The pile structure utilizes pile and small deformation of pre-stressed anchorage, which can control horizontal displacement of foundation pit slope support structure, and reduce the influence about the building around and municipal facilities; guarantee the safety of the civil house and facility and peace construction environment.

Pit Support Construction

On the basis of the characteristics of the foundation pit, this project takes piles in row as support structure. The structural arrangement is shown as Fig.1.



1. GL-1: width 1100×height 450; 2. ZC-1: width 600×height 450

Fig. 1 The structural arrangement for supporting

Manually Excavated Pile Support Construction. Plane arrangement for manually excavated pile support construction, plane arrangement chart is shown as Fig. 2

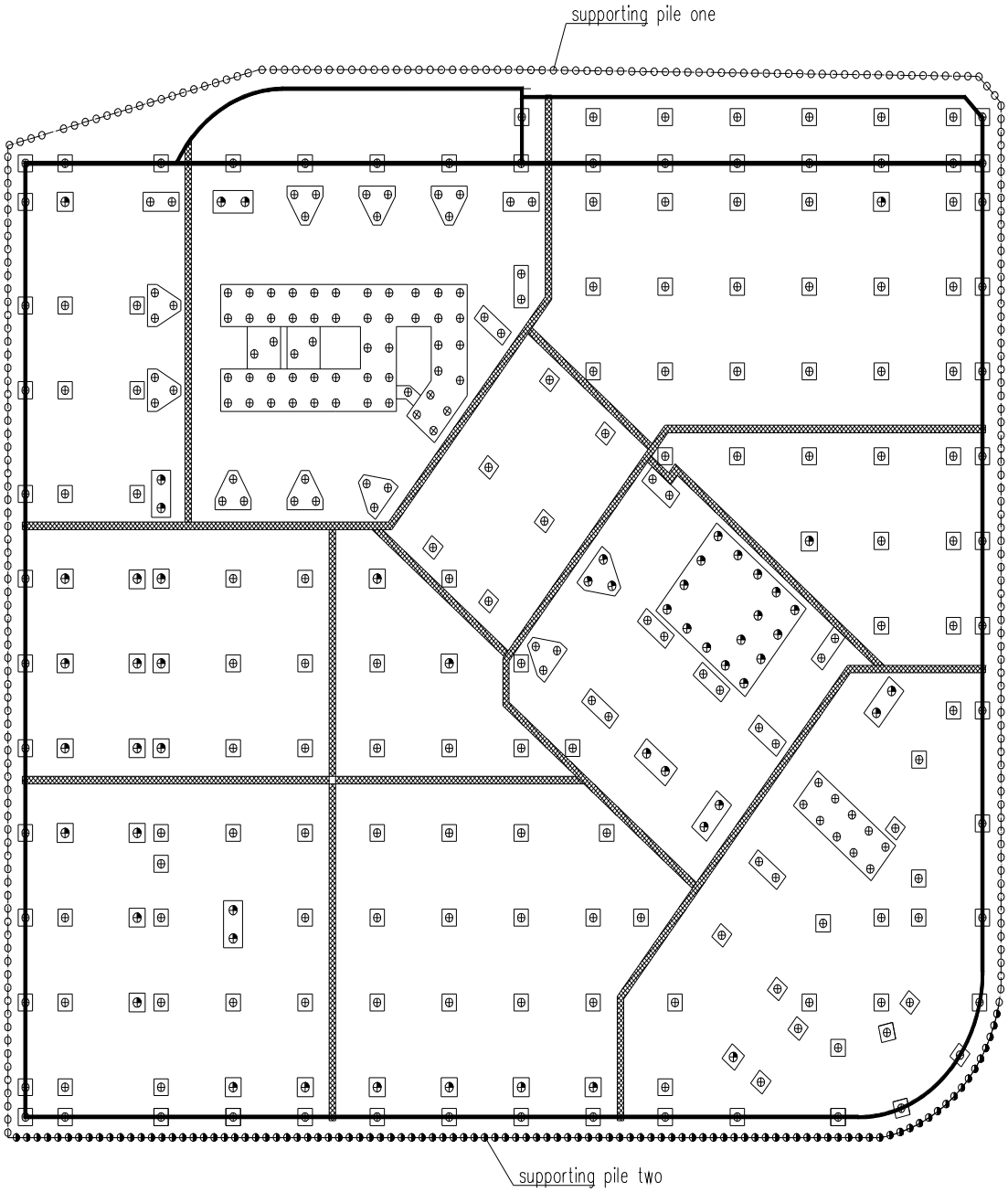


Fig. 2 The arrangement for the manually excavated pile support

Manually Excavated Pile Construction Process. The first step is paying off which fixes pile location and elevation, the second step is digging earthwork for the first quarter excavation pile hole, The third step is sustaining slurry-supported template and putting additional reinforced, The fourth step is pouring the first quarter concrete, the sixth step is checking the pile location (center) axis, the seventh step is setting up vertical transportation frame, the eighth step is Installing electric hoist (hoist or wood windlass), the ninth step is installing the bucket ,lighting , roll top, water pump, fanner etc, the tenth step is digging earthwork for the second quarter excavation pile hole, the eleventh step is dismantling the first quarter formwork and sustaining the second quarter slurry-supported template (putting additional bar), the twelfth step is pouring the second quarter concrete, the thirteenth step is checking the pile location (center) axis, the fourteenth step is looping down step by step, the fifteenth step is digging expansion place, the sixteenth step is checking and accepting , the seventeenth step is putting reinforcing cage, the eighteenth step is putting LiuTong concrete (catheter), the nineteenth step is pouring concrete pile.

Conclusions

Foundation pit supporting can use manually excavated pile for supporting if large foundation pit have good soil. Engineering practice shows which the supporting method is safe and reliable, cost is low, Increasingly in engineering construction, the construction unit by the attention, application will also more and more widely.

References

[1] W. Wang, Dredging row artificial dig-hole pile in the use of deep foundation pit, Journal of Geotechnical Engineering, 8 (2007) 45-49.
[2] A. Yao, Discussion about foundation pit supporting structure design method, Journal of Industrial Architecture, 11 (2001) 20-25
[3] Information on http://www.zhulong.com
[4] Information on http://www.tydf.cn

© (2012) Trans Tech Publications, Switzerland
doi:10.4028/www.scientific.net/AMM.238.803

Analysis of Settlement Reasons and Mechanism in Immersed Tunnel

Gang Wei [1.a], Huijie Qiu [2 b], and Xinjiang Wei [1,2 c]

[1] Department of Civil Engineering, Zhejiang University City College, Hangzhou 310015, China

[2] Institute of Geotechnical Engineering, Zhejiang University, Hangzhou 310058, China

[a]weig@zucc.edu.cn, [b]852038249@qq.com, [c]weixj@zucc.edu.cn

Keywords: immersed tube tunnel; mechanism; settlement reasons.

Abstract. The settlement of immersed tube tunnel may be influenced by variety factors in construction, operation and loads. The factors causing the immersed tube tunnel settlement were summarized and described in-depth by cases and data. Combined the mechanism analysis with the construction process, the action time of different loads along the construction process is summarized, the consolidation characteristics and settlement mechanism of original state soil layer and base layer are analyzed. The mechanisms and variations of tidal loading, siltation and dredging disturbance, groundwater level drawdown are elaborated.

Introduction

The pressure of the tunnel to the base is very small and hardly causes settlement due to the buoyancy effect on the pipe in the early settlement research of immersed tube tunnel. However the analysis of settlement data from 19 immersed tube tunnel at home and abroad indicates that the tunnel will have settlement or even uneven settlement and the average value of the largest settlement can be 108mm. Many immersed tube tunnel diseases like crack and leakage, joint failure, approach road destruction more or less connected with too large settlement. So it is very important to research the settlement reasons and mechanism of the immersed tube tunnel.

Some analysis around settlement reasons and mechanism of the immersed tube tunnel were made [1-3], pointed out the factors that affect the settlement but not comprehensive enough, explained the mechanism of some affective factors but not deep enough, and these jobs were not corresponded to the construction process.

This article summarizes the settlement reasons of immersed tube tunnel and explained them with project cases, combines settlement reasons and mechanism with project process. Settlement mechanism is analyzed from original soil and foundation layer two sides systematically along the construction process and loading time, some special loading mechanism are detailed described.

Analysis of Settlement Reasons

Construction Load. Construction load belongs to the additional load including the weight of construction appliances, grouting load Etc. The settlement during the construction mainly comes from the foundation layer settlement. Illustrate: the underwater tunnel from Huangsha to Huangcun in Guangzhou [4]. The average total settlement of the foundation layer 53.42mm. Compressibility of the foundation layer can be very different as the different foundation treatments. Thicker and looser the foundation layer is the more settlement it will be.

Cases: The Sixty-Third Street tunnel in New York USA 1973 treated its foundation with blasting, the final largest settlement on the dense soil was 50mm, mainly because the large deformation of the foundation layer caused by the construction load [5]. Similarly the Hampton road tunnel in Virginia USA 1976 happened with the largest settlement of 250mm on the soil mainly consisted with sand and weak silt clay during the construction.

Description settlement of immersed tube tunnel always associated with a variety of factors, list cases just explain this factor plays an important role in this case.

Vehicles and Pedestrians Load. Though a certain degree of live load was considered during the tunnel design, the actual live load is often greater than the design value especially in the areas the economic developing rapidly. Fig. 1 is the traffic statistics of Xianggang underwater tunnel 1972-1981 [4]. The figure reflects that the traffic statistics of 1981 is 8 times that of 1972, the vehicles overload seriously.

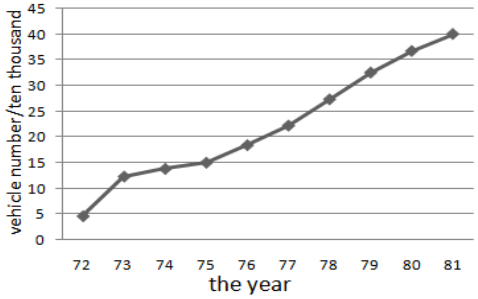


Fig. 1 Annual traffic statistics in Xianggang underwater tunnel 1972-1981

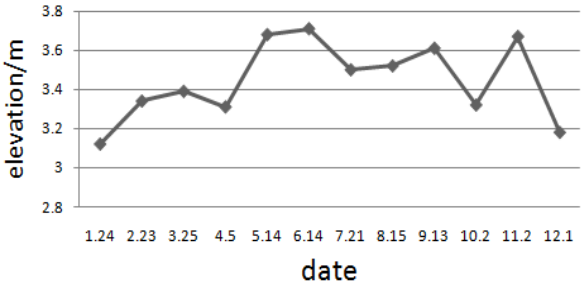


Fig. 2 Variation of groundwater level somewhere in Shanghai

Cases: the design standards of Ningbo Yongjiang tunnel in 1995 is automotive-20, trailer-100, average daily traffic volume 5500, corresponding design speed 60km/h. On the eve of the 2006 overhaul, due to the large traffic volume, the actual driving speed was limited to 30km/h, only half of the designed speed. Problems in the overhaul are mainly because that the tunnel in the port area and the traffic volume is large with high proportion of heavy vehicles and overloaded vehicles. The Tingstad tunnel in Gothenburg Sweden 1968 constructed upon pipes still happened with the largest settlement of 50mm, the main reason is also overloaded vehicle [2].

Siltation and Dredging Disturb. Siltation plays an important role in immersed tube tunnel settlement either in construction or operation. In construction, over siltation affect the safety and accuracy of the tube sinking; in operation, uneven siltation can cause overload lead to uneven settlement, which must be dredged from time to time, however, the cyclical silting and dredging disturbs the foundation and original soil.

Cases: the Ningbo Yongjiang tunnel, riverbed under the top section of pipe E3, E4, E5 silts seriously, the foundation trench siltation up to 3m per month during construction. The yearly average dredge is 55800.14 m^3 from 1998 to 2004 during operation. Tunnel settlement keeps increasing during the cycle of loading and unloading, local overload seriously. The largest settlement is 89mm in the section near the southern end of E4 and the northern end of E5 with serious uneven settlement due to the uneven siltation [3]. In addition, the Benelux tunnel in Netherlands Rotterdam 1967 [5], the Valake tunnel in Netherlands Zeeland 1975 [2], the Outer Ring immersed tube tunnel in Shanghai 2003 [6], all affected by siltation in different degrees.

Tidal Action. Tidal action affects the immersed tube tunnel in rivers and bay area normally. Such as the Shengjiamen port influenced by the rule semi-diurnal tide whose average rising tide lasts 5 hours and 37 minutes with the highest tide level of 3.26m, whose average ebb last 6 hours and 48 minutes with the lowest point of -2.44m [7]. Immersed tunnel in this area buffers from disturb of 5.7m ranging water load 2 times a day. The original soil will fluctuate and produce some permanent settlement under the long-term tidal effect while the weak soil layer likes the silt layer and disturbance layer is the main reason causing the daily fluctuation in settlement.

Cases: the Belgian Schelde tunnel suffer from the tidal gap of 5.4m water load, the settlement gap of high tidal and low tidal in the pipe near the shore up to 10mm, the settlement gap of the middle river up to 20mm. Though the fluctuation is a bit large, the accumulated settlement of 11 years after construction is only about 20~50mm; the Limfjord tunnel in Aalborg Denmark 1969 suffers from the tidal action, final largest settlement up to 119mm; the Kennedy tunnel in Antwerp Belgium also affected by the tidal and the largest final settlement is 186mm [5]. These cases have common points that their foundation trench silt seriously and the soil weak layer is very thick.

Changes in Regional Groundwater. Immersed tube tunnel as a long-term use underground structure will inevitably suffered with the change of groundwater level due to human action or nature change. The natural groundwater level changes are generally modest and cyclical, as shown

in Fig. 2 [8]. But the groundwater change caused by human action is always irreversible and affects the structure seriously.

Cases: the Baytown tunnel in Texas USA treated its foundation by the scraping sand method up on the hard clay and sand soil. The total tunnel settlement is 45cm and one area is leaking to 1960. Until 1978, the ground surface has sunk 1.5-2.5m all due to the over-exploitation of the underground water, gas and oil [5].

Earthquake Load. The major hazards of earthquake loading is shock and vibration, and it is easy to lead the liquefaction of foundation soil. To the less cohesion soil, it is easier to be liquefied and cause substantial settlement. To the cohesive, though it will not liquefied, but the earthquake load will causing the pore water pressure disappear leading to the soil consolidation settlement.

Deficiency during Construction. Deficiency during construction like the treatment of the foundation not dense enough, the gap between the foundation and pipe is too large, dredging disturbs the original soil too much, irregular over break Etc. can be not negligible factors considering the settlement. They affect the settlement together with the factors described before, and enlarged the influence.

Cases: Yingguang Fang and some other people took the sand diffusion model test of the immersed tube tunnel foundation treated by the sand flow method [9]. The test analyzed the diffusion law of the sand tray and many diffusion gaps were found in the model. That means it is inevitable to appear gaps during the foundation treatment resulting in accident settlement.

Settlement Mechanism of Original Soil and Foundation Layer during Construction

Tunnel settlement is mainly consisted by compression deformation of foundation layer and spring back of original soil--recompression deformation.

When analyze settlement mechanism of a non-pile foundation immersed tunnel, the changing of foundation load in construction processes should be considered. The construction process of a immersed tunnel is as follows: ①original soil-②excavation and unloading-③siltation-④pipe burying and treatment of foundation layer-⑤sinking of tube section-⑥refilling of overlaying soil-⑦operation.

Research shows that: (1) weak soil is mainly produced in process ② and ③ by disturbance and siltation ; (2) process ④ to ⑥ are construction period, tube section is subjected to basic load and additional load, which include construction loads and loads produced by concrete shrinkage; (3) tube section is subjected to several kinds of load including basic load, variable load like vehicles and pedestrians load, siltation, temperature load, and accidental load like blast and seismic load;

Settlement mechanism will be analyzed from the aspect of original soil and foundation layer as follows: to original layer:(1) It is a mechanical process of unloading-reloading in construction process ② and ③, original soil is unloaded by excavation, recompressed by silting, burying foundation layer, sinking tube section, and filling back. From the point of soil stress history, at stage ⑥ the cover soil pressure on original soil is lower than pre-consolidation pressure, original soil is still in the over-consolidated condition. (2) The process ⑦ is in operation period. With the increase of external load, the cladding pressure on original soil increases and exceeds the pre-consolidation. The original soil comes to be normally-consolidated soil. And with further consolidation, the settlement difference of swelled and recompressed is accumulated.

To the foundation layer:

(1) Compression begins with the progress ④. And the initial consolidation degree is zero.

(2) Progress ④ to ⑦ is a step-by-step load, compression and consolidation period. During this period, foundation layer is subjected to several kinds of load by burying and sinking tube section, backfilling the cover soil and operating. The particles of foundation layer are rearranged and the void ratio decreases.

(3) The main settlement of foundation layer by compression occurs in progress ④ to ⑥ that is construction period. Progress ⑦ is operating period, settlement also occurs in it, but its ratio is less, can be ignored, considering that with the same compression and consolidation, foundation layer is thinner than original soil.

Settlement Mechanism of Some Special Load

Tidal Action. Water pressure as the basic load was determined by the water level elevation during the load calculation. Tidal action on one side taken as the dead load considered in the load calculation from high tide and low tide two ways, on the ether side on the cycle of tide rising and ebb disturbs the original soil and foundation layer. Consider the soil swelling and recompression characteristics every swelling and recompression cycle accumulate a little settlement and it is a positive correlation between the settlement value and the soil compression modulus. The soil settlement variation caused by the tidal action is shown in Fig. 3 [10]. The settlement and the tidal water level both vary as wavy cycle. The curve peak of the tidal water level is broadly in line with the curve trough of the settlement with a little phase difference.

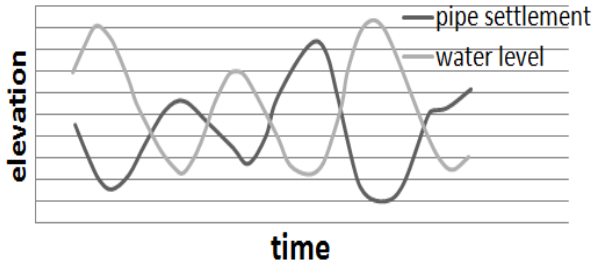


Fig 3 Variation of tide water lever and pipe settlement

Siltation and Dredging Disturb. Siltation affects the tunnel settlement in both construction and operation. The influence during the construction manifests as forming a weak silting layer to be an extra factor affects the settlement; during the operation one side as additional load roles directly on the soil, on the other side disturbs the soil in the cycle of siltation and dredging. To the soil the cycle of siltation and dredging equals to the mechanical process of gradually loading and suddenly unloading and the pipe sink and float in the cycle.

The load variation of siltation and dredging is as shown in Fig. 4, in the figure, Po represent for the siltation pressure before dredging, T represent for the siltation and dredging cycle. The load keep increasing with the siltation and suddenly decreases when dredging, this process cyclical changes, and the variation period is the same as the siltation and dredging period.

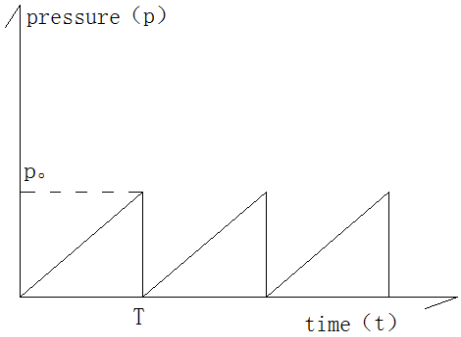


Fig.4 Load variation of siltation and dredging

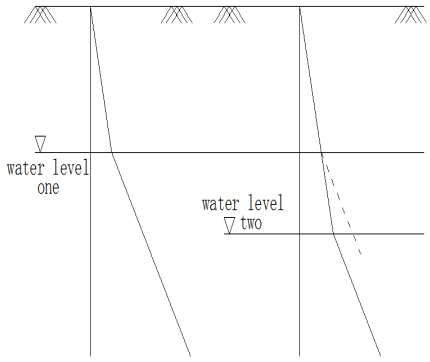


Fig.5 Total stress variation of the groundwater lowering

Groundwater Lowering. Non-normal groundwater lowering is a kind of accidental action no direct association with structure design construction or operation, it reduces the pore water pressure causing the soil effective stress increasing to balance the loose of pore water pressure, in this process the soil is compressed reflecting the settlement of the tunnel. The total stress variation of the groundwater lowering is shown in Fig. 5.

Groundwater lowering does not necessarily affect the soil around the tunnel structure. When the groundwater lowering happens in the soil layer far below the tunnel, as the mechanism the soil will be compressed, but the settlement caused by the compress still calculates on the structure upon the layer. Usually the influence scope of groundwater lowering is very large, so the effect immersed tube tunnel suffered is also serious.

Conclusions

Summarized 7 reasons lead to the immersed tube tunnel subsidence: construction load, vehicles and pedestrians load, siltation and dredging disturb, tidal action, changes in regional groundwater, earthquake load and deficiency during construction. Enumerate cases related to the reasons, finding that siltation and dredging disturb plays an important role in total settlement.

The settlement mechanism of foundation layer and original soil is analyzed from the angle of the degree of consolidation along the construction process. The foundation layer is consolidated from step to step, the original soil experiences the process of swelling and recompression.

A detailed description of variations and mechanisms of three special factors such as tidal action, siltation and dredging disturb, groundwater lowering is made.

Acknowledgements

This work was financially supported by The Chinese National Natural Science Foundation (51178428), and Zhejiang Provincial Natural Science Foundation of China (LZ12E08001).

References

[1] W. C. Grantz, Immersed tunnel settlements part 1：nature of settlements, Tunnelling and Underground Space Technology, 16 (2001) 195-201.

[2] J. Shao, Study on prediction and control for settlements of immersed tunnel, Tongji University, Shanghai, 2003.

[3] W. Li, D. Wu, X. Guo, et al, Overhaul design and construction of Ningbo Yongjiang immersed tube tunnel, Modern Tunnelling Technology, 1 (2011) 82-89.

[4] S. Chen, Immersed Tube Tunnel Design and Construction, Science Press, Beijing, 2002.

[5] W. C. Grantz, Immersed tunnel settlements Part 2：case histories, Tunnelling and Underground Space Technology, 16 (2001) 203-210.

[6] Y. Pan, J. Peng, S. Naotake, Technology of sand injection for the foundation of immersed tube elements on the external ring of Shanghai, Modern Tunnelling Technology, 41 (2004) 41–45.

[7] M. Ning, Design of Shenjiamengang undersea immersed tube tunnel, Modern Tunnelling Technology, 45 (2008) 61-69.

[8] W. Hu, G. Yang, The relative height of low pavement subgrade and the design of elevation of pavement in soft soil area, Shanghai Highways, 1 (2005) 11-13.

[9] Y. Fang, W. Li, H. Mo, R. Gu, J. Chen, Experiment and analysis of law of sand deposit expansion in foundation of immersed tube tunnel treated by sand flow method, Chinese Journal of Rock Mechanics and Engineering, 31 (2012) 206-216.

[10] W. Li, F. Xiong, Influence of oceanic tide on tunnel subsidence monitoring, Shanghai Geology, 2 (2007) 18-20.

© (2012) Trans Tech Publications, Switzerland
doi:10.4028/www.scientific.net/AMM.238.808

Monitoring Analysis on Tunnel Portal Shallow Burying Segment of Center Diaphragm Construction Method

Fei Zhou [a], Yongli Xie [b] and Jinxing Lai [c]

School of Highway, Chang'an University, Xi'an 710064, China

[a]122760135@qq.com, [b]xieyl263.net, [c]373159626@qq.com

Keywords: shallow burying segment; tunnel engineering; site monitoring; data analysis; guide the safe construction.

Abstract. Combined with highway tunnel monitoring measurement work of Bijia Mountain, the contents and methods of site monitoring and the analyzing methods for collected data of highway tunnel construction were studied. A comparative way was used to analyze the different curves of displacement with time on the two typical segments of ground settlement convergence and vault crown settlement. The result shows that the site monitoring curves of displacement with time can be divided into normal type and abnormal one. This article puts forward some feasible suggestions about how to guide the safe construction through the two types of curve. The aim of this article is to explore the changing of the abnormal curve before the dangerous accident occur, and give the causes of the reasonable analysis after collapse happened.

Introduction

The new Austrian tunneling method concept tends to be perfect, but there still lack common feasible scheme for how to construct safely for highway tunnel through the shallow buried segment [1, 2]. For the tunnel, the so-called tunnel buried or shallow buried is not simply refers to the stratum thickness above tunnel, it should be combined with the upper stratum of the engineering geological conditions and hydrology geographical conditions to judge comprehensively. As the definition of the buried and shallow buried, ultra- shallow buried tunnel depth is in accordance with the depth equal to the collapse statistical average of two times the height of the method to divide [3], this article is based on the project tunnel seems that near the entrance at the thickness of the overlying strata less than three times lots of the hole diameter as the shallow segment.

In recent years, monitoring measurement has frequently flashes its light in tunnel engineering design documents, specifications, papers and even bidding instruments. It's gradually becoming to a widespread popular technology in tunnel monitoring. This is because of monitoring measurement data processing and application, especially the lack of timely analysis and feedback information that the monitoring data often lags behind when it is conveyed to the monitoring unit. This factor hindered the monitor measuring technology to be widely used in actual highway tunnel construction, but the idea of monitoring measurements guiding the tunnel construction safety should never be overlooked [4, 5]. By analyzing the site monitoring displacement-time curves and combining with the tunnel support anomaly the author judges the possibility of dangerous situations occur, then sums up the cause of the collapse after the accident. The whole process proves the importance of monitoring measurements to guide the safe construction.

The Implementation of Site Monitoring

The project tunnel in this paper, Bijia Mountain tunnel, located in Zhenghe county of Nanping city, Fujian province, belongs to the hub of Ningwu expressway. It is a separated tunnel, the beginning and the end mileage pile are left hole ZK150+309~ZK152+955 and right hole YK150+305~ YK152+935. The entrance's terrain is mountain valley and territory flat, the vegetation is well developed, mostly cedar, pine forests and weed-tree. There is a paddy field on the right side of the upper left hole, which is good to the stability of the surrounding rock and the cave rock is priority to grade II and III, the level of entrance rock with more acidic soil and fractured surrounding rock near the entrance is IV and V.

Ground settlement measurements. Under the requirement of design and construction units, Bijia Mountain tunnel entrance should be taken observation of ground settlement measurements at its shallow section. The first excavation is this tunnel's right hole. Its ground settlement measurement points layout diagram are shown in Fig. 1. The dense vegetation of the hillside often spends a lot of twists and turns to search for the measuring point.

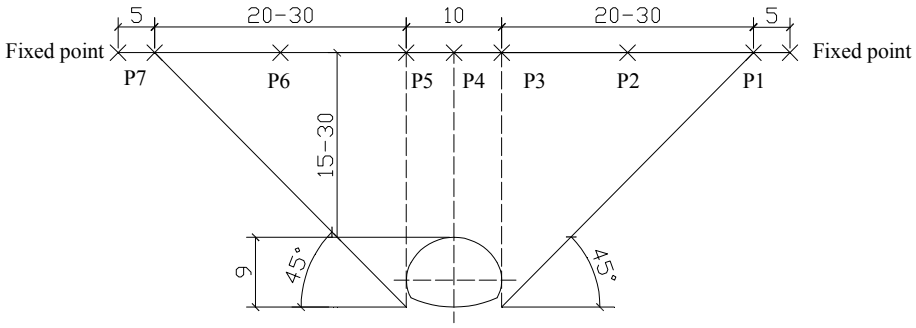


Fig. 1 Bijia Mountain tunnel imported surface settlement of the right hole distribution schematic

Vault crown settlement and convergence measurement. The Bijia Mountain tunnel uses Center Diaphragm method to excavate, as Fig. 2, according to the order of pilot tunnel excavation respectively. The measuring points A, B, C, D and E is arranged and the primary support concrete with certain intensity uses electric drill to take the measurement hook close to the wall rock. It should be noted that, the hook welded directly on the steel arch may be a convenient way, but tends to cause a large deviation of the measured data due to monitor the deformation of surrounding rock before it is deformed and passed to the steel arch.

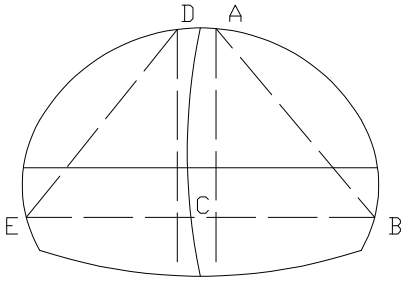


Fig. 2 Vault crown settlement and convergence arrangement diagram

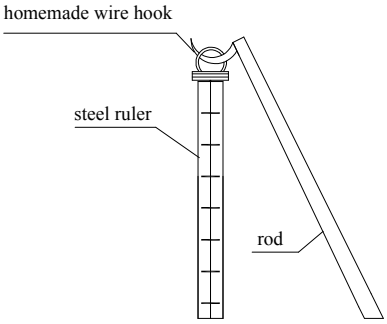


Fig. 3 With supplementary methods point take ruler on high schemes

Due to insufficient lighting intensity in the tunnel construction, a spotlight and a flashlight should be carried while doing measurements. Fig. 3 provides a metod that hang the ruler and convergence device end to high place. Homemade hook should have the stiffness that won't be tensile deformed with measuring tool, and the rod chosen is 5~6 meters of fibre glass rod.

Analyses of the Tunnel Entrance Monitoring Results

For site monitoring, relevant information literature gives some analysis method, and all sorts of displacement and deformation analysis commonly used regression analysis method and displacement back analysis method [6, 7]. Combined with Bijia Mountain import mileage pile YK150 + 340 and YK150 + 375 two sections of measured data, two different types of curve give substantial help to make suggestion on safety construction.

Normal type displacement-time curve. The right hole imports mileage pile YK150 +340 of tunnel excavate from March 1, 2010. The upper right of the pilot tunnel was first excavated, step length was 5 meters, because that entrance surrounding rock mostly fragile, the daily construction progress was less than one meter.

As Fig. 4, in the early stage of excavation, surface integral change was small. With upper right of the pilot tunnel excavation, the change of recent point 3, 4, and 5 of the tunnel center line significantly increased. After finished the right pilot tunnel excavation, the maximum settlement

was up to 4mm/d. Based on the monitoring group's advice, construction unit strengthened the primary support of concrete strength and completed the welding of mid-partition integrative rapidly, which made the subsidence relieved after stopping work and supporting structure for two days. After upper left of the pilot tunnel excavation on March 13, the settlement of surface showed increasing trend again and the settlement amount was up to 5mm/d, monitoring team immediately suggested that the inverted arch should be set up at a quicker speed, in order to make it closed into a ring to improve the overall stiffness. When the inverted arch got certain intensity on March 29, the surface subsidence mitigation and then continuously reduced until convergence.

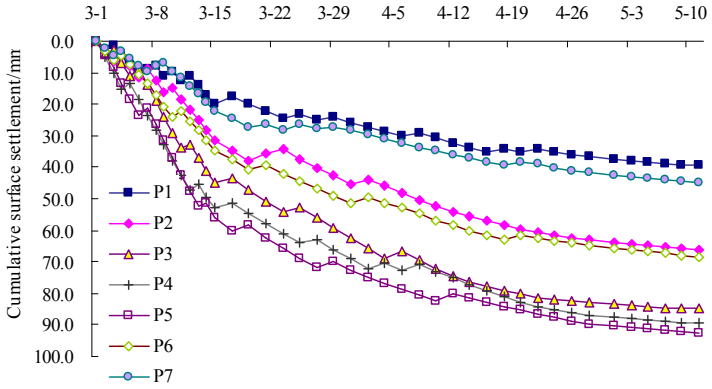


Fig. 4 YK150+340 curves of surface settlement variation with time

The construction process's impact on the surrounding rock can be seen from cumulative settlement curve of vault crown in Fig. 5. After March 10, completed lower right pilot tunnel excavation, point A began to be implemented with settlement observation and the surrounding rock had been a certain degree of settlement. With disturbance of upper left pilot tunnel excavation to the surrounding rocks, the vault crown settlement was increasing day by day. From the view of slope point D curve is consistent with point A, large deformation was generating in vaults crown above the surrounding rock. Construction unit should pay attention to excavation and supporting link closely. But by the calculation of the fitting equation about the curve changed greatly in Fig. 5, du/dt =0.13mm/d<0.15mm/d. No unfavorable effects would be produced on construction safety [8]. After the inverted arch with a certain intensity and the overall closed into a ring by the end of March, the two measuring points' settlement began to slow down and gradually convergence.

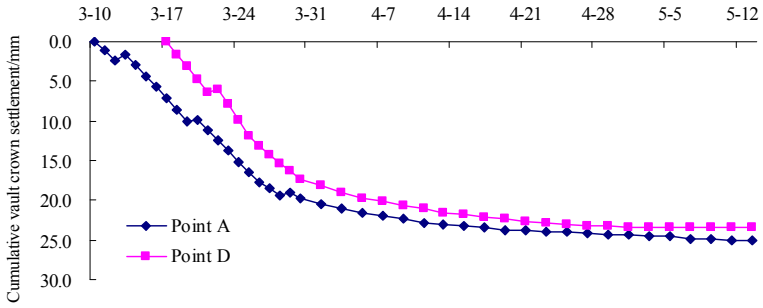


Fig. 5 YK150+340 curves of vault crown settlement variation with time

As right tunnel YK150 +340 the convergence time curve shown in Fig. 6, positive number indicates the inward contraction, negative means outward expansion [9]. The convergence of surrounding rock has large fluctuations in the construction process. After completion of the right lower pilot tunnel excavation, left side surrounding rock of mid-partition presses to the completion of the tunnel body which is reflected in the diagram on the measured line BC continuous to grow. When the left lower pilot tunnel excavation completed vault surrounding rock puts pressure to mid-partition causing it to produce the left deformation. A measuring line BC declines rapidly, the same changes are reflected in measuring line CE. If stability need to be maintained on tunnel body, BC extended CE section will shrink. After mid-partition was removed on April 10, monitor measuring began to implemented on line BE, with small-scale fluctuations, eventually converge to 2mm. Convergence accuracy of the instrument measured value is not only related with the professional skills of measurement, but also affected by the hook attached to the foreign bodies and

the temperature inside of the tunnel. So convergence measured values often show a small range of fluctuation, but for several months of repeated measurements by probability methods could be used to exclude these discrete points, and ultimately reflect real changes in surrounding rock.

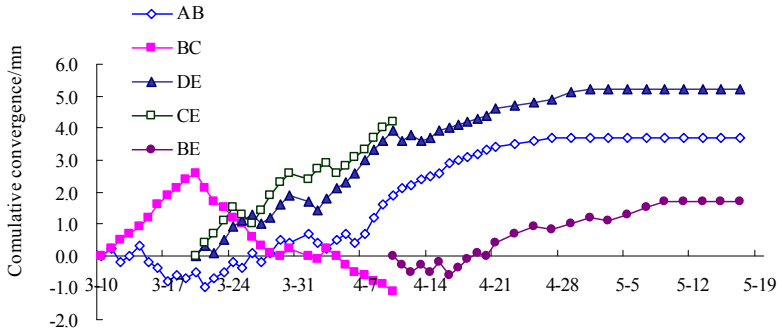


Fig. 6 YK150+340 curves of convergence total variation with time

Abnormal type displacement-time curve. The right hole imports mileage pile YK150+375 of Bijia Mountain tunnel excavation started from June 18, 2010, landslides occurred on August 3, 2010. Use this typical section to analysis the various anti-normal change of the monitoring measurement time curve before the collapse accident occurred.

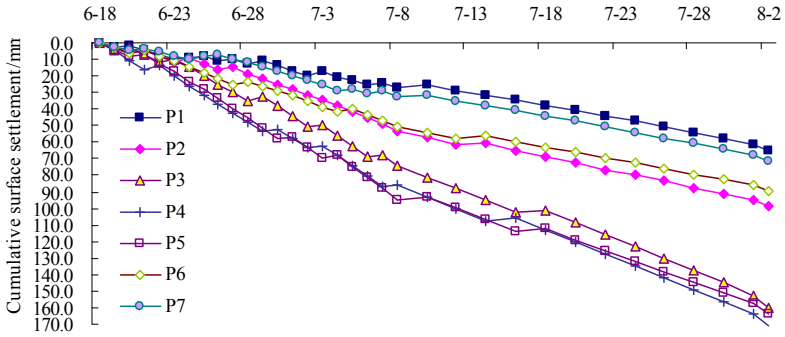


Fig. 7 YK150+375 curves of surface settlement total variation with time

From Fig. 7, at the beginning of excavation to the upper right of the pilot tunnel construction work, disturbance to the surrounding rock is very small and the reaction in the chart is the curve going down. When excavated the lower right of the pilot tunnel on June 23, the rate of surface subsidence increased significantly. It should be affected by the wide range of heavy rainfall, as most areas of Fujian province began to appear heavy rainfall on June 23, 2010. The owner of NingWu high-speed immediately ordered Bijia Mountain tunnel to stop construction until the weather improved. Hasty lay-off made the construction unit only did a simple support around the tunnel working face. Monitoring measurements of surrounding rock was poor and the primary support of tunnel must follow the principle of quickly into the hole and fast go out. The heavy rainfall had been continuing for 11 days, the surface settlement reached to the maximum 6mm/d until working on July 4. When the lower right pilot tunnel was excavated another time, settlement changed intensifies, while right tunnel body had been completed primary support. Surface subsidence tends to be slow down. But this trend only lasted for several days, as upper left pilot tunnel excavation disturbed surrounding rock. The surface of the maximum daily settlement reached 9mm/d on July 19 that monitoring team recommended construction unit to suspend excavation and strengthen support. However, in order to make up nearly half month lay-off losses, construction unit did not accept suggestions and determined to continue the excavation. The result was that the maximum daily settlement reached 12mm/d on July 19 and without any signs of easing. Then combining with the phenomenon of vault crown and convergence abnormal curve and obvious compressed deformation of tunnel mid-partition, monitoring group reported that Bijia mountain tunnel right hole imports YK150 +375 was likely to occur dangerous situation and great probability which might cause the collapse accident to the supervisor, the construction unit and the unit owners on August 1. Later, this region collapse occurred roof fall accident at 3:00 on the August 3 and collapsed objects pour into the tunnel buried almost all of YK150 +355 ~ 375 region.

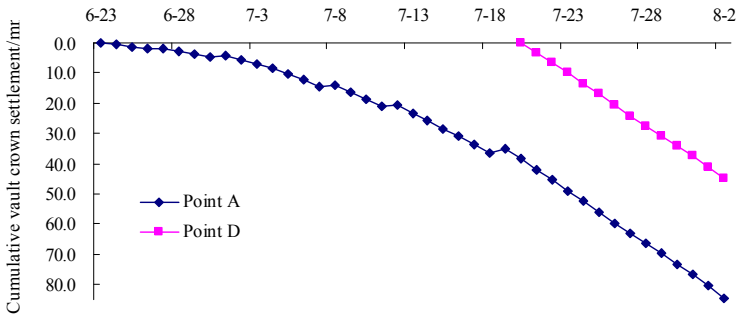


Fig. 8 YK150+375 curves of vault crown settlement total variation with time

As shown in Fig. 8, for 11 days heavy rain made the surface settlement curve accelerating changed while vault settlement-time curve changed relatively slow. The heavy rainfall brought a lot of rain water seeping into the soft rock and making loose rock constantly reinforced, resulting in surface subsidence with a large variation. With returning to work on July 4, the surrounding rock was disturbed again, the vault and subsidence was increasing day by day. Right side of the pilot tunnel excavation without made the inverted arch but direct excavation left part add to dismantled the former mid-partition earlier, heavy rainfall infiltration left on both sides of the tunnel and water in arch angle stagnant was not cleaned up. Not paying enough attention on all there risks, but to catch up with the construction progress intensifies the vault crown of subsidence. By doing regression analysis on measurement points A, D after July 20, du/dt=6.2mm/d, which have far exceeded construction standard required by the vault crown displacement sink rate, combined with surface and convergence abnormal curve deliberate decision reported dangerous situation.

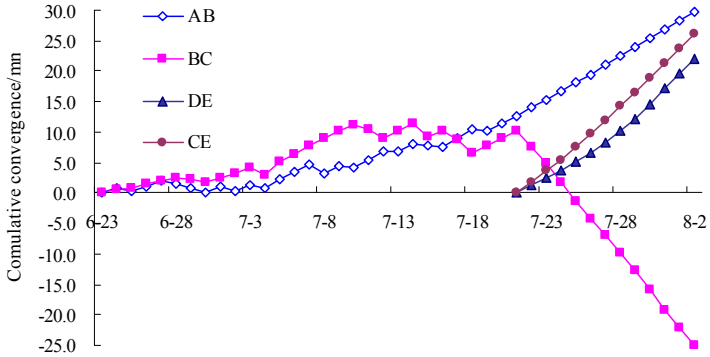


Fig. 9 YK150+375 curves of convergence total variation with time

The abnormal changes before the accident happened can be seen from the convergence schedule chart in Fig. 9. The mid-partition and left side of surrounding rock could work together under pressure from above strata before left pilot tunnel excavation, so that tunnel body could keep in a relatively stable state in this situation. It is shown on the chart as measuring line AB, BC, although they have slight fluctuations but still changing slowly. After left lower pilot tunnel excavation on July 17, the mid-partition became independent of the load-bearing structure and began bending deformation gradually and every change of measuring lines increased day by day. When measured in tunnel on July 30, the bending deformation of mid-partition near the tunnel working face was serious, and the top of the steel frame was exposed with the cover of concrete severely spalling. The water of the tunnel arch angle on both sides was still not clear, the danger was looming.

Listening to different experts and on the basis of observation and measured results from inside tunnels for several months, the reason of collapse can be summarized as following:

The demolition of the mid-partition in YK150 + 370~375 is too early. Only depending on the mid-partition near the working face is difficult to support the pressure of surrounding rock above vaults. After the completion of the pilot tunnel excavation, the inverted arch is not constructed in time, the bearing system do not close into a ring to increase its overall rigidity.

Blind pursuing the progress of construction lead to rough excavation process, the primary support cannot keep up with tunneling speed, the strength of primary support spray concrete cannot meet the design requirements. The mechanical strength of the surrounding rock of tunnel arch angle is

weakened due to both sides of the excavated plane soaked in water for half a month. The tunnel drainage is too lag that a great amount of water can be seen everywhere in the hole.

Irresistible bad weather has certain responsibilities for the accident, surface range of landslides roof caving just in the paddy fields which left by local villagers. Some experts consider that a half month of heavy rains cause paddy fields change into water containers, the rain affect the strength of the surrounding rock by permeating into the tunnel body through the roots of the vegetation.

Conclusions

Combined with the monitoring site data on tunnel project, displacement-time curves of the measurements of ground surface settlement, convergence and vault crown settlement are analyzed. Monitoring measurement is a practical measurement technology in instructing on-site construction.

By analyzing the schedule chart of monitor measuring displacement with typical sections, abnormal changes of monitoring curve that may arise were summarized before the accident. Besides, once danger happened, the curve anomalous change is often not alone, the ground surface settlement curve, convergence curve and vault crown settlement curve could present the abnormal changes. After eliminates human factors and possibility damage of hook and instruments, the alarm can be send to the construction, supervision and the owner. After all, nip in the bud, then guide construction safety is the basic purpose in monitoring measurement.

It is worthy of study on reasonable theoretical analysis method of all kinds of abnormal displacement-time curve. It is expected that this paper can attract more attention and a speedy site monitoring data analysis system will be established in the near future, which make the information feedback timely to the construction unit and the informatization construction be better implemented.

References

[1] H. Lai, J. Zheng, Y. Xie, Study on characteristics of surrounding rock pressure of undercut metro tunnel with shallow buried excavation in loess region, Journal of the China Railway Society, 3 (2012) 99-104.

[2] X. Wang, J. Chi, Y. Yuan, Study on characteristics of dynamic safety factor of construction process in shallow cover tunnel. Chinese Journal of Underground Space and Engineering, 7 (2011) 1454-1459.

[3] M. Wang, Tunnelling and Underground Engineering Technology in China, First edition. China Communications Press, Beijing, 2010.

[4] Y. Zhu, Monitoring measurement and results analysis of Luoping tunnel construction, Geotechnical Investigation & Surveying, 7 (2011) 7-11.

[5] Q. Liu, S. Bai, C. Xiao, Study on surrounding rock stability of Longtan Tunnel Based on in-situ monitoring measurements, Chinese Journal of Rock Mechanics and Engineering, 10 (2007) 1982-1990.

[6] T. Han, F. Huang, J. Zheng, Reinforcement construction and monitoring analysis of arch springing collapse of tunnel, Chinese Journal of Rock Mechanics and Engineering, 2 (2011) 3443-3449.

[7] M. Jiang, Z. Zhong, X. Liu, Research on informative monitoring and stability analysis of shallow covered asymmetrically loaded tunnel with small interval, Chinese Journal of Underground Space and Engineering, 6 (2010) 1465-1469.

[8] F. Ye, W. Ding, H. Zhu, Site monitoring and information feedback of highway tunnel, Journal of Chang'an University (Natural Science Edition), 5 (2007) 80-81.

[9] T. Han, J. Zheng, J. Zhu, Monitoring analysis of outlet section of tunnels with small clear-distance in half-hard and half-soft rock strata, Rock and Soil Mechanics, 2 (2010) 305-306.

© (2012) Trans Tech Publications, Switzerland
doi:10.4028/www.scientific.net/AMM.238.814

Stability Analysis of Underground Caverns by Jointed Finite Element Method

Jichang Wu[1 a], Yumin Zhang[2,b] and Hongxia Li[3 c]

[1]Dagangshan Branch of China Guodian Dadu River Hydropower Development Co. Ltd., Shimian 625409, China

[2] North China University of Water Resources and Electric Power, Zhengzhou 450011, China

[3]College of science, Naval University of Engineering, Wuhan 430033, China

[a]spddrwjc@163.com, [b]zhangyumin@ncwu.edu.cn, [c]26953296@qq.com

Key words: underground caverns; jointed finite element method; blocky rock mass; deformation; reinforcements.

Abstract. The jointed finite element method (JFEM) is used to analyze the deformation and failure characteristic of fractured rock mass and anchor reinforcement effect for the water collection shaft of the main power house of Dagangshan Hydropower Station. The results show that the JFEM not only simulates the actual rock mass structure very well, but also gives the reasonable simulation results for the common unstable rock mass. The JFEM may accurately simulate the major deformation characteristic and collapse mechanism, which is another effective way to analyze the stability of fractured rock mass. The on-site monitoring results show that the anchor reinforcement is effective for the water collection shaft.

Introduction

It is an economic, sometimes the only scheme to build the underground caverns for large hydropower stations of high water level in the southwest China. The excavation of underground caverns in complex geological environment will involve the special stratum and rock mass structure. The deformation and failure of surrounding rock mass are basically under the control of rock property and structural planes. The most broadly used Finite Element Method is hard to simulate the actual rock property and the reinforcement of anchors in complex rock structure. Thus, the Jointed Finite Element Method (JFEM) is introduced to solve this problem [1]. The JFEM established the geological model based on the fracture distribution obtained in the excavation period and by the 2D random joint net simulation method. Take the Dagangshan Hydropower Station for example, the JFEM is used to simulate the deformation and failure characteristic of fractured rock mass and anchor reinforcement effect for the water collection shaft of main power house.

Jointed Finite Element Method

The JFEM can simulate well the actual structure and failure characteristic of the rock joint network by inputting directly the investigated on-site joint into the model and permitting the joints to yield according to some failure criterion [2]. It is hard for the FEM and FDM software to simulate the actual structure of rock mass due to the difficulty in modeling and calculation convergence. In 2011, the Rocscience Inc. Company in Canada developed the Phase^2 8.0 FEM software that can simulate well the actual rock structure [1]. The Phase^2 8.0 provides a strong joint generator to create several sets of joints. The Goodman element is used to simulate the joint, and the shear behavior of joints is conducted by Mohr-Coulomb slide criterion or more advanced Barton-Bandis criterion.

The random joints in this paper are generated by Baecher disk model [3], assuming the middle points of joints distributs evenly in space and creates the disc-shape joints of specified radius and strike. The attitudes of structural planes are determined by single α and dip β, and the probability distribution models include Fisher, Bingham, normal double-variable, and uniform distribution, etc. The sizes of structural planes are basically described with outcropped joint length by line method or window method. The trace lengths of structural planes comply with lognormal or negative exponential distribution [4]. The trace lines in Fig. 1 are generated by Fisher distribution.

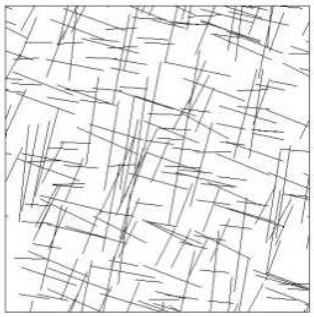


Fig. 1 Joints created by No.1826 random seed

Engineering Example

The underground caverns of Dagangshan Hydropower Station at the Daduhe basin in southwest China comprises a 30.80m-span main powerhouse, a 18.80m-span transformer chamber and a 20.50-24.00m span tailrace chamber in parallel distribution. The on-site terrain and geological condition are very complex with high geo-stress and some faults and dikes. Here take the typical section of water collection shaft of main powerhouse for example to analyze the deformation and failure characteristic of joints and anchor reinforcement by JFEM.

Parameters for Simulation. There are mainly four sets of joints in the 0+130.10~0+145.50 section under the deputy powerhouse uncovered during the construction period, as listed in Table 1. The outcropped joints have the length of meter- or ten-meter magnitude, and thus the rock cut by this kind of structural planes is about 0.5~10m long. The mechanical parameters of rock are determined by borehole tests or empirical estimation, and that of structural planes by on-site and indoor tests. The parameters for rock mass are listed in Table 2.

Table 1 Strike of main joints

Item	Dip/Single (°)	Trace length / Spacing (m)
A	EW/S(N) ∠60°~80°	20~30/10
B	N40°~50°E/N∠81°~85°	15~25/8
C	EW/S∠25°~35°	10~20/7
D	N20°~40°W/N∠28°~38°	8~12/4

Table 2 Mechanical parameters for rock mass

Jointed rock mass	E (GPa)	ν	K_n (MPa/m)	K_s (MPa/m)	c (MPa)	φ (°)
Rock	25	0.2	--	--	2.5	60
Structural planes	--	--	3000	1000	0.15	31

The parameters for anchor reinforcement are determined by rock mass quality. The pre-stressed and common mortar anchors are distributed alternately as listed in Table 3. The truss elements simulate the anchor behavior.

Table 3 Reinforcement scheme and parameters

Pre-stressed anchor	Mortar anchor	Spacing
Φ32，9m，T=150kN	Φ28，6m	1.5m

Typical Section of Well Collection Shaft. Local collapse of side wall of water collection shaft occurred during excavation period in the 0+130.10~0+145.50 section. Here the deformation and failure in this section is simulated in terms of geological data and underground cavern design. Only the shaft section is considered to simplify the problem, and the simulation model is shown in Fig. 3.



Fig. 2 Local collapse of shaft wall

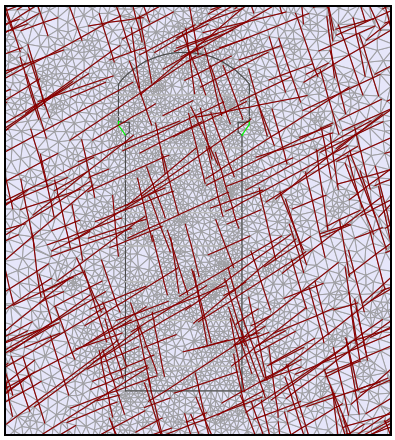


Fig. 3 Simulation model of local shaft

Simulation Results. Fig. 4 shows the deformation and failure contour of shaft wall without reinforcement. The deformation is generally affected by joint combination with max displacement of 21mm. For joints with small angle to shaft wall, the shear displacement easily occurs due to the difference of stress relaxation. For joints with steep angle, the open deformation can be found in the inverse-dip structural planes, and then may create the unstable blocks by combining the flat-dip structural planes. The red lines in Fig. 4 indicate the damaged joints, with steep-dip structural planes yielded in upward wall and flat-dip structural planes yielded in downward wall. The simulation results generally comply with the on-site investigation.

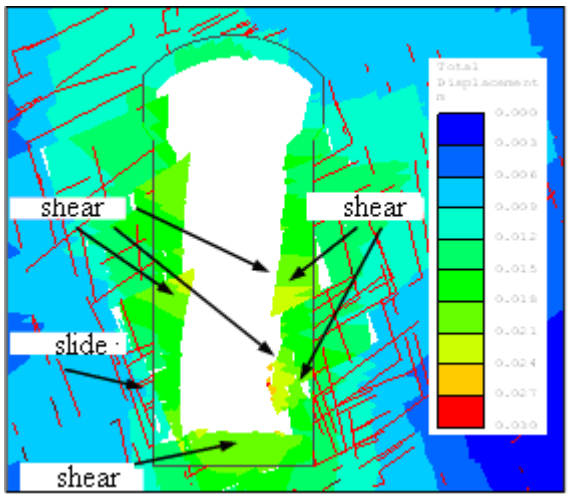


Fig. 4 Failure and deformation of shat without reinforcement

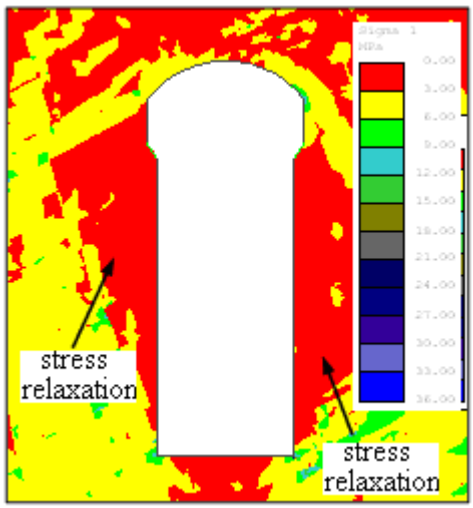


Fig. 5 Max principal stress of shat without reinforcement

The max principal stress contour of excavated shaft is shown in Fig. 5. The large shear and open deformation results in stress release, and the flat-dip structural planes have great effect on stress relaxation. The stress relaxation zone complies generally with the deformation zone of surrounding rock mass, which shows that the shear and open deformation basically results in stress relaxation. The deformation contour of reinforced shaft is shown in Fig. 6, which shows that the shaft walls are reinforced greatly with more uniform deformation. It is perhaps that the anchors limit the deformation of structural planes and improve the strength of structural planes [5]. Compared with the traditional FEM, the JFEM can simulate well the anchor reinforcement on rock mass. However, some rock blocks in the downward shaft wall may collapse and the slide deformation along the steep-dip structural planes of the upward wall may come into being. It is suggested that more concrete should be added in this area or additional anchors should be set. More attention should be paid to the evitable local block collapse.

The simulation results are well similar with the monitoring data from the displacement meters on the shaft walls, as shown in Table 4. The good similarity may explain the deformation progress with cavern excavation, and also shows that the joint model and parameters are reasonable.

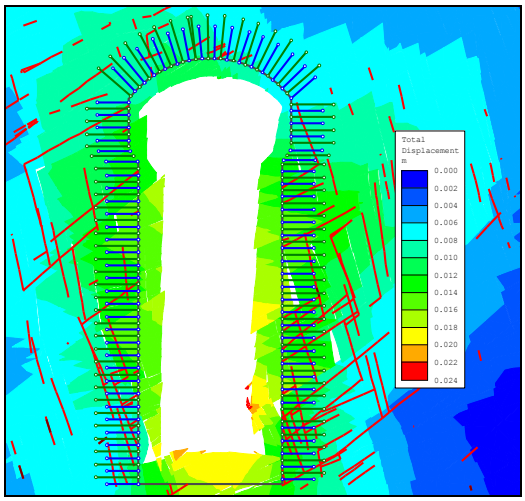


Fig. 6 Failure and deformation of shat with reinforcement

Table 4 Comparison between monitoring data and simulation results (mm)

Displacement meter No.	Location	Measurement		Simulation value after excavation
		Date	Value	
M^4_{1CFX}	Upward wall ▽959.5m	2011/07/18	18.85	23.2
M^4_{2CFX}	Upward wall ▽973.0m	2011/10/12	30.78	28.6
M^4_{3CFX}	Downward wall ▽977.5m	2011/10/13	7.09	12.5
M^4_{4CFX}	Downward wall ▽959.5m	2011/10/13	5.31	8.3

Conclusions

The JFEM can simulate well the deformation and failure characteristic of fractured rock mass and anchor reinforcement effect on rock mass. The comparison of simulation results and monitoring data shows that the JFEM may be a good method to analyze the stability of fractured rock mass and provide a reinforcement design for fractured rock mass.

The simulation of Dagangshan Hydropower Station shows that some rock blocks in the downward shaft wall may collapse and the slide deformation along the steep-dip structural planes of the upward wall may come into being. The reinforced shaft wall presents more uniform deformation.

Acknowledgements

This work was financially supported by the National Natural Science Foundation (51009130).

References

[1] Rocscience Inc.. Phase 2 Joint Network Verification. Rocscience Inc., Toronto, Ontario, 2011.

[2] H. Song, M. Huang, M. Sun: Application of finite elements with joint net to stability analysis of toppling slope, Rock and Soil Mechanics, 4 (2011) 1205-1210.

[3] Beacher G B, Lanney N A, Einsten H. H, Statistical description of rock properties and sampling, in: Proceedings of the 18th US Symposium on Rock Mechanics, 1977, pp. 1-8.

[4] Goodman R. E, Taylor R L, Brekke T L, A model for the mechanics of jointed rock, Journal of the Soil Mechanics and Foundations, 3 (1968) 637-659.

[5] Y. Wu, Y. Wang, D. Gu, Experimental study on effects of rock bolts resisting growth of surface structural planes, Chinese Journal of Rock Mechanics and Engineering, S1 (2006) 3046-3050.

© (2012) Trans Tech Publications, Switzerland
doi:10.4028/www.scientific.net/AMM.238.818

Controlling Criterion for Differential Settlement of Widened Expressway

Haofeng Xing [a], Haoming Li [b]

Department of Geotechnical Engineering, Tongji University, Shanghai 200092, China

[a]hfxing@tongji.edu.cn [b]liningqiang1988@163.com

Keywords: widening; pavement structure; differential Settlement; controlling criterion; ultimate tensile strength.

Abstract. The controlling criterion for differential settlement between the new and old subgrade of widened expressway is an important technical problem concerned by academia and engineering field. Based on an engineering project, finite element method was used to analyze the effects of foundation, embankment and road surface on the differential settlement, in which the foundation, embankment and pavement was considered as a whole structure, and the ultimate tensile strength was used to determine its strength. The calculation duration is from the construction of the original road to the post construction settlement of the widened road. The controlling criterion of differential settlement after bilateral widened expressway was explored. The analysis results show that the maximum differential settlement should be controlled in 5cm considering the mechanical response of pavement structure, and the integral analysis method is more reasonable to analyze the differential settlement of widened subgrade.

Introduction

Nowadays with the rapid development of China economy, more and more existing Expressways cannot meet the needs of traffic, and the measure such as widening the original highway is considered as the effective way to solve the traffic problem. While differential settlement is the main reason that cause longitudinal cracks and other related diseases [1]. Numerical researches on controlling criterion for differential settlement mostly put the subgrade separately from pavement structure, and the distribution curve for differential settlement of embankment is fit through the simulation for embankment consolidation settlement. The curve is exerted under the pavement to get the relations between pavement settlement and internal stress by changing maximum settlement of the curve, and then the controlling criterion for differential settlement which meet the pavement structural requirement is explored [2,3]. In fact, the settlement of old and new embankment is closely related to foundation treatment plan, foundation conditions, the scope of the project and the operation history. So considering the settlement as a curve simply is distorted and limited. The influence of settlement occurred before widening isn't considered in some literatures [4]. But the differential settlement of existing pavement has caused additional stress in base structure during the operation process before widening, which has important effects on the engineering response of whole pavement structure afer widening. Therefore the calculation duration of differential settlement should be from the construction of the original road. The load action for the existing road which comes from new road construction will cause the existing road structural stress changing that will lead to the existing road deformation, so the deformation of the old road caused by differential settlement during new construction period should be analyzed. The finite element program ABAQUS was used to analyze the effects of foundation, embankment and road surface on the differential settlement, in which the foundation, embankment and pavement was considered as a whole structure, and the ultimate tensile strength was used to determine its strength. The calculation duration of differential settlement is from the construction of the original road to the post construction settlement of the widened road. Its controlling criterion for bilateral widened expressway was explored as well, and compared with the method used currently that exerting differential settlement curve under the pavement, some useful results were obtained, which provided theoretical bases in order to improve highway safety use.

Finite Element Model and Calculation Parameters

The finite element analysis model was based on the Fokai Highway widening engineering project. The height of embankment was 5.19m, slope ratio was 1:1.5; The width of old embankment was 26m and both sides of the widened embankment was 8m. Geometric model of finite element analysis is shown as Fig. 1. Calculative depth of foundation was 30m and width was 80m. Took half of the structure to analyze according to the symmetry, in which the old road center was considered as symmetry plane. Left and right boundaries of structure were horizontal fixed constraint, no horizontal displacement; the bottom was horizontal and vertical constraint, no horizontal and vertical displacement; for calculating easily, assumed that only ground surface was permeable and the rest was impermeable.

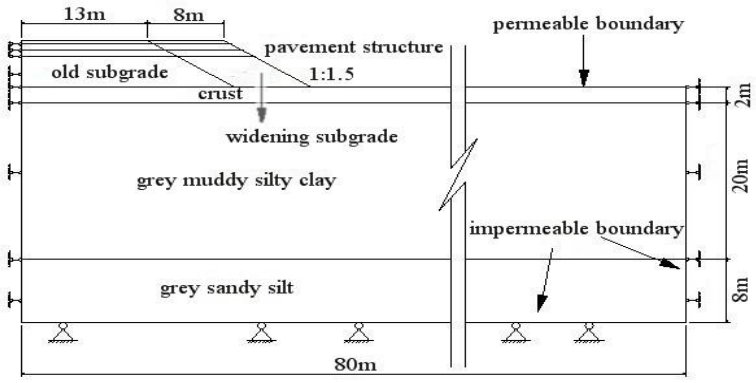


Fig. 1 Geometric model of finite element analysis

The new, old embankment and crust were used Mohr-Coulomb model to simulate. The grey muddy silty clay was simulated with Modified Cam-Clay model (MCC). Pavement structural layers (i.e. the surface, base, subbase) were considered with the linear elastic model. The assumptions for calculation are used as follows:

(1) A plane strain problem was considered.

(2) Pavement structural layers are homogeneous, isotropic linear and elastic materials.

(3) Pavement structural layers are completely continuous in the vertical direction.

(4) Uniform embankment sinking has little effect on the pavement structure.

Pavement structure and material parameters are listed in Table 1.

Table 1 Pavement structure and material parameters

Structural layer	Thickness h (cm)	Density ρ ($g \cdot cm^{-3}$)	Elastic modulus E (MPa)	Poisson ratio μ	Cleavage strength σ (MPa)
Asphalt concrete surface	18	2.5	1600	0.3	1.0 / 0.4
Cement stabilized graded macadam base	47	2.5	1500	0.25	0.5 / 0.2
Graded macadam subbase	16	2.5	220	0.3	—

The plane strain CPE4 was used to simulate pavement structure and embankment, the fluid-structure interaction unit CPE4P was used to simulate foundation. The surface and its base are respectively composed of 2 and 4 units, and its subbase and embankment are respectively divided into 2 and 4 units, crust is composed of 4 units, soft foundation is divided into 14 units, the foundation outside of widened embankment is divided into 17 units. Model mesh generation is shown in Fig. 2.

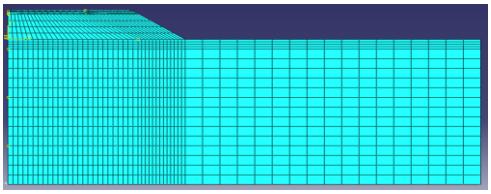


Fig. 2 Model mesh generation

The Mechanical Response of Pavement Structure for Differential Settlement

To simulate the actual process of construction and operation, the calculation duration is considered from the construction of the original road, and the embankment surface deformation at main different analysis steps are shown in Fig. 3, where step7 is the new embankment filling, Step8 reflects the new embankment preloading period, Step11 reflects for the pavement filling, Step13 shows widened highway operating for fifteen years. As shown from step7 and step8, two lines were substantially parallel. So the differential settlement of embankment surface is not obvious during new embankment preloading period. While unloading the old road self-weight and vehicle load in step11 made the center of the old road cock, settlement and differential settlement of new road both increased. Pavement self-weight and vehicle load influenced the differential settlement and pavement stress largely.

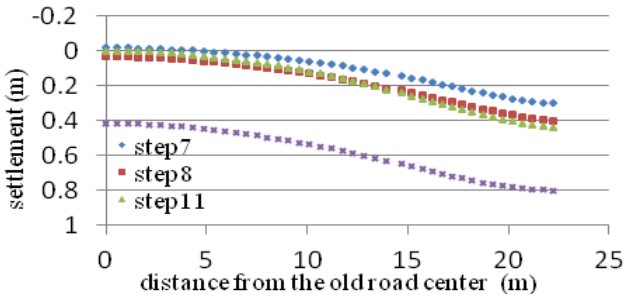


Fig. 3 The embankment surface deformation at the end of different analysis steps

Took structural layers, the depths of 0cm, 30cm, 42cm and 73cm represent respectively for the top surface, upper base, middle base and the middle subbase. The tensile stress distribution at 13 step is shown in Fig. 4. The maximum tensile stress is located at the new road base, 2m away from the old road shoulder.

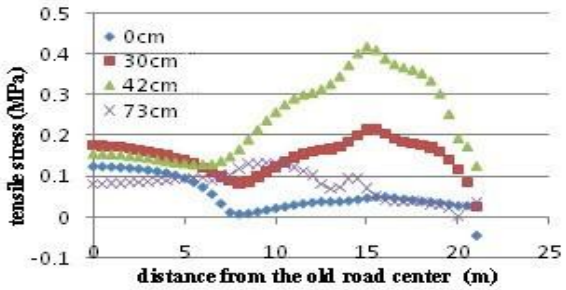


Fig. 4 Tensile stress distribution diagram of each layer

Therefore, when the maximum tensile stress reaches the ultimate base tensile strength, 0.5MPa, pavement is damaged due to the destruction of the base. Pavement tensile stress nephogram is shown as Fig. 5 when the maximum tensile stress of pavement reached 0.5MPa, and the maximum tensile stress was located at the new road base, at the distance of 2m away from the old road shoulder. The calculated time is 1880 days, i.e. five years and three months after laying the pavement.

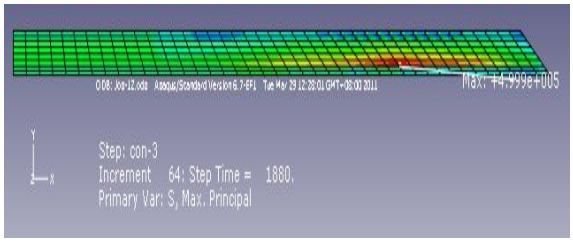


Fig. 5 Pavement tensile stress nephogram with the maximum reached the ultimate tensile strength

The differential settlement distribution curve of embankment surface is shown in Fig. 6, it is clear that the maximum differential settlement is 5cm and the variable slope rate is 0.24%. The maximum tensile stress of pavement base exceeds the ultimate tensile strength when the rate is greater than 0.24%, the pavement damages. Therefore, taking variable slope rate of 0.24% as controlling criterion for pavement structural damage is desirable.

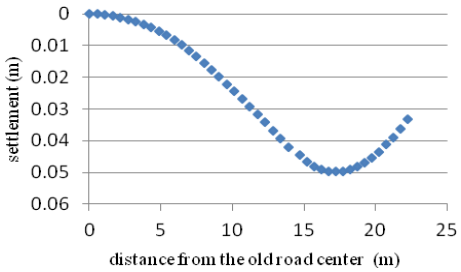


Fig. 6 Distribution curve of differential settlement when reached the ultimate tensile strength

Contrastive Analysis with Applying Curve Displacement Method

The integral analysis method used in this paper (the follow referred to as the integral method) is compared with the traditional applying curve displacement method, and the comparative result of different settlement is shown in Fig. 6, and the distribution curve of differential settlement on the new and old embankment of widened road is shown in Fig. 7.

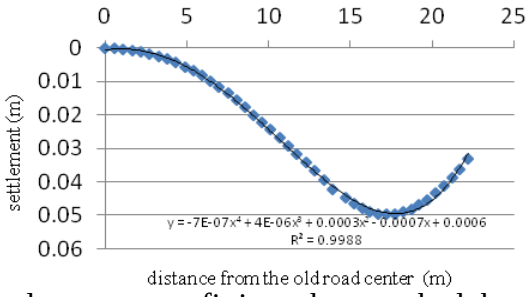


Fig. 7 Differential settlement curve fitting when reached the ultimate tensile strength

Through curve fitting method, formula1 is acquired, where α=0.05(m), is the maximum differential settlement value on top of embankment for the integral method when reached the ultimate tensile strength, μ is the differential settlement value where the distance is *x*(m) from the old road center. Using Formula1 and the pavement materials listed in Table1, the tensile stress nephogram at the bottom of widened road pavement is got as shown in Fig. 8.

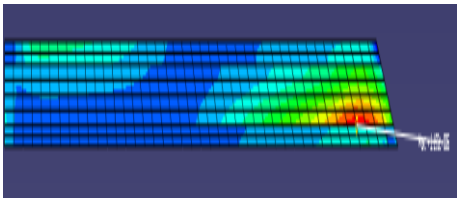


Fig. 8 Integral tensile stress nephogram of curve method

Through the adjustment of parameters such as coefficient of fitting equation and the loading to the bottom of widened road pavement, the settlement curve on top of embankment is shown in Fig. 9 in which maximum tensile stress reach 0.5MPa. The largest differential settlement was 1.5cm.

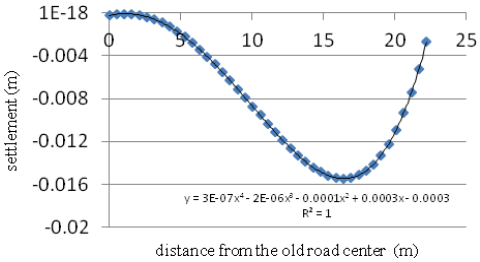


Fig. 9 The settlement curve of curve method when reached the ultimate tensile strength

Comparing Fig. 5 with Fig. 8, the maximum tensile stress value got form curve method was 1.195MPa, which occurs at the bottom of new road pavement base near the new road shoulder 2m, while the maximum tensile stress by integral method is 0.5MPa, which happens at the bottom of new road base where close to the old road shoulder 2m. It can be seen that the maximum tensile stress of the two kinds of methods are both distributed in the bottom of new pavement base. And maximum tensile stress of the curve method is larger than maximum tensile stress of integral method.

Through Fig. 7 and Fig. 9, the maximum differential settlement by integral method was 5cm, while the curve method was 1.5cm when the maximum tensile stress reached the ultimate tensile strength.

Comprehensively considering the above results and the controlling criterion for differential settlement in existing conclusions [5-7], integral method is relatively reasonable.

Conclusions

The effect of embankment and pavement on differential settlement of widened expressway should be considered during its analysis, it is better calculation duration is the time from the construction of the original road, and the deformation of the old road caused by differential settlement during widening construction period should be analyzed as well;

When the mechanical response of pavement structure is considered, the numerical analysis results of widened subgrade show the maximum tensile stress is located at the bottom of new road base, 2m away from the old road shoulder. The material ultimate tensile strength should be considered as the controlling criterion, the largest differential settlement of embankment should be controlled in 5cm, and its corresponding variable slope rate is 0.24%;

The maximum tensile stress of widened embankment is located at the bottom of new pavement base. Meanwhile, the maximum differential settlement is 1.5cm by curve method while the value is 5cm by integral method, and maximum tensile stress got from the curve method is larger than the value acquired from the integral method.

Since the differential settlement of old and new embankment is related to formation condition and its treatment method, using integral analysis method to analyze the allowable differential settlement of widened subgrade is more reasonable.

Acknowledgments

This study was supported by the National Natural Science Foundation of China (41172247).

References

[1] Q. Huang, J. Ling, J. Qian, Influence of pavement under discrepant deformation after construction between existing subgrade and that to be widened, Journal of Tongji University (Natural Science), 33 (2005), 759-762.

[2] X. Ma, L, Li, Influence analysis of pavement splicing under differential settlement in widening expressway, East China Highway, 6 (2009) 47-50.

[3] H. Liu, G. Zeng, R. Ying, Research on allowable differential settlements criterion after construction of widening, Highway, 3 (2004) 37-39.

[4] Z. Fu, X. Wang, X. Chen, et al, Influence of different settlement on pavement structure in expressway widening project, Journal of Chang'an University (Natural Science Edition), 28 (2008) 36-39.

[5] Z. Fu, X. Wang, X. Chen, et al, Controlling criterion of differential settlements after widening expressway, Journal of Chang'an University (Natural Science Edition), 28 (2008) 10-13.

[6] M. Zhang, Z. Xu, X. Huang, Research on classification and controlling criterion of differential settlement after widening expressway, Journal of Transportation Engineering and Information, 8 (2010) 109-113.

[7] X. Zheng, Research on controlling criterion of settlement in expressway widening project, Subgrade Engineering, 1 (2009) 38-39.

© (2012) Trans Tech Publications, Switzerland
doi:10.4028/www.scientific.net/AMM.238.823

Theory Study by CGM for Moving Force Identification

Zheng Chen [1, a] and Junling Han [2, b]

[1]School of Civil Engineering and Communication, North China University of Water Recourses and Electric Power, Zhengzhou 450011, China

[2]Henan Fifth Construction and Installation (group) Co, LTD Zhengzhou 450002, China

[1]yuchenfish@163.com; [2]hanjunling@163.com.

Keywords: theory study; moving force identification; conjugate gradient method (CGM); time domain method (TDM).

Abstract. The conjugate gradient method (CGM) is proposed in this paper to improve the ill-posed problem of moving force identification. Based on theoretical analysis, the CGM formula is deduced and applied in moving force identification. Related research shows that the CGM have higher identification accuracy and robust noise immunity as well as producing an acceptable solution to ill-posed cases to some extent comparing with the time domain method (TDM), when they are used to identify the moving force. The theoretical study results by CGM are practical significant to selection properly method for moving force identification.

Introduction

A number of methods for the identification of moving axle loads using bridge responses have been developed since 1952 [1-2]. Most of the moving forces identification methods eventually transformed to solve linear equations, which often cause different identification accuracy and robust noise immunity as ill-posed problem. In the last decade, a few indirect identification methods, such as the interpretive method I (IMI), the interpretive method II (IMII), the time domain method (TDM) and the frequency time domain method(FTDM) were successively proposed and incorporated into a moving force identification system(MFIS) [3].Numerical simulations, illustrative examples and comparative studies showed that each method involved in the MFIS could effectively identify moving forces with acceptable accuracy. Among these methods, the time domain method was found better than others, but it still has some limitations [4-6]. For example, the identification results were sensitive to noise, the ill-posed problem is very obvious when axles are going on or getting away bridge, and the identification accuracy is low when using bending moment responses alone. As no existing methods can be used to identify dynamic axle loads with these problems, it is necessary to adopt new methods to solve these matters. As for these reasons, a conjugate gradient method (CGM) has been developed based on the theory of moving force identification in this paper.

Basic Theory

Motion Equation of Bridge-vehicle System. A bridge superstructure is modeled as a simply supported beam as shown in Figure 1. The effects of shear deformation and rotary inertia are not taken into account. If the load f moves from left to right with speed c, then an equation of motion in terms of modal coordinate $q_n(t)$ can be expressed as

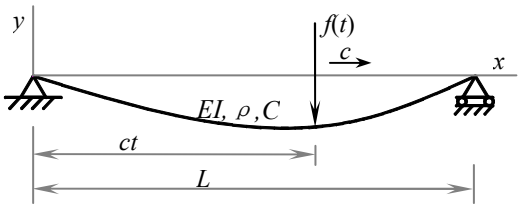


Fig. 1 Moving force Model

$$\ddot{q}_n(t) + 2\xi_n\omega_n\dot{q}_n(t) + \omega_n^2 q_n(t) = \frac{2}{\rho L} p_n(t) \qquad (n = 1,2,\cdots,\infty) \tag{1}$$

Where $p_n(t) = P(t)\sin(\frac{n\pi ct}{L})$, $\omega_n = \frac{n^2\pi^2}{L^2}\sqrt{\frac{EI}{\rho}}$, $\xi_n = \frac{C}{2\rho\omega_n}$, are the modal load, the nth modal frequency and the modal damping ratio respectively. C is the proportional damping. ρ and L are the constant mass per unit length and the span length of bridge respectively. The moving force identification is an inverse problem in structural dynamics, in which the unknown time-varying force $f(t)$ is identified from measured displacements, accelerations or bending moments of real structures.

Time Domain Method (TDM). Equation (1) can be solved in the time domain by the convolution integral and the dynamic deflection $v(x, t)$ of the beam at point x and time t can be obtained as

$$v(x,t) = \sum_{n=1}^{\infty} \frac{2}{\rho L\omega_n'} \sin\frac{n\pi ct}{L} \times \int_0^t e^{-\xi_n\omega_n(t-\tau)} \sin\omega_n'(t-\tau)\sin\frac{n\pi c\tau}{L} P(\tau)d\tau \tag{2}$$

Where $\omega_n' = \omega_n\sqrt{1-\xi_n^2}$.

So the bending moments of the beam at point x and time t is

$$M(x,t) = -EI\frac{\partial^2 v(x,t)}{\partial x^2} \tag{3}$$

The acceleration of at point x and time t is

$$\ddot{v}(x,t) = \sum_{n=1}^{\infty} \frac{2}{\rho L}\sin\frac{n\pi x}{L} \times \left[P_n(t) + \int_0^t \ddot{h}_n(t-\tau)P_n(\tau)d\tau \right] \tag{4}$$

Where $\ddot{h}_n(t) = \frac{1}{\omega_n'} e^{-\xi_n\omega_n t}\left\{\left[(\xi_n\omega_n)^2 - \omega_n'^2\right]\sin\omega_n' t + \left[-2\xi_n\omega_n\omega_n'\right]\cos\omega_n' t\right\}$, If the bending moments and acceleration responses are measured at the same time, both of them can be used together to identify the moving force. Whether using bending moments or acceleration responses or their combination, the TDM can be transformed to an equation as below

$$[A]_{N\times N_B}\{x\}_{N_B\times 1} = \{b\}_{N\times 1} \tag{5}$$

Where, x is a time series vector of time-varying load $f(t)$, b is a time vector of measured responses of the bridge deck. The coefficient matrix A is associated with the system of bridge deck and load. N and N_B are the number of data samples of the measured responses b and the load $\boldsymbol{x}$ respectively, when the load goes through the whole bridge deck. The time history of moving force $f(t)$ can be obtained by solving Equation (3).

Conjugate Gradient Method (CGM). The conjugate gradient method (CGM) is a common optimization method between the steepest descent method and the Newton method. It's well-known for solving sparse systems of equations with a symmetric positive definite coefficient matrix. In connection with ill-posed problems, the CGM algorithm is applied to solve the equation $A^{\mathrm{T}}Ax = A^{\mathrm{T}}b$. The calculation results show that the low frequency components of the solution tend to converge faster than the higher frequency components of the solution. Because of displacements or bending moment responses have better frequency response characteristics in low frequency band, the CGM has higher identification accuracy and robust noise immunity with displacements or bending moment responses. In addition, the CGM has many other merits, such as arithmetic is simple, it requires small storage and it is more suitable for very big matrix.

The kth iterative step of the CGM can be expressed as

$$\beta_k = \frac{\left\|q^{(k-1)}\right\|_2^2}{\left\|q^{(k-2)}\right\|_2^2};\ p^{(k)} = q^{(k-1)} + \beta_k p^{(k-1)};\ \alpha_k = \frac{\left\|q^{(k-1)}\right\|_2^2}{\left\|A^T A p^{(k)}\right\|_2^2} \quad x^{(k)} = x^{(k-1)} + \alpha_k p^{(k)};$$
$$q^{(k)} = q^{(k-1)} - \alpha_k A^T A p^{(k)} \tag{6}$$

Where $\boldsymbol{x}^{(k)}$ is the kth iterative step solution of $\boldsymbol{x}$, $\boldsymbol{p}^{(k)}$ and $\boldsymbol{q}^{(k)}$ are two auxiliary iteration vectors of length n.

To explain this regularizing effect of the CGM, introduce the Krylov subspace

$$K_k\left(A^T A, A^T b\right) = span\left\{A^T b, A^T A A^T b, ..., \left(A^T A\right)^{k-1} A^T b\right\} \tag{7}$$

Associate with the kth step of the CGM algorithm applied to $A^TAx=A^Tb$. It is also convenient to introduce the Ritz polynomial associated with step k.

The solution of $x^{(k)}$ after kth iterative steps can be defined as

$$\min\left\|\boldsymbol{Ax}-\boldsymbol{b}\right\|_2 \quad \boldsymbol{x} \in \boldsymbol{K}_k(\boldsymbol{A}^T\boldsymbol{A}, \boldsymbol{A}^T\boldsymbol{b}) \tag{8}$$

Where $Kk(A^TA, A^Tb)$ is the Krylov sub-matrix associated with the equation.

Conclusions

In this paper, the CGM is introduced and employed for the identification of moving force on bridge. Based on the theory study results, the proposed CGM is a successful method for the identification of moving forces from the responses induced by the moving vehicles on bridges. The CGM is more suitable for the time-varying loads identification compared with the time domain method, which will be proved in a companion paper.

Acknowledgements

The project is supported by North China Institute of Water Conservancy and Hydroelectric Power High-level talents scientific research startup project (001331).

References

[1] O. K. Normann, R. C. Hopkins, Weighing vehicles in motion, Highway Research Board Bulletin 50, National Research Council, Washington D.C., 1952.

[2] F. Moses, Weigh-in-motion system using instrumented bridge, Journal of Transport Engineering, ASCE, 105 (1984) 233-249.

[3] L.Yu, Accounting for bridge dynamic loads using moving force identification system (MFIS), The Hong Kong Polytechnic University, Hong Kong, 2002.

[4] L. Yu, T. H. T. Chan, Moving force identification from bending moment responses of bridge, Structural Engineering and Mechanics, 2 (2002) 151-170.

[5] T. H. T. Chan, L. Yu, S. S. Law, T. H. Yung, Moving force identification studies, I: THEORY, Journal of Sound and Vibration, 247 (2001) 59-76.

[6] T. H. T. Chan, L. Yu, S. S. Law, T. H. Yung, Moving force identification studies, II: comparative studies, Journal of Sound and Vibration, 247 (2001) 77-95.

© (2012) Trans Tech Publications, Switzerland
doi:10.4028/www.scientific.net/AMM.238.826

Numerical Simulation by CGM for Moving Force Identification

Zheng Chen[1,a] and Junling Han[2,b]

[1] North China University of Water Resources and Electric Power, Zhengzhou 450011, China

[2] Henan Fifth Construction and Installation (Group) Co., LTD, Zhengzhou, China

[a]yuchenfish@163.com, [b]hanjunling@163.com.

Keywords: moving force identification; numerical simulation; time domain method (TDM); conjugate gradient method (CGM).

Abstract. The conjugate gradient method (CGM) is compared with the time domain method (TDM) in the paper. The numerical simulation results show that the CGM have higher identification accuracy and robust noise immunity as well as producing an acceptable solution to ill-posed problems to some extent when they are used to identify the moving force. When the bending moment responses are used to identify the time-varying loads, the identification accuracy is more obviously improved than the TDM, which is more suitable for the time-varying loads identification.

Introduction

Identification of dynamic axle loads on bridges is an inverse problem of structural mechanics, and a notable feature of which is the presence of ill-posed problem [1]. The objective of the present study is to propose a new method to identify the axle loads of in-motion vehicles from responses of bridges. The bridge responses include displacements, bending moments and accelerations. Chan [2] employed a measurement method using strain gauges to measure bending moments, and then the measured bending moments were converted to displacements. Several weigh-in-motion systems were developed using strain gauges to acquire bridge response information for dynamic axle loads identification [3]. Numerical simulation has been conducted. Some results show that the identified results of the CGM have many advantages, such as has higher identification accuracy and less sensitive to noise as well as producing an acceptable solution to ill-posed problems to some extent when compared with the TDM [4]. When the bending moment responses are used to identify the time-varying loads, the identification accuracy is more obviously improved than the TDM, which is beneficial to the application of the force identification techniques in practice.

Basic Theory

Motion Equation of Bridge-vehicle System. A bridge superstructure is modeled as a simply supported beam as shown in Fig. 1. The effects of shear deformation and rotary inertia are not taken into account. If the load f moves from left to right with speed c, then an equation of motion in terms of modal coordinate $q_n(t)$ can be expressed as

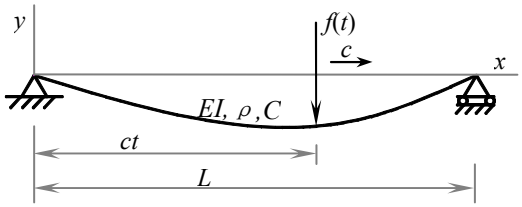


Fig. 1 Moving force Model

$$\ddot{q}_n(t) + 2\xi_n\omega_n\dot{q}_n(t) + \omega_n^2 q_n(t) = \frac{2}{\rho L} p_n(t) \qquad (n = 1,2,\cdots,\infty) \tag{1}$$

Where $\boldsymbol{p}_n(t)=\boldsymbol{P}(t)\sin(\frac{n\pi ct}{L})$, $\omega_n=\frac{n^2\pi^2}{L^2}\sqrt{\frac{EI}{\rho}}$, $\xi_n=\frac{C}{2\rho\omega_n}$, are the modal load, the nth modal frequency and the modal damping ratio respectively. C is the proportional damping. ρ and L are the constant mass per unit length and the span length of bridge respectively. The moving force identification is an inverse problem in structural dynamics, in which the unknown time-varying force $f(t)$ is identified from measured displacements, accelerations or bending moments of real structures.

Time Domain Method (TDM). Eq. (1) can be solved in the time domain by the convolution integral and the dynamic deflection $v(x, t)$ of the beam at point x and time t can be obtained as [4]

$$\nu(\boldsymbol{x},\boldsymbol{t})=\sum_{\boldsymbol{n}=1}^{\infty}\frac{2}{\rho\boldsymbol{L}\omega_{\boldsymbol{n}}^{'}}\sin\frac{\boldsymbol{n}\pi\boldsymbol{ct}}{\boldsymbol{L}}\times\int_0^{\boldsymbol{t}}\boldsymbol{e}^{-\xi_n\omega_n(t-\tau)}\sin\omega_{\boldsymbol{n}}^{'}(\boldsymbol{t}-\tau)\sin\frac{\boldsymbol{n}\pi\boldsymbol{c}\tau}{\boldsymbol{L}}\boldsymbol{P}(\tau)\boldsymbol{d}\tau\,. \tag{2}$$

Where $\omega_n^{'}=\omega_n\sqrt{1-\xi_n^2}$.

The TDM can be transformed to an equation as below

$$[\boldsymbol{A}]_{N\times N_B}\{\boldsymbol{x}\}_{N_B\times 1}=\{\boldsymbol{b}\}_{N\times 1} \tag{3}$$

Where, $\boldsymbol{x}$ is a time series vector of time-varying load $f(t)$, $\boldsymbol{b}$ is a time vector of measured responses of the bridge deck. The coefficient matrix $\boldsymbol{A}$ is associated with the system of bridge deck and load. N and N_B are the number of data samples of the measured responses $\boldsymbol{b}$ and the load $\boldsymbol{x}$ respectively, when the load goes through the whole bridge deck. The time history of moving force $f(t)$ can be obtained by solving Eq. (3).

Conjugate Gradient Method (CGM). The CGM is a common optimization method between the steepest descent method and the Newton method. It is well-known for solving sparse systems of equations with a symmetric positive definite coefficient matrix. In connection with ill-posed problems, the CGM algorithm is applied to solve the equation $A^{\mathrm{T}}Ax=A^{\mathrm{T}}b$ [5].

The kth iterative step of the CGM can be expressed as

$$\beta_k=\frac{\left\|\boldsymbol{q}^{(\boldsymbol{k}-1)}\right\|_2^2}{\left\|\boldsymbol{q}^{(\boldsymbol{k}-2)}\right\|_2^2};\ \boldsymbol{p}^{(\boldsymbol{k})}=\boldsymbol{q}^{(\boldsymbol{k}-1)}+\beta_k\boldsymbol{p}^{(\boldsymbol{k}-1)};\ \alpha_k=\frac{\left\|\boldsymbol{q}^{(\boldsymbol{k}-1)}\right\|_2^2}{\left\|\boldsymbol{A}^{\boldsymbol{T}}\boldsymbol{A}\boldsymbol{p}^{(\boldsymbol{k})}\right\|_2^2}$$

$$\boldsymbol{x}^{(\boldsymbol{k})}=\boldsymbol{x}^{(\boldsymbol{k}-1)}+\alpha_k\boldsymbol{p}^{(\boldsymbol{k})};\ \boldsymbol{q}^{(\boldsymbol{k})}=\boldsymbol{q}^{(\boldsymbol{k}-1)}-\alpha_k\boldsymbol{A}^{\boldsymbol{T}}\boldsymbol{A}\boldsymbol{p}^{(\boldsymbol{k})} \tag{4}$$

Where $x^{(k)}$ is the kth iterative step solution of $\boldsymbol{x}$, $p^{(k)}$ and $q^{(k)}$ are two auxiliary iteration vectors of length n.

The solution of $x^{(k)}$ after kth iterative steps can be defined as

$$\min\left\|\boldsymbol{A}\boldsymbol{x}-\boldsymbol{b}\right\|_2\quad\boldsymbol{x}\in\boldsymbol{K}_k(\boldsymbol{A}^{\boldsymbol{T}}\boldsymbol{A},\boldsymbol{A}^{\boldsymbol{T}}\boldsymbol{b}) \tag{5}$$

Where $K_{\mathrm{k}}(A^{\mathrm{T}}A, A^{\mathrm{T}}b)$ is the Krylov sub-matrix associated with the Equation.

Numerical Simulation

Bridge-Vehicle System and Parameters. In order to check the correctness and effectiveness of the proposed CGM, the following moving force identification cases are simulated and illustrated.

Two-axle vehicle time-varying loads are generated as follows

$$f_1(\mathrm{t})=58.8\times[1+0.1\times\sin(c\cdot\pi\cdot t)]\ \mathrm{kN}$$

$$f_2(t)=137.2\times[1+0.1\times\sin(c\cdot\pi\cdot t)]\ \ \mathrm{kN} \tag{6}$$

The wheelbase is l_s=8m, the vehicle speed is c=40m/s. The parameters of the beam are as follows: the flexural stiffness EI =1.27914×10^{11}N·m^2, the beam density ρ =12 000kg/m^3, the span length L =40m, the first three natural frequencies of the beam bridge are f_1 =3.2Hz, f_2 =12.8Hz, f_3 =28.8Hz. The analysis frequency bandwidth is from 0Hz to 40Hz and therefore the first three modes of the beam are included in the calculation. The sampling frequency is 200Hz.

Random noise is added to the calculated responses to simulate the contaminated measurements as

$$R_{measured} = R_{calculated}(1 + Ep \cdot N_{oise}) \tag{7}$$

Where Ep represents specified error level ranging from 0.0 to 1.0, Noise is a standard normal distribution vector with zero mean value and unit standard deviation.

To compare the true loads and the identified axle loads, relative percentage error term is introduced as follow

$$RPE = \frac{\left\| f_{ture} - f_{identified} \right\|}{\left\| f_{ture} \right\|} \times 100\% \tag{8}$$

Where f_{true} are the true axle loads, and $f_{identified}$ are the identified axle loads. In this study, f_{true} are the axle loads used to simulated bridge responses, and $f_{identified}$ are the axle loads identified from the simulated bridge responses. The relative percentage error is considered acceptable if it's less or equal to 10%.

Time-Varying Load Identification. The moving force identification from bending moment and/or acceleration responses at 1/4, 1/2, and 3/4 spans in 12 combinations have been conducted. The sensor arrangement is listed in Table 1. In the table, the letters 'm' and 'a' represent the bending moment and acceleration responses respectively. Fractions 1/4, 1/2 and 3/4 represent the measurement locations at quarter, middle and three-quarter spans respectively. There are the same meanings in the following tables if no further stated. The TDM and the CGM are used to moving force identification. In order to more clearly express the differences identification accuracy of them, numerical simulation results of TDM and CGM are compared as follow.

Table 1 Relative percent error (RPE) by TDM and CGM

case	Sensor Location	RPE (%)					
		1% Noise		5% Noise		10% Noise	
		Axle1	Axle2	Axle1	Axle2	Axle1	Axle2
1	1/4m & 1/2m	93.5	*	*	*	*	*
		89.2	81.1	*	*	*	*
2	1/4m & 1/2m & 3/4m	50.8	*	*	*	*	*
		41.2	50.5	*	*	*	*
3	1/4a & 1/2a	19.2	29.7	96.1	*	*	*
		9.8	10.7	12.7	11.8	19.5	14.7
4	1/4a & 1/2a & 3/4a	0.5	1.0	2.4	5.1	4.7	10.1
		1.1	7.0	2.2	9.2	4.3	11.8
5	1/2m & 1/2a	86.3	94.7	*	*	*	*
		24.9	21.1	*	*	*	*
6	1/4m & 1/2m & 1/2a	54.6	48.5	58.6	74.9	*	*
		15.9	16.3	78.2	79.1	*	*
7	1/4m & 1/2m & 1/4a & 1/2a	11.7	15.0	50.3	18.0	*	*
		10.8	9.8	14.4	13.3	21.1	18.8
8	1/4m & 1/4a	*	*	*	*	*	*
		15.3	15.4	41.5	42.2	89.1	87.8
9	1/4m & 1/4a & 1/2a	18.4	28.9	91.9	*	*	*
		10.6	9.8	14.5	13.3	21.5	18.7
10	1/2m & 1/4a	48.1	84.0	*	*	*	*
		16.8	17.1	66.8	55.2	*	*
11	1/4m & 1/2m & 1/4a	44.3	70.9	*	*	*	*
		15.6	14.3	55.9	44.6	*	*
12	1/2m & 1/4a & 1/2a	11.9	14.9	59.5	74.7	*	*
		10.9	10.5	14.4	12.8	21.1	16.9

Note: '*' indicates the RPE larger than 100%, the underlined values are relative percent error by CGM, others by TDM respectively.

Obviously, the identification accuracy of CGM is higher than that of TDM at each case. For cases failed to identify the moving forces by the TDM, the CGM can still give some acceptable solutions. While using bending moment responses, the identification results of the CGM have dramatically higher accuracy than TDM.

Conclusions

In this paper, the CGM has been proposed for the identification of moving force on bridge. Based on the numerical simulation results, the proposed CGM is a successful method for the identification of moving forces from the responses induced by the moving vehicles on bridges. The CGM is obviously better than the existed TDM from all the aspects and has higher robust immunity to the noise. It also can improve the solutions of ill-posed problem to some extent. As this advantage, the CGM is more suitable for the time-varying loads identification.

Acknowledgements

The project is supported by High-level Talents Scientific Research Startup Project of NCWU (001331).

References

[1] L. Fryba, Vibration of Solids and Structure under Moving forces, Noordhoff International Publishing, Prague, 1972.

[2] T. H. T. Chan, Highway bridge impact, Thesis for Ph.D., University of Queensland, Australia, 1988.

[3] C. O'Connor, T. H. T. Chan, Dynamic wheels loads from bridge strains, Journal of Structure Engineering, ASCE, 114 (1988) 1703–1723.

[4] S. S. Law, T. H. T. Chan, Q. H. Zeng, Moving force identification: a time domain method, Journal of Sound and Vibration, 201 (1997) 1-22.

[5] P. C. Hansen, Regularization tools: A matlab package for analysis and solution of discrete III-posed problems, Numerical Algorithms, 6 (1994) 1-31.

CHAPTER 5:

Earthquake and Seismic Engineering

© (2012) Trans Tech Publications, Switzerland
doi:10.4028/www.scientific.net/AMM.238.833

Mitigation of Seismic Risks to Soft-storey Structures using Toggle-brace-damper Systems

Ricky WK Chan [a] and Zhefei Zhao [b]

School of Civil, Environmental and Chemical Engineering, RMIT University, GPO Box 2476, Melbourne VIC 3000 Australia

[a]ricky.chan@rmit.edu.au, [b]s3184322@student.rmit.edu.au

Keywords: earthquake; soft-storey, toggle; passive energy dissipation.

Abstract. Soft-storey mechanism is characterized by a sudden reduction of lateral stiffness in one or more levels of a structure. Soft-storey is often observed in the ground level due to the absence of wall or cladding. With recent develop of energy dissipation systems, soft-storey mechanism can be corrected by addition of a damper-brace assembly. In particular, this paper investigates the effect of toggle-damper-brace systems on such situations. Governing equations including the magnification factor and lateral stiffness contributed by a toggle-damper-brace are formulated. It was found that a toggle-damper-brace system, if proportioned correctly, will significantly increase the travel in the damper and overall stiffness of structure can be enhanced. An illustrative example is presented using nonlinear time history analysis implemented on MATLAB.

Introduction

In the last few decades significant research and development has been made to make civil structures safer and more robust in the event of an earthquake. Since 1990's, rapid increase in implementation of energy dissipating systems have been reported [1]. In this technique designated energy dissipating devices (EDD) are installed in the structure such that a portion of the energy originated from ground shaking is diverted to. Among many energy dissipation mechanisms, metallic yielding is the most popular mechanism. They belong to the class of displacement-based device, which relies on relative displacement which the device travels. Metallic based EDD is generally inexpensive, insensitive to frequency of vibration, and require minimal maintenance. EDD which make use of such mechanism include the patented ADAS [2], its variants TADAS [3] and the Steel Slit Damper [4]. The Buckling-restrained brace (BRB) [5] and its variant Buckling-restrained lug [6], on the other hand, makes use of the axial deformation of steel. Shear yielding of thin steel plates have also been used to dissipate energy through displacement [7].

On the other hand, a very widespread structural problem is characterized by the absence of claddings or walls at the ground floor while they are present in upper levels. It causes a sudden reduce in stiffness in the ground level. It's commonly termed "soft-storey". This configuration permits good use of the ground floor space, but in structural point of view it is undesirable. Large lateral load may cause significant rotation ductility demand at the extreme sections of the columns of the first storey, while the superstructure behaves like a quasi-rigid body (Fig 1). Soft-storey failure is commonly observed in earthquake damages, claiming significant life and economical losses. Conventional strengthening approach often involves addition of braces to ground level such that the lateral stiffness is increased. In this approach, however, the braces occupy the spaces disturb normal use of the space, such as car parks or retail space, etc.

Toggle-brace-damper System

The main purpose to connect a damper to a toggle-brace is to magnify the displacement travelled in a damper. The configuration has been investigated by a number of researchers [8-9] and application in the US has been reported [8]. An upper toggle configuration presented in this paper is shown in Fig 2(a). Consider a single storey frame of dimension $h \times b$, the configuration is characterised by a lower brace of length l_1, and an upper brace of length l_2. The lower brace forms an angle θ with respect to

the ground. To maximize usable floor space, we shall limit our study with θ greater than 45 degrees. For a given building dimension, geometry is completely defined by l_1 and θ. The damper is supported between the eave and toggle brace intersection O. Upon horizontal displacement of u in the superstructure (Fig 2b), the lower brace undergoes a rotation ϕ together with the change in position of brace intersection O to O'. It will cause an axial deformation of damper. In this regard, displacement-based passive energy dissipater which operates in axial movement will be suitable, for example the Buckling-restrained Lug [7] which relies on plastic deformation of a steel bar under axial movement. Generally, benefits of toggle-brace-damper system include:

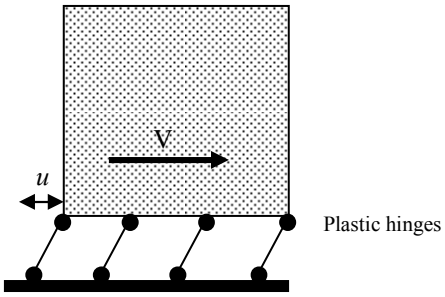
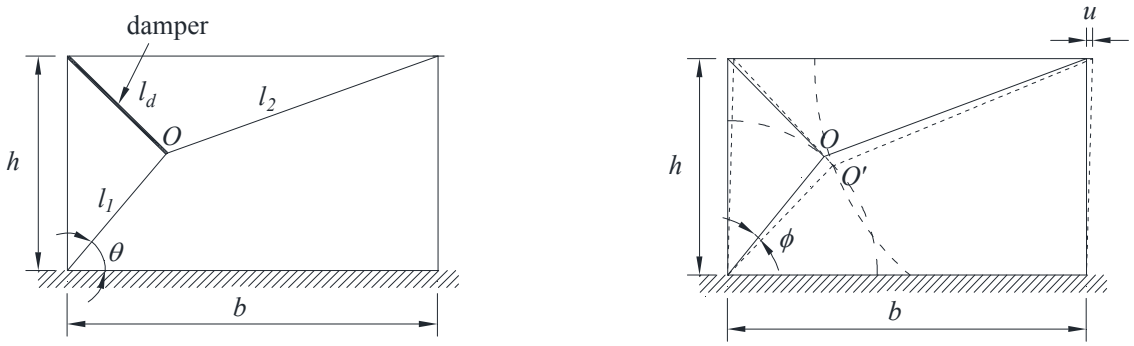


Fig. 1 Soft-storey mechanism

1) Damper increases effective damping of structure, hence it suppresses vibration magnitude and base shears;

2) The toggle arrangement magnifies damper travel; and

3) The toggle arrangement maximizes usable space which is architecturally attractive.



(a) (b)

Fig. 2 Toggle-brace-damper configuration

Magnification Factor

Consider Fig. 2(b), due to ground shaking the superstructure is displaced by u. Assuming the brace elements are axially stiff, the position of O' can be determined by the intersections of the two arcs of radii of l_1 and l_2. The change in damper length u_D can then be determined. The magnification factor f is defined as the ratio between the change in damper length and the horizontal displacement superstructure with respect to the ground, i.e.

$$f = \frac{u_D}{u} \tag{1}$$

The magnification factor varies with the magnitude of u, and it is affected by the geometry h, b, l_1 and θ. While h and b is determined by building geometry, l_1 and θ can be chosen by engineers. Fig 3 shows the magnification factor as a function of u for a number of l_1 and θ combinations. Generally f increases as θ decreases. Also, it can be observed that f is fairly constant over practical ranges of displacement, although it tends to increase slightly with increase in displacement. It should be noted that for values of f less than 1.0, it indicates the toggle-brace configuration reduces damper travel, which is contrary to our requirement.

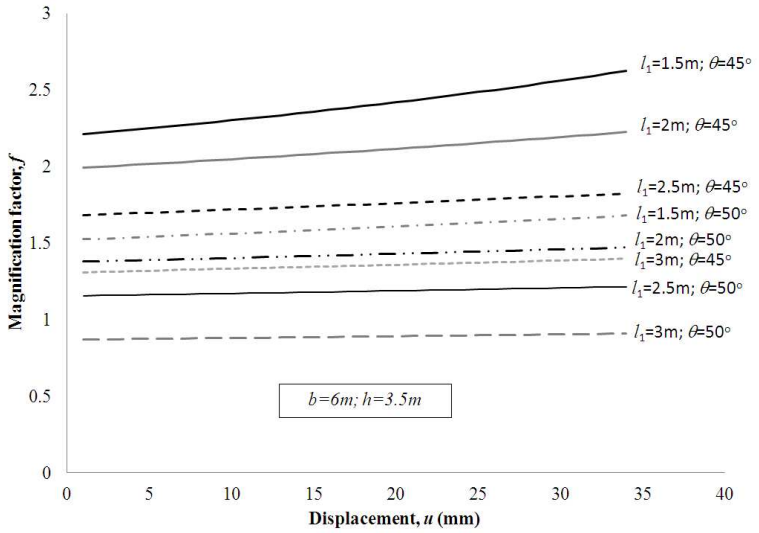


Fig. 3 Magnification factor

To study the effect of toggle brace in lateral stiffness of system, Assume the force exerted on the damper is F_D while the horizontal shear force on superstructure is V, the pinned beam-to-column joints, and assuming the brace members are axially rigid, all lateral stiffness is contributed by the damper. By equating external and internal work result,

$$F_D u_D = Vu \tag{2}$$

Overall horizontal stiffness of structure can be written as,

$$k = \frac{V}{u} \tag{3}$$

Substituting Eq. 1 in Eq. 3, and using damper stiffness $k_D = \frac{F_D}{u_D}$ we have,

$$k = \frac{V}{u} = \frac{F_D u_D}{u^2} = k_D \left(\frac{u_D}{u} \right)^2 = k_D f^2 \tag{4}$$

As a result the magnification factor has an effect on horizontal stiffness of structure. For a frame with inherent lateral stiffness k_s, such as for moment-resisting frames, the total horizontal stiffness after addition of a toggle-damper brace system can be expressed as numerical summation of stiffness, i.e.

$$k_{tot} = k_s + k \tag{5}$$

k_s denotes lateral stiffness of parent frame prior to addition of brace and device. Post-yield stiffness ratio α after yielding of damper is given by,

$$\alpha = \frac{k_s}{k_{tot}} = \frac{k_s}{k_s + k_D f^2} \tag{6}$$

α is an indication of stiffness contribution by the toggle-damper brace. When α approaches infinity it indicates an infinitely stiff toggle-damper brace. Yield displacement of complete system u_y equals u_D / f. Yield strength of the system with a toggle-damper assembly added is expressed as

$$P_y = k_{tot} u_y = \frac{k_s u_D}{\alpha f} \tag{7}$$

Consequently, the nonlinear behaviour of a structure installed with toggle-brace-damper system is completely defined by four parameters: k_s, f, α and u_D. In practice, k_s of the building can be estimated by structural analysis, whereas f and u_D are choices of the designer.

To model nonlinearity of dampers, a continuous Bouc-Wen's model [10] is adopted in this study. A single equation governs both elastic and inelastic range of the device under cyclic loading. Resilient force of complete system $P(t)$ is expressed by,

$$P(t) = \alpha k_{tot} u(t) + (1-\alpha) k_{tot} u_y z(t) \tag{8}$$

Where α and k are defined previously, γ, β and n are calibration parameters, and $z(t)$ is a variable contains hysteretic properties, which is defined by a first-order nonlinear differential equation,

$$u_y z(t) + \gamma |\dot{u}(t)| z(t) |z(t)|^{n-1} + \beta \dot{u}(t) |z(t)|^n - \dot{u}(t) = 0 \tag{9}$$

Numerical Example

To illustrate the effect of toggle damper-brace systems, consider an existing building that suffers from soft-storey mechanism as shown in Fig 4. This building is to be retrofitted by installing toggle damper-braces in the ground level. The superstructure weighs 600tons, which is elevated by 3.5m from the ground by 16 steel columns (200UC46.2). Lateral stiffness of structure prior to addition of braces is estimated to 41.1kN/mm. The structure is to be retrofitted by adding 4 toggle-damper braces, with 2.0m long lower brace at an angle of 45° from horizontal. This configuration results in a magnification factor f of approximately 2.0. By using a damper with axial stiffness of 5.2kN/mm, the overall stiffness of structure is increased, achieving an α value of 0.33. Table 1 shows the parameters used.

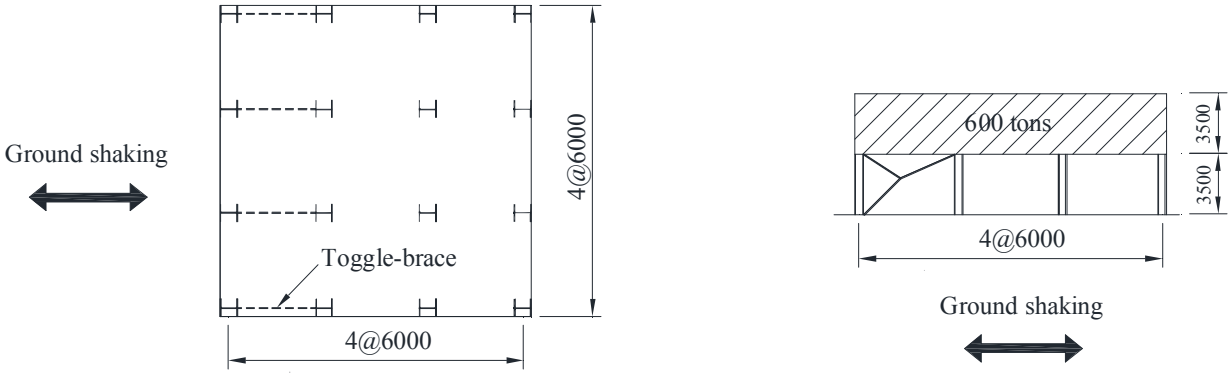
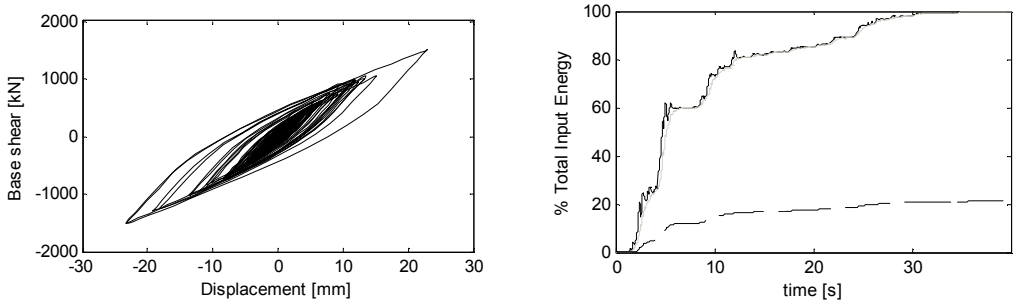


Fig. 4 Example soft-storey structure

Table 1

M	k_s	ζ	l_1	θ	f	k_D	u_D	α
600kNs^2/m	41.1kN/mm	3%	2.0m	45°	2.0	5.2kN/mm	3.5mm	0.33

For illustrative purpose, a single direction ground motion is applied. The input ground shaking is an un-scaled N-S component of 1940 El Centro Earthquake obtained from PEER Strong Motion Database [11]. Eqs 8 and 9 are implemented by numerical integration on MATLAB, the differential equations are solved using 4th order Runge-Kutta algorithm (MATLAB command ode45).



(a) (b)

Fig 5 (a) Base shear plot and (b) Cumulative energy dissipation

Fig. 5(a) shows the base shear plot. The nonlinearity of base shear is a consequence of nonlinear damper. Fig. 5(b) shows the cumulative energy diagram. At the end of ground shaking, approximately 79% of input energy is diverted to the damper, while the remaining energy is dissipated through viscous damping. Maximum displacement of superstructure is controlled within 23mm (1/152 of height of columns).

Conclusions

Soft-storey mechanism is a common problem observed in many historical earthquake events. It is characterized by a "soft-storey" which the horizontal stiffness of a particular storey is significantly smaller than the rest of the structure. When a strong earthquake hits the large shear force exerted on superstructure causes plastic rotations in columns, subsequently causes collapse of the soft-storey. This paper investigates the use of toggle-damper-brace system as a mitigation measure to soft-storey buildings. Governing equations of such system are presented in this paper. It was found that a toggle-damper-brace system, if proportioned correctly, will significantly increase the travel in the damper and overall stiffness of structure can be enhanced. A numerical example of a single storey structure retrofitted by addition of toggle-damper-braces is presented.

References

[1] M. D. Symans, F. A. Charney, A. S. Whittaker, M. C. Constantinou, C. A. Kircher, M. W. Johnson, R. J. McNamara, Energy Dissipation systems for seismic applications: current practice and recent developments, Journal of Structural Engineering, 1 (2008) 3-21.

[2] D. M. Bergman, S. C. Goel, Evaluation of cyclic testing of steel plate devices for added damping and stiffness, Report No. UMCE87-10, The University of Michigan, Ann Arbor, MI, USA, 1987.

[3] K. Tsai, H. Chen, C. Hong, Y. Su, Design of steel triangular plate energy absorbers for seimic-resistant construction, Earthquake Spectra, 3 (1993) 505-528.

[4] R. WK. Chan, F. Albermani, Experimental study of steel slit damper for passive energy dissipation, Engineering Structures, 4 (2008) 1058-1066.

[5] A. Watanabe, Y. Hitomi, E. Saeki, A. Wada, M. Fujimoto, Properties of brace encased in buckling-restraining concrete and steel tube, In: Proc., 9th conference on earthquake engineering. Vol. IV, 1988. p. 719-724.

[6] R. WK. Chan, F. Albermani, Buckling-restrained-lug connection for energy dissipation, 14th Asia Pacific Vibration Conference, 5-8 December 2011, Hong Kong.

[7] R. WK. Chan, F. Albermani, M. S. Williams, Evaluation of yielding shear panel device for passive energy dissipation, J. Constructional Steel Research, 65 (2009) 260-268.

[8] M. C. Constantinou, P. Tsopelas, W. Hammel, A. N. Sigher, Toggle-brace-damper seismic energy dissipation systems, J. Struct. Eng., 2 (2001) 105-112.

[9] J. S. Hwang, Y. N. Huan, Y. H. Hung, Analytical and experimental study of toggle-brace-damper systems, J. Struct. Eng., 7 (2005) 1035-1043.

[10] Y. K. Wen, Method for random vibration of hysteretic systems, J. Engr. Mech., 102 (1976) 249-263.

[11] PEER Strong Motion Database, Pacific Earthquake Engineering Research Center, University of California Berkeley.

© (2012) Trans Tech Publications, Switzerland
doi:10.4028/www.scientific.net/AMM.238.838

The Seismic Behavior of High-strength Concrete Frame Joints

Tingyan Wang[1,3 a], Junwei Zhang[2,3 b] and Danying Gao[3 c]

[1] School of Civil Engineering and communication, North China University of Water Resources and Electric Power, Zhengzhou 450011, China

[2] The New Campus Construction headquarters, Henan Agricultural University, Zhengzhou 450002, China

[3] Research Center of New Style Building Material and Structure, Zhengzhou University, Zhengzhou 450002, China

[a]wty@ncwu.edu.cn, [b]zhang_junwei2007@yahoo.com.cn, [c]gdy@zzu.edu.cn

Keywords: seismic behavior; frame joint; high-strength concrete; steel fiber concrete.

Abstract. By studying the two high-strength concrete frame joints by means of experimental investigate and finite element analysis with the low cycle reversed loading method, it discussed the influence of the steel fiber on the seismic behavior of the high-strength frame joints. The result shows that, mixed with steel fiber can enhance the constraint of the concrete at the joint core area, improve the seismic behavior. Amount of steel fiber can replace part of the stirrup.

Introduction

As an important part of building structure, frame joint is not only the central hub of structure transfer and distribution internal force, but also play an important role in keeping the structural integrity when structure goes into the elastic-plastic working period. The studies on the domestic and overseas earthquake damage show that, frame joint is the most fragile part when frame structure is under earthquake action, and the failure of it will usually cause the collapse of the whole building. As an effective method, mixed with steel fiber into the frame joint area has attracted great attention. However, the study on the seismic behavior of the steel fiber reinforced concrete frame joint under the low cycle loading is rare in and outside the country. Therefore, by experimental investigate and finite element analysis of the two high-strength concrete frame exterior joints under low cycle reversed loading, this paper discussed the influence of the steel fiber on the seismic behavior of the frame joints.

Experiment Survey

The reinforcement distribution condition and model size is shown in Fig. 1.

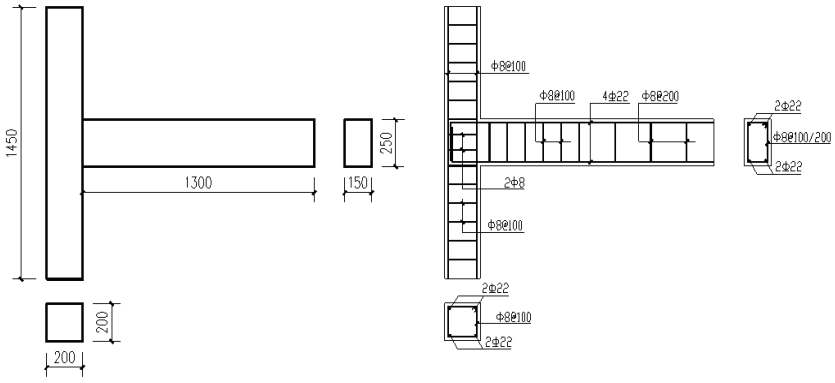


Fig. 1 The sizes and reinforcements of specimen

The specimen A uses the high-strength concrete C60, the 0.6% volume ratio stirrup is used in the joint core area. In the joint core area of specimen B, the 1.0% volume ratio steel fiber reinforced high-strength concrete CF60 is used, and the remaining part uses reinforced high-strength concrete

C60. The steel fiber additional range in the beam is fixed as 125 mm, the steel fiber additional range in the column is fixed as 50mm, and the axial compressive ratio is 0.3. In making specimen, ingot milling type fiber (AMI04-32-600) is used, and the length-diameter ratio is 35~40, equivalent diameter is 0.94mm, tensile strength ≥700Mpa, 42.5# high strength Portland concrete is also used, and 2.91 fineness modulus sand, and less than 20mm diameter cobble stone, powder high efficiency water reducer (FDN) is used, and water reduce ratio is 18%~25%. The material performance of high-strength concrete of specimens is seen in Table 1.

Table 1 The Material Performance of Concrete

No.	A	B	B(steel fiber concrete)
Cube compressive strength (MPa)	63.20	62.40	75.81
Axial compressive strength (MPa)	58.04	54.41	57.68
The tensile strength (MPa)	5.06	4.28	4.34
The elastic modulus (MPa)	44.71	44.37	44.13

The experiment uses electro-hydraulic dynamic fatigue tester to do low cyclic reversed load at beam end, and uses hydraulic jack to do axial load at column end. The first two circulations uses control forces to give loading, of which the first circulation loads till the 75% of the specimen's yielding load calculated value to simulate the stress state of normal uses. For the key of the research is at the specimen's plastic deformation period, then the second circulation loads to the yielding condition. Then uses control displacement loading, and takes the times of the displacement of the beam end yielding to give loading successive loading. For each level displacement value it circulates for twice till the utmost load is lower than 85% of the maximum load, then the specimen is broken.

Finite Element Analysis Model

The Constitutive Structure Relation of the Material. The axial compressive stress-strain curve of high-strength concrete uses Code for design of concrete structures (GB 50010-2002) [1]. The tensile stress-strain relationship of high-strength concrete describes as: upper period as line and lower period as index. The elastic modulus before crack is the same as that of the initial elastic modulus, after crack, the concrete is considered as non-brittle material. That is to say, the concrete tensile strength of the crack did not decline to zero immediately, but decline with the widening of the crack. For high strength concrete, the parameter of the calculation formula is from reference [2].

At the yielding period, the reinforcement's stress has small change, but strain increases dramatically, and the stress-strain curve is a 0.01E slope line. After the plastic hinge to form, the ultimate deformation of the plastic area concrete will seldom exceed 0.006, so the deformation of reinforcement has small change at hardening period, and the stress-strain curve is a 0.01E slope line, taking $E'=0.01E$ [3]. As metal material, steel fiber takes the ideal plastic stress-strain relationship as reinforcement. For the damage of steel fiber concrete is mainly as the pulling out of steel fiber from the concrete, not because of the broken of the steel fiber, therefore, taking the tensile stress when steel fiber is pulling out as the tensile strength of steel fiber, and in this paper it is taken as 250 MPa [4].

Concrete Failure Criterion and the Crack Treatment. The concrete failure criterion taking the William-Warnke model with five parameters, the formula is $F/f_c\text{-}S\geq 0$. In this formula, F is the function of the main stress σ_1, σ_2 and σ_3, S is the destroying section of the main stress σ_1, σ_2, σ_3 and the five parameters $f_t, f_c, f_{cb}, f_1, f_2$, and $f_t, f_c, f_{cb}, f_1, f_2$ stands for the single axes tensile strength, the axes compression strength, the biaxial compression strength constant pressure, the biaxial compression with ambient pressure and the multi-axial compression strength with ambient pressure. And the ANSYS method is used, when the ambient pressure is small, the failure surface can be made certain by two parameters f_t and f_c, and the other three are: $f_{cb}=1.2f_c, f_1=1.45f_c, f_2=1.725f_c$ [5].

In analysis, the dispersion crack model is used to treat frame joint cracking process. After cracks emerge, subsequent loading will produces sliding or shearing on the crack surface. In analysis, introducing split plane shear transfer coefficient (β_t) when crack opens and split plane transfer coefficient (β_c) to simulate the loss of the concrete shearing capacity. β_t has great influence on the

calculation result when crack emerges, and generally it is between 0.3~0.5, and in this paper $\beta_t = 0.3$. β_c has little influence on the result of monotonic loading load-carrying specimen, and generally it is between 0.9~1.0, and in this paper β_c=0.9. For not considering the concrete crush, it is hard to simulate the concrete failure process, and the normal failure surface will cause the premature crush invalidation. Therefore, using the expanded crush plane to consider the restriction effect of the steel fiber to the concrete, and the axis compressive strength parameter of the failure criterion is $1.2 f_c$~$2 f_c$.

Element Choosing. Reinforcement use Link8 unit and concrete uses Solid65 unit. The steel fibers are large in number and also they distribute in chaos, so it is impossible to model the role of each single steel fiber. Therefore, we take the steel fibers as distributing micro reinforcements. They distribute into the concrete Solid65 evenly according to volume ratio, and together with concrete, they compose integral model, that is steel fiber distributes along with the axes of the coordinates, and in each direction distributes volume ratio according to unit side length ratio, and also consider the influence of the steel fiber distribution effective coefficient and orientation coefficient. Moreover, because the steel fiber tensile strength is the tensile strength when steel fiber is pulling out, so there is no need to consider the bond-slip between the steel fiber and the concrete. For the steel fiber concrete and reinforcement, the discrete model is used for modeling. The bond-slip between the two uses Combin 39 to simulate, and the bond-slip constitutive construction relation uses the four line segment model advised by the CEB-FIPMC90 in reference [6].

Mesh Partition. When we do analysis by taking the whole model of joints, the size and the shape of the element mesh will both influence the analysis results. If the meshes are divided too meticulously, it will cause the instability of numerical calculation, and if the meshes are divided too coarsely, it will influence precision. Only the right meshes can get the convergence. By comparison, this paper does mesh partition by 5cm, the corresponding mesh partition needs to satisfy certain geometry topology rule. For it is necessary to consider the thickness of the protective layer of the beam and the column in modeling, so in this paper, besides 5.0cm, there are also 3.5cm and 4.0cm, and unit generation is shown in Fig. 2.

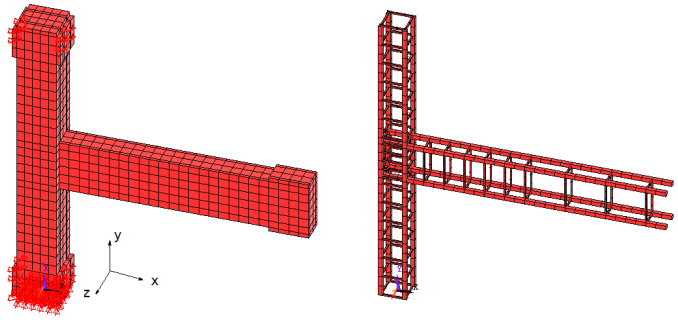


Fig. 2 Finite element model of frame exterior joints

Boundary Conditions and Load Application. In order to simulate the form of joint destruction under the low cycle loading, we supply X direction the two lateral surfaces of the upper and lower end of the column translation displacement constraint, and supply X,Y,Z three directions translation displacement constraint at the lower end of the column, supply Y axial force at the column top end, and supply Y reversed force or displacement at the beam ends. In the nonlinear analysis, by defining load step and load sub-step divides the load into a series of load increments. To solve by finite element, we make a series of linear approaching in the load increments to achieve balance. Considering the nonlinear influence of steel fiber concrete, we adopt Newton-Raphson method doing nonlinear iteration. Displacement convergence criterion is used and the convergence precision is 1%. In order to improve the convergence of nonlinear analysis, adaptive descend gene, linear searching, forecasting and dichotomy will be used at the same time.

Analysis of the Results

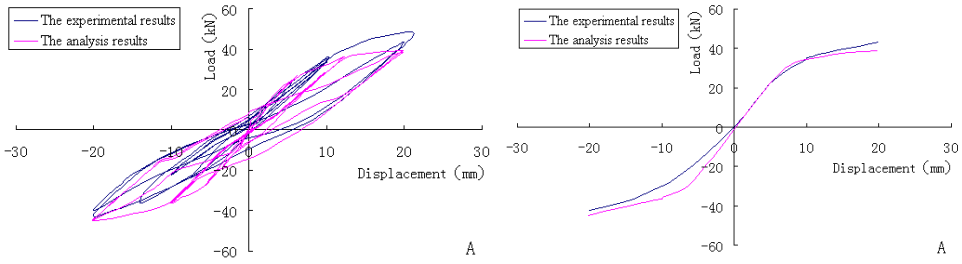
Table 2 has shown the experimental results and the analysis results of specimens. The result shows that, mixed with steel fiber can enhance the constraint of the concrete at the core area, improve the ultimate loading and the ultimate displacement. Amount of steel fiber can replace part of the stirrup.

At initial cracking state, the load of B is 80% of that of A, the displacement of B is 75% times of that of A. At yield state, the load of B is 1.01 times of that of A, the displacement of B is 88% of that of A. At ultimate state, the load of B is 1.03 times of that of A, the displacement of B is 1.17 times of that of A. Furthermore, the experimental results and the analysis results coincide well.

Table 2. The Results of Specimens

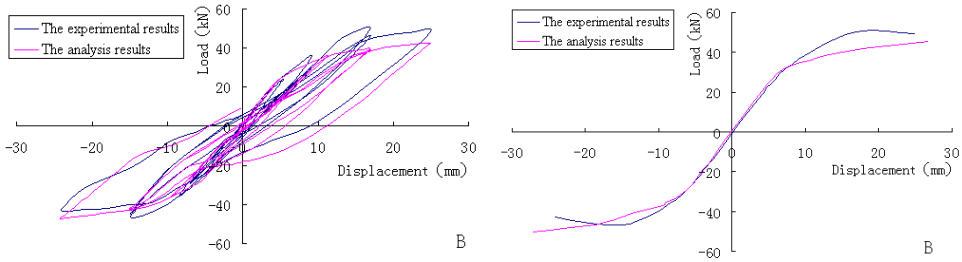
NO.		A		B	
		Experiment	Analysis	Experiment	Analysis
Initial cracking state	Load (kN)	20.00	15.61	16.00	13.77
	Displacement (mm)	4.07	2.94	3.07	2.36
Yield state	Load (kN)	36.00	36.00	36.30	36.30
	Displacement (mm)	10.26	12.10	9.06	11.22
Ultimate state	Load (kN)	47.83	39.58	49.21	42.50
	Displacement (mm)	21.28	19.89	25.00	24.89

Hysteresis Curve and Skeleton Curve. The hysteresis curve and the skeleton curve are shown in Fig. 3 and Fig. 4. The result shows, mixed with the steel fiber, the hysteresis curve becomes plumper, and the ultimate load, ultimate displacement and circulation time also increase. Amount of steel fiber can replace part of the stirrup. The hysteresis curve of B is plumper than that of A, because the ultimate load of B is 1.03 times of that of A, the ultimate displacement of B is 1.17 times of that of A. The coverage area of the skeleton curve of B is larger than that of A, and the circulation time of B is more than that of A.



a. The hysteresis curve b. The skeleton curve

Fig. 3 The hysteresis curve and the skeleton curve of specimen A



a. The hysteresis curve b. The skeleton curve

Fig. 4 The hysteresis curve and the skeleton curve of specimen B

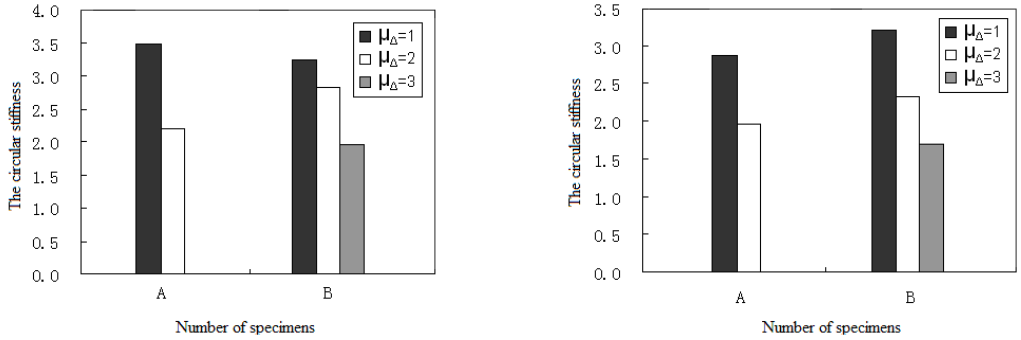
Table 3 Comparison of Loading Capacity Deterioration

NO.	A		B	
	Experiment	Analysis	Experiment	Analysis
Δy	0.973	0.997	0.987	0.996
$2\Delta y$	0.904	0.978	0.930	0.981
Ultimate load (kN)	47.830	39.580	49.210	42.500

Loading Capacity Deterioration. The loading capacity reducing coefficient is seen in Table 3. The result shows that mixed with steel fiber can enhance the constraint of the concrete at the core area, improve the shearing resistance capacity, and decrease the deterioration ratio of the loading

capacity. Amount of steel fiber can replace part of the stirrup. If the displacement ductility coefficient $\mu_\Delta = 1$, the loading capacity reducing coefficient of B is larger than that of A, and the displacement ductility coefficient $\mu_\Delta = 2$, the loading capacity reducing coefficient of B is larger than that of A. Therefore, the loading capacity reducing coefficient of B decreases more slowly than that of A.

Stiffness Degeneration. The circular stiffness is seen in Fig. 5. The result shows that mixed with steel fiber can enhance the constraint of the concrete at the core area, improve the shearing resistance capacity of the frame joints, increase the circulation times, and decrease the joint stiffness degeneration. If the displacement ductility coefficient $\mu_\Delta = 1$, the circular stiffness of B is smaller than that of A, but the displacement ductility coefficient $\mu_\Delta = 2$, the circular stiffness of B is larger than that of A, B can survive the displacement ductility coefficient $\mu_\Delta = 3$ process, but now A is broken. Therefore, the circular stiffness of B is larger than that of A.



a. The experimental results b. The analysis results

Fig. 5. Comparison of Stiffness Degeneration

Displacement Ductility. The displacement ductility is seen in Table 4. The result shows that mixed with steel fiber can increase ultimate displacement and displacement ductility coefficient. Amount of steel fiber can replace part of the stirrup. Yielding displacement of B is 88% of that of A, ultimate displacement of B is 1.17 times of that of A, displacement ductility coefficient of B is 1.33 times of that of A.

Table 4. Displacement Ductility of Specimens

NO.	A		B	
	Experiment	Analysis	Experiment	Analysis
Yielding displacement (mm)	10.26	12.10	9.06	11.22
Ultimate displacement (mm)	21.28	19.89	25.00	24.89
Displacement ductility	2.07	1.64	2.76	2.22

The Energy Dissipation Capacity. The energy dissipation capacity is seen in Table 5. The result shows that mixed with steel fiber can enhance the constraint of the concrete at the core area, improve the shearing resistance capacity, and increase circulation times. Therefore, the energy absorbed and the energy dissipated also increase. Amount of steel fiber can replace part of the stirrup. The absorbed energy of B is 1.27 times of that of A. The dissipated energy of B is 1.35 times of that of A.

Table 5. Energy Dissipation Capacity of Specimens

NO.	A		B	
	Experiment	Analysis	Experiment	Analysis
Dissipated energy (kN·mm)	1275.20	1164.04	1718.80	1752.35
Absorbed energy (kN·mm)	3436.40	3499.01	4363.70	4298.56

Conclusions

Mixed with steel fiber can enhance the constraint of the concrete at the core area, decrease the deterioration ratio of the loading capacity and stiffness degeneration, improve the ultimate loading, the ultimate displacement, displacement ductility coefficient, the shearing resistance capacity, the energy dissipation capacity, and circulation time. Amount of steel fiber can replace part of the stirrup.

In finite element analysis, steel fiber was equated with micro-reinforcement, and then put evenly into the concrete unit. The method of taking the steel fiber and concrete as a holistic model was thus validated. Therefore, it provides a reference for practical usage.

The experimental results and the analysis results coincide well. The results prove the rationality of element type, material constitutive relation and failure criterion used in the finite element analysis.

References

[1] GB 50010-02002, Code for Design of Concrete Structures, China Building Industry Press, Beijing, 2002.

[2] Z. Guo, Strength and deformation of concrete, China, 1997.

[3] Z. Liu, Nonlinear numerical simulation of prestressed concrete and reinforced concrete beam based on ANSYS, Xinjiang Agricultural University, Xinjiang, 2007.

[4] G. Zhao, S. Peng, C. Huang, Steel Fiber Reinforced Concrete Structures, China Building Industry Press, Beijing, 1999.

[5] S. Moaveni, Finite element analysis theory and application with ANSYS, China, 2008.

[6] B. Si, Z. Sun, Q. Ai, and D. Wang, Sensitive analysis and model modification for finite element analysis of R/C bridge piers under cyclic loading, Engineering Mechanics, 26 (2009) 174–180.

© (2012) Trans Tech Publications, Switzerland
doi:10.4028/www.scientific.net/AMM.238.844

Study on Relationship of Seismic and Pseudo Response Spectrums

Gonglian Chen[1,a], Wenfeng Liu[2,b] and Gang Li[3,c]

[1]School of Civil Engineering and Communication, North China University of Water Resources and Electric Power, Zhengzhou 450011, China

[2]School of civil engineering, Qingdao Technological University, Qingdao 266033, China

[3]Institute of Architectural Engineering, Qingdao Agricultural University, Qingdao 266109, China

[a]Chengonglian@gmail.com, [b]Lwfqdjg@263.net, [c]Qdndlg@163.com

Keywords: response spectrum; performance based seismic design; pseudo response spectrum.

Abstract. 153 seismic waves were input into the elastic-dynamic differential equations of single degree of freedom system, the acceleration response spectrum, velocity response spectrum and displacement response spectrum in different site characteristic periods were obtained. According to the pseudo-dynamic relationship between acceleration, velocity and displacement response spectrum, the pseudo response spectra were obtained by the deduction of the 3 real response spectra from the frequency relation. Compared with the value of the real and the pseudo response spectra, the basic characteristics and differences were studied, the correction formulas of the difference between the real response spectrum and the pseudo response spectrum were obtained, the correction formula will contribute to the development of performance based seismic design theory.

Introduction

With the development of economy and improvement of people's living standard, the increasingly high demand on the seismic performance of the structure by the community and the public arose. Many scholars believe that, under earthquake action, deformation can better reflect the performance of the structure than the strength, displacement based seismic design method is easier than traditional strength-based seismic design method, and also be possible to achieve performance-based seismic design concept. However, due to the lack of available design displacement response spectrum, the popularization and application of the method hindered [1]. So far, many scholars have studied displacement response spectrum [2]. The earthquake response spectrum is generally take a standardized absolute acceleration response spectrum, and doesn't directly give the relative displacement response spectrum. But according to the pseudo spectral relationship [4], the relative displacement response spectrum can be obtained by the acceleration response spectrum.

According to the response spectrum theory, when the system damping ratio is small enough and the sine and cosine relation is ignored, the pseudo spectral relationship can be described as:

$$S_d : S_v : S_a = 1 : \omega : \omega^2 \tag{1}$$

Where S_{d}, S_{v} and S_{a} are relative displacement response spectrum, relative velocity response spectrum and absolute acceleration response spectrum; ω is the circular frequency of the structure.

This paper takes the reinforced concrete structure as example, 153 seismic waves were input into the elastic-dynamic differential equations of single degree of freedom system, the acceleration, velocity and displacement response spectrum in different site characteristic periods were obtained. Based on the calculation, the pseudo response spectra were obtained by the deduction of the 3 real response spectra from the frequency relation, the correction formulas of the difference between the real spectrum and the pseudo response spectrum were obtained.

The Selected Seismic Waves

153 seismic waves were selected, including Elcentro, Kobe, Taft, BeiJing Hotel (EW), QianAn (EW), QianAn (SN), Tianjin Hospital (EW) and Tianjin Hospital (SN) earthquake waves.

Other 144 waves are shown in Table 1.

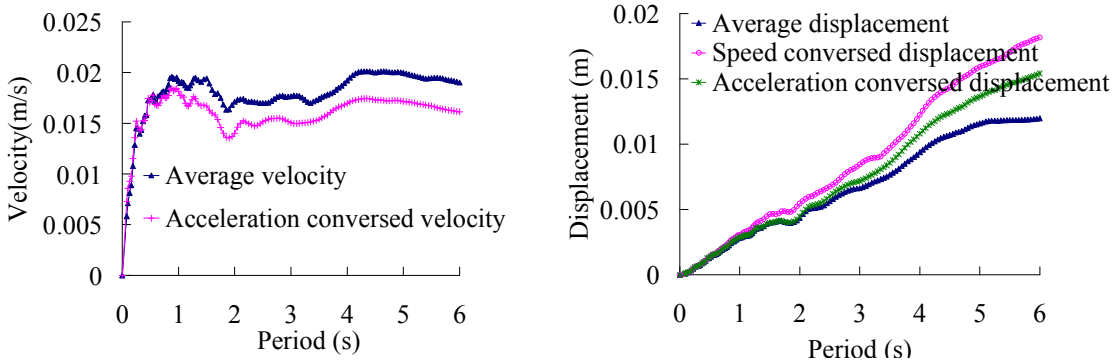
Table 1 The selected seismic waves in this paper

Site classification	Number	Earthquake data
B	36	Chi-Chi earthquake (9); Mexico earthquake (15); Northridge earthquake (12)
C	36	Chi-Chi earthquake (36)
D	36	Chi-Chi earthquake (9); Tangshan earthquake (15); Northridge earthquake (12)
E	36	Chi-Chi earthquake (15); Mexico earthquake (9); Northridge earthquake (12)

In Table 1, B, C, D, E site is detailed in UBC code 1997. Spectral analysis by response spectrum method of seismic waves, the characteristic period of the site can be obtained. In this paper, the characteristic period of the seismic waves is divided into nine groups, including 0.25s, 0.30s, 0.35s, 0.40s, 0.45s, 0.55s, 0.65s, 0.75s, 0.90s [5]。

Differences between Pseudo and Real Response Spectrum

The response spectra for each seismic waves were analysised by using Wilson-θ method, the comparison of the pseudo response spectrum and real response spectrum in different characteristic site can be obtained. Take the characteristic period of 0.25s for example, the relationship of pseudo and real response spectrum is shown in Fig. 1. It can be seen that from the shape of the curve, either the velocity response spectrum or displacement response spectrum, the shape of the pseudo response spectrum and the real response spectrum are roughly the same.



(a) Comparison of the velocity response spectrum (b) Comparison of the displacement response spectrum

Fig. 1 The comparison of the pseudo and real response spectrum at the characteristic period of 0.25s

Correction for Pseudo Response Spectrum

Relationship between Pseudo and Real Vecolity Response Spectrum. Take the characteristic site period 0.25s for example, the deviation between the pseudo and the real vecolity response spectrum are shown in Fig. 2. When the structural natural period is small, and about 0.1s, the vecolity of the absolute value is very small, small changes can have larger relative deviation, because the natural vibration period of the structure is generally bigger than 0.1s, and the study of this stage is of little significance; when the structural natural period increases, the relative deviation is gradually stabilized, the maximum value is about - 0.2.

The fitting formulate of relative deviation of the pseudo and real vecolity response spectrum is shown by Eq.(2).

$$f_1 = (T_g / T)^{a_1} \times b_1 + c_1 \tag{2}$$

Where f_1 is the relative deviation; T_g is the characteristic site period; T is the structural natural periods; a_1, b_1 and c_1 is the fitting parameters (Table 2).

When the damping ratio is 0.05, the correction for the pseudo response spectrum can be described as :

$$S_a = (1 + f_1)\omega S_v \tag{3}$$

Relationship between Pseudo and Real Displacement Response Spectrum. Displacement response spectrum conversed by acceleration response spectrum

Take the characteristic site period 0.25s for example, the deviation between the pseudo and the real displacement response spectrum is shown in Fig. 3. With the structure natural period increases the relative deviation of rapid growth.

Eq. (4) is the fitting formulate of relative deviation of the pseudo and real displacement response spectrum, the symbol in which is the same as Eq.(2). The fitting parameters is shown in Table 2.

$$f_2 = a_2^{(T/T_g)} \times b_2 \tag{4}$$

When the damping ratio is 0.05, the correction for the pseudo response spectrum can be described as

$$S_a = (1 + f_2)\omega^2 S_d \tag{5}$$

Displacement Response Spectrum Conversed by Vecolity Response Spectrum. Take the characteristic site period 0.25s for example, the deviation between the pseudo and the real displacement response spectrum is shown in Fig. 4. It can be seen that relative deviation of the slow growth in the long-period.

Eq. (6) is the fitting formulate of relative deviation of the pseudo and real displacement response spectrum, the symbol in which is the same as Eq.(2). The fitting parameters is shown in Table 2.

$$f_3 = \ln((T / T_g)^{a_3}) \times a_3 + b_3 \tag{6}$$

So when the damping ratio is 0.05, the correction for the pseudo response spectrum can be described as :

$$S_v = (1 + f_3)\omega S_d \tag{7}$$

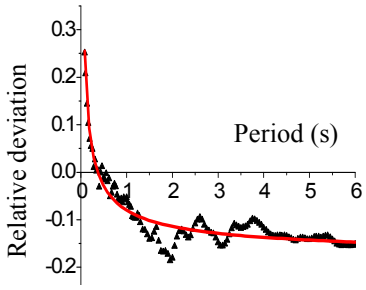


Fig. 2 Velocity response spectrum relative deviation fitting at the site characteristic period of 0.25s

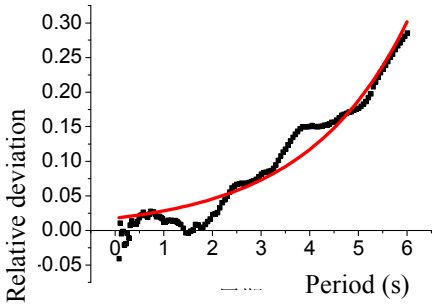


Fig. 3 Displacement response spectrum relative deviation fitting at the site characteristic period of 0.25s (1)

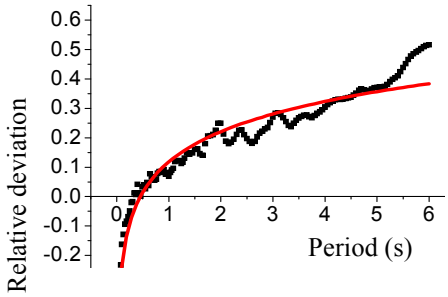


Fig. 4 Displacement response spectrum relative deviation fitting at the site characteristic period of 0.25s (2)

Pseudo Displacement Response Spectrum Calculated in Accordance with Code Defining

From Fig. 3, with the structure natural period increases the relative deviation of rapid growth. In Chinese *Code for seismic design of buildings*, the defined response spectrum is acceleration response spectrum, and if the displacement response spectrum is calculated by the acceleration response spectrum, the deviation occurred, and the pseudo displacement response spectrum can be revised by Eq. (4). Take T_g=0.30s and α_{max}=0.50 for example, the acceleration response spectrum in the *Code* is shown in Fig. 5, the displacement response spectrum calculated by the acceleration response spectrum before revise and revised are shown in Fig. 6.

By the relative displacement response spectrum statistical characteristics [3], when the structural natural period reaches a certain value, the relative displacement is not a linear growth with period increase. When the structural natural period is the displacement characteristic period, the relative displacement response spectrum is equal to the peak of the ground motion.

So, from Fig. 6, in the long structural natural period, the un-revised pseudo displacement response spectrum calculated by the acceleration response showed a high rising trend, which is inconsistent

with the statistical characteristics, but the rising trend of the revised pseudo displacement response spectrum in the long period is slow, so the revised displacement response spectrum has a more realistic reflection of the structure relative displacement variation.

Table 2 The fitting parameters in Eq.(2), Eq.(4) and Eq.(6)

Site characteristic period (s)	a_1	b_1	c_1	a_2	b_2	a_3	b_3
0.25	0.566	0.230	-0.185	1.125	0.017	0.385	-0.088
0.30	1.002	0.151	-0.130	1.160	0.019	0.380	-0.055
0.35	0.752	0.211	-0.161	1.186	0.012	0.378	-0.075
0.40	0.567	0.244	-0.147	1.152	0.013	0.321	-0.099
0.45	0.909	0.159	-0.141	1.291	0.013	0.406	-0.047
0.55	0.683	0.261	-0.216	1.580	0.001	0.390	-0.063
0.65	1.014	0.096	-0.123	1.317	0.023	0.382	0.026
0.75	0.606	0.245	-0.201	1.038	0.008	0.355	-0.059
0.90	0.187	1.319	-1.173	--	--	0.460	-0.095

Note: in Eq.(4), when the characteristic period is 0.90s, the deviation rule is not clear, and there is no fitting.

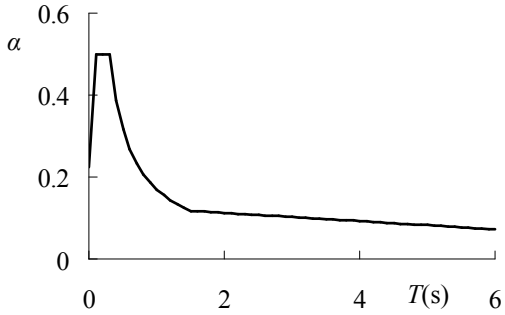


Fig. 5 Acceleration response spectrum in the Code（T_g=0.30s，α_{max}=0.50）

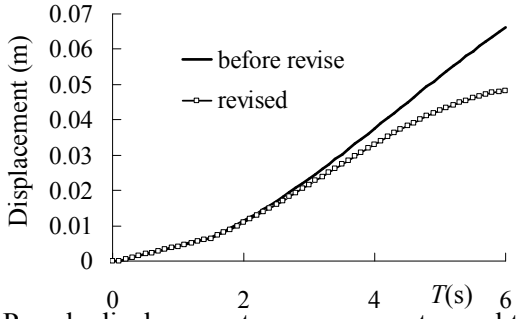


Fig. 6 Pseudo displacement response spectrum obtained by the Code and the revised pseudo displacement response spectrum (T_g=0.30s，α_{max}=0.50)

Conclusions

From the shape of the curve, for the 3 response spectrum, the shape of the pseudo and the real response spectrum are roughly the same. The correction formulas of the difference between the pseudo and the real response spectrum were obtained.

In the structure long period, the un-revised pseudo displacement response spectrum calculated by the acceleration response showed a high rising trend, but the rising trend of the revised pseudo displacement response spectrum in the long period is slow, the revised displacement response spectrum has a more realistic reflection of the structure relative displacement variation.

Acknowledgements

This work was financially supported by the National Natural Science Foundation (50878110) and High-level Personnel Research Sart-up Projects of NCWU (201159).

References

[1] Y. Wang, A review of seismic response spectra, time history analysis and energy method, Journal of Building Structures, 21 (2000), 21-28.

[2] K. Kawashima, J. Hoshikuma, K. Nagaya, Residual displacement response spectrum, Journal of Structural Engineering, 120(1998), 523-530.

[3] J. Cao, W. Shi, W. Liu, et al, Relative displacement response spectrum of a long-period structure, Journal of Vibration and Shock, 30(2011), 63-70.

[4] A. K. Chopra. Dynamics of Structures, Theory and applications to earthquake engineering, Prentice-Hall Inc, USA, 2004.

[5] G. Chen, Study on performance target based response spectrum, Qingdao Technological University, Qingdao, 2006.

© (2012) Trans Tech Publications, Switzerland
doi:10.4028/www.scientific.net/AMM.238.848

Feasibility of Vs Liquefication Evaluation Methods by Bachu Xinjiang Earthquake Data

Qianyu Zhao[1,a], Rui Sun[1,b], Yurun Li[2,3,c] and Weiming Wang[1,d]

[1]Key Laboratory of Earthquake Engineering and Engineering Vibration, Institute of Engineering Mechanics, CEA, Harbin 150080, China

[2]College of Civil Engineering, Hebei University of Technology, Tianjin 300401, China

[3]Civil Engineering Technology Research Center of Hebei Province, Tianjin, 300401, China

[a]zhaoqianyu_2006@yahoo.com.cn, [b]iemsr@163.com, [c]iemlyr7888@163.com, [d]wswwm1983@163.com

Keywords: shear Wave Velocity (Vs), soil liquefaction, probability analysis, discrimination model.

Abstract. A discrimination model for soil liquefaction is established by analyzing the liquefied and non-liquefied sites in the Bachu Xinjiang earthquake, based on 44 shear wave velocity data. One of them is based on the *Code for seismic design of buildings*, which is a linear model. The model is brief and convenient, while the evaluation success rate is 80%. But compared with the nonlinear model, the linear model is not advanced enough. The other model is based on probability analysis, and the evaluation success rate can reach up to 93%. And the discrimination results are high in reliability rely on real data analysis.

Introduction

In the free field case, soil liquefication is usually established based on the liquefied survey of earthquake site, which is an experimental verification method. With this method, the dynamic characteristics of soil can be expressed by field testing indicators, such as the CPT tip resistances, the SPT blow count and shear wave velocity. Although the standard penetration tests are informative and widely used, the experimental results are affected greatly by human factors. In contrast, shear wave velocity will become an important factor to determine the mechanics behavior of soil [1, 2].

The shear wave velocity data in this article comes from the Bachu Xinjiang earthquake, an M_s6.8 earthquake occurred in February 24, 2003. In this paper, we have 47 shear wave velocity test sites, 44 shear wave velocities are selected, including 19 liquefied and 25 non-liquefied sites.Among the records, 11 records are in intensity IX area, 21 out of 44 records are in intensity VIII area while 12 of them are in intensity VII area. In this paper, we use the theory of mathematical regression to analyze the Bachu Xinjiang earthquake shear wave velocity data, and then establish the relationship between the basic parameter and liquefaction probability. In this article, we raise two kinds of liquefaction evaluation model, and discuss them separately.

Discrimination Model Based on the Code for Seismic Design of Buildings

A standardized form of liquefaction discrimination equation is established according to the *Code for seismic design of buildings (GB50011-2001)*.It is similar with the SPT blow count liquefaction discrimination model, as the below Eq. 1 [3]:

$$V_{scri} = V_{s0}(1 + \alpha_w (d_w - 2) + \alpha_s (d_s - 3)) \quad (1)$$

Where V_{scri} is the limiting value of V_s for liquefaction occurrence,V_0 is the reference value of shear wave velocity, d_w is the underground water table depth, d_s is the liquefied or non-liquefied layer depth, a_w is the influence coefficient of underground water table depth, a_s is the influence coefficient of liquefied or non-liquefied layer depth. In this equation, set d_w=2m and d_s=3m as reference values.

Following the traditional procedure for correcting SPT blow count and CPT tip resistances to account for overburden stress, the V_s can be corrected to a reference overburden stress [4]

$$V_{S1} = V_s(P_a / \sigma_v^{'})^{0.25} = V_s((9d_s + 10d_w) / \sigma_v^{'})^{0.25} = V_s(47 / \sigma_v^{'})^{0.25} \quad (2)$$

Where V_{s1} is the overburden stress corrected shear wave velocity, P_a is reference stress of 47 kPa , $\sigma_v^{'}$ is the initial effective overburden stress (kPa).

By plotting intensity and corrected shear wave velocity in one figure, we can get the characteristic curve of critical stress corrected shear wave velocity, which is shown in Fig. 1, the boundaries between liquefied and non-liquefied sites is obvious, and the relationship between corrected shear wave velocity and intensity are shown in Table 1. To improve the evaluation rate, we use the surfer software to analyze the factors affecting liquefied and non-liquefied sites. In order to improve the success rate of Eq. 1 comprehensively, selected optimal a_s and a_w to meet the requirements of liquefaction and non-liquefaction evaluation success rate is shown in Fig. 2, which a_w=-0.02, a_s=0.04. It can be seen from the figure that the liquefied and non-liquefied discrimination success rates both reach 75%. Final equation as follow:

$$V_{scri} = V_{s0}(1 - 0.02(d_w - 2) + 0.04(d_s - 3)) \quad (3)$$

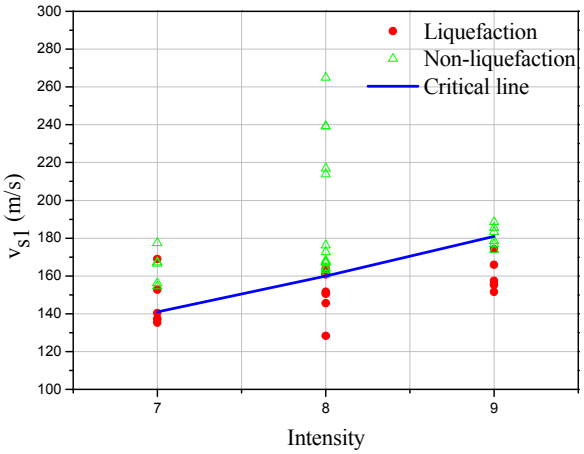


Fig. 1 Relationship between corrected shear wave velocity and intensity

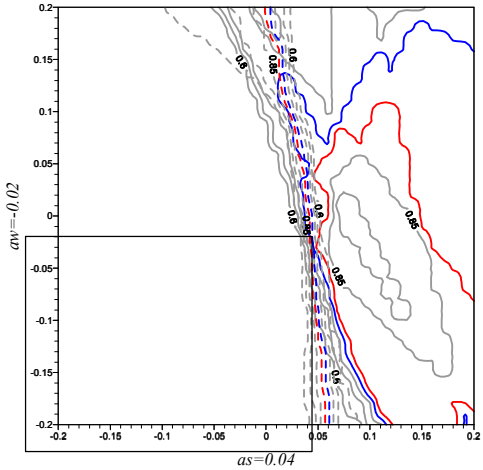


Fig. 2 Effects of a_w and a_s on discrimination success ratios for liquefied and non-liquefied sites

Table 1 The reference values of shear wave velocity in different intensity

Intensity	VII	VIII	IX
V_{s0}(m/s)	141	160	181

Discrimination Model Based on Probability Analysis

Liao (1988) proposed the regression model. The discrimination model based on probability analysis is expressed as:

$$P_L(X) = 1 / \{1 + \exp[-(\theta_0 + \theta_1 x_1 + \cdots + \theta_n x_n)]\} \quad (4)$$

Where $x_1, x_2, \cdots x_n$ are the influence factors of liquefaction, $\theta_0, \theta_1, \cdots \theta_n$ are the indefinite parameter of the relative mode [5,6].

The model assumes that there are two major factors affecting soil liquefication, shear wave velocity and cyclic stress ratio (CSR). Shear wave velocity represents the liquefaction resistant ability of soil. CSR represents the seismic intensity.The evaluation equation is as follows:

$$P_L(X) = 1 / \{1 + \exp[-(\theta_0 + \theta_1 V_s + \theta_2 \ln CSR)]\} \quad (5)$$

Then establish the likelihood function:

$$L(X;\theta) = \prod_{i=1}^{m} [P_L(X)]^{yi} [1 - P_L(X)]^{1-yi}$$

$$= \prod_{i=1}^{m} \left[\frac{1}{1+\exp[-(\theta_0+\theta_1 V_s+\theta_2 \ln CSR)]} \right]^{yi} \left[\frac{\exp[-(\theta_0+\theta_1 V_s+\theta_2 \ln CSR)}{1+\exp[-(\theta_0+\theta_1 V_s+\theta_2 \ln CSR)} \right]^{1-yi} \tag{6}$$

Where m is the total number of samples, yi=1 means liquefication, yi=0 when non-liquefication.

According to the maximum likelihood rule, when $L(X;\theta)$ take the maximum value, we can get the estimator $\hat{\theta}_0, \hat{\theta}_1, \hat{\theta}_2$, the best estimator of $\theta_0, \theta_1, \theta_2$. Both sides of Eq. 6 take logarithm as follows:

$$Ln\left(L(X;\theta)\right) = -\sum_{j=1}^{m} \ln\left\{1+\exp\left[-\left(\theta_0+\theta_1 V_{sj}+\theta_2 \ln CSR_j\right)\right]\right\} - \sum_{j=1}^{nm}[\theta_0+\theta_1 V_{sj}+\theta_2 \ln CSR_j] \tag{7}$$

Obviously logarithmic function increases monotonically . We can establish the likelihood equations:

$$\frac{\partial \ln[L(X;\theta)]}{\partial \theta_0} = \sum_{j=1}^{m} \frac{\exp\left[-\left(\theta_0+\theta_1 V_{sj}+\theta_2 \ln CSR_j\right)\right]}{1+\exp\left[-\left(\theta_0+\theta_1 V_{sj}+\theta_2 \ln CSR_j\right)\right]} - \sum_{j=1}^{nm} 1 \tag{8}$$

$$\frac{\partial \ln[L(X;\theta)]}{\partial \theta_1} = \sum_{j=1}^{m} \frac{V_{sj} \exp\left[-\left(\theta_0+\theta_1 V_{sj}+\theta_2 \ln CSR_j\right)\right]}{1+\exp\left[-\left(\theta_0+\theta_1 V_{sj}+\theta_2 \ln CSR_j\right)\right]} - \sum_{j=1}^{nm} V_{sj} \tag{9}$$

$$\frac{\partial \ln[L(X;\theta)]}{\partial \theta_2} = \sum_{j=1}^{m} \frac{\ln CSR_j \exp\left[-\left(\theta_0+\theta_1 V_{sj}+\theta_2 \ln CSR_j\right)\right]}{1+\exp\left[-\left(\theta_0+\theta_1 V_{sj}+\theta_2 \ln CSR_j\right)\right]} - \sum_{j=1}^{nm} \ln CSR_j \tag{10}$$

Where m is the total number of samples, nm is the number of non-liquefaction points, V_{sj} is the shear wave velocity values of the jth sample, $lnCSR_j$ is the logarithmic cyclic stress ratio of the jth sample.

By using MATLAB program plug the Bachu Xinjiang survey data which use in-situ test from shear wave velocity into the equation, we can get the values of indefinite parameters as, $\theta_0 = 27$, $\theta_1 = -0.12$, $\theta_2 = 3.17$. As a result, the liquefaction probability evaluation model becomes:

$$P_L(X) = 1/\{1+\exp[-(27-0.12V_s+3.17\ln CSR)]\} \tag{11}$$

Set P_L=50%. At this point, the shear wave velocity (V_s) is equal to the critical shear wave velocity (V_{scri}), the form of Eq. 11 can be turned into:

$$V_{scri} = (27+3.5\ln CSR)/0.12 \tag{12}$$

According to Eq. 12, set V_s as x-axis, cyclic stress ratio (CSR) as y-axis. We can see from the Fig. 3 that the boundary between liquefied and non-liquefied sites is obvious. And the regression model result fits well to the site records. Then set V_s/V_{scri} as x-axis, P_L as y-axis, the correspondence between regression liquefaction ratios and regression liquefaction probability shows as Fig. 4.

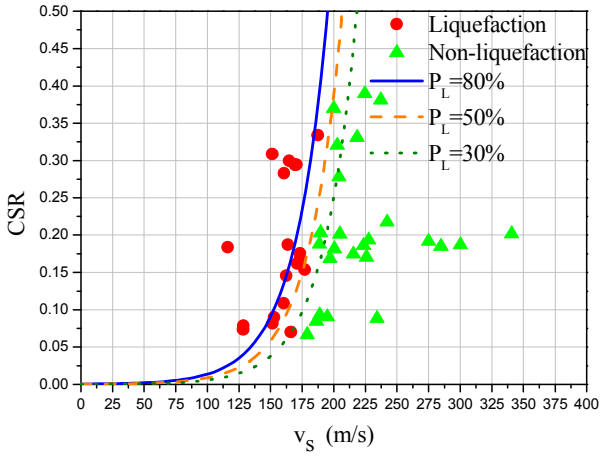


Fig. 3 Liquefaction strength under different probability conditions

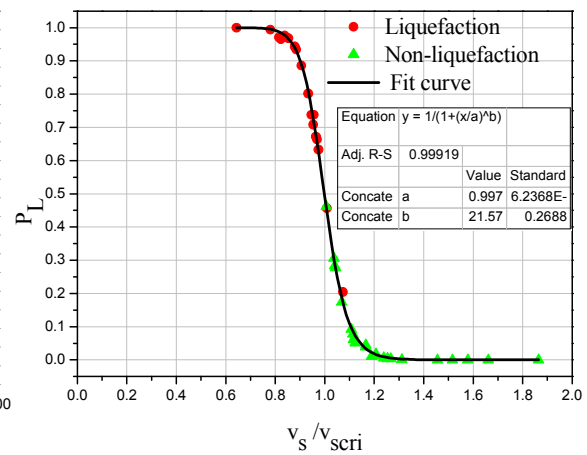


Fig. 4 Correspondence between regression liquefaction ratios and liquefaction probability

Results

From the above two discrimination model, the success ratios for liquefied and non-liquefied sites are in the Table 2.

Table 2 Discrimination success ratios of two the models

	Discrimination results based on the *Code for seismic design of buildings*	Discrimination results based on probability analysis
Liquefied site	74%	89%
Non-liquefied site	84%	96%
Successfully judging rates total	80%	93%

Conclusions

In this paper, two kinds of discrimination model are established based on statistic and analysis of Bachu Xinjiang shear wave velocity data. From Table 2 we can see the discrimination success ratios of the two models. The discrimination based on the code of seismic design of buildings, liquefied sites evaluation success rate is 74% and non-liquefied sites is 84%,with the total discrimination success rate as 80%. The discrimination based on probability analysis, evaluation success rate is 89% in liquefied and 96% in non-liquefied, while the total discrimination success rate is 93%. The two model's total evaluation success rate can reach 80%. Evaluation success rate of probability model is better than model based on building code. Based on the methods of probability analysis, probability model is more reliable.

Acknowledgements

This research is jointly supported by Fundamental Research Funds of Institute Engineering Mechanics and Earthquake (200708001) and National Natural Science Foundation of Youth Fund (51008110).

References

[1] G. Chen, K. Zhang, J. Xie, Methods of liquefaction potential with shear wave velocity as a field index and the adaptability. Journal of Harbin University of Architecture and Engineering, 1 (1996) 97-103.

[2] Z. Shi, S. Yu, The relationship between soil shear wave velocity and Liquefaction strength. Word Earthquake Engineering, 1991.

[3] GB50011–2001 Code for seismic design of buildings. China Architecture and Building Press, Beijing, 2001.

[4] R.D. Andrus, K.H. Stokoe II, Liquefaction resistance of soils from shear-wave velocity. Journal of Geotechnical and Geoenviromental Engineering, ASCE, 11 (2000) 1015-1025.

[5] Z. Cao, Study on reliability-based procedure for evaluating liquefaction potential. Institute of Engineering Mechanics China Earthquake Administration, 2006.

[6] Z. Cao, X. Yuan, Shear wave velocity-based approach for evaluating gravel soils liquefaction. Chinese Journal of Rock Mechanics and Engineering, 5 (2010) 943-951.

© (2012) Trans Tech Publications, Switzerland
doi:10.4028/www.scientific.net/AMM.238.852

Study on In-situ Test Based on Survey of Bachu Earthquake

Zhaoyan Li[1,a], Weiming Wang[1,b], Yurun Li[2,3,c] and Longwei Chen[1,d]

[1] Key Laboratory of Earthquake Engineering and Engineering Vibration，Institute of Engineering Mechanics, CEA, Heilongjiang, Harbin 150080, China

[2] College of Civil Engineering, Hebei University of Technology, Tianjin 300401

[3] Technology Research Center of Hebei Province, Tianjin, 300401

[a]hkjlizhaoyan@163.com, [b]wswwm1983@163.com, [c]iemlyr7888@163.com,

[d]chenlongwei83@126.com

Keywords: the Bachu-Jiashi Earthquake; in-situ test; soil liquefaction; SPT; CPT.

Abstract. Based on survey of the Bachu-Jiashi earthquake liquefaction sites, much new basic liquefaction information were obtained and China's liquefaction database was enriched. A detailed investigation of the Bachu earthquake liquefaction site was conducted, in which three kinds of in situ test measures were used to obtain the site information, and given China mainland SPT data of liquefaction site increase by 40%. By site investigation, international standard liquefaction site CPT data were obtained, and also, the first measurement of liquefaction site data by SPT and CPT index was conducted. With the new data, the feasibility of liquefaction discrimination methods of China was inspected.

Introduction

The February 24, 2003, Bachu-Jiashi earthquake, measured as 6.8 on the Richter scale, struck Kashi, Yarkand River valley, and caused extensive damage to buildings and utilities, is the most disastrous earthquake in China Xinjiang Uygur Autonomous Region since 1949 [1].

The site is mainly composed of silty sand, fine sand, silt soil and silty clay of the Holocene-late Pleistocene and the groundwater level is shallow. Extensive seismic damages such as soil liquefaction, ground cracks and slumping of steep river bank occurred in areas with seismic intensity of VII, VIII and IX. The Bachu-Jiashi earthquake caused a large scale of soil liquefaction damage and shown the most notable phenomena of sand liquefaction in China mainland since the Tangshan Great Earthquake in 1976, which provides a unique opportunity for soil liquefaction research [2].

Earthquake prevention is one of the most direct and effective means to mitigate earthquake disasters. The first step in preventing seismic liquefaction induced damages is site liquefaction prediction and discrimination. The rationality and reliability of the method for seismic liquefaction prediction is of particular importance for seismic disaster prevention and engineering costs. Also, seismic liquefaction prediction is one of the most important research topics for soil dynamics and earthquake engineering, and much attention has been paid by scholars and engineers [3-5].

Survey Sites

In September 2009, we selected 43 the typical area to resurvey for SPT and CPT in Bachu-Jiashi earthquake liquefied sites. The distribution of the investigation sites is shown in Fig. 1. Contribution to liquefaction database is shown in Table 1.

Table 1 Contribution to liquefaction database

	Original (sites)	Increase (sites)	Now (sites)	Augmenter (%)
SPT	119	47	166	40
CPT	47	40	87	85
Vs	30	40	70	130
Joint of diffrent methods	0	40	40	

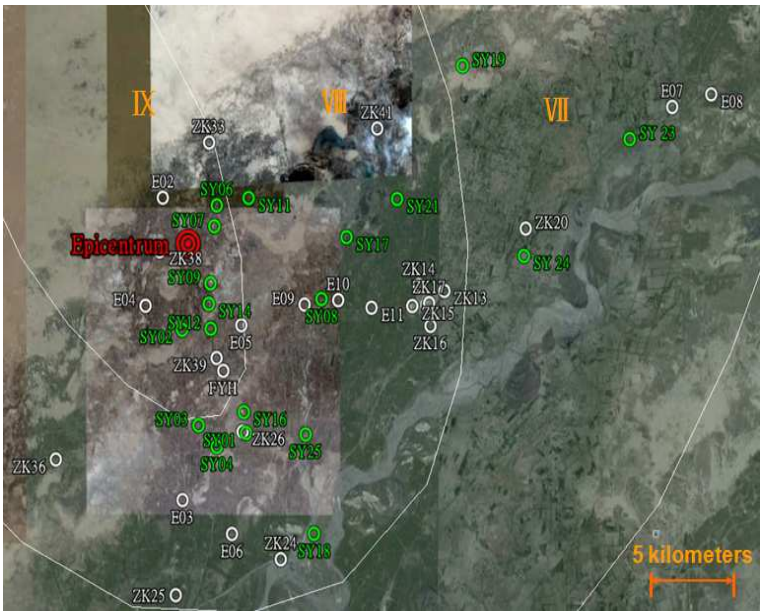


Fig. 1 The distribution of the investigation sites

CPT Liquefied Method

The code standard method is the compared empirical method, derived from the water spraying and sand emitting, subsidence and other ground deformation in liquefied region, which after the Xingtai earthquake (1966), Tonghai earthquake (1970), Haicheng earthquake (1975), the Tangshan earthquake (1976) and the overseas earthquake in history. The method use of probability statistics, thus has a strong practical and focused, becomes the main principles of sand liquefaction. The liquefied evaluation from the following equation [6]：

$$p_{scr} = p_{s0} \cdot a_w \cdot a_u \cdot a_p \tag{1}$$

$$q_{ccr} = q_{c0} \cdot a_w \cdot a_u \cdot a_p \tag{2}$$

$$a_w = [1 - 0.065(d_w - 2)] \tag{3}$$

$$a_u = [1 - 0.05(d_u - 2)] \tag{4}$$

Where p_{scr} and q_{ccr} are saturated soil liquefaction specific penetration resistance and critical value of tip resistance (MPa); p_{so} and q_{co} are saturated soil liquefaction specific penetration resistance and critical value of tip resistance, when d_u=2.0m, d_w=2.0m, is shown in Table 2. a_w is the groundwater depth of the coefficient; au is overlying non-liquefied soil thickness coefficient; a_p is CPT Sleeve friction coefficient, as noted is shown in Table 3.

Table 2 Fiducially values of specific penetration resistance and cone tip resistance

Intensity	VII	VIII	IX
p_{so}（MPa）	5.0-6.0	11.5-13.0	18.0-20.0
q_{co} (MPa)	4.6-5.5	10.5-11.8	16.4-18.2

Table 3 Soil property correction factor a_p value

	Soil type	Soil type	Soil type
CPT friction ratio R_f	$R_f \leq 0.4$	$0.4 < R_f \leq 0.9$	$R_f > 0.9$
a_p	1.00	0.60	0.45

SPT

The code sandard method for distinguishing liquefaction of foundation soil formula by the following equation [6]:

$$N_{cr} = N_0[0.9+0.1(d_s - d_w)]\sqrt{3/\rho_c}\ (d_s \le 15m) \tag{5}$$

$$N_{cr} = N_0(2.4-0.1d_s)\sqrt{3/\rho_c} \quad (15 < d_s \le 20m) \tag{6}$$

Where N_{cr} is critical SPT blow count, N_0 is under different intensity corresponding to SPT blow count, d_s is saturated soil depth of standard penetration point, d_w is groundwater depth, ρ_c is percentage of clay content, it is 3 for silt and sand in the study, $N_{63.5}$ is SPT blow count of measured value.

Liquefied Level Determination and Decision Results

The important step in survey data analysis is to determine the liquefied and non-liquefied layer position and thickness. This paper gives a typical Bachu earthquake liquefied layer evaluation, as shown in Fig. 2.

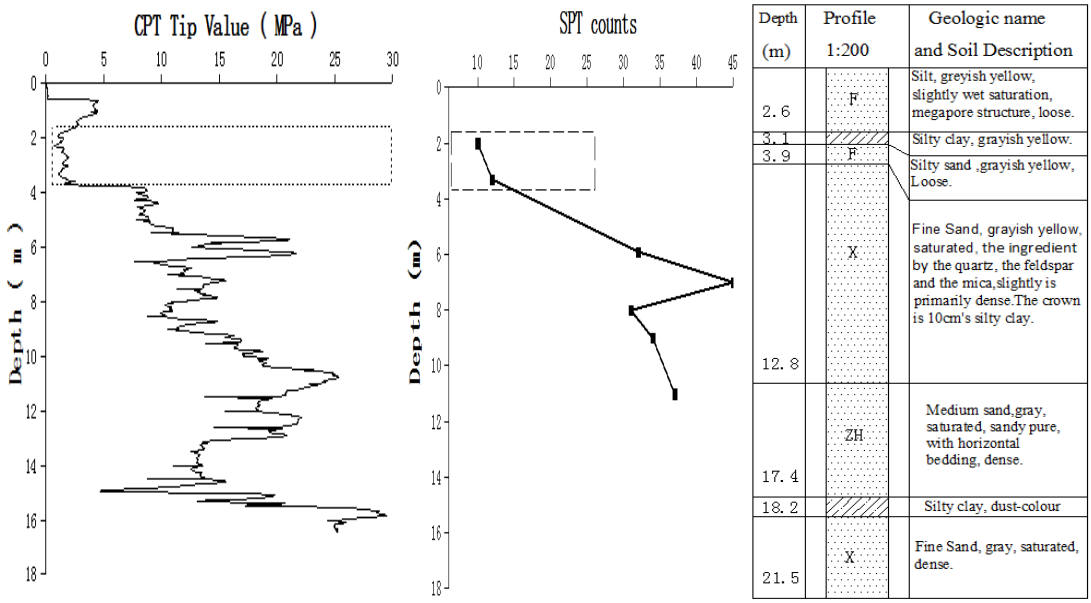


Fig. 2 Typical profiles of sites and position of liquefied layers

Discrimination Results

According to the Chinese code methods for discrimination results is shown in Table 4.

Table 4 Discrimination success ratio

	CPT method	SPT method
Liquefied site discrimination success rate	38%	55%
Non-liquefied site discrimination success rate	88%	88%

Conclusions

This paper, based on the soil liquefaction surveys in the Bachu Earthquake, obtains new basic data, enriches and supplements China's in-situ experiment records of soil liquefaction. With the new data, it validates the feasibility of soil liquefaction discrimination methods in practical by Chinese code.

A detailed investigation of the Bachu earthquake liquefaction site was conducted, in which three kinds of in situ test measures were used to obtain the site information, and given China mainland SPT data of liquefaction site increase by 40%.

By site investigation, international standard liquefaction site CPT data were obtained.

The first measurement of liquefaction site data by SPT, CPT and Vs index was conducted.

The area evaluation success rate is 88% in Bachu-Jiashi non-liquefied, when used CPT method for earthquake liquefaction discrimination and the liquefied sites success rate is only 38%, the obvious misjudgment in the liquefied sites.

Non-liquefied sites evaluation success rate is 88% when used SPT method and liquefied sites for 55%, liquefied sites misjudgment is obvious, and will give the results of tends to be dangerous.

Acknowledgements

This research is jointly supported by Fundamental Research Funds of Institute Engineering Mechanics and Earthquake (200708001) and National Natural Science Foundation of Youth Fund (51008110).

References

[1] Z. Li, X. Yuan, Z. Cao, et al, World earthquake engineering, Suppl. (2010) 282-285.

[2] Z. Li, R. Sun, Z. Cao, et al, Rock and Soil mechanics, 31 (2010) 3907-3911.

[3] H. B. Seed, I. M. Idriss: Journal of the Soil Mechanics and Foundations Division, ASCE, 9 (1971) 1249-l273.

[4] R. S. Olsen, M. I. Vicksburg, MI U.S. Army Corps of Engineers, 3 (1994) 201-209.

[5] T. L. Youd, I. M. Idriss, Journal of Geotechnical and Geoenvironment Engineering, 4 (2001) 297-300.

[6] The National Standards Compilation Group of People's Republic of China, China Architecture and Building Press, Beijing, 2001.

© (2012) Trans Tech Publications, Switzerland
doi:10.4028/www.scientific.net/AMM.238.856

Comparative Analysis on Liquefaction Macro-characteristics of the Three Major Regions in Wenchuan Earthquake

Weiming Wang[a], Zhuoshi Chen[b], Xiaoming Yuan[c] and Zhenzhong Cao[d]

Key Laboratory of Earthquake and Engineering Vibration, Institute of Engineering Mechanics, China Earthquake Administration, Harbin 150080, China

[a]wswwm1983@163.com, [b]various@163.com, [c]yxmiem@163.com, [d]iemczz@163.com

Keywords: Wenchuan earthquake; liquefaction; distribution; characteristic; comparison.

Abstract. Through the liquefaction-induced damage of Wenchuan earthquake investigation analysis, this paper studies that the liquefaction features and distribution of the three major liquefied regions in Wenchuan earthquake and the earthquake liquefied damage characteristics are preliminarily comparatively analyzed. The analytical results show that: Mianyang region, Deyang region and Chengdu region are the three major liquefaction affected regions in Wenchuan earthquake. Deyang region is the most serious liquefied region, Chengdu region is the second, and Mianyang region is the lightest. Liquefaction damage was considerably large, and basically was farmland. Liquefied sites mainly concentrated in intensities VIII in Deyang region, the categories of sand ejecta were abundant, and the percentage of gravel ejecta is largest in the three major liquefied regions. Liquefied sites mainly located in intensities VII in Chengdu region, and the sand ejecta covered many sand categories, including fine (silty) sand, medium sand, coarse sand and gravely sand. The liquefaction and relevant damage of Mianyang region were the lightest in the three major liquefied regions, and liquefied sites mainly located in intensities VII. 80% of the sand ejecta were fine-silty sand while coarse sand ejection was not found.

Introduction

Liquefaction of saturated sand is one of the most important factors resulting in engineering and construction, underground structure (objects) damage; earthquake liquefaction study focuses on the difficult and cutting-edge topics of geotechnical earthquake engineering. Liquefaction-induced damage phenomena occurred during many earthquakes in last century, such as Niigata, Alaska, Kobe, Chi-Chi, Xingtai, Haicheng, Tangshan earthquakes. The deep investigation and analysis of these earthquakes liquefaction field plays a role in founding and promotion in China even the world works of the theoretical methods for the development [1]. The Wenchuan 8.0 earthquake occurred in Sichuan Province on May 12, 2008, which was the most destructive and widely spreading earthquake since the founding of new China [2]. The range of seismic liquefaction is also the widely spreading in all the major earthquake affected areas. The study of liquefaction macro-phenomena and relevant damage is very important. It is the important foundation to acquaintance with this earthquake liquefaction and further studying, not only to the research of Wenchuan earthquake liquefaction but also the earthquake liquefaction research to a new height.

The liquefaction and relevant damage were very remarkable in Wenchuan earthquake. Comparatively, liquefaction in Wenchuan earthquake involves more areas and distributes in more regions than any of the previous earthquakes. The paper summarized and comparatively analyzed the major liquefied regions in Wenchuan earthquake and stated the situation of liquefaction macro-phenomena and damage in the major liquefaction regions in order to further grasp liquefaction characteristics and regulars in the Wenchuan earthquake.

Liquefaction Distribution Characteristics

So far, 118 liquefied sites have been detected. One liquefied site is defined as a typical village or town within which one or more liquefied points were observed. Thus, at least a 2-km distance exists between two adjacent liquefied sites [3-4]. Liquefied sites distribution in Wenchuan earthquake is shown in Fig. 1, in which a dot represents a liquefied site, and concentric elliptical lines represent

isoseismal lines which separately represent intensities VI, VII, VIII, IX, X and XI. In Fig.1 liquefaction phenomena had been found in all intensities such as VI, VII, VIII and IX, X, XI, and more covering eight regions of Chengdu, Deyang, Mianyang, Suining, Ya'an, Meishan, Guangyuan. As far as the east is Anju district in Suining city, which epicentral distance is 210km; South is Hanyuan country in Ya'an city, which epicentral distance is 200km; North is Longnan city in Gansu province, and the epicentral distance is 280km. the liquefaction in Wenchuan earthquake is the most destructive and widely spreading earthquake since the founding of new China, relative to the sizes of liquefaction areas with the earthquakes of Tangshan, Jiji, Haicheng and Bachu, the percentage is 1:33:8:1:1.

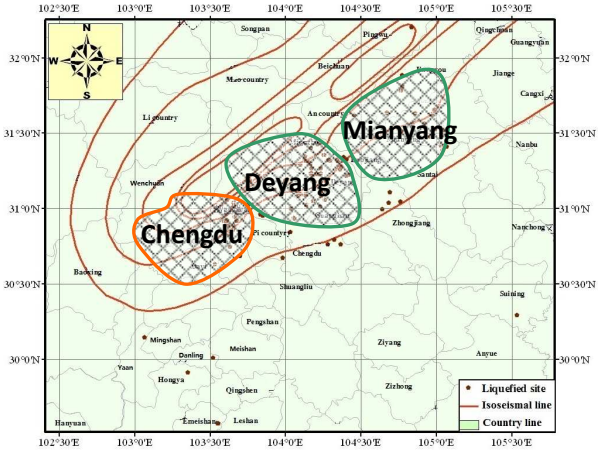


Fig. 1 Liquefied sites distribution in Wenchuan earthquake

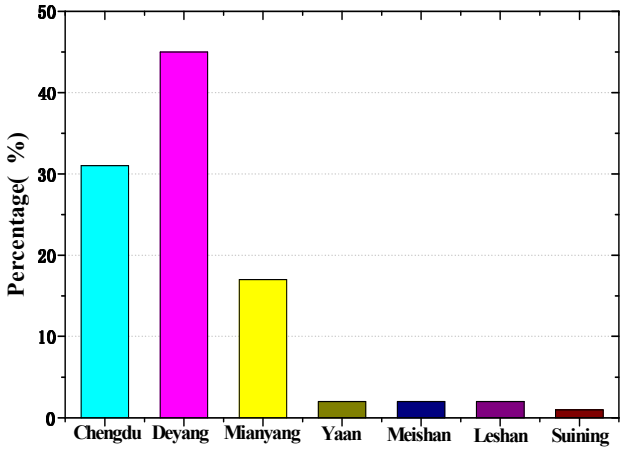


Fig. 2 Liquefied sites distribution in each region

The liquefied sites distribution was different among different regions. As shown in Fig. 2, the liquefaction mainly distributed in three regions, i.e., Chengdu, Mianyang and Deyang. Deyang is the most serious liquefied region, followed by Chengdu region, and the Mianyang region is the relatively lightest. Other areas include Meishan region, Leshan region, Suining region and Ya'an region etc, and all these regions were mostly located in intensity VI, and the liquefaction phenomenon was less. The major liquefied regions were Chengdu region, Deyang region and Mianyang region in Wenchuan earthquake. According to statistics, the number of investigative liquefied points is 38, 50 and 22 in Chengdu, Deyang and Mianyang region, respectively. Liquefaction generally occurred in the extensive villages, and most of liquefaction accompany with ground fissures and subsidence.

Liquefied points distribute in many intensity ranges. Fig.3 shows the distribution of liquefaction in different intensity of the three major liquefied areas. Liquefied sites of Chengdu region have been found in seismic intensities VI, VII, VIII, IX and X, but most were located in intensities VII. In Deyang region, liquefied sites have been found in seismic intensities VII, VIII, and IX, but most were located in intensities VIII. And in Mianyang region, liquefied sites have been found in seismic intensities VII and VIII, but most were located in intensities VII. Statistically, Wenchuan earthquake liquefaction mainly distributed in intensities VII and VIII, and the liquefaction distribution in different regions were different. Chengdu and Mianyang were similar in intensities VII and VIII, but Deyang mainly in intensity VIII. Less liquefaction phenomenon were found in intensities X and XI, the major reasons is that the highly seismic region were located in mountains.

Fig. 3 shows that the three major liquefied regions spanned more earthquake intensity zones from intensity VI to IX, but mainly were located in intensities VII and VIII. Liquefaction phenomenon was rarely found in high earthquake seismic intensity zone, meaning no reciprocal relationship exists between the occurrence of liquefaction and the seismic intensity in Wenchuan earthquake.

Sand Boils and Water Spray

The ejected materials in liquefied sites basically covered many soil categories, including fine-silty sand, medium sand, coarse sand and gravely sand. Gravely sand ejected rarely appeared in previous earthquakes. Over 80% of liquefaction caused ground fissure, leading to formation of sinkholes. But

the dimension of sand-spraying is not biggest, quality of sand-spraying is very small in single hole, the biggest is not more than few cubic meters, but the phenomenon of sand-spraying hundreds of cubic meters had appeared in Tangshan and Haicheng earthquakes.

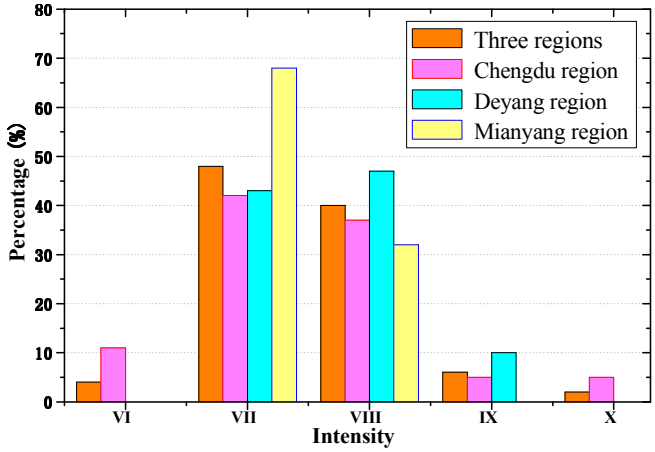


Fig. 3 Liquefied sites distribution in each intensity

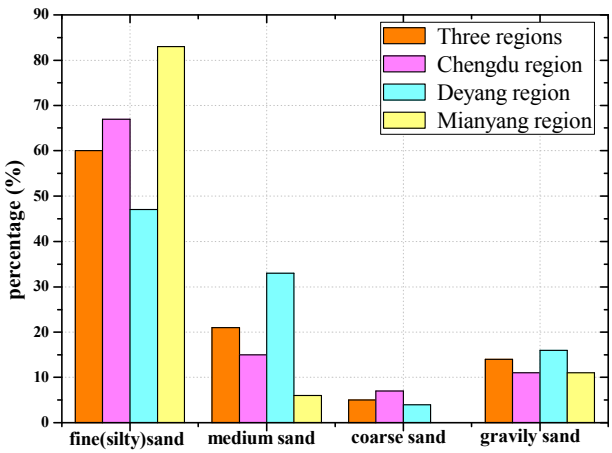


Fig. 4 Percentage of soil categories ejected to the ground

Liquefaction in Deyang region mainly concentrates in Mianzhu city, Shifang city and Deyang city, and Mianzhu city is the most serious. Liquefaction in Chengdu region mainly concentrated in Dujiangyan city and in Mianyang region majorly concentrate in Youxian region and Jiangyou city.

Sand-spraying materials contained fine sand, silty sand, medium sand, coarse sand and gravely sand. In Fig. 3, percentage histogram charts of soil categories ejected to the ground in three major liquefied regions shows that the sand categories of ejecta in Deyang region included about 50% fine (silty) sand, more than 30% medium sand, less than 5% coarse sand and about 16% gravely sand; the sand categories of ejecta in Chengdu region included more than 60% fine (silty) sand, about 15% medium sand, less than 10% coarse sand and about 10% gravely sand; the ejected materials in Mianyang liquefaction sites included 83% mealy-fine sand, 6% medium sand and 11% gravelly soil. Coarse sand ejection was not found in Mianyang region. The sand ejecta in Wenchuan earthquake liquefaction sites overall covered many sand categories, including more than 60% fine (silty) sand, about 21% medium sand, less than 5% coarse sand and about 15% gravely sand.

Liquefaction Damage

Seismic liquefaction damages were difference among three major liquefied regions. Table 1 shows the liquefaction damages situation of three major liquefied regions. As shown in table 1, Deyang region for seismic liquefaction damages was the most serious; Chengdu region ranged the second, and Mianyang region is the lightest.

According to preliminary statistics, about 1600-1800 mu farmlands were affected by liquefaction in Wenchuan earthquake. The fields were covered by sand-spraying materials, and the cracks leaded to soil and water loss. About tens of kilometers roads, 6 bridges, 7 schools and 4 factories were affected by liquefaction in different extents, involving in 100-120 villages.

Table 1 Liquefaction damages situation of three major liquefied regions

Region/types of damages	Farm land(mu)	Houses	Road(kilometer)	Bridge	School	Factory
Deyang region	800-900	40-50	tens	4	4	2
Chengdu region	500-600	40-50	tens	2	2	1
Mianyang region	about300	> 20	none	none	1	1

Conclusions

Through field investigation, the acquaintance of liquefaction in Wenchuan earthquake in three major liquefied regions was presented, and the macro-characteristics and damage features concerning on liquefaction issues were elucidated.

Mianyang region, Deyang region and Chengdu region are the three major liquefaction affected regions in Wenchuan earthquake. Deyang region is the most serious liquefied region followed by Chengdu region, and the Mianyang region is the lightest.

Liquefaction damage was considerably large, and basically was farmland. Liquefied sites mainly concentrated in intensities VIII in Deyang region, intensity VII in Chengdu region and intensity VII in Mianyang region.

In Deyang region, the percentage of gravel ejecta is the largest in the three major liquefied regions. In Chengdu region, the sand ejecta covered many sand categories. In Mianyang region, 80% of the sand ejected was fine-silty sand while coarse sand ejection was not found.

Acknowledgements

This work was financially supported by the Public Welfare Specialized Project in Earthquake Engineering (200708001).

References

[1] H. Liu, The great Tangshan earthquake of 1976, Published by Earthquake Engineering Research Laboratory, California Institute of Technology, Pasadena, 2002.
[2] W. Wang, X. Yuan, L. Chen, et al., Journal of Earthquake Engineering and Engineering Vibration 31 (2011) 145-154. (in Chinese)
[3] X. Yuan, Z. Cao, R. Sun, et al., Chinese Journal of Rok Mechanics and Engineering 6 (2009) 1288-1296. (in Chinese)
[4] Z. Cao, L. Hou, H. Xu, et al., Journal of Earthquake Engineering and Engineering Vibration 9 (2010) 167-175. (in Chinese)

© (2012) Trans Tech Publications, Switzerland
doi:10.4028/www.scientific.net/AMM.238.860

Research on Zoning Technology of the Liquefaction Seismic Settlement Based on MAPGIS

Xun Lu[1, a], Rui Sun[1, b], Yurun Li[2, c] and Longwei Chen[1, d]

[1.] Key Laboratory of Earthquake and Engineering Vibration, Institute of Engineering Mechanics, China Earthquake Administration, Heilongjiang, Harbin 150080, China

[2.] College of Civil Engineering, Hebei University of Technology, Civil Engineering Technology Research Center of Hebei Province, Tianjin, 300401，china

[a] 253413674@qq.com, [b] iemsr@163.com, [c] iemlyr7888@163.com, [d] longweichen83@gmail.com

Keywords: Liquefaction; seismic settlement; zoning technology; MAPGIS.

Abstract: Liquefaction seismic settlement is one of the typical nature disasters caused by earthquake, which always leads to wall cracking due to uneven settlement of the building. In the previous research work, scientists only study on the failure mechanism and the calculation method of the seismic settlement, the zoning technology about liquefaction seismic settlement have not been proposed. So that, utilizing the function of MAPGIS, this paper puts forward the zoning technology of the liquefaction seismic settlement.

Introduction

Seismic settlement refers to soil layer occurs permanent additional settlement by earthquake, and it is classified into even seismic settlement and uneven seismic settlement. Among them, uneven seismic settlement causes greater harm than even seismic settlement, which always leads to wall cracking.

In the earthquake occurred in Japan in 1964, the damage caused by seismic settlement is the most typical damage one among the world's previous earthquakes. In this earthquake, there were about 2300 buildings had been damaged by seismic settlement, and most of them were damaged by uneven seismic settlement. After 31 years, the similar damage occurred in the Kobe earthquake of Japan. Among the world's previous earthquakes, we can see that seismic settlement causes serious damage to buildings, roads, bridges, underground pipelines and so on, which leads to the great loss of property.

Calculation Method of the Liquefaction Seismic Settlement

Yoshimine and others (2006) proposed a calculation method of liquefaction seismic settlement as follows:

1) The correction of raw SPT blow count

The raw SPT blow count data were normalized and corrected to $(N_1)_{60}$ values by:

$$(N_1)_{60} = N_m C_N C_E C_B C_R C_S . \quad (1)$$

Where N_m is the measured standard penetration resistance (SPT blow count); C_N is used to normalize N_m to a common reference effective overburden stress of approximately 100 kPa, C_E varies from 0.5 to 1.3 depending on the type and efficiency of the hammer used in the SPT testing, C_B ranges from 1.0 for a 65-mm diameter hole to 1.15 for a 200-mm diameter hole, C_R ranges from 0.75 for less than 3 m of rod to 1.0 for 10 to 30 m of rod, C_S varies from 1.0 for samplers with liners to a value of 1.1 to 1.3 for samplers without lines.

Then correct $(N_1)_{60}$ values to clean sand values :

$$(N_1)_{60-CS} = \alpha + \beta (N_1)_{60} . \quad (2)$$

Where the α and β coefficients are determined by:

$\alpha = 0$, for $F_C \le 5\%$; $\alpha = \exp[1.76 - (190 / F_C^2)]$, for $5\% < F_C < 35\%$; $\alpha = 5.0$, for $F_C \ge 35\%$.

$\beta = 1.0$, for $F_C \ge 35\%$; $\beta = [0.99 + (F_C^{1.5} / 1000)]$, for $5\% < F_C < 35\%$; $\beta = 1.2$, for $F_C \ge 35\%$.

To implement Yoshimine and others (2006), the clean sand SPT blow count values were converted to N_1 values using Seed and others (1985) to account for traditional Japanese sampling practices and techniques:

$$N_1 = \frac{(N_1)_{60-CS}}{0.9} \quad \text{for } (N_1)_{60-CS} < 20 \tag{3a}$$

$$N_1 = (N_1)_{60-CS} \quad \text{for } (N_1)_{60-CS} \ge 20 \tag{3b}$$

2) Calculation of the relative density (*D*r):

$$D_r = 21\sqrt{\frac{N_1}{1.7}} \tag{4}$$

3) Calculation of the likelihood of liquefaction triggering (*FS*):

$$FS = \frac{R}{L} \tag{5}$$

$$R = 0.0882\sqrt{\frac{N_1}{1.7}} \quad \text{for } N_1 < 14 \tag{6a}$$

$$R = 0.0882\sqrt{\frac{N_1}{1.7}} + 1.6E^{-6}\left(\frac{N_1}{1.7}\right)^{4.5} \quad \text{for } N_1 \ge 14 \tag{6b}$$

$$L = \gamma_d \left(\frac{\sigma_v}{\sigma_v^{'}}\right)\left(\frac{\alpha}{g}\right) \tag{7}$$

$$\gamma_d = 1.0 - 0.015D \tag{8}$$

Where N_1 is the normalized and corrected Japanese-modified SPT blow count, σ_v is the total overburden pressures, $\sigma_v^{'}$ is the effective overburden pressures, α is the PGA, *D* is the depth from ground surface, γ_d is a stress reduction factor.

4) Calculation of the maximum single amplitude of shear strain ($\gamma_{\max}$):

$$\gamma_{\max} = 3.5 \times (2 - FS)\frac{1 - F_{ult}}{FS - F_{ult}} \quad \text{if } F_{ult} \le FS \le 2.0 \tag{9a}$$

$$\gamma_{\max} = 0 \quad \text{if } FS \ge 2.0 \tag{9b}$$

$$\gamma_{\max} = \infty \quad \text{if } F_{ult} \le FS \tag{9c}$$

$$F_{ult} = -0.0006D_{r,ini}^2 + 0.047D_{r,ini} + 0.032 \quad \text{if } D_{r,ini} \ge 39.2\% \tag{10a}$$

$$F_{ult} = 0.9524 \quad \text{if } D_{r,ini} < 39.2\% \tag{10b}$$

Where F_{ult} is a nameless intermediate variable, $D_{r,ini}$ is the initial relative density.

5) Calculation of the percent liquefaction-induced volumetric strains (ε_V):

$$\varepsilon_V = 1.5[\exp(-0.025D_{r,ini})]\gamma_{\max} \quad \text{if } \gamma_{\max} \le 8\% \tag{11a}$$

$$\varepsilon_V = 12\exp(-0.025D_{r,ini}) \quad \text{if } \gamma_{\max} > 8\% \tag{11b}$$

6) Calculation of the liquefaction seismic settlement (Δ_Y):

$$\Delta_Y = \sum_{i=1}^{n} t_i \times \varepsilon_{v,i} \tag{12}$$

The Zoning Technology of the Liquefaction Seismic Settlement

After liquefaction seismic settlement values of every borehole had been figured out by using the calculation method as the above, A zoning map (as Fig. 1) of liquefaction seismic settlement which based on MAPGIS had been completed by taking the Tangshan city and its south region as an object of research, and according to the method of Table 1 as follows.

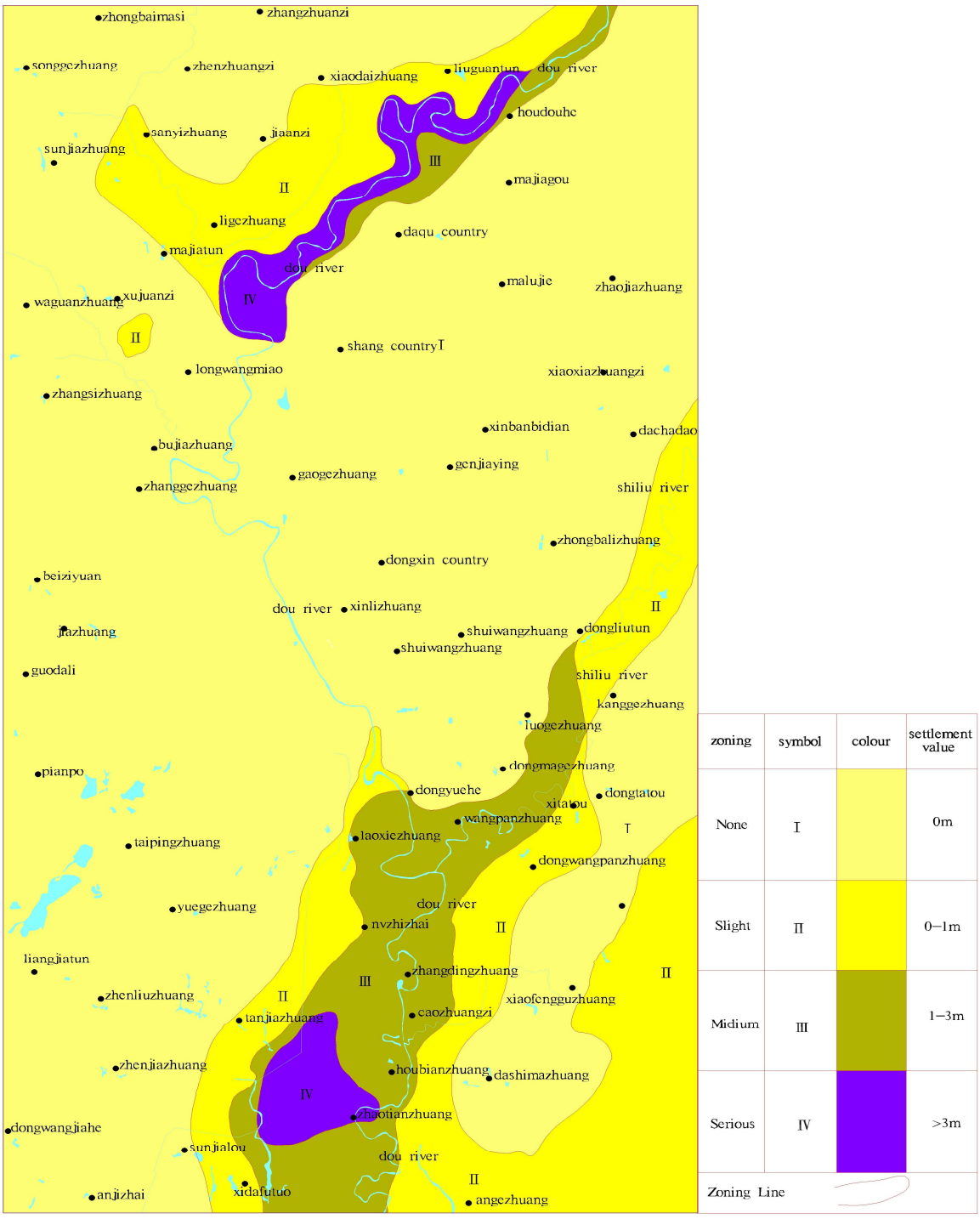


Fig. 1 Zoning map of liquefaction seismic settlement for Tangshan city and its south region

Table 1 Grade divition of liquefaction seismic settlement

Grade	None	Slight	Midium	Serious
Liquefaction seimic settlement value (mm)	0	0～10	10～20	≥20

Conclusions

A calculation method of liquefaction seismic settlement was introduced, and by using it, liquefaction seismic settlement values of every borehole were figured out.

Implemented the stimulation on zoning of liquefaction seismic settlement for Tangshan city and its south region based on MAPGIS, and finally a zoning map of liquefaction seismic settlement for Tangshan city and its south region was given, which can be used in site selection for large scale engineering.

Acknowledgements

This work was financially supported by Specific Item of Fundamental Scientific Research in Institute of Engineering Mechanics (2011B07).

References

[1] Daniel W. Hinckley, Liquefaction-induced Ground Displacement Mapping for The Salt Lake Valley, Utah. Salt Lack City, The University of Utah, 2010.

[2] Steven F. Bartlett, Utah's Plan for Developing the Next Generation of Liquefaction Hazard Maps, Salt Lack City, The University of Utah, 2010.

[3] X. Wu, MAPGIS Geographic Information System, Electronic Industry Press, Beijing, 2004.

© (2012) Trans Tech Publications, Switzerland
doi:10.4028/www.scientific.net/AMM.238.864

Correlation of Site Characteristic Period with Predominant Period of Ground Acceleration by a Simplified Model

Longwei Chen [a], Weiming Wang [b] and Rui Sun [c]

Key Laboratory of Earthquake Engineering and Engineering Vibration, Institute of Engineering Mechanics, CEA, 29 Xuefu Road, Harbin 150080, China

[a]longweichen83@gmail.com, [b]wswwm1983@163.com,[c]iemsr@163.com

Keywords: site characteristic period; predominant period; model; ground motion.

Abstract. Site characteristic period is an important index in seismic zonantion and seismic resistance design. The characteristics of the ground motions are conceptually related with site characteristics. A simplified single-layer model is used for simulating horizontal strata under seismic loading to calibrate the correlation of site characteristic period with the predominant period of ground motion. The analytical results show that the inputted motions were amplified considerably by the site typically for the period components which were close to the site characteristic periods; with the shear wave velocity of the soil layer decreases with respect to the initial shear wave velocity, the predominant period of ground motion increases; the site characteristic periods are consistent with the predominant periods of the ground motion.

Introduction

Seismic wave theories are the fundamental concepts in earthquake engineering and engineering seismology. In strong earthquakes, site soil exhibits non-linearity and the shear strength of the soil reduce, *i.e.*, softening. The soil nonlinearity can significantly change the soil characteristics and the characteristics of ground motions. Hence, site characteristic has strong influence on ground motions, and much research work has been done to contribute to such topics [1-4]. In the views of seismic records on liquefied sites, for example, the high-frequency components are dramatically reduced and, alternatively, low-frequency components or long-period components are enlarged. Youd [2] analyzed the records on liquefied site and found that liquefaction clearly amplified the long period (T>1.0) components in the acceleration response spectra. Meanwhile, he emphasized that the seismic design spectra for short period (T<1.0s) structures on liquefiable sites tend to be conservative while for long period (T>1.0s) structures generally they tend to be conservative for soft sites but non-conservative for hard sites in the current codes used in United States. The double effects of site liquefaction on ground motions have been focused on and preliminary results have been adopted in seismic design codes used in many countries. Sun [4] used theoretical calculation and analyzed the site records on liquefied sites and then pointed that the characteristic periods of acceleration spectra were shifted by at least 0.1s and on average 0.3s; a threshold of 0.8s in response spectra divided energy-absorption and shock aggravation effects by liquefaction. However, the correlation of site characters with the characters of ground motion has not been fully understood. The correlation of site characteristics and the characteristics of ground motions has not been linked.

In this paper, a simplified single-layer model is used to roughly simulate horizontal strata. Adopting the real time ground motion analysis method proposed by the authors [7], the ground surface accelerations were calculated and the corresponding response spectra were computed. The site characteristic period is compared with the predominant periods of the ground motion.

Model and Solution

A real site is roughly simplified by a single-layer model (Fig. 1) and the model parameters are listed in Table 1, in which v_s represents the initial shear wave velocity of the soil layer before loading while v_s' represents the shear wave velocity after soil softening. Even by such advantageous simplification, the physical meaning was remained but the calculation was easy.

By means of steady-state wave propagating in soil medium methods, an amplification coefficient function of the soil strata can be deduced. Using complex damping theories and supposing a Kelvin-Voigt viscous elastic soil medium, the amplification coefficient function of the soil strata under steady state wave incidence can be written as [5, 6],

$$R_1 = \frac{1}{\left|\cos\left(\frac{\beta_1}{1+\xi_1 \mathrm{i}}\right)\right|} \approx \frac{1}{\sqrt{\sinh^2(\xi_1\beta_1)+\cos^2\beta_1}} \tag{1}$$

Where $\beta_1=\omega h_1/v_s$; ω is frequency of incident wave; h_1 is the thickness of the soil layer; v_s is the shear wave velocity of soil layer; ξ_1 is the damping ratio.

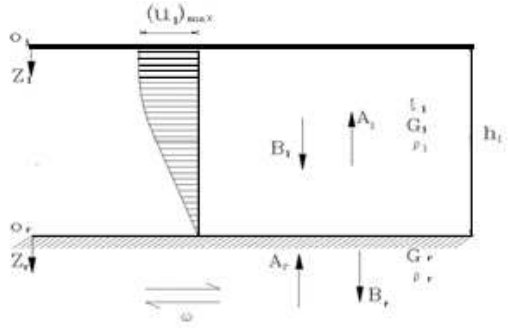


Fig. 1 Simplified models of 1D horizontal strata

The inputted motions were used Beijing wave time history which was recorded in 1976 Tangshan, China, earthquake and Northridge wave time history which was recorded in 1994 Northridge, USA, earthquake (Fig. 2). The PGAs are 2.0m/s^2 and 2.4m/s^2, respectively. In Fig. 3, the main period components of Beijing wave range from 0.1s to 1.5s while those of Northridge wave are in 0.2s to 1.5s.

Table 2 Parameters for 1D model

No.	v'/v_s	v_s/(m/s)	h_1/(m)	Characteristic period T_c/(s)
1	1.0	200	10	0.2
2	0.8	200	10	0.25
3	0.4	200	10	0.5
4	0.2	200	10	1.0

The site characteristic periods were estimated by,

$$T_c = \frac{4h_1}{v_s} \tag{2}$$

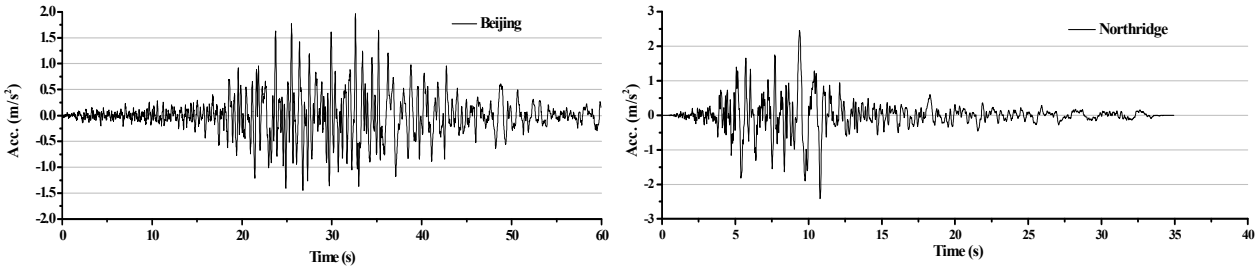


Fig.2 Time histories of the inputted motions (left: Beijing; right:Northridge)

Following the procedure for ground motion calculation in reference [7], the revevant ground motion time histiories (Fig. 3) under inputted motions were calculated and the corresponding response spectra were shown in Fig.4. With decreasing shear wave velocity of the soil layer, the predominant period of the ground motion increase, i.e., the peak values of the response spectra shift right. Meanwhile, the site characteristic period decreases. To characterize the site characteristic periods with the predominant periods of ground motions, Fig. 5 presents the characteristic periods with respect to the predominant periods the ground motions.

In Fig.3 of the calculated ground motions, the long period components in the calculated ground motions increase with decreasing shear wave veoity ratios and also the amplitudes increase except for the case of shear wave velocity ratio 0.2 under Beijing wave inputted. Hence, the high frequency components of the inputted motions were generally filtered by soil softening but the amplitude of long-period components were amplified.

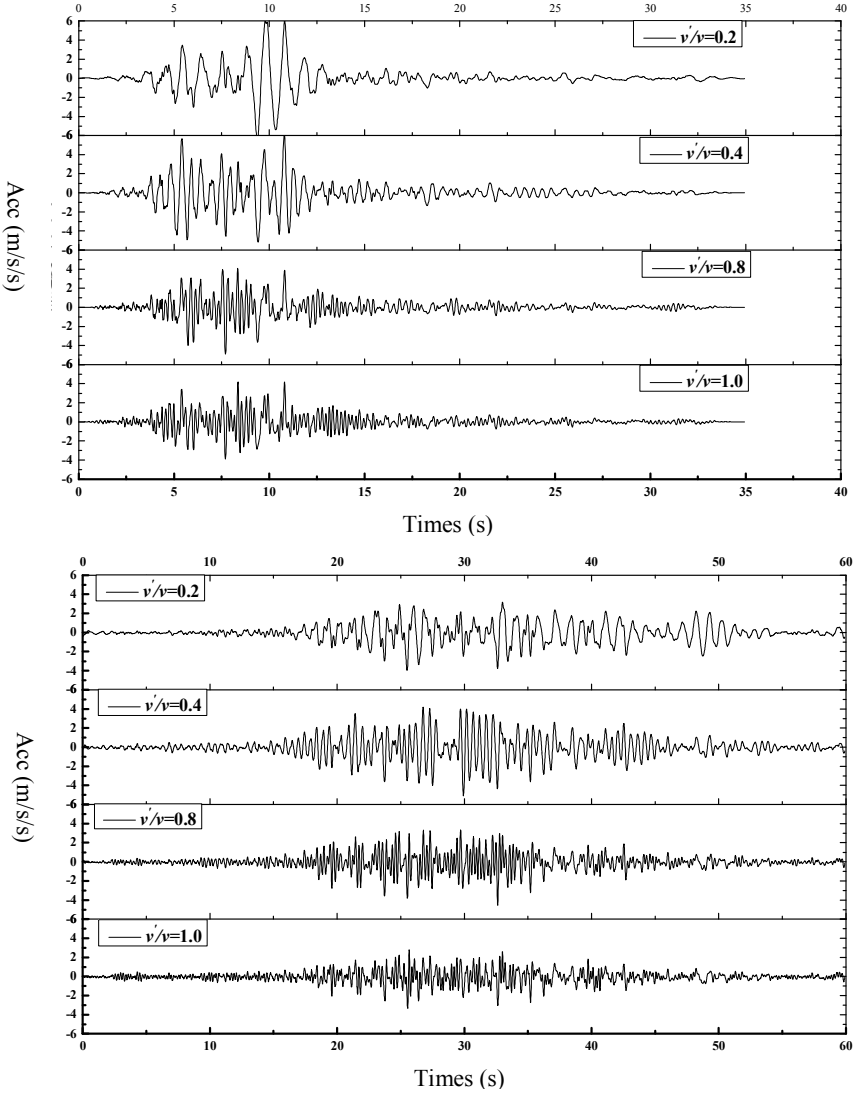


Fig.3 Calculated acceleration time histories under Northridge wave (left: Northridge; right: Beijing)

In the four cases, the site characteristic periods are 0.2s, 0.25s, 0.5s and 1.0s which are in the main period ranges of the inputted motions. Therefore, the amplifying effect of the site on inputted ground motions are considerable as shown in Fig.4, especially for the period components which are close to the site characteristic periods.

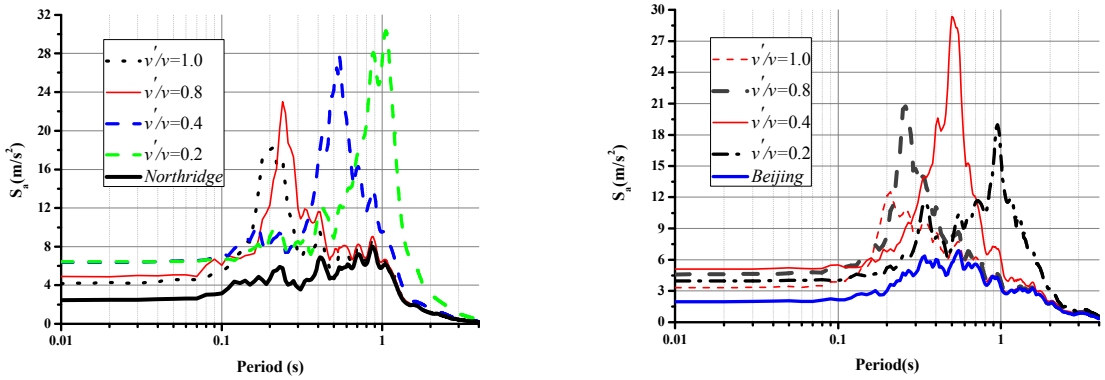


Fig.4 Site characteristic period ratios with respect to varing shear wave velocity ratios

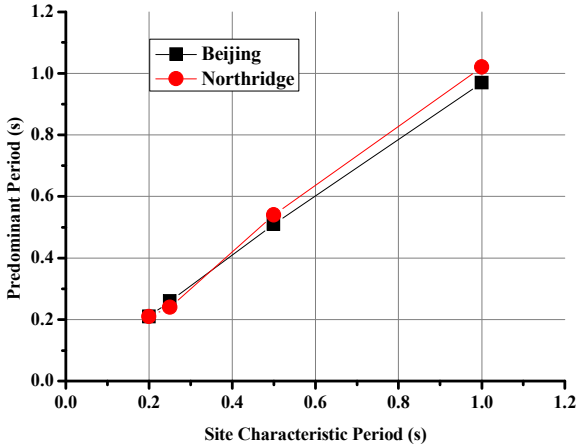


Fig.5 Relation of site characteristic periods with predominant periods of calculated ground motions

As shown in Fig.5, the site characteristic periods are consistent with the predominant periods of the ground motions, which means that predominant period of ground motion is typically determined by the combination of site characteristic period and the period components of inputted motion.

Conclusions

The main work and conclusions in the paper can be outlined as:

A simplified single-layer model is used for simulating horizontal strata under seismic loading, and the ground motions and corresponding spectra were calculated.

The inputted motions were amplified considerably by the site typically for the period components which were close to the site characteristic periods.

With the shear wave velocity of the soil layer decreases with respect to the initial shear wave velocity, the predominant period of ground motion increases.

The site characteristic periods are consistent with the predominant periods of the ground motion.

Acknowledgements

This work was financially supported by Specific Item of Fundamental Scientific Research in Institute of Engineering Mechanics (2011B07).

References

[1] G.T. Zorapapel, M. Vucetic: Earthquake Spectra, Vol. 10 No. 2 (1994) 403-438.

[2] T.L. Youd, B.L. Carter: Journal of Geotechnical and Geoenvironmental Engineering, Vol. 131 No. 7 (2005) 810-825.

[3] I.M. Idriss: Second International Conference on Recent Advances in Geotechnical Earthquake Engineering and Soil Dynamics, 1991.

[4] R. Sun, X. Yuan: Chinese Journal of Geotechnical Engineering Vol. 26, No. 5 (2004) 684-690.

[5] L. Chen, W. Wang and X. Yuan: Advanced Material Research Vols. 446-449 (2012) 1404-1407.

[6] Z.P. Liao: Wave Propagation Theory in Engineering Practice, Seismic Press, Beijing, 1996.

[7] L.W. Chen, X.M. Yuan and R. Sun: Rock and Soil Mechanics, Vol. 31 (2010) 3823-3828.

© (2012) Trans Tech Publications, Switzerland
doi:10.4028/www.scientific.net/AMM.238.868

Study on Anti-seismic Reliability of Urban Water Supply System

Xiaojuan Li[1,2,a] and Feimin Shen[1,b]

[1]College of Civil Engineering, Fuzhou University, Fuzhou 350001, China；

[2]Traffic College of Fujian Agriculture-Forest University, Fuzhou 350002, China；

[a]luckylxj2001@126.com; [b]1003474815@qq.com

Key words: buried pipeline; anti-seismic reliability; Monte-Carlo method; network connectivity.

Abstract. According to the seismic damage mechanism of the buried pipeline，the seismic performance of single pipeline is evaluated quantitatively. The network connectivity is analyzed with Monte-Carlo method and seismic performance of the whole network system is evaluated quantitatively. Finally, the anti-seismic reliability of the main water supply system is analyzed in the City of Fuzhou. The results indicate that the proposed method is feasible, accurate and effective, which provides references for further research of design, optimization and reformation of the urban buried pipeline.

Introduction

Urban Water Supply System is one important part of city lifeline engineering, and the buried pipelines is the basic structural unit .As a matter of experience, There are two reasons that cause the bury pipelines' damage by the earthquake [1]. One is that the earthquake destroy the place, and the other is that the transmission of the earthquake may cause great relative displacement. Based on the seismic performance of single pipeline under the effective of the earthquake, the single pipeline's axial deformation can be defined. According to the probability distribution of the pipe resistance, the probability of failure is calculated based on the reliability analysis method. And using Monte-Carlo, the connectivity and reliability of water supply system is calculated. So instance results show it is good.

Pipeline Monomer Earthquake Damage Calculation Method

Pipeline Seismic Response of a Simplified Calculation Model. Subjected to seismic waves, Pipeline around the land in a different point will have relative displacement, which make pipe bend and produce axial deformation. So bending deformation are negligible [2]. Calculation for the axial deformation, we often use Quasi-static analysis and seismic wave input. For the pipeline seismic deformation, we use Semi-theoretical semi-empirical seismic wave input generally [3].

Determination of Pipeline Failure Probability. Set pipeline state under function of the earthquake as

$$Z = f\ (R,S) = R - S \tag{1}$$

Where Z is a extraneous variable, R is the limit of pipeline axial deformation, S is the largest pipeline axial deformation under seismic action.

If R follows a normal distribution and S is a fixed value, then Z also follows a normal distribution, Density function:

$$f(z) = \frac{1}{\sqrt{2\pi}\sigma} \mathrm{e}^{-\frac{(x-\mu)^2}{2\sigma^2}} \tag{2}$$

In this formula, $u = u_R - \Delta L$; $\boldsymbol{\sigma} = \boldsymbol{\sigma}_R$.

U is the average of z, σ is the standard deviation of z;μ_{R}, σ_{R} are respectively meaning that standard deviation of the value of the limit and deformation of the pipe joints[4]; ΔL is pipeline's largest axial deformation under seismic action.

Probability of pipeline connectivity is

$$P_S=\Phi(u/\sigma) \tag{3}$$

In this Formula, $\Phi(\bullet)$ represents the standard normal distribution function.

Analysis on Pipe Network System Earthquake Damage Connectivity Reliability

Graph Theory and Graph Connectivity. Specializes in network diagram which consisting of a set of nodes and connections, some of which node the edge discipline called graph theory. Water supply system can simplify the diagram of the grounds of nodes and connecting rod. Therefore, you can use graph theory analysis system connectivity and reliability under seismic action. Usually the connectivity of each node in the graph with the adjacency matrix **A**. Assuming:

$$A^n=[a_{ij}] \tag{4}$$

In this formula, n is the number of edges i, j node connectivity through, a_{ij} denotes the node connectivity, when $a_{ij}\neq 0$, i, j node via n edges connected, when $a_{ij}=0$, I and j node can not be connected by n edges. Fig. 1 is a connected graph without node.

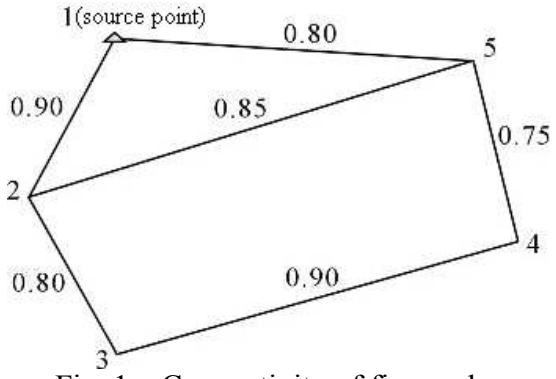


Fig. 1 Connectivity of five nodes

According to Fig. 1, the specific form of **A:** $A=\begin{bmatrix}1&1&0&1&1\\1&1&1&0&0\\0&1&1&1&0\\1&0&1&1&1\\1&0&0&1&1\end{bmatrix}$

The calculation based on the connectivity of the graph theory, in Fig. 1, each node which wants to connect several edges can be expressed as:

$$\mathbf{M}=\mathbf{A}+\mathbf{A}^2+\mathbf{A}^3+\mathbf{A}^4 \tag{5}$$

Where **M** is each node connected state matrix. Zero in **M** is on behalf of that corresponding nodes both after a few edges (the number of edges is less than the total number of nodes) are not passed. Otherwise, If **M** is non-zero elements, it said at least one path exists between any two nodes, and the graph is called connected graph [4].

Monte-carlo Method. Monte carlo method is commonly used algorithm for connectivity and reliability of the network system, using connectivity probability of each side of the network. Approximation to reproduce the connectivity status of each side by a large number of stochastic simulation, then it can calculate the network. In Figure 1, for example, the Monte-Carlo method to calculate the pipe network connectivity is the reliability of the following steps.

Step 1 According to the earthquake damage of the pipeline monomer calculated, the probability P of each side of the network connectivity on a seismic intensity is determined, so that the results marked on all sides.

Step 2 Using random number generator to generate a random number η in the matrix of the random number is composed of elements and contrast, the adjacency matrix **A**:

$$a_{ij} = \begin{cases} 1(P_s \le \eta) \\ 0(P_s > \eta) \end{cases} \tag{6}$$

Step 3 A compute nodes in step 2 of the connection state matrix:

$$M=A+A^2+\cdots+A^{n-1} \tag{7}$$

In this formula, n is the number of nodes, in this article, n = 5.

Step 4 According to **M** in step 3, record the Meeting Point and the connection of the source, and count the number.

Step 5 Repeating steps 2 through 4, make statistical frequency about each exchange point and the connectivity of source point. Enough for a long time when the number of simulations (analog 5000), the results become stable. Then the connectivity of the Meeting Point frequency can be approximate as the probability of connectivity of the Meeting Point.

Get connectivity probability by Monte-Carlo simulation of the Meeting Point in Fig. 1, and list in Table 1. It can be seen that the algorithm of the Monte-Carlo method is simple with high precision

Table 1 Connecting probability of meeting points

Meeting points	Monte-Carlo method	Exact solution	error/%
2nd	0.9704	0.9745	-0.42
3rd	0.9056	0.9095	-0.43
4th	0.8990	0.9038	-0.53
5th	0.9662	0.9676	-0.15

Practical Examples

Seismic reliability of a water supply system in Fuzhou, for example, its water supply pipes with ordinary cast iron pipes, socket-style apron asbestos gray flexible joints. The area of ground motion parameters in Table 2, according to the literature [5] , to calculate part of the pipeline buried in the area of small earthquakes, middle earthquake and large earthquake in shock. The connectivity probability of the earthquake is shown in Table 3, in which T_1 is the time of the earthquake response spectrum reached a peak value, T_2 site soil excellent cycle, β_m is the power coefficient, ∂_{max} is the maximum value for the coefficient of the earthquake.

Table 2 Ground motion parameters of region

50 probability of transcend (%)	T_1 (s)	T_2 (s)	β_m	α_{max}
63 (small earthquake）	0.1	0.40	2.5	0.075
10 (middle earthquake）	0.1	0.45	2.5	0.201
2 (large earthquake）	0.1	0.55	2.5	0.351

Table 3 Connectivity probability of single pipeline under different seismic intensity

Pipeline	Tube length	Diameter (mm)	Connectivity probability		
			Small earthquake	Middle earthquake	Large earthquake
1	1828	1200	0.928	0.892	0.874
2	1826	800	0.925	0.890	0.875
3	1325	800	0.938	0.903	0.886
4	1144	800	0.943	0.918	0.892
5	1101	800	0.945	0.921	0.896
6	785	500	0.965	0.943	0.913
7	783	400	0.961	0.938	0.907
8	789	350	0.957	0.934	0.906
9	2253	400	0.797	0.743	0.695
10	3281	800	0.744	0.692	0.628

In the pipeline on the basis of the single assessment, according to the method of network systems to earthquake damage evaluation in Section II, we can get down on the exchange point in the area of small earthquakes, middle earthquake and large earthquake connectivity probability in Table 4. The underground pipelines under the earthquake may easy destroyed, and thus impact shock production of the normal supply of domestic water.

Table 4 Connectivity probability of pipe network system under different seismic intensity

Meeting point	Connectivity probability		
	Small earthquakes	Middle earthquakes	Large earthquakes
1st	0.922	0.903	0.872
2nd	0.955	0.932	0.905
3rd	0.946	0.923	0.894
4th	0.876	0.852	0.823
5th	0.897	0.873	0.853
6th	0.863	0.842	0.824

In order to improve the seismic performance of urban water supply systems, we can do the following aspects: to minimize the length of a single pipeline. When you need long-distance water transfer, multi-stage pipeline can be laid and the use of flexible joints. Under the premise of considering the economy, demand for water, as much as possible the laying of pipelines and the establishment of water points.

Conclusions

The seismic analysis of the urban water supply systems can be divided into unit level and system level. Unit level of analysis can be used seismic waves to simplify the harmonic simplified calculation model, and the maximum deformation of the pipe earthquake reached the limits of deformation of the bearing capacity limit state. Monte Carlo algorithm for connectivity and reliable water supply network get earthquake probability of the Meeting Point and the connectivity of the water points. The whole method can solve accurately and efficiently the seismic reliability of large and complex water supply system, which provide a theoretical basis for the city water supply system optimized design and Retrofitting.

References

[1] Z. Hou: Underground pipelines earthquake, Academic Books Press, Beijing, 1990.

[2] T. Ariman and G. E. Muleski: The buried pipeline response under seismic excitation, Earthquake Engineering and Structural Dynamics, 9 (1999) 133-151.

[3] G. Bai: The lifeline earthquake damage prediction system based on GIS, Dalian University of Technology, Dalian, 2007.

[4] Y. Han. Urban underground pipe network system of seismic and reliable line, Dalian University of Technology, Dalian, 2002.

[5] X. Li, J. Zhou. Considering the nonlinear characteristics of the soil buried pipe-soil system dynamic response analysis, Journal of Computational Mechanics, 2 (2001) 167-172.

© (2012) Trans Tech Publications, Switzerland
doi:10.4028/www.scientific.net/AMM.238.872

A Study on the Analysis Method of Soil Layer Seismic Response in Seasonal Frozen Site

Zhuoshi Chen[1,2,a], Shangjiu Meng[3,b], Yurun Li[4,c] and Longwei Chen[1,2,d]

[1]Institute of Engineering Mechanics, China Earthquake Administration, Harbin 150080, China

[2]Key Laboratory of Earthquake Engineering and Engineering Vibration, Institute of Engineering Mechanics, CEA, Harbin 150080,

[3]Harbin University Of Science And Technology, Heilongjiang, Harbin 150080, China

[4]College of Civil Engineering, Hebei University of Technology, Tianjin 300401,China

[a]various@163.com, [b]iemmsj@163.com, [c]iemlyr7888@163.com, [d]chenlongwei83@126.com

Keywords: seasonal frozen site; shear wave velocity; dynamic shear modulus; soil layer seismic response.

Abstract. The analysis of ground motion on seasonal frozen soil mainly focused on the conventional soil, neglecting the impact of the permafrost which causes the obvious defeats in the existed calculation procedure. In this paper, the author proposed that we should apply the field test of shear wave velocity to the soil layer response calculation, improve the test method of dynamic shear modulus, and adopt the regular analysis method of soil layer response to the calculation of frozen soil site.

Introduction

The seasonal frozen grounds are widely distributed in China and many earthquakes occurred in the seasonal frozen soil areas. The soil layer will cause the effects of filtering and amplification to the seismic ground motion. The permafrost as a kind of special soil shows the significant mechanical properties from the following two aspects: the sensitivity to the temperature change, and the instability in the physical and mechanical properties. Compared with the soil in the normal temperature state, the shear modulus of frozen soil increases significantly, the shear strain decreases the compression modulus increase obviously, and the shear wave velocity increases which show part of the elastic characteristics. With the ground temperature rising, the pore ice in the permafrost melts into liquid water gradually, and a sharp attenuation of the elastic characteristics occurs in the permafrost. As a consequence, the creep and rheology will recover the permafrost to the soil in normal condition.

The unique mechanical properties of the seasonal frozen ground site are most likely to cause two kinds of engineering diseases. One is the frost heave phenomenon occurred during the frozen process of soil, which causes the damage to the foundation of engineering structure. The other is the occurrence of thawing settlement during the process of soil melting, which leads to the uneven subsidence damage to foundation. The seasonal frozen soil layers transform the homogeneous ground of normal state into double or even multi-layered soils with the uneven changes in the dynamic property, which changed the mechanical properties of ground layers, so that the soil seismic response impacts the upper structure directly. At present, the seismic engineering design bases on the calculation to the soil state at normal temperature was given out without considering the impact of permafrost though the engineering design basis. From the perspective of the building energy efficiency and environmental protection, the study on the seismic response of seasonal frozen areas has profound significance to design the structures rationally, saves the building materials organically, and improves the capacity of anti-seismic effectively.

The Basic Theories of Soil Layer Seismic Response

The theories of soil layer seismic response focus on studying the seismic response of the surface in the site under the condition of differ in soil thickness, ground structure, mechanical constitutive relation, seismic ground motion input, and mechanical parameters, etc. The soil layer seismic response is quit complicated which can be classified into two categories form the analysis to the research results: certainty analysis method and uncertainty analysis method. The differences between the two methods lie in the analytical methods to the seismic ground motion. The certainty analysis method defines the seismic ground motion as the function of time, whose model parameters are determined by the various constitutive relation models and the calculative condition of ground. The uncertainty analysis method regards the process of seismic ground motion as a random process with many discrete complex factors.

There are two research theories derived from the certainty analysis method: the equivalent linearization method, and the nonlinear method. The basic principle of the equivalent linearization method is that the discrete response parameters of soil layer can be replaced by the regular changed calculative parameters in the condition of rough equivalence to the mechanical effect. We represent the mechanical regression relation by a smooth regression curve, replace discrete shear modulus and damping ratio by the equivalent dynamic shear modulus, simplify the complex nonlinear calculation to the linear measure, and solve the matters in the frequency domain. The calculation of equivalent linearization method is simple with less number of iterations, which is used widely in the engineering design for the less using of the mechanical parameters and the simpler of the operation. The basic principle of the nonlinear method is that reflects the real laws of stress-strain by the study of the actual constitutive model of soil under the function of soil ground motion, and calculates the response of the soil layer exactly with the date points on the different hysteresis curve. The calculation of the nonlinear method is relatively complicated, but the results can simulate the actual change of soil better. However, this method hasn't been promoted in a wide range of the engineering project for the high technique level demanded in the selection of the stress-strain relation.

Corresponded with the certainty analysis method, the main principle of the uncertainty analysis method is that regards the soil ground motion as a series of random process which causes the uncertainty of the parameters selection. In the calculation of the uncertainty analysis method, the inputting soil ground motion and the calculative parameters are all uncertain under the certain site condition. The constitutive model selected by the uncertainty analysis method can make the selection based on the demand of the calculators which causes the calculation and the results relatively complicated so that the uncertainty analysis method hasn't been applied in the practice engineering process.

The Analysis of the Soil Layer Seismic Response in the Seasonal Frozen Area

The Calculation of the Permafrost Parameters. The general soil layer response analysis can calculate the acceleration of the soil in certain site of the surface or the ground, the response spectrum, and the maximum shear strain parameters by inputting the soil ground motion. After the determination of the soil layer analysis method, the frozen ground response calculation requires many parameters, including the soil ground motion, the soil thickness, the soil stratification state, the soil density, the shear wave velocity, shear modulus and the damping ratio, etc. in which the later three parameters affect the results of the soil layer response analysis significantly.

(1) Shear wave velocity is the most typical index of soil softness-hardness scale. The test of the shear wave velocity can be measured through the laboratory test and the field test. The current study of the shear wave velocity focuses on the test and calculation of the soil model through laboratory test. Because the remodeling mechanical properties of soil which differs from the actual site, whether the laboratory test can detect the variations of the soil shear wave velocity should be modified. The field test can adopt the single-hole method, the cross-hole method. With the steep rise of the shear wave velocity in winter, single-hole method and the cross-hole method are

inadequate to measure the soil shear wave velocity exactly for the limitations in the accuracy and condition of the test as well as the disturbance of human. The surface wave method is a new type of shear wave velocity test method of no soil constitutes damage and accurate test results, but the conditions of the test are so strict and the data processes are so complex that it isn't widely applied in the shear wave velocity test. In summary, the field test of the frozen soil shear wave velocity and the results from the laboratory test are very few, the values of the frozen soil shear wave velocity can only be analyzed qualitatively. The test results on the relative distribution of the amount of ice, the temperature, and the layer of the permafrost has not been published in public.

(2) The dynamic shear modulus and the damping ratio which reflect the nature of the soil can be obtained by the resonant column test. In terms of permafrost, the stiffness of soil caused the decrease of the shear strain and the increase of the dynamic shear modulus. In the maximum shear strain curve of the dynamic shear modulus and the damping ratio, the curve of the permafrost dynamic shear modulus ratio is relatively smooth compared with the normal soil curve, and the whole curve is located above it. The current studies apply the dynamic triaxial test to the test of dynamic shear modulus and damping ratio, but the maximum shear strain is much less than the normal condition, so that the dynamic triaxial test can't test the data accurately, only by fitting the permafrost strain modulus. This kind of test accuracy has been unable to meet the requirements of the soil response analysis. Existing on dynamic shear modulus and damping ratio of studies have been carried out a part, but not much soil, temperature dynamic shear modulus ratio -- shear strain values published. The value of the frozen soil dynamic shear modulus ratio and damping ratio can be selected only through the qualitative analysis, and the conducted study didn't display effective principles of the frozen soil layer on the soil dynamic characteristics parameters.

Research on the Seismic Response of Frozen Soil. Scholars have studied on frozen soil, given the different constitutive relation of models, and studied the macroscopic and microscopic mechanism of frozen soil. Frozen soil constitutive model is different from the normal soil, so it's very necessary to study the characteristics of seismic response. At present, the seasonal frozen soil seismic response analysis result is not much and clear.

Jilin Qi applied the scene of pulsation test and three triaxial tests of soil shear modulus and damping ratio in the seasonal frozen region [1]. Feng Gao studied the seasonal frozen soil and permafrost response acceleration, the law of response peak ground influence and the response spectrum [2]. U. Dutt studied different frequency spectrum under the permafrost ground motion according to ALASKA sites in different periods of seismic records [3]. Baipo Yang designed a six-story brick structure model of the foundation and structure in a category (type II) on the site, and argued that the existing rigid foundation assumptions of the multistory masonry buildings in terms of biased safety [4]. Lixia Wang studied the seismic engineering design and the different frozen soil roadbed under typical conditions of permafrost roadbed seismic response according to the construction of Qinghai-Tibet Railway [5]. Jiangang Sun studied the three categories of sites on the eight vertical storage tanks, and calculated the different seismic response of freezing and thawing soil in two under the conditions[6].

These studies analyzed the influence factors of ground surface response, built a variety of frozen soil mode and the seismic response analysis of soil layer. However, these work in understanding at present is not deep enough, even without calculation, with existing structural dynamics of general knowledge, we also can get some recognized qualitative knowledge, which is hard to solve engineering problems. Those existing examples are targeted at the particular venue of model, adapting the self-developed analysis program, calculating the diverse conclusions, conflicting actual earthquake damage phenomena, and the reliability of the method remains to be proved further. The selection of the calculation model and method affects the degree of reliability directly, and it lacks of the general calculating program on the frozen ground response analysis regulations.

Conclusions

At present, the studies of the frozen ground soil response analysis are fruitful, but the most important are listed as follows:

(1) Field test of the shear wave velocity in frozen soil site.
(2) The precision test of the frozen soil dynamic shear modulus and damping ratio.
(3) The study on the general program for calculation of frozen soil layer response.
(4) the research of the constitutive relationship of frozen soil.

Acknowledgements

This work was financially supported by Specific Item of Fundamental Scientific Research in Institute of Engineering Mechanics under grant No. 2011B07.

References

[1] J. Qi, W. Ma, Ground motion effect on the seasonal frozen soil in Zhangye Region, Chinese Journal of Rock Mechanics and Engineering, 24 (2005) 2082-2088.

[2] F. Gao, X. Chen, S. Yan. The impact of Seasonally frozen ground and permafrost to the seismic response, Chinese Journal of Rock Mechanics and Engineering, 25 (2006) 62-69.

[3] U. Dutta，Z. Yang, G. Xu and K. Hazirbaba, Effect of Seasonally Frozen Soil and Permafrost on Seismic Site Response. The 14th World Conference on Earthquake Engineering，Beijing，China, 2008.

[4] B. Yang, P. Sun, J. Shen, The damage prediction method for multi-storey brick house on the permafrost sites, Earthquake Engineering and Engineering Vibration, 6 (1999) 88-97.

[5] L. Wang, X. Ling, X. Xu, The characters of the earthquake dynamic stress response of the roadbed on permafrost site, Earthquake Engineering and Engineering Vibration, 27 (2004) 69-75.

[6] J. Sun, L. Wang, Z. Wei, The impact of seasonally frozen ground to the vertical storage tank seismic response, World Earthquake Engineering, 19 (2003) 55-59.

© (2012) Trans Tech Publications, Switzerland
doi:10.4028/www.scientific.net/AMM.238.876

Comparative Analysis of Seismic Responses of Different Layer Height Structures with Broken Stone Isolation Layers

Xinzhong Zhang[a], Lianjuan Miao[b] and Kedong Tang[c]

North China University of Water Resources and Electric Power, Zhengzhou 450011, China

[a]xinzhong.z@163.com , [b]mlj137@163.com, [c]tank0371@163.com

Keywords: sliding base isolation; applicability; finite element method; time-history analysis.

Abstract. For the purpose of doing modal and dynamic analysis, tall building structures and multistory building structures of vibration isolation foundation and non-isolation models were established respectively. To elaborate the broken stone isolating layer efficacy, top ten order frequencies and modes, sliding displacements of isolation layer, storey drift angles, storey accelerations, top floor relative displacements compared to the ground movement are obtained and contrasted. The result of the present work implies that the broken stone isolation layers are suitable for multistory buildings.

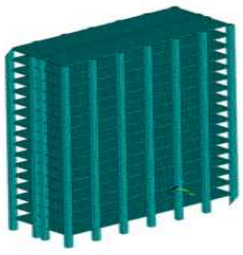
Introduction

Vibration isolation and vibration reduction were the milestone of the aseismic design of structures. Also, they were the hot topic of the engineering of protecting against mitigating earthquake disasters. Technology of base broken stone sliding isolation as a new method of protecting against mitigating earthquake disaster was suitable for our country for its low cost, easy construction technique and select-in-place material.

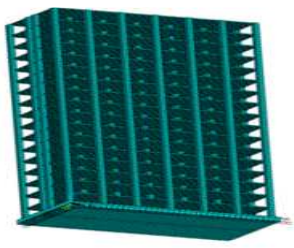
Models of Building

Tall building structures columns used element simulation with the section magnitude of $800\times800mm^2$, the floor slabs and the base isolation layer used element simulation in this research. Column models were mashed in 0.5 meter long, and floor slabs were mashed in $0.5\times0.5m^2$. The coincident nodes generated during the mashing work were coupled in each freedom to simulated together work of the connection of the columns and the floor slabs [1].

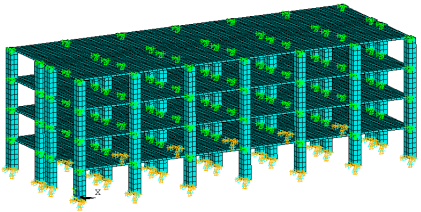
Multistory building structures were programmed in the same way like tall building structures and had same plan layout with the tall building structures [2]. The models were performed in Fig. 1. To consider the damping mechanism of the broken stone isolation layer, the damping ratio ξ was defined 0.015 [3].



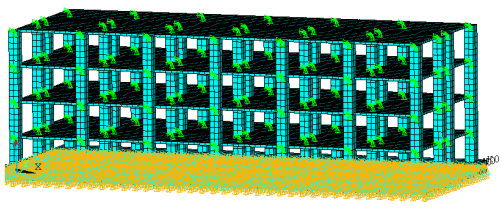
a) tall building structure with fixed base



b) tall building structure with broken stone isolation layer



c) multistory building structure with fixed base



d) multistory building structure with broken isolation layer

Fig. 1 Multi-storey structure models and tall building structure models

Modal Analysis

Modal analysis was the pre-work of transient analysis, basic vibration properties of structures such as fundamental frequencies and fundamental modes were obtained in this process[4]. Modal analysis was a modern method of studying dynamic behaviors of structures. It concludes two means[5]: calculated modal analysis and test modal analysis. Calculated modal analysis was used in this research. Modal solutions of tall building structures with fixed base, multistory structures with fixed base, tall building structures with broken stone isolation layer and multistory structures with broken stone isolation layer were listed in Table 1 and Table 2.

Table 1 Tall building frequencies of the two different modal (Hz)

Frequency order	Fixed base	With isolation layer
Primary frequency	0.4048	0
Second frequency	0.4194	0
Third frequency	0.4262	0
Forth frequency	1.4396	0.0033
Fifth frequency	1.5081	0.3567
Sixth frequency	1.5242	0.5297
Seventh frequency	3.0943	0.8546
Eighth frequency	3.2065	1.3473
Ninth frequency	3.3443	1.3508
Tenth frequency	5.4973	1.5056

Table 2 Multi-storey structure frequencies of the two different modal (Hz)

Frequency order	Fixed base	With isolation layer
Primary frequency	2.1417	0
Second frequency	2.5745	0
Third frequency	2.6737	0
Forth frequency	10.731	0.16406
Fifth frequency	10.732	0.7492
Sixth frequency	10.743	2.6737
Seventh frequency	10.746	2.8514
Eighth frequency	10.844	4.2638
Ninth frequency	10.847	10.732
Tenth frequency	10.862	10.827

The tall building model frequencies of the fixed bases and with isolation layers are shown in Table 1, the top frequencies of the models with fixed bases are greater than that of the models with isolation layers. Thus the periods of the structure models with isolation layers are greater than that of the fixed base models.

The multistory building structure models of the fixed bases and with isolation layers are shown in Table 2, the top frequencies of the models with fixed bases are larger than that of the models with isolation layers. And thus the periods of the structure models with isolation layers are larger than that of the fixed base models.

Transient Analysis

Transient Responses of Tall Building Structures. As shown in Table 3 and Table 4, the selected floors displacements of the tall building structures with base isolation layers and fixed bases are quite different. The displacements of the fixed base tall building structures increases with the floors increased. And the displacements of the tall building structures with isolation layers are in small change ranges.

Table 3 Max displacements of the selected floors exited by the Tianjin x seismic wave (cm)

floor	Foundational slab	Forth floor	Tenth floor	Sixteenth floor
Non-isolation	0.0000	0.9556	3.3282	5.4972
With isolation layer	0.0045	0.0018	0.0020	0.0021

Table 4 Max displacements of the selected floors exited by the EL CENTRO y seismic wave (cm)

floor	Foundational slab	Fourth floor	Tenth floor	Sixteenth floor
Non-isolation	0	0.2513	0.7365	1.0745
With isolation layer	5.4293	5.1623	4.7786	4.5127

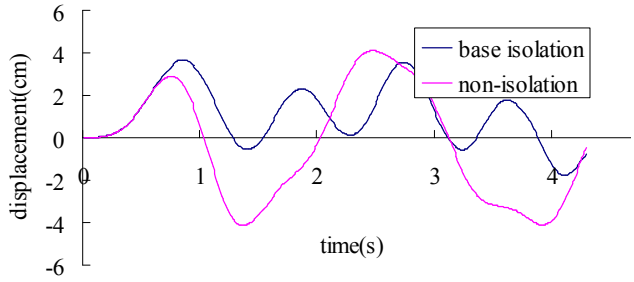


Fig. 2 Relative displacements timehist responses of the 16th floor under Tianjin y wave

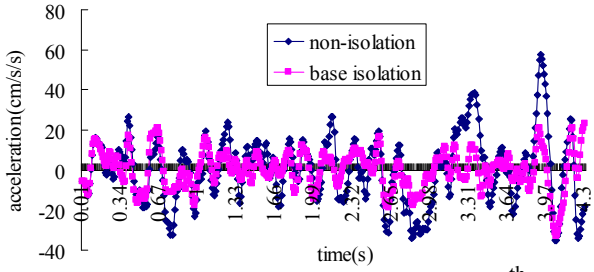


Fig. 3 Acceleration responses of the 16th floor under El Centro y wave

The tall building structures relative displacements timehist responses of the 16th floor under Tianjin y seismic wave are shown in figure 2. The displacements of non-isolation structures' 16th floor are much greater than that of the structures with fixed bases.

The tall building structures acceleration responses of the 16th floor under El Centro y seismic wave are shown in Fig. 3. It can be see from the figure that the acceleration of the tall building structures of the top floor are less than that of the fixed base tall building structures. Thus the forces entered in the structure with base isolation layers during earthquake are much less than the fixed base structures.

Acceleration timehist responses of the 16th floor under artificial y seismic wave are shown in Fig. 4. The forces entered in the tall building structures are a little greater than that of the fixed base structures with the seismic wave excitation time lasted. Tall building structures with base isolation layers are not safe during the excitation of the seismic waves.

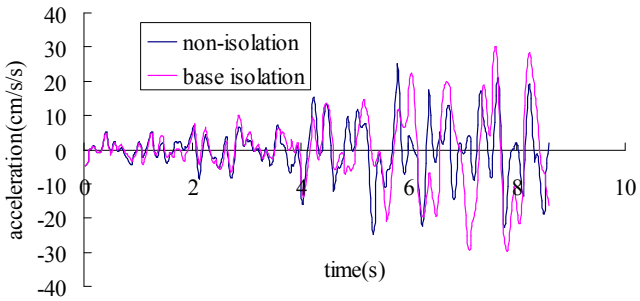


Fig. 4 Acceleration timehist responses of 16th floor under artificial y seismic wave

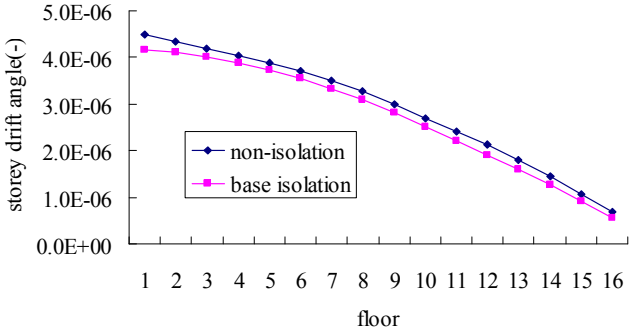


Fig. 5 Max storey drift angles of each floor of the building models excited by EL CENTRO z seismic wave

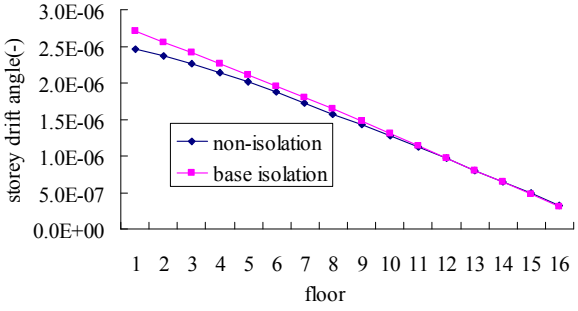


Fig. 6 Max storey drift angles of each floor under artificial z seismic wave

Max storey drift angles of each floor of multi-storey building structures excited by EL CENTRO y seismic wave and under artificial z seismic wave are shown in figure 5 and figure 6 respectively. As shown in the figures, tall building structures with isolation layers and fixed bases have similar displacement behaviors during the excitation of EL CENTRO y seismic wave and artificial z

seismic wave. The isolation layer applications in tall building structures have no distinguish effectives in isolating seismic forces transmission to supstructures. Especially under vertical seismic waves, large overturning moment may be in tall building structures which lead serious security problems in vertical direction.

Transient Responses of Multistory Building Structures. The peak displacements of the floors of the multistory structures excited by the Tianjin x seismic wave are listed in table 5. Structures with isolation layers occur large displacements up to 2.8932cm during seismic wave excitations, and they are changing in small ranges, the smallest value is 2.6832. The supstructures of multistory buildings move like rigid bodies during the earthquake. Structures with fixed bases occur very small displacements, the largest value is 0.0092 occurred at the fourth floor, values increases with the floor increased.

Table 5 Peak displacements of the floors exited by the Tianjin x seismic wave [cm]

floor	foundation	First floor	Second floor	Third floor	Fourth floor
Non-isolation	0.0000	0.0110	0.0358	0.0663	0.0992
With isolation layer	2.8932	2.8480	2.7945	2.7384	2.6823

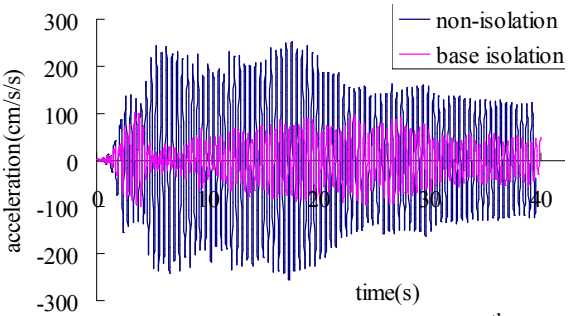


Fig. 7 Acceleration responses of the 4th floor under El Centro x seismic wave

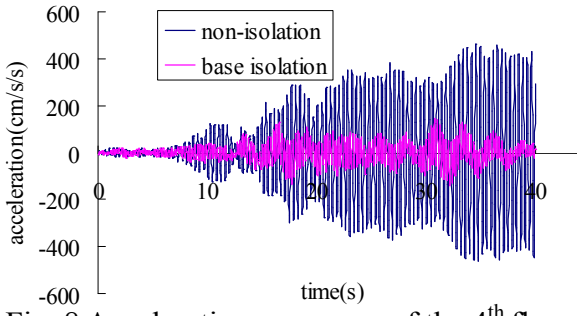


Fig. 8 Acceleration responses of the 4th floor under artificial y seismic wave

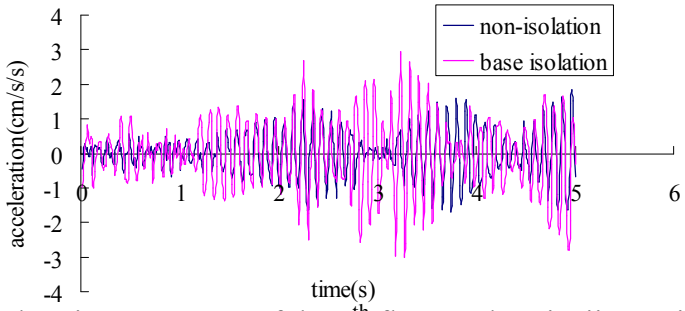


Fig. 9 Acceleration responses of the 4th floor under Tianjin z seismic wave

Acceleration responses of the top floor excited by EL Centro x seismic wave, artificial y seismic wave and Tianjin z seismic wave are shown in Fig. 7 to Fig. 9. As shown in Fig. 7 and Fig. 8, the horizontal forces entered in the supstructures of multistory building are reduced distinctively during the excitation of seismic waves. The reduction ranges between 32%~69%. As shown in Fig. 9, the vertical acceleration of the top floor of base isolation structures excited by vertical seismic wave are greater than that of the fixed base structures. So the forces entered in the base isolation supstructure are greater than that of the fixed base structures. Broken stone isolation layers used in multistory building structures also have no advantage effects in isolating seismic force responses. Considering that the aspect ratio of multistory building structures is not large, the structures' vertical direction is with little serious security problems.

Conclusions

Both the tall building and multistory building structures with broken stone isolation layers have better dynamic behaviors in horizontal direction seismic responses. But whenever the vertical seismic waves excited the structure models, the two different models are much alike in seismic responses. And the tall building structure models excited by vertical seismic waves may have

security problems due to the non-resistance of the broken stone isolation layers. Special attentions must be paid to the application of this technology in tall buildings. When comes to the multistory buildings, the broken stone isolation layers could be used to dissipate seismic energy during the displacements, thus, large displacements should be permitted whenever the earthquake happens, and a layer of broken stone must rather flexible in the horizontal direction but quite stiff in the vertical direction. For the isolation layer of broken stone has no restoring capacity, restoration devices should be used or the buildings be located to normal position artificially after large displacement occurred.

References

[1] J. Fan, J. Tang, Seismic response analysis of base sliding isolation structure, Earthquake Engineering, 3 (2001) 27 -31.

[2] Y. Zhou, Design of Tall Building Structures, Wuhan University of Technology Press, Wuhan, 2008.

[3] R. Clough, J. Peng, Structural Dynamics (U.S.), Higher Education Press, Beijing, 2006.

[4] J. Yu, Y. Wei, The Higher Structural Dynamics. Sichuan University Press, Chengdu, 2001.

[5] B. Zhu, Principle and Application of the Finite Element Method, China Water Power Press, Beijing, 1999.

© (2012) Trans Tech Publications, Switzerland
doi:10.4028/www.scientific.net/AMM.238.881

Introduction to ASCE7 Seismic Design and the Comparison with Chinese Code GB 50011-2010

Can Song [a] and Huijun Zheng [b]

North China University of Water Recourses and Electric Power, Zhengzhou 450011, China

[a] songcan@ncwu.edu.cn, [b]zhenghuijun@ncwu.edu.cn

Keywords: American code; Chinese standard; seismic design; response spectrum.

Abstract. Nowadays the design becomes more and more international. In order to effectively meet this trend, it is necessary to understand the similar or different concept and application of American code and Chinese code on seismic design. This article introduces the concept and design procedure of ASCE7 and compares the seismic analysis results of ASCE7 and GB 50011-2010 through a project example. The similarities and differences of American code and Chinese code on seismic design are summarized.

Introduction

With the rapid development of China, it is common for engineers to do analysis and design using American code. Except in American itself, American code is applied for other countries. For example, in Saudi Arabia, American code is applied directly. In Indonesia, American code is modified a bit and translated to Malay language. Essentially it is still American code. In order to meet the trend and requirement of international design, it is necessary to understand the differences and similarities of American code and Chinese code. This article introduces the analysis procedure and some concept of American code ASCE7, and compares with Chinese code GB 50011-2010 by a project example.

Seismic Analysis Procedure by American Code ASCE7

It is complex to analyze and design seismic effect following American code ASCE7. The procedure is summarized.

1) From ASCE7, according to the location of the project, find out mapped acceleration parameter, S_s and S_1. S_s is the mapped MCE_R spectral response acceleration parameter at short periods (0.2s) and S_1 the mapped MCE_R spectral response acceleration parameter at 1s.

2) According to the site soil properties, find site class A, B, C, D, E, or F.

3) The mapped acceleration is base site class B, so it is necessary to adjust MCE_R according to site class by applying F_a and F_v. Then calculate S_{Ms} and S_{M1} from equation (1) and (2)

$$S_{MS} = F_a S_s \tag{1}$$

$$S_{M1} = F_v S_1 \tag{2}$$

4) S_s and S_1 are 2475 year recurrence interval. So for design spectral acceleration parameters with 475 year recurrence interval, it is necessary to calculate S_{Ds} and S_{D1} based on E_q. (3) and (4)

$$S_{DS} = \frac{2}{3} S_{MS} \tag{3}$$

$$S_{D1} = \frac{2}{3} S_{M1} \tag{4}$$

5) Find long-period transition period, T_L

6) Calculate the spectrum based on Fig. 1.

7) Find Importance factor I_c.

8) Find seismic design category A, B, C or D

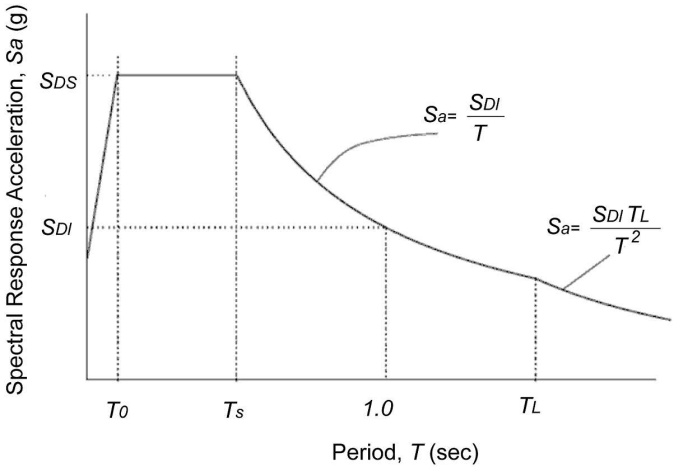


Fig. 1 Design Response Spectrum

9) Decide seismic force resisting system and find out response modification coefficient R, overstrength factor Ω and C_d

10) Study and decide flexible diaphragm, semirigid or rigid diaphragm

11) Find the irregular classification and increase in force if necessary

12) Find redundancy factor ρ

13) Work out load combination. Seismic load effect includes the redundancy factor ρ. When column, beam, trusses or slab support discontinuous walls or frames, structures shall be designed to resist the seismic load effects including overstrength factor Ω.

14) If seismic design category is B, only one direction of earthquake is applied once. If seismic design category is C and structures have horizontal irregularity, nonparallel system irregularity, or for SDC D~F, it needs combination of orthogonal direction by 1.0 of one direction and 0.3 of another direction or simultaneous application of orthogonal ground motion.

15) Define mass source

16) Modify the stiffness to consider the effects of cracked sections.

17) Calculate the fundamental period of structure. To pay attention to the upper limit of period

18) Calculate the base shear by equivalent lateral force procedure

19) Take note the accidental torsion for 5% if equivalent lateral force procedure is used.

20) In model response spectrum analysis, results should be divided by the quantity R/I_c. Displacement and drift shall multiply by the quantity of C_d/I_c.

21) Scale design force from response spectrum analysis based on equivalent lateral force procedure before if it is less than 85% of base shear using the equivalent lateral force procedure.

22) Calculate the drift and compare with allowable drift

23) Check if need to do P-delta analysis

24) Design the section.

Some Concept in ASCE7 and the Difference with Chinese Code

Design Concept. In ASCE7, the specified earthquake loads are based upon post-elastic energy dissipation in the structure in code. The design earthquake loads is based on ground acceleration corresponding to a 475 year recurrence interval and only a fraction of the estimated elastic seismic design force is economically designed. In additional to include complete lateral and vertical force–resisting systems capable of providing adequate strength, stiffness, and energy-dissipation capacity to withstand the design ground motions within the prescribed limits of deformation and strength demand, please keep in mind the ductility requirement for non-collapse during major earthquake corresponding to a 2475 year recurrence interval.

The seismic load in GB50011-2010 is actually corresponding to a 50 year recurrence interval. But GB50011-2010 requires the structure to remain elastic under this seismic load. For a 2475 year return period earthquake, both codes depend on seismic measure to ensure the strength, stiffness and ductility to dissipate the seismic energy.

***S_s* and *S_1* Meaning.** In ASCE7, S_s and S_1 is 0.2 and 1s spectral response accelerations corresponding to a 2475 year recurrence interval. S_s actually is ground acceleration times amplification factor. The amplification factor is the maximum response of the structure to ground acceleration and it is 2.5 in UBC97 ($2.5C_a$). S_1 is ground acceleration (C_v in UBC97). In ASCE7, the amplification factor is embedded in mapped acceleration parameters.

In GB50011-2010, the response spectrum depends on seismic ground motion parameter zonation map. The concept is similar to ASCE7 but the design basic acceleration of ground motion is not directly applied. Another concept, seismic precautionary intensity is used together with the design basic acceleration of ground motion.

1) 2/3 factor for design spectral acceleration parameters

In ASCE7, the acceleration corresponding to 2475 year and 475 is not simply 1.5 for everywhere. 2/3 is conservatively and conveniently applied.

In GB50011-2010, seismic ground motion parameter zonation map denotes ground peak acceleration (GPA) and it is the same as the design basic acceleration of ground motion.

2) Structure System

In ASCE7, for concrete structure system selection, there are only 5 systems: ordinary reinforced concrete moment frames, intermediate reinforced concrete moment frames, special reinforced concrete moment frames, ordinary reinforced concrete shear walls and special reinforced concrete shear walls. For dual system, the moment frames shall be capable of resisting at least 25% of design seismic forces.

In GB50011-2010, there are mainly four systems: framework; shear wall; wall-frame and tube structure.

3) Redundancy factor

In ASCE7, redundancy factor will be used in load combo. Furthermore, for element supporting discontinuous walls and frames, overstrength factor will be used.

In GB50011-2010, there is no redundancy factor. Although there is no explicit overstrength factor, some adjustment is made, for example, for transfer structure.

4) Effective seismic weight

Mass source doesn't include human live load in code. The reason is as follow. The effective seismic weight is the total weight of the building and other gravity loads that might reasonably be expected to be acting on the building at the time of an earthquake. It includes permanent and movable partitions and permanent equipments such as mechanical and electrical equipment, piping, and ceilings. The human live load is taken to be negligibly small in this contribution to the seismic lateral forces. Another reason is furniture and human is not strongly attached to building.

In GB50011-2010, effective weight include 50% of human live load.

5) Modified EI for ultimate limit states

In ASCE7, Stiffness properties of concrete and mansony elements shall consider the effects of cracked sections. According to ACI318, it shall be permitted to use the following properties for the members in the structure:

(a) Modulus of elasticity ..... E_c

(b) Moments of inertia
- Beams.... ... $0.35 I_g$
- Columns..... $0.70 I_g$
- Walls—Uncracked..... $0.70 I_g$
- —Cracked ..... $0.35 I_g$
- Flat plates and flat slabs .... $0.25 I_g$

(c) Area ..... $1.0 A_g$

In GB50011-2010, gross elastic section property is used in analysis.

6) Drift and deformation

In ASCE7, drift and deformation are for ultimate limit state check for seismic analysis. In GB50011-2010, there are two checks. First is a normal check that it is elastic drift and deformation under the seismic load for 50 year recurrence interval. Second check is elastoplastic drift and deformation under the seismic load for around 2000 year recurrence interval.

Project Example by ASCE7 and GB50011-2010

A four stories building consists of 3 bays in each direction and the span is 6m. The beams are 300 in width and 500 in depth. The columns are square section 450x450. Seismic design parameters in GB50011-2010 are as follow:

Design basic acceleration of ground motion: 0.2 g
Seismic precautionary intensity: 8 degree
Site class: II
Design Seismic group: 2
Design characteristic period of ground motion: 0.4s
The model is in Fig. 2.

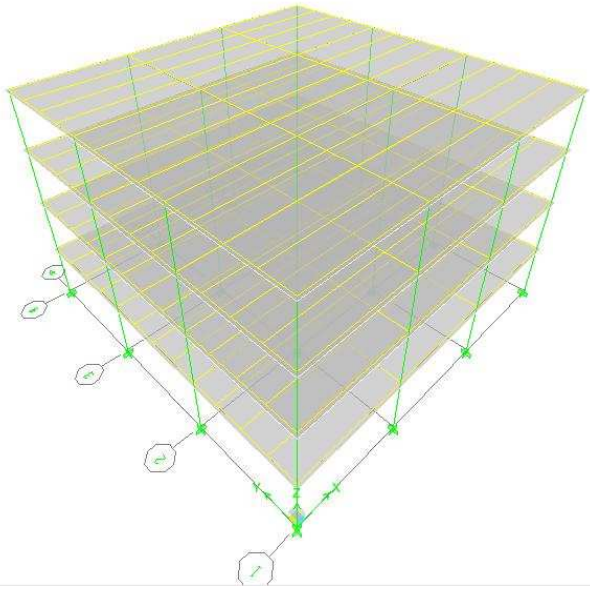


Fig. 2 Analysis model

Analysis Results by GB50011-2010. The fundamental period is 0.66s. The baseshear is 1227 kN. The elastic drift is 1/672. The bending moment diagram for grid line 2 is in Fig. 3.

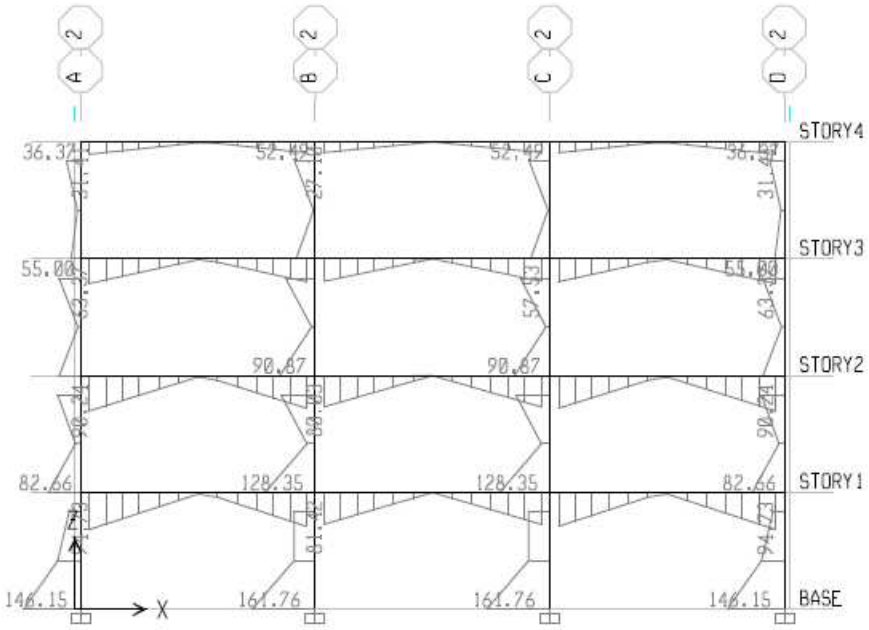


Fig. 3 Bending moment at GL2 by GB50011-2010

Analysis Results by ASCE7. According design basic acceleration of ground motion 0.2g, in ASCE7 S_s=1.13, S_1=0.3. The fundamental period is 0.918s after considering the crack effect. But from equivalent lateral force procedure, T_a=0.43 and the upper limitation is 0.65s. As ordinary

reinforced concrete moment frames, the response modification coefficient R is 3 and C_d is 2.5. The equivalent lateral force calculation is based on 0.65s and the base shear is 1247 kN. The base shear is 1278 kN from response spectrum analysis and it is not less than 85% of the force from equivalent lateral force procedure so there is no need to adjust. The drift is 1/46 and less than allowable drift 1/40. The bending moment diagram for grid line 2 is in Fig. 4.

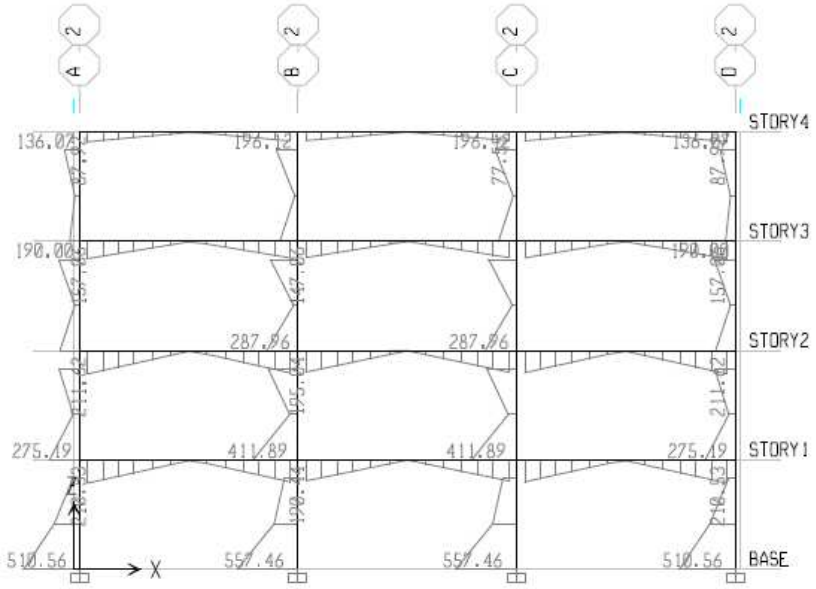


Fig. 4 Bending Moment at GL2 by ASCE7

From above comparison, the analysis results from ASCE7 and GB50011-2010 are very close. But in ASCE7, there are different R and C_d. For example, for special reinforced concrete moment frames, R=8 and C_d=5.5, the results will have significant difference.

Conclusions

This article introduces the seismic analysis procedure of ASCE7 and some concept in ASCE7. The similarities and difference with GB50011-2010 is illustrated. The comparison of seismic analysis by ASCE7 and GB50011-2011 are carried out. In ASCE7, the design earthquake loads are based on ground acceleration corresponding to a 475 years recurrence interval and only a fraction of the estimated elastic seismic design force is economically designed. In GB50011-2010 the earthquake load is actually corresponding to a 50 years recurrence interval and it requires the structure to remain elastic under this seismic load. The analysis results from ASCE7 and GB50011-2010 are very close for some cases.

References

[1] GB50010-2010, Code for design of concrete structures, China Building Industry Press，Beijing, 2010.

[2] GB50011-2010, Code for seismic design of buildings, China Building Industry Press, Beijing, 2010.

[3] American Society of Civil Engineers, Minimum Design Loads for Buildings and Other Structures, ASCE, 2010.

[4] ACI, ACI318-02, PCA, 2002

[5] S. Bungale. Taranath, Reinforced Concrete Design of Tall Buildings, CRC Press, 2010.

[6] L. Wei, Design of Building Structures Frequently Encountered Problems and Countermeasures, China Electric Power Press, Beijing, 2009.

© (2012) Trans Tech Publications, Switzerland
doi:10.4028/www.scientific.net/AMM.238.886

Analysis of Typical Example and Genesis of Landslide Triggered by Wenchuan Earthquake in China

Jinyu Dong[1,a], Zili Li [1,b], Zhiquan Huang[1,c], Jihong Yang [1,d] and Guoxiang Yang[2,e]

[1] North China University of Water Resources and Electric Power, Zhengzhou 450011, China

[2] Chinese Academy of Sciences Key Laboratory of Geomechanics, Institute of Geology and Geophysics, Chinese Academy of Sciences, Beijing 100029，China

[a]dongjy0552@126.com, [b]lizili@ncwu.edu.cn, [c]huangzhiquan@ncwu.edu.cn

[d]yjh04616@126.com, [e]yanggx@mail.igcas.ac.cn

Keywords: geological structure of slope; strong earthquake motion; structural surface; slope; failure process.

Abstract. As the main geohazard triggered by Wenchuan earthquake, landslide is widely distributed. It caused many people lost their lives and incipient fault. This paper analyzes the genesis of these landslides from the aspects of geomorphy, geological structure of slope body, rock characters, earthquake motion, stable condition of slope, weathering effect and stream action. Strong earthquake motion near the fracture zone and geological structure of slope body are the main reasons caused the slope failure. Take Wangjiayan landslide as the typical example, the genesis of earthquake-induced landslide is analyzed. Strong earthquake motion near the fracture zone and the extroversion structural surfaces are the main reasons caused the slide, and great slope and instable state of slope can also promote the slop failure. Failure process of slope is also analyzed.

Introduction

Wenchuan earthquake occurred at Longmenshan tectonic belt that east edge of Tibetan Plateau. Longmenshan tectonic belt is active for extruded fiercely by Tibetan Plateau and Sichuan basin. It is one area with the steepest mountain in the world. Wenchuan earthquake is with great insensitivity, shallow source, and long occurrence time. The main shock area is located at the western mountainous area of our country with gradient changed greatly and river cutting deeply. So many landslides, collapses and debris flow were occurred.

Genesis of Earthquake Induced Landslide in Wenchuan Earthquake Area

Topography and Geomorphy. Landslides triggered by Wenchuan earthquake are distributed linearly along rivers such as the main stream of the upstream of Minjiang river (from Dujiangyan to Yingxiu to Wenchuan to Maoxian) and the side stream of it, the Jianjiang river valley in Beichuan, the Qingzhujiang river valley in Qingchuan, the upstream of Mianyuanhe river and the upper stream of Chapinghe river in Anxian county. Secondary geo-hazards including collapse, landslide and rock fall were induced at both sides of the streams for the steep slope, deep river cutting and broken rockmass. Most of these landslides are with the slope of 40-50 degree. For influence of isolated topography on landslide has something to do with its height, so influence of local topography worth attention. Because isolated topography can induce resonance vibration, and displacement, velocity and acceleration at ground surface would be amplified by the multiple reflection of body earthquake wave in slope. So landslides were mainly occurred at isolated pediment and multiple free surfaces hill body or mountain ridge, and both sides of the landslide are river valley, which is benefit to occurrence of earthquake induced landslide.

Geological Structure of Slope Body. Geological structure is the decisive factor that can influence the stability of slope. Deformation and failure mode of slope during earthquake depend on the geological structure. According to field investigation and relative research results, geological structure of slope can be classified into bedrock-debris or bedrock slope geological structure, layered bedrock geological structure, blocky structure and cataclastic or granular structure etc. [1]. Layered bedrock slope structure can also be classified into bedding slope, counter-inclined slope and oblique layered slope. Upper part of most of the earthquake induced landslides is easy to fail for they are accumulative formation or strong weathering rock. So upper part of this kind of slope is the potential unstable area and would be destabilized under action of rainfall or gravitation.

As to the layered slope, bedding surface plays the controlling role in slope failure under earthquake force, large-scale sliding along the bedding surface would occur during earthquake; and to counter-inclined layered slope and oblique layered slope is mainly controlled by the weathering degree of rockmass and the structural surfaces in slope body. Take Wangjiayan landslide as an example, it is an typical oblique slope and there are three groups of joints developed in the slope two of which mainly cut the rockmass and the other one was the sliding surface of slope.

Rock mass with blocky structure is integrity, slope with this kind of structure is always steep and under action of earthquake force superficial rockmass of it would be loosened and small-scale sliding or rock fall usually occurred.

Slopes with cataclastic or granular structure were usually disintegrated and formed into debris flow under earthquake with long duration time, because rockmass of these slopes is brocked under long term weathering and unloading effect.

Formation Lithology. Strata developed in Wenchuan earthquake area are form the Mesoproterozoic to the Quaternary. According to research result of Huang, lithologic of the earthquake area includes the soil layer, sandstone, pudding stone, slate, phyllite, mud shale, carbonatite and magmatite. Landslides always occurred in soft rock strata with the soil layer, slate, phyllite and mud shale. And collapse always occurred in hard rock strata [2].

Earthquake Motion. Earthquake motion intensity and duration time are the dynamic conditions to the formation of earthquake-induced landslide. The stronger of the earthquake motion and longer of the duration time, the landslide is easier to slide. While earthquake occurred, the strong earthquake motion had progressive fracture effect on the potential slide surface. Vibration of slope body could cause subsidiary stress in slope, and then stress concentration would be appear at crack tip, which accelerated the expansion of cracks and they finally cut through to form the slide surface [3]. Duration time of earthquake is important to the occurrence of landslide for it can enlarge the damage area of potential slide surface. The spectrum characteristic of earthquake wave is another important factor to occurrence of landslide. Rock and soil body especially the loosening or soft soil near ground surface has special natural period for the different composition, thickness and structure. While the frequency of earthquake motion close to the natural vibration frequency of rockmass, resonance vibration would be occur, which can aggregate the earthquake intensity of ground surface and induced landslide easily.

Landslides triggered by Wenchuan earthquake distributed mainly along the fracture zone and within 20km from it. Remote sensing interpretation and field investigation illustrated that, density and scale of landslides occurred at hanging wall are bigger than that of the footwall. It indicated that impact effect of fault movement is relevant to occurrence of landslide. Earthquake motion is stronger at near fault and the intensity is bigger so landslides are prone to occur. Peak acceleration of hanging wall is bigger than that of the footwall, so landslides are easy to occur [2, 4].

Stable State of Slope Body. Stable state before of slope before earthquake can influence the failure of slope during earthquake. While the slope was with high safety reserves it can resist the earthquake force and would not failure during earthquake. But if the slope was in limited equilibrium state or unstable state, landslide would be induced under effect of earthquake force.

Weathering Effect. Landslides triggered by Wenchuan earthquake experienced multi-level sliding including large-scale sliding of superficial soil body and the subsequent sliding of the bedrock. Bedrock of the slope were always easily weathered rock, superficial rockmass was fractured

and broken for long time exposure in sunshine, washing of rainfall and unloading effect under gravity. Superficial rock and soil mass was fractured while the bedrock was relatively integrity. So under action of earthquake the superficial rock mass slid along the weathering interface.

River Action. Landslides induced by Wenchuan earthquake distributed along rivers which means that rivers had important impact on landslides. Most of these landslides located at river bend of the erosion bank and slope stability was lowered by long time erosion of river. River bend also has amplification effect on earthquake wave, so horizontal earthquake force at river bank is 0.5 to 1 times more than that at the river bed, and intensity at the slope is 1 degree more than that at the riparian. For long time down cutting erosion effect, unloading fissures were developed at the slope which made the rockmass broken, so strengthen of the slope was deduced and it was easy to slide under earthquake force.

Genesis Analysis on Typical Landslide

Wangjiayan landslide caused more than 1600 people lost their lives and damaged a large numbers of buildings and houses including the building of Beichuan hospital, family planning commission and elementary school and so on (see Fig.1 and Fig. 2). Length of the sliding body is 400m, width of it is 400m, thickness of the sliding body is 30m and the volume of it is $480\times10^4 m^3$. This landslide is 300m from the central fault zone [5, 6]. Slope body is gravel soil with the content of gravel is more than 50%, materials of the sliding bed are sandy shale, siltstone and thin sandy slate of Qingping group, lower Cambrian system ($\in_{1c}$). Posterior of the sliding surface is steep with the slope of 75°, slope of the middle part is 35° and slope of the anterior is less than 10°. Buried depth of the sliding surface is about 15m and tendency of it is 80°.



Fig. 1 Wanjiayan landslide



Fig. 2 Talus slideThrough analysis on

Through analysis on stereographic projection map (Fig. 3), it was found that occurrence of the third group of joint was the same as that of the sloping surface, and dip angle of it was steep dip with 67°, which is accordance with the measured occurrence of the posterior steep wall. So it was inferred that posterior wall of the slope was formed by the first group of joint. Included angle between the bedding surface and tendency of sloping surface is nearly 90°, which means that the slope is a oblique slope. The slope rockmass was with cataclastic texture under the cutting of two groups of joint and the bedding surface, which could be the condition for sliding.

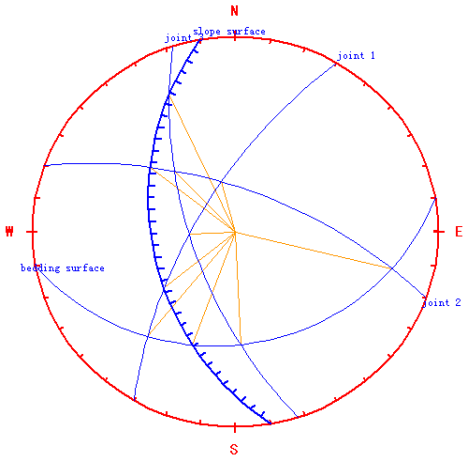


Fig.3 Stereographic projection of wanjiayan landslide

There were several factors that controlled the sliding of wanjiayan slope, the restricted canyon section, steep slope grade and convex slope surface formed the geomorphic conditions for landslide; the extrovert third group of joint formed the main sliding surface; wanjiayan landslide is 300m away from the main central fault zone, under strong

earthquake motion and amplification effect, rock and soil mass of slope was deformed and fractured, and then the sliding surface was cut through which led to high-speed slide of slope body and finally a large scale and high-speed rock landslide was occurred.

Failure process of Wanjiayan landslide can be divided into three stages: (1) The initial stage. Sliding surface was cut through under effect of gravity and unloading; oscillation energy of slope body and elastic strain energy accumulated near the sliding bed was transformed into kinetic energy partially and the initial speed made the sliding body to shear out. (2) High-speed sliding stage. While the slope start to deform, the rockmass can be seen as a rigid body and its potential energy would be transformed into kinetic energy rapidly, then the slope deformed seriously and the sliding body flied to the NEE direction toward the old Beichuan county, as a result a large number of buildings was buried. (3) Stage of impacting and stopping. While the sliding body flied for a certain distance, it would encounter the friction of sub face and be stopped by the buildings, and then stopped to be accumulated.

Conclusions

Genesis of landslide triggered by Wenchuan earthquake was analyzed from the aspects of geomorphy, geological structure of slope, lithologic characters, earthquake motion, slope stability, weathering effect and river etc.. The main factors that influencing the failure of slope are strong earthquake motion near the fault zone and the geological structure

Typical example of Wanjiayan landslide in Beichuan was analyzed, strong earthquake motion near the fault zone and existing of extrovert structural surface are the main reasons that caused the failure of the two slopes. Steep grade of slope promoted the occurrence of landslides. Failure process of typical landslide was preliminarily analyzed in this paper.

Acknowledgment

The work was supported by the Project of High-level Personnel of NCWU (201105) and National Natural Science Foundation of China (41102203).

References

[1] Z. Yang, R. Zhao, J. Wang, Earthquake-induced geological hazards in west of Anxian county and consideration of engineering geomechanical problems, Chinese Journal of Rock Mechanics and Engineering, 9 (2008) 1807~1813.

[2] R. Huang, W. Li, Fault effect analysis of geo-hazard triggered by Wenchuan earthquake, Chinese Journal of Rock Mechanics and Engineering, 12 (2008) 2585~2592.

[3] Y. Mao, G. Hu, X. Mao, Mechanism of set-out violent-slide of slope mass during earthquake and its simulation by using discrete element method, Journal of Engineering Geology, 1 (2001) 74~80.

[4] X. Wang, G. Nie, Characteristics of landslides induced by Wenchuan MS 8.0 Earthquake and preliminary analysis of their relations with ground motion parameters, Chinese Journal of Geotechnical Engineering, 9 (2009) 1378~1383.

[5] Y. Yin, Rapid and long run-out features of landslides triggered by the Wenchuan earthquake, Journal of Engineering Geology, 2 (2009) 153~166.

[6] G. Wang, J. Zhang, H. Liu, Investigation and preliminary analysis of geologic disasters in Beichuan county induced by Wenchuan Earthquake, The Chinese Journal of Geological Hazard and Control, 3 (2009) 47~51.

Keywords Index

3D FEM 292

A

ABAQUS 631
Abutment Slope 313
Activator 173
Adjacent Construction 777
Adjacent Roadway 783
After Fire 621
Aging 536
Air Cushion Surge Chamber 414
Air Pollution 791
Air Porosity 441
Airfield Drainage 455
American Code 881
Amount of Fly Ash 138
Analysis 382, 719
Anchorage Zone of Pylon 728
Anisotropic Damage 37
Annular Anchor 643
ANSYS 248, 765
Anti-Seismic 581
Anti-Seismic Performance 240
Anti-Seismic Reliability 868
Anti-Ship Collision 677
Applicability 876
Application 497
Application Groups 536
Aqueduct 329, 333
Aquifer 371
AR Model 585
Architectural Design 525
Architectural Style 543
ASHPS 478
Asphalt Concrete 22
Asphalt Pavement 201
Automatic Meshing 214
Axial Compression 13
Axial Deformation 652
Axial Force of Anchor 787
Axial Stress 329
Axial Tension 41

B

Bachu-Jiashi Earthquake 852
Ballastless Track 733
Barrier Free Environment 536
Basalt Fiber 17
Basalt Fiber Reinforcement Polymers (BFRP) 13
Bearing Capacity 666
Bearing Disengaging 705
Bending Stiffness EI 617
Bentonites 427
Bi-Level Programming Model 231
Binary Logistic 460
Biological Contact Oxidation 409
Blasting Vibration 783
Blocky Rock Mass 814
Bolt Connection 697
Bond Properties 176
Bond-Slip Relation 142
Borrow 490
BOTDA 346
Bracket Structure 701
Bridge 366
Bridge-Approach Embankment Section 719
Bridge Deck Negative Moment Zone 57
Bridge Deck Pavement 57
Bridge Deck Vibration 714
Bridge Engineering 689, 701, 753
Bridge Jacking 748
Bubble Pump 209
Buddhist Temple 551
Building Binder 173
Building Curtains 83
Buried Pipeline 868

C

Cable 709
Cable-Stayed Bridge 684, 728
CAD 555
Calculation Method 190
Canal Bank 308
Carbonation Resistance 161
Cement 96
Cement-Based Material 153
Central Plains Economic Zone 395
Ceramics 79

Ceramsite Concrete Short Pier Shear Wall 608
CFRP 223
Channel Slope 419
Characteristic 856
Checking Computation 689, 701
Chemical Composition 96
Chinese Standard 881
Chinese Traditional Culture 551
Chloride Permeability 75
Chord Member 576
Chulou Reservoir 317
Circumferential Stress 643
City Waterfront 395
Climate Change 350
Co-Rational 709
Coarse Aggregate 133
Coaxial Connect 61
Cold Recycling Technology 497
Collapsible Loess 435
Compaction Density 455
Compaction Loess 441
Comparison 856
Compensation Design 507
Complete Bond-Slip Curves 176
Complicated Building 555
Complicated Sedimentation Basin 292
Composite Foundation 196
Composite Shear Wall 640
Composite Strengthening Technique 723
Composition 17
Comprehensive Utilization 87
Compressive Strength 51, 87, 129, 133, 147
Computerized Tomography (CT) 422
Concentration of Pore Water Solutions 427
Concept 482
Concrete 46, 51, 71, 75, 129, 147, 157, 161, 165, 169, 350
Concrete Block 9
Concrete Column 240
Concrete Face Rockfill Dam 264
Concrete-Filled Steel Tube 666
Concrete Gravity Dam 252
Concrete Temperature Monitoring 346
Concrete Toughness 109
Concrete Well Pipe 378
Conjugate Gradient Method (CGM) 823, 826
Connective Corridor 738
Consolidator 196
Constant Stress 91
Construction 558, 562, 599, 663, 677
Construction Cost 333
Construction during Hot Season 272
Construction Equipment and Procedure 419
Construction Project 562
Construction Stage 753
Construction Standards 419
Construction Technology 697
Construction Test 419
Content 101
Continuous Beam Bridge 694
Continuous Compound Spiral Hoop 240, 663
Continuum Damage Mechanics (CDM) 37
Contract Condition 558
Contract Management 562
Controlling Criterion 818
COP 478
Corot-Truss 709
Corrosion Resistance 153
Cost 529
CPT 852
Crack 181, 341
Crack Extension 358
Crack Resistance 22
Crack States 201
Creep 733
Crossbar 329
Crossbeam Web Cutout 758
Crossing Speed 382
Curvature Rate of Change 493
Cylindrical Helical Spring 236

D

Dagangshan Hydropower Station 313
Dam 272
Dam Slope Stability 366
Damage Mechanism 46
Damage Variable 46
Damper 714
Data Analysis 808
Deck Arch Bridge 738

Deep-Sea Steel Catenary Riser 358
Deflection 669
Deformation 814
Deformed Steel Bar 176
Degree of Compaction 441
Design 482, 536, 677
Design Pattern 470
Design Theory 625
Detection of Bridge 694
Detection of Compactness 308
Deterioration 350
Develop 603
Development Application 608
Differential Settlement 818
Diffusion Absorption Refrigeration Cycle 209
Dimensional Analysis 256
Discrete Variable 400
Discrimination Model 848
Displacement Field 769
Displacement Time Histories 227
Distributed FBG 617
Distribution 856
Drainage System 482
Dry Density 441
Dry Shrinkage 165
Ductility 631, 635
Durability 26, 71
Dynamic Artificial Boundaries 227
Dynamic Force 292
Dynamic Impedance Functions 503
Dynamic Load Test 694
Dynamic Response 248, 260
Dynamic Shear Modulus 872
Dynamic Support 787

E

Early Plastic Cracking Resistance 109
Earthquake 833
Easy Grinding Property 87
ECC 57
Eccentric Capacity 666
Ecological Landscape Design 395
Ecological Restoration 395
Economic 529
Economic Analysis 581
Educational Scenes 532
Effective Porosity 378
Elastic Analysis 631
Elastic Mechanics 256
Elastic Modulus 75
Elastic-Plastic Analysis 652
Elastic-Plastic Theory 787
Elasto-Plastic 748
Elastoplastic Analysis 635
Elderly Population 382
Electrochemical Pretreatment 405
Embankment 431
Emission Reduction 486
Energy Absorption 3
Energy Conservation 486
Energy Efficiency Optimization Design 473
Energy Efficient Technology 513
Engineering Application 640
ENRG Method 66
Entropy Projection Method 565
Environment 532
Eulerian Method 218
Eutrophication 409
Evacuation 490
Excavation 313
Excavation Technology 773
Expansion Reinforcing Band 341
Expansive Soil 427
Experiment 185, 466, 748
Experimental Study 181
Exquisiteness 539

F

Face Rockfill Dam 260
Failure Process 886
Fatigue 190, 758
Fatigue Life 358
FBG 337
Fiber Reinforced Concrete (FRC) 37
FIDIC 558
Field Test 643
Finite Element (FE) 278, 723, 748
Finite Element Analysis (FEA) 593
Finite Element Method (FEM) 214, 876
Finite Element Technique 252
Fire Performance 621
Fire Prevention 490
Fire Resistant Time 684
First Excursion Dynamic Reliability 611
Flexural Performance 185

Flexural Strength 33, 51, 147, 669
Flexural Toughness 33
Flocculant 405
Flood Hazard 223
Flood Management 288
Flood Routing 304
Flowing Environment 153
Fly Ash Concrete 138
Forming Model 555
Foundation Excavation 777
Fractal 435
Fraction of Steel Fiber by Volume 33, 41
Fracture Energy 109
Frame-Core Tube Structures 648
Frame Joint 838
Free Vibration Analysis 648
Freezing-Thawing Durability 165
Friction Coefficient 643
FRP Bar 61
Full-Scale Model Test 728
Fundamental Frequency 278
Fuzzy-AHP 390

G

Gabled Frame 572
Gate Pier 341
Geological Structure of Slope 886
Geometric Nonlinear 709
Geometric Parameter 576
Geosynthetic Reinforcement Technology 419
GFRP 669
Gradation 133
GRAL-C Module 791
Gravity Dam 256
Green Office Buildings 513
Grid Structures 621
Ground Motion 864
Groundwater 371
Guide Safe Construction 808

H

H Sections 581
Harmonic Excitation 248
HAS 466
HEC 466
Height-Width Ratio 329
Hexahedron 214
High Bridge Pier 765
High Pressure Jet Grouting 317
High-Rise Residence 470
High-Strength 663
High-Strength Concrete 190, 838
Highway Alignment 493
Highway Engineering 201, 493, 507
Highway Landscape 507
Highway Safety 493
Historical Block 547
Homogeneous Clay Dam 366
HSC 669
Hybrid Reinforcements 669
Hydrate Heat 346
Hydraulic Calculation 385
Hydropower Design 414

I

Immersed Tube Tunnel 803
Impact Resistance 109
Impermeable Wall 317
Improved Response Surface Method 611
In Situ Test 852
Industrial Solid Waste 118
Influence Mechanism 138
Influencing Factors 308, 382
Inhabited Region 532
Integration 470
Integrity 539
Interfacial Bond Strength 185
Internal Model Control 66
Interval Metro Tunnel 773
Investigation 382
Irrigation Method 308
ITS 503

J

Jialu River 395
Jointed Finite Element Method 814

K

Kriging Model 611

L

Laboratory Tests 617
Landscape Design 529
Landslide 460

Large Centrifugal Shaker 795
Large Foundation Pit 799
Large Space 490
Lateral Dynamic Response 337
Life Cycle Cost 385
Lifecycle 513
Lime Stabilized Expansive Soils 431
Liquefaction 856, 860
Liquefaction-Induced Lateral Spreads 244
Liquefiable Soil 337
Liquid Storage Tank 248
Load Bearing Transform 593
Load Spreading Property 769
Load Stress 201
Loading Property 738
Local Architecture 532
Long Span Cable-Stayed Bridge 677
Long-Term Immersion 431
Low-Carbon Economy 486
Low-Cost 473
Low-Grade Thermal Energy 209
Lower Yellow River 304
Luffa Sponge 3

M

Machine Foundation Vibration 795
Machine-Made Sand Concrete (MSC) 142, 176
Magnesium Sulfate Attack 129
Manually Excavated Pile 799
MAPGIS 244, 860
Masonry 659
Mass 346
Material 419
Material Interface 218
Mathematical Model 795
MATLAB 390
Maximum Aggregate Size 147
Maximum Diameter 133
Maximum Single-Stage Charge 783
Mechanical Behaviour 26, 75, 333
Mechanical Derivation 666
Mechanical Properties 3, 9, 71, 161, 659
Mechanics Properties 138
Mechanism 803
Mesh Generating 169
Meso-Structure 169
Metro Station 777
Micro-Micromechanics 37
Microplane Constitutive Model 121
Microscope Lext OLS3000 150
Microstructure 435
Middle Line of SNWT 333
MIKE 21 304
Mining 625
Mix Proportion Design 26
Mixed Ground 773
Mixed Pile 196
Mixing Proportion 196
Modal Damping 714
Model 864
Model Analysis 581
Monitoring Test 593
Monte Carlo 611
Monte Carlo Method 868
Moving Force Identification 823, 826
Multi-Element Simulation Method 589
Multi-Objective Decision 288
Multi-Objective Optimization 321
Multiple Cracking 57

N

Nano-TiO_2 9
Nanomaterials 79
Natural Disaster 558
Natural Frequency 236
Natural Vibration Frequency 694
Network Connectivity 868
New Technology of Reinforcement 625
NO-NO_2-O_3 Recycle 791
Nominal Fracture Energy 57
Non-Quantification Factor 753
Non-Sand 378
Non-Square System 66
Normal Concrete 91
Northern Foot of Qinling Mountains 543
NSGA-II 321
Numerical Analysis 783
Numerical Discrete 121
Numerical Model 719
Numerical Simulation 176, 218, 223, 304, 313, 684, 728, 826

O

Objective Function 385

Ocean Engineering 71
Off-Axis Connect 61
Old Asphalt Pavement 497
Onstruction Scheme 333
OpenGL Display lists 555
Operation Parameter 209
Optimal Design 525
Optimal Operation 321
Optimization of Column Spacing 572
Optimum Pipe Diameter 385
Orientation 121
Orthogonal Enumeration Method 400
Orthogonal Test 173
Orthotropic Steel Bridge Deck 758
Outrigger 648
Over-Length Pile Groups 769
Overall Firmness 625
Overturning 705

P

P-δ Effect 589
Particle Gradation 87
Partner Selection 565
Partnering Mode 565
Passive Energy Dissipation 833
Pavement 278
Pavement Structure 818
Peak Acceleration 337
Pebble Concrete 133
Performance Based Seismic Design 844
Permeability Coefficient 451
Pharmaceutical Wastewater 405
Phase Distribution 282
Pile Foundation 337
Pile-Soil Action 743
Pit House 482
Plain Steel Bar 142, 176
Plain Strain 769
Plane Grid 473
Planning 536
Plastic Analysis 631
Plastic Zone 787
Polymer Mortar 185
Pore Water Pressure 451
PPC Hollow Slab Bridge 697
Pre-Stressed Concrete 643
Predominant Period 864
Preprocessing 214
Prestressed Concrete Box Girder 689, 701, 733
Prestressed Concrete Continuous Box Beam Bridges 723
Prestressed Continuous Box-Girder Bridge 743
Probabilistic Limit State 689, 701
Probability Analysis 848
Process 490
Proficiency Test 96
Property 17
Protect Rock Pillar 783
Protection 547
Pseudo Response Spectrum 844
Pull-Out Test 142
Pulsating Water Pressure 282
PZT 105

Q

Quality 529
Quality Detection 317
Quasi-Hydrostatic 298

R

Rainfall Infiltration 451
Rainfall Threshold 460
Random Aggregate 169
Randomness of Structural Parameters 611
Ratio of Cement to Stone 378
Raw Data 268
RCC 268
Reactive Powder Concrete 181
Regional Dividing 244
Reinforced Concrete Beam 185
Reinforcement Form 635
Reinforcements 814
Renewable Energy Technology 513
Renewal 547
Research Progress 61
Research Status 608
Residential Steel Structure 581
Resistance of Support 787
Response Spectrum 743, 844, 881
Rhombus Cradle System 689
Rice Hush Ash 75
Rigid Body Limit Equilibrium Method 252
Risk 513
Risk Management 753
Risk Responsibility 558

River Basin Network 288
Road-Construction Engineering 466
Road Engineering 22
Road Passenger Station 231
Road Property 22
Robust “Z-Score” 96
Roller Compacted Concrete (RCC) 272
Rotating Disc Method 153
Rural Building 223
Rural Drinking Water Safety 390
Rural Residence 473
Rural Road 497
Rural Supermarket 525

S

S-Transform 282
Safe 83
Safety Assessment 777
Saline Soil 118
Salt-Assistant Combustion Method 79
Saturation Line 371
Scale Design 231
Seaport 350
Seasonal Frozen Site 872
Second Plastic Hinge 765
Secondary Stress 576
Sedimentation Basin 298
Seepage Build Capacity 455
Seepage Field 451
Seepage Flow 366
Seismic Behaviour 838
Seismic Design 881
Seismic Performance 765
Seismic Reliability 400
Seismic Research 640
Seismic Resistance 743
Seismic Settlement 860
Seismic Strength 400
Seismic Wave 260
Sensing Technology 617
Settlement Reasons 803
Settling Velocity 298
SFRFAC 51
Shallow Burying Segment 808
Shanxi 551
Shear Capacity 240
Shear Strength 431
Shear Wave Velocity 848, 872
Shield Tunneling Method 773
Short Column 666
Silica Fume 157, 161, 165
Silt 196, 466
Simulation 390
Single Column Bridge 705
Single-Layer Cylinder Latticed Shell 589
Sintering Sludge-Shale Brick 101
Site Characteristic Period 864
Site Monitoring 808
Site Predominant Period 447
Site Selection 551
Slab Movement 260
Slag 71
Sliding Base Isolation 876
Slope 886
Sludge 101
Soft-Storey 833
Soil Consolidators 466
Soil Infiltration Rate 455
Soil Layer Seismic Response 872
Soil Liquefaction 848, 852
Soil Softening 447
Soil Surface Area 455
Sol-Gel Method 105
Solar Collector 478
Solid Waste 173
Solidification 118
Space Heating 478
Spacing Factor 150
Spatial Wall 652
Spectrum 292
Spherical Geometry 121
Spirit of Place 532
SPT 852
Square Steel Tube 581
Stability 22, 252, 705
Stabilizer 118
Stain 13
Stakeholders 513
Stamped 532
Static Analysis 264, 738
Static Force 292
Statistical Damage Constitutive Model 46
Stay Cable 714
Steady Thermal 325
Steel Bracket 748
Steel Fiber 190
Steel Fiber Concrete 838

Steel Fiber Reinforced Concrete (SFRC) 33, 41
Steel-Pipe Truss 576
Steel Plate 640
Steel-Polypropylene Hybrid Fiber Reinforced Concrete 26
Steel Structure Construction 603
Stepwise Regression Analysis 268
Stop Log Gate 282
Strain 91
Strength 91
Strength Model 13
Strengthening 185
Strengthening Effectiveness 723
Strengthening Principle 26
Stress Analysis 758
Stress Calculation 256
Stress-Strain Curve 41
Stretching 539
Strong Earthquake Motion 886
Structural Silicone Sealant 83
Structural Surface 886
Structure 482
Structure Evolution 422
Structure Style 333
Study 22, 378
Studying Style 603
Sulfate Attack 51
Sulfate-Ion Content 129
Support Flexibility 714
Supporting 799
Surface Treatment 150
Suspended Lattice Shell 599
Suspended Loads 572
Suspended Steel Cofferdam 677
Suspension Bridge 709
Sustainability 3
Sustainable 83
Sustainable Development 486
Swelling Pressure 427
Swelling Strain 427

T

T-Shaped Short-Limb Shear Walls 631
T-Shaped Short-Shear Walls 635
Tail Ore 87
Tangshan 244
Tanker Truck Fire 684
Teaching Model 603
Technology Analysis 581
Temperature Control 272
Temperature Differences Inside 341
Temperature Differences Outside 341
Temperature Monitoring 268
Temperature Stress 341
Tensile Cable 599
Tensile Membrane Action 621
Tensile Strength 129
Tension Slacken Analysis Method 599
Test 659
Tetrahedron 214
Theoretical Solution 447
Theory Study 823
Thermal Priority 473
Thermal Stress 325
Thickness of Cement Paste 33, 41
Three-Dimensional Finite Element 264
Three-Dimensional Reconstruction 422
Three-Spring Model 652
Time Domain Method (TDM) 823, 826
Time Frequency Transform 282
Time History Analysis 876
Time Series Analysis 585
Toggle 833
Touchdown Zone 358
Tower Structure 585
Track Deflection Angle 719
Traffic Flow Guidance System 503
Transient Thermal 325
Transparency 539
Transportation for CO_2 358
Transverse Bonded Structural Steel 697
Tree Path Pipe Network 385
Truss 593
Tunnel Engineering 808
Tunnel Portal 791
Tunnels 769

U

U-Shaped Aqueduct 325
Ultimate Bearing Capacity 589
Ultimate Tensile Strength 818
Ultrafiltration (UF) 409
Unbonded Prestressing 181
Underground Caverns 814
Underground Space Form 795
Underground Structure 414

Uniaxial Tension 46
Unload 593
Unsaturated Sediment Discharge Method 298
Unsaturated Soil 435
Update 470

V

V Norm Decouple 66
Value Remodeling 547
Vector 390
Vertical Projection Method 565
Vibration Mode 694
Virtual Simulation 603
Viscous Damper 648
Volcanic Ash 298
Volume of Station 231

W

Warping Effect 236
Water-Borne Polyurethane 109
Water Content 441
Water Depth 329
Water-Dropping Aeration 409
Water Impermeability 157
Water Quality Management 288
Water Resources 321
Water Resources Management 288
Water Supply Network 400
Water Treatment 405
Waterproof System 482
Wave Input 227
Weak Layer 447
Web Member 576
Weight 121
Wenchuan Earthquake 856
Whole Prestressing Reinforcement Technology 625
Widening 818
Wind-Induced Response 585
Wind Load 585
Winkler Foundation 278
Workability 157
Working Medium 209
Working Process 603

X

X-Ray 79
Xi'an Garden 543

Z

Zi/Ti Ratio 105
Zoning Technology 860

Authors Index

A

An, Z.Q. 395

B

Bai, L.H. 697
Bai, W.F. 46, 666
Bai, X.H. 435, 441
Bai, X.L. 214, 329
Bao, J. 419
Bao, J.C. 161
Bi, Q.T. 427

C

Cai, X.G. 617
Cai, Y.C. 366
Cai, Z.L. 455
Cai, Z.X. 451
Cao, C.J. 33, 41
Cao, S.G. 765
Cao, X. 181
Cao, Z.Z. 337, 856
Chan, R.W.K. 833
Chen, C. 697
Chen, G.L. 652, 659, 844
Chen, J.H. 697
Chen, L.W. 852, 860, 864, 872
Chen, R.L. 765
Chen, S.W. 298
Chen, X. 79, 105
Chen, Y. 478
Chen, Y.J. 87, 185
Chen, Y.Z. 22, 719
Chen, Z. 823, 826
Chen, Z.H. 422
Chen, Z.S. 795, 856, 872
Cheng, D. 409
Cheng, S.Z. 260, 264
Cheng, X.T. 96
Cui, B.X. 562
Cui, H.B. 256
Cui, L. 51
Cui, Y. 46
Cui, Z.P. 165

D

Deng, N. 181
Deng, Z.C. 13
Deng, Z.Y. 9, 799
Di, W.M. 385
Ding, B. 109
Ding, X.X. 129, 142, 176
Ding, Y. 532
Dobiáš, D. 153
Dong, B. 705
Dong, J.Y. 886
Dong, L.L. 292
Dong, Y. 431
Du, P.R. 218
Du, W.F. 572, 589, 599

F

Fan, Q.D. 507
Fang, W. 733
Feng, G.W. 333
Feng, H. 631, 635
Feng, Q. 539
Feng, Z.J. 677
Fu, D.F. 791
Fu, H. 753
Fu, Q. 181

G

Gan, W.K. 753
Gao, C.Z. 547
Gao, D.Y. 190, 838
Gao, H. 288
Gao, L.Q. 758
Gao, R.H. 765
Gao, S.L. 57
Gao, Y. 333, 419
Ge, X.D. 51
Guan, J.F. 46, 169, 236, 240, 663
Guo, D. 631, 635
Guo, S.L. 304
Guo, X.Y. 298
Guo, Z.D. 497
Guo, Z.L. 558

H

Han, B. 733, 758
Han, H. 313
Han, J.L. 823, 826
Han, L.W. 227
Han, P.F. 593, 643
Hao, L.J. 525
Hao, Y. 236
He, M.R. 777
He, S.H. 400, 723
He, W.Y. 346
He, W.Z. 431
He, X.D. 227
He, X.S. 390
He, Z.M. 451
Hu, B. 608
Hu, H.B. 765
Hu, S.N. 493, 507
Hu, Y.S. 414
Hu, Z.C. 677
Hu, Z.H. 507
Huang, B.B. 101
Huang, B.R. 447
Huang, H. 282
Huang, K. 308, 414
Huang, L. 585
Huang, S.M. 185
Huang, X.D. 3
Huang, Z.Q. 886
Huo, H.Y. 41

J

Ji, F.Q. 196, 466
Jia, B.Y. 611, 728
Jia, J.C. 427
Jia, M.X. 121
Jia, Y. 96
Jiang, Y.H. 390
Jiao, H.B. 723
Jin, L.H. 129
Jin, L.Z. 181
Jin, Q. 358
Jin, X.H. 513
Jin, Y.N. 133

K

Kang, Y.B. 308
Kolísko, J. 150
Kong, D. 350
Kostelecká, M. 150
Kuang, X.J. 666

L

Lai, J.X. 808
Lan, J.H. 565
Law, D.W. 350
Lei, H.J. 390
Li, C.B. 497
Li, C.C. 244
Li, C.Y. 33, 142
Li, F. 165
Li, F.L. 129, 743
Li, F.Z. 409
Li, G. 87, 844
Li, H. 427
Li, H.G. 482, 532
Li, H.M. 341, 818
Li, H.X. 814
Li, J. 91
Li, J.Y. 214, 329
Li, K.L. 71
Li, L.H. 555
Li, Q.F. 753
Li, Q.S. 625
Li, S. 157
Li, S.P. 227
Li, S.S. 121, 133, 138, 147, 341
Li, W.Z. 677
Li, X. 422
Li, X.J. 868
Li, X.K. 26, 593, 643, 738
Li, Y.R. 244, 337, 848, 852, 860, 872
Li, Y.X. 551
Li, Z.C. 231, 503
Li, Z.L. 886
Li, Z.M. 490, 536
Li, Z.P. 631, 635
Li, Z.X. 22, 719
Li, Z.Y. 852
Liang, L. 278
Liang, Q.H. 777
Liang, Y. 337
Liu, G.W. 621
Liu, H.J. 714

Liu, H.Q. 173
Liu, J. 497, 593, 643
Liu, J.C. 783
Liu, J.X. 395
Liu, J.Y. 631, 635
Liu, L.X. 738
Liu, Q. 470
Liu, R. 787
Liu, S.M. 176, 689, 701, 738, 743
Liu, W.F. 844
Liu, X.C. 292
Liu, Y.F. 777
Liu, Y.H. 669
Liu, Y.J. 223, 684
Liu, Y.Q. 532
Liu, Z.B. 758
Liu, Z.F. 201
Lu, J.M. 709
Lu, L.D. 79
Lu, M.J. 473
Lu, X. 860
Luo, G.J. 414
Luo, S. 714
Lv, B.F. 181
Lv, X.W. 409

M

Ma, B. 214, 329
Ma, F.L. 435, 441
Ma, L.H. 777
Ma, Q.Y. 51
Ma, X.T. 223
Ma, Z.C. 313
Meng, M.L. 366
Meng, S.J. 872
Mi, X. 405
Miao, C.W. 109
Miao, L.J. 876
Miao, S.J. 791
Molyneaux, T.C.K. 350
Mosly, I. 513

N

Ni, W. 118
Nie, X.T. 565
Ning, B. 684

P

Pan, H.W. 390
Peng, Q. 677
Peng, Q.W. 75
Pu, Q.H. 758

Q

Qiao, J.L. 57
Qing, L.B. 169
Qiu, H.J. 803
Quan, L. 66, 83

R

Raphael-Daud, J. 13
Ren, X.H. 209
Rjap, A. 308
Ruan, D. 3

S

Setunge, S. 350, 513
Shang, R.J. 91
Shao, W. 57
Shen, F.M. 868
Shen, J.H. 3
Shi, F.J. 17
Si, B.J. 358
Si, L.J. 652, 659
Song, C. 881
Song, J.Y. 709
Song, L. 490, 536
Song, L.S. 33, 41
Song, X.N. 382
Song, Y. 539
Song, Y.T. 547
Su, Z.M. 787
Sun, D.P. 298
Sun, L. 26, 33, 41
Sun, Q.X. 231
Sun, R. 244, 848, 860, 864
Sun, W. 529
Sun, X.Y. 75
Sun, Y.M. 223
Sun, Z.F. 572

T

Tan, Y.Y. 209

Tang, K.D. 876
Tang, Z. 765
Tang, Z.P. 581, 603
Tao, Z.T. 227
Tong, Y.P. 79, 218

W

Wan, C.F. 585
Wang, B.J. 709
Wang, B.T. 431
Wang, C.E. 551
Wang, F.H. 157
Wang, G.X. 482
Wang, G.Y. 621, 783
Wang, H. 576, 585
Wang, H.L. 75, 652
Wang, H.X. 478
Wang, J. 118, 169, 240, 585, 666
Wang, K. 769
Wang, L. 57
Wang, L.H. 441
Wang, L.J. 346
Wang, M. 435
Wang, M.J. 385
Wang, N. 529
Wang, Q. 46
Wang, Q.L. 161
Wang, Q.Y. 37
Wang, S.J. 422
Wang, T.C. 625
Wang, T.Y. 838
Wang, W.F. 728
Wang, W.M. 244, 447, 848, 852, 856, 864
Wang, X.Q. 621
Wang, Y. 201, 684
Wang, Y.K. 385
Wang, Y.L. 337, 617, 795
Wang, Y.Z. 447, 617, 795
Wang, Z. 91
Wang, Z.H. 593, 643, 648
Wang, Z.Q. 478
Wei, D. 96
Wei, G. 748, 803
Wei, X. 337
Wei, X.J. 803
Wei, Z. 278
Wei, Z.M. 390
Wen, J. 317, 321
Wen, Z.H. 252
Wu, H. 539
Wu, J.C. 814
Wu, J.L. 218
Wu, W. 451
Wu, Z.Y. 218

X

Xi, B.D. 390
Xiao, X.H. 507
Xiao, X.Q. 765
Xiao, Z.T. 543
Xie, W. 121, 133, 138, 147, 341
Xie, Y.L. 808
Xie, Y.M. 3
Xing, H.F. 346, 818
Xing, T. 33, 41
Xiong, J.H. 346
Xu, C.H. 539
Xu, H.B. 13
Xu, S.C. 539
Xu, S.L. 773
Xu, X.D. 272
Xu, X.Y. 282
Xu, Y.C. 581, 603
Xu, Z.D. 585
Xun, D.L. 196, 466, 677

Y

Yan, C.J. 378
Yan, Q.S. 611, 714, 728, 748
Yang, G.X. 886
Yang, J. 435, 441
Yang, J.H. 886
Yang, K. 313
Yang, S.K. 733
Yang, S.Q. 292
Yang, Y. 66
Yang, Y.B. 640
Yang, Z. 196, 466
Yang, Z.L. 689, 701
Yao, L. 227
Yao, Q.L. 185
Yin, C. 382
Yu, F.D. 572, 599
Yu, M.B. 470

Yu, X. 288
Yu, X.H. 697
Yu, X.L. 611, 728
Yuan, D.K. 147
Yuan, G.Q. 61
Yuan, S.F. 264
Yuan, X.M. 447, 617, 795, 856
Yuan, Y. 669
Yue, J.C. 256, 272

Z

Zeng, J. 677
Zeng, L. 451
Zeng, Y. 694
Zhang, A.L. 486
Zhang, B. 366
Zhang, D.X. 37
Zhang, G.M. 350, 513
Zhang, G.Z. 196
Zhang, H. 466, 558, 572
Zhang, H.J. 138
Zhang, H.L. 66, 83
Zhang, H.Y. 227, 486
Zhang, J.H. 325
Zhang, J.J. 470
Zhang, J.W. 46, 260, 264, 282, 666, 838
Zhang, M. 190
Zhang, Q. 663
Zhang, Q.H. 248
Zhang, S.B. 317, 321
Zhang, S.M. 743
Zhang, S.W. 490, 536
Zhang, T.W. 455
Zhang, X. 109
Zhang, X.F. 118
Zhang, X.H. 101
Zhang, X.L. 304
Zhang, X.M. 278, 705
Zhang, X.Q. 288
Zhang, X.Y. 292
Zhang, X.Z. 876
Zhang, Y.M. 814
Zhang, Y.Y. 371, 460
Zhao, C.Y. 185
Zhao, F.R. 455
Zhao, H. 689, 701
Zhao, Q.Y. 848
Zhao, S.B. 26, 79, 142, 176, 231, 697, 738
Zhao, T.H. 419
Zhao, Y. 260, 264
Zhao, Y.Q. 268
Zhao, Z.F. 833
Zheng, H.B. 748
Zheng, H.J. 881
Zheng, R.Y. 608
Zheng, Z.F. 473
Zhou, B.F. 608
Zhou, C. 748
Zhou, D.L. 109
Zhou, F. 808
Zhou, J. 252
Zhou, S.W. 3
Zhou, Y.Y. 26
Zhou, Z.Y. 589, 599
Zhu, H. 585
Zhu, H.T. 256
Zhu, J.Z. 101
Zhu, L.M. 599
Zhu, N. 61
Zhu, P. 589
Zhu, X.D. 551